SCHOLARLY PUBLICATIONS

A CURRENT AWARENESS BULLETIN
OF RESEARCH OUTPUT

@DTU

(76th Edition)

APRIL 2019

BY: CENTRAL LIBRARY

DELHI TECHNOLOGICAL UNIVERSITY
(FORMERLY *DELHI COLLEGE OF ENGINEERING)*
GOVT. OF N.C.T. OF DELHI
SHAHBAD DAULATPUR, MAIN BAWANA ROAD
DELHI 110042

PREFACE

This is the **Seventy Sixth** Issue of Current Awareness Bulletin started by Delhi Technological University, Central Library. The aim of the bulletin is to compile, preserve and disseminate information published by the faculty, students and alumni for mutual benefits. The bulletin also aims to propagate the intellectual contribution of Delhi Technological University (DTU) as a whole to the academia.

The bulletin contains information resources available in the internet in the form of articles, reports, presentations published in international journals, websites, etc. by the faculty and students of DTU. The publications of faculty and student which are not covered in this bulletin may be because of the reason that the full text either was not accessible or could not be searched by the search engine used by the library for this purpose.

The learned faculty and students are requested to provide their uncovered publications to the library either through email or in CD, etc. to make the bulletin more comprehensive.

This issue contains the information published during **April, 2019**. The arrangement of the contents is alphabetical. The full text of the article which is either subscribed by the university or available in the web is provided in this bulletin.

Central Library

CONTENTS

1. A Digital Twin Approach for Fault Diagnosis in Distributed Photovoltaic Systems, ***8.1.Palak Jain***, Jason Poon, Jai Prakash Singh, Costas Spanos, Seth R. Sanders and Sanjib Kumar Panda, Electrical, DTU

2. A Filter-Wrapper based Feature Selection for Optimized Website Quality Prediction, ***3.Akshi Kumar*** and ***6.Anshika Arora***, Computer Science, DTU

3. A framework for usage pattern–based power optimization and battery lifetime prediction in smartphones, ***6.Nirmal Pandey***, ***3.Om Prakash Verma*** and ***6.Amioy Kumar***, Electronics & Communication, DTU

4. A novel micro-solid oxide fuel cell (μ-SOFC) for detecting methane content in biogas, S PHAIJIT, M SUKLUENG2, S MARTHOSA, S NIYOMWAS, N Y VOO and ***3.A KUMAR***, MECHANICAL, DTU

5. A novel parallel classifier scheme for vulnerability detection in Android , ***7.1.Shivi Garg*** and Niyati Baliyan, IT, DTU

6. A short study of an SIR model with inclusion of an alert class, two explicit nonlinear incidence rates and saturated treatment rate, ***6.Abhishek Kumar***, ***3.Nilam*** and Raj Kishor, Applied Mathematics, DTU

7. A Theoretical Modeling of the Cu(In, Ga)Se2 Solar Cell, Gagandeep, ***3.M. Singh***, R. Kumar and F. Chand, Applied Physics, DTU

8. An Electron Paramagnetic Resonance and Photoluminescence Investigation of UVB Radiation Emitting Gadolinium-Activated CaY2Al4SiO12 Garnet Compound, VIJAY SINGH, ***6.SUMANDEEP KAUR***, ***3.A.S. RAO***, N. SINGH, M.S. PATHAK and J.L. RAO, Applied Physics, DTU

9. An Improved Nonlinear Flux Observer based Sensorless FOC IM Drive with Adaptive Predictive Current Control, ***6.Ambrish Devanshu***, ***3.Madhusudan Singh*** and ***3.Narendra Kumar***, Electrical, DTU

10. Biodegradable Polymeric Film for Food Packaging, ***3.Raminder Kaur*** and ***6.Neelam Yadav***, Applied Chemistry, DTU

11. Characterization and parametric optimization of tribological properties of Mo blend composite coating, ***6.Ankit Tyagi***, ***6.Shailesh Mani Pandey***, ***3.R.S. Walia*** and ***3.Prof. Qasim Murtaza***, Mechanical, DTU

12. Compact four-port MIMO antenna on slotted-edge substrate with dual-band rejection characteristics, ***3.Dinesh Kumar Raheja***, Binod Kumar Kanaujia and Sachin Kumar, Electronics and Communication, DTU

13. Continuous User Authentication System: A Risk Analysis Based Approach, Neha and ***6.1.Kakali Chatterjee***, Computer Science, DTU

14. Design of novel hybrid WDM/multiple-beam FSO system to improve the link length in rainy season, Disha Srivastava, ***3.Gurjit Kaur*** and Prabhjot Singh, ECE, DTU

15. Effect of biogas on the performance and emissions of diesel engine fuelled with biodiesel-ethanol blends through response surface methodology approach, Abhishek Sharma, ***3.Naushad Ahmad Ansari***, ***3.Amit Pal***, Yashvir Singh and ***7.S. Lalhriatpuia***, Mechanical, DTU

16. Effect of disorders on Half-Metallic Ferromagnetism in Cr2CoAl inverse Heusler alloy, ***8.Anushka Nagpal***, ***6.Bhuvan Agrawal***, Ramesh Kumar, Hardev S. Saini, Manish K. Kashyap and ***3.Mukhtiyar Singh***, Applied Physics, DTU

17. Epoxy-Glass Microballoon Syntactic Foams: Rheological Optimization of the Processing Window, ***6.A. V. Ullas***, ***3.Devendra Kumar*** and Prasun Kumar Roy, Applied Chemistry and Polymer Technology, DTU

18. Estimation of Source Wavelet From Seismic Traces Using Groebner Bases, Karthikeyan Elumalai, ***7.1.Brejesh Lall*** and R. K. Patney, ECE, DTU

19. Exergy destruction computation in three stages cascade vapour compression refrigeration systems for low temperature applications, ***3.R.S. Mishra***, Mechanical and Production Industrial and Automobiles, DTU

20. Finding significant keywords for document databases by two-phase Maximum Entropy Partitioning, ***3.Seba Susan*** and ***8.Juli Keshari***, Information Technology, DTU.

21. First-Principles Study on Electronic, Mechanical and Thermoelectric Transport Properties of Topological Insulator NaAuS, Nisha1, Hardev S.Saini1, a) Manish K. Kashyap2, Jyoti Thakur3 and ***3.Mukhtiyar Singh,*** Applied Physics, DTU

22. Fog removal in images using improved dark channel prior and contrast limited daptive histogram equalization, ***3.Rajiv Kapoor***, Rashmi Gupta, Le Hoang Son, Raghvendra Kumar and Sudan Jha, ECE, DTU

23. Green Computing in Sensors-Enabled Internet of Things: Neuro Fuzzy Logic-Based Load Balancing, Pankaj Kumar Kashyap, Sushil Kumar, Upasana Dohare, ***3.Vinod Kumar*** and Rupak Kharel, Computer, DTU

24. Identification of opinion leader in online social network using fuzzy trust system , ***6.Lokesh Jain*** and ***3.Rahul Katarya***, Computer Science, DTU

25. Implementation of 3L DPWM Techniques for Parallel Interleaved 2L VSIs, ***7.1.Kapil Shukla*** and Ramkrishan Maheshwari, Electrical, DTU

26. Improving dropClust scRNAseq analysis pipeline for online deployment, Improving dropClust scRNAseq analysis pipeline for online deployment, Debajyoti Sinha, ***8.Pradyumn Sinha***, ***8.Ritwik Saha***, Sanghamitra Bandyopadhyay and Debarka Sengupta, Computer Science, DTU

27. Influence of nanoadditives on ignition characteristics of Kusum (Schleichera oleosa) biodiesel, ***3.Naveen Kumar*** and ***6.Mukul Tomar***, Mechanical, DTU

28. MCML Dynamic Register Design, ***3.Neeta Pandey***, Kirti Gupta and ***6.Bharat Choudhary***, Electronics & Communication, DTU

29. Measurement of Benzo(a)pyrene in PM10 Collected in New Delhi, ***8.J. Pokhariyal***, ***3.A. Mandal*** and S. G. Aggarwal, Environmental, DTU

30. Mitigating the threat in space: Chinese military space capability and India's response, ***8.Rahul Krishna*** and ***8.Aradhya Shandilya***, Electronics and Communication, DTU

31. Numerical Simulation and Parametric Study of Carbon Deposition During Graphene Growth in PECVD System, ***7.Manish Kumar***, ***7.Sagar Khanna***, ***6.Neha Gupta***, ***6.Ravi Gupta*** and ***3.Suresh C. Sharma***, Applied Physics,, DTU

32. ONTOLOGY DRIVEN SOCIAL BIG DATA ANALYTICS FOR FOG ENABLED SENTIC-SOCIAL GOVERNANCE, ***3.AKSHI KUMAR*** AND ***3.ABHILASHA SHARMA***, Computer Science & Engineering,, DTU

33. Operational Transresistance Amplifier Based Wienbridge Oscillator and Its Harmonic Analysis, ***6.Gurumurthy Komanapalli***, ***3.Rajeshwari Pandey*** and ***3.Neeta Pandey***, Electronics and Communication, DTU

34. Optimization of protein extraction from detoxified Jatropha seed cake using response surface methodology and amino acid analysis, ***6.S. Ahluwalia[1]***, ***6.R. Bidlan[1]***, ***3.A.K. Shrivastav[1]***, R. K. Goswami, ***3.P. Singh[3]*** and ***3.J. G. Sharma[1]***, [1]Biotechnology and [3]Mechanical, DTU

35. Phosphazene Superbase-mediated Regio- and Stereoselective Iodoaminocyclization of 2-(1- Alkynyl)benzamides for the Synthesis of Isoindolin-1-ones, ***3.Saurabh Mehta*** and ***6.Dhirendra Brahmchari***, Applied Chemistry, DTU

36. Power Quality Enhancement Using Euclidean Direction Search Based Control Technique, ***6.1.Manoj Badoni***, ***8.1.Alka Singh*** and Bhim Singh, Electrical, DTU

37. Protein functionalised self assembled monolayer based biosensor for colon cancer detection, ***6.Tarun Narayana***, ***6.Saurabh Kumar***, ***6.Suveen Kumar***, ***7.Shine Augustine***, B.K. Yadavd, ***3.Bansi D. Malhotra,*** Biotechnology, DTU

38. QoS and Fuzzy Logic Based Routing Protocol for CRN, Gagan Deep Dhand, Rohit Kumar, Rishabh, Devashish Ghildiyal and ***7.1.Rachna Jain***, Computer Science, DTU

39. Resonator to Laser Cavity Decoupling Interface for Chemical Oxygen Iodine Laser, A.K. Varshney, Rajeev Kr. Dohare, Gaurav Singhal and ***7.1.Mainuddin***, Electronics and Electronics, DTU

40. Securing Data in Internet of Things (IoT) Using Cryptography and Steganography Techniques , Manju Khari, Aditya Kumar Garg, Amir H. Gandomi, ***6.1.Rashmi Gupta***, Rizwan Patan , and Balamurugan Balusamy, ECE, DTU

41. Short-Term PV Power Forecasting Using Adaptive Neuro-Fuzzy Inference System, Harendra Kumar Yadav, Yash Pal and ***3.M.M. Tripathi***, Electrical, DTU

42. Single-Feed Dual-Polarized High Gain Microstrip Antenna, Chandan Roy and ***3.1.Taimoor Khan***, DTU

43. SVM Tuned NARX Method for Wind speed & power Prediction in Electricity Generation, Vijay kumar, Yash Pal and ***3.M.M. Tripathi***, Electrical, DTU

44. Text area segmentation from document images by novel adaptive thresholding and template matching using texture cues, ***3.Seba Susan*** and ***7.1.K. M. Rachna Devi***, IT, DTU

45. THE IMPACT OF TECHNOLOGY ADOPTION ON AGRICULTURAL PRODUCTIVITY IN ETHIOPIA: ARDL APPROACH, ***6.AYNALEM SHITA***, ***3.NAND KUMAR*** AND ***3.SEEMA SINGH***, ECONOMICS, DTU

46. The Role of Wearable Technologies in Supply Chain Collaboration: A Case of Pharmaceutical Industry, MUHAMMAD NOMAN SHAFIQUE, MUHAMMAD MAHBOOB KHURSHID, HAJI RAHMAN, ASHISH KHANNA, ***7.1.DEEPAK GUPTA*** AND JOEL J. P. C. RODRIGUES, Computer, DTU

47. Thermodynamic performance evaluation of single effect Li/Br H2O vapour absorption refrigeration system cascaded with vapour compression system using ecofriendly HFC-134a and HFO-1234yf refrigerants, ***3.R.S. Mishra***, Mechanical and Production Industrial and Automobiles, DTU

48. Threshold Effect of Bank-specific Determinants of Non-performing Assets: An Application in Indian Banking, Samaresh Bardhan, ***3.Rajesh Sharma*** and Vivekananda Mukherjee, Management, DTU

49. Two-dimensional transition metal dichalcogenides assisted biofunctionalized optical fiber SPR biosensor for efficient and rapid detection of bovine serum albumin, Siddharth Kaushik, Umesh K. Tiwari, Akash Deep and ***3.Ravindra K. Sinha,*** Applied Physics, DTU

50. Two-Stage Spectrum Sensing Using Fuzzy Logic for Cognitive Radio Networks, Bhawna Ahuja and ***3.Gurjit Kaur***, Electronics and communication, DTU

51. Ultra Wide Band CPW-Fed Circularly Polarized Microstrip Antenna for Wearable Applications, ***7.1.Saumya Das***, Hashinur Islam, Tanushree Bose and Nisha Gupta, Electronics and Communication, DTU

52. Understanding the Nuances of Employees' Safety to Improve Job Satisfaction of Employees in Manufacturing Sector, ***3.Meha Joshi***, DSM, DTU

53. Voltage Differencing Buffered Amplifier based Voltage Mode Four Quadrant Analog Multiplier and its Applications, ***6.P. Gupta*** and ***3.R. Pandey***, ECE, DTU

1. *Chancellor*

2. *Pro Vice Chancellor*	***2.1.*** *Ex Pro Vice Chancellor*
3. *Faculty*	***3.1.*** *Ex Faculty*
4. *Teaching-cum-Research Fellow*	***4.1.****Asst. Librarian*
5. *Alumni*	
6. *Research Scholar*	***6.1.*** *Ex Research Scholar*
7. *PG Scholar*	***7.1.*** *Ex PG Scholar*
8. *Undergraduate Student*	***8.1.*** *Ex Undergraduate Student*

This article has been accepted for publication in a future issue of this journal, but has not been fully edited. Content may change prior to final publication. Citation information: DOI 10.1109/TPEL.2019.2911594, IEEE Transactions on Power Electronics

A Digital Twin Approach for Fault Diagnosis in Distributed Photovoltaic Systems

Palak Jain, *Student Member, IEEE,* Jason Poon, *Student Member, IEEE,* Jai Prakash Singh, Costas Spanos, *Fellow, IEEE,* Seth R. Sanders, *Fellow, IEEE,* Sanjib Kumar Panda, *Senior Member, IEEE*

***Abstract*—Rooftop and building-integrated distributed photovoltaic (PV) systems are emerging as key technologies for smart building applications. This paper presents the design methodology, mathematical analysis, simulation study, and experimental validation of a digital twin approach for fault diagnosis. We develop a digital twin that estimates the measurable characteristic outputs of a PV energy conversion unit (PVECU) in real-time. The PVECU constitutes a PV source and a source-level power converter. The fault diagnosis is performed by generating and evaluating an error residual vector, which is the difference between the estimated and measured outputs. A PV panel-level power converter prototype is built to demonstrate how the sensing, processing, and actuation capabilities of the converter can enable effective fault diagnosis in real-time. The experimental results show detection and identification of ten different faults in the PVECU. The time to fault detection in the power converter and the electrical sensors is less than 290 μs and the identification time is less than 4 ms. The time to fault detection and identification in the PV panel are less than 80 ms and 1.2 s, respectively. The proposed approach demonstrates higher fault sensitivity than that of existing approaches. It can diagnose a 20% drift in the electrical sensor gains and a 20% shading of a solar cell in the PV panel.**

***Index Terms*—Fault diagnosis, fault location, estimation, solar power generation, converters**

I. Introduction

Photovoltaic (PV) energy conversion architectures based on panel or subpanel-level distributed power electronic converters are increasingly ubiquitous for rooftop and building-integrated PV (BIPV) systems [2]–[5]. The unique advantages of a distributed power electronic-based PV system include higher energy yield (particularly, in partial shading conditions), higher performance reliability, lower installation costs, plug-and-play operation, and enhanced system flexibility, modularity, and scalability [3], [6]–[8]. The building block of a distributed PV system can be referred to as a *PV energy conversion unit* (PVECU). The PVECU constitutes a PV source (e.g. a PV panel or a PV subpanel) and a source-level power converter.

The distributed PV systems are vulnerable to a variety of faults due to their complex outdoor installations, increased number of power electronic converters at the PV panel-level, harsh mission profiles, manufacturing defects, and aging. A comprehensive analysis of common failure modes that could occur in these PV systems and their impacts on performance and reliability are given in [9]–[11]. These failures degrade system performance, and endanger the safety and security of the buildings and its occupants. Moreover, these failures are difficult to locate and repair in building applications because rooftop and BIPV systems have a very large number of PVECUs which can be physically inaccessible due to complex installations (exacerbating maintenance and inspection that incur high cost). Thus, robust and cost-effective methods for ensuring their dependability and fault tolerance are necessary.

Strategies for fault diagnosis have been explored to improve dependability and fault tolerance of complex systems. Fault diagnosis is a monitoring scheme that is comprised of two functions: 1) fault detection (FD), which is a binary decision on the occurrence of a fault; and 2) fault identification (FI), which is the process of classifying the precise fault type [12]. The successful fault diagnosis in a distributed PV system enables online fault remediation, increasing its availability and decreasing its maintenance costs.

Prior works in the literature address fault diagnosis of various subcomponents of PV systems. For example, the authors in [13]–[15] investigate various fault diagnosis approaches for power electronic converters in PV systems. Similarly, the authors in [16]–[18] report various methodologies for PV panel fault diagnosis. However, there is a lack of research work towards a holistic fault diagnosis approach for a complete PVECU. Table I presents common failure modes of each subcomponent in the PVECU. The holistic fault diagnosis approach should, at a minimum, be able to detect and identify these failure modes.

Commercial PV monitoring solutions are available that provide web-based monitoring and use data analytics to detect a fault event [24], [25]. However, these solutions typically lack: 1) the ability to perform FI; 2) require high bandwidth communication for data acquisition and control; 3) require additional central processing units (CPUs); and 4) add latency in the diagnostics of system performance and faults.

This work applies the concept of a *digital twin* to develop a holistic fault diagnosis approach. A digital twin is a digital emulation of a physical system that estimates the

This work is supported in part by Republic of Singapore's National Research Foundation through a grant to the Berkeley Education Alliance for Research in Singapore (BEARS) for the Singapore-Berkeley Building Efficiency and Sustainability in the Tropics (SinBerBEST) Program and in part by the NSF through the Graduate Research Fellowship program. This paper was presented in part at the 2016 IEEE 17th Control and Modelling for Power Electronics (COMPEL) on June 30, 2016 [1]. *(Corresponding author: Dr. Sanjib Kumar Panda)*

P. Jain and S. Panda are with the Department of Electrical and Computer Engineering at the National University of Singapore (NUS), Singapore 117583 (email: palakjain@u.nus.edu; sanjib.kumar.panda@nus.edu.sg).

J. P. Singh is with the Solar Energy Research Institute of Singapore, NUS, Singapore 117574 (email: jaiprakash.singh@nus.edu.sg).

J. Poon, C. Spanos, and S. Sanders are with the Department of Electrical Engineering and Computer Sciences at the University of California, Berkeley, CA 94720 USA (email: {jason, spanos, seth.sanders}@berkeley.edu).

0885-8993 (c) 2018 IEEE. Personal use is permitted, but republication/redistribution requires IEEE permission. See http://www.ieee.org/publications_standards/publications/rights/index.html for more information.

This article has been accepted for publication in a future issue of this journal, but has not been fully edited. Content may change prior to final publication. Citation information: DOI 10.1109/TPEL.2019.2911594, IEEE Transactions on Power Electronics

TABLE I
COMMON FAILURE MODES OF A PVECU.

COMPONENTS	COMMON FAILURE MODES
PV panel [11], [19], [20]	Soiling Continuous/repetitive partial shading conditions Cells breakage EVA browning Bypass diode failures Potential induced degradation (PID) Interconnect faults Internal faults related to PV shunt and series resistances
Power converter [21]–[23]	Switch open circuit Switch short circuit Capacitor or inductor degradation
Electrical sensors [15]	Open circuit Wear-out (tuning parameter drift)

characteristic outputs precisely in real-time [26]. To the best of our knowledge, the digital twin concept is relatively new for power electronic systems and has not yet been applied for fault diagnosis in a distributed PV system.

We present the design, development, and experimental validation of a digital twin approach for fault diagnosis in a distributed power electronic-based PV system. The proposed approach performs fault diagnosis of each individual PVECU and enhances the dependability of the overall PV system. A model-based digital twin is developed for each PVECU. An error residual vector is generated by comparing the outputs of the digital twin with the outputs of the physical twin. Analytic evaluation of the error residual vector enables to FD and FI.

The proposed approach operates by leveraging the sensing, processing, and actuation capabilities of the distributed power electronic converters (i.e. the panel-level power converters in these systems). Thus, such an approach obviates the need for extra hardware resources and relaxes the communication requirements which enable better performance than the state-of-the-art approaches.

The proposed fault diagnosis approach is validated in realistic outdoor field conditions. A 300 W panel-level power converter prototype is designed, developed, and tested to perform outdoor field experiments. Next, a PVECU is deployed on a building rooftop to demonstrate the proposed approach. The experimental results show the effectiveness of the proposed approach in detecting and identifying ten different faults in the PVECU which no other existing approach achieves. These ten faults are grouped into three categories: 1) PV panel faults, 2) panel-level power converter faults, and 3) electrical sensor faults. A central feature of the proposed approach is its ability to detect faults in the input energy source (i.e. the PV panel in this work) and distinguish them from the power converter and sensor faults. Moreover, the time to FD and FI is comparable to those of existing approaches. This work also demonstrates higher sensitivity to incipient PVECU faults (e.g. faults in an electrical sensor) than that of existing approaches.

The remainder of the paper is organized as follows. Section II presents an overview of a distributed power electronic-based PV system. Section III develops the modeling framework for the digital twin estimator. Section IV presents the digital twin approach for fault diagnosis, which includes both FD and FI methodologies. Section V presents the implementation details and hardware setup for the field experiments. The experimental results and related analysis that validate the digital twin approach for fault diagnosis are presented in Section VI. Section VII concludes the paper.

II. AN OVERVIEW OF THE DISTRIBUTED POWER ELECTRONIC-BASED PV SYSTEM

In this section, an overview of the distributed power electronic-based PV system is presented to illustrate the concepts put forward. Fig. 1 shows a candidate dc-based power conversion architecture using the PVECU concept. The panel-level power converter of each PVECU performs maximum power point tracking (MPPT). The PVECUs are connected in series to form a PV string which is connected to a 380 Vdc distribution bus. It is assumed that the bus voltage is maintained constant by another entity (e.g. a battery bank) in the distribution network and each PV string operates as a current source. Moreover, in this study, it is assumed that there are always sufficient loads in the system to sink the available PV power.

Fig. 2 shows the schematic of a PVECU power stage including a four-switch buck-boost converter circuit topology. The buck-boost converter is chosen because it can operate in three modes: buck, boost, and bridge, which provides design flexibility for the distributed PV system architecture and size [3]. Moreover, the authors in [8] evaluate various types of dc-dc converter topologies for the series-connected PVECUs and conclude that the four-switch buck-boost converter provides the greatest flexibility in placing any number of PV panels in a string and has an optimal efficiency-density Pareto front. The authors in [3], [8], [27] present additional advantages of the four-switch buck-boost converter in distributed PV systems including higher efficiency and reliability than those of the two-switch buck-boost converter.

Fig. 1 shows the PVECU control & monitoring stage which hosts the fault diagnosis and control on a single computing platform. It also presents the operational elements which perform fault diagnosis of each PVECU locally. The three main elements of the fault diagnosis approach are: 1) a digital twin which estimates the measurable characteristic outputs $\mathbf{z}(t)$ of the PVECU in real-time; 2) an error residual vector $\boldsymbol{\gamma}(t)$ which is the difference between the estimated outputs $\mathbf{z}(t)$ and the measured outputs $\mathbf{y}(t)$, and a FD methodology which triggers FD flag; and 3) analytic evaluation of the error residual vector $\boldsymbol{\gamma}(t)$ to precisely identify the faulted subcomponent and its failure mechanism (indicated by FI flag). Note that the fault signature library includes a priori knowledge about the possible fault events and is an ensemble of analytically computed n fault signatures $\mathbf{f}_i \; \forall \; i \in \{1, 2, ..., n\}$. These three elements are described in detail in the subsequent sections.

III. DIGITAL TWIN ESTIMATOR

A digital twin estimator is the first element of the fault diagnosis approach as shown in Fig. 1. It is a digital emulation of a physical system that analytically computes the measurable characteristic outputs in real-time [26]. It could

0885-8993 (c) 2018 IEEE. Personal use is permitted, but republication/redistribution requires IEEE permission. See http://www.ieee.org/publications_standards/publications/rights/index.html for more information.

This article has been accepted for publication in a future issue of this journal, but has not been fully edited. Content may change prior to final publication. Citation information: DOI 10.1109/TPEL.2019.2911594, IEEE Transactions on Power Electronics

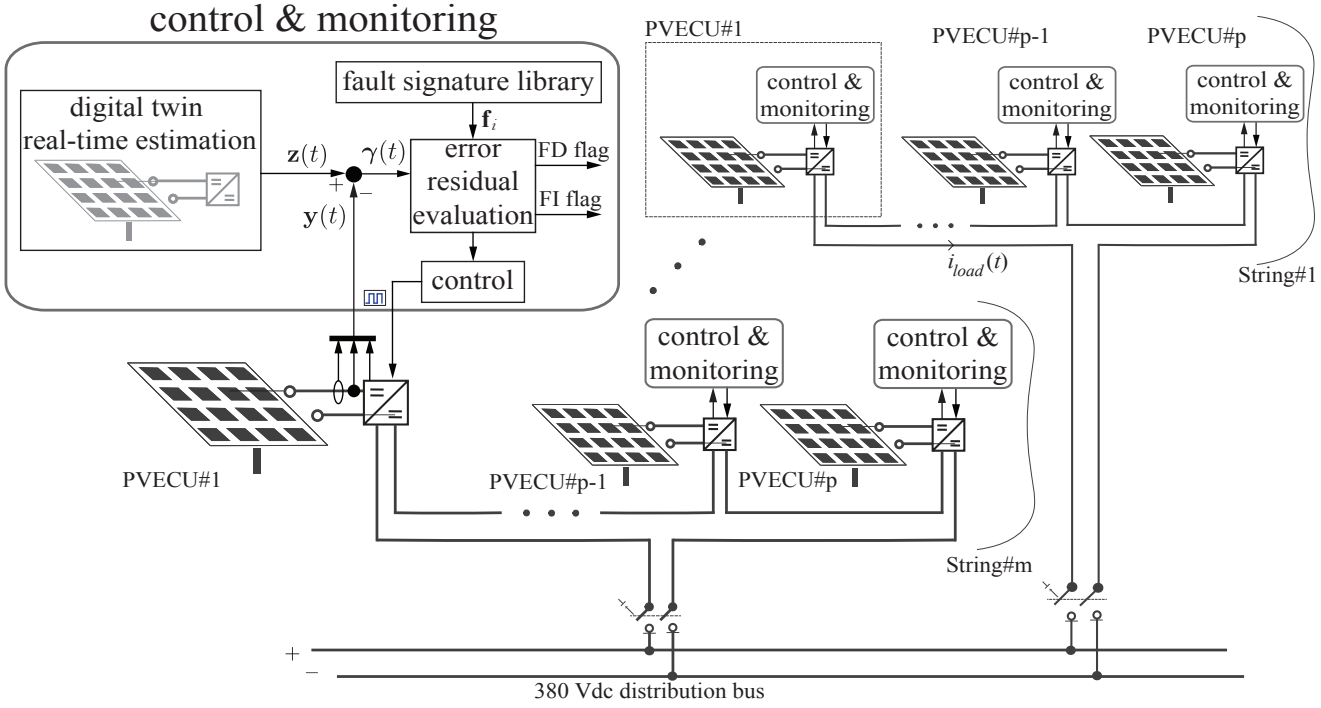

Fig. 1: A candidate distributed power electronic-based PV system for building applications. An overview of a digital twin approach for fault diagnosis of the complete PV system is also shown. p is the number of PVECUs in a string. m is the number of strings.

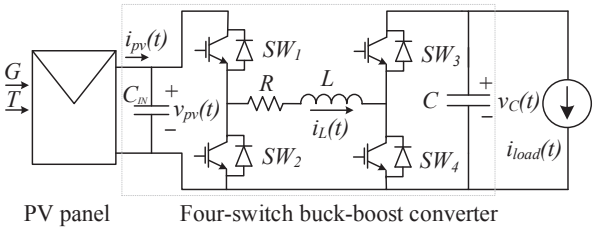

Fig. 2: Schematic of a PVECU power stage.

be model-based or data-driven or a combination of both. The following set of equations present the model-based digital twin estimator of a PVECU which has an arbitrary power electronic converter:

$$\mathbf{z}[k,G,T] = \mathbf{C}\begin{bmatrix}\mathbf{x}[k]\\ I_{pv}[G,T]\\ V_{pv}[G,T]\end{bmatrix} = \begin{bmatrix}\mathbf{x}[k]\ni\mathbf{x}[k+1]=\hat{\mathbf{A}}_j\mathbf{x}[k]+\hat{\mathbf{B}}_j\mathbf{u}[k]\\ \dfrac{I_{pv}^{ref}G\big(1+K_i(T-T^{ref})\big)}{G^{ref}}\\ \dfrac{V_{pv}^{ref}\big(1+K_p(T-T^{ref})\big)}{1+K_i(T-T^{ref})}\end{bmatrix},$$
$$\mathbf{C}=\mathbf{I}_{s_n\times s_n},\ k\in\mathbb{Z} \quad (1)$$

where $\mathbf{z}[k,G,T]\equiv\mathbf{z}(kT_s,G,T)$ is the estimated characteristic output vector in discrete-time with a sampling period of T_s; $\mathbf{x}[k]$ is the estimated power converter states; $I_{pv}[G,T]$ is the estimated PV panel operating current at maximum power point (MPP) and is a function of solar irradiance G and panel temperature T; $V_{pv}[G,T]$ is the estimated panel operating voltage at MPP and is a function of G and T; and $\mathbf{C}$ is an identity matrix representing s_n sensor gains (s_n represents identity matrix dimension).

Next, each equation in the digital twin estimator is discussed in detail. The first element of $\mathbf{z}[k,G,T]$ represents the forward Euler-based discretization of the linear-switched state space equation (i.e. $\dot{\mathbf{x}}(t)=\mathbf{A}_{\sigma(t)}\mathbf{x}(t)+\mathbf{B}_{\sigma(t)}\mathbf{u}(t)$ [15]) with a sampling period of T_s for an arbitrary power converter with piece-wise linear elements [28]. Thus, when $t=kT_s$ where $k\in\mathbb{Z}$, $\mathbf{x}(kT_s)\equiv\mathbf{x}[k]$ is the state vector; $\mathbf{u}(kT_s)\equiv\mathbf{u}[k]$ is the input vector; and the continuous-time switching function $\sigma(t)$ maps the time into an index set $\{1,2,...,nm\}$. Each of the indices indicates a particular model of the system given by the doublets $(\mathcal{A}_j,\mathcal{B}_j)$ where $j\in\{1,2,...,nm\}$. That is, $\mathbf{A}_{\sigma(t)}\in\mathcal{A}\triangleq\{\mathcal{A}_1,\mathcal{A}_2,...,\mathcal{A}_{nm}\}$ and $\mathbf{B}_{\sigma(t)}\in\mathcal{B}\triangleq\{\mathcal{B}_1,\mathcal{B}_2,...,\mathcal{B}_{nm}\}$. Thus, in $\mathbf{x}[k+1]=\hat{\mathbf{A}}_j\mathbf{x}[k]+\hat{\mathbf{B}}_j\mathbf{u}[k]$, $\hat{\mathbf{A}}_j=\mathbf{I}+T_s\mathbf{A}_{\sigma(t)}$ and $\hat{\mathbf{B}}_j=T_s\mathbf{B}_{\sigma(t)}$.

The second element of $\mathbf{z}[k,G,T]$ represents the operating current of the PV panel which corresponds to its MPP for a given G and T. Equation (2) models the panel operating current [29]:

$$I_{pv}[G,T]=\frac{I_{pv}^{ref}G\big(1+K_i(T-T^{ref})\big)}{G^{ref}} \quad (2)$$

where $I_{pv}[G,T]$ is the operational panel current at MPP when the incident solar irradiance is G and the panel temperature is T; I_{pv}^{ref} is the operating current at MPP at the reference solar irradiance G^{ref} and temperature T^{ref}; and K_i is the current temperature coefficient.

The last element of $\mathbf{z}[k,G,T]$ models the operating

0885-8993 (c) 2018 IEEE. Personal use is permitted, but republication/redistribution requires IEEE permission. See http://www.ieee.org/publications_standards/publications/rights/index.html for more information.

This article has been accepted for publication in a future issue of this journal, but has not been fully edited. Content may change prior to final publication. Citation information: DOI 10.1109/TPEL.2019.2911594, IEEE Transactions on Power Electronics

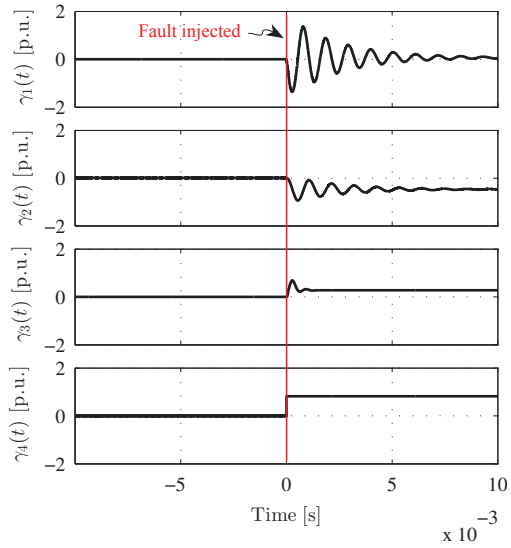

(a) Error residual $\boldsymbol{\gamma}(t)$ before and after a fault event in a PVECU.

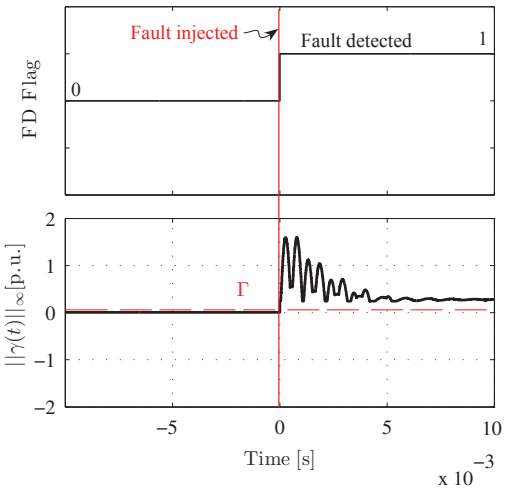

(b) FD logic. FD Flag indicating fault event (top). Comparison of the infinity norm of $\boldsymbol{\gamma}(t)$ and the threshold value Γ (bottom).

Fig. 3: Simulation results for the FD methodology.

voltage of the PV panel which corresponds to its MPP through (3) [30]:

$$V_{pv}[G,T] = \frac{P_{pv}[G,T]}{I_{pv}[G,T]} = \frac{P_{pv}^{ref}\dfrac{G}{G^{ref}}\big(1+K_p(T-T^{ref})\big)}{I_{pv}[G,T]} = \frac{V_{pv}^{ref}\big(1+K_p(T-T^{ref})\big)}{1+K_i(T-T^{ref})} \tag{3}$$

where $V_{pv}[G,T]$ is the operational panel voltage at MPP for a given G and T; P_{pv}^{ref} is the maximum panel power at G^{ref} and T^{ref}; V_{pv}^{ref} is the operating voltage at P_{pv}^{ref}; and K_p is the maximum panel power temperature coefficient.

Equations (2) and (3) approximate the panel current and voltage at MPP. These estimated values are compared with the measured values of a PV panel under regulated G and T conditions to calculate estimation errors for the digital twin estimator. The estimation errors for both equations are within $\pm 5\%$ for the operating range of G and T (see Appendix A). Note that field applications of these equations require a basic weather station to communicate the real-time information of solar irradiance and panel temperature.

This work presents a model-based digital twin estimator of a PVECU which has a four-switch buck-boost converter as shown in Fig. 2. The estimated outputs $\mathbf{z}(t)$ (in the continuous-time) of the PVECU digital twin include power converter inductor current $\hat{i}_L(t)$, power converter capacitor voltage $\hat{v}_C(t)$, PV panel MPP current $I_{pv}(G,T)$, and PV panel MPP voltage $V_{pv}(G,T)$. Note that in a fault-free (healthy) case, outputs of the digital twin are nominally the same as that of the physical twin irrespective of input conditions (G, T, and $i_{load}(t)$). Thus, the digital twin estimator for the PVECU in Fig. 2 (where $t = kT_s$) is:

$$\mathbf{z}[k,G,T] = \mathbf{C}\begin{bmatrix}\mathbf{x}[k]\\ I_{pv}[G,T]\\ V_{pv}[G,T]\end{bmatrix}, \mathbf{x}[k] = \begin{bmatrix}\hat{i}_L[k]\\ \hat{v}_C[k]\end{bmatrix},$$
$$\mathbf{u}[k] = \begin{bmatrix}v_{pv}[k]\\ i_{load}[k]\end{bmatrix}, \hat{\mathbf{A}}_j = \mathbf{I}_{2\times 2} + T_s\begin{bmatrix}-\frac{R}{L} & -\frac{s_3}{L}\\ \frac{s_3}{C} & 0\end{bmatrix},$$
$$\hat{\mathbf{B}}_j = T_s\begin{bmatrix}\frac{s_1}{L} & 0\\ 0 & -\frac{1}{C}\end{bmatrix}, \ \mathbf{C} = \mathbf{I}_{4\times 4},$$
$$j \in \{1,2,3,4\}, \ s_1 \in \{0,1\}, \ s_3 \in \{0,1\}$$

The reference values, I_{pv}^{ref} and V_{pv}^{ref} in (2) and (3) are chosen as the MPP current (I_{MPP}) and voltage (V_{MPP}) at standard test condition (i.e. $G^{ref} = 1000$ W/m^2 and $T^{ref} = 25°$C) which are generally available in a PV panel datasheet.

IV. Fault Diagnosis via Digital Twin

In this section, the FD and FI methodologies based on the digital twin estimator are illustrated with simulation results to describe their working principles and operation. Lastly, simulation results for the fault diagnosis of a representative distributed PV system are presented to demonstrate the operation of the proposed approach in a system setting.

A. FD Methodology

The generation of $\boldsymbol{\gamma}(t)$ for FD is the second element of the fault diagnosis approach as shown in Fig. 1. Note that (4) and (5) are also implemented digitally, but are presented in the continuous-time domain. The measured system outputs $\mathbf{y}(t)$ are subtracted from the estimated outputs $\mathbf{z}(t)$ to generate $\boldsymbol{\gamma}(t)$ as given in (4):

$$\boldsymbol{\gamma}(t) = \mathbf{z}(t) - \mathbf{y}(t) = \begin{bmatrix}\gamma_1(t)\\ \gamma_2(t)\\ \gamma_3(t)\\ \gamma_4(t)\end{bmatrix} = \begin{bmatrix}\hat{i}_L(t) - i_L(t)\\ \hat{v}_C(t) - v_C(t)\\ I_{pv}(G,T) - i_{pv}(t)\\ V_{pv}(G,T) - v_{pv}(t)\end{bmatrix} \tag{4}$$

To scale the heterogeneous elements of $\boldsymbol{\gamma}(t)$ to a common range, $\boldsymbol{\gamma}(t)$ is converted into per unit (p.u.) values. The L^∞ norm $||\boldsymbol{\gamma}(t)||_\infty$ can be easily computed and is used to detect a fault event. In the fault-free scenario, the norm is arbitrarily close to zero, with deviations arising due to analytical estimation errors, discretization errors, and system noises (e.g. due to sensors). To counteract these deviations and

0885-8993 (c) 2018 IEEE. Personal use is permitted, but republication/redistribution requires IEEE permission. See http://www.ieee.org/publications_standards/publications/rights/index.html for more information.

This article has been accepted for publication in a future issue of this journal, but has not been fully edited. Content may change prior to final publication. Citation information: DOI 10.1109/TPEL.2019.2911594, IEEE Transactions on Power Electronics

TABLE II
PV ENERGY CONVERSION SYSTEM SPECIFICATIONS

PV panel ratings	260 W, 8.95 A (I_{sc}), 37.7 V (V_{oc}), 8.58 A (I_{MPP}), 30.3 V (V_{MPP}) [CSUN 260-60P]
Controlled dc load	Resistor banks
Buck-Boost converter ratings	300 W, 100 V, 20 A [Table III]
Solar irradiance sensor	Pyranometer, Basis SMP11-A (4-20 mA) [KIPP & ZONEN]
Panel Temperature sensor	PT-100

to minimize false alarm rates in FD, the threshold value Γ is chosen by the following procedure:

1) the upper bound is computed for each element of the fault-free $\boldsymbol{\gamma}(t)$ (i.e. $\gamma_l(t)\ \forall\ l \in \{1,2,3,4\}$) such that $|\gamma_l(t)| \leq |\epsilon_l| + |n| + |d_e|$ where ϵ_l represents the estimation error in each element (see Appendix A), n is the noise determined from the experimental tests, and d_e is the error due to discretization and quantization deduced after the digital implementation.
2) the L^∞ norm $||\boldsymbol{\gamma}(t)||_\infty$ is calculated and a safety margin m_S is added to achieve tolerance against a maximum level of noise in the experimental conditions. Thus $\Gamma = ||\boldsymbol{\gamma}(t)||_\infty + |m_S|$.

A FD flag indicates the fault event according to the following logic:

$$\begin{aligned} ||\boldsymbol{\gamma}(t)||_\infty \geq \Gamma,\ \text{FD flag} = 1 \\ ||\boldsymbol{\gamma}(t)||_\infty < \Gamma,\ \text{FD flag} = 0 \end{aligned} \tag{5}$$

The PVECU and its digital twin estimator are simulated in MATLAB/Simulink using the Piecewise Linear Electrical Circuit Simulation (PLECS) toolbox. The simulation parameters are given in Table II. Fig. 3a shows $\boldsymbol{\gamma}(t)$ before and after a fault event. As shown, $\boldsymbol{\gamma}(t)$ is arbitrarily close to zero before the fault is injected. However, after the fault event, it evolves in time depending on the fault type. Fig. 3b shows the FD logic which compares $||\boldsymbol{\gamma}(t)||_\infty$ with $\Gamma = 0.2$. As shown, the fault is detected in one simulation time step after the fault is injected.

B. FI Methodology

Error residual evaluation for FI is the third element of the fault diagnosis approach as shown in Fig. 1. Note that the fault signatures and (9) are also implemented digitally, but are presented in the continuous-time domain. The FI methodology is broken into three parts as follows:

1) Residual Analysis for Fault Signatures: After a fault event, the dynamics of $\boldsymbol{\gamma}(t)$ evolve and take a unique direction in the fault space indicating the fault type. To determine the direction in the fault space, the error residual $\boldsymbol{\gamma}(t)$ is normalized to a unity vector $\mathbf{f}$ such that $\mathbf{f} = \xi(t)\boldsymbol{\gamma}(t)$ and $\xi(t) = \frac{1}{||\boldsymbol{\gamma}(t)||_2}$. Thus, the unit vector $\mathbf{f}$ represents the unique direction of the fault event and the L^2 norm $||\boldsymbol{\gamma}(t)||_2$ represents the fault magnitude (that is $\frac{1}{\xi(t)}$). Note that $\boldsymbol{\gamma}(t) = \frac{\mathbf{f}}{\xi(t)}$.

We analytically calculate $\boldsymbol{\gamma}(t)$ for every fault of interest in the system and validate the calculated $\boldsymbol{\gamma}(t)$ through simulation and experimental tests. The error residual vectors are then transformed into fault signatures through normalization and assembled into a *fault signature library*.

TABLE III
BUCK-BOOST CONVERTER SPECIFICATIONS

Input Voltage Range	15 V...50 V
Output Voltage Range	15 V...100 V
Max Output Power	300 W
Max Input Current	10 A
Max Output Current	20 A
Power components	
Input MOSFETS[1]	80 V, 1.9 mΩ, 180 A
Output MOSFETS[2]	150 V, 6.5 mΩ, 130 A
L	150 μH
R	80 mΩ
C	300 μF, 200 V
C_{IN}	1.6 mF, 63 V
Components for control & monitoring	
Computing device	Artix-35T FPGA
Device time step	500 ns
Switching Frequency	50 kHz
Voltage sensor bandwidth	500 kHz
Current sensor bandwidth	500 kHz

[1] [IPB019N08N3]
[2] [IPB065N15N3]

2) Fault Signature Calculation: Fault signatures are calculated analytically for sixteen types of faults which are grouped into three categories: 1) PV panel faults, 2) power converter faults, and 3) electrical sensor faults. The probabilities of the occurrence of these faults in a PVECU network depend upon operating conditions and the system specification and architecture.

PVECU faults are modeled on the digital twin estimator to analytically obtain their respective fault signatures. Thus, for a fault event in a physical system, a faulted digital twin is the one which estimates the outputs of the faulted physical system. For $\boldsymbol{\gamma}(t)$ generation in (4), the steady state outputs of a faulted digital twin are subtracted from those of a fault-free (healthy) digital twin. Note that the fault-free digital twin estimator in steady state is given by:

$$\mathbf{z}(t) = \mathbf{C} \begin{bmatrix} \frac{i_{load}(t)}{D_{s_3}}, -\frac{R*i_{load}(t) - D_{s_1}*D_{s_3}*v_{pv}(t)}{D_{s_3}^2}, \\ \frac{I_{pv}^{ref} G\left(1+K_i(T-T^{ref})\right)}{G^{ref}}, \\ \frac{V_{pv}^{ref}\left(1+K_p(T-T^{ref})\right)}{1+K_i(T-T^{ref})} \end{bmatrix}^T \tag{6}$$

where D_{s_3} is the duty cycle for SW_3 and D_{s_1} is the duty cycle for SW_1 (see Fig. 2). A fault signature $\mathbf{f}_i$ is extracted through the analysis of $\boldsymbol{\gamma}(t)$ as presented in Section IV-B1. Table VI in Appendix B presents $\mathbf{f}_i$ and $\frac{1}{\xi(t)}$ for all $i \in \{1, 2, ..., 16\}$.

The fault signature calculation is illustrated for a PV panel fault type $i = 1$. Consider the soiling of the PV panel. It causes the value of I_{pv}^{ref} for the faulted panel to change by a quantity ΔI_{pv}^{ref} for G^{ref} (note that the change in V_{pv}^{ref} is negligible). Thus, the faulted digital twin estimator in steady state is given

0885-8993 (c) 2018 IEEE. Personal use is permitted, but republication/redistribution requires IEEE permission. See http://www.ieee.org/publications_standards/publications/rights/index.html for more information.

This article has been accepted for publication in a future issue of this journal, but has not been fully edited. Content may change prior to final publication. Citation information: DOI 10.1109/TPEL.2019.2911594, IEEE Transactions on Power Electronics

by:

$$\tilde{\mathbf{z}}(t) = \mathbf{C}\begin{bmatrix} \frac{i_{load}(t)}{D_{s_3}}, -\frac{R*i_{load}(t)-D_{s_1}*D_{s_3}*v_{pv}(t)}{D_{s_3}^2}, \\ \frac{(I_{pv}^{ref}-\Delta I_{pv}^{ref})G\left(1+K_i(T-T^{ref})\right)}{G^{ref}}, \\ \frac{V_{pv}^{ref}\left(1+K_p(T-T^{ref})\right)}{1+K_i(T-T^{ref})} \end{bmatrix}^T \quad (7)$$

In this case, the error residual vector $\boldsymbol{\gamma}(t) = \mathbf{z}(t) - \tilde{\mathbf{z}}(t)$ is $\mathbf{C}\left[0, 0, \frac{\Delta I_{pv}^{ref} G\left(1+K_i(T-T^{ref})\right)}{G^{ref}}, 0\right]^T$. For its normalization, it is divided by $||\boldsymbol{\gamma}(t)||_2$ which represents the fault magnitude $\frac{1}{\xi(t)}$ and is $\frac{\Delta I_{pv}^{ref} G\left(1+K_i(T-T^{ref})\right)}{G^{ref}}$. This normalization results in a unity vector $\mathbf{f_1}$ which is the fault signature and is $[0, 0, 1, 0]^T$.

For power converter faults, the signature calculation for fault type $i = 4$ is illustrated. Consider an open switch fault in SW_1 in Fig. 2. The fault event causes the open circuit of the PV panel. Thus, the faulted digital twin estimator in steady state is $\tilde{\mathbf{z}}(t) = \mathbf{C}\left[\ 0, 0, 0, V_{oc}\right]^T$. The error residual $\boldsymbol{\gamma}(t)$ is generated and analyzed to obtain $\mathbf{f_4}$ and $\frac{1}{\xi(t)}$ which are given in Table VI in Appendix B.

For electrical sensor faults, the signature calculation for fault type $i = 12$ is illustrated. Consider a $\Delta c_{12}(t)$ drift and a $\Delta e_{12}(t)$ offset in $i_L(t)$ sensor. This sensor fault can be modeled in the measured physical system outputs as (see [15]):

$$\mathbf{y}(t) = (\mathbf{C} + \Delta\mathbf{C}(t))\begin{bmatrix} i_L(t) \\ v_C(t) \\ i_{pv}(t) \\ v_{pv}(t) \end{bmatrix} + \Delta\mathbf{E}(t),$$

$$\Delta\mathbf{C}(t) = \begin{bmatrix} \Delta c_{12}(t) & 0 \\ 0 & \mathbf{0}_{3\times 3} \end{bmatrix}, \ \Delta\mathbf{E}(t) = \begin{bmatrix} \Delta e_{12}(t) \\ 0 \\ 0 \\ 0 \end{bmatrix} \quad (8)$$

In this case, the error residual $\boldsymbol{\gamma}(t) = \mathbf{z}(t) - \mathbf{y}(t)$ is $[\Delta c_{12}(t) i_L(t) + \Delta e_{12}(t), 0, 0, 0]^T$. Thus, $\mathbf{f_{12}} = [1, 0, 0, 0]^T$ and $\frac{1}{\xi(t)} = \Delta c_{12}(t) i_L(t) + \Delta e_{12}(t)$. Note that $\mathbf{z}(t) = \mathbf{C}\left[\hat{i}_L(t), \hat{v}_C(t), I_{pv}(G,T), V_{pv}(G,T)\right]$ is nominally the same as $\mathbf{y}(t) = \mathbf{C}\left[i_L(t), v_C(t), i_{pv}(t), v_{pv}(t)\right]$ in a fault-free case.

Similarly, one can compute the fault signatures for other PVECU fault types listed in Table VI.

3) FI Logic: After a fault event, $\boldsymbol{\gamma}(t)$ takes a unique direction in the fault space that indicates the fault type. Thus after FD, an L^2 inner product is computed between $\boldsymbol{\gamma}(t)$ and every member of the fault signature library (i.e. $\{\mathbf{f_1}, \cdots, \mathbf{f_{16}}\}$) in real-time. It reveals the projection of $\boldsymbol{\gamma}(t)$ on each $\mathbf{f}_i$. Intuitively, the maximum magnitude of inner product will be between $\boldsymbol{\gamma}(t)$ and the $\mathbf{f}_i$ with which it most closely aligns to. The maximum inner product search indicates the fault type i identifying the fault event. Thus, a FI logic computes the inner products and performs the maximum inner product search.

The L^2 inner product is mathematically obtained as follows: $\langle \gamma(t), \mathbf{f}_i \rangle_{L^2} = \int_{t-W}^{t} \gamma^T(t-\tau)\mathbf{f}_i(\tau)\,\mathrm{d}\tau$ where W represents the window size over which the inner product is calculated. Thus, for a given fault signature library $\{\mathbf{f_1}, \cdots, \mathbf{f_{16}}\}$ (see Appendix B), the FI logic computes

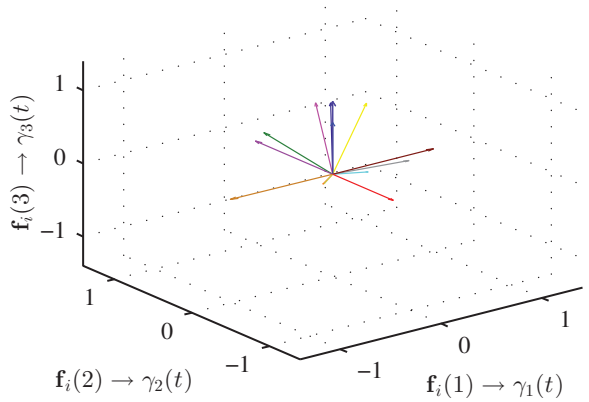

(a) First three elements of the sixteen fault signatures.

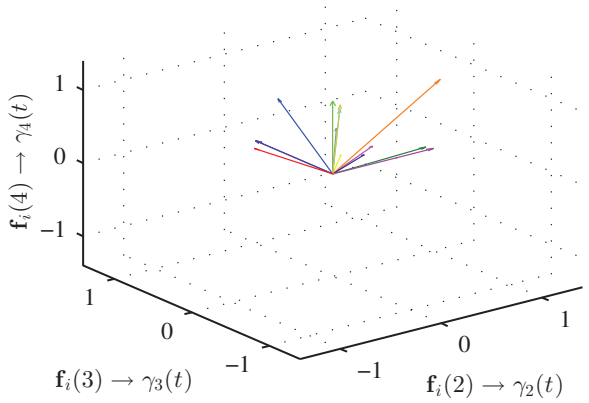

(b) Last three elements of the sixteen fault signatures.

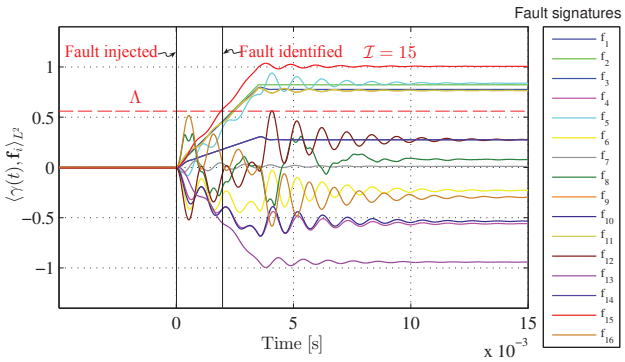

(c) Inner products between $\boldsymbol{\gamma}(t)$ and fault signature library to identify fault type.

Fig. 4: Simulation results for the FI methodology. Graphical representation of the fault signature library, where each fault signature $\mathbf{f}_i = \xi(t)[\gamma_1(t), \gamma_2(t), \gamma_3(t), \gamma_4(t)]^T \ \forall\ i \in \{1, \cdots, 16\}$ shows a unique direction in the fault space (top). FI logic (bottom).

$$\mathcal{I} = \begin{cases} i & \text{if } \max\limits_{i\in\{1,\cdots,16\}} \langle \gamma(t), \mathbf{f}_i \rangle_{L^2} \geq \Lambda \\ 0 & \text{if } \max\limits_{i\in\{1,\cdots,16\}} \langle \gamma(t), \mathbf{f}_i \rangle_{L^2} < \Lambda \end{cases} \quad (9)$$

where $\mathcal{I}$ indicates the fault type through the FI flag and Λ is the empirically calculated FI threshold to minimize the false identification of fault type during the transient.

Fig. 4 presents the simulation results for the FI methodology. The graphical representations of the fault signa-

0885-8993 (c) 2018 IEEE. Personal use is permitted, but republication/redistribution requires IEEE permission. See http://www.ieee.org/publications_standards/publications/rights/index.html for more information.

This article has been accepted for publication in a future issue of this journal, but has not been fully edited. Content may change prior to final publication. Citation information: DOI 10.1109/TPEL.2019.2911594, IEEE Transactions on Power Electronics

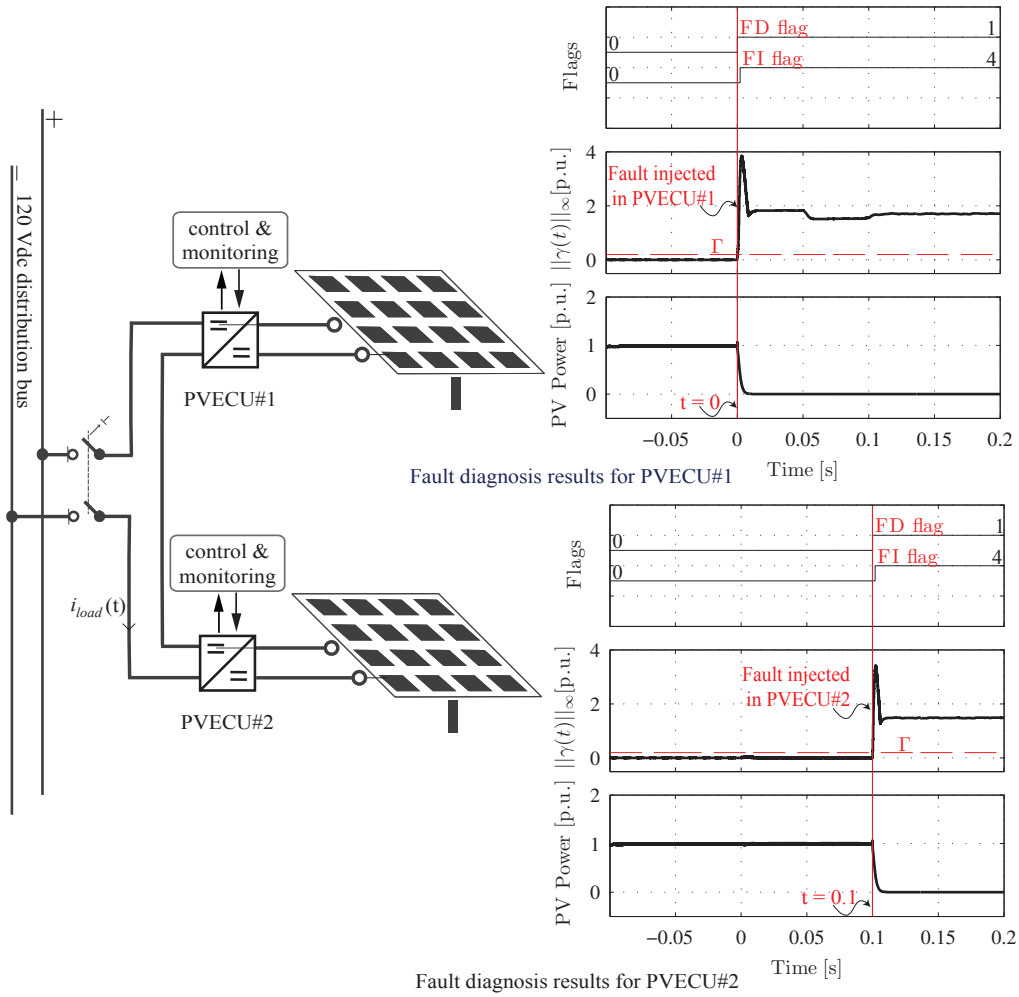

Fig. 5: Simulation results for fault diagnosis in a representative distributed PV system. Diagnosis of a fault injected at $t = 0$ [$t = 0.1$] in PVECU#1 [PVECU#2] is shown in the top [bottom] subfigure.

ture library show the direction taken by each $\mathbf{f}_i$ (a $\mathbf{f}_i = \xi(t)[\gamma_1(t), \gamma_2(t), \gamma_3(t), \gamma_4(t)]^T$). Fig. 4a presents the direction when the $\mathbf{f}_i$ has $\mathbf{f}_i(1), \mathbf{f}_i(2)$, and $\mathbf{f}_i(3)$ for all $i \in \{1, 2, ..., 16\}$. Fig. 4b presents the direction with the last three elements (i.e. $\mathbf{f}_i(2), \mathbf{f}_i(3)$, and $\mathbf{f}_i(4)$). Fig. 4c presents the FI logic which activates after FD. The logic identifies the fault event which is detected in Fig. 3b. It shows the evolution of the sixteen inner products performed between $\boldsymbol{\gamma}(t)$ and each $\mathbf{f}_i$ over a window size of 2 ms. These inner products are compared with $\Lambda = 0.6$ to prevent the initial false identification of fault type when $\boldsymbol{\gamma}(t)$ is still evolving in the fault space (during the transient). Fault type $\mathcal{I} = 15$ (see Table VI) is identified within 2 ms when the maximum inner product (out of all sixteen) exceeds the Λ.

C. Simulation Study for a Distributed PV System

To show the operation of the proposed fault diagnosis approach in a system setting, a simulation study is performed on a representative distributed PV system which is shown in Fig. 5. The system consists of a two series-connected PVECUs (i.e. PVECU#1 and PVECU#2) forming a string which is connected to a 120 V dc distribution bus (since only 2 PVECUs are considered). As shown in Fig. 5, both PVECUs have their own control & monitoring (which include the proposed fault diagnosis) stages. The simulation parameters for a PVECU are given in Table II and III. The simulation results for the fault diagnosis of each PVECU are presented adjacent to its schematic in Fig. 5. An open switch fault in SW_1 (see Fig. 2) is injected in PVECU#1 at $t = 0$ (see top subfigure in Fig. 5) and the same fault type is injected in PVECU#2 after 0.1s (see bottom subfigure in Fig. 5). As shown, after fault injection in the PVECU, the corresponding PV panel power goes to 0. This fault event causes $||\boldsymbol{\gamma}(t)||_\infty$ to become non-zero in each PVECU after the time of fault injection and triggers the FD and FI flags.

In PVECU#1, $||\boldsymbol{\gamma}(t)||_\infty$ exceeds the threshold and triggers the FD flag after one simulation time step (see top subfigure in Fig. 5). After FD, the FI function is activated that identifies the fault type as $i = 4$. Note that the FD and FI flags for PVECU#2 do not change during the fault event in PVECU#1. Later at $t = 0.1$, the open switch fault is injected in PVECU#2 which is also detected and identified correctly as shown in the bottom subfigure of Fig. 5. The fault event in PVECU#2

0885-8993 (c) 2018 IEEE. Personal use is permitted, but republication/redistribution requires IEEE permission. See http://www.ieee.org/publications_standards/publications/rights/index.html for more information.

This article has been accepted for publication in a future issue of this journal, but has not been fully edited. Content may change prior to final publication. Citation information: DOI 10.1109/TPEL.2019.2911594, IEEE Transactions on Power Electronics

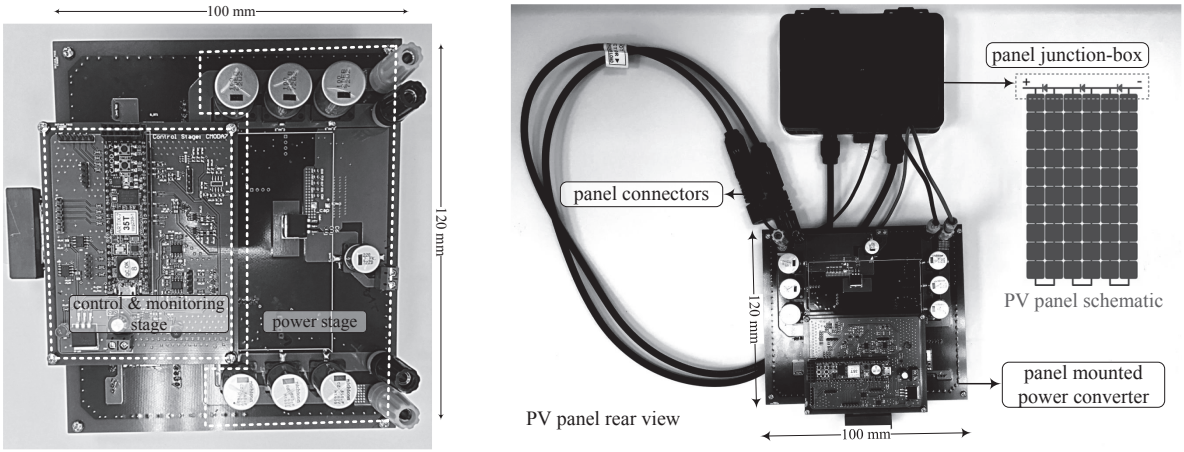

(a) Four-switch buck-boost converter prototype

(b) PV panel and its mounted power converter

Fig. 6: Annotated photographs presenting panel-level power converter and its mounting details on a PV panel for conducting outdoor field experiments.

does not alter the FD and FI flags of PVECU#1. Similarly, a distributed PV system with more than two PVECUs in a string or with multiple strings can also be simulated for other fault events.

V. Implementation details and Hardware Setup for field experiments

This section presents the implementation details and hardware setup for the outdoor field experiments to validate the proposed fault diagnosis approach. Since the dynamics of the PV panel faults are slow and can be better emulated in a real settings than through a PV emulator, we choose to perform experiments in an open space located on a flat roof of a building on the National University of Singapore campus. A 10 kW PV system along with a weather station has been installed in that space for various research purposes. The following are the step-by-step details for the outdoor field experimental validation.

A. Power Converter Prototype

First, a PV panel mounted 300 W buck-boost converter prototype is designed and developed. The power stage has four silicon MOSFET switches, four isolated gate drivers, a bank of input and output capacitors, an inductor, and on-board isolated current and voltage sensing devices. The control & monitoring stage uses a Xilinx Artix-7 FPGA based computing device, ADCs, and DACs. Fig. 6a shows the annotated photograph of the buck-boost converter prototype. Table III presents the complete specifications of the prototype and lists the details of the components for power and control & monitoring stages, respectively.

Fig. 6b presents the converter mounting details on the PV panel. In residential and commercial settings, a PV panel typically has three strings. Each string consists of 20 or 24 series connected silicon solar cells and terminates into an integrated junction box. These strings are further combined in series configuration at the junction box and an anti-parallel diode is placed across each string for PV panel protection purposes (see Fig. 6b). The converter prototype is connected across the output terminals of the panel junction box.

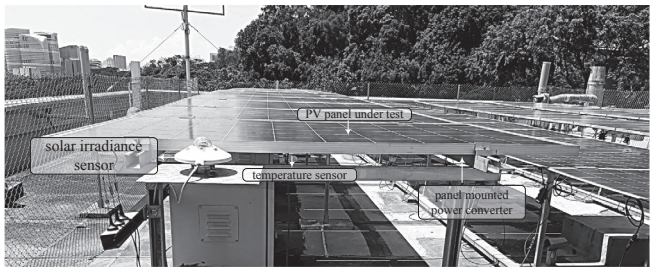

Fig. 7: Annotated photograph of the PV energy conversion system in field.

B. Implementation of Fault Diagnosis Approach and Control Logic

Next, the digital twin estimator, FD and FI methodologies, and control logic are implemented on the Artix-7 FPGA (i.e. XC7A35T-1CPG236C). The reasons for choosing this FPGA include its higher performance (in terms of speed and resources), lower power consumption, smaller size package and optimized cost compared to other computing devices.

The digital twin estimator (1), FD logic (5), FI logic (9), and control logic are discretized with a fixed device time step of 500 ns and implemented on the FPGA using finite state machines and pipelining. The fault signature library in Table VI is hardcoded onto the computing device. Thus, the FPGA performs the following tasks: 1) solves the digital twin estimator; 2) generates an error residual vector based on signals from the physical twin and the digital twin; 3) stores the fault signature library; and 4) triggers the FD and FI flags based on the L^∞ norm of the error residual vector and the L^2-inner product calculation. The ADCs sample the outputs of the PV panel, the power converter, and the load current at a frequency of 500 kHz for fault diagnosis and control. The solar irradiance and temperature data are sampled at a frequency of 0.1 Hz. Note that the overall digital design uses the 48%

0885-8993 (c) 2018 IEEE. Personal use is permitted, but republication/redistribution requires IEEE permission. See http://www.ieee.org/publications_standards/publications/rights/index.html for more information.

This article has been accepted for publication in a future issue of this journal, but has not been fully edited. Content may change prior to final publication. Citation information: DOI 10.1109/TPEL.2019.2911594, IEEE Transactions on Power Electronics

resources of the XC7A35T and the power consumption is 0.2 W.

In addition, the control logic includes a simple perturb and observe (P&O) method for tracking MPP under operating ranges of solar irradiance and temperature. The details of control logic are given in [3].

C. PV Energy Conversion System in Outdoor Field

Lastly, we installed a PVECU for the outdoor field experiments. Fig. 7 shows the annotated photograph of the field experimental testbed, where a 260 W PV panel is chosen and the power converter prototype is mounted on its rear side. The weather station provides the solar irradiance and panel temperature data. Table II presents addition details about the PV energy conversion system.

VI. Experimental Results and Discussions

This section presents the experimental results for diagnosis of a variety of faults listed in the fault signature library (see Table VI in Appendix B) using the field experimental testbed presented in Section V. Note that the experimental results are presented for diagnosis of those faults which have unique signatures. Later, the promptness and sensitivity [12] of the proposed approach is analyzed. Lastly, the proposed approach is compared with the prior works in the literature to display its unique and innovative features.

A. Fault Diagnosis Results

The fault diagnosis results show two types of the signals: 1) measured waveforms before and after a fault event; and 2) the digital FD and FI flag. Note that the FD flag is a *1-bit* signal which could be zero or one depending on the FD logic. Similarly, the FI flag is a *4-bit* signal presented in hexadecimal format which represents the fault type depending on the FI logic. The fault type number i corresponds to the fault event in Table VI in Appendix B.

1) PV Panel Faults: Three different types of PV panel faults are injected into the testbed.

A solar cell of the panel is shaded mildly (i.e. 20%) by an opaque object. That corresponds to $i = 1$ in Table VI. Fig. 8a presents the current-voltage and power-voltage characteristics of the PV panel before and after that fault event. Note that in a PV panel with bypass diodes, the mild shading (approximately up to 35% of a solar cell) significantly changes the MPP panel current while the change in (MPP) panel voltage from old to new MPP can be neglected. Fig. 8b shows the panel current $i_{pv}(t)$, the panel voltage $v_{pv}(t)$, and the load current $i_{load}(t)$, before and after the fault event. When the L^∞ norm of the $\boldsymbol{\gamma}(t)$ exceeds the FD threshold, the fault event is detected which takes 80 ms (see FD flag). Since the shading condition disturbs the MPP of the PV panel changing both the panel current and the panel voltage simultaneously at the point of fault injection, the fault is initially identified as $i = 3$. The control logic takes around 1.2 s to reach to a new MPP of the panel. The new MPP has decreased panel current and minor change in panel voltage in comparison to those of the fault-free case. Thus,

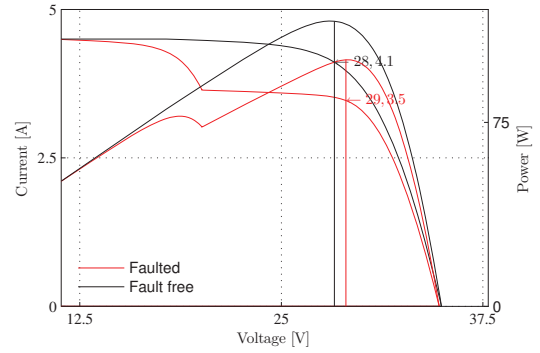

(a) PV panel characteristics for faulted and fault-free conditions.

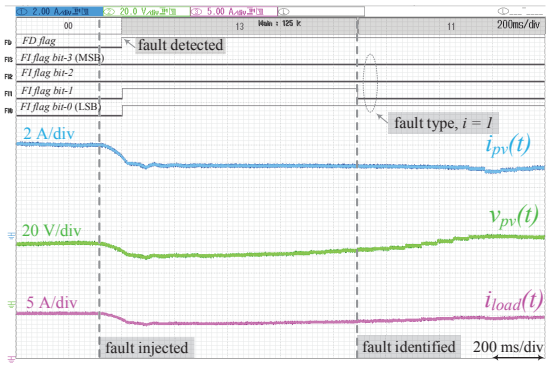

(b) Fault diagnosis.

Fig. 8: 20% shading of a solar cell in the PV panel (continuous/repetitive mild partial shading).

the fault type is identified correctly as $i = 1$, when the panel voltage is in the vicinity of the new MPP value. The time to FI is 939 ms when the inner product corresponding to $i = 1$ exceeds the FI threshold (see FI flag).

Similarly, for diagnosis of fault type $i = 2$, a solar cell of the panel is shaded severely (i.e. 40%) by an opaque object. In that scenario, one of the bypass diodes of the PV panel operates. That shifts the panel voltage to the new MPP (i.e. after severe shading) which is at the two-third of its old MPP value (i.e. fault-free) while the panel current at the new MPP remains the same as that at the old MPP. Fig. 9a presents the PV panel characteristics for fault-free and faulted (which include severe partial shading and bypass diode failures) conditions. Fig. 9b presents the panel current $i_{pv}(t)$, the panel voltage $v_{pv}(t)$, and the load current $i_{load}(t)$ before and after that fault event which is detected within 60 ms. Similar to the previous fault event, here also the initial fault type is identified as three. However, when the panel current is in the close proximity of the new MPP, the fault type is identified correctly as $i = 2$ within 1.14 s.

The fault type $i = 3$ corresponds to faults internal to the PV panel that change both its current and voltage at MPP, for instance PID of the solar cells or the interconnects. Fig. 10a presents the PV panel characteristics for $i = 3$ and fault-free conditions. We emulate PID of the PV panel by inserting a resistive element in shunt to its output terminals [31] that

0885-8993 (c) 2018 IEEE. Personal use is permitted, but republication/redistribution requires IEEE permission. See http://www.ieee.org/publications_standards/publications/rights/index.html for more information.

This article has been accepted for publication in a future issue of this journal, but has not been fully edited. Content may change prior to final publication. Citation information: DOI 10.1109/TPEL.2019.2911594, IEEE Transactions on Power Electronics

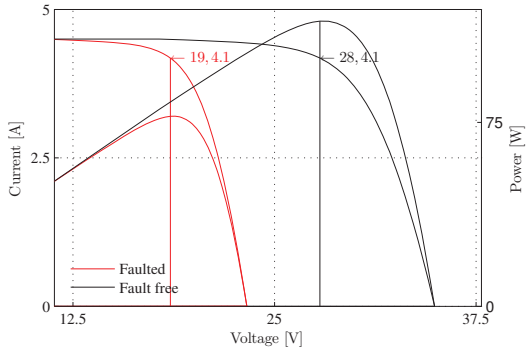

(a) PV panel characteristics for faulted and fault-free conditions.

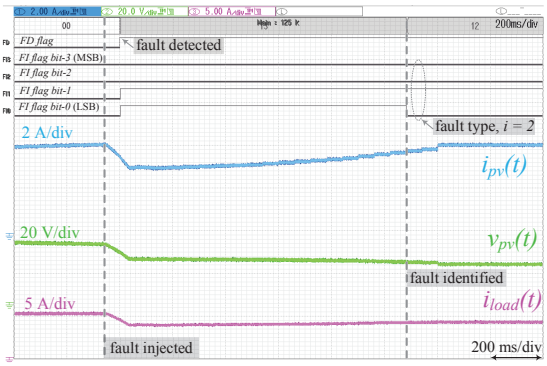

(b) Fault diagnosis.

Fig. 9: 40% shading of a solar cell in the PV panel (continuous/repetitive severe partial shading).

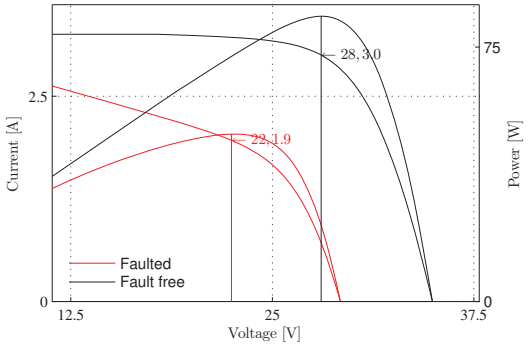

(a) PV panel characteristics for faulted and fault-free conditions.

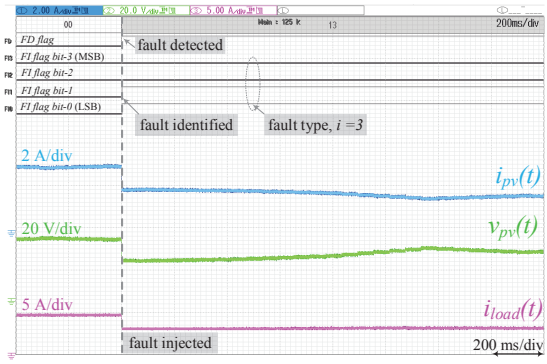

(b) Fault diagnosis.

Fig. 10: Faults internal to the PV panel.

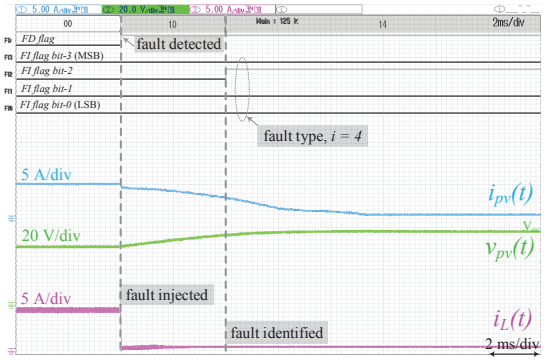

Fig. 11: Open switch fault in SW_1.

decreases the effective shunt resistance of the PV panel. Fig. 10b shows the panel current $i_{pv}(t)$, the panel voltage $v_{pv}(t)$, and the load current $i_{load}(t)$ before and after the insertion of the resistive element. The fault event is detected in 80 μs due to the instantaneous changes in the panel outputs. The fault event is identified as $i = 3$ in 2.08 ms. The control logic takes around 1.2 s to reach to a new MPP of the panel. The new MPP has both decreased, the panel current and voltage values in comparison to those of the fault-free case. Thus, in that scenario, the fault type does not change when the panel reaches the new MPP, contrary to the previous fault scenarios.

2) Power Converter Faults: The diagnosis of four types of converter switch faults (listed in Table VI) is demonstrated. Open circuit faults are injected through contactor switches and short circuit faults are injected by changing the related gating signal to one in the FPGA.

An open circuit fault in SW_1 (see Fig. 2) corresponding to $i = 4$ is injected. Fig. 11 presents the panel current $i_{pv}(t)$, the panel voltage $v_{pv}(t)$, and the inductor current $i_L(t)$ before and after the fault event. The fault event causes the open circuit of PV panel, thus the panel voltage goes to the open circuit value V_{oc}. The panel current and the inductor current go to zero. The time to FD is 14.8 μs and the fault is identified correctly as $i = 4$ within 4.01 ms. An assessment related to that performance is presented in Section VI-B.

Next, a short circuit fault in SW_2 is injected. Fig. 12 shows the panel current $i_{pv}(t)$, the panel voltage $v_{pv}(t)$, and the inductor current $i_L(t)$ before and after the fault event. The fault event shorts the PV panel terminal increasing the panel current to short circuit current I_{sc}. The transient in the panel current represents the discharging current of the panel capacitor, reducing the panel terminal voltage to zero. Due to shorting of the panel output terminals, the inductor discharges its stored energy and settles to zero value. The fault event is detected very fast (i.e. 5.6 μs) and correctly identified as $i = 7$ within 2.01 ms.

Fig. 13 presents the panel current $i_{pv}(t)$, the panel voltage

0885-8993 (c) 2018 IEEE. Personal use is permitted, but republication/redistribution requires IEEE permission. See http://www.ieee.org/publications_standards/publications/rights/index.html for more information.

This article has been accepted for publication in a future issue of this journal, but has not been fully edited. Content may change prior to final publication. Citation information: DOI 10.1109/TPEL.2019.2911594, IEEE Transactions on Power Electronics

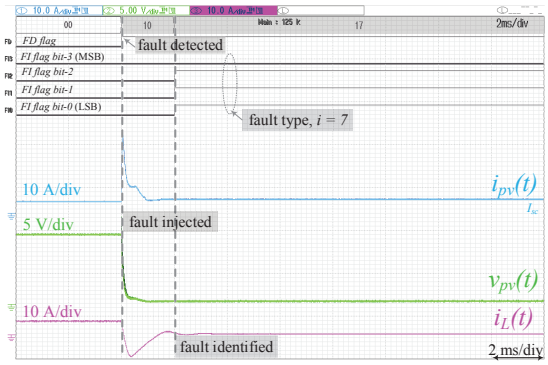

Fig. 12: Short switch fault in SW_2.

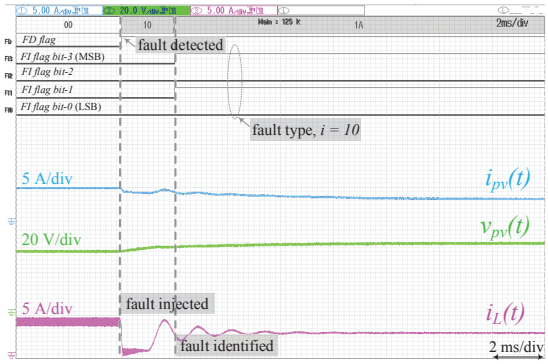

Fig. 13: Open switch fault in SW_4.

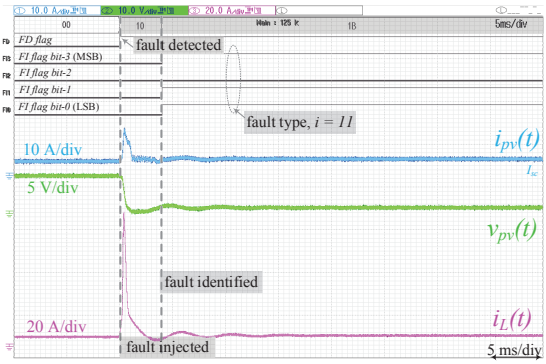

Fig. 14: Short switch fault in SW_4.

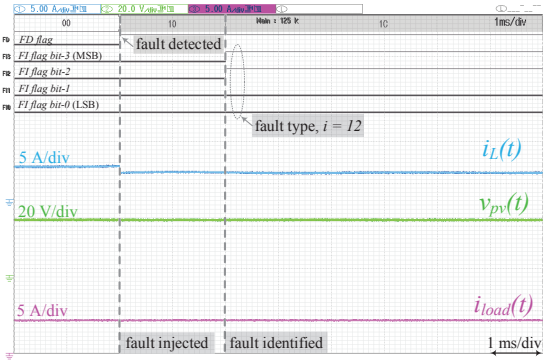

Fig. 15: 20% decrease in gain of inductor current sensor, $i_L(t)$.

$v_{pv}(t)$, and the inductor current $i_L(t)$ before and after an open fault in SW_4 is injected. The fault event can be detected and thus identified only if the power converter operates in the boost mode. That is because SW_4 is in open condition in all other modes. The open circuit in SW_4 causes the panel to work at some sub-optimal power point, thus changing the panel current and the panel voltage. The inductor discharges its pre-fault stored energy and charges to the same current value as the panel current. Time to FD is 33.6 μs and the fault event is identified as fault type $i = 10$ within 2.03 ms.

Fig. 14 shows the panel current $i_{pv}(t)$, the panel voltage $v_{pv}(t)$, and the inductor current $i_L(t)$ before and after a short fault in SW_4 is injected. The fault event shorts the PV panel through the inductor, increasing the panel current to short circuit current I_{sc}. The transient in the panel current represents the discharging current of the panel capacitance, reducing the panel terminal voltage to zero. Due to shorting of the panel output terminals through the inductor, the transient in the inductor current represents the discharging current of the input capacitance C_{IN} and its own energy. After the transient settles, the inductor current becomes equal to the panel current. The fault event is detected in 30 μs and correctly identified as fault type $i = 11$ within 4.03 ms.

3) Electrical Sensor Faults: In order to demonstrate the electrical sensor fault diagnosis, three different sensors (which include inductor current, panel output voltage, and load current sensor, respectively) are injected with a 20% decrease in their gains in the FPGA platform. Fig. 15, 16, and 17 present the inductor current $i_L(t)$, the panel voltage $v_{pv}(t)$, and the load current $i_{load}(t)$ for diagnosis of faults in three different sensors, respectively. As shown in Fig. 15, a 20% decrease in the inductor current sensor gain causes the FD flag trigger in 1.44 μs and the FI flag shows the fault type $i = 12$ within 2.00 ms. Similarly, for a 20% decrease in the load current sensor gain shown in Fig. 16, the time to FD is 290 μs and the fault type is identified as $i = 14$ within 2.29 ms. Lastly, a decrease of 20% gain in the panel voltage sensor is detected in 1.5 μs and identified as fault type $i = 15$ within 2.00 ms as shown in Fig. 17.

B. Promptness and Sensitivity

Promptness, fault sensitivity, and robustness (i.e. immunity to false alarms) assess the performance of a fault diagnosis approach [12]. Table IV presents the promptness and sensitivity for the proposed fault diagnosis approach.

Promptness refers to the *time to FD* and the *time to FI*. The time to FD primarily relies on the dynamics of an injected fault. Faster and greater fault dynamics imply a shorter time to FD. Since PV panel faults evolve slowly due to their characteristics, the detection time is the longest. The sensor faults have the least detection time. The time to FI primarily depends upon the averaging window W over which the inner

0885-8993 (c) 2018 IEEE. Personal use is permitted, but republication/redistribution requires IEEE permission. See http://www.ieee.org/publications_standards/publications/rights/index.html for more information.

This article has been accepted for publication in a future issue of this journal, but has not been fully edited. Content may change prior to final publication. Citation information: DOI 10.1109/TPEL.2019.2911594, IEEE Transactions on Power Electronics

TABLE IV
PROMPTNESS AND SENSITIVITY FOR THE PROPOSED FAULT DIAGNOSIS APPROACH

Fault type	Fault event	Minimum fault magnitude	Time to FD	Time to FI
PV panel faults				
$i = 1$	Continuous/repetitive mild partial shading	20%	80 ms	939 ms
$i = 2$	Continuous/repetitive severe partial shading	40%	60 ms	1.14 s
$i = 3$	Internal PV panel fault (panel PID)	–	80 μs	2.08 ms
Power converter faults				
$i = 4$	Open switch fault in SW_1	–	14.8 μs	4.01 ms
$i = 7$	Short switch fault in SW_2	–	5.6 μs	2.01 ms
$i = 10$	Open switch fault in SW_4	–	33.6 μs	2.03 ms
$i = 11$	Short switch fault in SW_4	–	30 μs	4.03 ms
Electrical sensor faults				
$i = 12$	Fault in $i_L(t)$ sensor	20%	1.44 μs	2.00 ms
$i = 14$	Fault in $i_{load}(t)$ sensor	20%	290 μs	2.29 ms
$i = 15$	Fault in $v_{pv}(t)$ sensor	20%	1.5 μs	2.00 ms

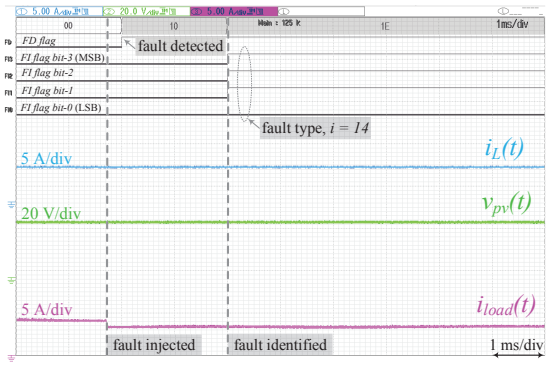

Fig. 16: 20% decrease in gain of load current sensor, $i_{load}(t)$.

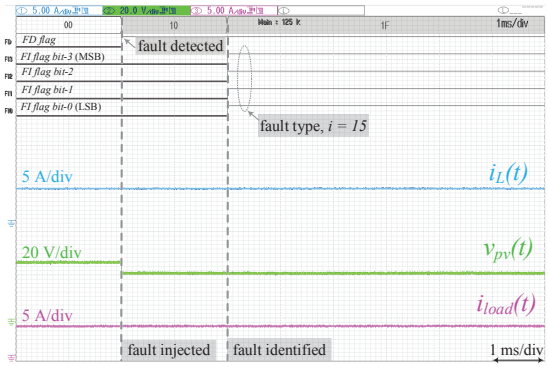

Fig. 17: 20% decrease in gain of PV panel voltage sensor, $v_{pv}(t)$.

product calculation is performed. Smaller window size implies a shorter time to FI. However, it also implies lesser reliability in FI. In our experiments, the size of FI window is 2 ms.

The threshold settings for FD and FI control the promptness, fault sensitivity, and robustness of the proposed approach. The choice of the FD threshold value $\Gamma = 0.2$ is the combination of the analytic and experimental study of the fault-free error residual vector as shown in Section IV-A. Similarly, FI threshold value $\Lambda = 0.6$ minimizes the false FI type.

Sensitivity refers to faults which develop slowly (i.e. incipient faults) for instance, drifts in sensor gains or hotspots due to shading conditions in a PV panel. It is quantified through the minimum fault magnitude which causes a change in the monitored variables that can be detected by the fault diagnosis approach. Robustness refers to the immunity of a fault diagnosis approach against various noises and uncertainties reducing the number of false alarms. Note that sensitivity and robustness are two conflicting attributes. Higher sensitivity trades off the robustness of the approach. With the above mentioned choice of Γ, the proposed algorithm detects 20% drift in sensor gains and 20% mild partial shading of a solar cell in the PV panel without false alarms.

Note that PV panel faults could be intermittent or temporal or continuous. In case of intermittent and temporal PV panel faults, the system operator should look for consistency in fault flags for sufficient time before taking any fault remedial action. Fault remedial action for any other faults could be immediate.

C. Performance Comparison with Prior Works

Table V presents the performance summary of this work and the comparison with prior works in the literature. As shown in the table, most of the existing approaches are fault- and application-specific and may not be applied to other power electronic-based energy conversion systems. For instance, a fault diagnosis approach for a wind energy system is investigated in [32] and may not be applicable to a PV system. On the other side, the framework of our approach is general in principle. That is, the idea of digital twin can be ported to other energy systems (e.g. digital twin of a wind or battery energy conversion unit). The digital twin can then be used to generate residuals which are evaluated using an application-specific fault signature library (as presented in Section IV-B).

The fault signature library consists of faults of interests which are generally the common failure modes of a system (in this work - a PVECU) enabling fault-agnosticism of the proposed approach. That is, the proposed approach detects and identifies a variety of fault types, which no other existing approach achieves. The unique feature is its ability to detect faults in the input energy source and distinguish them with other types of faults related to power converter and electrical sensors. Moreover, the time to FD and FI for converter and sensor faults are comparable to the state-of-the-art. Note that the diagnosis of the PV panel faults takes a longer time due to their characteristics. This work also demonstrates the diagnosis of minimum fault magnitude for sensor and PV

0885-8993 (c) 2018 IEEE. Personal use is permitted, but republication/redistribution requires IEEE permission. See http://www.ieee.org/publications_standards/publications/rights/index.html for more information.

This article has been accepted for publication in a future issue of this journal, but has not been fully edited. Content may change prior to final publication. Citation information: DOI 10.1109/TPEL.2019.2911594, IEEE Transactions on Power Electronics

TABLE V
PERFORMANCE COMPARISON OF PROPOSED FAULT DIAGNOSIS APPROACH WITH PRIOR WORKS

Work	[32]	[33]	[13]	[17]	[34]	[14]	[18]	[15]	This work
Application	wind energy systems	electrical railway traction	PV systems	PV systems	DC-DC converter systems	PV systems	PV systems	nano-grid	PV systems
Fault diagnosis approach	pole voltage estimation and error generation	state observer & residual generation	logic-based on PV panel parameters	PV panel data based	magnetic component voltage equation	shape of inductor current	online PV parameter estimation	state observer & residual generation	digital twin
Approach type	application-specific	fault-specific	application- & fault-specific	application- & fault-specific	fault-specific	fault-specific	fault-specific	general	general
Implementation platform	FPGA (quartus II)	microchip DSP	dSPACE	MatLab	DSP	FPGA	PLC	dSPACE & typhoon HIL	FPGA (Artix-7)
Power converter switching frequency	5 kHz	10 kHz	5 kHz	–	48 kHz	15 kHz	–	20 kHz	50 kHz
Fault diagnosis of energy source	no	no	no	yes	no	no	yes	no	yes
Time to FD	–	–	–	–	–	–	–	–	$\leq$ 80 ms
Time to FI	–	–	–	–	–	–	–	–	$<$ 1.2 s
Faults diagnosis of power converters	yes, OCF & SCF	no	yes, OCF	no	yes, OCF & SCF	yes, OCF & SCF	no	yes, OCF	yes
Time to FD	$<$ 10 μs	–	–	–	–	–	–	$\leq$ 340 μs	$\leq$ 33.6 μs
Time to FI	$<$ 10 μs	–	$\leq$250 ms	–	$<$ 10 μs	$\leq$ 66 μs	–	$\leq$ 113 ms	$\leq$ 4.03 ms
Fault diagnosis of sensors	no	yes	no	no	no	no	no	yes	yes
Time to FD	–	–	–	–	–	–	–	$\leq$ 360 μs	$\leq$ 290 μs
Time to FI	–	300 μs	–	–	–	–	–	$\leq$ 4.4 ms	$\leq$ 2.9 ms
Fault remediation	yes	yes	yes	no	no	yes	no	no	no
Sensitivity & robustness	no	no	no	yes	yes	no	yes	yes	yes
Threshold methodology	no	yes	–	yes	–	–	–	no	yes
Additional requirements	–	–	–	–	auxiliary winding in the magnetic core	–	auxiliary computing platform	–	G & T sensors (only for PV panel faults)

OCF = open circuit switch fault, SCF = short circuit switch fault

panel faults achieving higher sensitivity in comparison to the existing approaches. Note that fault remediation will be fault- and system architecture-specific, and is outside the scope of this paper.

VII. Conclusions

This paper presents a digital twin approach for fault diagnosis in PV installations such as rooftop and BIPV systems. These systems have decentralized and distributed power conversion architectures. The sensing, computation, and actuation capabilities of the distributed power electronics are leveraged for fault diagnosis in such systems. We design a digital twin which represents the model-based estimation of the characteristic outputs of the PV energy conversion unit in real-time. That is followed by the error residual generation and evaluation for fault diagnosis purposes.

A source-level power converter prototype is designed and developed for validation of the fault diagnosis in the outdoor field. It hosts the proposed approach on a low-cost FPGA. The outdoor field experiments demonstrate the operation of the proposed approach in real-time and field conditions for a variety of fault types. The experimental results and their analysis show the effectiveness of the fault diagnosis approach for easy maintenance and online fault remediation, thus integrating reliability and fault tolerance.

The broad benefits of the digital twin based fault diagnosis approach for distributed power electronic-based PV systems are: 1) it can quickly detect and precisely identify a variety

0885-8993 (c) 2018 IEEE. Personal use is permitted, but republication/redistribution requires IEEE permission. See http://www.ieee.org/publications_standards/publications/rights/index.html for more information.

This article has been accepted for publication in a future issue of this journal, but has not been fully edited. Content may change prior to final publication. Citation information: DOI 10.1109/TPEL.2019.2911594, IEEE Transactions on Power Electronics

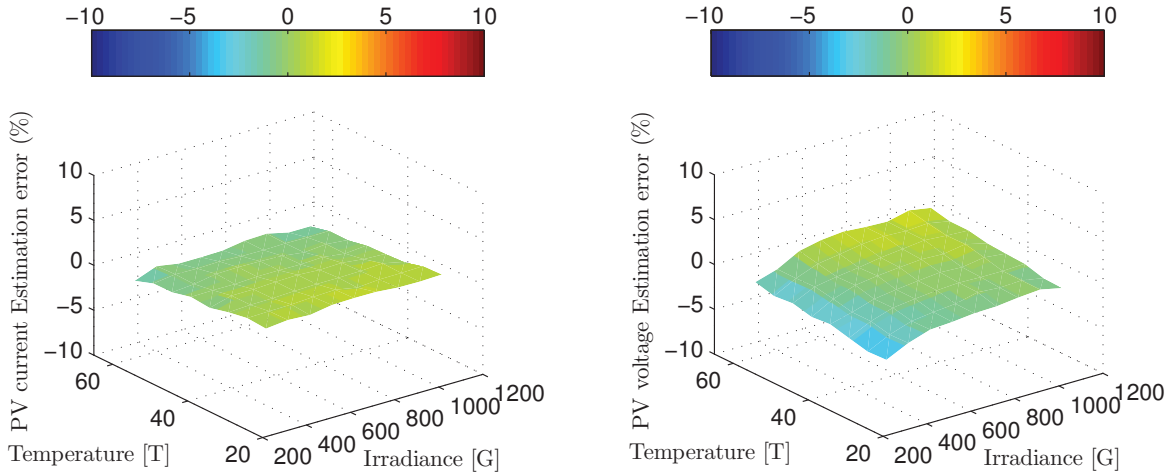

(a) Estimation error in % for PV panel current at MPP.

(b) Estimation error in % for PV panel voltage at MPP.

Fig. 18: Estimation errors with respect to the measured values for operating range of G and T for a PV panel.

of fault types including incipient faults; 2) its framework is converter topology-agnostic and independent of type of PV installation and power conversion architecture; 3) it adds minimal system complexity due to multitasking (i.e. both fault diagnosis and control) of a power converter computing platform. Moreover, the proposed approach is general in the sense that it can be applied to another energy conversion system (e.g. a battery energy system).

APPENDIX A
ESTIMATION ERRORS FOR PV PANEL OPERATING CURRENT AND VOLTAGE AT MPP

Fig. 18a [Fig. 18b] presents the estimation errors with respect to the measured values in the PV panel operating current [voltage] at MPP as a function of operating range of irradiance G and temperature T. The estimation error for a given G and T is computed by subtracting the real PV panel current [voltage] value at MPP from the estimated value by (2) [(3)]. The current-voltage $(I-V)$ curves of a crystalline silicon PV panel are measured to obtain the real PV panel values under regulated G and T conditions. It is shown that the estimation errors are well within $\pm 5\%$ envelope. The fault diagnosis approach is immune to these errors due to the careful selection of the threshold values.

APPENDIX B
FAULT SIGNATURE LIBRARY FOR FI IN A PVECU

Table VI presents the fault signature library which is used to identify the fault type in the FI methodology in Section IV-B.

REFERENCES

[1] P. Jain, J. X. Xu, S. K. Panda, J. Poon, C. Spanos, and S. R. Sanders, "Fault diagnosis via PV panel-integrated power electronics," in *2016 IEEE 17th Workshop on Control and Modeling for Power Electronics (COMPEL)*, pp. 1–6, June 2016.

[2] G. R. Walker and P. C. Sernia, "Cascaded DC-DC converter connection of photovoltaic modules," *IEEE Transactions on Power Electronics*, vol. 19, pp. 1130–1139, July 2004.

[3] L. Linares, R. W. Erickson, S. MacAlpine, and M. Brandemuehl, "Improved energy capture in series string photovoltaics via smart distributed power electronics," in *Twenty-Fourth Annual IEEE Applied Power Electronics Conference and Exposition (APEC), 2009.*, pp. 904–910, Feb 2009.

[4] NREL, "Building America case study: Photovoltaic systems with module-level power electronics. Technology solutions for new and existing homes, energy efficiency & renewable energy (EERE)," no. NREL/FS-5500-64876, pp. 1–2, 2015.

[5] U.S. Department of Energy, "Quadrennial technology review - an assessment of energy technologies and research opportunities," 2015.

[6] P. S. Shenoy, K. A. Kim, B. B. Johnson, and P. T. Krein, "Differential power processing for increased energy production and reliability of photovoltaic systems," *IEEE Transactions on Power Electronics*, vol. 28, pp. 2968–2979, June 2013.

[7] O. Carlos, M. Dragan, D. Chris, and M. Luis, "Impact of distributed power electronics on the lifetime and reliability of PV systems," *Progress in Photovoltaics: Research and Applications*, vol. 25, no. 10, pp. 821–835.

[8] M. Kasper, D. Bortis, and J. W. Kolar, "Classification and comparative evaluation of PV panel-integrated DC-DC converter concepts," *IEEE Transactions on Power Electronics*, vol. 29, pp. 2511–2526, May 2014.

[9] A. M. Bazzi, K. A. Kim, B. B. Johnson, P. T. Krein, and A. Dominguez-Garcia, "Fault impacts on solar power unit reliability," in *2011 Twenty-Sixth Annual IEEE Applied Power Electronics Conference and Exposition (APEC)*, pp. 1223–1231, March 2011.

[10] A. Sastry, S. Kulasekaran, J. Flicker, R. Ayyanar, G. TamizhMani, J. Roy, D. Srinivasan, and I. Tilford, "Failure modes and effect analysis of module level power electronics," in *2015 IEEE 42nd Photovoltaic Specialist Conference (PVSC)*, pp. 1–3, June 2015.

[11] M. K. et al., "Assessment of photovoltaic module failures in the field," in *International Energy Agency, Photovoltaic Power Systems Programme*, May 2017.

[12] R. J. Patton, P. M. Frank, and R. N. Clarke, *Fault Diagnosis in Dynamic Systems: Theory and Application*. Upper Saddle River, NJ: Prentice-Hall, Inc., Oct. 1989.

[13] E. Ribeiro, A. J. M. Cardoso, and C. Boccaletti, "Fault-tolerant strategy for a photovoltaic DC–DC converter," *IEEE Transactions on Power Electronics*, vol. 28, pp. 3008–3018, June 2013.

[14] E. Jamshidpour, P. Poure, and S. Saadate, "Photovoltaic systems reliability improvement by real-time FPGA-based switch failure diagnosis and fault-tolerant DC-DC converter," *IEEE Transactions on Industrial Electronics*, vol. 62, pp. 7247–7255, Nov 2015.

[15] J. Poon, P. Jain, I. C. Konstantakopoulos, C. Spanos, S. K. Panda, and S. R. Sanders, "Model-based fault detection and identification for switching power converters," *IEEE Transactions on Power Electronics*, vol. 32, pp. 1419–1430, Feb 2017.

[16] K. A. Kim, G. S. Seo, B. H. Cho, and P. T. Krein, "Photovoltaic hot-spot detection for solar panel substrings using AC parameter charac-

0885-8993 (c) 2018 IEEE. Personal use is permitted, but republication/redistribution requires IEEE permission. See http://www.ieee.org/publications_standards/publications/rights/index.html for more information.

This article has been accepted for publication in a future issue of this journal, but has not been fully edited. Content may change prior to final publication. Citation information: DOI 10.1109/TPEL.2019.2911594, IEEE Transactions on Power Electronics

TABLE VI
FAULT SIGNATURE LIBRARY

Fault type	Fault event	Fault magnitude ($\frac{1}{\xi(t)}$)	Fault signature ($\mathbf{f}_i$)
PV panel faults			
$i=1$	Soiling, Continuous mild partial shading, Mild cells breakage, EVA browning	$\frac{\Delta I_{pv}^{ref} G\left(1+K_i(T-T^{ref})\right)}{G^{ref}}$	$[0,0,1,0]^T$
$i=2$	Bypass diode failures, Continuous severe partial shading, Severe cells breakage	$\frac{\Delta V_{pv}^{ref}\left(1+K_p(T-T^{ref})\right)}{1+K_i(T-T^{ref})}$	$[0,0,0,1]^T$
$i=3$	Interconnect faults, PID, Faults related to PV shunt and series resistances	$\left\{ \begin{array}{l} \left(\frac{\Delta I_{pv}^{ref} G\left(1+K_i(T-T^{ref})\right)}{G^{ref}}\right)^2 \\ +\left(\frac{\Delta V_{pv}^{ref}\left(1+K_p(T-T^{ref})\right)}{1+K_i(T-T^{ref})}\right)^2 \end{array} \right\}^{\frac{1}{2}}$	$\xi \left[\begin{array}{l} 0,0, \\ \frac{\Delta I_{pv}^{ref} G\left(1+K_i(T-T^{ref})\right)}{G^{ref}}, \\ \frac{\Delta V_{pv}^{ref}\left(1+K_p(T-T^{ref})\right)}{1+K_i(T-T^{ref})} \end{array} \right]^T$
Power converter faults			
$i=4$	Open switch fault in SW_1	$\left\{ \begin{array}{l} \left(\frac{i_{load}(t)}{D_{s_3}}\right)^2 \\ +\left(\frac{R*i_{load}(t)-D_{s_1}*D_{s_3}*v_{pv}(t)}{D_{s_3}^2}\right)^2 \\ +\left(\frac{I_{pv}^{ref} G\left(1+K_i(T-T^{ref})\right)}{G^{ref}}\right)^2 \\ +\left(\frac{V_{pv}^{ref}\left(1+K_p(T-T^{ref})\right)}{1+K_i(T-T^{ref})}-V_{oc}\right)^2 \end{array} \right\}^{\frac{1}{2}}$	$\xi \left[\begin{array}{l} \frac{i_{load}(t)}{D_{s_3}}, \\ -\frac{R*i_{load}(t)-D_{s_1}*D_{s_3}*v_{pv}(t)}{D_{s_3}^2}, \\ \frac{I_{pv}^{ref} G\left(1+K_i(T-T^{ref})\right)}{G^{ref}}, \\ \frac{V_{pv}^{ref}\left(1+K_p(T-T^{ref})\right)}{1+K_i(T-T^{ref})}-V_{oc} \end{array} \right]^T$
$i=5$	Short switch fault in SW_1	$\left\{ \begin{array}{l} \left(\frac{i_{load}(t)}{D_{s_3}}-i_L(t)\right)^2 \\ +\left(\frac{I_{pv}^{ref} G\left(1+K_i(T-T^{ref})\right)}{G^{ref}}-i_{pv}(t)\right)^2 \\ +\left(\frac{V_{pv}^{ref}\left(1+K_p(T-T^{ref})\right)}{1+K_i(T-T^{ref})}-v_{pv}(t)\right)^2 \end{array} \right\}^{\frac{1}{2}}$	$\xi \left[\begin{array}{l} \frac{i_{load}(t)}{D_{s_3}}-i_L(t),0, \\ \frac{I_{pv}^{ref} G\left(1+K_i(T-T^{ref})\right)}{G^{ref}}-i_{pv}(t), \\ \frac{V_{pv}^{ref}\left(1+K_p(T-T^{ref})\right)}{1+K_i(T-T^{ref})}-v_{pv}(t) \end{array} \right]^T$
$i=6$	Open switch fault in SW_2	$\left\{ \begin{array}{l} \left(\frac{i_{load}(t)}{D_{s_3}}-i_L(t)\right)^2 \\ +\left(\frac{R*i_{load}(t)-D_{s_1}*D_{s_3}*v_{pv}(t)}{D_{s_3}^2}\right)^2 \\ +\left(\frac{I_{pv}^{ref} G\left(1+K_i(T-T^{ref})\right)}{G^{ref}}-i_{pv}(t)\right)^2 \\ +\left(\frac{V_{pv}^{ref}\left(1+K_p(T-T^{ref})\right)}{1+K_i(T-T^{ref})}-v_{pv}(t)\right)^2 \end{array} \right\}^{\frac{1}{2}}$	$\xi \left[\begin{array}{l} \frac{i_{load}(t)}{D_{s_3}}-i_L(t), \\ -\frac{R*i_{load}(t)-D_{s_1}*D_{s_3}*v_{pv}(t)}{D_{s_3}^2}, \\ \frac{I_{pv}^{ref} G\left(1+K_i(T-T^{ref})\right)}{G^{ref}}-i_{pv}(t), \\ \frac{V_{pv}^{ref}\left(1+K_p(T-T^{ref})\right)}{1+K_i(T-T^{ref})}-v_{pv}(t) \end{array} \right]^T$
$i=7$	Short switch fault in SW_2	$\left\{ \begin{array}{l} \left(\frac{i_{load}(t)}{D_{s_3}}\right)^2 \\ +\left(\frac{R*i_{load}(t)-D_{s_1}*D_{s_3}*v_{pv}(t)}{D_{s_3}^2}\right)^2 \\ +\left(\frac{I_{pv}^{ref} G\left(1+K_i(T-T^{ref})\right)}{G^{ref}}-I_{sc}\right)^2 \\ +\left(\frac{V_{pv}^{ref}\left(1+K_p(T-T^{ref})\right)}{1+K_i(T-T^{ref})}\right)^2 \end{array} \right\}^{\frac{1}{2}}$	$\xi \left[\begin{array}{l} \frac{i_{load}(t)}{D_{s_3}}, -\frac{R*i_{load}(t)-D_{s_1}*D_{s_3}*v_{pv}(t)}{D_{s_3}^2}, \\ \frac{I_{pv}^{ref} G\left(1+K_i(T-T^{ref})\right)}{G^{ref}}-I_{sc}, \\ \frac{V_{pv}^{ref}\left(1+K_p(T-T^{ref})\right)}{1+K_i(T-T^{ref})} \end{array} \right]^T$
$i=8$	Open switch fault in SW_3	$\left\{ \begin{array}{l} \left(\frac{i_{load}(t)}{D_{s_3}}\right)^2 \\ +\left(\frac{R*i_{load}(t)-D_{s_1}*D_{s_3}*v_{pv}(t)}{D_{s_3}^2}-v_C(t)\right)^2 \\ +\left(\frac{I_{pv}^{ref} G\left(1+K_i(T-T^{ref})\right)}{G^{ref}}\right)^2 \\ +\left(\frac{V_{pv}^{ref}\left(1+K_p(T-T^{ref})\right)}{1+K_i(T-T^{ref})}-V_{oc}\right)^2 \end{array} \right\}^{\frac{1}{2}}$	$\xi \left[\begin{array}{l} \frac{i_{load}(t)}{D_{s_3}}, \\ -\frac{R*i_{load}(t)-D_{s_1}*D_{s_3}*v_{pv}(t)}{D_{s_3}^2}-v_C(t), \\ \frac{I_{pv}^{ref} G\left(1+K_i(T-T^{ref})\right)}{G^{ref}}, \\ \frac{V_{pv}^{ref}\left(1+K_p(T-T^{ref})\right)}{1+K_i(T-T^{ref})}-V_{oc} \end{array} \right]^T$
$i=9$	Short switch fault in SW_3	$\left\{ \begin{array}{l} \left(\frac{i_{load}(t)}{D_{s_3}}-i_L(t)\right)^2, \\ +\left(\frac{I_{pv}^{ref} G\left(1+K_i(T-T^{ref})\right)}{G^{ref}}-i_{pv}(t)\right)^2 \\ +\left(\frac{V_{pv}^{ref}\left(1+K_p(T-T^{ref})\right)}{1+K_i(T-T^{ref})}-v_{pv}(t)\right)^2 \end{array} \right\}^{\frac{1}{2}}$	$\xi \left[\begin{array}{l} \frac{i_{load}(t)}{D_{s_3}}-i_L(t),0, \\ \frac{I_{pv}^{ref} G\left(1+K_i(T-T^{ref})\right)}{G^{ref}}-i_{pv}(t), \\ \frac{V_{pv}^{ref}\left(1+K_p(T-T^{ref})\right)}{1+K_i(T-T^{ref})}-v_{pv}(t) \end{array} \right]^T$

continued to next page

0885-8993 (c) 2018 IEEE. Personal use is permitted, but republication/redistribution requires IEEE permission. See http://www.ieee.org/publications_standards/publications/rights/index.html for more information.

This article has been accepted for publication in a future issue of this journal, but has not been fully edited. Content may change prior to final publication. Citation information: DOI 10.1109/TPEL.2019.2911594, IEEE Transactions on Power Electronics

TABLE VI: *CONTINUED FROM PREVIOUS PAGE*

Fault type	Fault event	Fault magnitude ($\frac{1}{\xi}$)	Fault signature ($\mathbf{f}_i$)
Power converter faults			
$i=10$	Open switch fault in SW_4	$\left\{ \begin{array}{l} \left(\frac{(1-D_{s_3})*i_{load}(t)}{D_{s_3}}\right)^2 + \\ \left(\frac{D_{s_3}^2 v_{pv}(t)+R*i_{load}(t)-D_{s_1}*D_{s_3}*v_{pv}(t)}{D_{s_3}^2}\right)^2 \\ + \left(\frac{I_{pv}^{ref} G\left(1+K_i(T-T^{ref})\right)}{G^{ref}} - i_{pv}(t)\right)^2 \\ + \left(\frac{V_{pv}^{ref}\left(1+K_p(T-T^{ref})\right)}{1+K_i(T-T^{ref})} - v_{pv}(t)\right)^2 \end{array} \right\}^{\frac{1}{2}}$	$\xi \left[\begin{array}{l} \frac{(1-D_{s_3})*i_{load}(t)}{D_{s_3}}, \\ \frac{-D_{s_3}^2 v_{pv}(t)-R*i_{load}(t)+D_{s_1}*D_{s_3}*v_{pv}(t)}{D_{s_3}^2}, \\ \frac{I_{pv}^{ref} G\left(1+K_i(T-T^{ref})\right)}{G^{ref}} - i_{pv}(t), \\ \frac{V_{pv}^{ref}\left(1+K_p(T-T^{ref})\right)}{1+K_i(T-T^{ref})} - v_{pv}(t) \end{array} \right]^T$
$i=11$	Short switch fault in SW_4	$\left\{ \begin{array}{l} \left(\frac{i_{load}(t)}{D_{s_3}} - i_L(t)\right)^2 \\ + \left(\frac{R*i_{load}(t)-D_{s_1}*D_{s_3}*v_{pv}(t)}{D_{s_3}^2}\right)^2 \\ + \left(\frac{I_{pv}^{ref} G\left(1+K_i(T-T^{ref})\right)}{G^{ref}} - I_{sc}\right)^2 \\ + \left(\frac{V_{pv}^{ref}\left(1+K_p(T-T^{ref})\right)}{1+K_i(T-T^{ref})}\right)^2 \end{array} \right\}^{\frac{1}{2}}$	$\xi \left[\begin{array}{l} \frac{i_{load}(t)}{D_{s_3}} - i_L(t), \\ -\frac{R*i_{load}(t)-D_{s_1}*D_{s_3}*v_{pv}(t)}{D_{s_3}^2}, \\ \frac{I_{pv}^{ref} G\left(1+K_i(T-T^{ref})\right)}{G^{ref}} - I_{sc}, \\ \frac{V_{pv}^{ref}\left(1+K_p(T-T^{ref})\right)}{1+K_i(T-T^{ref})} \end{array} \right]^T$
Electrical sensor faults			
$i=12$	Fault in $i_L(t)$ sensor	$\Delta c_{12}(t) i_L(t) + \Delta e_{12}(t)$	$[1,0,0,0]^T$
$i=13$	Fault in $v_C(t)$ sensor	$\Delta c_{13}(t) v_C(t) + \Delta e_{13}(t)$	$[0,1,0,0]^T$
$i=14$	Fault in $i_{load}(t)$ sensor	$\frac{\Delta c_{14}(t) i_{load}(t)+\Delta e_{14}(t)}{D_{s_3}} \sqrt{1+\left(\frac{R}{D_{s_3}}\right)^2}$	$\frac{1}{\sqrt{1+\left(\frac{R}{D_{s_3}}\right)^2}} [1, -\frac{R}{D_{s_3}}, 0, 0]^T$
$i=15$	Fault in $v_{pv}(t)$ sensor	$\Delta c_{15}(t) v_{pv}(t) + \Delta e_{15}(t) \sqrt{\left(\frac{D_{s_1}}{D_{s_3}}\right)^2 + 1}$	$\frac{1}{\sqrt{\left(\frac{D_{s_1}}{D_{s_3}}\right)^2+1}} [0, \frac{D_{s_1}}{D_{s_3}}, 0, 1]^T$
$i=16$	Fault in $i_{pv}(t)$ sensor	$\Delta c_{16}(t) i_{pv}(t) + \Delta e_{16}(t)$	$[0,0,1,0]^T$

I_{sc} = PV panel short circuit current, V_{oc} = PV panel open circuit voltage, D_{s_1} = duty cycle for SW_1, D_{s_3} = duty cycle for SW_3
$\Delta c_i(t)$ = drift in sensor gain, $\Delta e_i(t)$ = offset

terization," *IEEE Transactions on Power Electronics*, vol. 31, no. 2, pp. 1121–1130, 2016.

[17] J. Solrzano and M. A. Egido, "Automatic fault diagnosis in PV systems with distributed MPPT," *Energy Conversion and Management*, vol. 76, pp. 925–934, 2013.

[18] W. Wang, A. C. F. Liu, H. S. H. Chung, R. W. H. Lau, J. Zhang, and A. W. L. Lo, "Fault diagnosis of photovoltaic panels using dynamic Current-Voltage characteristics," *IEEE Transactions on Power Electronics*, vol. 31, pp. 1588–1599, Feb 2016.

[19] M. K. Alam, F. H. Khan, J. Johnson, and J. Flicker, "PV faults: Overview, modeling, prevention and detection techniques," in *2013 IEEE 14th Workshop on Control and Modeling for Power Electronics (COMPEL)*, pp. 1–7, June 2016.

[20] V. Sharma and S. S. Chandel, "Performance and degradation analysis for long term reliability of solar photovoltaic systems: A review," *Renewable and Sustainable Energy Reviews*, vol. 27, pp. 753–767, 2013.

[21] H. Wang, M. Liserre, and F. Blaabjerg, "Toward reliable power electronics: Challenges, design tools, and opportunities," *IEEE Industrial Electronics Magazine*, vol. 7, no. 2, pp. 17–26, 2013.

[22] H. Wang, M. Liserre, F. Blaabjerg, P. de Place Rimmen, J. B. Jacobsen, T. Kvisgaard, and J. Landkildehus, "Transitioning to physics-of-failure as a reliability driver in power electronics," *IEEE Journal of Emerging and Selected Topics in Power Electronics*, vol. 2, no. 1, pp. 97–114, 2014.

[23] S. Yang, D. Xiang, A. Bryant, P. Mawby, L. Ran, and P. Tavner, "Condition monitoring for device reliability in power electronic converters: A review," *IEEE Transactions on Power Electronics*, vol. 25, no. 11, pp. 2734–2752, 2010.

[24] "SunSpec logging in SolarEdge inverters," Technical Documentation, SolarEdge, July 2016.

[25] "Enlighten manager for Solar Professionals," Features Sheet, Enphase, 2017.

[26] E. H. Glaessgen and D. S. Stargel, "The digital twin paradigm for future NASA and U.S. air force vehicles," in *53rd AIAA/ASME/ASCE/AHS/ASC Structures, Structural Dynamics and Materials Conference - Special Session on the Digital Twin, Honolulu, HI, United States*, p. 20120008178, April 2012.

[27] R. K. Hester, C. Thornton, S. Dhople, Z. Zhao, N. Sridhar, and D. Freeman, "High efficiency wide load range buck/boost/bridge photovoltaic microconverter," in *Twenty-Sixth Annual IEEE Applied Power Electronics Conference and Exposition (APEC), 2011*, pp. 309–313, March 2011.

[28] J. G. Kassakian, M. Schlecht, and G. C. Verghese, *Principles of Power Electronics*. Addison-Wesley, 1991.

[29] M. G. Villalva, J. R. Gazoli, and E. R. Filho, "Comprehensive approach to modeling and simulation of photovoltaic arrays," *IEEE Transactions on Power Electronics*, vol. 24, pp. 1198–1208, May 2009.

[30] J. Rosell and M. Ibez, "Modelling power output in photovoltaic modules for outdoor operating conditions," *Energy Conversion and Management*, vol. 47, no. 15, pp. 2424 – 2430, 2006.

[31] W. Luo, Y. S. Khoo, P. Hacke, V. Naumann, D. Lausch, S. P. Harvey, J. P. Singh, J. Chai, Y. Wang, A. G. Aberle, and S. Ramakrishna, "Potential-induced degradation in photovoltaic modules: a critical review," *Energy Environ. Sci.*, vol. 10, pp. 43–68, 2017.

[32] S. Karimi, A. Gaillard, P. Poure, and S. Saadate, "FPGA-based real-time power converter failure diagnosis for wind energy conversion systems," *IEEE Transactions on Industrial Electronics*, vol. 55, pp. 4299–4308, Dec 2008.

[33] A. Youssef, S. El Khil, and I. Slama-Belkhodja, "State observer-based sensor fault detection and isolation, and fault tolerant control of a single-phase PWM rectifier for electric railway traction," *IEEE Transactions on Power Electronics*, vol. 28, pp. 5842–5853, Dec 2013.

[34] S. Nie, X. Pei, Y. Chen, and Y. Kang, "Fault diagnosis of PWM DC-DC converters based on magnetic component voltages equation," *IEEE Transactions on Power Electronics*, vol. 29, pp. 4978–4988, Sept 2014.

0885-8993 (c) 2018 IEEE. Personal use is permitted, but republication/redistribution requires IEEE permission. See http://www.ieee.org/publications_standards/publications/rights/index.html for more information.

This article has been accepted for publication in a future issue of this journal, but has not been fully edited. Content may change prior to final publication. Citation information: DOI 10.1109/TPEL.2019.2911594, IEEE Transactions on Power Electronics

Palak Jain (S'15) received her B.E. degree in electrical engineering from Delhi College of Engineering, University of Delhi, India in 2012. She is currently working on her Ph.D with the Department of Electrical and Computer Engineering, National University of Singapore, Singapore. Her research lies at the intersection of power electronics, cyber-physical systems, responsive and resilient energy systems, identification, estimation and learning techniques. She has held R&D positions with Xilinx Research Labs, Solar Energy Research Institute of Singapore, and University of California, Berkeley. Prior to her doctoral studies, she has worked and managed various power plant projects, both thermal and solar PV based at National thermal power Corporation (NTPC) Ltd., India. Ms. Palak is a recipient of a Best Paper Award at 2016 IEEE Workshop on Control and Modeling for Power Electronics, a General Manager Meritorious Award from NTPC Ltd., the Chief Minister's Gold Medal for the best undergraduate student, and the D. V. Kohli Gold Medal for the best electrical engineer from Delhi college of Engineering, University of Delhi, India.

Jason Poon (S'11) received the B.S. degree from the Olin College of Engineering, Needham, MA, USA, in 2012, and the M.S. degree from the University of California, Berkeley, CA, USA, in 2015, both in electrical engineering. He is currently working toward the Ph.D. degree with the Department of Electrical Engineering and Computer Sciences, University of California, Berkeley. He has held R&D positions with Dialog Semiconductor, ABB Corporate Research, the National Renewable Energy Laboratory, the Massachusetts Institute of Technology, the National University of Singapore, and Typhoon HIL. His research interests include the design, control, and optimization of power electronics circuits and systems. Mr. Poon is a recipient of the National Science Foundation Graduate Research Fellowship, the National Defense Science and Engineering Graduate Fellowship, and a Best Paper Award at the 2016 IEEE Workshop on Control and Modeling for Power Electronics for his work on distributed fault-tolerant power electronics.

Jai Prakash Singh is heading Advance PV Module Technology team at Solar Energy Research Institute of Singapore (SERIS). In 2015, he received his PhD degree in Electrical and Computer Engineering from National University of Singapore. He also holds M.Tech degree in Energy Science and Engineering from Indian Institute of Technology (IIT) Bombay, Mumbai and B.Tech degree in Electrical Engineering from Jamia Millia Islamia University, New Delhi. Jai Prakash has more than 10 years of experience on c-Si solar cell and module R&D. In 2008, he joined Moser Baer Photovoltaic as senior R&D engineer and in 2010, he joined PV module group at the SERIS. His research work focuses on advance PV module development, bifacial device characterization, simulation & loss analysis, failure analysis and reliability study of c-Si PV modules, Building-Integrated PV, smart module concepts and PV recycling.

Costas Spanos (M'87–SM'92–F'98) received the EE Diploma from the National Technical University of Athens, Greece in 1980 and the M.S. and Ph.D. degrees in ECE from Carnegie Mellon University in 1981 and 1985, respectively. In 1988 he joined the Faculty at the department of Electrical Engineering and Computer Sciences of the University of California, Berkeley. He has served as the Director of the Berkeley Microlab, the Associate Dean for Research in the College of Engineering and as the Chair of the Department of EECS. He works in statistical analysis in the design and fabrication of integrated circuits, and on novel sensors and computer-aided techniques in semiconductor manufacturing. He also works on statistical data mining techniques for energy efficiency applications. He has participated in two successful startup companies, Timbre Tech, (acquired by Tokyo Electron) and OnWafer Technologies (acquired by KLA-Tencor). He is presently the Director of the Center of Information Technology Research in the Interest of Society (CITRIS) and the Chief Technical Officer for the Berkeley Educational Alliance for Research in Singapore (BEARS).

Seth R. Sanders (S'88–M'88–SM'08–F'10) is Professor in the Department of Electrical Engineering and Computer Sciences at the University of California, Berkeley. He received B.S. degree (1981) in Electrical Engineering and Physics, and the M.S. (1985) and Ph.D. (1989) degrees in Electrical Engineering from the Massachusetts Institute of Technology, Cambridge. Following an early experience as a Design Engineer at the Honeywell Test Instruments Division in 1981-83, he joined the UC Berkeley faculty in 1989. Dr. Sanders technical interests are in electrical energy and power conversion systems . Dr. Sanders is presently or has recently been active in supervising research projects in the areas of flywheel energy storage, electric machine design, renewable energy systems, integrated power conversion circuits, and IC designs for power conversion applications. Dr. Sanders is co-founder and CTO of Amber Kinetics, Inc., a technology developer, manufacturer, and project developer of utility scale flywheel energy storage systems. During the 1992-1993 academic year, he was on industrial leave with National Semiconductor, Santa Clara, CA. Dr. Sanders received the NSF Young Investigator Award and multiple Best Paper Awards from the IEEE Power Electronics and the IEEE Industry Applications Societies. He has served as Chair of the IEEE PELS Technical Committee on Computers in Power Electronics, Chair of the IEEE PELS Technical Committee on Power Conversion Components and Systems, and as Member-At-Large of the IEEE PELS Adcom. He is an IEEE Fellow, a Distinguished Lecturer of the IEEE PELS and IAS societies, and recipient of the IEEE PELS Modeling and Control Technical Achievement Award.

Sanjib Kumar Panda (S'86-M'91-SM'01) received the B.Eng. degree from the South Gujarat University, Surat, India, in 1983, the M.Tech. degree from the Indian Institute of Technology, Banaras Hindu University, Varanasi, India, in 1987, and the Ph.D. degree from the University of Cambridge, Cambridge, U.K., in 1991, all in electrical engineering. Since 1992, he has been holding a Faculty Position in the Department of Electrical and Computer Engineering, National University of Singapore, Singapore, and currently serving as an Associate Professor and the Director of the Power & Energy Research Area. He has published more than 200 peer reviewed research papers, coauthored one book and contributed to several book chapters, and six patents. His research interests include high-performance control of motor drives and power electronic converters, condition monitoring and condition based maintenance, building energy efficiency, etc. Dr. Panda received the Cambridge-Nehru Scholarship and M. T. Mayer Graduate Scholarship during his Ph.D. study (1987-1991). He is serving as an Associate Editor of several IEEE Transactions and the Editor of the Journal of Power Electronics, South Korea. He has served in various capacities for the two key conferences IEEE Power Electronics and Drive Systems Conference and IEEE International Conference on Sustainable Energy Technologies Conference series organized and managed by the IEEE Joint Industry Applications Society/ Power Electronics Society (PELS) Society Chapter, Singapore Section. He has served the IEEE Section Congress 2014 as a member of the Program Committee. He is serving as the IEEE R-10 Asia Pacific Liaison Officer for the IEEE PELS. He has received the IEEE Third Millennium Medal, the IEEE Singapore Section Outstanding Volunteer Award in 2010, and the IEEE Region-10 Outstanding Volunteer Award in 2014.

0885-8993 (c) 2018 IEEE. Personal use is permitted, but republication/redistribution requires IEEE permission. See http://www.ieee.org/publications_standards/publications/rights/index.html for more information.

A Filter-Wrapper based Feature Selection for Optimized Website Quality Prediction

Akshi Kumar[#], Anshika Arora[*]

[#]*Department of Computer Science and Engineering, Delhi Technological University, Delhi, India*

[1]akshikumar@dce.ac.in

[*]*Department of Computer Science and Engineering, Delhi Technological University, Delhi, India*

[2]anshika.arora10nov@gmail.com

***Abstract*— A Website quality model essentially consists of a set of criteria used to determine if a website reaches certain levels of fineness. Quality attributes are imperative in predicting quality of a website. However large set features may increase model complexity and computational time for prediction. In this study an initial set of 13 quality attributes is prepared and two-stage feature selection based on hybrid filter-wrapper approach is used to optimize website quality prediction performance. In the first stage, each feature is ranked using the Information Gain (IG) method. In the second stage, Firefly Search Algorithm (FA) is applied to features which are ranked higher in the first stage and a feature sub-selection is carried out. In order to evaluate the effectiveness of feature selection method experiments are conducted using four baseline classification algorithms on a dataset prepared by 700 websites. The experimental results show that the proposed model is able to achieve high classification performance. An average of 36.53% reduction in features has been observed which leads to 0.015 seconds of average reduction in time for building a classifier and an average improvement of 5.420% in classification accuracy.**

***Keywords*— website quality, feature selection, classification, prediction, filter, wrapper, firefly search, information gain**

I. INTRODUCTION

The number of websites is progressively increasing with the growth of e-commerce engendering the need for website quality prediction. Website quality prediction includes development of a measure of website quality that predicts consumer use of a site. It is critical that an instrument specifically designed to measure the consumer's perception of website quality is developed. Website quality can be predicted using various quality attributes. In this work 16 quality attributes have been analysed that are necessary and sufficient for website quality prediction. Out of these 13 attributes are evaluated namely: Relevance, Total Size, Broken Links, Communication, Loading Time, Social Media Connectivity, Overall Theme, Compatibility, Global Audience, Resolution, Typography and Font, Colour Scheme, and Keyword matching or Page Rank. These quality attributes act as features for the dataset prepared by 700 websites constituting of 100 websites each from seven top-level domains namely: .com, .net, .org, .int, .gov, .edu and .mil further performing classification of these websites categorising them into three classes i.e. good, average, and poor. However, having a large set of features may increase computational complexity and training time for building a classifier. This may also bring about inefficiency and results of low accuracy due to redundant or irrelevant features in the feature space. For solving this problem, a two-stage filter-wrapper based feature selection using Information Gain as the filter method and Firefly Search Algorithm as the wrapper method has been developed.

978-1-5386-9346-9/19/$31.00 ©2019 IEEE

"Feature selection is a process of selecting a subset of features from the original feature set". This is done according to some criteria based on feature importance [1].

Existing feature selection techniques can be broadly classified into two groups: filter approaches and wrapper approaches depending on the evaluation measures that they use in distinguishing the different class labels. The key difference between the two algorithms is that filter algorithms select the feature subset prior to the application of any classification algorithm, i.e. they are classification independent. The filter approach eradicates the less important features by using statistical properties of features. Wrapper algorithms select the features according to the accuracy of the training data and afterwards learn and test the classification model using the test data. Generally, for the implementation of wrapper methods learning algorithm and the performance criteria are defined.

In this work a hybrid (filter-wrapper) feature selection model has been developed to reduce the feature dimension in order to predict website quality. In the first stage, each feature in the dataset is ranked using the Information Gain (IG) method. The features are ranked as per their importance for the classification in descending order where features of high importance are assigned to the first ranks and features of less importance are assigned to lower rank. Only high ranked features are selected and carried forward to the next stage. In the second stage, the Firefly Search method based on Firefly Algorithm (FA) is used for feature selection and dimension reduction is carried out. The feature subset selected by IG+FA is used to train four baseline classifiers namely: Naïve Bayes (NB), K-Nearest Neighbor (KNN), Decision Trees (DT), and Random Forest (RF). The results are expressed in terms of (i) reduction in features, (ii) reduction in training time of classifier, and (iii) improvement in performance of classifier.

The rest of the paper is structured as follows: Section 2 discusses the background work done within the domain of website quality and models. Section 3 describes the system architecture along with the details of the proposed optimal supervised learning model using filter-wrapper based feature selection. Section 4 discusses the results followed by section 5, which presents the conclusion of the empirical study.

II. RELATED WORK

The success with website's discoverability on the web

and visitor engagement is fundamentally related to the "quality" of website. Pertinent studies propose web quality models to facilitate website evaluation and assessment based on various quality parameters/attributes. WebQual is one such model developed by Loiacono et al. [2] which measures website quality based on 12 core dimensions. The instrument was developed and validated using 3 samples. In 2009, Sørum et al. [3], broadly categorised quality attributes as information quality, system quality, and service quality and address the norms used by national web awards to measure the website quality in Scandinavian countries. Hartmann et al.
[4] have explained how framing of website affects the user judgement of website quality and explored the contextual factors that influence user experience. The authors also focussed on how the presentation of information about a website influence user experience and gave a framework of user judgement and decision making. Sobecki and Żatuchin [5] have described methods for website usability evaluation, quality of website interface, and models for organizing data in frames further to be used in an expert system. WA—Web Assessment tool was also developed based on the three phases of a transaction (information, agreement, and settlement) by the Schubert and Selz [6, 7]. An extended model of the same, that is, an Extended Web Assessment Model (EWAM) which includes elements of TAM, social influence, and reviewing four practitioner reports on Web evaluation was also proposed by Schubert and Dettling [8]. As per the best of our knowledge, no work has been done up till now on Feature Selection in the domain of website quality evaluation. This research is the first one to adopt filter-wrapper based feature selection using IG and FA methods for Website Quality Prediction.

III. FILTER-WRAPPER BASED WEBSITE QUALITY PREDICTION MODEL

In this work, a two-stage feature selection model has been developed to improve the performance of website quality prediction. To evaluate the performance dimensionality reduction method on our proposed model, experiments are conducted using four classification algorithms on dataset consisting of 700 websites for website quality prediction.

Fig. 1 explains the system architecture giving insight to the step by step process of website quality prediction model using feature selection and supervised classification techniques.

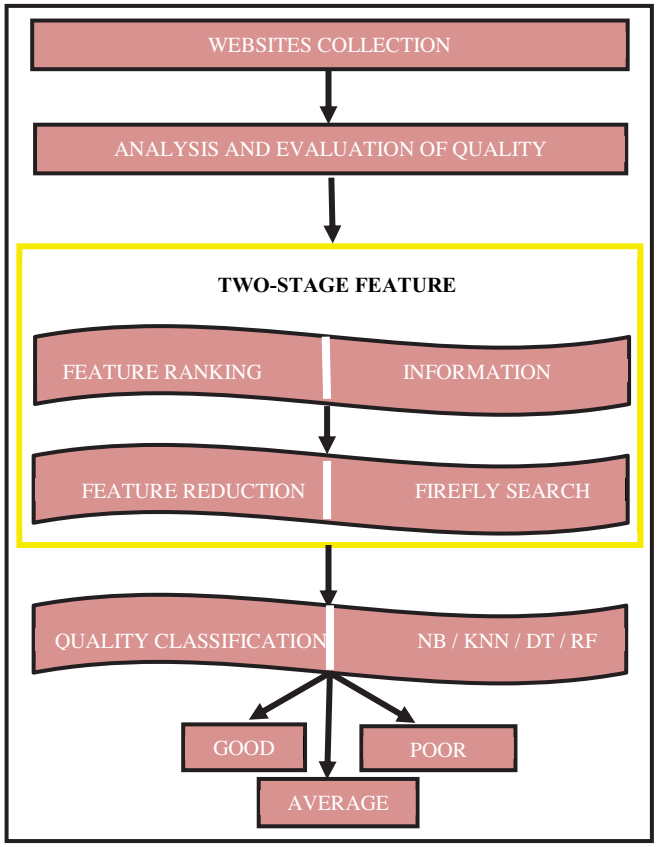

Fig. 1 System Architecture for Website Quality Prediction

Each of these steps are explained in detail in the following sub-sections.

A. Collection of Websites

In this work, 100 websites from each of the following Top-Level-Domains (total of 700 websites) have been considered for evaluation of the quality using optimized classification techniques. These Top-Level are- .com(commercial), .net(network), .org(organization), .gov(government), .int(international), .edu(educational), .mil(military).

B. Features Analysis and Evaluation

The dataset for this research has been formulated by identifying and extracting features which contribute to the quality of a website referred as quality features of a website. The identified quality attributes are extracted and evaluated for the 700 websites.

In this research we identified 16 quality attributes which contribute to the website quality. They were categorized into 6 major groups and 13 attributes out the 16 are quantifiable, which can be evaluated and rated based on scoring criteria. The Table I enlists the 6 groups, 16 attributes with their description, and the evaluation criteria for 13 quantifiable attributes.

C. Two-stage Feature Selection

Feature selection has ability to reduce the computation time and model complexity. Basically, feature selection is a technique of selecting a subset of important features and removing most irrelevant and redundant features [14] from the data for building an effective and efficient learning

model [15].

In this work filter-wrapper based feature selection is done where a filter method named as Information Gain is used to rank the features based on their importance followed by a wrapper method namely Firefly Search algorithm to select a subset of relevant features which improves the classification accuracy.

- *Information Gain*

"Information gain evaluates the worth of an attribute by measuring the information gain with respect to the class". It does so by measuring how each feature contributes in decreasing the overall entropy where entropy measures the degree of impurity. For each attribute it is calculated as follows:

$$InfoGain(Class, Attribute) = H(Class) - H(Class|Attribute)$$

where,

$H(Class)$ is the entropy of the class and is given by:

$$H(Class) = -\sum P_i * log_2(P_i)$$

where, P_i is the probability of class in the dataset.

In this work, InformationGainAttributeEval attribute evaluator method of WEKA has been used to rank the attributes along with the Ranker search method. These methods have been chosen based on the past studies which prove that Ranker+InfoGainAttributeEval takes less computational time among all the feature selection methods [16]. The 13 quality attributes have been reduced to 11 after this step eliminating the "resolution" and the "page rank".

- *Firefly Search Algorithm*

Firefly algorithm (FA) simulates the biochemical and the social characteristics of real fireflies. The algorithm was introduced by Xin-She Yang in late 2007 and 2008 [17]. It is a metaheuristic search algorithm based on the rhythmic flashing patterns that are used by fireflies to attract their mating partners as well as intelligent behaviors of these fireflies.

Firefly Algorithm formulates this flashing behavior determined by the objective function of the problem to be optimized. FA uses the following rules [18]:

i) The fireflies use flashing light to attract their mates.
ii) The fireflies are unisex and have tendency to attract each other irrespective of their sex.
iii) Attractiveness is proportional to their brightness. The brightness decreases as distance between two flies increases, and hence the attractiveness between them decreases. For any two flashing fireflies the less bright one always moves towards the brighter one. If there is no brighter present it will move randomly.
iv) The brightness of a firefly is determined by the landscape of the objective function.

The FA for feature section initially starts with n fireflies $x_i\ i = 1,2, \ldots . n$ corresponding to each feature in feature set.

TABLE I
QUALITY ATTRIBUTES AND THEIR EVALUATION CRITERIA

Domain	Attributes	Description	Evaluation
Information Quality	Relevance	The extent to which information of interest is relevant.	Crowed sourcing is done to rate the websites on a scale of 1-10 depending on the relevance of data and advertisement displayed on web page.
	Accuracy	The extent to which information on a webpage is accurate.	
	Completeness	The extent to which information is specified.	
	Updation	The recency of the update of information.	
Technical assessment	Total size	Total size of web page in KB or MB.	For measurement of webpage size, an online tool (https://gtmetrix.com/) has been used and scores are given as follows:

Web page size (in MB)	Score
< 1 MB (in KB)	10
1MB-3MB	9
3 – 5 MB	8
5 – 7 MB	7
7 – 9 MB	6
9 – 11 MB	5
11 – 13 MB	4

<table>
<tr><td></td><td></td><td></td><td><table>
<tr><td>13 – 15 MB</td><td>3</td></tr>
<tr><td>15 – 25 MB</td><td>2</td></tr>
<tr><td>25 – 50 MB</td><td>1</td></tr>
<tr><td>> 50 MB</td><td>0</td></tr>
</table></td></tr>
<tr><td></td><td>Broken Links</td><td>The presence of broken links throughout the website.</td><td>For the assessment of broken links an online tool (https://www.deadlinkchecker.com/) is used which crawls through the website to identify presence of broken links.
The scores have been given as follows:<table>
<tr><th>Percentage of broken links</th><th>Score</th></tr>
<tr><td>0</td><td>10</td></tr>
<tr><td>0 – 0.010</td><td>9</td></tr>
<tr><td>0.010 – 0.020</td><td>8</td></tr>
<tr><td>0.020 – 0.030</td><td>7</td></tr>
<tr><td>0.030 – 0.040</td><td>6</td></tr>
<tr><td>0.040 – 0.050</td><td>5</td></tr>
<tr><td>0.050 – 0.080</td><td>4</td></tr>
<tr><td>0.080 – 0.100</td><td>3</td></tr>
<tr><td>0.100 – 0.200</td><td>2</td></tr>
<tr><td>0.200 – 0.500</td><td>1</td></tr>
<tr><td>> 0.500</td><td>0</td></tr>
</table></td></tr>
<tr><td></td><td>Loading Time</td><td>The time taken by a web page to load completely.</td><td>An online tool (https://gtmetrix.com/) is used which gives us the page speed score in percentage. We have converted the percentage to score out of 10 as per its ceiling value. For example: 81% - 90% has been scored as 9.</td></tr>
<tr><td>Interaction</td><td>Communication</td><td>Search field
Address
Contact
Email</td><td>We have given score according to the four subfields giving 2.5 for the presence of each and a total of 10 if all of the four are present.</td></tr>
<tr><td></td><td>Social Media Connectivity</td><td>Google
Facebook
Twitter
Others</td><td>A good website should be allied to various social media sites budding today out of which Google, Facebook, and Twitter are most trending. So, we have given a score of 9 to the websites which are connected with three of these social media platforms, i.e. Google, Facebook, and Twitter (a score of 3 for each) and a score of 10 if other social media platforms like YouTube, LinkedIn are also linked.</td></tr>
<tr><td>Usage</td><td>Browser Compatibility</td><td>The compatibility of a website with different browsers.</td><td>We have tested websites with different browsers which are Internet Explorer, Google Chrome, and Mozilla Firefox. Different websites showed different behaviours and scores have been given in accordance with that behaviour.</td></tr>
<tr><td></td><td>Resolution</td><td>The appearance of website with different screen sizes.</td><td>On experiencing a website on different screen sizes some showed varied behaviour with different screen sizes and some showed same behaviour. Scores have been given according to the behaviours.</td></tr>
<tr><td></td><td>Global Audience</td><td>The language of information on the website.</td><td>Websites having information in English and used globally have been scored 10. Websites in a regional language have been given a score of 1. Websites having data in English but used regionally have been scored between 2 – 9.</td></tr>
<tr><td>Visual Appeal</td><td>Typography & Font</td><td>Font style and font size of the data on the website.</td><td>We have given highest score to 12 point Arial font as it is considered to be most legible and sharpest font and is most preferred by the users of websites [9]. We have given second highest score to 12 point Times New Roman as it is</td></tr>
</table>

			fastest to read [9]. The other fonts lagging behind in the queue are 12 point anti-aliased Arial, 10 point Arial, 12 point anti-aliased Times New Roman, 10 point times New Roman. Other fonts styles and size have been scored on the word of their readability.
	Colour Scheme	The colour combinations used to display the website.	Visually appealing colours on the websites likely lead to user satisfaction [10]. We have evaluated websites on the basis of colour combinations used and how these colours strike our eyes. Websites with blue and grey colour schemes have been scored highest as blue is associated with wealth, security and trust and is more aesthetically appealing [11]. Websites having cool colours like blue and green have been given higher score as compared to websites with warm colours such as red, yellow. as blue is more relaxing than red or yellow [12]. Unlike other warm colours, Orange is preferred by users [13] and we scored it higher as compared to pink, green or magenta. Websites with brown or black colour schemes have been scored the least as these colours are associated with sad and stale moods [10]. Websites with yellow background colour have been scored the least as it is distracting colour [10].
	Overall Theme	The association of data, images, tables used in the website.	The visual appeal people experience while visiting a web page via placement and association of its data, tables, and images have been scored.
Page Rank		The rank rendered to a website for its importance.	We used and online tool (https://www.checkpagerank.net/) that provided us with the page rank of all websites.

The following Fig. 2 describes the FA algorithm.

```
Objective function f(x), x = (x1,……xn)T
Generate initial population of fireflies xi (i=1,2,...n)
Light intensity Ii at xi is determined by f(xi)
Define light absorption coefficient γ
While(t>MaxGeneration)
   for i=1 to n
      for j=1 to i
         if (Ij>Ii), Move firefly i towards j in d-dimension;
         endif
Attractiveness varies with light absorption γ and distance r
Evaluate new solution and update light intensity
      endfor j
   endfor i
Rank the fireflies and find the current best
end while
Post process results and visualization.
```

Fig. 2 Firefly Algorithm

Attractiveness α varies with the distance r as follows:

$$\alpha = \alpha_o e^{-\gamma r^2}$$

where α_o is the attractiveness at $r = 0$

The movement of a firefly i towards a brighter firefly j is represented as follows:

$$x_i^{t+1} = x_i^t + \alpha_o e^{-\gamma r^2}\left(x_j^t - x_i^t\right) + \delta_t \in_i^t$$

where,

the second term represents the attraction, r being the distance between the fireflies i and j.

$\delta_t \in_i^t$ corresponds to randomization with δ_t being the randomization parameter and $\in_i^t$ is a vector of random numbers drawn from a Gaussian distribution or uniform distribution at time t.

If $\alpha_o = 0$ the equation becomes a simple random walk.

Out of the 11 features selected in the first stage FA is used to further optimize the features by selecting best feature subset for a classifier. WrapperSubsetEval method of WEKA is used with the FireFlySearch as the search method for this task. A Significant amount of feature reduction has been observed after the second stage. The results are discussed in the next section.

D. Quality Prediction using Classification

In this study, four classifier methods are used for website quality prediction; Naive Bayesian (NB) K-Nearest Neighbour (K-NN), Decision Tree (DT), and Random Forest (RF) to categorize them into classes good, average, and poor. The description of these techniques is available across pertinent literature on machine learning [19, 20]. These methods are separately trained with the original feature set and the reduced feature set obtained at the end of previous step. This is done to compare the performances and analyze the improvement in performance after feature selection. The performance of the proposed optimal learning model is evaluated using accuracy. All the parameters and settings are set to default during the conduction of experiment.

IV. EXPERIMENTAL RESULTS

The results of experimental study are discussed in terms of: (i) reduction in the number of features, (ii) reduction in time for training the classifier and building the model, (iii) improvement in classification accuracy. The following subsections discuss the same.

A. Reduction in Features

Initially IG filter method is used in order to rank each feature. Out of 13 attributes constituting the dataset, 11 are selected after this method eliminating the "resolution" and the "page rank". The following Table II gives top 11 ranked features in the decreasing order of rank.

TABLE II
TOP 11 RANKED FEATURES WITH THEIR IG SCORE

Rank	Feature	IG score
1.	social media connectivity	0.2044
2.	colour scheme	0.19
3.	typography and font	0.1899
4.	overall theme	0.1496
5.	relevance	0.1061
6.	global audience	0.0981
7.	broken links	0.0704
8.	communication	0.0651
9.	compatibility	0.0604
10.	size	0.0587
11.	loading time	0.0473

It can be clearly observed that "social media connectivity" is ranked 1st with the highest Information Gain score of 0.2044.

Following this, FA wrapper method is used to select the best subset of features which represents the dataset in order to decrease classification complexity and reduce the training time. The wrapper method uses a predetermined classifier to evaluate the best feature subset for that classifier. The following Table III enlists the features selected by FA for each classifier followed by the evaluation of the percentage feature reduction.

TABLE III
FEATURE SUBSET FOR EACH CLASSIFIER

Classifier	Feature Subset	Length of Subset
NB	1. communication 2. size 3. broken links 4. compatibility 5. global audience 6. loading time (page speed) 7. typography and font 8. colour scheme 9. social media connectivity	9
K-NN	1. communication 2. size 3. broken links 4. global audience 5. typography and font 6. colour scheme 7. social media connectivity	7
DT	1. communication 2. size 3. broken links 4. global audience 5. overall theme 6. colour scheme 7. social media connectivity	7
RF	1. relevance 2. communication 3. size	10

	4. broken links 5. global audience 6. loading time (page speed) 7. typography and font 8. overall theme 9. colour scheme 10. social media connectivity	

An average of 36.53% of feature reduction was observed after the two-stage feature selection method with K-NN and DT being the highest in percentage of feature reduction with 46.15%.

B. Reduction in Time

Reducing time for computation and the complexity of the resulting prediction model is the objective of feature selection and optimization techniques. The task of feature selection gives a reduced subset and is followed by training of four standard classifiers. A comparative analysis of the time taken to build the models for various classifiers is provided to assess time reduction and the effectiveness of the filter-wrapper feature selection approach.

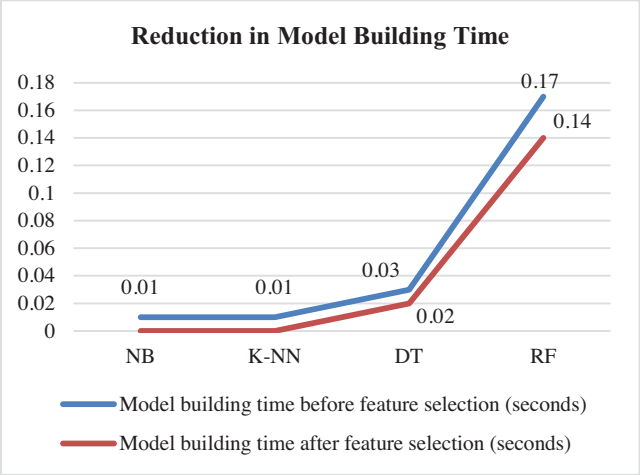

Fig. 3 Reduction in model building time

Maximum reduction in time was observed in building RF classifier method with the value of 0.03 seconds. Reduction of 0.01 seconds was found to build in all other classification models: NB, K-
NN, DT, RF.

C. Improvement in Classification Performance

Accuracy has been considered to measure the effectiveness and efficiency of a classifier. The performance of various classifiers before feature selection and after feature selection has been graphically illustrated in the Fig. 4. Also, improvement in accuracy has been evaluated and listed.

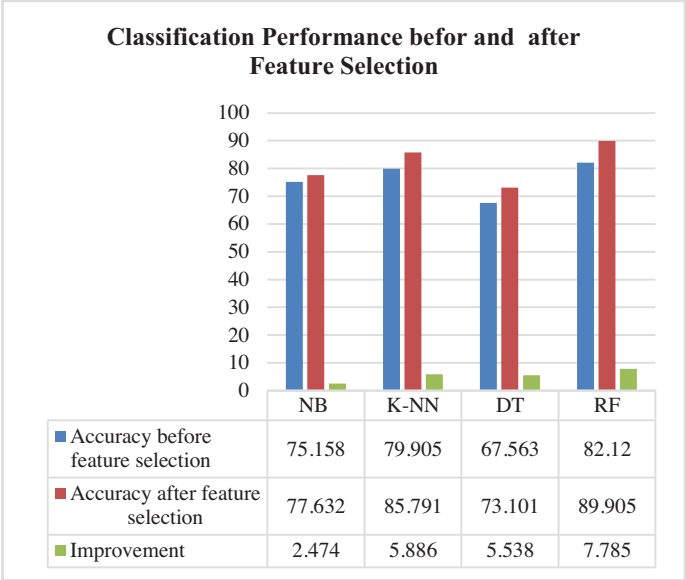

	NB	K-NN	DT	RF
Accuracy before feature selection	75.158	79.905	67.563	82.12
Accuracy after feature selection	77.632	85.791	73.101	89.905
Improvement	2.474	5.886	5.538	7.785

Fig. 4 Classification performance before and after feature selection

The results clearly convey that filter-wrapper feature selection leads to better performance of a classifier. Maximum accuracy gain was shown by RF (7.785%) with the average improvement of 5.420%.

V. CONCLUSION

This research proposes a predictive learning model to classify websites into good, average and poor quality based on 13 attributes related to user satisfaction and acceptance. A two-stage feature selection method consisting of a filter method at first stage and a wrapper method at second stage making it a hybrid filter-wrapper based feature selection has been implemented to reduce the dimension of feature space. An empirical study to evaluate the effectiveness of feature selection method and to classify websites from 7 top-level domains using four supervised learning techniques is conducted. An average of 36.53% reduction in features has been observed which leads to 0.015 seconds of average reduction in time for building a classifier and an average improvement of 5.420% in classification accuracy. RF gave the best performance with 23.37% of feature reduction and 7.785% improvement in accuracy giving the accuracy of 89.905%.

REFERENCES

[1] L. Liu, J. Kang, J. Yu, and Z. Wang, "A comparative study on unsupervised feature selection methods for text clustering," in *Proc. NLP-KE'O5*, 2005, pp. 597–601.

[2] E.T. Loiacono, R.T. Watson, and D.L. Goodhue, "WebQual: A measure of website quality," *Marketing theory and applications.*, vol. 13, no.3, pp.432-438, Feb. 2002.

[3] H. Sørum, R. and Medaglia, K.N. Andersen, "Assessment of website quality: Scandinavian web awards right on track?," in *Int. Conf. Electronic Government, Berlin, Heidelberg*, 2009, pp. 198-209, Springer.

[4] Hartmann, J., De Angeli, A., Sutcliffe, A.: 'Framing the user experience: information biases on website quality judgement'.Proc. SIGCHI Conf. Human Factors in Computing Systems, April 2008, pp. 855-864, ACM.

[5] J. Sobecki, and D. Żatuchin, "Knowledge and data processing in a process of website quality evaluation," in *New challenges in computational collective intelligence*, Berlin, Heidelberg, 2009, pp. 51-61, Springer.

[6] P. Schubert, and D. Selz, "Web assessment-measuring the effectiveness of e-commerce sites going beyond traditional marketing paradigms," in *Systems Sciences, HICSS-32. Proc. Annual Hawaii International Conference'32,* 1999. pp. 10-pp. IEEE.
[7] D. Selz, and P. Schubert, "Web assessment-a model for the evaluation and the assessment of successful electronic commerce applications," in *System Sciences, Proc. Hawaii International Conference'31,* 1998, vol. 4, pp. 222-231, IEEE.
[8] P. Schubert, and W. Dettling, "Extended Web assessment method (EWAM)-evaluation of e-commerce applications from the customer's viewpoint," in *System Sciences, HICSS. Proc. Annual Hawaii International Conference'35, 2002,* pp. 10-pp, IEEE.
[9] M. Bernard, and M. Mills, "So, what size and type of font should I use on my website," *Usability news*, vol.2, no.2, pp.1-5, July 2000.
[10] D. Cyr, M. Head, and H. Larios, "Colour appeal in website design within and across cultures: A multi-method evaluation," in *International journal of human-computer studies'68*, no. 1-2, 2010, pp.1-21.
[11] M.C. Lichtlé, "The effect of an advertisement's colour on emotions evoked by attitude towards the ad: The moderating role of the optimal stimulation level," *International Journal of Advertising*, vol. 26, no. 1, pp.37-62, Jan 2007.
[12] K.W. Jacobs, and G.H. Hustmyer, "Effects of four psychologically primary colors on GSR, heart rate, and respiration rate," *Perceptual and Motor Skills*, vol.38, no. 1, pp.763–766, Jun 1974.
[13] N. Bonnardel, A. Piolat, and L. Le Bigot, "The impact of colour on Website appeal and users' cognitive processes," *Displays*, vol. 32, no. 2, pp. 69-80, Apr 2011.
[14]. G.H. John, R. Kohavi, and K. Pfleger, "Irrelevant Features and the Subset Selection Problem," in *Proc. 11th Int. Conf. on Machine Learning, Morgan Kaufmann Publishers*, 1994, pp. 121-129.
[15]. M. Dash, and H. Liu, "Feature Selection for Classification," *Intelligent Data Analysis*, vol. 1, no. 3, 1997, pp. 131– 56.
[16] M. Aggarwal, "Performance analysis of different feature selection methods in intrusion detection," *International Journal of Scientific & Technology Research*, vol. 2, no. 6, Jun 2013, pp. 225-31.

[17] X. S. Yang, "Firefly Algorithm for Multimodal Optimization," in *International symposium on stochastic algorithms*, 2009, pp.169- 178.
[18] H. Banati, M. Bajaj, "Fire fly based feature selection approach," *International Journal of Computer Science Issues (IJCSI)*, vol. 8, no. 4, p. 473, July 2011.
[19] A. Kumar, S. R. Sangwan, "Rumour Detection using Machine Learning Techniques on Social Media," in *International Conference on Innovative Computing and Communication, Lecture Notes in Networks and Systems, Springer*, 2018.
[20] A. Kumar, A. Jaiswal, "Empirical Study of Twitter and Tumblr for Sentiment Analysis using Soft Computing Techniques," *in Proc. World Congress on Engineering and Computer Science,* 2017, pp. 1-5.

Personal and Ubiquitous Computing
https://doi.org/10.1007/s00779-019-01213-4

ORIGINAL ARTICLE

A framework for usage pattern–based power optimization and battery lifetime prediction in smartphones

Nirmal Pandey[1] · Om Prakash Verma[1] · Amioy Kumar[1]

Received: 22 March 2017 / Accepted: 14 March 2019
© Springer-Verlag London Ltd., part of Springer Nature 2019

Abstract
The use of mobile devices has increased many folds over the last few years. Smart phones are used not only for communication but also for storage of personal contents like photos, videos, documents, and bank account and credit/debit card details. Secure access to these contents is very important. Nowadays, many mobile devices come with inbuilt biometric-enabled security features like fingerprint, face recognition, and iris. However, additional battery power is consumed each time a user unlocks the device using any one of these security features. In order to enable prolonged use of the device, there is a strong need to find ways to conserve power in mobile devices. At the same time, it is also equally important that the smart phone user knows how long the battery of his device will last. In this paper, we present a novel power optimization and battery lifetime prediction framework called P4O (*P*attern, *P*rofiling, *P*rediction, and *P*ower *O*ptimization). Our contributions are threefold—(i) Propose a novel framework for power optimization in smart phones. (ii) Propose a new approach for battery lifetime forecast. (iii) Implement and validate the efficacy of the proposed framework. For experimental results, the proposed framework was implemented on the Android-based smartphone. The experimental results validate the proposed framework with power optimization up to 40% over default Linux and Android power saving features available in an Android operating system. This framework is also able to forecast battery lifetime with accuracy of up to 98%.

Keywords Energy efficiency · Mobile devices · Battery lifetime · Usage pattern · Power optimization

1 Introduction

The adoption of smart phones in society is increasing at a very fast pace. As per one estimate, about 432 million units of smart phones were sold worldwide in the last quarter of 2016 [1]. Till recently, patterns, personal identification numbers, passphrases, and passwords were the most common ways to unlock smart phones. According to a recent survey [2], one of the top concerns of the smart phone users was related to the security of the device. Due to these concerns, smart phone OEMs are enhancing the security features of mobile devices by adding biometric-enabled security features such as fingerprint scanners, face, and iris recognition [3, 4].

For the purpose of testing the power consumed by biometric components in smart phones, we used the Samsung Galaxy S7 Edge [4] mobile phone as the device under test. It has an inbuilt front-facing fingerprint scanner. For using the face recognition on Galaxy S7 Edge, we have used a third party app—the IOBit Applock [5]—for power measurement. As we observe the Galaxy S7 Edge power readings for a fingerprint and face unlock as given in Fig. 1, we see that for each unlock operation, 200 to 400 mA extra current is consumed. When added with the fact that on an average, one smart phone user unlocks his device 100 times daily [6], a total power consumed due to biometric sensors could range from 5 to 10% of total battery capacity in a day. Thus, biometric-enabled security features reduce the number of hours a smartphone can be used without charging. This reflects the severity of the power consumption problem in smart phones. This has been corroborated in many surveys and studies carried out in the past. Rahmati et al. [7] found that 80% of the mobile users

✉ Nirmal Pandey
writetonirmal@gmail.com

Om Prakash Verma
opverma.dce@gmail.com

Amioy Kumar
amioy.iitd@gmail.com

[1] Delhi Technological University (DTU), Shahbad Daulatpur, Main Bawana Road, Delhi 110042, India

Published online: 13 April 2019

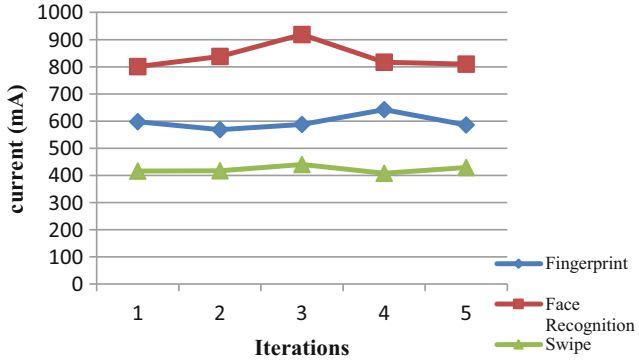

Fig. 1 Current consumption for fingerprint and face unlock features

were concerned with the battery life of the device. Therefore, a systematic and comprehensive approach is needed to overcome power consumption and fast battery drainage problem in smart phones.

A large number of studies have been carried out by many researchers to find out power consumption characteristics in mobile devices. Rahul Balani [8] analyzed energy consumption for various radio transmission technologies such as BT, Wi-Fi, 2G, and 3G. Andrew Rice et al. [9] developed a measurement framework that logs the traces of the consumed power. This was done to help in understanding the power consumption from the application perspective. Aaron Carroll et al. [10] analyzed and broke down power distribution into various components such as processors, display, and primary and secondary storage, and also developed an overall energy model of the device.

G.P. Perrucci et al. [11] studied energy consumption entities on the smart phone platform and identified various energy-hungry components of the mobile phones. Paul et al. [12] studied power consumption in Android devices. They proposed that more energy is consumed in the Android Dalvik VM (virtual machine) due to the lack of dynamic compiler in comparison with the Sun Embedded JVM (Java virtual machine).

By closely observing the power consumption profile of a mobile device, we find that some components of the device consume more power than others. Major power consuming components are CPU, GPU, display, radios, biometric sensors, other sensors (accelerometer, proximity, gyro, etc.), and audio components. During the unlocking of smartphones, the power consumed by biometric sensors is common in all use cases. Some or all of these components are active in various use cases of the device. Here are a few common instances:

1. Playing a video stored locally on the device (internal or storage card) involves unlocking the device (biometric sensors), CPU, GPU, display, speaker and storage card.
2. Playing a video from YouTube or any other streaming server involves unlocking the device (biometric sensors), radios, CPU, GPU, speaker, and display.
3. Making a voice call/video call involves unlocking the device (biometric sensors), radios, CPU, display (some part), sensors (proximity), camera, and speakers.
4. Playing a 2D/3D game involves unlocking the device (biometric sensors), CPU, GPU, display, speaker, and various other sensors.
5. Internet browsing involves unlocking the device (biometric sensors), radios, CPU, GPU, and display.

From these use case scenarios, it is obvious that any meaningful use of the smart phone involves a large number of software and hardware components. All of these components consume power. So, any power optimization system should encompass power saving in all or most of these components in order to be useful. The smartphones have many inbuilt power saving features available in the device. Figures 2 and 3 below show some of the power saving features available in the Samsung Galaxy S7 Edge [4] Android smart phone.

As we can see from the Figs. 2 and 3 above, in order to carry out effective power saving, a user must be technically conversant with power saving terminology such as screen brightness, screen resolution, CPU processing speeds, and network usage. along with the relationship between these parameters and corresponding power consumption. This is not the case with most of the users [7]. Therefore, an effective power optimization framework that does not require the user to fully understand power consumption domain is needed. To address this problem, a new framework is proposed in this work (detailed in the "Contributions" section). To optimize power and predict battery lifetime, a novel framework called P4O (*P*attern, *P*rofiling, *P*rediction, and *P*ower *O*ptimization) is proposed and investigated in detail in this work (detailed in the "P4O framework" section).

The rest of the paper is organized as below. In the "State of the art and contributions" section, we present a survey of prior research done related to the usage pattern–based mobile phone power consumption and battery lifetime prediction. The proposed power optimization framework P4O is presented in the "P4O framework" section. In the "Power consumption pattern and power states" section, we have covered the power consumption pattern and power states. The experimental results are provided under the "Experimental results" section. Under the "Conclusion and future work" section, the conclusion of the work done is given and the scope for future research is outlined.

2 State of the art and contributions

2.1 Prior work

Power optimization and accurate battery lifetime prediction problems have drawn the attention of many researchers to this

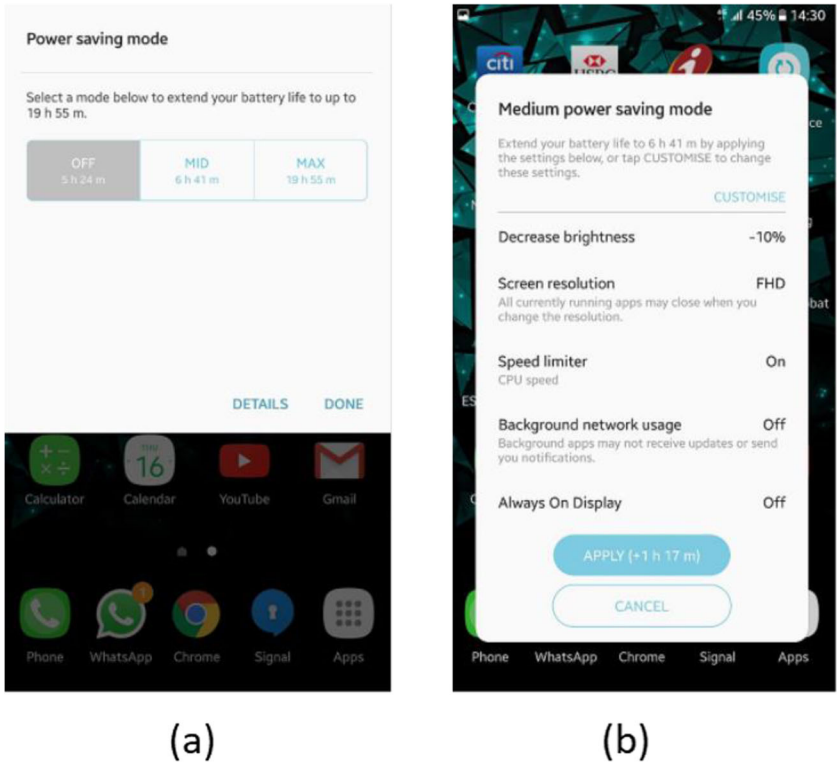

Fig. 2 Samsung Galaxy S7 Edge Power Saving. **a** Modes. **b** Medium power saving parameters

field. Analysis of user behavior as well as device usage patterns has been investigated by various researchers. Lyons et al. [13] conducted a 4-week investigation involving more than 4000 users, but they focused on the charging habits of smartphone users. R. Demumieux et al. [14] made use of various functions available on the device and collected the information along with the time taken for each of the activities. Rahmati et al. [7] studied the human-battery interaction of

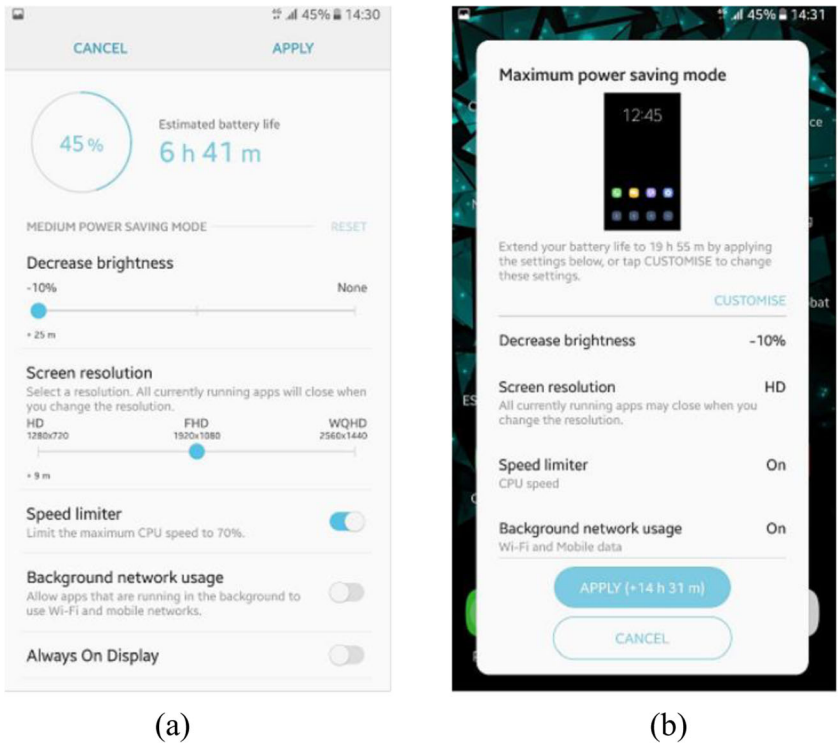

Fig. 3 **a**–**b** Samsung Galaxy S7 Edge maximum power saving mode

mobile phone users. They also studied GUI-related aspects of battery information in mobile phones. Kang et al. [15] analyzed the usage pattern of mobile phones. They took phone operations such as voice call into consideration and defined the various states of the device to understand user behavior. E. Oliver et al. [16] presented the challenges in conducting large-scale user studies. They examined user mobile interactions and energy consumption of the device. J. Lee et al. [17] proposed an automated power model generation approach taking usage patterns into consideration. The usage patterns were put under various baskets and tested for power model generation. H. Falaki et al. [18] focused on collating logs and presented a diversified usage pattern. Verkasalo [19] presented a framework called MobiTrack for the data collection and analysis of user behavior. Oulasvirta et al. [20] examined various data sources on the mobile device and concluded that mobile users form habits of device usage. Arun et al. attempted to provide an innovative plan for effective services to end users on the deployment of information services through mobile apps [21]. Alexander W. Min et al. [22] presented a framework called E2S3 (energy-efficient sleep-state selection). This framework minimizes battery consumption by adaptively going into an optimal low-power sleep state. In the direction of building IOT (Internet-of-things) sensors, a work done by Turjman [23] and Sing et al. [24] is also worth mentioning. The work in [24] attempted on information-gathering networks in large-scale IOT applications such as smart cities, which serve multiple users with diverse quality-of-information (QoI) requirements on the data delivered by the network.

Battery lifetime prediction has also been investigated by various researchers. J.M. Kang et al. [25] presented a battery lifetime prediction method that makes use of activities and the time spent in these activities as the basis for lifetime computation. Chandra et al. [26] presented application-level battery consumption. However, they did not consider the diversity of usage by various users. Zhang et al. [27] proposed an automated power model construction method called PowerBooter. They also proposed a power management tool called PowerTutor that works in conjunction with PowerBooter.

Various researchers have investigated the smartphone applications usage pattern. Some of them have investigated app usage to relate it to the stress level of the smartphone user. Research has also been done to investigate the app usage pattern based on the GPS location of the user, based on the wearable and sensor use in the smartphone. However, none of these investigations are focused on the relationship between the device usage pattern and battery drop rate, thus paving a way for opportunistic power optimization in the device.

A comparative study on some recent state of the art and the present work are shown in Table 1. It can be noted that the power optimization in smart phones and battery life forecast are a relevantly new area of research and carried out in none of the popularly available state of the arts.

2.2 Motivations

Every mobile user has a consistent and unique usage pattern [33]. Therefore, any power optimization technique also needs to be unique to each individual. Generic power conservation methods will have limited success as each individual differs in the way he interacts and makes use of his device. While capturing user behavior patterns, it is equally important that the data captured does not violate the privacy of individuals. Many usage pattern–based methods proposed in the literature make use of sensitive information such as user location, which applications user accesses and for how long, etc. These raise serious privacy issues, if such information is shared to web servers for processing. In addition to this, client-server-based power optimization architectures suffer from the lacunae that these are not real time, rather near real time. This affects the accuracy of these systems.

Some of the battery lifetime prediction methods available in the literature use static information for prediction, which gives incorrect output. Most other techniques available in the literature make use of the application usage pattern benchmarking. This also has the limitation as most users frequently change old applications and install new applications on the device.

2.3 Contributions

In this paper, our main contributions are as follows:

1. A novel framework for power optimization referred to as P4O (*P*attern, *P*rofiling, *P*rediction, and *P*ower *O*ptimization) is proposed. The proposed framework can learn the battery usage pattern of a user over a period of time. It utilizes the Kalman filter to provide knowledge base updates. This can optimize the battery power based on the state transition (see the "Power consumption pattern and power states" section for detail). Based on the learned pattern, it can minimize battery usage and hence optimize the battery power.
2. This framework has many advantages. It solely runs on the device. Therefore, there is no security or privacy aspects involved in the use of this framework. It makes use of the battery discharge rate information for benchmarking user behavior. This makes it independent of applications users tend to use, as users tend to install/uninstall applications.
3. It proposes a new approach for battery lifetime forecast. The proposed method makes an accurate prediction of battery lifetime based on the usage pattern analysis.
4. The proposed framework has been implemented on Android [34] smart phone. Its efficacy has been validated in experimental test results.

Table 1 State of the art in usage pattern analysis

S. no.	Ref	Application	Research methodology	Accuracy	Optimization
1	Ferdous et al. [28]	Smartphone app usage as a predictor of perceived stress levels at the workplace	- Studied the patterns of app usage, specifically the types of apps and their duration. - Proposed the relationship between the app usage pattern and the stress level of the user.	Average accuracy = 75% Precision = 85.7%.	Not available
2	Turjman et al. [29]	Ubiquitous cloud-based monitoring via a mobile app in smartphones: an overview	- Investigated the impact of wearable devices on user habits. - Focused on two areas—usage patterns and user mobility tracking using smartphones.	Not available	Not available
3	Elgedawy et al. [30]	IdProF: Identity provisioning framework for smart environments	- Proposed a secure context-sensitive seamless multi-modal identity provisioning framework for smart environments. - Can generate a disposable customized virtual inhabitant profile (DCVIP) on demand. - Creates a customized identity proxy to handle the identity verification for the required interaction.	Not available	Not available
4	Li et al. [31]	Characterizing smartphone usage patterns from millions of Android users	- Presented an empirical analysis of app usage behaviors collected from millions of users of Wandoujia, a leading Android app marketplace in China.	Not available	Not available
5	Lu et al. [32]	Mining mobile application sequential patterns for usage prediction	- Mining and prediction of mobile application usage behaviors. - Proposed a location-based approach to predict the mobile application usage behaviors.	Precision = 32% Recall = 40% (Both at 3% threshold)	Not available
6	This work	Novel power optimization and battery lifetime prediction framework	- A novel framework for power optimization in smart phones. - A new approach for battery lifetime forecast	Accuracy = 73% (With 2 weeks' usage pattern knowledge)	Available (Power optimization up to 30% over default Linux and Android systems)

3 P4O framework

The proposed P4O framework intends to record, analyze, learn, predict, and optimize the battery power consumption of the smart phone in a non-invasive way. Smartphone users exhibit a pattern of usage. This usage pattern is also reflected in the battery discharge pattern of the device as well. The P4O framework proposes to record the battery discharge pattern for each usage pattern slot of 30 min each. The usage pattern, so learned, will be used to predict the power state and take the device to a lower power state whenever the opportunity arises. It will also predict the battery lifetime of the device as per the learned usage pattern. The P4O framework is explained below.

The main components of the proposed framework are the following: logging and learning module, prediction module, decision-making module, power state controller, and battery lifetime forecast module. Figure 4 depicts the proposed P4O framework.

3.1 Logging and learning module

The purpose of logging and learning module is to monitor the battery consumption statistics of the device and record it in the usage pattern DB. It analyzes and learns the battery consumption pattern of the device. It takes inputs from battery monitoring service that is running on the device and monitors battery drop/charge status. It also takes into consideration the time of the day supplied by the system clock for pattern analysis and learning the usage pattern. Battery drop/charge rates are recorded by this module into the battery DB for the time slots that are pre-defined.

3.2 Prediction module

The prediction module takes inputs from the logging and learning module as well as the system clock. It predicts the most suitable power state for the system for the current usage time slot. For a given usage time slot, logging and learning module gives information about the past usage behavior of the device. The prediction module forecasts the power state by taking this information into consideration.

3.3 Decision-making module

The purpose of decision-making module is to decide whether the power state of the device for the current usage slot needs to be changed. For this purpose, it takes the predicted power state

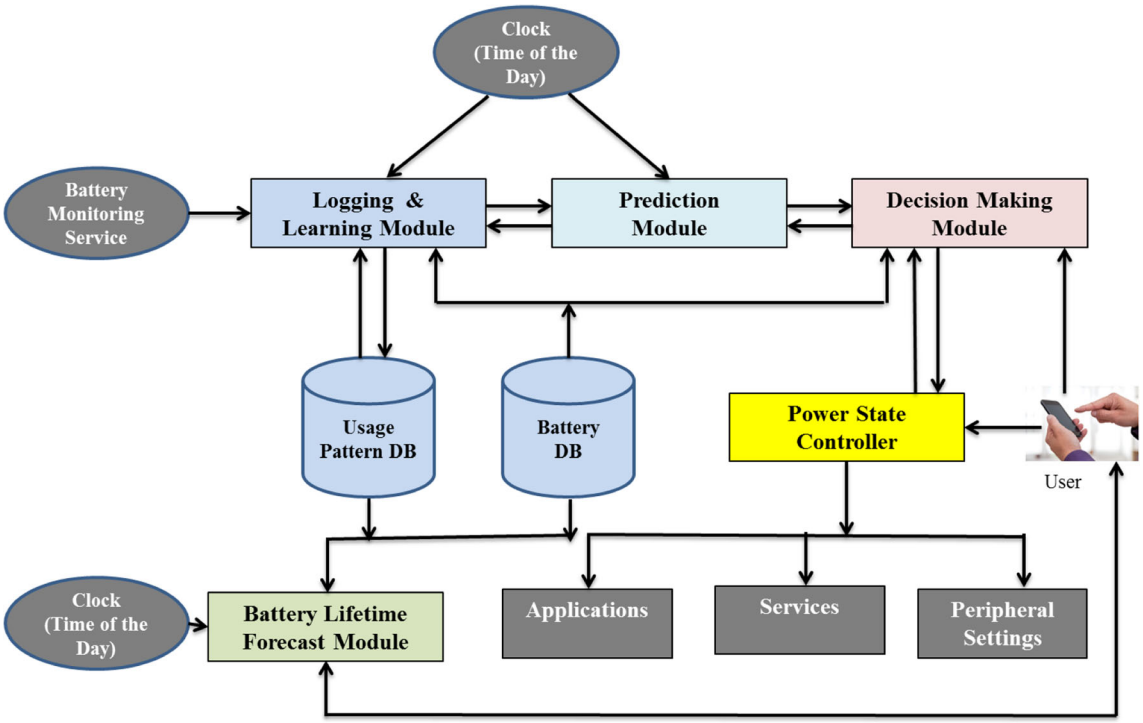

Fig. 4 P4O framework block diagram

from the prediction module, current user action, and time left in this usage slot as input, and decides the power state transition.

3.4 Power state controller

The P4O framework utilizes four power proposed states—high (H), medium (M), low (L), and very low (VL). These power states have been defined by taking the rate of battery discharge into consideration. If, for a given usage pattern slot, the battery drop rate is less than the computed threshold (refer to Table 2) but more than zero, the power state is declared a very low (VL) state. Similarly, other power states, low, medium, and high, are defined. The exact values of battery drop rates for these power states may vary from user to user. For example, if someone uses the device more for multimedia applications such as video streaming or high-end gaming, the value of battery discharge rate per usage pattern slot will be much higher than that for the person who uses the devices mostly for voice calls or sending messages. The power state controller takes the decision made by the decision-making module as input and does the actual work for making a transition from a higher power consumption state to a lower power consumption state. This module interacts with running applications, services, and various peripherals for actual power state transitions. However, if the system is woken up due to an external trigger, the power state controller rolls back the changes and takes the system from a lower power consumption state to a higher power consumption state depending upon the need of the system.

Table 2 Battery consumption rate to power state mapping

Power state	Battery consumption rate
Very low (VL)	DR
Low (L)	$> DR$ and $< (5 \times DR)$
Medium (M)	$> (5 \times DR)$ and $< (10 \times DR)$
High (H)	$> (10 \times DR)$

3.5 Battery lifetime forecast module

The purpose of battery lifetime forecast module is to predict the duration up to which the battery of the device will last or, after a given duration, how much battery will be left if there is no charging opportunity. This module takes the usage pattern of the device and the time duration from the user, and calculates the duration or battery lifetime.

4 Power consumption pattern and power states

The device usage pattern is reflected in the battery consumption or battery discharge pattern of the device. Therefore, recording this behavior becomes very important for any useful prediction and saving device power.

4.1 Building usage pattern knowledge base

For the purpose of recording the battery discharge pattern of the device, the period of interest is taken as 1 week. Each day of the week is further divided into "usage pattern slots" of 30 min each. Thus, we have 48 ($24 \times 2 = 48$) usage pattern slots for each day of the week. Initially, since there is no knowledge base of battery discharge pattern, the P4O framework records the battery discharge rates for each of these slots ($48 \times 7 = 336$ slots) for the entire week. This recorded information serves as the initial knowledge base of the usage pattern. All this information is recorded in real time in the device without user intervention. The flowchart below explains the building of the usage pattern knowledge base (Fig. 5).

4.2 Battery discharge pattern knowledge base update

The battery discharge rate information for each of the usage pattern slots is captured in real time. Even though the way any particular person uses the device shows some pattern, it may still change. Thus, the knowledge base, which stores the previous record of battery discharge rate for each of the 336 usage pattern slots, also needs to be updated in real time. In our system, we used the alpha-beta filter to calculate the updated battery discharge rate by taking the old value and the new value of the battery discharge rate.

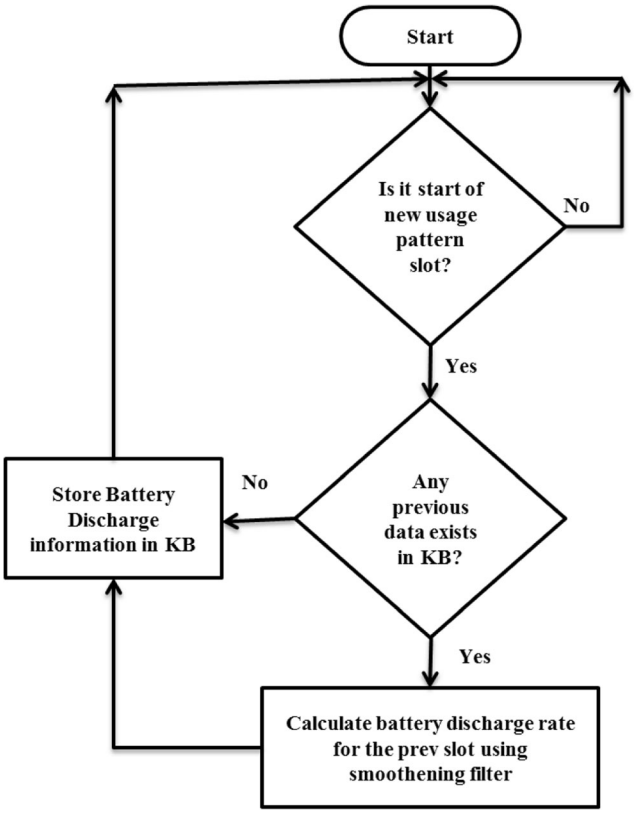

Fig. 5 Building battery discharge usage pattern knowledge base

The alpha-beta filter is a simpler form of the Kalman filter [35]. Let us assume that d_k is the battery discharge rate of the kth usage pattern slot and d_{k+1} is of the same slot during the same day of the next week. In that case, the new value of battery discharge rate for $k+1$st slot is given by the following equation:

$$d_{k+1} = d_k + \alpha\,(d_{k+1} - d_k) \tag{1}$$

Here, α is the smoothening factor between 0 and 1. A very high value of alpha means the system will catch up with the changes very fast, while a value of zero means the system will ignore any changes reported in the system. In the P4O framework, the value of alpha is kept at 0.5.

4.3 Power consumption states mapping

P4O framework defines four power consumption states. These states are dependent upon the value of battery discharge rates. The four power consumption states are high (H), medium (M), low (L), and very low (VL). The following algorithm is used to map the battery discharge rate to power states. This algorithm helps in creating the mapping between the battery consumption rate and the power state independent of battery capacity. The steps mentioned below are used in the algorithm:

1. Find the total battery capacity (T_B) of the device [in milliampere hours (mAH) units].
2. Assume the device base current (I_B). For Android smart phones, the base current is considered 10 mA in experiments after measurements [36].
3. Calculate the idle usage time of the device (T_U) [in hours unit]:

$$T_U = T_B / I_B \tag{2}$$

4. Calculate the battery discharge rate for one usage pattern slot of 30 min:

$$\text{Battery drop rate per hour} = 100/T_U$$

Therefore, the battery drop rate for 30 min will be given by the equation:

$$D_R = (0.5{*}100/T_U) \tag{3}$$

5. The value of D_R computed from Eq. 3 is mapped to the power state "Very Low" as this is the minimum current that the device will draw even when there is no load on the device.

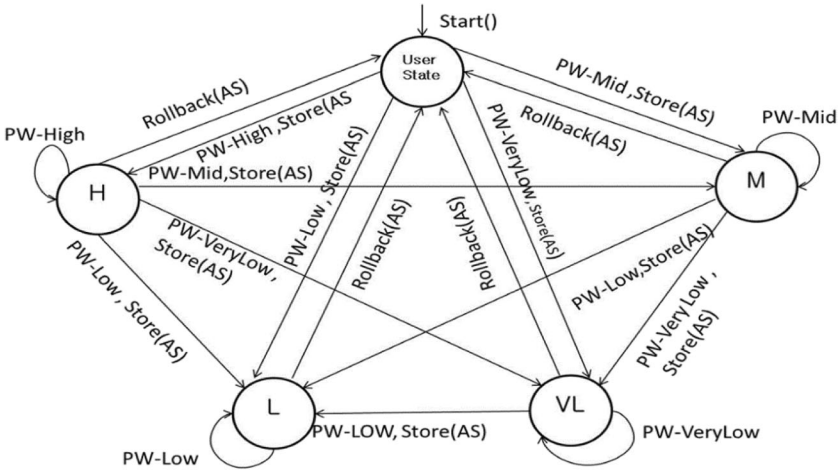

Fig. 6 Power state transitions

Table 3 Power state transition actions

Function	Very low	Low	Medium	High	Function	Very low	Low	Medium	High
Wi-Fi	X	X	O	O	Location/GPS	X	X	O	O
Bluetooth	X	X	X	O	CPU power Saving	X	X	X	O
Wi-Fi direct	X	X	X	O	Motion and gesture	X	X	O	O
Wi-Fi hotspot	X	X	X	O	Smart screen functions	X	X	X	O
Auto-sync	X	X	O	O	Tool box	X	X	X	O
Download booster	X	X	X	O	Bike mode/car mode	X	X	O	O
Smart bonding	O	X	X	X	Smart view	X	X	X	O
NFC	X	X	X	O	Glove mode	X	X	O	O
Brightness	X	X	O	O	Smart pause	X	X	X	O
Touch sensitivity	X	X	O	O	Smart stay	X	O	O	O
Screen rotation	X	X	O	O	Hands-free mode	X	O	O	O
Screen timeout	X	O	O	O	Reading mode	X	X	O	O
Screen power saving	X	X	X	O	S preview	X	O	O	O
Edge screen	X	X	X	O	Voice control	X	O	O	O
Key light duration	X	X	O	O	Air gesture	X	X	O	O
LED indicator	X	O	O	O	Air view	X	O	O	O
Battery level indicator	X	O	O	O	Multi window	X	X	O	O
Easy mode	X	X	X	O	Hands-free operation	X	O	O	O
Auto-rotate	X	X	O	O	Blocking mode	X	O	O	O
Volume intensity	X	O	O	O	Network restriction	X	O	O	O
Vibration intensity	X	X	O	O	Talk back	X	X	O	O
Haptic feedback	X	X	O	O	S pen	X	X	O	O
Volume	X	O	O	O	S cover	X	X	O	O

6. The remaining power states are mapped to the battery discharge rate as per Table 2.

4.4 Power consumption states transitions

The P4O framework is constantly on the lookout for conserving power. Power state transitions (higher power consumption state to lower power consumption state or vice versa) happen at either the start of a new usage pattern slot or when the system is woken up/goes to sleep due to user action (e.g., screen on/off) or some external trigger (e.g., incoming voice call/call disconnect). Figure 6 depicts the power state transitions. Each transition has a label which encapsulates various actions done by the P4O framework in carrying out that particular transition.

Some of the possible actions to be taken when changing power states are given in Table 3.

4.5 Battery lifetime forecast

As mentioned earlier, the logging and learning module of the P4O framework records the battery discharge rates for each of 336 usage pattern slots. It also updates the discharge rate values whenever there is a deviation from the previously stored value using a smoothening filter. Since this is recorded in real time as and when the mobile phone user uses the device, this information can be used to accurately compute the battery lifetime. The P4O framework also takes into consideration the user charging behavior of the device while computing the battery lifetime. While recording the battery discharge rate information for any of the usage pattern slots, if the device is undercharging, the battery discharge rate for that slot is considered zero. Thus, the recorded battery discharge rate information inherently incorporates the user device charging pattern as well.

Mathematically, we can represent this problem as follows. Let D_i denote battery discharge rate (in percentage terms) corresponding to usage pattern slot i. Let t represent the duration of the usage pattern slot, which is 0.5 h in our case. Let B_C be current battery level (in percentage terms). Battery lifetime is computed as per below flowchart (Fig. 7).

5 Experimental results

The P4O framework was implemented on a Samsung Galaxy J2 smartphone [37] running Android Marshmallow. Four volunteers were chosen, and the software of their devices was updated with the P4O framework–related changes. The volunteers were asked to use their devices normally as they would have used otherwise. The experimental information was extracted

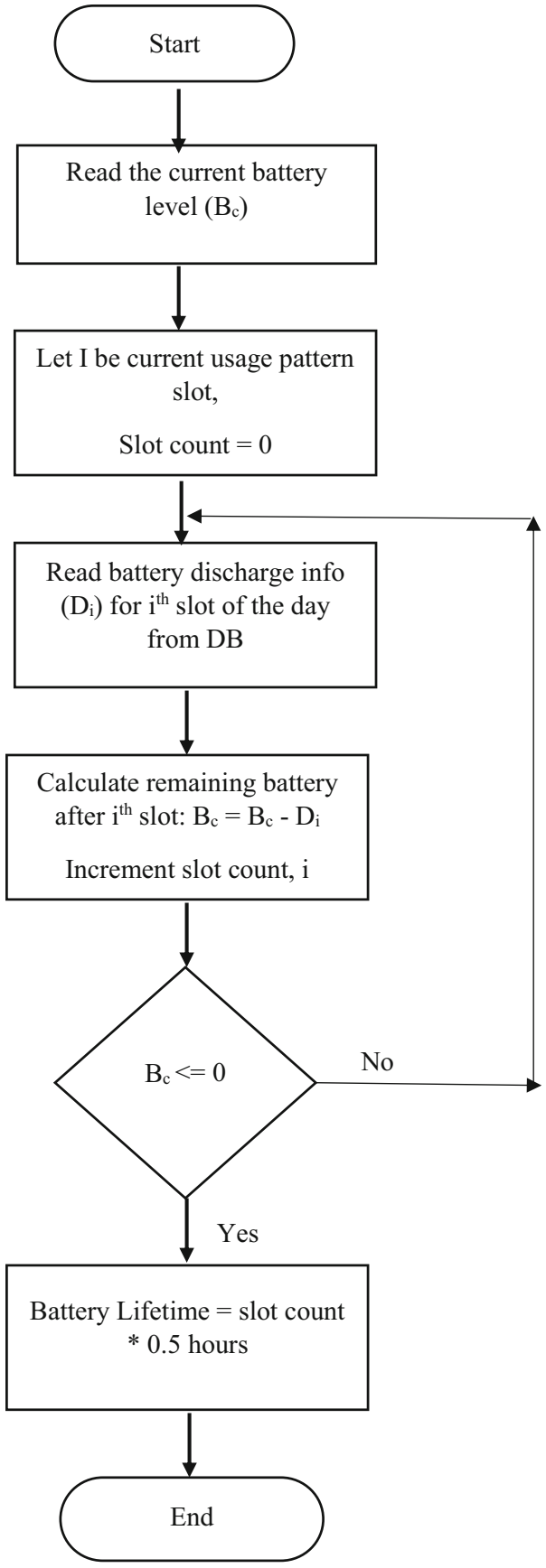

Fig. 7 Battery lifetime prediction algorithm

from these test devices every day. The overall results are grouped into four main sections: (1) battery power consumption pattern learning—here, normal devices (without P4O framework) are assigned to volunteers for usage pattern learning, (2) power state prediction of the learned patterns—here, the P4O framework–enabled devices are given to volunteers to test and provide the statistics on the power state prediction of the P4O framework, (3) battery power optimization as per predicted patterns—the P4O framework is tested for battery optimization in the real-time usage, and (4) battery lifetime forecast as per optimized battery power for user convenience. The outcomes from the abovementioned experiments are given in the below sections.

5.1 Battery consumption pattern learning

The purpose of this set of experiments is to train the device against the usage pattern data of the user. We selected 10 volunteers to do real-time experiments on the Samsung Galaxy J2 devices *without having the P4O framework*. We took volunteers from the staff group of Delhi Technological University, Delhi, India. It is important to note that these sets of experiments require a longer period of observation (at least 2 weeks) for reliable results. Hence, it requires a supportive set of volunteers who can judiciously use the device to provide trustworthy learning to the device in order to get reliable results at prediction. The usage pattern data of 10 volunteer test devices was observed for a period of 2 weeks. The 24 h of a day is divided into 48 windows of 30 min each, and the data of battery consumption is captured for each window. *These windows are referred to as slots from here onwards*. In each of these slots, the transition of the four states (high, medium, low, and very low) is marked (see the "Power consumption states mapping" and the "Power consumption states transitions" sections) and the battery data discharge rate is computed (See Table 2). This data (battery drop/consumed) is captured continuously and stored into a buffer until a broadcast of the shutdown, charging, or date change occurs. Whenever these changes occur or the buffer is full, the captured data is saved in a database in order to prevent any loss of the captured data.

In order to show that the battery usage by each user follows a pattern, we investigated the usage pattern slots (the "Building usage pattern knowledge base" section) for each user. We divided each day into 48 slots and hence each user has 336 slots to capture usage patterns in a week. We compared these 336 slots for each user for two consecutive weeks. The formula for calculating the matching percentage is given below:

$$\text{Slots matching percentage} = (\text{number of matching slots} \times 100/\text{total slots}) \quad (4)$$

For each of the 10 users, the slot-matching information is depicted in Fig. 8. It can be observed from the figure that 84 to 94% of the slots have matching battery discharge rates.

A bar graph for each of the 10 users is shown in Fig. 9 which shows the matching and non-matching slot scores for each user. The higher number of matching slots for each user shows that the battery discharge rates over a period of time follow a pattern.

From Figs. 8 and 9 above, we can conclude that the battery discharge rates over a period of time follow a pattern. This validates our assumption that every user exhibits a particular usage pattern which, in power consumption scenario, is reflected in the battery discharge pattern of the device.

5.2 Power state prediction

Based on the pattern learned in the above section, the next task is to test if the proposed P4O framework is able to predict the learned battery power consumption states in real time. This set

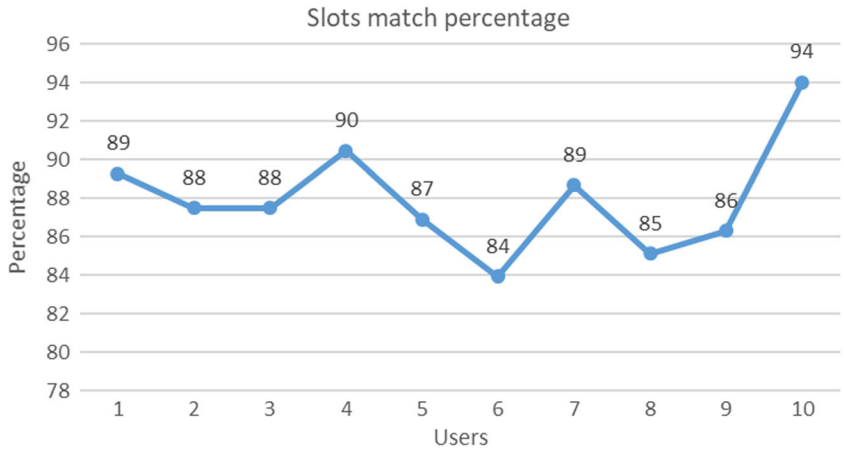

Fig. 8 Battery discharge slots match pattern (10 users)

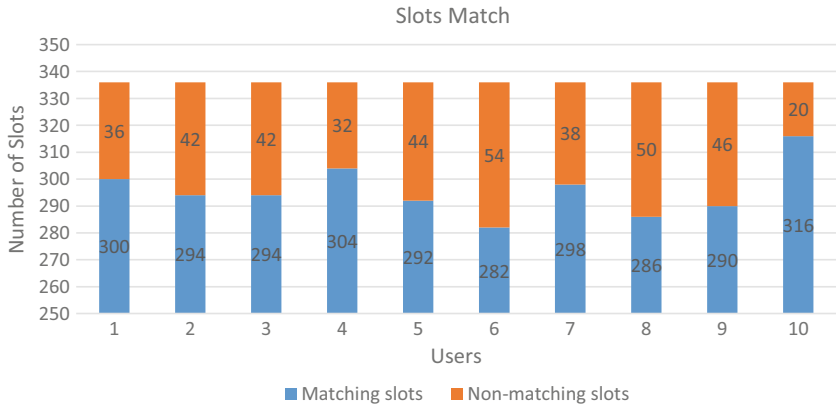

Fig. 9 Slots matching score (10 users)

of experiments is designed to evaluate the prediction capability of the P4O framework for the new time slots for the same user. *The same users have given the same devices (Samsung Galaxy J2) enabled with the P4O framework for 2 weeks*. The data collected with the predicted (P4O framework enabled) device is then compared with the actual (without P4O framework) device. Figure 10 depicts the comparison of the predicted versus the actual power state of one user for 1 day. It can be noted that the P4O framework is able to correctly predict the learned pattern of the power state for most of the usage pattern slots. The data depicted is taken for two consecutive weeks for experimental validation. However, with more learning or continuous learning mechanisms, the accuracy of the system would increase.

The accuracy and other statistics of the proposed P4O framework can be derived from the experimental results. As discussed in the previous section, there are 48 slots for each user and there are four users who are using P4O-enabled devices to predict the users' usage pattern. The patterns are predicted for 3 days, and hence, there are a total of 576 slots ($48 \times 4 \times 3 = 576$) where the proposed P4O framework predicted the usage pattern. Out of the 576 slots, the P4O framework correctly predicted the usage pattern for the 417 usage pattern slots. Hence, the accuracy can be calculated as follows:

$$\text{Accuracy} = \frac{\text{Total correctly predicted slots}}{\text{Total predicted slots}} \times 100 \tag{4}$$

As per Eq. 3, the accuracy of the proposed P4O framework is 73%. In order to provide further statistics about the performance of the P4O framework, the difference of the predicted versus the actual battery usage pattern data is plotted and is shown in Fig. 11. The difference is plotted as a standard normal distribution. It can be observed from the figure that the predictions in most of the slots are centered on zero (as the mean value). This implies that the predicted value coincides with the actual value of the battery usage at most of the usage pattern slot which further validates the accuracy of the proposed P4O framework.

5.3 Power optimization

In the latest set of experiments, the performance of the P4O framework is tested in real time. The experimental setup is as

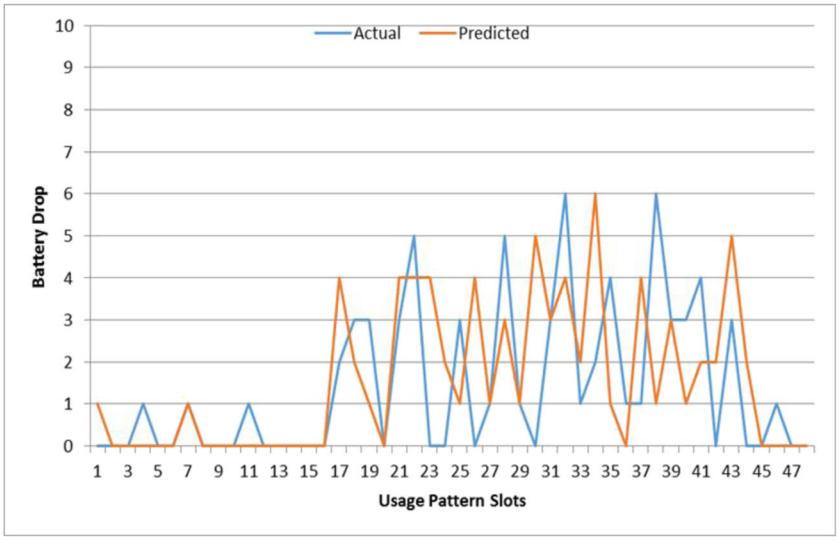

Fig. 10 Power state: actual vs predicted

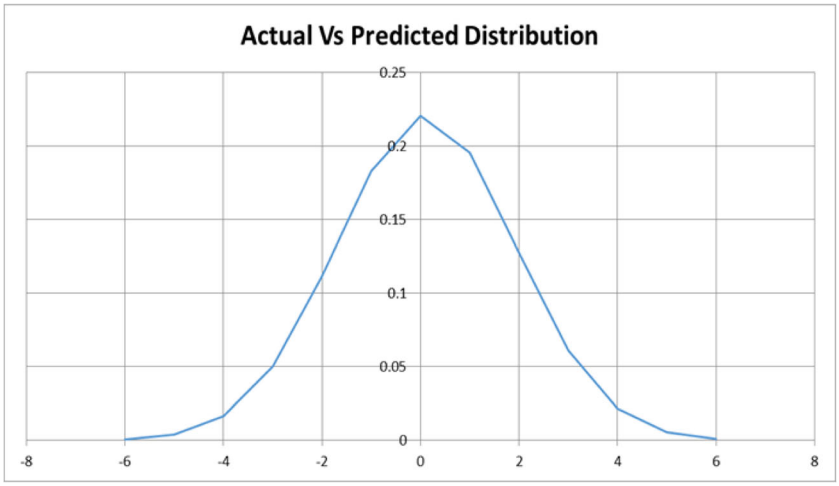

Fig. 11 Power state: actual vs predicted distribution

follows: 10 Samsung Galaxy J2 2016 devices are utilized for experiments. The experiment is divided into three phases. The first phase is the *benchmarking phase*, where these 10 devices, without P4O framework software, are given to 10 users for 1 week. We collected the battery consumption data of all 10 users for each day of the week (Monday to Sunday). The battery consumption data is shown in Table 4. As we can see from Table 4, the battery discharge values are different for every user; at the same time, it differs from day to day for the same user.

The second phase is the *learning phase* where all these 10 devices are enabled with the P4O framework in the learning mode for 2 weeks. As explained in the "Building usage pattern knowledge base" section, the P4O algorithm–learned battery consumption pattern for each of the 48 usage pattern slots during each day of the week (total $48 \times 7 = 336$ slots). The last phase is the *validation phase* where all these 10 devices trained with the P4O framework are tested for 1 week. Table 5 below shows the battery consumption data in actual devices at the benchmarking phase vs the P4O-optimized devices at the validation phase. As we can see from Table 5 below, the P4O algorithm consistently optimizes the power for each user each day.

It is evident from Table 5 that the P4O-optimized devices have low battery power consumption and hence are capable of saving more battery power in comparison with devices without the P4O framework. A snapshot of the battery level from 3 (out of 10) sample devices from the validation phase is shown in Fig. 12. It can be observed that the proposed P4O framework can learn the user pattern and can effectively use the pattern to optimize the battery power of the device.

The power saved by the P4O framework is further depicted in Figs. 13 and 14. In Fig. 13, the average weekly power savings with the P4O framework for 10 users are shown. On the *X*-axis, the user number is plotted, whereas on the *Y*-axis, the battery drop percentage is plotted. In the figure, bars in blue color show the average weekly battery discharge

Table 4 Daily percentage battery drop for 10 users

User no.	Day of the week						
	Monday (%)	Tuesday (%)	Wednesday (%)	Thursday (%)	Friday (%)	Saturday (%)	Sunday (%)
1	63	65	58	53	70	80	76
2	56	59	65	51	68	76	69
3	45	43	39	54	48	55	57
4	73	71	79	70	68	82	85
5	66	61	68	70	72	56	59
6	60	56	66	51	57	52	50
7	49	43	40	41	41	39	36
8	84	87	89	80	82	75	73
9	56	53	47	53	38	42	40
10	72	67	63	69	75	78	74

Table 5 Daily percentage battery drop vs optimized battery for 10 users

User no.	Day													
	Monday (%)		Tuesday (%)		Wednesday (%)		Thursday (%)		Friday (%)		Saturday (%)		Sunday (%)	
	Bench	Opt	Bench	Opt	Bench	Opt	Bench	Opt	Bench	Opt	Bench	Opt	Bench	Opt
1	63	42	65	46	58	37	53	34	70	47	80	55	76	51
2	56	43	59	46	65	47	51	39	68	54	76	55	69	53
3	45	32	43	34	39	28	54	39	48	36	55	36	57	41
4	73	56	71	55	79	60	70	55	68	51	82	61	85	68
5	66	47	61	46	68	46	70	46	72	58	56	40	59	42
6	60	47	56	45	66	55	51	40	57	45	52	39	50	40
7	49	30	43	27	40	26	41	27	41	26	39	23	36	25
8	84	60	87	70	89	68	80	58	82	64	75	55	73	52
9	56	41	53	38	47	33	53	40	38	29	42	31	40	28
10	72	52	67	46	63	49	69	50	75	56	78	54	74	56

percentages with the original software, whereas bars in red color show the average weekly battery discharge percentages with the P4O software. It is clearly visible from the figure that the P4O framework consistently optimizes power and has less battery consumption for each user. The value of power saved for various users differs from each other. Some of the users use device heavily whereas some users use device moderately (average battery drop minimum 41% for user no. 7 and maximum 81% for user no. 8).

The range of the power saved by the P4O framework for the 10 users for a day is depicted in Fig. 14. As we can see from the graph given in Fig. 14, the P4O framework is able to optimize the power from 20 to 40%. In this graph, the user numbers are plotted on the *X*-axis and their corresponding device power savings (percentages) are plotted on the *Y*-axis. It can be seen from the figure that for user 1, the percentage of power saving is 33.33%, for user 2, the percentage of power saving is 23.08%, and so on.

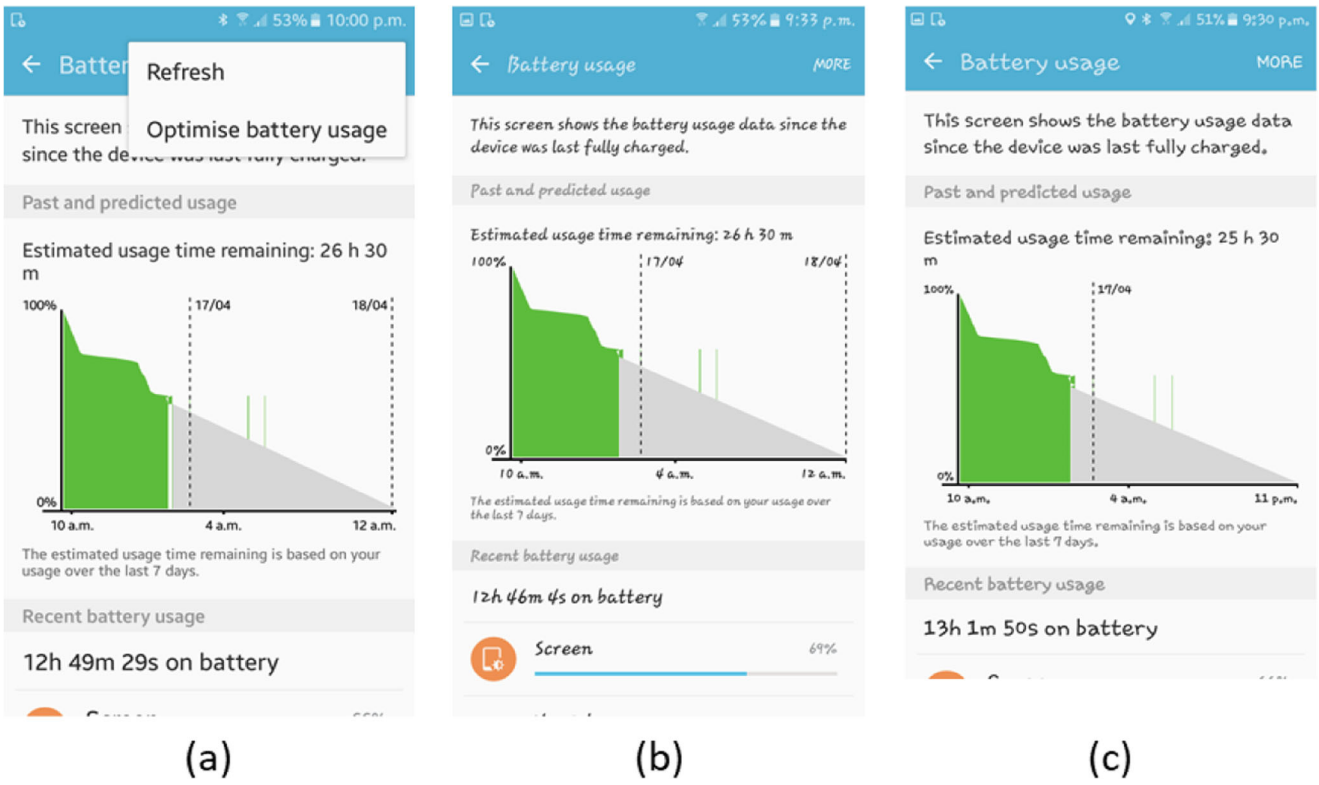

Fig. 12 **a**–**c** Test devices with power savings.

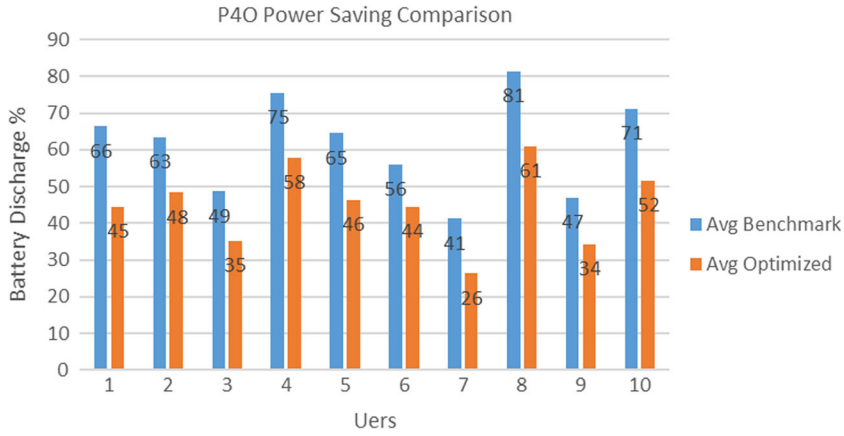

Fig. 13 Average weekly power savings with the P4O framework (10 users)

5.4 Battery lifetime forecast

Battery lifetime forecast is an important aspect of the P4O framework. Based on the recorded battery discharge pattern, the system can accurately predict the time up to when a battery can last without charging. For this experiment, 10 users were given 100% charged devices (Samsung J2) and were asked not to charge their devices until the battery is fully drained. The users noted the number of hours the battery of their devices lasted. For each user, at the start of the experiment, the P4O system predicted the number of hours the battery of that particular user will last based on the knowledge base that the P4O framework has learned. The experimental results are shown in Fig. 15. It can be seen from the figure that for all users, the graphs for the actual number of hours and the predicted hours overlap. From the percentage error graph, it can be seen that the percentage error between the actual battery lifetime hours and the predicted hours ranges from 2 to 26%. Thus, the best-case accuracy of the P4O framework for the battery lifetime prediction is 98%.

6 Conclusion and future work

Power conservation is central to the use of smart phones. The technology in fabrication has kept pace with the times following Moore's law; the battery technology has lagged behind. Therefore, power optimization plays a key role in enhancing the mobile users' satisfaction. To the best of our knowledge, very less or none of the earlier works (SOA) evaluated smart devices in these two directions. A comparative study on some recent state of the art and the present work is given in Table 1. It can be noted that the power optimization in smart phones and battery life forecast is a relatively new area of research. The contributions of this paper are twofold: (1) a novel framework for power optimization in smart phones, referred to as P4O, (2) a new approach for battery lifetime forecast. The proposed framework called P4O (*P*attern, *P*rofiling, *P*rediction, and *P*ower *O*ptimization) is detailed in the "P4O framework" section. This framework has many advantages. It solely runs on the device. Therefore, there is no security or

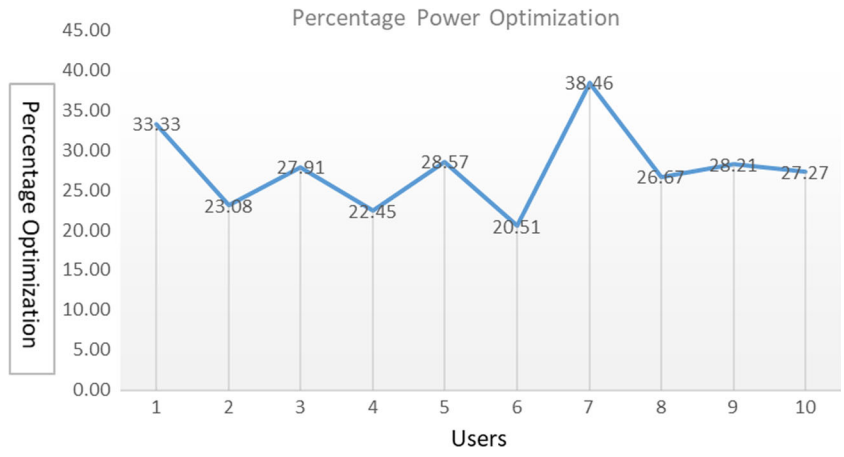

Fig. 14 Percentage of power savings with the P4O framework (10 users)

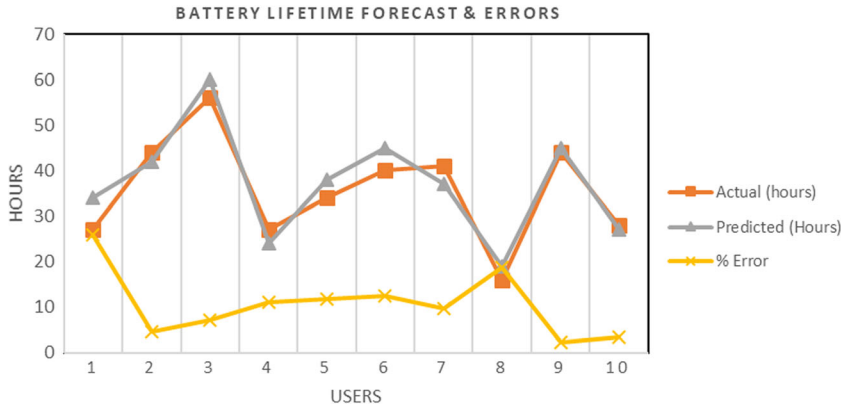

Fig. 15 Battery lifetime forecast and errors (10 users)

privacy aspects involved in the use of this framework. It directly makes use of the battery discharge rate information for benchmarking user behavior. This makes it independent of which application user uses, as the user tends to install/uninstall applications. This paper also proposed a new approach for battery lifetime forecast (the "Power consumption pattern and power states" section). The proposed method makes an accurate prediction of the battery lifetime.

The proposed framework has been implemented on the Android smart phone. Its efficacy has been validated in experimental test results. We conducted experiments at different stages. In the first set of experiments, users are given four mobile sets without the P4O framework to learn the usage patterns for 2 weeks. In the next set of experiments, we provided P4O-enabled devices to the same set of users to see if the proposed framework is able to predict the learned usage patterns. With this experiment, we established that the proposed P4O framework can predict the battery lifetime with 98% accuracy. In the third set of experiment, we validated the efficacy of the P4O framework as shown in Figs. 11 and 12. The experimental test results validate the proposed P4O framework with the power optimization of 20–40% over the default Linux and Android power saving features in an Android smartphone. More power savings can be achieved by the P4O framework by adding more low-power consuming actions in the power state transitions. This will be investigated in the future.

It may be noted here that this work requires the support of volunteers. We chose volunteers from the staff group of Delhi Technological University, Delhi, India. We carried out the experiments with four volunteers. It is important to note that the less number of probes (volunteers) is due to the nature of experiments. First, it requires a supportive set of volunteers who can judiciously use the device to provide trustworthy learning to the device in order to get reliable results at prediction. Second, the experiments need to be carried out for a longer period of time (at least 2 weeks). It requires large-scale effort to engage a huge number of volunteers for such a longer period of time while the scope of this manuscript is to introduce the proposed P4O framework and prove its efficacy with experimental results. Thus, to provide experiments on a large volume of users is in the scope of the future work.

References

1. Gartner Report, Egham, UK, February 15, 2017. Available at: http://www.gartner.com/newsroom/id/3609817. Accessed 27 March 2019
2. Deloitte 2015 Global mobile consumer survey. Available at: https://www2.deloitte.com/content/dam/Deloitte/us/Documents/technology-media-telecommunications/us-tmt-global-mobile-executive-summary-2015.pdf. Accessed 27 March 2019
3. Samsung Galaxy Note 7 with inbuilt Iris scanner. https://news.samsung.com/global/everything-you-need-to-know-about-the-galaxy-note7s-iris-scanner. Accessed 27 March 2019
4. Samsung Galaxy S7 Edge specifications. https://www.techradar.com/reviews/phones/mobile-phones/samsung-galaxy-s7-edge-1315189/review. Accessed 27 March 2019
5. IObit Applock face recognition unlock Android application. http://www.iobit.com/en/applock.php. Accessed 27 March 2019
6. Phone user behaviour report for unlocking phones. http://www.phonearena.com/news/Did-you-know-people-unlock-their-phones-an-average-100-times-a-day_id74189. Accessed 27 March 2019
7. Rahmati A, Qian A, Zhong L (2007) Understanding human-battery interaction on mobile phones. In: Proceedings of the 9th international conference on human computer interaction with mobile devices and services. ACM, Singapore
8. Balani R (2007) Energy consumption analysis for Bluetooth, Wi-Fi and cellular networks. White Paper, Tech Republic
9. Rice A, Hay S (2010) Decomposing power measurements for mobile devices. In: IEEE International Conference on Pervasive Computing and Communications. Manheim, Germany 29 March – 2 April 2010
10. Carroll A (2010) An analysis of power consumption in a smartphone. In: Proc. USENIX Annual Technical Conference. Boston, MA, USA, 23–25 June 2010
11. Perrucci GP, Fitzek FHP, Widmer J (2011) Survey on energy consumption entities on the smartphone platform. In: 73rd IEEE Vehicular Technology Conference (VTC). Yokohoma, Japan, 1–5 May 2011

12. Paul K, Kundu TK (2010) Android on mobile devices: an energy perspective. In: 10th IEEE International Conference on Computer and Information Technology (CIT). Bradford, UK, 29 June – 1 July 2010
13. Lyons K, Hightower J, Huang EM (eds) (2011) Understanding human-smartphone concerns: a study of battery life. Pervasive 2011, LNCS 6696. Springer-Verlag, Berlin Heidelberg, pp 19–33
14. Demumieux R, Losquin P (2005) Gather customer's real usage on mobile phones. In: Proceedings of the 7th international conference on Human computer interaction with mobile devices & services. ACM, pp 267–270
15. Kang JM, Seo S, Hong J (2011) Usage pattern analysis of smartphones. In: 13th Asia-Pacific Network Operations and Management Symposium. pp 1–8
16. Oliver E (2010) The challenges in large-scale smartphone user studies. In: Proceedings of the 2nd ACM International Workshop on Hot Topics in Planet-scale Measurement. ACM, pp 1–5
17. Lee J, Joe H, Kim H (2012) Smart phone power model generation using use pattern analysis. In: IEEE International Conference on Consumer Electronics. pp 412–413
18. Falaki H, Lymberopoulos D, Mahajan R, Govindan R, Kandula S, Estrin D (2010) Diversity in smartphone usage. In: Proc. ACM MOBISYS
19. Verkasalo H (2010) Analysis of smartphone user behavior. In: Mobile Business and 2010 Ninth Global Mobility Roundtable (ICMB-GMR), Ninth International Conference on IEEE, 2010, pp 258–263
20. Oulasvirta A, Rattenbury T, Ma L, Raita E (2012) Habits make smartphone use more pervasive. In Pers Ubiquit Comput 16:105–114
21. Adrakatti AF, Mulla KR (2017) A realistic approach to information services on mobile apps. J Access Serv 14(1)
22. Min AW, Wang R, Tsai J, Ergin MA, Tai TYC (2012) Improving energy efficiency for mobile platforms by exploiting low-power sleep states. CF'12, may 15–17, Cagliari, Italy
23. Al-Turjman F (2017) Cognitive-node architecture and a deployment strategy for the future sensor networks. Mobile Networks and Applications, Springer, ISBN 9781138102293 - CAT# K34952. https://doi.org/10.1007/s11036-017-0891-0
24. Singh GT, Al-Turjman FM (2016) Learning data delivery paths in QoI-aware information-centric sensor networks. IEEE Internet Things J 3(4):572–580
25. Kang J-M, Seo S-s, Hong JW-K (2011) Personalized battery lifetime prediction for mobile devices based on usage patterns. J Comput Sci Eng 5(4):338–345
26. Krintz C, Wen Y, Wolski R (2004) Application-level prediction of battery dissipation. In: Proceedings of the International Symposium on Lower Power Electronics and Design. Newport Beach, CA, pp 224–229
27. Zhang L, Tiwana B, Dick RP, Qian Z, Mao ZM, Wang Z, Yang L (2010) Accurate online power estimation and automatic battery behaviour based power model generation for smartphones. In: Proceedings of the 8th IEEE/ACM International Conference on Hardware/Software-Co-Design and System Synthesis. Scottsdale, AZ, pp 105–114
28. Ferdous R, Osmani V, Mayora O (2015) Smartphone app usage as a predictor of perceived stress levels at workplace. In: 9th IEEE International Conference on Pervasive Computing Technologies for Healthcare (Pervasive Health). Istanbul, Turkey
29. Al-Turjman F, Betin-Can A, Ever E, Alturjman S (2016) Ubiquitous cloud-based monitoring via a mobile app in smartphones: an overview. In: IEEE International Conference on Smart Cloud (SmartCloud). New York, NY, USA
30. Elgedawy I, Al-Turjman F (2016) IdProF: identity provisioning framework for smart environments. In: IEEE Conference HONET-ICT. Nicosia, Cyprus
31. Li H, Lu X, Liu X, Xie T, Bian K, Lin FX, Feng, F (2015) Characterizing smartphone usage patterns from millions of Android users. In: Proceedings of the 2015 ACM Conference on Internet Measurement Conference, pp 459–472
32. Lu EHC, Lin YW, Ciou JB (2014) Mining mobile application sequential patterns for usage prediction. In: 2014 IEEE International Conference on Granular Computing (GrC). Noboribetsu, Japan, pp 185–190
33. Zipf GK (1965) Human behaviour and the principle of least effort: an introduction to human ecology. Hafner Publishing Co., New York
34. Google Android developers information. Available at: https://developer.android.com/index.html. Accessed 27 March 2019
35. Kalman RE (1960) A new approach to linear filtering and prediction problems. J Basic Eng 82(1):35–45
36. Monsoon Power Monitor by Monsoon Solutions Inc. Available at: https://www.msoon.com/LabEquipment/PowerMonitor/. Accessed 27 March 2019
37. Samsung Galaxy J2 (2016) Available at: http://www.samsung.com/in/smartphones/galaxy-j2-2016-j210f/SM-J210FZDDINS/. Accessed 27 March 2019

Publisher's note Springer Nature remains neutral with regard to jurisdictional claims in published maps and institutional affiliations.

Bull. Mater. Sci. (2019) 42:129
https://doi.org/10.1007/s12034-019-1789-1

© Indian Academy of Sciences

A novel micro-solid oxide fuel cell (μ-SOFC) for detecting methane content in biogas

S PHAIJIT[1], M SUKLUENG[2,*], S MARTHOSA[3], S NIYOMWAS[4], N Y VOO[5] and A KUMAR[6]

[1]Energy Technology Program, Faculty of Engineering, Prince of Songkla University, Hat Yai, Songkhla 90110, Thailand
[2]PSU Energy Systems Research Institute (PERIN), Interdisciplinary Graduate School of Energy Systems, Prince of Songkla University, HatYai, Songkhla 90110, Thailand
[3]Faculty of Science and Industrial Technology, Prince of Songkla University, Suratthani Campus, Surat Thani 84000, Thailand
[4]Department of Mechanical Engineering, Faculty of Engineering, Prince of Songkla University, HatYai, Songkhla 90110, Thailand
[5]Centre for Advanced Material and Energy Sciences (CAMES), Universiti Brunei Darussalam, Jalan Tungku Link, Gadong BE1410, Brunei Darussalam
[6]Department of Mechanical Engineering, Delhi Technological University, Delhi 110042, India
*Author for correspondence (montri.su@psu.ac.th)

MS received 10 May 2018; accepted 19 December 2018

Abstract. A novel micro-solid oxide fuel cell (μ-SOFC), with a rectangular saw-tooth shape, was designed with a 50 wt% BYCF + 50 wt% GDC_{10} cathode and a 60 wt% NiO + 40 wt% GDC_{10} anode deposited on a GDC_{10} electrolyte substrate by the spray pyrolysis technique. μ-SOFC receives methane only (CH_4) as fuel gas from one side. The fuel gas was applied at a flow rate of 0.2 l min^{-1}. The power density obtained was 1.0 μW at 800°C. Voltage levels generated by the μ-SOFC at 40–99.99% CH_4 was highly accurate representing the quantity of CH_4. Low accuracy was observed at 10–30% of CH_4. Therefore, μ-SOFC is an application of SOFC technology to be a sensor for economically detecting CH_4 in a biogas system, while being capable of operating in humid conditions at high temperatures.

Keyword. μ-SOFCs; BYCF cathode; methane; biogas; sensor.

1. Introduction

A methane (CH_4) concentration in biogas of ∼60–70% [1,2] enables us to convert H_2 by a reforming process which further can be converted into electricity by a fuel cell. Thailand is the world's largest producer of dry natural rubber [3]. The waste water from oil palm, and rubber can be used to produce biogas [4]. CH_4 is one of such biogases produced which could be used as a possible alternative fuel in the drying process. The direct methane use is challenging as the fuel processing system needs to convert hydrocarbons into hydrogen for the fuel cells [5]. The gaseous components and composition of biogas depend on the operating conditions, raw materials, retention time and temperature [1]. Hence, the quality and quantity of biogas vary widely [3]. Particularly, the biogas steam reform technique is operated at temperatures 700−900°C with a CH_4/CO_2 molar ratio of 1–1.5 with a yield of around 50% H_2 [6]. Steam reform uses high temperatures of equal to or greater than 850°C to excite the chemical reaction in the presence of a Ni catalyst. At lower temperatures, this catalyst which proved efficient in steam reforming reactions is not sufficient to activate the chemical reaction [6]. This gas reform needs a sensor which can sustain at high temperatures. Micro-solid oxide fuel cells (μ-SOFCs) are electrochemical conversion devices that could support portable equipment such as laptop computers and mobile phones [7–9].

The high power density and the ability of continuous operation for long time periods without recharge is the speciality of this device [10,11]. Thus, μ-SOFCs are of particular interest, and more attractive due to their improved reliability and robustness with a ceramic structure [12]. They can operate at temperatures between 300 and 700°C, which is below the range of large-scale conventional SOFCs [13]. The decrease in overall thickness of SOFCs in order to increase the activation levels of ion oxide is required to lower temperatures [14]. Electrolytes, such as gadolinium-doped ceria (GDC), have also been improved in terms of their higher ionic conductivity [15]. Cathode and anode sides of the fuel cells have also evolved with decrease in resistivity, low thermal expansion, high porosity and the ability to operate at lower temperature [16–19]. The key reaction takes place between electrons, ions and gas molecules which occurs in the interfacial layer with

Published online: 25 April 2019

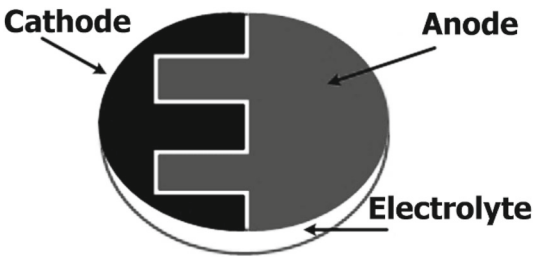

Figure 1. A novel μ-SOFC for detecting CH_4 in biogas.

anode/electrolyte/cathode interactions on the SOFC. Hence, the length of this triple phase boundary (TPB) should be maximized [20,21].

Suitable sensors could be used to monitor the multiple trace gases dissolved in transformer oil. The SOFC-based gas sensor is an alternative to detect H_2, CO, CH_4, C_2H_6, C_2H_4 and N_2 [22]. CH_4 is a very important and dangerous flammable gas used in domestic and industrial applications. High-performance methane gas sensors have been developed from nickel oxide (Ni_2O_3), decorated tin oxide (SnO_2) semiconducting films [23] and copper electrodes. Graphene oxide can be used to detect methane [24]. These sensors are based on materials with a high sensitivity to CH_4.

This investigation aims to design a novel gas sensor using a SOFC system to detect CH_4 in biogas for a reforming system. The sensor was constructed using GDC_{10} electrolyte as the substrate with a BYCF cathode and a nickel oxide (NiO) anode deposited on it, as shown in figure 1. The spray pyrolysis (SP) technique was used to deposit the cathode and anode layers on the electrolyte, in a rectangular saw-tooth shape, with a narrow space left between the cathode and the anode.

2. Experimental

A cathode composite BYCF ($Ba_{0.054}Y_{0.029}Co_{1.8}Fe_{0.062}O_{2.89}$) [25] was prepared using re-agent grade metal oxide powders from Sigma Aldrich, Germany. A mixture of 5 wt% BaO, 3 wt% Fe_2O_3, 2 wt% Y_2O_3 and 90 wt% Co_3O_4 was obtained by conventional ceramic powder processing. Commercial GDC_{10} (10% gadolinium-doped ceria, $Ce_{0.9}Gd_{0.1}O_{1.95}$) electrolyte powder with a surface area of 10–14 $m^2\ g^{-1}$ and particle size of 0.1–0.4 μm was obtained from Fuel Cell Materials, USA.The NiO anode powder with a surface area of 2.9 $m^2\ g^{-1}$ and particle size of 0.5–1.5 μm was also sourced from Fuel Cell Materials, USA.

The cathode was a 50:50 mixture of BYCF and GDC_{10}, while the anode was a 60:40 mixture of NiO and GDC_{10}. These compositions were used to control and maintain the thermal expansion coefficient close to that of GDC_{10}, which is $13.08 \times 10^{-6}{}^{\circ}C^{-1}$ at 900°C [26].

The electrolyte powders were ground for 1 h and mixed with distilled water, including 10% polyvinyl alcohol as a binder, by weight. The binder-added powder was pelletized

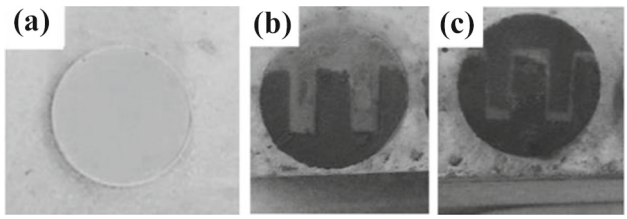

Figure 2. (**a**) GDC_{10} electrolyte. A uniaxial press was used to produce a pellet of 15 mm in diameter and 2 mm in thickness. (**b**) The SP technique was used to deposit a 50:50 BYCF + GDC_{10} cathode on the electrolyte substrate. (**c**) The μ-SOFC was completed by SP to deposit a 60:40 NiO + GDC_{10} anode with rectangular 'teeth' on the electrolyte substrate.

with the help of hydraulic press machine. The cathode and anode mixtures were milled for 12 h in a cylindrical-capped container with alumina balls as filling with the help of a horizontal rotary ball mill and dried in an oven at 150°C. The powders were ground again for 4 h in our in-house-made grinding machine and sieved through a 150 mesh.

In the SP technique, the spray gun was operated at 120 psi air pressure and the nozzle was set up at a height of 20 cm with a 16 cm spraying diameter. The pellet was placed on a stainless steel substrate and temperature was increased to 450°C. In order to use this technique, cathode and anode mixtures were needed in the form of slurries. The mixtures were mixed with distilled water in the ratio 30:70 vol%. All slurries were milled for 12 h in a horizontal rotary ball mill for obtaining highly homogeneous slurries.

In order to prepare a μ-SOFC sensor, the full fuel cell was fabricated with a 50:50 BYCF + GDC_{10} cathode and 60:40 NiO + GDC_{10} anode deposited on the GDC_{10} electrolyte pellet (50:50 BYCF + GDC_{10}|60:40 NiO + GDC_{10}|GDC_{10}) as shown in figure 1. The GDC_{10} powder was pressed to form pellets of 15 mm diameter and 2 mm thickness by using a uniaxial press under 3000 psi pressure. The GDC_{10} pellet, as seen in figure 2a, was sintered at 1400°C with a heating rate of 10°C min^{-1} for 10 h. This GDC_{10} pellet shows high density for ion conduction at high temperatures [27]. The 50:50 BYCF + GDC_{10} cathode was deposited on the GDC_{10} electrolyte pellet by SP in which the rectangular saw-tooth shape sticker covered the surface to control the shape of the cathode layer. After spraying the cathode, this pellet was co-sintered at 1100°C with a heating rate of 10°C min^{-1} for 10 h as shown in figure 2b. Meanwhile a 60:40 NiO + GDC_{10} anode was also deposited on the GDC_{10} electrolyte pellet, opposite to the cathode area, by SP, where the rectangular saw-tooth shape sticker covered the cathode layer to control the shape of the anode, and provided a space between the anode and cathode area. In order to obtain high porosity for the adsorption of gas and increase the electrochemical power density [28,29], this pellet was co-sintered at 1100°C with a heating rate of 10°C min^{-1} for 10 h under an atmosphere as shown in figure 2c. The symmetrical μ-SOFC

with a 50:50 BYCF+GDC_{10}|50:50 NiO+GDC_{10}|GDC_{10} was fabricated using the same process as the full μ-SOFC for measuring impedance spectra.

Figure 3 shows platinum electrodes as probes which were primed with platinum paste and pressed to ensure good contact. In the real experiment, the pellet with the platinum probes was placed in an in-house designed furnace. Microstructures were observed using a scanning electron microscope (SEM) (Gemini SEM, FE-SEM, and Zeiss). The ohmic and the interfacial resistance were determined by impedance spectroscopy using a Solarton 1286 electrochemical interface and a Solarton 1255 HF frequency response analyser. These were interfaced with a computer in the frequency range from 0.01 Hz to 1 MHz. A PROVA 200A PV analyser was used to measure power density. The biogas composition (H_2, CO_2, CH_4, N_2 and H_2S) was determined by gas chromatography with a flame thermal conductivity and photometric detector by using an Agilent GC7890. The mixture of gases used was 99.99% methane (CH_4) and 99.99% nitrogen (N_2), each at 60 psi pressure and mixed by a metreing valve from Swaglok as shown in figure 8b. The biogas was collected from a palm oil factory in the south of Thailand.

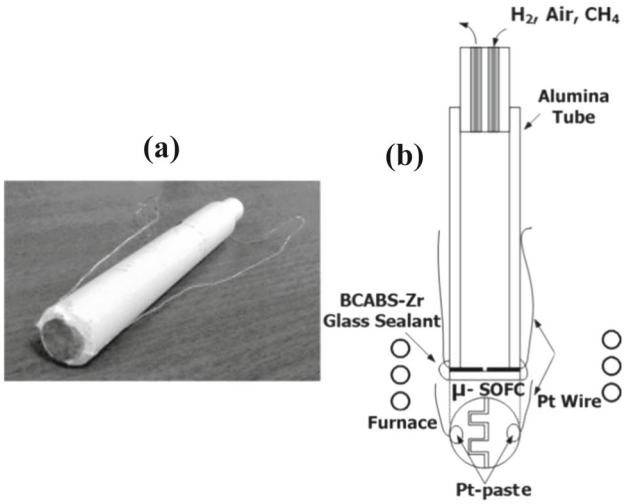

Figure 3. (**a**) The μ-SOFC with an alumina tube and platinum wire. (**b**) Diagram showing the μ-SOFC set-up for gas flow measurements.

3. Results and discussion

The μ-SOFC surface was examined using a SEM. Figure 4a shows the structure of the μ-SOFC surface with anode and cathode deposited on the electrolyte. The space (electrolyte) separating the anode and cathode was a rectangular sawtooth shape on the 15 mm diameter electrolyte substrate. Figure 4b shows the microstructure of the anode with ∼1 μm pin-holes. Figure 4c shows the microstructure of the cathode

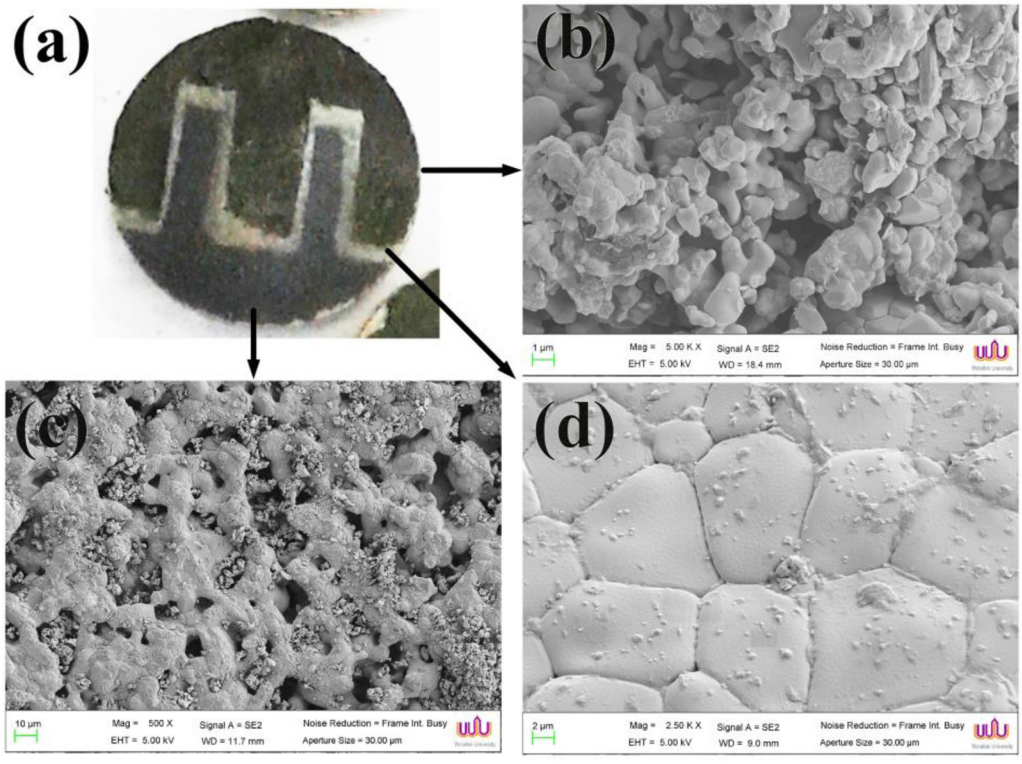

Figure 4. (**a**) The used μ-SOFC after gas sensing. (**b**) Microstructure of the 60:40 NiO + GDC_{10} anode. (**c**) Microstructure of the 50:50 BYCF + GDC_{10} cathode. (**d**) Microstructure of the GDC_{10} electrolyte.

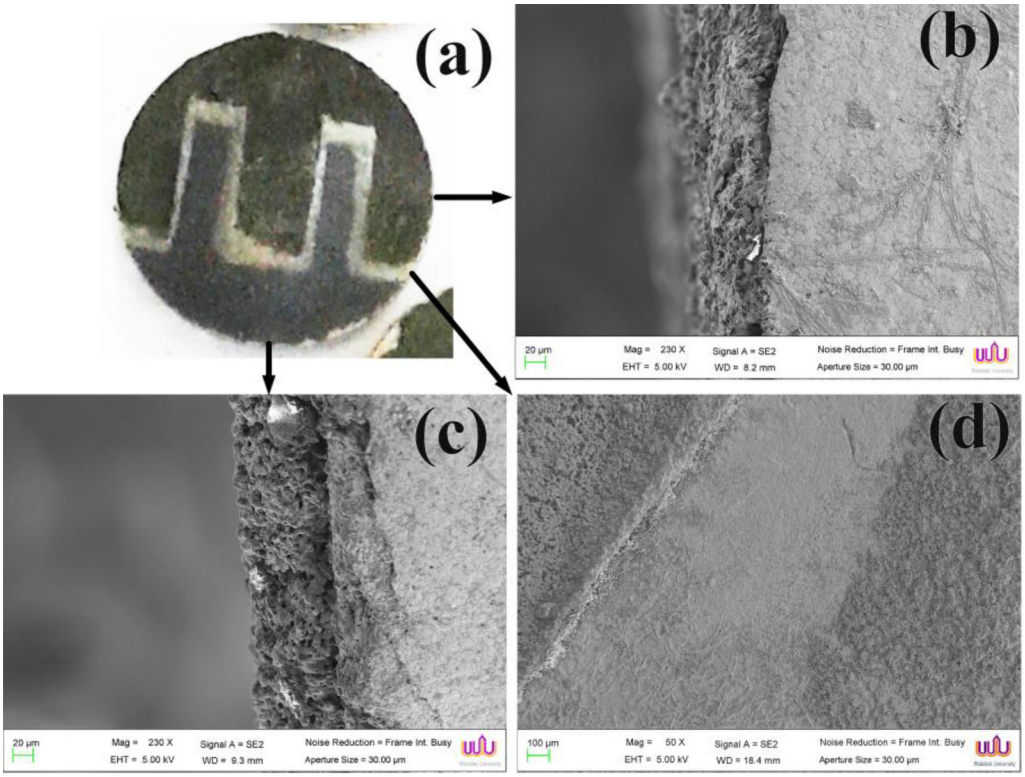

Figure 5. (**a**) The used μ-SOFC after gas sensing. (**b**) Cross-section of the microstructure between the 60:40 NiO + GDC_{10} anode and GDC_{10} electrolyte. (**c**) Cross-section showing the interface of the 50:50 BYCF + GDC_{10} cathode and the GDC_{10} electrolyte. (**d**) The free space separating the anode and cathode layers.

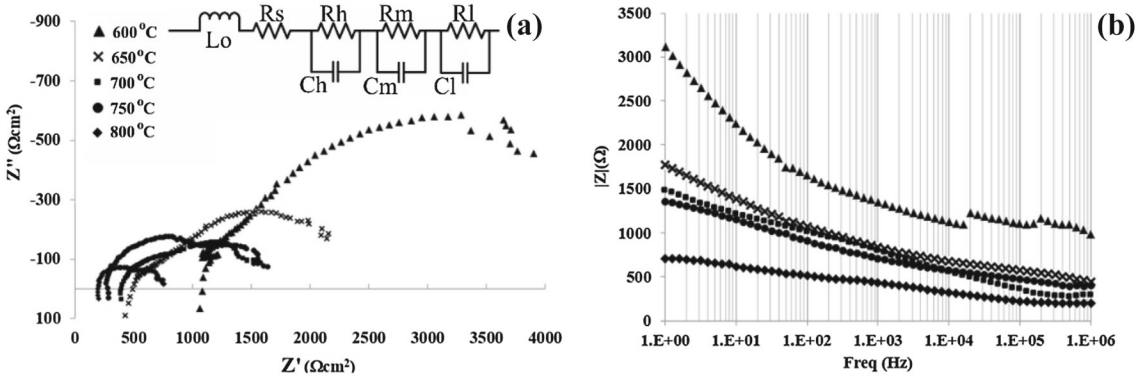

Figure 6. (**a**) Nyquist plots of the μ-SOFC impedance spectra at various temperatures in the range of 550−800°C. (**b**) Bode plots of the μ-SOFC at various temperatures.

with ~10 μm pin-holes. High porosity was observed from the microstructure of the cathode and anode [27]. Figure 4d shows the microstructure of the electrolyte with no pin-holes. This microstructure indicated that the electrolyte is highly dense. The deposited anode was 40 μm in thickness on the electrolyte substrate (figure 5b). The deposited cathode was 80 μm in thickness on the electrolyte substrate (figure 5c). SEM images clearly shows that the surfaces are well-connected to cathode–electrolyte and anode–electrolyte interfaces (figure 5b and c). The free space on the electrolyte surface was 900 μm wide between the anode and the cathode (figure 5d).

Impedance spectroscopy was utilized to assess the electrochemical properties and characteristics at different temperatures of the μ-SOFC. The impedance spectra of BYCF–GDC_{10}–NiO are fitted using Zview software with a proper equivalent circuit model as shown in figure 6a. In these models, L_o represents the inductance arising from equipment and cables during the measurements [28]. While R_s exhibits

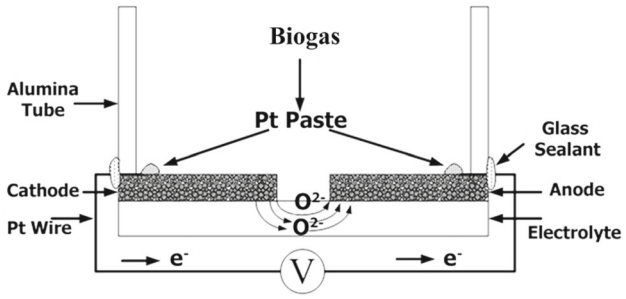

Figure 7. The conventional μ-SOFC set-up for determining the O^{2-} ion flow.

the ohmic resistance caused by electrolyte GDC_{10} and wires [29]. According to Li *et al*, the components (R_lC_l), (R_mC_m) and (R_hC_h) exhibit reaction steps in the low-frequency (LF), medium-frequency (MF) and high-frequency (HF) range, respectively [30]. The results of Nyquist and Bode plots are shown in figure 6a and b. An increase in temperature decreases the total impedance, depending on the electrical conductivity of the BYCF, NiO and GDC_{10} materials. The BYCF material shows high conductivity of 200–588.55 S cm^{-1} at 660−800°C and 3.23 eV [31]. After oxidation at 500°C, the NiO–GDC_{10} substrate shows grain boundary (GB) and grain interior (GI) conductivities at 0.107 and 0.0009 S cm^{-1}, respectively. The activation energies calculated from the Arrhenius plots for the GI and GB conductivities are 0.81 and 0.9 eV, respectively [32]. Figure 6a also shows the characteristic of the μ-SOFC at different operating temperatures. One large depressed arc is observed at 600 and 650°C and smaller arcs are observed when temperature is increased to 700, 750 and 800°C. The HF ($>10^3$ Hz) arcs correspond to the process of oxygen ionic exchange across the interfaces between the cathode and electrolyte [33]. The MF (10^3–10^2 Hz) arcs are probably associated with the diffusion of ion electrons at the surface of the cathode [28]. However, LF ($<10^2$ Hz) arcs are related to oxygen gas phase diffusion through the porous cathode layer [28]. This reaction occurred at the cathode interfaced with electrolyte that acted on the one side of the electrolyte layer. Ion (O^{2-}) transferred across the gap between cathode and anode as shown in figure 7. The impedance arising from the gas phase diffusion not only corresponds to the temperature and diffusion coefficient of oxygen in air, but also involves the microstructure of the cathode. Therefore, the addition of GDC_{10} into BYCF can enhance the processes of oxygen ions and electrode reactions [33].

Moreover, R_h and C_h corresponded to the resistance and capacitance between the anode and electrolyte; R_m and C_m corresponded to the resistance between the cathode and electrolyte, while R_l and C_l corresponded to fuel gas-diffusion impedance [34] as shown in table 1. The change in resistances (R_h, R_m, R_l) and capacitances (C_h, C_m, C_l) is dependent on the temperature, and the areas of the cathode/electrolyte/gas TPB active region [33].

The complex impedance of the μ-SOFC was recorded over 600−800°C. Figure 6a shows the usual three semicircles

Table 1. The fitting *R* (resistance) and *C* (capacitance) of impedance spectra for the symmetrical μ-SOFC (BYCF + GDC_{10}|BYCF + GDC_{10}|GDC_{10}) measured as a function of temperature in air.

	Parameters						
	R (Ω cm^2)				*C* (F cm^2)		
Temperature (°C)	R_s	R_l	R_m	R_h	C_l	C_m	C_h
600	1100	800	1500	650	1.205×10^{-06}	2.552×10^{-05}	1.552×10^{-08}
650	580	400	550	200	1.205×10^{-06}	2.552×10^{-04}	1.552×10^{-08}
700	400	180	120	200	6.184×10^{-03}	1.184×10^{-08}	1.184×10^{-05}
750	260	15	65	60	7.184×10^{-02}	1.004×10^{-07}	1.184×10^{-04}
800	150	6	8	27	1.918×10^{-01}	1.004×10^{-06}	1.184×10^{-04}

Table 2. Chemical composition of biogas from the palm oil factory in the south of Thailand.

Gas	Samples	H_2 (% volume)	N_2 (% volume)	CH_4 (% volume)	CO_2 (% volume)	H_2S (ppm)
Biogas	1	0.000	5.286	61.072	35.333	923.893
	2	0.000	4.921	60.592	34.781	953.304
	3	0.000	4.793	58.336	34.886	956.115
Average		0.000	5.000	60.000	35.000	944.437
Standard deviation		±0.000	±0.256	±1.461	±0.293	±17.847

GC was used for measurement.

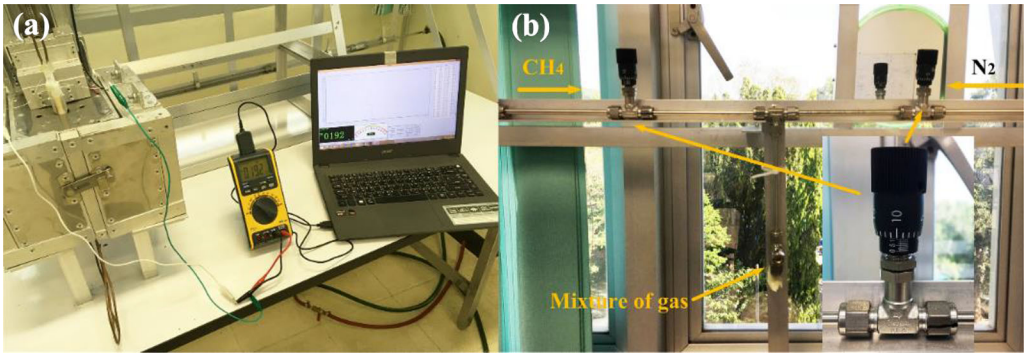

Figure 8. (**a**) The μ-SOFC sensor was set-up in the furnace for application of the gas sensing. (**b**) The conventional gas mixing technology by using metring valve to mix the CH_4 and N_2 gas.

in the complex impedance corresponding to the cathode–electrolyte and electrolyte–anode interfacial impedance contributions to the total impedance of the system. The total impedance decreases with frequency and temperature as shown in figure 6b. It is affected by porous-media transport, elementary heterogeneous chemical reaction, ion conduction and electrochemical charge transfer, as shown in equation (1):

$$Z_{\text{tot}} = Z_{\text{rd}} + \frac{R_{\text{ct,a}}}{i + j\omega R_{\text{ct,a}} C_{\text{dl,a}}} + R_{\text{ele}} + \frac{R_{\text{ct,c}}}{i + j\omega R_{\text{ct,c}} C_{\text{dl,c}}}. \quad (1)$$

Here, $C_{\text{dl,a}}$ and $C_{\text{dl,c}}$ are the double layer capacitances at the anode–electrolyte and cathode–electrolyte interfaces respectively; $R_{\text{ct,a}}$ and $R_{\text{ct,c}}$ are the charge transfer resistances at the anode and cathode respectively; R_{ele} is the ohmic resistance of the electrolyte; Z_{rd} is the effective reaction-diffusion resistance and $\omega = 2\pi f$ is the angular frequency [34].

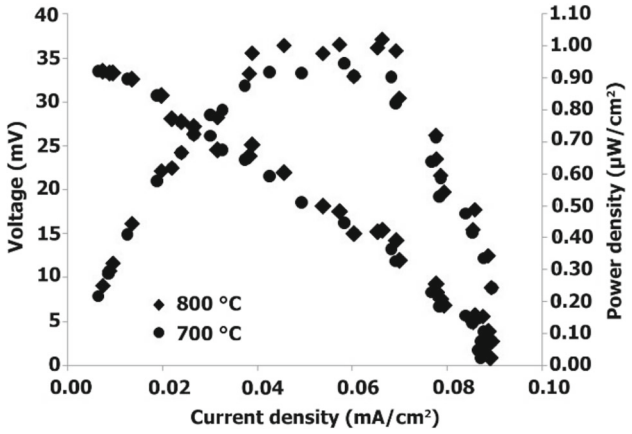

Figure 9. Current–voltage characteristics of biogas from the palm oil factory in the south of Thailand and the corresponding power densities for the μ-SOFC with a flow rate of $CH_4 = 0.2$ l min^{-1} at 700–800°C.

Therefore, the frequency also affects the total impedance through capacitances.

The biogas, as the fuel for the sensor was collected from a palm oil factory in the south of Thailand. Table 2 indicates that the biogas was measured three times by GC machine which contains N_2, CH_4, CO_2 and H_2S. The average biogas composition was 5% N_2, 60% CH_4 and 35% CO_2 by % volume. Hydrogen sulphide (H_2S) was obtained in biogas in the small amount of 944.437 ppm due to the palm wood materials. Lau *et al* [35] reported that biogas produced by palm oil mill effluent anaerobic digestion contains small amounts of H_2S. Figure 8a shows the set-up for measuring the voltage generated by the μ-SOFC sensor at 700–800°C temperature of the furnace. The calibration on the μ-SOFC sensor needs various percentages of CH_4 to generate the voltage because biogas from the factory contains 60% CH_4. Therefore, calibration of the sensor was conducted at various percentage levels of methane gas as shown in figure 8b. Figure 9 exhibits power density and voltage as a function of biogas, the palm factory, fed to the sensor at 700 and 800°C. The maximum power density of the μ-SOFC sensor was 1.00 μW cm^{-2} at 700 and 800°C. This means almost the same power density generated at both temperatures. Therefore, the μ-SOFC sensor can be operated at 700°C to save on energy consumption as well as thermal stress relief. Le *et al* [36] observed

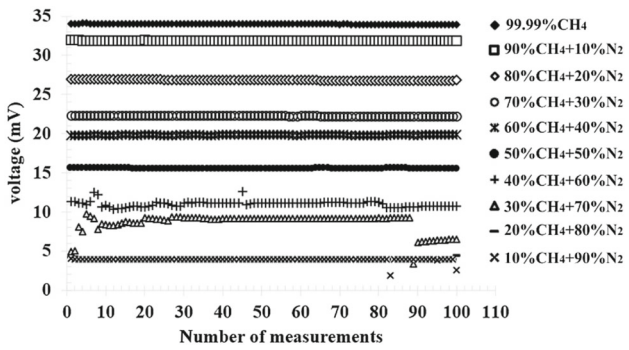

Figure 10. Measured voltage levels for different gas mixtures fed to the μ-SOFC at 800°C with the gas flow rate of 0.2 l min^{-1}.

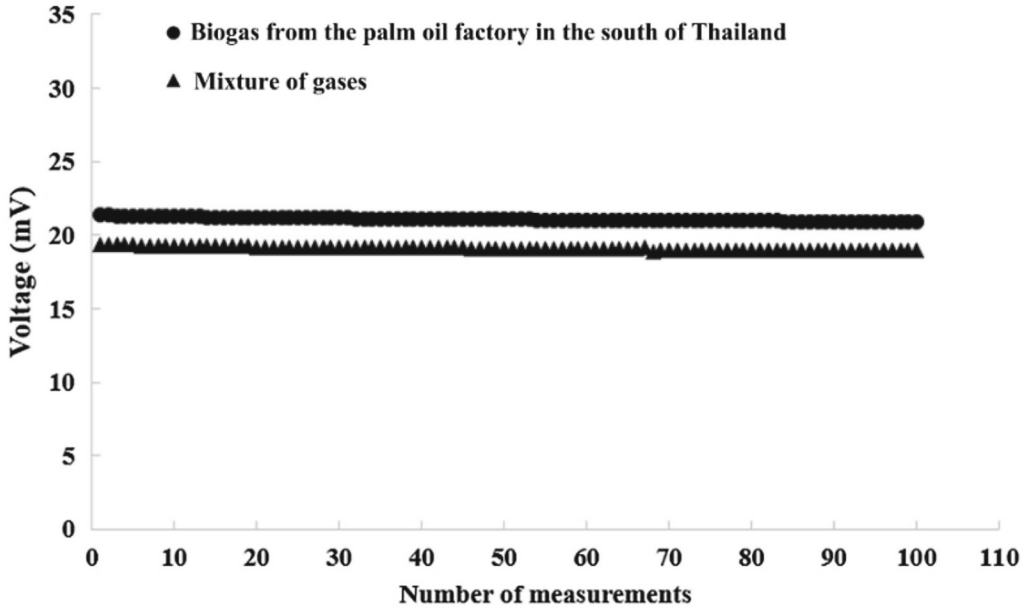

Figure 11. Comparison of voltage levels of biogas from the palm oil factory in the south of Thailand and the mixture of gases measured by the μ-SOFC at 800°C, with a flow rate of 0.2 l min^{-1}.

a power density of 0.26 W cm^{-2} from the full fuel cell fabricated from $Ba_{0.5}Sr_{0.5}Co_{0.8}Fe_{0.2}O_3$ (BSCF) + GDC cathode, $La_{1.8}Dy_{0.2}Mo_{0.2}O_9$ (LDM) electrolyte and GDC+NiO+ LDM anode which operated in an atmospheric reactant with a 1.5:1 (CH_4:O_2) ratio. At high temperatures, the composition of the BSCF + GDC cathode reacted to thermal expansions; however, it performed steadily in the temperature range of 652−700°C.

The measured voltage levels correspond to the amount of methane gas fed to the sensor. Experiments used mixture of gases which involves percentages of CH_4 and N_2 varying from 10 to 99.99%. The voltage levels of 50% CH_4 to 99.99% CH_4 were highly stable and can be used for reference. Meanwhile the voltage levels of 30% CH_4 to 40% CH_4 were unstable and had high error levels. For 10% CH_4 to 20% CH_4, it was not possible to separate the exact voltage level as shown in figure 10. There are three-layer fuel cells of BSCF/GDC/NiO which have a current level of around 0.55 A cm^2 spending 200 h, based on a 700 mV voltage level at 550°C [37]. Therefore, the μ-SOFC is a potential option for CH_4 gas detectors at high temperature.

There is insufficient methane to react in the reforming to convert CH_4 to hydrogen when the CH_4 concentration was below 40% (equation (2)). Hence, a low voltage level was detected with high error levels. CH_4 quantity should be sufficient to produce a typical endothermic reaction at high temperatures of 700−900°C. High catalysts are required to promote the conversion of syngas when the NiO-based material is used. Other reactions also occur concurrently during the dry reforming process. One typical side chemical reaction is a reverse water gas shift which can reduce the H_2/CO ratio in the syngas product. This chemical reaction contributes to proper adjustment of the H_2/CO ratio for production of higher hydrocarbons [38].

Biogas was compared with the mixture of gases as shown in figure 11. Biogas-generated voltage level is 20.90 mV while the mixture was reported at 18.84 mV (figure 11). All gas samples were measured under the same conditions. The biogas from the factory was higher than the mixture of gas by around 10.93%, because H_2 was reformed from CH_4 gas on the anode side and mixed with the air in the alumina tube chamber. The NiO composition included in the anode side of the μ-SOFC, activated and contributed to CH_4-dry reforming as shown in equation (2) [5]. The biogas from the factory contained higher CO_2 levels than the mixture of gas, and H_2S was also detected in biogas. It may also be the case that H_2S causes the generation of the H_2 which is used by CH_4 dry reforming to produce the voltage, but it has a very small effect. Normally, the SOFC technology can produce the electricity (voltage level; e^-) by H_2 and O_2, following $H_2 + O^{2-} \rightarrow H_2O + 2e^-$ and $1/2O_2 + e^- \rightarrow O^{2-}$. Therefore, the biogas from factory can produce high voltage levels that occurred in the chemical reaction following equation (2):

$$CH_4 + CO_2 \leftrightarrow 2CO + 2H_2. \quad (2)$$

Therefore, CH_4 is used to generate electricity using the μ-SOFC. A μ-SOFC with small-sized pellets cannot produce enough electricity to act as a power source. However, μ-SOFC can still be used as a low-cost sensor for CH_4 in biogas.

4. Conclusions

A novel μ-SOFC, consisted of a 50:50 BYCF + GDC_{10} cathode and 60:40 NiO + a GDC_{10} anode deposited on a GDC_{10} electrolyte substrate in rectangular saw-tooth shapes, was fabricated. This μ-SOFC only allowed the fuel gas to be fed on one side and produced microwatt power density. CH_4 gas generated with 1 μW cm^{-2} of power density and the device can be adapted to a low-cost sensor for detecting methane in the biogas which contains H_2S, CO_2, N_2 and CH_4 with CH_4 the major component at 60% (based on biogas from oil palm wood). The sensor was monitored in terms of voltage level corresponding to the quantity of CH_4 in the biogas. This sensor cannot represent accurate voltage levels for 10–40% CH_4. The μ-SOFC sensor can be usefully operated at high temperatures which would be suitable in gas forming systems and biogas power plants. The electronic sensors are sensitive to humidity, which affects both metals and semiconductors. In contrast, the μ-SOFC can be operated at comparatively high temperatures and is mainly ceramic. Therefore, the novel μ-SOFC has potential for use as a low-cost sensor to detect biogas composition.

Acknowledgements

This research was supported by the Innovation Fund (RDO590769S), Prince of Songkla University. We thank our colleagues from the Faculty of Engineering; PSU Energy Systems Research Institute (PERIN), Centre of Excellence in Materials Engineering (CEME) and Centre for Advanced Material and Energy Sciences (CAMES, Universiti Brunei Darrusalam) and all those who provided their insight and expertise that greatly assisted this research.

References

[1] Charnnok B, Suksaroj T, Boonswang P and Chaiprapat S 2013 *Bioresour. Technol.* **131** 492
[2] Chaiprapat S, Wongchana S, Loykulnant S, Kongkaew C and Charnnok B 2015 *Process Saf. Environ. Prot.* **94** 420
[3] Choosong T, Phakthongsuk P, Tekasakul S and Tekasakul P 2014 *Saf. Health Work* **5** 86
[4] Chaikitkaew S, Kongjan P and Thong S O 2015 *Energy Procedia* **79** 838
[5] González-Gil R, Herrera C, Larrubia M Á, Kowalik P, Pieta I S and Alemany L J 2016 *Int. J. Hydrog. Energy* **41** 19781
[6] Tuna C E, Silveira J L, da Silva M E, Boloy R M, Braga L B and Pérez N P 2018 *Int. J. Hydrog. Energy* **43** 2108
[7] Bornapour M, Hooshmand R-A, Khodabakhshian A and Parastegari M 2016 *Energy* **117** 176
[8] Rottmayer M, Singh R and Huang H 2016 *J. Power Sources* **332** 139
[9] Timurkutluk B, Timurkutluk C, Mat M D and Kaplan Y 2016 *Renew. Sustain. Energy Rev.* **56** 1101
[10] Patil T C and Duttagupta S P 2016 *Appl. Energy* **168** 534
[11] Pla D, Sánchez-González A, Garbayo I, Salleras M, Morata A and Tarancón A 2015 *J. Power Sources* **293** 264
[12] Wang J 2015 *Energy* **80** 509
[13] Sohn S, Baek S M, Nam J H and Kim C-J 2016 *Int. J. Hydrog. Energy* **41** 5582
[14] Kim K-J, Choi S-W, Kim M-Y, Lee M-S, Kim Y-S and Kim H-S 2016 *J. Ind. Eng. Chem.* **42** 69
[15] Yao C, Meng J, Liu X, Zhang X, Liu X, Meng F *et al* 2015 *Solid State Sci.* **49** 90
[16] Jin F, Liu J, Shen Y and He T 2016 *J. Alloys Compd.* **685** 483
[17] Yi S, Shen Y, Zhao H, Du Z, Chen N and Huang B 2016 *Electrochim. Acta* **219** 394
[18] Patro P K, Delahaye T and Bouyer E 2010 *Solid State Ion.* **181** 1378
[19] Handal H T and Thangadurai V 2014 *Solid State Ion.* **262** 359
[20] Doraswami U, Shearing P, Droushiotis N, Li K, Brandon N P and Kelsall G H 2011 *Solid State Ion.* **192** 494
[21] Mukhopadhyay M, Mukhopadhyay J, Sharma A D and Basu R N 2011 *Int. J. Hydrog. Energy* **36** 7677
[22] Ding J, Li X, Cao J, Sheng L, Yin L and Xu X 2014 *Sens. Actuators B* **202** 232
[23] Vuong N M, Hieu N M, Hieu H N, Yi H, Kim D, Han Y-S *et al* 2014 *Sens. Actuators B* **192** 327
[24] Assar M and Karimzadeh R 2016 *J. Colloid Interface Sci.* **483** 275
[25] Hing P 2015 *ECS Conference on Electrochemical Energy Conversion & Storage with SOFC-XIV (July 26–31, 2015)*, ECS
[26] Wongthong P, Nakason C, Pan Q, Rempel G L and Kiatkamjornwong S 2015 *J. Appl. Polym. Sci.* **132** 42520
[27] Hanifi A R, Laguna-Bercero M A, Sandhu N K, Etsell T H and Sarkar P 2016 *Sci. Rep.* **6** 27359
[28] Pang S, Jiang X, Li X, Wang Q and Su Z 2012 *J. Power Sources* **204** 53
[29] Çelikbilek Ö, Siebert E, Jauffrès D, Martin C L and Djurado E 2017 *Electrochim. Acta* **246** 1248
[30] Li R, Ge L, Chen H and Guo L 2012 *Electrochim. Acta* **85** 273
[31] Suklueng M, Yoong V N, Hing P and Ming L C 2014 *Walailak J. Sci. Technol. (WJST)* **12** 373
[32] Chourashiya M G and Jadhav L D 2011 *Int. J. Hydrog. Energy* **36** 14984
[33] Pang S, Jiang X, Li X, Wang Q and Su Z 2012 *Int. J. Hydrog. Energy* **37** 2157
[34] Huang Q-A, Hui R, Wang B and Zhang J 2007 *Electrochim. Acta* **52** 8144
[35] Ohimain E I and Izah S C 2017 *Renew. Sustain. Energy Rev.* **70** 242
[36] Le M-V, Tsai D-S and Nguyen T-A 2018 *Ceram. Int.* **44** 1726
[37] Kim C, Park H, Jang I, Kim S, Kim K, Yoon H *et al* 2018 *J. Power Sources* **378** 404
[38] Gao Y, Jiang J, Meng Y, Yan F and Aihemaiti A 2018 *Energy Convers. Manage* **171** 133

Computers and Electrical Engineering 77 (2019) 12–26

Contents lists available at ScienceDirect

Computers and Electrical Engineering

journal homepage: www.elsevier.com/locate/compeleceng

A novel parallel classifier scheme for vulnerability detection in Android ☆

Shivi Garg [a,b], Niyati Baliyan [a,*]

[a] Department of Information Technology, IGDTUW, Delhi, 110006, India
[b] Department of Computer Engineering, J.C. Bose University of Science and Technology YMCA, Faridabad, 121006, India

ARTICLE INFO

Article history:
Received 29 August 2018
Revised 24 April 2019
Accepted 24 April 2019

Keywords:
Android
Hybrid analysis
Machine learning
Malware
Parallel classifiers

ABSTRACT

Android is one of the most commonly used mobile operating systems; however, its open-source nature and flexibility of usage attract a lot of attention from cybercriminals. In recent years, the rapid increase in malware has become a major cause of concern amongst Android users. The cybercriminals either aim to exploit confidential information from users or try to corrupt their systems by infecting them with malicious code. In order to make Android systems more secure, several malware detection techniques using static, dynamic, and hybrid analysis have been introduced in recent times; however, these techniques are inaccurate and have low efficiency. The paper not only explains how distinctive parallel classifiers can be used for detecting zero-day android malware but also addresses the oncoming highly elusive vulnerabilities. The proposed methodology combines characteristics from various parallel classifiers using expectation maximization to achieve 98.27% accuracy.

© 2019 Elsevier Ltd. All rights reserved.

1. Introduction

Internet of Things (IoT) has emerged as a strong communication link that interconnects a large number of devices like home-appliances, smartphones, etc., with people, processes, and data, thereby allowing them to communicate seamlessly. The smartphone-enabling technologies, such as built-in sensors, Bluetooth, Radio-Frequency Identification (RFID) tracking, etc. allow it to be an integral part of the IoT world [1]. However, its use imposes severe security and privacy threats since smartphones usually contain and communicate sensitive private information. With an accelerated evolution in the field of mobile computing, smartphones have become more sophisticated in recent years. These days, smartphones are not only being used for personal conversations, but also for shopping, flight booking, Internet banking, etc., which makes users store their confidential information within smartphone applications. Therefore, a large number of new malware is being developed and introduced to steal sensitive data from users. This malware can steal personal information, encode or encrypt private data, and install fraudulent programs [2], as mentioned in Fig. 1.

There were more than 2.3 billion smartphone users globally in 2017, and by 2019, this number is likely to increase to nearly 2.7 billion [3]. Various mobile operating systems (OS) are available globally; however, Android and iOS are the most used [3]. Android scores over other mobile OS since it is open-source in nature, has a Linux-based kernel, and is a

☆ This paper is for regular issues of CAEE. Reviews processed and recommended for publication to the Editor-in-Chief by Area Editor Dr. G. Martinez Perez.

* Corresponding author.
E-mail address: niyatibaliyan@igdtuw.ac.in (N. Baliyan).

https://doi.org/10.1016/j.compeleceng.2019.04.019
0045-7906/© 2019 Elsevier Ltd. All rights reserved.

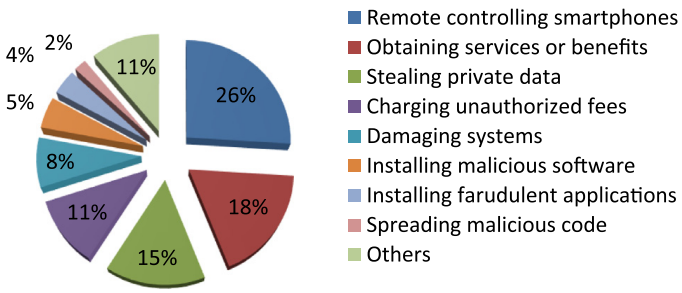

Fig. 1. Percentage distribution of various cyber crimes committed in the year 2017.

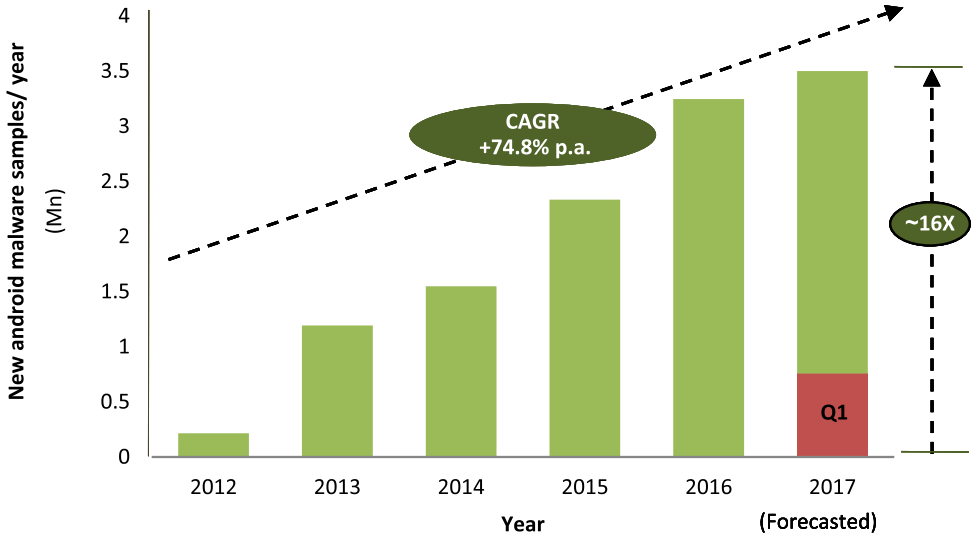

Fig. 2. Growth of Android malware.

light-weight cost-effective platform. However, these features make Android susceptible to attacks. Google Play store and third-party unreliable resources majorly contribute to the expansion of malicious applications on Android [4]. Google's 2015 report[1] claimed that almost 30 percent of all active Android phones and tablets (nearly 420 million out of 1.4 billion at that point of time) below 4.4.4 version did not receive patches. Also, 2016's report[2] mentioned that over 100 security researchers made public contribution to Android for a total of $1 million. In the year 2017, 50 malicious apps entered Google Play store that led to 4.2 million downloads[3] of the rogue program. Fig. 2 explains the growth of Android malware from the year 2013 to 2017, where the count is in millions and Compound Annual Growth Rate (CAGR) is in percentage [5].

Security in Cyber-Physical Systems (CPS) is a critical element. If proper security and privacy rules are not followed, the deployment of CPS may be hindered [6]. Therefore, various security models provide effective security for the IoT network to protect it from both external and internal threats and attacks.

1.1. Related work

With an exponential increase in Android malware in recent years, several approaches are introduced to detect the inherent vulnerabilities present in the Android OS. The first Android malware detection technique used static analysis, where individual sections of the code are analyzed without actually executing the application on an external device or an Android Emulator. This is a cost-friendly, quick and resource efficient method for finding vulnerabilities. In static analysis, two main approaches are reviewed:

(i) Signature-based detection: It is the foundation of AndroSimilar [7], which is used to detect only the samples of known malware. DroidAnalytics [8] predominately carries out collection, extraction, and analysis of malware affected Android APKs.

[1] Google, "Android security 2015 year in Review," Feb. 27, 2018. [Online]. Available: https://source.android.com/security/reports/Google_Android_Security_2015_Report_Final.pdf.

[2] Google, "Android security 2016 year in Review," Feb. 27, 2018. [Online]. Available: https://source.android.com/security/reports/Google_Android_Security_2016_Report_Final.pdf.

[3] Liam Tung, "Android malware in Google Play racked up 4.2 M downloads: Are you a victim?," zdnet.com.[Online]. Available:https://www.zdnet.com/article/android-malware-in-google-play-racked-up-4-2-million-downloads-so-are-you-a-victim/. [Accessed: March. 15, 2018].

(ii) Permission-based detection: This method can detect unknown malware samples that remained undetected in Signature-based technique. Several tools are based on permission-based detection method, of which three were reviewed in detail. The first tool, Stowaway [9], can identify malware by tracking Application Programming Interface (API) calls. The second tool, proposed by R. Sato [10], is able to analyze AndroidManifest.xml file and calculate malignancy score. The third tool, PUMA [11] is able to take the extracted permissions into consideration to detect malware.

However, the technique that uses static analysis has a drawback, i.e., code obfuscation makes matching pattern a major problem in detecting malicious behaviour of applications, also it does not allow dynamic loading of code. The similarity score in signature-based detection technique sometimes misclassifies non-harmful apps as malicious and thus, cannot detect unknown malware types. Permission-based detection technique neither analyzes reflective calls nor identifies adware and thereby gives a high false positive rate.

The second technique uses dynamic analysis, which aims to overcome the limitations of the static analysis. In this technique, the behaviour of the application in a real-time environment is monitored. This approach checks the performance of the application in the running state, which successfully resolves the issue of dynamic code loading in static analysis. In dynamic analysis, there are three key approaches:

(i) Anomaly-based detection: It is used in various mechanisms like CrowDroid [12], Andromaly [13], and AntiMalDroid [14], etc. CrowDroid identifies malware by initiating and executing system calls in the client-server architecture. Andromaly detects malware by focusing on and observing the behavior of events in the Android application. AntiMalDroid detects malware during run-time. It generates signatures by recording inputs and corresponding outputs based on the application features.
(ii) Taint Analysis: It is particularly used by TaintDroid [15], which is based on the scientific approach known as dynamic taint analysis. This tool monitors the movement of the tainted information and performs an automatic tagging of sensitive data, such as GPS or microphone.
(iii) Emulation-based detection: It is used by DroidScope [16] which has functionalities that depend on the inspection of the OS, Dalvik Semantics and AASandbox [17]. It performs both static and dynamic analysis in the sandbox by working on the class.dex file. It breaks the file into an easily understandable form using the Monkey tool [18].

However, dynamic analysis is not feasible for battery operated devices since they consume a lot of resources (e.g., time, memory, etc.). Anomaly-based detection techniques consume time and power, and fabricate incorrect results when a legitimate app invokes more system calls. Taint analysis does not track control flow, while emulation-based detection provides limited coverage and neglects new malware. The third technique combines both static and dynamic analysis methods and is known as hybrid analysis. It extracts information and executes application simultaneously. The hybrid analysis provides better results as compared to the results obtained from static and dynamic analysis; however, it increases the time complexity of the system. The paper reviews different tools used in the hybrid analysis:

(i) Mobile Sandbox [19] works on the principle of signature-based and permission-based methods, where it examines the manifest file, user permissions, and anti-virus to identify any malicious code and then checks the behaviour of the application in the running state.
(ii) Andrubis [20] feeds the result of a static analysis, which is obtained by analyzing byte-code and AndroidManifest.xml file, as an input to the dynamic analysis which further performs taint tracing, method tracing, and system level analysis while executing the application.
(iii) SAMADroid [21], a 3-level hybrid malware detection model for Android, is an accurate and efficient solution for malware detection. However, it depends on server communication and therefore, the malicious behavior of Android APKs is detected at the remote site.
(iv) DroidRanger [22] is a heuristics scheme that detects known malware sample through permission-based filtering and behavioral foot-printing. However, it focuses only on 10 permissions for each malware family.
(v) DroidDolphin [23] obtains static and dynamic features through APIMonitor and APE_BOX, and uses SVM for classification. Its drawback is that it is easily evaded by anti-emulator techniques.

These techniques have failed to deliver efficient malware detection as both static and dynamic analysis have managed to achieve a maximum accuracy of 93%, while hybrid analysis has achieved 94% accuracy [24]. Techniques using hybrid analysis have their own limitations that inhibit them from conveying an impeccable result. Previously used techniques deploying hybrid analysis produced results that were worse than the fully static case for all the families.

The fourth technique, Machine Learning (ML), is non-conventional. ML is based on Artificial Intelligence, which allows the system to learn and adapt from experience without the need to be programmed explicitly. ML has proved to be efficient not only in computer science but also in diverse applications like – electromagnetics, circuit theory, atomic physics [25], etc. In this technique, several features from Android Package Kit (APKs) are extracted with which the dataset is trained and APKs are classified. The classifiers are programmed to detect malicious APKs from the testing dataset. ML algorithms are perceived to be more efficient than other available techniques. The paper aims to surpass the best accuracy achieved by ML to date, with the set of algorithms defined in Section 3. Previous ML approaches for malware detection in Android were not efficient and scalable [26]. The paper proposes a novel approach to provide better results and to overcome the limitations of previous ML approaches. Proposed methodology detects malware at an early stage by deploying parallel ML classifiers and their features. Table 1 provides a comparative study of existing Android malware detection techniques.

Table 1
Comparative study of Android malware detection techniques.

Approach	Technique used	Tools	Description	Limitations
Static	Signature-based	AndroSimilar [7]	Used to detect only the samples of known malware	- Classifies non-harmful apps as malicious - Cannot detect unknown malware types - Produces a high false positive rate - Does not analyse reflective calls and adware samples
		DroidAnalytics [8]	Collects, analyses, extracts the association of malware affected android APKs	
	Permission-based	Stowaway [9]	Identifies using API call track down	
		Sato [10]	Analyses the manifest file of an application and calculates the malignancy score	
		PUMA [11]	Performs malware detection by taking the extracted permissions into consideration	
Dynamic	Anomaly-based	CrowDroid [12]	Identifies vulnerabilities by initiating system calls and executing in a client-server architecture	- Consumes time and battery and fabricate incorrect results - Does not track control flow - Provides limited coverage and neglects new malware
		Andromaly [13]	Focuses on behavior and event of the application	
		AntiMalDroid [14]	Records the I/O based on the features performed in the application for the generation of a signature	
	Taint Analysis	TaintDroid [15]	Monitors the movement of data and its automatic tagging	
	Emulation-based	DroidScope [16]	Functionality depends on OS, Dalvik Semantic, and AASandbox	
Hybrid	NA	Mobile sandbox [19]	Examines permissions and AV to identify malicious code to check apps behavior in running state	- Produces worse results than the fully static case for all families - Primarily dependent on server communications - High resource consumption - Malware detection at the remote site instead of localhost - Focuses on 10 permissions for each malware family -It was easily evaded by anti-emulator techniques
	NA	Andrubis [20]	Static analysis results fed to dynamic analysis, to perform taint tracing, method tracing, and system level analysis	
	NA	SAMADroid [21]	Provides high malware detection accuracy since it combines three techniques: -Static and Dynamic Analysis; -Local and Remote Host; -Machine Learning Intelligence.	
	NA	DroidRanger [22]	Heuristics scheme that detects known malware sample based on permission-based filtering and behavioral foot-printing.	
	NA	DroidDolphin [23]	Obtains static and dynamic features through APIMonitor and APE_BOX and used SVM for classification. It could only achieve 86% efficiency.	

1.2. Innovative contributions

The approach proposed in the paper significantly differs from the methodology proposed by Suleiman, Sezer, and Muttik [27]. Their approach is limited to only static features like API calls, commands, and permissions. However, the current work extracts dynamic features along with additional static features, as described in Section 4. The paper also proposes the best combination of the most efficient ML algorithms. Consequently, upgrading the precision and recall. Hence, the accuracy of detecting Android malware is improved considerably.

Following are the innovative contributions of the paper:

- A thorough investigation of Android malware detection techniques with strengths and limitations
- A novel and effective approach for vulnerability detection in Android that combines multiple classifiers
- Relevant APK dataset collection, which is comprehensive and aligned to the scope of the research. The data is taken from Google play store,[4] Wandoujia[5] (third party), Android Malware Detection (AMD) community[6] and Androzoo[7]

[4] Google play store apps. Available: https://play.google.com/store/apps [Accessed: April. 15, 2018].
[5] Wandoujia apps. Available: http://www.wandoujia.com/apps [Accessed: April. 15, 2018].
[6] Wei, Fengguo, Yuping Li, Sankardas Roy, XinmingOu, and Wu Zhou. "Deep ground truth analysis of current android malware." In International Conference on Detection of Intrusions and Malware, and Vulnerability Assessment, pp. 252-276. Springer, Cham, 2017.
[7] Allix, Kevin, Tegawendé F. Bissyandé, Jacques Klein, and Yves Le Traon. "Androzoo: Collecting millions of android apps for the research community." In Mining Software Repositories (MSR), 2016 IEEE/ACM 13th Working Conference on, pp. 468-471. IEEE, 2016.

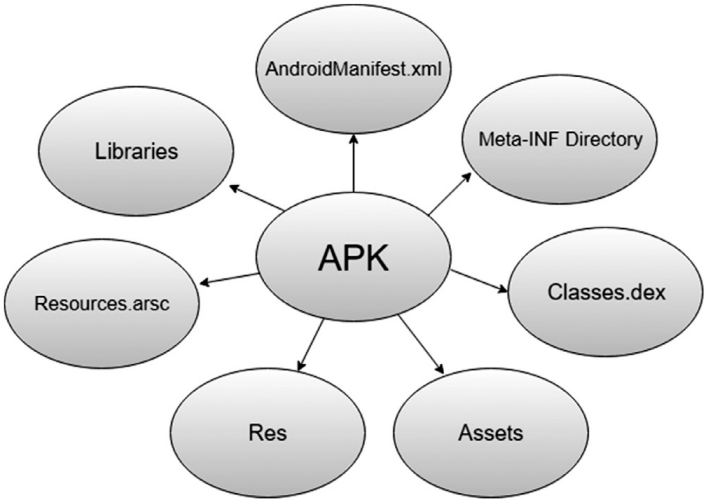

Fig. 3. De-compilation of an APK.

1.3. Organization

The rest of the paper is structured as follows: Section 2 describes the structure of Android application and explains how different application features are extracted. Section 3 presents and explains parallel classifiers in ML paradigm that are used to build malware detection model. Section 4 describes the proposed methodology and presents the performance metrics that are used to evaluate ML algorithms. Section 5 explains the experimental setup and system configuration. Section 6 lists all the results obtained from individual and parallel classifiers. Finally, Section 7 draws out the conclusion.

2. Android architecture and feature extraction

An android application has four fundamentals components that are responsible for defining its overall behavior. They are known as Activities, Broadcast Receivers, Services, and Content Providers. These components are loosely connected by the AndroidManifest.xml file, which explains the interaction amongst all components. Each component has a unique function and life process and is detailed below.

Activities (invoked via intents) control User Interface (UI) and maneuver user interaction, while Services operate background processing. Broadcast Receivers supervise communication between Android OS and applications. Content providers manage data and deal with issues of database management.

Android applications are written in Java. They are then compiled by the Android Software Development Kit (SDK) tools with data and resource files, and are archived as a file (with an extension .APK) named 'Android package'. This file is then used by an Android device to install the application. Fig. 3 shows several components of an APK.

In the paper, the methodology used to detect malware, extracts certain features from APKs, which are then used to classify an application as malicious or benign. Thus, the classification model must be effectively trained to provide correct results. These features, which are further used to train the model, are extracted using Python script from the dataset of 25,450 malware applications obtained from Google play store, Wandoujia APKs, AMD Community, and 60,000 benign applications from Androzoo.

Static features, which are extracted and used in the ML algorithms to determine the presence or absence of the malware in the Android applications, are: Permissions, API Calls, Version, Broadcast Receivers and Services, and Libraries Used. These features are illustrated as follows:

- **Permissions** – Applications in Android request permissions before they can use necessary resources and system data. Based on the application features, the permission is granted by the system or by the user.
- **API Calls** – Android applications use API Calls to interact with the functionality within various devices.
- **Version** – Version decides whether the app is capable of running on installed OS or on its lower versions.
- **Services** – They perform long-running operations running in the background with no need for user interaction.
- **Libraries Used** – Android Libraries encompass specific Java-based libraries, including application framework libraries, and those that promote graphic drawing, UI, and database access.
- **Broadcast Receivers** – Defined earlier

A sample of the features named and explained above is shown in Table 2.

Table 2
Extracted features in a CSV.

APK features	Extracted format
Name	['0d02b9d5539893efc674fbacae14944a.APK']
Permission	['android.permission.INTERNET', 'android.permission.RECEIVE_SMS', ... 'android.permission.CALL_PHONE', 'android.permission. SEND_SMS']
Version	[u'3.0']
Services	[['*my.app.client.Client*']]
Broadcast Receivers	[['*my.app.client.BootReceiver*', '*my.app.client.AlarmListener*']]
Libraries	[['*android.test.runner*']]

3. Machine learning models used with parallel classifiers

A classifier algorithm in ML maps the input data to a category. It generally produces class labels as output using a set of certain extracted features. Over many years these classification algorithms have contributed to the growth of Artificial Intelligence in multiple areas because of which they are now widely preferred to detect malware on almost all electronic mechanisms. ML can be implemented in many ways, e.g., Supervised, Unsupervised, Reinforced, and Semi-supervised learning.

The paper focuses on Supervised Learning. The training dataset has data that is labeled with either of the two classes-malicious or benign. The class for each APK is already known. This becomes the basis for constructing the classification model.

Our methodology incorporates ML algorithms like Pruning Rule-Based Classification Tree (PART), Ripple Down Rule Learner (RIDOR), Support Vector Machine (SVM) and Multilayer Perceptron (MLP). We have used these four algorithms in particular as only a few of the previous studies had used them. Since SVM has a decent accuracy as compared to other ML classifiers, it has been used a few times in the past research projects. In addition, the combination of SVM, RIDOR, PART, and MLP has never been used before in malware detection and the paper aims to improve accuracy using these parallel classifiers.

Fig. 4 explains the methodology used in the paper that combines the disparate ML parallel classifiers. One CPU core is assigned to each algorithm and then made to run simultaneously to obtain higher accuracy by producing a single classification judgment. This is done to detect malware at an early stage with the least possible errors. The scheme of parallel classifiers is followed by decision fusion in which the results from different classifiers can be combined to give better quality estimates than those obtained from any of the individual sources alone. In other words, it improves the generalization capability of individual classifiers. Given below is a brief description of the working of the ML classifiers.

3.1. Multi-Layer Perceptron

MLP is often known as a feed-forward neural network that has one or more hidden layers between the input and output layer. In feed-forward, data flows only in the forward direction, i.e., from input to the output layer. A back-propagation algorithm is used to train the network. Problems that are not linearly separable are generally solved using MLP, e.g., pattern recognition, classification, prediction, and approximation.

3.2. Support vector machine

It is a supervised ML algorithm that can solve both classification and regression problems. However, it is commonly used for classification problems. In SVM, each data item is plotted as a point in n-dimensional space, where n denotes the number of features present; and a particular coordinate is the feature value.

3.3. Pruning rule-based classification tree

It combines two basic strategies of rule learning, i.e., separate-and-conquer and divide-and-conquer. It produces decision lists, which are ordered set of rules. PART builds a partial decision tree iteratively and the largest coverage leaf is turned into a rule.

3.4. Ripple down rule learner

RIDOR is a separate-and-conquer rule classifier. It first generates a default rule and finds exceptions with the least error rate. It then finds the best exception for each exception iteratively. This approach is known as incremental reduced error pruning. The exceptions are common rules that predict classes other than the default.

4. Proposed methodology

Various steps involved in the methodology are elaborated as follows:

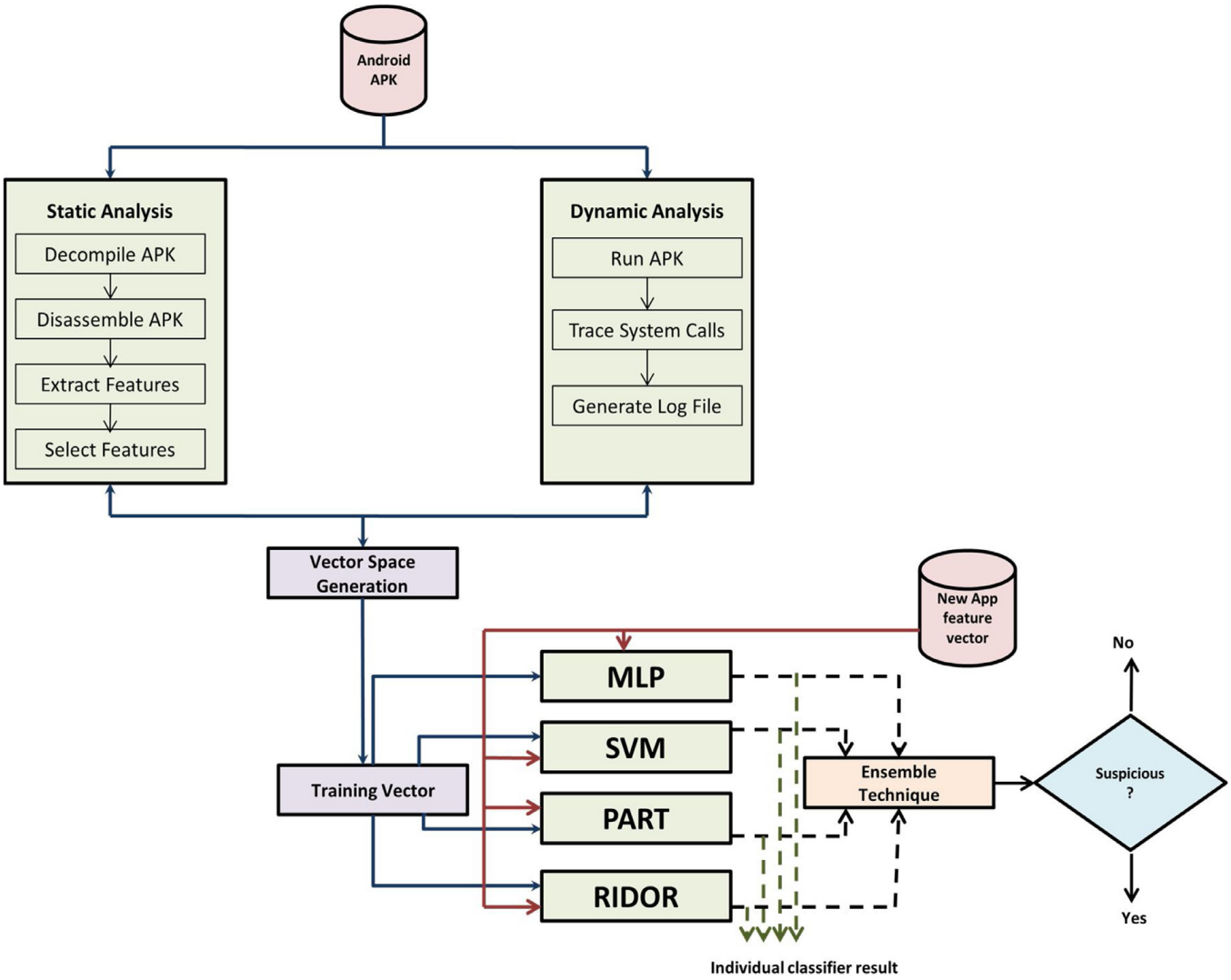

Fig. 4. Schematic representation of parallel classifier.

Table 3
The data source of Android APKs.

Data Source	No. of APKs	Benign/ Malicious
Google Play store,Wandoujia (3rd Party)	800	Benign + Malicious
AMD	24,650	Malicious
Androzoo	60,000	Benign

4.1. Input preprocessing

A dataset of ~85,000 Android applications (benign and malicious) was used from benchmarked datasets as shown in Table 3. With the help of the Apktool, we decompiled the input of APKs. Post de-compilation, we obtained the components of APKs as an outcome in a separate folder as shown in Fig. 3. A further detailed description of the dataset and pseudo codes can be found in [28].

4.2. Feature extraction

For feature extraction, we extracted the static and dynamic features from the collected dataset [29].

4.2.1. Static analysis

Android applications are in the form of an Android package, or APK archive. The APK archive includes the manifest, gradle, resources, and other folders. To extract the features that interest us, we first need to reverse engineer the APK files, which we accomplished using the Apktool. We then designed our own custom Python script to parse the decompiled folders

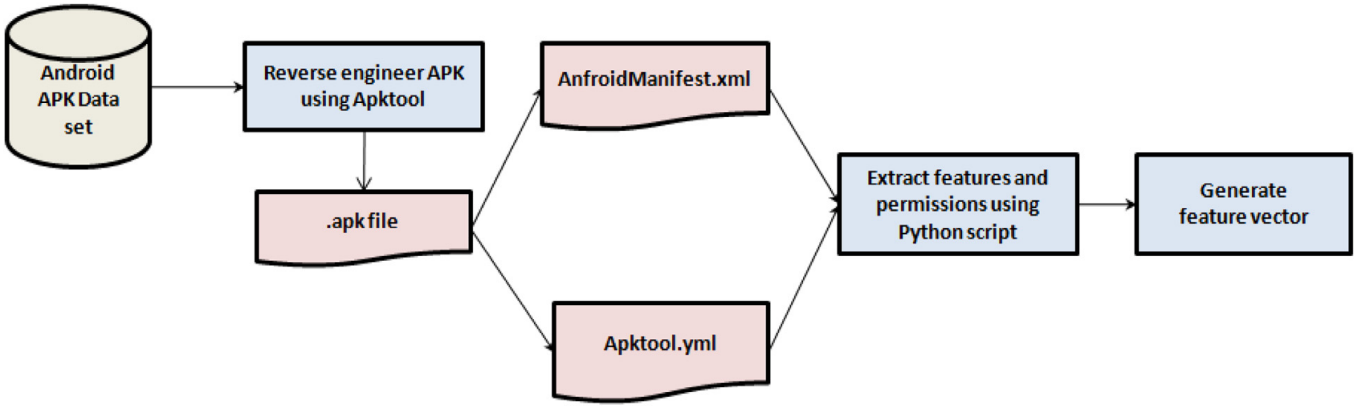

Fig. 5. Schematic diagram for static feature extraction.

and extracted the required permissions, libraries, API calls, version, and broadcast receivers from AndroidManifest.xml and Apktool.yml files.

There is a total of 135 Android permissions. A binary feature vector is constructed from the extracted features. We denote this feature vector as $F = (f_1, f_2, \ldots, f_3)$, where

$$f_i = \begin{cases} 1, & if\ the\ i^{th}\ permission\ is\ present \\ 0, & otherwise \end{cases}$$

The following steps describe the process used for feature extraction as shown in Fig. 5:

- Reverse engineer the Android applications using the Apktool
- Extract permissions and other requested features from the AndroidManifest.xml and Apktool.yml files using Python script
- Generate a binary feature vector, as shown in Eq. (1)
- Finally, create a feature vector dataset for all the APKs in the dataset and store it in .csv file format as shown in Table 1

The binary sequence 1 denotes that the permission is present while binary sequence 0 denotes that the permission is absent. Further, another variable G is introduced where $G \in \{malicious,\ benign\}$ and indicates 1 for benign application and -1 for a malicious application.

For example, the benign and malicious vectors from an APK are represented by Eqs. (1) and (2) respectively. Here, $F_{\alpha\beta\ Benign}$ and $F_{\alpha\beta\ Malicious}$ denote benign and malicious vectors, where α and β denote row and column respectively:

$$F_{\alpha\beta\ Benign} = \begin{pmatrix} 0 & 0 & 0 & 0 & 0 & 0 & 0 & 1 & 0 & 0 & 0 & 0 & 0 & 0 & 0 & 0 & 0 & 0 & 0 \\ 0 & 0 & 0 & 0 & 0 & 0 & 0 & 0 & 0 & 0 & 0 & 0 & 0 & 0 & 0 & 0 & 0 & 0 & 0 \\ 0 & 0 & 0 & 0 & 0 & 1 & 0 & 0 & 0 & 0 & 0 & 0 & 0 & 0 & 0 & 0 & 0 & 0 & 0 \\ 0 & 0 & 0 & 0 & 0 & 1 & 0 & 0 & 0 & 0 & 0 & 0 & 0 & 0 & 0 & 0 & 0 & 0 & 0 \\ 0 & 0 & 0 & 0 & 1 & 0 & 0 & 0 & 0 & 0 & 0 & 0 & 0 & 0 & 0 & 0 & 0 & 0 & 0 \end{pmatrix} \quad (1)$$

$$F_{\alpha\beta\ Malicious} = \begin{pmatrix} 0 & 0 & 0 & 0 & 0 & 0 & 0 & 1 & 0 & 0 & 0 & 0 & 0 & 0 & 0 & 0 & 0 & 0 & 0 \\ 0 & 0 & 0 & 0 & 0 & 0 & 0 & 0 & 0 & 0 & 0 & 0 & 0 & 0 & 0 & 0 & 0 & 0 & 0 \\ 0 & 0 & 0 & 0 & 0 & -1 & 0 & 0 & 0 & 0 & 0 & 0 & 0 & 0 & 0 & 0 & 0 & 0 & 0 \\ 0 & 0 & 0 & 0 & 0 & 1 & 0 & 0 & 0 & 0 & 0 & 0 & 0 & 0 & 0 & 0 & 0 & 0 & 0 \\ 0 & 0 & 0 & 0 & -1 & 0 & 0 & 0 & 0 & 0 & 0 & 0 & 0 & 0 & 0 & 0 & 0 & 0 & 0 \end{pmatrix} \quad (2)$$

4.2.2. Dynamic analysis

An android application communicates wth the OS using system calls, which we extract using dynamic analysis. Dynamic features like battery charging status, temperature of battery (while charging), memory, network traffic, CPU, SMS, etc., are extracted as shown in Table 4.

For dynamic analysis, we used the in-built emulator in Android studio and connect it with the ADB shell (a command line tool). It generates n number of random events (UI interactions) like clicks, touches, etc., and sends it to the system or an application that captures the system calls. We record system calls using a monitoring tool Strace [30].

Given an Android application, the following steps describe the process that we use to extract dynamic features as shown in Fig. 6:

- Create an emulator instance by opening the AVD manager and run it
- Check whether the ADB is working or not

Table 4
Extracted dynamic features.

Dynamic feature	Feature parameter
BattIsCharging	Battery amount on charging (Percentage)
BattTemperature	Battery temperature while charging (Degree Celsius)
Network traffic	Receive Packet, Transmission Packet (Bytes)
Memory	Allocated, Free, Shared (Bytes)
CPU	Usage of CPU (Percentage)
SMS	Send SMS, Receive SMS (Bytes)

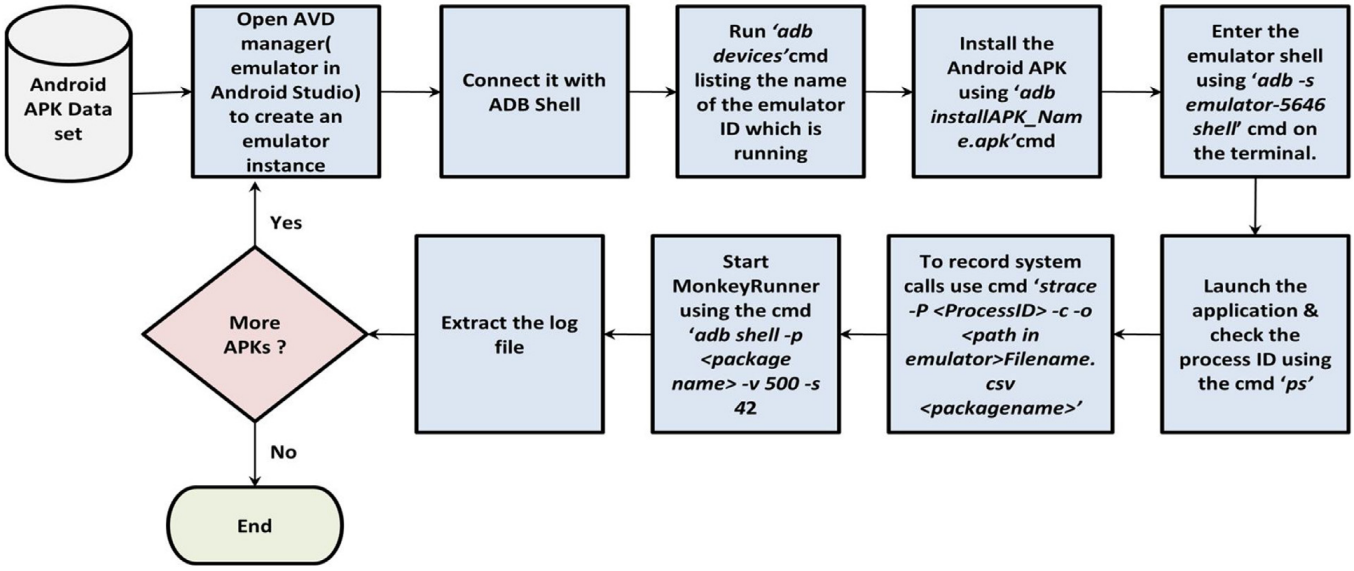

Fig. 6. Schematic diagram for dynamic feature extraction.

- Issue command *adb devices*
- Give the command *adb install APK-name.APK (*assuming the Android application is named *APK-name.APK*)
- Enter *adb -s emulator-5646 shell* command at the terminal
- Launch the application and check the process ID using the command *ps*
- Enter the *Strace* commands
- Start Monkey Runner
- Extract the log file

Let $S = (s_1, s_2, \ldots, s_n)$ be the set of all possible system calls available in the Android OS. Then element j in system call feature vector contains the count for the number of occurrences of system calls s_j. The parameter ξ is an n-length sequence that denotes the frequency of system call captured in a log file for each application.

Let $\xi = (m_1, m_2, \ldots, m_n)$, where $m_i \in S$ is i^{th} observed system call in the log file.

Feature vector obtained above is then passed to the next phase of feature extraction. Here, every attribute in the feature vector denotes the frequency of occurrence of system calls in the strace log. Using this sequence ξ, feature vector $y = [y_1, y_2, \ldots, y_{|s|}]$ is defined, where y_i is the frequency of system call $s_i \in \xi$.

We define a permission vector as a variable G, where $G \in \{malicious, benign\}$ indicates 1 for benign applications, and -1 for the malicious applications. The feature vector for system calls is obtained for benign and malicious application as per Eqs. (3) and (4) respectively.

$$F_{\alpha\beta\ Benign} = \begin{pmatrix} 0 & 0 & 0 & 0 & 2500 & 0 & 0 & 1 & 0 & 0 & 0 & 1500 & 0 & 0 & 0 & 0 & 1 & 0 & 32 \\ 0 & 0 & 36 & 0 & 0 & 0 & 0 & 0 & 753 & 0 & 0 & 0 & 0 & 1 & 0 & 0 & 90 & 0 & 56 \\ 0 & 150 & 0 & 0 & 110 & 1 & 0 & 0 & 0 & 0 & 0 & 1 & 0 & 0 & 0 & 0 & 0 & 0 & 0 \\ 0 & 0 & 0 & 55 & 0 & 1 & 0 & 0 & 0 & 0 & 0 & 0 & 0 & 87 & 0 & 0 & 0 & 1 & 0 \\ 0 & 0 & 0 & 0 & 1 & 0 & 0 & 0 & 65 & 0 & 0 & 425 & 0 & 0 & 0 & 0 & 1 & 0 & 0 \end{pmatrix} \tag{3}$$

$$F_{\alpha\beta\ Malicious} = \begin{pmatrix} 0 & 0 & 0 & 0 & 500 & 0 & 0 & 1 & 0 & 0 & 0 & 1500 & 0 & 0 & 0 & 0 & 1 & 0 & 32 \\ 0 & 0 & 86 & 0 & 0 & 0 & 0 & 0 & 653 & 0 & 0 & 0 & 0 & 1 & 0 & 0 & 90 & 0 & 56 \\ 0 & 150 & 0 & 0 & 110 & -1 & 0 & 0 & 0 & 0 & 0 & 1 & 0 & 0 & 0 & 0 & 0 & 0 & 0 \\ 0 & 0 & 0 & 55 & 0 & 0 & 0 & 0 & 0 & 0 & 0 & 0 & 0 & 887 & 0 & 0 & 0 & 1 & 0 \\ 2238 & 0 & 0 & 0 & 1 & 0 & 0 & 0 & 65 & 0 & 0 & 425 & 0 & 0 & 0 & 0 & 1 & 0 & -1 \end{pmatrix} \tag{4}$$

Table 5
Confusion matrix.

Predicted				
		Positive	Negative	Total
Observed	Positive	TP (a)	FN (b)	a + b
	Negative	FP (c)	TN (d)	c + d
	Total	a + c	b + d	a + b + c + d

4.3. Model training

In this phase, the pre-processed matrix obtained in the Section 4.2.1 and 4.2.2 of our proposed methodology is divided into two datasets, namely Training dataset and Testing dataset. The Training dataset is modeled using the ML algorithms described in Section 3. Thereafter, the Testing dataset is used to do a test run using the feature vectors from trained models to classify APKs and to capture their respective performance metrics.

4.4. Model evaluation

Ten-fold cross-validation technique is used to calculate the performance of the classifiers in various parallel combination strategies. As the name suggests, the dataset is divided into ten equal parts such that there is no overlapping. They can be termed as part1, part2, part3 up to part10. For the evaluation process, at every level, one portion is taken as the testing dataset and the other nine portions are supposed to administer the training model. The ML model is trained using the cross-validation training dataset and thereafter the accuracy of the model is calculated by validating the predicted results against the validation dataset. Accuracy of the ML model is estimated by averaging the accuracies derived in all the ten cases of cross-validation. The reason behind the selection of this technique is to ensure that our approach also helps identify the unknown harmful applications.

Table 5 lists the terms used in the confusion matrix that are used to express the efficiency and the efficacy of the applied method.

- *True Positive Ratio (TPR)/ Sensitivity:*

The proportion of harmful APKs classified accurately to the total number of harmful APKs present in the dataset.

$$TPR = \frac{a}{a+b}$$

- *True Negative Ratio (TNR)/ Specificity:*

The proportion of non-harmful APKs classified correctly divided by the total number of non-harmful APKs in the dataset.

$$TNR = \frac{d}{c+d}$$

- *False Positive Ratio (FPR):*

The proportion of non-harmful classified incorrectly APKs to the total number of non-harmful APKs in the dataset.

$$FPR = 1 - TNR = 1 - Specificity$$
$$FPR = \frac{c}{c+d}$$

- *False Negative Ratio (FNR):*

The proportion of harmful apps classified incorrectly to the total number of harmful apps in the dataset.

$$FNR = \frac{b}{a+b}$$

- *Accuracy (Acc):*

The proportion of correct predictions to the total number of predictions in the dataset.

$$Acc = \frac{a+d}{(a+b+c+d)}$$

- *Error ratio (Err):*

The proportion of incorrect predictions to the total number of predictions in a dataset.

$$Err = 1 - Acc$$

Table 6
System configuration.

Host machine	
Model	Dell Latitude e5250
Processor	Intel(R) Core^{TM} i5-5300 U CPU @ 2.30 GHz 2.29 GHz
RAM	16.0 GB
System Type	64-bit Operating System
Operating System	Windows 10
Guest Machine	
Operating System Image	Ubuntu 14.04 LTS
Memory	226.0 GB
System type	32-bit Operating System
Android Emulator Configuration	
Platform	Android Studio 1.5.1
Device	Nexus 7
Target	Android 4.2.2 – API Level 17
CPU/ ABI	Intel Atom(x86)
RAM	512 MiB
SD Card	200 MiB

Table 7
Performance metrics of the individual classifiers (in%).

Algorithm	TPR	TNR	FPR	FNR	Acc	Err
MLP	96.11	95.67	4.33	3.89	95.89	4.11
SVM	93.29	94.81	5.19	6.71	94.05	5.95
PART	95.36	96.59	3.41	4.64	95.87	4.03
RIDOR	95.68	94.37	5.63	4.32	95.02	4.98

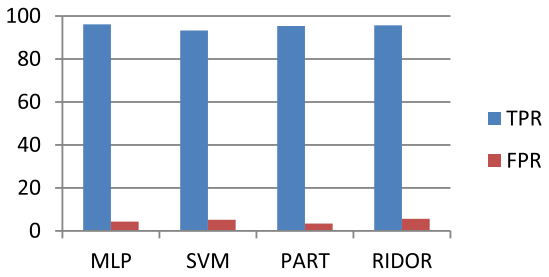

Fig. 7. Comparison of different individual classifiers.

5. Experimental setup and system configuration

Table 6 summarizes the experimental set up used for Android malware detection. The system configuration for host and guest machine (Memory requirements, OS types, etc.) is also shown in Table 6.

6. Results

Sections 6.1 and 6.2 present the summary of results obtained using different ML classifiers.

6.1. Results of individual classifiers

The first part of the research is conducted using individual classifiers that are listed and discussed in the current section. Then, using the same individual classifiers, we create a combined model, known as parallel classifiers to obtain higher accuracy. Table 7 presents the result of the individual classifiers.

It can be clearly seen from Table 7 that MLP is the best classifier amongst the four. TPR or the detection rate of MLP is 96.11% with the least FPR of 4.33% as shown in Fig. 7. The accuracy of MLP is the highest (95.89%) while the accuracy of SVM was the lowest (94.05%) as shown in Fig. 8. ROC curve for MLP (0.9589) is shown in Fig. 9.

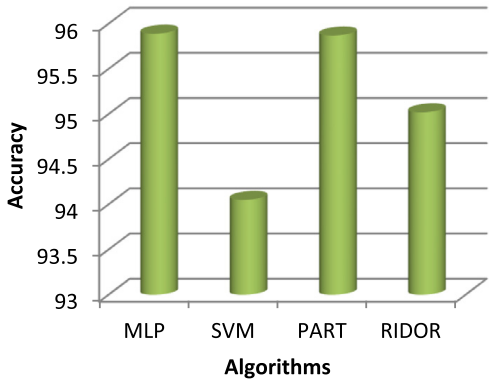

Fig. 8. Accuracy for different algorithms.

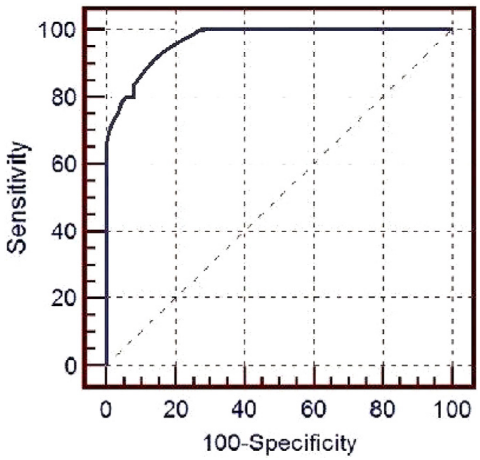

Fig. 9. ROC for high ranked individual classifier MLP.

6.2. Results of the parallel classifiers

The second part of the research is conducted using the composite model where the results (obtained from Section 6.1) are executed in a parallel manner. Four parameters are considered to estimate the efficiency of the cumulative approach. Probability of detection of malware from individual classifiers is combined to create parallel classifiers. The two classes obtained are malicious (Mal) and benign (Ben).

6.2.1. Average probabilities (AvgProb)

It is an average of the probabilities of each class. If the average of the probabilities from malicious *classMal* $[(P1+P2+P3+P4)/4]$ is greater than the average of the probabilities from benign *classBen* $[(P1+P2+P3+P4)/4]$ then the APK is categorized as malicious, otherwise benign.

6.2.2. Product of probabilities (ProdProb)

It is a product of the probabilities of each class. If the product of the probabilities from malicious *classMal*($P1$.$P2$.$P3$.$P4$) is greater than the product of the probabilities from benign *classBen*($P1$.$P2$.$P3$.$P4$), then the APK is categorized as malicious, otherwise benign.

6.2.3. Maximum probability (MaxProb)

It is the maximum of the probabilities for each class. If the maximum of the probabilities from malicious *classMax*[*Mal*($P1$, $P2$, $P3$, $P4$)] is greater than the maximum of the probabilities from benign *classMax*[*Ben*($P1$, $P2$, $P3$, $P4$)], then the APK is categorized as malicious, otherwise benign.

6.2.4. Majority vote (MVote)

It is the decision that is taken when an individual classifier has obtained the highest majority of the vote. If the majority votes from the classifier *MVote*($C1$, $C2$, $C3$, $C4$) = *Mal*, then the APK is categorized as malicious, otherwise benign.

Table 8 presents the result of the four different parameters used in the proposed methodology. After comparing Table 7 and Table 8, it is seen that TPR has improved in MaxProb and ProdProb.

Table 8
Performance metrics of parallel classifiers (in%).

Ensemble technique	TPR	TNR	FPR	FNR	Acc	Err
MaxProb	98.79	97.75	2.25	1.21	98.27	1.73
ProdProb	96.02	95.81	4.19	3.98	95.91	4.09
AvgProb	95.82	93.63	6.37	4.18	94.72	5.28
MVote	92.06	93.13	6.87	7.94	92.59	7.41

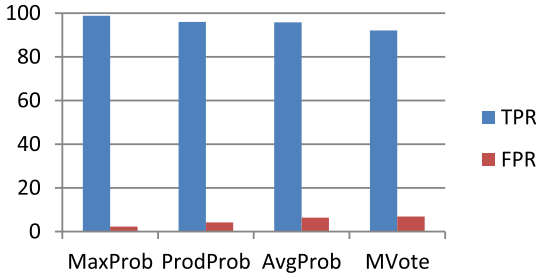

Fig. 10. Comparison of different parallel classifiers.

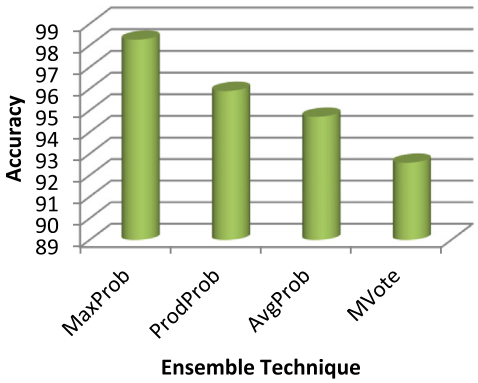

Fig. 11. Accuracy values for different algorithm combination.

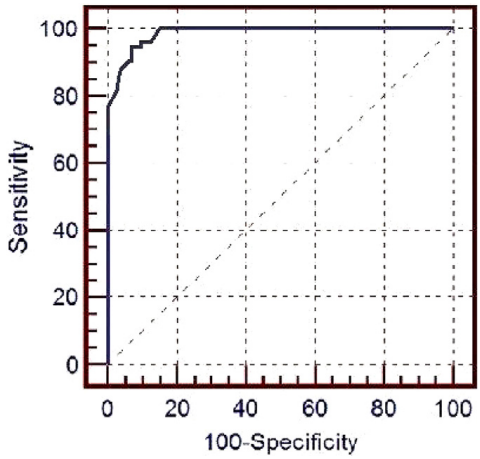

Fig. 12. ROC for high ranked parallel classifier.

The results in Table 8 validate the need for implementing the parallel ML classifiers for detecting malware in Android. Parallel ML classifiers (MaxProb and ProdProb) not only improve the accuracy of detection of malware but also help overcome the gaps and limitations of the existing techniques (described in Section 1). As per obtained results, the best parallel classifier is MaxProd and the best individual classifier is MLP. The TPR of MaxProd stands at 98.79%, which is 2.68% higher than the TPR obtained from MLP. In addition, MaxProd shows an improvement in accuracy by 2.38% and reduction in error rate by 2.38% over MLP. Fig. 10 compares TPR and FPR for all parallel classifiers. Accuracy for different parallel classifiers is shown in Fig. 11. ROC curve for MaxProd (0.9827) is shown in Fig. 12.

7. Conclusion and future scope

Android mobile platforms are susceptible to malware threats and, although previously researchers have handled such malware detection and categorization, the accuracy of their methods is not beyond improvement. Hence, the paper demonstrates the use of parallel classifiers to efficiently detect and classify malware (as malicious or benign) in Android applications. A number of static features (e.g., Permissions, API Calls, Version, Receiver Broadcast, Services and Libraries used), as well as dynamic features (e.g., battery temperature, battery charging percentage, network traffic, SMS sent and received, CPU and memory usage, etc.), were tested and correlated. The methodology proposed in the paper uses individual classifiers, namely, MLP, SVM, PART, and RIDOR and ensembles them to create a solution that is more accurate and efficient. This method not only detects the malware in the Android OS with an accuracy of 98.27% but also overcomes the gaps and limitations of the previous approaches. This methodology leverages the capabilities and strong-points inherent to each individual classifier and averages out their individual limitations. Hence, the overall method is more robust and has a lower error rate.

As part of the future work, we aim to create more parallel classifiers by taking new combinations of individual classifiers. Our goal is also to detect and predict vulnerabilities and malware using deep-learning models on a large real-world dataset. There is a strong hypothesis that the existent malware can be clustered into various families and useful patterns can be drawn from them using advanced ML models. In addition, we also aim to perform an in-detail impact analysis of Android vulnerabilities on Confidentiality, Integrity and Availability triad at the architectural level.

Conflicts of interest

The authors have no conflicts of interest to disclose.

Acknowledgements

We thankfully acknowledge all the help and support of Dr. Arun Sharma in guiding us throughout the project. We would also like to acknowledge AMD community and Androzoo for providing us with the dataset of 24,650 malware and 60,000 of benign applications respectively.

References

[1] Al-Turjman F. 5G-enabled devices and smart-spaces in social-IoT: an overview. Future Generation Comput Syst 2019;92:732–44. https://doi.org/10.1016/j.future.2017.11.035.
[2] Smith G. Mobile Malware: gGrowth stuns, storms and threatens, anewdomain.net. [Online]. Available: http://anewdomain.net/mobile-malware-growth-stuns-storms-and-threatens. [Accessed: Feb. 12, 2018].
[3] Statista Number of smartphone users in India from 2015 to 2022. The Statistics Portal 2017. [Online]. Available: https://www.statista.com Accessed:Mar. 20, 2018.
[4] Maier D, Müller T, Protsenko M. Divide-and-conquer: why android malware cannot be stopped. 9th international conference on availability, reliability and security. IEEE; 2014.
[5] González D. In Android the Malware has a free way: 350 malicious applications increase every hour, voltaico.lavozdegalicia.es. [Online]. Available: https://voltaico.lavozdegalicia.es/2017/05/android-malware-via-libre-350-aplicaciones-maliciosas-aumentan-hora/. [Accessed: Mar. 18, 2018].
[6] Song H, Fink GA, Jeschke S. Security and privacy in cyber-physical systems: foundations, principles, and applications. John Wiley & Sons; 2017.
[7] Faruki P, Ganmoor V, Laxmi V, Gaur MS, Bharmal A. AndroSimilar: robust statistical feature signature for Android malware detection. In: Proceedings of the 6th international conference on security of information and networks. ACM; 2013. p. 152–9. doi: 10.1145/2523514.2523539.
[8] Zheng M, Sun M, Lui J. Droidanalytics: a signature based analytic system to collect, extract, analyze and associate android malware. arXiv:1302.7212, 2013. doi:10.1109/TrustCom.2013.25.
[9] Felt AP, Chin E, Hanna S, Song D, Wagner D. Android permissions demystified. In Proceedings of the 18th ACM conference on computer and communications security, ACM. pp. 627–638.
[10] Sato R, Chiba D, Goto S. Detecting Android malware by analyzing manifest files. Proc Asia-Pacific Adv Netw 2013;36(23–31):17.
[11] Sanz B, Santos I, Laorden C, Ugarte-Pedrero X, Bringas PG, Álvarez G. Puma: permission usage to detect malware in android. In: International joint conference CISIS'12-ICEUTE 12-SOCO 12 special sessions. Berlin, Heidelberg: Springer; 2013. p. 289–98.
[12] Burguera I, Zurutuza U, Nadjm-Tehrani S. Crowdroid: behavior-based malware detection system for android. In: Proceedings of the 1st ACM workshop on security and privacy in smartphones and mobile devices. ACM; 2011. p. 15–26. doi: 10.1145/2046614.2046619.
[13] Shabtai A, Kanonov U, Elovici Y, Glezer C, Weiss Y. "Andromaly": a behavioral malware detection framework for android devices. J Intell Inf Syst 2012;38(1):161–90.
[14] Zhao M, Ge F, Zhang T, Yuan Z. AntiMalDroid: an efficient SVM-based malware detection framework for android. In: International conference on information computing and applications. Berlin, Heidelberg: Springer; 2011. p. 158–66.
[15] Enck W, Gilbert P, Seungyeop H, Tendulkar V, Byung-Gon C, Cox LP, Jung J, McDaniel P, Sheth AN. TaintDroid: an information-flow tracking system for realtime privacy monitoring on smartphones. ACM Transactions on Computer Systems (TOCS) 2014;32(2):5.
[16] Yan L-K, Yin H. DroidScope: seamlessly reconstructing the OS and Dalvik semantic views for dynamic Android Malware analysis. In: USENIX security symposium; 2012. p. 569–84.
[17] Blasing T, Batyuk L, Schmidt A-D, Camtepe SA, Albayrak S. An android application sandbox system for suspicious software detection. In: 2010 5th international conference on malicious and unwanted software (MALWARE 2010). IEEE; 2010. p. 55–62. doi: 10.1109/MALWARE.2010.5665792.
[18] Bae C, Shin S. A collaborative approach on host and network level android malware detection. Secur Commun Netw 2016;9(18):5639–50. https://doi.org/10.1002/sec.1723.
[19] Spreitzenbarth M, Freiling F, Echtler F, Schreck T, Hoffmann J. Mobile-sandbox: having a deeper look into android applications. In: Proceedings of the 28th annual ACM symposium on applied computing. ACM; 2013. p. 1808–15. doi: 10.1145/2480362.2480701.
[20] Barsiya TK, Gyanchandani M, Wadhwani R. Android Malware analysis: a survey paper. Int J Control Autom Commun Syst (IJCACS) 2016;1(1):35–42.
[21] Arshad S, Shah MA, Wahid A, Mehmood A, Song H, Yu H. SAMADroid: a novel 3-level hybrid malware detection model for android operating system. IEEE Access 2018;6:4321–39.
[22] Zhou Y, Wang Z, Zhou W, Jiang X. Hey, you, get off of my market: detecting malicious apps in official and alternative android markets. NDSS 2012;25(4):50–2.

[23] Wu W-C, Hung S-H. DroidDolphin: a dynamic Android malware detection framework using big data and machine learning. In: Proceedings of the 2014 conference on research *in Adaptive and Convergent Systems*. ACM; 2014. p. 247–52. doi: 10.1145/2663761.2664223.
[24] Baskaran B, Ralescu A. A study of android malware detection techniques and machine learning. MAICS 2016:15–23.
[25] Mehmood A, Mukherjee M, Ahmed SH, Song H, Malik KM. NBC-MAIDS: naïve Bayesian classification technique in multi-agent system-enriched IDS for securing IoT against DDoS attacks. J Supercomput 2018:1–15. https://doi.org/10.1007/s11227-018-2413-7.
[26] Rehman Z-U, Khan SN, Muhammad K, Lee JW, ZhihanLv SW, Shah PA, Awan K, Mehmood I. Machine learning-assisted signature and heuristic-based detection of malwares in Android devices. Comput Electric Eng 2018;69:828–41.
[27] Yerima SY, Sezer S, Muttik I. Android malware detection using parallel machine learning classifiers. In: 2014 eighth international conference on next generation mobile apps, services and technologies. IEEE; 2014. p. 37–42. doi: 10.1109/NGMAST.2014.23.
[28] Garg S, Baliyan N. Data on vulnerability detection in Android. Data in Brief 2019;22:1081–7.
[29] Milosevic N, Dehghantanha A, Choo K-KR. Machine learning aided android malware classification. Comput Electric Eng 2017;61:266–74.
[30] Ham YJ, Moon D, Lee H-W, Lim JD, Kim JN. Android mobile application systems call event pattern analysis for determination of malicious attack. Int J Secur Appl 2014;8(1):231–46. doi: 10.14257/ijsia.2014.8.1.22.

Shivi Garg received her M.Tech in Information Security from Delhi Technological University, India, in 2014. She is an Assistant Professor in J.C. Bose University of Science & Technology YMCA, since September 2018. She is also a Ph.D. scholar at Indira Gandhi Delhi Technical University for Women, since August 2016. Her research interests include Cyber Security, Data Mining and Machine learning.

Niyati Baliyan is an Assistant Professor at Information Technology Department, Indira Gandhi Delhi Technical University for Women, Delhi. She received her Ph.D. from Indian Institute of Technology Roorkee. She also attained Post Graduate Certificate with Honors in Information Technology from Sheffield Hallam University, UK, as an exchange student on scholarship. Her research interests are Knowledge Engineering and Machine Learning.

SeMA Journal
https://doi.org/10.1007/s40324-019-00189-8

A short study of an SIR model with inclusion of an alert class, two explicit nonlinear incidence rates and saturated treatment rate

Abhishek Kumar[1] · **Nilam**[1] · **Raj Kishor**[2]

Received: 4 December 2018 / Accepted: 5 April 2019
© Sociedad Española de Matemática Aplicada 2019

Abstract
In this paper, we present a susceptible–alert–infected–recovered (SAIR) epidemic model with the consideration of two explicit saturated incidence rates and Holling functional type II treatment rate. Awareness about the epidemic may play a vital role in the control of the spread of an epidemic. Hence, an alert compartment has been incorporated into the model. It strives us to take two incidence rates: one from the susceptible class to infected class and another from alert class to infected class. Holling functional type II treatment rate has been introduced to capture the effects of resource limitation in treating infectives. The model has a disease-free equilibrium (DFE), which is locally asymptotically stable when $R_0 < 1$. Using the center manifold theory, we show that DFE exhibits the forward bifurcation at $R_0 = 1$. Stability of the endemic equilibrium has also been analyzed and discussed. Numerical simulations have been done by MATLAB 2012b and the outcomes have been discussed with the help of graphs in the paper.

Keywords Epidemic · SAIR model · Saturated treatment rate · Basic reproduction number · Center manifold theory · Stability

Mathematics Subject Classification 34D20 · 92B05 · 37M05

1 Introduction

In mathematical epidemiology literature, numerous epidemic models [1, 2, 6–9, 11–16, 19–21] like SIR, SEIR, SVEIR, etc. have been proposed for infection transmission and

✉ Nilam
rathi.nilam@gmail.com

Abhishek Kumar
abhishek.dtu14@gmail.com

Raj Kishor
rajkishoredpr@gmail.com

[1] Department of Applied Mathematics, Delhi Technological University, Delhi 110042, India

[2] Raj Tutors, Dhampur, Bijnor, Uttar Pradesh 246761, India

control. Still, the control of the epidemics is a major problem for the doctors and health agencies. Consequently, in this paper, we propose a novel susceptible–alert–infected–recovered (SAIR) model with two explicit nonlinear incidence rates alongside the Holling type II treatment rate. We know that the incidence rate and treatment rate play an important part in modeling transmission and control of the epidemic. Numerous researchers have studied that the disease transmission process may have a nonlinear incidence rate. In various epidemic models [6, 8, 10], the bilinear incidence rate βSI is as often as possible utilized. In epidemiology literature, the bilinear incidence rate relies upon the law of mass action which is unrealistic for a large number of populations. The probability of infection per contact is likely influenced by the number of infected individuals, since a large number of infected individuals can build the disease hazard [20]. Capasso and Serio [3] considered a saturated incidence rate $g(I)S$ into the disease transmission models, where $g(I)$ tends to a saturation level when I gets large, i.e.,

$$g(I) = \frac{\beta I}{1 + \alpha I},$$

where I estimates the force of infection and $\frac{1}{1+\alpha I}$ measures the inhibition effect from the behavioral change of the vulnerable (susceptible) people when their number increases or from the crowding effect of the infective people. This incidence rate appears to be more sensible than the bilinear incidence rate βIS, in light of the fact that it incorporates the behavioral change and crowding effect of the infectives and keeps the unboundedness of the contact rate by choosing reasonable parameters [20].

Proper and timely treatment approach can considerably lessen the impact of infection on society. In classical epidemic models, the treatment rate of infected individuals is assumed to be either constant or proportional to the number of infected individuals. However, there is low availability of treatment resources in the community. Therefore, it is very important to choose a suitable treatment rate of a disease. In the absence of effective treatments and vaccines, the epidemical control techniques depend on taking appropriate preventive measures. Wang and Ruan [19] in 2004 proposed an SIR epidemic model with constant treatment rate as given below:

$$\mathrm{H(I)} = \begin{cases} b, & I > 0 \\ 0, & I = 0 \end{cases},$$

where b is a positive constant and I is the number of infected individuals. They studied long term behavior of the model and showed the various bifurcations. Further, Zhou and Fan [22] in 2012 modified the treatment rate to Holling type II

$$\mathrm{H(I)} = \frac{aI}{1 + bI}, \quad I \geq 0, \quad a > 0, \quad b > 0.$$

They showed that, with varying amount of medical resources and their supply efficiency, the target model admits both backward and Hopf bifurcation.

In this article, we propose a model for the epidemic by introducing two explicit nonlinear incidence rates alongside the Holling type II treatment rate. We investigate the basic reproduction number R_0, analyze the dynamical behavior of the model at equilibrium points. The stability analysis of the model at equilibrium points has been done using Descartes' rule of signs [18] alongside the Routh–Hurwitz criterion.

The rest of paper is organized as follow: A SAIR mathematical model with two explicit nonlinear incidence rates alongside the Holling type II treatment rate for the epidemic is formulated in Sect. 2. Basic properties of the model are presented in Sect. 3. Equilibrium

points and their stability analysis are discussed in Sect. 4. Model is simulated numerically using MATLAB 2012b in Sect. 5. Lastly, a discussion is given in Sect. 6.

2 Mathematical model

To formulate the mathematical epidemic model, the total population $N(t)$ is divided into four compartments (or classes); susceptible individual class (S), alert individual class (A), infected individual class (I), and recovered individual class (R). Vulnerable (susceptible) people are those individuals who are healthy and can get the infection under appropriate conditions. Alert people are the individuals who know about the effect of disease, infection and symptoms and taking necessary precautions to control the infection, and can get the infection under appropriate conditions. Infected people are the individuals who have caught the infection and can transmit it to susceptible and alert people via contacts. As time passes, either via auto recuperation which could be due to the immune system reaction of the body or by treatment, the infected individuals lose infectivity and transfer to the recover class. We consider the Holling functional type II treatment rate for the recovery of the infected people since it considers the cure rate along with the limitation rate in treatment availability which is more realistic. The transfer diagram of the epidemic in numerous classes is shown in the block diagram (Fig. 1) below:

The proposed model is given by the following system of nonlinear ordinary differential equations:

$$\begin{aligned}
\frac{dS}{dt} &= \pi - \delta S - \mu S - \frac{\beta SI}{1+\alpha I},\\
\frac{dA}{dt} &= \delta S - \mu A - \frac{\gamma AI}{1+\alpha I},\\
\frac{dI}{dt} &= \frac{\beta SI}{1+\alpha I} + \frac{\gamma AI}{1+\alpha I} - (\mu + d + \theta)I - \frac{aI}{1+bI},\\
\frac{dR}{dt} &= \frac{aI}{1+bI} + \theta I - \mu R,
\end{aligned} \tag{1}$$

where $S(0) > 0,\ A(0) \geq 0,\ I(0) \geq 0,$ and $R(0) \geq 0$.

In the model (1), $\frac{d}{dt}$ denotes the rate of change in each compartment. The parameter π represents the constant recruitment rate of susceptible by birth or immigration. We consider

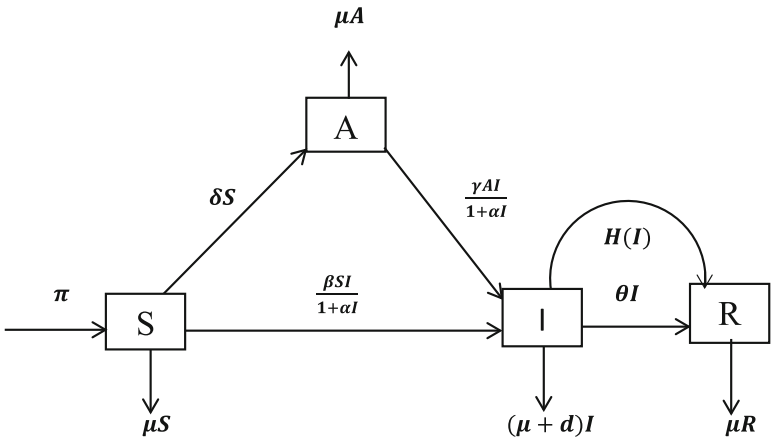

Fig. 1 Transfer diagram of the epidemic for the model (1)

that the susceptible individuals are moving in alert class at a rate δ, hence δ defines the rate of alertness of susceptible individuals. The incidence term $\frac{\beta SI}{1+\alpha I}$ represents the nonlinear saturated rate (where β denotes the transmission rate of susceptible to infected individuals and α is the measure of inhibition taken by infectives), describing the rate of new infection when the susceptible individuals are becoming infected. μ is the natural mortality rate. The term $\frac{\gamma AI}{1+\alpha I}$ represents the incidence rate of alert population (where γ denotes the transmission rate of alert to infected individuals), describing the number of new infections when the alert individuals are becoming infected. The parameters d and θ represent the disease-induced death rate and recovery rate of the infected individuals, respectively. The term $H(I) = \frac{aI}{1+bI}$ represents the Holling functional type II treatment rate, where a is the cure rate and b is the rate, taking into account as resource limitations [21, 22].

3 Basic properties

Since the model (1) monitors the population, therefore for the biological reasons it is supposed that all the state variables are nonnegative and all the parameters of the model are positive.

For the model (1), we find that all the solutions with nonnegative initial data will remain non-negative and bounded for all time t. It can be observed as follows:

The total population $N(t)$ is

$$N(t) = S(t) + A(t) + I(t) + R(t).$$

The rate of change in the total population is

$$\frac{dN(t)}{dt} = \frac{dS(t)}{dt} + \frac{dA(t)}{dt} + \frac{dI(t)}{dt} + \frac{dR(t)}{dt} = A - \mu N(t) - dI(t).$$

It implies that,

$$N(t) \leq N(0)e^{-\mu t} + \frac{A}{\mu}(1 - e^{-\mu t}).$$

Thus, we get

$$\lim_{t\to\infty} N(t) \leq \frac{A}{\mu}.$$

Furthermore, $\frac{dN(t)}{dt} < 0$ if $N(t) > 0$. Thus, all the solutions of the model (1) tend to the positively invariant region $D = \{(S, A, I, R) \in \mathbb{R}^4_+ : 0 < S + A + I + R \leq \frac{A}{\mu}\}$. Hence, all the solutions of the model (1) are bounded and nonnegative. Thus, the model (1) is well-posed mathematically and epidemiologically.

Hence, we establish the following lemma:

Lemma 1 *The set* $D = \{(S, A, I, R) \in \mathbb{R}^4_+ : 0 < S + A + I + R \leq \frac{A}{\mu}\}$ *is a positively invariant region of the model* (1).

Since the recovered population $R(t)$ does not feature in the first three equations of the model (1). Therefore, without loss of generality, this equation can be omitted for theoretical analysis. Thus, we consider the following reduced system for the study:

$$\begin{aligned}
\frac{dS}{dt} &= \pi - \delta S - \mu S - \frac{\beta SI}{1+\alpha I},\\
\frac{dA}{dt} &= \delta S - \mu A - \frac{\gamma AI}{1+\alpha I},\\
\frac{dI}{dt} &= \frac{\beta SI}{1+\alpha I} + \frac{\gamma AI}{1+\alpha I} - (\mu + d + \theta)I - \frac{aI}{1+bI}.
\end{aligned} \tag{2}$$

In the next section, we obtain the equilibria of the system (2) and discuss their stability behavior.

4 Equilibria and their stability analysis

The system (2) has two equilibria which are obtained by equating the derivatives of the system (2) to zero. These are as follows:

i. Disease-free equilibrium (DFE) $Q\left(\frac{\pi}{\mu+\delta}, \frac{\delta\pi}{\mu(\mu+\delta)}, 0\right)$.
ii. Endemic (positive) equilibrium (EE) $Q^*(S^*, A^*, I^*)$.

To investigate the stability of the system (2) at obtained equilibria, we first find the linearized matrix. For this, we assume that $F = (F_1, F_2, F_3)^T$, where F_1, F_2 and F_3 represent the right-hand sides of the system (2) respectively. Furthermore, let $X = (S, A, I)^T$. Then, the linearized matrix for the system (2) is obtained as follows:

$$J = \begin{pmatrix} \left(-\delta - \mu - \frac{\beta I}{1+\alpha I}\right) & 0 & -\frac{\beta S}{(1+\alpha I)^2} \\ \delta & \left(-\mu - \frac{\gamma I}{1+\alpha I}\right) & -\frac{\gamma A}{(1+\alpha I)^2} \\ \frac{\beta I}{1+\alpha I} & \frac{\gamma I}{1+\alpha I} & \left(\frac{\beta S}{(1+\alpha I)^2} + \frac{\gamma A}{(1+\alpha I)^2} - d - \mu - \theta - \frac{a}{(1+bI)^2}\right) \end{pmatrix}.$$

Further, we obtain the threshold parameter R_0, known as the basic reproduction number, which determines the stability of the equilibria.

4.1 Computation of R_0

The characteristic equation of the matrix J in λ at DFE (Q) is given by

$$(\mu + \lambda)(\mu + \delta + \lambda)[\lambda - (d + \mu + \theta + a)(R_0 - 1)] = 0. \tag{3}$$

The characteristic Eq. (3) has three roots $\lambda_1 = -\mu$, $\lambda_2 = -(\mu + \delta)$, and $\lambda_3 = (d + \mu + \theta + a)(R_0 - 1)$,

where,

$$R_0 = \frac{\pi(\mu\beta + \gamma\delta)}{\mu(\mu + \delta)(d + \mu + \theta + a)}.$$

The term R_0 is known as the basic reproduction number. The basic reproduction number is defined as "the expected number of secondary cases produced, in a completely susceptible population, by a typical infective individual" [5].

4.2 Stability analysis of disease-free equilibrium

In this subsection, we analyze the stability of the disease-free equilibrium (Q).

4.2.1 Analysis for $R_0 \neq 1$

From Eq. (3) we note that the matrix J evaluated at Q has two negative eigenvalues $\lambda_1 = -\mu$ and $\lambda_2 = -\mu - \delta$, and the sign of the third eigenvalue λ_3 depends on the basic reproduction number R_0. λ_3 is negative if and only if $R_0 < 1$. Thus, with the help of the Routh–Hurwitz criterion, we propose the following theorem:

Theorem 1 *The DFE* $Q\left(\frac{\pi}{\mu+\delta}, \frac{\delta\pi}{\mu(\mu+\delta)}, 0\right)$ *is locally asymptotically stable if* $R_0 < 1$ *and unstable if* $R_0 > 1$.

4.2.2 Analysis at $R_0 = 1$

We notice that the matrix J of the system (2) evaluated at $R_0 = 1$ and bifurcation parameter $\beta = \beta^* = \left(\frac{(\delta+\mu)(d+\mu+\theta+a)}{\pi} - \frac{\gamma\delta}{\mu}\right)$ has a simple zero eigenvalue and the other eigenvalues are negative. Therefore, the disease-free equilibrium Q is a non-hyperbolic equilibrium when $R_0 = 1$. To analyze the behavior of the system (2) for the basic reproduction number R_0 equals to one, we use the bifurcation theory approach which is based on the center manifold theory [4, 17]. Through this approach, we are interested to access if there is a stable coexistence equilibrium bifurcating from Q, and Q changes from being stable to unstable. This behavior is known as forward bifurcation [4]. For the analysis, we assume that $S = x_1$, $A = x_2$ and $I = x_3$ then the system (2) can be rewritten as

$$\begin{aligned}
\frac{dx_1}{dt} &= \pi - \delta x_1 - \mu x_1 - \frac{\beta x_1 x_3}{1+\alpha x_3} \equiv f_1,\\
\frac{dx_2}{dt} &= \delta x_1 - \mu x_2 - \frac{\gamma x_2 x_3}{1+\alpha x_3} \equiv f_2,\\
\frac{dx_3}{dt} &= \frac{\beta x_1 x_3}{1+\alpha x_3} + \frac{\gamma x_2 x_3}{1+\alpha x_3} - (\mu + d + \theta)x_3 - \frac{a x_3}{1+b x_3} \equiv f_3.
\end{aligned} \tag{4}$$

The Jacobian matrix J^* evaluated at $R_0 = 1$ and $\beta = \beta^*$ is obtained as

$$J^* = \begin{pmatrix} (-\delta-\mu) & 0 & -\frac{\beta^*\pi}{(\mu+\delta)} \\ \delta & -\mu & -\frac{\gamma\delta\pi}{\mu(\mu+\delta)} \\ 0 & 0 & 0 \end{pmatrix}.$$

Let $u = [u_1, u_2, u_3]$ denotes the left eigenvector and $w = [w_1, w_2, w_3]^T$ denotes the right eigenvector of J^* corresponding to the zero eigenvalue. Then, we obtain that

$$u_1 = 0,\ u_2 = 0,\ u_3 = 1 \text{ and } w_1 = -\frac{\beta^*\pi}{(\delta+\mu)^2},\quad w_2 = -\frac{\delta\pi(\gamma\delta + \gamma\mu + \mu\beta^*)}{\mu^2(\delta+\mu)^2},\quad w_3 = 1.$$

The non-zero partial derivatives associated with the functions f_1, f_2, and f_3 of the system (4) calculated at $R_0 = 1$ and $\beta = \beta^*$ are

$$\left(\frac{\partial^2 f_3}{\partial x_1 \partial x_3}\right)_Q = \beta^*, \quad \left(\frac{\partial^2 f_3}{\partial x_2 \partial x_3}\right)_Q = \gamma, \quad \left(\frac{\partial^2 f_3}{\partial x_3 \partial x_1}\right)_Q = \beta^*,$$

$$\left(\frac{\partial^2 f_3}{\partial x_3 \partial x_2}\right)_Q = \gamma, \quad \left(\frac{\partial^2 f_3}{\partial x_3^2}\right)_Q = -\frac{2\alpha\pi}{\mu(\mu+\delta)}(\mu\beta^* + \gamma\delta), \text{ and} \left(\frac{\partial^2 f_3}{\partial x_3 \partial \beta^*}\right)_Q = \frac{\pi}{(\delta+\mu)}.$$

From [4], we obtain the bifurcation constants a_1 and b_1 as given below:

$$\begin{aligned} a_1 &= \sum_{k,i,j=1}^{3} u_k w_i w_j \left(\frac{\partial^2 f_k}{\partial x_i \partial x_j}\right)_Q \\ &= u_3\left(w_1 w_3 \beta^* + w_2 w_3 \gamma + w_3 w_1 \beta^* + w_3 w_2 \gamma - w_3^2 \frac{2\alpha\pi}{\mu(\mu+\delta)}(\mu\beta^* + \gamma\delta)\right) \\ &= -\left(2\frac{\beta^{*2}\pi}{(\delta+\mu)^2} + 2\frac{\delta\gamma\pi(\gamma\delta + \gamma\mu + \mu\beta^*)}{\mu^2(\delta+\mu)^2} + \frac{2\alpha\pi}{\mu(\delta+\mu)}(\mu\beta^* + \gamma\delta)\right) < 0, \end{aligned}$$

$$\begin{aligned} b_1 &= \sum_{k,i=1}^{3} u_k w_i \left(\frac{\partial^2 f_k}{\partial x_i \partial \beta^*}\right)_Q \\ &= w_3\left(\frac{\pi}{(\delta+\mu)}\right) \\ &= \frac{\pi}{(\delta+\mu)} > 0. \end{aligned}$$

Thus, we propose the following theorem:

Theorem 2 *The DFE* $Q\left(\frac{\pi}{\mu+\delta}, \frac{\delta\pi}{\mu(\mu+\delta)}, 0\right)$ *exhibits a forward bifurcation at* $R_0 = 1$. *Hence, there exists a positive equilibrium as* R_0 *crosses one.* Theorems 1 and 2 can be observed numerically in Fig. 2.

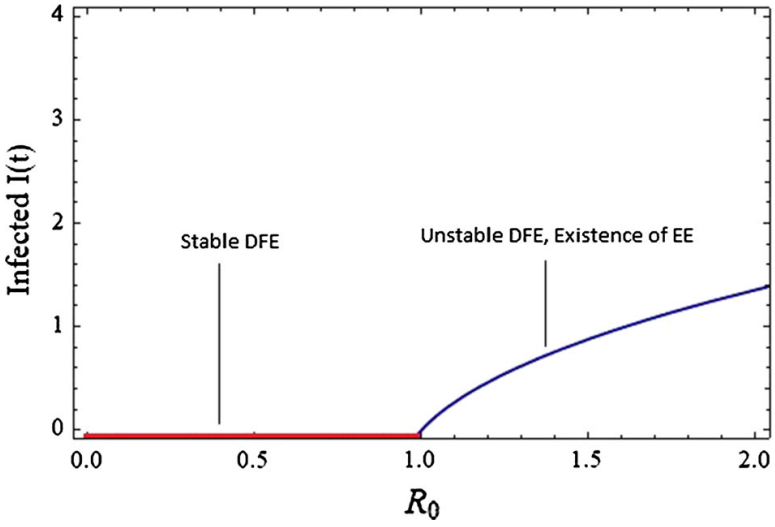

Fig. 2 Graph in support of Theorems 1 and 2 with parameter values $\pi = 2, \alpha = 0.5, \gamma = 0.0009, \mu = 0.007, d = 0.05, \delta = 0.002, b = 0.2, a = 0.2, \theta = 0.002, \beta = 0.0012$

4.3 Endemic equilibrium (EE)

To obtain the conditions for the existence of the endemic equilibrium $Q^* = (S^*, A^*, I^*)$, the system (2) is rearranged to get S^*, A^*andI^* which gives:

$$S^* = \frac{\pi(1+\alpha I^*)}{(\delta+\mu)(1+\alpha I^*)+\beta I^*}, \quad A^* = \frac{\delta S^*(1+\alpha I^*)}{\mu(1+\alpha I^*)+\gamma I^*},$$

and I^* is given by the cubic equation

$$C_4 I^{*3} + C_3 I^{*2} + C_2 I^* + C_1 = 0, \tag{5}$$

where,

$$C_1 = \mu(\delta+\mu)(a+d+\theta+\mu) - \pi(\gamma\delta+\beta\mu) = \mu(\delta+\mu)(a+d+\theta+\mu)(1-R_0),$$

$$\begin{aligned} C_2 = &-\pi((b+\alpha)\gamma\delta + \beta(\gamma+(b+\alpha)\mu)) + a(\gamma(\delta+\mu)+\mu(\beta+2\alpha(\delta+\mu))) \\ &+(d+\theta+\mu)(\gamma(\delta+\mu)+\mu(\beta+(b+2\alpha)(\delta+\mu))), \end{aligned}$$

$$\begin{aligned} C_3 = &\, a(\gamma+\alpha\mu)(\beta+\alpha(\delta+\mu)) - \pi b(\alpha\gamma\delta+\beta(\gamma+\alpha\mu)) \\ &+(d+\theta+\mu)(\beta(\gamma+(b+\alpha)\mu)+(\delta+\mu)(\alpha(\gamma+\alpha\mu)+b(\gamma+2\alpha\mu))), \end{aligned}$$

$$C_4 = b(d+\theta+\mu)(\gamma+\alpha\mu)(\beta+\alpha(\delta+\mu)).$$

After simplifying the coefficients C_2 and C_3, we get that

$$C_2 = -\pi((b+\alpha)\gamma\delta+\beta(\gamma+(b+\alpha)\mu)) + a(\gamma n+\mu(\beta+2\alpha n)) + m(\gamma n+\mu(\beta+(b+2\alpha)n)),$$

$$C_3 = -\pi b(\alpha\gamma\delta+\beta(\gamma+\alpha\mu)) + a(\gamma+\alpha\mu)(\beta+\alpha n) + m(\beta(\gamma+(b+\alpha)\mu)+n((b+\alpha)\gamma+\alpha(2b+\alpha)\mu),$$

where, $m = d+\theta+\mu$, and $n = \delta+\mu$.

Using Descartes' rule of the signs [18], for $R_0 > 1$, the Eq. (5) has a unique positive real root I^* if any one of the following holds:

i. $C_1 < 0, C_2 > 0, C_3 > 0, C_4 > 0$.
ii. $C_1 < 0, C_2 < 0, C_3 > 0, C_4 > 0$.
iii. $C_1 < 0, C_2 < 0, C_3 < 0, C_4 > 0$.

Here, C_1 is negative for $R_0 > 1$, and C_4 is always positive whereas the coefficients C_2, and C_3 are positive or negative under the conditions given below:

$$C_2 \begin{cases} > 0 & \text{when } \pi((b+\alpha)\gamma\delta < \beta(\gamma+(b+\alpha)\mu)) + a(\gamma n+\mu(\beta+2\alpha n)) + m(\gamma n+\mu(\beta+(b+2\alpha)n)). \\ < 0 & \text{when } \pi((b+\alpha)\gamma\delta > \beta(\gamma+(b+\alpha)\mu)) + a(\gamma n+\mu(\beta+2\alpha n)) + m(\gamma n+\mu(\beta+(b+2\alpha)n)). \end{cases}$$

and

$$C_3 \begin{cases} > 0 & \text{when } \pi b(\alpha\gamma\delta+\beta(\gamma+\alpha\mu)) < a(\gamma+\alpha\mu)(\beta+\alpha n) + m(\beta(\gamma+(b+\alpha)\mu)+n((b+\alpha)\gamma+\alpha(2b+\alpha)\mu)). \\ < 0 & \text{when } \pi b(\alpha\gamma\delta+\beta(\gamma+\alpha\mu)) > a(\gamma+\alpha\mu)(\beta+\alpha n) + m(\beta(\gamma+(b+\alpha)\mu)+n((b+\alpha)\gamma+\alpha(2b+\alpha)\mu)). \end{cases}$$

After getting the value of I^* we can obtain the values of S^* and A^*. It indicates the existence of a unique positive equilibrium $Q^*(S^*, A^*, I^*)$ if anyone of the above conditions is satisfied.

The local stability analysis of the endemic equilibrium Q^* is explored as follows: The characteristic equation of the system (2) evaluated at Q^* is a third degree polynomial:

$$\lambda^3 + p_0\lambda^2 + p_1\lambda + p_2 = 0, \tag{6}$$

where,

$$p_0 = \delta + 2\mu + \frac{(\beta+\gamma)I^*}{1+\alpha I^*} + \left(\frac{a}{(1+bI^*)^2} + \mu + d + \theta - \frac{(\beta I^* + \gamma A^*)}{(1+\alpha I^*)^2}\right),$$

$$p_1 = \left(\delta + \mu + \frac{\beta I^*}{1+\alpha I^*}\right)\left(\mu + \frac{\gamma I^*}{1+\alpha I^*}\right) + \frac{(\beta^2 S^* + \gamma^2 A^*)I^*}{(1+\alpha I^*)^3} + \left(\delta + 2\mu + \frac{(\beta+\gamma)I^*}{1+\alpha I^*}\right)\left(\frac{a}{(1+bI^*)^2} + \mu + d + \theta - \frac{(\beta I^* + \gamma A^*)}{(1+\alpha I^*)^2}\right),$$

$$p_2 = \left(\delta + \mu + \frac{\beta I^*}{1+\alpha I^*}\right)\left(\mu + \frac{\gamma I^*}{1+\alpha I^*}\right)\left(\frac{a}{(1+bI^*)^2} + \mu + d + \theta - \frac{(\beta I^* + \gamma A^*)}{(1+\alpha I^*)^2}\right) + \frac{\gamma^2 A^* I^*}{(1+\alpha I^*)^2}\left(\delta + \mu + \frac{\beta I^*}{1+\alpha I^*}\right) + \frac{\beta\delta\gamma S^* I^*}{(1+\alpha I^*)^3} + \frac{\beta S^* I^*}{(1+\alpha I^*)^3}\left(\mu + \frac{\gamma I^*}{1+\alpha I^*}\right).$$

Theorem 3 *The endemic equilibrium Q^* is locally asymptotically stable when* $\frac{(\beta I^*+\gamma A^*)}{(1+\alpha I^*)^2} \leq \frac{a}{(1+bI^*)^2} + \mu + d + \theta$.

Proof From Eq. (6), it is clear that the coefficients p_0, $p_1$andp_2 of λ^2, λ and1, respectively, are positive if $\frac{(\beta I^*+\gamma A^*)}{(1+\alpha I^*)^2} \leq \frac{a}{(1+bI^*)^2} + \mu + d + \theta$. Therefore, by the Descartes's rule of the signs [18], it is clear that all the eigenvalues of Eq. (6) are negative. Hence, by the definition of the Routh–Hurwitz criterion Q^* is locally asymptotically stable when the condition $\frac{(\beta I^*+\gamma A^*)}{(1+\alpha I^*)^2} \leq \frac{a}{(1+bI^*)^2} + \mu + d + \theta$ is satisfied.

5 Numerical simulation

We simulate the system (2) numerically. For simulation, we take the following numerically experimental values of parameters:

$$\pi = 2,\ \alpha = 0.5,\ \beta = 0.003,\ \mu = 0.007,\ d = 0.05,\ \gamma = 0.001,\ \delta = 0.002,$$
$$a = 0.2,\ b = 0.2,\ \theta = 0.002.$$

With the above values of parameters, we calculate the coefficients of Eq. (5) as $C_1 = -0.0000044829$, $C_2 = 0.000004607$, $C_3 = 0.00000503207$, $C_4 = 3.0267 \times 10^{-7}$ with the basic reproduction number $R_0 = 1.274$ which satisfies the condition (i) i.e.$C_1 < 0, C_2 > 0, C_3 > 0, C_4 > 0$ for the existence of a unique positive I^*. Trajectories of S, A, I, and R with initial conditions $S(0) = 200$, $A(0) = 15$, $I(0) = 2$, $R(0) = 1$ approaches to the endemic equilibrium $Q^*(154.6402,\ 37.1406, 3.8084,\ 62.1365)$ as shown in Fig. 3.

In Fig. 3, we plot the graphs for S, A, I and R populations. We observe that the number of infected individuals increase up, and after some days it decreases and become constant due to Holling type II treatment, and these individuals once recovered, become immunized to the infection and will not get re-infected in future. Susceptible individuals decrease to attain a steady state. This decrease may be due to an increase in the number of alert individuals. Further, the alert population increases as the alertness behavior prevent infection and finally, the population settles down to its steady state. This increase may be due to a decrease in the number of infected individuals because of alertness in society. Furthermore, the recovered individuals increase which may be due to the Holling type II treatment of infected individuals, and settles to the steady state.

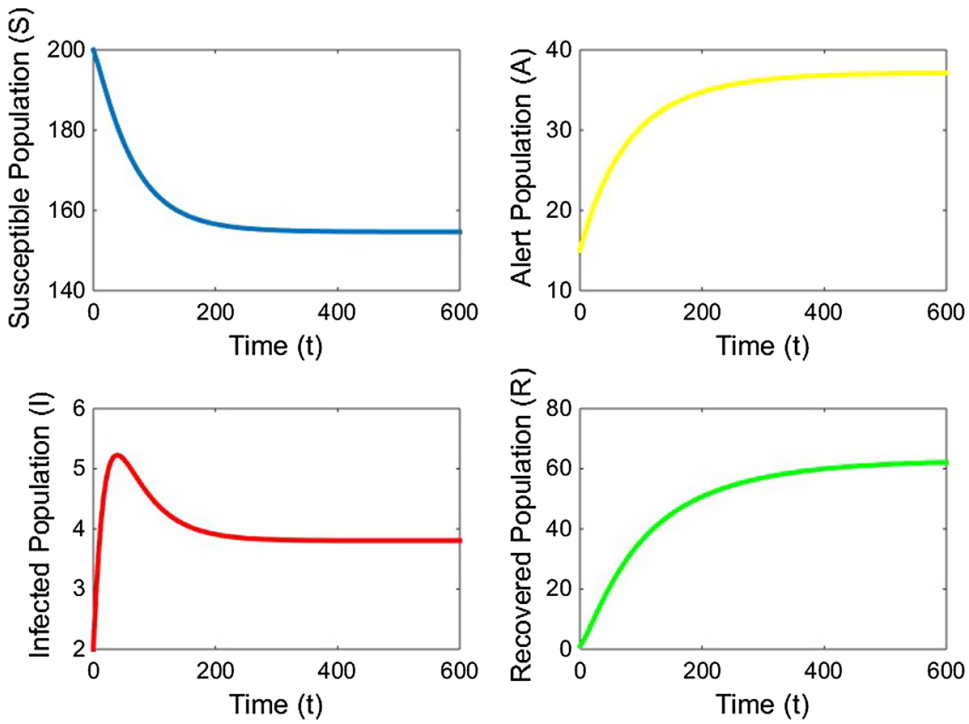

Fig. 3 Susceptible (S), alert (A), infected (I) and recovered (R) population

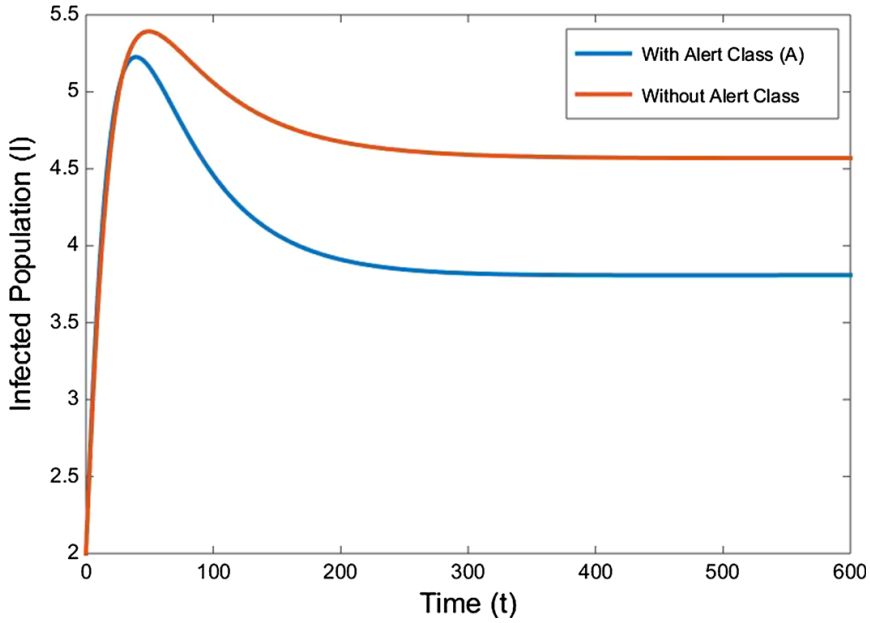

Fig. 4 The infected population with and without the alert class

Figure 4 shows the difference between the infectives with alert and without alert class. It can be seen that the number of infected individuals without the alert class is higher than the number of infected individuals with the alert class. Hence, the alert class plays a vital role in controlling the infection of an epidemic in society.

Figure 5 shows the difference between the infected population with Holling type II treatment rate and without the Holling type II treatment rate. Clearly, in this figure, the number of infected individuals without the Holling type II treatment rate is very high in comparison to the number of infected individuals with Holling type II treatment rate. Hence, the Holling

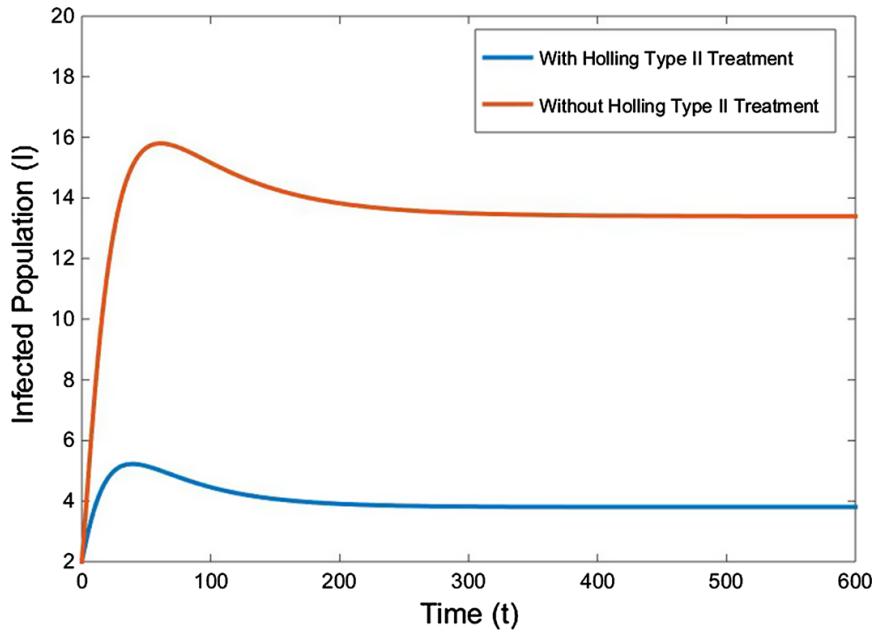

Fig. 5 Graph depicting the behavior of the infected population with and without Holling type II treatment

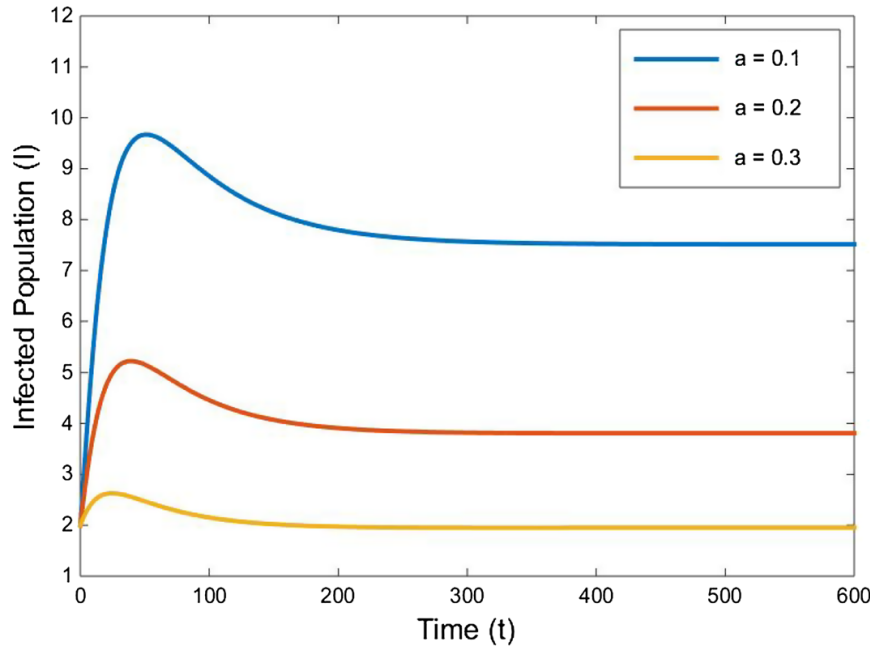

Fig. 6 Impact of the cure rate a on infected population

type II treatment rate has an important role in reducing the infection of the epidemic in society.

Figures 6 and 7 show the effect of the cure rate a and limitation rate b in treatment availability on the infected population at numerous values of a and b. Figure 6 shows the decrease in the infected population as the cure rate a increases and it settles down at its steady state, but the disease is not eliminating entirely as it will persist at a much lower level. Figure 7 shows an increase in the infected population as b increases, which is due to the limited availability of resources in the society.

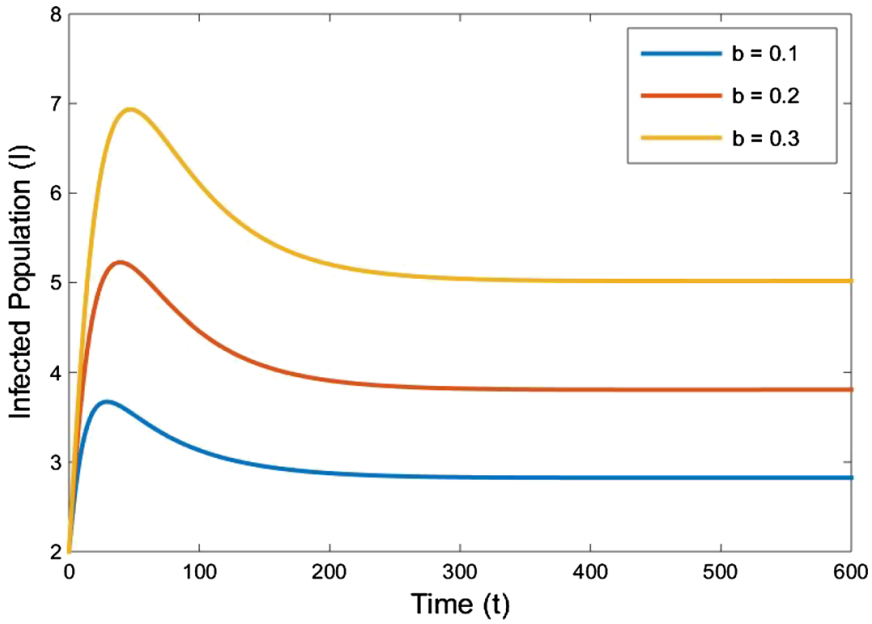

Fig. 7 Impact of limitation rate b in treatment availability on the infected population

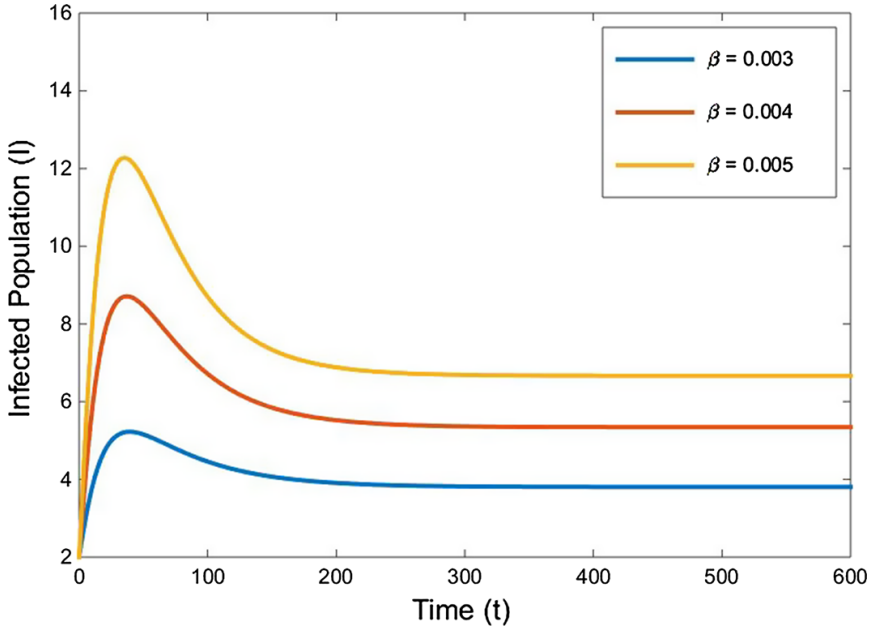

Fig. 8 Impact of β on infected population

Figures 8 and 9 depict the infected population at numerous values of transmission rate β and γ, respectively. Clearly, in these figures, the infected population (I) increases with the increase in the values of $\beta$and γ.

Figure 10 depicts the infected population at numerous values of α. It can be seen that the number of infected individuals decreases as the values of α increases.

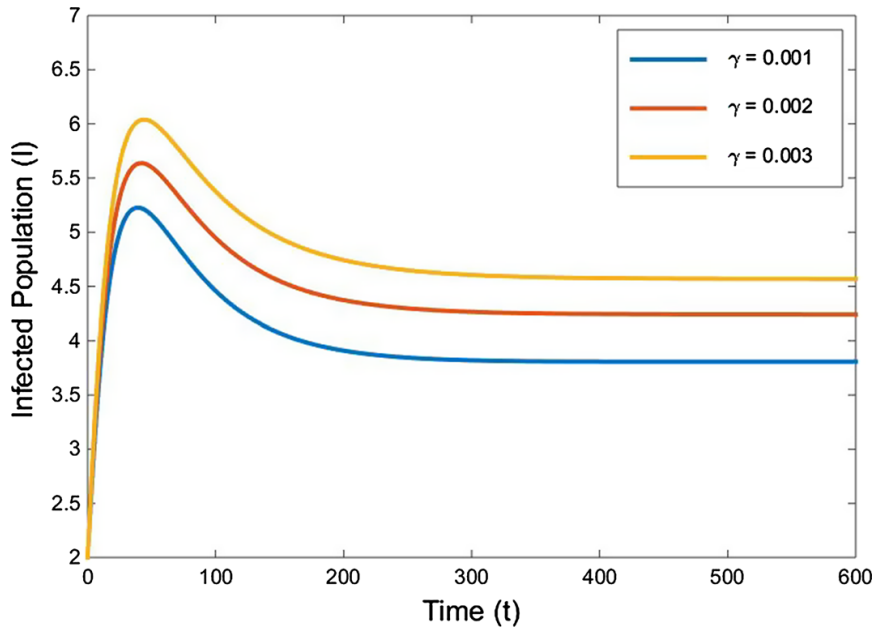

Fig. 9 Impact of transmission rate γ on infected population

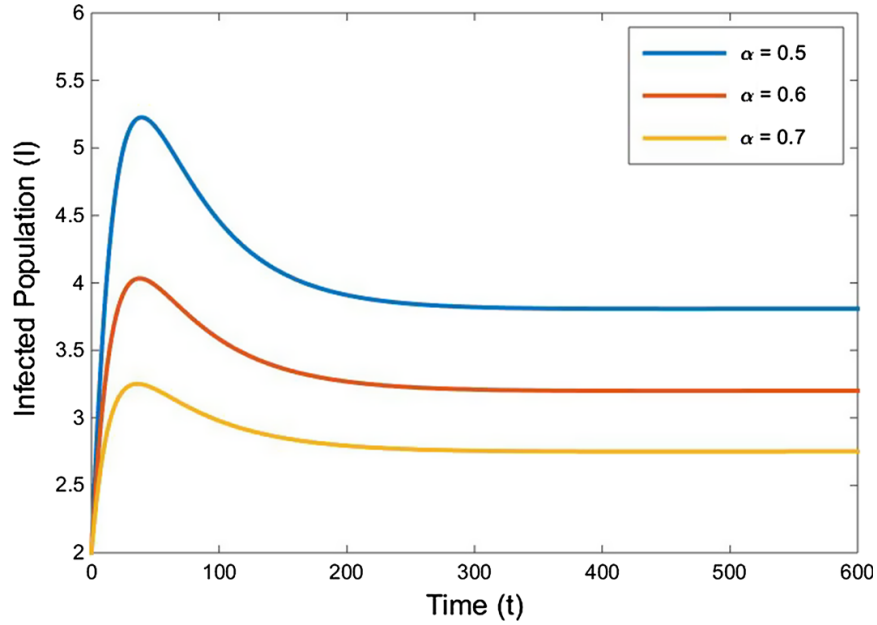

Fig. 10 Number of infected individuals at various values of α

6 Discussion

Mathematical modeling is a valuable tool to understand the dynamics of the epidemics and for planning and evaluating the interventions. In the present article, we have proposed and analyzed a susceptible–alert–infected–recovered (SAIR) model with two explicit saturated incidence rates along with Holling type II treatment rate to study the transmission and control of the epidemic. We have discussed the stability of DFE using the basic reproduction number R_0 and proved that the disease dies out from the society when $R_0 < 1$ and persists if $R_0 > 1$. We have discussed the stability at DFE for $R_0 = 1$ and evaluated that DFE exhibits the forward bifurcation and hence there exists a positive equilibrium as R_0 crosses one. We also investigated the stability for the endemic equilibrium (EE) and showed that EE is

locally asymptotically stable when the condition stated in Theorem 3 is satisfied. Numerical simulations have been carried out to see the effect of alertness and Holling type II treatment rate. It is observed that the number of infected individuals decreases as the cure rate increases. However, the number of infected individuals increases as the limitation rate in treatment availability increases. It shows that for effective treatment, the resource limitation should be minimized. We also observed that the number of infected individuals increases as the transmission rate increases and it decreases as the rate of inhibition increases.

Acknowledgements The authors are thankful to Delhi Technological University, Delhi, for monetary support for this research. The authors also gratefully acknowledge the handling editor and anonymous reviewers for their valuable suggestions which enhance the quality of the paper.

References

1. Alexander, M.E., Bowman, C., Moghadas, S.M., Summers, R., Gumel, A.B., Sahai, B.M.: A vaccination model for transmission dynamics of influenza. SIAM J. Appl. Dyn. Syst. **3**(4), 503–524 (2004)
2. Buonomo, B., d'Onofrio, A., Lacitignola, D.: Global stability of an SIR epidemic model with information dependent vaccination. Math. Biosci. **216**(1), 9–16 (2008)
3. Capasso, V., Serio, G.: A generalization of the Kermack–Mckendrick deterministic epidemic model. Math. Biosci. **42**, 41–61 (1978)
4. Castillo-Chavez, C., Song, B.: Dynamical models of tuberculosis and their applications. Math. Biosci. Eng. **1**, 361–404 (2004)
5. Driessche, P.V.D., Watmough, J.: Reproduction numbers and sub-threshold endemic equilibria for compartment models of disease transmission. Math. Biosci. **180**, 29–48 (2002)
6. Dubey, B., Patara, A., Srivastava, P.K., Dubey, U.S.: Modeling and analysis of a SEIR model with different types of nonlinear treatment rates. J. Biol. Syst. **21**(3), 1350023 (2013)
7. Goel, K., Nilam, : A mathematical and numerical study of a SIR epidemic model with time delay, nonlinear incidence and treatment rates. Theory Biosci. (2019). https://doi.org/10.1007/s12064-019-00275-5
8. Gumel, A.B., Mccluskey, C.C., Watmough, J.: An SVEIR model for assessing the potential impact of an imperfect anti-SARS vaccine. Math. Biosci. Eng. **3**, 485–494 (2006)
9. Hattaf, K., Lashari, A.A., Louartassi, Y., Yousfi, N.: A delayed SIR epidemic model with general incidence rate. Electron. J. Qual. Theory Differ. Equ. **3**, 1–9 (2013)
10. Karim, S.A.A., Razali, R.: A proposed mathematical model of influenza A, H1N1 for Malaysia. J. Appl. Sci. **11**(8), 1457–1460 (2011)
11. Kumar, A., Nilam, : Stability of a time delayed SIR epidemic model along with nonlinear incidence rate and Holling type II treatment rate. Int. J. Comput. Methods **15**(6), 1850055 (2018)
12. Kumar, A., Nilam, : Dynamical model of epidemic along with time delay; Holling type II incidence rate and Monod-Haldane treatment rate. Differ. Equ. Dyn. Syst. **27**(1–3), 299–312 (2019)
13. Li Michael, Y., Graef, J.R., Wang, L., Karsai, J.: Global dynamics of a SEIR model with varying total population size. Math. Biosci. **160**, 191–213 (1999)
14. Li, G.H., Zhang, Y.X.: Dynamic behavior of a modified SIR model in epidemic diseases using nonlinear incidence and recovery rates. PLoS ONE **12**(4), e0175789 (2017)
15. Liu, W.M., Hethcote, H.W., Levin, S.A.: Dynamical behavior of epidemiological models with nonlinear incidence rates. J. Math. Biol. **25**(4), 359–380 (1987)
16. Mena-Lorca, J., Hethcote, H.W.: Dynamic models of infectious disease as regulators of population size. J. Math. Biol. **30**(7), 693–716 (1992)
17. Sastry, S.: Analysis, Stability and Control. Springer, New York (1999)
18. Wang, X.: A simple proof of Descartes's rule of signs. Am. Math. Mon. (2004). https://doi.org/10.2307/4145072
19. Wang, W., Ruan, S.: Bifurcation in an epidemic model with constant removal rates of the infectives. J. Math. Anal. Appl. **21**, 775–793 (2004)
20. Xu, R., Ma, Z.: Stability of a delayed SIRS epidemic model with a nonlinear incidence rate. Chaos Solut. Fractals **41**, 2319–2325 (2009)
21. Zhang, Z., Suo, S.: Qualitative analysis of a SIR epidemic model with saturated treatment rate. J. Appl. Math. Comput. **34**, 177–194 (2010)

22. Zhou, L., Fan, M.: Dynamics of a SIR epidemic model with limited medical resources revisited. Nonlinear Anal. RWA **13**, 312–324 (2012)

Publisher's Note Springer Nature remains neutral with regard to jurisdictional claims in published maps and institutional affiliations.

AIP Conference Proceedings

A theoretical modeling of the Cu(In, Ga)Se_2 solar cell

Cite as: AIP Conference Proceedings **2093**, 020018 (2019); https://doi.org/10.1063/1.5097087
Published Online: 15 April 2019

Gagandeep, M. Singh, R. Kumar, and F. Chand

View Online Export Citation

ARTICLES YOU MAY BE INTERESTED IN

First-principles study on electronic, mechanical and thermoelectric transport properties of topological insulator NaAuS
AIP Conference Proceedings **2093**, 020016 (2019); https://doi.org/10.1063/1.5097085

Structural, electronic and magnetic properties of Ti-doped MgSe diluted magnetic semiconductor compound
AIP Conference Proceedings **2093**, 020001 (2019); https://doi.org/10.1063/1.5097070

Modifications in optical parameters of PVA by embedded Au-Ag core-shell nanoparticles
AIP Conference Proceedings **2093**, 020006 (2019); https://doi.org/10.1063/1.5097075

AIP Publishing

© 2019 Author(s).

A Theoretical Modeling of the Cu(In, Ga)Se_2 Solar Cell

Gagandeep[1, a)], M. Singh[2], R. Kumar[1,b)] and F. Chand[3]

[1]*Department of Physics, Guru Jambheshwar University of Science & Technology, Hisar*
[2]*Department of Applied Physics, Delhi Technological University, Delhi*
[3]*Department of Physics, Kurukshetra University, Kurukshetra*

[a)] *gagankundu22@gmail.com*
[b)] Corresponding author: *rameshkumar.bibiyan@gmail.com*

Abstract. The recent research work in solar cell based on chalcopyrite Cu (In, Ga) Se_2(CIGS) materials have more potential to enhance the efficiency of solar cells. In this theoretical work, we studied the working conditions of CIGS solar cell. The CIGS solar cells can be considered as single diode model. We implemented the diode equations in MATLAB software. From these equations, we calculate current density-voltage (J-V) and power-voltage (P-V) characteristics under the illumination condition of AM 1.5G. We investigate the efficiency (η) changes for various values of series resistance (R_S) and parallel resistance (R_P). The efficiency and fill factor of CIGS solar cell under optimized values of R_S=0.5 Ω, R_P=20 KΩ are 21.86% and 0.8014 respectively. It is seen that our theoretical results are in good matching with the other research studies.

Key Words: CIGS, Diode, Solar Cell, Resistance, Efficiency

INTRODUCTION

At the beginning of 21st century, various types of energy sources are employed to fulfill the world's demand for energy. Till now the more contribution in energy is from fossil fuels such as coal, oil and natural gas. Other alternatives for energy are renewable sources such as water, wind and solar. Solar energy has more advantage as compared to other renewable sources. Solar cells are made from crystalline Si, amorphous Si and from thin film technologies. Thin film technologies widely employed the chalcopyrite or CIGS material for solar cell.

Recently, the researchers have paid much attention to CIGS as promising material for thin film solar cells. These type of solar cells have high conversion efficiency and low production cost. The energy gap of CIGS can be tuned in between 1.04 eV and 1.68 eV by varying the gallium concentration [1,2]. Thus, the energy gap of CIGS can be changed to better match with the visible part of sunlight spectra. The high performance of CIGS solar cell using flexible substrate is still challenging, but a record efficiency of 18.7% on polyimide film has been attained [3]. The CIGS conversion efficiency of 20.3% is obtained in lab [4] and commercially reach 10-12 %. A record efficiency of 20.8% have obtained for thin film CIGS solar cell [5]. This record did not last for long due to the development of alkali post deposition treatment (PDT) [6]. With new techniques in various laboratories, the CIGS solar cell efficiency has raised from 20.4% to 21.8% (SOLAR frontier: 20.9% [7], Solibro 21.0% [8]). Recently, the authors [9] with PDT technique have once again enhanced the efficiency of thin film CIGS solar cell up to 21.7%.

Hence, it is essential to analyze the efficiency variation of CIGS solar cells with different parameters, which presents important physical views to further increase the efficiency of CIGS photovoltaic cells. In this theoretical work, CIGS solar cell has been modeled as diode equivalent circuit in MATLAB software. Using this diode model

Proceedings of the National Conference on Recent Advances in Condensed Matter Physics
AIP Conf. Proc. 2093, 020018-1–020018-4; https://doi.org/10.1063/1.5097087
Published by AIP Publishing. 978-0-7354-1823-3/$30.00

we verified the experimental results reported by the authors in [9]. The variations of current density (J) and power (P) with voltage (V) of CIGS solar cell have been obtained and the influence of R_S and R_P on the solar cell parameters are analyzed. We obtained the largest CIGS solar cell efficiency and fill factor (FF) under optimized values of R_S=0.5 Ω, R_P=20 KΩ are 21.86% and 0.8014 respectively.

THEORETICAL DETAILS

In this theoretical works, the CIGS solar cell is considered as single diode model by considering the different physical aspects such as ideality factor of diode and values of resistances during fabrication conditions. The diode equations derived from the diode model is implemented in MATLAB software. The diode equivalent model of CIGS solar cell with series and shunt resistances are given in Figure 1.

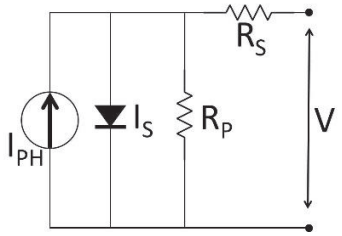

FIGURE 1. Equivalent circuit for CIGS solar cell.

The photo induced current in solar is presented by $I_{ph} = I_{sc} + K_i(T - 298)] \times I_r/1000$. The I_{sc} represents the current at short circuit; K_i, I_r are the temperature current constant parameter at T, and intensity of solar radiation respectively. The mathematical equations using equivalent model [10, 11] are obtained. The reverse saturation current is mentioned below

$$I_{on} = \frac{I_{scn}}{\left(\exp\left(\frac{V_{ocn}}{a*V_{tn}}\right)\right) - 1} \tag{1}$$

The device saturation current I_o and voltage variations with temperature is given as:

$$I_o = I_{on} * \left(\left(\frac{T_n}{T}\right)^3\right) * \exp\left(\left(q * \frac{E_g}{a * k}\right) * \left(\left(\frac{1}{T_n}\right) - \left(\frac{1}{T}\right)\right)\right) \tag{2}$$

$$V_{tn} = N_s * \left(k * \frac{T_n}{q}\right) \tag{3}$$

Where N_s =no. of cell, V_{ocn} = open circuit voltage, V_{tn}= voltage at nominal temperature, I_{scn} = short circuit current, E_g = energy band gap, k is Boltzmann's constant (1.38×10^{-23}J/K), T_n= nominal temperature, T(298K) = operating temperature, I_o= reverse saturation current, a= diode ideality constant and q= electron charge (1.6×10^{-19}C). The mathematical equations (1) and (2) are implanted in MATLAB software using some experimental fitting parameters [9] shown in Table 1.

Table 1. Computational parameters for CIGS materials

Working parameters	I_{sc}(A)	V_{oc} (V)	K_v(V/K) (%)	K_i (A/K)(%)	G (W/m^2)	E_g(eV)	N_S	a	R_S (Ω)	R_P (K Ω)
Values	0.0182	0.746	-0.33%	0.03%	1000	1.67	1	1.38	0.644	3539.82

RESULTS AND DISCUSSIONS

In this theoretical work, CIGS materials based solar cell has been studied using diode model in MATLAB software. This is a widely used material for power conversion efficiency of solar cells due to its energy gap of 1.67 eV and high

absorption co-efficient ($10^5 cm^{-1}$). From this equivalent model as shown in fig. 1, the basic diode equations that relate the saturation current to the bias voltage, temperature and energy gap have been derived i.e. given by equations (1), (2), (3). The value of J is obtained for the CIGS solar cell by considering the area of solar cell of about 0.4977 cm^2. Other parameters of CIGS solar cell is tabulated in the table 1. We calculated the J-V behavior of the CIGS cell under radiance of AM 1.5G, given in figure 2 (a). By taking the values for R_S = 0.644 Ω, R_P = 3539.82 Ω in figure 1, the efficiency, 21.56% and FF, 0.79 are procured. These theoretical calculations are in good matching with the experimental study [9]. The P-V curve of the device linking to the J-V characteristics and is presented in figure 2 (b). P-V curve maxima gives the maximum power point (P_{max}). This point presents the idea about the highest power that can be taken out from a device. If P_{max} is divided by the incoming power, then it represents the power conversion efficiency of the solar cell. The efficient working of a photovoltaic device requires a small value of R_S and larger value of R_P.

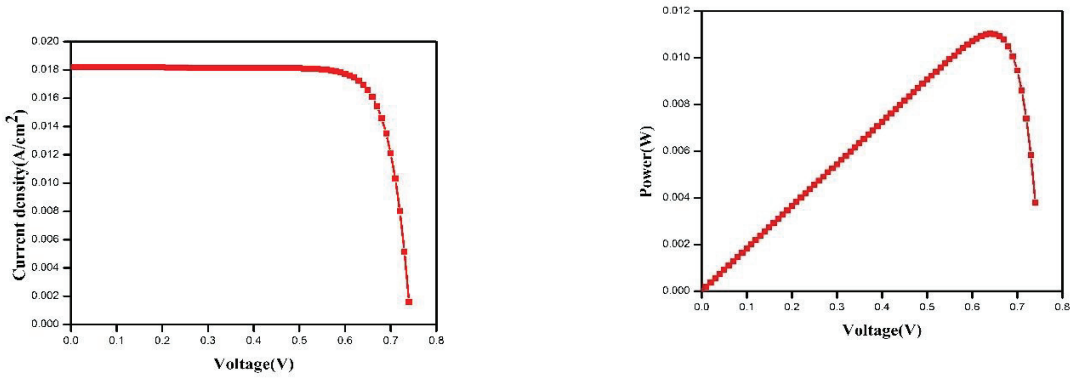

(a) (b)

FIGURE 2. (a) I – V curve. (b) P-V curve.

Table 2. Effect of R_S on FF and efficiency

S.No.	R_S (Ω)	R_P (Ω)	FF	η(%)
1	0.5	8000	0.7991	21.79
2	5	8000	0.7018	19.14
3	10	8000	0.5976	16.30
4	15	8000	0.5017	13.68

Table 3. Effect of R_P on FF and efficiency

S.No.	R_S (Ω)	R_P (Ω)	FF	η(%)
1	0.5	2000	0.7878	21.49
2	0.5	5000	0.7968	21.73
3	0.5	8000	0.7991	21.76
4	0.5	20000	0.8014	21.86

In order to analyze the effect of R_S and R_P on the working of CIGS solar cell, the values of R_S and R_P varied independently, taking other parameters that affected the performance of device are fixed. The effect of series resistance on J-V curve, keeping R_P = 8000 Ω is given in figure 3 (a), and the obtained outcomes are mentioned in Table 2. These results show a clear variation that when we rise in value of R_S, the values of FF and the efficiency of the solar cell decreases. The rise in R_S links to rise in bulk resistance and contact resistance of the device. Due to increase in resistance, the charge collection of the cell is reduced, thus, lowering the power conversion efficiency. The variation in the solar cell device efficiency and FF are clearly visible for the different values of R_S and a significant lowering is computed at 15 Ω. For CIGS solar cell, the largest efficiency of 21.79% and FF of 0.7991 is obtained for R_S = 0.5 Ω. But, practically it is not feasible to obtain such small value of R_S and one can advise to take the optimistic values in the range 5-15 Ω.

Further we studied the influence of shunt resistance on cell working, holding R_S constant at 0.5. The change in the behavior of J-V curve with R_P are given in figure 3 (b). The device performance is improved i.e. the efficiency and FF increases with rise in R_P. We correlated the results with the diode equivalent model given in Fig. 1. When we rise the value of R_P, more current draws through R_S, then the FF and efficiency increases. For CIGS solar cell, the largest efficiency of 21.86% with a FF of 0.8041 is obtained at R_P = 20KΩ. The variation in the cell working is low prominent

for the higher values of R_p as tabulated in table 3. Therefore, the practical feasible value of R_P = 5 kΩ was chosen. Hence, from this theoretically study, we may be concluded that in spites getting a small value of R_S and a large value of R_P, some other material properties such as energy gap, mobility and morphology require to be studied to construct a high efficiency solar cells.

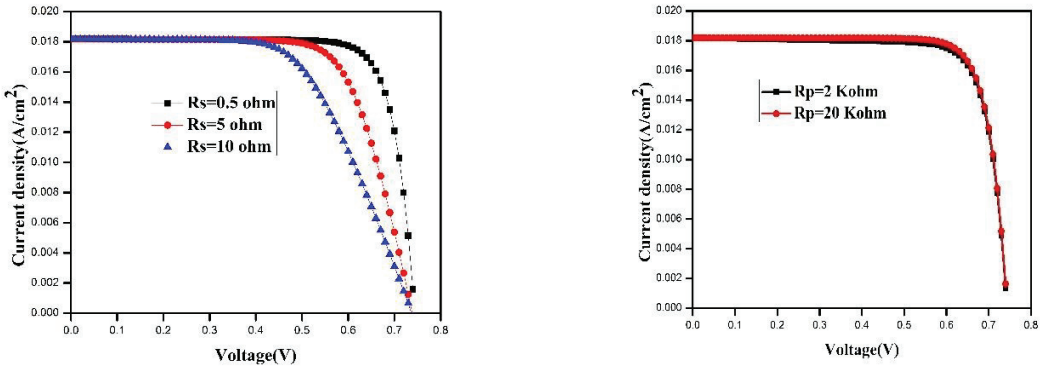

(a) (b)

FIGURE 3. J-V curve variation with (a)R_S, keeping R_P fixed(b)R_P, keeping R_S fixed.

CONCLUSIONS

Based on the above theoretical works, we calculated the efficiency and FF of CIGS solar cell using diode model in MATLAB software. The efficiency and FF of the cell are computed for R_S = 0.644 Ω, R_P = 3539.82 Ω and have values 21.56% and 0.79 respectively. The modeling results are in very excellent matching with the other theoretical as well as experimental results reported in literature. We optimized the better values of series and parallel resistance for CIGS solar cell. The highest efficiency and fill factor of CIGS solar cell under optimized values of R_S=0.5 Ω, R_P=20 KΩ are 21.86% and 0.8014 respectively. Therefore, we conclude that a small value of R_S and a larger R_P is needed for a good working of the solar cells.

ACKNOWLEDGMENT

One of the author (**RK**) gratefully acknowledges the **University Grants Commission, INDIA** for providing the financial support through **START-UP GRANT** (No. F.30-364/2017 (BSR), Dated 15/12/2017).

REFERENCES

1. S. H. Wei, S. B. Zhang and A. Zunger, App. Phys. Lett.**72,**3199, (1998).
2. C. H. Huang, Journal of Physics and Chemistry Solids**69**, 330-334, (2008).
3. M. Powalla et. al. IEEE J. Photovoltaics**4**,440-6(2014).
4. P. Jackson et. al., Prog. Photovolt: Res. Appl.**19**, 894-897, (2011).
5. P. Jackson et.al. Phys. Status Solidi RRL **8**, 219, (2014).
6. A. Chirila et. al., Nature Mater.**12**, 1107, (2013).
7. K. Kushia, Current Status and Future Prospects of Solar Frontier K.K., presented at the IW-CIGSTech 5, Berlin, Germany, April 2-3, (2014).
8. D. Herrmann et. al., CIGS module manufacturing with high deposition rates and efficiencies, presented at 40th IEEE PVSC, Denver, CO, USA, June 8-13, (2014).
9. P. Jackson et.al. Phys. Status Solidi RRL,1-4, (2014).
10. P. Bhatt, M. Kumar, P. Chandra Kant, M. K. Panday and B. Tripathi, Organic Electronics **39**,258-266, (2016).
11. Gagandeep, M. Singh, R. Kumar, V. Singh and F. Chand, AIP Conference Proceedings **2006**, 030018, (2018).

Journal of ELECTRONIC MATERIALS
https://doi.org/10.1007/s11664-019-07175-w
© 2019 The Minerals, Metals & Materials Society

An Electron Paramagnetic Resonance and Photoluminescence Investigation of UVB Radiation Emitting Gadolinium-Activated $CaY_2Al_4SiO_{12}$ Garnet Compound

VIJAY SINGH,[1,4] SUMANDEEP KAUR,[2] A.S. RAO,[2] N. SINGH,[1] M.S. PATHAK,[1] and J.L. RAO[3]

1.—Department of Chemical Engineering, Konkuk University, Seoul 05029, Korea. 2.—Department of Applied Physics, Delhi Technological University, Bawana Road, Delhi 110042, India. 3.—Department of Physics, S.V. University, Tirupati, Andhra Pradesh 517502, India. 4.—e-mail: vijayjiin2006@yahoo.com

Trivalent gadolinium (Gd^{3+}) activated $CaY_2Al_4SiO_{12}$ garnet compounds with a variable concentration of Gd^{3+} ions were synthesized by a sol–gel method. The synthesized garnet compounds were characterized for their structural, morphological, luminescent, and magnetic properties. The x-ray diffraction data of Gd^{3+} activated $CaY_2Al_4SiO_{12}$ garnet compound reveal the cubic structure with I*a3d* space group. The scanning electron microscope images represent the morphology of the particles. The photoluminescence properties were analyzed from the excitation and emission spectra. The emission spectra of the $CaY_2Al_4SiO_{12}$:Gd^{3+} garnet compound under 273 nm excitation exhibit two emission peaks at 308 nm and 314 nm and are attributed to $^6P_{5/2} \rightarrow {}^8S_{7/2}$ and $^6P_{7/2} \rightarrow {}^8S_{7/2}$ transitions, respectively. The emission peak observed at 314 nm is more intense than the peak observed at 308 nm. The high-intensity peak at 314 nm is used to cure various skin disorders, and hence is beneficial in phototherapy. The intensity of the emission peaks increases up to 0.09 mol of Gd^{3+} ion concentration in the $CaY_2Al_4SiO_{12}$ garnet compound, and beyond, then decreases, showing concentration quenching. The electron paramagnetic resonance of Gd^{3+} ions in the prepared garnet compound exhibits resonance signals with effective g values at $g \approx 6.5$, 5.0, 2.6, 2.2, 2.0, and 1.6 of the U-spectrum, due to cubic, octahedral, or tetrahedral distorted sites.

Key words: Sol–gel, EPR, Gd^{3+}, $CaY_2Al_4SiO_{12}$, garnet, luminescence

INTRODUCTION

Garnet host materials are one of the most important host materials for rare earth (RE) ions, because of their physical stability, high luminescent efficiency, good chemical stability, and high thermal properties.[1–5] Garnet-type structure offers promising candidates for electrolytes in solid-state electrochemical devices, and in rechargeable lithium batteries.[6,7] Garnet compounds have the general crystal formula $\{A_3\}[B_2](C_3)O_{12}$, where A, B, and C are in dodecahedral, octahedral, and tetrahedral coordinates, respectively.[8,9] In recent years, by combining the ions of different valence states, such as A = RE^{3+}, Ca^{2+}, Ba^{2+}, Sr^{2+}, or Mg^{2+}; B = Sc^{3+}, Ga^{3+}, or Al^{3+}; and C = Ga^{3+}, Al^{3+}, or Si^{4+} at various crystallographic sites, a significant number of different compositions were obtained, without changing the garnet structure.[10,11] Although the structure of garnet does not show any change, the local coordination structure of the sites can be changed, depending on the garnet composition. Exploiting the isomorphism in garnets is another approach to obtain new compounds with garnet structure that belong to the *Ia3d* space group.[12] In recent years, $MY_2Al_4SiO_{12}$ (where M = Ca, Ba, Sr,

(Received September 14, 2018; accepted March 28, 2019)

Published online: 08 April 2019

Mg) garnet compounds were investigated by several research groups. Garnet compound $MgY_2Al_4SiO_{12}:Ce^{3+}$ was successfully prepared in which Mg^{2+} substituting into the dodecahedral Y^{3+} site.[13] The optical properties of yellow-emissive $CaY_2Al_4SiO_{12}:Ce^{3+}$ garnet compound for phosphor-converted LEDs were also studied and reported.[14] High thermal emission stability of $Y_2BaAl_4SiO_{12}:Ce^{3+}$ yellow phosphor was studied and discussed in detail.[15] The co-doped phosphor ($MgY_2Al_4SiO_{12}:Ce^{3+}$, Mn^{2+}) with high quantum yields (up to 89.0%) was studied and suggested as a potential candidate to obtain a warm white LED.[16] The $CaY_2Al_4SiO_{12}$ lattice contains (CaY_2) sites in dodecahedral, [Al^{3+}] sites in octahedral, and (Al_2Si) sites in tetrahedral sites. However, in the literature, a dearth of knowledge remains in terms of the luminescent property of the RE-doped $CaY_2Al_4SiO_{12}$ garnet.

Among various RE ions, trivalent gadolinium (Gd^{3+}) ion exhibits emission in the ultraviolet (UV) region, which is quite apt for medical applications.[17] In general, UV radiation has various applications in the cosmetic, germicidal, photolithographic, photochemical, photobiological, medical, polymer hardening, and atmospheric sensing areas, and is also important for the synthesis of vitamin D.[18–25] Besides these applications, UV sources play a vital role in gas lasers, and optical parametric oscillators.[26,27] The Gd^{3+} ions give the emission in the narrowband ultraviolet B (NB-UVB) region, due to their $^6P_{7/2} \rightarrow {}^8S_{7/2}$ transition. The NB-UVB emission from Gd^{3+} ions is vital in the phototherapy lamp for the treatment of skin diseases.[28] LaB_3O_6: Bi, Gd, and $CeMgB_5O_{10}:Gd^{3+}$ are commercial samples that are used in low-pressure fluorescent lamps for NB-UVB treatment.[29,30] The excited state ($^6P_{7/2}$) of Gd^{3+} ions lies in the ultraviolet region, and, due to this, the Gd^{3+} ion is able to absorb ultraviolet light, and can transfer energy to other RE ions, such as Sm^{3+}, Eu^{3+}, and Tb^{3+} through charge transfer, which leads to improved luminescence efficiency.[31–33] Nowadays, Gd^{3+} ions co-doped with upconversion nanocrystals can be used for magnetic or optical bimodal detection.[34] Besides these applications, gadolinium ions could be used for neutron capture therapy, due to their high neutron capture cross-section of non-radiative radiation.[35] Currently, the development of novel NB-UVB radiation-emitting gadolinium-doped host compounds for phototherapy lamp are gaining much attention. The synthesis method plays an important role in developing strong NB-UVB radiation compounds. Traditionally, RE-doped compounds were prepared by the solid-state method. But the solid-state method requires high temperature and a lengthy heating process. In comparison with the solid-state method, the wet chemical method, especially the sol–gel process, has advantages over the solid-state method regarding low annealing temperature, and good particle homogeneity.[36]

It is well known that EPR is very sensitive, and can detect paramagnetic ions, such as Gd^{3+}, Eu^{2+}, Mn^{2+}, and Cr^{3+}.[37–40] EPR signals of these ions can give information about their own environment in the host lattice. In particular, Gd^{3+} ions containing host compounds are very interesting, due to their paramagnetic properties. The EPR signal of the Gd^{3+} ions exhibits a complex nature, which is popularly known as the "U" spectrum, due to its "ubiquity". In recent years, several researchers have investigated the EPR properties of various Gd^{3+} doped inorganic oxides, such as aluminates, zirconate, silicates, and phosphates.[41–44]

Among various hosts, silicate-based garnet host materials have been investigated widely due to their high physical, chemical, thermal, and structural diversity of luminescent properties.[45–47] Therefore, in this article, we prepared silicate-based Gd^{3+}-activated $CaY_2Al_4SiO_{12}$ garnet compound using a sol–gel method to explore the structural and luminescent properties of the synthesized garnet compound. The final product was characterized by XRD and SEM techniques. PL and EPR techniques were used to study the local site of the Gd^{3+} ion incorporated in the garnet host.

EXPERIMENTAL

A series of $CaY_2Al_4SiO_{12}:Gd_{0.005–0.11}$ (CYS1–CYS7) samples were prepared by a sol–gel method using $Ca(NO_3)_2{\cdot}4H_2O$, $Y(NO_3)_3{\cdot}6H_2O$, $Al(NO_3)_3{\cdot}9H_2O$, SiO_2, citric acid, and $Gd(NO_3)_3{\cdot}6H_2O$ as starting materials. Table I gives the details of sample composition, sample code, and starting materials. In the typical synthesis, stoichiometric amounts of calcium nitrate, yttrium nitrate, aluminum nitrate, fumed silica, gadolinium nitrate, and citric acid (citric acid/metal ion = 2:1, molar ratio) were dissolved in 10 mL de-ionized water in a 150 mL glass beaker under stirring at 500 rpm for 1 h, to get a completely homogeneous solution.[48–52] The obtained aqueous solution was kept in an oven at 110°C to get the dried gel. Afterwards, the dried gel was sintered at 400°C for 2 h to evaporate the gaseous compounds. Finally, the resulting brown-color residual samples were crushed using mortar and pestle and annealed at 1100°C for 3 h for the crystallization of the prepared samples. After natural cooling of the sample to room temperature, ground samples were taken for characterization.

The XRD patterns of the samples were recorded by a RIGAKU Miniflex-II diffractometer. Cu-Kα radiation (λ = 1.5406 Å) was used as an x-ray source. The XRD patterns were taken with a scan rate of 5°/min in the 2θ range of 10°–80°. Morphology details were obtained by SEM (S-3400, Hitachi, Japan). PL measurements were carried out at room temperature by a Shimadzu RF-5301PC, spectrofluorophotometer equipped with Xenon flash lamp. The EPR spectra of the samples were recorded by a

Table I. Detailed information of sample composition, sample code and starting materials

Sample composition	Sample code	Starting materials				
$CaY_2Al_4SiO_{12}:Gd_{0.005}$	CYS1	Ca = 0.4722 g	Y = 0.7660 g	Al = 1.5 g	Si = 0.0600 g	C.A = 3.0736 g	Gd = 0.0022 g
$CaY_2Al_4SiO_{12}:Gd_{0.015}$	CYS2	Ca = 0.4722 g	Y = 0.7660 g	Al = 1.5 g	Si = 0.0600 g	C.A = 3.0736 g	Gd = 0.0067 g
$CaY_2Al_4SiO_{12}:Gd_{0.03}$	CYS3	Ca = 0.4722 g	Y = 0.7660 g	Al = 1.5 g	Si = 0.0600 g	C.A = 3.0736 g	Gd = 0.0135 g
$CaY_2Al_4SiO_{12}:Gd_{0.05}$	CYS4	Ca = 0.4722 g	Y = 0.7660 g	Al = 1.5 g	Si = 0.0600 g	C.A = 3.0736 g	Gd = 0.0225 g
$CaY_2Al_4SiO_{12}:Gd_{0.07}$	CYS5	Ca = 0.4722 g	Y = 0.7660 g	Al = 1.5 g	Si = 0.0600 g	C.A = 3.0736 g	Gd = 0.0315 g
$CaY_2Al_4SiO_{12}:Gd_{0.09}$	CYS6	Ca = 0.4722 g	Y = 0.7660 g	Al = 1.5 g	Si = 0.0600 g	C.A = 3.0736 g	Gd = 0.0406 g
$CaY_2Al_4SiO_{12}:Gd_{0.11}$	CYS7	Ca = 0.4722 g	Y = 0.7660 g	Al = 1.5 g	Si = 0.0600 g	C.A = 3.0736 g	Gd = 0.0496 g

Ca = $Ca(NO_3)_2{\cdot}4H_2O$, Y = $Y(NO_3)_3{\cdot}6H_2O$, Si = SiO_2, Al = $Al(NO_3)_3{\cdot}9H_2O$, C.A = Citric acid, Gd = $Gd(NO_3)_3{\cdot}6H_2O$.

JEOL FE1X ESR Spectrometer, operating in the X-band frequencies, with a field modulation of 100 kHz.

RESULTS AND DISCUSSION

X-ray Diffraction Studies

Figure 1 shows the XRD patterns of the sol–gel synthesized $CaY_2Al_4SiO_{12}:Gd^{3+}$ (CYS1–CYS7) garnet compound. The XRD patterns reveal the matching peaks of the experimentally observed data with the standard JCPDS data (JCPDS file no. 33-0040) of $Y_3Al_5O_{12}$ garnet. All the major peaks reveal the cubic structure of garnet with a *Ia3d* space group. The XRD pattern also reveals a few peaks of impurity indicated by (*), which might belong to $Ca_2Al_2SiO_7$, as reported in Ref. [14]. Figure 1 conspicuously shows that the XRD patterns for all of the prepared compounds are similar except for their intensity. This is probably because of the difference in ionic radii of Y^{3+} and Gd^{3+} ions. The ionic radius of Y^{3+} ions in eight coordination is 1.019 Å and that of Gd^{3+} and Ca^{2+} are 1.053 Å, and 1.120 Å, respectively. The Gd^{3+} ions are most likely to substitute for Y^{3+} ions as their ionic radii are in close proximity to each other. The XRD pattern shows that $CaY_2Al_4SiO_{12}$ doped with Gd^{3+} has been successfully synthesized by the sol–gel method. The full-width at half-maximum (FWHM) of the strongest diffraction peak is used to calculate the crystalline size by the well-known Scherrer equation: $D = 0.9\lambda/\beta\cos\theta$, where λ is the wavelength of incident x-ray, θ is the corresponding Bragg's diffraction angle, and β is the FWHM of the (420) peak.[53,54] The calculated crystallite sizes were found to be in the range of 25–39 nm.

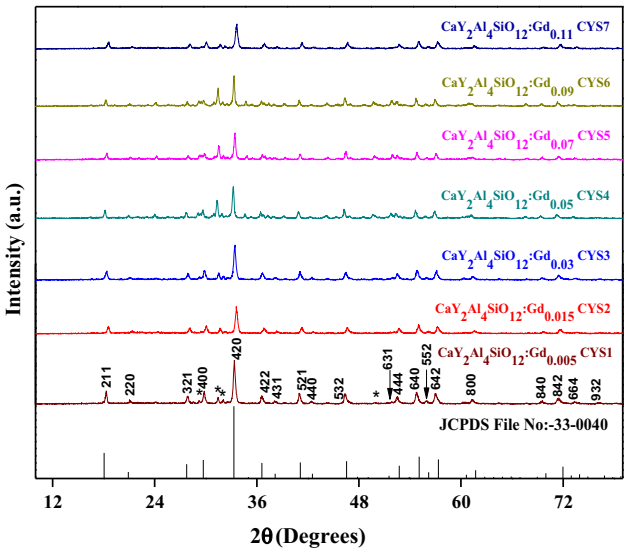

Fig. 1. Powder XRD patterns of $CaY_2Al_4SiO_{12}:Gd^{3+}$ (CYS1–CYS7) garnet compound.

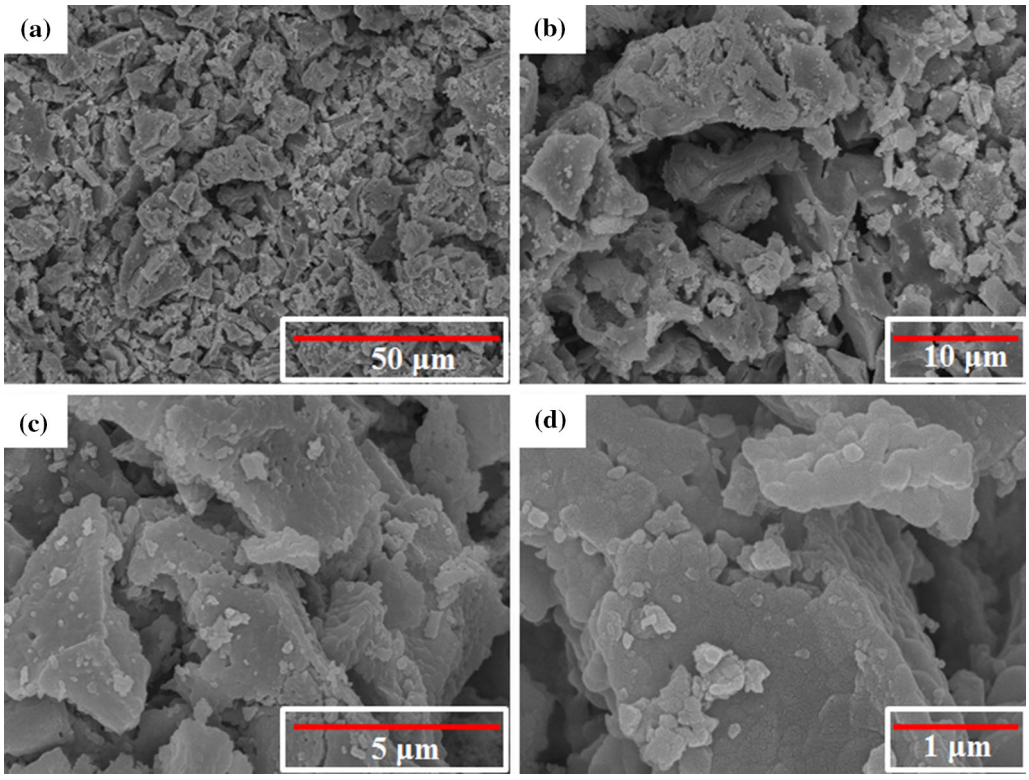

Fig. 2. SEM images of $CaY_2Al_4SiO_{12}:Gd_{0.09}$ (CYS6) garnet compound. (a) and (b) The irregular and inhomogeneous morphology of the agglomerated particles. (c) That the particle contains minor amounts of pores and voids. (d) The formation of smaller particles on the surface of larger particles.

SEM Studies

Figure 2a–d show the morphology of $CaY_2Al_4SiO_{12}:Gd_{0.09}$ (CYS6) that was inspected by taking SEM pictures. The SEM images in Fig. 2a and b show the irregular and inhomogeneous morphology of the agglomerated particles. The average particle size ranges from sub-micrometer to a few micrometers. The nonuniformity of the particle sizes can be attributed to the non-uniform distribution of the temperature during the sintering process. Figure 2c shows that the particle contains minor amounts of pores and voids. Figure 2d shows the formation of smaller particles on the surface of larger particles. The pores, voids, and small particles might be formed due to the escaping of a larger amount of gases molecules during the sintering process.

Photoluminescence Studies

Figure 3a shows the photoluminescence excitation spectra of the $CaY_2Al_4SiO_{12}:Gd^{3+}$ (CYS1–CYS7) compound for different concentrations of dopant ions (Gd^{3+}) under 314 nm emission wavelength. The excitation spectra exhibit excitation peaks due to f–f intra-configurational transitions at 244 nm, 246 nm, 253 nm, 273 nm, 276 nm, and 279 nm, and are attributed to transitions from $^8S_{7/2}$ to $^6D_{5/2,\ 3/2}$, $^6D_{7/2}$, $^6D_{9/2}$, $^6I_{11/2}$, $^6I_{9/2,\ 17/2}$, and $^6I_{7/2}$, respectively.[41,55] A narrow band has been observed at 274 nm in the $Zn_{1-y}B_2O_4:Gd^{3+}$ compound reported elsewhere.[56] Two excitation peaks in the UV region, one major excitation peak at 274 nm and another minor peak at 245 nm have also been reported in the $K_3Gd(PO_4)_2$ compound.[57] In other reported work, the excitation bands have been observed at 246 nm, 252 nm, 274 nm, and 278 nm in the $BaB_8O_{13}:Gd^{3+}$ compound.[58] Among these excitation peaks, the peak at 273 nm is highly intense, which demonstrates the prime absorption of incident radiation in the UV region. Figure 3b shows the emission spectra of $CaY_2Al_4SiO_{12}:Gd^{3+}$ samples under the excitation wavelength at 273 nm. The emission spectra of the $CaY_2Al_4SiO_{12}:Gd^{3+}$ compound exhibit two emission peaks at 308 nm and 314 nm, attributed to $^6P_{5/2} \rightarrow {}^8S_{7/2}$ and $^6P_{7/2} \rightarrow {}^8S_{7/2}$ transitions, respectively, as shown in Fig. 3b.[59,60] The emission peak at 308 nm is very low in intensity, whereas the peak at 314 nm is highly intense corresponding to the $^6P_{7/2} \rightarrow {}^8S_{7/2}$ electronic transition, which is desired to cure various skin disorders, and hence beneficial in phototherapy. The luminescence properties of Gd^{3+} ions in $LaAlGe_2O_7$ have been studied, and there was observed a major emission peak of Gd^{3+} in $LaAlGe_2O_7$ at 312 nm, which corresponds to the transition $^6P_J \rightarrow {}^8S_{7/2}$.[61] In the $Gd_2Zr_2O_7$ compound, two emission bands were observed at 307 nm and 313 nm in the emission spectrum under 273 nm excitation.[62] A weak emission peak at

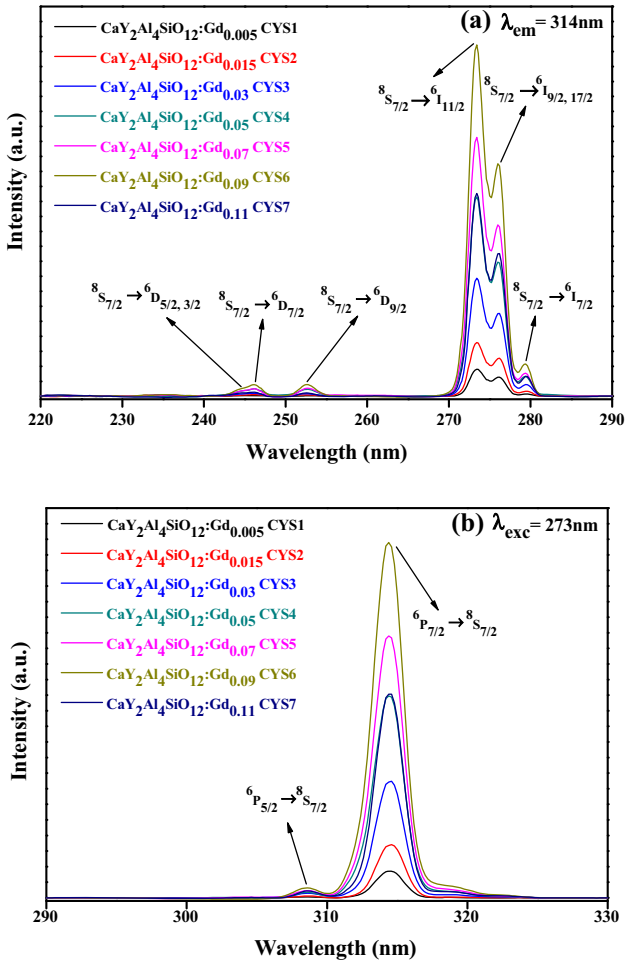

Fig. 3. Photoluminescence spectra of $CaY_2Al_4SiO_{12}:Gd^{3+}$ garnet compound (a) excitation spectrum of $CaY_2Al_4SiO_{12}:Gd^{3+}$ (λ_{em} = 314 nm) and (b) emission spectrum of $CaY_2Al_4SiO_{12}:Gd^{3+}$ (λ_{exc} = 273 nm).

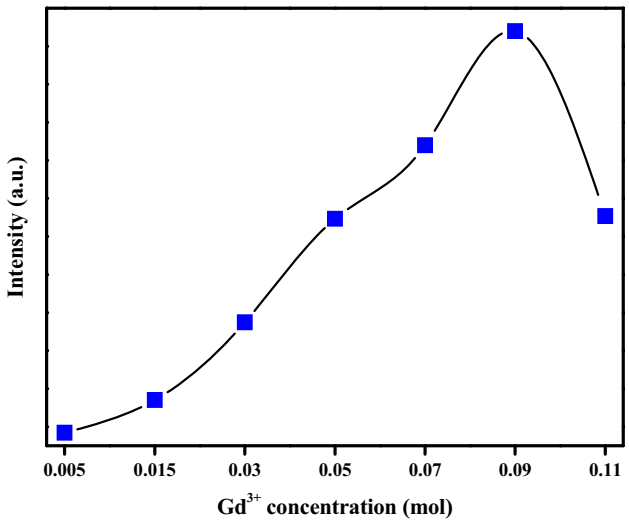

Fig. 4. Variation in the emission intensity of strong emission (314 nm) as a function of Gd^{3+} concentration.

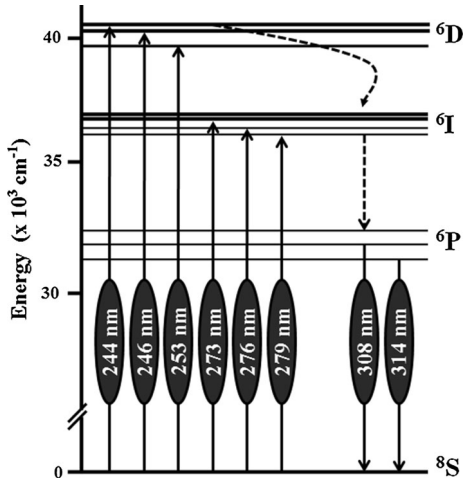

Fig. 5. Energy level diagram of Gd^{3+} ions.

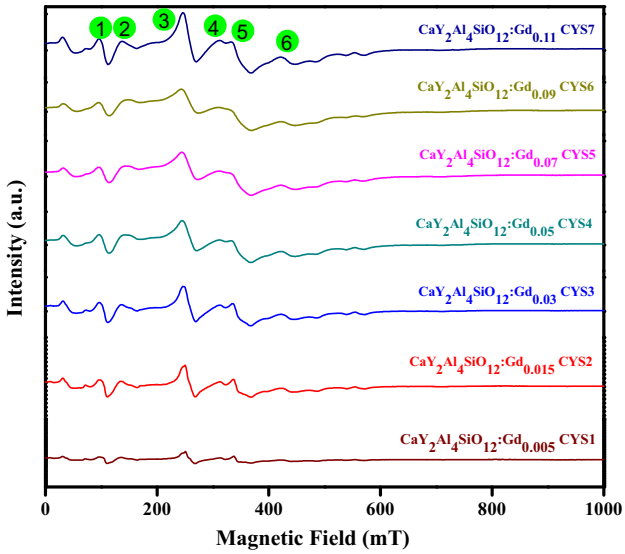

Fig. 6. EPR spectra of $CaY_2Al_4SiO_{12}:Gd^{3+}$ (CYS1–CYS7) garnet compound.

306.6 nm, followed by a strong emission peak at 312.5 nm in the $La_2Zr_2O_7:Gd^{3+}$ compound are also reported elsewhere.[63] Moreover, the emission spectra for all the garnet compounds show resemblance in their peak profile, except for their emission intensity. The emission intensity of $CaY_2Al_4SiO_{12}:Gd^{3+}$ compound initially rises for varying concentrations (0.005–0.09) mol of Gd^{3+} ions, and beyond, the intensity of emission declines. The reduction in the intensity of emission, beyond a certain concentration of dopant ions in the host is due to concentration quenching. The phenomenon of luminescence quenching at higher concentration of dopant ions is attributed to the reduction of space between the nearest luminescent centers, which thereby increase the possibility of non-radiative

energy transfer.[64,65] Figure 4 plots the emission intensity of $CaY_2Al_4SiO_{12}:Gd^{3+}$ compound versus the concentration of Gd^{3+} ions. The optimized concentration of Gd^{3+} ions in $CaY_2Al_4SiO_{12}$ is found to be 0.09 mol. Hence, $CaY_2Al_4SiO_{12}$ compound with 0.09 mol of Gd^{3+} ions is efficient for its applications in phototherapy lamps. Figure 5 shows the energy-level diagram of the Gd^{3+} ion, which shows the possible transitions that are involved in the process. The energy level diagram shows the Gd^{3+} ions were excited from ground state $^8S_{7/2}$ to the upper states ^6D_J and ^6I_J. Afterward, the electrons of the Gd^{3+} non-radiatively decayed through the multiphonon relaxations up to the ^6P_J level and finally, relaxed radiatively to $^8S_{7/2}$ state, giving rise to the emission in the NB-UVB at 314 nm.

Electron Paramagnetic Resonance Studies

Figure 6 shows the EPR spectra of $CaY_2Al_4SiO_{12}:Gd^{3+}$ (CYS1–CYS7) garnet compound. It is well known that when doped in a host matrix, Gd^{3+} ions impose their own environment. In general, Gd^{3+} ions are characterized by a fully spin-polarized half-filled 4f-shell. The ground state of Gd^{3+} ion is $^8S_{7/2}$ with $L = 0$, which indicates zero orbital magnetic moments with a spherically symmetric charge cloud. The spin–orbit interaction instigates splitting of the ground state, resulting in crystal field effects, and induces resonance signals due to the variation in local symmetry of the ion. The spin relaxation time is long and therefore the EPR spectra are observable in crystalline material. In crystalline materials, crystal field interaction is experienced by a probe ion due to the disordered arrangement in the occupancy of certain available sites. Under such circumstances, the crystalline material may exhibit EPR spectra similar to that of a glassy material.[66] The resonance spectra exhibit resonance signals due to the presence of Gd^{3+} ions in the host with effective g values at $g \approx (6.5, 5.0, 2.6, 2.2, 2.0,$ and $1.6)$ of the U-spectrum for the resonance signals marked as (1, 2, 3, 4, 5, and 6), respectively, in Fig. 6. The effective g values ($g \approx 6.5$, 2.6, and 2.0) are attributed to cubic, octahedral, and tetrahedral distorted sites. In these sites, Gd^{3+} ions are supposed to have the coordination of more than six, having a weak crystal field. In such sites, Gd^{3+} ions coordinate more with non-bridging oxygen, and thereby decrease the number of Gd^{3+} ions. The effective g value of 5.0 is assigned to the vitreous disordered polycrystalline structure in sites of a strong crystal field with lower coordination.[67,68] The $g \approx 2.0$ reveals the presence of paramagnetic ions in a weak ligand field, while $g > 2.0$ reveals the presence of paramagnetic ions in a strong ligand field. The resonance signal at $g \approx 2.2$ arises due to the large separation between two Kramers doublets.[69,70] Moreover, with an increase in Gd^{3+} ions concentration, the EPR spectra show insignificant variation in intensity.

CONCLUSIONS

A series of Gd^{3+} activated $CaY_2Al_4SiO_{12}$ garnet compounds have been successfully prepared by a sol–gel method. All of the synthesized garnet compounds show a cubic structure, where Gd^{3+} ions do not influence the crystal structure of the host lattice ($CaY_2Al_4SiO_{12}$). The irregular agglomerated morphology of the particles with denser distribution is observed from SEM micrographs. The PL spectra of Gd^{3+}-activated $CaY_2Al_4SiO_{12}$ garnet compound exhibit UV emission peaks at 314 nm, under 273 nm excitation. The optimized concentration of Gd^{3+} ions is observed as 0.09 mol. The EPR studies reveal several resonance signals with effective g values at (6.5, 5.0, 2.6, 2.2, 2.0, and 1.6) that exhibit weak, intermediate, and strong cubic symmetry fields. The aforementioned studies potentiate the use of Gd^{3+}-activated $CaY_2Al_4SiO_{12}$ garnet compound in phototherapy lamps.

ACKNOWLEDGMENTS

This work was supported by the National Research Foundation of Korea (NRF) Grant funded by the Korea Government (MSIT) (2018M2B2A9 065656).

REFERENCES

1. Z. Jiang, J. Gou, Y. Min, C. Huang, W. Lv, X. Yu, X. Su, and L. Duan, *J. Alloys Compd.* 727, 63 (2017).
2. P. Haritha, C.S. Dwaraka Viswanath, K. Linganna, P. Babu, C.K. Jayashankar, V. Lavin, and V. Venkatramu, *J. Lumin.* 179, 533 (2016).
3. A.A. Trofimov, C. Li, K.S. Brinkman, and L.G. Jacobsohn, *Opt. Mater.* 68, 7 (2017).
4. B. Malysa, A. Meijerink, and T. Jüstel, *J. Lumin.* 202, 523 (2018).
5. J. Wang, F. Xu, R.J. Wheatley, N. Neate, and X. Hou, *Ceram. Int.* 42, 14228 (2016).
6. S. Ramakumar, C. Deviannapoorani, L. Dhivya, L.S. Shankar, and R. Murugan, *Prog. Mater Sci.* 88, 325 (2017).
7. K. Hofstetter, A. Junio Samson, S. Narayanan, and V. Thangadurai, *J. Power Sources* 390, 297 (2018).
8. P. Loiko, N. Khaidukov, A. Volokitina, I. Zhidkova, E. Vilejshikova, A. Novichkov, V. Aseev, J.M. Serres, X. Mateos, and K. Yumashev, *Dyes Pigments* 150, 158 (2018).
9. K. Asami, J. Ueda, M. Kitaura, and S. Tanabe, *J. Lumin.* 198, 418 (2018).
10. M.S. Bhagat, K.N. Shinde, N. Singh, M.S. Pathak, P.K. Singh, S.U. Pawar, and V. Singh, *Optik* 161, 111 (2018).
11. K. Sawada, T. Nakamura, and S. Adachi, *Ceram. Int.* 43, 14225 (2017).
12. S. Zhang, P. Zhang, X. Liu, Z. Yang, Y. Huang, and H.J. Seo, *J. Lumin.* 203, 152 (2018).
13. Z. Pan, W. Li, Y. Xu, Q. Hu, and Y. Zheng, *RSC Adv.* 6, 20458 (2016).
14. A. Katelnikovas, S. Sakirzanovas, D. Dutczak, J. Plewa, D. Enseling, H. Winkler, A. Kareiva, and T. Jüstel, *J. Lumin.* 136, 17 (2013).
15. H. Ji, L. Wang, Y. Cho, N. Hirosaki, M.S. Molokeev, Z. Xia, Z. Huang, and R.-J. Xie, *J. Mater. Chem. C* 4, 9872 (2016).
16. Z. Pan, J. Chen, H. Wu, and W. Li, *Opt. Mater.* 72, 257 (2017).
17. R. Singh and H.S. Nalwa, *J. Biomed. Nanotechnol.* 7, 489 (2011).
18. B.L. Diffey and J. Robson, *J. Soc. Cosmet. Chem.* 40, 127 (1989).

19. C. Stevens, V.A. Khan, J.Y. Lu, C.L. Wilson, P.L. Pusey, M.K. Kabwe, E.C.K. Lgwegbe, E. Chalutz, and S. Droby, *Crop Prot.* 17, 75 (1998).
20. J.G. Goodberlet, *Appl. Phys. Lett.* 76, 667 (2000).
21. D. Costa, A.M. Galvão, R.E. Di Paolo, A.A. Freitas, J.C. Lima, F.H. Quina, and A.L. Maçanita, *Tetrahedron* 71, 3157 (2015).
22. A.R. Young, J. Claveau, and A.B. Rossi, *J. Am. Acad. Dermatol.* 76, S100 (2017).
23. S. Tamboli and S.J. Dhoble, *Spectrochim. Acta A Mol. Biomol. Spectrosc.* 184, 119 (2017).
24. W. Zeng, S. Wu, J. Wen, and Z. Chen, *Constr. Build. Mater.* 93, 1125 (2015).
25. M.F. Holick, *Anticancer Res.* 36, 1345 (2016).
26. M.Yu. Glyavin, S.V. Golubev, I.V. Izotov, A.G. Litvak, A.G. Luchinin, S.V. Razin, A.V. Sidorov, V.A. Skalyga, and A.V. Vodopyanov, *Appl. Phys. Lett.* 10, 174101 (2014).
27. B.R. Halls, P.S. Hsu, N. Jiang, E.S. Legge, J.J. Felver, M.N. Slipchenko, S. Roy, T.R. Meyer, and J.R. Gord, *Optica* 4, 897 (2017).
28. S. Dogra and A.J. Kanwar, *Indian J. Dermatol. Venereol. Leprol.* 70, 205 (2004).
29. A.B. Gawande, R.P. Sonekar, and S.K. Omanwar, *Optik* 127, 3925 (2016).
30. D.S. Thakare, S.K. Omanwar, P.L. Muthal, S.M. Dhopte, V.K. Kondawar, and S.V. Moharil, *Phys. Stat. Sol. A* 201, 574 (2004).
31. M. Runowski and S. Lis, *J. Alloys Compd.* 661, 182 (2016).
32. B. Fan, S. Qi, W. Zhao, S. Li, and S. An, *J. Lumin.* 196, 520 (2018).
33. S.K. Omanwar, S.R. Jaiswal, N.S. Sawala, K.A. Koparkar, and V.B. Bhatkar, *Mater. Discov.* 7, 15 (2017).
34. T. Jiang, Y. Liu, S. Liu, N. Liu, and W. Qin, *J. Colloid Interface Sci.* 377, 81 (2012).
35. P. Sharma, S.C. Brown, G. Walter, S. Santra, E. Scott, H. Ichikawa, Y. Fukumori, and B.M. Moudgil, *Adv. Powder Technol.* 18, 663 (2007).
36. M. Song, L. Wang, Y. Feng, H. Wang, X. Wang, and D. Li, *Opt. Mater.* 84, 284 (2018).
37. V. Singh, G. Sivaramaiah, J.L. Rao, and S.H. Kim, *J. Electron. Mater.* 43, 3486 (2014).
38. V. Singh, N. Singh, M.S. Pathak, H. Jeong, S. Wantanabe, T.K. Gundu Rao, V. Dubey, and V.K. Rai, *J. Mater. Sci.: Mater. Electron.* 29, 3006 (2018).
39. V. Singh, G. Sivaramaiah, J.L. Rao, S.J. Dhoble, and S.H. Kim, *Mater. Chem. Phys.* 149–150, 202 (2015).
40. V. Singh, R.P.S. Chakradhar, J.L. Rao, and S.H. Kim, *J. Lumin.* 154, 328 (2014).
41. V. Singh, S. Borkotoky, A. Murali, J.L. Rao, T.K. Gundu Rao, and S.J. Dhoble, *Spectrochim. Acta A Mol. Biomol. Spectrosc.* 139, 1 (2015).
42. V. Singh, G. Sivaramaiah, J.L. Rao, S. Watanabe, T.K. Gundu Rao, S.S. Jagtap, and P.K. Singh, *J. Alloys Compd.* 648, 1083 (2015).
43. V. Singh, G. Sivaramaiah, N. Singh, M.S. Pathak, J.L. Rao, H.D. Jirimali, and V. Natarajan, *Optik* 169, 397 (2018).
44. A.O. Chauhan, A.B. Gawande, and S.K. Omanwar, *Optik* 127, 6647 (2016).
45. V. Gorbenko, T. Zorenko, S. Witkiewicz, K. Paprocki, A. Iskaliyeva, A.M. Kaczmarek, R. Van Deun, M.N. Khaidukov, M. Batentschuk, and Y. Zorenko, *J. Lumin.* 199, 245 (2018).
46. A.A. Setlur, W.J. Heward, Y. Gao, A.M. Srivastava, R. Gopi Chandran, and M.V. Shankar, *Chem. Mater.* 18, 3314 (2006).
47. N. Khaidukov, T. Zorenko, A. Iskaliyeva, K. Paprocki, K. Paprocki, M. Batentschuk, A. Osvet, R. Van Deun, Y. Zhydaczevskii, A. Suchocki, and Y. Zorenko, *J. Lumin.* 192, 328 (2017).
48. K. Sadhana, S.R. Murthy, and K. Praveena, *Mater. Sci. Semicond. Process.* 34, 305 (2015).
49. K. Sadhana, S.R. Murthy, and K. Praveena, *J. Mater. Sci.: Mater. Electron.* 25, 5130 (2014).
50. K. Praveena, K. Sadhana, S. Srinath, and S.R. Murthy, *Mater. Res. Innov.* 18, 69 (2014).
51. K. Sadhana, S.E.N. Vinodini, R. Sandhya, and K. Praveena, *Adv. Mater. Lett.* 6, 717 (2015).
52. K. Praveena, S. Matteppanavar, H.-L. Liu, and K. Sadhana, *J. Mater. Sci.: Mater. Electron.* 28, 4179 (2017).
53. A. Patterson, *Phys. Rev.* 56, 978 (1939).
54. S. Kaur, M. Jayasimhadri, and A.S. Rao, *J. Alloys Compd.* 697, 367 (2017).
55. V. Singh, G. Sivaramaiah, J.L. Rao, and S.H. Kim, *J. Lumin.* 143, 162 (2013).
56. Z. Mu, Y. Hu, L. Chen, X. Wang, R. Chen, T. Wang, Y. Fu, and J. Xu, *Displays* 35, 147 (2014).
57. P. Gupta, A.K. Bedyal, V. Kumar, Y. Khajuria, V. Sharma, O.M. Ntwaeaborwa, and H.C. Swart, *Mater. Res. Express* 2, 076202 (2015).
58. S. Tamboli, G.B. Nair, S.J. Dhoble, and D.K. Burghate, *Phys. B* 535, 232 (2018).
59. H. Jeong, N. Singh, M.S. Pathak, S. Watanabe, T.K.G. Rao, V. Dubey, and V. Singh, *Optik* 157, 1199 (2018).
60. M.S. Pathak, N. Singh, V. Singh, S. Watanbe, T.K. Gundu Rao, and J.K. Lee, *Mater. Res. Bull.* 97, 512 (2018).
61. Y.-C. Li, Y.-H. Chang, Y.-S. Chang, Y.-J. Lin, and C.-H. Laing, *J. Phys. Chem. C* 111, 10682 (2007).
62. V. Singh, G. Sivaramaiah, J.L. Rao, and S.H. Kim, *Phys. B* 416, 101 (2013).
63. V. Singh, G. Sivaramaiah, J.L. Rao, R.S. Kumaran, P.K. Singh, T.-S. Kim, and L.K. Kim, *J. Mater. Sci.: Mater. Electron.* 26, 5195 (2015).
64. A.K. Vishwakarma and M. Jayasimhadri, *J. Lumin.* 176, 112 (2016).
65. B.V. Ratnam, M.K. Sahu, A.K. Vishwakarma, K. Jha, H. Woo, K. Jang, and M. Jayasimhadri, *J. Lumin.* 185, 99 (2017).
66. L.E. Iton, C.M. Brodbeck, S.L. Suib, and G.D. Stucky, *J. Chem. Phys.* 79, 1185 (1983).
67. E. Culea, L. Pop, and S. Simon, *Mater. Sci. Eng., B* 112, 59 (2004).
68. K. Srinivasulu, I. Omkaram, H. Obeid, A.S. Kumar, and J.L. Rao, *J. Mol. Struct.* 1036, 63 (2013).
69. V. Singh, G. Sivaramaiah, J.L. Rao, and S.H. Kim, *J. Lumin.* 157, 82 (2015).
70. V. Singh, G. Sivaramaiah, J.L. Rao, and S.H. Kim, *Mater. Res. Bull.* 60, 397 (2014).

Publisher's Note Springer Nature remains neutral with regard to jurisdictional claims in published maps and institutional affiliations.

This article has been accepted for publication in a future issue of this journal, but has not been fully edited. Content may change prior to final publication. Citation information: DOI 10.1109/TPEL.2019.2912265, IEEE Transactions on Power Electronics

An Improved Nonlinear Flux Observer based Sensorless FOC IM Drive with Adaptive Predictive Current Control

Ambrish Devanshu*, Madhusudan Singh, Senior Member, *IEEE* and Narendra Kumar Senior Member, *IEEE*
ambrish.devanshu@gmail.com*, madhusudan@dce.ac.in, ndeshwalus@gmail.com
Electrical Engineering Department, Delhi Technological University, Delhi, India

***Abstract*- This paper presents a novel adaptive predictive current controller (PCC) with improved flux estimator for a sensorless direct field oriented control (DFOC) induction motor (IM) drive. Classical PCC performance depends on the stator resistance of the motor which varies with temperature. In the proposed method a discrete stator resistance estimator is developed to increase the robustness of the system towards stator resistance variations. An improved nonlinear discrete stator flux estimator is also developed to replace the pure integrator which reduces the initial value and dc offset problems. Sensorless operation of IM drive has advantages of reduced overall cost and increased reliability of motor operation. Dynamic and steady state performances of the IM under different operating conditions are analysed in MATLAB/Simulink as well as experimentally using dSPACE1104 controller and have been compared with conventional PCC. The simulation results of the classical and proposed methods are also validated experimentally. Smooth starting, reduced oscillations in speed and flux at low speed operation, fast speed and torque dynamics, robust operation of drive against load and variation in stator resistance, fast and smooth speed reversal are the main advantages of the proposed method over classical PCC based DFOC IM drive.**

I. INTRODUCTION

The IM is widely used in industry due to its low cost, less maintenance, and rugged construction. With the advancement in the different control techniques of the IM, several current-regulation methods have been developed for control of voltage source inverter (VSI) fed IM drives. These advance control methods of the IM can provide high performance, high accuracy, fast dynamic response and excellent tracking ability of the drive. The different current regulation techniques such as Hysteresis Control, Linear Pulse Width Modulator (PWM), Predictive Control, Sliding Mode Control, Delta and Sigma Delta Modulation, Neural Networks, Fuzzy Logic and Neuro-Fuzzy Controls can be used to minimize the current ripple and improve the performance of the IM drives [1]. Recent evolution in the digital electronics and availability of faster and more powerful processors with the high computational speed, predictive current control has emerged as a powerful current control method which provide switching signals to solid state switches in VSI based on optimized algorithm and cost function [1], [8]. Generalized predictive control (GPC) technique has been applied to current source inverter (CSI) for the regulation of the current to the resistive inductive (RL) circuit model of the IM [2]. The GPC is developed in synchronously rotating reference frame and play useful role in the control of stator current of the IM [3]. Based on the electromotive force concept, current controller has been developed which require one period prediction and delay introduced by the measurement. It is reported that this control technique is more affected by the variations in load inductances than the rotor and stator resistances [4], [5]. A PCC based on space vector modulation is proposed using discrete motor modelling [6]. The performance of the PCC method proposed in [7] is being compared with PWM and hysteresis current controller (HCC). In this method, for all the value of voltage vectors, predicted value of load current is generated by the inverter. Long range model based PCC is designed for an input-output linearized IM [9]. However, modelling of the inverter is not taken into account in the conventional FOC. Whereas, state of the inverter is defined as discrete control variable when PCC strategy is used. Flux and time constant of the rotor is estimated using reduced order extended high gain observer [10]. An improved version of PCC is proposed [11] which considers a control technique of neutral point potential and optimized description of inverter switching transitions. This approach enables fast motor current control while maintaining a low switching and excluding excitation of the filter resonance. The FOC of five phase IM is discussed for the verification of the model predictive control to achieve ripple free stator current and fast current response [12]. It has been observed that predictive control method offers faster torque and current response than PI controllers [13] with SVPWM techniques for multiphase drives. However, PCC technique is implemented for speed sensorless FOC IM drive system along with SVPWM to ensure fixed switching frequency [14].

The bandwidth of the traditional current controller with PI regulator is limited by the switching frequency and this limitation is removed by the PCC in sensorless FOC system [15]. For managing post fault operation of multiphase drives, PCC is being proposed [16]. An improved current control in IM, robust PCC is implemented based on polytopic uncertainties and linear matrix inequalities. Offline multi-parametric semidefinite programming and quadratic search tree is applied for the current control resulting into significantly suppressed overshooting [17]. The dynamic performance of the current loop is also improved using robust PCC combined with a speed adaptive full order observer [18].

The classical PCC has drawbacks of large torque and flux ripple, large THDs in voltages and currents and dependency

0885-8993 (c) 2018 IEEE. Personal use is permitted, but republication/redistribution requires IEEE permission. See http://www.ieee.org/publications_standards/publications/rights/index.html for more information.

This article has been accepted for publication in a future issue of this journal, but has not been fully edited. Content may change prior to final publication. Citation information: DOI 10.1109/TPEL.2019.2912265, IEEE Transactions on Power Electronics

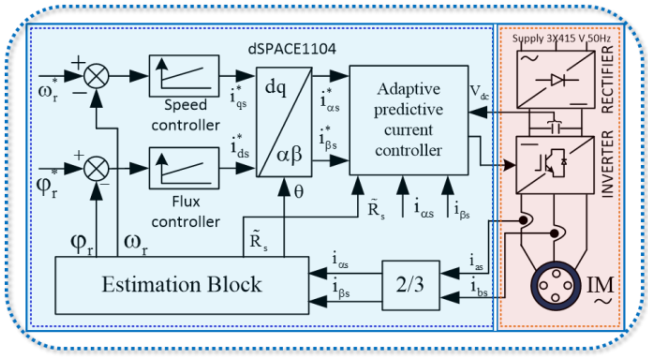

Fig. 1a Block diagram of proposed DFOC IM drive

on the motor parameter such as stator resistance. Slip speed of the IM drive also depends on the rotor time constant of the motor. The rotor and stator resistance are important parameters of IM whose variations may lead to improper performance of the PCC and improper estimation of speed over the wide operating range in sensorless drives [25].

An adaptive PCC is implemented in this paper and stator resistance is estimated to overcome the uncertainty due to the stator resistance variations. The rotor time constant is also estimated using Popov's stability criteria as slip speed depends on this parameter of the motor. For the correct estimation of the parameters and high performance of the drive, accurate information of the fluxes are also needed. Additionally, in the stator voltage model of the flux estimation, an integrator is being used in the majority of the work reported in the literature [19]-[22]. However, existing dc drift in the system and initial value of the pure integrator will cause integrator to saturate resulting into distorted estimated flux. Thus, an improved nonlinear discrete stator flux estimator is also proposed to replace the pure integrator to reduce the dc offset and initial value problem. The sensorless DFOC IM drive with non-linear flux observer and adaptive predictive current controller is analysed in MATLAB/ Simulink as shown in Fig. 1a. A complete experimental setup of DFOC IM drive with estimators is implemented in the laboratory using dSPACE 1104 controller. The simulation and experimental results are discussed for sensorless speed control of IM to validate the effectiveness of the proposed estimation and control algorithms. A comparison of the IM drive performance with conventional PCC and proposed PCC method show that the proposed method can effectively improve the overall performance of the drive.

In this paper, the major contributions on DFOC IM drive by the authors are as follows:

- Performance of the system for direct field oriented controlled IM drive is analysed. An adaptive PCC is developed for more robust performance of the DFOC IM motor drive.
- Discrete stator resistance estimator is established for the controller to adapt for changes in stator resistance of the IM. The rotor time constant of the motor is also calculated using Popov's stability criteria.
- A discrete non-linear stator and rotor flux observer is developed to mitigate the effect of the existing dc offset problem in the system due to inverter nonlinearity, current measurement, biasing in sensors, operational amplifier, A/D converter, variations in stator resistance, and unknown integral initial conditions at the starting of the drive.
- Mechanical sensorless technique with proposed stationary discrete non-linear flux observer is developed to minimize the cost of the system.

II. MATHEMATICAL MODELLING OF IM

Dynamic modelling of the IM in stationary reference frame is described by the following state equations:

$$\dot{x} = Ax + Bu \qquad (1)$$
$$y = Cx$$

Where,

$$A = \begin{bmatrix} -\left(\frac{L_m^2}{\sigma L_s L_r \tau_r} + \frac{R_s}{\sigma L_s}\right) & 0 & \frac{L_m}{\sigma L_s L_r \tau_r} & \frac{L_m \omega_r}{\sigma L_s L_r} \\ 0 & -\left(\frac{L_m^2}{\sigma L_s L_r \tau_r} + \frac{R_s}{\sigma L_s}\right) & \frac{L_m \omega_r}{\sigma L_s L_r} & \frac{L_m}{\sigma L_s L_r \tau_r} \\ \frac{L_m}{\tau_r} & 0 & -\frac{1}{\tau_r} & -\omega_r \\ 0 & \frac{L_m}{\tau_r} & -\omega_r & \frac{1}{\tau_r} \end{bmatrix}$$

$$B = \begin{bmatrix} \frac{1}{\sigma L_s} & 0 & 0 & 0 \\ 0 & \frac{1}{\sigma L_s} & 0 & 0 \end{bmatrix} \quad C = \begin{bmatrix} 1 & 0 & 0 & 0 \\ 0 & 1 & 0 & 0 \end{bmatrix}$$

$$x = \begin{bmatrix} i_{\alpha s} & i_{\beta s} & \varphi_{\alpha r} & \varphi_{\beta r} \end{bmatrix}^T, \quad u = \begin{bmatrix} u_{\alpha s} & u_{\beta s} & 0 & 0 \end{bmatrix}^T$$

$$\omega_r = 1/J \int (T_e - T_L) dt \qquad (2)$$

$$Te = \frac{3PL_m}{4L_r}\left(i_{\beta s}\varphi_{\alpha r} - i_{\alpha s}\varphi_{\beta r}\right) \qquad (3)$$

Where R_s is stator resistance per phase, L_m is magnetizing inductance per phase, R_r is rotor resistance per phase, L_r is rotor inductance per phase, L_s = stator inductance per phase, L_m is magnetizing inductance per phase, P is number of poles, ω_r is rotor electrical angular speed, J is the moment of inertia of rotor, T_e is the electromagnetic torque, T_l is the external load torque, $u_{\beta s}$ ($u_{\alpha s}$) is β -axis (α -axis) stator voltage, $i_{\beta s}$ ($i_{\alpha s}$) is β -axis (α -axis) stator current, $\varphi_{\beta r}$ ($\varphi_{\alpha r}$) is β -axis (α -axis) rotor flux, and $\sigma = 1 - \left(L_m^2 / L_r L_s\right)$.

0885-8993 (c) 2018 IEEE. Personal use is permitted, but republication/redistribution requires IEEE permission. See http://www.ieee.org/publications_standards/publications/rights/index.html for more information.

This article has been accepted for publication in a future issue of this journal, but has not been fully edited. Content may change prior to final publication. Citation information: DOI 10.1109/TPEL.2019.2912265, IEEE Transactions on Power Electronics

III. DIRECT FIELD ORIENTED CONTROL OF IM DRIVE

Field oriented control of IM is implemented by independent control of field flux component and the torque component of the stator current. The torque component of the stator current is in the quadrature of the rotor flux and flux component of the current is oriented in phase of it. Following equations are used for the implementation of DFOC IM drive:

Motor stator terminal voltages and currents are sensed and fluxes are computed in stationary reference frame as follows

$$\begin{bmatrix} u_{\alpha s} \\ u_{\beta s} \end{bmatrix} = \begin{bmatrix} \frac{2}{3} & -\frac{1}{3} & \frac{1}{3} \\ 0 & \frac{2}{\sqrt{3}} & -\frac{2}{\sqrt{3}} \end{bmatrix} \begin{bmatrix} u_{as} \\ u_{bs} \\ u_{cs} \end{bmatrix}, \quad (4)$$

$$\begin{bmatrix} i_{\alpha s} \\ i_{\beta s} \end{bmatrix} = \begin{bmatrix} \frac{2}{3} & -\frac{1}{3} & \frac{1}{3} \\ 0 & \frac{2}{\sqrt{3}} & -\frac{2}{\sqrt{3}} \end{bmatrix} \begin{bmatrix} i_{as} \\ i_{bs} \\ i_{cs} \end{bmatrix}$$

Where, u_{as}, u_{bs}, u_{cs} are stator three phase terminal voltage and i_{as}, i_{bs}, i_{cs} are stator line currents.

Stator flux equations of IM are written as follows:

$$\varphi_{\alpha s} = \int \left(u_{\alpha s} - i_{\alpha s} R_s\right) dt, \ \varphi_{\beta s} = \int \left(u_{\beta s} - i_{\beta s} R_s\right) dt \quad (5)$$

$$\varphi_{\alpha s} = L_s i_{\alpha s} + L_m i_{\alpha r}, \ \varphi_{\beta s} = L_s i_{\beta s} + L_m i_{\beta r} \quad (6)$$

Resultant stator flux φ_s and phase angle θ_s between $\varphi_{\alpha s}$ and $\varphi_{\beta s}$ can be evaluated as follows:

$$\varphi_s = \sqrt{\varphi_{\alpha s}^2 + \varphi_{\beta s}^2}, \ \theta_s = \tan^{-1}\left(\varphi_{\beta s} / \varphi_{\alpha s}\right) \quad (7)$$

Rotor currents are determined as follows:

$$i_{\alpha r} = \frac{1}{L_m}\left(\int \left(u_{\alpha s} - i_{\alpha s} R_s\right) dt - L_s i_{\alpha s}\right),$$
$$i_{\beta r} = \frac{1}{L_m}\left(\int \left(u_{\beta s} - i_{\beta s} R_s\right) dt - L_s i_{\beta s}\right) \quad (8)$$

Therefore, rotor flux is evaluated as follows

$$\varphi_{\alpha r} = L_r i_{\alpha r} + L_m i_{\alpha s}, \ \varphi_{\beta r} = L_r i_{\beta r} + L_m i_{\beta s}, \quad (9)$$

$$\varphi_r = \sqrt{\varphi_{\alpha r}^2 + \varphi_{\beta r}^2} \quad (9.1)$$

$$\theta_r = \tan^{-1}\left(\varphi_{\beta r} / \varphi_{\alpha r}\right)$$

IV. FLUX EXSTIMATION USING MODIFIED INTEGRATION

The high performance motor drives such as field oriented control, direct torque control and feedback linearization control of AC drives require an accurate estimation of flux. Estimation of flux is usually implemented using two existing methods namely voltage model and current model. The voltage model for stator flux estimation is being considered in this work. Estimation of stator flux using voltage model requires pure integrator, which creates drift signal component caused by the inverter problems [20], [21]. To eliminate the drawbacks of a

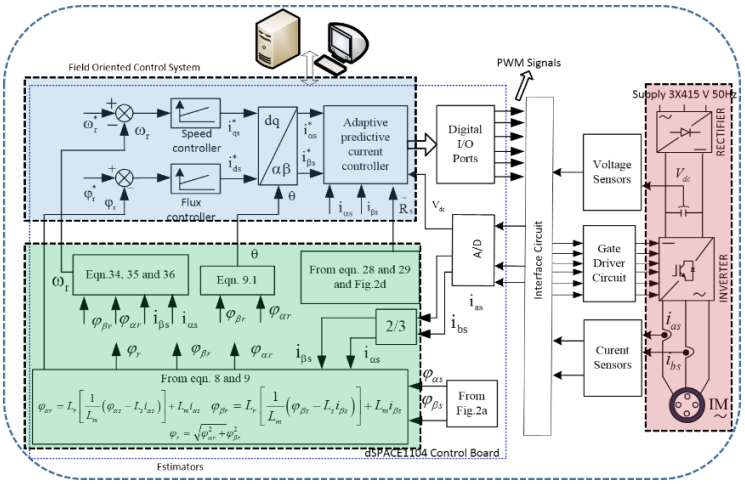

Fig. 1b Simulation and experimental schematic diagram of proposed method with estimators

pure integrator in voltage model based stator flux estimation, a low pass filter with feedback compensation integration algorithm is implemented as shown in Fig.2a-b. The stator flux estimated using modified integration is described as follows

$$\varphi_s = e_s \frac{1}{s+\omega_c} + \varphi_s^L \frac{\omega_c}{s+\omega_c}, \ \varphi_s = \varphi_s^F + \varphi_s^C \quad (10)$$

$$\text{Where, } \varphi_s^F = e_s \frac{1}{s+\omega_c} \text{ and } \varphi_s^C = \varphi_s \frac{\omega_c}{s+\omega_c} \quad (11)$$

First part of the eqn. (10) is a low pass filter (LPF) and second part is a compensating feedback signal which is used to counterbalance the error in the output. The term φ_s^L is the output of the saturation block used to stop the integration as soon as signals go above the reference stator flux amplitude. The value of φ_s^L is obtained using the stator angle which is calculated from flux components $\varphi_{\alpha s}$ and $\varphi_{\beta s}$. Therefore, the accuracy of the estimated flux is strongly dependent on the angle θ_s given in Eqn. (7). Application of this method at lower frequency of operation for IM leads to improvement in the ripple in flux, torque and speed.

Several discretization methods for second order generalized integrator are implemented [19]. For the implementation of the discrete flux controller, modified integrator eqn. (11) can be expressed as follows

$$e_s = \varphi_s^F (s+\omega_c), \ e_s = \varphi_s^F \times s + \varphi_s^F \times \omega_c \quad (12)$$

In order to achieve the better performance, advanced numerical method such as trapezoidal method for discrete time integration is used for the flux estimation [22]. In trapezoidal method, integrator is defined as $1/s = \frac{T_s}{2}\frac{z+1}{z-1}$.

In this way, realization of eqn. (12) in discrete form can be written as:

0885-8993 (c) 2018 IEEE. Personal use is permitted, but republication/redistribution requires IEEE permission. See http://www.ieee.org/publications_standards/publications/rights/index.html for more information.

This article has been accepted for publication in a future issue of this journal, but has not been fully edited. Content may change prior to final publication. Citation information: DOI 10.1109/TPEL.2019.2912265, IEEE Transactions on Power Electronics

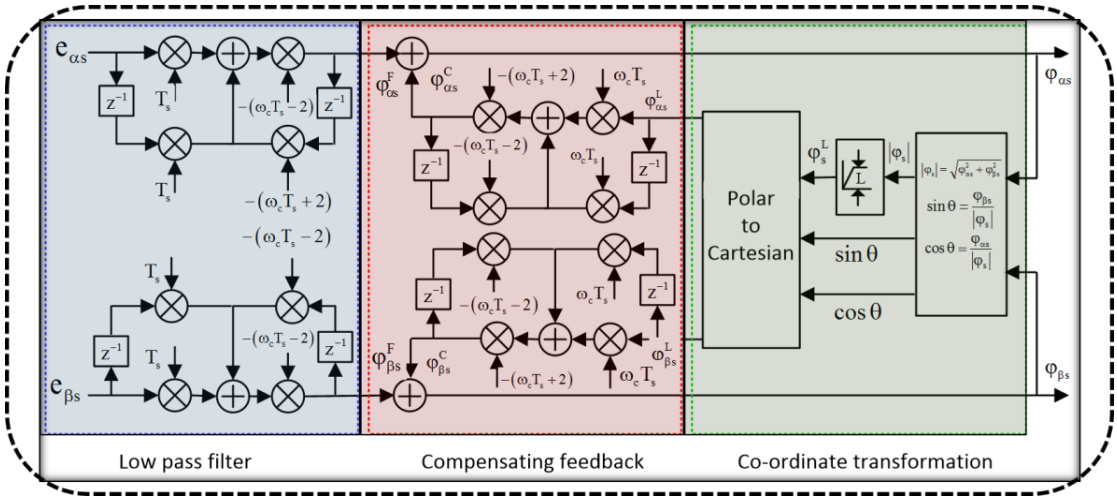

Fig. 2a. Discrete time realization of modified flux integration

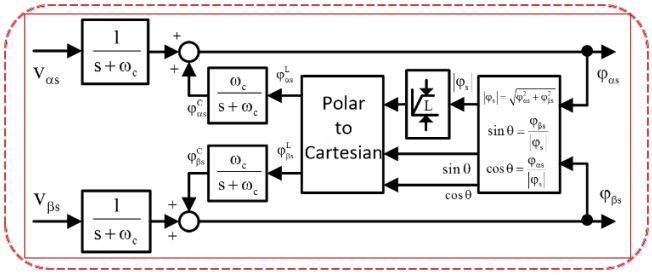

Fig. 2b. Modified flux integration in s-domain

$$\varphi_s^F(k) = \frac{T_s + T_s z^{-1}}{(\omega_c T_s + 2) + (\omega_c T_s - 2) z^{-1}} \tag{13}$$

Similarly, second term of the Eqn. (10) is the compensating feedback signal in the discrete form can be written as:

$$\varphi_s^C(k) = \frac{\omega_c T_s + \omega_c T_s z^{-1}}{(\omega_c T_s + 2) + (\omega_c T_s - 2) z^{-1}} \tag{14}$$

Realization of eqn. (13) and eqn. (14) in MATLAB/Simulink is shown Fig.2a.

V. ADAPTIVE PREDICTIVE CURRENT CONTROLLER

The predictive control is an advanced and powerful control with ability to consider constraints and actuators limitations. The adaptive PCC has been used in the IM drive system specially to achieve good performance at a low speed operation and satisfactory robustness in drive operation. Fig. 1c shows the basic principle of the proposed adaptive PCC.

A. Objective Function

The induction motor is considered as a combination of resistance, inductance and back emf for VSI which is used to predict the nature of the stator currents for every switching state generated by VSI. An objective function is defined for the selection of the best switching state which is applied to control VSI and this objective function is calculated for the predicted values to be controlled. The error signal between predicted stator currents and reference stator currents minimized using the cost function defined with PCC [6, 7, 24]. The best

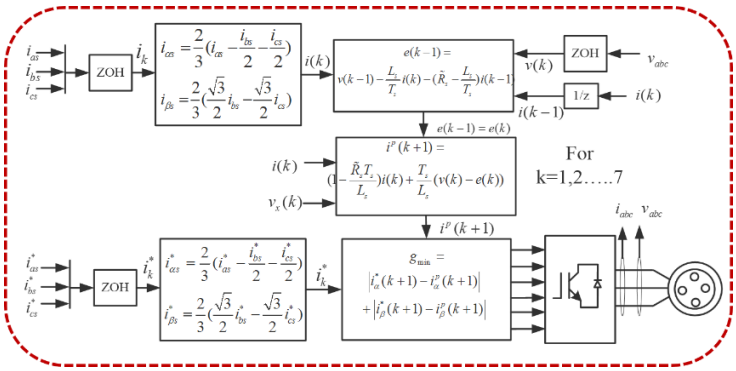

Fig. 2c. Block Diagram of PCC

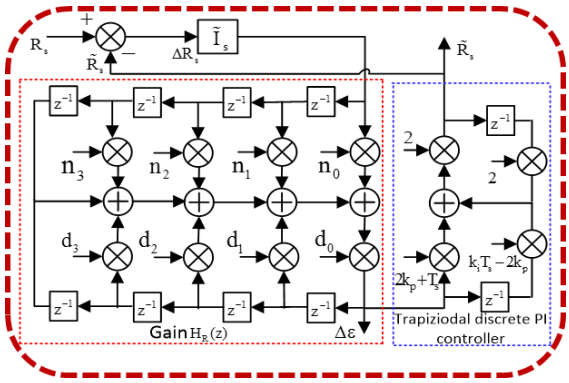

Fig. 2d. Discrete time realization of stator resistance estimation

0885-8993 (c) 2018 IEEE. Personal use is permitted, but republication/redistribution requires IEEE permission. See http://www.ieee.org/publications_standards/publications/rights/index.html for more information.

This article has been accepted for publication in a future issue of this journal, but has not been fully edited. Content may change prior to final publication. Citation information: DOI 10.1109/TPEL.2019.2912265, IEEE Transactions on Power Electronics

switching state which gives the minimum value of cost function is selected and applied to the three-leg VSI without any use of modulation stage and linear regulators. The error between reference currents generated using indirect FOC and predicted currents are measured by cost function which is expressed in vector form as

$$\vec{g} = \vec{i}^{*}(k+1) - \vec{i}^{\,p}(k+1) \tag{15}$$

Where $\vec{i}^{*}(k+1) = i_{\alpha}^{*}(k+1) + j i_{\beta}^{*}(k+1)$

and $\vec{i}^{\,p}(k+1) = \vec{i}_{\alpha}^{\,p}(k+1) + j\vec{i}_{\beta}^{\,p}(k+1)$

Here $\vec{i}^{*}(k+1)$ is the reference stator current vector produced using DFOC algorithm, $\vec{i}_{\alpha}^{*}(k+1)$ and $\vec{i}_{\beta}^{*}(k+1)$ are the real and fictitious constituent of this current vector, $\vec{i}^{\,p}(k+1)$ is the predicted stator current vector. Currents $\vec{i}_{\alpha}^{\,p}(k+1)$ and $\vec{i}_{\beta}^{\,p}(k+1)$ are the real and fictitious constituent of the current vector $\vec{i}^{\,p}(k+1)$ for a given voltage vector. Superscript 'p' is used for the predicted variables. Now, the objective function in $\alpha\beta$ co- ordinate system can be defined for every voltage vector as

$$\vec{g} = \left|i_{\alpha}^{*}(k+1) - i_{\alpha}^{p}(k+1)\right| + \left|i_{\beta}^{*}(k+1) - i_{\beta}^{p}(k+1)\right| \tag{16}$$

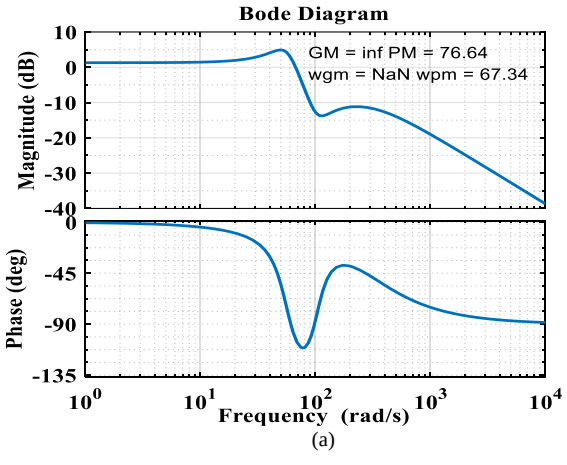

(a)

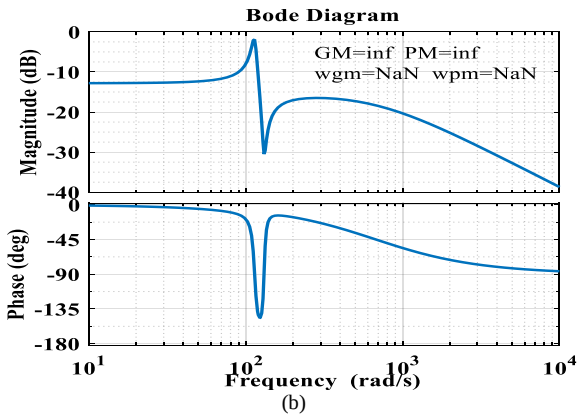

(b)

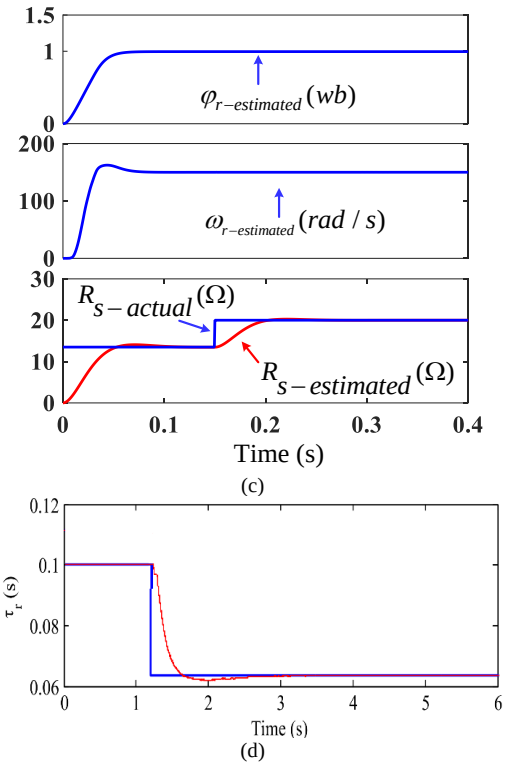

(c)

(d)

Fig.3 Stator resistance and rotor time constant adaptation (a) Bode plot at Rs (b) Bode plot at 5Rs (c) Stator resistance adaption (d) Rotor time constant adaption

B. Modelling of Voltage Source Inverter

A the three phase VSI is comprised of six insulated gate bipolar transistor (IGBT) switches (S_1 S_2…S_6), which forms 3-leg of VSI. Each leg of VSI is controlled in complementary mode. Different switching states of the VSI are governed by the gating signals S_a, S_b and S_c as follows

$$S_a = \begin{cases} 1 \text{ if } S_1 \text{ on and } S_4 \text{ off} \\ 0 \text{ if } S_1 \text{ off and } S_4 \text{ on} \end{cases}$$

$$S_b = \begin{cases} 1 \text{ if } S_2 \text{ on and } S_5 \text{ off} \\ 0 \text{ if } S_2 \text{ off and } S_5 \text{ on} \end{cases}$$

$$S_c = \begin{cases} 1 \text{ if } S_3 \text{ on and } S_6 \text{ off} \\ 0 \text{ if } S_3 \text{ off and } S_6 \text{ on} \end{cases}$$

The value of output voltage generated by inverter with different switching signals can be defined as

$$v = V_{dc} S \tag{17}$$

Where $S = \frac{2}{3}(S_a + aS_b + a^2 S_c)$, **is** the inverter switching state vector and $v = \frac{2}{3}(v_{aN} + av_{bN} + a^2 v_{cN})$ is the output voltage vector generated by the inverter. V_{dc} is the DC link voltage, $a = e^{j2\Pi/3}$ is the unitary vector which gives $120°$ phase shift in different phases. For simplicity, diode forward voltage, dead time and IGBT saturation voltage is not considered in this inverter model.

0885-8993 (c) 2018 IEEE. Personal use is permitted, but republication/redistribution requires IEEE permission. See http://www.ieee.org/publications_standards/publications/rights/index.html for more information.

This article has been accepted for publication in a future issue of this journal, but has not been fully edited. Content may change prior to final publication. Citation information: DOI 10.1109/TPEL.2019.2912265, IEEE Transactions on Power Electronics

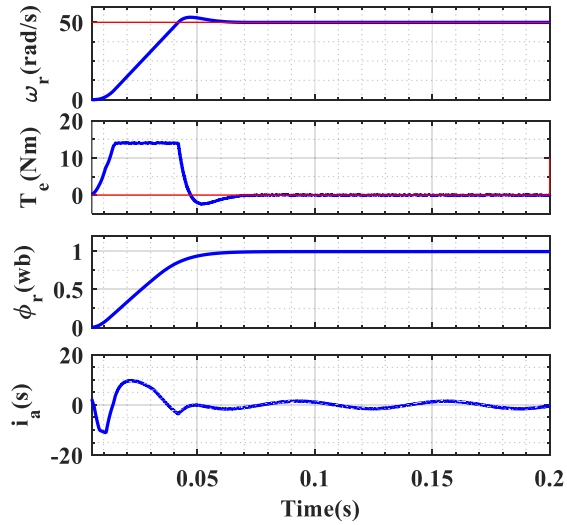

(a)

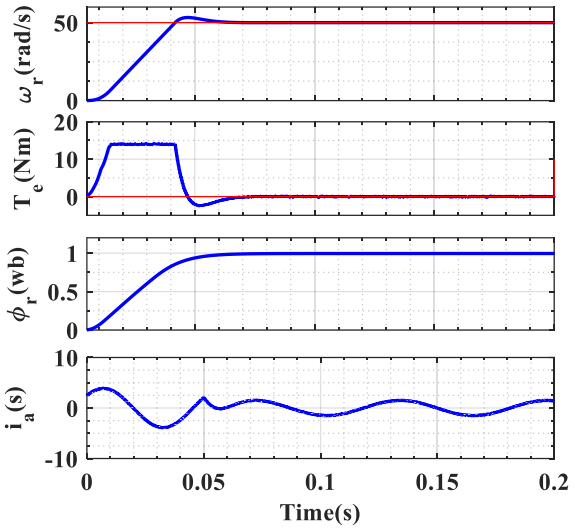

(b)

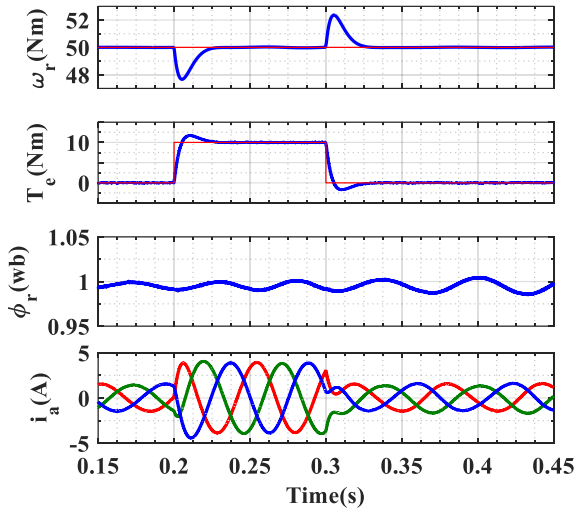

(c)

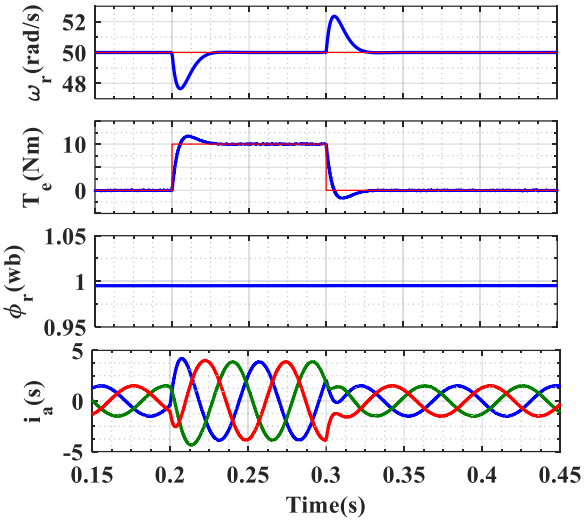

(d)

Fig.4 Starting and load torque dynamic response of IM drive
(a) Starting dynamics with conventional PCC and LPF flux integration
(b) Starting dynamics with proposed PCC and modified LPF flux integration
(c) Load dynamics with conventional PCC and LPF flux integration
(d) Load dynamics with proposed PCC and modified LPF flux integration

C. Discrete Time Model for Prediction

A discrete model considering IM as load on the inverter is developed here. From equivalent circuit of the IM, the continuous time model equation is written as:

$$v = i\tilde{R}_s + L_s \frac{di}{dt} + e \tag{18}$$

Where v and i is the voltage and current vector produced at the inverter terminal, which is also stator voltage and stator current for the IM, e is back emf vector of IM. At the k_{th} sampling instant, stator voltage and current is predicted here using discrete time model of the stator current. Sampling time used for the entire discretization process is T_s. Using the forward Euler approximation, stator current derivative di/dt can be written as

$$\frac{di}{dt} \approx \frac{i(k+1) - i(k)}{T_s} \tag{19}$$

For every voltage vector $v_x(k)$ which is produced by the inverter, future stator current can be predicted by substituting the value of $\frac{di}{dt}$ in eqn. (18) from eqn. (19) as

$$i^p(k+1) = (1 - \frac{\tilde{R}_s T_s}{L_s}) i(k) + \frac{T_s}{L_s}(v(k) - e(k)) \tag{20}$$

Using eqn. (20) back-emf can be calculated as

$$e(k-1) = v(k-1) - \frac{L_s}{T_s} i(k) - (\tilde{R}_s - \frac{L_s}{T_s}) i(k-1) \tag{21}$$

0885-8993 (c) 2018 IEEE. Personal use is permitted, but republication/redistribution requires IEEE permission. See http://www.ieee.org/publications_standards/publications/rights/index.html for more information.

This article has been accepted for publication in a future issue of this journal, but has not been fully edited. Content may change prior to final publication. Citation information: DOI 10.1109/TPEL.2019.2912265, IEEE Transactions on Power Electronics

Using an extrapolation of past back-emf $e(k-1)$, the present value $e(k)$ of the back emf can be estimated. Further, the value of sampling frequency is much larger than the frequency of the back-emf and it is assumed that back emf will not change significantly in one sampling period. Therefore, it is assumed that $e(k)=e(k-1)$.

D. Adaptive Predictive Current Controller Algorithm

A block diagram of PCC is shown in Fig.2c. It shows the implementation of control algorithm for predictive current controller used for DFOC IM drive system. Reference currents are being generated from DFOC IM drive system where one PI controller is used for the regulation of the speed and rotor flux. The three phase stator current i_{abc} are measured from the stator terminals of IM and the reference stator current i^*_{abc} are calculated from DFOC method. The back emf is calculated with the help of discrete stator current and voltage vector at the motor stator terminals. Predicted current $i_p(k+1)$ is determined for back emf $e(k)$ and each voltage vector $v(k)$. The error between predicted stator current and reference current generated using control algorithm is minimized using minimum function block of the MATLAB/Simulink for each voltage vector for each sampling interval. The best switching state which gives the minimum value of cost function are selected and applied to control the three-leg VSI.

VI. PARAMETER ADAPTATION

A. Stator Resistance Adaptation

The state space representation of the machine in stationary reference frame with stator current and rotor flux as state variables, are given in eqn. (1). On linearization of eqn. (1), the linearized equations can be written as:

$$\dot{\Delta x} = A\Delta x + B\Delta u + \Delta A x_0 \tag{22}$$

$$\Delta y = C\Delta x \tag{23}$$

Where $x_0=\begin{bmatrix} i_{\alpha s0} & i_{\beta s0} & \varphi_{\alpha r0} & \varphi_{\beta r0}\end{bmatrix}^T$ $\Delta u=\begin{bmatrix}\Delta u_{\alpha s} & \Delta u_{\beta s} & 0 & 0\end{bmatrix}^T$

$$\Delta A=\begin{bmatrix} -1/\rho L_s & 0 & 0 & 0\\ 0 & -1/\rho L_s & 0 & 0\\ -L_r'/L_m & 0 & 0 & 0\\ 0 & -L_r'/L_m & 0 & 0\end{bmatrix}\Delta R_s$$

By taking Laplace transform of eqn. (22) and eqn. (23), the transformed equation is given as,

$$\Delta y = C\left(sI-A\right)^{-1}\left(\Delta A x_0 + B\Delta u\right) \tag{24}$$

Equation of the stator resistance using machine dynamics can be written as:

$$\tilde{R}_s = k_p\left[\tilde{i}_{\alpha s}e_{i\alpha s} - \tilde{i}_{\beta s}e_{i\beta s}\right] + k_I\int\left[\tilde{i}_{\alpha s}e_{i\alpha s} - \tilde{i}_{\beta s}e_{i\beta s}\right]dt \tag{25}$$

Where $\begin{bmatrix} e_{i\alpha s} & e_{i\beta s}\end{bmatrix}^T = \begin{bmatrix} i_{\alpha s}-\tilde{i}_{\alpha s} & i_{\beta s}-\tilde{i}_{\beta s}\end{bmatrix}^T$

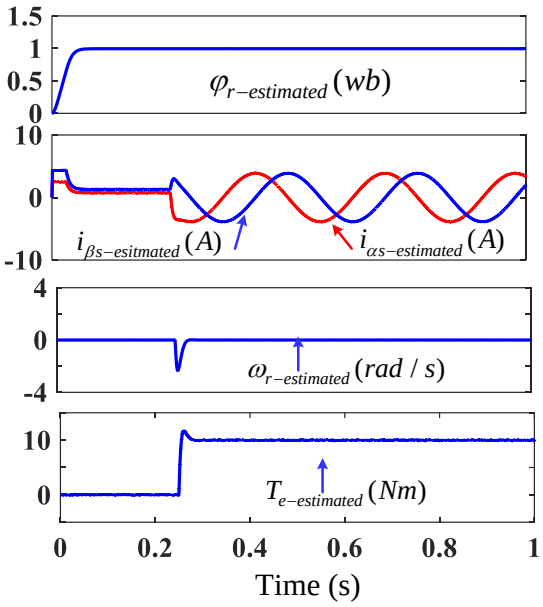

Fig. 4e. Zero speed and load dynamic with proposed PCC and modified LPF flux integration

Fig.2c represents the discrete block diagram of the stator resistance estimator. From fig.2c the error in continuous domain is described as that $\Delta\varepsilon = H_R(s)\tilde{i}_s\Delta R_s$, Where $\tilde{i}_s=\begin{bmatrix}\tilde{i}_\alpha & \tilde{i}_\beta\end{bmatrix}^T$ and Δε are *dq* axes stator current error.

Considering only the *d*-axis component, the error equation is written as,

$$\Delta\varepsilon = H_{R1}(s)\tilde{i}_s\Delta R_s \tag{26}$$

Therefore, the open loop transfer function of the stator resistance estimator is given in eqn. (26) can be written as

$$H_{R1}(s)=\frac{s^3+s^2p_1+sp_2+p_3}{s^4+2s^3p_4+s^2p_5+sp_6+p_7} \tag{27}$$

The final closed loop transfer function is given as,

$$\frac{\tilde{R}_s}{R_s}=\frac{H_{R1}(s)\tilde{i}_s\left(k_P+k_I\frac{T_s}{2}\frac{z+1}{z-1}\right)}{1+H_{R1}(s)\tilde{i}\left(k_P+k_I\frac{T_s}{2}\frac{z+1}{z-1}\right)} \tag{28}$$

Where, $p_1=2c+a$, $p_2=c^2+2ac-d^2-bj$,

$p_3=a\left(c^2-d^2\right)-j\left(fd+cb\right)$, $p_4=2\left(a+c\right)$

$p_5=\left(\left(a+c\right)^2+2ac-d^2-2bj\right)$,

$p_6=\left(2\left(a+c\right)\left(ac-bj\right)-2i\left(fj+ad\right)\right)$,

$p_7=a^2\left(c^2-i^2\right)+j^2\left(b^2-e^2\right)-2aj\left(ei+cb\right)$

$a=\frac{L_m^2}{\sigma L_s L_r\tau_r}+\frac{R_s}{\sigma L_s}, b=\frac{L_m}{\sigma L_s L_r\tau_r}, c=\frac{1}{\tau_r}, d=\omega_r, j=\frac{L_m}{\tau_r}, f=\frac{L_m\omega_r}{\sigma L_s L_r}$

Discretized form of transfer function given in eqn. (28) by replacing $s=\frac{2}{T_s}\frac{z-1}{z+1}$ can be written as below

0885-8993 (c) 2018 IEEE. Personal use is permitted, but republication/redistribution requires IEEE permission. See http://www.ieee.org/publications_standards/publications/rights/index.html for more information.

This article has been accepted for publication in a future issue of this journal, but has not been fully edited. Content may change prior to final publication. Citation information: DOI 10.1109/TPEL.2019.2912265, IEEE Transactions on Power Electronics

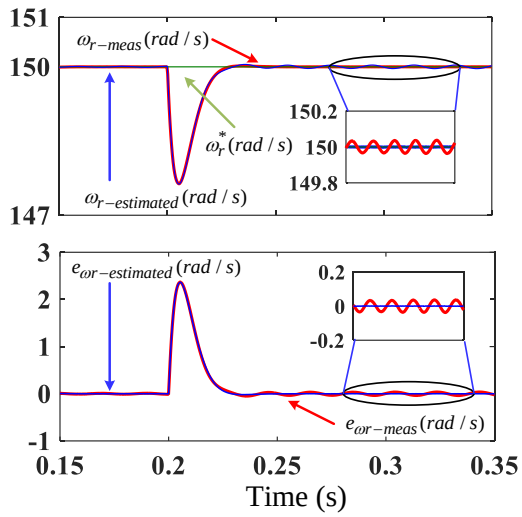

(a)

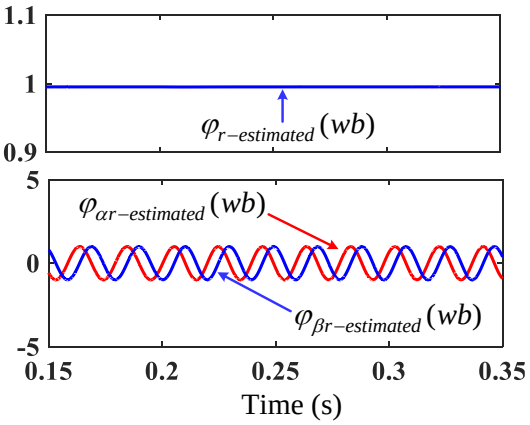

(b)

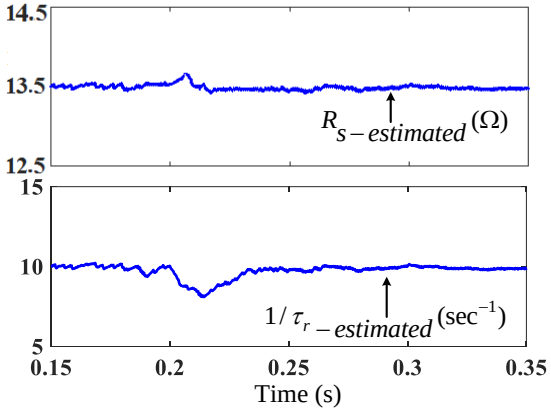

(c)

$$H_{R1}(z)=\frac{n_0+n_1z^{-1}+n_2z^{-2}+n_3z^{-3}+n_4z^{-4}}{d_0+d_1z^{-1}+d_2z^{-2}+d_3z^{-3}+d_4z^{-4}} \tag{29}$$

Where, $n_0=8T_s+4T_s^2p_1+2T_s^3p_2+T_s^4p_4$,

$n_1=-16T_s+4T_s^3p_2+4T_s^4p_3$, $n_2=-8T_s^2p_1+6T_s^4p_3$,

$n_3=16T_s-4T_s^3p_2+T_s^4p_3$ $n_4=-8T_s+4T_s^2p_1-2T_s^3p_2+4T_s^4p_4$,

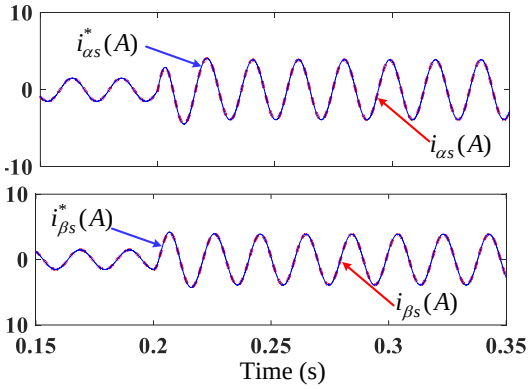

(d)

Fig.5 Load torque dynamic response of IM drive with proposed method (a) Measured and estimated speed (b) Measured and estimated flux (c) Estimated stator resistance and inverse rotor time constant (d) Reference and measured current components

$d_0=16+8T_sp_4+4T_s^2p_5+2T_s^3p_6+T_s^4p_4$,

$d_1=-64-16T_sp_4+4T_s^3p_6+2T_s^4p_7$, $d_2=96-8T_s^2p_5+6T_s^4p_7$,

$d_3=-64-16T_sp_4-4T_s^3p_6+4T_s^4p_7$,

$d_4=16+8T_sp_4+4T_s^2p_5+2T_s^3p_6+T_s^4p_4$

B. Rotor Time Constant Adaptation

The rotor time constant τ_r of the IM is estimated. The error matrix [w] for τ_r can be written as,

$$\Delta A\tilde{x}=w=\begin{bmatrix}\frac{-L_m^2}{\rho L_sL_r}\left[\frac{1}{\tilde{\tau}_r}-\frac{1}{\tau_r}\right] & 0 & \frac{L_m}{\rho L_sL_r}\left[\frac{1}{\tilde{\tau}_r}-\frac{1}{\tau_r}\right] & 0\\ 0 & \frac{-L_m^2}{\rho L_sL_r}\left[\frac{1}{\tilde{\tau}_r}-\frac{1}{\tau_r}\right] & 0 & \frac{L_m}{\rho L_sL_r}\left[\frac{1}{\tilde{\tau}_r}-\frac{1}{\tau_r}\right]\\ L_m\left[\frac{1}{\tilde{\tau}_r}-\frac{1}{\tau_r}\right] & 0 & -\left[\frac{1}{\tilde{\tau}_r}-\frac{1}{\tau_r}\right] & 0\\ 0 & L_m\left[\frac{1}{\tilde{\tau}_r}-\frac{1}{\tau_r}\right] & 0 & \left[\frac{1}{\tilde{\tau}_r}-\frac{1}{\tau_r}\right]\end{bmatrix}\begin{bmatrix}\tilde{i}_\alpha\\ \tilde{i}_\beta\\ \tilde{\varphi}_{\alpha r}\\ \tilde{\varphi}_{\beta r}\end{bmatrix} \tag{30}$$

$$w^Te=e^Tw=\left[\frac{1}{\tilde{\tau}_r}-\frac{1}{\tau_r}\right]\begin{bmatrix}\left(K_M\tilde{i}_\alpha+K_N\tilde{\varphi}_{\alpha r}\right)e_{i\alpha}+\left(K_M\tilde{i}_\beta+K_N\tilde{\varphi}_{\beta r}\right)e_{i\beta}\\ +\left(L_m\tilde{i}_\alpha-\tilde{\varphi}_{\alpha r}\right)e_{\varphi\alpha r}+\left(L_m\tilde{i}_\beta-\tilde{\varphi}_{\beta r}\right)e_{\varphi\beta r}\end{bmatrix} \tag{31}$$

Therefore, the system has forward path matrix with strictly positive real values. Now, to check the stability of nonlinear feedback path matrix, the Popov's inequality criterion is used. By Popov's inequality,

$$\int_0^{t1}\frac{d}{dt}fn(t)\,fn(t)dt\geq-\frac{fn^2(0)}{2} \tag{32}$$

The Popov's inequality is satisfied and the solution can be derived as:

$$\int_0^{t1}\mathrm{Re}\left(e^Tw\right)dt\geq-\frac{1}{2}\left[\frac{1}{\tilde{\tau}_r}-\frac{1}{\tau_r}\right]^2\geq-\frac{q_0^2}{2} \tag{33}$$

Therefore, the following inequality satisfies the Popov's theorem. Further, the adaptive rotor-time constant is identified as:

0885-8993 (c) 2018 IEEE. Personal use is permitted, but republication/redistribution requires IEEE permission. See http://www.ieee.org/publications_standards/publications/rights/index.html for more information.

This article has been accepted for publication in a future issue of this journal, but has not been fully edited. Content may change prior to final publication. Citation information: DOI 10.1109/TPEL.2019.2912265, IEEE Transactions on Power Electronics

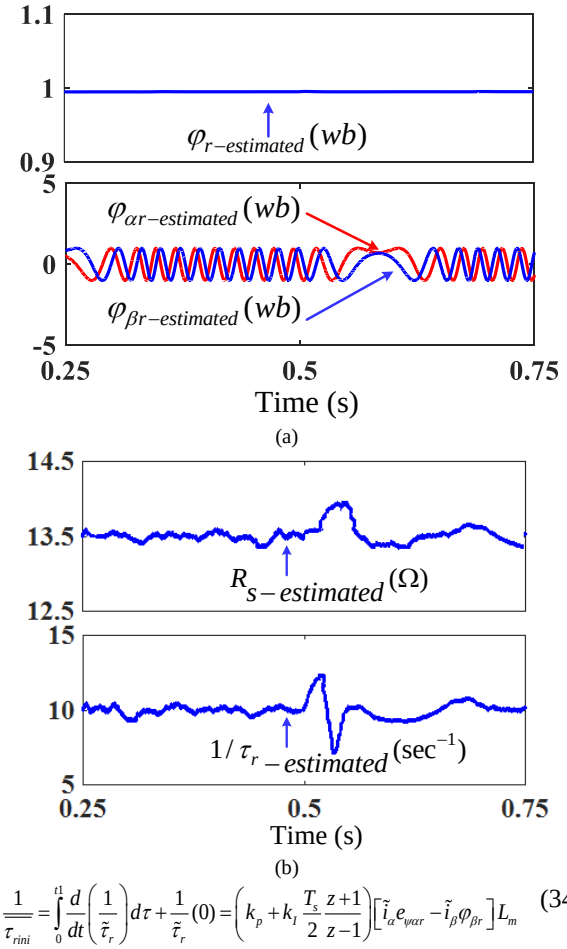

$$\frac{1}{\tau_{rini}} = \int_0^{t1} \frac{d}{dt}\left(\frac{1}{\tilde{\tau}_r}\right) d\tau + \frac{1}{\tilde{\tau}_r}(0) = \left(k_p + k_I \frac{T_s}{2}\frac{z+1}{z-1}\right)\left[\tilde{i}_\alpha e_{\psi\alpha r} - \tilde{i}_\beta \varphi_{\beta r}\right] L_m \quad (34)$$

C. Speed Estimation

The accurate speed estimation involves, accurate estimation of motor fluxes in stationary rotor reference frame [23]. Using eqn. (9.1) the estimated slip speed is given as

$$\omega_{sl} = \left(\varphi_{\alpha r} i_{\beta s} - \varphi_{\beta r} i_{\alpha s}\right) / \varphi_r \times \frac{L_m}{\tau_r} \text{ and } \omega_e = \left(\varphi_{\alpha s} \dot{\varphi}_{\beta s} - \varphi_{\beta s} \dot{\varphi}_{\alpha s}\right) / \varphi_s \quad (35)$$

Where, $\varphi_{\alpha r}$ and $\varphi_{\beta r}$ are rotor fluxes in stationary reference frame, ω_e is the synchronous speed, $\tau_r = L_r / R_r$ is rotor time constant. The motor speed is given as:

$$\tilde{\omega}_r = \omega_e - \omega_{sl} \quad (36)$$

D. Stability Analysis of the System with Rotor Resistance Adaptation

The stability of the system is analyzed by varying the stator resistance from its nominal value. It is expected that the actual stator resistance is constant. Fig.3a shows the Bode plot of the system at rated stator resistance and the stability is analyzed by observing the gain margin (GM) and the phase margin (PM) of the plot. It is observed that both GM and PM are positive, which implies that the system is stable. Furthermore, the GM is at infinity, which proves the robustness of the parameter estimation method. The adaptability of the system is confirmed for one more operating condition in which the motor resistance is fixed at 5 times the nominal stator resistance. Fig.3b validates the stability of the system for this large variation in stator resistance under worst operating condition. The GM is infinite in this case, which again validates the robustness of the system.

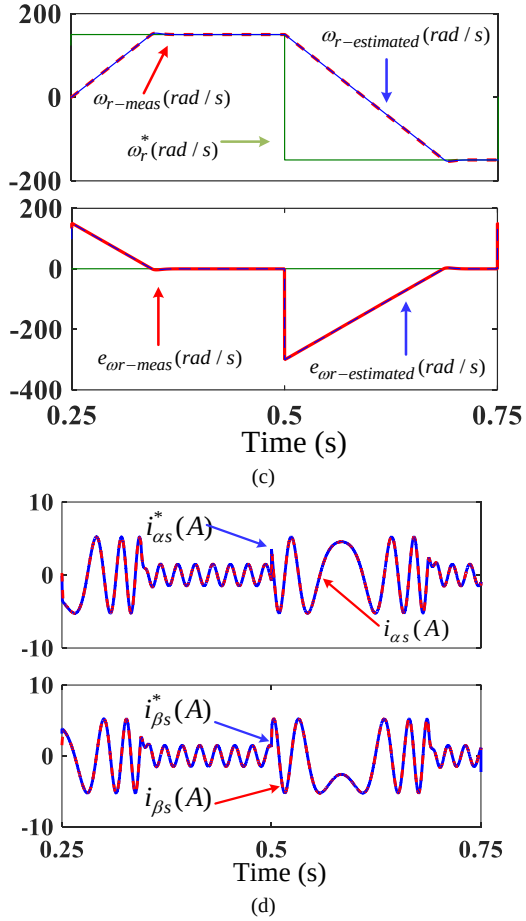

Fig.6 Speed reversal dynamic response of IM drive with proposed method (a) Measured and estimated flux (b) Estimated stator resistance and inverse rotor time constant (c) Measured and estimated speed (d) Reference and measured current components

VII. SIMULATION RESULTS AND DISCUSSIONS

The proposed PCC for DFOC IM drive system is modelled and simulated in MATLAB/Simulink. The results obtained under different operating conditions with conventional PCC and proposed PCC are presented for comparison performance of the drive. The parameters and ratings of IM used for the simulation studies are given in Table I.

0885-8993 (c) 2018 IEEE. Personal use is permitted, but republication/redistribution requires IEEE permission. See http://www.ieee.org/publications_standards/publications/rights/index.html for more information.

This article has been accepted for publication in a future issue of this journal, but has not been fully edited. Content may change prior to final publication. Citation information: DOI 10.1109/TPEL.2019.2912265, IEEE Transactions on Power Electronics

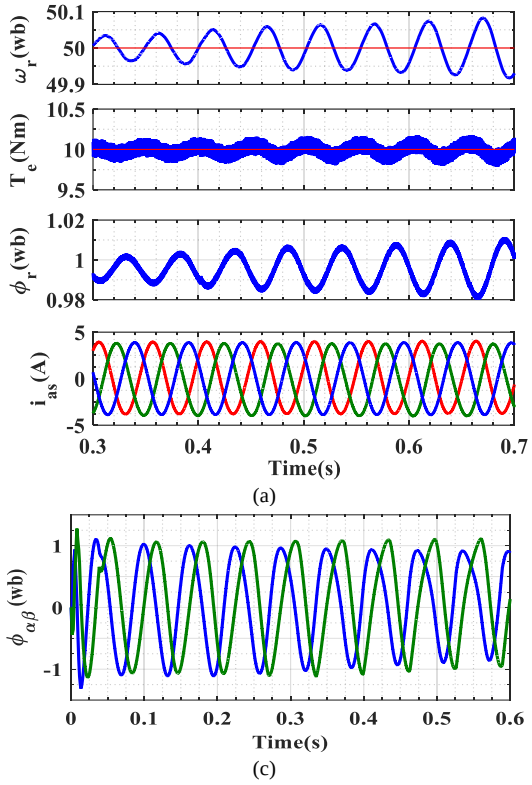

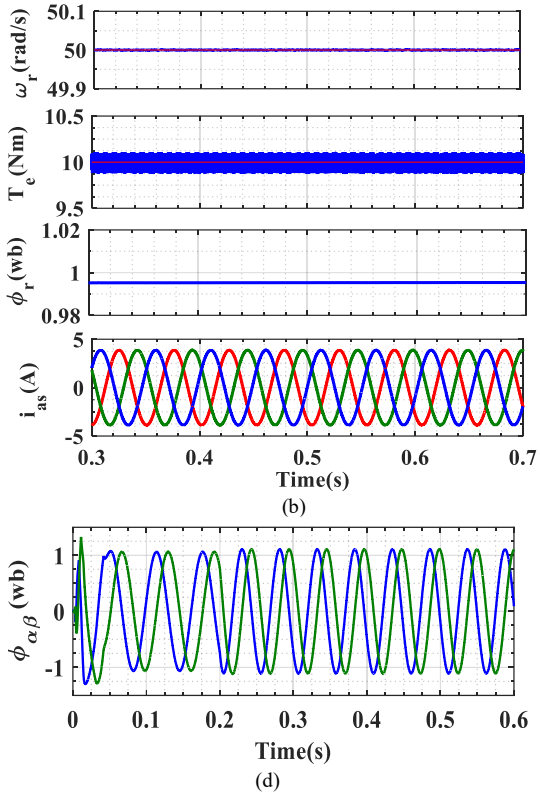

Fig.7 Steady state response of IM drive (a), (c) With conventional PCC and LPF flux integration (b), (d) with proposed PCC and modified LPF flux integration

A. Motor Stator Resistance and Rotor Time Constant Adaptation

Figs.3c shows the adaptability of the predictive current controller (PCC) to the stator resistance variation and Fig.3d shows the adaptability of the system to the rotor time constant. Initially, motor runs at 150 rad/s without load and the nominal stator resistance value is 13.5 Ω. It is observed from Fig.3c that estimated value of the stator resistance track the nominal value of stator resistance of the motor. At t=0.15 sec the stator resistance is increased by 50% and it can be observed that the drive performance is satisfactory. Speed and flux in the motor are constant with increased stator resistance value, which proves the robustness of the controller. When rotor time constant reduced by 50 % of the rated value it also tracks the reference value as shown in Fig.3d. The estimated value of stator resistance and rotor time constant closely track the nominal value of motor parameters with the stable motor operation.

B. Starting Dynamics of IM Drive

The starting behavior of a classical PCC based DFOC and proposed DFOC IM drive is investigated. The profiles of rotor speed (ω_r), torque (T_e) and rotor flux (φ_r), and stator currents (i_a) are shown for classical PCC based DFOC and proposed method in Fig.4a and Fig.4b respectively. Initially, the IM runs at low speed 50 rad/s without load. From Fig.4a and Fig.4b, it is observed that starting transients in speed, torque and flux with proposed method is smoother than the classical PCC based DFOC. It is also observed that the speed and flux response in proposed method is faster than the PCC based DFOC as it reaches to the steady state value comparatively in lesser time. The speed of the motor rise to the steady state value in 0.09 s when conventional PCC based DFOC is used, whereas it requires 0.08 s with proposed PCC control. The overshoot in speed is 3.3 rad/s in the case of conventional PCC based FOC whereas 3.2 rad/s with proposed PCC controlled drive. It is observed that the accuracy of the flux estimation during startup period is improved by the proposed modified flux estimator.

C. Starting Dynamics of IM Drive under Sudden Load Disturbance and Speed Reversal

Fig.4c and Fig.4d show the dynamic performance of the IM with the PCC based DFOC and the proposed PCC method, when a sudden load torque is applied on IM. The IM is driven at $\omega_r = 50\, rad/s$ and load torque $T_l = 10$ Nm is suddenly applied at $t = 0.2\, sec$ in both cases. When motor runs with the PCC and the proposed PCC based DFOC, speed is dropped by 2.35 rad/s and then recovers in t= 0.045 s to the reference speed as shown in Fig.4c and Fig. 4d respectively. The torque developed reaches to the load torque T_l =10 Nm

0885-8993 (c) 2018 IEEE. Personal use is permitted, but republication/redistribution requires IEEE permission. See http://www.ieee.org/publications_standards/publications/rights/index.html for more information.

This article has been accepted for publication in a future issue of this journal, but has not been fully edited. Content may change prior to final publication. Citation information: DOI 10.1109/TPEL.2019.2912265, IEEE Transactions on Power Electronics

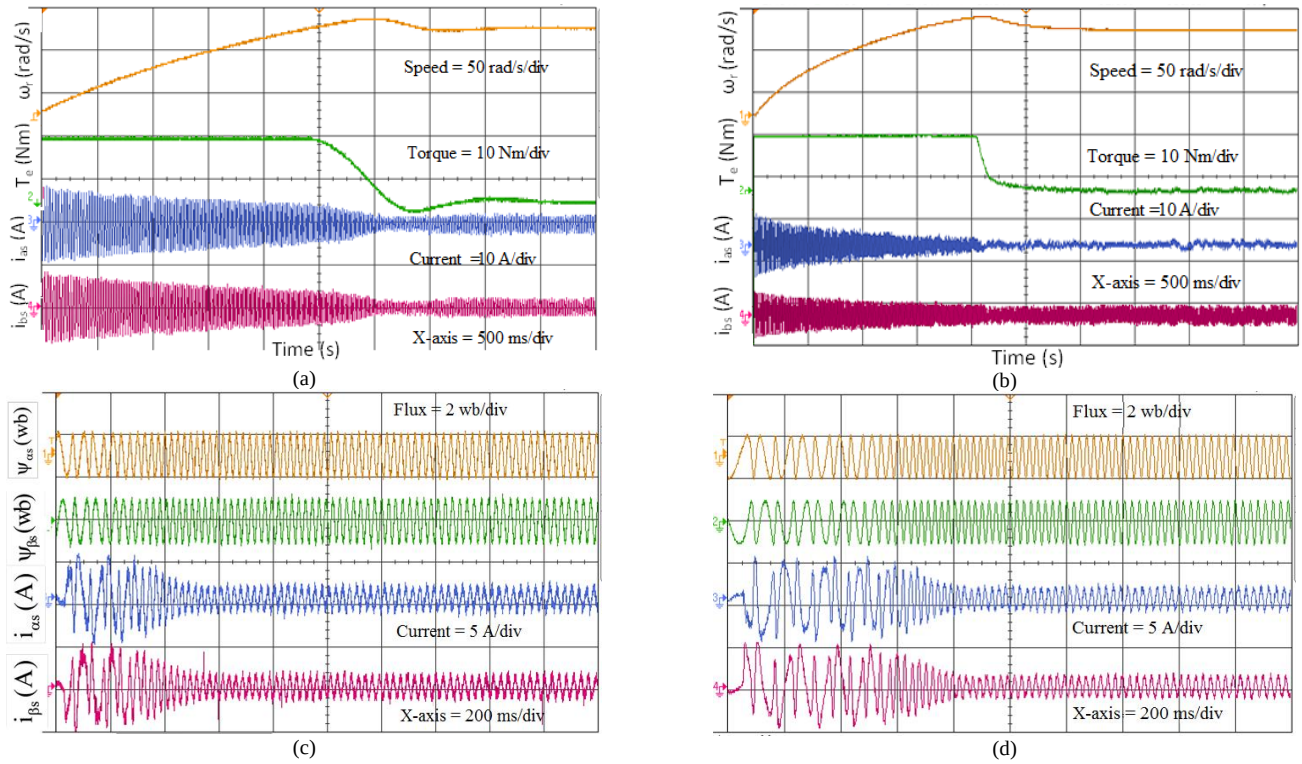

Fig.8 Starting response of IM drive (a), (c) With conventional PCC and LPF flux integration (b),(d) With proposed PCC and modified LPF flux integration

in t = 0.03 s as shown in Fig.4c Fig. 4d. When load torque is suddenly removed at $t = 0.3$ s, there is an overshoot in speed by 2.36 rad/s but it settles to the reference speed in t=0.03 sec by the controller in both the cases. It is also observed in Fig.4c that as soon as motor is loaded, flux has some ripples. However, these ripples are not observed in the proposed PCC controlled drive as shown in Fig.4d. There are some ripples in the stator currents of the IM as shown in Fig. 4c when motor operates at no load but smoother current response is observed under load conditions as shown in Fig.4d. The Fig. 4d shows that the rotor flux is almost constant even with sudden change in the load torque which also indicates the improved behaviour of the IM drive with proposed PCC control. Fig. 4e shows the zero speed dynamics of the proposed method. It is observed that motor start smoothly and after 2.5 s, the load torque of 10 Nm is suddenly applied. It can be observed from the Fig. 4e that speed drops momentarily but it recovers quickly to reference level and reaches its steady state value in few seconds. The flux is observed to be constant even after the change in load. The current $i_{\alpha s}$ and $i_{\beta s}$ are constant initially as there is no frequency at zero speed. The overall, dynamic performance of the motor is stable and satisfactory at zero speed.

Effect of the load torque on measured speed, estimated speed, speed error, flux, stator resistance, inverse rotor time constant, reference and estimated components of stator currents are shown in Fig. 5a, 5b, 5c and 5d respectively with the proposed controller. Effect of sudden change in load torque is observed as small deviation in estimated stator resistance and inverse rotor time constant but this deviation is recovered by the controller in next few seconds and the estimated values of all these parameters and variables are settled at their steady state values quickly. The speed reversal performance of the motor is specially demonstrated through measured speed, estimated speed, speed error, flux, stator resistance, inverse rotor time constant, reference and estimated components of current in Fig. 6a, 6b, 6c and 6d respectively with the proposed controller. The speed reversal of the speed from 150 rad/s to -150 rad/s is made by varying reference speed. It is observed that estimated inverse rotor time constant and stator resistance have very small deviation in magnitude. However, the estimated quantities recovers to its nominal value and reaches its steady state values quickly

D. Steady State Response of IM Drive

Fig.7a and Fig.7b show zoomed waveform of the steady state behaviour of the motor rotor speed (ω_r), torque (T_e), rotor flux (φ_r), and stator current i_a . Fig. 7c and Fig. 7d show the steady state behaviour of $\varphi_{\alpha\beta}$ when PCC based DFOC with LPF flux estimator and proposed DFOC with modified flux estimator is used respectively. It is clearly observed in Fig.7a that the speed, torque and rotor flux has some ripples. However, there are no such ripples observed in Fig. 7b and

0885-8993 (c) 2018 IEEE. Personal use is permitted, but republication/redistribution requires IEEE permission. See http://www.ieee.org/publications_standards/publications/rights/index.html for more information.

This article has been accepted for publication in a future issue of this journal, but has not been fully edited. Content may change prior to final publication. Citation information: DOI 10.1109/TPEL.2019.2912265, IEEE Transactions on Power Electronics

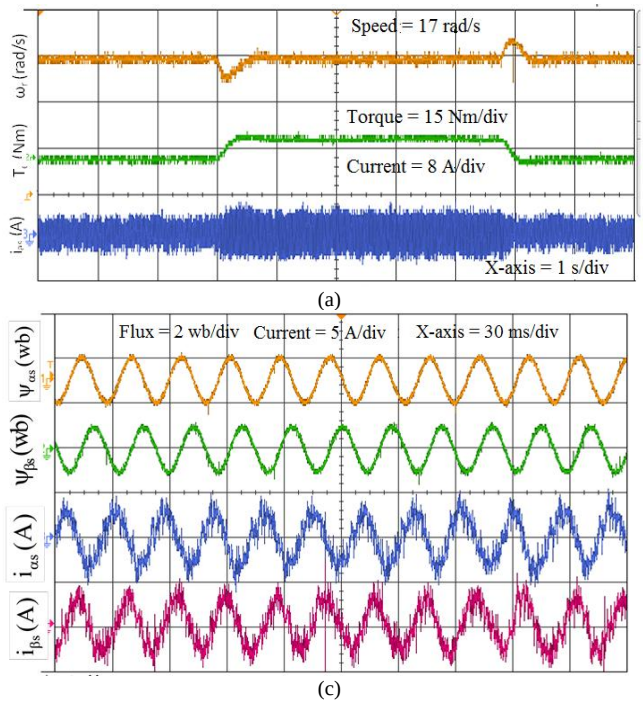

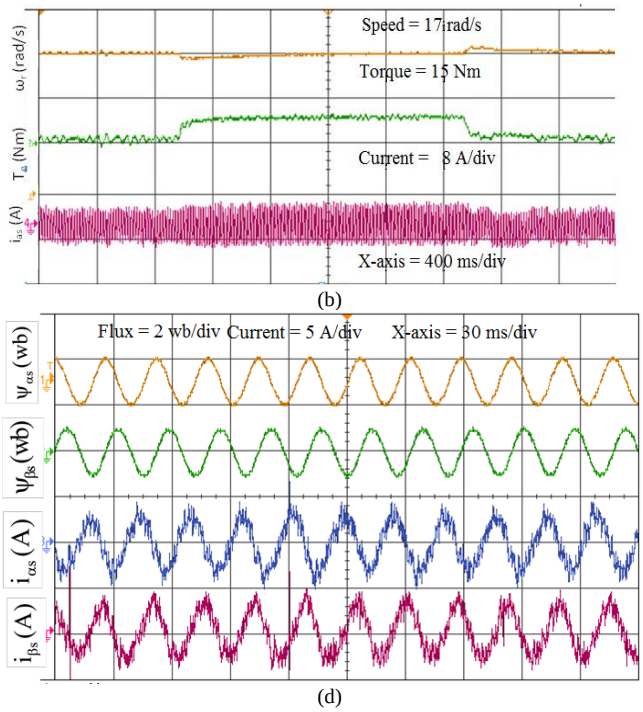

Fig. 7c. Fig. 5d shows the $\alpha\beta$-stator flux waveforms when a small dc signal is introduced to the back emf signal. It is observed that there is DC drift in the estimated flux and small flux distortions in classical method. However, DC drift problem and distortion in flux is resolved using the proposed flux eliminated method. Sampling period for simulation in both the cases is $T_s = 2\mu s$.

VIII. EXPERIMENTAL RESULTS AND DISCUSSIONS

Fig. 12 shows the photograph of the experimental prototype setup used for experimental validation of the proposed PCC control of DFOC IM drive. A complete schematic diagram is shown in Fig. 1a and Fig 1b. The DFOC IM drive consists of the VSI, driver circuit, dS dsp1104 controller, current sensors and power supplies. The dSPACE system with dS1104 TMS320F240 controller board with MATLAB/Simulink is used for implementing control strategy. The different controllers are implemented and operation of drive is analysed under different operating conditions for real time validation. The parameters of drive used for the experimental study is given in the Table 1. The stator voltage to the IM is fed by the VSI, which is controlled by the gate pulses produced through dS1104 controller using different control algorithms. A DC machine is coupled with IM to arrange electrical loading on the IM. Stator currents of the IM are sensed by the two current sensors. A four channel digital storage oscilloscope is used for the recording the waveform of IM under different operating conditions. The sampling time of the control structure is selected at 50μs in both the cases.

Fig.9 Load response of IM drive (a), (c) With conventional PCC and LPF flux integration (b), (d) with proposed PCC and modified LPF flux integration

A. Performance of the IM Drive during Starting

Figure 8 shows the starting response of the IM drive with classical and proposed method. Fig.8a and Fig.8b show the starting response of the rotor speed (ω_r), Torque (T_e), stator current ($i_{\alpha s}$) and stator currents ($i_{\beta s}$). The IM requires few seconds to reach to the steady state speed and the torque developed is adequate enough to rotate the rotor on steady state level. It is observed that the current drawn by the motor during starting is high in magnitude but it reduces to no load current level. The dynamic response of the drive using proposed method is observed to be faster than the classical PCC based DFOC. Fig.8c and Fig.8d show the response of the α-axis flux ($\varphi_{\alpha s}$), β-axis flux ($\varphi_{\beta s}$), α-axis stator current ($i_{\alpha s}$) and β-axis stator currents ($i_{\beta s}$). These waveforms are observed to have lesser ripple in the case of proposed method than the classical PCC based DFOC.

B. Performance of the IM Drive on Load

Fig.9a and Fig.9b show the dynamic response of the motor rotor speed (ω_r), torque (T_e) and stator current (i_{as}) with conventional PCC and proposed PCC respectively. Fig.9c and Fig.9d show the response of the α-axis flux ($\varphi_{\alpha s}$), β-axis flux ($\varphi_{\beta s}$), α-axis stator current ($i_{\alpha s}$) and β-axis stator currents

0885-8993 (c) 2018 IEEE. Personal use is permitted, but republication/redistribution requires IEEE permission. See http://www.ieee.org/publications_standards/publications/rights/index.html for more information.

This article has been accepted for publication in a future issue of this journal, but has not been fully edited. Content may change prior to final publication. Citation information: DOI 10.1109/TPEL.2019.2912265, IEEE Transactions on Power Electronics

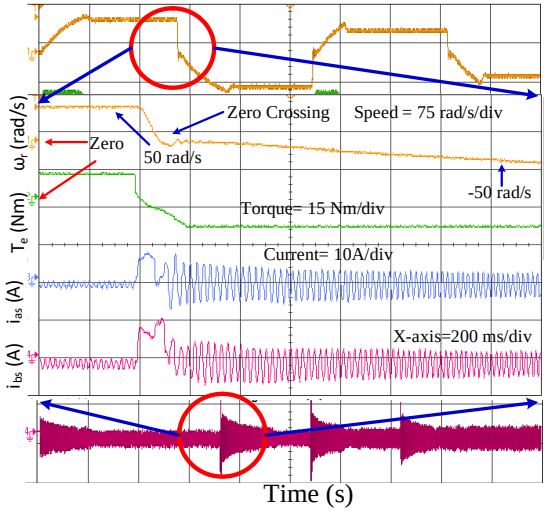

(a)

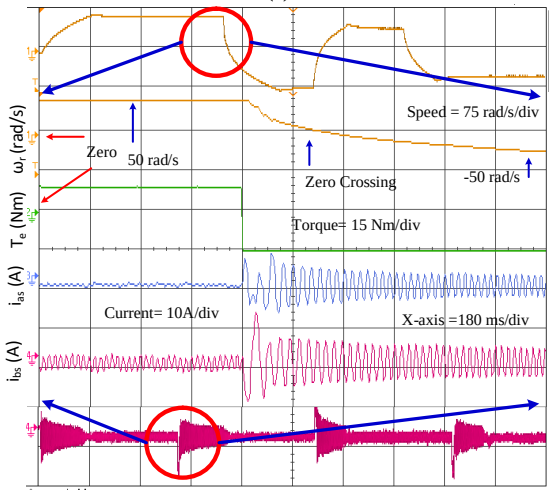

(b)

($i_{\beta s}$) for classical PCC based DFOC and proposed drive respectively. In Fig.9a and Fig.9b, the load torque is suddenly changed to 10Nm and it is observed that motor current increases to increase the motor torque and motor speed settles to reference speed in few seconds. After few seconds the load torque is suddenly removed and speed of the motor overshoot for short interval but it settled down to reference speed. Torque and speed response is observed to be faster in the case of proposed method.

Fig.9c and Fig.9d also show the steady state response of the stator fluxes in the case of classical PCC based DFOC and proposed method. Steady state response of proposed method is observed to be better than the classical method.

C. Performance of the IM Drive under Sudden Change in Speed

Fig.10a and Fig.10b show the speed reversal dynamics from 50 rad/s to -50 rad/s and 30 rad/s to -30 rad/s with PCC based DFOC and proposed method. Zoomed speed response of speed reversal from 50 rad/s to -50 is also shown to demonstrate the effect of controller at zero crossing. It is

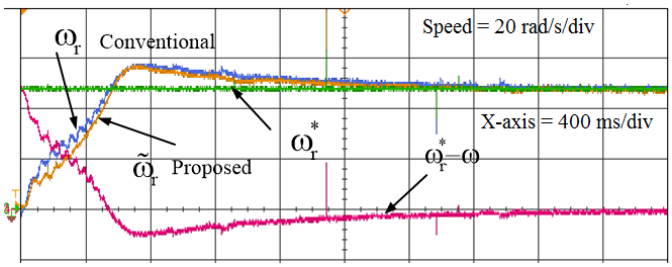

(c)

Fig.10 Speed reversal dynamics of IM drive (a) With conventional PCC and LPF flux integration (b) With proposed PCC and modified LPF flux integration (c) Speed response with conventional PCC and LPF flux integration and proposed PCC and modified LPF flux integration

closely observed that the speed reversal dynamics of the motor is faster with proposed method. Phase sequence reversal of the current is also observed. At zero crossing speed and torque are also found to have smooth response with proposed method compared to that in the classical method.

Fig.10c shows the reference speed, estimated speed with PCC based DOFC, estimated speed with proposed method and speed error between reference speed and estimated speed with PCC based DFOC. Starting speed transients are observed smoother in the case of proposed method.

Fig. 11a shows the effect of variations in speed on stator resistance in proposed techniques. It is observed that initially when motor runs at speed 50 rad/s, estimated stator resistance is 13.5 ohm. After few seconds speed changes from 50 rad/s to -50 rad/s, it is observed that there is small glitch in estimated value of stator resistance but settles down to its rated value. In next few seconds speed reduces from -50 rad/s to zero and it is observed that the estimated stator resistance remains at its rated value except a small dip during transient period. It shows the robustness of the proposed controller. Fig. 11b shows the steady state response of the rotor flux with the proposed method.

Fig. 11c shows the effect of stator resistance variations. Initially, motor is set to run at 50 rad/s at 50% of the full load with rated stator resistance. When estimated speed, flux and stator resistance of motor attain steady state value, the stator resistance is increased by inserting external resistance into stator winding in series. The estimated speed and flux settle to their reference value with small disturbances during transient state. The estimated stator resistance is observed to track the change in actual value closely.

Figure 11d shows the effect of the step change in speed on inverse rotor time constant. Initially, motor is set to run at 50 rad/s so that the estimated speed, measured speed and inverse rotor time constant attain steady state value. After some time, the speed changes from 50 rad/s to 100 rad/s and it is observed that estimated and measured speed, closely follow the reference speed. There is a small change in rotor time constant during the transient state but it settles down to its rated value in next few seconds, which shows the robustness of inverse rotor time constant against speed variations.

Simulation and experimental investigations validate the effectiveness of the proposed adaptive PCC based DFOC of IM drive under dynamic and steady state study conditions.

0885-8993 (c) 2018 IEEE. Personal use is permitted, but republication/redistribution requires IEEE permission. See http://www.ieee.org/publications_standards/publications/rights/index.html for more information.

This article has been accepted for publication in a future issue of this journal, but has not been fully edited. Content may change prior to final publication. Citation information: DOI 10.1109/TPEL.2019.2912265, IEEE Transactions on Power Electronics

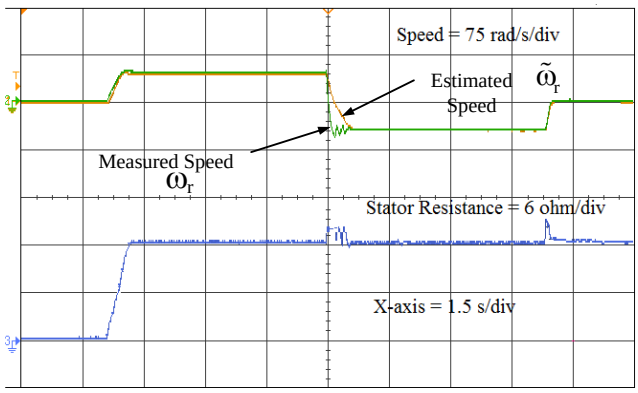

(a)

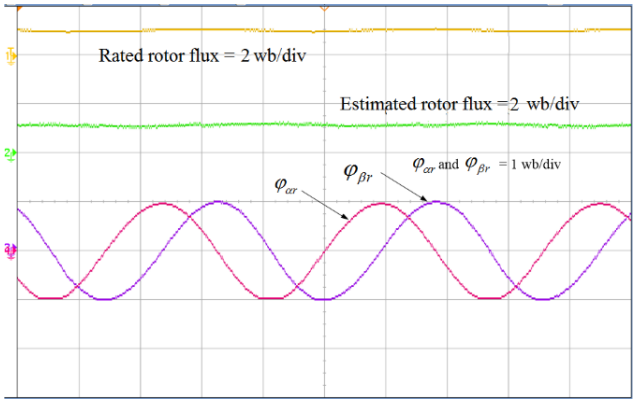

(b)

TABLE 1
INDUCTION MOTOR PARAMETER AND RATINGS

Parameters	Value
Rated power	3 HP
Rated speed(ω_r)	1430 rpm
Number of poles(P)	4
Stator phase voltage(V)	415
Rotor resistance per phase(R_r)	6.82 Ω
Stator resistance per phase (R_S)	13.5 Ω
Rotor leakage inductance per phase(L_{lr})	0.045 H
Stator leakage inductance per phase(L_{lr})	0.045H
Magnetizing inductance per phase (L_m)	0.664H
Rotor inertia(J)	0.00873Kgm^2
Frequency(f)	50 Hz

IX. CONCLUSION

The performance analysis of PCC based sensorless DFOC IM drive with pure integrator voltage model flux estimator and adaptive PCC based DFOC IM drive with modified LPF voltage model flux estimator are investigated through simulation and experimentation. The stator resistance of the motor is estimated for implementation of adaptive PCC in DFOC of IM drive. Robustness and stability of the system

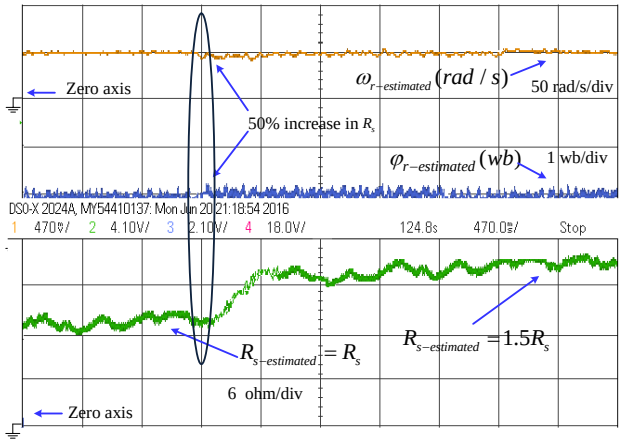

(c)

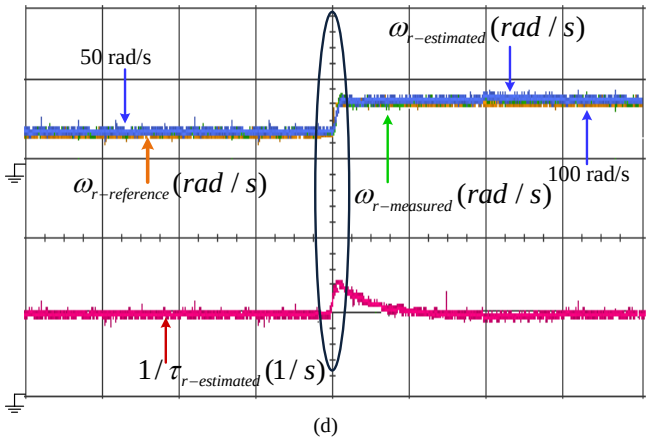

(d)

Fig. 11. (a) Speed reversal and its effect on estimated stator resistance. (b) Rotor flux in steady state (c) Change in stator resistance and its effect on speed and flux (d) Change of reference speed and its effect on inverse rotor time constant

with variation in the stator resistance is validated in frequency domain using Bode plot. Robustness of the drive against rotor time constant is verified using Popov's stability criteria. The proposed method is capable to overcome, parameter mismatches, current and voltage detection errors, unknown integral initial value problem and problems caused by dc offset, effectively. The usefulness of proposed method is demonstrated in low speed region of operation for DFOC IM drive and it also gives better dynamic response especially better speed reversal, starting and low steady state speed error. The experimental and simulation results show that the proposed PCC can effectively improve the dynamic and steady state performance of IM drive.

REFERENCES

[1] L. Malesani and P. Tomasin, "PWM current control techniques of voltage source converters-a survey," *Proc. IECON '93 - 19th Annu. Conf. IEEE Ind. Electron.*, pp. 670–675, 1993.

[2] L. Zhang and H. R. Tayebi, "Field-oriented CSI induction motor drive with optimal predictive current regulation," *1994 Fifth International Conference on Power Electronics and Variable-Speed Drives*, London, 1994, pp. 48-53

0885-8993 (c) 2018 IEEE. Personal use is permitted, but republication/redistribution requires IEEE permission. See http://www.ieee.org/publications_standards/publications/rights/index.html for more information.

This article has been accepted for publication in a future issue of this journal, but has not been fully edited. Content may change prior to final publication. Citation information: DOI 10.1109/TPEL.2019.2912265, IEEE Transactions on Power Electronics

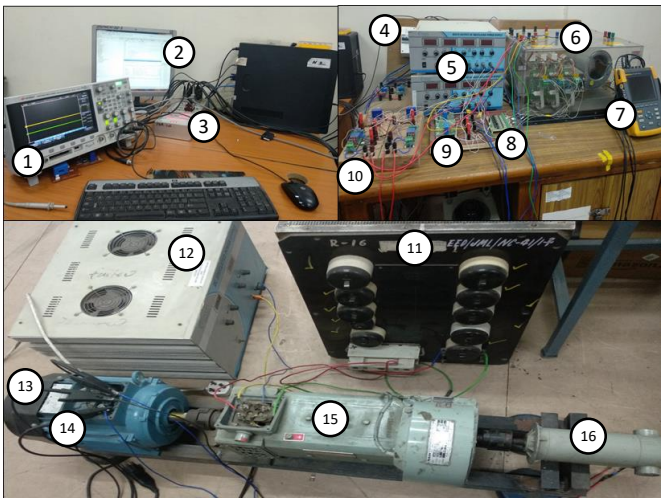

Fig.12 Experimental prototype setup: 1 –four channel digital oscilloscope, 2 – PC, 3 -dSPACE 1104, 4 –Grid, 5 –dc power supply, 6 –three phase rectifier plus inverter, 7 –three phase power analyser, 8 –driver circuit, 9 –current sensor, 10 –voltage sensor, 11 –resistive load, 12 -300V dc power supply, 13 –three phase induction motor, 14 –voltage probe, 15 –dc generator 16 –tachogenerator

[3] L. Zhang, R. Norman, and W. Shepherd, “Long-range predictive control of current regulated PWM for induction motor drives using the synchronous reference frame,” *IEEE Trans. Control Syst. Technol.*, vol. 5, no. 1, pp. 119–126, 1996.

[4] W. Bank, P. Autonomy, J. Guzinski, Z. Krzeminski, and H. A. Toliyat, “Predictive Current Control of Voltage Source Inverters,” vol. 0, no. C, pp. 1195–1200, 2001.

[5] H. Abu-Rub, J. Guziński, Z. Krzeminski, and H. A. Toliyat, “Predictive current control of voltage-source inverters,” *IEEE Trans. Ind. Electron.*, vol. 51, no. 3, pp. 585–593, 2004.

[6] R. Kennel, E. El-kholy, S. Mahmoud, A. El-refaei, and F. Elkady, “A Simple High Performance Current Control Scheme for Induction Motor Drives,” *Ind. Electron. Soc. 2005. IECON 2005. 31st Annu. Conf. IEEE*, p. 6 pp., 2005.

[7] J. Rodriguez, J. Pontt, C. A. Silva, P. Correa, P. Lezana, P. Cortes, U. Ammann, R. Jos, P. Jorge, a S. Csar, C. Pablo, L. Pablo, C. Patricio, and A. Ulrich, “Predictive Current Control of a Voltage Source Inverter,” *Ind. Electron. IEEE Trans.*, vol. 54, no. 1, pp. 495–503, 2007.

[8] P. Cortes, M. P. Kazmierkowski, R. M. Kennel, D. E. Quevedo, J. Rodriguez, P. Cortés, S. Member, and J. Rodríguez, “Predictive Control in Power Electronics and Drives,” *IEEE Trans. Ind. Electron.*, vol. 55, no. 12, pp. 4312–4324, 2008.

[9] N. Kutasi, A. Kelemen, and M. Imecs, “Vector Control of Induction Motor Drives with Model Based Predictive Current Controller,” *2008 IEEE Int. Conf. Comput. Cybern.*, no. 1, pp. 21–26, 2008.

[10] J. M. Retif, L.-S. Xuefang, and F. Morel, “Predictive Current Control for an Induction Motor,” *Power Electron. Spec. Conf. 2008. PESC 2008. IEEE*, pp. 3463–3468, 2008.

[11] T. Laczynski and A. Mertens, “Predictive stator current control for medium voltage drives with LC filters,” *IEEE Trans. Power Electron.*, vol. 24, no. 11, pp. 2427–2435, 2009.

[12] C. S. Lim, N. a. Rahim, W. P. Hew, M. Jones, and E. Levi, “Model predictive current control of a five-phase induction motor,” *IECON 2011 - 37th Annu. Conf. IEEE Ind. Electron. Soc.*, pp. 1934–1940, 2011.

[13] J. Prieto, F. Barrero, C. S. Lim, and E. Levi, “Predictive Current Control with Modulation in Asymmetrical Six – phase Motor Drives,” pp. 1–8, 2012.

[14] J. Guzinski and H. Abu-Rub, “Speed Sensorless Induction Motor Drive With Predictive Current Controller,” *Ind. Electron. IEEE Trans.*, vol. 60, no. 2, pp. 699–709, 2013.

[15] S. Wei, Y. Yong, X. Dianguo, X. Jin, and D. Li, “Predictive Current Control Method in Induction Motor Speed Sensorless Drive,” no. 3, pp. 341–345, 2014.

[16] H. Guzman, F. Barrero, S. Member, M. J. Duran, and I. O. P. M. Ode, “IGBT-Gating Failure Effect on a Fault-Tolerant Induction Motor Drive,” *IEEE Trans. Ind. Electron.*, vol. 62, no. 1, pp. 15–20, 2015.

[17] Z. Hu and K. Hameyer, “Robust predictive current control for performance improvement of induction motors with parameter variation,” *IECON 2015 - 41st Annu. Conf. IEEE Ind. Electron. Soc.*, pp. 000451–000456, 2015.

[18] B. Wang, H. Wang, Y. Yu, X. Lv, G. Wang, and Di. Xu, “Sensorless robust predictive current control for induction motor using a speed adaptive full-order observer,” *9th Int. Conf. Power Electron. - ECCE Asia "Green World with Power Electron. ICPE 2015-ECCE Asia*, no. 1, pp. 1149–1154, 2015.

[19] M. Ciobotaru, R. Teodorescu and F. Blaabjerg, "A new single-phase PLL structure based on second order generalized integrator," *2006 37th IEEE Power Electronics Specialists Conference*, Jeju, 2006, pp.1-6.

[20] M. Hinkkanen and J. Luomi, “Modified integrator for voltage model flux estimation of induction motors,” *IEEE Trans. Ind. Electron*, vol. 50, no. 4, pp. 818–820, 2003.

[21] Z. Xin, R. Zhao, F. Blaabjerg, L. Zhang and P. C. Loh, "An Improved Flux Observer for Field-Oriented Control of Induction Motors Based on Dual Second-Order Generalized Integrator Frequency-Locked Loop," in *IEEE Journal of Emerging and Selected Topics in Power Electronics*, vol. 5, no. 1, pp. 513-525, March 2017.

[22] W. Xu, Y. Jiang, C. Mu and F. Blaabjerg, "Improved Nonlinear Flux Observer Based Second-Order SOIFO for PMSM Sensorless Control," in *IEEE Transactions on Power Electronics, 2018*.

[23] J. Guzinski and H. Abu-Rub, "Speed Sensorless Induction Motor Drive With Predictive Current Controller," in *IEEE Transactions on Industrial Electronics*, vol. 60, no. 2, pp. 699-709, Feb. 2013.

[24] A. Devanshu, M. Sinah and N. Kumar, "Predictive Current Control of Feedback Linearized Induction Motor Drive," *2018 3rd IEEE International Conference on Intelligent Transportation Engineering (ICITE)*, Singapore, 2018, pp. 132-136.

[25] J. Wang, F. Wang, G. Wang, S. Li and L. Yu, "Generalized Proportional Integral Observer Based Robust Finite Control Set Predictive Current Control for Induction Motor Systems With Time-Varying Disturbances," in *IEEE Transactions on Industrial Informatics*, vol. 14, no. 9, pp. 4159-4168, Sept. 2018.

0885-8993 (c) 2018 IEEE. Personal use is permitted, but republication/redistribution requires IEEE permission. See http://www.ieee.org/publications_standards/publications/rights/index.html for more information.

Journal of
APPLIED PACKAGING RESEARCH

RESEARCH ARTICLE

Biodegradable Polymeric Film for Food Packaging

Raminder Kaur
Delhi Technological University

Neelam Yadav*
Delhi Technological University

ABSTRACT

Food packaging films that show post-consumer biodegradability are rarely explored by researchers. The present study was carried out to investigate the physicomechanical characteristics of ethyl cellulose (EC) based films to be used in food packaging. Ethyl cellulose was plasticized with different percentage of polyethylene glycol (PEG). The samples of standard dimensions were subjected to different testing such as soluble matter content, moisture content, oil permeability, surface morphology, mechanical testing etc. The data obtained was analysed to decide the moderate percentage of plasticizer that can be used to provide a rational explanation of a perfect quality specimen. It has been revealed that too high or too low percentage of plasticizer was not appropriate for a good film. Tensile stress analysis was used to estimate the mechanical properties of the films. The results have shown an increase in tensile properties with increase in coalescence temperature. Temperature-dependent plastic deformation was observed for coalescence temperatures above 50°C.

KEY WORDS

Ethyl cellulose, Plasticizer, Biopolymers, Food packaging.

***Raminder Kaur**
Corresponding Author
rkwaliadtu@gmail.com

INTRODUCTION

Packaging protects food from the external environment and provides information to the consumers about the food inside the package. Foods are packaged to deliver safe, wholesome and nutritious food to the consumers and it gives a high significance of link between packaging and consumer protection [1]. Plastics commonly used in food packaging include polyethylene (both HDPE and LDPE), polypropylene, polyvinyl chloride, polyethylene terephthalate and polystyrene [2].These plastics used in food packaging, are derived from petroleum and generate greenhouse gases, thus cause a huge impact on environment. Moreover, they also interact with food material and may release toxic chemicals into food [3]. In addition, the quality of the packaged food is likely to be deteriorate during its storage due to change in its natural ingredients, which may include the loss in the moisture content or volatile odour. However, this deterioration can be reduced by selecting passable food packaging or coatings. Many researchers have reported the enrichment of these packaging films by the addition of other active agents such as O_2 and CO_2 absorbers, antimicrobial agents and antioxidants etc. in order to enhance their utility [4-7]. However, the food packaging films which show post-consumer biodegradability, without causing much burden on the environment were not much explored [8]. Like other polymeric products [9-15], researches are now focused on the development of the bio-based performance end products in the food packaging, with an attention to make them environment friendly. Most widely used bio-based polymers are the cellulose derivatives, such as methyl cellulose, cellulose acetate, hydroxypropyl cellulose and ethyl cellulose, that, have a backbone of cellulose with repeating structure of anhydrous glucose units, each having three reactive -OH (hydroxyl) sites [16]. Ample of work has been done in the past for the preparation and investigation of modified atmosphere packaging films based on protein, lipid and polysaccharide, which provide barrier to the volatile component of food as well as its moisture content [17,18]. However, the main concern is that, these bio-degradable packaging films lack many desirable characteristics of packaging materials to be used at a commercial scale. Various approaches may be used to overcome these problems, including the modification of raw material or the incorporation of plasticizers to improve their film forming characteristics. The type of plasticizer and its concentration can modify the different physical properties of the films [19]. The present study has been conducted to synthesize ethyl cellulose based bio-degradable films with improved physical properties by the incorporation of polyethylene glycol as plasticizer. The ethyl cellulose films were synthesized by taking different ratios of ethyl cellulose and polyethylene glycol and their various properties are studied.

MATERIALS AND METHOD

2.1 Materials

Ethyl cellulose containing ethoxy content of about 48-49.5% was used for film formation. Ethanol (99.9%) was used as solvent for dissolving ethyl cellulose to form a 2.5% w/v solution with viscosity about 18-24 cp. Polyethylene glycol (MW 400) was used as plasticizer. All the chemicals used were of AR grade and were supplied by CDH (P) Ltd., New Delhi.

2.2 Method

2.2.1 Preparation of Ethyl Cellulose Film

All films were prepared by simple casting method. A 2.5% (w/v) solution of ethyl cellulose in ethanol was prepared by constant stirring at 100 rpm for 20-25 minutes using a magnetic stirrer at room temperature. After the formation of a homogenized solution, polyethylene glycol (PEG); as a plasticizer was added to it. The ethyl cellulose and polyethylene

glycol used were in the ratio 4:1, 2:1 and 4:3 for different samples i.e. Sample 1, 2 and 3 respectively. The cast solution was then gently poured into a petridish (diameter = 4 cm) avoiding any bubble formation. The content of the petridish was then dried overnight at room temperature on a levelled surface, thus, resulting in a spotless film that was manually peeled unbroken from the casting surface.

2.3 Assessment of Ethyl Cellulose Films for their Suitability as Food Packaging Material

The samples of ethyl cellulose films containing different ratio of PEG were assessed for the physical and chemical properties so as to be used in a food packaging. Five replicates of each sample was tested for assuring the reproducibility of the results.

2.3.1 Film Appearance

The appearance of the ethyl cellulose films having different ratio of polyethylene glycol was assessed by its texture and uniformity.

2.3.2 Film Thickness

All ethyl cellulose films i.e. Sample1, Sample 2 and Sample 3 were acclimatised at 24°C ± 2°C and 75% RH for 24 hours and the thickness was determined using micro-meter, which recorded upto exactness of ± 0.001mm. The thickness measurements was done at 6 diverse points of the ethyl cellulose films. Mean value was used to estimate the thickness of the resulted ethyl cellulose films [20, 21].

2.3.3 Soluble Matter (SM)

The soluble matter percentage of the resulted films were estimated by immersing the samples (2.0 cm in diameter each) in 50 ml of distilled water, which was slowly stirred for a duration of 24 hrs. The samples were removed and dried in oven for 24 hrs. The following equation was used to calculate the amount of soluble matter in the resulted films [22].

$$\textit{Soluble matter \%} = \left(\frac{\textit{Initial dry weight} - \textit{Final dry weight}}{\textit{Initial dry weight}}\right) x\ 100 \quad (1)$$

2.3.4 Moisture Content (MC)

The moisture content of all samples was calculated by measuring the weight loss of films by drying it in a furnace at 105°C ± 3°C for approximately 12 hrs, till a constant weight had been achieved (dry sample weight). Moisture content was determined as percentage loss in mass during drying of the films using following equation [23, 24].

$$\textit{Moisture content}\ (\%) = \left(\frac{\textit{Intial mass} - \textit{Final mass}}{\textit{Initial mass}}\right) * 100 \quad (2)$$

2.3.5 Scanning Electron Microscopy (SEM)

The microstructural examination of ethyl cellulose films was done using a scanning electron microscope (SEM). Film samples to be tested for SEM were confirmed for no water present in them. For the purpose, they were kept in desiccators with P2O5 for 2 weeks. Further, ethyl cellulose films were frozen using liquid nitrogen and then a cryo-fractured cross section of these films were gold sputtered (*placing gold layer of about 100 A° so as to escape charging up of the films under electron beam*) and then observed under scanning electron microscope (Hitachi S3700 SEM) at 10 kV as accelerating voltage [21].

2.3.6 Mechanical Properties

The wet films were dried in a levelled- forced air drying oven, pre-set at a desired coalescence temperature (The temperature at which the components of miscible solution attract each other) for 24hrs [25]. Mechanical properties like tensile strength (σ_{ut}), elongation at break (EAB %), elastic modulus (E) and work of failure for these ethyl cellulose films were determined by ASTM method, using an Universal Testing Machine (Micro UTM KLA Tencor T150 UTM with a gauge length of 2 mm to 10 mm and a load variable of 50mN to 20 kN.).The samples of each ethyl cellulose film was

cut into a rectangular shape having a measurement of 60 mm x 60 mm and with an average thickness of 1 mm. The samples was griped on the device with a gap of 1 mm and pulled away at a speed of 0.1 mm/s and load of 1 N. The curves plotted between stress (Tension force (F) / cross sectional area(S)) and strain (change in length (**ΔL**) /original length ($\mathbf{L_0}$) were used to determine the tensile properties as per equation 3 and 4, given below. [24, 26].

$$\sigma_{ut} = F/S \quad (3)$$

$$EAB = \Delta L / L_0 \times 100\% \quad (4)$$

Equation 3 was used to calculate the elastic modulus of the ethyl cellulose films, which was calculated by taking the ratio of the maximum force exerted on the film by the cross sectional area and is represented in MPa. Equation 4 represents the percentage change in strain.

Equation 5 is used to calculate the elastic modulus which is the ratio of stress and strain at elastic limit

$$E = \sigma/\epsilon \quad (5)$$

Where, σ denotes stress and ϵ denotes strain at elastic limit

(6)

Work of failure = (Area under curve x cross head speed)/ (film thickness x film width)

Work of failure represented by Equation 6 is a function of work done in breaking the film specimen and is representative of the film thickness.

Applied load is an important parameter to be considered, especially when comparing the results of two studies, since the strain or percent elongation of a polymeric film is normally inversely proportional to the rate of strain and the parameter changes due to various reasons namely sample preparation method, coalescence temperature and also on coating process variables.

2.3.7 Anti-permeability for Oils

To test the anti-permeability of ethyl cellulose films (incorporated with different percentage of PEG) for liquid oils and oily foods, the samples of resulted films of size 2 cm x 2 cm was firmly pressed on the open end of the test tube (inner diameter- 25 mm, outer diameter-27 mm) containing liquid oil (soya bean oil). Further, the test tube was placed upside down on the filter paper, and was observed for the permeability of the oil through the ethyl cellulose films as time went. Observations were repeated on 5 samples of similar composition, for a duration of 3 days storage under normal conditions of temperature, pressure and relative humidity [27].

2.3.8 Reliability, Collapsibility and Water-solubility of Ethyl Cellulose films

The samples of the ethyl cellulose films were considered reliable, as they maintained the integrity of appearance, when peeled from petri dish. Also, the samples of resulted ethyl cellulose films were creased for 20 times at the same line to test its plasticity or collapsibility. Water solubility of the samples were examined by immersing a square piece of each film in 100 ml of distilled water, without stirring, at a temperature of 25°C. Water solubility of ethyl cellulose film was estimated by observing the time taken for the film to totally dissolve in water [21].

RESULTS AND DISCUSSIONS

3.1 Film appearance

The samples of ethyl cellulose films formed on a flattened surface was peeled off unspoiled from the petri-dish. The appearance of the sample 1 was hazy and that of sample 3 was translucent while the appearance of sample 2 was opaque, as seen from Figure 1. However the texture of all the samples was smooth and homogeneous and showed no breakage while peeling from the surface. These same samples were used for further testing.

(a)

(b)

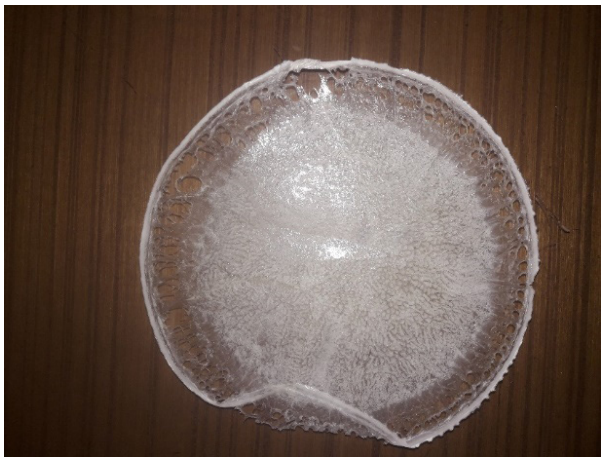

(c)

Fig. 1: Appearance of surface of Ethyl cellulose film containing different ratio of ethyl cellulose and polyethylene glycol in ethanol (a) EC: PEG-4:1 (b) EC: PEG-2:1 (c) EC: PEG-4:3

Table 1: Mean values of weights (mg) and soluble matter (%) of various samples

SAMPLE	EC : PEG	INITIAL WEIGHT(sd)	FINAL WEIGHT (sd)	SOLUBLE MATTER (sd)
1	4:1	0.041 (0.00018)	0.016 (0.00028)	60.97 (0.00023)
2	2:1	0.032 (0.00029)	0.014 (0.00035)	56.25 (0.00032)
3	4:3	0.052 (0.000167)	0.013 (0.00061)	75 (0.00039)

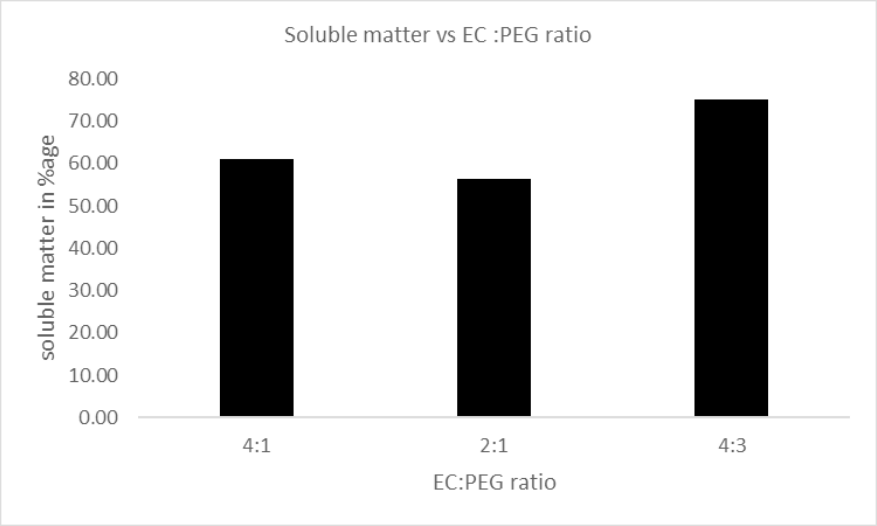

Fig. 2: Soluble Matter Content for Ethyl Cellulose Films of Different EC: PEG Compositions

3.2 Films Thickness

The samples of resulted films were measured for the film thickness at 6 different points (centre of each film, at centre of each quarter of the film and edges of the film). Average value of all the points was calculated to determine the thickness of each ethyl cellulose film. The mean thickness of various samples was measured as 1.010 mm with a standard deviation of 0.01, 1.017 mm with standard deviation of 0.04 and 1.014 mm with a standard deviation of 0.02 for sample 1 (EC:PEG-4:1), sample 2 (EC:PEG-2:1)and sample 3 (EC:PEG-4:3) respectively.

3.3 Soluble Matter (SM)

The samples of the resulted ethyl cellulose films immersed in distilled water for 24 hrs, showed no swelling, as well as, they maintained their structure. The result of soluble matter among different categories of ethyl cellulose film was maximum for the ethyl cellulose film containing EC: PEG ratio 4:3, which showed approximately 75.00 % total soluble matter and minimum for the ethyl cellulose film containing EC: PEG ratio 2:1, having approximately 56.25% total soluble matter. However, the soluble matter for ethyl cellulose film containing EC: PEG ratio 4:1 showed the total soluble matter of about 60.97 %. The mean values of initial and final weights (with standard deviation) for each sample their Percentage of soluable matter is as given in Table 1. The soluble matter content for ethyl cellulose films of different EC: PEG compositions is as shown in Figure 2.

Sample of ethyl cellulose film with EC: PEG 2:1 ratio showed a slight lower moisture percentage (about 10% decrease) as compared with the sample having EC: PEG 4:1 ratio, while the ethyl cellulose film having EC: PEG 4:3 ratio showed a great increase in moisture content. Figure 3 gives the moisture content for ethyl cellulose films of different EC: PEG

Table 2: Mean values of weights (mg) and moisture content (%) of different EC: PEG Compositions

SAMPLE	EC:PEG	INITIAL WEIGHT (mg)	FINAL WEIGHT (mg)	MOISTURE CONTENT (%)
1	4:1	0.043	0.016	62.79
2	2:1	0.022	0.011	50.00
3	4:3	0.044	0.014	68.18

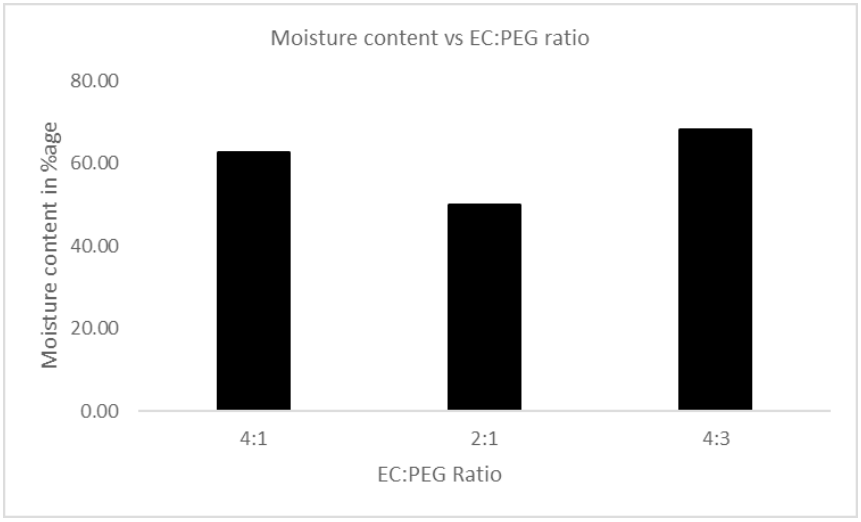

Fig. 3: Moisture Content for Ethyl Cellulose Films of Different EC: PEG Compositions

compositions.The low moisture percentage of EC: PEG 2:1 can be explained as a result of interference of water structure in the binding condition. The mean values of weights (mg) and moisture content (%) of different EC: PEG compositions are given in Table 2.

3.5 Scanning Electron Microscopy (SEM)

The microstructural examination of the ethyl cellulose films was qualitatively studied using scanning electron microscopy (SEM). The images of the surface and cross section of EC films revealed the effects of addition of different percentage of PEG. Figure 4 show the SEM images of PEG plasticized ethyl cellulose films with EC: PEG ratio 4:1, EC: PEG ratio 2:1 and EC: PEG ratio 4:3 respectively. The surface image of both ethyl cellulose films with EC:PEG ratio 4:1 and 2:1 showed unbroken, compact and smooth traits without any micro-cracks, which meant polyethylene glycol has been easily incorporated into ethyl cellulose as plasticizer. However the EC film with ratio 4:3 showed few cracks and the surface was not apparently smooth, which might be due to decreased polymer-polymer cohesiveness, with increases content of plasticizer, leading to the deterioration of the quality of film. After observing all the three films, it is inferred that the EC: PEG ratio of 2:1 and EC: PEG ratio of 4:1 both are considered suitable for uniform and good quality film.

The structure of the film is affected by the organization of various constituents in the film making solution and the interaction taking place between the constituents during the drying of the ethyl cellulose film. The microstructural analysis of the film is also helpful to know the mechanism of water vapor permeability across the films and the arrangement of components in the film and their effect on mechanical properties of the film [28].

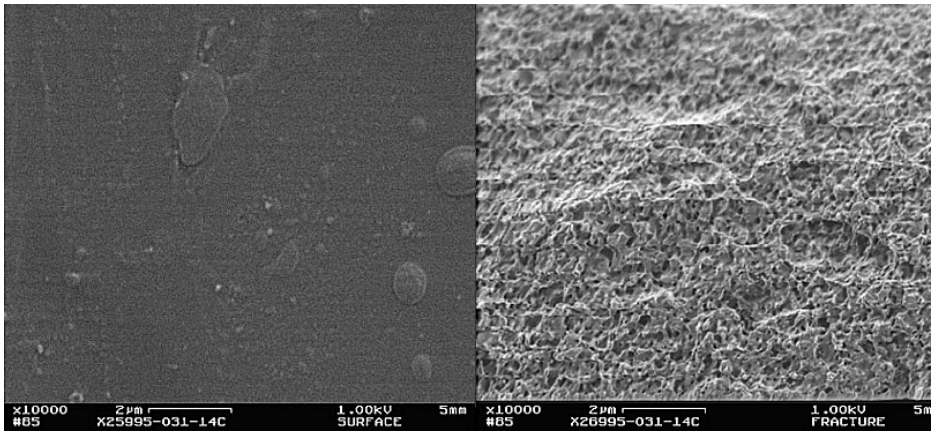

(i) (ii)

(a) EC: PEG - 4:1

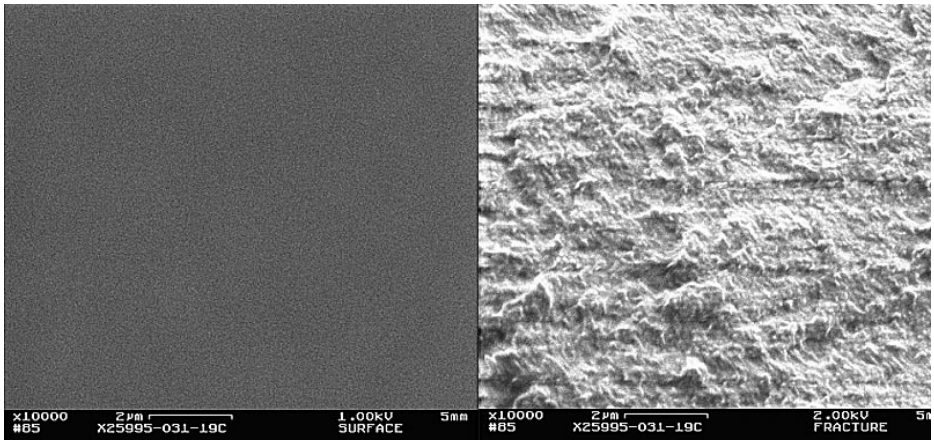

(i) (ii)

(a) EC: PEG - 2:1

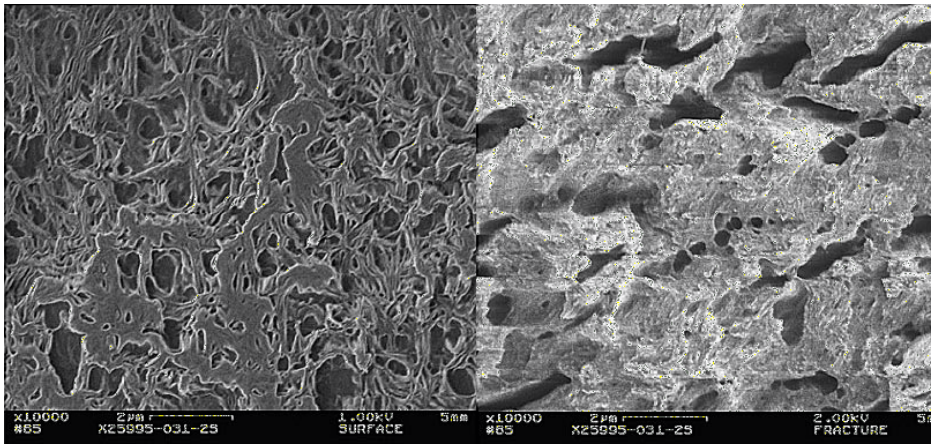

(i) (ii)

(a) EC: PEG - 4:3

Fig. 4: SEM Images of PEG 400 Plasticized Ethyl Cellulose Films (a) EC: PEG ratio: 4:1; (i) surface of the film, (ii) cross section of the film (b) EC: PEG ratio: 2:1; (i) surface of the film, (ii) cross section of the film. (c) EC: PEG ratio: 4:3; (i) surface of the film, (ii) cross section of the film.

Table 3: Mean values of tensile strength of various samples at different coalescence temperature

Coalescence temperature in (°C)	Tensile strength in (MPa)		
	SAMPLE 1 (sd)	SAMPLE 2 (sd)	SAMPLE 3 (sd)
30	0.007 (0.00015)	0.014 (0.001)	0.013 (0.00125)
40	0.013 (0.0017)	0.015 (0.00146)	0.014 (0.00115)
50	0.016 (0.00114)	0.017 (0.00126)	0.016 (0.00321)
60	0.016 (0.00125)	0.017 (0.00111)	0.015 (0.00167)
70	0.0149 (0.00143)	0.0156 (0.00129)	0.0149 (0.00125)

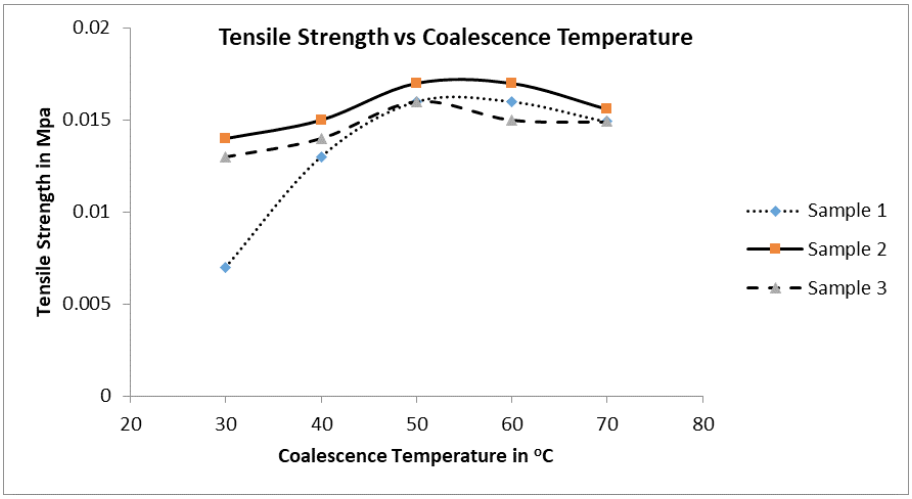

Fig. 5: Plot of Tensile Strength Vs Coalescence Temperature (Sample1-EC: PEG - 4:1; Sample 2- EC: PEG- 2:1; Sample 3 – EC: PEG- 4:3).

3.6 Mechanical Properties

Characteristic features of the load-time or typical stress-strain profiles from tensile tests are routinely used to characterize the polymer properties. Toughness is directly proportional to the area under a load time or load-displacement curve which is quantitated as energy. The higher the amount of energy a polymeric film can absorb prior to break under load, the higher is its toughness. Elastic modulus is an indicator of the elasticity of the film, with lower values corresponding to higher elasticity. On the other hand, tensile strength is an indicator of the film strength, with larger values corresponding to the stronger films. Ideally a film coating must be both strong and elastic and, therefore, must yield a higher tensile strength-to-elastic modulus ratio. This ratio has been used as an indicator of the overall mechanical quality of the films.

Figure 5 depicts the plot of tensile strength as a function of coalescence temperature for the samples prepared. The tensile strength of the films increased with a corresponding increase in coalescence temperature and did not reach a plateau within the temperature range used in this investigation. It was observed that sample 2 showed best characteristics in comparison to other samples. At temperatures above 60°C, no appreciable differences were observed in the tensile strengths of the films cast from all formulations. This could possibly be due to evaporation of the plasticizers from the films at elevated temperatures. Mean values of tensile strength of various samples at different coalescence temperatures is as given in Table 3.

Mean values of work of failure of various samples at different coalescence temperatures are given in Table 4. The values of work of failure

Table 4: Mean values of work of failure of various samples at different coalescence temperature

Coalescence temperature in °C	Work of failure (Nm/sec)		
	SAMPLE 1 (sd)	SAMPLE 2 (sd)	SAMPLE 3 (sd)
30	5 (0.67)	5.4 (0.78)	0.1 (0.0124)
40	4 (0.45)	5.9 (0.64)	3 (0.21)
50	5.5 (0.167)	6.1 (0.51)	5 (0.14)
60	15 (0.253)	19 (0.92)	13 (1.5)
70	30 (1.67)	32 (1.12)	17 (2.1)

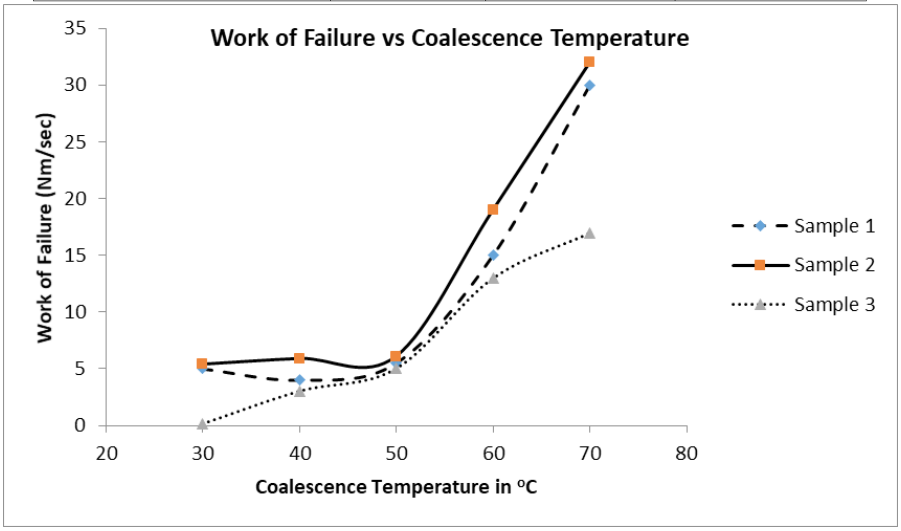

Fig. 6: Work of Failure vs Coalescence Temperature of Different Ethyl Cellulose Films (Sample1-EC: PEG - 4:1; Sample 2- EC: PEG - 2:1; Sample 3 – EC: PEG - 4:3).

plotted as a function of coalescence temperature for all the three samples are shown by Figure 6. No significant difference was observed in the work of failure for the films cast from formulation EC:PEG ratios 4:1 and 2:1. The work of failure value for the formulation with EC:PEG ratio 4:3 is almost approaching zero at lower coalescence temperature i.e. at 30°C. At higher coalescence temperatures, the higher values of work of failure depict a significantly higher absorption of energy, possibly due to the complete penetrate of plasticizer molecules into the polymeric network. From the load-time profiles, it was observed that the films at and above 50°C exhibited distinct and prolonged plastic deformation with the resultant increase in the area under the curve. This could be due to strong interaction between the neighboring polymer particles at and above the coalescence formulation.

The influence of coalescence temperature on the elastic modulus values of the films is shown in Figure 7. Plot of applied load with time is used to calculate the value of elastic modulus. Higher value of load carrying ability indicate a high value of elastic modulus, thus reflects the strength of the film. In general, it is observed that as the coalescence temperature get increased, the elastic modulus of the films increased almost linearly, for all the samples of the polymeric films, until they achieved a peak. A decline in the values of elastic modulus values was further observed, at elevated coalescence temperatures, which is due to the softening of the film at elevated temperature. Mean values of load

Table 5: Mean values of load carrying capacities for various time periods

Time in (sec)	Applied load (Elastic Modulus in MPa)		
	Sample 1	Sample 2	Sample 3
0	0.3 (91.52)	0.5 (152.54)	0.31 (94.57)
2	0.3 (91.52)	0.9 (274.57)	0.31 (94.57)
5	0.35 (106.78)	1.5 (457.62)	0.32 (97.62)
10	1.1 (335.58)	2.2 (671.17)	0.97 (295.92)
12	0.3 (91.52)	2.5 (762.69)	1.5 (457.62)
15	0.3 (91.52)	2.6 (793.2)	1.8 (549.42)
20	0.31 (94.57)	2.4 (732.18)	0.29 (88.47)
25	0.3 (91.52)	0.5 (152.54)	0.29 (88.47)
30	0.31 (94.57)	0.5 (152.54)	0.295 (90)
35	0.3 (91.52)	0.5 (152.54)	0.29 (88.47)
40	0.31 (94.57)	0.51 (155.59)	0.295 (90)

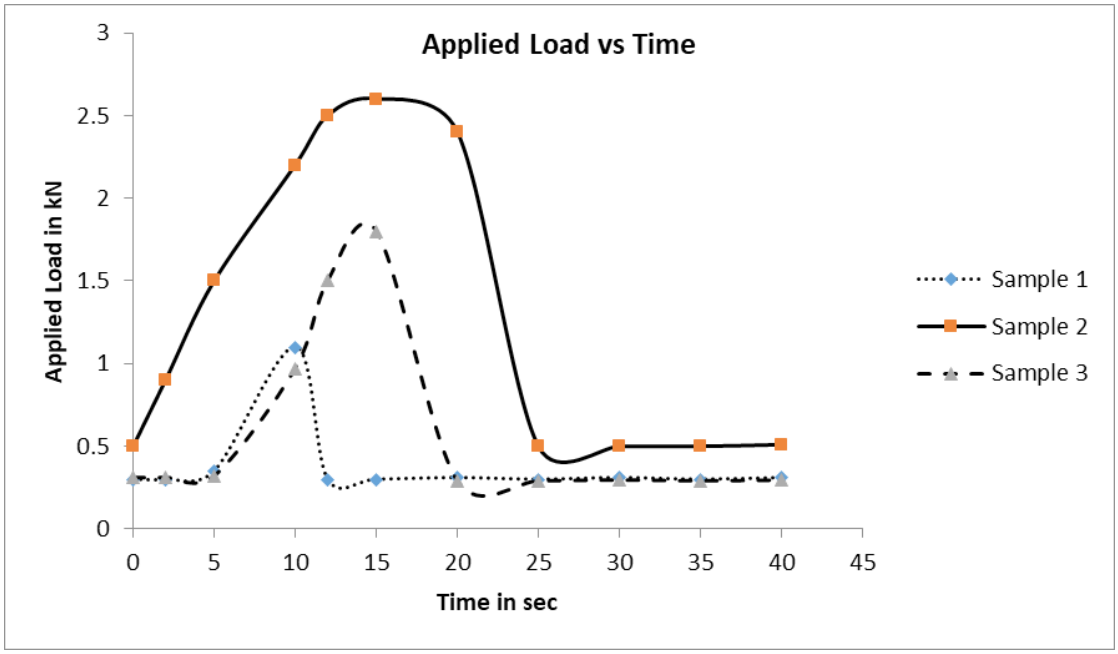

Fig. 7: Applied Load Vs Time of Different Ethyl Cellulose Films (Sample1-EC: PEG - 4:1; Sample 2- EC: PEG - 2:1; Sample 3 – EC: PEG - 4:3) used for calculation for elastic modulus.

Table 6: Comparison of properties of ethyl cellulose film with different EC: PEG ratios

SAMPLE	EC:PEG	APPEARANCE	THICKNESS (mm)	COLLAPSIBILITY (folding at a point)
1	4:1	Hazy	1.02	NO FISSURE
2	2:1	Opaque	1.01	NO FISSURE
3	4:3	Translucent	1.01	SLIGHT FISSURE

carrying capacities for different ethyl cellulose films at various time periods is as given in Table 5.

The independent interpretation of these three parameters, i.e., tensile strength, work of failure, and elastic modulus may not always lead to meaningful conclusions with respect to the in situ performance of the films. The mechanical properties of the films was observed to be dependent on the type of the plasticizer and the coalescence temperature. With an increase in the coalescence temperature, the films exhibited a characteristic transition in their mechanical properties, i.e., from a soft and weak system(as evident from lower values of tensile strength, strain at break and elastic modulus) to a hard and tough system (as evident from higher values of tensile strength, strain at break, and elastic modulus). The optimal values of the tensile strength-to-elastic modulus ratio obtained for films of all three formulations dried at 50°C indicate that the films coalesced at or around this temperature may be less susceptible to physical defects.

3.7 Anti-permeability for Oil

The bio polymeric films used for packaging food, especially oily foods or liquid oil containing edibles, should be anti-permeable for oils, otherwise leakage of oil from packaging films will cause decline in the appearance, flavor and shelf life of packaged foods. So, the anti-permeability test of different sample of ethyl cellulose was carried out. The result showed no trace of oil leakage through the ethyl cellulose films, thus offering good anti-permeability for oil [29].

3.8 Reliability, Collapsibility and Water-solubility of Ethyl Cellulose Films

Samples of ethyl cellulose film formed by casting method showed complete integrity while peeling off from the surface of the petri-dish. The thickness of the resulted films are as reported in Table 1. The folding test performed for finding the collapsibility of ethyl cellulose films showed that 20 times folding of film at a particular trace did not showed any fissure in sample1 and sample 2 but in sample 3 slight marking was observed. The visual test showed that the sample 2 had a good flexibility of all the films. Further the water solubility of the samples of ethyl cellulose films with different ratio of EC: PEG also indicated a delayed water solubility in sample 2 in comparison to sample 1 and sample 3. The comparison of the properties of ethyl cellulose films with different EC: PEG ratios is as given in Table 6.

CONCLUSION

The ethyl cellulose films with different amount of polyethylene glycol, as plasticizer, had been casted to be used as a bio-degradable food packaging material. Among the different EC: PEG ratios used, the film with EC: PEG ratio 2:1 was found to have better suitability for food packaging applications and showed a very good flexibility and collapsibility. The soluble matter and moisture content of the film with EC: PEG ratio 2:1 was found to be minimum, among all the films tested. The developed film showed a maximum tensile strength of 0.0165 MPa at a coalescence temperature of 50^{o}C and a maximum work of failure of magnitude 29.5 Nm/sec was observed at temperature of 70^{o}C. The

film also exhibited a maximum load of 2.65 kN for a substantially good amount of time. The film was hence found to be mechanically stable of handling sufficient amount of load. The three parameters, characterising mechanical strength of the film namely tensile strength, work of failure, and elastic modulus were found to be good for the reported polymeric films.

CONFLICT OF INTEREST

The work presented in this manuscript has been carried out for the research purpose only and there is no conflict of interest involved in it.

REFERENCES

[1] B. L. Ottoni , R. M. Deus, J. A. G. Junior, Â. M. G. de Carvalho and R. A. G. Battistelle, "Communication and Biodegradable Packaging Relationship: A Paradigm for Final Disposal", *Journal of Applied Packaging Research, vol 10* (1). 10-27, 2018.

[2] American Chemistry Council (ACC). Plastics Division: Resin Identification Codes.2010.http://www.americanchemistry.com/s_plastics/doc.asp?CID=1102 & DID=4644

[3] I.S. Arvanitoyannis, "Totally and partially biodegradable polymer blends based on natural and synthetic macromolecules: preparation, physical properties, and potential as food packaging materials, *Journal of Macromolecular Science", Reviews in Macromolecular Chemistry and Physics, vol 39*. 205–271, 1999.

[4] 4T. Labuza, W. M. Breene, "Applications of "active packaging" for improvement of shelf life and nutritional quality of fresh and extended shelf life foods", *J. Food Process. Preser, vol 13.1-69*, 1989.

[5] T. P. Labuza, "An introduction to active packaging for foods", *Food Technol., vol 50*. 68-71, 1996.

[6] S.K.Bajpai, C. Navin and L.Ruchi, "Water vapor permeation and antimicrobial properties of sago starch based films formed via microwave irradiation", *International Food Research Journal, vol 18*, 417-426, 2011.

[7] K.Petersen, P. V.Nielsen, G. Bertelsen, M. Lawther, M. B Olsen, N. H. Nilsson and G. Mortensen, "Potential of bio-based materials for food packaging", *Trends Food Sci. Technol., vol 10*. 52-68, 1999.

[8] J. M. Krochta and C. De Mulder-Johnston, "Edible films and biodegradable films: Challenges and Opportunities", *Food Technol, vol 51*. 61-74, 1997.

[9] M. Malik and R. Kaur, "Synthesis of NIPU by the carbonation of canola oil using highly efficient 5,10,15-tris(pentafluorophenyl) corrolato-manganese(III) complex as novel catalyst", *Polym. Adv. Tech., vol 29* (3). 1078-1085, 2018.

[10] A. Aggarwal, R. Kaur and R.S.Walia, "PU Foam Derived from Renewable Sources: Perspective on Properties Enhancement: An Overview", *Europ. Polym. Jl., vol 95*. 255-274, 2017.

[11] M.Kumar and R.Kaur, "Glass fiber reinforced rigid polyurethane foam: synthesis and characterization", *e-Polymers., vol 7 (*6). 517-521, 2017.

[12] M. Malik and R. Kaur, "Influence of aliphatic and aromatic isocyanates on the properties of polyether-ester polyol based PU adhesive system", *Polym. Eng. Sci., vol 58* (1).112-117, 2018.

[13] M. Malik and R. Kaur, ".Mechanical and Thermal Properties of Castor Oil–Based Polyurethane Adhesive: Effect of TiO_2 Filler", *Adv. Polym. Tech., vol 37*(1). 24-30, 2018.

[14] R. Kaur and M. Kumar, "Function of Silicon Oil in the Castor Oil Based Rigid Polyurethane Foams", *Jl. Polym. Eng., vol 33* (9). 857-861, 2013.

[15] M. Kumar and R. Kaur, "Effect of Different Formulations of MDI on Rigid Polyurethane Foams based on Castor Oil", *Int. Jl. Sci. Res. Review, vol 2* (1) Special Issue April – May. 29-42, 2013.

[16] G. S. Rekhi and S. S. Jambhekar, "Ethyl-cellulose -- a polymer review, *Drug development and industrial pharmacy", vol 21* (1).61-77, 1995.

[17] M. B. Perez-Gago and J.M. Krochta, "Lipid particle size effect on water vapor permeability and mechanical properties of whey protein-beeswax emulsion films", *J. Agric. Food Chem., vol 49*. 996-1002, 2001.

[18] H. M. Lai and G.W. Padua, "Water vapor barrier properties of zein films plasticized with oleic acid, *Cereal Chem.", vol 75.* 194-199, 1998.

[19] R.L. Carmen and B. Roland, "Mechanical and Water Vapor Transmission Properties of Polysaccharide Films, Drug Dev." *Ind. Pharm., vol 22* (12). 1201–1209, 1996.

[20] S Yuvaraj and N Rajeswari," Chitosan/ Modified Banana Epidermis Starch Composite Films for Food Packaging Applications" *Journal of Applied Packaging Research, vol 10* (4),14-27,2018.

[21] G. Chen, B. Zhang, J. Zhao, and H. Chen, "Development and characterization of food packaging film from cellulose sulfate, Food Hydrocoll.", *vol 35.* 476–483, 2014.

[22] E. M. Ciannamea, P. M. Stefani, and R. A. Ruseckaite, "Physical and mechanical properties of compression molded and solution casting soybean protein concentrate based films", *Food Hydrocoll., vol 38.* 193–204, 2014.

[23] T. Chowdhury and M. Das, "Moisture sorption isotherm and isosteric heat of sorption of edible films from blends of starch, amylose and methyl cellulose", *International Food Research Journal, vol 19* (4) 1669- 1678, 2012.

[24] ASTM. (1995). Standard test methods for water vapour transmission of materials. Standards designations: E96-95 Annual book of ASTM standards (pp. 406-413). Philadelphia, *PA: American Society for Testing and Materials.*

[25] N.H. Parikh, S.C. Porter and B.D.Rohera, "Tensile properties of free films cast from aqueous ethyl cellulose dispersions", *Pharmaceutical Research, Vol.10* (6) 810-815, 1993.

[26] W.Y.Weng, Z. Tao, G.M. Liu, W.J. Su, K. Dsako, M.Tanaka and M.J. Cao, "Mechanical, barrier, optical properties and antimicrobial activity of edible films prepared from silver carp surimi incorporated with ε-polylysine", *Packaging Technology and Science, vol 27* (1), 37-47, 2014.

[27] G. Hu, J. Chen and J. Gao, "Preparation and characteristics of oxidized potato starch films. Carbohydrate Polymers", *vol 76* (2). 291-298, 2009.

[28] S. Wang, X. Kuang, Li, B., Wu, X., and T. Huang, "Physical properties and antimicrobial activity of chilled meat pads containing sodium carboxy-methyl cellulose", *Journal of Applied Polymer Science, vol 127* (1). 612-619, 2013.

[29] M. R. De Moura, M. V. Lorevice, L. H. C. Mattoso and V. Zucolotto, "Highly stable, edible cellulose films incorporating chitosan nanoparticles", *Journal of Food Science, vol 76* (2). 25-29, 2011.

Materials Research Express

ACCEPTED MANUSCRIPT

Characterization and parametric optimization of tribological properties of Mo blend composite coating

To cite this article before publication: Ankit Tyagi *et al* 2019 *Mater. Res. Express* in press https://doi.org/10.1088/2053-1591/ab1d0a

Manuscript version: Accepted Manuscript

Accepted Manuscript is "the version of the article accepted for publication including all changes made as a result of the peer review process, and which may also include the addition to the article by IOP Publishing of a header, an article ID, a cover sheet and/or an 'Accepted Manuscript' watermark, but excluding any other editing, typesetting or other changes made by IOP Publishing and/or its licensors"

This Accepted Manuscript is **© 2019 IOP Publishing Ltd**.

During the embargo period (the 12 month period from the publication of the Version of Record of this article), the Accepted Manuscript is fully protected by copyright and cannot be reused or reposted elsewhere.
As the Version of Record of this article is going to be / has been published on a subscription basis, this Accepted Manuscript is available for reuse under a CC BY-NC-ND 3.0 licence after the 12 month embargo period.

After the embargo period, everyone is permitted to use copy and redistribute this article for non-commercial purposes only, provided that they adhere to all the terms of the licence https://creativecommons.org/licences/by-nc-nd/3.0

Although reasonable endeavours have been taken to obtain all necessary permissions from third parties to include their copyrighted content within this article, their full citation and copyright line may not be present in this Accepted Manuscript version. Before using any content from this article, please refer to the Version of Record on IOPscience once published for full citation and copyright details, as permissions will likely be required. All third party content is fully copyright protected, unless specifically stated otherwise in the figure caption in the Version of Record.

View the article online for updates and enhancements.

This content was downloaded from IP address 14.139.251.100 on 30/04/2019 at 10:11

Characterization and parametric optimization of tribological properties of Mo blend composite coating

Ankit Tyagi[a]; Dr. Shailesh Mani Pandey[a]; Prof. R.S. Walia[a]; Prof. Qasim Murtaza[a]*

[a] Department of Mechanical Engineering, Delhi Technological University, Delhi

*Corresponding author: Email-qasimmurtaza@gmail.com

Abstract

The aim of present work was to develop Mo-blend composite coating using atmospheric plasma spray technique and to optimize its tribological properties such as temperature, frequency and load as process parameters, using Taguchi L9 orthogonal array (OA). The SEM microstructures also help in confirming the optimal process conditions for tribological properties of a composite coating, while EDS was used to confirm the elemental peaks of composite coating. HRXRD was used to confirm the phase deposition of composite coating. Calculation and prediction of optimum process parameters were done by using raw data and signal to noise (S/N) ratio of ANOVA (Analysis of variance). The significant process parameters for COF according to their contribution percentage are frequency (51.20) followed by the load (30.36 %), and temperature (17.12 %). The percentage contribution of frequency (87.81 %) was highest followed by temperature (2.69 %) and load (2.53 %) for weight loss.

Keywords: Atmospheric plasma spray coating, coefficient of friction (COF), weight loss, Taguchi optimization.

1. Introduction

In recent years, development of engine start-stop system in the automobiles has significantly reduced emission of harmful gases into the atmosphere. A study reveals that implementation of this system can considerably reduce emission of CO_2 upto 20% per vehicle and 3-8% fuel consumption [1-3]. Plenty of research has been going on to encounter the challenges caused by the friction and wear between the components. To reduce these losses one approach is using friction modifiers in the lubricating oil, such as Al_2O_3 and TiO_2 nanoparticle which were able to reduce COF upto 50% [4-7]. Another approach to mitigate these losses is to use different advanced coating methods. To enhance surface properties, different surface modification technology can be used such as physical vapour deposition, chrome plating [8], flame spraying, high velocity oxy-fuel coating and atmospheric plasma spray coating [9]. Atmospheric plasma spray coating is an extensively used technique for deposition of anti-wear and anti-corrosion materials. Atmospheric plasma spray technique has higher deposition efficiency and thermal energy density, hence lower amount of heat is transferred

Accepted Manuscript

to the substrate material as Mo cladding on NiCr powders improves inter lamellar bonding. Mo has low hardness, high melting temperature and has tribo oxidation behavior, so MoO_2 layer can be generated on the rubbing surfaces under dry condition thereby significantly reducing friction between them, by behaving as a solid lubricant [10-12]. For the above mentioned reasons Mo has been regularly used in automotive applications. Mo and NiCrC can be used for fabrication of a composite material having excellent tribological properties. It has been examined that anti-seizure performance of materials can be improved by doping Mo in NiCrC coating. During dry conditions, Mo is oxidized into MoO_2 and rapidly forms a film having good lubricating property on rubbing surfaces and prevents direct adhesion between them, which finally helps in reduction of friction. On the other hand, Mo formed a MoS_2 film having anti corrosion and good lubrication properties under oil-lubricated conditions. Particularly in oil starvation and boundary lubrication, MoS_2 tribofilm carries the substantial load and hampers the direct rubbing between friction pair [13-14]. Niranatlumpong et al. [15] in his research studied the effect of Mo coating on coefficient of friction and wear performance under dry condition. It is observed from the results that 25 wt. % Mo-NiCrBSi coating exhibits high porosity, low hardness and better wear performance. However, excessive use of Mo results in inter lamellar debonding due to reduction in the interlayer adhesion [16, 17]. However, the dependence of the tribological performance on Mo content has not been demonstrated.

In the present work, multiple contents of Mo-blended composite coatings are prepared by atmospheric plasma spray coating. Taguchi L9 orthogonal array (OA) have been used for optimization of the tribological properties and wear mechanism of Mo- blend composite coating by varying process parameters, i.e. temperature, frequency, and load. The process parameter of the Mo-blend composite coatings so produced is analyzed in term of Coefficient of friction (COF), and weight loss. Calculation and prediction of optimum process parameters was done by using raw data and signal to noise (S/N) ratio of ANOVA (Analysis of variance). The aim of the work is to find out the optimal conditions for COF, and weight loss of developed composite coating. Mo- blend composite coating on cast iron substrate are selected keeping in mind their present application in the field of engine assembly. The present study, tis relevant in exploring the opportunity of using composite coating in order to achieve a lower coefficient of friction, lower weight loss and lesser percentage residual stress.

Accepted Manuscript

2. Experimental procedure

2.1. Material and methods

The substrate material of dimension 80*240*2mm has been fabricated with its constituent particles using sand casting process. Initially, the substrate was ground in order to obtain smoother surface, then after, the substrate plate was grit blasted using 40 mesh of Al_2O_3 at 0.6 MPa compressed air pressure, so that adhesion strength of deposited coating could be increased. The particle size distribution of NiCr, Mo and CrC were in the range of 40-75µm. The chemical composition of the substrate material is illustrated in table 1. V-type of the mixer were used to mix the composite powders and was dried to remove the moisture before spraying. Atmospheric plasma spray torch, PT F4 (Sulzer-Metco make) was used in a sealed chamber for coating deposition. A robot to ensure controlled speed and reproducible trajectories was used. Hydrogen and argon were choosen as primary and secondary gases respectively. The composite powder deposition rate was controlled at 50±5 gram/min. During spraying the substrate temperature was controlled with continuously flowing water jets around. The coating thickness ranged from 350-450µm. The SEM images were used to study the surface morphology of composite coating, while EDS was used to examine and evaluate the elemental peaks of composite coating. HRXRD was used to confirms the deposition phases of composite coating.

Table 1 Chemical composition of cast iron substrate material

Element	C (%)	S (%)	Cu (%)	Mn (%)	Cr (%)	Si (%)	P (%)
Composition	3.75±0.05	0.06±0.005	0.035±0.03	0.53±0.01	0.04±0.01	2.70±0.05	0.36±0.02

2.2.Measurement of coefficient of friction (COF), and weight loss for the composite coating

The wear behavior of developed coating was performed on the pin on disc high temperature linear reciprocating tribometer having pin diameter and coating sample size of 8 mm and 20*20*5mm respectively, with maximum temperature range of tribometer is 550^{o}C and data acquisition system for appropriate identification of coefficient of friction and wear characteristics of mating components.

It was concluded from the literature review that temperature, frequency and applied load are the processing parameters that influence tribological behavior of developed coating. Table 2 shows trial condition parameters chosen for the experiment at all process condition in the procedure of COF, and weight loss of the composite coating.

Accepted Manuscript

Table 2 Design parameters and trial conditions chosen for the Taguchi's experiment

Designation	Parameters	Trial 1	Trial 2	Trail 3
A	Temperature (^oC)	100	200	300
B	Frequency (Hz)	10	15	20
C	Load (N)	10	25	40

The experimental results for all process condition was recorded in the table 3 and were examined to find out the effects of all parameters. Lower-the-better type, quality characteristic was chosen for calculation of S/N ratio data for COF, weight loss and residual stress and test results at all condition were converted into S/N ratio.

Table 3 Experimental results of Taguchi L_9 OA of COF, and weight loss

Experiments	COF			S/N ratio (db)	Weight loss (mg)			S/N ratio (db)
	R_1	R_2	R_3		R_1	R_2	R_3	
1	0.78	0.78	0.72	2.37	7.22	7.44	7.50	-17.37
2	0.51	0.52	0.52	5.73	9.61	9.30	9.01	-19.37
3	0.35	0.35	0.35	9.03	10.90	11.30	11.12	-20.91
4	0.60	0.61	0.62	4.29	7.30	7.51	7.38	-17.38
5	0.48	0.48	0.47	6.43	10.29	10.65	10.34	-20.36
6	0.52	0.52	0.52	5.67	11.01	11.07	11.31	-20.93
7	0.47	0.47	0.47	6.55	8.22	8.19	8.18	-18.27
8	0.51	0.51	0.51	5.84	10.04	10.23	10.07	-20.09
9	0.31	0.31	0.31	10.17	11.06	11.75	11.04	-21.05
T= overall mean of COF= 0.50					T= overall mean of weight loss = 9.59			

The practice of S/N ratio is recommended by Taguchi in order to measure better quality characteristics deviating. Therefore higher S/N ratio will be the best level for the optimum trial for process parameters. The S/N ratio for lower-the-better type trial process can be figured as:

$$(S/N)_{LB} = -10\log\left[\frac{1}{R}\sum_{J=1}^{R}(X_j^2\right] \quad (1)$$

where X_j, j= 1,2,3….n are the response values lower than the test conditions.

ANOVA (Analysis of variance) was implemented to recognize parameters that were statistically significant in the test experimental results. Through ANOVA and S/N ratio analyses, optimum arrangement of parameters were predicted.

Accepted Manuscript

3. Results and discussions

3.1.Coating characterization

Fig. 1(a-d) shows the cross-sectional morphology and bonding conformity of developed coating using scanning electron micrograph (SEM). SEM images shows uniform melting of powder expect very few partially melted powder. Formation of lamellae with molten, partially molten & non-melted particles was also observed. Presence of splats confirmed homogeneous coating and uniform bonding of sprayed material. EDS results confirm homogeneous mixing of composite powders as shown in fig. 1(e). Presence of Mo, Cr, S, O and C confirms formation of carbide, sulphide and oxide layers.

Fig. 1 (f) shows phase deposition of composite coating using HRXRD. The peaks obtained during deposition was at 40.4º and 73.6º, which confirms the presence of Cr_2C_2 and $Cr_{0.5}Mo_{0.5}$ respectively. The HRXRD peaks also confirm the presence of hard phases such as MoO_2 and Mo_2C in the composite coating.

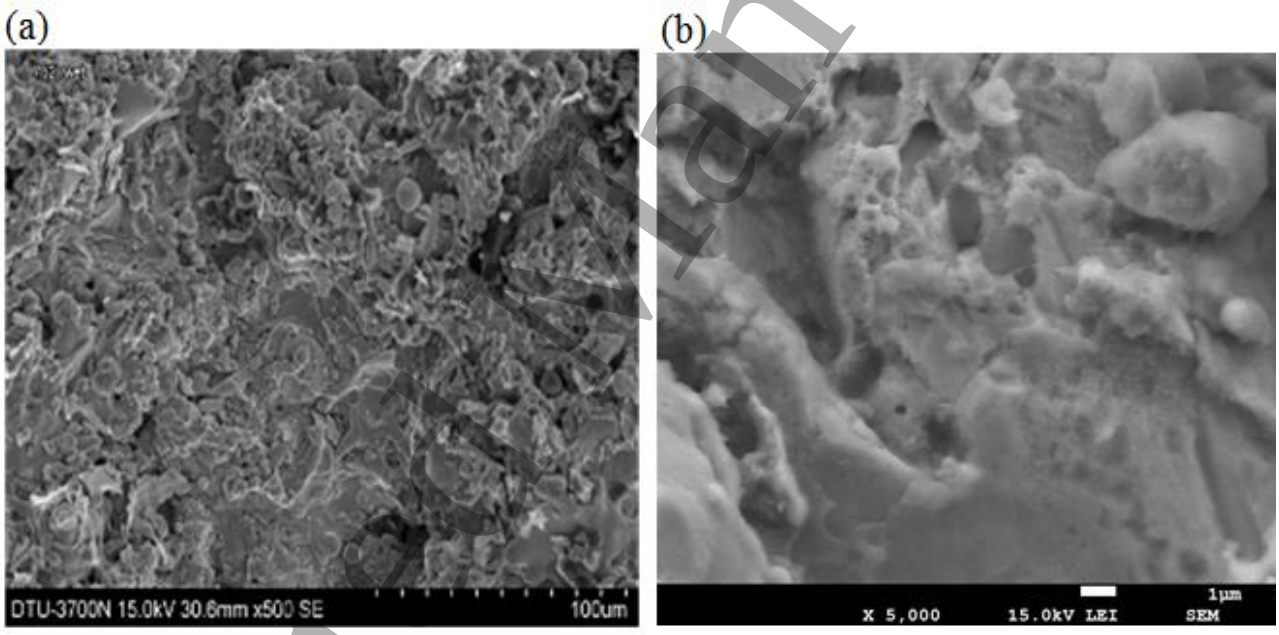

Accepted Manuscript

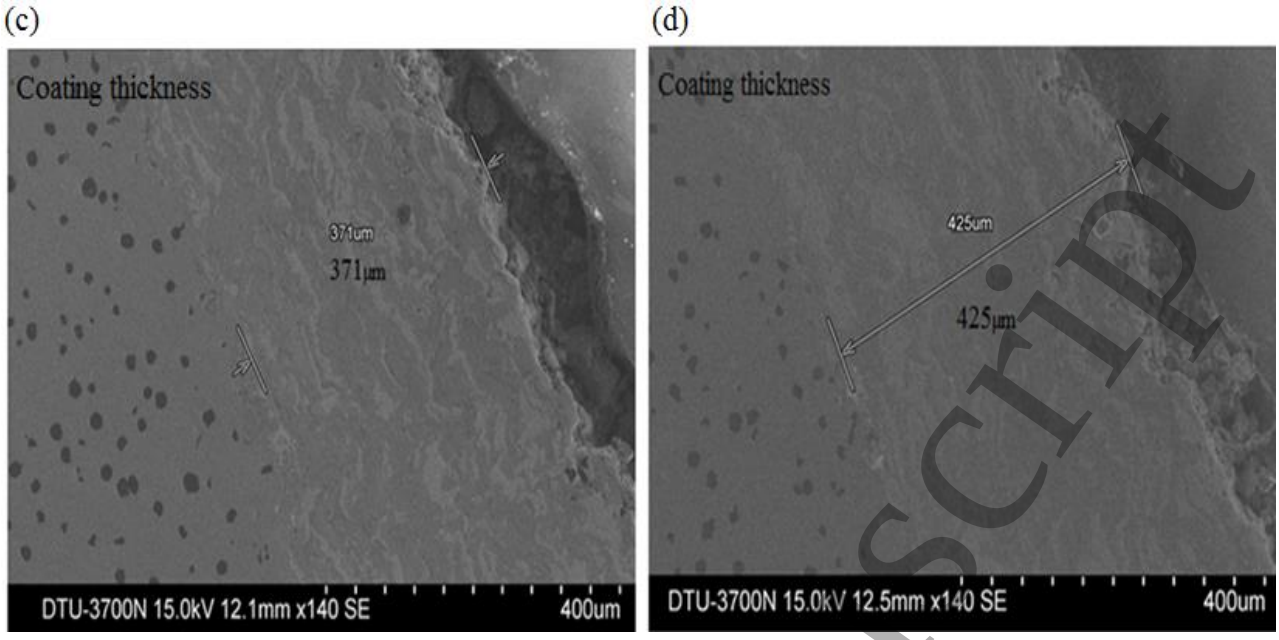

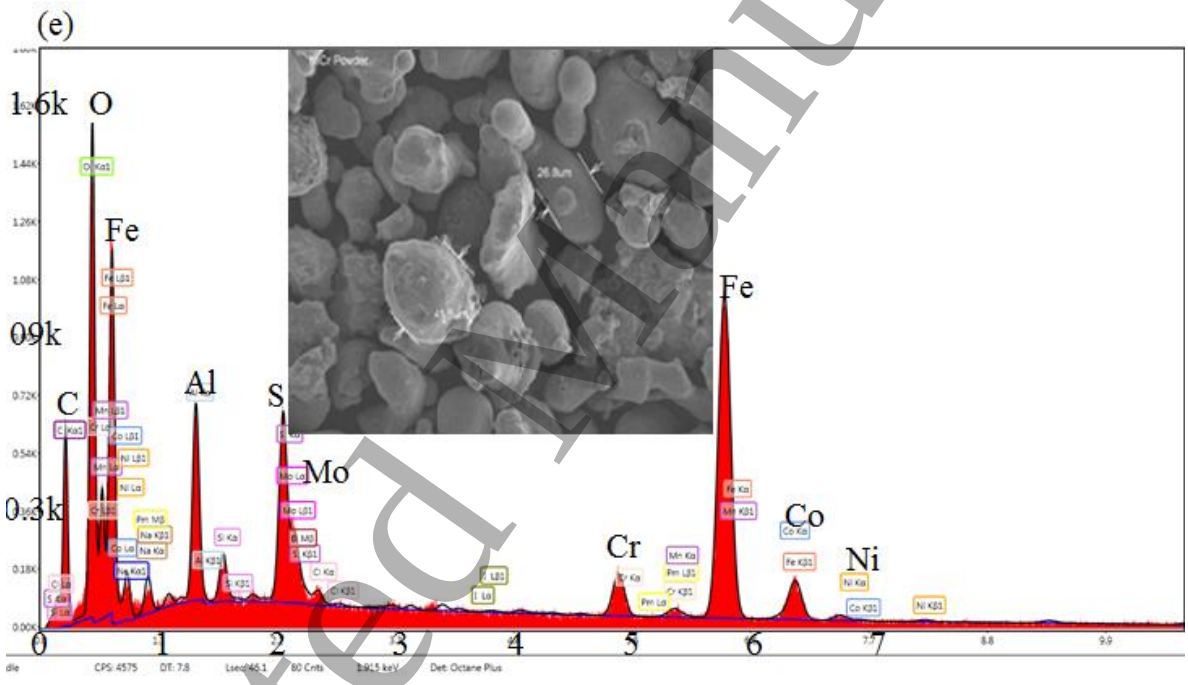

Accepted Manuscript

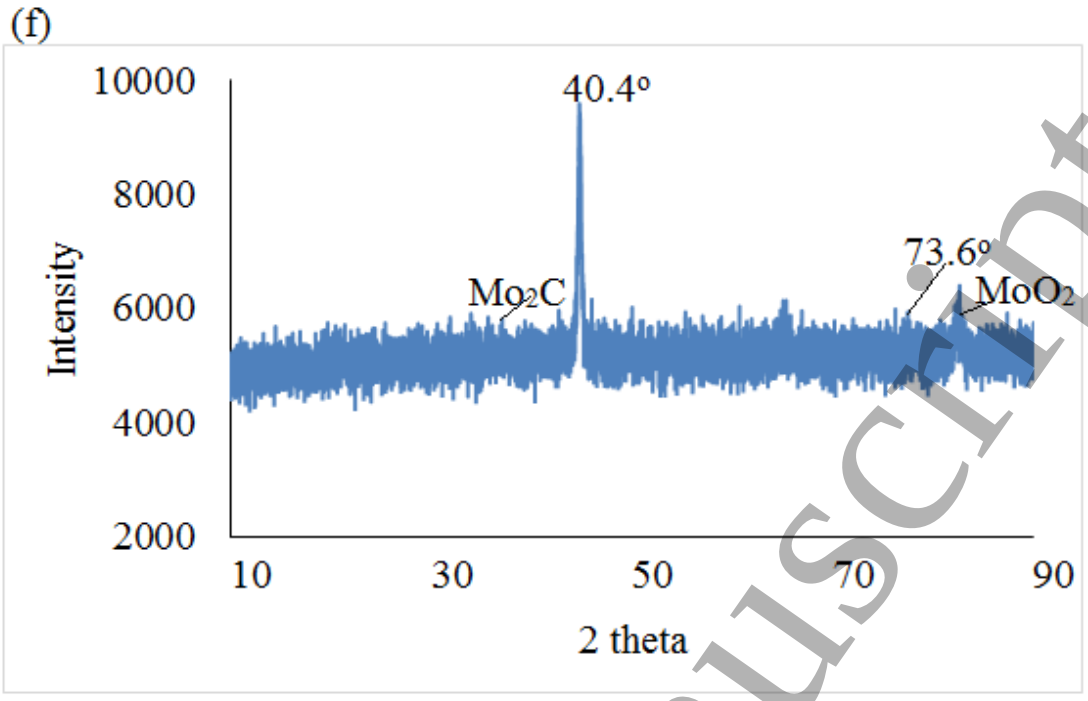

Fig. 1 (a-d) SEM image (e) EDS result (f) HRXRD result of composite coating

3.2.Effects of parameters on coefficient of friction (COF)

The main effects and average values of COF and S/N ratio for all parameters at trail T1, T2 and T3 were calculated and are illustrated in table 4 and also plotted in fig. 2.

Table 4 Main effects and average values of COF (S/N ratio and raw data)

Parameter	Trial	Temperature (°C)		Frequency (Hz)		Load (N)	
Data		Raw Data	S/N Ratio	Raw Data	S/N Ratio	Raw Data	S/N Ratio
Average values (weight loss)	T1	0.54	5.71	0.61	4.40	0.59	4.63
	T2	0.53	5.46	0.50	6.00	0.47	6.73
	T3	0.43	7.52	0.39	8.29	0.43	7.34
Main effect of weight loss	T2-T1	-0.008	-0.24	-0.11	1.59	-0.11	2.09
	T3-T2	-0.10	2.057	-0.10	2.29	-0.046	0.60
Difference (T3-T2)-(T2-T1)		-0.098	2.30	0.06	-0.69	0.72	-1.48

Fig. 2 (a) shows deviation of COF with respect to the temperature on the composite coating. The result shows that COF obtained at 300°C temperature is lowest on comparing at 100°C and 200°C temperature for the composite coating, while the S/N ratio is highest at 300°C. The above result suggests a stronger signal and lesser noise, hence offers an optimum test results at the same trial condition.

Accepted Manuscript

From the fig. 2 (b) it can be observed that there is a decrease in the value of COF as the frequency increases from 10 to 20 Hz. The lowest value of COF is obtained for the highest frequency of 20 Hz, while COF obtained is highest at 10 Hz frequency for the chosen range. The S/N ratio corresponds to 20 Hz is highest and decreases as the frequency decreases. Figure 2 (c) shows deviation of COF with respect to the load. The results show that the COF obtained is maximum at load of 10N and decreases with increase in load from 10 to 40N. However, S/N ratio value for COF (raw data) is maximum at a load 40 N followed by 25 N and 10N, while S/N ratio value is minimum at 40N and maximum at 10N. Fig. 3 shows the experimental results of average COF with respect to sliding distance. It can be observed that as the load, frequency and temperature increase, the COF decreases probably due to formation of tribo-oxidative, solid lubricant sulphide layer during wear test as reported earlier [17-21]. It has been previously reported that during the wear test, increase in temperature results in increase in thermal stresses that cause plastic flow of material which reduces COF and also provide abrasive wear resistance [19]. A study based on APS composite alloy coating observed that composite coating was temperature dependent. It was also observed that as the temperature, load and sliding velocity increase, the COF and wear rate decrease for piston ring application due to formation of solid lubricant layer [18]. Zabala et al. [20] observed that MoS_2 (0.15) and CrN (0.22) coating show low COF for piston ring due to tribolayer formation on the coated surface and having anti-wear property.

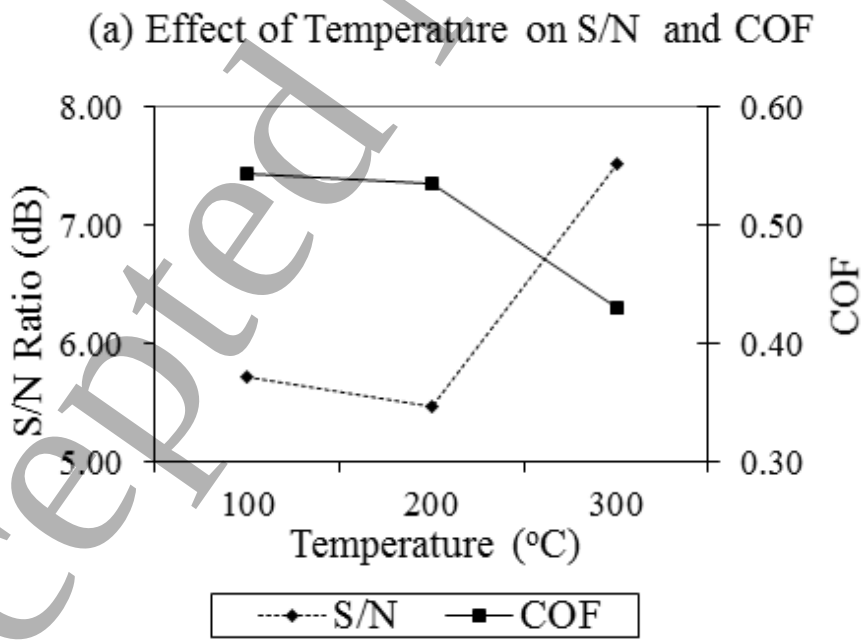

Accepted Manuscript

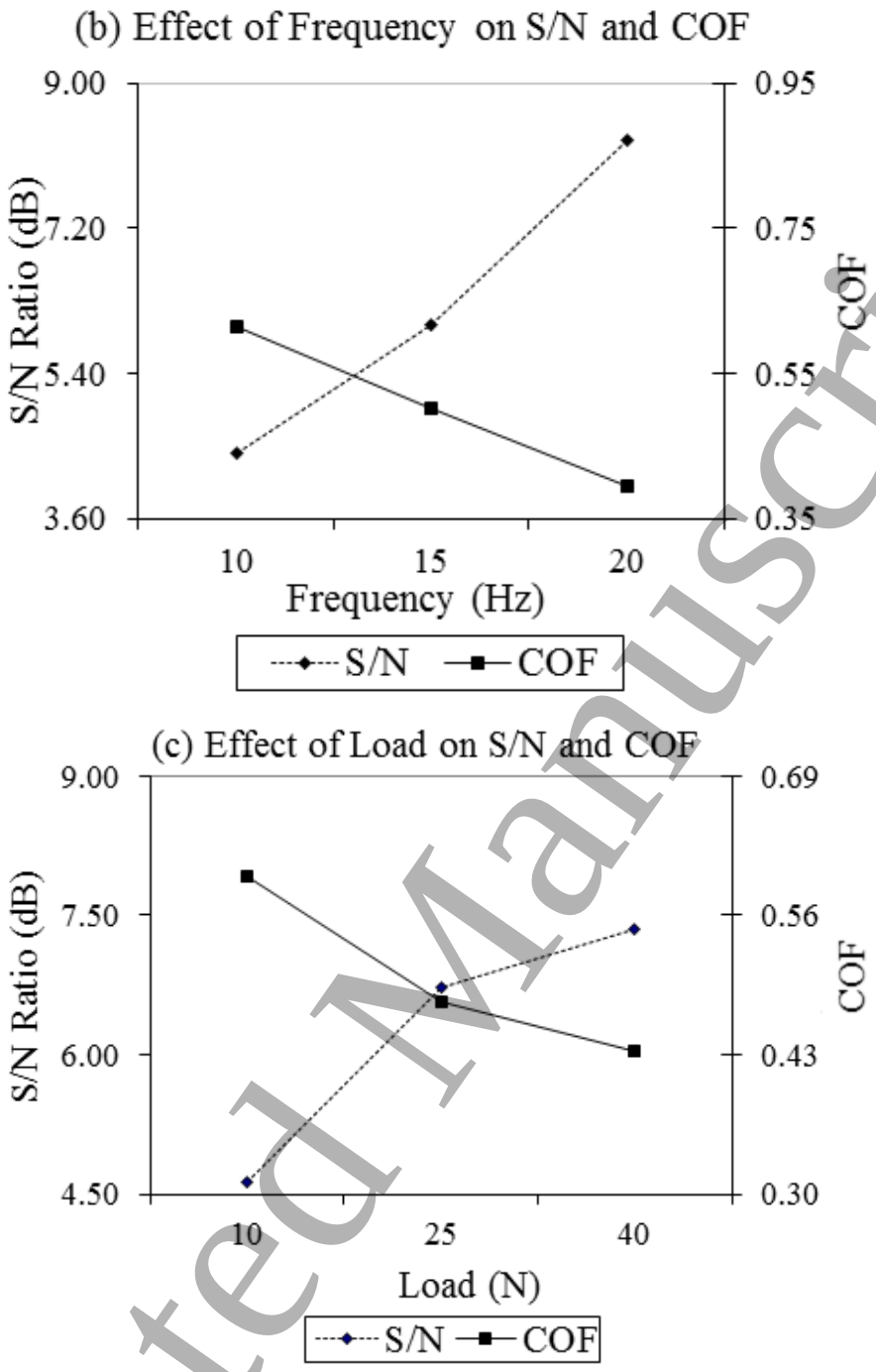

Fig. 2 Deviation of COF with parameters (a) Temperature (^{O}C) (b) Frequency (Hz) (c) Load (N)

As lower-the-better type of quality characteristic was chosen for better results, lower values of COF was sought. It is quite evident from fig. 2 that COF is optimum i.e. minimum at trial 3 of parameter A (300^{o}C), trial 3of the parameter B (20Hz) and trial 3 of the parameter C (40N). On the other hand, the trial parameters A, B and C, the lowest values of mean response correspond to the highest values of S/N ratio. From the above discussion it is clear that COF increases as the temperature, frequency and load increases and may be attributed due to tribo-

Accepted Manuscript

oxidation or running wear encountered by the flow of metal during the rubbing process. Fig. 3 shows the experimental results of average COF with respect to sliding distance. It can be seen that as the load, frequency and temperature increase, the COF decreases due to formation of tribo-oxidative, solid lubricant sulphide layer during wear test. From fig. 4 it can be observed that due to the presence of delamination, tribo-oxidative layer appears as a dominant wear mechanism during the process in accordance with earlier reports [17-20]. EDS result confirms homogeneous mixing of composite powders with presence of Mo, Cr, S, O and C elements together with, the formation of carbide, sulphide (MoS_2) and oxide (MoO_2) layers. The HRXRD peaks also confirm the presence of hard structured phases such as MoO_2 and Mo_2C in the composite coating as shown in fig 1 (g).

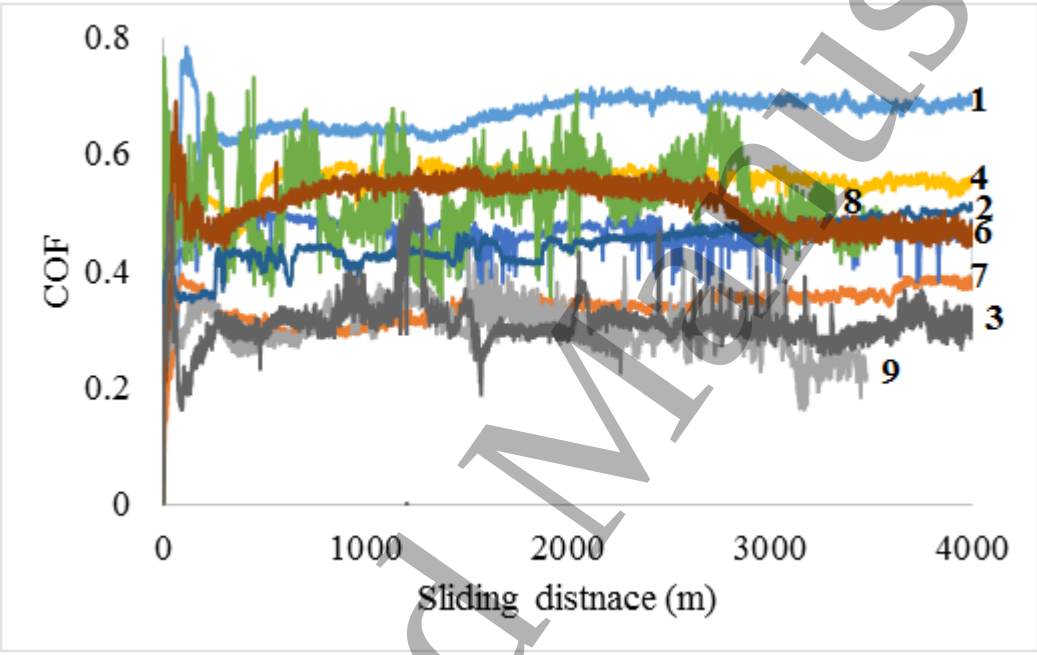

Fig. 3 Experimental results of sliding distance Vs COF

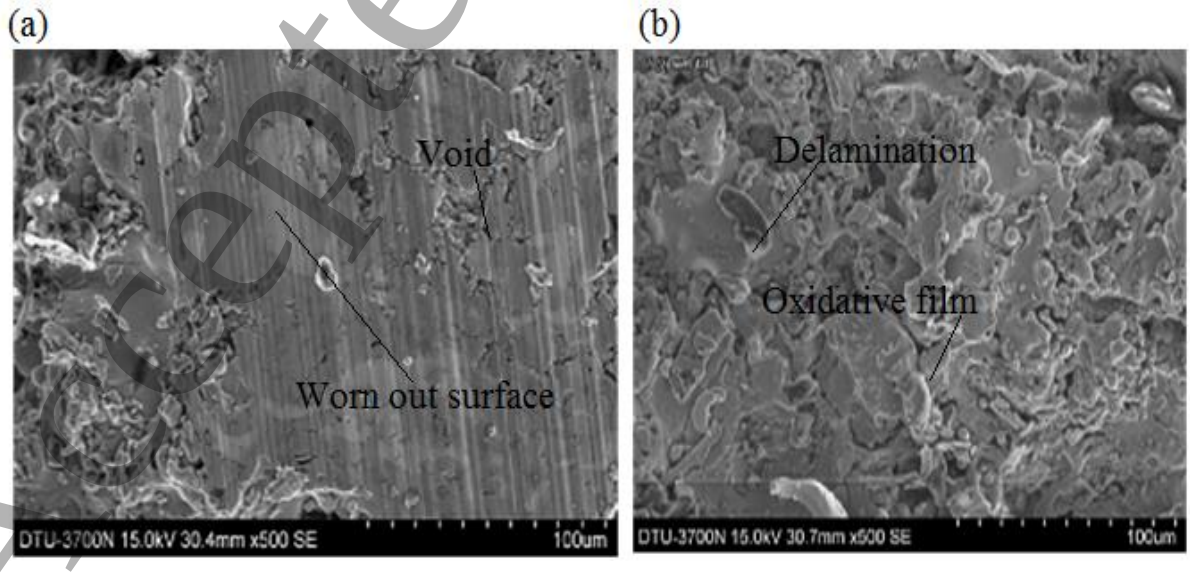

Accepted Manuscript

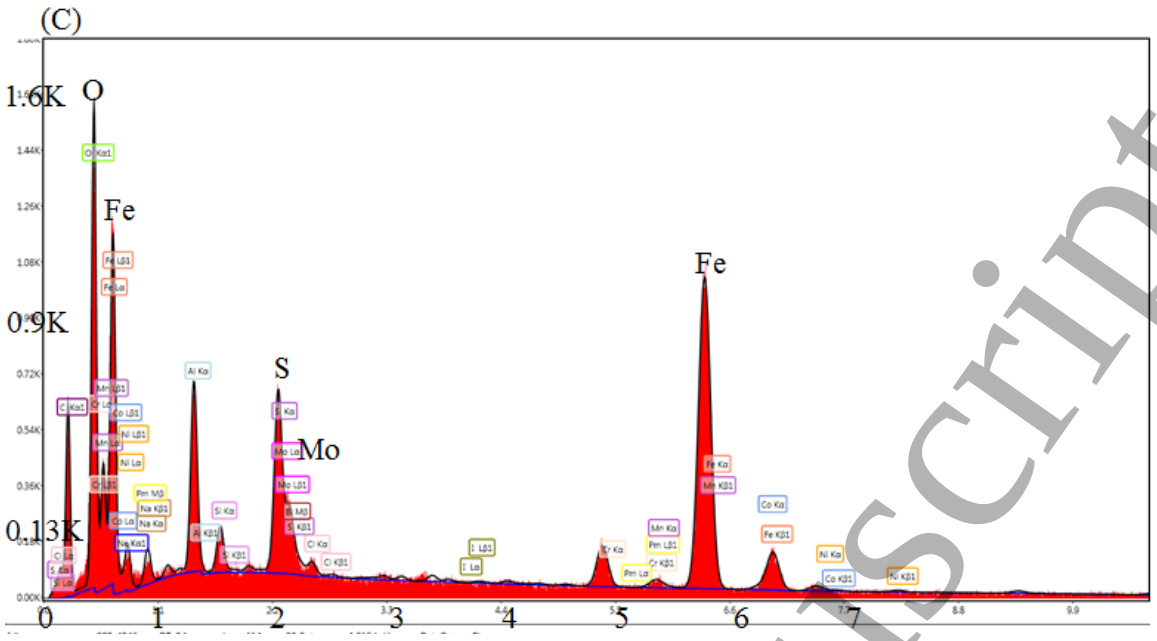

Fig. 4 (a) SEM images (b) EDS result of worn out surfaces.

To examine the significance of parameters of COF, ANOVA was performed. Table 5 shows the pooled ANOVA S/N data and raw data of COF. It is quite evident that process parameters A, B, and C considerably affect mean and variation in COF. The percentage contribution of frequency (51.20 %) was highest followed by load (30.36 %), and temperature (17.12 %) for COF.

Table 5 Pooled ANOVA for COF (S/N ratio and raw data)

Source type	SS		DOF		V		F-Ratio		SS'		P (%)	
	Raw data	S/N data	Raw data	S/N data	Raw data	S/N data	Raw data	S/N data	Raw data	S/N data	Raw data	S/N data
Temperature (°C)	0.072	7.57	2	2	0.036	3.78	131.25	27.15	0.07	7.29	17.12	17.66
Frequency (Hz)	0.21	22.89	2	2	0.107	11.44	392.35	82.12	0.21	22.62	51.20	53.43
Load (N)	0.12	12.10	2	2	0.063	6.05	232.65	43.41	0.12	11.82	30.36	28.24
E (Pooled)	0.0054	0.27	20	2	0.00027	0.13	-	-	0.0071	1..11	1.30	0.65
Total	0.42	42.85	26	8	-	-	-	-	0.42	42.85	100	100

SS= Sum of squares; DOF= Degree of freedom; V= Variance; SS'= pure sum of squares

3.2.1. Estimation of optimal performance characteristics

3.2.1.1.Optimal values of response characteristics for COF (predicted mean)

Table 6 shows the average values of COF at optimum level of significant parameters. The

Accepted Manuscript

optimum value of the estimated mean (μ) COF can be obtained as follow [21-24]:

$\mu_{COF} = A_3 + B_3 + C_3 - 2T$ (2)

$\mu_{COF} = 0.25$

Table 6 Average values of COF at optimal levels

Trail	COF
A_3	0.43
B_3	0.39
C_3	0.43
T	0.50

A3= trail 3 of temperature; B3= trail 3 of frequency; C3 = trail 3 of load; T= average value of response

The Confirmation experiments (CI_{CE}) for 95 % confidence interval and confidence interval population (CI_{POP}) was calculated by using equations:

$$CI_{CE} = \sqrt{F_a(1, f_e)V_e\left[\frac{1}{n_{eff}} + \frac{1}{R}\right]} \quad (3)$$

$$CI_{POP} = \sqrt{\frac{F_a(1, f_e)V_e}{n_{eff}}} \quad (4)$$

Where, $F_a(1,f_e)$ = F ratio at the confidence level of (1-a) against DOF 1 and degree of freedom error f_e; R= sample size for confirmation experiments; V_e = variance error; $n_{eff.} = \left(\frac{N}{1+DOF}\right)$; N= total no. of trials; and DOF = total degree freedom associated in the estimate of mean response.

The values obtained by the ANOVA is:

N= 27; $f_e = 20$; $V_e = 0.00027$; $n_{eff.} = 3.86$; R= 3; $F_{0.05}(1, 20) = 3.49$

From eq. 3 $CI_{CE} = \pm 0.024$

From eq. 4 $CI_{POP} = \pm 0.016$

The predicted optimum values for COF is given by:

CI_{CE}: $0.22 < \mu < 0.27$

CI_{POP}: $0.23 < \mu < 0.26$

The optimum values of COF were predicted at the designated trials of significant parameters.

Temperature (A, trial 3) = 300°C

Frequency (B, trial 3) = 20 Hz

Load (C, trial 3) = 40N

Accepted Manuscript

3.2.1.2.Confirmation experiments

Three confirmation tests were performed at the optimal situation of the process parameters. For COF process parameters are set temperature at trail 3 (300^{o}C), frequency at trail 3 (20 Hz), and load at trail 3 (40N). The average value for COF of composite coating was measured as 0.25 which was in the predicted optimum range of 95 % confidence interval for COF for the composite coating.

3.3.Effects of parameters on weight loss (mg)

The main effects and average values of weight loss and S/N ratio for all parameters at trail T1, T2 and T3 were calculated and are illustrated in table 7 and also plotted in fig. 5.

Fig. 5 (a) shows a deviation of weight loss with respect to the temperature on the composite coating. The result shows that weight loss obtained at 300^{o}C temperature is highest while the S/N ratio is lowest when compared to 100^{o}C and 200^{o}C temperature for the composite coating at the same condition.

Table 7 Main Effects and average values of weight Loss (S/N ratio and raw data)

Parameter	Trial	Temperature (^{o}C)		Frequency (Hz)		Load (N)	
Data		Raw Data	S/N Ratio	Raw Data	S/N Ratio	Raw Data	S/N Ratio
Average values (weight loss)	T1	9.26	-19.22	7.66	-17.67	9.54	-19.46
	T2	9.65	-19.55	9.94	-19.94	9.32	-19.27
	T3	9.86	-19.80	11.17	-20.96	9.91	-19.85
Main effect of weight loss	T2-T1	0.38	-0.33	2.28	-2.27	-0.21	0.195
	T3-T2	0.21	-0.24	1.22	-1.01	0.58	-0.57
Difference (T3-T2)-(T2-T1)			0.08	-1.06	1.25	0.79	-0.77

From the fig. 5 (b), it can be observed that there is an increase in the value of weight loss as the frequency increases from 10 to 20 Hz. The highest value of weight loss is obtained for the highest frequency of 20 Hz, while weight loss obtained is lowest at 10 Hz frequency for the chosen range. The S/N ratio corresponds to 20 Hz is lowest and increases as the frequency decreases.

Figure 5 (c) shows the deviation of weight loss with respect to load. The results show that the weight loss obtained is minimum at load of 25N and maximum at 40N. However, S/N ratio value is minimum at a load 40 N followed by 10 N and maximum at 25N.

Accepted Manuscript

As lower-the-better type quality characteristic was chosen for better results, lower values of weight loss were sought. It is quite evident from fig. 5 that weight loss is optimum i.e. minimum at trial 1 of parameter A (100^{o}C), trial 1 of the parameter B (10Hz) and trial 2 of the parameter C (25N). However, for the parameters A, B and C, the minimum values of average data correspond to the maximum values of S/N ratio. From the above discussion it is clear that weight loss increases as the temperature and frequency increases and may be attributed to running wear encountered by the flow of metal. Initially as the load increases from 10-25N, weight loss of composite coating decreases due to the formation of oxide layer and later increases as the load increases from 25- 40N.

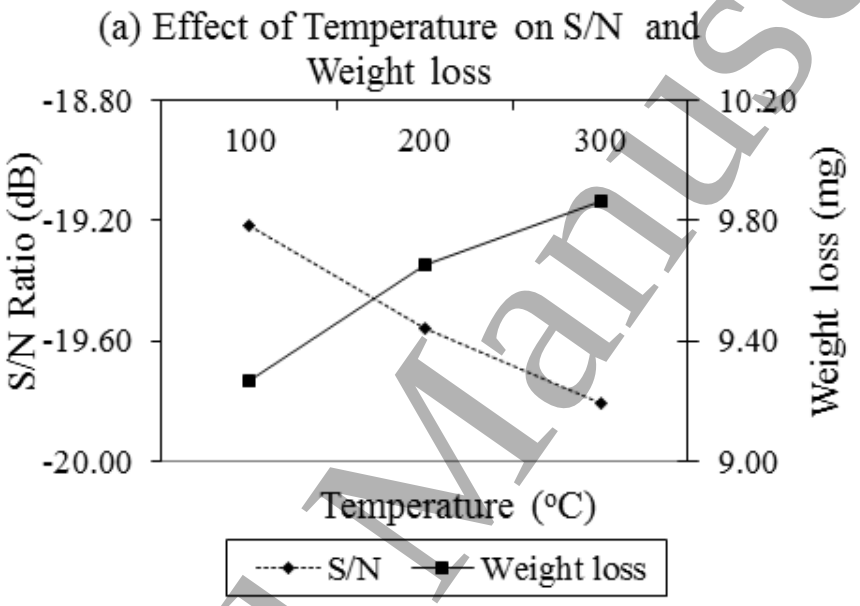

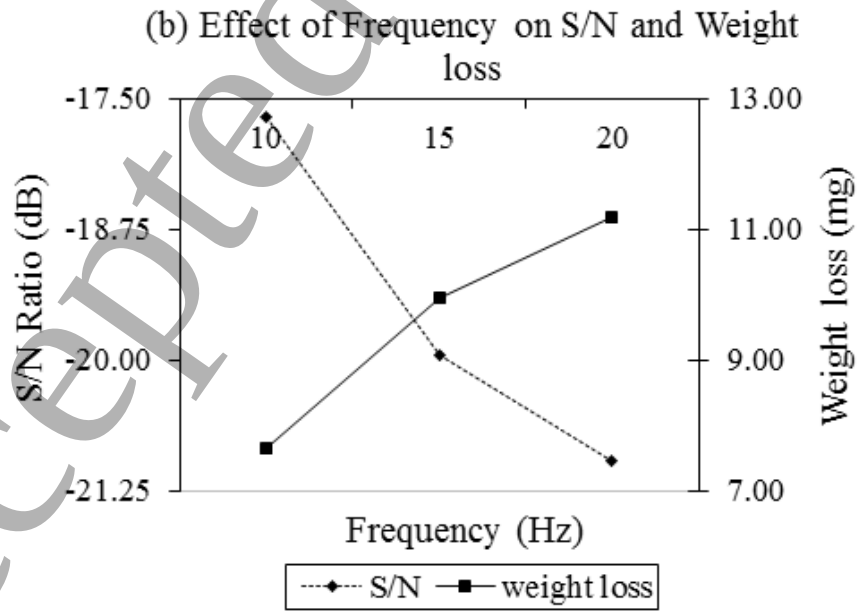

Accepted Manuscript

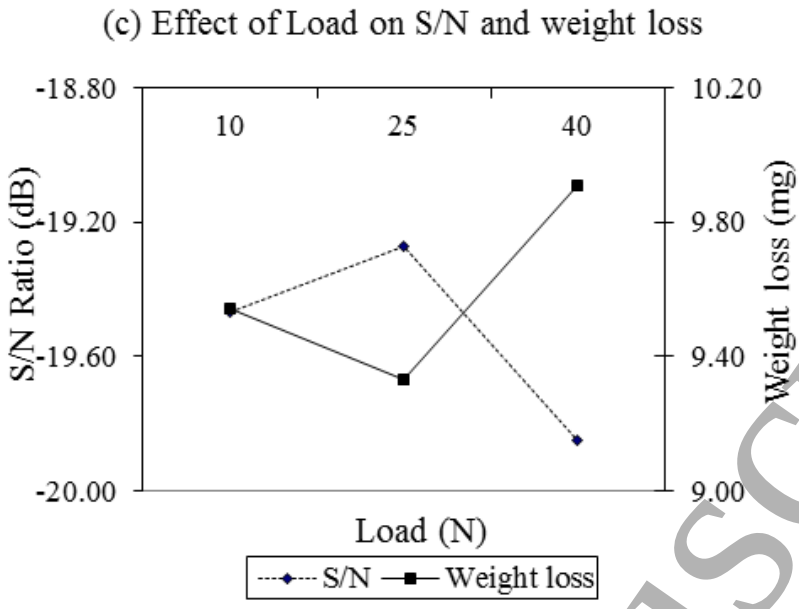

Fig. 5 Deviation of weight loss with parameters (a) Temperature (^{O}C) (b) Frequency (Hz) (c) Load (N)

To examine the significance of parameters of weight loss, ANOVA was performed. Table 8 shows the pooled ANOVA S/N data and raw data of weight loss. It is quite evident that process parameters A, B, and C considerably affect mean and variation in weight loss values. The percentage contribution of frequency (87.81 %) was highest followed by temperature (2.69 %) and load (2.53 %) for weight loss.

Table 8 Pooled ANOVA for weight loss (S/N ratio and raw data)

Source type	SS		DOF		V		F-Ratio		SS'		P (%)	
	Raw data	S/N data	Raw data	S/N data	Raw data	S/N data	Raw data	S/N data	Raw data	S/N data	Raw data	S/N data
Temperature (°C)	1.65	0.52	2	2	0.82	0.26	3.86	20.09	1.22	0.49	2.69	2.88
Frequency (Hz)	53.92	17.02	2	2	26.96	8.51	126.12	656.50	53.49	17.00	87.81	94.10
Load (N)	1.55	0.52	2	2	0.77	0.26	3.63	20.06	1.12	0.49	2.53	2.87
E (Pooled)	4.27	0.026	20	2	0.21	0.01	-	-	5.55	0.10	6.96	0.14
Total	61.40	18.09	26	8	2.36	-	-	-	61.40	18.09	100	100

3.3.1. Estimation of optimal performance characteristics

3.3.1.1. Optimal values of response characteristics for weight loss (predicted mean)

Table 9 shows the average values of weight loss at optimum level of significant parameters.

Accepted Manuscript

The optimum value of the estimated mean (μ) for weight loss can be obtained by using equation 2.

$\mu_{weight\ loss} = 7.06$

The Confirmation experiments (CI_{CE}) for 95 % confidence interval and confidence interval population (CI_{POP}) was calculated by using equations 3 and 4.

The values obtained by the ANOVA is:

N= 27; $f_e = 20$; $V_e = 0.21$; $n_{eff.} = 3.86$; R= 3; $F_{0.05}(1, 20) = 3.49$

From eq. 3 $CI_{CE} = \pm 0.66$

From eq. 4 $CI_{POP} = \pm 0.44$

The predicted optimum values for weight loss is:

CI_{CE}: $6.4 < \mu < 7.72$

CI_{POP}: $6.62 < \mu < 7.5$

Table 9 Average values of weight loss at optimal level

Trails	Weight loss
A_1	9.26
B_1	7.66
C_2	9.32
T	9.59
A1= trail 1 of temperature; B1= trail 1 of frequency;C1=trail 1 of load; T= average value of response	

The optimum values of weight loss were predicted at the designated trial of significant parameters.

Temperature (A, trial 1) = 100°C

Frequency (B, trial 1) = 10 Hz

Load (C, trial 2) = 25N

3.3.1.2.Confirmation experiments

Three confirmation tests were performed at the optimal situation of the process parameters. For weight loss process parameters are set temperature at trail 1 (100°C), frequency at trail 1 (10 Hz), and load at trail 2 (25N). The average value for weight loss of composite coating was measured as 7.06 mg which was in the predicted optimum range of 95 % confidence interval for weight loss for the composite coating.

4. Conclusions

Mo blend composite coating was successfully deposited on cast iron as substrates material by using atmospheric plasma spray coating. Tribological behavior of composite coating was

Accepted Manuscript

studied using temperature, frequency and load as process parameters and following conclusions can be computed from the present study:

- It is possible to achieve a comparatively lower value of COF using 300ºC temperature and 20 Hz frequency. On the other end lower weight loss at 100ºC temperature and 10 Hz frequency can also be achieved. This may be attributed due to tribo-oxidation or running wear encountered by the flow of metal during the rubbing process for better quality of results.
- It is also observed that COF decreases as the load increases from 10N to 40N, however it is noted that weight loss first decreases upto 9.32 mg at 25N load.
- The predicted optimum range for COF is
  CI_{POP}: $0.23 < \mu < 0.26$, and for weight loss is CI_{POP}: $6.62 < \mu < 7.5$
- The predicted mean range of 95% confidence interval for COF is
  CI_{CE}: $0.22 < \mu < 0.27$, for weight loss is CI_{CE}: $6.4 < \mu < 7.72$

References

1. A. Ozdemir, A. Mugan, Stop/Start system integration to diesel engine and system modelling & validation, IFAC Proc., 2013, 46, 95-100.
2. E. Bent, P. Shayler, A. La Rocca, C. Rouaud, The effectiveness of stop-start and thermal management measures to improve fuel economy, Vehicle Thermal Management Systems Conference Proceedings, 2013, 27-39.
3. N. Fonseca, J. Casanova, M. Valdes, Influence of the stop/start system on CO2 emissions of a diesel vehicle in urban traffic, Transp. Res. Part D Transp. Environ., 2011, 16, 194-200.
4. Wu YY, Tsui WC, Liu TC, Experimental analysis of tribological properties of lubricating oils with nanoparticle additives, Wear, 2007, 262, 819–825.
5. Tyagi, A., Murtaza, Q., Walia, RS., Pandey, SM., Tyagi, P., Bajaj, B., A critical review of Diamond like Carbon Coating for Wear Resistance Applications, International Journal of Refractory Metals & Hard Materials, 2019, 78, 107–122.
6. Ali MKA, Xianjun H, Mai L, Qingping C, Turkson RF, Bicheng C, Improving the tribological characteristics of piston ring assembly in automotive engines using Al_2O_3 and TiO_2 nanomaterials as nano-lubricant additives, Tribol Int., 2016, 103, 540–554.
7. Gara L, Zou Q, Friction and Wear Characteristics of Water-Based ZnO and Al_2O_3 Nanofluids", Tribol Trans., 2012, 55, 345–350.
8. Holmberg K, Andersson P, Erdemir A, Global energy consumption due to friction in

Accepted Manuscript

passenger cars, Tribol Int., 2012 47, 221–234.

9. Ronen A, Etsion I, Kligerman Y, Friction-Reducing Surface-Texturing in Reciprocating Automotive Components, Tribol Trans., 2001, 44, 359–366.
10. M. Laribi, A.B. Vannes, D. Treheux, Study of mechanical behavior of molybdenum coating using sliding wear and impact tests, Wear, 2007, 262, 1330-1336.
11. J. Ahn, B. Hwang, S. Lee, Improvement of wear resistance of plasma-sprayed molybdenum blend coatings, J. Therm. Spray Technol., 2005, 14, 251-257.
12. S. Wayne, S. Sampath, V. Anand, Wear mechanisms in thermally-sprayed Mo based coatings, Tribol. Trans., 1994, 37, 636-640.
13. M.I. De Barros Bouchet, J.M. Martin, Th. Le Mogne, P. Bilas, B. Vacher, Y. Yamada, Mechanisms of MoS_2 formation by MoDTC in presence of ZnDTP: effect of oxidative degradation, Wear, 2005, 258, 1643-1650.
14. P.E. Hovsepiana, P. Mandal, A.P. Ehiasarian, G. Safran, R. Tietema, D. Doerwald, Friction and wear behaviour of Mo-W doped carbon-based coating during boundary lubricated sliding, Appl. Surf. Sci., 2016, 366, 260-274.
15. P. Niranatlumpong, H. Koiprasert, The effect of Mo content in plasma-sprayed Mo-NiCrBSi coating on the tribological behavior, Surf. Coatings Technol., 2010, 205, 483-489.
16. S. Usmani, S. Sampath, Time-dependent friction response of plasma-sprayed molybdenum, Wear, 1999, 225-229, 1131-1136.
17. S.F. Wayne, S. Sampath, V. Anand, Wear mechanisms in thermally-sprayed Mo based coatings, Tribol. Trans., 1994, 37, 636-640.
18. Tyagi, A., Murtaza, Q., Walia, RS., Effect of Reciprocating Frequency and Load on Wear Behaviour of Mo blend Composite Coating, International conference of advance research and innovation, 2019, 978-93- 5346-3243.
19. SM Pandey, Q Murtaza, RS Walia, Study of dry wear behavior and morphological characteristic of 60% Mo-20% NiCr-10% CrC-10% Mo+ Fe based alloy coating by atmospheric plasma spray technique, Advances in Materials and Processing Technologies, 2018, 3, 393-406.
20. H. Wu, X.D. Lan, Y. Liu, F. Li, W.D. Zhang, Z.J. Chen, X.F. Zai, H. Zeng, Fabrication, tribological and corrosion behaviors of detonation gun sprayed Fe-based metallic glass coating, Trans. Nonferrous Metals Soc. China, 2016, 26(6), 1629–1637.
21. B. Zabala, A. Igartua, X. Fernández, C. Priestner, H. Ofner, O. Knaus, M. Abramczuk, P. Tribotte, F. Girot, E. Roman, R. Nevshupa, Friction and wear of a piston

Accepted Manuscript

ring/cylinder liner at the top dead centre: Experimental study and modelling, Tribology International, 2017, 106, 23–33.

22. T Goyal, RS Walia, TS Sidhu, Study of coating thickness of cold spray process using Taguchi method, Materials and Manufacturing Processes, 2012, 27, 185-192.
23. RS Walia, HS Shan, P Kumar, Parametric optimization of centrifugal force-assisted abrasive flow machining (CFAAFM) by the Taguchi method, Materials and Manufacturing Processes, 2006, 21, 375-382.
24. BS Brar, RS Walia, VP Singh, Electrochemical-aided abrasive flow machining (ECA^2FM) process: a hybrid machining process, The International Journal of Advanced Manufacturing Technology, 2015, 79, 329-342.
25. T Goyal, RS Walia, TS Sidhu, Effect of parameters on coating density for cold spray process, Materials and Manufacturing Processes, 2012, 27, 193-200.

Accepted Manuscript

Received: 29 October 2018 | Revised and accepted: 25 February 2019

DOI: 10.1002/mmce.21756

RESEARCH ARTICLE

INTERNATIONAL JOURNAL OF RF AND MICROWAVE COMPUTER-AIDED ENGINEERING WILEY

Compact four-port MIMO antenna on slotted-edge substrate with dual-band rejection characteristics

Dinesh Kumar Raheja[1,2] | **Binod Kumar Kanaujia**[3] | **Sachin Kumar**[4]

[1]Department of Electronics and Communication Engineering, Ambedkar Institute of Advanced Communication Technologies and Research, Delhi, India

[2]University School of Information, Communication and Technology, Guru Gobind Singh Indraprastha University, New Delhi, India

[3]School of Computational and Integrative Sciences, Jawaharlal Nehru University, New Delhi, India

[4]Department of Electronics and Communication Engineering, SRM Institute of Science and Technology, Chennai, India

Correspondence
Binod Kumar Kanaujia, School of Computational and Integrative Sciences, Jawaharlal Nehru University, New Delhi 110067, India.
Email: bkkanaujia@ieee.org

Abstract

A compact ultra-wideband (UWB) multiple-input-multiple-output (MIMO) antenna with dual band elimination characteristics is presented. The proposed MIMO antenna is comprised of four identical elliptical shaped monopole radiators located orthogonally to each other. A second order Koch fractal geometry is applied on the edges of the ground planes of the radiating elements; to reduce the overall size of the MIMO antenna, without compromising the lower frequency response. Further, in order to eliminate the undesired resonant bands (3.5 and 5.5 GHz) from UWB, an elliptical complementary split ring resonator is introduced in the monopole radiator. For reducing inter-element coupling in the proposed MIMO antenna, a different approach (of slotted edge substrate) is used, as a substitute of traditional decoupling stub/elements. In the entire operating band of 3 to 13.5 GHz, inter-element isolation more than 22 dB and envelope correlation coefficient less than 0.008 are obtained. The measured parameters of the fabricated prototype antenna are found in good agreement with the simulated results.

KEYWORDS

CSRR, elliptical, Koch fractal, MIMO, UWB

1 | INTRODUCTION

Recently, rapid development in the field of communication is seen with modern systems using ultra-wideband (UWB) and spread-spectrum based wireless technologies. After the official declaration of 3.1 to 10.6 GHz spectrum as an unlicensed band by Federal Communication Commission (FCC) in 2002,[1] the UWB based communication had established a new paradigm in civil and military applications. With the ever-increasing popularity of UWB systems in microwave imaging, cognitive radio, sensing networks, high data rate communication and multi-user environment, many engineers and researchers focused their attention toward UWB antenna configuration.[2,3] The UWB signal suffers adversely from multipath fading effects such as diffraction, scattering, reflections from large buildings and other similar objects, and so on. To overcome these challenges and to enhance data throughput, UWB systems with various diversity techniques (spatial, frequency, or polarization) have been deployed.[4–6] The combination of UWB and multiple-input-multiple-output (MIMO) significantly improves the data rate transmission capacity, spectrum efficiency and overall quality of the communication link in comparison to single antenna systems.[7]

While designing MIMO antenna systems, the most challenging task is to overcome the limitations of available space, especially for portable terminals. It is difficult to place a large number of radiating elements within a limited space. Inevitably, due to the close vicinity, there is a significant rise in mutual coupling and envelope correlation coefficient (ECC) among the radiating elements, which deteriorates the overall performance of the MIMO system. The space between the antenna elements and mutual coupling are inversely related to each other. Thus, minimizing the inter-element coupling,

 © 2019 Wiley Periodicals, Inc.

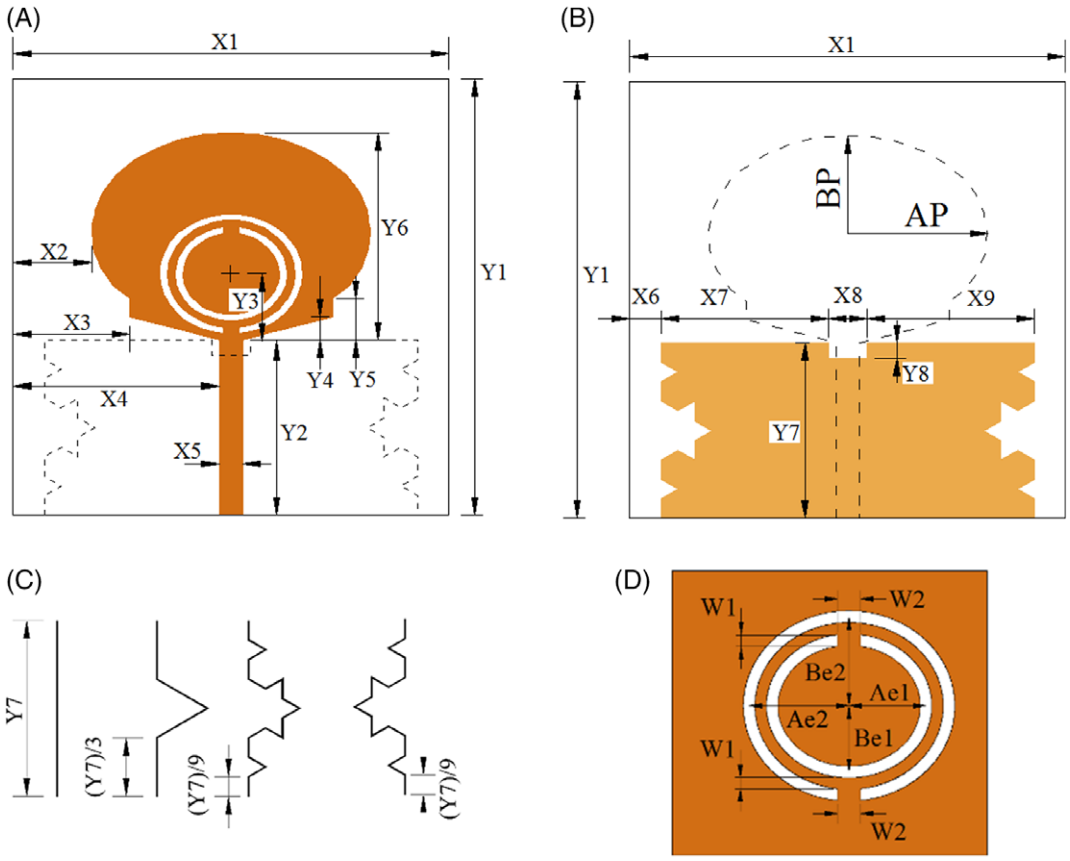

FIGURE 1 Antenna element geometry (A) monopole radiator (B) ground plane (C) first and second order iterations of Koch fractal (D) elliptical CSRR

without considerably increasing the overall size of the MIMO antenna, raises critical problems for practically useful designs. Designing an antenna for quad-port MIMO systems becomes more complex, because it has to deal with much higher levels of mutual coupling and ECC, in comparison to the dual-port MIMO systems.[8,9]

Furthermore, various commercial gadgets partially share (eg, WLAN/Wi-MAX) bands within the UWB spectrum, which affects the performance of portable UWB terminals. Therefore, in many UWB antenna design problems, it becomes essential to eliminate the interfering bands. Various UWB MIMO antennas exhibiting single/multiple band rejection characteristics have been reported in the last few years.[10–18] However, MIMO antennas deploying elliptical patches with a high value of eccentricity are relatively less explored. So far, in most of the MIMO antenna configurations, the authors have used grounded stubs in order to increase inter-element isolation or to reduce mutual coupling level.[19–21] In this article, a novel approach using the slotted-edges substrate to increase inter-element isolation is presented. Here, each element is configured around a highly eccentric elliptical patch, loaded with elliptical complementary split ring resonator (CSRR) for obtaining dual band elimination characteristics. A two-element MIMO is also analyzed, before proposing the four-element MIMO antenna system. The rigorous simulations related to antenna designing and optimizations are performed on Ansys HFSS software platform.[22]

2 | ANTENNA DESIGN

2.1 | UWB MIMO antenna unit cell

The schematic layout and geometrical details of the proposed monopole antenna and its ground plane are given in Figure 1A,B, respectively. The monopole antenna element is comprised of an elliptical radiator, excited by means of the microstrip feed line and a ground plane with second order Koch fractal geometry on the two opposite edges as illustrated in Figure 1C. For achieving dual band notched characteristics within the UWB, an elliptical CSRR is loaded onto the radiating patch of the proposed monopole antenna. The details related to the dimensions of elliptical CSRR are represented in Figure 1D. Beneath the feed line, a U-shaped slot is etched from the upper edge of the ground surface, for obtaining better impedance matching within the UWB range. A low-cost FR-4 epoxy substrate having $\varepsilon_r = 4.4$, tan $\delta = 0.02$, and thickness of 0.8 mm is used for designing the

TABLE 1 Design parameters of the proposed antenna

Dimension	Value (mm)	Dimension	Value (mm)
AP	9	*X8*	2.5
BP	6.3	*X9*	10.75
Ae1	3.35	*X10*	58
Be1	2.85	*X11*	2
Ae2	4.35	*Y1*	28
Be2	3.85	*Y2*	11.25
W1	0.5	*Y3*	4.25
W2	1	*Y4*	1.5
X1	28	*Y5*	2.65
X2	5	*Y6*	13.35
X3	7.5	*Y7*	11.25
X4	13.25	*Y8*	1
X5	1.53	*Y9*	10
X6	2	*Y10*	18
X7	10.75		

antenna. The details regarding the antenna parameters and dimensions are given in Table 1.

The evolution of the proposed antenna unit cell is shown in Figure 2. Firstly, an elliptical monopole radiating element excited through a microstrip line of 50 Ω is designed as shown in Figure 2A. It possesses high eccentricity of ~71% to support multiple modes, required for UWB operation. The elliptical radiating patch semi-major and semi-minor axes are represented as *AP* and *BP*, respectively. Since the surface beneath the resonant patch is not grounded, it behaves like an unbalanced impedance. The monopole radiating element needs to be excited by a grounded microstrip feed line having 50 Ω balanced characteristic impedance. So, a small rectangular slot of dimensions *X8* × *Y8* is etched from the ground plane of the microstrip line to provide necessary balanced-to-unbalanced (BALUN) impedance matching between the feeding microstrip line and the radiating monopole. A tapered conducting patch is placed between the elliptical radiator and the feeding line, to maintain good impedance bandwidth throughout the UWB as shown in Figure 2B.

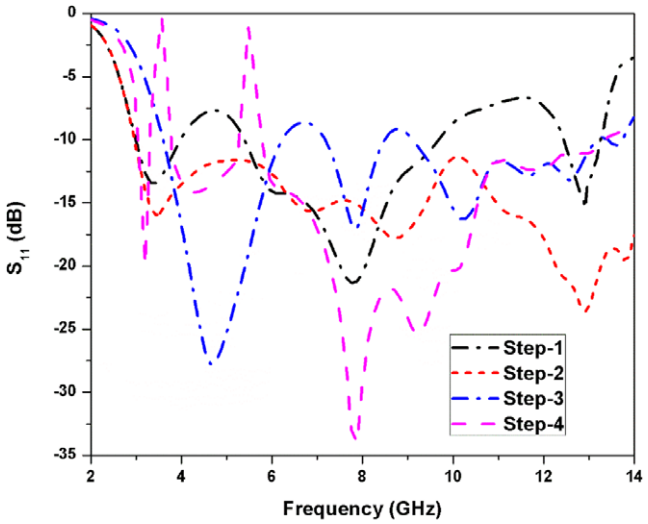

FIGURE 3 S_{11} comparison of UWB antenna designing steps

While designing an antenna for portable MIMO systems, the overall size of the antenna is important, due to the space constraints. But, the peripheral length of the ground plane affects the impedance bandwidth of the UWB antenna.[23] In printed or patch antennas, the peripheral length of the conductor provides the maximum path length available for current flow. If the current path length is changed, the wavelength also changes and thus the frequency response of the antenna changes, accordingly. Here, the space-filling property of second order Koch fractal geometry[24] is applied at the two opposite edges of the ground patch, to minimize the overall size of the ground plane, without changing its peripheral dimensions. In this way, miniaturization of approximately 9/16 is realized in the ground surface, without compromising the lower frequency response. Similarly, a reduction in the size of the proposed four-port UWB MIMO antenna is achieved. Figure 3 shows reflection coefficients comparison at different development stages of the proposed UWB monopole antenna.

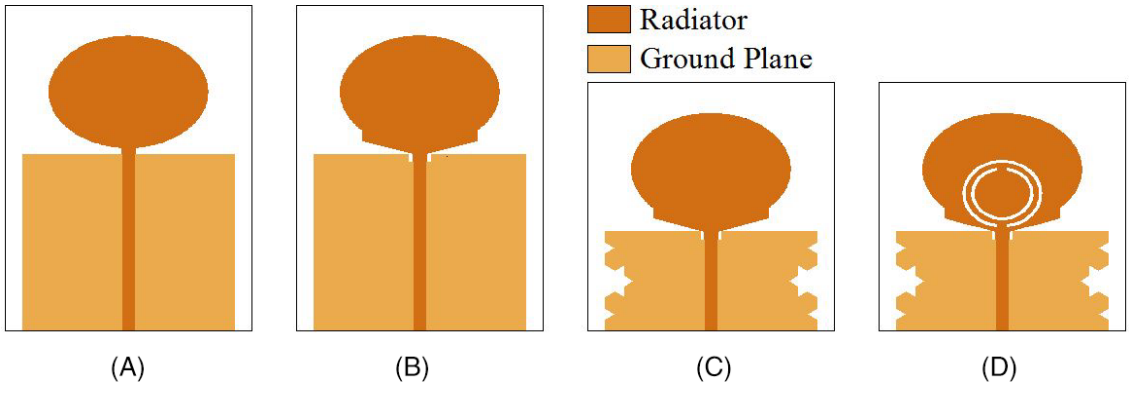

FIGURE 2 UWB antenna evolution steps (A) step-1 (B) step-2 (C) step-3 (D) step-4

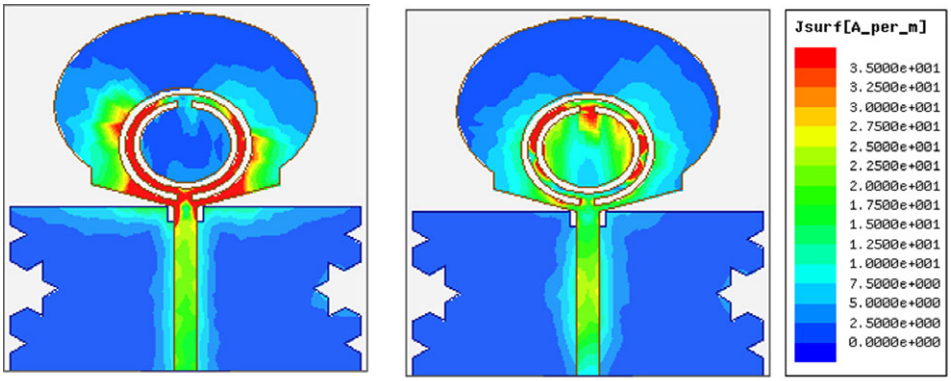

FIGURE 4 Current distribution in proposed monopole antenna (A) 3.5 GHz (B) 5.5 GHz

Further, in order to eliminate the undesired interfering bands from the UWB spectrum, an elliptical CSRR slot is loaded on the antenna radiating element. The CSRR geometry is formed by closely placing two concentric elliptical slots of somewhat different radii, with the same width and gap (*W1*) as indicated in Figure 1D. The resonant frequency f_{ri} of each interfering band can be obtained as[25]

$$f_{ri} = \frac{c}{2L_i\sqrt{\varepsilon_{\mathrm{r,eff}}}} \tag{1}$$

where c is the velocity of light in free space, L_i is the average length of each elliptical slot of CSRR and $\varepsilon_{\mathrm{r,eff}}$ is the effective dielectric constant of the substrate. The average length L_i of the elliptical slot is calculated as

$$L_i = \{\pi(A_{ei} + B_{ei}) - W_2\}; i = 1,2 \tag{2}$$

where A_{ei} and B_{ei} are the respective semi-major and semi-minor axes of the elliptical slots. The combined effect of balun impedance matching, Koch fractal geometry in the ground plane and dual band elimination (3.5 and 5.5 GHz) from UWB can be seen in step-4 of Figure 3. The surface current distribution in Figure 4A indicates that the current is mainly concentrated close to outer elliptical split-ring, which is responsible for the elimination of 3.5 GHz band. Similarly, in Figure 4B, the current concentration is high close to the inner elliptical split ring, which is accountable for the elimination of 5.5 GHz band.

2.2 | Two-element UWB MIMO antenna

A two-element UWB MIMO antenna is developed by placing two identical antenna elements orthogonally. A perpendicular slot of dimensions *X11* × *Y9* is cut from the lower edge of the dielectric substrate, in order to obtain very good inter-element isolation and ECC. The schematic layout of the proposed two-port MIMO antenna is shown in Figure 5.

Figure 6 shows simulated *S*-parameters of the two-element MIMO antenna, indicating UWB and dual-band elimination characteristics. The S_{21} curve shows that the inter-element isolation larger than 20 dB is obtained throughout the UWB. The simulated gain (Figure 7) of the antenna varies from 1 to 6.8 dBi and it is also noticed that at the two notch band frequencies the proposed antenna is behaving as a notched band filter. In MIMO antennas the mutual coupling between the

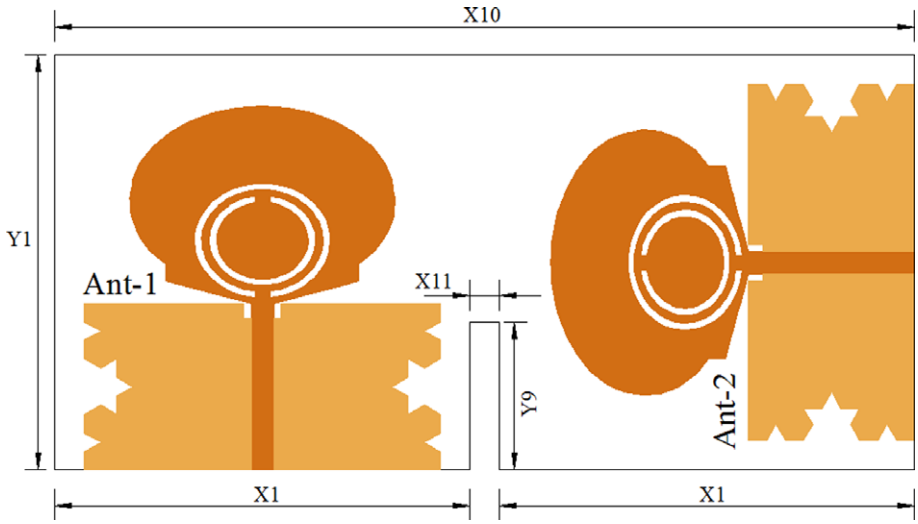

FIGURE 5 Schematic of proposed two-element UWB MIMO antenna

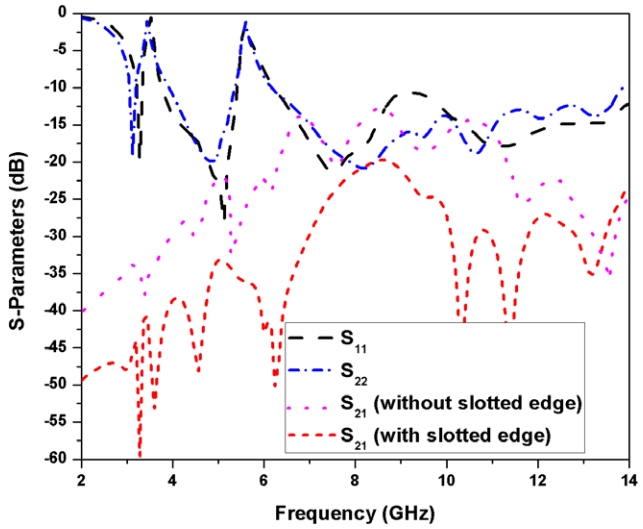

FIGURE 6 *S*-parameters of proposed two-element UWB MIMO antenna

two adjacent antenna elements can be studied by calculating the value of ECC. The ECC between the adjacent antenna elements i and j for N-port MIMO system can be calculated by the relation[26]

$$\rho_e(i,j,N) = \left| \frac{\sum_{n=1}^{N} S_{i,n}^{*} S_{n,j}}{\left| \prod_{k=i,j} \left(1 - \sum_{n=1}^{N} S_{k,n}^{*} S_{n,k}\right) \right|^{1/2}} \right|^2 \quad (3)$$

For a two-port MIMO system, $i = 1$, $j = 2$, $N = 2$ and the ECC is expressed as

$$\rho_e(1,2,2) = \frac{\left| S_{11}^{*} S_{12} + S_{21}^{*} S_{22} \right|^2}{\left(1 - |S_{11}|^2 - |S_{21}|^2\right)\left(1 - |S_{22}|^2 - |S_{12}|^2\right)} \quad (4)$$

The ECC calculated is less than 0.001 within the resonating band and is plotted in Figure 7.

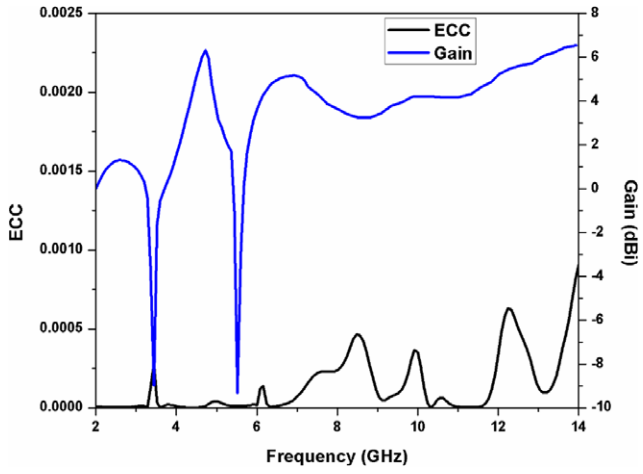

FIGURE 7 ECC and gain of proposed two-element UWB MIMO antenna

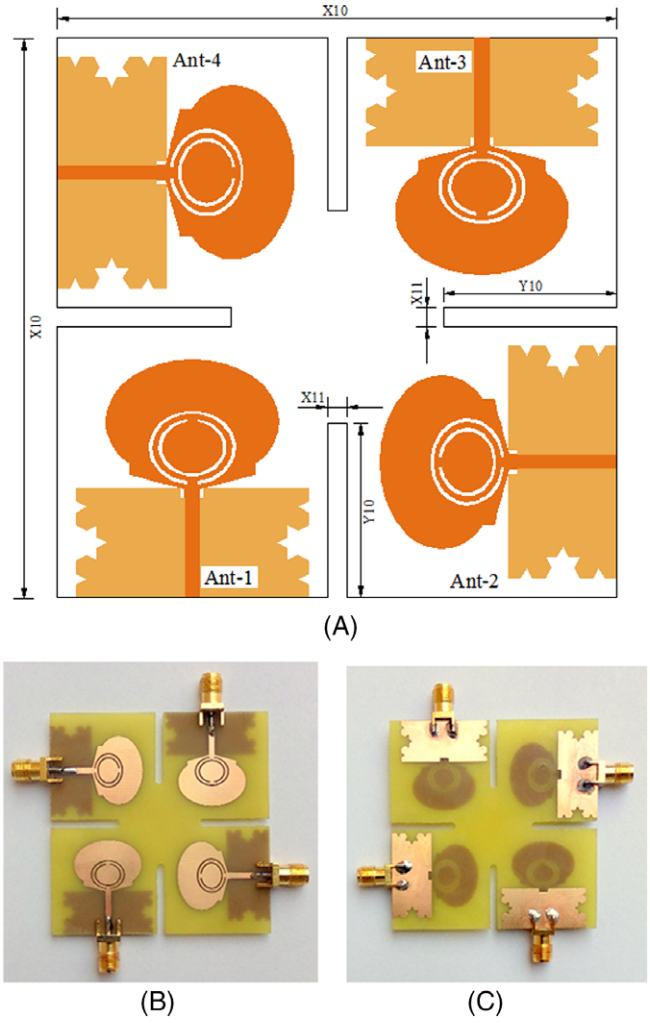

FIGURE 8 Proposed four-element UWB MIMO antenna (A) schematic (B) fabricated prototype top view (C) fabricated prototype bottom view

2.3 | Four-element UWB MIMO antenna

Here, the antenna for four-element MIMO systems is developed by placing four antenna elements orthogonally, in a way to reduce the overall size of the MIMO antenna. Instead of using space occupying decoupling elements, four orthogonal slots of size *X11* × *Y10* are cut from the middle of the four edges of the dielectric substrate. The schematic layout details for the four-port UWB MIMO antenna are given in Figure 8A. The MIMO fabricated antenna prototype from top and bottom are represented in Figure 8B,C, respectively.

3 | RESULTS AND DISCUSSION

The antenna is fabricated using photo-etching process and its parameters are measured by means of Agilent vector network analyzer (PNA L-Series) and Rhode & Schwarz FSP spectrum analyzer. The SMA 50 Ω connectors are used for

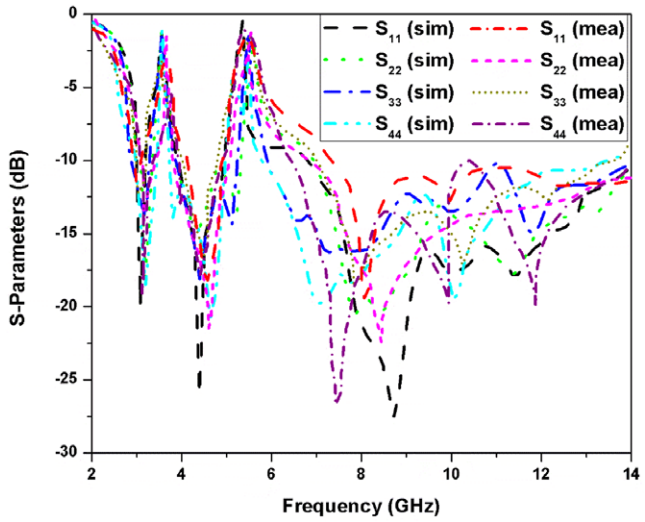

FIGURE 9 *S*-parameters of proposed four-element UWB MIMO antenna

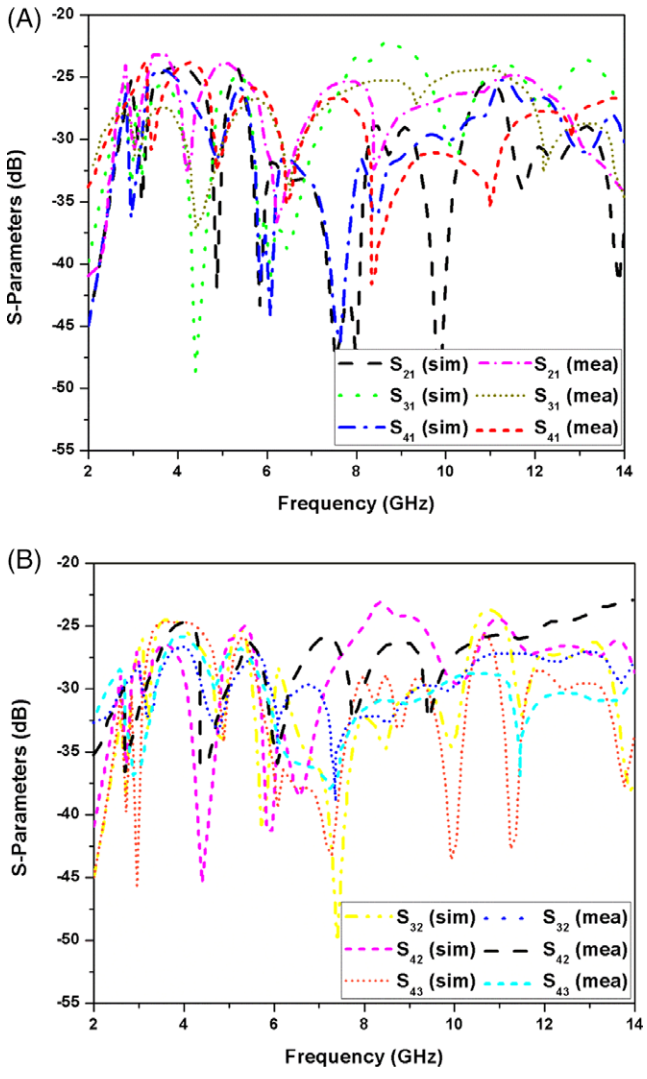

FIGURE 10 *S*-parameters of proposed four-element UWB MIMO antenna (A) with reference to port-1 (B) other ports

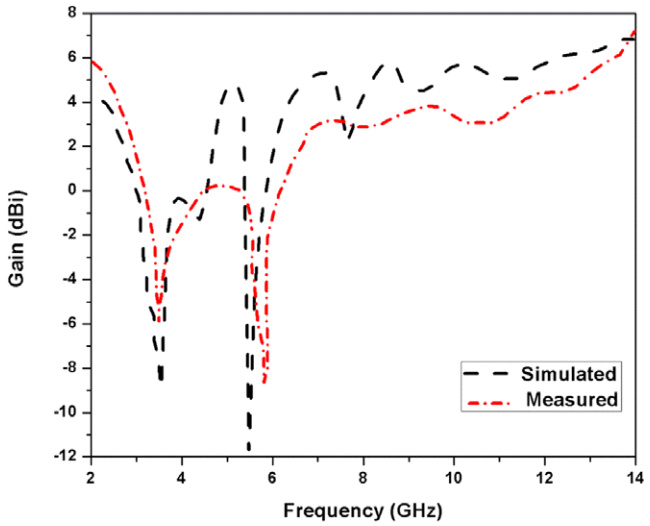

FIGURE 11 Gain of proposed four-element UWB MIMO antenna

measuring the electrical performance of the proposed antenna. Figure 9 shows simulated and measured reflection coefficients at different antenna ports. During the S_{11} measurement at port-1, other ports in the MIMO antenna are terminated with the help of standard 50 Ω load. The same procedure is followed for the measurement of S_{22}, S_{33}, and S_{44}. From the measured response, it can be observed that the antenna has a −10 dB impedance bandwidth of 3 to 13.5 GHz (10.5 GHz). The centre frequencies of the two notch bands are 3.5 GHz (3.25-3.75 GHz) and 5.5 GHz

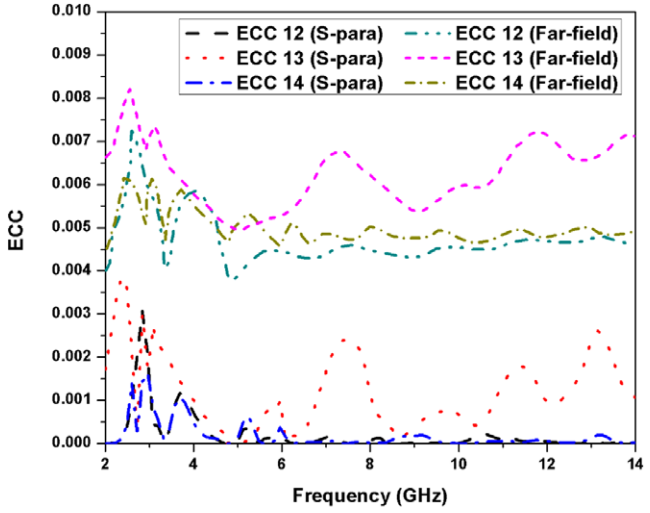

FIGURE 12 ECC of proposed four-element UWB MIMO antenna

TABLE 2 Performance parameters of the proposed four-element UWB MIMO antenna

Frequency (GHz)	Isolation (dB)	ECC	ADG
8	>25	<0.002	10
10	>23	<0.002	9.98
12	>23	<0.002	10

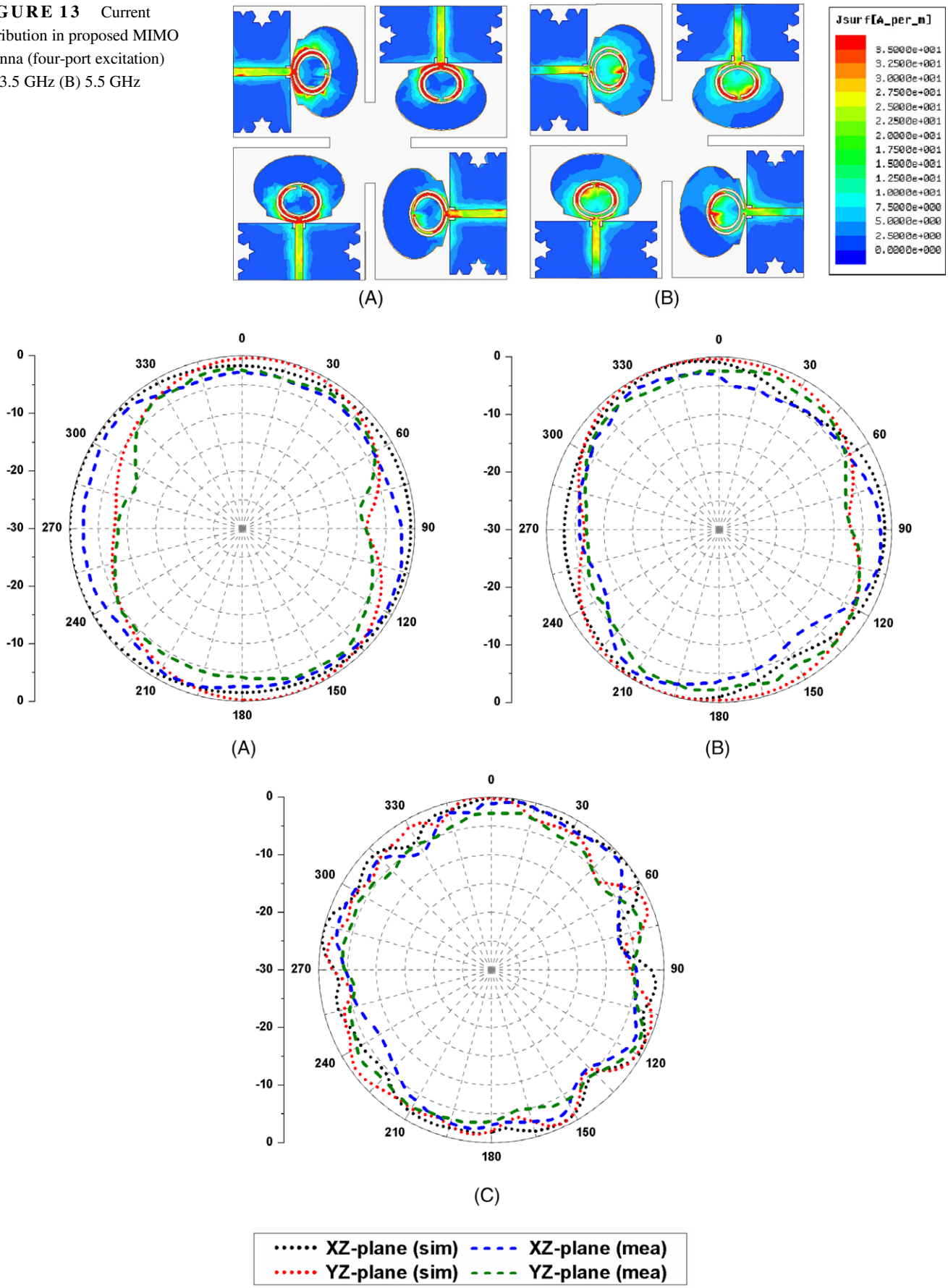

FIGURE 13 Current distribution in proposed MIMO antenna (four-port excitation) (A) 3.5 GHz (B) 5.5 GHz

FIGURE 14 Radiation patterns of the proposed antenna (A) 8 GHz (B) 10 GHz (C) 12 GHz

TABLE 3 Comparison of proposed band notched antenna with other reported antennas

Ref.	Number of elements	Antenna size (mm^3)	Bandwidth (GHz)	Number of notch bands	Notch frequency (GHz)	ECC	Isolation (dB)
10	2	22 × 36 × 1.6	3.1-11	1	5.15-5.85	<0.1	>15
11	2	48 × 48 × 0.8	2.5 12	1	5.5	<0.005	>15
12	2	30 × 22 × 0.8	3.1-10.6	1	5–6	<0.05	>15
13	2	30 × 40 × 0.8	3.1–10.6	2	3.4-3.7, 5.15-5.825	<0.05	>15
14	2	41 × 41 × 0.8	2.95-10.65	2	3.5/5.5	<0.15	>16
15	2	35 × 68 × 1	3.1-10.6	2	3.35-3.55, 5.65-5.95	<0.002	>20
16	4	60 × 60 × 1.6	3-16.2	1	4.6	<0.4	>17.5
17	4	44 × 44 × 1.6	2.95-10.8	1	5.10-5.95	<0.1	>15.5
18	4	100 × 100× 1.6	2–15	2	3.5/5.5	<0.1	>20
This work	4	58 × 58 × 0.8	3–13.5	2	3.5/5.5	<0.008	>22

(5.3-5.7 GHz). However, by adjusting the dimensions of SRR, the notch frequencies can be controlled.

Figures 10 and 11 represent isolation and gain of the proposed antenna, respectively. The isolation achieved is more than 22 dB within the impedance bandwidth range. For gain measurement, the antenna under test is used as the receiving antenna and recorded power is converted into gain by using the Friss transmission equation. In the higher frequency range, the antenna peak gain obtained is 7 dBi. The measured results of the designed UWB MIMO antenna are in good match with the simulated results. A small deviation is seen in measured and simulated results which is due to customary photo-etching fabrication process, SMA connector soldering and cable effects.

The ECC for a four-port MIMO system ($N = 4$) between antenna elements-1 and -2 (Figure 8A) is expressed as

$$\rho_e(1,2,4) = \frac{\left|S_{11}^* S_{12} + S_{21}^* S_{22} + S_{13}^* S_{32} + S_{14}^* S_{42}\right|^2}{\left(1-|S_{11}|^2-|S_{21}|^2-|S_{31}|^2-|S_{41}|^2\right)\left(1-|S_{12}|^2-|S_{22}|^2-|S_{32}|^2-|S_{42}|^2\right)} \quad (5)$$

Similarly, the ECC between other antenna elements is calculated. Alternatively, the ECC can be calculated in terms of antenna far-field radiation pattern as[27]

$$\rho_e = \frac{\left|\int\int\left[\vec{F_1}(\theta,\varphi)\,\vec{F_2}(\theta,\varphi)\right] d\Omega\right|^2}{\int\int\left|\vec{F_1}(\theta,\varphi)\right|^2 d\Omega \int\int\left|\vec{F_2}(\theta,\varphi)\right|^2 d\Omega} \quad (6)$$

where F is the radiated field of two considered antenna elements out of four antennas, Ω, θ, and φ are the solid, elevation, and azimuthal angles, respectively. The ECC is less than 0.008 (as plotted in Figure 12) within the resonating UWB which assures that the MIMO antenna has good diversity performance. Further, the antenna apparent diversity gain (ADG) is also calculated and found within the desired limits.[27] The ADG signifies the increment in the quality of signal due to the introduction of diversity scheme in the MIMO systems and here, it can be observed that the ADG is more than 9.9 dB as shown in Table 2.

The surface current distribution in MIMO antenna at the interfering bands 3.5 and 5.5 GHz is presented in Figure 13A,B, respectively. The maximum current (shown in red) is concentrated near the respective slot of the CSRR at the chosen frequency. The outer slot of the SRR eliminates lower band around 3.5 GHz and the inner slot removes the upper band of 5.5 GHz. Thus, due to CSRR loading, dual band notch characteristics are obtained in the UWB spectrum, further justifying the S-parameters and gain curve of the MIMO antenna. The simulated and measured radiation patterns of the proposed antenna in the XZ- and YZ-planes at 8, 10, and 12 GHz frequencies are shown in Figure 14. For the radiation pattern measurement, the antenna under test is used as a receiving antenna and fixed to the stand, whose rotation can be controlled by a stepper motor controller. The proposed antenna and standard horn antenna are placed in the line of sight aligned with each other. The receiving antenna is connected to the spectrum analyzer to measure the received power. Further, a comparison of proposed dual

notched band UWB MIMO antenna with other reported notch band MIMO antennas is given in Table 3. It is noticed that the proposed MIMO antenna covers complete UWB with good isolation between adjacent antenna elements.

4 | CONCLUSION

This article presents a microstrip line fed dual band notched quad-port UWB MIMO antenna. The proposed MIMO antenna is composed of four identical monopole radiating elements placed orthogonally to each other and for introducing band rejection characteristics, an elliptical CSRR slot is loaded in the radiator. A slotted-edge substrate is used in the proposed MIMO antenna to increase inter-element isolation between adjacent antenna elements. The MIMO antenna performance parameters such as isolation, ECC and ADG are calculated which verifies that the proposed antenna could be a suitable candidate for modern UWB based MIMO applications.

ORCID

Binod Kumar Kanaujia https://orcid.org/0000-0002-7849-5299
Sachin Kumar https://orcid.org/0000-0002-6260-6353

REFERENCES

1. Federal Communications Commission, First report and order, revision of part 15 of the commission's rules regarding ultrawideband transmission systems, Washington, DC, 2002.
2. Chen ZN, Ammann MJ, Qing XM, Wu XH, See TSP, Cai A. Planar antennas. *IEEE Microw Mag*. 2006;7(6):63-73.
3. Liang JX, Chian CC, Chen XD, Parini CG. Study of a printed circular disc monopole antenna for UWB systems. *IEEE Trans Antennas Propag*. 2005;53(11):3500-3504.
4. OuYang J, Yang F, Wang ZM. Reducing mutual coupling of closely spaced microstrip MIMO antennas for WLAN application. *IEEE Antennas Wirel Propag Lett*. 2011;10:310-313.
5. Khan MS, Capobianco AD, Asif SM, Anagnostou DE, Shubair RM, Braaten BD. A compact CSRR-enabled UWB diversity antenna. *IEEE Antennas Wirel Propag Lett*. 2017;16:808-812.
6. Deng J, Li J, Zhao L, Guo L. A dual-band inverted-F MIMO antenna with enhanced isolation for WLAN applications. *IEEE Antennas Wirel Propag Lett*. 2017;16:2270-2273.
7. Chandel R, Gautam AK. Compact MIMO/diversity slot antenna for UWB applications with band-notched characteristic. *Electron Lett*. 2016;52(5):336-338.
8. Sarkar D, Srivastava KV. Compact four-element SRR-loaded dual-band MIMO antenna for WLAN/WiMAX/WiFi/4G-LTE and 5G applications. *Electron Lett*. 2017;53(25):1623-1624.
9. Ramachandran A, Pushpakaran SV, Pezholil M, Kesavath V. A four-port MIMO antenna using concentric square-ring patches loaded with CSRR for high isolation. *IEEE Antennas Wirel Propag Lett*. 2016;15:1196-1199.
10. Liu L, Cheung SW, Yuk TI. Compact MIMO antenna for portable UWB applications with band-notched characteristic. *IEEE Trans Antennas Propag*. 2015;63(5):1917-1924.
11. Gao P, He S, Wei X, Xu Z, Wang N, Zheng Y. Compact printed UWB diversity slot antenna with 5.5-GHz band-notched characteristics. *IEEE Antennas Wirel Propag Lett*. 2014;13:376-379.
12. Tao J, Feng Q. Compact UWB band-notch MIMO antenna with embedded antenna element for improved band notch filtering. *Prog Electromagn Res C*. 2016;67:117-125.
13. Tang TC, Lin KH. An ultrawideband MIMO antenna with dual band-notched function. *IEEE Antennas Wirel Propag Lett*. 2014;13:1076-1079.
14. Srivastava G, Kanuijia BK. Compact dual band-notched UWB MIMO antenna with shared radiator. *Microw Opt Technol Lett*. 2015;57(12):2886-2891.
15. Li WT, Hei YQ, Subbaraman H, Shi XW, Chen RT. Novel printed filtenna with dual notches and good out-of-band characteristics for UWB-MIMO applications. *IEEE Microw Wirel Compon Lett*. 2016;26(10):765-767.
16. Wu W, Yuan B, Wu A. A quad-element UWB-MIMO antenna with band-notch and reduced mutual coupling based on EBG structures. *Int J Antennas Propag*. 2018, article ID 8490740, 10 pages;2018:1-10.
17. Liu Y, Tu Z. Compact differential band-notched stepped-slot UWB-MIMO antenna with common-mode suppression. *IEEE Antennas Wirel Propag Lett*. 2017;16:593-596.
18. Shehata M, Said MS, Mostafa H. Dual notched band quad-element MIMO antenna with multi-tone interference suppression for IR-UWB wireless applications. *IEEE Trans Antennas Propag*. 66:5737-5746. https://doi.org/10.1109/TAP.2018.2868725.
19. Zhang S, Ying Z, Xiong J, He S. Ultrawideband MIMO/-diversity antennas with a tree-like structure to enhance wideband isolation. *IEEE Antennas Wirel Propag Lett*. 2009;8:1279-1282.
20. Khan MS, Capobianco AD, Najam AI, Shoaib I, Autizi E, Shafique MF. Compact ultra-wideband diversity antenna with a floating parasitic digitated decoupling structure. *IET Microw Antennas Propag*. 2014;8(10):747-753.
21. Roshna TK, Deepak U, Sajitha VR, Vasudevan K, Mohanan P. A compact UWB MIMO antenna with reflector to enhance isolation. *IEEE Trans Antennas Propag*. 2015;63(4):1873-1877.
22. Ansys Corporation, *HFSS, Suite v15.* Pittsburg, PA; 2014.
23. Mandal K, Sarkar PP. High gain wide-band U-shaped patch antennas with modified ground planes. *IEEE Trans Antennas Propag*. 2013;61(4):2279-2282.
24. Best SR, Morrow JD. The effectiveness of space-filling fractal geometry in lowering resonant frequency. *IEEE Antennas Wirel Propag Lett*. 2002;1:112-115.
25. Chandel R, Gautam AK, Rambabu K. Tapered fed compact UWB MIMO-diversity antenna with dual band-notched characteristics. *IEEE Trans Antennas Propag*. 2018;66(4):1677-1684.
26. Blanch S, Romeu J, Corbella I. Exact representation of antenna system diversity performance from input parameter description. *Electron Lett*. 2003;39(9):705-707.
27. Singh HS, Shalini, Meshram MK. Printed monopole diversity antenna for USB dongle applications. *Wireless Pers Commun*. 2016;86(2):771-787.

AUTHOR BIOGRAPHIES

DINESH KUMAR RAHEJA received his BE (Electronics) degree in 1991, from Marathwada University, Aurangabad, India. In industry he worked, as R&D Engineer/Senior Engineer in Calcom Electronics Ltd; Samtel India Ltd; and Ahuja Radios, New Delhi, till 1998; before joining as Lecturer at Ambedkar Polytechnic, Delhi. He received his ME (Electronics and Communication Engineering) degree in 2005 from Delhi College of Engineering, Delhi, India. Currently, he is working as Associate Professor (Electronics and Communication Engineering) in Ambedkar Institute of Advanced Communication Technologies and Research, Delhi, India. His area of interest includes microstrip antennas, RF and microwave systems.

BINOD KUMAR KANAUJIA received his BTech degree in Electronics Engineering from Kamla Nehru Institute of Technology, Sultanpur, India in 1994. He did his MTech and PhD in 1998 and 2004, respectively, from Department of Electronics Engineering, Indian Institute of Technology Banaras Hindu University, Varanasi, India. At present, he is working as Professor in School of Computational & Integrative Sciences, Jawaharlal Nehru University, New Delhi, India. He has been credited to publish more than 250 research articles with more than 1200 citations and h-index of 18 in several peer-reviewed journals and conferences. He had supervised 50 MTech and 15 PhD scholars in the field of RF and microwave engineering. He is currently on the editorial board of several international journals. Dr. Kanaujia had successfully executed five research projects sponsored by several agencies of Government of India, that is, DRDO, DST, AICTE, and ISRO. He is also a member of several academic and professional bodies, that is, IEEE, Institution of Engineers (India), Indian Society for Technical Education and The Institute of Electronics and Telecommunication Engineers of India.

SACHIN KUMAR received his BTech degree in Electronics and Communication Engineering from Uttar Pradesh Technical University, Lucknow, India in 2009. He received his MTech and PhD degrees in Electronics and Communication Engineering from Guru Gobind Singh Indraprastha University, New Delhi, India, in 2011 and 2016, respectively. At present, he is working as Research Assistant Professor in the Department of Electronics and Communication Engineering, SRM Institute of Science and Technology, Chennai, India. His research interest includes circularly polarized microstrip antennas, reconfigurable antennas, ultra-wideband antennas, defected ground structure, and microwave components.

How to cite this article: Raheja DK, Kanaujia BK, Kumar S. Compact four-port MIMO antenna on slotted-edge substrate with dual-band rejection characteristics. *Int J RF Microw Comput Aided Eng*. 2019;e21756. https://doi.org/10.1002/mmce.21756

Wireless Personal Communications
https://doi.org/10.1007/s11277-019-06403-0

Continuous User Authentication System: A Risk Analysis Based Approach

Neha[1] · **Kakali Chatterjee**[1]

© Springer Science+Business Media, LLC, part of Springer Nature 2019

Abstract
With the expansion of smart device users, the security mechanism of these devices in terms of user authentication has been advanced a lot. These mechanisms consist of a pattern based authentication, biometric based authentication, etc. For security purpose whenever a user fails to authenticate themselves, these devices get locked. But as these devices consist of numerous applications (document creator, pdf viewer, e-banking, Social networking app, etc.), locking of the whole devices prevents the user from using any of the applications. Since the variety of applications provided by the devices have different security needs, we feel it is better to have application level security rather than device level. Here, in this paper, we have proposed a behavioral biometric based user authentication mechanism for application level security. First, we have performed a risk assessment of different applications. Then for complete protection, static multi-modal (keystroke and mouse dynamics) authentication at the start of an interactive session, and a continuous keystroke authentication during this session is performed. An analysis of the proposed authentication mechanism has been conducted on the basis of false acceptance rate (FAR), false rejection rate (FRR) and equal error rate (EER). The static multi-modal authentication achieved a FAR of 0.89%, FRR of 1.2% and EER of 1.04% using J48 classification algorithm. Whereas the continuous keystroke authentication has been analyzed by the time (no. of keystrokes pressed) taken to capture an intruder.

Keywords Authentication · Keystroke · Biometrics · Behavioral · Application

1 Introduction

With the advancement of technology use of personalized electronic devices like: laptops, tablets ,etc. has increased tremendously. These devices are very popular due to the portability and different types of useful applications they provide, which fulfill our

✉ Neha
neha.cse14@nitp.ac.in

Kakali Chatterjee
kakali@nitp.ac.in

[1] Department of Computer Science and Engineering, National Institute of Technology Patna, Patna, Bihar, India

Published online: 24 April 2019

daily needs. The various applications are e-shopping, e-learning, e-mails, document creator (word, text, excel, latex, etc.), social networking, web browser, music players, etc. Numerous applications are being introduced every day by the service providers through the application stores. These applications provide us an easy way to access various services. A lot of sensitive and important data like e-cash, e-wallet, e-banking statements, secret document files, etc. are accessed and saved in our personalized devices while using these applications. These data/files may be accessed by others without knowledge of the device owner. For the security of these data, user authentication is a very important step in these devices. With the existing traditional password based security, nowadays various smart device support biometric (fingerprint) based and graphical pattern based authentication for user verification. Many works have been done in the direction of user authentication through memory based [1–5], graphical pattern based [6–8], static biometric based [9–13] techniques. Among these most of the memory based techniques are vulnerable to many attacks like password guessing attack, replay attack, modification attack, etc. In pattern based authentication user tends to use the same pattern for a long time, for their convenience. This may produce oily smudge on the screen of these devices, which can be detected in very high resolution images [14] causing smudge attack. Whereas static unimodal biometrics may face issues like [15]: *Noise in the data, Intraclass variation, Distinctiveness, Non-universality, Spoof Attacks*. To overcome these, multi-modal biometrics provides a solution. Multi-modal biometrics combines two or more biometrics traits for user authentication. The different biometric traits are fused together to reach a unique decision. The various fusion techniques include *Feature level fusion, Matching level fusion and Decision level fusion*.

A major limitation of all these security mechanisms is that these are being implemented only once at the start of any session. It means after authenticating users at the start of any session there is no provision of authenticating the user in between the sessions. Hence, an intruder can establish a post authentication session after verification of the real user. So, for complete security along with initial static authentication, there is a need to implement *continuous user authentication* mechanism. *Continuous user authentication* is a process where after authentication at the start of the session, the user is being authenticated continuously during the whole duration of usage of the system in the current session. Behavioral biometric techniques(voice, signature, gait, keystroke dynamics, etc.) can be used for continuous authentication. Keystroke dynamics in one of the behavioral biometrics that can be captured without any extra hardware. In this paper, we are using keystroke dynamics for continuous user authentication. A few works [16–28] has been done in the direction of continuous user authentication through behavioral biometrics.

One of the limitation of all the above proposed continuous authentication mechanism is that in case of detection of an unauthorized user, the locking and unlocking of whole device is performed, rather than locking the particular sensitive applications only. As the different application deals with data having different security needs, locking the whole device will decrease the device usability. Also it creates a very helpless condition for the device owner, since they are unable to access any of the applications in those devices, even those which needs the least security. so there is a need of application level security mechanism.

Considering the above two limitations, in this paper, we are proposing an application based security mechanism, through which user is authenticated at the start of the session with static multi-modal (keystroke and mouse dynamics) behavioral biometric technique, and then periodically during the session with continuous keystroke dynamics.

Our contribution in this work are:

- We have proposed a biometric user authentication mechanism for data security in the personal devices. It not only helps to identify the valid user but also provide application level security to the device.
- This mechanism uses static multi-modal behavioral biometric at the entry point and continuous authentication of user using keystroke dynamics. This will help to reduce the intrinsic failure of the behavioral biometric.
- The proposed mechanism provides application security by using risk analysis based approach. It prioritizes the various applications on the basis of risk score and secures the applications accordingly.
- The proposed continuous authentication mechanism identifies the attacker within a very few keys pressed. It helps in locking the various applications according to their priority, rather than locking the whole device.
- The proposed mechanism achieved less false acceptance rate (FAR), less false rejection rate (FRR) and less equal error rate(EER) in comparison with other authentication protocol.

2 Related Work

In keystroke dynamics, user style (time and speed) of typing on a keyboard or typing behavior while pressing keys on the keyboard is used to identify the user. Keystroke dynamics authentication is of two types: *Fixed text* and *Free text based.* In *Fixed text*, the user is authenticated based on the typing dynamics for a given text (fixed). Many works have been done for user authentication through fixed text keystroke dynamics [29–35]. It is used in case of static user authentication, i.e. to improve the security of entry point authentication. But in *free text authentication*, there is no fixed text. The user needs to be authenticated based upon whatever they type. Not much work has been done in the area of user authentication through free text keystroke dynamics. Gunetti and Picardi [16] experimented with free text, keystroke dynamics with a wide set of experimenters (205 individuals). In his paper, the author used two measures: R-measure and A-measure for comparison of free text typing sample. Pusara [17] proposed an examination of user behavior for user re-authentication. Here the user is being authenticated through user input on GUI, keystroke and mouse dynamics. They achieved a FAR of 23.33% and FRR of 1.50% using J48 classification algorithm. Latter Marsters [18] analyzed user authentication through free text, keystroke dynamics using a Bayesian Network Classifier. The author achieved an equal error rate (ERR) of 0.27% with 10-fold cross-validation. Li et al. [19] proposed a behavioral based profiling technique for authentication in mobile devices. It used MIT reality database for experimental purpose. Then Bours [20] proposed a continuous keystroke dynamics authentication mechanism in contrast to the static keystroke dynamics authentication. The author stressed on the way to evaluate the performance of such a biometric authentication system, and how it is different from the existing one. He proposed an authentication performance measure for continuous keystroke dynamics as the number of keystrokes typed, before being detected as an intruder, rather than FAR and FRR. Later Kyle et al. [21] proposed a behavioral biometric system that fuses user data from keyboard, mouse and graphical user interface interaction. Roth et al. [22] proposed a novel behavioral biometrics "Typing behavior" for continuous user authentication. The author claims to provide authentication with short delay compared to the keystroke dynamics. Li et al. [23] proposed a continuous and transparent authentication of mobile users using behavioral

profile. The proposal makes a balance between the security and usability, by authenticating the user on the basis of consecutive application usage, but not the single application. Clark et al. [24] proposed a continuous user authentication using multi-modal biometrics. Patel et al. [25] proposed a survey on progress and existing challenges in continuous user authentication on mobile devices. In this paper, the author has well justified the problems in the previous authentication technique and shift to the biometrics. It has dealt with the various physiological and behavioral biometric modalities. Mondal and Bours [26] proposed a context independent continuous authentication system. In this paper, the author proposed a trust model algorithm for user authentication and performance reporting technique for the continuous authentication system. Fenu et al. [27] proposed a " Multibiometric system for continuous student authentication in e-learning platforms." The approach is found to be flexible and provide reliable support on a large set of online experiences. Kim et al. [28] proposed a user adaptive feature extraction method which captures individual users distinctive typing behaviors embedded in relative typing speed for different digraphs. The author achieved an EER of 0.44

3 Proposed Work

In this section, the scenario for the proposed user authentication mechanism has been discussed. The control flow diagram of the proposed authentication mechanism has been explained in detail, and the application risk analysis rules have been proposed.

Application Scenario We are considering the scenario for the suitability of our proposed user authentication mechanism. Let's suppose a user has a few electronic devices like laptop, tab, etc. All these systems facilitate the user with different applications. The list of various applications may include network applications, system applications, and user applications, etc. The various application deals with various personalized data, having different security needs. So with the risk analysis method, different applications are being provided with different risk scores in the range of 1–30. Now through the static authentication mechanism user will also be provided with a confidence score of genuineness in the range of 0–30. After successful static authentication at the beginning of the session user confidence score will be 30. And in between the session with the help of continuous authentication, it will be adjusted accordingly. A user will be only allowed to use those applications whose risk score are less than or equal to the confidence score of the user.

3.1 Authentication Mechanism

The proposed authentication mechanism as shown in Fig. 1, has been divided into two parts:

- One is *static authentication* at the start of the session or cases where continuous authentication raises an alert.
- Second is*continuous authentication* for the system usage in between the session.

Each of these authentication stages consists of two phases: *Registration Phase* and *Authentication Phase*.

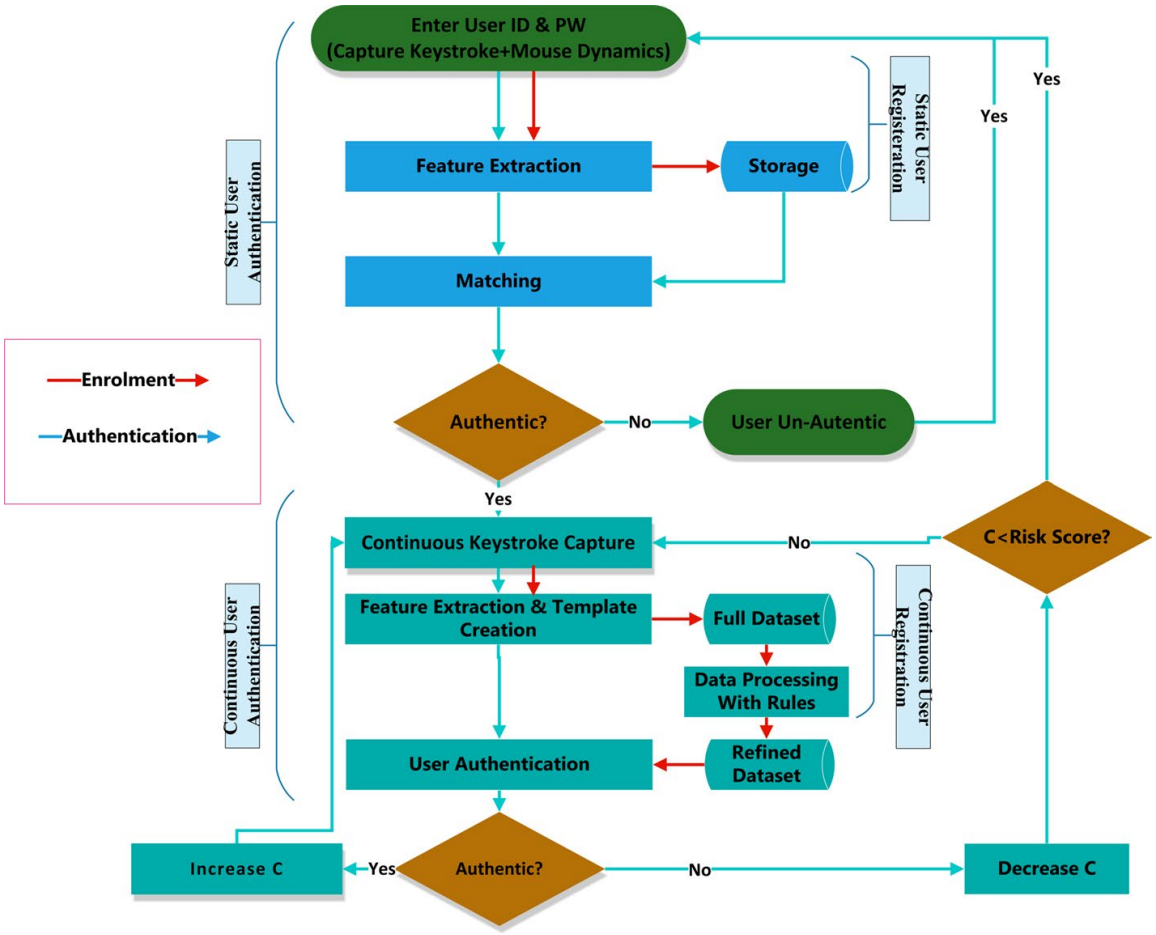

Fig. 1 User authentication work flow diagram

3.1.1 Static Authentication

At the start of the session, when the user opens the system, the system will authenticate the user by user ID and password. Here along with these memory based parameter user's keystroke dynamics as well as mouse dynamics, behavioral parameters during system interaction are also being captured. Now the system will authenticate the user based upon the fused authentication score of these two behavioral modalities.

1. **Registration Phase**
   For registration of the user in the static authentication process we will capture the keystroke and mouse dynamics behavioral parameters of the user for entering a fixed password. Following activities are done in the process:

   – A registration page has been created, where the user will enter their ID and password. While doing this the keystroke and mouse dynamic values for given features were captured.
   – The static keystroke and mouse dynamics features were taken, here are shown in Table 1.
   – Where t_i is the time of pressing the present key. X_i and Y_i are horizontal and vertical distance covered respectively while dragging the mouse. T_i is the current time of the mouse click.
   – After extracting the values, these features are saved in storage for further reference.

Table 1 Static keystroke and mouse dynamics features

S. No.	Biometric modality	Features	Calculation formula
1	Keystroke dynamics	Dwell time (D_i)	$D_i = t_i^{up} - t_i^{down}$
		Flight time (F_i)	$F_i = t_{i+1}^{down} - t_i^{up}$
2	Mouse dynamics	Horizontal velocity (HV)	$HV = \frac{\sum_{i=0}^{n} X_{i+1} - X_i}{\sum_{i=0}^{n} T_{i+1} - T_i}$
		Vertical velocity (VV)	$VV = \frac{\sum_{i=0}^{n} Y_{i+1} - Y_i}{\sum_{i=0}^{n} T_{i+1} - T_i}$
		Tangential acceleration (TA)	$TA = \frac{TV}{\sum_{i=0}^{n} T_{i+1} - T_i}$

2. **Authentication Phase**
   The steps involved in this phase are:

   – First, the user will enter the same ID and password into the login page. The keystroke and mouse dynamic behavior is captured parallelly.
   – Then after feature extraction, static user authentication is performed by matching the login phase data with the corresponding user's registered data from the storage.
   – Here keystroke matching and mouse dynamics matching are done separately, and the decision level fusion is done to get a result.

3.1.2 Continuous Authentication

After the initial intrusive (static) authentication, the user is allowed to use the system. Now, once the session has started, the continuous user authentication will be done. After the initial authentication user will be given a confidence score. Now during continuous authentication after each key press, the authentication is performed. If the user is found to be authentic the confidence level will be increased otherwise decreased.

1. **Registration Phase**
   Registering a user for authentication in continuous text, keystroke dynamics are slightly different from the fixed text keystroke dynamics. Here we need to authenticate the user based on any character they type. So, for that, we will capture users typing behavior continuously on our system for 2 days. The steps for registration are:

   – Keystroke features of each letter typed by the user need to be captured.
   – Features are extracted and arranged in proper format to save in *Full Storage database*. The format in which we are saving the values are:
     $||CurrentKey||DwellTime||FlightTime||NextKey||$.
   – But to authenticate a user correctly, we need their consistent typing timings. Hence, it's not useful to keep those keys typing timings which have rarely used and which have a high coefficient of variation [36]. Using rules in Table 2, the *Full Dataset* is minimized to *Final Dataset1* for single key and *Final Dataset2* for digraph.

Table 2 Rules for dataset refinement

S. No.	Feature type	No. of repitation (NR)	Coefficient of variation (CV)
1	Single key	NR > 50	CV < 0.7
2	Diagraph	NR > 20	CV of single key < 0.7
			CV of all flight times < 1.12

Table 3 User confidence score (CS) variation

S. No.	Matching score (MS)	Confidence score (CS)
1	If $MS < Tdistance$	$CS = minimum(CS + (T_{distance} - MS), 30)$
2	If $MS > Tdistance$	$CS = CS - (MS - T_{distance})$
3	If character not in database?	

2. **Authentication Phase**
   In the continuous authentication phase, the user will be continuously authenticated after each key press. Following steps are involved:

   – After initial authentication, the user will be given a confidence score (CS).
   – Authentication is done by matching a single key and digraph combination.
   – There will be a threshold, $T_{distance}$.
   – During continuous authentication three cases may arise shown in Table 3:
   – When the CS of the user falls below the risk score of the application, the user will be unable to access that application. That application will be locked, and the user is asked for static authentication to proceed forward with that application.

3.2 Risk Analysis of Applications

The computer systems or mobile devices facilitate us with a variety of applications. Different users personalize their device applications according to their needs. The security of these applications assures the security of personal devices. So, when we are talking about our personal computer or mobile systems, the applications are our *assets* which need to be protected. Different applications have different security needs. We have to find out the risk associated with each of the applications we are using. Risk mainly depends on threat and vulnerability associated with an asset. Hence, risk [37] can be defined as:

Risk to an asset is defined as the potential for loss, damage or destruction of an asset as a result of a threat exploiting a vulnerability.

Formally risk is defined as:

$$Risk = Asset * Threat * Vulnerability \tag{1}$$

For risk analysis of applications, following steps will be followed:

Table 4 Examples of possible user assets(UA_i) in a personalized electronic devices

Assets category	
Network applications	
Email (Gmail, Yahoo etc.)	E-banking
Social networking (Facebook, Whatsapp, Twitter etc.)	E-commerce (Paytm, E-shopping, E-ticketing etc.)
News and information	games, entertainment, E-books etc.
User applications	
Offline applications/utilities (doc file, spread sheets etc.)	Multimedia data stored on device(image, video etc.)
Password storage	
System applications	
Bluetooth	Wireless connectivity
LAN settings	

Table 5 Identified threats (T_i)

S. No.	Threats	Notation
1	T.Denial of service	T_1
2	T.Unauthorized access	T_2
3	T.Impersonation	T_3
4	T.Data theft	T_4
5	T.Replace	T_5
6	T.Change of data	T_6
7	T.System failure	T_7
8	T.Copy	T_8

- *Asset identification and ranking* In this step the assets are first categorized and ranked according to the usage preference of the user. Some of the asset categorization of the proposed scenario according to the rank are shown in Table 4.
- *Threat identification* After asset identification, the possible threat on the given assets are identified. Table 5 shows some of them.
- *Mapping of Asset and Threats* In this step the different identified asset in the project are mapped with the all possible threat on it. This mapping are shown in Table 6.
- *Vulnerability Assessment* The vulnerability related to the assets are divided into three categories. Value of vulnerability defined by CRAMM [37] will be taken that are low (.1), medium (.5), high (1), Table 7 shows this.
- *Estimate the Value of Risk* Now to find out the risk value related to the applications, we will use a lookup Table 9 similar to the CRAMM [37] (where the value of the asset, the strength of the threat and the vulnerability value are input parameters), which gives the final value of risk in the range 1 through 30. Here the asset and the threat values are identified with the help of Table 8. The asset value is determined as the number of threat occurring in them, and the threat value is derived as the number of assets it is affecting in the present system. Now the calculated risk will be fixed as the risk level of the application.

Table 6 User asset-threat mapping ($UA_i \longrightarrow T_i$)

S. No.	Asset	Threat
Network applications		
1	E-banking (UA_1)	T_1, T_3, T_2, T_6, T_4
2	E-commerce (UA_2)	T_1, T_3, T_2, T_6
3	E-mail (UA_3)	T_1, T_3, T_2, T_6, T_4
4	Social networking (UA_4)	T_3, T_4, T_5, T_6
5	Games and entertainment (UA_5)	T_5, T_6
User applications		
6	Password storage file (UA_6)	T_1, T_4, T_8, T_6, T_5
7	Document, multimedia files (UA_7)	T_1, T_4, T_6, T_8
System applications		
8	Wireless connectivity (UA_8)	T_1, T_7
9	Anti-virus (UA_9)	T_2, T_7

Table 7 Vulnerability asset mapping

Low (.1)	Medium (.5)	High (1)
Vulnerability categories		
Games and Entertainment (UA_5)	E-Commerce (UA_2)	E-banking (UA_1)
Multimedia data stored and doc files, spread sheets (UA_7)	E-Mail (UA_3)	Password storage (UA_6)
	Social network (UA_4)	Anti-virus (UA_9)

Table 8 Asset value and threat value lookup table (where ✓ denotes applicable and X denotes not applicable)

	UA1	UA2	UA3	UA4	UA5	UA6	UA7	UA8	UA9
T1	✓	✓	✓	X	X	✓	✓	✓	X
T2	✓	✓	✓	X	X	X	X	X	✓
T3	✓	✓	✓	✓	X	X	X	X	X
T4	✓	X	✓	✓	X	✓	✓	X	X
T5	X	X	X	✓	✓	✓	X	X	X
T6	✓	✓	✓	✓	✓	✓	✓	X	X
T7	X	X	X	X	X	X	X	✓	✓
T8	X	X	X	X	X	X	✓	X	X

4 Implementation and Results

We have implemented the proposed authentication mechanism on a prototype scenario having only three applications. All the implementation interfaces have been created and tested on the system with 64-bit windows operating systems, with 16 GB RAM, Intel(R) Core(TM)i5-7200U CPU 2.50 GHz 2.17 GHz processor.

According to the proposal, first, the risk score of different applications was calculated and assigned in the range of (1–30). Then to access the applications user need to intrusively

Table 9 Risk value calculation of all the categorized assets

Assets	Asset value	Threats applicable	Threat level, average value ($= \frac{\sum Threat\ Value}{No.\ of\ threats}$)	Vulnerability value	Calculated risk
UA1	5	T1,T2,T3,T4,T6	6,4,4,5,7 (5.5)	1	26.5
UA2	4	T1,T2,T3,T6	6,4,4,7 (5.5)	0.5	11.8
UA3	5	T1,T2,T3,T4,T6	6,4,4,5,7 (5.5)	0.5	13.75
UA4	4	T3,T4,T5,T6	4,5,3,7 (4.7)	0.5	9.4
UA5	2	T5,T6	3,7 (5)	0.1	1
UA6	4	T1,T4,T5,T6,T8	6,5,3,7,1 (4.4)	1	17.6
UA7	4	T1,T4,T6,T8	6,5,7,1 (4.7)	0.1	1.8
UA8	2	T1,T7	6,2 (4)	0.1	4
UA9	2	T2,T7	4,2 (6)	1	6

authenticate themselves by entering their user ID and password in the login page. For this purpose, static multi-modal behavioral biometric authentication was performed. Each authenticated user will be awarded the highest Confidence level (30) and able to use any of the applications whose risk score is below their confidence level. In the post authentication session, user was continuously observed and authenticated based upon whatever they type, and accordingly, the user confidence level was adjusted. So, to implement the proposed application scenario, we need to register the user by creating the dataset. The dataset we need to create here consists of, data set for static user authentication and continuous keystroke dynamics. We have implemented the proposed work in the following subsections.

Dataset Creation First of all, to create the dataset for static user authentication, we captured the features of keystroke and mouse dynamics mentioned in Table 1, through the registration interface. Our created dataset consists of a total of 60 users with each user's 50 repeated entries. The repeated entries were taken to capture the user's consistent behavior. After that the registered data were stored in the database *Keystroked* and *Mouse*.

Then dataset for continuous keystroke dynamics was created by continuously capturing the keystroke features for 2 days of each typed character in any of the three applications. At a time user can write in any one of the applications only. As this process resulted in with the key press duration of all the keys typed during those 2 day period, so the data set consisted of keys and key combinations that are pressed many times and some that are pressed very less number of times like once or twice only. All these data, we captured were inserted into the database named ***Full Storage***. This table consists of attributes: current key, dwell time, flight time, next key, app no, and user name. To capture the users consistent data for better accuracy, application administrator logged in and analyzed user's data that were collected and filtered them according to the rules mentioned in Table 2, and created two refined databases one for single key ***(Final Dataset1)*** and other for di-graph ***(Final Dataset2)***.

Risk Assessment After dataset creation, we need to calculate the risk score of various classified assets. For this, we followed the steps proposed in Sect. 3.2. The calculated risk values of the assets are shown in Table 9. But here we have performed an analysis over three applications only. For that, we created an interface having three applications (E-banking, Password Storage File and Notes), each having different risk levels. The calculated risk levels of the applications E-banking, Password Storage File and Notes were found to be

Table 10 Classification result of keystroke and mouse dynamics data

Algorithms		FAR	FRR	EER	Accuracy (%)
Keystroke dynamics	Bayes net	0.99	1.79	1.39	94.36
	J48	0.93	1.66	1.29	93.29
Mouse dynamics	Bayes bet	1.82	1.94	1.88	66.02
	J48	1.65	2.99	2.32	64.91
Keystroke dynamics and mouse dynamics	Bayes net	0.82	1.72	1.27	93.82
	J48	0.89	1.2	1.04	95.66

26.5, 17.6 and 1.8 respectively as calculated in Table 9. After the risk score assessment, the user authentication process will be started.

Authentication For using the system, the user entered their credentials through the login page. Then matching of user's entered credentials with the registered data was performed. Here we have used two classification algorithms: Bayes Net and J48 for matching of both keystroke and mouse dynamics. We used Weka 3.8 version for all the statistical analysis. A comparative analysis has been made here which shows that the multi-modal biometrics, i.e., mouse dynamics and keystroke dynamics together gave a better authentication performance than the single modalities. Table 10 shows the result.

As mentioned in Sect. 3.1 after the successful static multi-modal user authentication, the user will be continuously authenticated for each key they pressed. After static user authentication, the user was given a confidence score of 30. Now, for every key press, while using any of these applications matching scores were generated for a single key and di-graph using Euclidean distance algorithm [38] at the given threshold ($T_{distance}$). According to the obtained matching score the confidence level was adjusted based upon the rules in Table 3. In cases was confidence score is below the threshold T_{action}, the application were temporarily locked, and the user are asked for static multi-modal authentication.

5 Performance Analysis and Comparison

In this section, a performance analysis of static authentication and continuous authentication has been performed. A performance comparison of proposed work with previous work has also been done here.

For static authentication, we simulated the authentication process of the three modalities at a varying range of normalized threshold values between 0 and 1 using the j48 algorithm, as shown in Fig. 2.

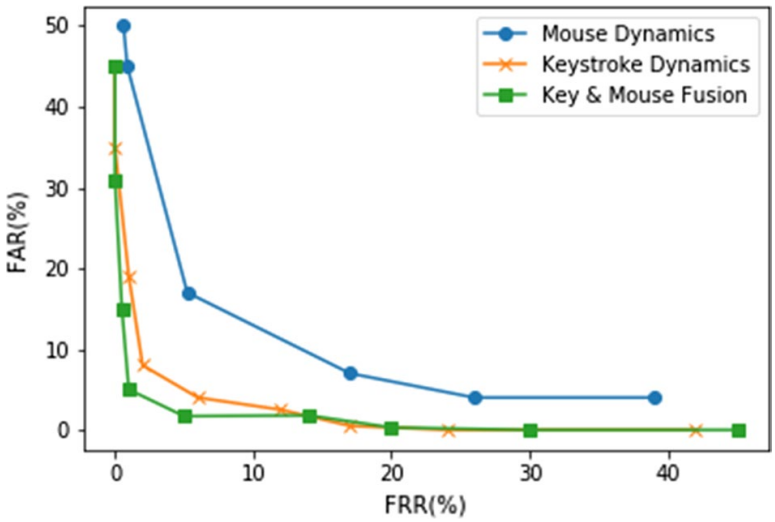

Fig. 2 Receiver operating curve for keystroke dynamics, mouse dynamics and fused keystroke and mouse dynamics

Table 11 Performance analysis of continuous keystroke dynamics

p Applications	Risk level	Attacker1	Attecker2	Attacker3	Attacker4	Attacker5
E-banking	26.5	63	46	99	65	54
Password file	17.6	97	76	112	71	68
Notes	1.8	108	79	135	88	97

As observed from the plot 2 we found the EER value of multi-modal biometrics are more near to zero compared to keystroke dynamics and mouse dynamics. This plot reveals the robustness of multi-modal biometrics in the verification task. Also at most of the observed threshold, the performance of multi-modal biometrics are found better compared to the uni-modal biometrics in the given scenario. The result justifies our selection of multi-modal biometric in static authentication.

For the performance evaluation of continuous authentication, first, the thresholds T_{action} for each user need to be determined. This T_{action} will help to adjust the value of confidence level of particular user. For determining T_{action} the user's test data are compared against their own registered data. Now to evaluate the continuous keystroke dynamics performance, number of key pressed by an intruder before being restricted to use particular application need to be identified, it means when the confidence score (CS) goes below the risk score (RS) of particular application. We have tested with around five attackers for the given three applications. The results are shown in Table 11.

The table shows applications with their risk levels, and different attackers with the number of the key pressed before reaching the threshold. We found that, for almost all the five attackers, the number of key pressed before being detected as imposture increases with the decreasing risk level of applications. And on an average 46–135 number of keys were pressed by an attacker before being detected. A plot showing five different attackers being captured after the number of keys they pressed in three different applications are shown in Fig. 3.

A comparative analysis with the previous works in continuous keystroke dynamics has been presented with our proposed work in Table 12. The analysis shows a satisfactory results.

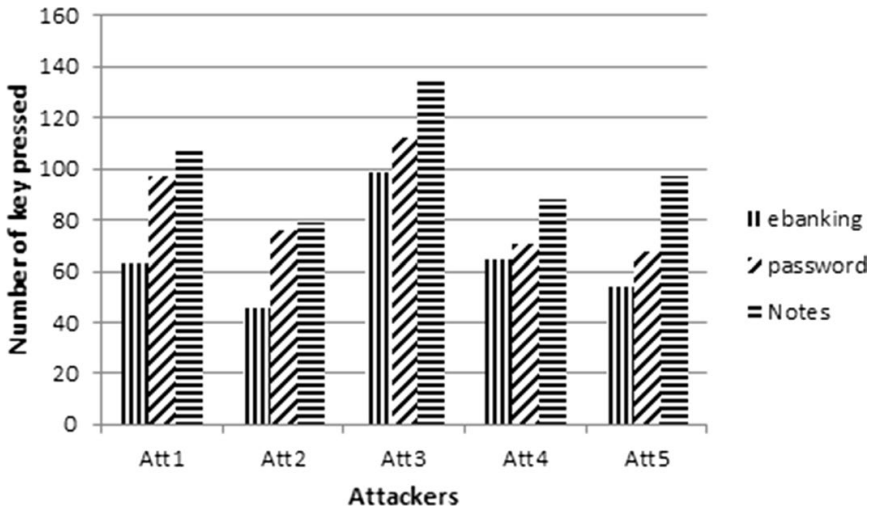

Fig. 3 A plot of different attacker (Att1, Att2, Att3, Att4, Att5) with no. of key they pressed before being detected using given three applications

Table 12 Comparison analysis

Research works	No. of users	Features used	Classification technique	Results
Pusara et al. [17]	61	KS,MD,GUI	J48	FAR 23.33%
				FRR 1.50%
Marsters et al. [18]	10	KS	Bayes net	EER 0.27%
Li et al. [19]	22	calls	Neural Net	EER 2.2%
Bours [20]	25	KS	No. of key pressed	EER 41.8%
Bailey et al. [21]	31	KS,MD,GUI	EBDL fusion	FAR 2.24%
				FRR 2.10%
Roth et al. [22]	63	TB	Bag of MD phrase	EER 4.9%
Li et al. [23]	22	Historical usage data	Neural net	EER 9.8%
Proposed work	60	KS,MD	J48	EER 1.04%

6 Conclusion

In this paper, we have shown the importance of application based user authentication mechanism compared to the device level, as the device based user authentication mechanisms, locks the whole device irrespective of application risk level. For providing full proof security, a biometric based authentication mechanism has been proposed. Here for static authentication behavioral multi-modal biometric authentication has been used. And for continuous authentication keystroke dynamics has been used.

References

1. Fan, C. I., Chan, Y. C., & Zhang, Z. K. (2005). Robust remote authentication scheme with smart cards. *Computers and Security*, *24*(8), 619–628.
2. Lee, S. W., Kim, H. S., & Yoo, K. Y. (2005). Efficient nonce-based remote user authentication scheme using smart cards. *Applied Mathematics and Computation*, *167*(1), 355–361.

3. Liu, J. Y., Zhou, A. M., & Gao, M. X. (2008). A new mutual authentication scheme based on nonce and smart cards. *Computer Communications*, *31*(10), 2205–2209.
4. Xu, J., Zhu, W.-T., & Feng, D.-G. (2009). An improved smart card based password authentication scheme with provable security. *Computer Standards and Interfaces*, *31*(4), 723–728.
5. Li, L.-H., Lin, I.-C., & Hwang, M.-S. (2001). A remote password authentication scheme for multiserver architecture using neural networks. *IEEE Transactions on Neural Networks*, *12*(6), 1498–1504.
6. Weiss, R., & De Luca, A. (2008). PassShapes: Utilizing stroke based authentication to increase password memorability. In *Proceedings of the 5th Nordic conference on human–computer interaction: building bridges* (pp. 383–392). ACM.
7. Gao, H., Guo, X., Chen, X., Wang, L., & Liu, X. (2008). Yagp: Yet another graphical password strategy. In *Computer security applications conference, 2008. ACSAC 2008. Annual* (pp. 121–129). IEEE.
8. Bicakci, K., Atalay, N. B., Yuceel, M., Gurbaslar, H., & Erdeniz, B. (2009). Towards usable solutions to graphical password hotspot problem. In *Computer software and applications conference, 2009. COMPSAC'09. 33rd annual IEEE international* (Vol. 2, pp. 318–323). IEEE.
9. Chang, C. C., & Lin, I. C. (2004). Remarks on fingerprint-based remote user authentication scheme using smart cards. *ACM SIGOPS Operating Systems Review*, *38*(4), 91–96.
10. Kim, H. S., Lee, S. W., & Yoo, K. Y. (2003). ID-based password authentication scheme using smart cards and fingerprints. *ACM SIGOPS Operating Systems Review*, *37*(4), 32–41.
11. Scott, M. (2004). Cryptanalysis of an ID-based password authentication scheme using smart cards and fingerprints. *ACM SIGOPS Operating Systems Review*, *38*(2), 73–75.
12. Choi, H., Choi, K., & Kim, J. (2011). Fingerprint matching incorporating ridge features with minutiae. *IEEE Transactions on Information Forensics and Security*, *6*(2), 338–345.
13. Das, R. K., Mukhopadhyay, S., & Bhattacharya, P. (2014). User authentication based on keystroke dynamics. *IETE Journal of Research*, *60*(3), 229–239.
14. Aviv, A. J., Gibson, K. L., Mossop, E., Blaze, M., & Smith, J. M. (2010). Smudge attacks on smartphone touch screens. *Woot*, *10*, 1–7.
15. Jain, A. K., Ross, A., & Prabhakar, S. (2004). An introduction to biometric recognition. *IEEE Transactions on Circuits and Systems for Video Technology*, *14*(1), 4–20.
16. Gunetti, D., & Picardi, C. (2005). Keystroke analysis of free text. *ACM Transactions on Information and System Security (TISSEC)*, *8*(3), 312–347.
17. Pusara, M. (2007). *An examination of user behavior for user re-authentication*. Ph.D diss., Purdue University.
18. Marsters, J.-D. (2009). *Keystroke dynamics as a biometric*. Ph.D. diss, University of Southampton.
19. Li, F., Clarke, N., Papadaki, M., & Dowland, P. (2011). *Behaviour profiling for transparent authentication for mobile devices*. Academic Publishing Ltd, UK.
20. Bours, P. (2012). Continuous keystroke dynamics: A different perspective towards biometric evaluation. *Information Security Technical Report*, *17*(1–2), 36–43.
21. Bailey, K. O., Okolica, J. S., & Peterson, G. L. (2014). User identification and authentication using multimodal behavioral biometrics. *Computers and Security*, *43*, 77–89.
22. Roth, J., Liu, X., & Metaxas, D. (2014). On continuous user authentication via typing behavior. *IEEE Transactions on Image Processing*, *23*(10), 4611–4624.
23. Li, F., Clarke, N., Papadaki, M., & Dowland, P. (2014). Active authentication for mobile devices utilising behaviour profiling. *International Journal of Information Security*, *13*(3), 229–244.
24. Saevanee, H., Clarke, N., Furnell, S., & Biscione, V. (2015). Continuous user authentication using multimodal biometrics. *Computers and Security*, *53*, 234–246.
25. Patel, V. M., Chellappa, R., Chandra, D., & Barbello, B. (2016). Continuous user authentication on mobile devices: Recent progress and remaining challenges. *IEEE Signal Processing Magazine*, *33*(4), 49–61.
26. Mondal, S., & Bours, P. (2017). A study on continuous authentication using a combination of keystroke and mouse biometrics. *Neurocomputing*, *230*, 1–22.
27. Fenu, G., Marras, M., & Boratto, L. (2018). A multi-biometric system for continuous student authentication in e-learning platforms. *Pattern Recognition Letters*, *113*, 83–92.
28. Kim, J., Kim, H., & Kang, P. (2018). Keystroke dynamics-based user authentication using freely typed text based on user-adaptive feature extraction and novelty detection. *Applied Soft Computing*, *62*, 1077–1087.
29. Liew, K.-M., Shen, H., See, S., Cai, W., Fan, P., & Horiguchi, S. (Eds.). (2004). *Parallel and distributed computing: applications and technologies: 5th international conference, PDCAT 2004, Singapore, December 8–10, 2004, Proceedings* (Vol. 3320). Springer.
30. Cho, S., & Hwang, S. (2006). Artificial rhythms and cues for keystroke dynamics based authentication. In *International conference on biometrics* (pp. 626–632). Berlin: Springer.
31. Hocquet, S., Ramel, J.-Y., & Cardot, H. (2007). User classification for keystroke dynamics authentication. In *Advances in biometrics* (pp. 531–539).

32. Rybnik, M., Tabedzki, M., & Saeed, K. (2008). A keystroke dynamics based system for user identification. In *Computer information systems and industrial management applications, 2008. CISIM'08. 7th* (pp. 225–230). IEEE.
33. Revett, K. (2009). A bioinformatics based approach to user authentication via keystroke dynamics. *International Journal of Control, Automation and Systems*, *7*(1), 7–15.
34. Giot, R., El-Abed, M., Hemery, B., & Rosenberger, C. (2011). Unconstrained keystroke dynamics authentication with shared secret. *Computers and Security*, *30*(6), 427–445.
35. Visumathi, J., & Jesu Jayarin., P. (2015). A secured and reliable biometric user authentication using keystroke template method. *Journal of Applied Security Research*, *10*(3), 375–384.
36. Abdi, H. (2010). Coefficient of variation. *Encyclopedia of Research Design*, *1*, 169–171.
37. Yazar, Z. (2002). A qualitative risk analysis and management tool—CRAMM. *SANS InfoSec Reading Room White Paper*, *11*, 12–32.
38. Danielsson, P.-E. (1980). Euclidean distance mapping. *Computer Graphics and Image Processing*, *14*(3), 227–248.

Publisher's Note Springer Nature remains neutral with regard to jurisdictional claims in published maps and institutional affiliations

Neha is a Ph.D. scholar at National Institute of Technology Patna, in computer science department. She has completed her M.Tech from National Institute of Technology Durgapur, India. She has some published research papers in CCIS (Springer) and reputed International Journals. Presently, she is working in the field of Information Security.

Kakali Chatterjee is Assistant Professor in Computer Science and Engineering Department of National Institute of Technology Patna, India. She has completed her Ph.D. from Delhi University (formerly Delhi College of Engineering). She has done M.Tech from Centre for Development of Advanced Computing, a R&D and Academic centre of Govt. of India. She has many published research papers in LNCS (Springer) and reputed International Journals. She is working in the field of Information Security and Cryptography.

J Opt
https://doi.org/10.1007/s12596-019-00534-0

RESEARCH ARTICLE

Design of novel hybrid WDM/multiple-beam FSO system to improve the link length in rainy season

Disha Srivastava[1] · **Gurjit Kaur**[3] · **Prabhjot Singh**[2]

Received: 14 June 2017 / Accepted: 24 April 2019
© The Optical Society of India 2019

Abstract As single laser beam cannot deal with the effect of turbulent atmospheric channels in free space optic (FSO) system, so we have proposed a novel hybrid WDM/multiple-beam system which can reduce the effects of tropical rain weather condition and provide a significant enhancement in the link range, scalability and received optical power. The result indicates that the SNR and FSO link ranges are improved by 20 dB and 3 km, respectively, by using the proposed technique in contrast to previous techniques.

Keywords Free space optical communication · Wavelength division multiplexing · Rain attenuation · Signal-to-noise ratio · Link length

Introduction

The Free space optical communication (FSO) is an attractive and alternative solution to the present microwave systems by offering high bandwidth, light weight, smaller size and low-power economical systems for future broadband network. The FSO technology offers ultra-high data rate due to extremely large available bandwidth and operates in unlicensed spectrum band which can be quickly set up and reconfigured. The integration of FSO technology into existing access networks is more rapid since it is transparent to the traffic type and the protocol [1–3]. Its narrow optical beams are very directive and provide secure connections and spatial isolation from eavesdroppers. Although the biggest challenges are the atmospheric attenuation and attainment of high link availability [3–6], the main atmospheric impairments that affect the propagation of optical signal through the atmosphere unguided media are absorption, scintillation, atmospheric scattering and the region in which link is being established. In temperate region, fog and heavy snow are two main weather conditions and in tropical region, haze and heavy rain are two main constraints which have the major impact on the FSO link [7, 8].

The FSO systems with wavelength division multiplexing (WDM) technique employing single laser beam have been demonstrated in [9–11]. But the quality of an FSO transmission link using single-beam transceiver is less adequate. As signal passes through the turbulent atmospheric channel, FSO with single laser beam experiences random beam wander, beam broadening and wavefront distortion [12, 14, 15]. These meteorological effects create random power fluctuation at the receiver. This single laser beam faces temperature gradients due to heavy fog and solar heating; hence, the link performance can be extremely influenced by scintillation and heavy rain condition and cause fluctuation in the air refractive index. At the receiver, these factors give rise to the intensity variations which turns into a high BER and reduced channel capacity. To combat these problems, we are proposing one remarkable solution to apply the multiple-beam concept in FSO system.

✉ Gurjit Kaur
gurjeet_kaur@rediffmail.com

Disha Srivastava
disha17srivastava@gmail.com

Prabhjot Singh
prabhjot27@gmail.com

[1] Department of Electronics and Communication Engineering, Gautam Buddha University, Greater Noida, UP, India

[2] Salesforce, San Francisco, Bay Area, USA

[3] Department of Electronics and Communication Engineering, Delhi Technological University, Delhi, India

Published online: 03 May 2019

In this research paper, we have designed the hybrid WDM/multiple-beam technique that will reduce the atmospheric attenuation significantly. It also achieves the increasing requirements for scalability and enlarged communication bandwidth by employing multiple-optical beams under heavy rain situation.

We examine the performance of proposed system by taking the actual rain weather data of Delhi which improves the viability of results. Delhi being a capital of India is the hub of IT companies where FSO systems can provide ultra-high speed and bridge multiple buildings in campus and corporate networks. We consider the 5-month rainfall data collected from Agricultural Research Institute, New Delhi [13], and performance is examined in terms of bit error rate (BER), received optical power, signal-to-noise ratio (SNR) and eye diagram for various FSO link ranges. Delhi weather is monsoon influenced where the monsoon starts in late May and lasts until the mid of September. The driest weather in Delhi is in November and December, and the wettest weather is in July. The rainfall attenuation in FSO communication system is given as

$$\mathrm{Att}_{\mathrm{Rainfall}} = 1.076 \times (R_{\mathrm{Rain}})^{0.67} \tag{1}$$

where $\mathrm{Att}_{\mathrm{Rainfall}}$ is rainfall attenuation and R_{Rain} is the rainfall rate. Hence, the collected rainfall data of 5 months have been used for the calculation of attenuation of the FSO link as represented in Eq. (1). FSO system in Delhi oversees the 5-month rainfall attenuation of 29 dB/km. The data are shown in Table 1.

The rest of paper is organized as: Sect. 2 describes the simulation design of the proposed hybrid WDM/multiple-beam FSO system. The results are discussed in Sect. 3, and the conclusion is presented in Sect. 4.

Simulation design of the proposed system

We propose a hybrid WDM/multiple-beam FSO communication system where multiple beams are incident from the source plane at $z = 0$ and propagate along the z-axis $(z > 0)$ in the atmosphere where the turbulence is present.

Table 1 Measured rainfall data [7] and rainfall attenuation for 5 months in Delhi for the year 2015

Month	Rainfall rate (mm/h)	Rainfall attenuation (dB/km)	Average rainfall attenuation of five months
May 2015	0.8	0.92	29 dB/km
June 2015	124.4	27.24	
July 2015	377.8	57.35	
August 2015	261.3	44.8	
September 2015	67.2	18.04	

In Cartesian coordinate system, the electric field of multiple-optical beams in source plane can be represented as

$$E_{\mathrm{s}}(x, y, z = 0) = \sum_{n=1}^{N} E_{\mathrm{n}}(x, y, z = 0) \tag{2}$$

where $E_{\mathrm{n}}(x, y, z = 0)$ expresses the electric field of nth optical beam in a multiple-beam FSO communication system and N is number of beams. If the beams are flat-topped in nature, then at source plane ($z = 0$), the electric field has circular symmetry and can be represented by the summation of Gaussian beam as

$$E_{\mathrm{n}}(x, y, z = 0) = \sum_{m=1}^{P} \frac{(-1)^m}{P} \binom{P}{m} \times \exp\left[\frac{-m\left[(x - a_{\mathrm{n}})^2 + (y - b_{\mathrm{n}})^2\right]}{w_0^2}\right] \tag{3}$$

where P represents the order of beam flatness, $\binom{P}{m}$ is binomial coefficient, $(a_{\mathrm{n}}, b_{\mathrm{n}})$ is center coordinate of nth beam in the source plane and w_0 is beam width of Gaussian beam. Therefore, at source the electric field of multiple beams can be formulated as

$$E_{\mathrm{s}}(x, y, z = 0) = \sum_{n=1}^{N} \sum_{m=1}^{P} \frac{(-1)^m}{P} \binom{P}{m} \times \exp\left[\frac{-m\left[(x - a_{\mathrm{n}})^2 + (y - b_{\mathrm{n}})^2\right]}{w_0^2}\right] \tag{4}$$

.

We consider four beam FSO systems for three end users as shown in Fig. 1. The design parameters of the proposed hybrid WDM/multiple-beam FSO system are shown in Table 2.

We consider pseudo-random binary sequence (PRBS) generator of 5 to 10 Gbps used by each end user to generate its information. Non-return to zero (NRZ) pulse generator is used to translate the user data into binary signals, and then these signals are modulated with laser of 1550 nm wavelength having spacing of 0.8 nm by Mach–Zehnder modulator. These modulated optical signals from each end user are optically multiplexed using the WDM multiplexer into one signal carrying the wavelengths 1550 nm, 1550.8 nm and 1551.6 nm. The multiplexed signal is split into four beams using optical power splitter as shown in Fig. 2 and send to the turbulent atmospheric medium through an optical transmitter.

At the receiver, the signals are combined with power combiner and de-multiplexed to convert the optical signal of each user into corresponding electrical signal. The receiver is composed of three PIN photodiodes which

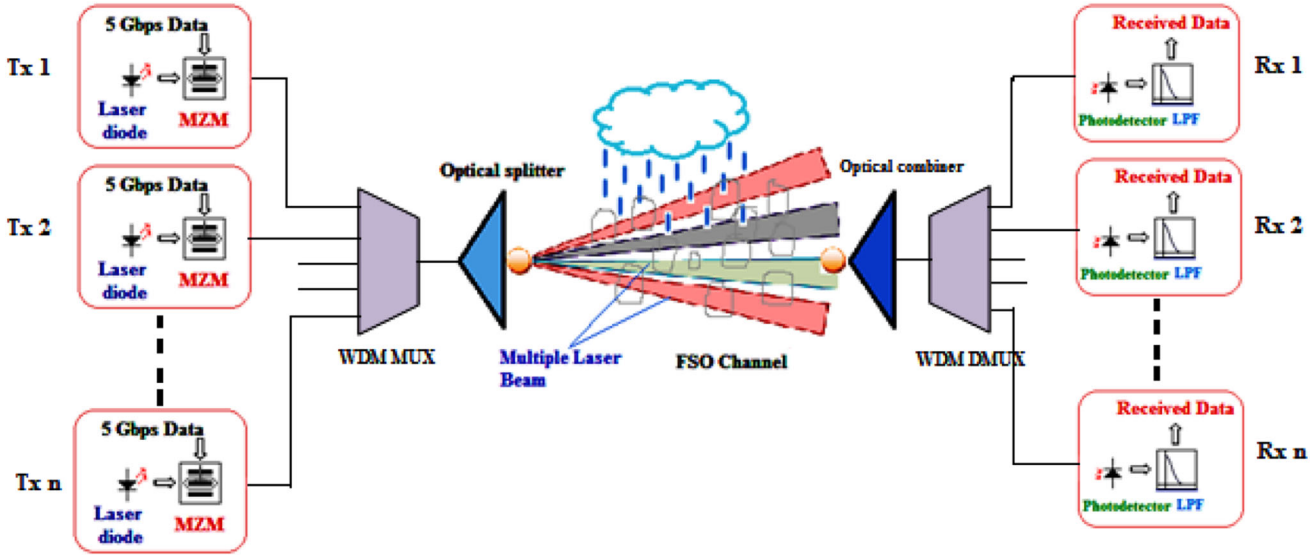

Fig. 1 Proposed hybrid WDM/multiple-beam FSO communication system

Table 2 Design parameters of the hybrid WDM/multiple-beam FSO communication link

Component	Parameter	Value
PRBS generator	Data rate	5 and 10 Gbps
CW laser	Wavelength	1550 nm
	Spacing	0.8 nm
Optical amplifier	Gain	20 dB
FSO channel	Link length	1–8 km
	Attenuation (due to rainfall)	29 dB/km
	Transmitter aperture diameter	5 cm
	Receiver aperture diameter	30 cm

detect the electrical signals. To analyze performance of hybrid WDM/multiple-beam FSO system, the received signal is sent to WDM signal analyzer, eye diagram analyzer and power meter.

Results and discussion

The performance of the proposed system is improved by employing hybrid WDM/multiple-beam concept as shown in Fig. 3. The FSO system using single beam is much vulnerable to rain attenuation in tropical rainy weather and gives the BER of 10^{-39} for link length of 3 km whereas using four multiple beams, 10^{-69} BER can be achieved for the same distance.

According to the Meteorological Department of India [11], the rainfall in Delhi is at its peak during the monsoon seasons and in July the rainfall rate is 377.8 mm/h, which is very high. So rainfall causes very much degradation on FSO system performance during this month which induces fluctuations of signal intensity at receiver and gives an SNR of 10 dB for 3 km link length in heavy rain condition.

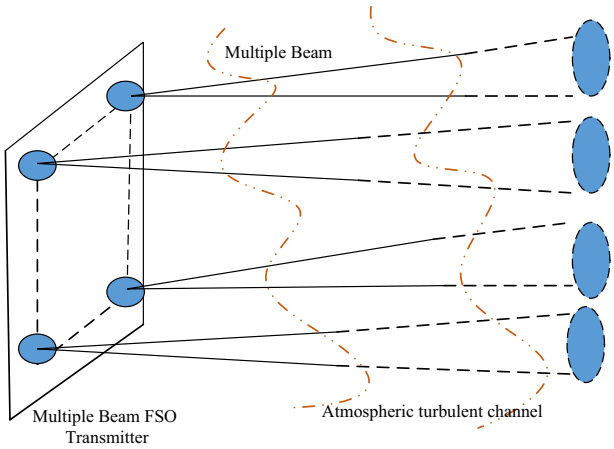

Fig. 2 Concept of multiple-beam FSO system transmitter

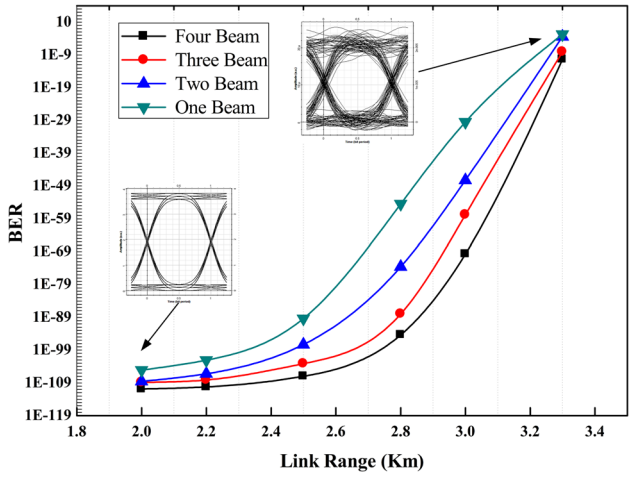

Fig. 3 BER versus link range

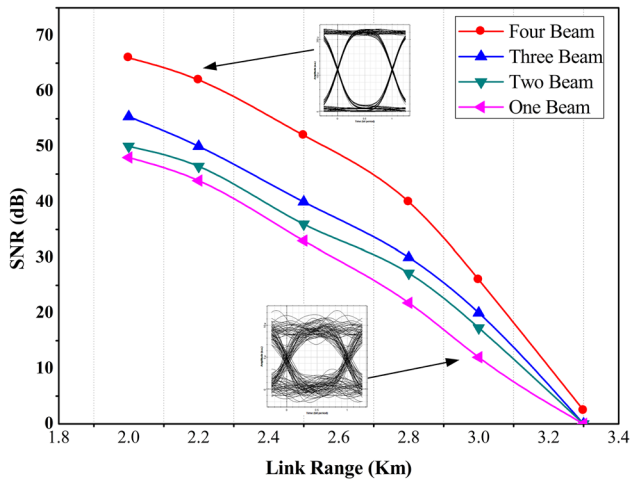

Fig. 4 SNR versus link range

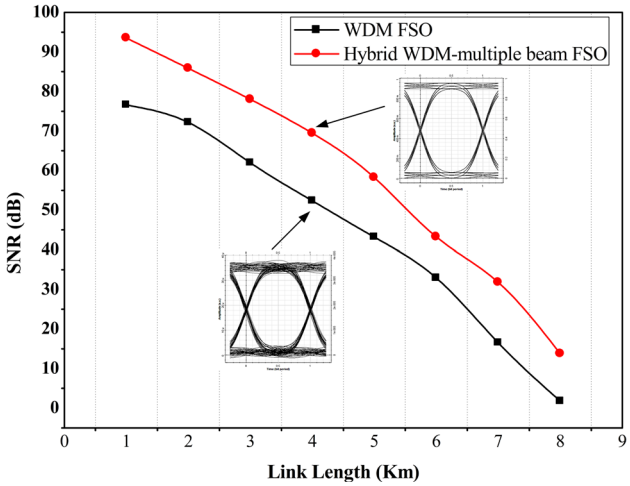

Fig. 6 SNR versus link range

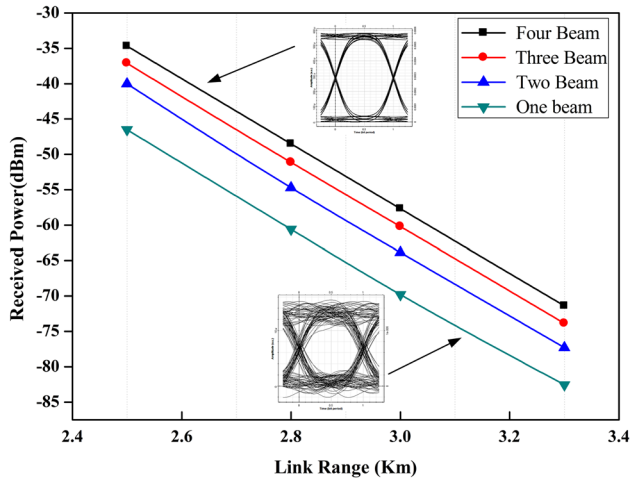

Fig. 5 Received optical power versus link length

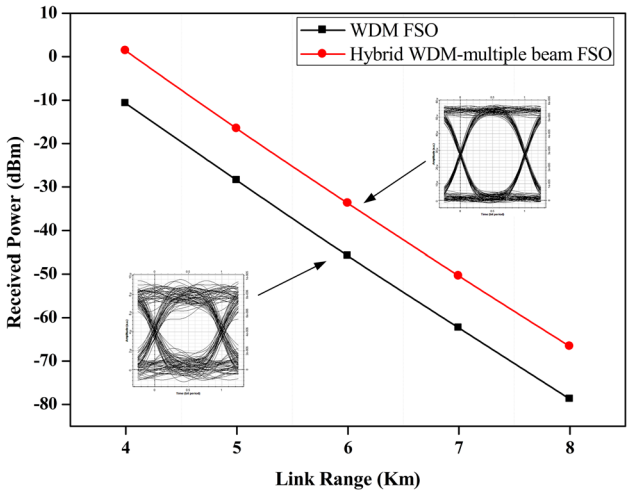

Fig. 7 Received optical power versus link range

By replacing single-beam channel with hybrid-WDM/multiple beams, the signal is less attenuated and can reach to the receiver even at 3 km away from the transmitter with an SNR of 30 dB during heavy rain in Delhi. FSO system with four beams can encounter a higher received optical power up to − 55 dBm for 3 km link length as shown in Figs. 4 and 5.

Figures 6 and 7 conclude the comparison between WDM and hybrid WDM/multiple-beam FSO system under medium rain condition. With the help of WDM technique, the FSO systems attract huge bandwidth demanding applications and conquer the limited scalability, confined reach and reduced optical power. Employing WDM technique with multiple-beam concept ensures an increased in number of end users at very high data rate.

Figure 8 illustrates the measure of BER values versus link range for different users. The maximum achievable range is 3.5 km at a BER of 10^{-9} that explains that as link

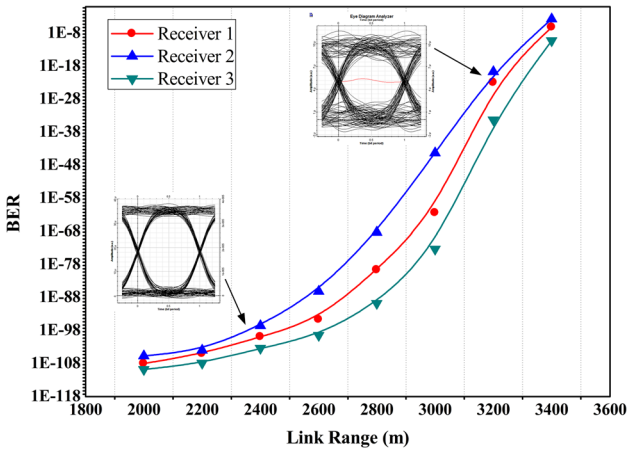

Fig. 8 BER versus link range

length increases, the beams get overlapped and decrease the system performance. Figure 9 demonstrates the optical

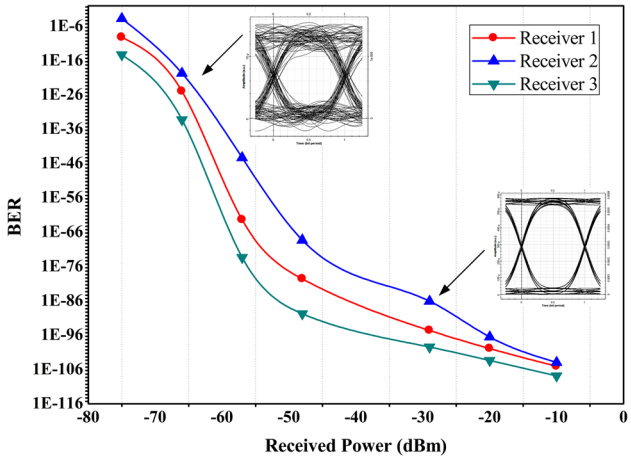

Fig. 9 BER versus received optical power

power sensitivity by different receivers at required BER of 10^{-9}.

Conclusion

In this paper, the performance of hybrid WDM/multiple-beam FSO system is investigated for Delhi rain weather. For the analysis, the rainfall rate of 5 months for the year 2015 is collected. The outcome demonstrates that multiple-beam concept has given a noteworthy change in link availability during heavy rain in Delhi with link span successfully up to 3.3 km. The result also shows that by replacing single beam with multiple-beam FSO channel, the SNR is improved by 20 dB and rise in received signal power is 15 dBm for 3 km link range. Additionally, from an operational point of view, utilizing multiple lasers on transmitter side and multiple apertures on receiver side, redundancy in the transmission path can be provided and it is helpful if a particular laser gets failed. From an atmospheric prospective, multiple-beam concept is exceptionally powerful in reduction in the attenuation caused by heavy rain and scintillation.

Acknowledgements I would like to thank Gautam Buddha University for providing Optical Communication Laboratory for research work.

References

1. Z. Zhao, S.D. Lyke, and M.C. Roggemann, Adaptive optical communication through turbulent atmospheric channels, in IEEE International Conference Communications, ICC, Beijing, pp. 5432–5436, May 2008
2. X. Qiu, Red Bank, K. Chawla, On the performance of adaptive modulation in cellular systems. IEEE Trans. Commun. **47**(6), 884–895 (2002)
3. T.S. Rappaport, *Wireless Communications: Principles and Practice*, vol. 3, 2nd edn. (Prentice Hall, New Jersey, 2010)
4. D. Kedar, S. Arnon, Urban optical wireless communication networks: the main challenges and possible solutions. IEEE Commun. Mag. **42**(5), 2–7 (2004)
5. M. Toyoshima, W.R. Leeb, H. Kunimori, T. Takano, Comparison of microwave and light wave communication systems in space applications. Opt. Eng. **46**, 015003-1–015003-7 (2007)
6. T.H. Carbonneau, D.R. Wisley, Opportunities and challenges for optical wireless; the competitive advantage of free space telecommunications links in today's crowded market place, in SPIE Conference on Optical Wireless Communications, Massachusetts, vol. 3232, pp. 119–128, 1998
7. http://www.iari.res.in/?option=com_content&view=article&id=402&Itemid=322. Accessed 5 June 2016
8. S.A. Zabidi, M.R. Islam, W. AL-Khateeb, A.W. Naji, Analysis of rain effects on terrestrial free space optics based on data measured in tropical climate. IIUM Eng. J. **12**(5), 469–472 (2011)
9. H.A. Fadhila, A. Amphawanb, H.A.B. Shamsuddina, T.H. Abda, H.M.R. Al-Khafajia, S.A. Aljunida, N. Ahmed, Optimization of free space optics parameters: an optimum solution for bad weather conditions. Optik **124**(19), 3969–3973 (2013)
10. F.D. Kashani, M.R.H. Rad, M.R. Mahzoun, B. Ghafary, Beam propagation analysis of a multi beam FSO system with partially flat-topped laser beams in turbulent atmosphere. Optik **123**, 879–886 (2011)
11. http://www.imd.gov.in. Accessed 5 June 2016
12. S.A. Al-Gailani, A.B. Mohammad, R.Q. Shaddad, Enhancement of free space optical link in heavy rain attenuation using multiple beam concept. Optik **124**, 4798–4801 (2013)
13. S. Hitam, S.N. Suhaimi, A.S.M. Noor, S.B.A.A. Sahbudin, R.K. Zakiah, Performance analysis on 16-channels wavelength division multiplexing in free space optical transmission under tropical regions environment. J. Computer Sci. **8**(1), 145–148 (2012)
14. G. Kaur, D. Srivastava, Optimization of FSO system parameters under varying meteorological conditions in Delhi (May 8, 2018). IUP J. Telecommun. **IX**(1), 29–39 (2017)
15. G. Kaur, D. Srivastava, P. Singh, Y. Parasher, Development of a novel hybrid PDM/OFDM technique for FSO system and its performance analysis. Opt Laser Technol. **109**, 256–262 (2019)

Publisher's Note Springer Nature remains neutral with regard to jurisdictional claims in published maps and institutional affiliations.

Renewable Energy 141 (2019) 657–668

Contents lists available at ScienceDirect

Renewable Energy

journal homepage: www.elsevier.com/locate/renene

Effect of biogas on the performance and emissions of diesel engine fuelled with biodiesel-ethanol blends through response surface methodology approach

Abhishek Sharma [b], Naushad Ahmad Ansari [a], Amit Pal [a], Yashvir Singh [c, *], S. Lalhriatpuia [a]

[a] Department of Mechanical Engineering, Delhi Technological University, Delhi, India
[b] Department of Mechanical Engineering, G L Bajaj Institute of Technology and Management, Greater Noida, UP, India
[c] Department of Mechanical Engineering, Sir Padampat Singhania University, Udaipur, Rajasthan, India

ARTICLE INFO

Article history:
Received 22 January 2019
Received in revised form
26 March 2019
Accepted 8 April 2019
Available online 11 April 2019

Keywords:
Dual fuel
Biogas
Soya biodiesel
Diesel engine
Response surface methodology

ABSTRACT

Fossil fuels consumption rate is an important issue which needs to be addressed regarding future perspectives in terms of the world overall energy requirement due to its exhausting nature and also due to environmental concern. Hence, more diversified research for alternate sources of fuel is needed, even to the extent of using only dual fuels; a mixture of high and low viscous fuel to eliminate diesel from compression ignition (CI) engines completely. In the present study, soya and soya ethanol blends are used as fuels for the CI engine. Besides the use blends in a diesel engine, the response surface methodology technique is also implemented for getting better responses. RSM results confirm that the use of dual fuel results in satisfactory engine performance and emission in a standard diesel engine without any modification in the engine. Blends, engine speed, air flow rate, and engine load are the input variables considered for attaining better BTE, VE, CO, HC, and NO_x as the responses. From all the tested fuel blends considered in the study, the result shows that a blend of soya biodiesel with 8% blending with dual fuel mode at 1486 RPM, 49.5 mm manometer air flow, 6.27 kg engine load show an overall good engine performance. The performance and emission characteristics (BTE, VE, CO, HC, and NO_x emission) are found to be 24.29%, 68.53%, 0.0715% volume, 51.6 ppmv and 1080.2 ppmv respectively.

© 2019 Elsevier Ltd. All rights reserved.

1. Introduction

Researchers from around the world are exploring different possibilities to overcome two major problems namely, shortage of fossil fuels and environmental pollution. In the literature, many researchers found that the best alternative method would be the implementation of renewable fuels that should be environment-friendly and reduces pollution [1]. By keeping these points in mind, the present scenario emphasis on the power generation through internal combustion engines (ICE) by utilizing the biomass as the alternative source of energy which may be in liquid or gaseous forms. Biogas is one of the most attractive biofuels due to its easy availability, economical and easy to use in diesel engine while considering dual fuel mode (DFM) [2–4]. Biogas is a clean fuel for internal combustion engines and it can be generated by cellulose biomass using anaerobic fermentation. In the oil crunch, it can be used as an encouraging alternative fuel for diesel engines, by replacing a substantial quantity of fossil fuels. Engines based on diesel may be easily rehabilitated to fumigated dual fuel (FDF) engines. Biogas is the most effective and practical technique to use large spontaneous ignition temperature alternative fuels [5]. The FDF process includes the biogas mixing with air before inserting this blend into the combustion chamber with an amount of diesel used to insert at the end of the compression stroke which is called the pilot injection [6]. The pilot injection is used to ignite the biogas and air mixture. The FDF process includes a benefit in which the system has the ability to go back to only diesel fuel operation mode in case of a deficit in biogas availability during the desired operation. Due to the benefits stated above, dual fuelling of diesel and biogas [7–10], as well as NG, LPG, hydrogen, or producer gas [11–13], have been studied broadly worldwide during the past

* Corresponding author.
E-mail addresses: yashvirsingh21@gmail.com, yashvir.singh@spsu.ac.in (Y. Singh).

https://doi.org/10.1016/j.renene.2019.04.031
0960-1481/© 2019 Elsevier Ltd. All rights reserved.

Nomenclature

BP	Brake power
η_{bth}	Brake thermal efficiency (%)
BSEC	Brake specific energy consumption
BSFC	Brake specific fuel consumption
CI	Compression ignition
CO_2	Carbon dioxide
CO	Carbon monoxide
DBG	Diesel biogas mode
DFM	Dual fuel mode
DICI	Direct injection compression ignition
EL	Engine load
EGT	Exhaust gas temperature
HC	Hydrocarbon
IC	Internal combustion
K	Number of cylinders
LFR	Liquid fuel Replacement
LHV_g	Low heating value of biogas (MJ/kg)
LHV_d	Low heating value of diesel (MJ/kg)
$\dot{m}_g$	Mass flow rate of biogas in Kg/sec
$\dot{m}_d$	Mass flow rate of diesel in Kg/sec
$\dot{m}_p$	Mass flow rate of pilot fuel in Kg/sec
NO_X	Oxides of nitrogen
PM	Particulate matter
RSM	Response surface methodology
RPM	Revolution per minute
R	Universal gas constant
SBD	Soya biodiesel blend
SED	Soya ethanol blend
F_2	Volume of intake air
VE	Volumetric efficiency
W	Dynamometer load
PPMV	Parts per million volume

decades. Karim et al. [14] investigated dual fuel operation with various fuels (methane, propane, hydrogen, LPG, CNG) with respect to combustion characteristics, exhaust gas emissions, engine performance, and factors influencing them.

Yuanli et al. [15] investigated engine performance by operating gasoline/diesel dual-fuel engine (DFE) and performed experiments on the basis of optimization of gasoline ratio, diesel injection timing, injection pressure, EGR rate under different combinations of engine speed and torque. They concluded that at high and medium load, the two times injection was better than a single one. Two times injection could successfully decrease the extreme pressure rise by delaying the first injection timing although the engine load could be enhanced by the second injection. Singh et al. [16] studied eucalyptus oil (EU) and aamla seed oil biodiesel (AB) blends which were utilized as fuels for a CI engine. In the context of the environment, they found that the emissions reduced in terms of unburnt hydrocarbon (HC), carbon monoxide (CO), and smoke, whereas nitrogen oxides emission was nearly same in comparison to the diesel. Veinblat et al. [17] reported about the biodiesel which is derived from linseed oil-derived and comparative study had been done on a compression ignition engine (CIE) for the analysis of combustion and its performance. They found that opposite to soybean biodiesel, the linseed-derived biodiesel shown reduced NOx emission in comparison to diesel at higher engine loads.

Dong et al. [18] studied the dual fuel engine fuelled with ethanol/diesel blends. The study included the simulations and experiments to find aspects which affect fuel stratification as well as the combustion process and auto-ignition. They also realized from the experiments that the heat release rate and peak pressure could reduce with reduced nozzle holes. Sarkar and Saha [19] studied DFE with biogas and tried to increase its efficiency through the variation of fuel-air equivalence ratio and preheating of biogas.

Chen et al. [20] explored methanol as an alternative fuel of DFE which might be also helpful in reducing the particulate matter emissions. Bora et al. [21] explored dual fuel engine and relative evaluation was carried out of biogas with methyl eater of pongamia oil, palm oil and rice bran oil as pilot fuels. Authors observed the increase in brake thermal efficiency in all three mentioned fuel cases with biogas. Duc and Wattanavichien [22] performed research on a dual fuel diesel engine with biogas run at different loads and engine speed. They found the smooth engine functioning with biogas in dual fuel mode (DFM). Although, the researchers got lesser energy transformation at lower loads in comparison to larger loads, and also found that the larger unburned hydrocarbon emission (HCE) was due to the lower energy change of biogas. Papagiannakis and Hountalas [23] found that the combustion duration to be larger and vice versa in a natural gas run in DFE for better performance of the engine.

Based on the previous studies, the author came to the conclusion that the introduction of the biogas has a significant effect on the performance of the engine which is summarized as:

- Improvement in the combustion and the performance of the engine.
- Reduction in the amount of exhaust emissions.
- There is a significant role of the engine load and air flow rate on the performance characteristics of the engine.
- Implementation of biogas with different blends plays a vital role.

From the above literature review, it is also predicted that the comparative study on dual fuel mode with biogas and various commonly alternative biodiesel blends like soya and ethanol are not mentioned earlier. In the context of the previous researches, optimization using response surface method is an important issue as it reduces time, resources and effort.

By considering these points, the objective of the work is to include engine input parameters which are fuel type at dual mode as well as conventional mode, engine load, air flow rate and speed (rpm). Optimization of these input parameters is carried out using response surface methodology. In this work engine output responses are BTE, volumetric efficiency, carbon mono-oxide, unburnt hydrocarbon, and NOx.

2. Materials and methods

2.1. Physicochemical properties of the fuel

The soya oil was purchased from the local vendor of the city of New Delhi, India. The transesterification process was applied for its conversion to the biodiesel and the author followed the same process for its conversion as mentioned in the previous work [24,25]. The blending of the biodiesel was done using stirrer which was run at 700 rpm speed. The fuels injected as a pilot fuel, which acts as the source of ignition. The biodiesel blend of soya or ethanol with 20% blend are used as the tested fuels and the diesel fuel was considered as the reference fuel. The biodiesel blends used in this

Table 1
Properties of the different blends tested.

S. No	Characteristics	Diesel	Soya blends	Soya Ethanol blend	ASTM
1	Chemical formula	C13H24	–	–	–
2	Density (kg/m^3)	832	852	852	D6751
3	Lower heating value (MJ/kg)	43.99	39.19	39.19	–
4	Kinematic Viscosity at 40 °C (cSt)	2.91	3.31	3.31	D445
5	Flashpoint (°C)	76	90	90	D93
6	Cetane number	45–55	42	42	D613
7	Carbon residue (%)	0.1	–	–	D4530
8	Cloud point	6.4	8.1	8.1	D2500
	Boiling point (°C)	180–330	315–350		
9	Pour point	−5.1	−1.2	−1.2	–
10	Molecular weight	181	–	–	–
11	Auto ignition temperature (°C)	261	283	283	–
12	Ash content (% by mass)	0.58	–	–	D874
13	Oxidation stability	High	No	No	EN1412

study meets the ASTM D6751 specifications. Table 1 shows the physicochemical properties of the fuels considered during the study.

Biogas is very stable gas, colourless and has a smell like rotten eggs. The toxicity of the biogas depends on the type of feedstock's utilized for its production. When a mixture of biogas burns, it results in the appearance of the blue flame which produces a large amount of heat and energy. Different sources of the production of biogas lead to different specific compositions. The presence of H_2S, CO_2, and water makes biogas very corrosive and it leads to the requirement of the adapted materials. Table 2 shows the biogas test fuel physicochemical properties. The composition of biogas mentioned in Table 2 is based on the previous work stated earlier [26,27].

2.2. Response surface methodology

Response surface methodology is a gathering of the statistical-based mathematical methods which is among the most relevant multivariate techniques for the optimization and engine modeling. In this method, the foremost emphasis is to boost the engine retorts which are influenced by different engine input parameters. Response surface methodology also measures the assembly among the governing engine input factors and the resulting output responses of the engine [5,25,28]. Conferring to the RSM, each of the engine input parameters is presumed to be computable; the parallel engine responses can be stated by:

$$y = f(x_1, x_2, x_3 \ldots\ldots\ldots\ldots, x_p) \quad (1)$$

Where $x_1, x_2, x_3 \ldots\ldots\ldots, x_p$ are the engine input factors and y is the engine output which is required for the improvement. Now, it can be presumed that the self-governing engine input factors are uninterrupted as well as controllable by the experiments through insignificant inaccuracies. A second-order regression modeling by RSM is utilized during the analysis part.

$$y = b_o + \sum_{i=1}^{k} b_i X_i + \sum_{i=1}^{k} b_{ii} X_i^2 + \sum\sum_{j} b_i X_i X_j \quad (2)$$

Where b represents regression coefficients (RC) determined by the least square method. To assess the RC for the model, every variable X_i needs to be engaged with three different levels. Thus, 3^p number of engine experiments in factorial design is needed. For the appropriate second-order engine modeling, rotatable central composite design (RCCD) method is commonly used. This involves the experiments to be performed by using the factorial design with 2^p number of experiments and $2p + 1$ incorporation of the supplementary factors. These permutations are given below:

$$(0, 0, \ldots., 0);\ (-a, 0, \ldots., 0);\ (a, 0, \ldots, 0);\ (0, -a, \ldots., 0);$$
$$(0, a, \ldots., 0) \ldots (0, 0, \ldots, -a);\ (0, 0, \ldots, a)$$

Here, the significance of code 'a' is equivalent to $(2^p)^{1/4}$ which is introduced to provide the orthogonal property to the array. The central value of input factors is denoted by the coded level '0'.

It is very essential for a second-order engine modeling to specify the best estimate about the engine performance within the fixed range of all values of the engine input factors. Therefore, the engine model must have a realistically steady and constant forecast for the engine output responses at points of interest, X_i and it is realized by RCCD.

Table 2
Physicochemical properties of the biogas.

Composition	55–70% methane, 30–45% carbon dioxide, traces of other gases
Calorific value, kcal/m^3	4500–5000
Explosion limits	6–12% biogas in air
Ignition temperature, °C	650–750
Critical pressure, bar	75–89
Critical temperature, °C	−82.5
Normal density, kg/m^3	1.2
Flame speed, cm/s	25
Stoichiometric A/F ratio	10:1
Octane rating	130
Odor	Bad eggs (the smell of hydrogen sulphide)

Table 3
Single-cylinder, Kirloskar, Model TV1, 4-stroke, DI diesel engine Specifications.

Rated power (diesel)	5.2 kW (7 BHP) @1500 rpm
Type of cooling	Water cooled
Bore × Stroke	87.5 × 110 mm
Swept volume	0.661 L
Compression ratio	17.5:1
Speed	1500 rpm, constant
Injection pressure	20 MPa
Injection timing (diesel)	23° bTDC
Combustion chamber	Hemispherical bowl-in piston type
Governor	Mechanical governing (centrifugal)
Air flow	Orifice meter and manometer (100–0–100 mm)
Fuel flow	Fuel measuring unit, range 0–450 ml
Temperature sensor	K type thermocouple
Rotameters	Engine cooling 40–400 lph, calorimeter 10–100 lph
Engine software	'Enginesoft' engine performance analysis software

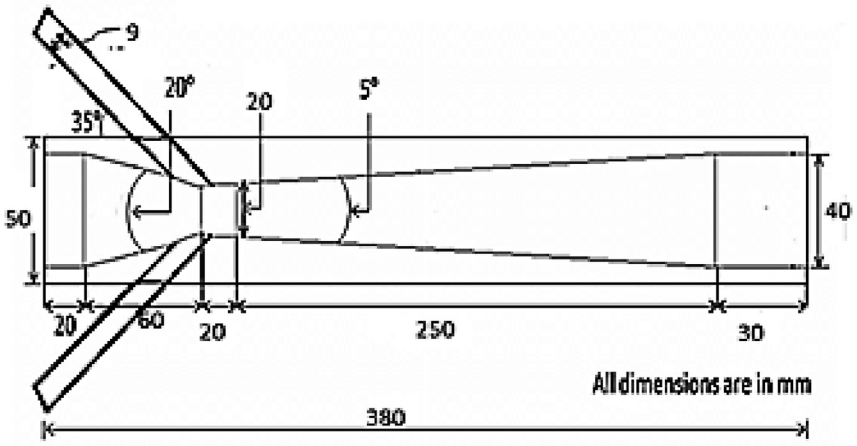

Fig. 1. Design of fuel-air mixing chamber.

$$X_1^2 + X_2^2 + X_3^2 \ldots\ldots\ldots X_p^2 = \text{constant} \quad (3)$$

RCCD needs five levels of engine input methods to calculate the regression coefficients. In the present condition, the total number of permutations needed are $2^p + 2^p +$ which are more than one run at a centre. In the present study of the engine with four control parameters, a standard RCCD matrix with seven central point run is selected.

2.3. Experimental setup

The experiments are carried out on a Kirloskar TV1 diesel engine installed at the Internal Combustion Engine Lab, Delhi Technological University, Delhi, India. The detail about the technical specifications of the experimental setup is shown in Table 3.

The engine test setup is modified to biogas run dual fuel mode set up by connecting a venturi gas mixer at its inlet manifold as depicted in Fig. 1. Fig. 1 shows the procedure used in the design and fabrication of the various components, as well as the set-up of the experiment mentioning the engine and its auxiliary components. For changing the diesel engine to the dual fuel mode, the real alteration required is to associate a fuel-air mixing chamber to the inlet manifold. The fuel-air mixing chamber is vital in dual fuel mode, as it provides a burnable blend of biogas and air in the required amount and the quality for the proficient operation of the engine under all conditions. The design of a fuel-air mixing chamber for a specific engine mostly relies on its volumetric efficiency, rated power, speed, specific fuel consumption, swept volume and manifold connection diameter which are considered for the design of fuel-air mixing chamber.

The modification is also done at the engine stop lever to allow for the regulation of the amount of diesel fuel injected into the combustion chamber during each cycle which is shown by Fig. 2. This is to allow reduction of the diesel fuel injection quantity during the dual fuel mode operation since diesel has to be used in small quantity as a pilot fuel to ignite biogas. It also assists to calculate the amount of the liquid fuel replacement at any specific load corresponding to any particular speed. The engine is connected to a computer employed with engine software designed by Engine soft agency. Initially, the engine is running on pure diesel for 10 min before changing the mode of the fuel supplied until the temperature of the lubricant reached around 80 °C to maintain the steady state condition. Originally, the test engine is designed for diesel fuel having injection timing 23°bTDC and 20 MP fuel injection pressure. The performance and emission parameters of the engine are determined by utilizing diesel, soya and ethanol blending up to 20% in single fuel mode. Biogas is used as a primary fuel and a pilot fuel

Fig. 2. Image of the modifications done at engine stop level.

Table 4
Technical specifications of AVL DiGas 444 exhaust gas analyser.

Parameters	Exhaust gas analyser
Measurement	CO and NO_x
Range of measurement	CO = 0 to 11 vol % NO_x = 0 to 5000 ppmv (as Nitric oxide) Smoke = 0–100%
Accuracy	CO = 0.002 vol % NO_x = 10 ppmv
Resolution	CO = 0.01 (vol. %) NO_x = 1 ppmv Smoke = 0.1%
Warm up time	10 min (self-controlled) at 20 °C
Response time	Within 10 s for 90% response

Table 5
Input parameters with their levels.

Coded level	Test fuel (F)	Load (kg) (EL)	Speed (RPM)	Air flow (H)
−2	Diesel	2.4	1523	52
−1	DBG	4.8	1509	50
0	SBG	7.2	1493	48
1	SBD	9.6	1480	46
2	SED	12	1471	44

F-Fuel; EL-Engine load; RPM-Revolution per minute; H-Flow of air.

in dual fuel mode. During the initial stage, the engine is run with diesel at standard conditions. At 20%, 40%, 60%, 80%, and 100% load, the engine is tested during the experiment. The air flow rate and engine speed are other input variables which affect the engine response. The air flow rate is recorded by measuring the difference in height of the water column in the manometer. The additional energy that the engine obtained due to the combustion of biogas results in the increment of the engine speed. Until the engine rpm becomes steady, the flow of biogas is slowly increased. In the meantime, the governor helped in reducing the speed of the engine. However, to perfectly match the rpm at any particular load in diesel mode, pilot fuel regulating device helped by minimizing the pilot fuel consumption. The engine is allowed to operate for a few minutes and the readings are obtained from the biogas flow meter. For every test, the initial and final reading of the meter is recorded for 30 s. The volume of gas consumed is calculated by taking the difference between the initial and the final gas consumption reading.

The experiment is performed three times for each condition and the average value is considered for the analysis. The engine performance parameter BTE is obtained with the help of Legion brother's engine data acquisition software. CO and NOx are observed by using AVL di 444-gas analyser and the smoke is measured by AVL smoke meter and their technical specification is mentioned in Table 4.

2.4. Response surface modeling

The second-order RSM model for the BTE, VE, CO, HC, and NOx has been established from the engine trial response values which have been achieved by considering the levels given in Table 5. The central value of the engine input parameters conforming to code '0' is the optimum engine operating parameter level. Here, the coded values for RCCD at diverse levels are −2, −1, 0, 1, and 2.

In this work, five different test fuel mode are used which is pure diesel, DBG mode (diesel biogas dual mode), 20% soya biodiesel with diesel, soya biogas mode including pilot fuel blend of 20% soya biodiesel with diesel and biogas. The 20% soya biodiesel performed better in terms of improving the thermal efficiency of diesel engine and decreasing emissions like CO_2, CO and HC as stated in the literature. Therefore, 20% soya biodiesel was utilized during the test without any increment or decrement in the blend percentage of soya biodiesel [29]. Soya-ethanol-diesel mode is prepared by blending of 10% soya biodiesel and 10% of ethanol with diesel. In this work, engine speed is one of the important engine input parameters. Here, five different engine speeds are taken which are mentioned in the RCCD matrix. The air flow is also among one of the main parameters of the engine which affect the engine output response. In this work, five different combinations of the air flow rate are also considered to find the impact on the engine responses. The engine responses according to the L31 orthogonal array at different engine input are shown in Table 6.

This model has been developed by using MINITAB 15 software and the equations obtained after the analysis for output responses BTE, volumetric efficiency, CO, HC, and NOx are given below which are designated by equation number 4–8.

Table 6
Experimental design matrix.

Exp. Run	Fuel	Load (kg)	Speed (RPM)	Air flow (h)	BTE (%)	VE (%)	CO (Vol. %)	HC (ppmv)	NOx (ppmv)
1	1	1	1	1	15.31	65.20	0.135	33.75	1338
2	0	0	0	0	23.76	68.50	0.195	43.75	1226
3	0	0	0	0	22.60	68.40	0.195	44.75	1229
4	0	0	2	0	17.12	77.30	0.168	42.00	1251
5	1	−1	1	−1	16.91	68.50	0.141	45.25	848
6	−1	−1	1	−1	21.45	68.97	0.199	44.75	635
7	1	1	1	−1	15.62	65.60	0.138	34.50	1345
8	−1	−1	−1	1	19.91	56.01	0.182	49.50	703
9	−1	−1	1	−1	21.50	69.05	0.193	48.25	716
10	0	0	0	−2	27.05	59.11	0.198	44.50	1222
11	0	0	0	0	26.78	68.60	0.195	44.75	1228
12	0	0	−2	0	28.26	68.80	0.132	33.00	1205
13	−1	1	−1	1	17.26	64.91	0.196	43.00	1113
14	0	0	0	0	22.80	68.60	0.192	48.00	1225
15	0	0	0	2	20.01	58.00	0.132	43.00	1242
16	1	1	−1	−1	20.81	65.40	0.111	27.75	1341
17	−1	1	1	1	16.25	55.33	0.199	51.75	1175
18	−2	0	0	0	23.57	58.71	0.078	29.50	1056
19	−1	1	1	−1	18.91	85.86	0.132	46.00	1310
20	0	−2	0	0	13.11	49.67	0.045	56.25	650
21	0	2	0	0	25.12	68.10	0.105	36.25	1422
22	−1	−1	1	1	13.76	56.02	0.219	54.75	703
23	0	0	0	0	26.79	68.65	0.195	42.75	1210
24	0	0	0	0	26.71	68.63	0.195	42.75	1235
25	1	−1	−1	1	17.67	65.70	0.048	12.00	1015
26	1	1	−1	1	26.20	85.00	0.018	14.50	1295
27	1	−1	1	1	16.92	65.70	0.135	33.75	870
28	−1	1	−1	−1	27.32	65.66	0.132	39.00	1150
29	0	0	0	0	26.81	68.70	0.195	43.75	1205
30	1	−1	−1	−1	12.42	46.00	0.153	38.25	865
31	2	0	0	0	16.90	67.80	0.048	22.00	1421

BT-Brake thermal efficiency; VE-Volumetric efficiency; CO-Carbon monoxide; HC-Hydrocarbon; NO_x-Nitrogen oxide.

Table 7
ANOVA analysis with F values.

Source	BTE	VE	CO	HC	NOx
Regression	18.1	16.01	24.84	45.06	8.83
Linear	24.54	19.72	15.96	31.42	14.33
Square	29.9	31.34	57.2	118.94	13.03
Interaction	6.66	21.15	9.83	2.5	1.27
Lack of fit	1.75	1696.86	7.83	3187.53	3.34

BTE-Brake thermal efficiency; VE-Volumetric efficiency; CO- Carbon monoxide; HC-Hydrocarbon; NO_x- Nitrogen oxide.

Table 8
RSM approach with ANOVA analysis and p values.

Source	BTE	VE	CO	HC	NOx
Regression	0.000	0.000	0.000	0.000	0.000
Linear	0.000	0.000	0.000	0.000	0.000
Square	0.000	0.000	0.000	0.000	0.000
Interaction	0.001	0.000	0.000	0.067	0.324
Lack of fit	0.237	0.000	0.006	0.000	0.063

BTE-Brake thermal efficiency; VE-Volumetric efficiency; CO- Carbon monoxide; HC-Hydrocarbon; NO_x- Nitrogen oxide.

$$\boldsymbol{BTE} = 25.18 - 1.08F + EL - 6.7RPM - 3H - 5.7F^2 - 17.8EL^2 - 3.3RPM^2 - 0.41H^2 - 0.6F{*}EL - 1.8F{*}RPM + 10.8F{*}H + 2.04EL{*}RPM + 1.7EL{*}H - 2.1RPM{*}H \quad (4)$$

$$\boldsymbol{VE} = 68.58 + 4.2F + 10EL + 4.17RPM + 0.26H - 5F^2 - 9.4EL^2 + 4.78RPM^2 - 9.72H^2 - 3.23F{*}EL - 7.42F{*}RPM + 6F{*}H - 13.36EL{*}RPM - 7.38EL{*}H - 23.56RPM{*}H \quad (5)$$

$$\boldsymbol{CO} = 0.062 - 0.06F - 0.01EL - 0.09RPM + 0.1H + 0.4F^2 + 0.38EL^2 + 0.13RPM^2 + 0.08H^2 - 0.05F{*}EL - 0.14F{*}RPM + 0.14F{*}H - 0.12EL{*}RPM - 0.02EL{*}H - 0.24RPM{*}H \quad (6)$$

$$\boldsymbol{HC} = 27.14 + 37.68F - 262.8EL - 39.2RPM - 43.1H + 756F^2 + 344EL^2 + 393.2RPM^2 + 524.7H^2 - 198.05F{*}EL - 25.78F{*}RPM - 79.55F{*}H - 74.78EL{*}RPM + 17.5EL{*}H + 43.7RPM{*}H \quad (7)$$

$$\boldsymbol{NOx} = 1169.7 + 175.10.5F + 519.6EL - 234RPM - 58.2H - 949.4F^2 - 571.9EL^2 - 269.9RPM^2 - 175.9H^2 + 177F{*}EL - 92.31F{*}RPM + 214F{*}H + 324.7EL{*}RPM - 332.9EL{*}H + 40.2RPM{*}H \quad (8)$$

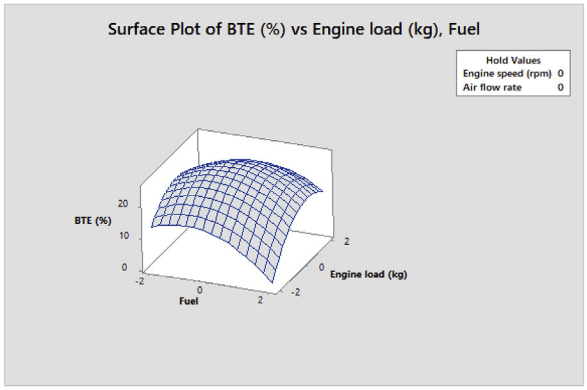

(a)

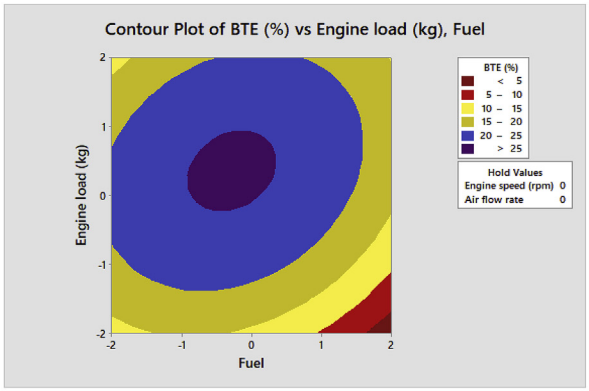

(b)

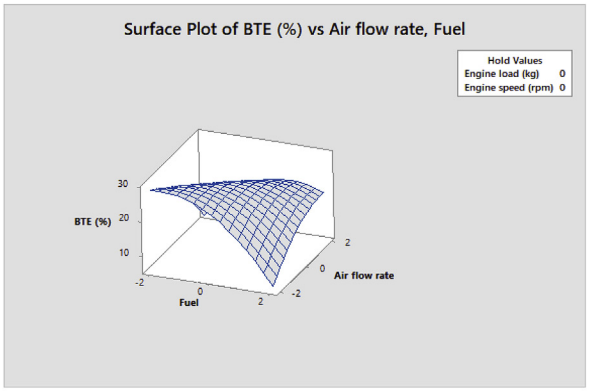

(c)

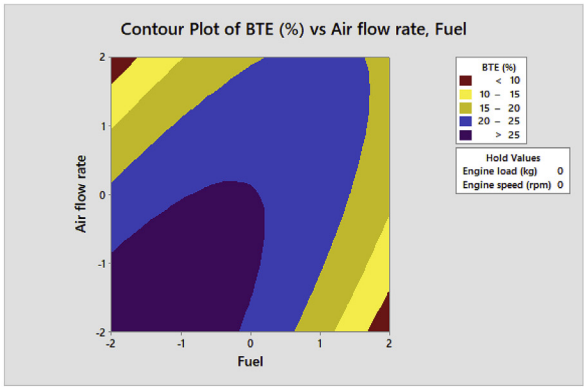

(d)

Fig. 3. BTE Surface and contour plots.

To evaluate that the data are well fitted in these models, S value was analyzed of the regression, here for BTE, VE, CO, HC and NOx emission S value was obtained 2.22968, 2.9672, 0.0480851, 57.3937 and 197.068 respectively and seen to be quite satisfactory. R2 value for five engine responses are 94.06%, 93.34%, 95.6%, 97.53% and 88.54%, respectively also, R2 (adj) for BTE, VE, CO, HC, and NOx emission are 88.86%, 87.5%, 91.75%, 95.36% and 78.51%, respectively means also conclude that data was well fitted. Analysis of variance (ANOVA) and subsequently F-ratio test and p-value test have been carried out to test the adequacy of the developed mathematical models for BTE, VE, CO, HC and NOx emission. ANOVA, F value is mentioned in Table 7, p-value is mentioned in Table 8 source of regression model and linear effects are lower than 0.05 for all engine responses. The established regression model and linear effect of engine parameters for all engine responses are meaningful. Hence, the developed second-order regression model for BTE, VE, CO, HC, and NOx emission are obtained suitable for 95% confidence level.

3. Results and discussions

The discussion incorporates the effect of four input variables of the diesel engine on five engine output responses (BTE, VE, CO, HC, and NOx). During plotting of surface and contour plot, all these four engine input parameters (fuel type and mode, engine load, engine speed, and air flow rate) variation are not possible simultaneously. Seven combinations are possible between four engine input parameters. During the surface and contour plots of engine responses, three main engine variables (fuel and mode of operation, engine load, and air flow rate) are considered and remaining two engine input variables was put on hold at centre according to RCCD matrix. In this work, more stress was applied on engine parameters like different biodiesel with dual mode method, air flow rate, engine loading at different engine speed. The second observation plots are between fuel and air flow rate when engine hold parameters are engine load and engine speed (7.2 kg engine load and 1493 RPM). In the proceeding Figures, engine hold parameters are mentioned on the upper right-hand corner of each surface plot and contour plots. All given surface and contour plots are generated by MINITAB 17.

3.1. The effect of input engine parameter on BTE

The Brake thermal efficiency estimate about the efficiency of the engine capacity to transform the heat from fuel into mechanical energy. Fig. 3 shows the effect on BTE with engine input parameters. Fig. 3 (a) shows the effect of BTE with fuel type and engine load when hold values are (engine RPM, air flow rate) constant (1493 RPM and 48 mm manometer reading). It is seen that maximum thermal efficiency was obtained with conventional diesel fuel that is due to the more calorific value of diesel fuel among all the tested fuels. When fuel mode changes to duel fuel mode as well as with biodiesel blending, BTE found to decreased slightly due to the low heating value of test fuel. Fig. 3 (b) also shows that BTE enhances with respect to engine load, BTE increases and reaches to peak at around 60% of rated engine load due to good mixing of fuels and adequate combustion at a higher temperature. The maximum value of BTE was obtained (more than 25%) with dual fuel mode at 55–60% of rated engine load.

Fig. 3 (c) shows the BTE with fuel and air flow rate when hold values are (engine load, RPM) constant. BTE decreases for the

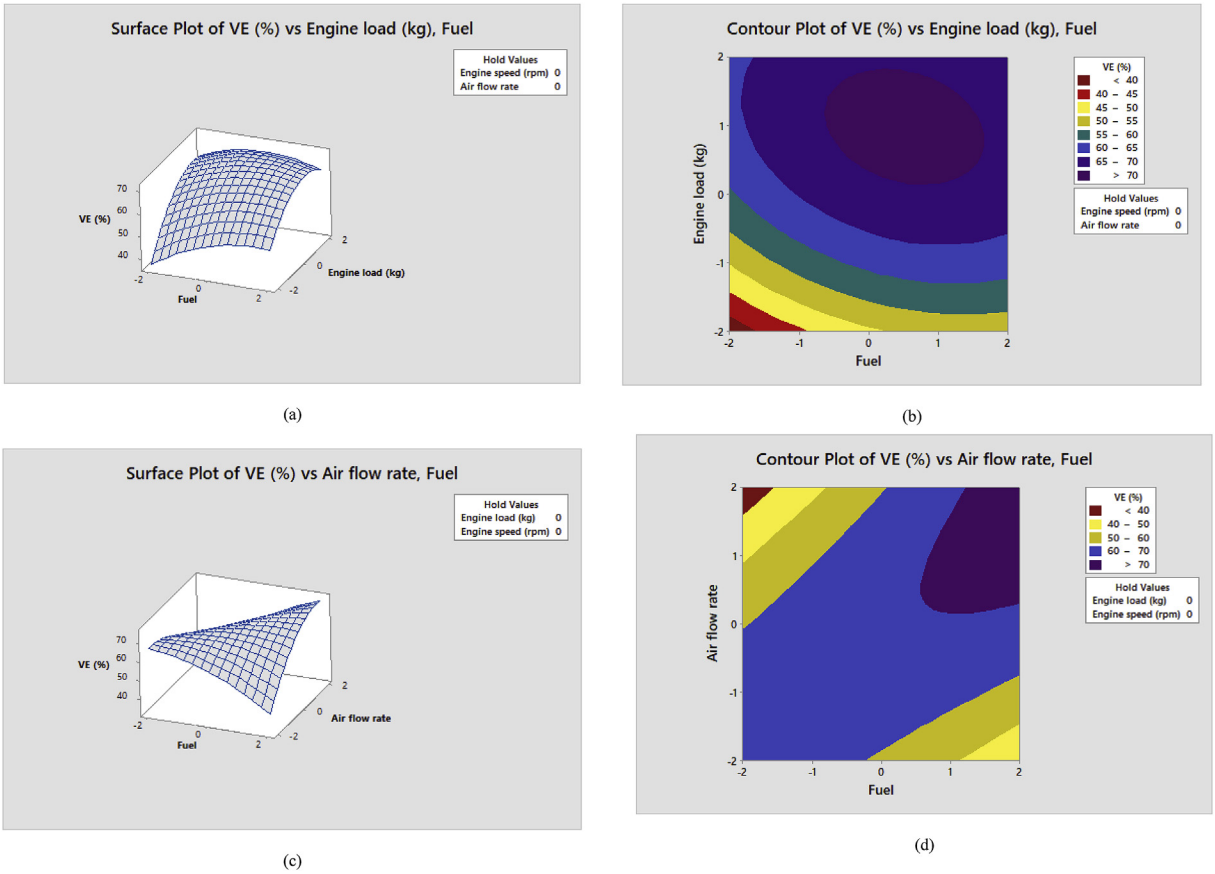

Fig. 4. Volumetric efficiency surface and contour plots.

change in fuel mode from conventional diesel fuel. This is due to higher heating value for the initial and inadequate combustion, but with increasing air flow rate, BTE enhanced sharply that is due to the good amount of air available for the test fuel during combustion. From Fig. 3 (d), it was observed that BTE reaches more than 25% available at diesel mode when test fuel is supplied in dual mode and the air flow rate is more than 50 mm of manometer reading.

3.2. The effect of input engine parameter on volumetric efficiency

Volumetric efficiency in simple terms can be defined as the breathing capacity of the engine. Fig. 4 shows the effect of BTE with all engine input parameters. Fig. 4 (a) shows engine response i.e. volumetric efficiency with fuel type mode and engine load when hold values are constant at 1493 engine RPM and 48 mm manometer reading. From Fig. 4 (a), it can be observed that VE increases when input fuel mode is changed due to the fact that in dual fuel mode, biogas displaces some air which then affects the VE. With respect to engine load, VE increases and reaches to peak at around 80% due to an increase in exhaust gas temperature with increase of load which thereby preheats the air resulting in lower VE. Fig. 4 (b) shows the contour shape, it is observed that maximum range of VE which is more than 70% occurs when the engine was operated on biodiesel blends dual mode at more than 75% of engine rated load.

Fig. 4 (c) shows VE with fuel and air flow rate when hold values are constant at 7.2 kg engine load and 1493 engine RPM. At this hold values, VE decreases because higher substitution of biogas with a change in fuel due to better fuel mixture obtained at later fuel used which result in proper combustion compared to the initial one. With respect to air flow manometer reading, volumetric efficiency enhances that is due to more air available for the combustion. From Fig. 4(d), it is concluded that more than 70% volumetric efficiency was observed with biodiesel blending and with more than 50 mm manometer reading.

3.3. The effect of input engine parameter on CO

Formation of CO is mainly due to the shortage of oxygen. Fig. 5 shows the effect of CO with all engine input parameters. Fig. 5 (a) shows the effect on CO emission with different fuel and engine load while holding the value of engine speed and air flow rate. CO emission was more at dual gas mode due to the presence of CO_2 (42% by volume) in biogas, the stoichiometric flame speed of biogas (about 25 cm/s) is lower than that of diesel fuel (about 30 cm/s). Hence, the flame front cannot propagate faster enough and far enough to consume the entire air-biogas mixture within the combustion time period available. CO emissions found lower when using biodiesel blends as a test fuel that is due to more oxygen contents present. At lower load, the high value of CO emission was observed due to low cylinder temperature at lower engine load resulting in improper fuel combustion. At higher engine load, CO emissions become more. At higher engine loading, cylinder has rich air-fuel mixture and then incomplete combustion of test fuel resulting in more CO emission. Fig. 5 (b) shows the average response of CO emissions for the tested fuel modes. When increasing the load beyond 35%, a fall in CO level was observed.

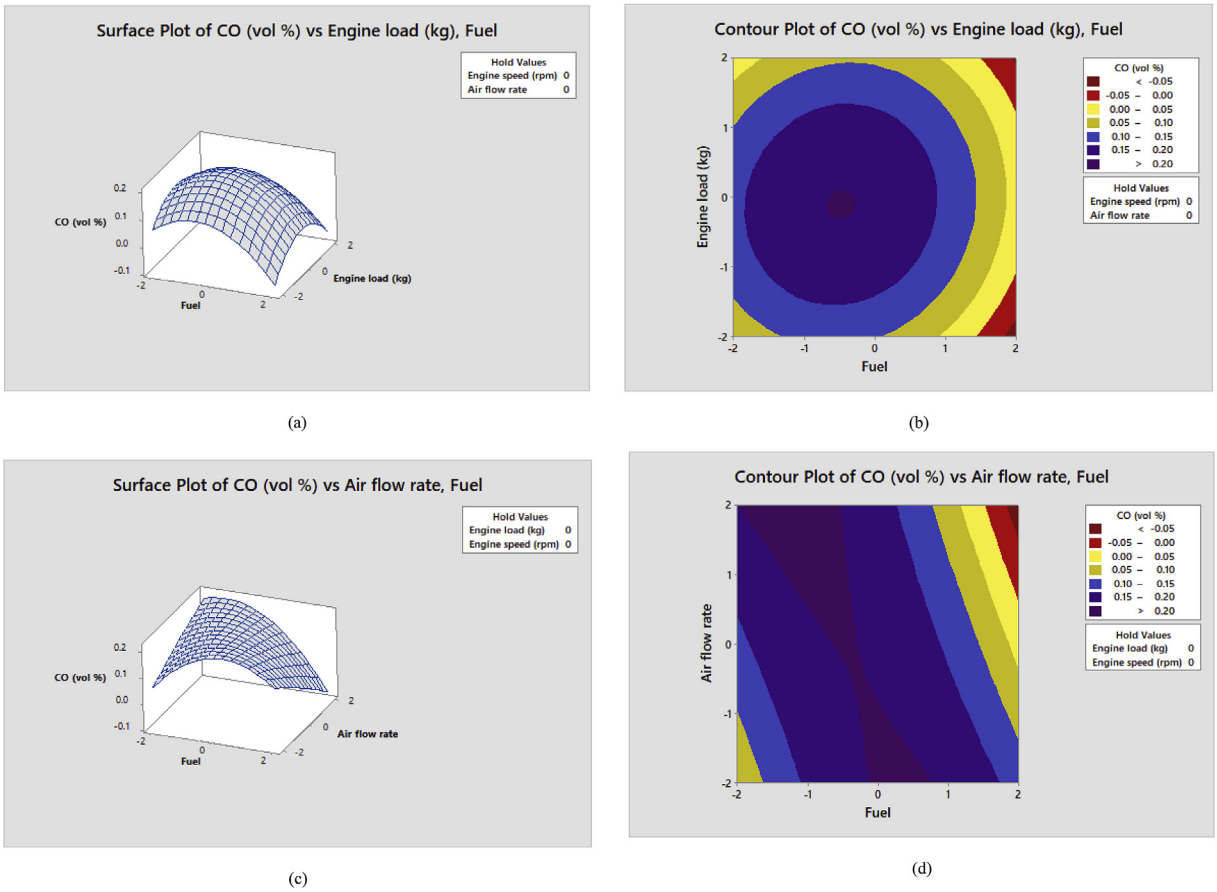

Fig. 5. CO surface plot and contour plots.

Minimum range of CO emission up to 0.05% volume was seen for soya ethanol biodiesel blending at 7.2 kg of engine load at above-mentioned hold value.

Fig. 5 (c) shows the CO emission with fuel types and air flow rate. The engine hold parameters are engine load and speed (7.2 kg and 1493 RPM). The CO emission enhanced when fuel is changed to dual mode as biogas displaces air which results in the deficiency of oxygen aiding the formation of CO. This is due to deficiency of oxygen as for dual fuel mode. With air flow rate, CO emission decreases due to more air available promoting a proper mixture of fuel resulting in proper combustion. From Fig. 5 (d), the minimum value of CO emission can be found for the combination of SBD and SED mode with an air flow rate of up to 50 mm manometer reading.

3.4. The effect of input engine parameter on HC

Formation of HC is mainly due to incomplete combustion of test fuel. Fig. 6 shows the effect of HC with engine input parameters. Fig. 6 (a) shows the effect of HC with different fuels and engine load at which engine speed and air flow rate are on hold. From Fig. 6 (a), it can be observed that more HC emission occurs when running on a dual-mode fuel supply due to the lesser flame velocity of biogas which enhances more formation of HC emission. Using biodiesel as a test fuel, HC emission found less in comparison with other test fuels, it may be due to good combustion of fuel which is attributed to more oxygen content. With respect to engine load, HC increases with an increase in load, since with increase in load there is a higher substitution of biogas which leads to maximum combustion of biogas. Including this, the flame quenching and incomplete combustion also led to high HC levels. This is due to more formation of HC due to a lower flame velocity of biogas. From Fig. 6 (b), a minimum value of HC emission around 20 ppmv was seen with SED fuel at 75% engine load.

Fig. 6 (c) shows the HC emission with fuel type and air flow rate. In this case, hold values are 7.2 kg engine load, 1493 engine RPM. The HC emission increases at a dual mode of DBG and SBG biogas mode. This was probably because of the unburned portion of the charge which is thought to be composed of biogas becomes richer. It is to recall here that the dual fuel operation was executed to a maximum biogas level up to engine misfire. Hence, at higher loads, for the maximum biogas combustion, there was a sudden rise in the HC levels. But at biodiesel blends mode SBD and SED, a hydrocarbon found lesser due to good combustion of fuel due to more oxygen content. Air flow rate plays an important role in the formation of hydrocarbon, more air flow rate decreases the value of HC emissions. It was seen from Fig. 6 (d) that the minimum value of HC emission less than 20 ppmv was obtained with a combination of SBD and SED biodiesels fuel mode.

3.5. The effect of input engine parameter on NOx

Formation of NOx emission basically depends on the combustion chamber temperature which is influenced by some input engine parameters. Fig. 7 shows the effect of NOx with engine input parameters. Fig. 7 (a) shows the effect on NOx emission with fuel mode and engine load during which engine RPM and air flow rate put on hold. NOx emission was found lesser at DBG and SBG mode. However, at dual mode fuel, due to the effect of CO_2, low energetic

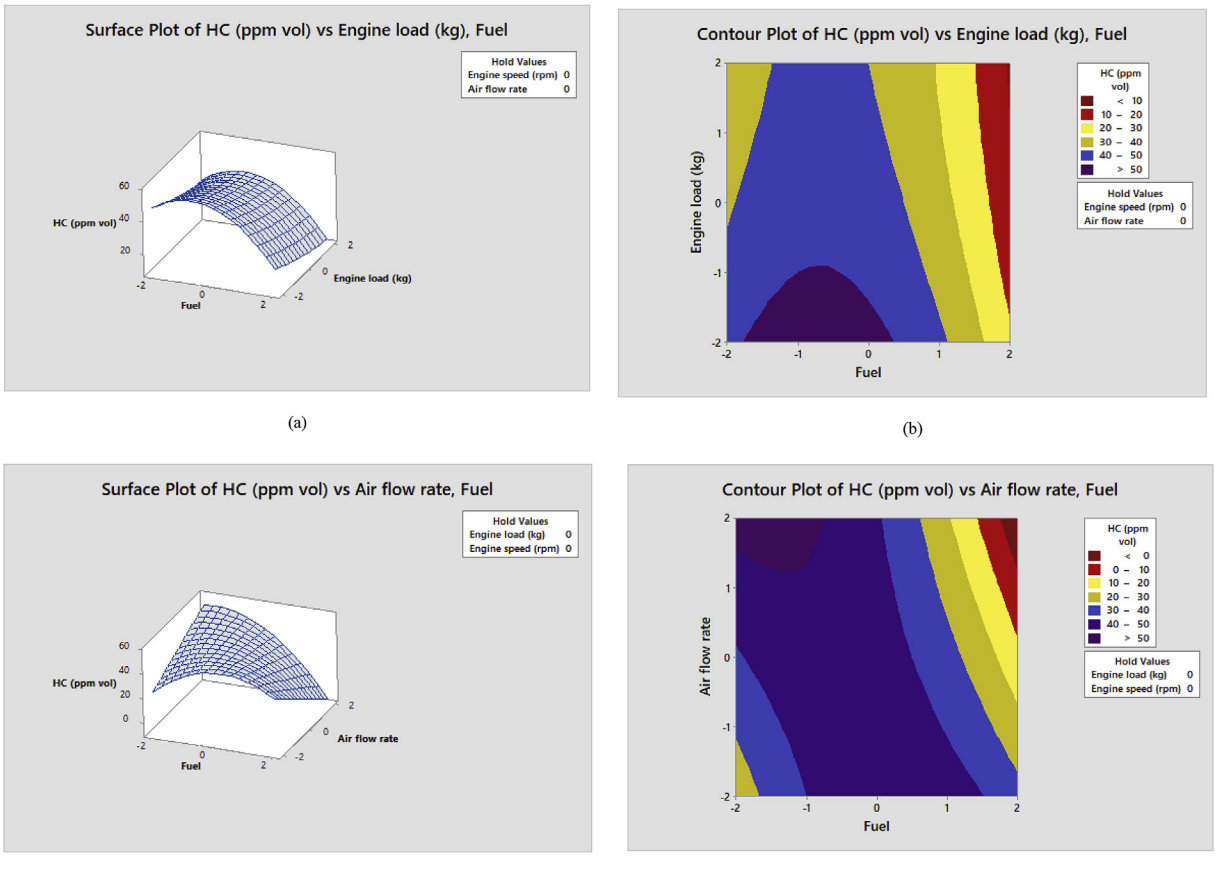

Fig. 6. HC surface plot and contour plots.

dual fuel operation produced much lower NOx compared to diesel mode. This was due to poor air-fuel mixing rates which reduces charge temperature. At SBD and SED biodiesel mode, NOx emission found more due to the high temperature of the cylinder due to more oxygen content in the test fuel. The NOx emission depends upon the combustion chamber temperature which in turn depends on the applied load. Therefore, with an increase in load, there is always an increase in NOx emission. From the experiments, it was found that NOx emissions increased with increase in load for all the fuels tried on the engine. Fig. 7 (b) shows the minimum value of NOx emission less than 750 ppmv which was obtained for SBG dual fuel mode at 35% of rated engine load.

Fig. 7 (c) shows NOx with different fuel mode and air flow rate in which 7.2 kg engine load and 1493 engine RPM are on hold. NOx increases and then decreases for the change in fuel. This is due to increasing of heating value at the initial stage and then decreases at a later stage. As for air flow rate, NOx increases due to more oxygen content available with air flow rate resulting in more temperature during the combustion which enhances the formation of more NOx emission.

3.6. Optimization response

In this work, RSM optimizer is used to determine the best engine setting based on an alternative fuel setting. The multi-objectives optimization test was carried out the best combination of BTE, VE, CO, HC, and NOx emission are the important engine response hence, these five variables are optimized where BTE and volumetric efficiency should be maximum, while try to achieve the lowest value of CO, HC, and NOx.

Fig. 8 shows the RSM optimizer results. Optimum values of BTE, VE, CO, HC and NOx emission are 24.29%, 68.53%, 0.0715% volume, 51.6 ppmv and 1080.2 ppmv respectively when engine input parameters of the test engine fuel was operated on dual fuel mode with soya biodiesel with 8% blending, air flow rate at 49.5 mm manometer reading and at 6.27 kg engine load with 1486 RPM engine speed.

3.7. Validation of robust engine analysis

In order to authenticate the RSM results, engine experiments were carried out at 1486 RPM, air flow rate 49.5 mm, 6.27 kg engine load with SBG dual fuel mode operation. The details of the engine experimental response are shown in Table 9.

Responding BTE, VE, CO, HC, and NOx emission were experimentally determined and the outcomes were compared with the optimized values obtained from the RSM model. The average percentage error for the output responses BTE, VE, CO, HC, and NOx emission are 2.42, 3.85, 3.4, 6.7, and 6.2 respectively, and were well within the acceptable limit.

4. Conclusions

The influence of single cylinder diesel engine input parameters which includes type and methodology of alternative fuel, engine speed, engine load, and air flow rate on the corresponding engine output responses i.e. BTE, VE, CO, HC, and NOx emission is evaluated in this work. It is observed that SBG dual fuel mode (soya

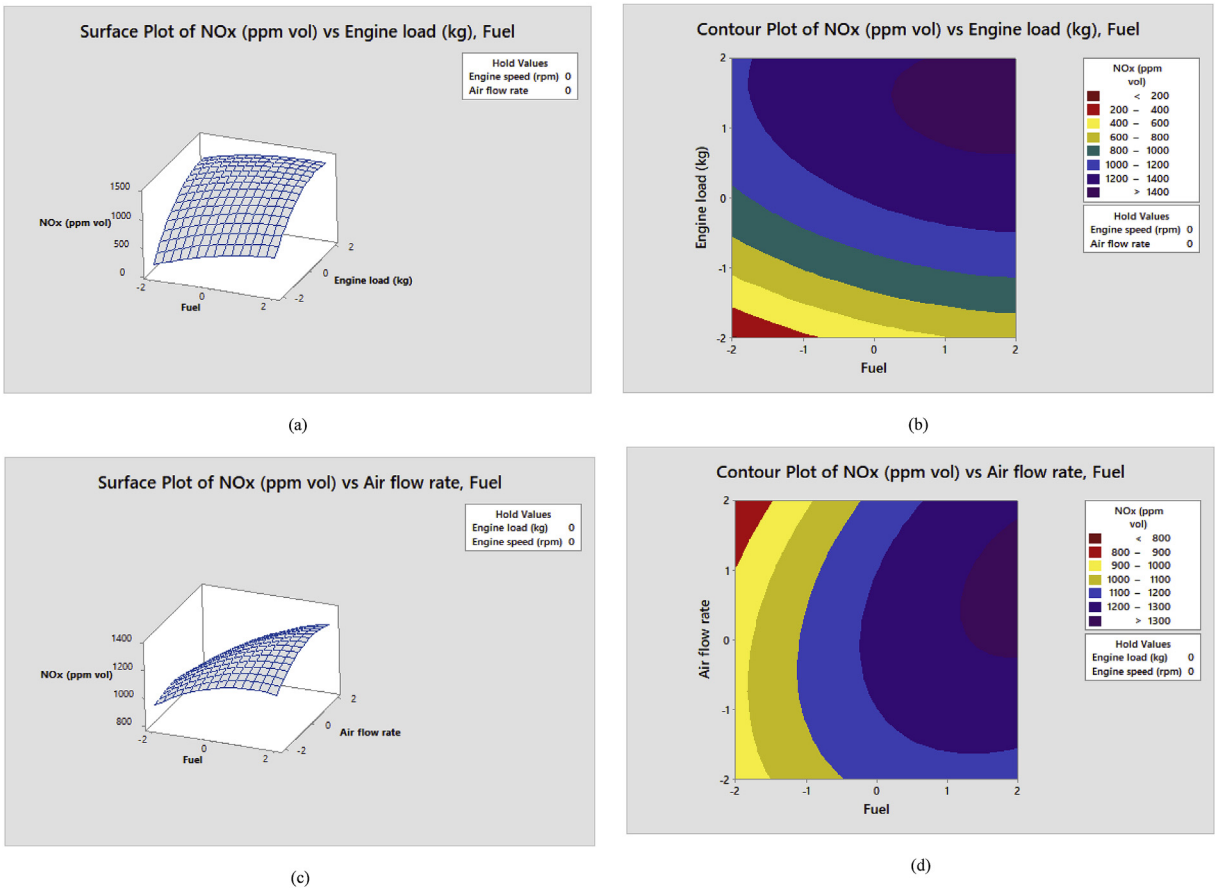

Fig. 7. NOx surface plot and contour plots.

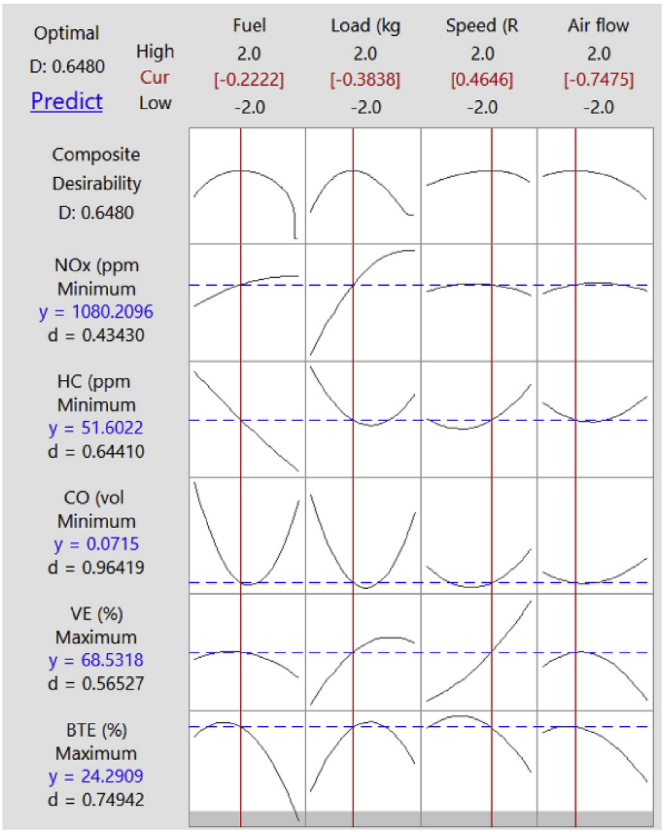

Fig. 8. RSM optimizer.

Table 9
Validation of the results.

Engine Response at SBG mode, 1486 RPM engine speed, air flow rate 49.5 mm, at 6.27 kg EL			
Engine Response	Predicted	Actual	% Error
BTE(%)	24.29	23.7	2.42
VE(%)	68.53	71.24	3.85
CO (% Vol.)	0.0715	0.074	3.4
HC (ppmv)	51.6	55.1	6.7
NOx (ppmv)	1080.2	1012	6.2

BTE-Brake thermal efficiency; VE-Volumetric efficiency; CO- Carbon monoxide; HC-Hydrocarbon; NO_x- Nitrogen oxide; SBG- Soya biogas; RPM- Revolution per minute; EL-Engine load.

biodiesel blend with 8% blending) alternative fuel. The performance parameters, namely BTE, VE, CO, HC, and NOx emission are optimized and modelled using the RSM techniques. The developed RSM models for BTE, VE, CO, HC, and NOx emission are validated experimentally and found within a specified error range. For testing the significance of the RSM model, ANOVA analysis has also been done to obtain the percentage significance of each operating parameters. Results show that the optimum values of BTE, VE, CO, HC, and NOx emission are 24.29%, 68.53%, 0.0715% volume, 51.6 ppmv, and 1080.2 ppmv respectively. Furthermore, it may be concluded that RSM models can be effectively applied to optimize the performance of the engine using optimal operating parameters. This research may help to develop a robust dependable and knowledge base by the early prediction of the optimum conditions for improving the performance of an internal combustion engine with a minimum number of experiments.

Acknowledgements

The author would be thankful to the faculty and staff of the department of mechanical engineering, Delhi Technological University, Delhi for providing the experimental facilities to make this study successful.

References

[1] S.J. Jabłoński, M. Kułażyński, I. Sikora, M. Łukaszewicz, The influence of different pretreatment methods on biogas production from Jatropha curcas oil cake, J. Environ. Manag. 203 (2017) 714–719.
[2] S.H. Park, S.H. Yoon, J. Cha, C.S. Lee, Mixing effects of biogas and dimethyl ether (DME) on combustion and emission characteristics of DME fueled high-speed diesel engine, Energy 66 (2014) 413–422.
[3] V. Uusitalo, R. Soukka, M. Horttanainen, A. Niskanen, J. Havukainen, Economics and greenhouse gas balance of biogas use systems in the Finnish transportation sector, Renew. Energy 51 (2013) 132–140.
[4] X. Wang, Y. Qian, Q. Zhou, X. Lu, Modulated diesel fuel injection strategy for efficient-clean utilization of low-grade biogas, Appl. Therm. Eng. 107 (2016) 844–852.
[5] Y. Singh, A. Sharma, G. Kumar Singh, A. Singla, N. Kumar Singh, Optimization of performance and emission parameters of direct injection diesel engine fuelled with pongamia methyl esters-response surface methodology approach, Ind. Crops Prod. 126 (2018b) 218–226.
[6] M.J. Nosratpour, K. Karimi, M. Sadeghi, Improvement of ethanol and biogas production from sugarcane bagasse using sodium alkaline pretreatments, J. Environ. Manag. 226 (2018) 329–339.
[7] J. Cheng-qiu, L. Tian-wei, Z. Jian-li, A study on compressed biogas and its application to the compression ignition dual-fuel engine, Biomass 20 (1–2) (1989) 53–59.
[8] L. Gustavsson, P. Börjesson, B. Johansson, P. Svenningsson, Reducing CO2 emissions by substituting biomass for fossil fuels, Energy 20 (11) (1995) 1097–1113.
[9] A. Henham, M. Makkar, Combustion of simulated biogas in a dual-fuel diesel engine, Energy Convers. Manag. 39 (16–18) (1998) 2001–2009.
[10] T. Kapur, T. Kandpal, H. Garg, Electricity generation from rice husk in Indian rice mills: potential and financial viability, Biomass Bioenergy 10 (5–6) (1996) 393–403.
[11] J.G. Cleland, C.R. Purvis, Independent power plant using wood waste, Energy Convers. Manag. 37 (6–8) (1996) 1205–1209.
[12] C. Uma Maheswari, K. Obi Reddy, E. Muzenda, B.R. Guduri, A. Varada Rajulu, Extraction and characterization of cellulose microfibrils from agricultural residue – Cocos nucifera L, Biomass Bioenergy 46 (2012) 555–563.
[13] F. Vyarawalla, P. Parikh, H. Dak, B. Jain, Utilisation of biomass for motive power generation—gasifier engine system, Biomass 5 (3) (1984) 227–242.
[14] G. Karim, An examination of some measures for improving the performance of gas fuelled diesel engines at light load, SAE Trans. (1991) 966–974.
[15] Y. Xu, H. Kang, J. Gong, S. Zhang, X. Li, A study on the combustion strategy of gasoline/diesel dual-fuel engine, Fuel 225 (2018) 426–435.
[16] P. Singh, S. Chauhan, V. Goel, Assessment of diesel engine combustion, performance and emission characteristics fuelled with dual fuel blends, Renew. Energy 125 (2018a) 501–510.
[17] M. Veinblat, V. Baibikov, D. Katoshevski, Z. Wiesman, L. Tartakovsky, Impact of various blends of linseed oil-derived biodiesel on combustion and particle emissions of a compression ignition engine–A comparison with diesel and soybean fuels, Energy Convers. Manag. 178 (2018) 178–189.
[18] S. Dong, Z. Wang, C. Yang, B. Ou, H. Lu, H. Xu, X. Cheng, Investigations on the effects of fuel stratification on auto-ignition and combustion process of an ethanol/diesel dual-fuel engine, Appl. Energy 230 (2018) 19–30.
[19] A. Sarkar, U.K. Saha, Role of global fuel-air equivalence ratio and preheating on the behaviour of a biogas driven dual fuel diesel engine, Fuel 232 (2018) 743–754.
[20] C. Chen, A. Yao, C. Yao, B. Wang, H. Lu, J. Feng, L. Feng, Study of the characteristics of PM and the correlation of soot and smoke opacity on the diesel methanol dual fuel engine, Appl. Therm. Eng. 148 (2019) 391–403.
[21] B.J. Bora, U.K. Saha, Comparative assessment of a biogas run dual fuel diesel engine with rice bran oil methyl ester, pongamia oil methyl ester and palm oil methyl ester as pilot fuels, Renew. Energy 81 (2015) 490–498.
[22] P.M. Duc, K. Wattanavichien, Study on biogas premixed charge diesel dual fuelled engine, Energy Convers. Manag. 48 (8) (2007) 2286–2308.
[23] R. Papagiannakis, D. Hountalas, Combustion and exhaust emission characteristics of a dual fuel compression ignition engine operated with pilot diesel fuel and natural gas, Energy Convers. Manag. 45 (18–19) (2004) 2971–2987.
[24] N.A. Ansari, A. Sharma, Y. Singh, Performance and emission analysis of a diesel engine implementing polanga biodiesel and optimization using Taguchi method, Process Saf. Environ. Protect. 120 (2018a) 146–154.
[25] A. Sharma, Y. Singh, G.K. Singh, A.T. Habte, N. Singh, Production of polanga methyl esters and optimization of diesel engine parameters through response surface methodology approach, Process Saf. Environ. Protect. 121 (2019) 94–102.
[26] M. Khalil, M.A. Berawi, R. Heryanto, A. Rizalie, Waste to energy technology:

the potential of sustainable biogas production from animal waste in Indonesia, Renew. Sustain. Energy Rev. 105 (2019) 323–331.
[27] M. Parsaee, M. Kiani Deh Kiani, K. Karimi, A review of biogas production from sugarcane vinasse, Biomass Bioenergy 122 (2019) 117–125.
[28] N.A. Ansari, A. Sharma, Y. Singh, Performance and Emission Analysis of A Diesel Engine Implementing Polanga Biodiesel and Optimization Using Taguchi Method, Process Safety and Environmental Protection, 2018b.
[29] C. Patel, N. Tiwari, A.K. Agarwal, Experimental investigations of Soyabean and Rapeseed SVO and biodiesels on engine noise, vibrations, and engine characteristics, Fuel 238 (2019) 86–97.

AIP Conference Proceedings

Effect of disorders on half-metallic ferromagnetism in Cr_2CoAl inverse Heusler alloy

Cite as: AIP Conference Proceedings **2093**, 020023 (2019); https://doi.org/10.1063/1.5097092
Published Online: 15 April 2019

Anushka Nagpal, Bhuvan Agrawal, Ramesh Kumar, Hardev S. Saini, Manish K. Kashyap, and Mukhtiyar Singh

View Online Export Citation

ARTICLES YOU MAY BE INTERESTED IN

Study of $FeCrSn_{1-x}Ga_x$ Heusler alloys: Tuning Fermi level to attain half-metallic ferromagnetism
AIP Conference Proceedings **2093**, 020019 (2019); https://doi.org/10.1063/1.5097088

Study of magnetic, Mössbauer and microwave properties of $Ba_3Co_{2-x-y}Zn_xCu_yFe_{24}O_{41}$ hexaferrite
AIP Conference Proceedings **2093**, 020021 (2019); https://doi.org/10.1063/1.5097090

Structural and optical properties of Cu doped CeO_2 nanoparticles
AIP Conference Proceedings **2093**, 020026 (2019); https://doi.org/10.1063/1.5097095

AIP Conference Proceedings
Get 30% off all print proceedings!
Enter Promotion Code PDF30 at checkout

AIP Publishing

© 2019 Author(s).

Effect of disorders on Half-Metallic Ferromagnetism in Cr_2CoAl inverse Heusler alloy

Anushka Nagpal[1], Bhuvan Agrawal[1], Ramesh Kumar[2], Hardev S. Saini[2], Manish K. Kashyap[3] and Mukhtiyar Singh[1, a)]

[1]*Department of Applied Physics, Delhi Technological University, Delhi-110042 (India)*
[2] *Department of Physics, Guru Jambheshwar University of Science & Technology, Hisar-125001 (India)*
[3]*Department of Physics, Kurukshetra University, Kurukshetra-136119 (India)*

[a)] *Corresponding Author: mukhtiyarsingh@dtu.ac.in*

Abstract. The chromium based fully compensated ferrimagnet, Cr_2CoAl has been earlier proposed to show half-metallic ferromagnetism. In this paper, we thoroughly study the effect of atomic disorders on spin polarization, half-metallic character and magnetism in Cr_2CoAl using Full-Potential Linearized Augmented Plane Wave method as implemented in WIEN2k code. Cr_2CoAl exists in Inverse Heusler alloy structure with space group $F\bar{4}3m$ (No. 216). This study includes five types of disorders namely $A2_a$-, $A2_b$-, DO_{3a}-, DO_{3b}- and *B2*-type (as suggested by Singh *et al* for Inverse Heusler alloy). Our calculations predict Cr_2CoAl as near half-metallic ferromagnet with 97% spin polarization. $A2_a$-, $A2_b$- and DO_{3a}-type disorders exhibit high spin polarization of 98%, 99%, and 81%, respectively, whereas DO_{3b}-and *B2*- type disorder exhibit 61% and 70% spin polarization, respectively. The energetics of these disorders suggest that DO_{3a}-type disorder is more probable to occur but the high spin polarization in spite of disorder favors its application in spintronics devices. The total spin magnetic moment of Cr_2CoAl is 0 μ_B, which increases with the disorders.

INTRODUCTION

Heusler alloys exhibit number of diverse magnetic phenomena ranging from heavy fermionic to spectacular magnetic behaviour which includes anti-ferromagnetism, helimagnetism, Pauli paramagnetism itinerant and localized magnetism [1,2]. Heusler alloys generally exist in $L2_1$ structure and are called full-Heusler alloys, having formula X_2YZ where X and Y are transition metal elements and Z is *sp* element. The other possible structures of these alloys are half-heusler, inverse-heusler and quaternary-heusler alloys. The unit cell of full-Heusler alloy contains four atoms as basis which are positioned at the following Wyckoff positions: X atom at 4c (¼,¼,¼) and 4d (¾,¾,¾), with center of inversion symmetry, and Y and Z atoms at 4b (½,½,½) and 4a (0,0,0), respectively. In 1983, Groot *et al.* [3] discovered that a particular arrangement of constituent atoms of Heusler alloys leads to a different peculiar property i.e. half-metallic ferromagnetism (HMF). This unique property of these alloys makes them the promising candidates to be used as spintronic materials [4]. Since the discovery of HMF in NiMnSb, many researchers have demonstrated the HMF in other Heusler alloys [5-7]. Later, it is found that this peculiar behavior is adversely affected by disorders, spin wave excitation and temperature [8]. The disorders in full-heusler alloys are mainly of three types i.e. DO_3, *A2* and *B2*. The DO_3-type disorder, BiF_3-type structure, is result of occupation of X position by atoms at Z position. In *B2*-type disorder (CsCl-type structure), the Y and Z atoms are equally distributed at 4a and 4b positions which reduces the symmetry of original $L2_1$-type structure and the resulting space group becomes Pm3m. The *A2*-type disorder, generally, occurs when the disordering between the X and YZ sublattices takes place. A detail study of possible disorders in X_2YZ and XYZ structures is presented in a review article by Bacon and Plant [9]. There are numerous studies existing in the literature which focussed on the perseverance of half-metallic nature of Heusler

Proceedings of the National Conference on Recent Advances in Condensed Matter Physics
AIP Conf. Proc. 2093, 020023-1–020023-4; https://doi.org/10.1063/1.5097092
Published by AIP Publishing. 978-0-7354-1823-3/$30.00

alloys against various disorders. Piccozi *et al.* [10] showed that the half-metallicity is retained for Mn antisite disorder in Co_2MnGe and Co_2MnSi full-heusler alloys whereas the Co antisite disorder destroys the half-metallicity. Gerci *et al.* [11] obtained the high spin polarization in the disordered Co_2Fe-based heusler alloys except for *A2*-type disorder. Similarly, Miura *et al.* [12] in his investigation showed that Co–Cr disorder significantly reduces the spin polarization whilst the Cr–Al disorder hardly effects the spin polarization at Fermi level [13]. These studies motivated us to study the effect of various disorders in Cr_2CoAl, which has already been synthesised by Jamer et al [14]. Our aim is to understand the structure-to-property relation of this Heusler alloy i.e. to check the perseverance of half-metallic nature of Cr_2CoAl under the possible disorders.

STRUCTURAL AND COMPUTATIONAL DETAILS

Cr_2CoAl is an inverse Heusler alloy which crystallizes in *X*-structure (prototype $CuHg_2Ti$) with Cr atoms lying at two inequivalent positions: 4a (0,0,0) and 4c (¼,¼,¼). On the other hand, Co and Al remain present at 4b (½,½,½) and 4d (¾,¾,¾) site, respectively. We have used the same disorder scheme for Cr_2CoAl inverse-Heusler alloy as proposed by Singh *et al*. for such type of systems [13]. According to them, five different types of disorders can be possible for an inverse Heusler alloy structure, namely, $A2_a$, $A2_b$, DO_{3a}, DO_{3b} and B_2 type. The $A2_a$ disorder is obtained by the occupation of Al atom on the Cr^I site whereas the $A2_b$ disorder is produced by the occupation of Al atom on the Cr^I site. In DO_{3a}/DO_{3b} disorder, the Co atom occupies Cr^I/Cr^{II} site. The *B2* disorder is generated by the occupation of Al atom on the Co site.

The calculations for Cr_2CoAl and for all disordered concentrations were performed using the density functional theory (DFT) based Full-Potential Linearized Augmented Plane Wave (FPLAPW) method as implemented in WIEN2k code [15]. The exchange and correlation potentials were taken in to account using Perdew-Burke-Ernzerhof (PBE) version of the generalized gradient approximation (GGA) [16]. To simulate all the disordered concentrations, we were used a convention cell (1×1×1) of 16 atoms. The k-space integration was carried out by modified tetrahedron method in the irreducible Brillouin zone (IBZ). The accuracy of calculations was ensured by applying a strict convergence criterion of 0.0001 for both energy and charge and by using plane wave cut-off parameters: $R_{MT}k_{max} = 8$ (where k_{max} is the largest wave vector of the basis set such that k_{max} controls the accuracy of the calculation).

RESULTS AND DISCUSSION

First of all, a systematic structural optimization has been performed in order to obtain the equilibrium lattice parameters for Cr_2CoAl. We have optimized (Fig.1) this alloy in both in $L2_1$- and *X*-structures and found that the latter is more stable structure.

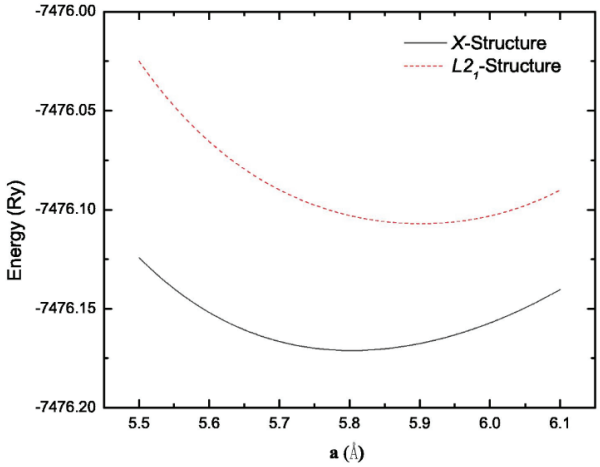

Figure 1.: Calculated total energy versus lattice constants of Cr_2CoAl in the *X*- and $L2_1$-structures.

The optimized lattice parameters for Cr_2CoAl is found to be 5.80 Å, which is in a very close agreement with experimental one (5.794 Å) [14]. The ordered phase is found to be a compensated ferrimagnet (having vanishing

magnetic moment) which is again in excellent agreement with the experimental observation [14] and other theoretical prediction [17]. Since ordered phase of Cr_2CoAl is already studied well and predicted as a compensated half-metal, we have only focused on its disordered phases and restricted to have minimum possible disorder concentration in the conventional cell (1×1×1).

Table 1. The calculated formation energy/atom (eV), spin-polarization, and total magnetic moment of various disordered phases of Cr_2CoAl inverse Heusler alloy.

Disorder type	% of disorder	Formation Energy	Spin-Polarization $\mathcal{P}(E_F)$	Total Magnetic Moment (μ_B)
DO_{3a}	12.5	-0.09	0.81	1.00
DO_{3b}	12.5	-0.15	0.61	2.53
$A2_a$	12.5	-0.11	0.98	1.00
$A2_b$	12.5	-0.16	0.99	2.39
$B2$	25.0	-0.10	0.70	-0.65

In a (1×1×1) cell, the minimum possible values of $DO3_a$-/$DO3_b$-type and $A2_a$-/$A2_b$-type disorders are 12.5% which have been obtained by replacing one Cr^I/Cr^{II} by Co and Al atom, respectively. On the other hand, a minimum value (25%) of $B2$-type disorder has been realized via replacing one Co atom by Al atom [14].

After having the equilibrium lattice parameters, we calculated the formation energies for all studied disorder concentrations with respect to the ordered phase which are listed in Table-1. The 12.5% of DO_{3b}-type disorder has the lowest formation energy (-0.09 eV/atom). In all other cases the formation energies are higher than this value. On analyzing the values of spin-polarization (Table-1) for each disordered system, the half-metallicity is found quite robust even in the presence of the disorder except DO_{3a}-type and $B2$-type disorder, therefore, these disorders need not be a barrier to the practical applications of parent Heusler alloy (Cr_2CoAl).

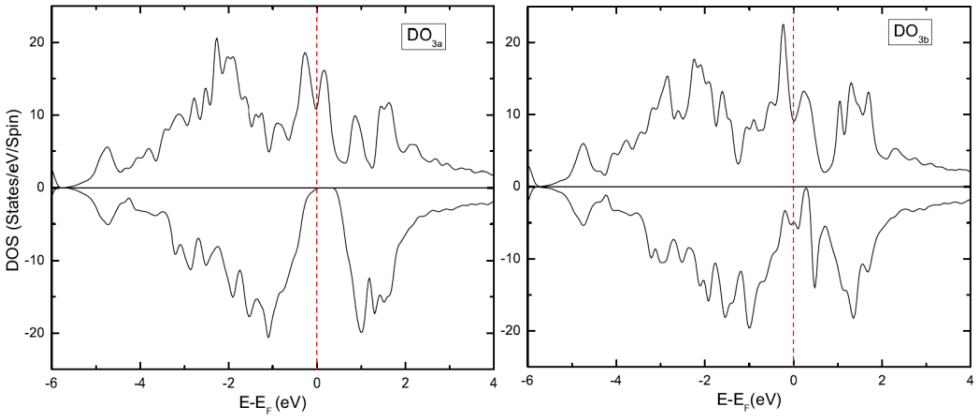

Figure 2.: Total DOS of Cr_2CoAl with DO_{3a}- and DO_{3b}-type disorders

We have plotted the total density of states (DOS) Cr_2CoAl inverse Heusler alloy with DO_{3a}- and DO_{3b}-type disorders in Fig. 1 and with $A2_a$- and $A2_b$-type disorders in Fig. 2. It is clear from the figures that for DO_{3a}-, $A2_a$- and $A2_b$-type disorders, Cr_2CoAl shows the high spin polarization. The partial DOS (not shown here) affirm that there is a strong covalent hybridization between the d states of Cr^I, Co, and Cr^{II} atoms which leads to the formation of the bonding and antibonding in minority spin channel. In case of DO_{3a}-, $A2_a$- and $A2_b$-type disorders, these states are separated by a band gap which essentially arises from covalent hybridization. The calculated total magnetic moment for each disorder shows a rather non-uniform behavior and exhibits a strong dependence on the type of disorder and the change in chemical environment [13].

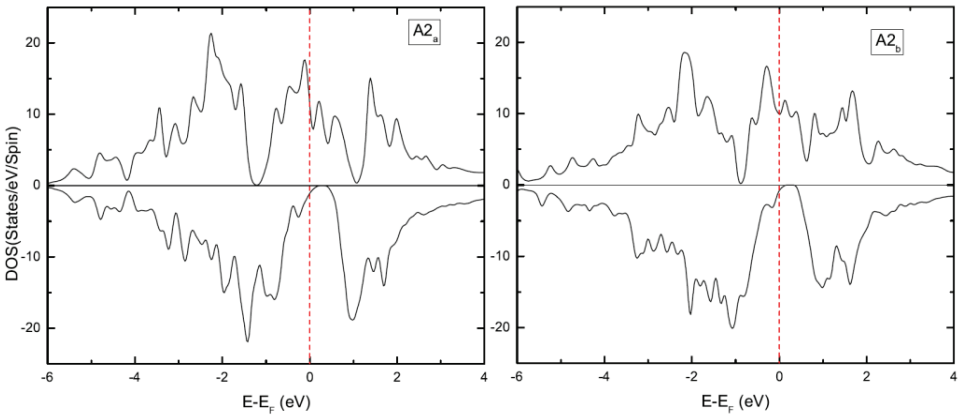

Figure 3: Total DOS of Cr_2CoAl with $A2_a$- and $A2_b$-type disorders

CONCLUSION

In present work, we have focused on the study of various possible disorders in Cr_2CoAl inverse Heusler alloy which is a compensated ferrimagnet (having vanishing total magnetic moment). We have investigated five types of disorders namely; $A2_a$-, $A2_b$-, DO_{3a}-, DO_{3b}- and $B2$-type. The lowest formation energy in case of DO_{3a}-type disorder suggests that probability of occurrence of this disorder is highest but the high spin polarization (81%) favours its use in spintronics devices, even in the presence of this disorder. The magnetic moment of all disorder concentrations exhibit a strong dependence on both the disorder and the change in chemical environment.

ACKNOWLEDGMENTS

The theoretical work presented in this paper has been carried out on the computational facilities provided by Delhi Technological University, New Delhi.

REFERENCES

1. P.J. Webster, K.R.A. Ziebeck, in: H.R.J. Wijn (Ed.), Alloys and Compounds of d-Elements with Main Group Elements. Part 2, Landolt-Bornstein, New Series, Group III, 19, Springer, Berlin, 1986, pp. 75–184.
2. T. Graf, F. Casper, J. Winterlik, B. Balke, G.H. Fecher, and C. Felser, Z. Anorg. Allg. Chem. 635, 976 (2009).
3. R.A. de Groot, F.M. Mueller, P.G. van Engen, K.H.J. Buschow, Phys. Rev. Lett. 50, 2024 (1983).
4. J. R. M. Hashimoto, J. Herfort, H.-P.Schönherr, and K.H.Ploog, Appl.Phys.Lett.87,102506 (2005).
5. M. Singh, H.S. Saini, S. Kumar, and M.K. Kashyap, Comput. Mater. Sci. 53, 431 (2012).
6. I. Galanakis, P.H. Dederichs, and N. Papanikolaou, Phys. Rev. B 66, 134428 (2002).
7. I. Galanakis, and P.H. Dederichs, Phys. Rev. B 66, 174429 (2002).
8. J.J. Attema, G.A. de Wijs, and R.A. de Groot, J. Phys. Condens. Matter 19, 315212 (2007).
9. G.E. Bacon, and J.S. Plant, J. Phys. F: Met. Phys. 1, 524 (1971).
10. S. Picozzi, A. Continenza, and A.J. Freeman, Phys. Rev. B 69, 094423 (2014).
11. Z. Gercsi, and K. Hono, J. Phys.: Condens. Matter 19, 326216 (2007).
12. Y. Miura, and K. Nagao, M. Shirai, Phys. Rev. B 69, 144413 (2004).
13. M. Singh, H.S. Saini, J. Thakur, A.H. Reshak, and M.K. Kashyap, J. Solid State Chem. 208, 71 (2013).
14. M.E. Jamer, L.G. Marshall, G.E. Sterbinsky, L.H. Lewis, and D. Heiman, J. Magn. Magn. Mater. 394, 32 (2015).
15. P. Blaha, K. Schwarz, G. K. H. Madsen, D. Kvasnicka, J. Luitz, R. Laskowski, F. Tran and L. D. Marks, 2018 WIEN2k, An Augmented Plane Wave + Local Orbitals Program for Calculating Crystal Properties, revised edition WIEN2k 18.2, ed K. Schwarz (Austria: Techn. Universität Wien), ISBN 3-9501031-1-2
16. J. P. Perdew, K. Burke, and M. Ernzerhof, Phys. Rev. Lett. 77, 3865 (1996).
17. H-S. Jin, and K-W. Lee, arXiv:1802.00125v1 [cond-mat.mtrl-sci] 1 Feb 2018.

Hindawi
Advances in Polymer Technology
Volume 2019, Article ID 9180302, 12 pages
https://doi.org/10.1155/2019/9180302

Research Article

Epoxy-Glass Microballoon Syntactic Foams: Rheological Optimization of the Processing Window

A. V. Ullas,[1,2] **Devendra Kumar**,[2] **and Prasun Kumar Roy**[1]

[1]*Centre for Fire, Explosive and Environment Safety, DRDO, Timarpur, Delhi 110054, India*
[2]*Department of Applied Chemistry and Polymer Technology, Delhi Technological University, Delhi 110042, India*

Correspondence should be addressed to Prasun Kumar Roy; pkroy@cfees.drdo.in

Received 30 October 2018; Accepted 24 February 2019; Published 1 April 2019

Academic Editor: Minna Hakkarainen

Copyright © 2019 A. V. Ullas et al. This is an open access article distributed under the Creative Commons Attribution License, which permits unrestricted use, distribution, and reproduction in any medium, provided the original work is properly cited.

In this paper, we discuss the chemorheology of epoxy based syntactic foams containing glass microballoons of varying density, with an aim of establishing the effect of microballoon loading on its processability. The primary objective is to determine the maximum microballoon loading that disperses uniformly in the resin without the aid of any diluent. The viscosity and dynamic mechanical properties of epoxy formulations containing varying amounts of glass microballoons were established by parallel plate rheometry. Our studies reveal that solventless processing of formulations with microballoon loading > 60% poses practical difficulties due to prohibitively high viscosities, although a packing efficiency of 74% is theoretically allowed in the case of hexagonal close packing. The presence of microballoons does not alter the curing mechanism. The mechanical properties of syntactic foams were inversely proportional to the loading and type of glass microballoons.

1. Introduction

Syntactic foams are lightweight composite materials prepared by incorporating hollow microballoons of glass [1], polymer [2, 3], or metal [4] in a suitable matrix. The inclusion of these hollow counterparts allows for significant weight savings, which is crucial for certain applications, especially marine [5, 6], aerospace [7, 8], and blast mitigation [9]. Polymeric syntactic foams refer to a subclass of cellular material, where hollow fillers are dispersed within a mechanically robust polymeric matrix. Apart from the nature of the matrix, concentration and type of microballoon are critical parameters, which decide its final properties [10]. Amongst hollow fillers, glass microballoons (HGM) are most extensively used [11–14], due to their low coefficient of thermal expansion and chemical inertness. Amongst all polymeric matrices, epoxy has been extensively studied [15–20], in view of its excellent mechanical properties and low shrinkage [21, 22].

The density of syntactic foam decreases with increasing concentration of purposely placed voids and for maximal weight savings, high loadings of the microballoon are desirable. The density of the syntactic foam can further be tuned by astute choice of microballoons, which are available in a variety of sizes and grades. Hexagonal close packing of rigid spheres is expected for microballoon loading to 74% v/v [23]. However, it is very unlikely to achieve hexagonal close packing under conventional conditions employed for processing. Interestingly, assuming random packing, the upper limit of microballoon loading is restricted to ~ 64% v/v [24–26]. It is perhaps for this reason that very few studies deal with syntactic foams with very high microballoon loading (ϕ > 60%) [8, 27–30].

Syntactic foams are conventionally processed using molding, casting, extrusion, rotational molding, or buoyancy methods, with the choice of technique depending upon the microballoon loading and the type of product being manufactured [31–33]. Processing using conventional techniques mandates fluidity of formulation for subsequent casting into molds. Increasing the microballoon loading beyond a critical value may render its processing impracticable by stir-casting techniques, which is perhaps most common. It is very important to establish the relationship of viscosity with curing time to ascertain optimal conditions required for processing. Surprisingly, rheological studies on syntactic

Table 1: Characteristics of hollow glass microballoons [2].

HGM	Density (kgm^{-3})	Wall thickness (μm)	Radius ratio	Microballoon size (mean diameter) (μm)	Isostatic crush strength (MPa)	Thermal conductivity ($Wm^{-1}K^{-1}$) at 21°C
K15	150	0.70	0.9839	43.6	2	0.055
K46	460	1.29	0.9356	40	41	0.153

foam formulations are rather scarce, with most of the studies dealing with the thermoplastic matrix [34–36]. In general, processing of compositions containing high microballoon loading is possible through molding [31], and casting mandates the use of solvent [14]. Unfortunately, there are issues associated with the subsequent solvent removal step, which in turn leads to void formation and a concomitant decrease in mechanical properties and increased production costs.

Chemorheology of curing thermosets has been widely studied and extensive reviews are available [37, 38]. Surprisingly, the rheological behavior of HGM-epoxy formulations has not been reported, which instigated us to undertake this work. Here, in this work, we attempt to establish the role played by HGM towards the curing of epoxy with an aim of determining the maximum amount of microballoons that can be dispersed properly within the resin in the absence of a diluent. It has been brought out in the literature that the presence of glass fibers does not affect the curing mechanism, but notable difference in the reaction rates has been observed [39, 40]. We hypothesize that, in view of the physical restraint posed by the glass balloons, the curing process will be adversely affected, especially at high microballoon loadings.

In this article, the rheological profile of glass microballoon filled polymeric syntactic foams using a cycloaliphatic epoxy resin in the presence of two different types of hollow glass microballoons of varying crushing strengths and densities is discussed, to establish the optimal processing conditions.

2. Materials and Methods

A low viscosity cycloaliphatic epoxy resin (Ciba Geigy, Araldite CY 230; epoxy equivalent 200 eq g^{-1}, η~1000 mPa.s at 30°C ($\dot{\gamma}$=0.1 s^{-1})), a hardener (HY 951; amine content 24 eq kg^{-1}), and hollow glass microballoons (Grades K46 and K15, 3M®) were used without any further treatment. The physical properties of hollow glass microballoons (HGM) used for the preparation of syntactic foams are presented in Table 1.

2.1. Rheological Studies. Rheological studies were carried out for HGM-epoxy formulations using an Anton Paar rheometer (MCR 102) using 25 mm disposable aluminum parallel plates. During the experiments, the shear stress was maintained at 1000 Pa to produce reliable and reproducible results. Shear rate sensitivity studies were performed, while varying the shear rate over the range of 0.1 to 1 s^{-1} under isothermal conditions (30°C). The oscillatory shear flow studies were conducted under both isothermal and dynamic conditions. The test fixture was initially preheated to the desired temperature. The plates were subsequently separated and the HGM-resin formulation was rapidly inserted. The plates were then brought back to a gap of approximately 1.0 mm and excess sample was trimmed. The experiment was finally initiated when the desired set temperature was achieved. The viscoelastic properties of the sample during cure, including the complex dynamic viscosity ($\eta*$), shear storage modulus (G'), and shear loss modulus (G"), were monitored. Experiments were performed over temperatures ranging from 60°C to 100°C in increments of 20°C and temperature sweeps from 30°C to 150°C at a heating rate of 5°C/min were performed using a constant frequency of 1 Hz for all experiments.

2.2. Processing of Syntactic Foams. Epoxy based syntactic foams were prepared as per the procedure reported in the literature [10]. The processing steps are as follows: firstly, precalculated amounts of epoxy and hardener (mix ratio of 100:13 by weight) are weighed and mixed together in a suitable beaker for about 5 min. Then, the precalculated amount of microballoon (0–70 vol %) is added while mixing the constituents together by stirring, using a wooden hand spatula (Supplementary Section S1, Table S1). To prevent breakage of hollow microballoons, slow stirring was performed for the uniform dispersion of microspheres. Moreover, due to the low density of the microballoons in comparison to the epoxy resin, the former has a tendency to drift towards the surface of the mold during the curing process. To circumvent the same, the stirring time was adjusted depending upon the amount of microballoon added, to achieve an optimal increase in the viscosity of the mixture. The formulation was degassed and was transferred into silicone molds and placed at 65°C inside an oven for 24 h. Finally, test samples are machined from the cured panel for mechanical and thermal characterization. The nomenclature for the sample is SFxx-yy, where SF refers to syntactic foams, xx denotes the type of glass microballoon employed for processing, i.e., 15 for K15 and 46 for K46, and yy corresponds to the volume percentage of glass microballoons.

2.3. Quasi-Static Testing. Mechanical testing was performed on syntactic foams containing 10-70% (v/v) of hollow glass microballoons (K15 and K46) using the Universal Testing Machine (International Equipments). The sample compositions that underwent testing are detailed in the supplementary section, Table S1. For compression, standard specimens of 12 mm diameter and 6 mm thickness were compressed at a crosshead speed of 1.3 mm min^{-1}. Five specimens of each composition were tested and compressive strength was

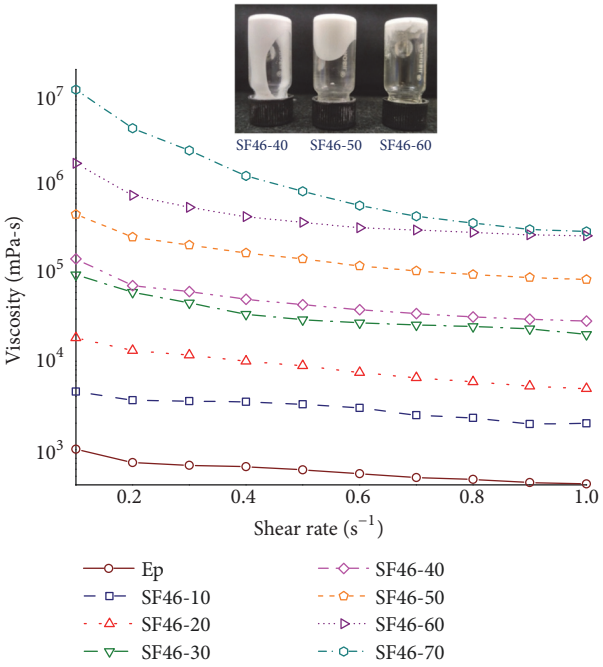

FIGURE 1: Dependence of increasing shear rate and microballoon loading (ϕ) on viscosity. Inset shows flowability of formulations at 40-60% (v/v) loadings of glass microballoons.

determined from the load-displacement data obtained from the tests. The area under the compressive stress-strain curve till the end of plateau region was quantified to determine the amount of energy absorbed by the foams [41]:

$$E_a = \frac{1}{2}\left(\sigma_c \times \varepsilon_{crush}\right) + \left(\sigma_c \times \varepsilon_{crush}\right), \quad (1)$$

where E_a, σ_c, and ε_{crush} refer to the energy absorbed, compressive yield strength, and crushing strain of the foam, respectively.

Flexural testing of syntactic foam specimens of standard dimensions (127 mm length × 12.5 mm width × 3.5 mm thickness) was performed by subjecting them to a deformation rate of 2 mm min^{-1} and span length of 60 mm under a three-point bending mode as per ASTM D790. The tensile properties were determined as per ASTM D638 using a Universal Testing System (International Equipments) at ambient temperature. The dog bone shaped specimens used for tensile testing were 165 mm long, 3 mm thick, and 13 mm wide along the center of the casting for syntactic foams. The samples were subjected to a crosshead speed of 10 mm min^{-1}.

2.4. Density Determination. Syntactic foams are usually three phase systems consisting of voids, microballoons, and resin. The presence of voids accounts for a reduction in the experimental density of the syntactic foams [42]. Theoretical density of syntactic foam (ρ_{th}) was estimated as per the standard rule of mixtures:

$$\rho_{th} = \rho_{HGM} * \Phi_{HGM} + \rho_{matrix} * \Phi_{matrix}. \quad (2)$$

Experimental density was determined by averaging the mass: volume ratio of five specimens as per ASTM D1622–98. The ratio of the difference between theoretical and experimental densities to the theoretical density was used to quantify the air void porosity trapped in the matrix during fabrication according to the following equation:

$$Void\ volume\ \% = \frac{\rho_{th} - \rho_{ex}}{\rho_{th}} \times 100. \quad (3)$$

The thermal degradation behavior was investigated using Perkin Elmer Diamond STG-DTA under N_2 atmosphere in the temperature range 50-600°C. A heating rate of 15°C/min and sample mass of 5.0 ± 0.5 mg were used for each experiment. Calorimetric studies were performed on a differential scanning calorimeter (DSC) (TA Instruments Q20). For dynamic DSC scans, samples (10±2 mg) were sealed in aluminum pans and heated from 0 to 200°C at 5°C/min. The experiments were performed under flowing N_2 (50 mL/min) to minimize oxidative degradation of the sample during the curing process. Visual inspection of the hollow glass microballoons was performed using an optical microscope (Olympus) at 40x magnification.

3. Results and Discussion

The chemorheological behavior of cycloaliphatic epoxy containing different types of hollow glass microballoons is studied to arrive at the optimal conditions required for processing of syntactic foam formulations.

3.1. Effect of Microballoon Loading on Viscosity. The effect of increasing microballoon loading (K46) on the viscosity of the composition in terms of viscosity-shear rate dependence is presented in Figure 1. Compositions prepared using lighter

microballoons (K15) also exhibit a similar profile. It can be seen that the cycloaliphatic epoxy resin exhibits a viscosity of ~ 1000 mPa.s at 30°C ($\dot{\gamma}$=0.1 s^{-1}) and the inclusion of microballoons leads to a considerable increase in its viscosity, the extent of which is proportional to the microballoon loading. The data associated with an increase in viscosity as a function of microballoon loading and shear rate is presented in the supplementary section (Figure S1). It is to be noted that, at microballoon loadings ~ 60%, the viscosity of the formulation is too high to permit solventless processing. For the sake of visualization, photographs of the representative formulation (ϕ=40-60%) are also included as an inset in Figure 1. It is clear that, for the present system, a microballoon loading of 60% v/v is the upper limit of fluidity and formulations with higher loading are too viscous to be processed in the absence of a diluent. Our studies indicate that although a theoretical packing efficiency of 74% is achievable for hexagonal close packing, it is only practical to process foam formulations with HGM loadings 40-60% v/v, where the packing of microballoons is random (upper limit = 64% v/v).

It is to be noted that, in view of the substantial difference in the density of HGM and epoxy, the lighter microballoons tend to drift to the surface of the resin, the time for drifting depending on the density difference. Digital photographs of representative formulations containing varying microballoon (K46) loadings are presented in the supplementary section (Figure S2). At loadings less than or equal to 30% v/v, separation of the components into distinct layers is evident, with the formation of an upper layer of light, hollow microballoons with epoxy layer at the bottom.

Our study clearly highlights that the curing temperature of epoxy-HGM formulations should be astutely chosen such that the rate of network formation is rapid enough to prevent microballoon agglomeration to the top. The DSC traces associated with the curing of epoxy at different isothermal temperatures are presented in Figure 2. The time associated with the curing process decreases from 200 min to 20 min as the temperature is raised from 40 to 70°C. For the present scenario, a temperature of 65°C appears to be appropriate.

Rheological studies can generate valuable inputs with regard to the viscoelastic nature of the material. The rheological profile associated with the curing of microballoon filled compositions was studied under an oscillatory mode using a parallel plate geometry which is routinely used for studying epoxy based systems [43]. The variation in the viscosity for both unfilled and glass microballoon filled compositions (40-60% microballoon loading) is presented in Figure 3. Three distinct regions are clearly evidenced. Initially, a slight decrease in viscosity is observed as the temperature was increased to ~ 90°C, which could be attributed to the overcoming of intermolecular interactions with increasing temperature. Further increase in temperature (90-120°C) leads to a sudden and exponential increase in viscosity: a feature attributable to the autocatalytic nature of curing. As the temperature approaches 120°C, the viscosity levels off indicating complete curing of the system.

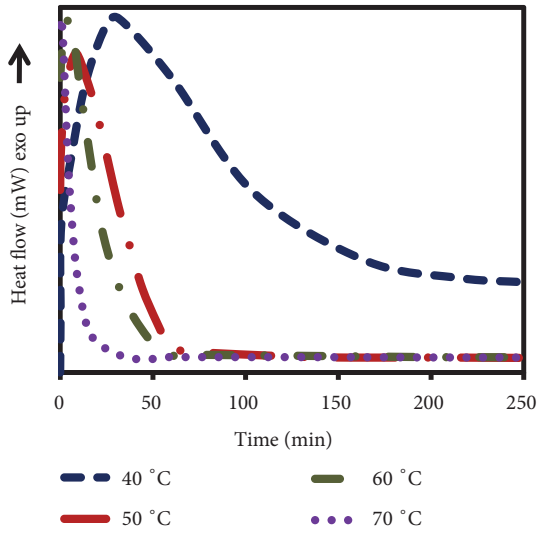

Figure 2: Calorimetric traces associated with curing of epoxy at different isothermal temperatures.

The evolution of storage and loss modulus due to curing of representative formulations (ϕ= 40%) was studied under isothermal temperatures (60-100°C) to arrive at the optimal temperature required for processing, and the results are presented in Figure 4. The loss modulus is initially higher than the storage modulus because the reactants are in a liquid state. Due to the reaction of the epoxy with amine, both G' and G" increase swiftly and a gelation region is observed denoted by crossover of storage and loss modulus. This region marks a sudden transition of the viscous liquid to an elastic solid, where the material can store and dissipate an equal amount of energy and the time required for this is referred to as gelation time (t_{gel}).

Interestingly, when the curing was performed at T= 60°C, after the initial increase in storage modulus, a slight decrease (in the form of a kink) was observed in the microballoon filled formulations (Figure 4(a)), irrespective of the type of microballoon employed. At lower temperatures, the curing process requires much longer time periods, which reflects in terms of longer "t_{gel}." Spherical microballoons tend to roll due to shearing action offered by the plates, and the polymeric network formed is not strong enough to withstand the shearing force offered by the oscillating plates, thereby resulting in its disruption. The network subsequently evolves with time, and the complete curing mandates ~ 1 h. When the curing is performed at higher temperatures (isothermal temperature = 80-100°C), the rate of emergence of the cross-linked structure is much more rapid; therefore the shear force offered by the plates is insufficient to result in any disruption of the network. Although storage and loss modulus are not design parameters, these data can be used to accurately predict the elastic modulus of syntactic foams which will be helpful in engineering applications of such foams [44, 45].

The delay in the curing phenomenon due to inclusion of microballoons in the resin is also evident from the calorimetric studies performed on formulations. Representative

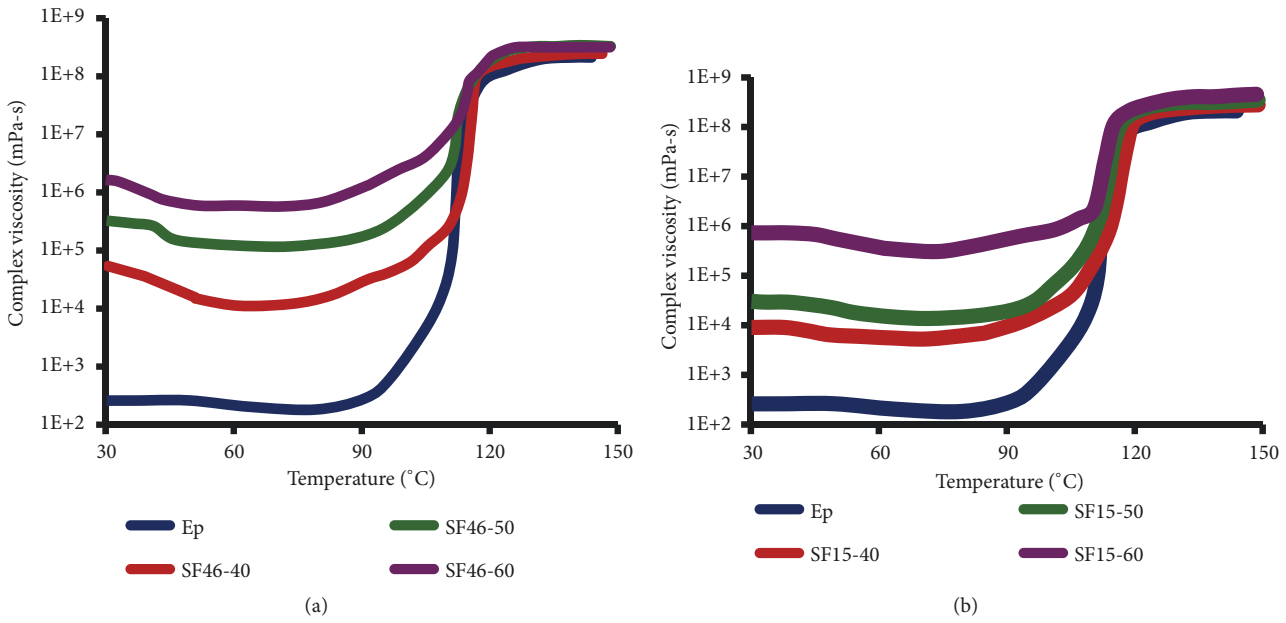

Figure 3: The effect of increasing microballoon loading on complex viscosity: (a) K46-epoxy formulations and (b) K15-epoxy formulations.

nonisothermal DSC traces (heating rate= 10°C min^{-1}) are presented in Figure 5. It can be seen that neat epoxy cures at 89°C (T_{peak}), which is relatively lesser than the T_{peak} value associated with formulations containing microballoons.

Gelation time-temperature dependence was used to arrive at the activation energy (E_a) associated with the curing process of epoxy, and the results are presented in Figure 6. The detailed procedure for the calculation of E_a is presented in the supplementary section (Section S2). A substantial delay in curing (as evidenced in terms of longer gelation time) is clear in formulations containing microballoons, a phenomenon attributable to the physical hindrance posed by the microballoons.

The presence of K15 results in a larger delay, which in turn can be attributed to the difference in the thermal conductivity of the microballoons (0.05 $Wm^{-1}K^{-1}$ for K15 and 0.15 $Wm^{-1}K^{-1}$ for K46), which leads to difference in the heat flow into the epoxy resin [46]. In addition, the role of the difference in the dimensions of the constituent fillers (K15: diameter 43 μm) as compared to K46 (diameter: 40 μm) cannot be ruled out.

Interestingly, the activation energy was found to be of the same order in all the formulations, which indicates that the presence of microballoons does not alter the epoxy-amine curing mechanism, which is a classical nucleophilic substitution reaction, reportedly following second-order kinetics [47] (Scheme 1). Our studies are in line with previous studies on glass fiber-epoxy compositions, which revealed that the glass fibers decrease the reaction rate associated with the curing process, without altering the mechanism [39].

3.2. Voidage in Syntactic Foam. The theoretical and experimental densities associated with syntactic foams (ϕ=10-70%) are presented in Figure 7. Owing to the higher density of K46 compared to K15 microballoons, cellular samples containing the former microballoons (ρ= 460 kg/m^3) exhibit relatively higher densities than samples containing K15 (ρ= 150 kg/m^3), under similar loadings. The experimental density, however, was much lower than the theoretical values. The difference in the densities was used to evaluate the voidage, which too is included in the figure, the noticeable feature being the higher voidage content in specimens containing high microballoon loading (ϕ = 70%).

3.3. Mechanical Properties. The low density of syntactic foam is the most favorable feature of cellular materials; hence the trends in mechanical properties need to be analyzed with respect to their density, which is best described in terms of specific mechanical properties. The quasi-static properties of the syntactic foams containing varying loadings (10-70% v/v) and different types of microballoons (K15 and K46) are presented in Figure 8. The difference in the crushing strength of the constituent microballoons clearly reflects in the mechanical properties of syntactic foams. The compressive stress-strain curves of epoxy-microballoon syntactic foams at different microballoon volume fractions are presented in the supplementary section (Figure S3). The stress-strain profiles reveal an initial linear elastic (Hookean) region, followed by an energy absorbing plateau region. The peak stress value is the compressive strength of the sample and the plateau region is visualized by an increase in strain without an appreciable increase in stress. In this plateau region, the microballoons are subjected to extensive compressive loads, which results in their crushing. Beyond this, there is an exponential increase in stress without any appreciable increase in strain: a region signaling the onset of densification [8].

Five specimens of each composition were subjected to mechanical tests. All, quasi-static mechanical properties

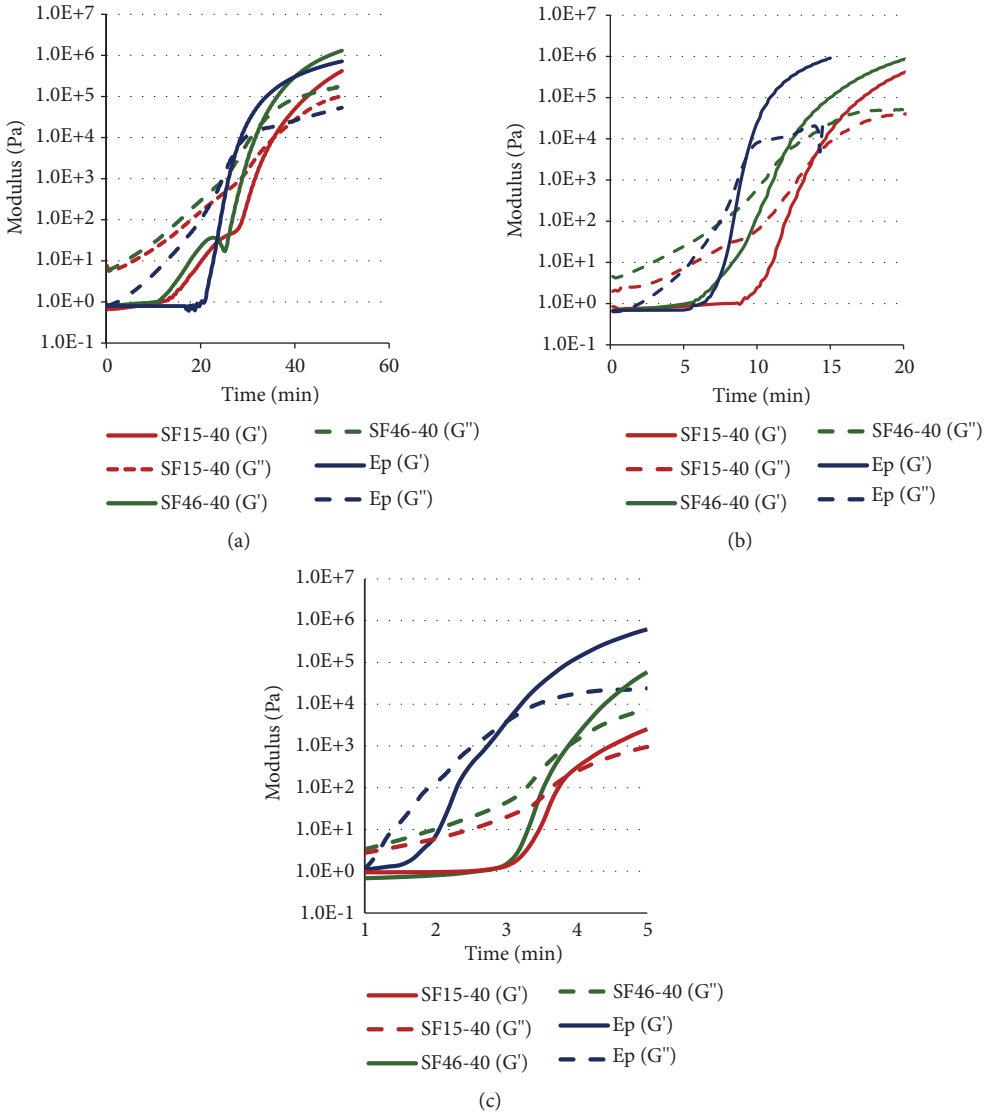

Figure 4: Isothermal gelation profiles of resin and syntactic foam formulations at different temperatures: (a) 60°C, (b) 80°C, and (c) 100°C (dotted lines G", solid lines G').

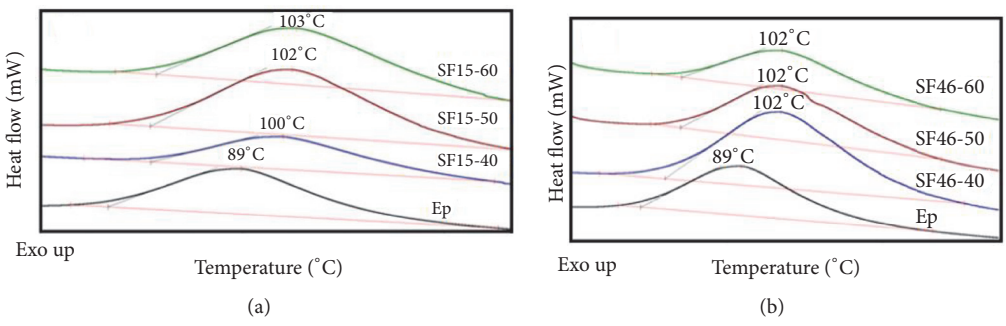

Figure 5: Nonisothermal DSC traces for epoxy-HGM formulations with increasing glass microballoons loadings: (a) SF15 and (b) SF46.

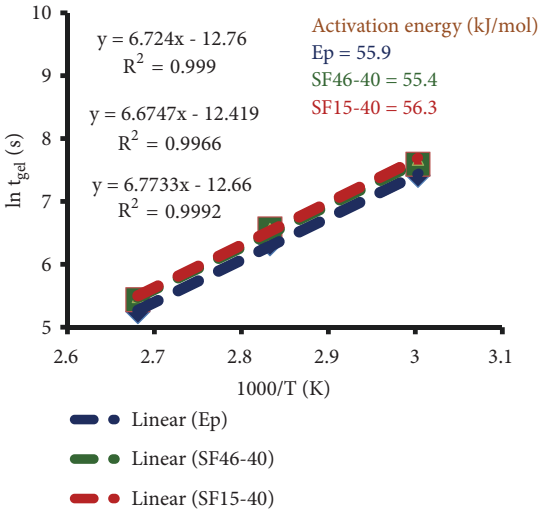

FIGURE 6: Arrhenius plot of $\ln(t_{gel})$ versus 1/temperature.

irrespective of the testing mode (compressive, tensile, and flexure) were found to decrease with increasing microballoon loading. Microballoon crushing is the primary mechanism responsible for the energy absorption of the foams in the compressive mode [48], which is usually quantified in terms of the area under the stress-strain curve till the end of the plateau region. Under flexural and tensile loadings, the difference between the strengths of two types of a syntactic foam specimen discernibly reduces. It is to be noted that, under the flexure and tensile mode, the microballoons are not the primary load bearing phase and failure depends to a large extent upon the matrix failure [18, 49]. The highest energy absorption ability was exhibited by syntactic foam compositions containing 40% microballoon loading.

What is particularly interesting to note is that the mechanical properties of the cellular materials drop significantly as the microballoon loading is increased to 70% v/v. It is to be noted that the properties of any reinforced material are decided by the extent of interfacial adhesion between the filler and the matrix. A condensation reaction between the surface hydroxyl groups of silica and oxirane rings of epoxy resin is responsible for the excellent adhesion between the glass and epoxy (Scheme S1). The inferior mechanical properties can be attributed to the fact that, in the specimens containing high microballoon loading (~70%), the resin is unable to penetrate into the interstitial regions and inclusion of a large volume percentage of glass microballoons which reportedly exhibit poor crushing strength compared to epoxy. This, in turn, is expected to lead to high voidage, which has also been observed experimentally (Figure 7). The decrease in mechanical properties exceeds the lowering in density; therefore the specific properties are also substantially reduced.

It appears that it is impossible to obtain a hexagonal close-packed structure in syntactic foams using common stir-casting techniques. In common words, packing is defined as a collection of nonoverlapping solid objects in n-dimensional space. An important attribute of packing is its density ϕ, which is defined as the fraction of space covered by the particles. Previously, computer algorithms have been used to study idealized random packing associated with monodisperse spheres. A rate-dependent densification algorithm [24] has indicated that a packing fraction between 0.642 and 0.649 is common. A Monte Carlo scheme yields $\phi = 0.68$, while a "drop and roll" algorithm yields a maximal packing efficiency (ϕ) of 0.60 [25]. Subsequently, a concept of a "Maximally Random Jammed" (MRJ) state was developed, which can be viewed as prototypical glasses in that they are maximally disordered while simultaneously being mechanically rigid. This is associated with a maximum limit of $\phi = 0.64$ [26]. A pictorial representation of hexagonal packing and random packing is presented in the supplementary section (Figure S4). Our studies indicate that, under the ordinary processing conditions, the "jammed" state appears to be the upper limit of packing with a packing efficiency of 64% [50].

3.4. Thermal Degradation. TG-DTG traces of syntactic foams containing K46 microballoons are presented in Figure 9. The thermogravimetric traces of neat epoxy and syntactic foams demonstrated similar profiles barring the progressive increase in the char content from 15.7% to 53% (at 600°C) with increasing microballoons content (10-70% (SF46)). The thermal properties of foams containing K15 present a similar trend and are included in the figure (Figure 9(b)).

Processing of epoxy-glass balloon formulations (40-60% microballoon loading) did not lead to any rupture of glass microballoons under the experimental conditions employed. This was determined by performing oxidative degradation of epoxy syntactic foam specimens in a muffle furnace (at 600°C), and the leftover char was observed under an optical microscope. Representative images of the char obtained from SF46-60 and SF15-60 are presented in Figure 10. It is clear that all the microballoons retained their physical appearance with no evidence of glass rupture.

4. Conclusions

In this paper, the rheological behavior associated with the curing of cycloaliphatic epoxy resin in the presence of hollow glass microballoons has been studied to establish optimal conditions for processing. For all practical purposes, compositions with microballoon loading < 60% can be conveniently processed using common techniques like stir casting. Formulations with high microballoon loading (≥ 60% v/v) exhibit too high viscosities to permit solventless processing of these compositions. This is substantially lower than the theoretical limit of 74% associated with hexagonal close packing. Under ordinary processing conditions, a "random jammed" state appears to be the upper limit of packing, with a packing efficiency of 64%. The presence of microballoons does not alter the epoxy-amine mechanism but the rate of reaction is adversely affected. In view of the density variation between the epoxy and hollow microballoons, the latter tend to drift to the surface. Hence, the curing temperature should be so chosen such that the rate of network formation exceeds the rate of microballoon drifting. In view of the same, a processing temperature of 65°C was found to be

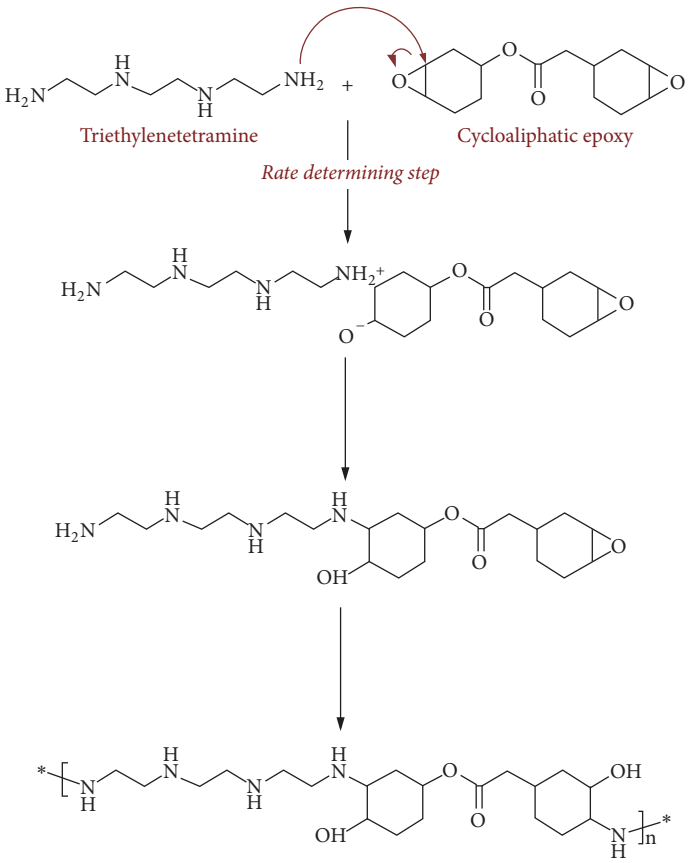

Scheme 1: Cycloaliphatic epoxy-amine curing reaction mechanism.

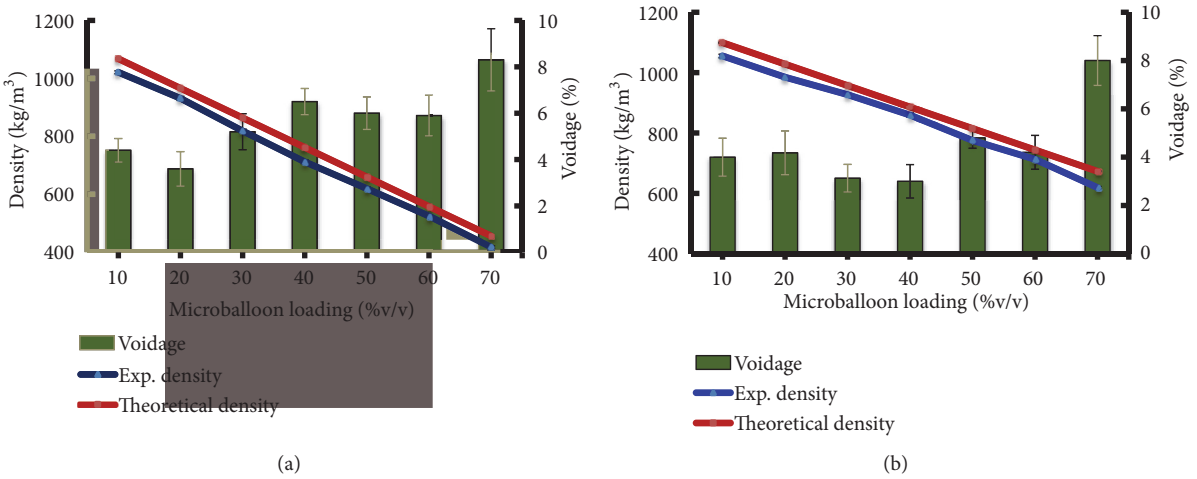

Figure 7: Theoretical and experimental densities of syntactic foam specimens: (a) SF15 and (b) SF46. The voidage is presented in the secondary axis.

most appropriate. Mechanical characterization reveals that the quasi-static properties associated with syntactic foams are higher in compositions containing microballoons with higher crushing strength. A concomitant decrease in the quasi-static properties is observed on increasing loadings of either type of glass microballoons; however the mechanical properties decrease precipitously as the microballoon loading is increased to 70%. An increase of approximately 72% and 192% is observed in the specific toughness values of SF15-40 and SF46-40 syntactic foams, respectively, compared to neat epoxy. The microballoons did not undergo any significant rupture under the conditions employed during processing.

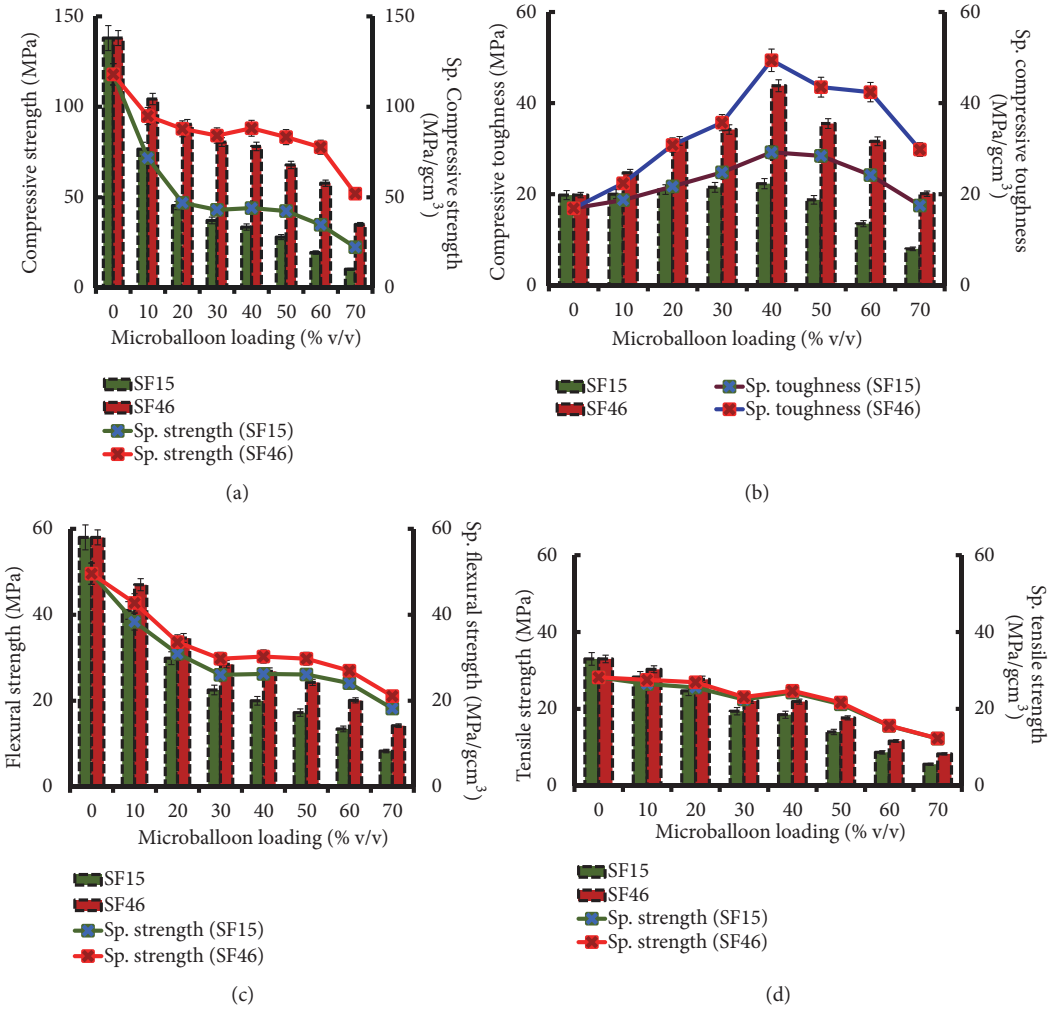

FIGURE 8: (a-b) Compressive, (c) flexural, and (d) tensile properties of epoxy syntactic foams containing different microballoons at varying loadings.

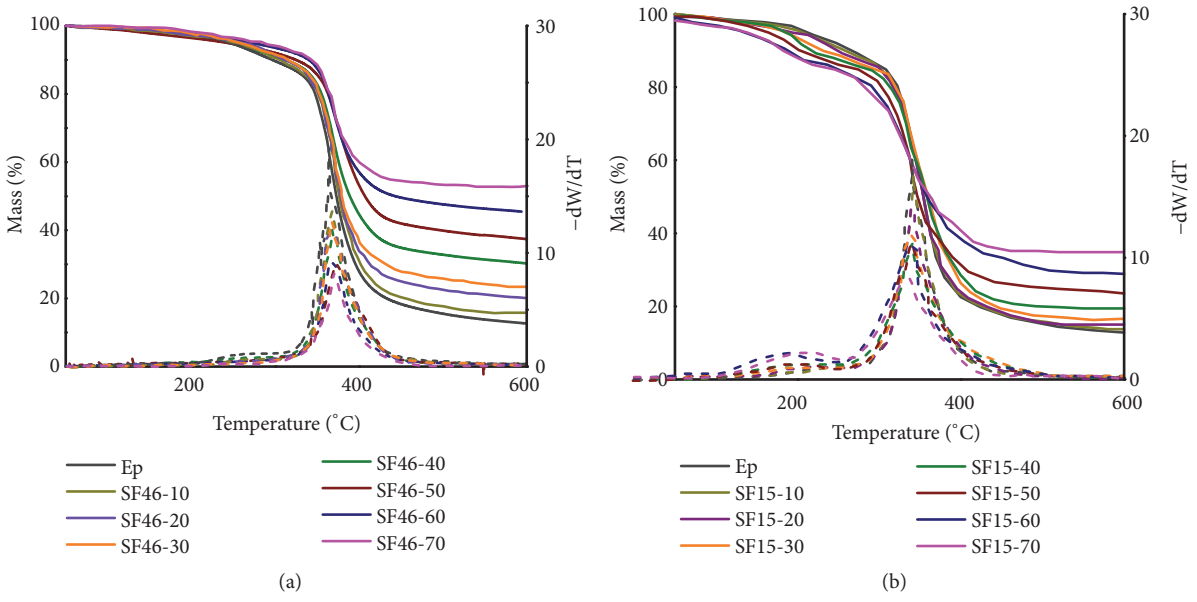

FIGURE 9: TG-DTG traces of epoxy syntactic foams: (a) SF46 and (b) SF15 (dotted lines represent DTG).

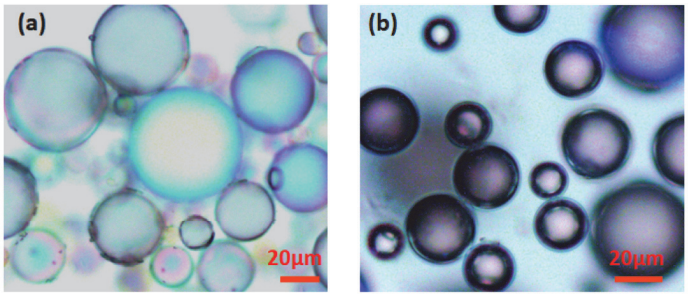

(a) (b)

Figure 10: Optical images of the char obtained after oxidative degradation of (a) SF15-60 and (b) SF46-60.

Data Availability

The data used to support the findings of this study are included in the manuscript and supplementary material.

Conflicts of Interest

The authors declare that there are no conflicts of interest regarding the publication of this paper.

Acknowledgments

The authors would like to thank DRDO for funding this work through ST/14-15/CFE-1311. A. V. Ullas is pleased to acknowledge DTU for providing financial support.

Supplementary Materials

Section S1: calculation of the amount of hollow glass microballoons. Table S1: compositional details of syntactic foam. Figure S1: increase in viscosity as a function of microballoon loading and shear rate ($\dot{\gamma}$). Figure S2: drifting of microballoons to the surface of epoxy-HGM formulations with varying glass microballoon loadings: (a) 10, (b) 20, (c) 30, and (d) 40% (v/v). Section S2: activation energy calculation. Table S2: variation of gelation time (t_{gel}) with temperature (T) and activation energy for syntactic foam compositions. Figure S3: representative compressive stress-strain curves of (a) SF15 and (b) SF46 syntactic foams. Figure S4: close packing in syntactic foams: (a) random packing (packing efficiency ~ 64%) and (b) hexagonal close packing (packing efficiency ~74%). Scheme S1: reaction of hydroxyl groups in glass with epoxy. *(Supplementary Materials)*

References

[1] D. Pinisetty, V. C. Shunmugasamy, and N. Gupta, *6 - Hollow Glass Microspheres in Thermosets—Epoxy Syntactic Foams*, William Andrew Publishing: Oxford, UK, 2015.

[2] A. Ullas, D. Kumar, and P. K. Roy, "Poly(dimethylsiloxane)-toughened syntactic foams," *Journal of Applied Polymer Science*, vol. 135, no. 8, p. 45882, 2018.

[3] H. Mae, M. Omiya, and K. Kishimoto, "Effects of strain rate and density on tensile behavior of polypropylene syntactic foam with polymer microballoons," *Materials Science and Engineering: A Structural Materials: Properties, Microstructure and Processing*, vol. 477, no. 1-2, pp. 168–178, 2008.

[4] N. Jha, D. P. Mondal, M. D. Goel, J. D. Majumdar, S. Das, and O. P. Modi, "Titanium cenosphere syntactic foam with coarser cenosphere fabricated by powder metallurgy at lower compaction load," *Transactions of Nonferrous Metals Society of China*, vol. 24, no. 1, pp. 89–99, 2014.

[5] R. L. Poveda and N. Gupta, "Carbon-nanofiber-reinforced syntactic foams: compressive properties and strain rate sensitivity," *JOM: The Journal of The Minerals, Metals & Materials Society (TMS)*, vol. 66, no. 1, pp. 66–77, 2013.

[6] D. Benderly, Y. Rezek, J. Zafran, and D. Gorni, "Effect of composition on the fracture toughness and flexural strength of syntactic foams," *Polymer Composites*, vol. 25, no. 2, pp. 229–236, 2004.

[7] M. Colloca, N. Gupta, and M. Porfiri, "Tensile properties of carbon nanofiber reinforced multiscale syntactic foams," *Composites Part B: Engineering*, vol. 44, no. 1, pp. 584–591, 2013.

[8] N. Gupta, Kishore, E. Woldesenbet, and S. Sankaran, "Studies on compressive failure features in syntactic foam material," *Journal of Materials Science*, vol. 36, no. 18, pp. 4485–4491, 2001.

[9] A. V. Ullas, P. K. Shaima, P. Chandel et al., "Epoxy-glass microballoon syntactic foams for blast mitigating application," *Defence Science Journal*, vol. 68, no. 2, pp. 210–217, 2018.

[10] A. V. Ullas, B. Qayyum, D. Kumar, and P. K. Roy, "Electrospun polyamide nanofiber-reinforced hybrid syntactic foams," *Polymer—Plastics Technology and Engineering*, vol. 55, no. 17, pp. 1797–1806, 2016.

[11] A. Pellegrino, V. L. Tagarielli, R. Gerlach, and N. Petrinic, "The mechanical response of a syntactic polyurethane foam at low and high rates of strain," *International Journal of Impact Engineering*, vol. 75, pp. 214–221, 2015.

[12] L. Bardella, F. Malanca, P. Ponzo, A. Panteghini, and M. Porfiri, "A micromechanical model for quasi-brittle compressive failure of glass-microballoons/thermoset-matrix syntactic foams," *Journal of the European Ceramic Society*, vol. 34, no. 11, pp. 2605–2616, 2014.

[13] A. Panteghini and L. Bardella, "On the compressive strength of glass microballoons-based syntactic foams," *Mechanics of Materials*, vol. 82, pp. 63–77, 2015.

[14] K. A. Devi, B. John, C. P. R. Nair, and K. N. Ninan, "Syntactic foam composites of epoxy-allyl phenol-bismaleimide ternary blend - processing and properties," *Journal of Applied Polymer Science*, vol. 105, no. 6, pp. 3715–3722, 2007.

[15] J. R. M. D'Almeida, "An analysis of the effect of the diameters of glass microspheres on the mechanical behavior of glass-microsphere/epoxy-matrix composites," *Composites Science and Technology*, vol. 59, no. 14, pp. 2087–2091, 1999.

[16] R. Huang and P. Li, "Elastic behaviour and failure mechanism in epoxy syntactic foams: The effect of glass microballoon volume fractions," *Composites Part B: Engineering*, vol. 78, pp. 401–408, 2015.

[17] C. S. Karthikeyan, S. Sankaran, and Kishore, "Elastic behaviour of plain and fibre-reinforced syntactic foams under compression," *Materials Letters*, vol. 58, no. 6, pp. 995–999, 2004.

[18] L. Wang, J. Zhang, X. Yang, C. Zhang, W. Gong, and J. Yu, "Flexural properties of epoxy syntactic foams reinforced by fiberglass mesh and/or short glass fiber," *Materials and Corrosion*, vol. 55, pp. 929–936, 2014.

[19] M. V. Alonso, M. L. Auad, and S. Nutt, "Short-fiber-reinforced epoxy foams," *Composites Part A: Applied Science and Manufacturing*, vol. 37, no. 11, pp. 1952–1960, 2006.

[20] T. C. Lin, N. Gupta, and A. Talalayev, "Thermoanalytical characterization of epoxy matrix-glass microballoon syntactic foams," *Journal of Materials Science*, vol. 44, no. 6, pp. 1520–1527, 2009.

[21] S. Kang, S. I. Hong, C. R. Choe, M. Park, S. Rim, and J. Kim, "Preparation and characterization of epoxy composites filled with functionalized nanosilica particles obtained via sol-gel process," *Polymer Journal*, vol. 42, no. 3, pp. 879–887, 2001.

[22] J. Gassan and A. K. Bledzki, "Possibilities for improving the mechanical properties of jute/epoxy composites by alkali treatment of fibres," *Composites Science and Technology*, vol. 59, no. 9, pp. 1303–1309, 1999.

[23] K. R. Dando, W. M. Cross, M. J. Robinson, and D. R. Salem, "Production and characterization of epoxy syntactic foams highly loaded with thermoplastic microballoons," *Journal of Cellular Plastics*, vol. 54, no. 3, pp. 499–514, 2018.

[24] W. S. Jodrey and E. M. Tory, "Computer simulation of close random packing of equal spheres," *Physical Review A: Atomic, Molecular and Optical Physics*, vol. 32, no. 4, pp. 2347–2351, 1985.

[25] W. M. Visscher and M. Bolsterli, "Random packing of equal and unequal spheres in two and three dimensions," *Nature*, vol. 239, no. 5374, pp. 504–507, 1972.

[26] S. Torquato, T. M. Truskett, and P. G. Debenedetti, "Is random close packing of spheres well defined?" *Physical Review Letters*, vol. 84, no. 10, pp. 2064–2067, 2000.

[27] M. C. Saha, S. Nilufar, M. Major, and S. Jeelani, "Processing and performance evaluation of hollow microspheres filled epoxy composites," *Polymer Composites*, vol. 29, no. 3, pp. 293–301, 2008.

[28] N. Gupta and E. Woldesenbet, "Hygrothermal studies on syntactic foams and compressive strength determination," *Composite Structures*, vol. 61, no. 4, pp. 311–320, 2003.

[29] R. R. Maharsia and H. D. Jerro, "Enhancing tensile strength and toughness in syntactic foams through nanoclay reinforcement," *Materials Science and Engineering: A Structural Materials: Properties, Microstructure and Processing*, vol. 454-455, pp. 416–422, 2007.

[30] K. S. Santhosh Kumar, C. P. Reghunadhan Nair, and K. N. Ninan, "Mechanical properties of polybenzoxazine syntactic foams," *Journal of Applied Polymer Science*, vol. 108, no. 2, pp. 1021–1028, 2008.

[31] F. A. Shutov, "Syntactic polymer foams," in *Chromatography/Foams/Copolymers*, vol. 73/74 of *Advances in Polymer Science*, pp. 63–123, Springer Berlin Heidelberg, Berlin, Germany, 1986.

[32] P. Bunn and J. T. Mottram, "Manufacture and compression properties of syntactic foams," *Composites Part B: Engineering*, vol. 24, no. 7, pp. 565–571, 1993.

[33] M. M. Islam and H. S. Kim, "Manufacture of syntactic foams: pre-mold processing," *Materials and Manufacturing Processes*, vol. 22, no. 1, pp. 28–36, 2007.

[34] P. Pötschke, T. D. Fornes, and D. R. Paul, "Rheological behavior of multiwalled carbon nanotube/polycarbonate composites," *Polymer Journal*, vol. 43, no. 11, pp. 3247–3255, 2002.

[35] H.-W. Xiao, S.-Q. Huang, and T. Jiang, "Morphology, rheology, and mechanical properties of dynamically cured epdm/pp blend: effect of curing agent dose variation," *Journal of Applied Polymer Science*, vol. 92, no. 1, pp. 357–362, 2004.

[36] A. K. Jain, N. K. Gupta, and A. K. Nagpal, "Effect of dynamic cross-linking on melt rheological properties of polypropylene/ethylene-propylene-diene rubber blends," *Journal of Applied Polymer Science*, vol. 77, no. 7, pp. 1488–1505, 2000.

[37] P. J. Halley and M. E. Mackay, "Chemorheology of thermosets—an overview," *Polymer Engineering & Science*, vol. 36, no. 5, pp. 593–609, 1996.

[38] M. B. Roller, "Rheology of curing thermosets: a review," *Polymer Engineering & Science*, vol. 26, no. 6, pp. 432–440, 1986.

[39] M.-F. Grenier-Loustalot and P. Grenier, "The mechanism of epoxy-resin curing in the presence of glass and carbon fibres," *Polymer Journal*, vol. 33, no. 6, pp. 1187–1199, 1992.

[40] V. M. Karbhari and R. Lee, "On the effect of E-glass fiber on the cure behavior of vinylester composites," *Journal of Reinforced Plastics and Composites*, vol. 21, no. 11, pp. 901–918, 2002.

[41] P. Raghu, S. Kunigal, and R. Larry, "Energy absorption performance of a eco-core - a syntactic foam," in *Proceedings of the 48th Aiaa/Asme/Asce/Ahs/Asc Structures, Structural Dynamics, And Materials Conference*, American Institute of Aeronautics and Astronautics, 2007.

[42] M. Narkis, S. Kenig, and M. Puterman, "Three-phase syntactic foams," *Polymer Composites*, vol. 5, no. 2, pp. 159–165, 1984.

[43] M. Ivankovic, L. Incarnato, J. M. Kenny, and L. Nicolais, "Curing kinetics and chemorheology of epoxy/anhydride system," *Journal of Applied Polymer Science*, vol. 90, no. 11, pp. 3012–3019, 2003.

[44] S. E. Zeltmann, K. A. Prakash, M. Doddamani, and N. Gupta, "Prediction of modulus at various strain rates from dynamic mechanical analysis data for polymer matrix composites," *Composites Part B: Engineering*, vol. 120, pp. 27–34, 2017.

[45] S. E. Zeltmann, B. R. Bharath Kumar, M. Doddamani, and N. Gupta, "Prediction of strain rate sensitivity of high density polyethylene using integral transform of dynamic mechanical analysis data," *Polymer Journal*, vol. 101, pp. 1–6, 2016.

[46] S. Park, F. Jin, and C. Lee, "Preparation and physical properties of hollow glass microspheres-reinforced epoxy matrix resins," *Materials Science and Engineering: A Structural Materials: Properties, Microstructure and Processing*, vol. 402, no. 1-2, pp. 335–340, 2005.

[47] J.-E. Ehlers, N. G. Rondan, L. K. Huynh, H. Pham, M. Marks, and T. N. Truong, "Theoretical study on mechanisms of the epoxy-amine curing reaction," *Macromolecules* , vol. 40, no. 12, pp. 4370–4377, 2007.

[48] M. Dimchev, R. Caeti, and N. Gupta, "Effect of carbon nanofibers on tensile and compressive characteristics of hollow particle filled composites," *Materials and Corrosion*, vol. 31, no. 3, pp. 1332–1337, 2010.

[49] N. Gupta and R. Nagorny, "Tensile properties of glass microballoon-epoxy resin syntactic foams," *Journal of Applied Polymer Science*, vol. 102, no. 2, pp. 1254–1261, 2006.

[50] C. Song, P. Wang, and H. A. Makse, "A phase diagram for jammed matter," *Nature*, vol. 453, no. 7195, pp. 629–632, 2008.

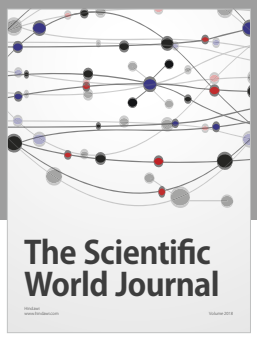

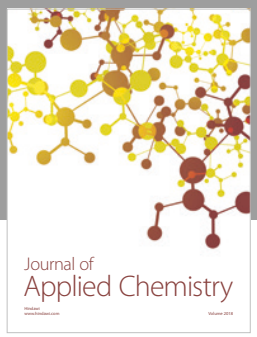

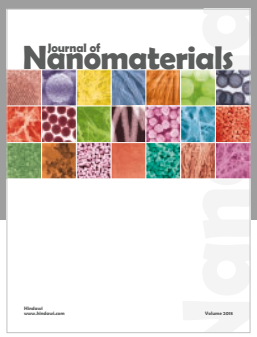

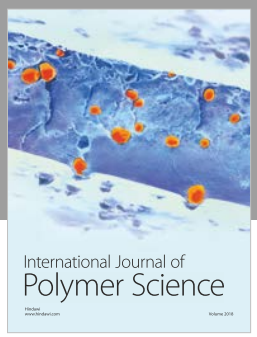

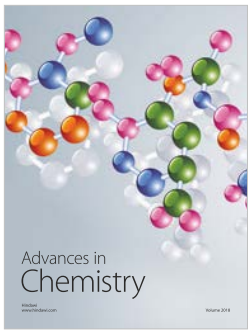

Hindawi
Submit your manuscripts at
www.hindawi.com
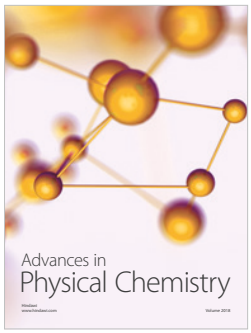

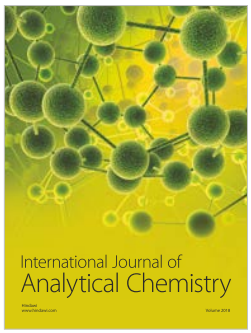

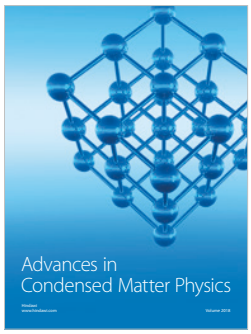

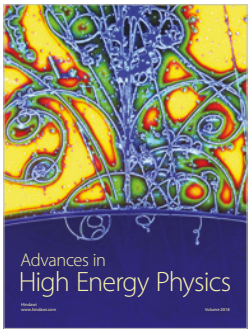

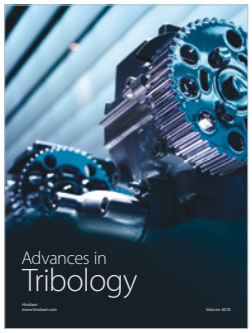

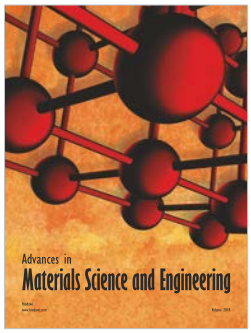

This article has been accepted for inclusion in a future issue of this journal. Content is final as presented, with the exception of pagination.

Estimation of Source Wavelet From Seismic Traces Using Groebner Bases

Karthikeyan Elumalai, *Student Member, IEEE*, Brejesh Lall, *Member, IEEE*, and R. K. Patney, *Senior Member, IEEE*

***Abstract*— An accurate and effective seismic wavelet estimation technique has extreme significance in the seismic data processing for analyzing the earth's subsurface layer information. The seismic wavelet to be determined is modeled as a moving average (MA) process and assumed to be driven by a zero mean, non-Gaussian, statistically independent, and identically distributed (IID) process. In order to estimate the MA model parameter from the observed noisy seismic signal, we pose this as a blind system identification (BSI) problem. In the BSI, a set of multivariate polynomial equations is obtained by matching higher order cumulant of observed noisy data with a higher order moment of blind system's impulse response. The Groebner bases that form the solution to this set of equations are obtained using the proposed algorithm. Numerical results demonstrate that the proposed method has a lower estimation error as compared to the previously reported methods.**

***Index Terms*— Blind system, groebner basis, higher order statistics (HOS), seismic wavelet.**

I. Introduction

A Major challenge in prospecting/extracting subsurface layer information from the observed seismic signal is seismic wavelet estimation. The estimation of seismic wavelet is generally posed as a blind system identification (BSI) problem [1]–[3]. To this end, we present a novel approach to BSI, which is used for wavelet estimation. In general, the goal of BSI is to identify system parameters using the responses (output) of the system to unknown input. The observed system response $y(n)$ to an unknown input $r(n)$ can be mathematically modeled as [4]

$$y(n) = \underbrace{r(n) * h(n)}_{x(n)} + N(n) \tag{1}$$

where $h(n)$ is the finite impulse response (FIR) of the system, $N(n)$ is the noise sequence, and $*$ denotes the convolution. The impulse response can be modeled as a minimum phase/nonminimum phase autoregressive (AR) [5], moving average (MA) [6], [7], or ARMA [8] process. The noise $N(n)$ is modeled as a Gaussian white or as a colored Gaussian sequence with zero mean and is assumed to be independent of the input $r(n)$. The ideal output of the system denoted as $x(n)$ in (1) is given as

$$x(n) = \sum_{n=0}^{q} h(n) r(n-i) \tag{2}$$

where $h(n) = \{h(0), h(1), \ldots h(q)\}$, $h(n) \neq 0 \ \ \forall\ 0 \leq n \leq q$. Here, q represents the order of system.

The aim of BSI is to estimate the system parameters $\{h(n), n = 1, \ldots, q\}$ using only the observation $y(n)$. Since the input and noise are unknown, the system identification is an ill-posed problem. In order to obtain system parameters, we require that certain assumptions be made regarding the system impulse response and the statistics of $x(n)$, $N(n)$. The assumptions made in this paper are generally valid in seismic signal processing [9], [10] and wireless channel estimation [11]. The key assumptions are as follows.

1) The input signal $r(n)$ is independent and identically distributed (IID) non-Gaussian sequence with zero mean and it is kth order white. The kth order cumulant [12], [13] of input $r(n)$ denoted by γ_k^r satisfies the condition

$$0 < \left|\gamma_k^r\right| < \infty, \quad \forall\ k > 2. \tag{3}$$

2) The FIR system parameters are real and $h(0) = 1$.
3) The noise sequence $N(n)$ is a zero-mean IID Gaussian sequence independent of $r(n)$. The mean and the variance of $r(n)$ are unknown.

The system identification using second-order statistics (SOS) was pioneered in [14] and [15]. The input was assumed to be white Gaussian noise sequence, and consequently, the autocorrelation of the output is equal to the scaled version of second-order moment of the impulse response [13]. The SOS does not preserve the phase information and can be used to obtain only the amplitude information of the system. Therefore, the estimation technique with SOS works well for an ideal minimum phase system given in (2) with the phase spectrum close to zero [16]. In order to overcome the limitations of SOS for a general nonminimum phase system with non-Gaussian input sequence, higher order statistics (HOS) was introduced for system identification by Giannakis [17]. The advantage of using HOS stems from its properties that preserve the system phase information and insensitivity to

Manuscript received January 27, 2018; revised July 8, 2018, November 18, 2018, and January 2, 2019; accepted March 3, 2019. *(Corresponding author: Karthikeyan Elumalai.)*

The authors are with the Signal Processing Group, Department of Electrical Engineering, IIT Delhi, New Delhi 110016, India (e-mail: imkarthi@gmail.com; brejesh@ee.iitd.ernet.in; rkpatney@ee.iitd.ernet.in).

Color versions of one or more of the figures in this paper are available online at http://ieeexplore.ieee.org.

Digital Object Identifier 10.1109/TGRS.2019.2905151

0196-2892 © 2019 IEEE. Personal use is permitted, but republication/redistribution requires IEEE permission.
See http://www.ieee.org/publications_standards/publications/rights/index.html for more information.

This article has been accepted for inclusion in a future issue of this journal. Content is final as presented, with the exception of pagination.

Gaussian noise. The algorithms for identification of the nonminimum phase FIR system using higher order cumulants have been summarized in [10], [12], and [18]– [20]. These methods can be broadly classified into three categories: 1) closed-form solution [21], [22]; 2) linear algebraic solution [9], [23]–[25]; and 3) optimization method [26]–[28].

Jian-hua and Ze-Min [21] obtain a set of equations from bispectrum and trispectrum of the observed noisy signal to identify system parameters of the MA model. The closed-form solution to these equations is obtained using the least-square method. Another recursive closed-form algorithm to estimate the parameters of MA model for a known order was studied in [22]. The authors utilize autocorrelation and diagonal slice of the third-order cumulant of $y(n)$. The algorithms based on linear algebraic solutions [9], [23]–[25] have been found to be more robust in the presence of additive noise. These studies provide a lower error variance of the estimated system parameters as compared to the closed-form solutions. Most studies on linear algebraic methods use the autocorrelation sequence of an observed noisy output $y(n)$. This approach leads to inconsistent estimates in the presence of colored Gaussian noise. Fonollosa and Vidal [24] alleviated this drawback by expressing the FIR system parameters as a linear combination of the cumulant slices. The studies in [29] have extended the work in [24] and incorporated higher order cumulant. In [26], the system parameters are obtained by minimizing the sum of the squared difference between the cumulant of observed output and the cumulant of the proposed model. Tugnait [27] presented a unified second-order and fourth-order cumulant matching methods. They consider a nonminimum-phase ARMA model for $h(n)$, whose parameters are estimated using the second-order and the fourth-order cumulants of the observed output.

With recent advances and widespread availability of computational resources, the exhaustive nonlinear optimization methods, which have a better performance than linear algebraic algorithms, are becoming viable. However, nonlinear optimization methods require a good initial guess for proper convergence. In view of this, linear algebraic algorithms are not only computationally attractive but also provide a good initial guess for the nonlinear optimization methods. In this paper, we propose a new method for BSI using Groebner bases (GB). A set of multivariate polynomials is generated from the kth order cumulant matching method and the GB method is utilized to obtain the unknown system parameters. Conventional optimization methods for BSI become computationally cumbersome as the number of system parameters increases. In [30] and [31], the set of polynomial functions is solved using the linear algebraic method; however, their method returns a large number of possible solutions. This makes the task of converging to the true system parameters arduous. In the proposed method, the new algorithm overcomes this problem. Numerical results show that the proposed method has a lower error variance as compared to previous studies in [9] and [32] and much smaller solution space.

Rest of the paper is organized as follows. In Section II, we discuss the preliminaries of HOS and GB. In Section III, we describe the proposed BSI method. In Section IV, we describe the seismic signal model, and in Section V, the accuracy of the proposed method is verified. In Section VI, we present the numerical results with real seismic data.

II. Mathematical Model

In this section, we provide some mathematical preliminaries about HOS and Groebner basis that will be useful in the later sections of this paper.

A. Higher Order Statistics

Let $y(n)$ be a kth order stationary random process with zero mean, then the kth order cumulant of this process $C_k^y(\tau_1, \tau_2, \ldots, \tau_{k-1})$ is given as [12]

$$C_k^y(\tau_1, \ldots, \tau_{k-1}) = \mathbb{E}\{y(n)y(n+\tau_1)\cdots y(n+\tau_{k-1})\}. \quad (4)$$

Here, $\mathbb{E}\{\cdot\}$ represents the expectation operator, and τ_i are the time delays. Using the independence of noise sequence $N(n)$ and the input $x(n)$, kth order cumulant of $y(n)$ in (4) can be rewritten as follows:

$$C_k^y(\tau_1, \ldots, \tau_{k-1}) = C_k^x(\tau_1, \ldots, \tau_{k-1}) + C_k^N(\tau_1, \ldots, \tau_{k-1}). \quad (5)$$

Since $x(n) = r(n) * h(n)$, using Brillinger Rosenblatt formula [33] in (5), we have

$$C_k^y(\tau_1, \ldots, \tau_{k-1}) = C_k^r(\tau_1, \ldots, \tau_{k-1}) * M_k^h(\tau_1, \ldots, \tau_{k-1}) + C_k^N(\tau_1, \ldots, \tau_{k-1}) \quad (6)$$

where

$$M_k^h = \sum_{n=0}^{q} h(n)h(n+\tau_1)h(n+\tau_2)h(n+\tau_{k-1}) \quad (7)$$

and

$$C_k^r(\tau_1, \tau_2, \ldots, \tau_{k-1}) = \gamma_k^r \delta(\tau_1, \tau_2, \ldots, \tau_{k-1}). \quad (8)$$

In (8), $\gamma_3^r = C_3^r(0,0)$ is a measure of skewness, $\gamma_4^r = C_4^r(0,0,0)$ is a measure of the kurtosis of $r(n)$, and $\delta(\tau_1, \tau_2, \ldots, \tau_{k-1})$ is the $k-1$ dimensional Kronecker delta function. Substituting (7) and (8) into (6), the expression for kth order cumulant of $y(n)$ is given as

$$C_k^y(\tau_1, \ldots, \tau_{k-1}) = \gamma_k^r \sum_{n=0}^{q} h(n)h(n+\tau_1)\cdots h(n+\tau_{k-1}) + C_k^N(\tau_1, \ldots, \tau_{k-1}) \quad (9)$$

where $C_k^N(\tau_1, \tau_2, \ldots, \tau_{k-1})$ is the kth order cumulant of a noise $N(n)$. For Gaussian noise, the higher order moments $\{k > 2\}$ are zero and (9) can be written as

$$C_k^y(\tau_1, \tau_2, \ldots, \tau_{k-1}) = \gamma_k^r \sum_{n=0}^{q} h(n)h(n+\tau_1)\cdots h(n+\tau_{k-1}). \quad (10)$$

Therefore, the kth order cumulant of $y(n)$ is equal to scaled version of kth order moment of system parameters in the presence of Gaussian noise.

This article has been accepted for inclusion in a future issue of this journal. Content is final as presented, with the exception of pagination.

B. Groebner Bases

GB, first proposed by Buchberger in [34], is used to solve a wide range of problems involving multivariate polynomials. The Buchberger algorithm [34] is used to find the GB of a set of multivariate polynomial functions given in Algorithm 1. To introduce GB, the following notation and definition are important and are being reproduced here from [35]–[38].

1) Monomial: A monomial is a number, a variable or a product of a number and a variable where all exponents are positive numbers. Let $x_1, \ldots x_n$ be n variables and $x^\alpha = x_1^{\alpha_1} \ldots x_n^{\alpha_n}$ is called a monomial where $\alpha_i \in \mathbb{N}$ for $i = 1, \ldots n$. Example: $x_1^2, 4x_2^3, 24xyz$.

The degree of the monomial is the sum of the exponents of all included variables $\alpha = \{\alpha_1 + \cdots + \alpha_n\}$. Constants have the monomial degree of 0. For example, the monomial $24xyz$ has degree 3 because the sum of degrees of x, y, and z is $1 + 1 + 1 = 3$.

2) Polynomial: A polynomial f in $x_1, \ldots x_n$ with the coefficients in K (where K is any field such as real numbers, $\mathbb{R}$, rational numbers, $\mathbb{Q}$, complex numbers, $\mathbb{C}$, etc.) is a finite linear combination of monomials, written as

$$f = \sum_{\alpha} \beta_\alpha x^\alpha \tag{11}$$

where coefficient $\beta_\alpha \in K$. Example: $f = 2x_1^2 + 4x_2^3$
A polynomial as oppose to the monomial is a sum of monomials where each monomial is called a term. If $\beta_\alpha \neq 0$, then we call $\beta_\alpha x^\alpha$ a term of f. The degree of the polynomial is the greatest degree of its terms. Example: let $f = 3x^2y + 6xy^3 - 9y^4$, a polynomial with three terms and maximum degree 4.

3) Polynomial Ring: A ring (K) is a set with two binary structures, namely, $+$ and $\times$, which satisfy the following conditions.

1) $(K,+)$ is an abelian group with identity 0.
2) $(K,.)$ is an associative binary structure with identity 1.
3) For all a,b,c $\in K$.

(a+b).c=a.c+b.c, c.(a+b) =c.a+c.b

Given a ring K, consider the set of polynomials $K[x] = K[x_1, \ldots x_n]$ in the variables $x = x_1, \ldots x_n$ with coefficients from K. These polynomials in n variables, over a field K, together with operations of addition and multiplication, satisfy all axioms of ring, and so form a commutative polynomial ring.

4) Ideals: Let $K[x_1 \ldots x_n]$ be a polynomial ring over a field K. Then the subset $I \subset K[x_1 \ldots x_n]$ is an ideal if and only if the following properties are satisfied.

1) $0 \in$ I.
2) If $f_i, f_j \in I$, then $f_i + f_j \in I$.
3) If $f \in I$ and $h \in K[x_1 \ldots x_n]$, then $h.f \in I$.

Let $f_1, f_2, \ldots f_s$ be polynomials such that $f_1, f_2, \ldots f_s \in K[x_1 \ldots x_n]$. Then ideal $< f_1, f_2, f_3 \ldots f_s >$ defined as

$$\langle f_1, f_2, f_3 \ldots f_s \rangle = \left\{ \sum_{i=1}^{s} h_i f_i | h_1, ..h_s \in K[x_1 \ldots x_n] \right\}. \tag{12}$$

5) Lexicographic Order: In order to arrange the terms of polynomial, one must be able to compare every pair of polynomials. In this paper, we need to choose a method for ordering set of monomials. The chosen method is Lexicographic ordering ($>_{\text{lex}}$). Let x^α and x^β be two different monomials, i.e., $\alpha = (\alpha_1, \ldots, \alpha_n), \alpha \in \mathbb{Z}_{\geq 0}^n$ and $\beta = (\beta_1, \ldots, \beta_n), \beta \in \mathbb{Z}_{\geq 0}^n$. If $x^\alpha >_{\text{lex}} x^\beta$ then the nonzero element on the leftmost nonzero entry of $\alpha - \beta \in \mathbb{Z}_{\geq 0}^n$ is positive.
Example: $x^2y >_{\text{lex}} xy$, since (2, 1) $>_{\text{lex}}$ (1, 1) because $\alpha - \beta =$ (2, 1)−(1, 1) = (1, 0).

6) S-Polynomial: To introduce the algorithm for computing GB, Buchberger first defined the notion of S-polynomials. It eliminates the leading term (LT) of the polynomial. Let $f = \sum_\alpha \beta_\alpha x^\alpha$ is nonzero polynomial in $K[x] = K[x_1, \ldots x_n]$ and let $>_{\text{lex}}$ be the monomial ordering then:

1) *multidegree of f: $multideg(f) = max\{\alpha \in \mathbb{Z}_{\geq 0}^n, \beta_\alpha \neq 0\}$;*
2) *leading coefficient (LC) of f: $LC(f) = \beta_{multideg(f)} \in K[x_1 \ldots x_n]$;*
3) *leading monomial (LM) of f:$LM(f) = x^{multideg(f)}$;*
4) *LT of f: $LT(f) = LC(f).LM(f)$;*
5) *least common multiple (LCM): $L = Lcm\{LT(f_i), LT(f_j)\}$.*

Given two multivariate polynomials f_i and f_j, suppose that L is the LCM of the LMs of f_i and f_j with respect to a fixed ordering of monomials

$$S(f_i, f_j) = \frac{L}{LT(f_i)}(f_i) - \frac{L}{LT(f_j)}(f_j). \tag{13}$$

Example: Let $f_1 = xy - x$, and $f_2 = x^2 - y$. Here, $L = Lcm\{LT(f_1), LT(f_2)\}$, where $LT(f_1) = xy$ and $LT(f_2) = x^2$ Therefore, $L = Lcm\{xy, x^2\} = x^2y$. Substitute L, f_1, and f_2 in (13)

$$S(f_1, f_2) = \frac{x^2y}{xy}\{xy - x\} - \frac{x^2y}{x^2}\{x^2 - y\} = -x^2 + y^2. \tag{14}$$

Note: The S-polynomials can be constructed by any two polynomials f_1 and f_2. First, it involves multiplication of the two polynomials by such monomial factors that the leading power product of both polynomials becomes equal, namely, the least common multiple of the leading power products of the two polynomials. By the subsequent subtraction, this LCM power product then vanishes.

7) Groebner Bases: A finite set of polynomials $\{g_1, g_2 \ldots g_t\} \subset I$ is a GB for an Ideal I if and only if $\forall f \in I$, $LT(f)$ is divisible by $LT(g_i)$ for some i.

8) Buchberger's Criteria: A finite polynomial set $G = \{g_1, g_2 \ldots g_t\}$ is a GB for an Ideal I if and only if for all $i \neq j$, the remainder on division of $S(g_i, g_j)$ by G is zero. The notation $\overline{S(g_i, g_j)}^{\,G}$ is used to represent the division process.

9) Buchberger Algorithm: The algorithm proceeds as follows: take a set of polynomials F and set initially $G := F$, where G will be the desired Groebner basis of F at the end of this procedure. Next, apply the Buchberger criterion to see if G is already a Groebner basis. If this is the case, reduce each polynomial in G with respect to other polynomials in G and stop. Otherwise, pick a pair of polynomials f_1 and f_2 from G, and compute their S-polynomial. If the remainder with respect to G of the S-polynomial is nonzero, then adjoin it to G. Iterate until G is a Groebner basis.

This article has been accepted for inclusion in a future issue of this journal. Content is final as presented, with the exception of pagination.

Algorithm 1 Buchberger's Algorithm

Input: $F = \{f_1, f_2, f_3, \ldots, f_s\}$
Output: Groebner bases $G = \{g_1, g_2, \ldots, g_t\}$ for an Ideal $I =< \{f_1, f_2, f_3, \ldots, f_k\} >$, with $F \subset G$
Initialize: $G = F$
repeat
$Gr = G$
for each pair $\{i, j\}$ such that $g_i, g_j \in Gr$ and $i \neq j$ **do**
$S = \overline{S(g_i, g_j)}^{Gr}$
if $S \neq 0$ **then**
$G = G \bigcup \{S\}$
end if
end for
Until $G = Gr$

Let us analyze Algorithm 1 step-by-step. In the first step, we assign G with the input system of polynomial equations F and generate a set with all (unordered) pairs of polynomials from F. We will use this set to verify the Buchberger criterion for G. Next, we enter a loop, which will execute until there are critical pairs to check. If there are no more pairs, then the Buchberger criterion is satisfied and G is a Groebner basis. In the loop, we take a pair of polynomials f_1 and f_2, and compute their S-polynomial and its reduction with respect to the current basis. If the reduction is nonzero, we adjoin new element to G and update the set of critical pairs. When the loop terminates, we obtain a Groebner basis of F. In the final step of the algorithm, if the reduced flag is set, we reduce each element of the basis with respect to other elements and make each element monic, obtaining a reduced Groebner basis.

III. Blind System Identification

In cumulant matching method, the kth order cumulant of observed data (6) and kth order moment of impulse response (7) are matched in mean square error (MSE) sense to estimate the unknown system parameters. The objective function can be mathematically expressed as

$$J = \sum_{\tau_1}\sum_{\tau_2}\cdots\sum_{\tau_{k-1}}\left[C_k^y(\tau_1, \tau_2, \ldots, \tau_{k-1}) - \gamma_k^r M_k^h(\tau_1, \tau_2, \ldots, \tau_{k-1})\right]^2. \quad (15)$$

In view of (7) the above-mentioned function can be rewritten as

$$J = \sum_{\tau_1}\sum_{\tau_2}\cdots\sum_{\tau_{k-1}}\left[C_k^y(\tau_1, \ldots, \tau_{k-1}) - \gamma_k^r \sum_{n=0}^{q} h(n)h(n+\tau_1)\cdots h(n+\tau_{k-1})\right]^2). \quad (16)$$

The solution for (16) can be obtained using the algorithms proposed in [7] and [28]. However, the solution requires a good initial guess and may converge to local minima. In this paper, we propose a method to solve the moment matching problem analytically based on Groebner basis method. The proposed method obtains all the finite number of possible solutions for (16), and hence overcomes the local minima problem. The desired solution is then chosen according to the assumption on system parameters. In the proposed method, we obtain a set of nonlinear equations by matching the kth order moment of impulse response with kth order cumulant of observed noisy signal and force it to be zero, that is,

$$\gamma_k^r \sum_{n=0}^{q} h(n)h(n+\tau_1)\cdots h(n+\tau_{k-1}) - C_k^y(\tau_1, \ldots, \tau_{k-1}) = 0. \quad (17)$$

In order to proceed, the higher order cumulant dimension is reduced by slicing it diagonally [7], [39]. Performing diagonal slicing by substituting $\tau_1, \tau_2, \ldots, \tau_{k-1} = \tau$ into (16), we have

$$\gamma_k^r \sum_{n=0}^{q} h(n)h^{k-1}(n+\tau) - C_k^y(\tau) = 0. \quad (18)$$

For $n = 0, 1, \ldots, q$ expand the summation in (18) and map the obtained nonlinear equation to a multivariate polynomial function $f_\tau(h(0), h(1), \ldots, h(q))$ as

$$f_\tau(h(0), \cdots, h(q)) \triangleq \gamma_k^r\{h(0)h^{k-1}(\tau) + \cdots + h(q)h^{k-1}(q+\tau)\} - C_k^y(\tau) = 0. \quad (19)$$

For $\tau = -q, \ldots, 0, \ldots, q$, we obtain a set of multivariate polynomial function by substituting τ in (19) and $f_i(h(0), \ldots, h(q)) = f_i$

$$\begin{aligned}
&\tau = -q : f_{-q} \triangleq \gamma_k^r\{h(q)h^{k-1}(0)\} - C_k^y(-q) \quad (20)\\
&\quad\vdots\\
&\tau = -1 : f_{-q+1} \triangleq \gamma_k^r\{h(1)h^{k-1}(0) + h(2)h^{k-1}(1) + \cdots + h(q)h^{k-1}(q-1)\} - C_k^y(-1)\\
&\tau = 0 : f_0 \triangleq \gamma_k^r\{h^{k-1}(0) + h^{k-1}(1) + \cdots + h^{k-1}(q)\} - C_k^y(0)\\
&\tau = 1 : \quad f_1 \triangleq \gamma_k^r\{h(0)h^{k-1}(1) + h(1)h^{k-1}(2) + \cdots + h(q)h^{k-1}(q+1)\} - C_k^y(1)\\
&\quad\vdots\\
&\tau = q : \quad f_q \triangleq \gamma_k^r\{h(0)h^{k-1}(q)\} - C_k^y(q).
\end{aligned}$$

In the above-mentioned set of functions, we note that there are $2q + 1$ number of multivariate polynomial functions, q unknown variables, and $C_k^y(\tau)$ known functions. For any real signal $y(n)$, the cumulant $C_k^y(\tau)$ is calculated using (4). From the property of kth order cumulant $C_k^y(-\tau) \neq C_k^y(\tau)$ for $k > 2$. Therefore, we need to obtain the unknown system parameters $\{h(0), \ldots, h(q)\}$ for kth order cumulant of $y(n)$ by solving the set of multivariate polynomial functions.
Choose a set of polynomial functions to solve out of $2q + 1$ functions and identify the unknown system parameters. For any combination of equations, we end up with finite number of solutions only. The obtained solutions are the desired system parameters. The obtained solutions may be real or complex.

The algorithm to choose a set of the multivariate polynomial equation for $k > 2$ is given in Algorithm 2.

Case 1: Here, we explain our approach in detail to identify the unknown system parameters for the case when $q = 2$

This article has been accepted for inclusion in a future issue of this journal. Content is final as presented, with the exception of pagination.

Algorithm 2 Algorithm to Find System Parameters

Step 1: Select two multivariate polynomial functions out of $2q+1$ which contains a minimum number of variables and find Groebner Bases for them.
Step 2: Find the possible roots for variables form the univariate polynomial present in the Groebner Bases.
Step 3: If there exist repeated roots and complex roots for variables remove them to reduce the solution space. Here we consider only the real roots for variables (if unknown system parameters assumed as real) and substitute in equation set to find possible real roots for other variables.
Step 4: Stop if all the possible roots are obtained for all variables, otherwise choose other two polynomial equations which contains minimum variable to solve using Groebner Bases and find the roots. Repeat this process for q times in order to obtain roots for q variables

and $k=3$. The set of multivariate polynomial equations is obtained by substituting the values of q and k in (20) as follows:

$$\begin{aligned} f_{-2} &\triangleq \gamma_3^r\{h(2)h^2(0)\} - C_3^y(-2) = 0 \qquad (21)\\ f_{-1} &\triangleq \gamma_3^r\{h(1)h^2(0) + h(2)h^2(1)\} - C_3^y(-1) = 0\\ f_0 &\triangleq \gamma_3^r\{h^3(0) + h^3(1) + h^3(2)\} - C_3^y(0) = 0\\ f_1 &\triangleq \gamma_3^r\{h(0)h^2(1) + h(1)h^2(2)\} - C_3^y(1) = 0\\ f_2 &\triangleq \gamma_3^r\{h(0)h^2(2)\} - C_3^y(2) = 0. \end{aligned}$$

We define $a \triangleq C_3^y(-2), b \triangleq C_3^y(-1), c \triangleq C_3^y(0), d \triangleq C_3^y(1), g \triangleq C_3^y(2)$, and $s \triangleq \gamma_3^r$ and proceed to find the system parameters using the algorithm proposed.
Step 1: Find GB for a multivariate polynomial function $\{f_{-2}, f_2\}$ explained in the Appendix.

$$f_6 \triangleq gh(0) - ah(2) = 0 \qquad (22a)$$
$$f_7 \triangleq -ash^3(2) + g^2 = 0. \qquad (22b)$$

Step 2: From the univariate polynomial function (22a), we find all the possible three roots of $h(2)$. Substituting the value of $h(2)$ into (22b) and obtain all three roots for $h(0)$, where

$$h(0) = \frac{1}{\left(\gamma_3^r\right)^{1/3}} \frac{C_3^y(-2)}{C_3^y(2)} \left\{ \frac{C_3^y(2)^2}{C_3^y(-2)} \right\}^{1/3} \quad \text{and}$$
$$h(2) = \frac{1}{\left(\gamma_3^r\right)^{1/3}} \left\{ \frac{C_3^y(2)^2}{C_3^y(-2)} \right\}^{1/3}.$$

Step 3: If there are repeated roots or complex roots for $h(0)$ or $h(2)$ in Step 2 above, we eliminate them to reduce the solution space. We consider the real roots only since the unknown system parameters assumed as real. Next, we obtain $h(1)$ corresponding to each pair of $(h(0), h(2))$ by substituting in f_{-1} or f_0 or f_1. Invoking the aforementioned assumption $h(0)=1$ on system parameter, we have $\gamma_3^r = ((C_3^y(-2)^2)/(C_3^y(2)))$. Note that using this method, we can estimate both minimum and nonminimum phase FIR systems. In Section IV, we show how this technique can be used for seismic wavelet estimation.

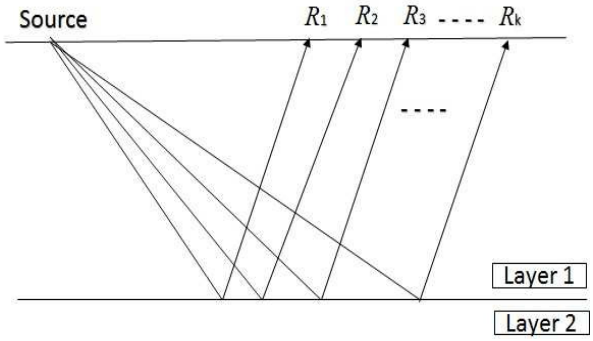

Fig. 1. Example of shot gather, source denotes the shot, and $R_1 \ldots R_k$ are the number of geophones. The seismic wave gets reflected due to impedance contrast at the end of Layer 1.

IV. Seismic Wavelet Estimation

In seismic exploration, a short duration seismic wave (seismic wavelet) is transmitted from the earth's surface. There are various types of sources used to seismic waves such as dynamite, hammer/weight drops, and vibrosis. The source selection is dependent on the desired signal to noise ratio, the human environment, the target depth desired, and the geological environment. The dynamite and hammer/weight drops are called impulse sources. The shape of seismic wavelet looks as if most of the energy is concentrated in the front of the pulse [2], [40]. The hammer/weight drops are used to analyze shallow depths [42]. The dynamite sources have been widely used for land seismic surveys for many decades [46]–[48]. Due to the high energy density of the dynamite explosion, the seismic wave propagates into deep earth layers. As an alternative to explosives and hammer, vibrators on land have been used for traditional reflection seismic profiling for petroleum exploration and deep seismic profiling. The signal emitted by the seismic vibrator is not impulsive, but typically has a duration of some 10–15 s [41], [43]–[45].

The seismic wavelet propagates through earth's different subsurface layers. The wave gets reflected due to impedance (the product of each layer's density and wave velocity) contrast between two layers. The reflected signals are being received by a number of geophones, which are arranged horizontally on the earth surface as shown in Fig. 1. The geophone converts the elastic wave motion of the ground into an electrical signal, known as seismic trace [2]. The geophysical structure and the layer's information are analyzed from the seismic trace up to certain depth at a particular place. The primary applications such as oil and gas exploration, and the higher resolution seismic method in coal exploration, and so on. The earth layer's information is not directly accessible from seismic trace. The trace contains seismic wavelet, reflection coefficients (ratio of incident and reflected wave energy), and noise informations. The ultimate goal of seismic signal processing is to interpret earth properties without complications of the source wavelet [7]. To retrieve the reflection coefficients from trace, seismic deconvolution is one of the steps in seismic signal processing. In order to perform deconvolution, the seismic wavelet must be known. However, the shape and statistical

This article has been accepted for inclusion in a future issue of this journal. Content is final as presented, with the exception of pagination.

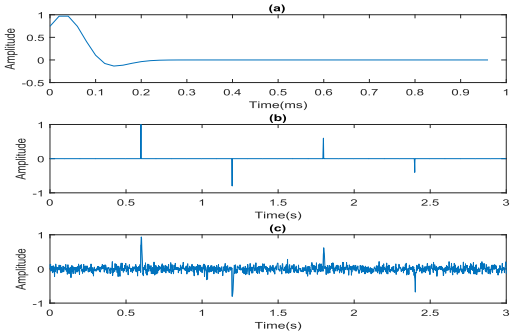

Fig. 2. (a) Short duration seismic wavelet used for exploration. (b) Reflection coefficient sequence generated for 3 s. (c) Seismic trace generated by convolving reflection coefficients sequence with seismic wavelet and additive Gaussian noise.

properties of a seismic wavelet are not known *a priori* in practical scenarios and it is difficult to estimate reflection coefficients directly from seismic trace [52]. We estimate the unknown seismic wavelet amplitude [49] and phase [50], [51] from observed noisy seismic trace using the solution proposed for BSI. The seismic trace can be mathematically modeled as the convolution between a source wavelet and a reflectivity sequence, in the presence of additive noise as

$$\text{Trace}(n) = \text{Reflection}(n) * \text{Wavelet}(n) + \text{Noise}(n) \quad (23)$$

where "Trace" represents the observed noisy seismic trace, "Reflection" represents the reflection coefficients sequence, "Wavelet" represents the seismic wavelet or seismic source used for exploration, and "Noise" represents the additive noise in the seismic trace and "n" denotes the discrete time samples. The synthetic seismic trace [2] generated based on (23) as shown in Fig. 2.

The seismic wavelet modeled as minimum/nonminimum phase FIR system. The use of HOS-based MA model for seismic wavelet estimation was introduced in [7]. In this model, the length of the wavelet is its order (i.e., q), and the amplitude values of the wavelet are the values of the model parameters. Dai *et al.* [28] proposed a seismic wavelet model based on the ARMA. Unlike the MA model, the orders p and q of the ARMA model are not directly related to the length of the seismic wavelet. An approximate seismic wavelet is then obtained using the ARMA parameters. However, in ARMA process, the order of AR estimation is difficult. It is also difficult to derive a multivariate polynomial function using a higher order cumulant. Therefore, we have assumed the seismic wavelet as an MA model and it is easy to derive a multivariate polynomial function using higher order cumulant.

In order to estimate the seismic wavelet form seismic trace, generally, fourth-order statistics $k = 4$ is used. A set of multivariate polynomial function obtained by substituting $k = 4$ in (20) and find Groebner basis using Algorithm 2. The performance of the proposed method is presented and discussed in section III and Appendix A.

V. Results and Discussion

In order to evaluate the performance of the proposed method, we consider an example of both minimum phase and nonminimum phase systems with known order q. The output $y(n)$ of this system is corrupted by an additive colored Gaussian noise $N(n)$. The input $r(n)$ is independent exponentially distributed random process with zero mean ($\mu_r = 0$), unit variance ($\sigma_r^2 = 1$), and skewness ($\gamma_r^3 = 2$). We use the proposed method to identify parameters of the MA model from noisy output process. Let σ_y^2 be the variance of the output signal and σ_N^2 be the noise variance. We define the signal-to-noise ratio (SNR) as

$$SNR = 10 \log \left(\frac{\sigma_y^2}{\sigma_N^2} \right).$$

A finite number of Monte Carlo simulation runs are used to validate the performance of proposed method. The mean and variance ($\pm\sigma$) of estimated parameters are considered. To measure accuracy of the proposed method, MSE of estimated parameter ($\hat{h}(i)$) and the true parameter ($h(i)$) for $i = 0, \ldots, q$ is given as

$$MSE = \frac{1}{q} \sum_{i=0}^{q} \left(\frac{h(i) - \hat{h}(i)}{h(i)} \right)^2.$$

Example 1: In this example, we consider a minimum phase MA(2) system with true system parameters as $h(0) = 1, h(1) = -0.86, h(2) = 0.74$. The system response $y(n)$ generated by using (1) where

$$y(n) = r(n) - 0.86r(n-1) + 0.74r(n-2) + N(n). \quad (24)$$

The estimation of system parameters is performed using only third-order statistics. We compare the MSE of the proposed estimation method with existing estimation method given in [32]. We obtain the set of multivariate polynomial equations based on third-order ($k = 3$) statistics. The system parameters are then retrieved using the proposed algorithm. The proposed method is compared with existing Zidane method [32], Zhang method [53], and Safi method [54]. In Table I, we consider different numbers of input signal samples (N=500,1500, 2000), and use the proposed method to estimate the unknown system parameters in the absence of noise using third-order statistics.

We observe in Table I that the MSE values of the proposed method are very small as compared to those obtained by Algo-Z, Algo-safi, and Algo-Zhang methods. The error variance is also less as compared to other methods. This implies that the estimated parameters are comparable with the true system parameters. It is also observed that if we increase the number of samples, the accuracy of the proposed algorithm increases. In Table II, we consider a fixed sample size of $N = 2000$ and different SNRs to compare the proposed method using third-order statistics. The proposed method has a better performance as compared to other methods, even at low SNRs as can be observed from Table II.

Example 2: In this example, we consider a nonminimum phase MA(2) system with true system parameters are $h(0) = 1$, $h(1) = -2.33, h(2) = 0.667$. The system response $y(n)$ generated by using (1) where

$$y(n) = r(n) - 2.33r(n-1) + 0.667r(n-2) + N(n). \quad (25)$$

This article has been accepted for inclusion in a future issue of this journal. Content is final as presented, with the exception of pagination.

TABLE I

MINIMUM PHASE FIR PARAMETERS ESTIMATED USING THIRD-ORDER STATISTICS FOR NOISE-FREE CASE AND 50 MONTE CARLO RUNS

Data length	Method	h(0)±σ	h(1)±σ	h(2)±σ	MSE
500	Proposed method	1 ±0.010	-0.853 ±0.013	0.731±0.016	7.1x10-05
	AlgoZ	1	-0.7715±0.1341	0.5662±0.3289	0.0219
	Algo-safi	1	-0.6879±0.5040	0.4499±0.7337	0.0646
	Algo-Zhang	1	-6461±0.2046	0.6729±0.2402	0.0234
1500	Proposed method	1 ±0.006	-0.856 ±0.021	0.734 ±0.015	2.9x10-5
	AlgoZ	1	-0.9007±0.1246	0.6403±0.2625	0.0068
	Algo-safi	1	-0.9106±0.2005	0.8008±0.2344	0.0034
	Algo-Zhang	1	-0.6913±0.1241	0.6638±0.0921	0.0164
2000	Proposed method	1 ±0.003	-0.861 ±0.005	0.741 ± 0.006	1.05x10-6
	Algo-Z	1	-0.8411±0.085	0.6939±0.1420	0.0015
	Algo-safi	1	-8922±0.0749	0.8009±0.1349	0.0027
	Algo-Zhang	1	-7460±0.0811	0.6570±0.0696	0.0101

TABLE II

FIR SYSTEM PARAMETER ESTIMATED USING HIGHER ODER STATISTICS FOR DIFFERENT SNR, $N = 2000$ AND FOR 50 MONTE CARLO RUNS

SNR	Method	w(0)±σ	w(1)±σ	w(2)±σ	MSE
0 dB	Proposed method	1 ±0.013	-0.866 ±0.041	0.749 ±0.079	6.5x10-5
	AlgoZ	1	-0.857 ±0.1990	0.8298±0.3080	0.0049
	Algo-safi	1	-0.817 ±0.3625	1.0176±0.3745	0.0477
	Algo-Zhang	1	-0.290 ±0.2338	0.6317±0.1018	0.1538
15 dB	Proposed method	1 ±0.012	-0.865 ±0.037	0.747 ±0.015	4.1x10-5
	AlgoZ	1	-0.8439±0.1032	0.6705±0.1751	0.0031
	Algo-safi	1	-0.9429±0.0884	0.8897±0.1270	0.0167
	Algo-Zhang	1	-0.7272±0.0803	0.6494±0.0531	0.0129
30dB	Proposed method	1 ±0.01	-0.864 ±0.013	0.746 ±0.014	2.9x10-5
	AlgoZ	1	- 0.8679±0.069	0.6788±0.1405	0.0023
	Algo-safi	1	-0.9406±0.0811	0.8581±0.1276	0.0114
	Algo-Zhang	1	-0.7423±0.0765	0.6511±0.0444	0.0111
45dB	Proposed method	1 ±0.005	-0.855 ±0.011	0.735 ±0.012	2.6x10-5
	AlgoZ	1	- 0.8648±0.084	0.6894±0.1445	0.0016
	Algo-safi	1	-0.9131±0.1190	0.8512±0.1792	0.0088
	Algo-Zhang	1	-0.7372±0.0685	0.6582±0.0502	0.0109

TABLE III

NONMINIMUM PHASE CHANNEL SYSTEM PARAMETER ESTIMATED FOR DIFFERENT SNR (50 MONTE CARLO RUNS, $N = 640$)

	Method	h(0)±σ	h(1)±σ	h(2)±σ	MSE
SNR=∞ (with out noise)	Proposed	1 ±0.004	-2.31 ±0.012	0.663 ±0.03	3.6x10-5
	G-M	1	-2.255 ±0.225	0.786 ±0.141	1.3
SNR=100	Proposed	1 ±0.013	-2.34 ±0.014	0.661 ±0.013	6.12x10-5
	G-M	1	- 2.423 ±0.421	0.863 ±0.458	1.41
SNR=10	Proposed	1 ±0.014	2.31 ±0.015	0.658 ±0.016	8.5x10-4
	G-M	1	-2.429±1.140	0.797±0.262	1.403

TABLE IV

NONMINIMUM PHASE CHANNEL SYSTEM PARAMETER ESTIMATED FOR VARIOUS DATA LENGTHS FOR 50 MONTE CARLO RUNS

Data length	Method	h(0)±σ	h(1)±σ	h(2)±σ	MSE
640	Proposed method	1±0.011	-2.31±0.012	0.663±0.01	3.6x10-5
1024	Proposed method	1±0.012	-2.32±0.01	0.664±0.011	1.2x10-5
2048	Proposed method	1±0.004	-2.32±0.005	0.665±0.006	9.1x10-6

In this example, we focus on nonminimum phase system estimation using third-order statistics. We compare our proposed method with this existing *G–M* method detailed in [9] for various SNRs and sample length $N = 640$. It is observed from Table III that the proposed method has a better performance as compared to the *G–M* method under various SNR= 100 and 10 dB. In Table IV, we considered different input signal sample lengths ($N = 1024, 2048$). The proposed method is used to estimate the unknown system parameters with third-order statistics. It is observed that the error variance reduces with increase in sample length.

VI. REAL SEISMIC DATA

The experimental seismic data are used for testing the proposed wavelet estimation method. The real data used in this paper comes from the east Texas, USA [55]. Dynamite is used as source (wavelet) for explorations. The reflected waves were observed by an array of geophones and recorded for a period of 3 s with a sampling interval of 2 ms. The seismic data are sorted based on the common midpoint (CMP) between the source and the receiver [2]. The time delays between the CMP gathers are corrected by the normal move out (NMO) correction method [56]. The CMP gathered and NMO corrected

This article has been accepted for inclusion in a future issue of this journal. Content is final as presented, with the exception of pagination.

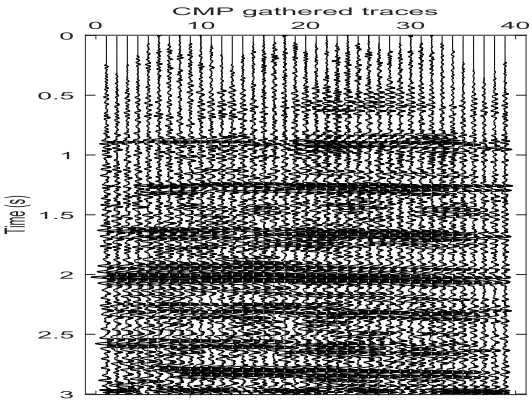

Fig. 3. CMP gathered and NMO corrected real seismic data.

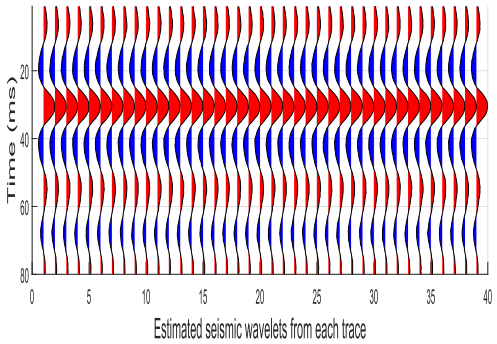

Fig. 4. Seismic wavelet estimated from each CMP gathered traces.

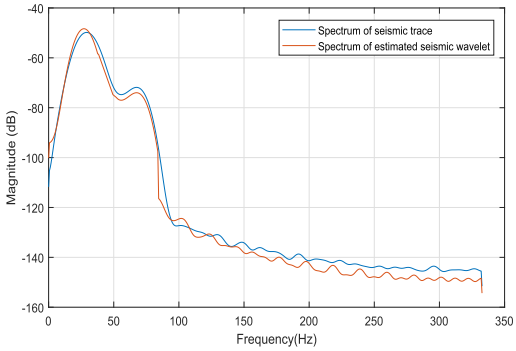

Fig. 5. Magnitude spectrum of seismic trace overlaid with magnitude spectrum of seismic wavelet.

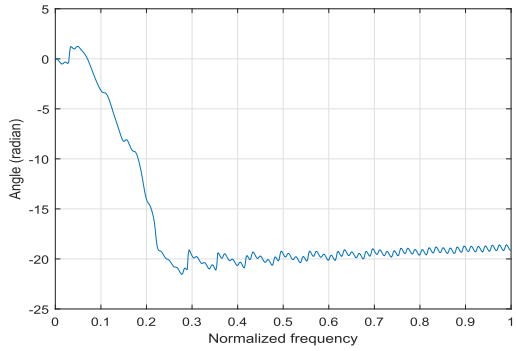

Fig. 6. Unwarped phase spectrum of stacked (averaged) seismic wavelet.

data shown in Fig. 3, which contains 39 traces. Those traces contain the same reflection point and the source informations. The procedure to estimate the seismic wavelet through the proposed method was the same as the one applied on the synthetic model: first, we have to calculate the higher order cumulant from trace. The reflection coefficient sequence is assumed to have a symmetrically distributed IID non-Gaussian distribution. Therefore, the fourth-order cumulant is used to estimate the wavelet parameters. The fourth-order cumulant is calculated by substituting $k = 4$ in (17) and the system of polynomial equations is derived using (20). Finally, the polynomial equations are solved by finding Groebner basis to obtain the desired parameters using Buchburger's algorithm.

We have estimated the seismic wavelet for a time duration of 80 ms. We observe that the estimated wavelet for the real data has large energy content in the low-frequency range as shown in Fig. 4. This observation is consistent with the fact that dynamite is an impulsive source and it generates a front-loaded signal (i.e., most of the energy is concentrated at the beginning of the wave) and the energy in the side lobes is very less. In Fig. 4, each column represents estimated seismic wavelet, the red color represents the positive amplitude and the blue color represents negative amplitude. The magnitude spectrum of normalized seismic wavelet overlaid with magnitude spectrum of the normalized seismic trace is shown in Fig. 5. The spectrum matches approximately, therefore, the estimated wavelet is more reliable. The unwarped phase spectrum of the stacked seismic wavelet is shown in Fig. 6. The seismic wavelets estimated from different seismic traces are very consistent. This proves that the stability of the extraction approach proposed in this paper. This accurate seismic wavelet estimation helps in accurately estimating the reflection coefficients by performing deconvolution and, thus, helps in studying the earth layers accurately.

VII. Conclusion

In this paper, we propose a novel method for seismic wavelet estimation using GB from the observed seismic data. The performance of the proposed method and the existing methods is analyzed using numerical simulations based on third-order cumulants. It was observed that the MSE of the proposed method is lower as compared to the existing methods. The advantage of the proposed method is that it does not require a good initial guess for global convergence. The proposed method also provides a consistent estimate of the system parameters even in the presence of colored Gaussian noise. Furthermore, we have used the real CMP gathered seismic data to estimate the seismic wavelet from each trace separately. The magnitude spectrum of the estimated seismic wavelet is close to the magnitude spectrum of the seismic trace.

Appendix

In this appendix we show the steps to find a Groebner Bases for our multivariate polynomial function f_{-2} and f_2 using

This article has been accepted for inclusion in a future issue of this journal. Content is final as presented, with the exception of pagination.

Buchberger Algorithm.

$$\begin{aligned} f_{-2} &\triangleq \gamma_3^r\{h(2)h^2(0)\} - C_3^y(-2) = 0 \\ f_2 &\triangleq \gamma_3^r\{h(0)h^2(2)\} - C_3^y(2) = 0 \end{aligned} \tag{26}$$

where $a \triangleq C_3^y(-2)$, $g \triangleq C_3^y(2)$ and $s \triangleq \gamma_3^r$
solve set of polynomial $\{f_{-2}, f_2\}$ using Buchberger's algorithm given in **Algorithm** 1 to find GB.
Buchberger's Algorithm
$Ideals =< f_{-2}, f_2 >$
$Initialize : G = \{f_{-2}, f_2\}$
Step 1:
$Gr = \{f_{-2}, f_2\}$
Find S-polynomial for $\{f_{-2}, f_2\}$ using (13)

$$S(f_{-2}, f_2) = \frac{L}{LT(f_{-2})}(f_2) - \frac{L}{LT(f_2)}(f_2) \tag{27}$$

Here $L = Lcm\{LT(f_{-2}), LT(f_2)\}$, where $LT(f_{-2}) = sh(2)h^2(0)$ and $LT(f_2) = sh(0)h^2(2)$
Therefore, $L = Lcm\{sh(2)h^2(0), sh(0)h^2(2)\} = sh^2(0)h^2(2)$.

Substitute L, f_{-2} and f_2 in the above equation

$$\begin{aligned} S(f_{-2}, f_2) = &\frac{sh^2(0)h^2(2)}{sh(2)h^2(0)}\{sh^2(0)h(2) - a\} \\ &-\frac{sh^2(0)h^2(2)}{sh(0)h^2(2)}\{sh(0)h^2(2) - g\} \end{aligned}$$

$S(f_{-2}, f_2) = gh(0) - ah(2)$, {reduced with respect to G}
Let $f_6 \triangleq gh(0) - ah(2)$
Step 2:
$G = \{f_{-2}, f_2, f_6\}$
$Gr = \{\{f_{-2}, f_6\}, \{f_2, f_6\}\}$
Find S-polynomial for $\{f_2, f_6\}$ using (13)

$$S(f_2, f_6) = \frac{L}{LT(f_2)}(f_2) - \frac{L}{LT(f_6)}(f_6) \tag{28}$$

$L = Lcm\{LT(f_2), LT(f_6)\}$, where $LT(f_2) = sh(0)h^2(2)$ and $LT(f_6) = gh(0)$
Therefore, $L = Lcm\{sh(0)h^2(2), gh(0)\} = gsh(0)h^2(2)$.
Substitute L, f_2 and f_6 in the above equation

$$\begin{aligned} S(f_2, f_6) = &\frac{gsh(0)h^2(2)}{sh(0)h^2(2)}\{sh(0)h^2(2) - a\} \\ &-\frac{gsh(0)h^2(2)}{gh(0)}\{gh(0) - ah(2)\} \end{aligned}$$

$S(f_2, f_6) = -ash^3(2) - g^2$, {reduced with respect to G}
Let $f_7 \triangleq -ash^3(2) + g^2$

REFERENCES

[1] D. G. Stone, "Wavelet estimation," *Proc. IEEE*, vol. 72, no. 10, pp. 1394–1402, Oct. 1984.

[2] O. Z. Yilmaz, *Seismic Data Analysis: Processing, Inversion, and Interpretation of Seismic Data*. Tulsa, OK, USA: Society of exploration geophysicists., 2001.

[3] X. Lü and Y. Wang, "Mixed-phase wavelet estimation by iterative linear inversion of high-order statistics," *J. Geophys. Eng.*, vol. 4, no. 2, pp. 184–193, Mar. 2007.

[4] A. G. Stogioglou and S. McLaughlin, "MA parameter estimation and cumulant enhancement," *IEEE Trans. Signal Process.*, vol. 44, no. 7, pp. 1704–1718, Jul. 1996.

[5] J. Vidal and J. R. Fonollosa, "Causal AR modeling using a linear combination of cumulant slices," *Signal Process.*, vol. 36, no. 3, pp. 329–340, Apr. 1994.

[6] J. Antari, A. E. Khadimi, A. Zeroual, and Y. Zaz, "Identification parameters of MA model and non-minumum phase channel using adaptive method," in *Proc. Int. Conf. Multimedia Comput. Syst.*, May 2012, pp. 394–398.

[7] G. D. Lazear, "Mixed-phase wavelet estimation using fourth-order cumulants," *Geophysics*, vol. 58, no. 7, pp. 924–1060, Jul. 1993.

[8] B. Nsiri, T. Chonavel, and J.-M. Boucher, "SEM blind identification of ARMA models application to seismic data," in *Proc. IEEE 12th Eur. Signal Process. Conf.*, Sep. 2004, pp. 1099–1102.

[9] G. B. Giannakis and J. M. Mendel, "Identification of nonminimum phase systems using higher order statistics," *IEEE Trans. Acoust., Speech, Signal Process.*, vol. 37, no. 3, pp. 360–377, Mar. 1989.

[10] G. B. Giannakis, "Wavelet parameter and phase estimation using cumulant slices," *IEEE Trans. Geosci. Remote Sens.*, vol. 27, no. 4, pp. 452–455, Jul. 1989.

[11] D. P. Ruiz, A. Gallego, and M. C. Carrion, "Fourth-order cumulant-based algorithms for non-minimum phase MA system identification," in *Proc. 9th Eur. Signal Process. Conf. (EUSIPCO)*, Rhodes, Greece, Sep. 1998, pp. 1–4.

[12] J. M. Mendel, "Tutorial on higher-order statistics (spectra) in signal processing and system theory: Theoretical results and some applications," *Proc. IEEE*, vol. 79, no. 3, pp. 278–305, Mar. 1991.

[13] C. L. Nikias and J. M. Mendel, "Signal processing with higher-order spectra," *IEEE Signal Process. Mag.*, vol. 10, no. 3, pp. 10–37, Jul. 1993.

[14] Y. Li and Z. Ding, "ARMA system identification based on second-order cyclostationarity," *IEEE Trans. Signal Process.*, vol. 42, no. 12, pp. 3483–3494, Dec. 1994.

[15] M. K. Hasan, N. M. Hossain, and P. A. Naylor, "Autocorrelation model-based identification method for ARMA systems in noise," *IEE Proc.-Vision, Image Signal Process.*, vol. 152, no. 5, pp. 520–526, Oct. 2005.

[16] S. Ouyang, "Bi-iterative least squares algorithms for blind channel identification and equalization with second-order statistics," *Sci. China Ser. F, Inf. Sci.*, vol. 52, no. 10, pp. 1905–1914, Oct. 2009.

[17] G. B. Giannakis, "Cumulants: A powerful tool in signal processing," *Proc. IEEE*, vol. 75, no. 9, pp. 1333–1334, Sep. 1987.

[18] K. Abderrahim, H. Mathlouthi, and F. Msahli, "New approaches to finite impulse response systems identification using higher-order statistics," *IET Signal Process.*, vol. 4, no. 5, pp. 488–501, Oct. 2010.

[19] K. Abederrahim, H. Mathlouthi, and F. Msahli, "FIR system identification using higher-order statistics," in *Proc. Amer. Control Conf.*, St. Louis, MO, USA, pp. 5598–5603, Jun. 2009.

[20] A. K. Nandi, "Blind identification of FIR systems using third order cumulants," *Signal Process.*, vol. 39, nos. 1–2, pp. 131–147, Sep. 1994.

[21] W. Jian-hua, and L. Ze-Min, "A simple closed form solution for FIR system identification using higher order st atistics," in *Proc. TENCON IEEE Region Int. Conf. Comput., Commun. Automat.*, Beijing, China, Oct. 1993, pp. 591–593.

[22] A. Swami and J. M. Mendel, "Closed-form recursive estimation of MA coefficients using autocorrelations and third-order cumulants," *IEEE Trans. Acoust., Speech Signal Process.*, vol. 37, no. 11, pp. 1794–1795, Nov. 1989.

[23] J. K. Tugnait, "Approaches of FIR system identification with noisy data using higher order statistics," *IEEE Trans. Acoust., Speech, Signal Process.*, vol. 38, no. 7, pp. 1307–1317, Jul. 1990.

[24] J. A. R. Fonollosa and J. Vidal, "System identification using a linear combination of cumulant slices," *IEEE Trans. Signal Process.*, vol. 41, no. 7, pp. 2405–2412, Jul. 1993.

[25] L. Srinivas and K. V. S. Hari, "FIR system identification using higher order cumulants-a generalized approach," *IEEE Trans. Signal Process.*, vol. 43, no. 12, pp. 3061–3064, Dec. 1995.

[26] K.-S. Lii and M. Rosenblatt, "Deconvolution and estimation of transfer function phase and coefficients for nonGaussian linear processes," *Ann. Statist.*, vol. 10, no. 4, pp. 1195–1208, Dec. 1982.

[27] J. Tugnait, "Identification of linear stochastic systems via second-and fourth-order cumulant matching," *IEEE Trans. Inf. Theory*, vol. 33, no. 3, pp. 393–407, May 1987.

This article has been accepted for inclusion in a future issue of this journal. Content is final as presented, with the exception of pagination.

[28] Y. Dai, Y. Wei, J. Chen, Y. Zhang, and J. Ding, "Seismic wavelet estimation based on adaptive chaotic embedded particle swarm optimization algorithm," in *Proc. 5th Int. Symp. Comput. Intell. Des.*, Oct. 2012, pp. 57–60.
[29] M. Zidane, S. Safi, M. Sabri, and A. Boumezzough, "Comparative study between blind identification algorithms and least mean square algorithm for non minimum phase channel," in *Proc. Int. Conf. Multimedia Comput. Syst. (ICMCS)*, Marrakech, Morocco, Apr. 2014, pp. 191–196.
[30] J. Lebrun and P. Comon, "A linear algebra approach to systems of polynomial equations with application to digital communications," in *Proc. IEEE 12th Eur. conf. Signal Process.*, Sep. 2004, pp. 213–216.
[31] O. Grellier, P. Comon, B. Mourrain, and P. Trebuchet, "Analytical blind channel identification," *IEEE Trans. Signal Process.*, vol. 50, no. 9, pp. 2196–2207, Sep. 2002.
[32] M. Zidane, S. Safi, M. Sabri, and A. Boumezzough, "Higher order statistics for identification of minimum phase channels," *World Acad. Sci., Eng. Technol. Int. J. Math. Comput. Sci.*, vol. 8, no. 5, pp. 831–836, Jun. 2014.
[33] D. R. Brillinger and M. Rosenblatt, *Computation and Interpretation of k-th Order Spectra*. Hoboken, NJ, USA: Wiley 1967, pp. 189–232.
[34] B. Buchberger, "Gröbner bases: A short introduction for systems theorists," *Pro. Comput. Aided Syst. Theory - EUROCAST*, 2001, pp. 1–19.
[35] D. Cox, J. Little, and D. O'shea, *Ideals, Varieties, and Algorithms*. New York, NY, USA: Springer, 1992.
[36] W. W. Adams and P. Loustaunau, "An introduction to Grbner bases," *Amer. Math. Soc.*, to be published.
[37] T. Matsumoto, M. Takata, and S. Moro, "Reachability analyses in Petri nets by groebner bases," *Proc. 41st SICE Annu. Conf.*, vol. 2, Aug. 2002, pp. 841–846.
[38] J. Ning, W. Gao, G. Radman, and J. Liu, "The application of the Groebner basis technique in power flow study," in *Proc. 41st North Amer. Power Symp.*, Oct. 2009, pp. 1–7.
[39] D. R. Velis, and T. J. Ulrych, "Simulated annealing wavelet estimation via fourth-order cumulant matching," *Geophysics*, vol. 61, no. 6, pp. 1939–1948, Nov. 1996.
[40] A. Ziolkowski, "Determination of the signature of a dynamite source using source scaling, Part 1: Theory," *Geophysics*, vol. 58, no. 8, pp. 1074–1182, Aug. 1993.
[41] Z. J. Jiang, X. J. Qiu, H. W. Chen, J. Lin and Z. B. Chen, "Reflection extraction with wavelet package transform in Vibroseis mineral deposit exploration," in *Proc. Mineral Deposit Res., Meeting Global Challenge*, Berlin, Germany, Aug. 2005, pp. 1465–1468.
[42] R. D. Miller, S. E. Pullan, D. W. Steeples, and J. A. Hunter, "Field comparison of shallow seismic sources near Chino, California," *Geophysics*, vol. 57, no. 5, pp. 693–709, May 1992.
[43] D. N. Steer, L. D. Brown, J. H. Knapp and D. J. Baird, "Comparison of explosive and vibroseis source energy penetration during COCORP deep seismic reflection profiling in the Williston Basin," *Geophysics*, vol. 61, no. 1, pp. 211–221, Jan. 1996.
[44] D. Woodward, "Contributions to a shallow aquifer study by reprocessed seismic sections from petroleum exploration surveys, eastern Abu Dhabi, United Arab Emirates," *J. Appl. Geophys.*, vol. 31, nos. 1–4, pp. 271–289, May 1994.
[45] D. W. Steeples and R. D. Miller, "Seismic Reflection Methods Applied to Engineering, Environmental, and Groundwater Problems," in *Proc. Geotech. Environ. Geophys., Volume I, Rev. Tutorial*, Jan. 1990, pp. 1–30.
[46] S. E. Pullan and H. A. MacAulay, "An in-hole shotgun source for engineering seismic surveys," *Geophysics*, vol. 52, no. 7, pp. 985–996, Jul. 1987.
[47] P. Jongerius and K. Helbig, "Onshore high-resolution seismic profiling applied to sedimentology," *Geophysics*, vol. 53, no. 10, pp. 1276–1283, Oct. 1988.
[48] C. Wright, J. A. Wright, and J. Hall, "Seismic reflection techniques for base metal exploration in eastern Canada: examples from Buchans, Newfoundland," *J. Appl. Geophys.*, vol. 32, nos. 2–3, pp. 105–116, Aug. 1994.
[49] J. Gao, B. Zhang, W. Han, J. Peng, and Z. Xu, "A new approach for extracting the amplitude spectrum of the seismic wavelet from the seismic traces," *Inverse Problems*, vol. 33, no. 8, Jun. 2017, Art. no. 085005.
[50] Z. Wang, B. Zhang, and J. Gao, "The residual phase estimation of a seismic wavelet using a Rényi divergence-based criterion," *J. Appl. Geophys.*, vol. 106, pp. 96–105, Jul. 2014.
[51] S. Wang, S. Yuan, M. Ma, R. Zhang, and C. Luo, "Wavelet phase estimation using ant colony optimization algorithm," *J. Appl. Geophysics*, vol. 122, pp. 159–166, Nov. 2015.
[52] A. F. M. Hani, M. S. Younis, and M. F. M. Halim, "A HOS-based blind deconvolution algorithm for the improvement of time resolution of mixed phase low SNR seismic data," *J. Geophys. Eng.*, vol. 6, no. 1, p. 87, Feb. 2009.
[53] X.-D. Zhang and Y.-S. Zhang, "FIR system identification using higher order statistics alone," *IEEE Trans. Signal Process.*, vol. 42, no. 10, pp. 2854–2858, Oct. 1994.
[54] S. Safi, M. Frikel, A. Zeroual, and M. M'Saad, "Higher Order Cumulants for Identification and Equalization of Multicarrier Spreading Spectrum Systems," in *Proc. J. Telecommun. Inf. Technol.*, 2011. pp. 74–84.
[55] W. A. Mousa and A. A. Al-Shuhail, "Processing of seismic reflection data using MATLAB," *Synth. Lectures Signal Process.*, vol. 5, no. 1, pp. 1–97, Sep. 2011.
[56] P. Deng, Y. Chen, Y. Zhang, and H.-W. Zhou, "Weighted stacking of seismic avo data using hybrid AB semblance and local similarity," *J. Geophys. Eng.*, vol. 13, no. 2, p. 152, 2016.

Karthikeyan Elumalai (S'18) received the B.E. degree in electronics and communication engineering and the M.E degree in communication system from Anna University, Chennai, India, in 2007 and 2009, respectively. He is currently pursuing the Ph.D. degree with the Department of Electrical Engineering, IIT Delhi, New Delhi, India.

Brejesh Lall (M'05) received the B.E. and M.E. degrees in electronics and communications from Delhi Technological University, New Delhi, India, in 1991 and 1993, respectively, and the Ph.D. degree in signal processing from IIT Delhi, New Delhi, in 1997.

He is currently a Professor with the Department of Electrical Engineering, Bharti School of Telecommunication Technology and Management, IIT Delhi. His research interests include computer vision, stochastic processing, and video communications systems.

R. K. Patney (M'00–SM'01) received the B.Tech. degree in electrical engineering from IIT Kanpur, Kanpur, India, in 1969, and the M.Tech. degree in electronics/electrical communication engineering and the Ph.D. degree in digital signal processing from IIT Delhi, New Delhi, India, in 1971 and 1979, respectively.

Since 1979, he has been with IIT Delhi, where he is currently a Professor with the Electrical Engineering Department. His research interests include signal processing and related areas.

International Journal of Research in Engineering and Innovation (IJREI)
journal home page: http://www.ijrei.com
ISSN (Online): 2456-6934

Exergy destruction computation in three stages cascade vapour compression refrigeration systems for low temperature applications

R.S. Mishra

Department of Mechanical and Production Industrial and Automobiles Engineering, Delhi Technological University, Delhi, India

Abstract

Cascade refrigeration systems work with two or more cycles in serial and can obtain internal temperatures below -80°C, necessary to several activities in medicine and scientific research. The main objective of this paper is to present a thermodynamic analysis of three stages vapour compression cascade refrigeration system with the use of HFO refrigerants in the high temperature cycle and HFO and HFC refrigerants in intermediate (medium temperature cycle and HFC refrigerants & hydrocarbon fluids in the low temperature cycle. The energy and exergy analysis for three stages cascade vapour compression refrigeration systems were carried out for two different conditions (i) temperature 103ºC and (ii) 95ºC and thermodynamic model based on the law of conservation of mass, on the first and second laws of Thermodynamics was developed. The numerical computed results of developed model were compared to validate results obtained from developed models using R12 in the high temperature circuit and R22 in intermediate (medium)at -60ºC temperature circuit and R13 in the low temperature circuit at -90ºCand found that our model validates results with the variation in overall first law efficiency of cascade system (1.67 % (higher) $COP_{Overall}$) , total electrical power required to run whole system (i.e. running three compressors) in terms of 1.667% (lower) exergy of fuel, 10.96% (higher) circuit high temperature cycle first law efficiency (COP_{HTC}) , 1.27% (lower) intermediate circuit (Medium) temperature cycle first law efficiency (COP_{ITC}) and 0.615% (higher) Low temperature circuit first law efficiency (COP_{LTC}) .The Detailed comparison of two different conditions have been predicted for twenty four cascade three stages vapour compression refrigeration systems using various ecofriendly refrigerants for low temperature applications and important conclusions were drawn. © 2019 ijrei.com. All rights reserved

Keywords: Ecofriendly refrigerants, Exergy Destruction Computations, Cascade Vapour Compression Refrigeration Systems

1. Introduction

Biomedical preservation requires storing biological specimens like stem cells, sperm, blood and organs, at a storage temperature of around -90ºC. For long-term storage of biological materials, temperatures below -100ºC are generally considered to safeguard against the effects of devitrification and Crystallization. The use of a single-cycle vapour compression refrigeration system can only achieve effective cooling of about -40ºC, and the efficiency begins to deteriorate under -35ºC due to the vast difference between the evaporating and condensing temperatures.

2. Cascade refrigeration system

Cascade refrigeration systems contained minimum two or more refrigeration cycles that work individualistically. The three refrigeration cycles are connected by a cascade heat exchanger where heat is released in the condenser low-temperature circuit and it is absorbed from the evaporator high-temperature circuit). Therefore, the desired refrigeration effect occurs in the evaporator low-temperature, and rejection of heat from the cycle as a whole takes place in the high temperature condenser. In these three cascade refrigeration systems in which the same refrigerant passes through the stages of high and low temperature, extreme values of pressure and specific volume can cause problems. In fact, when the evaporation temperature is too low, the specific volume of refrigerant vapor in the compressor suction is high, which implies a high volumetric capacity compressor. The important aspect of the three cascade system is that the refrigerant in three stages can be selected so as to present reasonable pressures in the evaporator and the condenser in three temperature intervals. In a three stages cascade vapour compression system, a

Corresponding author: Prof. R.S. Mishra
Email Address: hod.mechanical.rsm@dtu.ac.in

refrigerant to be selected for each of the cycle has a relationship between the saturation pressure and temperature that permits refrigeration at a relatively low temperature without excessively low pressure in the evaporator. The refrigerant cycle B and C must have characteristics of saturation that allows condensation to the desired temperature in the absence of excessively high pressures in the condenser. The two stage cascade refrigeration systems consist of at least two refrigeration systems that work independently. The two refrigeration systems are connected by a cascade heat exchanger where heat is released in the condenser low temperature circuit (LTC) using HFO-1234yf up to -53ºC and is absorbed from the evaporator high-temperature circuit (HTC) using HFO-1234ze up to -30ºC. While by using two stage cascade refrigeration one can reach minimum temperature of -70ºC to -80ºC using hydrocarbons and HFC refrigerants. Bhattacharyya et al. [3] studied a carbon dioxide–propane (R744–R290) optimum cascade evaporating system to define an evaporating temperature of R744 for application in heating circuits.

3. Concept of Exergy

Exergy is the maximum theoretical work that can be obtained from a global system, as it comes into equilibrium with the environment (reaches the dead state). Thus, if the pressure and temperature are equal to room temperature, this is the dead state, with no longer able to generate work. Therefore, exergy is a property that measures the availability of a system, which is generally largely destroyed because of the irreversible nature of thermodynamic processes. However, the exergy not only can be destroyed by irreversibilities, but can also be transferred to others systems. The exergy transferred from one system to its surroundings and which is not used usually represents a loss for better utilization of energy resources by reducing the exergy destruction within a system and / or reducing exergy losses in terms of exergy destruction ratio based on exergy of fuel/input known as rational exergy destruction ratio or reducing exergy losses in terms of exergy destruction ratio based on exergy of product known as exergy destruction ratio of the system [1] H.M. Getu and P.K. Bansal [2] carried out Thermodynamic analysis of an R744–R717 cascade Refrigeration system, and found that an increase in condensing temperature resulted in a decrease in first law efficiency (COP) and an increase in refrigerant mass flow ratios. Similarly the increase in evaporating temperature increased COP of the system and decreased mass flow ratios. An increase in temperature difference in cascade condenser reduced both COP and mass flow ratios. Kilicarslan [4] experimentally inspected the effects of the refrigeration load and water mass flow rate on the performance of cascade and single stage refrigeration systems both using R134a and compared the COP, work of compression, discharge pressure and refrigerant mass flow rate of the cascade system with those of the single stage refrigeration system.

4. Refrigerant fluids used in the cascade refrigeration systems

Since the establishment of the Montreal Protocol, the refrigeration engineering has required substitutes for CFCs and HCFCs refrigerants. The use of hydrocarbons (HCs) as refrigerants in some applications of refrigeration and air conditioning has been an effective alternative. Compared with CFCs, hydro-choro-fluocarbons (HCFCs) and hydrofluorocarbons (HFCs), hydrocarbons refrigerants offer zero Ozone Depletion Potential (ODP) and extremely low Global Warming Potential (GWP). In regard the performances, they offer in general use for high efficiency, reduces charge sizes, good miscibility with mineral oils, lower compressor discharge temperatures, and slightly better heat transfer within heat exchangers.

5. Use of hydrocarbons in cascade refrigeration systems

Several Hydrocarbons are used in the vapour compression refrigeration system which includes (i) isobutene (R600a) is the maximum commonly used refrigerant. Even in the Europe, the R600a (isobutene) is used in household refrigerators, with a market share of more than 95% in the many European countries. Propane (R290) and propylene (R1270) are also used in the heat pump systems, and have also been used in air conditioners in commercial refrigeration systems (Palm, 2008). Ethylene (R-1150) is one of the greatest important raw materials in the petrochemical industry which is also used in the synthesis of a series of products such as: ethylene oxide, ethylene glycol, ethyl alcohol, and polyethylene, polystyrene. These fluids are HFCs, are not inflammable and have low toxicity were used in the cascade refrigeration systems. The cascade systems still uses refrigerant fluids with high GWP, such as R-508B and R-404a which has low thermodynamic performances.

6. Applicability of several refrigerants in cascade refrigeration systems

In vapour compression cascade refrigeration systems, several refrigerants (such as R-717, R152a, R134a, R-12, R22, R410a, R407c, R-404A, HFO-1234yf, R1234ze etc) are used from high temperature cycle and R134a, R410a, R407c, HFO-1234yf, R123, R125,R143a, R141b, R227ea, R236fa, R245fa R507a,and hydrocarbons (R-290, R600 and R600a) etc are used in the medium temperature cycle (i.e. intermediate temperature cycle) and R13, R404a, R134a, R-508B, R290, R600a, R 600,etc R-508B refrigerant fluids are used temperature below -90ºC from low temperature cycle. The global warming potential (GWP) of hydrocarbons is 3, while for R-508B it is 10350 very high, and for R-404A it is 3260 (Hansen and Haukas, 2000). Thus, R404a, R134a, and R125, R407c up to -95ºC and hydrocarbons can be substitutes also relevant for these systems, being technically feasible and can operate over a wide range of evaporation temperature up the lower limit of -170 °C

7. Results and Discussions

For validation data from developed model for R12 in high temperature circuit and R22 in intermediate circuit and R13 in low temperature circuit, the following input data have been taken from ref [5]

(i) Condenser temperature of High Temperature circuit 40^0C.
(ii) Evaporator temperature of High Temperature circuit -22^0C.
(iii) Condenser temperature of High Temperature circuit -12^0C.
(iv) Evaporator temperature of Intermediate Temperature circuit -60^0C.
(v) Condenser temperature of High Temperature circuit -22^0C.
(vi) Evaporator temperature of Intermediate Temperature circuit -90^0C.
(vii) Compressor efficiency of HTC circuit=100%.
(viii) Compressor efficiency of ITC circuit=100%.
(ix) Compressor efficiency of LTC circuit=100%.
(x) Temperature overlapping of Condenser Temperature $_{ITC}$-Evaporator Temperature $_{HTC}$) and = 10.
(xi) Temperature overlapping of Condenser Temperature $_{LTC}$-Evaporator Temperature_$_{ITC}$) = 10.
(xii) Load on LTC evaporator=(50*3.5) kW

Table 1: Validation of data for three stages cascade vapour compression refrigeration system

Parameters	Ref [5]	Model	% variation
COP_CASCADE	0.858	0.8723	1.667% (higher)
EXERGY_FUEL (kW)	204.0	200.6	1.667% (lower)
COP_HTC (i.e.COP_R12)	2.72	3.018	10.956%(higher)
COP_ITC (i.e.COP_R22)	3.7	3.653	1.2703% (lower)
COP_LTC (i.e.COP_R13)	3.74	3.763	0.615% (higher)

Case-1: Vapour compression cascade refrigeration system using R1234ze in HTC (High temperature circuit) and R1234yf in Intermediate (Medium) temperature circuit and Following refrigerants in low temperature circuit below -100°C.

System-1: Vapour compression cascade refrigeration system using R1234ze in HTC (High temperature circuit) and R1234yf in Intermediate (Medium) temperature circuit and HFC-134a refrigerant in low temperature circuit.

System-2: Vapour compression cascade refrigeration system using R1234ze in HTC (High temperature circuit) and R1234yf in Intermediate (Medium) temperature circuit and HFC-404a refrigerant in low temperature circuit.

System-3: Vapour compression cascade refrigeration system using R1234ze in HTC (High temperature circuit) and R1234yf in Intermediate (Medium) temperature circuit and R-236fa refrigerant in low temperature circuit.

System-4: Vapour compression cascade refrigeration system using R1234ze in HTC (High temperature circuit) and R1234yf in Intermediate (Medium) temperature circuit and R-141b refrigerant in low temperature circuit.

System-5: Vapour compression cascade refrigeration system using R1234ze in HTC (High temperature circuit) and R1234yf in Intermediate (Medium) temperature circuit and R-32 refrigerant in low temperature circuit.

System-6: Vapour compression cascade refrigeration system using R1234yf in HTC (High temperature circuit) and R134a in Intermediate (Medium) temperature circuit and R-32 refrigerant in low temperature circuit.

System-7: Vapour compression cascade refrigeration system using R1234yf in HTC (High temperature circuit) and R134a in Intermediate (Medium) temperature circuit and HFC-404a refrigerant in low temperature circuit.

System-8: Vapour compression cascade refrigeration system using R1234yf in HTC (High temperature circuit) and R134a in Intermediate (Medium) temperature circuit and R-236fa refrigerant in low temperature circuit.

System-9: Vapour compression cascade refrigeration system using R1234yf in HTC (High temperature circuit) and R134a in Intermediate (Medium) temperature circuit and R-141b refrigerant in low temperature circuit.

System-10: Vapour compression cascade refrigeration system using R1234yf in HTC (High temperature circuit) and R134a in Intermediate (Medium) temperature circuit and R-143a refrigerant in low temperature circuit.

System-11: Vapour compression cascade refrigeration system using R1234yf in HTC (High temperature circuit) and R134a in Intermediate (Medium) temperature circuit and R-290 refrigerant in low temperature circuit.

System-12: Vapour compression cascade refrigeration system using R1234yf in HTC (High temperature circuit) and R134a in Intermediate (Medium) temperature circuit and R-600a refrigerant in low temperature circuit.

The following input data have been taken for computation of thermal performances of following cascade systems.

(i) Condenser temperature of High Temperature circuit (°C)= 50.
(ii) Evaporator temperature of High Temperature circuit (°C)= 0
(iii) Evaporator temperature of Intermediate Temperature

circuit (ºC)= -50.
(iv) Evaporator temperature of Intermediate Temperature Circuit(ºC)= -103
(v) Compressor efficiency of HTC circuit=0.8.
(vi) Compressor efficiency of ITC circuit=0.8.
(vii) Compressor efficiency of LTC circuit=0.8.
(viii) Temperature overlapping=zero, 5, 10, 15.
(ix) Load on LTC evaporator=35 kW

Table-2(a) and Table-2(b) shows the comparison of various thermodynamic performance parameters for twelve cascade systems. It is found that first law efficiency of system-1 to system-5 containing HFO-1234ze in high temperature circuit is higher than system-6 to system-12 containing HFO-1234yf in HTC circuit.

Table 2(a): Variation of First law efficiencies of various cascade vapour compression refrigeration systems using HFO-1234ze in HTC and HFO-1234yf in ITC and other ecofriendly refrigerants in the low temperature circuit.

Various systems	$COP_{Overall}$	COP_{HTC}	COP_{ITC}	COP_{LTC}
System-1	0.6106	3.215	2.844	2.047
System-2	0.6001	3.215	2.844	1.981
System-3	0.6142	3.215	2.844	2.07
System-4	0.6198	3.215	2.844	2.105
System-5	0.6081	3.215	2.844	2.105

Table 2(b): Variation of First law efficiencies of various cascade vapour compression refrigeration systems using HFO-1234yf in HTC and HFC-134a in ITC and other ecofriendly refrigerants in the low temperature circuit.

Various systems	$COP_{Overall}$	COP_{HTC}	COP_{ITC}	COP_{LTC}
System-6	0.6026	3.215	2.844	2.068
System-7	0.6062	3.215	2.844	2.092
System-8	0.5983	3.215	2.844	2.04
System-9	0.5973	3.215	2.844	2.033
System-10	0.5844	3.215	2.844	1.952
System-11	0.5701	3.215	2.844	1865
System-12	0.5805	3.215	2.844	1.864

It is also found that cyclic first law efficiency of low temperature circuit changes due to different ecofriendly refrigerants flowing in the low temperature circuit. It does not affect high temperature and intermediate temperature circuit first law efficiency as shown in Table-2(a) and Table-2(b) respectively. From table 2(a) and table-2(b), the first law efficiency of system-4 (cascade vapour compression refrigeration system using R1234ze in High temperature circuit (HTC)and R1234yf in Intermediate (Medium) temperature circuit (ITC) and R-141b refrigerant in low temperature circuit(LTC) gives highest coefficient of performance ($COP_{_Overall_Cascade\ _System}$) which is also higher than system-1: cascade vapour compression refrigeration system using R1234ze in High temperature circuit (HTC)and R1234yf in Intermediate (Medium) temperature circuit (ITC) and HFC-134a refrigerant in low temperature circuit(LTC) and lowest first law thermodynamic performance was found for system-11 consisting of R1234yf in High temperature circuit (HTC)and R134a in the Intermediate (Medium) temperature circuit (ITC) and R-290 refrigerant in low temperature circuit(LTC). It is also found that system-12 consisting of R1234yf in High temperature circuit (HTC) and R134a in the Intermediate (Medium) temperature circuit (ITC) and R-600a refrigerant in low temperature circuit (LTC is higher first law performance than system11 consisting of R1234yf in High temperature circuit (HTC) and R134a in the Intermediate (Medium) temperature circuit (ITC) and R-290 refrigerant in low temperature circuit (LTC).

Table-3(a) and Table-3(b) shows the comparison of various thermodynamic performance parameters for twelve cascade systems. It is found that exergetic efficiency of system-1 to system-5 containing HFO-1234ze in high temperature circuit is higher than the exergetic efficiency of system-6 to system-12 containing HFO-1234yf in HTC circuit. Similarly Exergy destruction ratio of cascade system and rational exergy destruction ratio of system-1 to system 5 is lower than system 6 to system -12 as shown in Table-3(b).

Table 3(a): Variation of Exergetic law efficiencies and exergy destruction variation of various cascade vapour compression refrigeration systems using HFO-1234ze in HTC and HFO-1234yf in ITC and other ecofriendly refrigerants in the low temperature circuit.

Various systems	$COP_{Overall}$	Exergetic Efficiency	Rational $EDR_{Cascade}$	$EDR_{cascade}$
System1	0.6106	0.3443	0.6557	1.904
System2	0.6001	0.3357	0.6643	1.917
System3	0.6142	0.3544	0.6456	1.970
System4	0.6198	0.3377	0.6623	1.821
System5	0.6081	0.3564	0.6436	1.805

Table 3(b): Variation of Exergetic law efficiencies and exergy destruction variation of various cascade vapour compression refrigeration systems using HFO-1234yf in HTC and HFC-134a in ITC and other ecofriendly refrigerants in the low temperature circuit.

Various systems	$COP_{Overall}$	Exergetic Efficiency	Rational $EDR_{Cascade}$	$EDR_{cascade}$
System6	0.6026	0.3333	0.6667	2.001
System7	0.6062	0.3323	0.6677	2.009
System8	0.5983	0.3522	0.6478	1.839
System9	0.5973	0.3391	0.6609	1.949
System10	0.5844	0.3425	0.6575	1.920
System11	0.5701	0.3409	0.6591	1.934
System12	0.5805	0.3589	0.6411	1.787

Table-4(a) and Table-4(b) shows the variation of various thermodynamic performance parameters for twelve cascade systems. It is found that the second law efficiency of system-1 to system-5 containing HFO-1234ze in high temperature circuit is higher than the second law efficiency of system-6 to system-12 containing HFO-1234yf in HTC circuit. Similarly Exergy destruction ratio of cascade system and rational exergy destruction ratio of system-1 to system 5 is lower than system 6 to system -12 as shown in Table-4(b).

Table 4(a): Variation of second law efficiencies and exergy destruction variation with system of various systems

Various systems	$COP_{Overall}$	Second law efficiency	Rational EDR	EDR_{System}
System-1	0.6106	0.4598	0.5402	1.175
System-2	0.6001	0.4518	0.5482	1.213
System-3	0.6142	0.4625	0.5375	1.162
System-4	0.6198	0.4665	0.5335	1.143
System-5	0.6081	0.4579	0.5421	1.184

Table 4(b): Variation of second law efficiencies and exergy destruction variation with system of various systems

Various systems	$COP_{Overall}$	Second law efficiency	Rational EDR	EDR_{System}
System-6	0.6026	0.4537	0.5463	1.204
System-7	0.6062	0.4564	0.5434	1.191
System-8	0.5983	0.4504	0.5496	1.22
System-9	0.5973	0.4497	0.5503	1.224
System-10	0.5844	0.440	0.560	2.001
System-11	0.5701	0.4293	0.5707	1.329
System-12	0.5805	0.4371	0.5623	1.288

Table 5(a): Percentage variation of exergy losses in various temperature circuit of three stages cascade refrigeration systems

Various systems	$COP_{Overall}$	% Exergy Destruction in HTC	% Exergy Destruction in ITC	% Exergy Destruction in LTC
System-1	0.6106	20.47.	17.28	27.82
System-2	0.6001	20.17	17.03	29.23
System-3	0.6142	19.94	16.83	29.56
System-4	0.6198	20.88	17.62	26.05
System-5	0.6081	22.66	16.23	25.89

Table-5(a)and Table-5(b) shows the variation of exergy destruction in HTC circuit (%) ,and exergy destruction in ITC circuit(%) and exergy destruction in LTC circuit(%) for all twelve cascade systems and it is found that Exergy Destruction in HTC (%) of system-1 to system-5 containing HFO-1234ze in high temperature circuit is lower than the second law efficiency of system-6 to system-12 containing HFO-1234yf in HTC circuit. Similarly Exergy destruction in ITC (%) of system-1 to system 5 of cascade system is higher than system-6 to 11 but less than system-12 due to variation of refrigerating properties of low temperature circuit refrigerant. The exergy destruction in low temperature circuit (%) of system-1 to system 5 is slightly less than system 6 to system -12 as shown in Table-5(b).

Table 5(b): Percentage variation of exergy losses in various temperature circuit of three stages cascade refrigeration systems

Various systems	$COP_{Overall}$	% Exergy Destruction in HTC	% Exergy Destruction in ITC	% Exergy Destruction in LTC
System-6	0.6026	22.16	15.88	27.71
System-7	0.6062	21.97	15.74	28.20
System-8	0.5983	22.04	15.79	28.26
System-9	0.5973	21.62	15.49	29.66
System10	0.5844	21.98	15.75	28.95
System11	0.5701	23.88	17.11	23.37
System12	0.5805	22.02	18.58	23.05

Table 6 (a): Percentage variation of various systems using energy-exergy concept

Various systems	% (Total) Exergy Destruction in Condensers	% (Total) Exergy Destruction in compressors	% (Total) Exergy Destruction in Valves	% (Total) Exergy Destruction in Evaporators
System-1	27.9543	14.87	13.08	9.1857
System-2	27.391	15.0	13.31	9.839
System-3	28.4024	14.94	13.37	9.2276
System-4	27.5077	14.82	12.6	9.6623
System-5	27.112	14.72	13.03	9.70782

Table 6 (b): Percentage variation of various systems using energy-exergy concept

Various systems	% (Total) Exergy Destruction in Condensers	% (Total) Exergy Destruction in compressors	% (Total) Exergy Destruction in Valves	% (Total) Exergy Destruction in Evaporators
System-6	27.557	14.8	13.77	9.4234
System-7	27.6852	14.8	13.75	9.49477
System-8	27.50	14.84	14.11	9.4486
System-9	27.90	14.87	14.43	9.268
System10	27.02	14.95	14.51	9.7099
System11	24.9244	15.01	14.0	10.2156
System12	26.994	14.82	12.6	10.176

The cumulative sum of exergy destruction in all three compressors, cumulative sum of exergy destruction in all three condensers, cumulative sum of exergy destruction in all three expansion valves and cumulative sum of exergy destruction in all three evaporators are shown in Table-6(a) and Table-6(b) respectively. The Exergy Destruction (%) of all three condensers (of system-1 to system-5 containing HFO-1234ze in high temperature circuit) is slightly higher than the Total exergy destruction in all condensers (of system-6 to system-12 containing HFO-1234yf in HTC circuit). Similarly The Exergy Destruction (%) of all three compressors (of system-1 to system-5 containing HFO-1234ze in high temperature circuit) is similar with small variations (slightly higher) than the Total exergy destruction in all compressors (of system-6 to system-12 containing HFO-1234yf in HTC circuit).

The Exergy Destruction (%) of all three expansion valves (of system-1 to system-5 containing HFO-1234ze in high temperature circuit) is similar with small variations (slightly higher) than the total exergy destruction in all three expansion valves (of system-6 to system-12 containing HFO-1234yf in HTC circuit). The Exergy Destruction (%) of all three evaporators (of system-1 to system-5 containing HFO-1234ze in high temperature circuit) is similar with small variations (slightly higher) than the total exergy destruction in all three evaporators (of system-6 to system-12 containing HFO-1234yf in HTC circuit). The all three compressors are running on 80% of isentropic compressor efficiency, therefore exergy destruction have been computed by considering 80% of compressor efficiencies. It is found that maximum exergy destruction (%) based on the exergy of input occurred in the condenser and lowest were found in the evaporators. The

exergy destruction in the compressors are higher than expansion valves due to expansions valves have international irreversibilities occurred but less than sum of all condensers in the systems.

Case-2: Vapour compression cascade refrigeration system using R1234ze in HTC (High temperature circuit) and R1234yf in Intermediate (Medium) temperature circuit and ecofriendly Refrigerants in low temperature circuit.

The input data have been taken for computation of thermal performances of following cascade systems.

System-13: Vapour compression cascade refrigeration system using R1234ze in HTC (High temperature circuit) and R1234yf in Intermediate (Medium) temperature circuit and HFC-134a refrigerant in low temperature circuit.

System-14: Vapour compression cascade refrigeration system using R1234ze in HTC (High temperature circuit) and R1234yf in Intermediate (Medium) temperature circuit and HFC-404a refrigerant in low temperature circuit.

System-15: Vapour compression cascade refrigeration system using R1234ze in HTC (High temperature circuit) and R1234yf in Intermediate (Medium) temperature circuit and R-236fa refrigerant in low temperature circuit.

System-16: Vapour compression cascade refrigeration system using R1234ze in HTC (High temperature circuit) and R1234yf in Intermediate (Medium) temperature circuit and R-141b refrigerant in low temperature circuit.

System-17: Vapour compression cascade refrigeration system using R1234ze in HTC (High temperature circuit) and R1234yf in Intermediate (Medium) temperature circuit and R-32 refrigerant in low temperature circuit.

System-18: Vapour compression cascade refrigeration system using R1234ze in HTC (High temperature circuit) and R1234yf in Intermediate (Medium) temperature circuit and R-123 refrigerant in low temperature circuit.

System-19: Vapour compression cascade refrigeration system using R1234ze in HTC (High temperature circuit) and R1234yf in Intermediate (Medium) temperature circuit and HFC-143a refrigerant in low temperature circuit.

System-20: Vapour compression cascade refrigeration system using R1234ze in HTC (High temperature circuit) and R1234yf in Intermediate (Medium) temperature circuit and R-227ea refrigerant in low temperature circuit.

System-21: Vapour compression cascade refrigeration system using R1234ze in HTC (High temperature circuit) and R1234yf in Intermediate (Medium) temperature circuit and R-245fa refrigerant in low temperature circuit.

System-22: Vapour compression cascade refrigeration system using R1234ze in HTC (High temperature circuit) and R1234yf in Intermediate (Medium) temperature circuit and R-410a refrigerant in low temperature circuit.

System-23: Vapour compression cascade refrigeration system using R1234ze in HTC (High temperature circuit) and R1234yf in Intermediate (Medium) temperature circuit and R-125 refrigerant in low temperature circuit.

System-24: Vapour compression cascade refrigeration system using R1234yf in HTC (High temperature circuit) and R1234yf in Intermediate (Medium) temperature circuit and R-407c refrigerant in low temperature circuit.
For computation of thermal performances, the following input data have been taken of for cascade system-13 to cascade system-24.

(i) Condenser temperature of High Temperature circuit (^oC)= 50
(ii) Evaporator temperature of High Temperature circuit (^oC)= 0.
(iii) Evaporator temperature of Intermediate Temperature circuit (^oC)= -50.
(iv) Evaporator temperature of Intermediate Temperature Circuit (^oC)= -95
(v) Compressor efficiency of HTC circuit=0.8
(vi) Compressor efficiency of ITC circuit=0.8
(vii) Compressor efficiency of LTC circuit=0.8

Table-7 shows the comparison of various thermodynamic performance parameters such as first law efficiency of whole cascade three stages vapour compression refrigeration systems using HFO-1234ze in high temperature cycle and HFO-1234yf in Intermediate temperature and following ecofriendly refrigerants in the low temperature cycle for twelve cascade systems. It is found that first law efficiency of system-16 (containing HFO-1234ze in high temperature cycle and HFO-1234yf in intermediate (medium) temperature and R-141b in low temperature circuit is higher than system-24 containing HFO-1234ze in high temperature cycle and HFO-1234yf in Intermediate temperature and HFC-407c in LTC circuit. Similarly Low temperature cycle first law efficiency (COP_{LTC}) using HFC-407c is also found and also no effect on COP_HTC and COP_ITC were observed. Table-8 shows the variation of various thermodynamic performance parameters for twelve cascade systems. It is found that the second law efficiency of system-17 containing HFO-1234ze in high temperature circuit and HFO-1234yf in ITC circuit is higher and R32in LTC than the system-24 containingR407c in low temperature circuit. . Similarly Exergy destruction ratio of cascade system and rational exergy destruction ratio of system-24 is higher than system 17.

Table 7: Variation of First law efficiencies of various systems

Various systems	$COP_{Overall}$	COP_{HTC}	COP_{ITC}	COP_{LTC}
System-13	0.6759	3.027	2.844	2.639
System-14	0.6646	3.027	2.844	2.546
System-15	0.6784	3.027	2.844	2.660
System-16	0.6833	3.027	2.844	2.703
System-17	0.6524	3.027	2.844	2.448
System-18	0.6770	3.027	2.844	2.649
System-19	0.6747	3.027	2.844	2.629
System-20	0.6717	3.027	2.844	2.604
System-21	0.6767	3.027	2.844	2.663
System-22	0.6731	3.027	2.844	2.615
System-23	0.6739	3.027	2.844	2.623
System-24	0.5833	3.027	2.844	1.963

Table 8: Variation of second law efficiencies and exergy destruction variation with system of various systems

Various systems	$COP_{Overall}$	Exergetic Efficiency	Rational $EDR_{Cascade}$	$EDR_{cascade}$
System13	0.6759	0.3307	0.6693	2.024
System14	0.6646	0.3239	0.6761	2.087
System15	0.6784	0.3255	0.6745	2.072
System16	0.6833	0.3377	0.6623	1.961
System17	0.6524	0.3404	0.6596	1.938
System18	0.6770	0.3329	0.6671	2.004
System19	0.6747	0.3285	0.6715	2.044
System20	0.6717	0.3208	0.6792	2.118
System21	0.6767	0.3302	0.6698	2.028
System22	0.6731	0.3367	0.6633	1.970
System23	0.6739	0.3236	0.6764	2.091
System24	0.5833	0.3046	0.6954	2.284

Table-8 shows the comparison of exergetic efficiency (performance parameter) for twelve cascade systems. It is found that exergetic efficiency of system-17 containing HFO-1234ze in high temperature circuit and HFO-1234yf in intermediate temperature circuit and R-32 in low temperature circuit containing is higher than the exergetic efficiency of system-24 (containing HFO-1234ze in HTC circuit HFO-1234yf in ITC circuit and R-407c in low temperature circuit). Similarly Exergy destruction ratio of cascade system and rational exergy destruction ratio of system-24 is higher than system 16 containing HFO-1234ze in high temperature circuit and HFO-1234yf in intermediate temperature circuit and R141b in low temperature circuit. Similarly Exergy destruction ratio of cascade system and rational exergy destruction ratio of system-17 is lower than system 24.

Table 9: Percentage variation of exergy losses in various temperature circuit of three stages cascade refrigeration systems

Various systems	$COP_{Overall}$	% Exergy Destruction in HTC	% Exergy Destruction in ITC	% Exergy Destruction in LTC
System13	0.6759	22.54	17.17	22.27
System14	0.6646	22.3	16.99	28.32
System15	0.6784	22.13	16.86	28.45
System16	0.6833	22.86	17.42	25.95
System17	0.6524	23.69	18.05	24.22
System18	0.6770	22.66	17.26	26.79
System19	0.6747	22.41	17.07	27.67
System20	0.6717	21.94	16.71	29.27
System21	0.6767	22.45	17.1	27.43
System22	0.6731	23.0	17.52	25.81
System23	0.6739	22.09	16.82	28.73
System24	0.5833	22.72	17.31	29.52

Table-9 shows the variation of exergy destruction in HTC circuit (%) ,and exergy destruction in ITC circuit(%) and exergy destruction in LTC circuit(%) for all twelve cascade systems and it is found that Exergy Destruction in HTC (%) of system-1 containing HFO-1234ze in high temperature circuit and HFO-1234yf in intermediate (medium) temperature circuit and R125 in low temperature circuit is higher than the % % Exergy Destruction in HTC of system-22 containing HFO-1234ze in high temperature circuit and HFO-1234yf in intermediate (medium) temperature circuit and HFO-227ea in LTC circuit.

Table-10: Percentage variation of exergy destruction of various components in the three stages cascade vapour compression refrigeration systems

Various systems	% Exergy Destruction in Condensers	% (Total) Exergy Destruction in compressors	% (Total) Exergy Destruction in Valves	% (Total) Exergy Destruction in Evaporators
System13	27.94	14.57	13.10	10.66
System14	27.61	14.7	13.22	10.98
System15	28.50	14.66	13.29	10.40
System16	27.82	14.52	12.45	10.82
System17	26.39	14.68	13.12	11.13
System18	27.94	14.58	12.92	10.66
System19	28.14	14.63	13.24	10.54
System20	28.60	14.76	13.71	10.28
System21	28.09	14.57	13.05	10.60
System22	27.57	14.60	12.76	10.79
System23	28.34	14.67	13.55	10.43
System24	20.18	15.0	12.37	16.29

Table-10 shows Exergy Destruction (%) of all three compressors (of system-12 to system-24 and it is found that the system-20 containing HFO-1234ze in high temperature circuit and HFO-1234yf in ITC circuit and R227ea in low temperature is higher condenser exergy destruction (%) than the system-14 containing HFO-1234ze in high temperature circuit and HFO-1234yf in ITC circuit and R407c in low temperature circuit. The all three compressors are running on 80% of isentropic compressor efficiency, therefore exergy destruction have been computed by considering 80% of compressor efficiencies. It is found that maximum exergy destruction (%) based on the exergy of input occurred in the condenser and lowest were found in the evaporators. The exergy destruction in the compressors are higher than expansion valves due to expansions valves have international irreversibility occurred but less than sum of all condensers in the systems

The Exergy Destruction (%) of all three expansion valves (of system-1 containing HFO-1234ze in high temperature circuit and HFO-1234yf in ITC circuit) and R227ea is higher than the system-24 containing HFO-1234ze in high temperature circuit and HFO-1234yf in ITC circuit) and R-407c. The Exergy Destruction (%) of all three compressors (of system-16 containing HFO-1234ze in high temperature circuit and HFO-1234yf in intermediate (Medium) temperature circuit and R141b in lower temperature circuit is lower than system-24 containing HFO-1234ze in high temperature circuit and HFO-1234yf in intermediate (Medium) temperature circuit and R407c in lower temperature circuit. The Exergy Destruction (%) of all three evaporators (of system-20 containing HFO-1234ze in high temperature circuit and HFO-1234yf in intermediate (Medium) temperature circuit and R227ea in lower temperature circuit is lower than system-24 containing HFO-1234ze in high temperature circuit and HFO-1234yf in intermediate (Medium) temperature circuit and R407c in lower temperature circuit.

8. Conclusions

The following conclusions were made from present investigation

- The thermal performance of three stage cascade refrigeration system using HFO-1234ze in HTC and HFO-1234yf in ITC and HFC-134a in LTC gives better thermodynamic performance.
- The numerical computed results of developed model were compared to validate results obtained from developed models using R12 in the high temperature circuit and R22 in intermediate (medium)at -60^{o}C temperature circuit and R13 in the low temperature circuit at -90^{o}C and found that our model validates results well in terms of 1.67 % (higher) first law efficiency of cascade refrigeration system and 1.667% (lower) total power required to run the whole cascade systems (containing all three running compressors) , 10.96% (higher) circuit high temperature cycle first law efficiency ($COP_{_HTC}$) , 1.27% (lower) intermediate circuit (Medium) temperature cycle first law efficiency ($COP_{_ITC}$) and 0.615% (higher) Low temperature circuit first law efficiency ($COP_{_LTC}$).
- The developed thermal model predicts thermodynamic performance parameters for all twenty four systems.
- Exergetic efficiency of system-17 (containing HFO-1234ze in high temperature circuit and HFO-1234yf in intermediate temperature circuit and R-32 in low temperature circuit) is higher than the exergetic efficiency of system-24 (containing HFO-1234ze in HTC circuit HFO-1234yf in ITC circuit and R-407c in low temperature circuit.
- The Exergy Destruction (%) of all three evaporators of all cascade refrigeration systems are lower and highest exergy destruction is found in the condensers.
- The Exergy Destruction (%) of all three compressors is higher than Exergy Destruction (%) of all three expansion valves in the all cascade systems
- The Exergy Destruction (%) of all three expansion valves (of system-1 containing HFO-1234ze in high temperature circuit and HFO-1234yf in ITC circuit) and R227ea is higher than the system-24 (containing HFO-1234ze in high temperature circuit and HFO-1234yf in ITC circuit) and R-407cin lower temperature circuit.
- The Exergy Destruction (%) of all three condensers (of system-16 containing HFO-1234ze in high temperature circuit and HFO-1234yf in intermediate (Medium) temperature circuit and R141b in lower temperature circuit is lower than system-24 containing HFO-1234ze in high temperature circuit and HFO-1234yf in intermediate (Medium) temperature circuit and R407c in lower temperature circuit
- The Exergy Destruction (%) of all three compressors of system-20 (containing HFO-1234ze in high temperature circuit and HFO-1234yf in ITC circuit and R227ea in low temperature) is higher exergy destruction (%) than the system-24 containing HFO-1234ze in high temperature circuit and HFO-1234yf in ITC circuit and R407c in low temperature circuit.
- The Exergy Destruction (%) of all three evaporators (of system-20 containing HFO-1234ze in high temperature circuit and HFO-1234yf in intermediate (Medium) temperature circuit and R227ea in lower temperature circuit is lower than system-24 containing HFO-1234ze in high temperature circuit and HFO-1234yf in intermediate (Medium) temperature circuit and R407c in lower temperature circuit

References

[1] Ahamed J.U, Saidur R, Masjuki H, A review on exergy analysis of vapor compression refrigeration system, Renewable and Sustainable Energy Reviews, 15, 2011, 1593–1600

[2] Getu, H.M. and Bansal, P.K., 2008. “Thermodynamic analysis of an R744–R717 cascade refrigeration system”. International Journal of Refrigeration, Vol. 31(1), p. 45-54.

[3] Souvik Bhattacharyya S, Bose J, Sarkar, Exergy maximization of cascade refrigeration cycles and its numerical verification for a transcritical CO2-C3H8 system, 30, 2007, 624 – 632.

[4] Kilicarslan A, Hosoz M, Energy and Irreversibility analysis of a cascade refrigeration system for various refrigerant couples, Energy Conversion and Management, 51, 2010, 2947-2954.

[5] Domkundwar , [2010]Refrigeration and air conditioning . Dhanpat Rai & sons , Delhi-11002.

Cite this article as: R.S. Mishra, Exergy destruction computation in three stages cascade vapour compression refrigeration systems for low temperature applications, International Journal of Research in Engineering and Innovation Vol-3, Issue-3 (2019), 187-194.

AIP Conference Proceedings

First-principles study on electronic, mechanical and thermoelectric transport properties of topological insulator NaAuS

Cite as: AIP Conference Proceedings **2093**, 020016 (2019); https://doi.org/10.1063/1.5097085
Published Online: 15 April 2019

Nisha, Hardev S. Saini, Manish K. Kashyap, Jyoti Thakur, and Mukhtiyar Singh

View Online

Export Citation

ARTICLES YOU MAY BE INTERESTED IN

Structural, electronic and magnetic properties of Ti-doped MgSe diluted magnetic semiconductor compound
AIP Conference Proceedings **2093**, 020001 (2019); https://doi.org/10.1063/1.5097070

Modifications in optical parameters of PVA by embedded Au-Ag core-shell nanoparticles
AIP Conference Proceedings **2093**, 020006 (2019); https://doi.org/10.1063/1.5097075

A theoretical modeling of the Cu(In, Ga)Se_2 solar cell
AIP Conference Proceedings **2093**, 020018 (2019); https://doi.org/10.1063/1.5097087

© 2019 Author(s).

First-Principles Study on Electronic, Mechanical and Thermoelectric Transport Properties of Topological Insulator NaAuS

Nisha[1], Hardev S.Saini[1, a)] Manish K. Kashyap[2], Jyoti Thakur[3] and Mukhtiyar Singh[4]

[1]*Department of Physics, Guru Jambheshwar University of Science & Technology, Hisar-125001, Haryana (India)*
[2]*Department of Physics, Kurukshetra University Kurukshetra, Kurukshetra-136119, Haryana (India)*
[3]*Department of Physics & Astrophysics, University of Delhi - 110007, Delhi (India)*
[4]*Department of Applied Physics, Delhi Technological University, Delhi - 110042, Delhi (India)*

[a)]hardevdft@gmail.com

Abstract. We have investigated the mechanical, electronic and thermoelectric transport properties of material using density functional theory. Our calculated results predict that NaAuS is elastically and thermodynamically stable material. We have calculated band gap of 0.15eV for this material using PBE functional including spin-orbit coupling (SOC). Band inversion at gamma point indicates about the topological behavior of material. The calculated value of power factor and Seebeck Coefficient is 8.874×10^{11} W/msK^2 and 140.42 μV/K, respectively; at T=1000K. Lattice thermal conductivity which plays a significant role in thermoelectric efficiency of a material, is found to be 5.62 W/mK at T=300K. The lattice thermal conductivity of this material decreases with increase in temperature. The figure of merit (ZT) comes out to be 0.79 at T=1000K, thus this material can act as good thermoelectric material.

INTRODUCTION

In the present era of large scale of industrial growth and excessive exploitation of natural resources, the demand for sustainable and clean energy sources increases, and this forces us to look for alternate energy resources and also to take necessary steps for reducing the energy consumption. Therefore, we need such materials which may act smartly in response to the external fields and fulfill our needs. Thermoelectric (TE) materials are able to convert the heat to electricity and vice-versa [1]. The performance of TE materials is characterized by the dimensionless figure of merit (ZT):

$$ZT = \frac{\sigma S^2 T}{k_e + k_l} \quad (1)$$

where S, σ, T, k_e and k_l are Seebeck coefficient, electrical conductivity, absolute temperature, electronic and lattice part of thermal conductivity, respectively. $S^2\sigma$ is called as power factor (PF). To attain high ZT value, we require large value of PF and low value of thermal conductivity. But improving ZT is quite challenging as it is a combination of conflicting physical quantities [2].

There are large numbers of materials such as half-Heusler alloys, clathrates, perovskites, and telluride based materials etc. [3] which have been investigated in search of good thermoelectric response; among them the most widely used TE materials are newly discovered Topological Insulator (TI) which have ZT>1. The TIs are characterized by full insulating gap and gapless edge states which are topologically protected against backscattering at non-magnetic impurities and defects.

By reviewing the literature, we found that Lin et al. [4] predicted that NaAuS compound to be topological insulator by showing band inversion at gamma point. Sihi et. al. [5] studied the effect of different exchange correlation functionals on the structural and electronic properties of NaAuS compound. In this paper, we report the

Proceedings of the National Conference on Recent Advances in Condensed Matter Physics
AIP Conf. Proc. 2093, 020016-1–020016-4; https://doi.org/10.1063/1.5097085
Published by AIP Publishing. 978-0-7354-1823-3/$30.00

electronic, mechanical and thermoelectric properties of NaAuS compound, and planned to find out the figure of merit which is very useful to predict the efficiency of thermoelectric materials.

METHODOLOGY

We have calculated the structural, electronic and thermoelectric properties based on the full-potential linearized augmented plane wave (FPLAPW) method as implemented in WIEN2k [6]. The NaAuS crystallizes in cubic phase having spacegroup F-43m (216) with Na presented at 4c (½,½,½), Au at 4b (¼,¼,¼) and S at 4a (0,0,0) Wyckoff positions. We have used cut off energy = -6.0 Ry, $R_{MT}K_{max}$=7 and 6000 k-points in full Brillouin zone (FBZ) to create 18×18×18 k-mesh. BoltzTraP code is used for the calculation of transport properties which is based on semi-classical Boltzmann transport theory within the constant relaxation time approximation. Denser mesh (41×41×41) of k-points is used for calculating TE transport properties. The calculation was performed including spin-orbit coupling (SOC). IRelast method as implemented in WIEN2k was used for the calculations of elastic constants and these elastic constants were furtther used for the calculation of mechanical properties. For the calculation of Debye temperature we have used GIBBS code.

RESULTS AND DISCUSSION

Electronic and Elastic properties:The lattice parameters and bulk modulus are calculated by computing the total energy for different volumes based on Murnaghan's equation of state. The data shown in Table I is the output of volume optimization. This compound also satisfies the 18-electron rule [7] such that it is non-magnetic and semiconducting in nature.

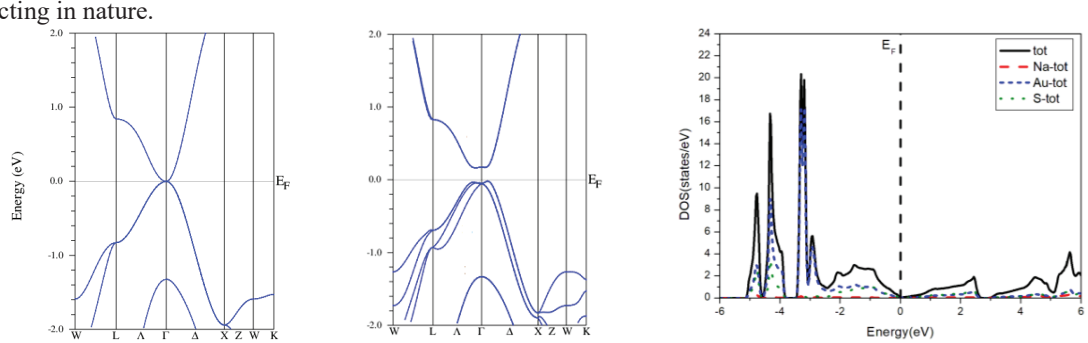

(a) (b) (c)

FIGURE 1:(a) Band-structure of NaAuS using PBE-GGA potential (b) Band-structure of NaAuS using PBE-GGA+SOC (c) DOS plot of NaAuS using PBE-GGA+SOC

We have also calculated the elastic properties to check the mechanical stability of our compound. The elastic constants (including C_{11}, $C_{12}$and C_{44}), Bulk modulus (B), Shear modulus (G), and other properties are listed in Table II. The necessary and sufficient conditions of stability of the material are checked by using Born-Huang stability criteria [8] as mentioned below:

$$C_{11}-C_{12}>0,\ C_{11}>0,\ C_{44}>0 \text{ and } C_{11}+2C_{12}>0 \quad (2)$$

Our calculated elastic constants indicate that our compound is elastically stable.

Pugh's ratio is defined as the ratio of bulk and shear modulus which is greater than 1.75 [9] which means the material is ductile in nature. The calculated value of Frantsevich's ratio (G/B) is less than 1.06, indicating about low resistance against shear deformation.

TABLE I. Calculated lattice parametera (A^o), bulk modulus (B) and its pressure derivative ($B^{'}$) of NaAuS compound

Compound	Our Result a (A^o) B (GPa) $B^{'}$	Available Theoretical/expt. Data a (A^o) B (GPa) $B^{'}$	References
NaAuS	6.34 50.80 5.2705	6.30 - -	[4] theoretical

The energy band structures and DOS of NaAuS using PBE and PBE+SOC is shown in Fig.1. As shown in fig. 1(a), the top of the valence band (VBM) and bottom of conduction band (CBM) touch each other at gamma point in

absence of SOC at Fermi level (E_F). In the presence of SOC, the widening of band gap is observed due to the movement of VBM and CBM away from E_F as shown in Fig. 1(b). The negative value of band inversion strength gives indication about topological non-trivial behavior of NaAuS compounds. The value of band gap using PBE+SOC calculation is 0.15 eV, which is in good agreement with available theoretical data [4] which is 0.19 eV. The total density of states (TDOS) of NaAuS compound along with the TDOS of individual atoms is shown in the Fig. 1(c).At the vicinity of the Fermi level (E_F), the Au atom and S atom playmajor rolein both valence and conduction band, whereas the contribution of Na atom is negligible.

TABLE II: Elastic and Thermodynamic properties of NaAuS compound

Properties	Calculated Value(in GPa)	Properties	Calculated Values
C_{11}	51.284	Poisson's ratio(ϑ)	0.412
C_{12}	49.451	Pugh' Ratio(B/G)	5.3718
C_{44}	26.808	Frantsevich' Ratio(G/B)	0.186
C_{11}-C_{12}	1.838	Debye Temperature(θ_D)	255.26K
C_{11}+2C_{12}	150.186	GruneisenParameter(γ)	2.77
B(Bulk modulus)	50.060		
G(Shear modulus)	9.319		
Y(Young's modulus)	26.324		

***Thermoelectric Properties*: -** We have calculated the value of lattice thermal conductivity (K_l) using Slack [10] equations given as:-

$$K_l = \frac{AM\delta\theta_D^3}{\gamma^2 n^{2/3} T} \quad (3)$$

Here M is the average atomic weight, δ^3 is volume per atom, T is absolute temperature, n is the number of atom per unit cell and γ is Gruneisen parameter and A is the coefficient depending upon γ . We have found out the value of Grunesian parameter and coefficient A using following expression:-

$$\gamma = \frac{3(1+\vartheta)}{2(2-3\vartheta)} \quad \& \quad A(\gamma) = \frac{2.43*10^{-8}}{1-\frac{0.514}{\gamma}+\frac{0.228}{\gamma^2}} \quad (4)$$

The calculated value of 'γ' for NaAuS is 2.77 this gives indication about stronger anharmonic scattering of phonons which results low value of lattice thermal conductivity.The Debye temperature (θ_D)comes out to be 255.26K at room temperature

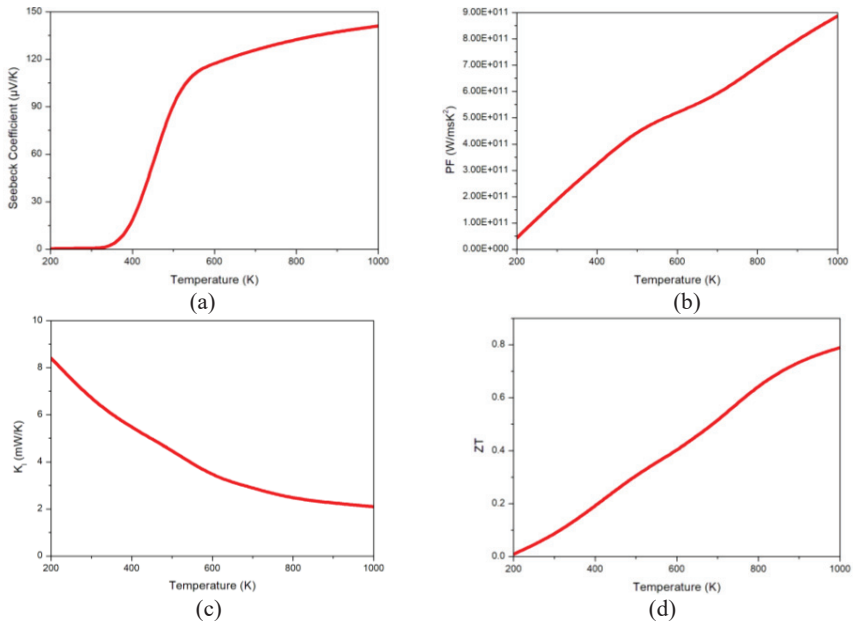

FIGURE 2: Variation of (a) Seebeck coefficient (b) Power factor (PF) (c) Lattice thermal conductivity (k_l) (d) Figure of merit (ZT) w.r.t temperature

One of the limitations of BoltzTraP is that relaxation time is not known, so we assumed its value to be 10^{-14} sec [11]. The various thermoelectric properties such as Seebeck coefficient, Power factor, lattice component of thermal conductivity and Figure of merit of NaAuS compound as a function of temperature is shown in Fig.2. Fig.2 (a) shows that the value of Seebeck coefficient increases with increase in temperature and attains maximum value 140.42 μV/K at T=1000K. Due to which, the power factor ($S^2\sigma$) reaches to a maximum value of 8.874×10^{11} W/msK^2 at T=1000K, which is beneficial for high thermoelectric performance as shown in Fig. 4 (b). The positive value of Seebeck coefficient indicates that the conduction is due to holes and predicts that our material is of p-type which is confirmed by other studies [12]. Lattice thermal conductivity decreases with increase in temperature and attains minimum value 2.40 W/mK at T=1000K. This shows the enhancement of ZT in higher temperature region. The figure of merit shows increasing trend from 200-1000K and achieves a maximum value 0.79 at T=1000K which is useful to make thermoelectric devices in higher temperature region.

CONCLUSIONS

In present work, we have studied the electronic, mechanical and thermoelectric transport properties of topological insulator NaAuS. The calculated value of lattice thermal conductivity at T=300K is 5.62W/mK, which is beneficial for high efficiency thermoelectric material. The calculated maximum value of figure of merit 0.79 and the minimum value of lattice thermal conductivity 2.34W/mK at T=1000K make NaAuS compoundas a potential thermoelectric material in higher temperature region.

ACKNOWLEDGMENTS

H. S. Saini gratefully acknowledges the support from University Grant Commission (UGC), New Delhi, INDIA for providing financial assistanceship through start up research grant under Faculty Research Promotion Schemes (FRPS) scheme (No. F. 30-364-2017 (BSR)

REFERENCES

1. M. Zebarjadi, K. Esfarjani, M.S. Dresselhaus, Z.F. Ren, G. Chen , Energy Environ. Sci.**5**, 5147- 5153 (2012).
2. Z. Fan, J. Zheng, H.Q. Wang, J.C Zheng, Enhanced thermoelectric performance in three-dimensional superlattice of topological insulator thin films, Nanoscale Res. Lett. **7,** 1931-7573, (2012)
3. H. Kleinke, Chem. Mater. **22**, 604-611, (2010).
4. Shi-Yuan Lin, Ming Chen, Xiao-Bao Yang, Yu-Jun Zhao, Physical Review B **91,** 094107-1-6, (2015).
5. AntikSihi, Sohan Lal, Sudhir K. Pandey, Cond-mat.str-el, (2017).
6. P. Blaha, K. Schwarz, G. Madsen, D. Kavinscka and J. Luitz, WIEN2k, An Augmented Plane Wave Plus Local Orbitals Program for Calculating Crystal Properties (Vienna University of Technology, Vienna, Austria),(2001).
7. I. Galanakis, P. Mavropoulos, P.H. Dederichs, J. Phys. D: Appl. Phys. **39(5),** 705-711, (2005).
8. M. Born, K. Huang, *Dynamical Theory of Crystal Lattices*, Claendron, Oxford,(1954).
9. S.F Pugh, XCII., Philos. Mag.**45**, 823-843, (1954).
10. D.T. Morelli, G.A. Slack, High Lattice Thermal Conductivity Solids, Springer, New York, USA, 37-68,(2006).
11. L. Chaput, H. Scherrer, Phys. Rev. B **75**, 045116-1-5, (2007).
12. Kulwinder Kaur, EPL (Europhysics Letters) **117,** 47002-p1-p6, (2017).

Multimedia Tools and Applications
https://doi.org/10.1007/s11042-019-7574-8

Fog removal in images using improved dark channel prior and contrast limited adaptive histogram equalization

Rajiv Kapoor[1] · Rashmi Gupta[2] · Le Hoang Son[3,4] · Raghvendra Kumar[5] · Sudan Jha[6]

Received: 8 February 2018 / Revised: 6 September 2018 / Accepted: 2 April 2019
Published online: 02 May 2019
© Springer Science+Business Media, LLC, part of Springer Nature 2019

Abstract

It is necessary to perform fog removal from an image based on the estimation of depth to increase the visibility of a scene. In this paper, we propose a new algorithm to eradicate fog from images in which fog is defined as a state or cause of perplexity or confusion with respect to the image. It runs at high speed and simultaneously minimizes the halo-artifact with a new median operator in dark channel prior. The proposed method is based on Guided Filter for transmission-map refinement and Contrast Limited Adaptive Histogram Equalization (CLAHE) for visibility improvement. It preserves small details while remaining robust against density of fog, and recovers scene contrast simultaneously. Guided filter improved the transmission map acquired from Median dark channel prior (MDCP), which is an improvement of the Dark Channel Prior DCP by the use of median operation. All of the parameters used in our method are data driven. The quality of algorithm has been validated on several types of fog-degraded images where considerable variation in contrast and illumination exists. Moreover, its performance is compared with the other state-of-the-art methods. The experimental results indicate that the proposed method effectively restores the color and contrast of scene as well as produces satisfactory information in homogeneous fog. It outperforms the existing fog removal methods for run time computational time and other evaluation metrics for rating of visibility enhancement. The proposed method conserves small details part of the image when outstanding vigorous against concentration of fog, and recuperate scene contrast instantaneously. It controls at a high speed than the existing approaches and can diminish the halo effect.

Keywords Atmospheric dichromatic model · Computer vision · Contrast limited adaptive histogram equalization · Dark channel prior · Defogging · Guided filter

✉ Le Hoang Son
sonlh@vnu.edu.vn

Extended author information available on the last page of the article

1 Introduction

Outdoor scene images may be degraded through various reasons in which the most notable source is bad weather conditions such as haze, smoke and fog [5]. The outdoor surveillance systems effect is obviously limited through fog [18]. Recently, many challenges have been encountered in computer vision and graphics communities to remove fog by using minimal inputs, i.e. a single image [13]. In outdoor environments when images are captured from optical devices, light after reflecting from an object leads to scattering of light in the atmosphere prior to reaching the camera [43]. In the presence of pollutants or atmospheric particles in the air in forms of dust, smoke, fog, rain and snow, these atmospheric particles result in two fundamental phenomena called 'direct distortion' and 'distortion contributed by atmospheric light' [33]. Direct distortion reduces the contrast and atmospheric light distortion adds whiteness in the scene which creates a problem of color ambiguity [21]. As a result, images taken under such conditions are characterized by having poor contrast and visibility [20]. Therefore, elimination of air-light and restoration of contrast is essential for outdoor vision application used for object recognition, tracking and navigation [32].

A reliable visibility restoration method requires accurate estimation of air-light and transmission map [13]. From the past few decades, several methods have been proposed to remove fog using many numbers of images. In [21, 27], the authors removed fog by taking more than two images of the same scenes (e.g. one in dense fog and another in normal fog). However in general scenarios, these strategies are not practical since weather may remain unchanged for several minutes or even hours [26]. Another class of methods is the polarization-based technique proposed by Schechner et al. [26]. The major disadvantage of this method is camera setting which captures two strictly aligned polarized images only [2]. Another disadvantage is that it requires dedicated hardware for rotating the polarizer. The relevant methods in [21, 26–28] are not able to adapt themselves to practical scenarios since only one degraded image is available as an input; thus, more flexible approaches are preferable [26]. As a summary, the main disadvantage of these multiple image restoration methods is that several images with identical scene and dissimilar weather environments are required.

Single image restorations are a difficult task [23]. Nowadays, only one degraded image is available on which various algorithms can be applied [33]. In [9], an independent-component analysis algorithm was suggested. This method is related to local statistic and requires color information and variance. It achieves good results when the image is affected by thin fog but has trouble with dense fog where color is light-sensitive and the variance is not reliable to estimate the transmission map. The method in [9] is not suitable for grayscale images and requires deep knowledge of color. In another work [16], the restored image looks over saturated and unnatural looking. A different approach proposed in [11] called the deep photo system heavily relies on 3D model where no dehazing was performed if no model on the scene is available [1, 7, 45].

A more popular method that has been explored in recent years is using the dark channel prior (DCP) [19], which is one of the most simple, elegant and effective in single image defogging. Yong et al. [42] suggested the enhancement of Contrast Limited Adaptive Histogram Equalization (CLAHE) algorithm on the basis of archive monitoring and low illumination. Yadav et al. [40] argued how a digitally filtered image can be enhanced using CLAHE algorithm in order to improve its contrast. Other works on image handling can be seen in [22, 29, 30, 35–38].To sum up, some drawbacks of the single image restoration methods are shown as follows:

- Prominence of the reinstated image is very low.
- There are some Halo artifacts on the subsequent images.
- Some of these mentioned methods are unacceptable when a scene object is akin to air light like vehicle head lights, snow-white ground, etc.
- Correct prediction of transmission map is not estimated.
- Estimation of air light is not measured accurately.
- Improvement of the contrast of an image is difficult.
- More computational time.

It has been realized that CLAHE achieves good results compared to the other algorithms. In this article, we aim to enhance this algorithm by proposed a new method that combines Guided Filter and CLAHE for visibility improvement in fog removal. Our main contributions in this research are as follows:

- The proposed work uses Guided Filter for improvement of transmission map obtained from Median dark channel prior (MDCP), which is an improvement of the DCP with the new median operation. It has few data driven parameters and constants.
- The proposed method uses Contrast-Limited Adaptive Histogram Equalization (CLAHE) for visibility improvement of fog removal. In spite of the fact that there are different strategies for enhancing the view by expelling mist; however the greater part of them obliterates the shape and appearance of foggy images prompting a misdiagnosis. Thus, in this work CLAHE is utilized for identification of mist. The difference, particularly in homogeneous zones, can be constrained to abstain from intensifying any commotion that may be available in the image. It replaces each pixel in a given image by histogram of the surrendered areas to estimate pixels. Moreover, the CLAHE calculation is a broadly utilized system which brings differentiation improvement of images. Each tile's complexity is upgraded so that the histogram of the yield locale roughly coordinates that indicated by the 'Dispersion' parameter. CLAHE works on a little locale, called tile, as opposed to the whole image. It causes no harm on symptomatic outcomes. Alternate strategies utilized for the most part are: wavelet change, un-sharp concealing, and morphological administrator.
- The proposed method will be validated on the datasets in various types of climatic images against the relevant works namely Kopf et al.; Fattal's; Tan et al.; He et according to the evaluation metrics such as VM, PNSR and AMBE. The dataset contains more than 100 images of outside scenes and for each scene there are 5 unmistakable climate conditions are rehashed.
- The proposed method preserves small details while remaining robust against density of fog, and recovers scene contrast simultaneously. It is simple but effective in removing fog from a single degraded image. The proposed method operates at a high speed than existing ones and can minimize the halo artifact.
- To the best of our knowledge, none of the existing methods work well in three major factors (Contrast, Halo effect and transmission map) of fog removal simultaneously. Thus, we believe that the proposed method will put some extra value in this research field.

This article is organized into eight sections. Section 2 showsthe related works for fog removal. Section 3 shows the basic theory of atmospheric dichromatic model to describe the formation of fog. In Sections 4 and 5, we illustrate the proposed approach and its instantiation respectively. Experimental environment and performance evaluations of the proposed method are discussed in Sections 6 and 7 respectively. Finally, Section 8 concludes the research article and delineates further studies.

2 Related work

In this section, we discuss some previous approaches about fog removal techniques and their pros and cons (See Table 1).

3 Background

In computer vision, the atmospheric dichromatic model [21] is used in description of formation of foggy images as indicated in Fig. 1:

$$\hat{X}(a,b) = X(a,b)t(a,b) + a_{ir}(1-t(a,b)). \tag{1}$$

RGB color of the fog image $\hat{X}$ at pixel position (a. b) is expressed in Eq. 2:

$$\hat{X}(a,b) = \left[\hat{X}(a,b,r), \hat{X}(a,b,g), \hat{X}(a,b,b1)\right]^T. \tag{2}$$

RGB color image without fog at pixel position (a, b) is shown in Eq. 3:

$$X(a,b) = [X(a,b,r), X(a,b,g), X(a,b,b1)]^T. \tag{3}$$

In Eq. 1, the first term X(a, b) t(a, b) is called 'direct distortion' which produces a multiplicative distortion of scene radiance and reduces the contrast. The later term $a_{ir}(1 - t(a, b))$ is called the 'local atmospheric light distortion' which produces additive effects and adds the whiteness in a scene. Intuitively, an image received by observer is the combination of the attenuated version of underlying scene radiance with an additive atmospheric light [23]. The atmosphere is assumed to be homogenous [18]. This has two simplifying consequences: the atmospheric light is constant throughout the image (which means that it has to be estimated only once), and the transmission t(a, b) follows the Beer-Lambert law in Eq.4:

$$t(a,b) = e^{-\beta d(a,b)}. \tag{4}$$

Here, β is the extinction coefficient and d(a, b) represents the distance from the observer to the scene at pixel (a, b). When we assume the atmosphere is homogenous, it restricts β to be constant. The medium transmission coefficient has a scalar value within $0 \le t(a,b) \le 1$ for each pixel which attenuates the target color. Putting value of t(a, b) in Eq. 1, we gain Eq. 5:

$$\hat{X}(a,b) = X(a,b)e^{-\beta d(a,b)} + a_{ir}\left(1-e^{-\beta d(a,b)}\right). \tag{5}$$

The main aim of fog removal is finding X(a, b) which also requires information regarding of distance (d) between the scene and camera, extinction coefficient (β) and air light (a_{ir}). Eq. 5 indicates that the distance attenuates exponentially [13]. The depth up to an unknown distance can be recovered by recovering the transmission.

The ultimate goal of 'single image fog removal' is to recover a true image X(a, b) from the observed fog-image $\hat{X}(a,b)$ which requires knowledge of three unknown parameters, β, d and a_{ir}. He et al. [11] introduced a successful algorithm of dark channel prior (DCP). Low value of

Table 1 A brief review of the related works

Method	Description	Pros	Cons
Polarization filter [26]	Air light is incompletely polarized. In this method, the input image is mixture of two unidentified mechanisms. The first one is the sight without the fog and another one is air light	Fog is detached by the polarization filter. No halo effect	Numerous images with similar scene and changed weather environments are compulsory
Dark channel prior (DCP) [11]	Some particular pixels consume small strength in any of the color channel	Single image is mandatory for haze elimination. Transmission map is evaluated correctly	Air light approximation hypothesis is required that only 0.1% positive pixels are reserved. It creates some halo effects on the resulting images
Improved dark channel prior (IDCP) [27]	Soft-matting is applied with the help of bilateral filter which smoothen the slight textures of image	Accurate estimated air light and less computation time	It creates halo effects in specific regions of the image. Transmission map is not projected correctly
IDCP using guided filter [12]	Image dehazing is completed by merging dark channel prior (DCP) and guided filter. Guided filter is an operator of preserve the edge and smoothen the image	Halo effects are detached proficiently. For the decent result, advanced transmission is applied by guided filter	It cannot be competent to develop the contrast of the image
DCP with histogram specification [41]	Recover the contrast of a recuperated image. Histogram of fog removal image has an affinity of left-shifting. Some sharpen area arises in the high concentrating region	Haze is detached from the huge contextual region and dump region of images. It enhances the contrast of fog free image	Size of the image and computation time are increased tremendously
Anisotropic diffusion method [6]	Post processing is used for the contrast enhancement which is appropriate for hazy images. The color model decreases the computation time	Estimation of air light is completed precisely. Contrast is boosted in the resulting image	Transmission map is not appraised correctly. Prominence of the reestablished image is poor
Parametric model, [24]	Hypothesis testing based on Long range transportation (LRT) detector	Compare LRT design by using the proposed one	The proposed method is hypotheticalimages re-sampled from mixed compressed and uncompressed images due to which uniformity is not maintained. It lacks of accurate model
Steganography, [39]	Steganalys is analysis was done using steganography tools	Calibration is done with features decreasing the influence of image content. It is helpful to detect stego messages hidden by Least significant bit (LSB) matching	Experimental results calculate non-adjacent pixels. Dependencies between the random pixel pairs were considered due to which the

Table 1 (continued)

Method	Description	Pros	Cons
			detection is influenced. Thus, it yields out non accurate results.
Image Retrieval Approach [4]	Standard texture databases and a color dataset show the benefits which can be drawn from the proposed retrieval approaches	Three different quantization schemes have been used. Quantization effect used in this work helps in efficient retrieval of fog	Drops in the reduction of retrieval strategy are most likely to occur. It was carried out on 3 standard texture databases including a colored dataset. This mismatches the accurate results

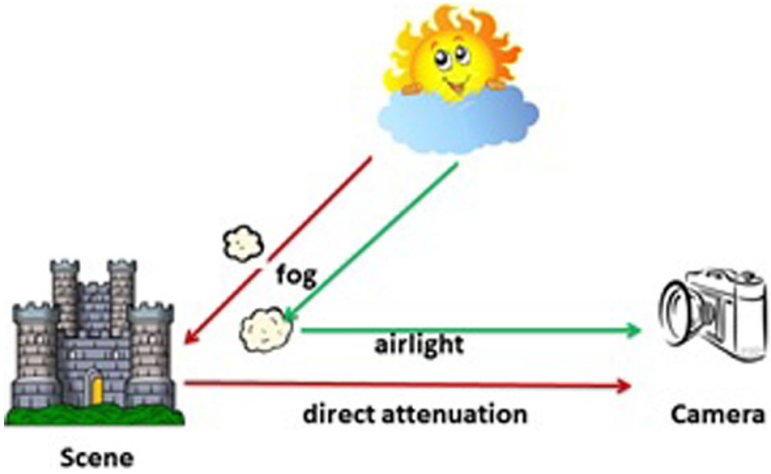

Fig. 1 The atmospheric dichromatic model

intensity is caused by lacking of color in a channel which may be due to shadows of buildings, trees and dark objects shown in Eq. 6.

$$\theta_D(a,b)=\min_{m,n\in\Omega(u,v)}\left(\min_{c\in(r,g,b)}\frac{X(a,b)^c}{a_{ir}(c)}\right). \tag{6}$$

Thus, θ_D is used as a prior to estimate the transmission-map given by Eq. 7:

$$\tilde{t_D}(a,b) = 1-w\theta_D(a,b). \tag{7}$$

The parameter $w(0 \le w \le 1)$ is introduced to prevent removing fog thoroughly and to keep the feeling of depth in a distant object as 0.95. The transmission obtained by Eq.7 is only a coarse estimation. If we try to recover X(a, b) directly from Eq. 7, the result contains severe halo-artifact. Thus, it is necessary to refine the transmission. In order to remove these artifacts, transmission–map obtained by Eq. 7 is refined by using matting Laplacian in Eq.8:

$$E(t) = t^T Lt + \lambda\left(t-\tilde{t_D}\right)^T\left(t-\tilde{t_D}\right). \tag{8}$$

The solution is found by solving for t_D from the following Eq. 9:

$$(L + \lambda U)t_D = \lambda\tilde{t_D}. \tag{9}$$

The (l,p) element of L is defined as in Eq. 10:

$$L(l,p) = \sum_{(k|l,p)\in w_k}\left(\delta_{l,p}-\frac{1}{|w_k|}\right)\left(1+(X_i-\mu_k)^T\left(\sum k+\frac{\varepsilon}{|w_k|}U_3\right)^{-1}(X_j-\mu_k)\right), \tag{10}$$

where L is the (MN × MN) Matting Laplacian matrix for an image of size (M × N), $\delta_{l,p}$ is the Kronecker delta function, μ_k and $\sum k$ are the mean and covariance of the pixel in window (w_k) centered around k, $|w_k|$ is the number of pixels in each window, ε is a small regularization parameter (10^{-3} to 10^{-4}), U is an identity matrix with the same size as (L) and λ is a small value (10^{-3} to 10^{-4}) so that t_D is softly constrained by $\tilde{t_D}$. Figure 2 indicates the result of recovered scene radiance using DCP followed by matting Laplacian. We can clearly see in Fig. 2d that the recovered de-foggy image contains some block artifact near the complicated edge structure.

In the proposed method, we conserved small details part of images when outstanding vigorous against concentration of fog, and recuperate scene contrast instantaneously. The new procedure is simple but actual in eliminating fog from a single tainted image. The proposed method controls at a high speed than existing approaches and can diminish the halo effect. Guided filter improves the transmission map acquired from Median dark channel prior

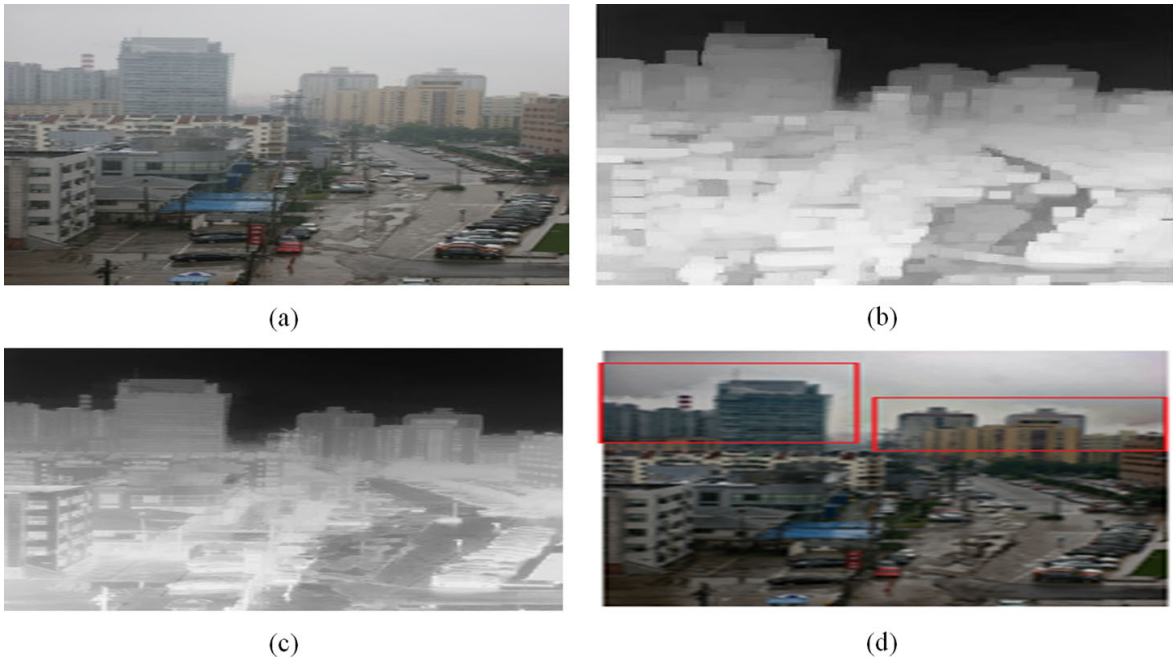

Fig. 2 Recovering the scene radiance using the transmission map refined by Matting Laplacian. **a** Original Fog Image, **b** Estimated Transmission Map from DCP, **c** Refined Transmission Map by Matting Laplacian, **d** Recovered Scene Radiance

(MDCP), which is an improvement of the Dark Channel Prior DCP by the use of median operation. All of the parameters used in our method are data driven.

4 The proposed work

4.1 Median dark-channel prior (MDCP)

We proposed a visibility restoration algorithm based on the utilization of median filtering operation. The proposed method is an improvement to the Dark Channel Prior [11] by replacing the second minimum operator in Eq. 6 with a median operator. The median operator performs a non-linear filtering operation which can effectively suppress impulsive noise components while preserving edge information in detailed areas and permitting dehazing [3, 8, 25] in smooth areas. The flow diagram of the algorithm is indicated in Fig. 3.

From a given foggy image, the atmospheric light, and transmission map are estimated. Once air light and transmission map are obtained, it is then refined by using the guided filter and scene radiance. To improve the overall contrast of an output image, CLAHE is performed as the post processing operation. The proposed median dark channel prior (MDCP) is given as Eq. 11:

$$\theta_M(a,b)=\underset{m,n\in\Omega(a,b)}{\text{med}}\left(\min_{c\in(r,g,b)}\frac{X(m,n)^c}{a_{ir}(c)}\right). \tag{11}$$

Here Ω represents a patch of size 15×15. Likewise, θ_M is then used to estimate the transmission-map given by Eq. 12:

$$\widetilde{t_M}(a,b)=1-w\theta_M(a,b). \tag{12}$$

The transmission map estimation using Eq. 12 can be used for further refinement. Despite several techniques soft matting [10], bilateral filter [14] and anisotropic diffusion [31] were

proposed to enhance the transmission map, they are computational intensive and may make the fog removal algorithm impracticable.

4.2 Transmission map refinement

The Matting Laplacian, which was used for refinement of transmission map in [11], produces visually satisfying results, but the computational cost is very high as it involves solving a large linear system. Therefore to speed up the defogging process, the transmission map obtained by Eq. 13 is refined by using the guided filter [12]. In the guided filter, kernel can be built by using a guidance image I_g and then applied to the target image $\widetilde{t_M}$ through a standard linear filtering process in the pixel domain. In general, the filtering process can be described by Eq. 14:

$$t_l = \sum_p W_{l,p}(I_g)\widetilde{t_J}, \tag{13}$$

$$W_{lp}(I_g) = \frac{1}{|w|^2}\sum_{k:(l,p)\in w_k}\left(1 + \frac{(I_l - \mu_k)(I - \mu_k)}{\sigma_k^2 + \varepsilon}\right), \tag{14}$$

where l and p are pixel indexes, t is the final result, W is the weight depending on the guidance image I_g, and $\widetilde{t_j}$ is the input image. For a color image, derivation of the guided filter relies on a linear assumption between the guidance image I_g and the refined transmission map t in Eq. 15.

$$t_l = a_k^T I_g + b_k, \forall_l \in w_k, \tag{15}$$

where t_l are the filter output, (a_k, b_k) are some linear coefficient's assumed to be constant in a window (w_k). Windows size is typically defined by their radius (r), which is the pixel distance from the center pixel to the outer pixel. Since square window are used, the total window size is therefore $(2r + 1) \times (2r + 1)$. The guided filter seeks for coefficient (a_k, b_k) that minimizes the difference between the output and input, by using following cost function in Eq. 16:

$$E(a_k, b_k) = \sum_{l\in w_k}\left(\left(a_k I_g + b_k - \tilde{t}\right) + \varepsilon a_k^2\right), \tag{16}$$

where ε is a regularization parameter to prevent a_k from being too large. The solution of Eq. 16 is found as in Eq. 17(a & b):

$$a_k = (\sum_k \varepsilon U)^{-1}\left(\frac{1}{|w|}\sum_{l\in w_k} Ig\widetilde{t_J} - \mu_k \overline{t_k}\right) \tag{17a}$$

$$b_k = \overline{t_k} - a_k^T \mu_k \tag{17b}$$

Here, μ_k and σ_k^2 are the mean and variance of I_g in a window w_k, and $|w|$ is the number of pixels in w_k. $\overline{t_k}$ is the mean of t in w_k. $\sum_k$ is the 3×3 covariance matrix of I_g in w_k and U is a 3×3 identity matrix. Since a pixel l belongs to many windows, the final output t_l is averaged over all possible windows. After computing all filter coefficients (a_k, b_k) in the image, the final output is:

$$t_l = \frac{1}{|w|}\sum_{k:(l)\in w_k}\left(a_k^T Ig + b_k\right) \tag{18}$$

Thus, the guided filter simply measures the normalized correlation between two pixels. Spatial distance is taken into account by the fact that when two pixels l and p are close together, they share more windows compared to when they are far apart.

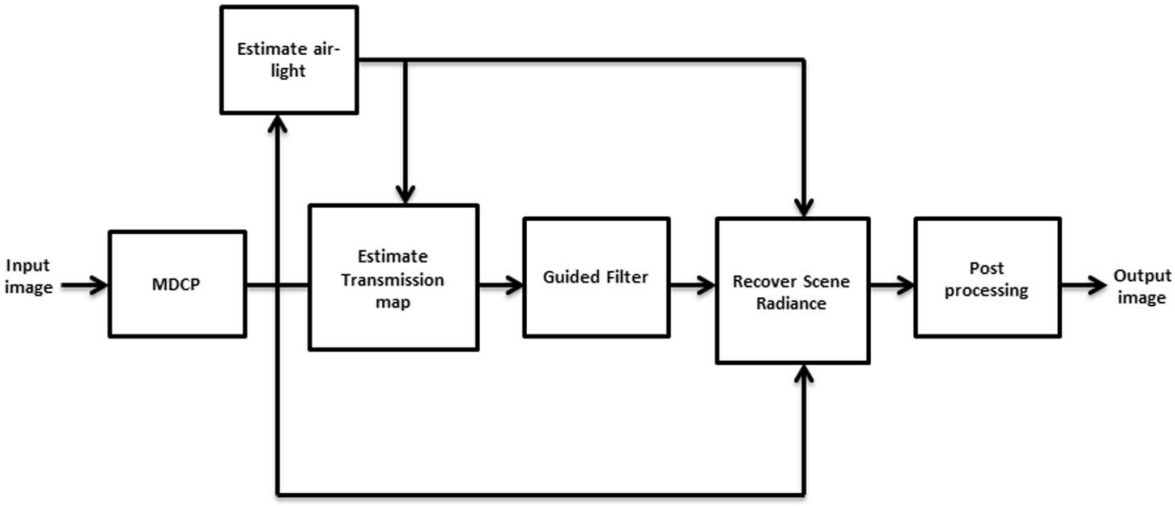

Fig. 3 Block Diagram of fog removal method

4.3 Behavior of guided filter

The input images are filtered by edge preserving smoothing filter, fast, accurate, non-iterative guided filter. The main benefit of this guided filter is that it has good behavior near edges and does not suffer from the problem of gradient-reversal artifact. Guided filter take advantages of reducing the problem of solving a large linear system of equations to a simple filtering process. It is demonstrated below.

Algorithm: Guided Filter

Input: Transmission map $(\tilde{t})$, Guidance Image (I_g) , Regularization parameter (ε).

Output: Filtered transmission map t.

Step 1: Compute:

$$\text{mean}_{I_g} = f_{\text{mean}}(I_g),$$

$$\text{mean}_{\tilde{t}} = f_{\text{mean}}(\tilde{t}),$$

$$\text{corr}_{I_g} = f_{\text{mean}}(I_g .* I_g),$$

$$\text{corr}_{I_g\tilde{t}} = f_{\text{mean}}(I_g .* \tilde{t}).$$

Step 2: Calculate:

$$\text{var}_{I_g} = \text{corr}_{I_g} - \text{mean}_{I_g} .* \text{mean}_{I_g},$$

$$\text{cov}_{I_g\tilde{t}} = \text{corr}_{I_g.\tilde{t}} - \text{mean}_{I_g} .* \text{mean}_{\tilde{t}}.$$

Step 3: Compute:

$$a = \text{cov}_{I_g\tilde{t}} ./ \text{var}_{I_g} + \varepsilon,$$

$$b = \text{mean}_{\tilde{t}} – a .* \text{mean}_{I_g}.$$

Step 4: Compute the mean values:

$$\text{mean}_a = f_{\text{mean}}(a),$$

$$\text{mean}_b = f_{\text{mean}}(b).$$

Step 5: Finally calculate the transmission map:

$$t = f_{\text{mean}}(a) .* I_g + f_{\text{mean}}(b).$$

4.4 Recovering the scene radiance

The map (t), and air light (a_{ir}) are known. The scene radiance can be estimated by using Eq. 19:

$$X(a,b) = \frac{\hat{X}(a,b) - a_{ir}}{\max(t, t_o)} + a_{ir} \tag{19}$$

Using Eq. 19, t_o is typically bounded to a low number such as 0.1 to avoid instability. Figure 4 shows the result of a recovered scene radiance using the guided filter.

4.5 Post-Processing using CLAHE

It is found that image after removal of fog loses some contrasts and appears dim. This can improve the visibility. The most common method for visibility enhancement is the histogram equalization and histogram stretching. Histogram equalization is the most well-known methodby using the gray-scale transformation. However, its major disadvantage is that it over-enhances the image and shifts mean brightness and consequently creates an unnatural look. While in histogram stretching, we have to be careful of clipping; otherwise it eliminates visual information in bright and in dark region. Therefore, instead of using the histogram equalization and histogram stretching which affect the whole image, we use the CLAHE algorithm as indicated in Fig. 5a and b.

CLAHE is a visibility enhancement algorithm which can provide optimal equalization and overcome the problem of standard histogram equalization. As proposed in [34], CLAHE divides an images into small contextual region [8 × 8], and applies the histogram equalization to each region for contrast-enhancement. It also combines neighboring blocks into an image bilinear interpolation to eliminate artificially induced boundaries. There are two parameters in CLAHE to control image quality namely block-size and clip-limit. Block-size specifies the size of contextual-region, and clip-limit is a scalar parameter in range [0,1] specifying the contrast enhancement limit and preventing over-saturation. The CLAHE method can be derived from following steps in Eq. 20:

$$N_{avg} = \frac{N_x \times N_y}{N_{Gray}}. \tag{20}$$

Based on Eq. 20, the N_{CL} can be calculated by Eq. 21:

$$N_{CL} = N_{clip} \times N_{avg}, \tag{21}$$

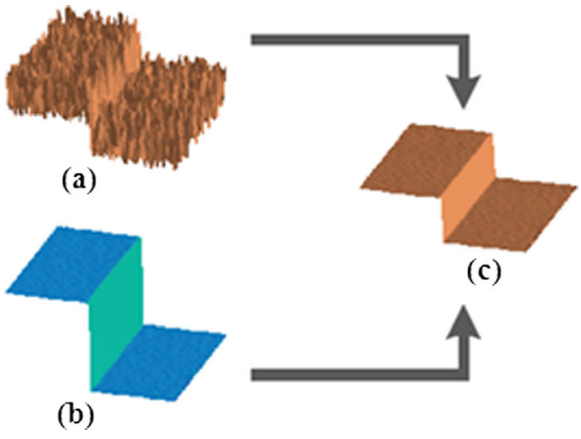

Fig. 4 Behavior of guided filter after filtering, the edges of the guide image is transferred to the filtering image: **a** Noisy Image, **b** Guidance image, **c** Image after guided filtering

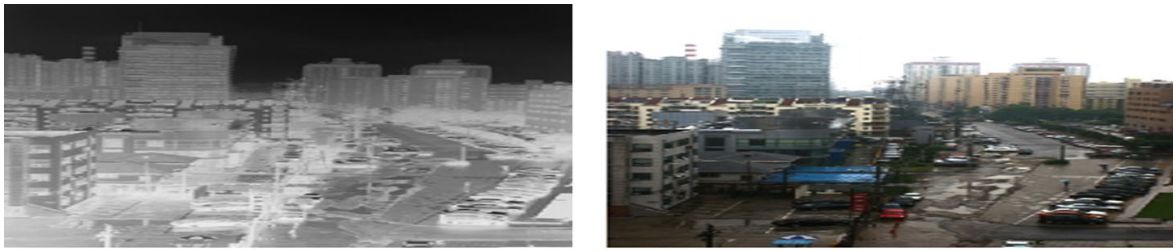

(a) (b)

Fig. 5 Recovering scene radiance using the MDCP and Guided Filter: **a** Enhanced Transmission Map by Guided Filter, **b** Restored Scene Radiance

where,

N_{avg} Average Number of Pixels.
N_x Number of pixels in X-axis.
N_y Y-axis.
N_{Gray} Number of gray levels.
N_{CL} Actual Clip-Limit.
N_{clip} Maximum multiple of average pixels in each gray level.

The original and clipped histograms are indicated in Fig. 6a. We can observe in Fig. 6b that if pixels are greater than N_{clip}then they result in clipping of the pixels. $N_{\sum clip}$ Indicates the total numbers of clipped pixels in each gray level given in Eq. 22:

$$N_{acp} = \frac{N_{\sum clip}}{N_{gray}}. \tag{22}$$

The contextual region can be calculated by using the following rules:

- *Rule 1:* If $N_x(i) > N_{CL}$, $N_x(i) = N_{CL}$
- *Rule 2*: Elseif $N_x(i) + N_{acp} \geq N_{CL}$, $N_x(i) = N_{CL}$
- *Rule 3:* Else $N_x(i) = N_x(i) + N_{ap}$

The step of distributed pixels can be calculated by using the Eq. 23:

$$S = \frac{N_{Gray}}{N_{RP}}, \tag{23}$$

where N_{RP} denotes the remaining number of clipped pixel.

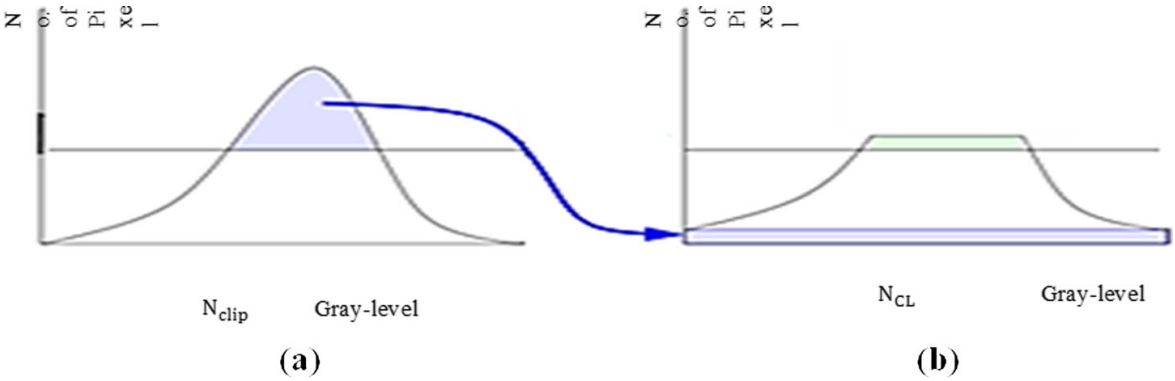

Fig. 6 Representation of the original and clipped histogram (CLAHE): **a** Original histogram **b** Clipped histogram

4.6 Description of the proposed algorithm

The algorithm is shown in Table 2 where I is the input image and I_F is the output. The time complexity of the guided filter algorithm (Steps 3 and 4) is *O (n)* where *n* is number of the pixels in the image. The time complexity of other procedures like MDCP, transmission map refinement, recovering scene radiance and CLAHE is O(1). Therefore, the total time complexity is *(O (n) + O (1)) = O (n)*.

5 Instantiation

In any case, using a clock rate comparable to pixel landing rate, the mean number of required mapping RAMs is 32. For this circumstance, when all operations are driven at the pixel passage rate, there is a prerequisite for another extra eight mapping RAM's to fill in as a pad for authentic pipe covering of all operations. The time laps between utilization of the fundamental regional mapping sequentially and the last common mapping in a comparative segment, for 512×512 pictures, is, at most, proportional to the arrival time of $7 \times 64 = 448$ pixels. Under best conditions, using a higher clock rate, the base required number of mapping RAM's is 24. The accompanying and last operation is to framework of the image, as shown by the most ideal blend of the regional mappings. For the underlying 32 sections of an image, only eight commonplace mappings are required. The final pixel mapping is planned based on the assumption that regional mappings are available for the pixel under process. Realization of this engine depends on the way that six products are

Table 2 The proposed method

Input: I is the input image
Output: I_F (Fog / haze removed image)
Algorithm:
1. Apply the Median Dark Channel Prior (MDCP) to the image I and calculate θ_M to estimate the transmission map t_M.
2. The output of MDCP t_M is converted to refined transmission map t_l using transmission map refinement.
3. Guided filtering algorithm is applied to the transmission map. The inputs of this algorithm are transmission map (tl), guidance image (I_g), regularization parameter (ε). The output is filtered transmission map t.
4. Recover the scene radiance using known parameters i.e. the filtered transmission map (t), and air light (a_{ir}).
5. Process the final image in the Post-Processing step using CLAHE for visibility enhancement.
6. Finally we get the final output as I_F (Fog removed image).

calculated. It is possible to simplify hardware realization as follows. Let η and μ be defined as

$$\eta = \frac{X}{X+Y},$$
$$\mu = \frac{S}{R+S}.$$

This mapping can be solved by using the following given equation:

$$P_{new} = \mu\left[\eta f_{i-1,j-1}(P_{old}) + (1-\eta) f_{i,j-1}(P_{old})\right] + (1-\mu)\left[\eta f_{i-1,j}(P_{old}) + (1-\eta) f_{i,j}(P_{old})\right].$$

Since the scales in the multipliers, for square districts with size of forces of two, are dyadic numbers, the multipliers may have more productive equipment usage. The quantity of time-keepers expected to finish each mapping operation relies upon how the multipliers are executed. In the event that the multipliers are likewise legitimately pipelined, with an inertness of at most 30 pixels, for every pixel entry, one-pixel mapping is finished. On account of 512 square images, the locales are of size 64 by 64 and the scaling factors are numbers separated by 64.

6 Experimental setup

This section presents an assessment of the proposed method by using MATLAB 7.0.4, 64-bit Intel Core i3–2600 processor with memory of 2GB. To compare the performance of our method, benchmark images such as foggy images namely Mountain '01', Tower '02', 'Sweden' are derived from well-known sources in Google database. The Haze RD dataset contains 15 actual outdoor scenes, and for each scene there are 5 different climate conditions are replicated. Besides, we also collected more than 50 extra images with different outdoor scene and added to the Haze RD dataset for the experiment. Thus, in this experiment we use more than 100 images for verifying the proposed method. The objective of evaluation is to check how well the images are restored by the algorithm. In order to do so, image quality metrics are necessary to assess the quality of images. Performance of the algorithms are measured in terms of Visibility Metric (VM), Absolute Mean Brightness Error (AMBE), Peak Signal to Noise Ratio (PSNR), and Run Time (t_{comp}).

6.1 Visibility metric (VM)

The visually enhancement performance is defined by visibility metric. Visibility is a measure of image quality and used to tell how well an observer can view a texture and color of image.

Table 3 Run time (seconds) comparison of the proposed method with the other methods

Method	t_{run}(mean ± SD)
Kim et al. [15]	$21.16 \pm 4.2 \times 10^{-3}$
Fattal [9]	$19.36 \pm 4.2 \times 10^{-3}$
Kopf et al. [17]	$17.48 \pm 7.2 \times 10^{-3}$
He et al. [11]	$15.42 \pm 4.2 \times 10^{-3}$
Ren et al. [25]	$16.24 \pm 5.1 \times 10^{-3}$
Berman and Avidan [3]	$15.34 \pm 5.2 \times 10^{-3}$
Fan et al. [8]	$13.38 \pm 6.2 \times 10^{-3}$
Proposed Method	$5.12 \pm 7.2 \times 10^{-3}$

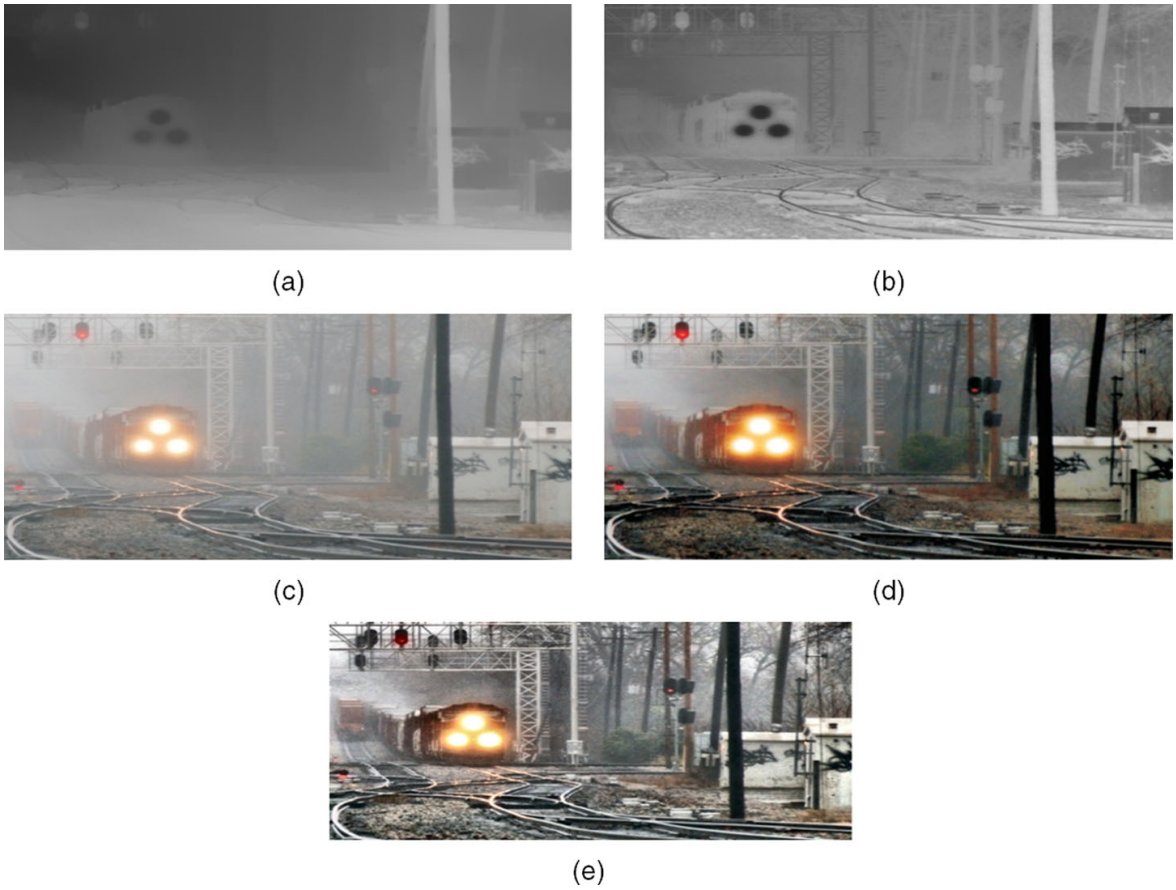

Fig. 7 Intermediate steps of proposed method: **a** Original fog image 'train' **b** Estimated Transmission map using MDCP, **c** Enhanced transmission map using Guided filter **d** Restored image **e** Final fog free image followed by post- processing

Visibility metric gives an objective measure of detail enhancement. The enhancement in contrast and edge sharpness is useful for measuring the enhancement. The visibility metric is calculated in Eqs. 24, 25, 26, 27 and 28.

$$n(l,p) = r(l,p) - e(l,p), \tag{24}$$

$$\mu_r = \frac{1}{M \times N} \sum_{i=0}^{M-1} \sum_{i=0}^{N-1} r(l.p), \tag{25}$$

$$\mu_n = \frac{1}{M \times N} \sum_{i=0}^{M-1} \sum_{j=0}^{N-1} n(l,p), \tag{26}$$

$$\sigma_n^2 = \frac{1}{(M \times N) - 1} \sum_{i=0}^{M-1} \sum_{i=0}^{N-1} (n(l,p) - \mu_n)^2, \tag{27}$$

$$VM = CNR(r,e) = \frac{\mu_r - \mu_n}{\sigma_n}. \tag{28}$$

r (l, p) and e(l, p) denote the image taken as reference and improved images (M × N), n(l,p) visibility of the image, μ_n, μ_r and σ_n^2, are mean and variance. The effectiveness is described by high value of visibility metric.

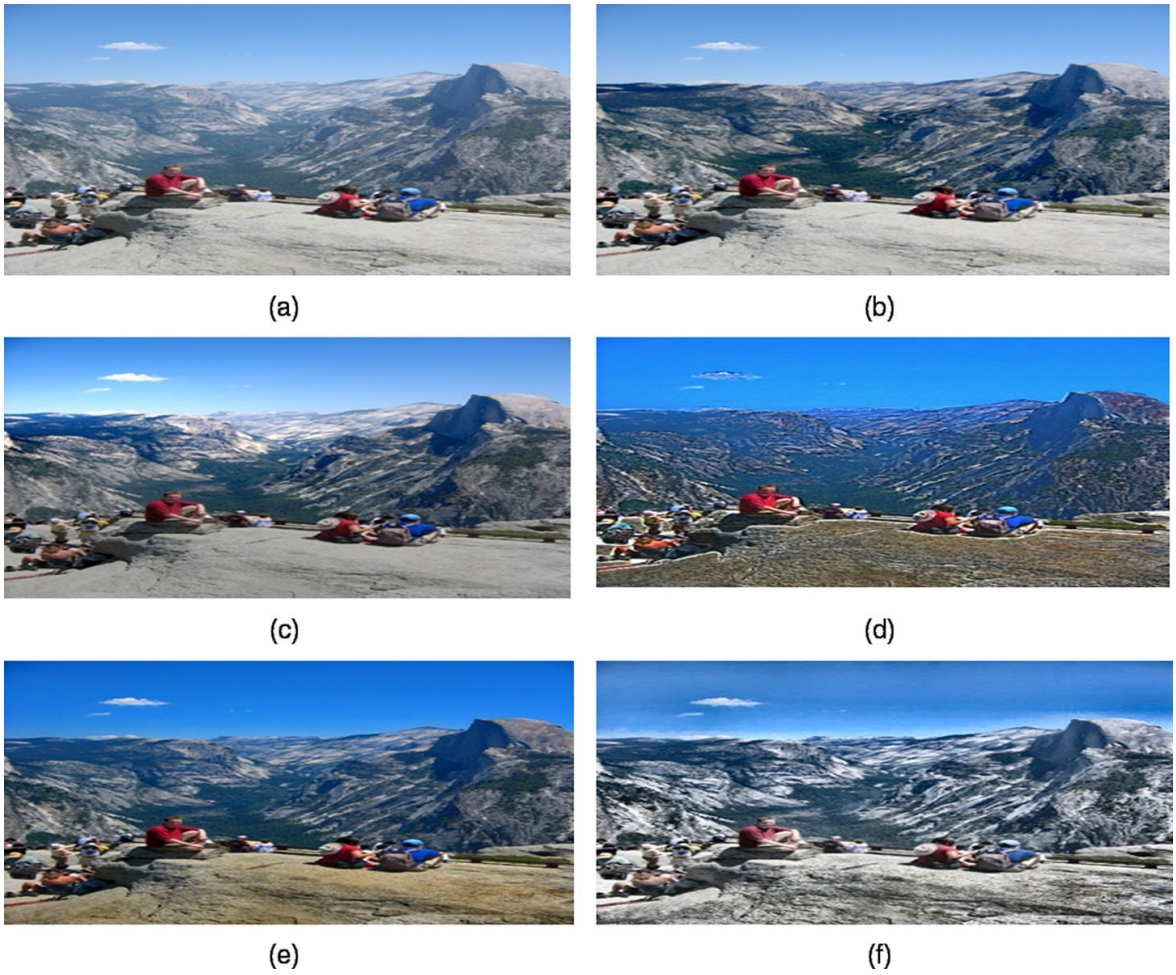

Fig. 8 Visual comparison of defogging result with recent state-of-the-art methods: **a** Original foggy image 'mountain 01' recovered by the algorithm; **b** Kopf et al.; **c** Fattal's; **d** Tan et al.; **e** He et al.; **f** The proposed algorithm

6.2 Absolute mean brightness error (AMBE)

A qualitative measure of visibility enhancement is checked in terms of AMBE. To examine how the appearance of image has changed after removal of fog, the deviation of the reference image is computed in Eq. 29.

$$\mathrm{AMBE} = |\mu_r - \mu_n|. \tag{29}$$

For better similarity between two images, the AMBE must be as small as possible.

6.3 Peak signal to noise ratio (PSNR)

There are many version of SNR, but the PSNR are simpler and widely used for fidelity measurement. PSNR, calculated in decibels units, measures the ratio of the peak signal (Eq. 30) and the Mean-Square-Error between two images. It is defined in Eq. 31:

$$\mathrm{MSE} = \frac{1}{\mathrm{M} \times \mathrm{N}} \sum_{i=0}^{M-1} \sum_{i=0}^{N-1} (r(l,p) - e(l,p))^2, \tag{30}$$

$$\mathrm{PSNR} = 10\log_{10}\left(\frac{(L-1)^2}{\mathrm{MSE}}\right), \tag{31}$$

Fig. 9 Visual comparison of defogging result with recent state-of-the-art methods: **a** Original hazy image 'tower 02' recovered by the algorithm; **b** Kopf et al.; **c** Fattal's; **d** Tan et al.; (e) He et al.; **f** The proposed algorithm

where r(l,p) denotes the original foggy image and e(l,p) denotes the enhanced fog-free image. (M × N) represents the size of image and L is dynamic range of pixel values (256 for 8-bit grayscale image).

6.4 Run time(t_{run})

Run time (t_{run}) is the period during which the computer program is executing to remove fog from image. Therefore, the efficiency of an image depends on how fast the algorithm is. For the fog removal,t_{run} is related to the size of image. For fast execution,t_{run} must be low. (Table 3).

7 Results and discussions

Firstly, intermediate steps of proposed method are illustrated in Fig. 7.

To check the effectiveness of the proposed method, we carry out simulation on various foggy images: Mountain'01′, Tower '02', 'Sweden' in Figs. 8, 9 and 10.

The Visibility Metric in comparison with other methods is shown in Table 4 in which the 2nd column represents the actual visibility of fog images whereas the restored visibility are depicted in last column of this table. We observe that actual visibility of the fog image-

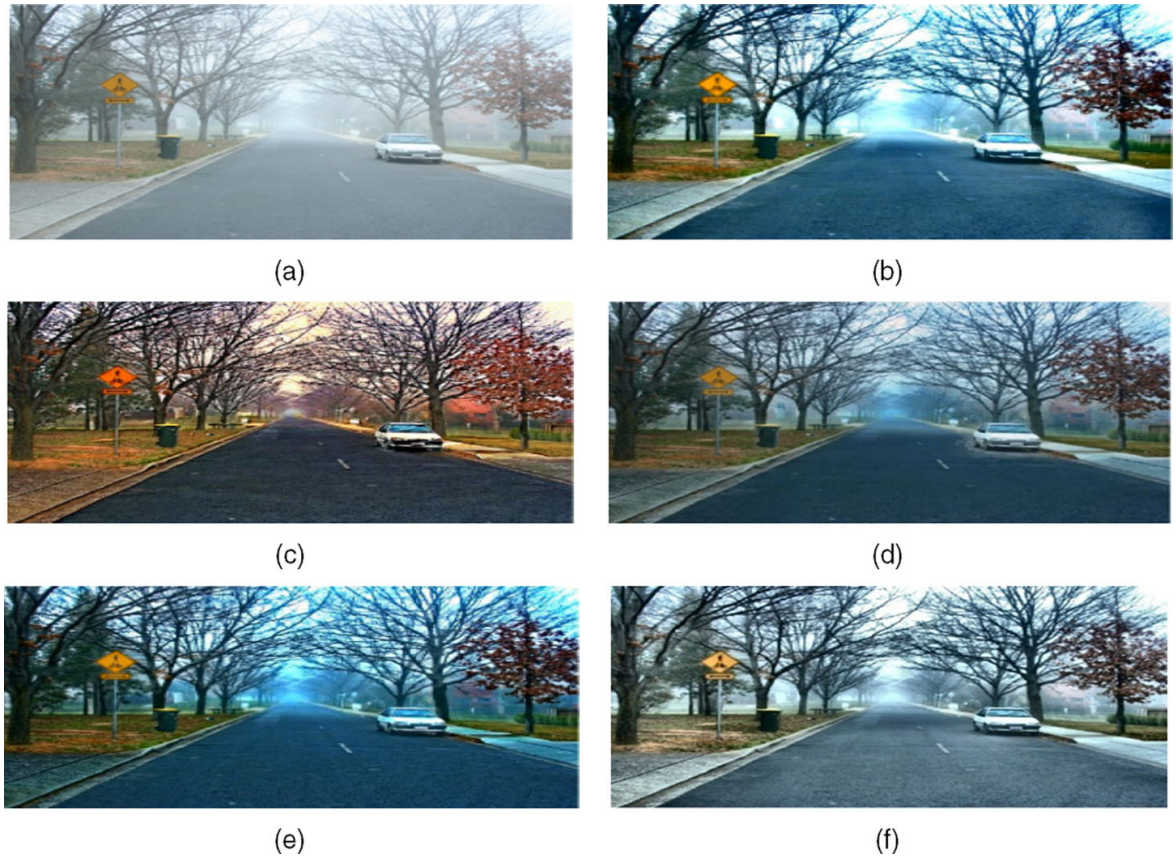

Fig. 10 Visual comparison of defogging result with recent state-of-the-art methods: **a** Original hazy image 'Sweden', recovered by the algorithm; **b** Kopf et al.; **c** Fattal's; **d** Tan et al.; **e** He et al.; **f** The proposed algorithm

Mountain '01' is 70.59 which is increased to 115.62 after fog removal. Similarly, in Tables 5 and 6, we compare the PSNR and AMBE with the other state-of-art methods. The effectiveness of the proposed method is described by high value of VM and low value of AMBE, ηand t_{run}.

Likewise, from Table 4, the visibility metric produced by the proposed method yields out 40% more enhanced visibility than the others. The PSNR produced by the proposed method is 12.5% more than those of the existing works (Table 5). Especially for Mountain 01, the proposed method achieves 36% higher value of PSNR than that of He et al. However, AMBE comparison in Table 6 indicates that the proposed method works well with the ambience of the other but does not yield out effective results. The proposed method gives from 3% to 5% of PSNR more than Kopf et al., and Tan et al. for Tower '02'. The experimental result clearly indicates that the proposed method has the best result over all other approaches. Knowing the ground truth of any degraded images have been a difficult issues since long. However, we have adopted a common and well-known manually investigated image pixels into foreground and

Table 4 Visibility metric comparison produced by the proposed method and others

Image	VM	Kopf et al.	Fattal et al.	Tan et al.	He et al.	Ren et al.	Berman et al.	Fan et al.	Proposed Work
'Mountain 01'	70.59	80.14	78.18	76.62	87.95	88.96	87.98	89.58	115.62
'Tower 02'	65.92	99.61	99.26	97.48	103.41	104.52	105.12	104.84	150.63
'Sweden'	62.99	100.87	85.21	114.15	113.24	105.63	104.98	103.25	115.98

Table 5 PSNR comparison produced by the proposed method and others

Image	Kopf et al.	Fattal et al.	Tan et al.	He et al.	Ren et al.	Berman et al.	Fan et al.	Proposed Work
'Mountain 01'	34.83	45.74	30.07	32.16	33.54	34.63	36.84	48.40
'Tower 02'	31.47	36.82	28.62	33.87	34.85	37.85	34.14	42.83
'Sweden'	22.67	22.71	22.50	24.60	25.36	24.52	24.62	28.74

background classes. These include presence of degradation effects such as lack of contrast, interfering patterns and color fading. We have identified these images as degraded in the following way:

a) The difficulty in taking a decision that which pixel should be considered as text or background as the pixels are mislabeled is such images. Hence, they are mentioned in our work as haze images (Misty, Foggy, Cloudy Images).
b) The confusion between text and background rises which makes the separation task quite difficult (gray-scale intensity). We found these RGB (Red, Green Blue) images with redundant luminance information. Thus, these segments appear as if they are fog. This happens in most of the historical and old images.

Now, we compare all algorithms on the HazeRD dataset [44] with respect to the Average VM (Avg_VM), Average PSNR (Avg_PSNR) and Average AMBE (Avg_AMBE). In Table 7, it is clear that the proposed method produces the highest average VM and PSNR values and lower AMBE values. It has been shown that the proposed method gives the best result over all.

Figures 11 and 12 demonstrate defogging of the proposed method and the others. An illustration of refining the transmission map using the guided filter with various window sizes is indicated in Fig. 13a and b. Herein, we adapt a simple strategy to adjust r^{dark} according to the area of image. When the number of pixels in the image is less than (2×10^5), the radius is fixed as 15 preventing the patch size become too small. When the number of pixels is more than (2×10^5), the radius is fixed as 30, preventing the patch size from growing too large. For the guided filter, the regularization parameter ε fix to be 10^{-2}. The parameter t_o is set to be 0.1, but its value needs to be increased when an image contains sky regions. The parameter $\lambda = 10–4$ is chosen corresponding to the best PSNR. The value of parameter wis depended on applications but we fix it to 0.95 for all result reported in this paper.

An important parameter for computing the dark channel is patch size. We denote its radius as r^{dark}. Since the computational cost in soft matting is quite high, we cannot use it for refinement of large images. In [12], the patch size is fixed as 15×15 which is relatively small. However, the complexity of the proposed method is quite low, and it is capable of processing

Table 6 AMBE comparison of the proposed method and others

Image	Kopf et al.	Fattal et al.	Tan et al.	He et al.	Ren et al.	Berman et al.	Fan et al.	Proposed Work
Mountain'01'	22.61	17.86	47.97	48.27	38.52	34.21	35.27	10.92
Tower '02'	16.54	34.46	47.80	34.88	31.24	30.14	31.42	5.51
Sweden	45.00	76.38	75.86	71.06	68.54	67.52	54.21	43.58

Table 7 Comparison on the Haze RD dataset in terms of the basic comparative factors

Method	Avg_VM	Avg_PSNR	Avg_AMBE
Tan et al. (2011)	102.89	25.98	59.98
Fattal [9]	88.56	38.09	62.28
Kopf et al. [17]	91.25	30.68	43.89
He et al. [11]	108.98	31.87	55.76
Ren et al. [25]	108.92	21.27	46.85
Berman and Avidan [3]	109.81	24.47	47.89
Fan et al. [8]	112.28	29.57	41.29
Proposed Method	131.85	40.78	41.65

the large image with short running time. Thus, it is not appropriate to use fixed patch size. From the local linear model in Section 4, large radius r implies that filtering output is linear to guidance images in order to reduce the halo artifact in recovered image. But if r is too large, the transmission map will capture too much detail from the guidance; making the recovered image over saturated. Failure of transmission refinement using the guided filter is indicated in Fig. 14a and b.

In those images, the uppermost right corner is destroyed because of using DCP. The dark channel prior (DCP) is statistically based; thus it is likely that particular spots in the image do not follow this prior. Indeed, this method fails when some objects in a particular image is inherently gray or white. It assumes that a part of the images is a part of the fog. That is why the white patches are appeared in the image. Our method may misjudge the fatness of the haze (underestimate the transmission). Thus, the color saturation is occurred in the recovered image.

Fig. 11 Defogging of the proposed method vs. He et al. method **a** Input image, **b** He's result, **c** Proposed method's **d** Input image, **e** He's result, **f** Proposed method's

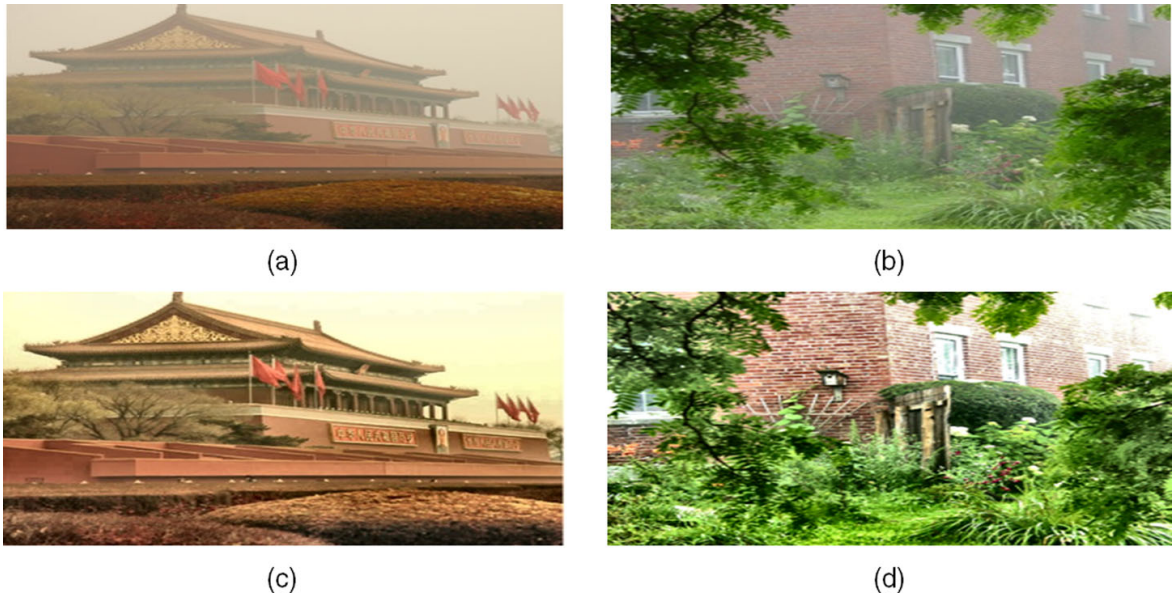

Fig. 12 Defogging for heavy fog images by the proposed method: **a** Foggy 'Monastery' image, **b** Foggy 'Hostel' image, **c** Restored 'Monastery' image, **d** Restored 'Hostel' image

In the future, we will try to use Edge Aware Filtering to overcome this limitation. Edge-aware filtering become inherent, e.g. through answering a linear arrangement. The weighted least squares (WLS) filter uses the matrix operations according to gradient of the image. There are two cases in Edge-aware filtering such as Flat patches and Edge or high variance. When a pixel is in the center of a flat patch region, its value is converted into the average of adjacent pixels. If it is in the center of an edge or high variance region, its value will be constant. Because edge-aware filter is time consuming, we can try minimizing the time complexity of this filter by using fast and high quality explicit filter.

8 Conclusion

Through the survey on state-of-the-arts on fog removal, it is a fact that they ignored every phase or circumstances. The existing techniques neglect utilization of the dark channels prior to reduce noises and uneven illuminate problems. To overcome the previous circumstance, we proposed in this paper an integrated algorithm to improve the visibility of fog degraded images. It is a combination of Guided filter and CLAHE, where the Guided filter is an edge-preserving filter which is used for quickly refinement of transmission map and CLAHE

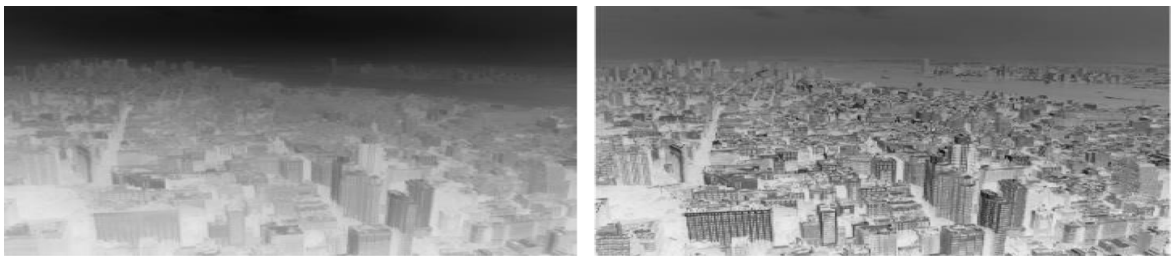

Fig. 13 Refining the transmission map using guided filter with various window sizes ($\varepsilon = 10^{-2}$)

(a) (b)

Fig. 14 Failure of suggested image: **a** Foggy input image and **b** Our result

is used to improve the local contrast of image by portioning the image into small boxes. The proposed methods has been empirically validated on benchmark images such as foggy images namely Mountain '01', Tower '02', 'Sweden', and the HazeRD datasets. Performance of the algorithms were measured in terms of Visibility Metric (VM), Absolute Mean Brightness Error (AMBE), Peak Signal to Noise Ratio (PSNR), and Run Time (t_{comp}).It was observed that in restored image, no oversaturated region exist due to which there is a negligible appearance of halo-artifact. The advantages of proposed method are multiple: It is simple in principle and hence easy to implement; it provides good result in most cases (homogenous fog), without introducing artifact and efficient for various type of fog images.

The proposed method outperforms the other existing methods by enhancing details in fog degraded images. However, guided image filtering is actually an approximation of soft matting; this method fails when the input image contains abrupt depth changes. Failure of transmission refinement using guided filter is aforementioned. To address the mention problem, we will try to use Edge Aware filtering with weighted least squares (WLS) filter. The idea is intuitively: when a pixel is in the center of a flat patch region, its value is converted into the average of adjacent pixels. If it is in the center of an edge or high variance region, its value will be constant. Because edge-aware filter is time consuming, we can try minimizing the time complexity of this filter by using fast and high quality explicit filter. All of these will be our future works in progress.

Acknowledgements The author (Le Hoang Son) would like to express a sincere thank to the sponsor of a project regarding Computer Vision and Artificial Intelligence from the Duy Tan University

Compliance with ethical standards

Conflict of interest The authors declare that they have no conflict of interest.

References

1. Aizenberg I, Bregin T, Butakoff C, Karnaukhov V, Merzlyakov N, Milukova O (2002) Type of blur and blur parameters identification using neural network and its application to image restoration. Artificial Neural Networks:138–139
2. Ancuti C, Ancuti C, Hermans C, Bekaert P (2011) A fast semi-inverse approach to detect and remove the haze from a single image. Computer Vision–ACCV:501–514

3. Berman D, Avidan S (2016) Non-local image dehazing. In: CVPR, https://www.eng.tau.ac.il/~berman/NonLocalDehazing/index.html
4. Chaker A, Kaaniche M, Benazza-Benyahia A, Antonini M (2018) Efficient transform-based texture image retrieval techniques under quantization effects. Multimed Tools Appl 77(1):1–25
5. Cheng FC, Cheng CC, Lin PH, Huang SC (2015) A hierarchical airlight estimation method for image fog removal. Eng Appl Artif Intell 43:27–34
6. Dobler G, Cholis I, Weiner N (2011) The Fermi gamma-ray haze from dark matter annihilations and anisotropic diffusion. Astrophys J 741(1):25–34
7. Dong W, Zhang L, Shi G, Wu X (2011) Image deblurring and super-resolution by adaptive sparse domain selection and adaptive regularization. IEEE Trans Image Process 20(7):1838–1857
8. Fan X, Wang Y, Tang X et al (2017) Two-Layer Gaussian Process Regression with Example Selection for Image Dehazing. IEEE Transactions on Circuits & Systems for Video Technology 27(12):2505–2517
9. Fattal R (2014) Dehazing using color-lines. ACM Trans Graph 34(1):13–27
10. He K, Sun J (2015) Fast guided filter. arXiv preprint arXiv:1505.00996, 54, 147–158
11. He K, Sun J, Tang X (2011) Single image haze removal using dark channel prior. IEEE Trans Pattern Anal Mach Intell 33(12):2341–2353
12. He K, Sun J, Tang X (2013) Guided image filtering. IEEE Trans Pattern Anal Mach Intell 35(6):1397–1409
13. Huang SC, Chen BH, Wang WJ (2014) Visibility restoration of single hazy images captured in real-world weather conditions. IEEE Transactions on Circuits and Systems for Video Technology 24(10):1814–1824
14. Jiang J, Hou T, Qi M (2011) Improved algorithm on image haze removal using dark channel prior. Journal of circuits and systems 16(2):7–12
15. Kim JH, Sim JY, Kim CS (2011) Single image dehazing based on contrast enhancement. In: Proc. 2011 IEEE International Conference on Acoustics, Speech and Signal Processing (ICASSP), Prague, Czech Republic, pp 1273–1276
16. Kim JH, Jang WD, Sim JY, Kim CS (2013) Optimized contrast enhancement for real-time image and video dehazing. J Vis Commun Image Represent 24(3):410–425
17. Kopf J, Neubert B, Chen B, Cohen M, Cohen-Or D (2008) Deussen, O.,& Lischinski, D. Deep photo: Model-based photograph enhancement and viewing ACM 27(5):116–124
18. Kundur D, Hatzinakos D (1998) A novel blind deconvolution scheme for image restoration using recursive filtering. IEEE Trans Signal Process 46(2):375–390
19. Levin A, Lischinski D, Weiss Y (2008) A closed-form solution to natural image matting. IEEE Trans Pattern Anal Mach Intell 30(2):228–242
20. Levin A, Weiss Y, Durand F, Freeman WT (2011) Understanding blind deconvolution algorithms. IEEE Trans Pattern Anal Mach Intell 33(12):2354–2367
21. Narasimhan SG, Nayar SK (2003) Contrast restoration of weather degraded images. IEEE Trans Pattern Anal Mach Intell 25(6):713–724
22. Ngan TT, Tuan TM, Son LH, Minh NH, Dey N (2016) Decision Making Based on Fuzzy Aggregation Operators for Medical Diagnosis from Dental X-ray images. J Med Syst 40(12):1–7
23. Park D, Ko H (2012) Fog-degraded image restoration using characteristics of RGB channel in single monocular image. 2012 IEEE International Conference on Consumer Electronics, (pp. 139–140)
24. Qiao T, Zhu A, Retraint F (2018) Exposing image resampling forgery by using linear parametric model. Multimed Tools Appl 77(2):1501–1523
25. Ren W, Liu S, Zhang H, Pan X, Cao J, Yang MH (2016) Single image dehazing via multi-scale convolutional neural networks. In: ECCV, (pp.154–169)
26. Schechner YY, Narasimhan SG, Nayar SK (2001) Instant dehazing of images using polarization. Proceedings of the 2001 IEEE Computer Society Conference on Computer Vision and Pattern Recognition, 1, (pp. 124–134)
27. Shi L, Cui X, Yang L, Gai Z, Chu S, Shi J (2016) Image Haze Removal Using Dark Channel Prior and Inverse Image. MATEC Web of Conferences 75:30–38
28. Shi J, Malik J (2000) Normalized cuts and image segmentation. IEEE Trans Pattern Anal Mach Intell 22(8):888–905
29. Son LH, Tuan TM (2016) A cooperative semi-supervised fuzzy clustering framework for dental X-ray image segmentation. Expert Syst Appl 46:380–393
30. Son LH, Tuan TM (2017) Dental segmentation from X-ray images using semi-supervised fuzzy clustering with spatial constraints. Eng Appl Artif Intell 59:186–195
31. Sun XM, Sun JX, Zhao LR, Cao Y (2014) Improved algorithm for single image haze removing using dark channel prior. Journal of Image and Graphics 19(3):381–385
32. Tai YW, Tan P, Brown MS (2011) Richardson-lucydeblurring for scenes under a projective motion path. IEEE Trans Pattern Anal Mach Intell 33(8):1603–1618
33. Tan RT (2008) Visibility in bad weather from a single image. IEEE Conference on Computer Vision and Pattern Recognition, (pp. 1–8)

34. Tang K, Yang J, Wang J (2014) Investigating haze-relevant features in a learning framework for image dehazing. Proceedings of the IEEE Conference on Computer Vision and Pattern Recognition, (pp. 2995–3000)
35. Tuan TM, Duc NT, Hai PV, Son LH (2017) Dental diagnosis from X-Ray images using fuzzy rule-based systems. International Journal of Fuzzy System Applications 6(1):1–16
36. Tuan TM, Ngan TT, Son LH (2016) A novel semi-supervised fuzzy clustering method based on interactive fuzzy satisficing for dental x-ray image segmentation. Appl Intell 45(2):402–428
37. Vo BN, Vo BT, Hoang H (2016) An Efficient Implementation of the Generalized Labeled Multi-Bernoulli Filter. IEEE Trans Signal Process 65(8):1975–1987
38. Wang G, Ren G, Jiang L, Quan T (2013) Single image dehazing algorithm based on sky region segmentation. Inf Technol J 12(6):1168–1175
39. Xia Z, Wang X, Sun X, Liu Q, Xiong N (2016) Steganalysis of lsb matching using differences between nonadjacent pixels. Multimed Tools Appl 75(4):1947–1962
40. Yadav G, Maheshwari S, Agarwal A (2014) Foggy image enhancement using contrast limited adaptive histogram equalization of digitally filtered image: Performance improvement. 2014 IEEE International Conference on Advances in Computing, Communications and Informatics, (pp. 2225–2231)
41. Yang S, Zhu Q, Wang J, Wu D, Xie Y (2013) An improved single image haze removal algorithm based on dark channel prior and histogram specification. In Proceedings of 3rd International Conf. On Multimedia Technology, Atlantis Press (pp. 279–292)
42. Yong W, Ting L, Yongsheng Q (2015) Image enhancement algorithm research based on the archives monitoring under low illumination. 2015 12th IEEE International Conference on Electronic Measurement & Instruments, 3, (pp. 1270–1274)
43. Yuan L, Sun J, Quan L, Shum HY (2007) Image deblurring with blurred/noisy image pairs. ACM Trans Graph 26(3):1–12
44. Zhang Y, Ding L, Sharma G (2017) HAZERD: an outdoor scene dataset and benchmark for single image dehazing, ICIP-2017, IEEE, (pp. 3205–3209)
45. Zhao S, Shmaliy YS, Liu F (2016) Fast Kalman-like optimal unbiased FIR filtering with applications. IEEE Trans Signal Process 64(9):2284–2297

Publisher's note Springer Nature remains neutral with regard to jurisdictional claims in published maps and institutional affiliations.

Rajiv Kapoor received M.E. and Ph.D. degree in Electronics & Communication Engineering from Delhi College of Engineering, Delhi University. Dr. Kapoor presently working as Professor in Electronics & Communication Engineering Department, AIACT&R (Govt. of NCT of Delhi). He has authored over 90 research papers in various renowned international journal and conferences. His primary research interests are machine learning, computer vision, signal and image processing.

Rashmi Gupta received M.E. and Ph.D. degree in Electronics & Communication Engineering from Delhi College of Engineering, Delhi University. Dr. Gupta held the position of Sr. Engineer in Calcom group of companies from 1991 to 1999, position of Lecturer in Electronics & Communication Engineering Department at Hindu Institute of Technology and Senior Lecturer in Maharaja AgrasenIntitute of Technology, Delhi from 1999 to 2003. Dr. Gupta presently working as Associate Professor in Electronics & Communication Engineering Department, AIACT&R (Govt. of NCT of Delhi). She has authored over 40 research papers in various renowned international journal and conferences. Her primary research interests are machine learning, computer vision, signal and image processing.

Le Hoang Son obtained the PhD degree on Mathematics – Informatics at VNU University of Science, Vietnam National University (VNU) in 2013. He has been promoted to Associate Professor in Information Technology since 2017. Dr. Son worked as senior researcher and Vice Director at the Center for High Performance Computing, VNU University of Science, Vietnam National University during 2007–2018. From August 2018, he is Head of Department of Multimedia and Virtual Reality, VNU Information Technology Institute, VNU. He is also the Consultant of Vietnam Office of the Government from October 2018. His major fields include Artificial Intelligence, Data Mining, Soft Computing, Fuzzy Computing, Fuzzy Recommender Systems, and Geographic Information System. He is a member of International Association of Computer Science and Information Technology, Vietnam Society for Applications of Mathematics, and Key Laboratory of Geotechnical Engineering and Artificial Intelligence in University of Transport Technology (Vietnam). Dr. Son is an Associate Editor of Journal of Intelligent & Fuzzy Systems (SCIE), IEEE Access (SCIE), Neutrosophic Sets and Systems (ESCI), Vietnam Research and Development on Information and Communication Technology, VNU Journal of Science: Computer Science and Communication Engineering, Frontiers in Artificial Intelligence. He serves as Editorial Board of Applied Soft Computing (SCIE), PLOS ONE (SCIE), International Journal of Ambient Computing and Intelligence (ESCI), and Vietnam Journal of Computer Science and Cybernetics. Recently, Dr. Son has been

appointed as Consultant of Vietnam Government Office. So far, he has awarded “2014 VNU Research Award for Young Scientists”, “2015 VNU Annual Research Award”, “2015 Vietnamese Mathematical Award”, and “2017 Vietnamese Mathematical Award”.

Raghvendra Kumar is working as Assistant Professor in Computer Science and Engineering Department at L.N.C.T Group of College Jabalpur, M.P. India. He received B. Tech. in Computer Science and Engineering from SRM University Chennai (Tamil Nadu), India, M. Tech. in Computer Science and Engineering from KIIT University, Bhubaneswar, (Odisha) India and Ph.D. in Computer Science and Engineering from Jodhpur National University, Jodhpur (Rajasthan), India. He has published 86 research papers in international / National journal and conferences including IEEE, Springer and ACM as well as serve as session chair, Co-chair, Technical program Committee members in many international and national conferences and serve as guest editors in many special issues from reputed journals (Indexed By: Scopus, ESCI). He also received best paper award in IEEE Conference 2013 and Young Achiever Award-2016 by IEAE Association for his research work in the field of distributed database. His researches areas are Computer Networks, Data Mining, cloud computing and Secure Multiparty Computations, Theory of Computer Science and Design of Algorithms. He authored 12 computer science books in field of Data Mining, Robotics, Graph Theory, and Turing Machine by IGI Global Publication, USA, IOS Press Netherland, Lambert Publication, Scholar Press, Kataria Publication, Narosa, Edupedia Publication, S. Chand Publication and Laxmi Publication.

Sudan Jha was born on October 22 at the Capital city Kathmandu of Himalayan Country Nepal, he received proficiency in certificate level from Saint Xavier's College Kathmandu and then Bachelor of Engineering in Electronics Engineering from Motilal Nehru Regional College, Allahabad. Uttar Pradesh, India, in 2001; joined as a Lecturer in one of the premium and largest Engineering College and the first one in the private domain in Nepal ("Nepal Engineering College (nec)"), where he got full sponsorship from the employer (nec) to pursue "Masters in Computer Science". In due course of time, he chaired and organized 5 International Conferences, some of the proceedings of those conferences been published by Springer Verlag, World Science Series, Imperial Press London, etc. He was promoted to Assistant Professor in the Department of Computer Science and Engineering after completion of his Masters Degree and no sooner than later, he became the Head of the Computer Science and Engineering Department.

Affiliations

Rajiv Kapoor [1] · Rashmi Gupta [2] · Le Hoang Son [3,4] · Raghvendra Kumar [5] · Sudan Jha [6]

Rajiv Kapoor
rajivkapoor@dce.ac.in

Rashmi Gupta
rashmig71@yahoo.com

Raghvendra Kumar
raghvendraagrawal7@gmail.com

Sudan Jha
jhasudan@hotmail.com

1 ECE Department, Delhi Technological University, Delhi, India

2 ECE Department, AIACT&R, GGSIPU, Delhi, India

3 Institute of Research and Development, Duy Tan University, Da Nang, Vietnam

4 VNU Information Technology Institute, Vietnam National University, Hanoi, Vietnam

5 Computer Science and Engineering Department, LNCT College, Bhopal, MP, India

6 School of Computer Engineering, Kalinga Institute of Industrial Technology, Bhubaneswar, Odisha, India

electronics

MDPI

Article

Green Computing in Sensors-Enabled Internet of Things: Neuro Fuzzy Logic-Based Load Balancing

Pankaj Kumar Kashyap [1], Sushil Kumar [1], Upasana Dohare [1], Vinod Kumar [2] and Rupak Kharel [3,*]

1 School of Computer and Systems Sciences, Jawaharlal Nehru University, New Delhi 110067, India; pankaj76_scs@jnu.ac.in (P.K.K.); skdohare@mail.jnu.ac.in (S.K.); upasanadohare@yahoo.com (U.D.)
2 Department of Computer Engineering, Delhi Technological University (DTU), New Delhi 110042, India; vinod_k@dtu.ac.in
3 School of Engineering, Manchester Metropolitan University, Manchester M1 5GD, UK
* Correspondence: r.kharel@mmu.ac.uk

Received: 1 March 2019; Accepted: 25 March 2019; Published: 29 March 2019

Abstract: Energy is a precious resource in the sensors-enabled Internet of Things (IoT). Unequal load on sensors deplete their energy quickly, which may interrupt the operations in the network. Further, a single artificial intelligence technique is not enough to solve the problem of load balancing and minimize energy consumption, because of the integration of ubiquitous smart-sensors-enabled IoT. In this paper, we present an adaptive neuro fuzzy clustering algorithm (ANFCA) to balance the load evenly among sensors. We synthesized fuzzy logic and a neural network to counterbalance the selection of the optimal number of cluster heads and even distribution of load among the sensors. We developed fuzzy rules, sets, and membership functions of an adaptive neuro fuzzy inference system to decide whether a sensor can play the role of a cluster head based on the parameters of residual energy, node distance to the base station, and node density. The proposed ANFCA outperformed the state-of-the-art algorithms in terms of node death rate percentage, number of remaining functioning nodes, average energy consumption, and standard deviation of residual energy.

Keywords: fuzzy logic; neural network; load balancing; supervised learning; back-propagation learning; clustering

1. Introduction

Sensors enabled Internet of Things (IoT) networks have been regarded as reasonable data collection and control applications over various network communication infrastructures through smart sensors called IoT nodes [1–3]. Sensors-enabled IoT networks are comprised of various smart sensor nodes (RFID enabled) that assemble facts (data) from the encompassing conditions and convey the data to the static base station (BS) or overload the data to cloud applications where users download the data for processing [4–6]. Sensors-enabled IoT networks have gained impressive attention in view of their broad application in animal or human tracking and surveillance, medical environments [7], military services, automobile industries [8], stock administration in industrial production [9], environment monitoring, natural hazards and seismic detection, fleet navigation and management, agricultural advancements [10], etc. However, these smart sensor nodes have a limited amount of energy for computation and data communication, and it is troublesome to substitute the power source. In addition, some sensor nodes quickly deplete their energy, which causes network partitions and reduces the lifetime of the network [11]. Reference [12] proposed a model which uses ant colony optimization technique coupled with Huffman coding to deduce the energy consumption in green computing wireless networks. Therefore, the proper use of the energy of the sensors is the primary challenge.

Hence, there is a need to find an approach that schedules the load among the smart sensors, particularly among those that have higher computational power and transmission capabilities.

Clustering is one potential load balancing approach which exists in the literature. Clustering is a technique which divides the entire network into small clusters. The maximum number of cluster heads per cluster is limited to one; each of the cluster heads have the mandatory duty of collecting data from their respective member nodes [13,14]. These member nodes are normally distributed in the same topographical region, so they have correlated data. After obtaining the data from its member nodes, cluster heads apply data aggregation techniques to eliminate any data redundancies, as a result, it effectively truncates the quantity of data to be transferred to the base station. Since only one cluster head per cluster is accountable for routing, to scale down the amount of data transferred, one must make the network scalable and mitigate the load balance problem [15]. There are three major aspects for designing a cluster-based network for data collection and transfer, namely, 1) optimal selection procedure for cluster head, 2) cluster binding, and 3) inter-cluster routing phase for transfer of aggregated data from each cluster head to the base station.

In clustering, cluster head selection procedure is a primary issue. Cluster head selection using traditional mathematical models is not appropriate for complex sensors-enabled Internet of Things. A fuzzy inference system is an appropriate tool to construct a model for cluster head selection since a fuzzy inference system processes the subjective part of human understanding and thinking without using any kind of mathematical tools. Zadeh [16] in 1965 first proposed the theory of fuzzy sets. Later on, Takagi and Sugeno [17] (1985) proposed the fuzzy modeling fuzzy identification or fuzzy modeling to alleviate the problem of various pragmatic applications such as control, inference, prediction, and estimation. As fuzzy modeling provides some great advantages such as the capacity to translate the immanent indecisiveness of human aspects into linguistic variables and effortless understanding of outcomes, as a result of the natural rule portrayal, simple augmentation of rule to the base knowledge is achieved through the expansion of new principles and robustness of system. Although, there are some disadvantages with this approach, there is no proper method defined which can transform human practical knowledge into fuzzy rule databases. Fuzzy modelling is only capable of giving an answer to a question that is written in the rules database. It cannot handle out-of-the-box problems, or in other words, generalization is very difficult. To alleviate this generalization problem, there is the need for a method of tuning or learning the membership function to cut down the error rates and to increase the performance index.

McCulloch and Pitts [18] developed the first artificial neural network model. Both Rosenblatt and Widrow first trained and named the trained variant of the artificial neural network model as the "adaptive liner neuron", later on called the "adaptive linear element algorithm" [19–24]. An artificial neural network is a "connectionist" computation model, which attempts to carve the biological neurons of a human cerebrum. The main advantage of neural networks is learning capacity; this model can learn from training data vectors and input–output pairs of the system. The neural network itself maps the weight functions or membership functions according to the problem up to an acceptable error rate of the system, which makes the system more efficient in terms of performance. Thus, it leads to the idea of augmenting the learning algorithm and generalization capability into the fuzzy system. A neural network receives the clarity of logical interpretation from fuzzy systems to rectify problems. In the early 1990s, Jang and Lin [25], Berenji [26] and Nauck [27] developed a hybrid system called a neuro-fuzzy system. There is diversity in neuro-fuzzy systems, which include fuzzy adaptive learning control networks [25,28], generalized approximate reasoning-based intelligence control [26], neuronal fuzzy controllers [27], fuzzy inference environment software with tuning [29], self-constructing neural fuzzy inference networks [30], fuzzy neural networks [31], evolving/dynamic fuzzy neural networks [32], and adaptive network-based fuzzy inference systems [33].

In this paper, a hybrid system based on two different soft-computing techniques—adaptive neural networks and fuzzy inference systems—is proposed to optimize the number of cluster heads that evenly

distribute the load among sensors in a network. We refer to this hybrid system as an adaptive neuro fuzzy clustering algorithm (ANFCA). The main contribution of the paper is highlighted as follows:

1. Firstly, in the system model, a first-order energy radio model was used to examine the energy consumption throughout the network.
2. Secondly, we designed an adaptive fuzzy logic inference system (AFLIS) with the help of fuzzy rules, sets, and membership functions that were updated (rules of AFLIS were updated) using input–output mapping of the hybrid systems. The output of the AFLIS was used as input for the neural network.
3. Thirdly, in ANFCA, the metrics were input into the fuzzy logic inference system and output was produced, which provided the information about the sensor nodes, whether it was capable or not of playing the role of cluster head. The output of the fuzzy logic inference system was handed to the neuro fuzzy logic inference system to elect the cluster head for the next round. The ANFCA used a supervised learning strategy to adjust the weight of the membership function of the AFLIS.
4. Fourthly, we present an approach to form clusters in which cluster heads aggregate data and send that data to the base station.
5. Finally, the proposed algorithm was simulated and the results were compared with LEACH, CHEF, and LEACH-ERE algorithms to shows the effectiveness of the ANFCA.

This paper is split into well-regulated systematic sections as follow: Section 2 provides a description about related works on green computing without heuristics and fuzzy-centric heuristics. Section 3 presents the proposed adaptive neuro-fuzzy algorithm for green computing in the IoT. Section 4 discusses the simulation and the analysis of the results. Section 5 describes the conclusion of the paper with future perspectives.

2. Related Works

There exist discreet numbers of clustering algorithms in the literature. Here, we reviewed the appropriate papers which were related to the proposed work.

2.1. Green Computing without Heuristics

Low-energy adaptive clustering hierarchy (LEACH) [34] was the first hierarchical clustering algorithm in sensor networks. There are two stages per clustering round in LEACH. The first one is related to cluster head election and formation of clusters within the network and the second one deals with data transmission to the cluster head known as the steady-state stage. A probabilistic model is proposed to choose a cluster head in the cluster setup phase; each sensor node has a certain probability of being assigned as cluster head per round. In general, the probability of a sensor node being elected as a cluster head depends upon a predefined threshold value. Every sensor node generates an arbitrary value between 0 and 1. Generated values of each sensor are compared with the threshold value to become cluster head for an ongoing epoch or round when generated value is below the threshold value. Each elected cluster head broadcasts a message using the carrier-sense multiple-access protocol to avoid inter-cluster interference. The strength of the received signal is used by each sensor node to determine which cluster head they want to join. After that, every cluster head gathers information from their member sensor nodes, and applies data aggregation, and then forwards the aggregated packet to the base station [35]. Thus, LEACH provides equal opportunity for each sensor node to become a cluster head with equal probability. But there are major shortcomings, as it does not take into account the energy consumption of each node, the geographical location of nodes are not included which causes asymmetrical classification of clusters in a network, and it does not use multi-hop nodes for transmission of data. Hybrid energy efficient distributed (HEED) [36] clustering protocol rectifies the shortcomings of LEACH in terms of uneven formation of clusters by including one extra parameter: the residual energy of nodes with nodes density (i.e., the proximity of neighbors' sensor nodes) for selection of cluster heads. Node density plays a major role in reducing the intra-cluster communication.

Hybrid energy efficient distributed clustering also uses a probabilistic model to elect temporary cluster heads, and every sensor node increases the probability of being a cluster head by twice in between rotations. Hybrid energy efficient distributed clustering also suffers from problems where some of the nodes are exempted from the cluster head selection process, and these nodes resolve this problem by pronouncing themselves as cluster head. In addition, several sensors may be exempted from all clusters or be freely available. Power-efficient gathering in sensor information systems (PEGASIS) [37] was introduced to save energy by making a chain of sensor nodes; it uses a greedy approach which means every node accepts delivery of data from its closest neighbors, and these acquired data are then transferred to another closest neighbor node. These assembled data keep on moving subsequently between nodes. Data are fused and then transmitted from specified nodes to the base station. The role of the designated node is replaced by another random node. Therefore, all the nodes deplete their energy proportionally or evenly distribute the load among nodes. Further, average energy spent in each cycle is reduced.

2.2. Green Computing Using Fuzzy-Centric Heuristics

Recently, fuzzy logic systems have been applied to elect cluster heads in sensors-enabled IoT networks. Gupta et al. [38] have proposed to choose a node as cluster head based on energy, density, and centrality of nodes. The main difference between the protocol proposed in Reference [38] and LEACH clustering is that this information is sent by node to the base station (known as a centralized approach). The base station is solely responsible for the selection of the cluster head. The base station processes these data with the help of a Mamdani-type fuzzy inference system, which gives output as a chance to decide the future of the preferred node if that would be suitable as a cluster head or not. The rest of the operations for a steady-state phase of that kind are similar to LEACH clustering. In Reference [39], another cluster head selection mechanism (CHEF) is proposed based on residual energy and local distance. Nodes select a cluster head using local information gathered from neighboring nodes, whereas in Reference [38] the cluster head is elected by the base station. Another improvement over the low-energy adaptive clustering hierarchy (LEACH) protocol is based on fuzzy logic (LEACH-FL) [40]. This protocol is proposed by Reference [37], apart from it, LEACH-FL has three distinct fuzzy variables: node density, energy level, and distance to base station. In this mechanism, the base station gathers information from sensor nodes and applies a Mamdani-type fuzzy inference system to figure out whether a node would be interpreted as a cluster head or not. Lee et al. [41] put forward a clustering head selection algorithm (LEACH-ERE) with the use of energy prediction techniques in accordance with fuzzy logic for homogenous WSNs. All of the above cluster head election mechanisms are based on fuzzy logic, and are intended to equalize the load among sensor nodes, but these are not able to tune the membership function or weight of the fuzzy descriptor to adapt to the environment.

The next one in this series is the cluster head election mechanism using the fuzzy logic (CHEF) protocol [39] that is almost the same as the Gupta fuzzy protocol. In CHEF, the base station is not responsible for selection of the cluster head; it does not gather any information from sensor nodes. The mechanism for selection of the cluster head is localized (a distributed approach) within a cluster. The setup phase is similar to the setup phase of LEACH. The CHEF protocol uses two fuzzy parameters: residual energy and local distance. The CHEF protocol works in rounds; in each round the sensor nodes select random numbers between 0 and 1, much like LEACH. If the chosen value is less than the threshold value, they calculate their chance using the fuzzy inference system. If the chance value of a tentative node is greater than all other chance values of sensor nodes, than it becomes the cluster head for the current round. It does far better than the Gupta protocol in terms of the number of cluster head selections; the Gupta protocol selects only a single cluster head per network (simulation was done under certain circumstances), although it is claimed that it can be increased, the process of creating more clusters is unclear [38].

Another improved version of the LEACH protocol based on fuzzy logic is LEACH-FL [40]. This protocol coupled with the above Gupta protocol (a centralized approach) has three distinct fuzzy variables: node density, energy level, and distance to base station. In this protocol, the base station gathers information from sensor nodes and applies a Mamdani-type fuzzy inference system to determine whether a node would be interpreted as a cluster head or not. Lee et al. [41] put forward a clustering head selection algorithm (LEACH-ERE) to predict residual energy in accordance with fuzzy logic for homogenous sensors-enabled IoT. The chance value of a cluster head is determined with the aid of two fuzzy norms, expected residual energy, and residual energy of a node. It is similar to the LEACH protocol where each node makes the decision itself to become a cluster head or not, without the help of the base station (called a distributed or localized approach). The sensor node having both extra residual energy as well as expected residual energy, gains additional benefit in becoming a cluster head. However, LEACH-ERE does not consider the distance between the cluster head and base station, or the node density around the sensor node which can lead to uneven energy consumption over the network.

Recently Nayak and Devulpalli [42,43] proposed a new fuzzy-logic-based clustering algorithm where the base station is mobile, and each cluster head does not send aggregated data to the mobile station. There is one super cluster head (SCH) in the network area that gathers the aggregated data from cluster heads and only the SCH dispatches information to the base station. Similar to LEACH, in each round the cluster heads are selected using a probabilistic model. Furthermore, the SCH is elected among cluster heads based on a Mamdani-type fuzzy inference system. According to a distributed approach, each cluster head is determined by its chance value using three fuzzy descriptors: remaining battery power (residual energy), mobility (referring to when the BS changes its position, and then the distance between the SCH and the BS increases or decreases), and centrality (primarily focusing on how central the SCH is to other cluster heads for communication). The chance value is the summation of the centrality mobility and battery power. These fuzzy labels are taken as additives due to the increase or decrease in the mobility and centrality upon the increase or decrease in the mobility of the base station. The chance value that is greater, this cluster head becomes a super cluster head. So, the SCH degrades the transmission taken by nodes, consequently, it reduces the duration of the first node dead over a number of rounds and enhances the network lifetime over LEACH.

In Reference [44], Abidoye et al. present the significance of the IoT in wireless sensor networks. Energy-efficient models are presented for enabling service-oriented applications in IoT-enabled WSN areas in two stages: in the first stage, the clustering-based model is used for service of the application, and in second phase, an energy-aware model is designed. Basically, those approaches are good, but not good enough for IoT networks, and their performances are poor when considering those networks are static. As the IoT provides dynamic networks, there is a need to improve the algorithms, so we emphasize fuzzy-based techniques with adaptive neural networks, which adapt to the dynamic networks of the IoT as well. In Reference [45], Yan li et al. proposed an analytic hierarchy process and fuzzy-based energy management system for industrial equipment management, and showed intensive case studies over IoT networks. In Reference [46], fuzzy-based vehicular physical systems were analyzed in the Internet of Vehicles (IoV), which uses fuzzy frameworks with the Markov chain to optimize location-oriented channel access delay. Signal-to-inference ratios and channel access delays are used as parameters for channel quality measurement. Hu et al. proposed [47] another aspect of the IoV which enables communication at the edge with the help of fuzzy logic. The cluster heads or gateways (smart vehicle) are chosen using fuzzy parameter velocity, vehicle neighboring density, and antenna height. The proposed algorithm provides an optimal number of gateways to bridge the licensed sub 6-GHz communication with millimeter wave to enhance network throughput. In Reference [48], a genetic-based virtualization approach was used to develop a method to overcome the torrent delay and minimize the energy consumption in IoT-enabled sensor networks. In Reference [10], the proposed algorithm was used for proper deployment of sensor nodes for coverage and connectivity for agricultural purposes. There are two methods for deployment of sensor nodes based on seven metrics that quantified the qualities measurement of sensor nodes.

Test-bed-based experiment (INDRIYA) is done for simulation purposes to show the effectiveness of the proposed algorithm.

All of the above protocols deal with fuzzy-logic-based algorithms, but none of them are able to tune the membership function or weight of the fuzzy descriptor. To the best of our knowledge, none of the above are up to the mark for real implementation, where input–output pairs are changing according to the environment. An adaptive artificial neural network is another soft-computing technique where a supervised learning approach is used to adapt to the environment. Therefore, we propose a novel adaptive neuro-fuzzy clustering algorithm (ANFCA) using both fuzzy logic and a neural network to address the problem of leaning rate of membership function, balancing the load, and minimizing the energy consumption to improve the lifetime of the sensor-enabled IoT.

3. Adaptive Neuro-Fuzzy for Green Computing in IoT

In this section, the details of the proposed adaptive neuro fuzzy for green computing in IoT is presented.

3.1. System Model

We consider that there are N sensor nodes deployed randomly in the sensing field in order to sense the surroundings of the environment periodically. These sensor nodes form clusters using the proposed neuro-fuzzy system. Each cluster has one cluster head, which receives data from cluster members. All the sensors are stationary in nature, having equal initial energy and capability for sensing the environment, processing the data, and transmission. The radio link between the nodes is symmetric. It means the nodes require equal energy for transmission in both directions. The base station is outside of the network. Sensor nodes have the capability to adjust their transmission power depending upon the distance between receiving nodes.

We consider the first-order radio model to compute the energy requirement in the proposed work. Let the size of **the** packet be m bits. The total energy consumed in transmitting a packet of m bits across l meter distance between the sender and receiver is given by

$$E_{TNE}(m,l) = \begin{cases} m * E_{elect} + m * \varepsilon_{fsp} * l^2 & if\ l < l_o \\ m * E_{elect} + m * \varepsilon_{mpf} * l^4 & if\ l \geq l_o \end{cases} \quad (1)$$

The energy consumed to receive a packet of m bits from the sender node is given by

$$E_{RCE}(m) = m * E_{elect} \quad (2)$$

where E_{elect} represents information about electronic energy dissipation in the electronic circuit per bit. This is affected by several factors such as digital coding, acceptable bit-rate, modulation, etc. The ε_{fsp} and ε_{mpf} are the energy consumption factor in the free space path and multipath fading, respectively. When the source and receiver nodes are separated within the limit of the threshold value $l_o (l_o = \sqrt{\varepsilon_{fsp}/\varepsilon_{mp}})$, it uses the free space model, otherwise its multipath fading channel will be used to computing the energy consumption for transmitting the message.

3.2. Adaptive Neuro-Fuzzy Clustering Algorithm

In this section, we propose our adaptive neuro-fuzzy clustering algorithm (ANFCA). The proposed algorithm combines the features of the adaptive fuzzy logic algorithm (ALFIS) and the adaptive neural fuzzy feature inference system (ANFIS), described in the following sections. The ALFIS is used to obtain training data for ANFIS. The output of the ANFLIS is used as input for the ANFIS, where the result is tuning, with weight adjustment, of the membership function of the antecedent and consequent of the fuzzy-rule-based system. In the last section, the phase of the proposed algorithm is presented.

3.2.1. Adaptive Fuzzy Logic Inference System

In this section, an adaptive fuzzy logic inference system (AFLIS) is presented to obtain information about a sensor node to become a cluster head. The output of the fuzzy logic inference system is passed as input data set for the next proposed adaptive neuro fuzzy inference system (ANFIS). We employed a Mamdani engine in the adaptive fuzzy logic inference system. Three metrics: residual energy (RE), node density (ND), and node distance to the base station (NDBS) were considered to compute the observation about a node, whether it can play the role of cluster head or not. As a sensor node has limited power for computation and communication, and these battery powers are almost irreplaceable in nature, residual energy is the most viable parameter for cluster head selection. In addition, these cluster heads are not very far away from base station otherwise data transfer would consume more energy from the nodes. Therefore, node distance to the base station is taken as another factor. Those nodes in the vicinity of the cluster head define the second criterion of node density, as sensor nodes are dispersed in the surrounding area by air support, artificial arrangement or any other method. As a result, each sensor node has a different number of neighbor nodes; if we select nodes with a lower number of neighbors in their communication range and these neighbors are not much closer to each other, these nodes cannot communicate directly to the cluster head and need intermediate nodes for transmission, thus increasing communication cost. Therefore, node density was another parameter taken into account.

The linguistic variables of the three metrics are defined as follows: residual energy (RE) = (below, fair, top); node distance to the base station (NDBS) = (adjacent, midway, distant); and node density (ND) = (deficient, medium, compact). The triangular and trapezoidal fuzzy membership function was used over other membership functions (such as Gaussian, Bell or Sigmoidal) for achieving better performance in real-time scenarios. For below and top values of residual energy, adjacent and distant values of node distance to base station, and deficient and compact values of node density, trapezoidal membership functions were used. The triangular membership function was used for the rest of the values as illustrated in Figures 1–4. The probability (output of adaptive fuzzy inference system) of sensor nodes to be assigned with the responsibility of cluster head was defined by linguistic variable chance (CH) = (weakest, weaker, weak, medium, strong, stronger, strongest). Since we used three metrics in fuzzification, therefore it required a total $3^3 = 27$ rules that are shown in the Table 1. These rules were stored in the knowledge base component of the fuzzy inference system. There were two extreme rules: The first one was related to creating strong chances for assigning the responsibility of cluster head to a sensor node when the value of the residual energy of that sensor node was equal to top, the node density was compact in nature, and the node was adjacent to the base station. The second one was if the value of the residual energy was equal to below, the node was distant from the base station, and the node was deficient in node density, then a node would have a very weak chance to become a cluster head.

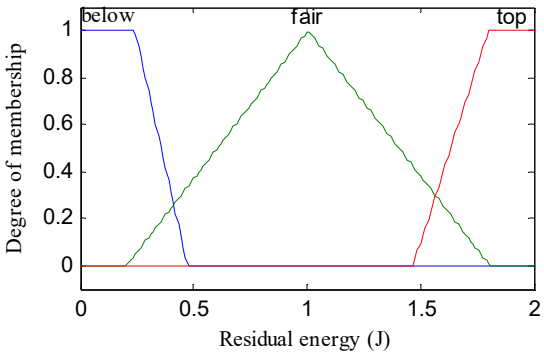

Figure 1. Membership function of RE (residual energy).

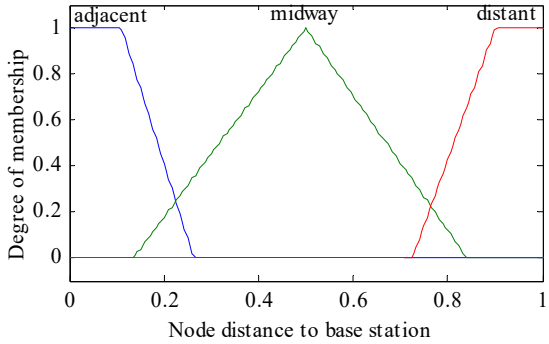

Figure 2. Membership function of NDBS (node distance to the base station).

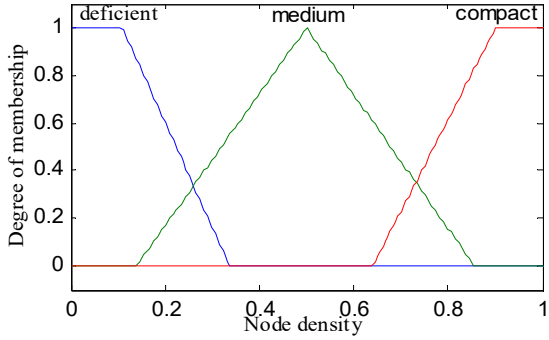

Figure 3. Membership function of ND (node density).

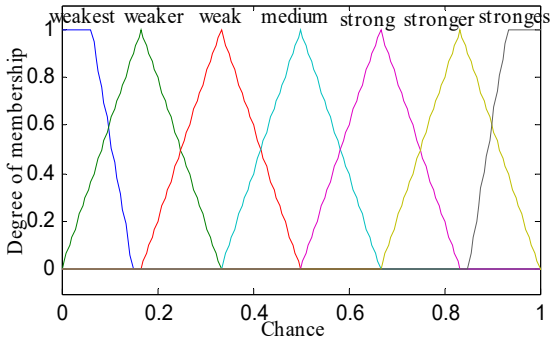

Figure 4. Membership function of CH (chance).

Table 1. Fuzzy knowledge database rules.

Rule	IF		THEN		Rule	IF		THEN	
	RE	NDBS	ND	CH		RE	NDBS	ND	CH
1.	below	adjacent	deficient	weakest	15.	fair	midway	compact	medium
2.	below	adjacent	medium	weaker	16.	fair	distant	deficient	weakest
3.	below	adjacent	compact	weak	17.	fair	distant	medium	weaker
4.	below	midway	deficient	weakest	18.	fair	distant	compact	weaker
5.	below	midway	medium	weakest	19.	top	adjacent	deficient	strong
6.	below	midway	compact	weaker	20.	top	adjacent	Medium	stronger
7.	below	distant	deficient	weaker	21.	top	adjacent	compact	strongest
8.	below	distant	medium	weakest	22.	top	midway	deficient	medium
9.	below	distant	compact	weakest	23.	top	midway	medium	strong
10.	fair	adjacent	deficient	weak	24.	top	midway	compact	stronger
11.	fair	adjacent	medium	medium	25.	top	distant	deficient	strong
12.	fair	adjacent	compact	strong	26.	top	distant	medium	stronger
13.	fair	midway	deficient	weak	27.	top	distant	compact	stronger
14.	fair	midway	medium	weak	-	-	-	-	-

The adaptive fuzzy inference system works in four steps to compute the possibility of a node to evolve into a cluster head.

a. Fuzzification or Input Crisp Value: In this step, we input the three metrics: residual energy, node density, and distance to base station as crisp values in the fuzzy inference system. In this step, the inference system creates membership functions for each metric that is the intersection points.
b. Knowledge Base or If–Then Rules: The knowledge base consists of all 27 rules, which runs concurrently on inputs and generates output as chance values. There are multiple inputs (three membership values), but selection is done among the minimum membership values which use fuzzy AND operator.
c. Aggregation: There are 27 rules in the fuzzy inference system, which give multiple outputs. In this step, we aggregate all the output to generate a single fuzzy output set using union fuzzy OR operator which choose maximum of rule evaluation.
d. Defuzzification: In this step, whether a sensor node can act as a cluster head or not is computed. For this purpose, we use a centroid method in the defuzzification step under the fuzzy set to get from aggregation, which is given by Equation (3).

$$NODE\ CHANCE\ (CH) = \int u_c(z) * z dy / u_c(z) dz \tag{3}$$

where $u_c(z)$ measures the rate of the membership function of the entity z within fuzzy set C, which is described as follows: $C = \{(z, u_P(z))/\ z\ \epsilon\ Z$, where Z denotes the universe of discourse.

3.2.2. Adaptive Neuro-Fuzzy Inference System

Fuzzy logic and artificial neural networks are good candidates for making smart artificial intelligence systems because of their generalization and non-linearity properties. We developed a hybrid system which consists of two different soft-computing techniques: fuzzy logic and artificial neural networks. We named the hybrid system an adaptive neuro fuzzy inference system (ANFIS). Fuzzy logic has expertise in the area of shapes but not on the subjective aspects of human learning into the procedure of exact quantitative analysis. But in any case, it does not have a characterized technique that can be utilized as a guide during the change from human idea into knowledge or rules-based fuzzy inference systems. It is also requires much time to adjust the membership function. Not at all like artificial neural networks, it has a higher ability in the learning procedure to adjust to its condition. Along these lines, the artificial neural network can be used to consequently alter the membership function and lower the rate of error in the assurance of tenets in fluffy rationale. Artificial neural networks are used for weight adjustment of the membership function of the antecedent and consequent of fuzzy-rule-based systems. Jang [49] proposed the ANFIS, which implements the Takagi–Sugeno fuzzy inference system of five layers. The ANFIS technique was intended to permit membership function and if–then rules to be developed in the light of already acquired data of metrics that are input or output data from the previously designed adaptive fuzzy inference system (AFLIS) in Section 4.1. In addition to the ANFIS, the fuzzy rules are tuned automatically, which is already used in adaptive fuzzy inference systems by using supervised learning. The ANFIS uses a trapezoidal membership function for weight adjustment. These membership functions were used with product inference rules in fuzzification level. The model of the proposed ANFIS with three inputs and one output is shown in Figure 5. Each input used the three membership functions following the Takagi–Sugeno type model containing 27 rules, and each of the nodes were governed by the if–then rules shown in Table 1. The antecedent part of the rules depicts a fuzzy subspace, whereas the subsequent part determines the output inside the fuzzy subspace.

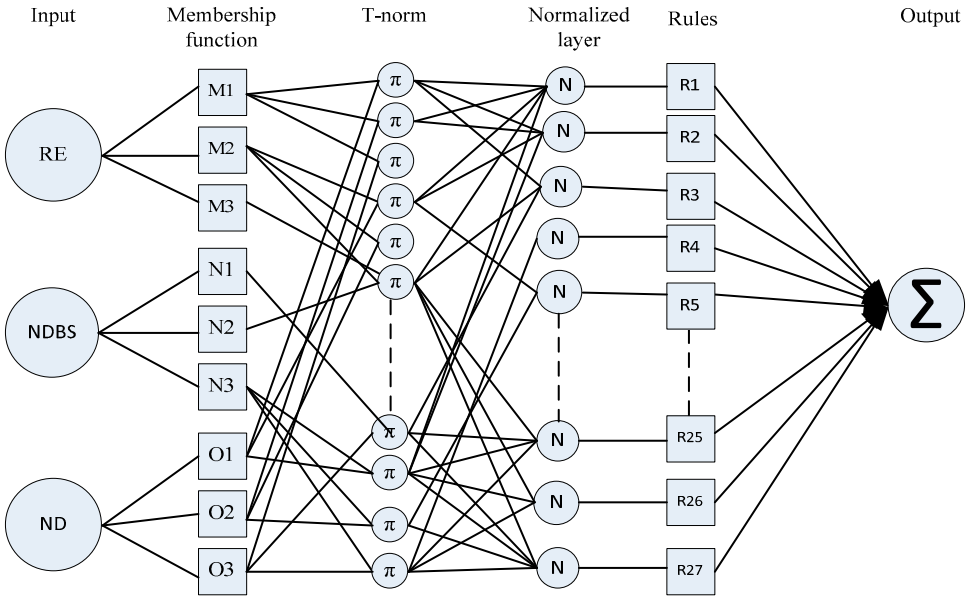

Figure 5. Three input type-3 adaptive neuro fuzzy inference system (ANFIS) with 27 rules and one output.

The ANFIS system is a feed-forward neural network with five layers using a supervised learning algorithm. These layers are denoted as fuzzy layer, T-norm layer, normalized layer, defuzzy layer, and aggregated layer, which represent the first, second, third, fourth, and fifth layers, respectively. The first and fourth layers have adaptive nodes, and the remaining layers have fixed nodes. There are three inputs: residual energy (RE), node distance to base station (NDBS), and node density (ND), and one output: chance (CH). We developed twenty-seven rules of "if–then" for the proposed ANFIS system based on the Takagi–Sugeno fuzzy inference model. These rules are

Rule 1 = If RE is below, NDBS is adjacent and ND is deficient Then $F_1 = S_1m + T_1n + U_1o + P_1$
Rule 2 = If RE is below, NDBS is adjacent and ND is medium Then $F_2 = S_2m + T_2n + U_2o + P_2$
Rule 3 = If RE is below, NDBS is adjacent and ND is compact Then $F_3 = S_3m + T_3n + U_3o + P_3$
…
Rule 25 = If RE is top, NDBS is distant and ND is deficient Then $F_{25} = S_{25}m + T_{25}n + U_{25}o + P_{25}$
Rule 26 = If RE is top, NDBS is distant and ND is medium Then $F_{26} = S_{26}m + T_{26}n + U_{26}o + P_{26}$
Rule 27 = If RE is top, NDBS is distant and ND is compact Then $F_{27} = S_{27}m + T_{27}n + U_{27}o + P_{27}$

where below, adjacent, and deficient are the membership functions or linguistic variables of inputs RE, NDBS, and ND (part of antecedent), respectively, and S_i, T_j, U_k are linear parameters of then part (consequent) of the Takagi–Sugeno fuzzy inference model. The linguistic variable for residual energy RE (M) = (below, fair, top) is represented as (M_1, M_2, M_3), node distance to base station NDBS (N) = (adjacent, midway, distant) is represented as (N_1, N_2, N_3) and node density ND (O) = (deficient, medium, compact) is represented as (O_1, O_2, O_3).

1. Fuzzy Layer: This section describes the nature of the node which is actually flexible according to backward pass (denoted by square adaptable node) that resembles each input variable relative to membership function. The membership function graph is plotted against each adaptable node to describe their output. Membership function follows Gaussian distribution as shown in Equation (4) or generalized bell-shaped membership function (see Equation (5)) which gives a value in the range of 0 and 1.

$$\mu_{M\alpha}(M) = exp\left[-\left(\frac{m - f_\alpha}{2d_\alpha}\right)^2\right] \quad (4)$$

$$\mu_{M\alpha}(M) = \frac{1}{1 + \left|\frac{m - f_\alpha}{d}\right|^2 e_\alpha} \tag{5}$$

The output of the first layer is given by

$$R_{1,\alpha} = \mu_{M\alpha}(M),\ \alpha = 1,2,3$$
$$R_{1,\alpha} = \mu_{N\alpha}(N),\ \alpha = 1,2,3$$
$$R_{1,\alpha} = \mu_{O\alpha}(O),\ \alpha = 1,2,3$$

where M is the input node to α and μ_{Mi}, μ_{Ni}, μ_{Oi} are the degree of membership function cross-ponding to linguistic variables M_i, N_i, and O_i and $\{d_i, e_i, f_i\}$ are referred to as a parameter set of the membership function or premise parameter. The bell-shaped membership function varies along with the values of the premise parameter set. In this layer, we can also use the triangular and trapezoidal membership function for the input node; they are also valid quantifiers for this node.

2. T-Norm Layer: In this layer, each node is non-adaptive in nature, and called as rule nodes which are depicted by the circle labeled with π (see Figure 5). These nodes represent the firing strength of each rule connected to it. To determine the results of each node, multiply all the signals (membership function) coming to the node. The T-norm operator uses generalized AND to calculate the antecedents/outputs at second layer of the rule.

$$R_{2\alpha} = T_\alpha = \mu_{M\alpha}(M) * \mu_{N\alpha}(N) * \mu_{O\alpha}(O),\ \alpha = 1,2,3 \tag{6}$$

where T_α is the output of each node which stands for each rule's firing strength.

3. Normalized Layer: Non-adaptive in nature nodes found in the normalized layer, which is known as normalized mode, are depicted by circles labeled as N (see Figure 5). The output of every node is an estimation of the proportion between the αth rule's firing strength to the summation of firing strength of all rules. The result at the third layer or normalized output can be expressed as

$$R_{3\alpha} = T_{n\alpha} = \frac{T_\alpha}{\sum_\alpha T_\alpha},\ \alpha = 1,2,3 \tag{7}$$

4. Defuzzy Layer: This layer consists of those nodes which have adaptive essence depicted by a square (see Figure 5). The output of the node is the product of normalized firing strength and individual rule. The output at the fourth layer can be given by

$$R_{4\alpha} = T_{n\alpha}\ f_\alpha = T_{n\alpha}(s_\alpha m + t_\alpha n + u_\alpha o + p_\alpha) \tag{8}$$

where $T_{n\alpha(s_\alpha m + t_\alpha n + u_\alpha o + p_\alpha)}$ is the normalized firing strength from the normalized layer and $(s_\alpha m + t_\alpha n + u_\alpha o + p_\alpha)$ is a parameter in the node. Defuzzy layer parameters are also known as a consequent parameter.

5. Aggregated Output Layer: This layer consists of a single consolidated node as an output which is specified as non-adaptive in nature. This non-adaptive node gives information about the complete system performance evaluated by adding up all the approaching signals arriving at this layer from the previous node. Summation sign $\sum$ is used inside a circle to represent this aggregated output node. The output of the fifth layer is computed as

$$R_{5\alpha} = \sum_\alpha T_{n\alpha}\ f_\alpha = \frac{\sum_\alpha W_\alpha f_\alpha}{\sum_\alpha w_\alpha} \tag{9}$$

The ANFIS uses the adaptive neuro fuzzy clustering algorithm (Algorithm 1) to train the premise and consequent parameters. The first layer resembles the adaptive node, which contains the non-linear premise parameter, and the fourth layer consists of the linear consequent parameters. Initially, the gradient descent or back propagation method is used as a learning algorithm. There may be a chance to stick in local minima and slow convergence rates while using back propagation. To rectify these problems Jang [49] uses a hybrid learning algorithm in which two learning strategies—least mean squares and gradient descent—are merged. The convergence rate of the hybrid learning algorithm is much faster than general artificial neural networks that never include local minima. The working strategy of the ANFCA incorporates two passes: forward pass and backward pass. In the forward pass, input signals (premise metrics) are propagated layer by layer until the fourth layer. These metrics are fixed, and consequent metrics are updated using the least mean squares method. After obtaining the output data at the fourth layer, the data are compared with the actual output and the error is calculated. Now, in the backward pass, the errors which occurred due to the comparison of the output generated in the forward pass and the actual output are sent back to the adaptive node of the first layer. At the same time, the membership functions (premise metrics) are updated using the gradient descent method or back propagation method. During this time, consequent metrics are fixed. Each level of learning is called an epoch. The proposed algorithm works in three phases: selection phase, cluster formation phase, and transfer phase. In the first phase, cluster heads are selected. In the second phase, clusters are formed by calculating their area based upon radius. In the final phase, cluster heads transfer the aggregated data to the base station. The precise description of each phase is presented in the next section.

Algorithm 1- Adaptive Neuro Fuzzy Clustering Algorithm (ANFCA)	
1.	**Begin**
2.	**Input:** Given input training pattern, {RE, NDBS, ND} and maximum number of Epoch to E_{max}. // obtained from first modeling mamdani type fuzzy inference system.
3.	**Output** {CH}
4.	**Process**
5.	**for** E=1 to E_{max}.
6.	Input the training data into first layer of Takagi-sugeno inference engine.
7.	Membership function $\mu_{M\alpha}(M)$ tuned using Equations (4) and (5).
8.	Adjust the firing strength of each node (T_α), using Equation (6) in non-adaptive T-norm layer.
9.	Normalize the firing strength of each node (W_{ni}) using Equation (7) in normalized layer.
10.	Defuzzification of each node using Equation (8).
11.	Aggregated output is produced for each node using Equation (9) in fifth layer.
12.	**END**

3.2.3. Phases of the Algorithm

The proposed algorithm of the ANFCA works in three phases as follow.

Selection Phase

Initially, the base station starts the operation of clustering; it broadcasts a beacon message (request for IDs, residual energy, distance to base station, and its density) in the network. All the sensor nodes reply an acknowledgment with requested information. Every node estimates the distance between base station and itself using received signal strength indicator. Equation (10) determines the received signal strength.

$$S_r = S_o + 10\beta\, log\left(\frac{a_r}{a_o}\right) + \delta \tag{10}$$

$$S_r = S_o 10^{\frac{RSSI-\theta}{10\alpha}} \tag{11}$$

where S_o (in decibel meter) is the reference signal strength at distance a_o, β is used to represent path loss exponent ($2 \leq \beta \leq 4$), and a_r is the actual distance. Gaussian random variable is represented by δ having mean zero and variance σ^2 (in decibel meter $4 \leq \sigma \leq 12$). The distance between the base station and a node is calculated using Equation (11). Where θ is the received signal strength in one meter distance from the base station without any obstacles. The base station triggers election procedures for cluster heads choosing some nodes as cluster heads randomly. These temporary cluster head nodes are gone through AFLIS to check the validity of each node whether they can play the role of cluster head or not. Afterwards, output of AFLIS is recorded and trained using ANFIS, and the final output is recorded. If the nodes have fulfilled the selection criteria for a cluster head, then these nodes are designated as permanent cluster heads for the present round. The selection procedure for a cluster head is rehashed in each cycle so it is potentially able for the sensor to get opportunity to become a part of cluster head group, therefore all nodes exhaust their energy relatively that upgrades the network lifetime.

Cluster Formation Phase

The ANFCA forms variable sizes of clusters; the cluster head manages the number of nodes or cluster sizes that eventually balances the load with periodic replacement of cluster heads. Initially, selected cluster heads calculate their radius for formation of cluster phase. The mean radius of each cluster head is obtained by the Equation (12)

$$Cr_{minimum} = \sqrt{\frac{A \times A}{\pi \times n \times k}} \tag{12}$$

whereas n represents the number of nodes deployed inside the network of area $A \times A$, and k represents the number of clusters. Generally, a cluster has at least a radius equal to Cr. After radius calculation, each cluster head acquires an area according to their radius then sends a join message to each node within the cluster. The nodes make the decision based upon the received signal strength to join which cluster. The sensor node which does not receive any join message declares themselves as cluster head and sends their data directly to the base station. The nodes within the defined radius are called member nodes for their respective clusters. Now, cluster heads schedule a time-division multiple-access approach to gather data from member nodes. This time-division multiple-access schedule reduces intra-cluster collision in addition to cutting down on energy utilization because of the limit on the number of messages exchanged between member nodes. Each cluster head broadcasts time-division multiple-access schedule information in their clusters to their member nodes on when they are able to send messages to their cluster head. The cluster head dictates the time slot for every node, only in their specific time slot can nodes send their message to the cluster head. Therefore, nodes enter the wake-up mode in their time slot, otherwise they go into sleep mode. In this way, nodes conserve their energy. The cluster heads gather messages from their member nodes and apply data aggregation to form single packets of a fixed size.

Transfer Phase

According to the time-division multiple-access schedule, the cluster head gathers and aggregates data, and then communicates to the base station directly without using any relay node. The number of messages exchanged is limited to the number of cluster heads which reduces the energy consumption.

4. Simulation

In this section, the performance of the proposed adaptive neuro fuzzy clustering algorithm (ANFCA) was analyzed. The proposed algorithm was simulated by writing a script in MATLAB (R2019a, MathWorks, Natick, MA, USA) and using simulator tools: FIS and ANFIS. The simulator FIS consists of a fuzzy inference model and membership function for each considered metric: residual

energy, node density, and node distance to the base station. The ANFIS simulator produced the output that determined the cluster head. The proposed algorithm ANFCA was compared with LEACH, fuzzy-logic-based CHEF, and energy prediction technique using fuzzy-logic-based LEACH-ERE to show its effectiveness.

4.1. Simulation Environment

In this section, the simulation parameters used to conduct simulation of the ANFCA are presented. We considered a 200 × 200 node simulation area of the network, where 200 sensor nodes were distributed randomly. The sensing capabilities of the nodes were limited to 5 m and they were allowed to transfer data within a 25-meter range in a symmetric way. The simulation cycle time was approximately 60 µs, and it ran until all nodes had died. The size of the packets were 512 bits. The simulation metrics and their values are shown in Table 2.

Table 2. Modeling framework.

Metrics	Specification
Number of nodes	200
Rectangular area	200 × 200 m^2
Node sensing range	5 m
Node transmission range	25 m
Base station location	(200,170)
Packet size m	512 bits
Initial Energy	2 J
E_{TDA}	5 nJ/bit/message
E_{TNE}	50 nJ/bit
ε_{fsp}	10 pJ/bit/m^2
ε_{mpf}	0.0013 pJ/bit/m^4
Cycle time	60 µs

Evaluation Metrics

- Network Lifetime: Lifetime definition of the network is application dependent, and it may be stated that as the tenure spans from the start, it is the functioning of the network to a moment when a certain percentage of the nodes have died or the network will be disconnected. In this paper, we considered the simulation time until 90% of the nodes were dead.
- (First node death) FND, (Half node death) HND and (Last node death) LND: The round at which the death of the first node occurred was defined as FND. Similarly, the round at which half of the nodes had died was defined as HND. The round at which the last node death has occurred was taken as LND.
- Average Residual Energy: Defined as the mean of residual energy of alive nodes in the network with respect to rounds.
- Average Energy Consumption: Defined as the summation of overall energy consumption taken place during the sensing and transmission by each sensor node to the number of sensor nodes with respect to rounds.
- Standard Deviation of Residual Energy: The standard deviation of residual energy is the square root of variance of residual energy of all the sensor nodes. It shows the variation of residual energy around the mean.

4.2. Simulation Results

4.2.1. Network Lifetime Over Rounds

Figure 6 shows the results obtained in the simulation for functioning nodes with respect to each round. It was observed that 90% of all 200 nodes had died by 2000 rounds, and the remaining 10%

stretched the lifetime of the network up to another 100 rounds (total: 2100 rounds) for the LEACH algorithm, whereas CHEF showed little improvement over the classical LEACH (20% improvement in network lifetime) which ran up to 2220 rounds smoothly, and there were still 20 nodes alive. The LEACH-ERE initially showed up to 800 rounds with only 20–30 nodes having died, and thereafter the death rate of the nodes increased and almost followed the CHEF curve. The LEACH-ERE showed a 4–5% enhancement over the CHEF and 25% over LEACH. The LEACH-ERE ran up to 2300 rounds. Apart from this proposed algorithm, the ANFCA showed a steady death rate of sensor nodes; at up to 1000 rounds, only 10% of sensor nodes (20 nodes) had died, and thereafter it followed almost a similar curve to the LEACH-ERE up to 1200 rounds. The ANFCA lasted up to 2300 rounds until all 200 sensor nodes (100%) had died. It was clearly observed that the proposed ANFCA runs for a longer time compared with the state-of-the-art algorithms. It is due to the fact that the neuro fuzzy system is employed to rotate the cluster head responsibility among the sensors.

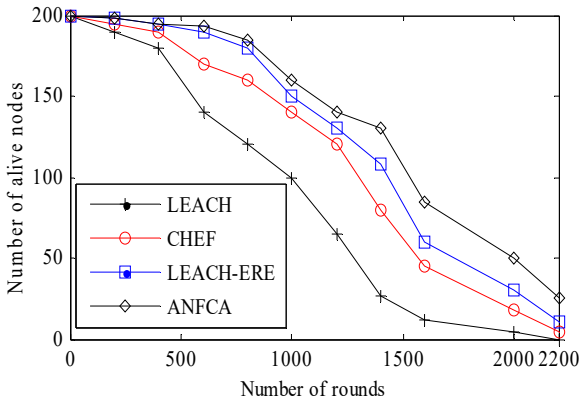

Figure 6. Number of functioning nodes over the rounds.

Figure 7 shows the percentage of nodes that died over the increasing number of rounds. From the simulation results, it was observed that the proposed ANFCA does far better than LEACH and LEACH-ERE. Initially, in the LEACH algorithm, the node death percentage rate slowly increased up to 500 rounds, but thereafter there was a sharp drop from 1400 rounds onwards, and all 200 nodes (100%) died before reaching 2200 rounds. In the case of the ANFCA, about 15% more nodes were still alive compared with the LEACH, and 5% of nodes were still alive compared with the LEACH-ERE after completing 2200 rounds, respectively. The rate of node death for the ANFCA was very slow compared to the state-of-the-art algorithms. It is because the proposed algorithm uses a supervised learning approach for the membership function, which is responsible for updating the membership weight function and lowering the energy consumption rate.

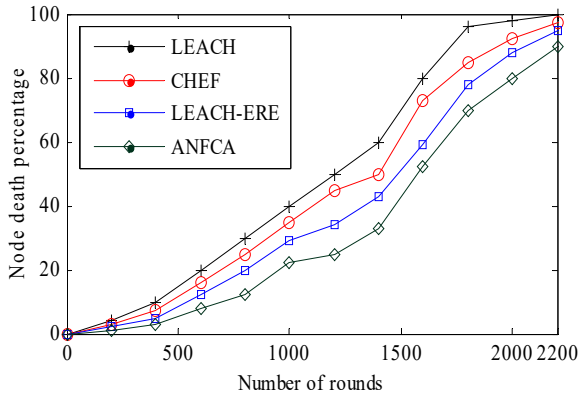

Figure 7. Node death percentages over the rounds.

Table 3 shows the comparative view of the metrics FND, HND, and LND for the proposed algorithm ANFCA and all of the state-of-the-art algorithms with respect to rounds. Figure 8 shows a comparative view of the death percentages' connections with FND, HND, and LND for LEACH, CHEF, LEACH-ERE, and ANFCA. It was observed that FND for LEACH was around the 96th round, FND occurred for ANFCA at the 260th round, which was almost two and half times more than that of LEACH, and the last node died at 1970 rounds for LEACH, whereas LND occurred for ANFCA at the 2310th round. Figure 8 and Table 3 show that the proposed algorithm did far better than the state-of-the-art algorithms, and that the lifetime of the network was enhanced because of the lower death rate of the nodes.

Table 3. Node death rate percentages up to 2500 rounds.

Death Percentage (%)	LEACH	CHEF	LEACH-ERE	ANFCA
FND	96	150	205	260
20	600	827	1107	1224
40	934	1223	1536	1707
HND	1167	1400	1665	1810
60	1386	1631	1885	1972
80	1600	1795	1994	2206
LND	1970	2056	2140	2310

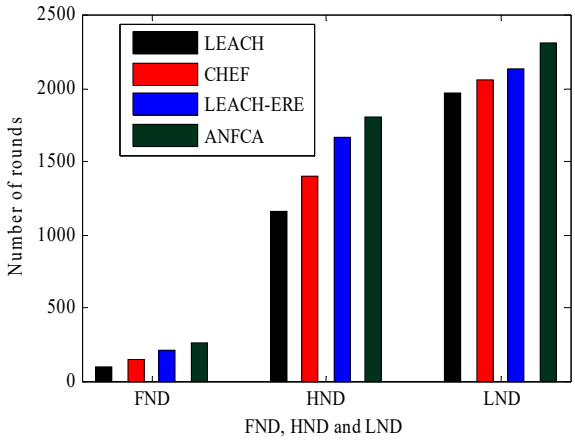

Figure 8. FND, HND, and LND results over the rounds.

4.2.2. Energy Expenditure over Rounds

In this simulation, we show the comparative study of energy expenditure across LEACH, CHEF, LEACH-ERE, and ANFCA. Figure 9 depicts the average residual energy versus the number of rounds for the ANFCA and the state-of-the-art algorithms. Initially, all the sensor nodes had equal energy at 2 joules. The LEACH, CHEF, and LEACH-ERE lost almost equal amounts of energy at 425 rounds, and around 1.72 joule of the average residual energy was remaining out of the initial 2 joules. The energy consumption of the nodes was calculated with the help of Equation (1). The ANFCA outperformed compared to the state-of-the-art algorithms; at the same point (425 rounds), the residual energy of the nodes was approximately 1.86 joule. As the number of rounds increased, LEACH performed the worst among the other algorithms, and all the remaining energy of the nodes was exhausted near 1800 rounds. The CHEF and LEACH-ERE showed better performance than LEACH, in terms of energy usage, with about 11% (up to 2000 rounds) and 20% (up to 2200 rounds), respectively. Overall, in this simulation the proposed algorithm ANFCA did far better than all the other algorithms. The ANFCA ran up to 2480 rounds, and the average remaining residual energy of the nodes was still 0.45 joule.

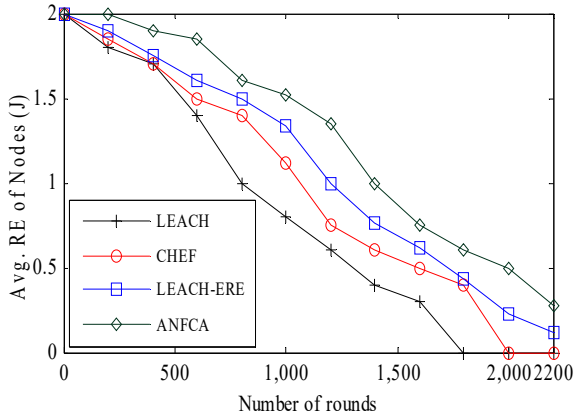

Figure 9. Avgerage residual energy over the rounds.

Figure 10 depicts the average energy consumption versus number of rounds for the ANFCA and the other algorithms. It was observed that, initially, all four algorithms—LEACH, CHEF, LEACH-ERE, and ANFCA—followed the same curvature and consumed almost an equal amount of energy up to 455 rounds, around 0.25 joule. Yet, the ANFCA consumed only 1.67 joule out of 2 joules up to 2200 rounds. In fact, as there was growth in the number of rounds, the LEACH consumed energy much faster than other algorithms because of the probabilistic selection cluster head method and because it does not include the residual energy parameter, whereas CHEF, LEACH-ERE, and ANFCA include fuzzy logic to select a cluster head. The CHEF consumed more energy towards increasing the number of rounds compared with the LEACH-ERE, whereas the proposed algorithm ANFCA showed that the rate of consuming energy by nodes was uniform until the last node death. The ANFCA consumed 10%, 15%, and 40% less energy than LEACH-ERE, CHEF, and LEACH, respectively. This is because cluster head selection is done initially with the AFLIS model, and thereafter it is refined through the selected cluster head ANFIS model. Thus, overall, the ANFCA appears to be energy-efficient, which ultimately enhances the network's lifetime.

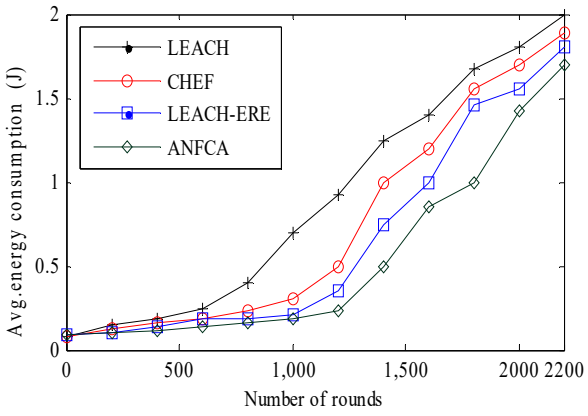

Figure 10. Avgerage energy consumed by nodes over the rounds.

4.2.3. Standard Deviation of Residual Energy

Uniform consumption of energy is highly desirable for load balancing among the sensor nodes which increases the lifetime of the networks. Therefore, we examined the standard deviation of residual energy for all the nodes in the networks and show the variation around the rounds as well as the diaspora from the mean. The energy dissipated by the cluster head and member node per cycle "c" (rounds) was evaluated. The energy consumption by cluster head is expressed as

$$E^c_{dst}(h) = \begin{cases} (x_n - 1)mE_{elect} + x_n mE_{da} + mE_{elect} + m\varepsilon_{mpf} l^4_{h\ to\ BS} & , \quad h\ \epsilon\ CH \\ mE_{elect} + m\varepsilon_{fsp} l^2_{h\ to\ BS} & , \quad h\ \epsilon\ non - CH \end{cases} \tag{13}$$

where x_n represents the total number of sensor nodes that are actually connected to the cluster head as well as the cluster head node, h is used to represent the nodes, and m is the m-bit data. The average (mean) dissipated energy for a cycle can be computed as

$$u(E_{dst}) = \frac{\sum_{h\ \epsilon\ \mathrm{N}} E^c_{dst}(h)}{N} \tag{14}$$

The residual energy for the next cycle (c + 1) is calculated as

$$E^{c+1}_{res}(h) = E^c_{res}(h) - E^c_{dst}(h) \tag{15}$$

The average (mean) residual energy for next cycle is expressed as

$$u(E_{res}) = \frac{1}{N} \sum_{i\ \epsilon\ \mathrm{n}} E^c_{res}(h) \tag{16}$$

The standard deviation of residual energy is the square root of the variance of the residual energy, and is given by

$$\sigma(E_{resdiual}) = \sqrt{\frac{1}{N} \sum_{i\ \epsilon\ \mathrm{n}} [u(E_{res}) - E_{res}(h)]^2} \tag{17}$$

Figure 11 shows the standard deviation of residual energy versus the rounds for all of the algorithms considered in this simulation. The broader the area of standard deviation, the higher the value of a node's residual energy within one mean (that means that each node dissipates almost equal amounts of energy relatively). The LEACH showed a lower coverage of area among the other algorithms, which means that nodes in the LEACH method have variable amounts of energy dissipation. The CHEF showed much improvement over the LEACH by 27%, as 80% of nodes were within one mean (all 80% had almost equal amounts of residual energy). The LEACH-ERE and the ANFCA were closer to each other on basis of coverage; both the algorithms had coverage of 95% of total nodes. The ANFCA provided a little smoother graph over the LEACH-ERE. For example, as the ANFCA ran up to 2000 rounds, the graph progressed more smoothly. This is because the ANFCA balanced the load using a fuzzy neural system and fairly balanced the energy consumption among the sensor nodes.

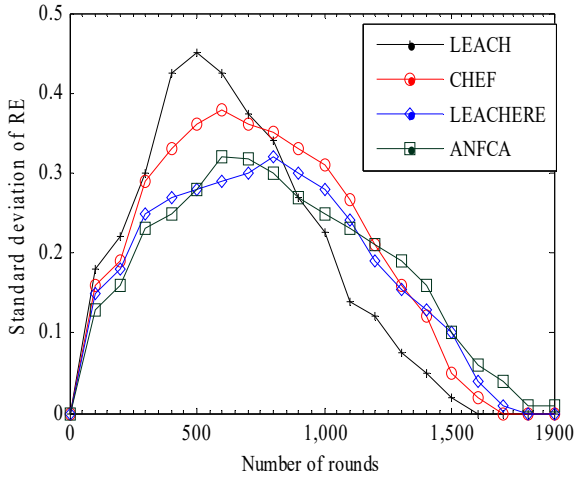

Figure 11. Standard deviation over rounds.

Figure 12 shows the alternative representation of the standard deviation of residual energy of functioning nodes for better visualization. As seen from the bar graph in Figure 12, when the number of functioning nodes was 40, the value of the standard deviation for LEACH was 0.045. This was higher than the other state-of-the-art algorithms, whereas the ANFCA had a standard deviation of residual energy equal to 0.027, which means that the load among the nodes was shared fairly in terms of energy consumption. Lowering the value of the standard deviation means a uniform distribution of the load from the mean. That means energy consumption of the load is evenly distributed among the sensor nodes. When the number of alive nodes was between 80 and 120, the values of the standard deviation for the LEACH-ERE was less than the ANFCA. This shows that for lower numbers of nodes, the LEACH-ERE distributed the load more fairly than the proposed algorithm ANFCA, but when the number of nodes increased between 160 and 200, the ANFCA did better than the state-of-the-art algorithms. Lowering the value of the standard deviation of energy means broadening the coverage area, which includes all the sensors nodes within one mean. This shows that the ANFCA has a better capability to distribute the load evenly among the sensor nodes. This is due to the fact that the membership function of residual energy is updated as a result of the role of the cluster head being changed every round among the other sensor nodes.

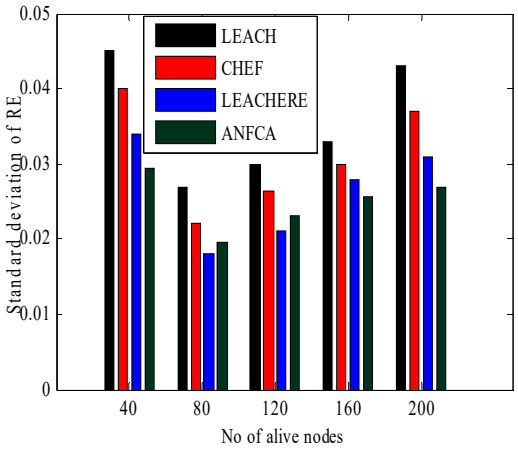

Figure 12. Standard deviation over alive nodes.

5. Conclusions and Future Perspectives

Cluster formation in an evenly and energy-efficient manner is of the utmost priority in a sensors-enabled IoT environment. In this paper, an energy-efficient neuro fuzzy hybrid approach for load balancing was proposed. The key components of the ANFCA are an adaptive neural network and a fuzzy logic inference system, which combined the use of residual energy, node distance to base station, and node density to select a cluster head. With the training data of ANFIS from the fuzzy logic system, the membership function and rules can be legitimately tuned to refine the cluster formation process according to the current situation of the network. The results proved that the proposed algorithm ANFCA formulated the evenly distributed clusters, as well as lowered the energy dissipation in the network, which directly improved the network's lifetime. The simulation results revealed that the proposed algorithm's performance was one step ahead of LEACH and the fuzzy-logic-based CHEF and LEACH-ERE with regards to cluster formation, energy dissipation, and network lifetime, because ANFCA combined the features of an artificial neural network learning strategy into fuzzy logic. The proposed algorithm could be useful in monitoring in the agriculture field. Our proposed work follows a centralized algorithm where all decisions are made by the base station only. In the future, we plan to extend this work to a distributed algorithm rather than a centralized algorithm, which is suitable for a scalable, fault-tolerant, cluster-based network, which considers RFID-enabled smart sensors with multiple gateways for IoT networks. These multiple gateways are loaded with heavy data, thus it must use distributed approaches to balance the load.

Author Contributions: Conceptualization, P.K.K.; Formal analysis, R.K.; Investigation, P.K.K.; Methodology, P.K.K.; Resources, V.K.; Supervision, S.K.; Writing—review and editing, U.D.

Funding: The research was supported by Jawaharlal Nehru University, New Delhi, India, under the grant DST-PURSE-II Programme.

Acknowledgments: The research was supported by Jawaharlal Nehru University, New Delhi, India, under the grant DST PURSE-II Programme.

Conflicts of Interest: The authors declare no conflict of interest.

References

1. Farhan, L.; Kharel, R.; Kaiwartya, O.; Hammoudeh, M.; Adebisi, B. Towards green computing for Internet of things: Energy oriented path and message scheduling approach. *Sustain. Cities Soc.* **2018**, *38*, 195–204. [CrossRef]
2. Aliyu, A.; Abdullah, A.H.; Kaiwartya, O.; Cao, Y.; Lloret, J.; Aslam, N.; Joda, U.M. Towards video streaming in IoT Environments: Vehicular communication perspective. *Comput. Commun.* **2018**, *118*, 93–119. [CrossRef]
3. Kaiwartya, O.; Abdullah, A.H.; Cao, Y.; Altameem, A.; Prasad, M.; Lin, C.T.; Liu, X. Internet of Vehicles: Motivation, Layered Architecture, Network Model, Challenges, and Future Aspects. *IEEE Access* **2016**, *4*, 5356–5373. [CrossRef]
4. Kumar, K.; Kumar, S.; Kaiwartya, O.; Cao, Y.; Lloret, J.; Aslam, N. Cross-Layer Energy Optimization for IoT Environments: Technical Advances and Opportunities. *Energies* **2017**, *10*, 2073. [CrossRef]
5. Verma, J.K.; Kumar, S.; Kaiwartya, O.; Cao, Y.; Lloret, J.; Katti, C.P.; Kharel, R. Enabling green computing in cloud environments: Network virtualization approach toward 5G support. *Trans. Emerg. Telecommun. Technol.* **2014**, *25*, 81–93. [CrossRef]
6. Kaiwartya, O.; Kumar, S.; Lobiyal, D.; Abdullah, A.; Hassan, A. Performance improvement in geographic routing for vehicular Ad Hoc networks. *Sensors* **2014**, *14*, 22342–22371. [CrossRef] [PubMed]
7. Ullah, F.; Abdullah, A.; Kaiwartya, O.; Arshad, M. Traffic priority-aware adaptive slot allocation for medium access control protocol in wireless body area network. *Computers* **2017**, *6*, 9. [CrossRef]
8. Cao, Y.; Yang, S.; Min, G.; Zhang, X.; Song, H.; Kaiwartya, O.; Aslam, N. A Cost-Efficient Communication Framework for Battery-Switch-Based Electric Vehicle Charging. *IEEE Commun. Mag.* **2017**, *55*, 162–169. [CrossRef]
9. Kaiwartya, O.; Kumar, S.; Abdullah, H.A. Analytical model of Deployment Methods for Application of Sensors in non-Hostile Environment. *Wireless Pers. Commun.* **2017**, *97*, 1517–1536. [CrossRef]
10. Kaiwartya, O.; Abdullah, A.H.; Cao, Y.; Raw, R.S.; Kumar, S.; Lobiyal, D.K.; Isnin, I.F.; Liu, X.; Shah, R.R. T-MQM: Testbed-Based Multi-Metric Quality Measurement of Sensor Deployment for Precision Agriculture—A Case Study. *IEEE Sens. J.* **2016**, *16*, 8649–8664. [CrossRef]
11. Dohare, U.; Lobiyal, D.K.; Kumar, S. Energy balanced model for lifetime maximization in randomly distributed wireless sensor networks. *Wireless Pers. Commun.* **2014**, *78*, 407–428. [CrossRef]
12. Aanchal, Kumar, S.; Kaiwartya, O.; Abdullah, A.H. Green computing for wireless sensor networks: Optimization and Huffman coding approach. *Peer-to-Peer Netw. Appl.* **2017**, *10*, 592–609. [CrossRef]
13. Liu, A.-F.; Zhang, P.-H.; Chen, Z.-G. Theoretical analysis of the lifetime and energy hole in cluster based wireless sensor networks. Journal of parallel and distributed computing. *J. Parallel Distrib. Comput.* **2011**, *71*, 1327–1355. [CrossRef]
14. Khasawneh, A.; Latiff, M.; Kaiwartya, O.; Chizari, H. Next forwarding node selection in underwater wireless sensor networks (UWSNs): Techniques and challenges. *Information* **2016**, *8*, 3. [CrossRef]
15. Khatri, A.; Kumar, S.; Kaiwartya, O.; Aslam, N.; Meena, N.; Abdullah, A.H. Towards green computing in wireless sensor networks: Controlled mobility–aided balanced tree approach. *Int. J. Commun. Syst.* **2017**, *31*, e3463. [CrossRef]
16. Zadeh, L.A. Fuzzy sets. *Inf. Control* **1965**, *8*, 338–353. [CrossRef]
17. Takagi, T.; Sugeno, M. Fuzzy identification of systems and its applications to' modeling and control. *IEEE Trans. Syst. Man Cybern.* **1985**, *15*, 116–132. [CrossRef]
18. McCulloch, W.S.; Pitts, W.H. A logical calculus of the ideas immanent in nervous activity. *Bull. Math. Biophys.* **1943**, *5*, 115–133. [CrossRef]

19. Rosenblatt, F. The Perceptron: A Probabilistic Model for Information Storage and Organization in the Brain. *Psychol. Rev.* **1958**, *65*, 386–408. [CrossRef]
20. Rosenblatt, F. *Principles of Neurodynamics; Perceptrons and the Theory of Brain Mechanisms*; Spartan Books: Washington, DC, USA, 1962. Available online: https://catalog.hathitrust.org/Record/000203591 (accessed on 21 February 2019).
21. Rosenblatt, F. *On the Convergence of Reinforcement Procedures in Simple Perceptron*; Cornell Aeronautical Laboratory: Buffalo, NY, USA, 1960.
22. Widrow, B.; Lehr, M.A. 30 years of adaptive neural networks: perceptron, Madaline, and back propagation. *Proc. IEEE* **1990**, *78*, 1415–1442. [CrossRef]
23. Widrow, B.; Winter, R.G.; Baxter, R.A. Layered neural nets for pattern recognition. *IEEE Trans. Acoust. Speech Signal Process.* **1988**, *36*, 1109–1118. [CrossRef]
24. Winter, R.; Widrow, B. MADALINE RULE II: A training algorithm for neural networks. In Proceedings of the IEEE 1988 International Conference on Neural Networks, San Diego, CA, USA, 24–27 July 1988; pp. 401–408.
25. Lin, C.-T.; Lee, C.S.G. Neural-network-based fuzzy logic control and decision system. *IEEE Trans. Comput.* **1991**, *40*, 1320–1336. [CrossRef]
26. Berenji, H.R.; Khedkar, P. Learning and tuning fuzzy logic controllers through reinforcements. *IEEE Trans. Neural Netw.* **1992**, *3*, 724–740. [CrossRef]
27. Nauck, D.; Kruse, R. Neuro-Fuzzy Systems for Function Approximation. *Fuzzy Sets Syst.* **1999**, *101*, 261–271. [CrossRef]
28. Lin, C.-T. FALCON: A fuzzy adaptive learning control network. In *NAFIPS/IFIS/NASA '94, Proceedings of the First International Joint Conference of The North American Fuzzy Information Processing Society Biannual Conference. The Industrial Fuzzy Control and Intellige, San Antonio, TX, USA, 18–21 December 1994*; IEEE: Piscataway, NJ, USA; pp. 228–232.
29. Tano, S.; Oyama, T.; Arnold, T. Deep Combination of Fuzzy Inference. *Fuzzy Sets Syst.* **1996**, *8*, 338–353.
30. Juang, C.F.; Lin, C.-T. An online self-constructing neural fuzzy inference network and its applications. *IEEE Trans. Fuzzy Syst.* **1998**, *6*, 12–32. [CrossRef]
31. Figueiredo, M.; Gomide, F. Design of fuzzy systems using neuro fuzzy networks. *IEEE Trans. Neural Netw.* **1999**, *10*, 815–827. [CrossRef]
32. Nauck, D.; Kalwon, F.; Kruse, R. *Foundation of Neuro-Fuzzy Systems*; John Wiley & Sons, Inc.: New York, NY, USA, 1997.
33. Jang, R. Neuro-Fuzzy Modeling: Architectures, Analysis and Application. Ph.D. Thesis, University of California, Berkley, CA, USA, July 1992.
34. Heinzelman, W.R.; Chandrakasan, A.; Balakrishnan, H. Energy efficient communication protocol for wireless micro sensor networks. In Proceedings of the 33rd Annual Hawaii International Conference on System Sciences, Maui, HI, USA, 7 January 2000; pp. 3005–3014.
35. Heinzelman, W.B.; Chandrakasan, A.P.; Balakrishnan, H. An application-specific protocol architecture for wireless micro sensor networks. *IEEE Trans. Wireless Commun.* **2002**, *1*, 660–670. [CrossRef]
36. Younis, O.; Fahmy, S. HEED: A Hybrid, Energy Efficient, Distributed clustering approach for Ad Hoc sensor networks. *IEEE Trans. Mobile Comput.* **2004**, *3*, 366–379. [CrossRef]
37. Lindsey, S.; Raghavendra, C.S. PEGASIS: Power efficient gathering in sensor information systems. In Proceedings of the IEEE Aerospace Conference, Big Sky, MT, USA, 9–16 March 2002; pp. 1125–1130.
38. Sampalli, S.; Riordan, D.; Gupta, I. Cluster-head election using fuzzy logic for wireless sensor networks. In Proceedings of the 3rd Annual Communication Networks and Services Research Conference, Halifax, NS, Canada, May 2005.
39. Kim, J.; Park, S.; Han, Y.; Chung, T. CHEF: Cluster head election mechanism using fuzzy logic in wireless sensor networks. In Proceedings of the 2008 10th International Conference on Advanced Communication Technology, Gangwon-Do, Korea, 17–20 February 2008; pp. 654–659.
40. Ran, G.; Zhang, H.; Gong, S. Improving on LEACH protocol of wireless sensor networks using fuzzy logic. *J. Inf. Comput. Sci.* **2010**, *7*, 767–775.
41. Lee, J.S.; Cheng, W.L. Fuzzy-Logic-Based Clustering Approach for Wireless Sensor Networks Using Energy Predication. *IEEE Sens. J.* **2012**, *12*, 2891–2897. [CrossRef]
42. Nayak, P.; Devulapalli, A. A Fuzzy Logic-Based Clustering Algorithm for WSN to Extend the Network Lifetime. *IEEE Sens. J.* **2016**, *16*, 137–144. [CrossRef]

43. Nayak, P.; Anurag, D.; Bhargavi, V.V.N.A. Fuzzy based method super cluster head election for wireless sensor network with mobile base station (FM-SCHM). In Proceedings of the 2nd International Conference Advance Computational Methodology, 2013; pp. 422–427.
44. Abidoye, A.P.; Obagbuwa, I.C. Models for integrating wireless sensor networks into the Internet of Things. *IET Wirel. Sens. Syst.* **2017**, *7*, 65–72. [CrossRef]
45. Li, Y.; Sun, Z.; Han, L.; Mei, N. Fuzzy Comprehensive Evaluation Method for Energy Management Systems Based on an Internet of Things. *IEEE Access* **2017**, *5*, 21312–21322. [CrossRef]
46. Kasana, R.; Kumar, S.; Kaiwartya, O.; Kharel, R.; Lloret, J.; Aslam, N.; Wang, T. Fuzzy-Based Channel Selection for Location Oriented Services in Multichannel VCPS Environments. *IEEE Internet Things J.* **2018**, *5*, 4642–4651. [CrossRef]
47. Hu, Q.; Wu, C.; Zhao, X.; Chen, X.; Ji, Y.; Yoshinaga, T. Vehicular Multi-Access Edge Computing With Licensed Sub-6 GHz, IEEE 802.11p and mmWave. *IEEE Access* **2018**, *6*, 1995–2004. [CrossRef]
48. Kaiwartya, O.; Abdullah, A.H.; Cao, Y.; Lloret, J.; Kumar, S.; Shah, R.R.; Prasad, M.; Prakash, S. Virtualization in wireless sensor networks: Fault tolerant embedding for internet of things. *IEEE Internet Things J.* **2018**, *5*, 571–580. [CrossRef]
49. Jang, J.S.R. ANFIS: adaptive-network-based fuzzy inference system. *IEEE Trans. Syst. Man Cybern.* **1993**, *23*, 665–685. [CrossRef]

© 2019 by the authors. Licensee MDPI, Basel, Switzerland. This article is an open access article distributed under the terms and conditions of the Creative Commons Attribution (CC BY) license (http://creativecommons.org/licenses/by/4.0/).

Identification of opinion leader in online social network using fuzzy trust system

Lokesh Jain
Department of Computer Science
Delhi Technological University, New Delhi-India
nsitlokesh.jain@gmail.com

Rahul Katarya
Department of Computer Science
Delhi Technological University, New Delhi-India
rahulkatarya@dtu.ac.in

Abstract - In today human life, a social network plays a significant role in the user's decision-making. In the social network, an opinion leader is a critical person who influences the behavior of the person with their own knowledge and skills. The major contribution of this paper is to recommend an advance approach to discover the opinion leader in the social network using fuzzy logic and trust generation model. In the first step, we evaluate the fuzzy trust rules based on the user's trust. In the next step, these fuzzy trust rules apply to the online social network and then the de-fuzzification process applied to find out the trust value for each user and at last, identify the top-N user according to their prominence value that directly used to obtain their trust value for each user. We demonstrate our approach on the synthesized dataset and show the result that is better than the standard Social network analysis measures with respect to accuracy, precision, F1-score, and recall.

Keywords— Fuzzy logic, online social network, opinion leader, trust model.

I. INTRODUCTION

In the current web scenario, social networking is an integral part of human life. The Social networking site provides the opportunity to interact with another unknown world of known things and human being. Now a day, these sites also provide the facility for the diffusion of the new product and merchandise. Opinion leader has the significant function in the diffusion of the new product. There is a significant role of an opinion leader behind the success of the product and invention [1]. Opinion leader also affected the consumer behavior and decision making by their own knowledge and experience about a particular product. Sometimes, People interact with each in this virtual world and may betray for others. Hence, People need to follow only those persons who are trusted and authenticated opinion leader [2], [3].

According to Day et al. [4], an Opinion Leader is a person or set of persons having more influence on the customer's adoption process and decision making. The main idea of opinion leader was introduced by Katz and Lazarsfeld's [5] in their seminar in 1940 and 1950. According to them, identification of opinion leader is a two-step procedure, In the first step, Opinion leader analyzes, examine and understand the end user's requirements and in the second step, Opinion leader derived their own opinion on the basis of the first step incorporate with their own knowledge and skills.

One of the prevalent obscurities with the social network is trustworthiness. A system is not capable to gain credibility without trust. In any system, a trust can be defined as a belief or expectation that a person expects from others. In social networking, it is very difficult to identify the trustworthy person. In a complex situation, trust can also be the basis for critical decision-making system. In the online social network, trust plays an important, remarkable and valuable role to influence the behavior of another person. There are various areas, such as decision making, marketing, banking, credit rating, online community, etc., in which trust has a great implication.

The Growth of Online community is more and more popular due to an improvement of the Web. Nowadays most of the persons connected with numerous social network groups such as Facebook, Twitter, Google+, Flixster, and many others to share their views and ideas. These online social networking sites grant a place for a person to contribute their views about any products, movies, politics, and celebrity, etc. sometimes the online public opinion is closely related with very sensitive and contradictory. All the registered user in this social network sites is not necessarily being trusted and reliable [6]. Therefore, it is very critical to find out the trusted and reliable ideas for these groups. Opinion leader plays an important role to boost up the communication among users and enhance the probability to exchange information [7].

In any system, apparently, there may be both an opinion leader and other innovative people who are in competition with the changes. These other innovation people either may help to promote the ideas suggested by opinion leader or may take stand against them to diffuse their own idea.

In general, when opinion leader compared with another person, we state that:

1. An Opinion leader is observable to peripheral communication in all forms.
2. An Opinion leader is a more sophisticated and deep thinker.
3. Opinion leader has a somewhat higher social status and higher competence level.
4. An Opinion leader is more advanced and groundbreaking.

But one of the most unresolved characteristics of opinion leaders is that they have an exclusive and exceptional reputation in their communication structure of the system. They behave like a bull's eye and exist in the middle of interpersonal communication networks. A communication network consists of interrelated persons and all of these persons are coupled with decorative flows of information. The existence of the opinion leader in interpersonal networks treated as a social model whose innovative actions are copied by numerous other followers in the system [8].

978-1-5386-6678-4/18/$31.00 ©2018 IEEE

Hence, in this paper, we attempted to find out the answer by following queries:

1. *A fuzzy logic-based trust model has been announced in associated with the online social network.*
2. *A new attribute has been introduced, called 'Prominence' to compute the opinion leader.*
3. *The whole performance of the projected model is improved as compared to the other standard measures with respect to accuracy, precision, recall, and F1-score.*

The whole paper constitutes as follow: in the first segment, we will confer the various approaches and literature survey to find out the opinion leader in a social network. In the next segment, we will discuss our proposed methodology, a fuzzy model, and fuzzy rules. We will also discuss the fuzzy membership for each and every possible relationship exists between the users. In the next segment, we will present the experimental setup and result in the synthesized dataset and compared the results with the other social network measures. In the final segment, we will confer the conclusion, limitations and future scope of the proposed approach.

II. Related Work

The current segment includes the diverse approaches that have been proposed to classify opinion leaders in the social network. A systematic study has been carried out to find out the opinion leader. Vincent et al. [3], proposed a model, that describe null or weak results with the help of game-theoretic outlook on the relationship of opinion leader-followers. The proposed prototype aggregates social network, word-of-mouth communication, customer heterogeneity, and time predilection.

R. van der Merwe et al. [9] proposed a hypothesis to linking of the opinion leader to social network and test the hypothesis that opinion leadership is monomorphic (topic specific) by screening that domain-specific opinion leadership is powerfully related to universal opinion leadership. But this approach is not so useful for all type of domain-specific social network due to lack of understanding of attributes.

Freimut B et al. [10] proposed a concept based on text mining and social networking in which the user identified as opinion leader based on the quality of the text of the comment that they post on social networking site. But this approach is not able to handle all types of text due to various languages semantics. Y. Cho et al. [11] design a statistical method in which opinion leaders are acknowledged based on diffusion rapidity and more sociality. They also suggested that the discovering of opinion leader is also depends upon the initial no of adopters, the category of a social network, and variety of modernism.

M. Zubair Shafiq et al. [12] proposed a novel model, known as a Longitudinal User Centered Influence (LUCI) model. In this model, user collaboration data used as input and on the basis of this data, divide the users into four clusters which are classified according to the user interaction characteristic. Samad Mohammad Aghdam et al. [13] designed a model that applies the user's trust relationship with the other users and estimates the aggregate trust value of the all the users and choose those users as opinion leader having the maximum aggregate trust value among all of them.

Seyed Ali et al. [14] proposed a model in which the computation of item matrix sparseness is done using MIPFGWC algorithm and the sparseness later uses to find opinion leader. In this paper author also proposed that opinion leader can also help to solve the cold start problem of the recommended system.

Abolfazl Aleahmad et al.[15] projected an algorithm called OLfinder, that will identify the main subject of argument in the domain and calculate the competency and popularity score for each user and on the basis of these parameters, find the list of an opinion leader.

Kim et al. [16] anticipated an extended the Advogato trust metric that is used for the identification of respectable and users for every particular user as well as on the bases of capacity propagation, they also identified the ordered set of reliable and unreliable users. The unreliable users are prohibited to reach the personal network. This work can further be extended to find that reliable person, considered as an opinion leader, having a higher degree of trust. Opinion leader can also be considered as whisperer of word-of-mouth information, that only depends upon the degree of trust in the virtual internet environment[17].

B Huang et al. [18], anticipated a dynamic rank technique to find the opinion leader in the remarks of Chinese Weibo news. Initially find the most influential remarks chosen from the group of remarks and then discover the opinion leader based on three level mapping structure.

Therefore, in the social network, Trust is one of the major factors that characterized the significance and importance of opinion leader. Once the opinion leader gains the trust of the users, it is very easy to diffuse the new product or service in digital marketing as well [19].

Lots of studies carried out to discover the opinion leader in the social network but only a few approaches used the concept of trust. In the proposed work, we not only used the concept of trust but fuzzy logic also to identify the opinion leader.

III. Background

The formation of a social network can be well thought-out as an assortment of nodes and edges. The Social network can be mocked-up as un-directed graph $G = (V, E)$ where V implies the collection of nodes indicating actors or user and E implies the collection of edges indicating the relationship between the actors [20]. In realism, people follow those persons having high trust rather than others feedback. Therefore, trust is major factors, which obviously improve the probability to find out the accurate and correct opinion leader in the online social network. We proposed a narrative approach which uses the fuzzy trust model to find out the opinion leader.

A. Evaluation of trust

In social networking, trust is a foremost element in the service-oriented situation. It is also helpful for decision making and for the diffusion of new products on the social networking platform. Most of the approach [21], [22] uses the various statistical, probabilistic, classification, heuristic, and the nature-inspired algorithm is proposed to compute the trust but usually, it is extremely rigid to figure the exact discrete

value of trust. According to our proposed approach, trust is not a discrete value, it is a fuzzy element and the value of trust should be obtained from the various surveys, interview, and personal discussion. In this paper, we obtained trust from various sources like an informal discussion, personal interview, survey and group discussion with various friends, relatives, colleagues, and acquaintance. Although, we only consider only three values as strong, moderate, and low for trust based on a person's opinion as shown in Fig. 1.

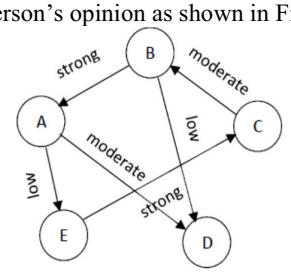

Fig. 1 trust representation between the users in a social network

B. Fuzzy rule and fuzzy set

The concept of Fuzzy logic is analogous to the individual sense, perception, and implication procedure. The tradition control strategy theory is a point-to-point supervisor that does not include any partial membership of an element in the set while the theory of fuzzy logic regulator is a range-to-point or range-to-range control that also includes the partial membership of an element in the set. The impression of fuzzy logic was developed by L. A. Zadeh at Berkeley in 1965 [23], [24]. According to Zadeh, an element can have a fractional degree in the fuzzy set. If an element *i* belongs to a set S, then it can be represented in Eq. 3.

$$\mu_S(i) \in [0,1] \quad (1)$$

And the membership of element i in set S can be represented as in Eq. 4.

$$A = (i, \mu_S(i) \mid i \in X) \quad (2)$$

Where X represents the universe of discourse.

Furthermore, the fuzzy rules can be defined in the form of if then else form. For example, consider the following rule:

R: IF A is HIGH and B is Low THEN C is MEDIUM.

In the above rule, HIGH, LOW, and MEDIUM are linguistic variables defined by a fuzzy set on the domain A and B (universe of discourse) and for each fuzzy set.

IV. Proposed Methodology

In the proposed system, initially we derive hypothesis to implement our algorithm as follows:

H1: all the users are categorized into two classes: trusted and untrusted.

H2: all the users have a significant amount of information regarding other users in the network.

H3: there are only two types of relation friend and foe exists in the network.

The pseudo code of the proposed algorithm is as follow:

Algorithm: Fuzzy Trust Model based Opinion Leader (FTMOL)

Input: total n no of users,

Output: prominence value for each user

Steps:

1. Compute the clustering coefficient for each user.
2. Compute the reputation of each user using Eq. (3).
3. Compute the degree of trust for each user using Eq. (4).
4. Apply the fuzzy rules to compute the prominence value for each user with de-fuzzification using centroid methods.
5. Rank the user according to their prominence value.

The flow chart of the proposed model can be shown in Fig. 2.

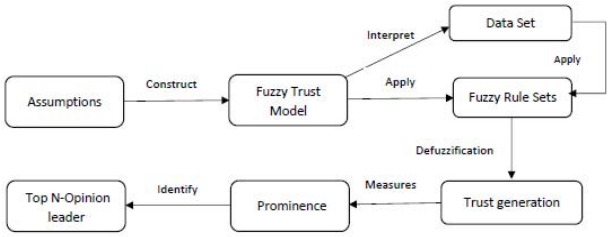

Fig. 2 Proposed methodology flow chart

A. Fuzzy trust model

Initially, we design some hypothesis and assumptions. Next, we design the fuzzy trust model in which we define the trust relationship between the users. For figure out the trust for a user, initially, we identify the reputation of the user. The reputation r of the user is based on clustering coefficient C(x) and centrality which can be computed using Eq. 3.

$$r = \frac{\{\sqrt[2]{(CC*BC)}\}}{DC} - (1 - C(x)) \quad (3)$$

The clustering coefficient of a node depends upon the triadic closure and strong ties or weak ties with the other nodes. The clustering coefficient of a node is computed as:

$$C(x) = \frac{\text{actual no of relationships among neighbors}}{\text{total no of possible relationships among neighbors}}$$

Trust between the users may be unidirectional or may be bidirectional. The degree of trust T_{xy} between the users is represented using Eq. 4.

$$T_{xy} = f(d_{xy}, d_{yx}, d^z_{xy}, d^z_{yx}, r_x, r_y) \quad (4)$$

Where d_{xy} is the degree of trust gained by user x on user y, d_{yx} is the degree of trust gained by user y on user x, d^z_{xy} is the degree of trust that is supposed to be suggested by user x to user y on user z, d^z_{yx} is the degree of trust that is supposed to be suggested by user y to user x on user z. r_x and r_y are the reputations of user x and user y respectively. The trust can be direct, indirect, and recommended trust. The overall description can be shown in Fig. 3.

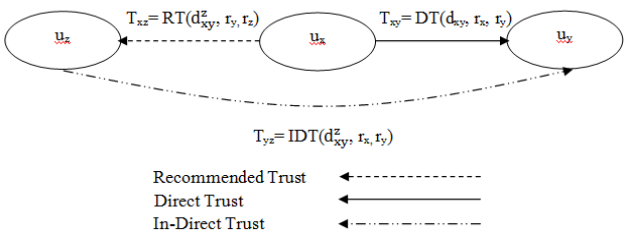

Fig. 3 Trust Model

Whenever the user established the degree of trust, they can set their own linguistics relationship with the other users because it is not possible to prove the trust by some discrete value. Although, we have calculated the degree of trust for each user, yet it is only used for signifying the preceding social status and trust relationship with the other users in the social network; because, if a person has some prior information about the other person, it may be easier to derive their own interpretation about a person or community in the network. The structure of the fuzzy trust model is shown in Fig 4.

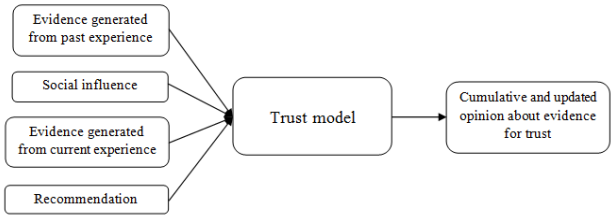

Fig. 4 fuzzy trust model

In this model, initially, user gathered information about the particular user from the real world either directly or indirectly through other's recommendation, past or current experience, and social influence. These inputs are analyzed by the trust model and produce some evidence for obtaining the trust. Now, we also defined fuzzy rules for each fuzzy relation. In the social network, usually, two types of relationship exist between a pair of the user as a friend and foe. But ordinarily, in the social network, no one is a true friend or foe until the trust is considered. Sometimes, we also refer the opinion of the anonymous user during the online review community or in recommendation system.

B. Fuzzy Set for the proposed model

Now, on the basis of the above assumptions and discussion, we have defined the four fuzzy sets: friendship, foe, trust, and opinion follow. Friendship can be strong, moderate and low and the membership of an element can be represented using Eq. 5:

$$\mu_S(i) = \begin{cases} 0\,, & x \le a \\ 2\left(\frac{x-a}{b-a}\right)^2, & a \le x < \frac{a+b}{2} \\ 1-2\left(\frac{x-b}{b-a}\right)^2, & \frac{a+b}{2} \le x \le b \\ 1-2\left(\frac{x-c}{d-c}\right)^2, & c \le x \le \frac{c+d}{2} \\ 2\left(\frac{x-d}{d-c}\right)^2, & \frac{c+d}{2} \le x \le d \\ 0, & x \ge d \end{cases} \quad (5)$$

Here, the parameters a and d are the bottom of the curve, while b and c are the shoulders of the curve.

Similarly, Foe can be strong, moderate and less and the membership of an element can be represented using Eq. 6:

$$\mu_S(i) = \begin{cases} 0 & , \quad x \le a \\ \frac{x-a}{b-a} & , \quad a \le x \le b \\ 1 & , \quad b \le x < c \\ \frac{d-x}{d-c} & , \quad c \le x \le d \\ 0 & , \quad x \ge d \end{cases} \quad (6)$$

Here, the parameters a and d are the lower and upper limit, respectively. Parameters b and c are a lower support and an upper support respectively, and a < b < c < d.

Trust can be low, medium and high and the membership of an element is representing in Eq. 7:

$$\mu_S(i) = \begin{cases} 0 & , \quad x \le a \\ \frac{x-a}{b-a} & , \quad a \le x \le b \\ \frac{c-x}{c-b} & , \quad b \le x \le c \\ 0 & , \quad x \ge c \end{cases} \quad (7)$$

Here, parameter a and c are the bottom left and right limit, respectively and b is a peak real value such that a<b<c.

Similarly, follow can be strong, moderate and less and the membership of an element can be represented using Eq. 8.

$$\mu_S(i) = \begin{cases} 0 & , \quad x \le a \\ 2\left(\frac{x-a}{b-a}\right)^2 & , \quad a \le x \le \frac{a+b}{2} \\ 1-2\left(\frac{x-b}{b-a}\right)^2 & , \quad \frac{a+b}{2} \le x \le b \\ 0 & , \quad x \ge b \end{cases} \quad (8)$$

Where, the parameters a and b are the lower and upper limit, respectively.

C. Fuzzy Rules

From the above discussion, we will identify the following fuzzy rule for the social network that can be represented with the help of Table 1and Table II:

Table I
RULES FOR FRIENDSHIP, TRUST, AND OPINION FOLLOW

Friendship \ Trust	Strong	Moderate	Low
High	High	High	Moderate
Medium	High	Moderate	Less
Low	Moderate	Less	Less

TABLE II
RULES FOR FOE, TRUST AND OPINION FOLLOW

foe \ Trust	Strong	Medium	Low
High	NA	NA	Less
Medium	NA	NA	Less
Low	NA	NA	NA

For example, one of the rules that we can infer from the above table is:

IF friendship is MODERATE and trust is STRONG, then follow the opinion of a person is HIGH.

Now, at last, apply the de-fuzzification process to find out the prominence of each user in the social network. In the social network, Prominence of a person can be denied as the prestige that can be evaluated on the basis of trust. Whenever the trust for each person has computed according to the mentioned fuzzy rules, apply the de-fuzzification process to find the discrete value of trust for each person. For the de-fuzzification purpose, we use the classical centroid method that can be computed using the midpoint of gravity of the fuzzy set. The centroid of the fuzzy set can be computed using Eq. 9.

$$\bar{\bar{C}} = \frac{\int_{i=1}^{i=n} i * \mu_S(i)}{\int_{i=1}^{i=n} \mu_S(i)} \quad (9)$$

Here n is the total no of users in the network.

Finally, ranked the user according to their prominence that can be calculated using the value obtained after the de-fuzzification process as shown in Eq. 10.

$$P \; \alpha \; |\bar{\bar{C}}| \quad (10)$$

So, prominence of a user is one of the aspects to find out the opinion leader in the social network.

V. EXPERIMENTAL RESULT

For implementing the proposed approach, we use the synthesized data set that indicates the petite view of the world. The ties between the users are chosen on the basis of similarity. Although, the users with the same type of behavior or community, have more tendency to link together in a rapid manner. This dataset represents a network of friends and an association between them. The dataset has the total of 3182 nodes and total 8621 edges that can be drawn using Gephi software [25] as shown in Fig 5. In this figure, the different colors specify the different community that they belong to on the basis of their modularity. There are only 2 kinds of relation exists in the dataset as friend and foe. There are total 4 columns user_id1, user_id2, type_of_relation, and type_of_trust exists in the dataset.

Fig. 5 synthesized social network structure

Now we apply the proposed fuzzy trust model on our dataset and calculate the prominence value for each user. When we calculated the prominence value for each user then, find the top -10 opinion leader as shown in Table III.

TABLE III
TOP-10 OPINION LEADER ACCORDING TO THEIR PROMINENCE VALUES

Rank	Node id	Degree of Trust (T_{xy})	Prominence
1	108	0.85494	0.621012
2	1685	0.85322	0.619457
3	98	0.85125	0.617872
4	2098	0.84228	0.604912
5	390	0.84013	0.598897
6	720	0.83796	0.590068
7	894	0.83242	0.582458
8	1963	0.82647	0.551254
9	3022	0.82019	0.550078
10	2725	0.81724	0.550005

Furthermore, we compare our approach with the other SNA standard measures; it gives the best result with respect to the rate of convergences shown in Fig.6.

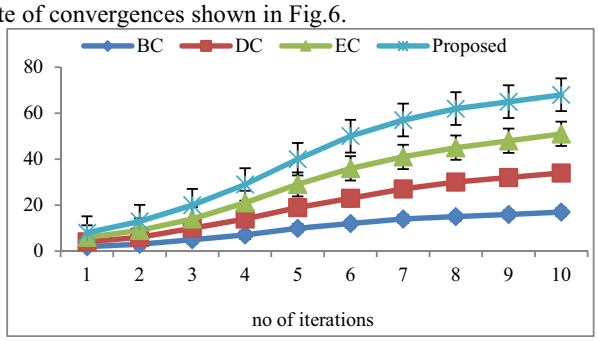

Fig. 6 Rate of convergence of BC, DC, EC, and Proposed approach

Where EC, BC, and DC are Eigenvalue centrality, betweenness centrality, and closeness centrality respectively.

These measures are used to compute the centrality of a node in the social network [26]. From the mentioned analysis, we can say that our proposed method is better in term of convergence with other SNA measures.

For measuring the accuracy of an algorithm, there are 3 main performance measures are precision, recall, and F1-score. These measures not only compute the accuracy of the

model but also govern how virtuous our model is [27]. The complexity of the proposed algorithm depends upon the total no of users, clustering coefficient, reputation of the users, and compute the prominence value. Now, we compared the precision, recall, and F_1-score of our proposed model with the other standard SNA measures and indicate the result that the proposed approach is better than the other measures as shown in Table IV and Fig. 7.

TABLE IV
COMPARISON OF PRECISION, RECALL, F_1-SCORE, AND ACCURACY

Measures	Precision	Recall	F1-score	Accuracy
EC	0.94382	0.94382	0.94382	0.918
DC	0.953488	0.942529	0.947977	0.925
BC	0.965116	0.954023	0.959538	0.934
Proposed	0.967033	0.967033	0.967033	0.953

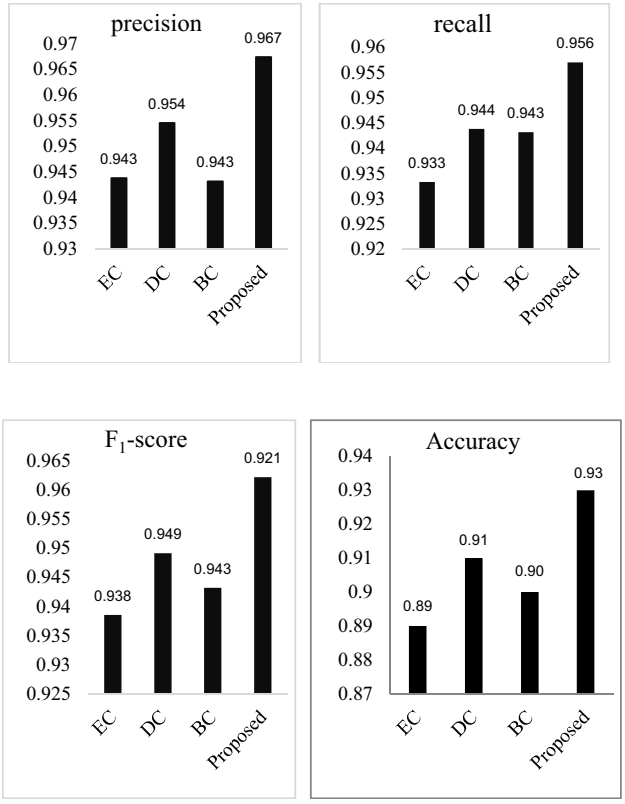

Fig.7 Comparison of EC, DC, BC and proposed model w.r.t precision, recall, F1-score and accuracy

Further, we compared the total execution time required by the proposed algorithm with the other SNA measures as shown in Fig. 8. Institutively, The time complexity in social network merely depends upon the fact that how promptly user share information and link to each other [28]. In the proposed model, we consider the relationship on the basis of fuzzy logic hence; our approach takes lesser total time with respect to other SNA measures because only those users considered having the high prominence value.

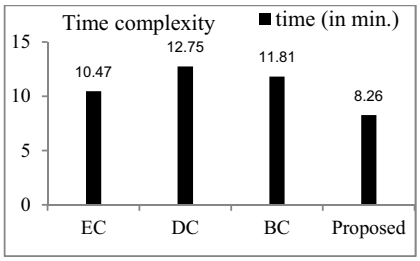

Fig. 8 Comparison over the time taken to identify opinion leader based on Table III

VI. CONCLUSION AND FUTURE SCOPE

In this paper, we have presented a new approach to discovering the opinion leader in the social network using the fuzzy logic trust system. Although, it is very tough to find out the opinion leader, because there is no standard method present to discover it, yet we have attempted to find the opinion leader. We can also use some other factor, such as total no of tweets, response time, centrality, PageRank with the proposed model to find the opinion leader in the most precise way. Besides these factors, we can also practice some naturally meta-heuristic algorithms such as PSO, ant colony, cuckoo search and many more [30]–[32].

One of the real world applications of the proposed approach is that it is used to resolve the cold start problem in the recommended system. Whenever an organization manufactures and launches its new product in the market, it is very harsh to gain the user trust on that product because lots of products of the same quality are already available in the market. But if some of the opinion leaders impose this product with their positive feedback, it may be possible to diffuse the product easily through cascading behavior. So the proposed model is awfully beneficial for e-commerce environment.

The other applicability of this proposed model is that it can also be used for improving cascading behavior in the social network. Cascading behavior in the network also depends upon the user's degree of trust. In this model, if a user having the higher degree of trust, it may be possible that the user may get the high pay off by trusting on most trustworthy user although the user ha lesser number of out-degree in the network.

One of the restrictions of this paper is that we have proposed an algorithm for the static social network. In the future, we will attempt to implement the model on the dynamic social network [33], [34], because nowadays, the relation between the user changes frequently.

.

REFERENCES

[1] A. E. Reppel, I. Szmigin, and T. Gruber, "The iPod phenomenon: Identifying a market leader's secrets through qualitative marketing research," *J. Prod. Brand Manag.*, 2006.

[2] D. K. Kim, "PhD Thesis - Identifying Opinion Leaders by Using Social Network Analysis: A Synthesis of Opinion Leadership Data Collection Methods and Instruments," no. August, p. 220, 2007.

[3] V. Mak, "The Emergence of Opinion Leaders in Social Networks," *SSRN Electron. J.*, 2008.

[4] R. Dye, "The buzz on buzz.," *Harv. Bus. Rev.*, 2000.

[5] D. Gold, E. Katz, P. F. Lazarsfeld, and E. Roper, "Personal

Influence: The Part Played by People in the Flow of Mass Communications.," *Am. Sociol. Rev.*, 1956.
[6] C. Fernandez-Gago, I. Agudo, and J. Lopez, "Building trust from context similarity measures," *Comput. Stand. Interfaces*, 2014.
[7] J. Turcotte, C. York, J. Irving, R. M. Scholl, and R. J. Pingree, "News Recommendations from Social Media Opinion Leaders: Effects on Media Trust and Information Seeking," *J. Comput. Commun.*, 2015.
[8] K. K. Chan and S. Misra, "Characteristics of the opinion leader: A new dimension," *J. Advert.*, 1990.
[9] G. van der Merwe, R.; van Heerden, "Finding and utilizing opinion leaders: Social networks and the power of relationships," *outh African J. Bus. Manag.*, 2009.
[10] F. Bodendorf and C. Kaiser, "Detecting opinion leaders and trends in online communities," *4th Int. Conf. Digit. Soc. ICDS 2010, Incl. CYBERLAWS 2010 1st Int. Conf. Tech. Leg. Asp. e-Society*, pp. 124–129, 2010.
[11] Y. Cho, J. Hwang, D. Lee, J. Wang, and D. Lee, "Identification of effective opinion leaders in the diffusion of technological innovation: A social network approach," *Technol. Forecast. Soc. Change*, 2012.
[12] M. Z. Shafiq, M. U. Ilyas, A. X. Liu, and H. Radha, "Identifying leaders and followers in online social networks," *IEEE J. Sel. Areas Commun.*, vol. 31, no. 9, pp. 618–628, 2013.
[13] S. M. Aghdam and N. Jafari Navimipour, "Opinion leaders selection in the social networks based on trust relationships propagation," *Karbala Int. J. Mod. Sci.*, vol. 2, no. 2, pp. 88–97, 2016.
[14] S. A. Mohammadi and A. Andalib, "Using the opinion leaders in social networks to improve the cold start challenge in recommender systems," *2017 3rd Int. Conf. Web Res. ICWR 2017*, pp. 62–66, 2017.
[15] A. Aleahmad, P. Karisani, M. Rahgozar, and F. Oroumchian, "OLFinder: Finding opinion leaders in online social networks," *J. Inf. Sci.*, 2016.
[16] Y. S. Kim and V. L. Tran, "Assessing the ripple effects of online opinion leaders with trust and distrust metrics," *Expert Syst. Appl.*, 2013.
[17] E. Dichter, "How Word of Mouth Advertising Works," *Harv. Bus. Rev.*, 1966.
[18] B. Huang, G. Yu, and H. R. Karimi, "The finding and dynamic detection of opinion leaders in social network," *Math. Probl. Eng.*, vol. 2014, pp. 1–8, 2014.
[19] W. Sherchan, S. Nepal, and C. Paris, "A survey of trust in social networks," *ACM Comput. Surv.*, 2013.
[20] J. Scott, "Social network analysis: A handbook," *SAGE Publications*. 2000.
[21] S. E. Chang, A. Y. Liu, and W. C. Shen, "User trust in social networking services: A comparison of Facebook and LinkedIn," *Comput. Human Behav.*, vol. 69, pp. 207–217, 2017.
[22] Z. Yan, S. Member, and M. Wang, "on Two-Dimensional Trust Levels," *IEEE Syst. J.*, no. 99, pp. 1–12, 2014.
[23] L. A. Zadeh, "Fuzzy logic," *Computer (Long. Beach. Calif).*, 1988.
[24] L. A. Zadeh, "Is there a need for fuzzy logic?," *Inf. Sci. (Ny).*, 2008.
[25] Gephi.org, "Gephi - The Open Graph Viz Platform," *Gephi*, 2017. .
[26] L. C. Freeman, "Centrality in Social Networks," *Soc. Networks*, 1978.
[27] D. M. W. POWERS, "Evaluation: From Precision, Recall and F-Measure To Roc, Informedness, Markedness & Correlation," *J. Mach. Learn. Technol.*, 2011.
[28] G. Kossinets and D. J. Watts, "Empirical analysis of an evolving social network," *Science (80-.).*, 2006.
[29] M. McPherson, L. Smith-Lovin, and J. M. Cook, "Birds of a Feather: Homophily in Social Networks," *Annu. Rev. Sociol.*, 2001.
[30] X.-S. Yang, *Nature-Inspired Metaheuristic Algorithms*. 2010.
[31] M. Mafarja and S. Mirjalili, "Whale optimization approaches for wrapper feature selection," *Appl. Soft Comput. J.*, 2018.
[32] S. Mirjalili and A. Lewis, "The Whale Optimization Algorithm," *Adv. Eng. Softw.*, 2016.
[33] Y. Chen, L. Hui, C. I. Wu, H. Liu, and S. Chen, "Opinion Leaders Discovery in Dynamic Social Network," 2017.
[34] B. Skyrms and R. Pemantle, "A dynamic model of social network formation.," *Proc. Natl. Acad. Sci. U. S. A.*, 2000.

This article has been accepted for publication in a future issue of this journal, but has not been fully edited. Content may change prior to final publication. Citation information: DOI 10.1109/TIA.2019.2913618, IEEE Transactions on Industry Applications

Implementation of 3L DPWM Techniques for Parallel Interleaved 2L VSIs

Kapil Shukla and Ramkrishan Maheshwari, *Senior Member*, *IEEE*

***Abstract*— Parallel interleaved two-level (2L) three-phase voltage source inverters (VSIs) are widely used due to their distinct advantages of high power delivery, modularity, low current rating devices, etc. Along with these advantages, the parallel interleaved 2L VSIs could also be analyzed as a single three-level (3L) VSI. Conventionally parallel interleaved 2L VSIs are modulated using the 2L pulse-width modulation (PWM) techniques. However, implementation of parallel interleaved 2L VSIs using the 2L PWM techniques may generate a higher ac side current ripple as compared to implementing the parallel interleaved 2L VSIs using 3L PWM techniques. This paper proposes a carrier-based method for implementing different 3L discontinuous PWM (DPWM) techniques for parallel interleaved 2L three-phase VSIs. Comparison of different 2L switching sequences for implementing a 3L DPWM switching sequence based on circulating current, line current ripple, and switching loss is also carried out. Simulation and experimental results are also displayed to validate the proposal.**

***Index Terms*— Two-level (2L), Three-level (3L), Interleaving, Pulse-width Modulation (PWM).**

I. INTRODUCTION

Two-level (2L) voltage source inverters (VSIs) are generally connected in parallel to deliver high current [1]. Other major advantages of paralleling the VSIs are the reduction of current rating of individual switches, lower thermal stress, modularity, higher efficiency, etc. [2] - [4]. The high frequency carrier signals are normally used for modulating any 2L VSI. In case of parallel connected 2L VSIs, the carrier signals are interleaved to reduce the harmonic content in the ac side quantities [5] - [6]. The interleaving angle varies on the number of parallel connected VSIs. For N parallel interleaved VSIs, an interleaving angle of $2\pi/N$ is generally preferred. However, interleaving of carrier signals introduces a common-mode (CM) voltage difference between the VSIs and hence due to this CM voltage difference a circulating current starts to flow between the VSIs. Various active and passive methods are already proposed in the literature to reduce the circulating current [7] - [9].

The N parallel interleaved 2L VSIs could be analyzed as a single N+1 level VSI [10] - [15]. In literature, different methods are proposed to implement a three-level (3L) conventional space-vector pulse-width modulation (SVPWM) technique for parallel interleaved 2L VSIs [12] - [14]. However, none of these methods have implemented a 3L discontinuous PWM (DPWM) [16] - [20]. A generalized carrier-based method to implement different 3L PWM techniques is proposed in [15]. However, the proposed method does not give insight to the 2L switching sequences which are required to generate the 3L switching sequences for parallel interleaved 2L VSIs. The main contributions of the paper are given in the following.

(1) A 3L switching sequence could be generated from different 2L switching sequences. Multiple 2L switching sequences are presented to implement a particular 3L switching sequence.

(2) Different 2L switching sequences have different impact on the system performance indices such as circulating current, individual VSI ac side current ripple, and switching loss. Moreover, each 2L switching sequence could not be implemented using the carrier-based approach. Therefore, an appropriate 2L switching sequence is found in this paper on the basis of abovementioned system performance indices along-with the ease of implementation for implementing a particular 3L switching sequence.

(3) Appropriate 2L switching sequences required to implement 3L DPWM techniques are listed in the paper. This also improves the understanding of 2L VSI PWM sequences applied which was not present in [15].

In this paper, two parallel interleaved 2L VSIs are analyzed as a single 3L VSI. Different 3L discontinuous PWM (DPWM) techniques are already proposed in the literature for modulating a 3L VSI. Corresponding to each 3L DPWM technique, there will be a 3L switching sequence. Based on the 3L switching sequences, the 2L switching sequences are formulated. To carrier-based implement these formulated 2L switching sequences, a common-mode (CM) offset is calculated. This calculated CM offset is added to the given low frequency reference voltage signals to generate the required 3L switching sequence. Furthermore, the proposed method relates the space vectors of the individual VSIs and corresponding equivalent 3L space vector which can further be generalized.

The paper is organized as follows. Section II discusses about the operation of parallel interleaved 2L VSIs analyzed as a single 3L VSI and generation of 3L switching sequences. Section III discusses about the 3L DPWM techniques, different 2L switching sequences, and the CM offset calculation. Simulation and experimental results are displayed

Manuscript received November 21, 2018; revised January 21, 2019 and March 05, 2019; accepted April 23, 2019.

The authors are with the department of Electrical Engineering, Indian Institute of Technology Delhi, New Delhi, India (e-mail: kapilstriker@gmail.com, rkmahesh@ee.iitd.ac.in).

0093-9994 (c) 2018 IEEE. Personal use is permitted, but republication/redistribution requires IEEE permission. See http://www.ieee.org/publications_standards/publications/rights/index.html for more information.

This article has been accepted for publication in a future issue of this journal, but has not been fully edited. Content may change prior to final publication. Citation information: DOI 10.1109/TIA.2019.2913618, IEEE Transactions on Industry Applications

in sections IV and V, respectively. Conclusions are presented in section VI.

II. GENERATION OF 3L SWITCHING SEQUENCES

Two parallel interleaved 2L VSIs connected with a common dc-link are shown in Fig. 1. The ac sides of the VSIs are connected through inductors, and these inductors could be common-mode (CM) or differential-mode (DM) inductors. A resistive load is connected to the ac side common point of the VSIs. The load could vary depending on the application.

The two parallel interleaved 2L VSIs are analyzed as a single 3L VSI. If Phase A of both the 2L VSIs are considered, the Thevenin's equivalent circuit is shown in Fig. 2. The equivalent 3L pole voltage (v_{AO}) is given by [10], [14]

$$v_{AO} = \frac{v_{A1O} + v_{A2O}}{2} \tag{1}$$

where v_{A1O} and v_{A2O} are the phase A pole voltages of the individual VSIs. The pole voltage levels of a 2L VSI are, $+V_{dc}/2$ or $-V_{dc}/2$. Therefore, by using these two levels, it is possible to get all the three voltage levels of a 3L VSI. The three levels of the pole voltage of a phase are $+V_{dc}/2$, 0, and $-V_{dc}/2$. Therefore, the 2L interleaved VSIs can be analyzed as a single 3L VSI. A state of 3L VSI is represented by a combination of three numerals (0, 1, and 2). 0, 1, and 2 correspond to voltage levels $-V_{dc}/2$, 0, and $V_{dc}/2$, respectively. The SV diagram of a 3L VSI is divided into six sectors (dark-lines) as shown in Fig 3. Each sector is further divided into six sub-sectors (p1, p2, q1, q2, r, s) as shown in Fig. 3 For a given reference voltage vector (V_{ref}), the dwell times of active and zero voltage vectors of 2L SV diagram [21] (Fig. 4) is given by [24]

$$T_1 = \frac{V_{ref}}{V_{dc}} \frac{\sin(60-\theta)}{\sin(60)} T_s = \frac{v_{max} - v_{mid}}{V_{dc}} T_s \tag{2}$$

$$T_2 = \frac{V_{ref}}{V_{dc}} \frac{\sin(\theta)}{\sin(60)} T_s = \frac{v_{mid} - v_{min}}{V_{dc}} T_s \tag{3}$$

$$T_z = T_s - T_1 - T_2 \tag{4}$$

Here, T_1, T_2, and T_z are the dwell times of the 2L voltage vectors V_1^{2L} (+ − −), V_2^{2L} (+ + −), and zero voltage vectors (V_0^{2L} & V_7^{2L}), respectively. The maximum, minimum, and middle values of the reference voltage signals ($v_{A,ref}$, $v_{B,ref}$, $v_{C,ref}$) are termed as v_{max}, v_{min}, and v_{mid}, respectively. T_s is the switching period. Now, using the conventional 2L SVPWM, the generated equivalent 3L switching sequence for time period $T_s/2$ is shown in Table I. Since an interleaving angle of 180° is used among the carrier signals to modulate the individual VSIs, the 2L switching sequences of VSI 2 would be in reverse order of that of VSI 1 as shown in Table I [2]. The equivalent 3L switching sequence generated using the conventional 2L SVPWM is comprised of the 3L SV diagram voltage vectors. Therefore, any 3L switching sequence could be generated using the two 2L parallel interleaved VSIs.

III. 2L SWITCHING SEQUENCES FOR 3L DPWM TECHNQIUES

Different 3L continuous and discontinuous PWM techniques are already discussed in literature [18]. In case of 2L DPWM techniques, one out of three phases clamps to $+V_{dc}/2$ or to $-V_{dc}/2$. This clamping of a phase reduces the switching of a phase in a switching period (Ts) and hence reduces the switching loss **[**23**]**. However, in case of a 3L VSI, an additional zero voltage value is available for clamping. Therefore, depending on the 3L DPWM technique, there will be different switching sequences in different sub-sectors of a sector of a 3L SV diagram. For each sub-sector, a CM offset (v_{off}) is calculated in terms of maximum, minimum, and middle values of the given reference voltage signals ($v_{A,ref}$, $v_{B,ref}$, $v_{C,ref}$) to implement a particular 3L switching sequence. Due to the six fold symmetry of a 3L SV diagram [25], the calculated CM offsets for sub-sectors of sector 1 would be valid for corresponding sub-sectors of other sectors.

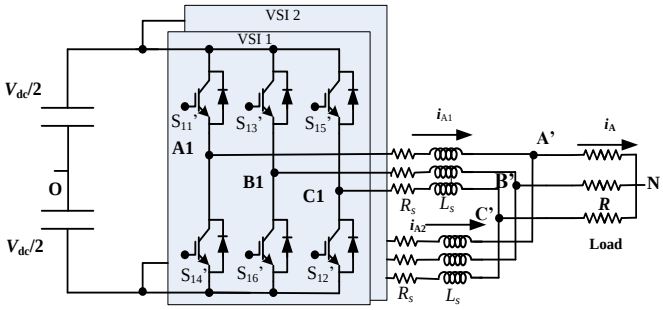

Fig. 1. Parallel interleaved 2L VSIs connected to load fed from a common dc-link.

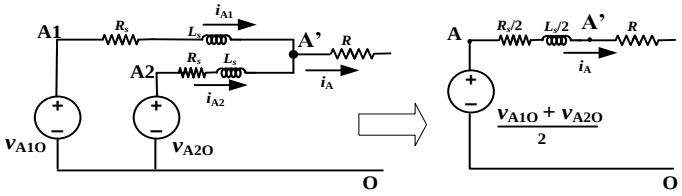

Fig. 2. Thevenin's equivalent circuit**.**

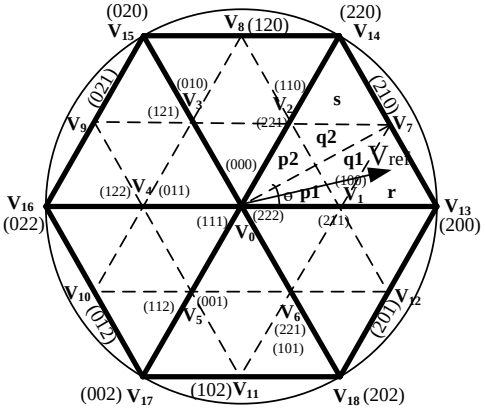

Fig. 3. Space-vector diagram of a 3L VSI.

A. 3L DPWM Switching Sequences

The switching sequences corresponding to 3L DPWM1 and 3L DPWM3 techniques are tabulated in Table II and Table III, respectively [18]. Using these switching sequences of 3L DPWM1 and 3L DPWM3, other 3L DPWM techniques could easily be implemented. Therefore, only DPWM1 and DPWM3 are considered in this paper. In addition to, for implementing a 3L switching sequences, there could be multiple 2L switching

0093-9994 (c) 2018 IEEE. Personal use is permitted, but republication/redistribution requires IEEE permission. See http://www.ieee.org/publications_standards/publications/rights/index.html for more information.

This article has been accepted for publication in a future issue of this journal, but has not been fully edited. Content may change prior to final publication. Citation information: DOI 10.1109/TIA.2019.2913618, IEEE Transactions on Industry Applications

sequences. For example, using Table II, the multiple 2L switching sequences corresponding to the 3L switching sequence of sub-sector q1 are tabulated in Table IV. Since an interleaving angle of 180° is considered between the carrier signals, the switching sequences of both the VSIs are 180° shifted to each other. Moreover, in all the switching sequences (Table IV), the average value of the difference in the common mode voltages of the VSIs is also kept to zero [21] , i.e.

$$< v_{cm,1} - v_{cm,2} >_{T_s} = \frac{1}{T_s}\int_{T_s} \left(v_{cm,1} - v_{cm,2}\right)\cdot dt = 0 \quad (5)$$

where $v_{cm,1}$ and $v_{cm,2}$ are the common-mode voltages of the individual 2L VSIs. Since the circulating current is proportional to the integration of the CM voltage differences of the individual VSIs [15], the constraint in (5) should be met to keep the net change in the circulating current over a switching period to be zero and hence avoiding the CM inductors to get saturated. The CM voltage differences of all the four 2L sequences (Table IV) are shown in Fig. 5. The CM voltage difference would decide the peak-peak and root mean square (rms) values of the circulating current [21]. The switching sequences of Table IV are also compared on the basis of individual VSI ac side current ripple [3] for modulation index (m_a) value of 0.7 and is shown in Fig. 6. The modulation index (m_a) is defined as the ratio of peak of reference phase voltage and ($V_{dc}/2$).

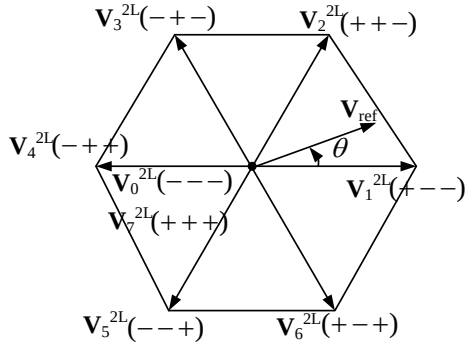

Fig. 4. Space-vector diagram of a 2L VSI.

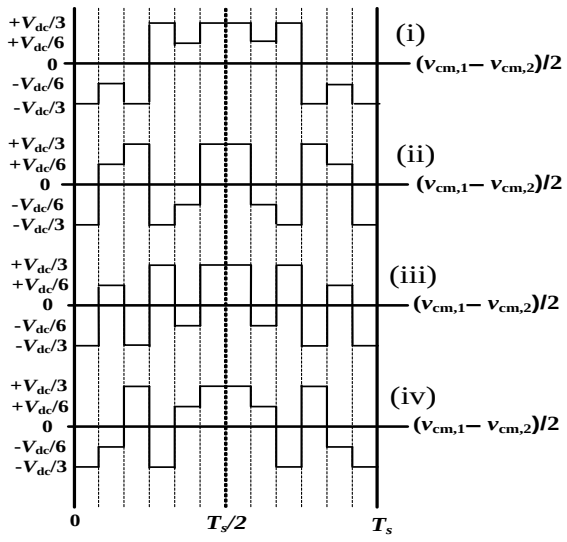

Fig. 5. CM Voltage difference for different 2L switching sequences (Table IV).

Since the same 3L switching sequence is implemented using different 2L switching sequences, the load side current ripple would be same for all the 2L switching sequences mentioned in Table IV. However, the individual VSI ac side current ripple would vary depending on the 2L switching sequence as shown in Fig. 6. The sequence (iii) provides minimum individual VSI current ripple. However, due to multiple switching, the switching loss [22] of sequence (iii) would be maximum among the all four sequences for the same modulation index value as shown in Fig. 7. Moreover, carrier-based implementation of the multiple switching sequences is very complicated. Therefore, depending on all the system performance indices: ac side current ripple, circulating current, and switching loss along-with the ease of implementation, the 2L switching sequence (i) is found most suitable for generating the equivalent 3L switching sequences. Based on the 3L switching sequences, appropriate 2L switching sequences are found for each sub-sector of sector 1 and are tabulated in Table V and Table VI for DPWM1 and DPWM3, respectively. Similarly, switching sequences for other sectors could be formulated.

Table I.
Switching sequences using 2L SVPWM

VSI1	(− − −),(+ − −),(+ − −),(+ + −),(+ + +)
VSI2	(+ + +),(+ + −),(+ − −),(+ − −),(− − −)
Equivalent 3L	(111),(210),(200),(210),(111)

Table II.
Switching sequences for 3L DPWM1 Technique

Sub-sector		3L Switching Sequence
p	p1	(211),(111),(110),(110),(111),(211)
	p2	(211),(111),(110),(110),(111),(211)
q	q1	(211),(210),(110),(110),(210),(211)
	q2	(211),(210),(110),(110),(210),(211)
r		(211),(210),(200),(200),(210),(211)
s		(110),(210),(220),(220),(210),(110)

Table III.
Switching sequences for 3L DPWM3 Technique

Sub-sector		3L Switching Sequence
p	p1	(111),(110),(100),(100),(110),(111)
	p2	(111),(211),(221),(221),(211),(111)
q	q1	(210),(110),(100),(100),(110),(210)
	q2	(221),(211),(210),(210),(211),(221)
r		(210),(200),(100),(100),(200),(210)
s		(221),(220),(210),(210),(220),(221)

B. *CM Offset Calculation*

For implementing the 2L switching sequences mentioned in Tables V and VI, a CM offset has to be calculated for each sub-sector. This CM offset is added to the given sinusoidal three-phase reference signals to implement a PWM technique. Conventionally during the implementation of continuous and discontinuous PWM techniques, each phase pole voltage changes once or does not change during a sampling period ($T_s/2$). However, during the implementation of a 3L PWM technique using the parallel interleaved 2L VSIs, one of the

0093-9994 (c) 2018 IEEE. Personal use is permitted, but republication/redistribution requires IEEE permission. See http://www.ieee.org/publications_standards/publications/rights/index.html for more information.

This article has been accepted for publication in a future issue of this journal, but has not been fully edited. Content may change prior to final publication. Citation information: DOI 10.1109/TIA.2019.2913618, IEEE Transactions on Industry Applications

three pole voltages changes twice in the sampling period. For example, phase A pole voltage in the highlighted 2L switching sequence in Table VI changes twice during the sampling period. This double transition could not be implemented using the conventional carrier based approach. In the conventional carrier based approach, the three phase low frequency reference signals are compared with the high frequency carrier signals. This comparison of signals would lead to either no or one transition in a phase pole voltage during a sampling period. However, the 2L switching sequences proposed in this paper requires double transition of a pole voltage in the sampling period. Therefore, the following procedure is to be followed: Firstly, depending on the 2L switching sequence an appropriate CM offset is calculated, which is added to the given sinusoidal three phase reference signals. Secondly, the reference signal of the phase whose pole voltage changes twice is divided into two signals. These two signals are then compared with the high frequency carrier signals. The output pulses produced by the comparison are then passed through a logic gate to generate the required gate pulse. The gate pulses and the pole voltage waveforms for implementing the 3L DPWM3 technique, when V_{ref} lies in sub-sector r is shown in Fig. 8. Here, $v_{A,ref}$', $v_{B,ref}$', $v_{C,ref}$' are the updated reference voltage signals, as given by

$$\begin{aligned} v_{A,ref}' &= v_{A,ref} + v_{off} \\ v_{B,ref}' &= v_{B,ref} + v_{off} \\ v_{C,ref}' &= v_{C,ref} + v_{off} \end{aligned} \quad (6)$$

where v_{off} is the CM offset signal and is calculated such that the phase C remains clamped to $-V_{dc}/2$, as given by

$$v_{off} = - v_{C,ref} - V_{dc}/2 \quad (7)$$

After the abovementioned step, the phase with double transition has to be identified. Since the phase A pole voltage changes twice in a sampling period to implement 3L DPWM3 technique (Table VI, sub-sector r), the phase A reference signal ($v_{A,ref}$') is divided into two signals, $v_{A,ref1}$' and $v_{A,ref2}$', which are given by

$$v_{A,ref1}' = 0, \;\; v_{A,ref2}' = +V_{dc}/2 - v_{A,ref}' \quad (8)$$

These divided signals are then compared with a high frequency carrier 1 signal to generate two signals, g_{vA1O1} and g_{vA1O2}. These signals are then passed through an EXNOR logic gate to get the gate signal of top IGBT of phase A of VSI 1. Similarly, the divided signals are compared with the carrier 2 signal to generate the gate signal of top IGBT of phase A of VSI 2.

The average value of the difference in the CM voltages of the VSIs is also equal to zero as shown in Fig. 8. Similarly, to implement switching sequences of sub-sector s (Table VI), a CM offset (v_{off1}) has to be added to the three phase reference signals such that the phase A is clamped at $+V_{dc}/2$ and is given as

$$v_{off1} = - v_{A,ref} + V_{dc}/2 \quad (9)$$

After addition of v_{off1}, the reference signal of phase B is divided into two signals, $v_{B,ref1}$' and $v_{B,ref2}$', as given by

$$v_{B,ref1}' = 0, \;\; v_{B,ref2}' = +V_{dc}/2 - v_{B,ref}' \quad (10)$$

Now, similar to sector r, these divided signals are then compared with a high frequency carrier1 signal to generate two signals, g_{vB1O1} and g_{vB1O2}. These signals are then passed through an EXNOR logic gate to get the gate signal of top IGBT of phase B. Similarly, pole voltages of VSI 2 are generated. The reference signals, carrier signals, and pole voltages corresponding to the abovementioned case is shown in Fig. 9.

Table IV.
2L switching sequences for 3L DPWM1 (q1)

Sequence	VSI	2L Switching Sequence
(i)	1	(+ − −),(+ − −),(− − −),(+ + −),(+ + −),(+ + +)
	2	(+ + +),(+ + −),(+ + −),(− − −), (+ − −),(+ − −)
(ii)	1	(+ − −),(+ + −),(+ + −),(− − −),(+ − −),(+ + +)
	2	(+ + +),(+ − −),(− − −),(+ + −), (+ + −),(+ − −)
(iii)	1	(+ − −),(+ + −),(− − −),(+ + −),(+ − −),(+ + +)
	2	(+ + +),(+ − −),(+ + −),(− − −), (+ + −),(+ − −)
(iv)	1	(+ − −),(+ − −),(+ + −),(− − −),(+ + −),(+ + +)
	2	(+ + +),(+ + −),(− − −),(+ + −), (+ − −),(+ − −)

The switching sequences to implement the 3L DPWM3 technique for medium and higher value of modulation indices either clamps the phase having maximum value to $+V_{dc}/2$ or the phase having minimum value to $-V_{dc}/2$. For example, in sector 1, the phase A is clamped to $+V_{dc}/2$ in sub-sectors q2 and s (Table III), while the phase C is clamped to $-V_{dc}/2$ in sub-sectors q1 and r (Table III). However, in case of 3L DPWM1 technique, the 3L switching sequences in sub-sectors q1 and q2 are such that the phase having middle value among the three phases is clamped to the zero voltage value (Table II). Therefore, to clamp the middle value phase, i.e. phase B in sub-sector q1 to zero voltage value, an appropriate CM offset (v_{off2}) is added to the three given reference signals, as given by

$$v_{off2} = - v_{B,ref} \quad (11)$$

After addition of v_{off2}, the reference signal of phase A is divided into two signals, $v_{A,ref1}$' and $v_{A,ref2}$', as given by

$$v_{A,ref1}' = 0, \;\; v_{A,ref2}' = +V_{dc}/2 - v_{A,ref}' \quad (12)$$

Now, similar to the DPWM3 technique, these divided signals are then compared with a high frequency carrier1 signal to generate two signals, g_{vA1O1} and g_{vA1O2}. These signals are then passed through an EXNOR logic gate to get the gate signal of top IGBT of phase A. Similarly, pole voltages of VSI 2 are generated. The reference signals, carrier signals, and pole voltages corresponding to the DPWM1 technique are shown in Fig. 10.The average value of the difference in the CM voltages of the VSIs is also kept to zero as shown in Fig. 10. However, the CM voltage difference for 3L DPWM1 is higher as compared to that of 3L DPWM3 (Figs. 8 & 9). This higher CM voltage difference would lead to higher peak-peak and root mean square (rms) circulating current.

The CM offset signals for 3L DPWM1 and 3L DPWM3 techniques are listed in Tables VII and VIII, respectively. To generalize, the CM offset signals are calculated in terms of maximum (v_{max}), minimum (v_{min}), and middle (v_{mid}) values of the given voltage reference signals ($v_{A,ref}$, $v_{B,ref}$, $v_{C,ref}$).

0093-9994 (c) 2018 IEEE. Personal use is permitted, but republication/redistribution requires IEEE permission. See http://www.ieee.org/publications_standards/publications/rights/index.html for more information.

This article has been accepted for publication in a future issue of this journal, but has not been fully edited. Content may change prior to final publication. Citation information: DOI 10.1109/TIA.2019.2913618, IEEE Transactions on Industry Applications

Table V.
2L switching sequences for 3L DPWM1 Technique

Sub-sector		VSI	2L Switching Sequence
p	p1	1	(+ − −),(− − −),(− − −),(+ + −),(+ + +),(+ + +)
		2	(+ + +),(+ + +),(+ + −),(− − −), (− − −),(+ − −)
	p2	1	(+ − −),(− − −),(− − −),(+ + −),(+ + +),(+ + +)
		2	(+ + +),(+ + +),(+ + −),(− − −), (− − −),(+ − −)
q	q1	1	(+ − −),(+ − −),(− − −),(+ + −),(+ + −),(+ + +)
		2	(+ + +),(+ + −),(+ + −),(− − −), (+ − −),(+ − −)
	q2	1	(+ − −),(+ − −),(− − −),(+ + −),(+ + −),(+ + +)
		2	(+ + +),(+ + −),(+ + −),(− − −), (+ − −),(+ − −)
	r	1	(+ − −),(+ − −),(+ − −),(+ − −),(+ + −),(+ + +)
		2	(+ + +),(+ + −),(+ − −),(+ − −), (+ − −),(+ − −)
	s	1	(− − −),(+ − −),(+ + −),(+ + −),(+ + −),(+ + −)
		2	(+ + −),(+ + −),(+ + −),(+ + −), (+ − −),(− − −)

Table VI.
2L switching sequences for 3L DPWM3 Technique

Sub-sector		VSI	2L Switching Sequence
p	p1	1	(− − −),(− − −),(− − −),(+ − −),(+ + −),(+ + +)
		2	(+ + +),(+ + −),(+ − −),(− − −), (− − −),(− − −)
	p2	1	(− − −),(+ − −),(+ + −),(+ + +),(+ + +),(+ + +)
		2	(+ + +),(+ + +),(+ + +),(+ + −), (+ − −),(− − −)
q	q1	1	(+ − −),(− − −),(− − −),(+ − −),(+ + −),(+ + −)
		2	(+ + −),(+ + −),(+ − −),(− − −), (− − −),(+ − −)
	q2	1	(+ + −),(+ − −),(+ − −),(+ + −),(+ + +),(+ + +)
		2	(+ + +),(+ + +),(+ + −),(+ − −), (+ − −),(+ + −)
	r	1	(+ − −),(+ − −),(− − −),(+ − −),(+ − −),(+ + −)
		2	(+ + −),(+ − −),(+ − −),(− − −), (+ − −),(+ − −)
	s	1	(+ + −),(+ + −),(+ − −),(+ + −),(+ + −),(+ + +)
		2	(+ + +),(+ + −),(+ + −),(+ − −), (+ + −),(+ + −)

Table VII.
Common-mode offset signal for 3L DPWM1

Sub-sector		Common-mode offset
p	$v_{mid} \le 0$	$v_{off} = -v_{mid}$
		$v_{max1}' = 0 \;\&\; v_{max2}' = +V_{dc}/2 - v_{max}'$
	$v_{mid} > 0$	$v_{off} = -v_{mid}$
		$v_{max1}' = 0 \;\&\; v_{max2}' = +V_{dc}/2 - v_{max}'$
q	$v_{mid} \le 0$	$v_{off} = -v_{mid}$
		$v_{max1}' = 0 \;\&\; v_{max2}' = +V_{dc}/2 - v_{max}'$
	$v_{mid} > 0$	$v_{off} = -v_{mid}$
		$v_{max1}' = 0 \;\&\; v_{max2}' = +V_{dc}/2 - v_{max}'$
r		$v_{off} = -v_{max} + \frac{V_{dc}}{2}$
s		$v_{off} = -v_{min} - \frac{V_{dc}}{2}$

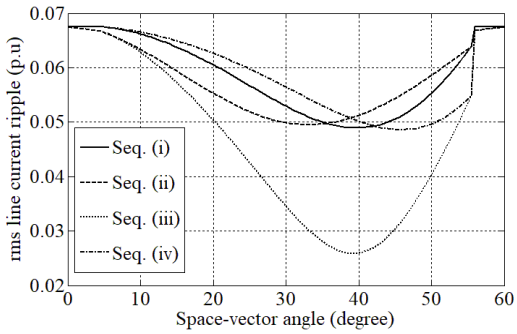

Fig. 6. RMS line current ripple variation (p.u) of individual VSIs over a sector for 3L DPWM1, $m_a = 0.7$.

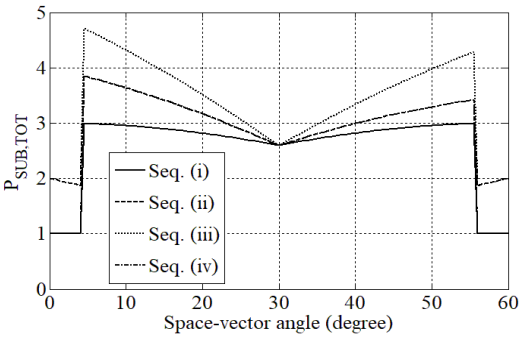

Fig. 7. Normalized total switching loss ($P_{SUB,TOT}$) variation over a sector for 3L DPWM1, $m_a = 0.7$.

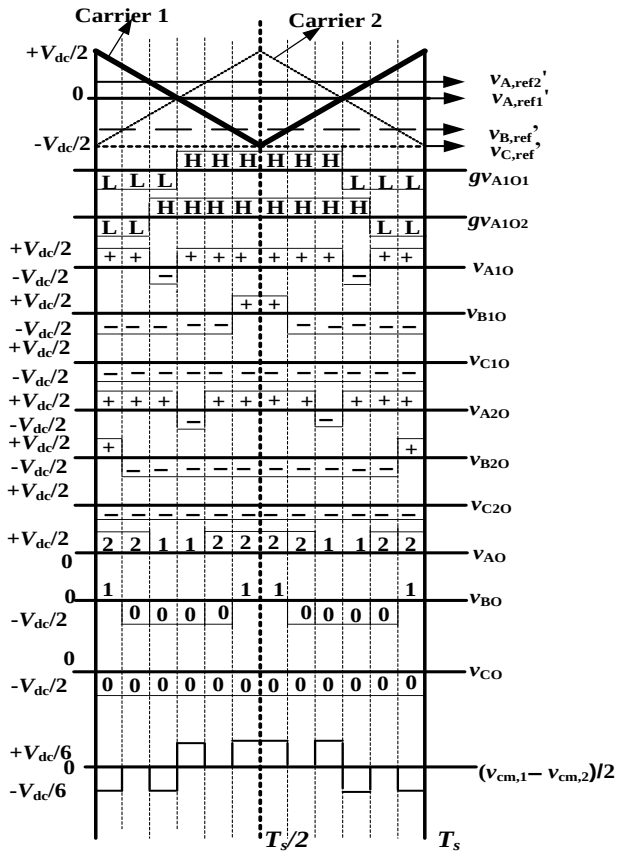

Fig. 8. Voltage waveforms for 3L DPWM3, when V_{ref} lies in sub-sector r.

0093-9994 (c) 2018 IEEE. Personal use is permitted, but republication/redistribution requires IEEE permission. See http://www.ieee.org/publications_standards/publications/rights/index.html for more information.

This article has been accepted for publication in a future issue of this journal, but has not been fully edited. Content may change prior to final publication. Citation information: DOI 10.1109/TIA.2019.2913618, IEEE Transactions on Industry Applications

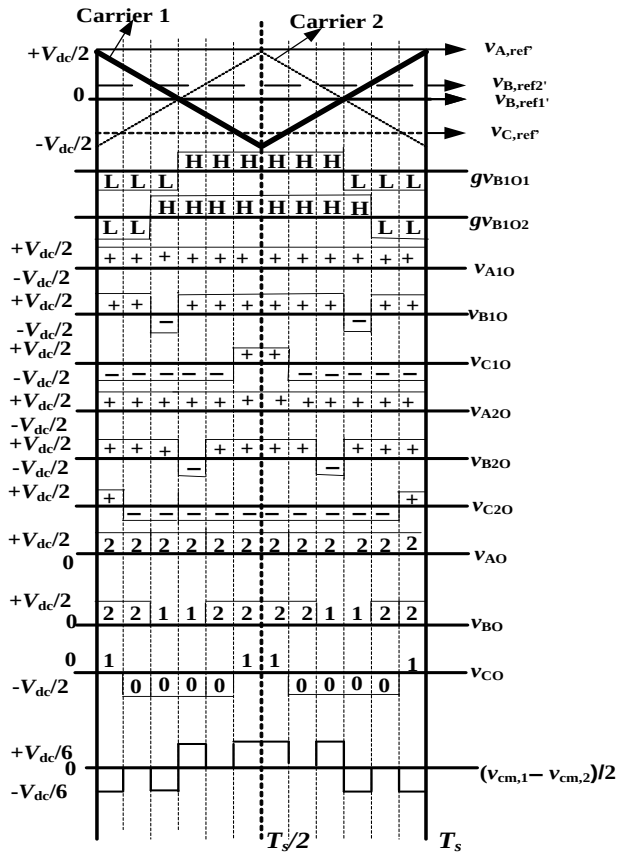

Fig. 9. Voltage waveforms for 3L DPWM3, when V_{ref} lies in sub-sector s.

Table VIII.
Common-mode offset signal for 3L DPWM3

Sub-sector		Common-mode offset
p	$v_{mid} \le 0$	$v_{off} = -v_{max}$
	$v_{mid} > 0$	$v_{off} = -v_{min}$
q	$v_{mid} \le 0$	$v_{off} = -V_{dc}/2 - v_{min}$
		$v_{max1}' = 0$ & $v_{max2}' = +V_{dc}/2 - v_{max}'$
	$v_{mid} > 0$	$v_{off} = +V_{dc}/2 - v_{max}$
		$v_{mid1}' = 0$ & $v_{mid2}' = +V_{dc}/2 - v_{mid}'$
r		$v_{off} = -V_{dc}/2 - v_{min}$
		$v_{max1}' = 0$ & $v_{max2}' = +V_{dc}/2 - v_{max}'$
s		$v_{off} = +V_{dc}/2 - v_{max}$
		$v_{mid1}' = 0$ & $v_{mid2}' = +V_{dc}/2 - v_{mid}'$

IV. Simulation Results

The different 2L and 3L PWM techniques for the parallel interleaved VSIs are compared with each other on the basis of ac side line current ripple [15], and switching loss [22]. The ac side line current ripple variation w.r.t modulation index (m_a) is shown in Fig. 11. The 3L PWM techniques offers lesser ac side current ripple w.r.t 2L PWM techniques. The 3L SVPWM technique provides minimum ac side current ripple w.r.t other 2L and 3L PWM techniques. Moreover, among the 2L and 3L DPWM techniques, the 3L DPWM1 technique provides minimum ac side current ripple. The reduction in the ac side line current ripple is quite significant for 3L PWM techniques as compared to the 2L PWM techniques. This reduction in line current ripple in parallel interleaved 2L VSIs system signifies the importance of implementation of 3L PWM techniques over the conventional 2L PWM techniques. The 2L and 3L PWM techniques are also compared on the basis of switching loss [22]. As the DPWM techniques have lesser switching of phases in a sampling period as compared to the continuous PWM techniques. Therefore, the switching loss for DPWM techniques would be lesser as compared to the continuous PWM techniques. The switching loss of both 2L and 3L PWM techniques for a single VSI at unity power factor condition is displayed in Fig. 12.

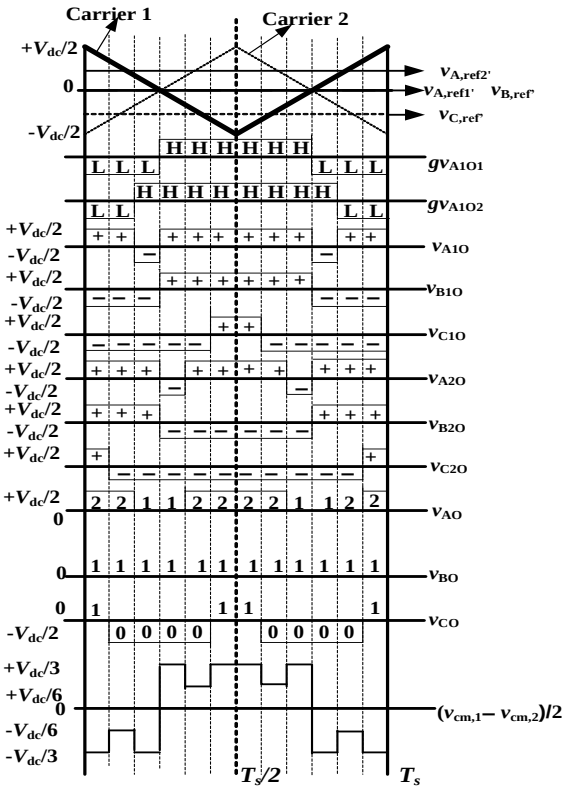

Fig. 10. Voltage waveforms for 3L DPWM1, when V_{ref} lies in sub-sector q1.

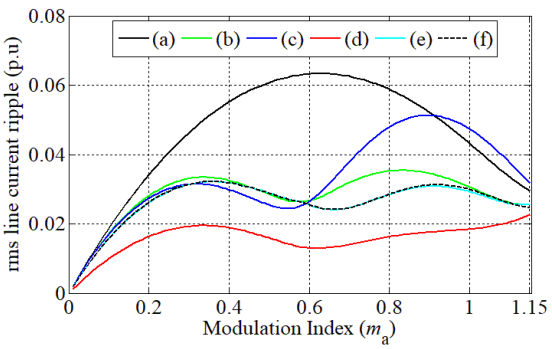

Fig. 11. RMS line current ripple variation (p.u) w.r.t modulation index (m_a). (a) 2L SVPWM, (b) 2L DPWM1, (c) 2L DPWM3, (d) 3L SVPWM, (e) 3L DPWM1, and (f) 3L DPWM3.

0093-9994 (c) 2018 IEEE. Personal use is permitted, but republication/redistribution requires IEEE permission. See http://www.ieee.org/publications_standards/publications/rights/index.html for more information.

This article has been accepted for publication in a future issue of this journal, but has not been fully edited. Content may change prior to final publication. Citation information: DOI 10.1109/TIA.2019.2913618, IEEE Transactions on Industry Applications

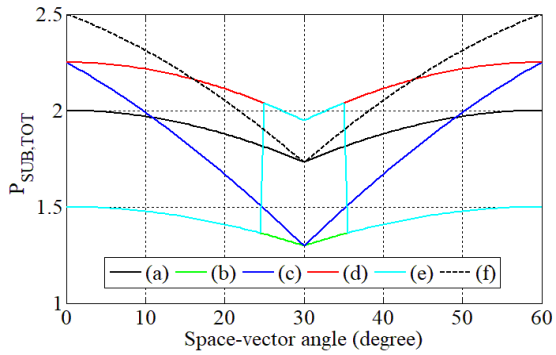

Fig. 12. Normalized total switching loss ($P_{SUB,TOT}$) variation over a sector. (a) 2L SVPWM, (b) 2L DPWM1, (c) 2L DPWM3, (d) 3L SVPWM, (e) 3L DPWM1, and (f) 3L DPWM3.

A MATLAB-Simulink model has been developed having parameters as shown in Table IX. The simulated waveforms of pole voltages (v_{A1O}, v_{A2O}, v_{B1O}, v_{B2O}) using 3L DPWM1 and 3L DPWM3 technique for modulation index (m_a) value of 0.7 are shown in Figs. 13 and 14, respectively. The equivalent 3L pole voltages (v_{AO} and v_{BO}) are calculated using (1). As could be seen from the Figs. 13 and 14, the pole voltages are clamped for certain duration of time to the positive value ($+V_{dc}/2$) or to the negative value ($-V_{dc}/2$) of half the dc-link (V_{dc}) or to the zero voltage level depending on the 3L DPWM technique. This clamping of phases ensures less switching and hence lower switching loss.

TABLE IX.
SYSTEM PARAMETERS

R	R_s	L_s	V_{dc}	f_c
60 Ω	2.5 Ω	24 mH	600 V	5 kHz

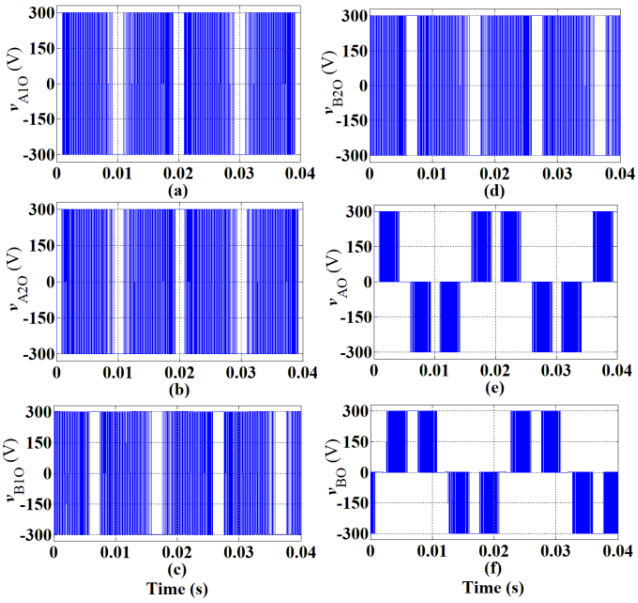

Fig. 13. Simulated pole voltage waveforms using 3L DPWM1, m_a = 0.7.

V. EXPERIMENTAL RESULTS

The experimental implementation of the system is done with the help of the digital signal controller (DSC) TMS320F28335 from Texas Instruments. Parameters used for experimental purpose are same as that of simulation. The experimental waveforms of pole voltages (v_{A1O}, v_{A2O}, v_{B1O}, v_{B2O}) using 3L DPWM3 technique at m_a value of 0.7 are shown in Fig. 15. The simulation and experimental results accompany each other. Here, due to measuring instrument limitation, the dc-link is kept at 200 V. However, for all the other experimental results, the dc-link is kept at 600 V. The FFT comparison of simulated and experimental pole voltage, v_{AO} using 3L DPWM3 at m_a value of 0.7 is also shown in Fig. 16. Here, the magnitude is shown in per unit (p.u) for a base value of 300 V for simulation and 100 V for experimental. The two plots are similar to each other. Moreover, the equivalent 3L switching sequences have a double the frequency to that of a single 2L VSI switching sequence as shown in Figs. 8 10. Therefore, the dominant harmonics and its sidebands would occur - at 10 kHz and multiples of 10 kHz for a carrier frequency of 5 kHz as displayed in Fig. 16.

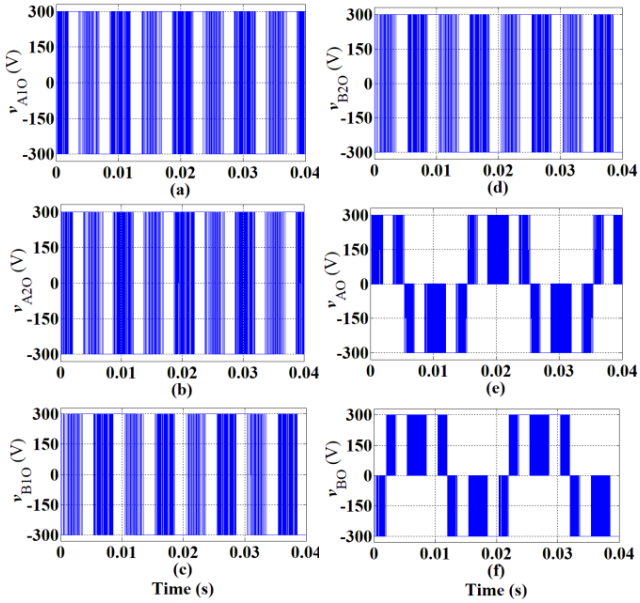

Fig. 14. Simulated pole voltage waveforms using 3L DPWM3, m_a = 0.7.

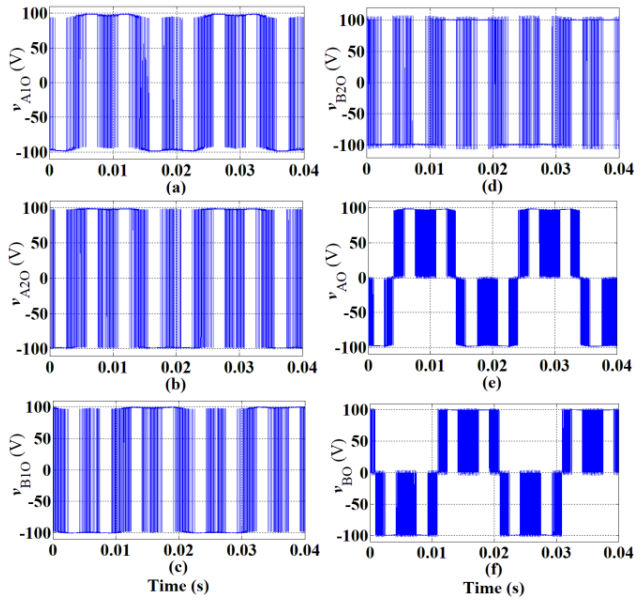

Fig. 15. Experimental pole voltage waveforms using 3L DPWM3, m_a = 0.7.

0093-9994 (c) 2018 IEEE. Personal use is permitted, but republication/redistribution requires IEEE permission. See http://www.ieee.org/publications_standards/publications/rights/index.html for more information.

This article has been accepted for publication in a future issue of this journal, but has not been fully edited. Content may change prior to final publication. Citation information: DOI 10.1109/TIA.2019.2913618, IEEE Transactions on Industry Applications

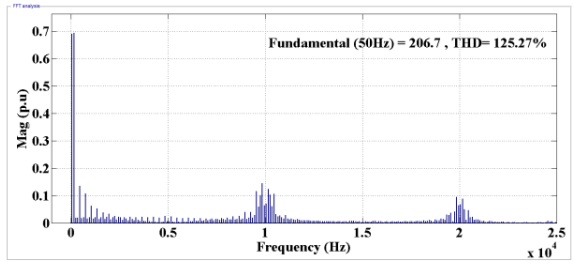

(a)

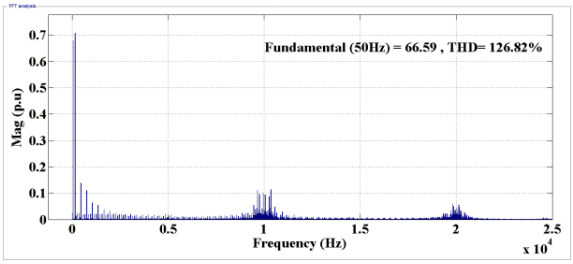

(b)

Fig. 16. FFT plots of v_{AO} using 3L DPWM3, m_a = 0.7. (a) Simulation (b) Experimental.

The experimental line-line voltages (v_{AB}) for both the 3L DPWM1 and 3L DPWM3 techniques for modulation index values of 0.4 and 0.7 are displayed in Figs. 17 and 18, respectively. The line-line voltages in Figs. 17 and 18 show the accurate implementation of 3L DPWM techniques using the proposed CM offsets. The 3L DPWM techniques could be implemented over the entire linear modulation index range, i.e. $0 < m_a < 1.154$. Since the DPWM techniques are conventionally used for reducing the switching losses and that are dominating at medium and high value of modulation indices. Therefore, the current waveforms are displayed for modulation index values of 0.7 and 1.0. The line currents (i_{A1}, i_{A2}, and i_A) and circulating currents ($3.i_{CC}$) for both the 3L DPWM1 and 3L DPWM3 techniques are displayed in Figs. 19 - 22, respectively. The individual VSI ac side currents (i_{A1}, i_{A2}) have higher amount of ripple content as compared to the load current (i_A). This reduction of ripple content in the load current is due to the interleaving of the carrier signals.

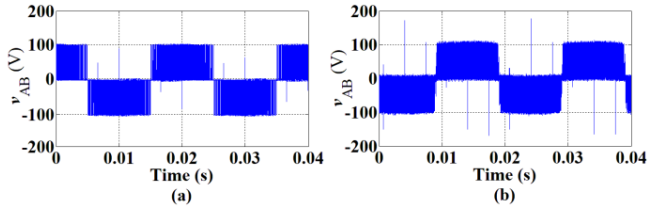

Fig. 17. Experimental line-line voltage waveforms, m_a = 0.4. (a) 3L DPWM1 (b) 3L DPWM3.

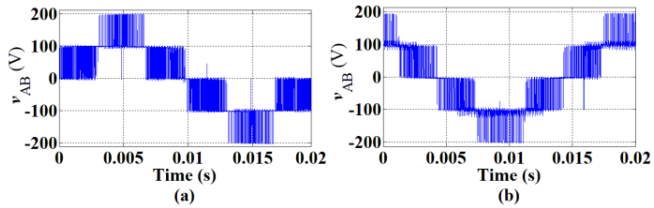

Fig. 18. Experimental line-line voltage waveforms, m_a = 0.7. (a) 3L DPWM1 (b) 3L DPWM3.

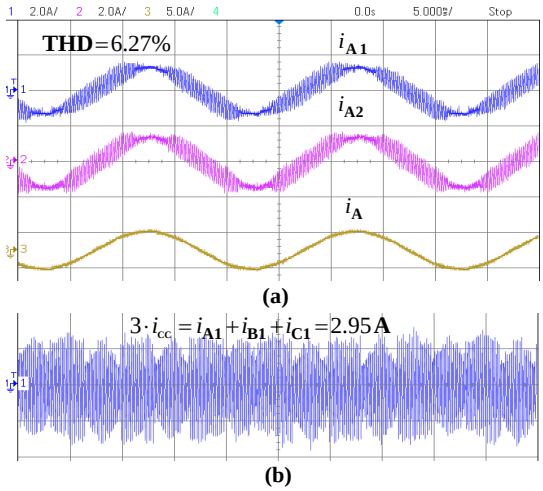

(a)

(b)

Fig. 19. Experimental result of 3L DPWM1, m_a = 0.7. (a) Line currents (2A/div, 2A/div, and 5A/div) (b) 3·Circulating current (i_{CC}) (1 A/div).

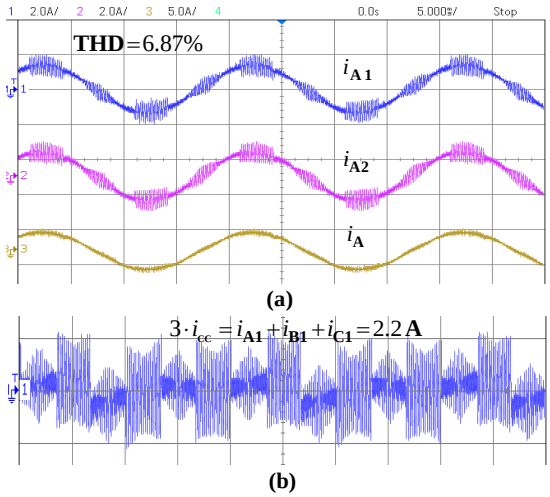

(a)

(b)

Fig. 20. Experimental result of 3L DPWM3, m_a = 0.7. (a) Line currents (2A/div, 2A/div, and 5A/div) (b) 3·Circulating current (i_{CC}) (1 A/div).

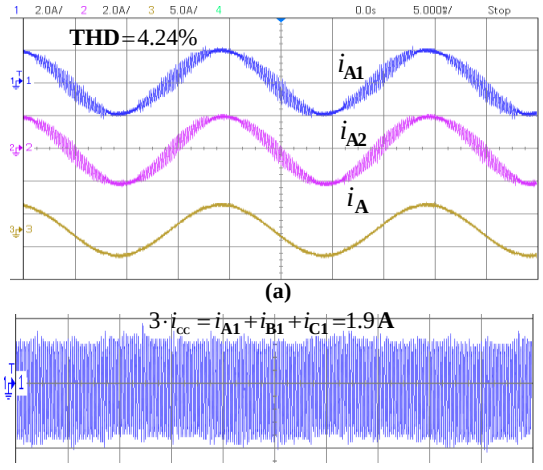

(a)

(b)

Fig. 21. Experimental result of 3L DPWM1, m_a = 1.0. (a) Line currents (2A/div, 2A/div, and 5A/div) (b) 3·Circulating current (i_{CC}) (1 A/div).

The total harmonic distortion (THD) value of load current (i_A) is also displayed in Figs. 19 - 22. It could be seen that the 3L DPWM1 technique provides lesser ac side current ripple as

0093-9994 (c) 2018 IEEE. Personal use is permitted, but republication/redistribution requires IEEE permission. See http://www.ieee.org/publications_standards/publications/rights/index.html for more information.

This article has been accepted for publication in a future issue of this journal, but has not been fully edited. Content may change prior to final publication. Citation information: DOI 10.1109/TIA.2019.2913618, IEEE Transactions on Industry Applications

compared to 3L DPWM3 technique. However, the circulating current produced due to the 3L DPWM1 technique is higher as compared to the 3L DPWM3 technique. Therefore, while operating any PWM technique using the parallel interleaved VSI system there must be a trade-off between the circulating current and the ac side line current ripple. The dynamic performance of the 3L DPWM1 is also shown in Fig. 23. Here, both the current and frequency variations are displayed. The load is kept constant.

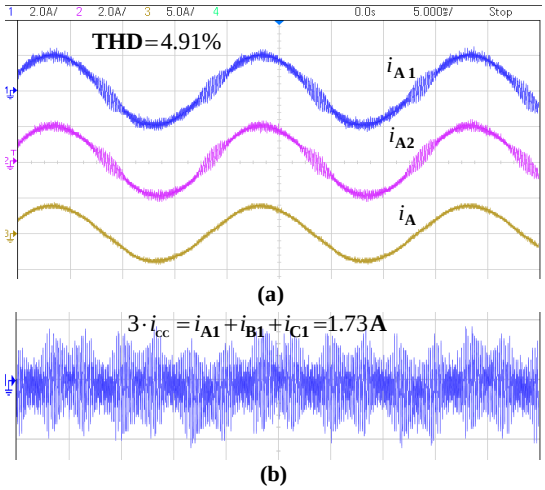

Fig. 22. Experimental result of 3L DPWM3, m_a = 1.0. (a) Line currents (2A/div, 2A/div, and 5A/div) (b) 3·Circulating current (i_{CC}) (1 A/div).

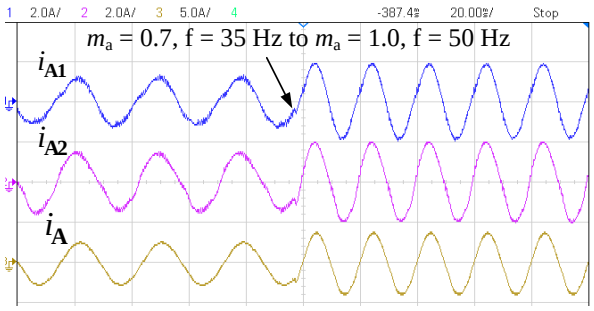

Fig. 23. Dynamic response of 3L DPWM1. Line currents (2A/div, 2A/div, and 5A/div).

VI. Conclusions

Two parallel interleaved 2L VSIs are analyzed as a single 3L VSI. A carrier-based method is developed for implementing different 3L DPWM techniques. A 3L SV diagram is divided into different sub-sectors and for each sub-sector equivalent 3L switching sequence is found. Depending on the 3L switching sequence, multiple 2L switching sequences are formulated. Depending on the system performance indices such as circulating current, ac side individual VSI current ripple, switching loss, and ease of implementation, an appropriate 2L switching sequence is found among the multiple 2L switching sequences. For implementing the most suitable 2L switching sequence, a CM offset is calculated. The calculated CM offset is derived in terms of maximum, minimum, and middle values of the reference voltage signals such that it is applicable for each sector of a 3L SV diagram. The net change in the circulating current is also kept to zero in a switching period by keeping the average value of the difference in the common mode voltages of the VSIs to zero.

Acknowledgement

This work is supported by the Ministry of Electronics and Information Technology (Meity), Government of India.

References

[1] G. Gohil, L. Bede, R. Teodorescu, T. Kerekes, and F. Blaabjerg, "Line filter design of parallel interleaved VSCs for high power wind energy conversion system," *IEEE Trans. Power Electron.*, vol. 30, no. 12, pp. 6775–6790, Dec. 2015.

[2] G. Gohil, L. Bede, R. Teodorescu, T. Kerekes, and F. Blaabjerg, "An integrated inductor for parallel interleaved VSCs and PWM schemes for flux minimization," *IEEE Trans. Ind. Electron.*, vol. 62, no. 12, pp. 7534-7546, Dec. 2015.

[3] M. Xiaolin, A. K. Jain, and R. Ayyanar, "Hybrid interleaved space Vector PWM for ripple reduction in modular converters," *IEEE Trans. Power Electron.*, vol. 26, no. 7, pp. 1954-1967, July 2011.

[4] B.Cougo, T. Neynard, and G. Gateau, "Parallel three-phase inverters: Optimal PWM method for flux reduction in intercell transformers," *IEEE Trans. Power Electron.*, vol. 26, no. 8, pp. 2184-2191, Aug. 2011.

[5] J. S. S. Prasad and G. Narayanan, "Minimization of grid current distortion in parallel-connected converters through carrier interleaving," *IEEE Trans. Ind. Electron.*, vol. 61, no. 1, pp. 76-91, Jan. 2014.

[6] Di Zhang, F. Wang, R. Burgos, L. Rixin, and D. Boroyevich, "Impact of interleaving on ac passive components of paralleled three-phase voltage-source converters," *IEEE Trans. Ind. Appl.*, vol. 46, no.3, pp. 1042-1054, June 2010.

[7] D. Shin, J. Lee, D. Yoo, and H. Kim, "Stability improvement of interleaved voltage source inverters employing coupled inductors for grid-connected applications", *IEEE Trans. Ind. Electron.*, vol. 63, no. 10, pp. 6014-6023, 2015.

[8] J. Ewanchuk, and J. Salmon, "Three-limb coupled inductor operation for paralleled multi-level three-phase voltage sourced inverters," *IEEE Trans. Ind. Electron.*, vol. 60, no. 5, pp. 1979–1988, Mar. 2013.

[9] D. Zhang, F. Wang, R. Burgo., and D. Boroyevich, "Common-mode circulating current control of paralleled interleaved three-phase two-level voltage-source converters with discontinuous space-vector modulation," *IEEE Trans. Power Electron.* , vol. 26, no. 12, pp. 3925-3935, Dec. 2011.

[10] G. Konstantinou, J. Pou, G. J. Capella, K. Song, S. Ceballos, and V. G. Agelidis, "Interleaved operation of three-level neutral point clamped converter legs and reduction of circulating currents under SHE-PWM", *IEEE Trans. Ind. Electron.*, vol. 63, no. 6, pp. 3323-3332, June 2016.

[11] Z. Quan and Y. W. Li "A three-level space vector modulation scheme for parallel converters to reduce circulating current and common-mode voltage," *IEEE Trans. Power Electron.*, vol.32, no.1, pp. 703–714, Jan. 2017.

[12] B. Cougo, G. Gateau, T. Meynard, M. Bobrowska-Rafal, and M. Cousineau, "PD Modulation Scheme for Three-Phase Parallel Multilevel Inverters," *IEEE Trans. Ind. Electron.*, vol. 59, no. 2, pp. 690-700, Feb. 2012.

[13] G. Gohil, L. Bede, R. Teodorescu, T. Kerekes, and F. Blaabjerg, "Flux-Balancing Scheme for PD-Modulated Parallel-Interleaved Inverters," *IEEE Trans. Power Electron.*, vol. 32, no. 5, pp. 3442-3457, May 2017.

[14] K. Shukla, V. Malyala, and R. Maheshwari, "A novel carrier-based hybrid PWM technique for minimization of line current ripple in two parallel interleaved two-level VSIs," *IEEE Trans. Ind. Electron,* vol. 65, no. 3, pp. 1908-1918, Mar. 2018.

[15] K. Shukla and R. Maheshwari, "A generalized method to generate carrier-based 3L PWM techniques using two parallel interleaved 2L VSIs," early access *IEEE Trans. Ind. Electron.*

[16] J. Rodriguez, S. Bernet, B. Wu, J. O. Pontt, and S. Kouro, "Multi-level voltage-source-converter topologies for industrial medium-voltage drives," *IEEE Trans. Ind. Electron.*, vol. 54, no. 6, pp. 2930–2945, Dec. 2007.

[17] J. Rodriguez, S. Bernet, P. Steimer, and I. Lizama, "A survey on neutral-point-clamped inverters," *IEEE Trans. Ind. Electron.*, vol. 57, no. 7, pp. 2219–2230, Jul. 2010.

0093-9994 (c) 2018 IEEE. Personal use is permitted, but republication/redistribution requires IEEE permission. See http://www.ieee.org/publications_standards/publications/rights/index.html for more information.

This article has been accepted for publication in a future issue of this journal, but has not been fully edited. Content may change prior to final publication. Citation information: DOI 10.1109/TIA.2019.2913618, IEEE Transactions on Industry Applications

[18] T. Bruckner and D. G. Holmes, "Optimal pulse-width modulation for three-level inverters," *IEEE Trans. Power Electron*., vol. 20, no. 1, pp. 82–89, Jan. 2005.
[19] S. Das, G. Narayanan, and M. Pandey, "Space- vector-based hybrid pulsewidth modulation techniques for a three-level inverter," *IEEE Trans. Power Electron*., vol. 29, no. 9, pp. 4580-4591, Sep. 2014.
[20] S. Das and G. Narayanan, "Novel switching sequences for a space-vector- modulated three- level inverter," *IEEE Trans. Ind. Electron*., vol. 59, no. 3, pp. 1477-1487, Mar. 2012.
[21] R. Maheshwari, G. Gohil, L. Bede, and S. Munk-Nielsen, "Analysis and modelling of circulating current in two parallel-connected inverters," *IET Power Electron.*, vol. 8, no. 7, pp. 1273-1283, 2015.
[22] D. Zhao, V. S. S. P. K. Hari, G. Narayanan, and R. Ayyanar, "Space-vector-based hybrid pulsewidth modulation techniques for reduced harmonic distortion and switching loss," *IEEE Trans. Power Electron*., vol. 25, no. 3, pp. 760-774, Mar. 2010.
[23] Emre Ün and A. M. Hava, "A Near-State PWM Method With Reduced Switching Losses and Reduced Common-Mode Voltage for Three-Phase Voltage Source Inverters," *IEEE Trans. Ind. Appl*., vol. 45, no.2, pp. 782-793, Apr. 2009.
[24] H. W. Van der Broeck, H. C. Skudelny, and G. V. Stanke, "Analysis and realization of a pulsewidth modulator based on voltage space vectors," *IEEE Trans. Ind. Appl.*, vol. 24, no. 1, pp. 142-150, Jan/Feb 1988.
[25] A. M. Hava, R. J. Kerkman, and T. A. Lipo, "Simple analytical and graphical methods for carrier-based PWM-VSI drives," *IEEE Trans. Power Electron.*, vol.14, no.1, pp.49-61, Jan 1999.

Kapil Shukla was born in Dungarpur, India. He received the bachelor of technology (B.Tech.) degree in electrical engineering from the Rajasthan Technical University, Kota, India in 2010 and the master of technology (M.Tech.) degree in power systems from the Delhi Technological University (DTU), New Delhi, India in 2012. Since 2015, he has been working toward the Ph.D degree in the Department of Electrical Engineering, Indian Institute of Technology Delhi, New Delhi, India.

From 2012 to 2014, he was with the Department of Electrical and Electronics Engineering, Galgotias University, Greater Noida, U.P, India, as an Assistant Professor. He then joined the Electrical Engineering Department, Manipal University Jaipur, India as an Assistant Professor. His research interests include parallel operation of voltage source inverters and pulse-width modulation techniques.

Ramkrishan Maheshwari (S'10 – M'11) was born in Allahabad, India. He received the master of engineering (M.E.) degree in electrical engineering from the Indian Institute of Science (IISc), Bangalore, India in 2005 and the Ph.D. degree in electrical engineering from Aalborg University, Aalborg, Denmark in 2012.

From 2005 to 2008, he was with Honeywell Technology Solution Lab, Bangalore, India. From 2012 to 2014, he was with the Department of Energy Technology, Aalborg University, Denmark. He is currently working as an assistant professor with the Department of Electrical Engineering, Indian Institute of Technology, Delhi, India. His research interests include modeling and control of power converters.

0093-9994 (c) 2018 IEEE. Personal use is permitted, but republication/redistribution requires IEEE permission. See http://www.ieee.org/publications_standards/publications/rights/index.html for more information.

Received: 24 September 2018 | Revised: 5 December 2018 | Accepted: 5 December 2018

DOI: 10.1002/er.4446

RESEARCH ARTICLE

WILEY INTERNATIONAL JOURNAL OF ENERGY RESEARCH

Influence of nanoadditives on ignition characteristics of Kusum (*Schleichera oleosa*) biodiesel

Naveen Kumar | Mukul Tomar

Centre for Advanced Studies and Research in Automotive Engineering, Department of Mechanical Engineering, Delhi Technological University, Delhi, India

Correspondence
Mukul Tomar, Centre for Advanced Studies and Research in Automotive Engineering, Department of Mechanical Engineering, Delhi Technological University, Bawana Road, Delhi 110042, India.
Email: mukultomar007@gmail.com

Summary

Biodiesel obtained from inedible sources emerged as a productive approach in Indian energy scenario due to the scarcity of food resources come up with extensive usage of edible crops. Kusum (*Schleichera oleosa*) oil is abundantly available in India and can be used as feedstock to produce biodiesel. However, issues such as higher viscosity, poor stability, and lower calorific value result in poor ignition characteristics, hence limiting its use in combustion applications. An improvement in performance and emission characteristics can be achieved by doping nanoparticles in Kusum biodiesel (KBD). The present work examines the impact of a metal compound and carbon-primarily based nanoparticles on the evaporation time and ignition probability of the KBD. During the experimental process, different fuel samples of KBD were prepared by amalgamating nanoparticles; then, a sequence of hot plate (stainless steel) ignition test was conducted on these test fuels. The comparative assessment of neat biodiesel and the biodiesel fuel doped with 30 ppm each of alumina (Al2O3), and multiwalled carbon nanotubes (MWCNTs) nanoparticles were carried out. The Kusum oil was converted to biodiesel using two-stage transesterification process. In the initial stage, refined oil was gone through the acid catalyst esterification process followed by the transesterification reaction. The prepared methyl ester was confirmed and characterized using GC-MS technique. The thermophysical and spray properties of the test fuels including density, viscosity, calorific value, cloud/pour point, Sauter mean diameter (SMD), and specific surface area (SSA) were also calculated. The experimental result showed a significant increase in ignition probability and heat conduction properties due to improved surface area/volume ratio. Also, lower evaporation time was noted for metal/carbon-based nanoparticles doped biodiesel as compared with neat biodiesel.

KEYWORDS

Evaporation time, GC-MS technique, hot surface ignition, ignition probability, Kusum (*Schleichera oleosa*) biodiesel, nanoparticles, Sauter mean diameter, Specific surface area

 © 2019 John Wiley & Sons, Ltd.

1 | INTRODUCTION

The development of a country can be gaged from its energy consumption pattern. India is a developing nation and has abundant coal and renewable energy resources. However, India imports more than 80% of its petroleum oil requirement since crude reserves are only 0.6 billion tonnes, and with the escalating exchange rate, the import bill has increased substantially. In the year 2016, the primary energy consumption of India is 12.9% of Asia-Pacific region and 5.5% of world.[1] The per capita energy consumption of the country remains low as 743 kilogram of oil equivalent (KGOE).[2] In the year 2016 to 2017, India imported 182.50 million tonnes of crude oil as consumption rate surpasses the production rate, ie, 40.20 to 212.70 million tonnes per annum (MTPA). India is spending Rs. 3682.15 billion on the purchase of petroleum products, which could have been used for other development work that may be remunerative to the Indian community.[3] The current energy scenario can only be improved if future energy needs of the nation can be made sustainable that includes shifting toward renewable fuel, increasing efficiency of fuel conversion, reducing environmental impacts, and increasing awareness among the humanity.

At present, developing countries are heavily dependent upon diesel fuel as it is driving industrial/transportation engines, marine and farm machinery, etc. The diesel imparts better fuel economy, durability, fidelity, and flexibility. However, the harmful emissions (such as carbon monoxide [CO], nitrogen oxide [NOx], hydrocarbons [HC], and particulate matter [PM] and smoke) emitted with the usage of diesel fuel in compression ignition (CI) engines are causing severe hazards to the atmosphere by increasing acid rain, ozone layer depletion, greenhouse effect, climatic changes, and smog.[4,5] The ongoing circumstances suggest that there is an immediate requirement to substitute diesel fuel as the world population is increasing significantly and shall give rise to petroleum demand in the coming years.[6] The research is underway all around the world to find the substitute to diesel, which can adhere with the stringent emission norms (Euro VI) and also lease a new life to hundreds of thousands of the engines.

Biodiesel is a promising substitute for diesel and produced from the edible, nonedible, and waste sources.[7-9] Currently, the world's biodiesel production is dominated by food crops such as soybean, olive, palm, coconut, and sunflower. However, the excessive use of edible oils for biodiesel production is a threat to mankind since chaos in the food chain is created.[10] The transition toward nonedible sources is of paramount significance as these crops can be grown in a barren land, and also, their properties make them unsuitable for human consumption. Biodiesel has an advantage over conventional fuels due to renewable nature[11]; however, there are challenges as well, eg, poor stability, clogging, lower calorific value, and lower evaporation rate resulting in incomplete combustion and reduced engine life.[12-14]The difficulties associated with the use of biodiesel precludes its complete replacement and most of the times it is used as an extender.

Kusum (*Schleichera oleosa*), belonging to Sapindaceae family, are abundantly available in tropical states of India, ie, southern Punjab, Haryana, Western Uttar Pradesh, warm regions of Madhya Pradesh, Rajasthan, and Gujarat.[15] The nonesterified fatty acid present in the Kusum oil is 5% to 11%, whereas iodine absorption value is 215 to 220, and total fatty acid content is 91.6%.[16,17] By modifying and improving the ignition and thermal properties, Kusum oil methyl ester (KOME) can be used as a potential substitute for diesel fuel. Fuel reformulation technique is of paramount significance, which can be a breakthrough in biofuel production and commercialization not only in India but also globally. The improvement in performance and emission characteristics of CI engines can be achieved by deploying the applications of nanoparticles in hydrocarbon-based and alternative fuels. Nanofuels are the very promising as they can improve the efficiency of diesel engines without any engine modifications.[18-22] Annamalai et al[23] doped cerium oxide nanoparticles with lemongrass-water emulsion (LWE) and found an improvement in thermal efficiency of the CI engine due to reduced evaporation time of fuel. Recent advancements in the field of nanotechnology have made it possible to improve the properties and quality of the fuels. The potential advantages associated with nanoadditives are that these microscopic particles provide a higher surface area to volume ratio, quick evaporation, and shorter ignition delay characteristics. These properties of nanoparticles make it a propitious fuel-borne catalyst, which can address the leading issues of engine performance and emission attached with the usage of neat biodiesel and diesel.[24] To overcome the difficulty of lengthier ignition lag, some previous investigations have been carried on the use of nanoparticles in CI engines. Somandepalli et al[25] conducted an ignition test using hot plate setup. Comparative assessment of ignition properties was investigated using different flammable and combustible liquids in different proportions. Later, further research on hot plate ignition test concluded that amalgamating Al_2O_3 nanoparticles to the diesel fuel immediately boost the initiation temperature and also provided reduced ignition lag.[26] As of late, Shams and Moghiman[24] investigated the outcome of distinct nanoparticles on the combustion properties of the fossil diesel. In their experiment, diesel fuel samples both with and without nanoparticles were employed for hot plate

ignition analysis. Samples containing metal oxide nanoparticles were found to have significantly higher ignition probability when compared with neat diesel samples. The mixing of carbon nanotubes with Jatropha biodiesel resulted in a drop in maximum cylinder pressure and heat release rate. Carbon-based nanoparticles act as a catalyst during the combustion process, which thus decreases the ignition delay effect.[27] Higher viscosity and lower calorific value associated with neem biodiesel result in lower evaporation rate, hence limiting its use in combustion applications. The evaporation rate of fuel plays a crucial role in combustion. An improvement in evaporation rate was achieved by doping nanoparticles in Neem biodiesel.[28] The ignition delay was lowered from 1.6 to 1.4 seconds, whereas the peak temperature was brought down from 659 to 611 K with the addition of graphene oxide in palm biodiesel. The doping of nanoadditives in neat biodiesel reduces the exhaust emissions and also improve the performance parameters.[29] Basha and Anand[27] in their experimental study showed that an enhancement in evaporation rate and reduction in ignition delay was observed when carbon-based nanoparticles (CNT) were blended with neat diesel fuel. Colwell and Reza[30] proposed a correlation between hot plate temperature and ignition expectancy. The authors conducted a series of ignition test on the hot surface by using 14 frequently used automotive and aviation fuels.

The spray distribution pattern of biodiesel fuel such as Sauter mean diameter (SMD), specific surface area (SSA), transmittance, and velocity of spray particles plays an important role in ignition properties and emission characteristics. However, neat biodiesel shows inferior spray characteristics as compared with that of diesel fuel. Therefore, there is a need to explore the relationship between physicochemical properties and the atomization attributes of different fuel blends. The atomization properties of the fuel are also dependent on injection pressure. High injection pressure (1500 bar) improves the quality of mixing and also facilitates lower soot formation during combustion. The ignition properties of diesel fuel are better as compared with that of biodiesel. The logic behind this is that smaller is the droplet size distribution better will be the atomization and droplet momentum.[31] Chen et al[32] conducted a comparative study of three different fuels, ie, neat biodiesel, jet, and diesel fuel. Jet fuel displayed better ignition/spray characteristics as compared with that of other fuels, due to lower viscosity and surface tension. However, enlarged spray tip penetration and bigger droplet size were found for neat biodiesel (B100).

Thus, from the foregoing discussion, it is important to conclude that very few research work had been done on the ignition prospects of next generation alternative fuels such as nanoparticle blended fuels and higher alcohols. The objectives were to investigate the ignition characteristics of biodiesel derived from Kusum (*S. oleosa*) oil by the process of transesterification. Secondly, to improve the performance characteristics such as stability, lower calorific value, and poor atomization properties of inedible vegetable oil, which restricts the use of biodiesel as a complete replacement fuel in CI engines. Later, the biodiesel obtained was doped with microscopic particles such as aluminum oxide and multiwalled carbon nanotubes (MWCNTs) with the assistance of ultrasonic bath. Four different samples containing neat biodiesel and nanoparticles mixed biodiesel were prepared for the present work. The critical temperature (the temperature of least evaporation time) of these different blends was also determined. The heat transfer mechanism of droplets was also evaluated on the hot surface in order to understand the Leidenfrost phenomenon,[33] which can serve as a gateway in other applications as well.

2 | EXPERIMENTAL METHODS

2.1 | Preparation of KOME

Kusum oil has high free fatty acid (FFA) content (5%-11%). Therefore, it was necessary to adopt two-step transesterification processes. The alkaline catalyst saponifies free fatty acids and transesterification becomes difficult. So esterification of FFA was carried before the start of the transesterification process. The alcohol used was methanol and KOH (potassium hydroxide) as an alkaline catalyst with PTSA (p-Toluenesulfonic acid) as an acid catalyst. The schematic of biodiesel formation after completion of the two-step transesterification process is shown in Figure 1.

In the acid catalyzed esterification reaction, Kusum oil was mixed with PTSA and methanol. The solution was mixed in a magnetic stirrer for 120 minutes at 60°C. After completion of the esterification process, the layer of alcohol (methanol) formed was separated. Later, in the second stage, potassium hydroxide—which act as a strong base catalyst—and methanol were mixed with Kusum oil and the mixture was stirred for 100 minutes at 60°C temperature. A 6:1 molar ratio was used for complete conversion of triglyceride. The glycerine and biodiesel were separated using a centrifuge. The biodiesel was washed with warm water to remove any alcohol, and again, it was heated to higher than 100°C to remove moisture (Figure 2).

2.2 | Preparation of test fuels

Nanoparticles, MWCNTs were purchased from Reinste Nano Ventures and alumina/aluminum oxide (Al_2O_3) from Nanobeach Organization. The detailed

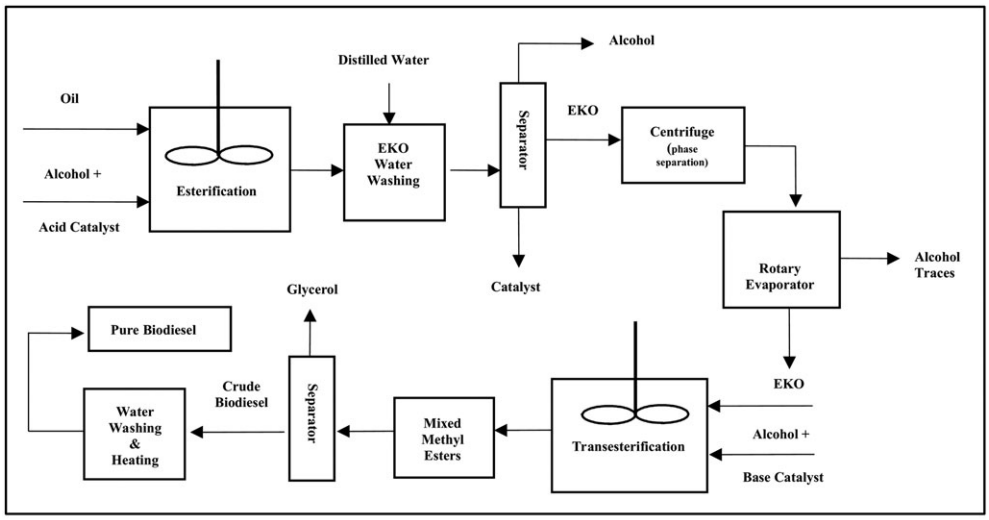

Abbreviations: EKO, Esterified Kusum oil.

FIGURE 1 Schematic of biodiesel production of Kusum (*Schleichera oleosa*) oil using two-step transesterification process

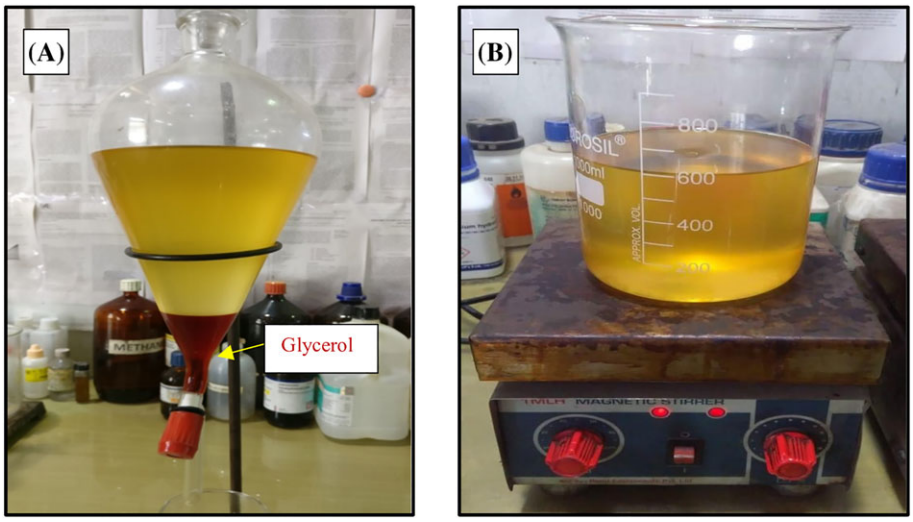

FIGURE 2 Photographic view of Kusum (*Schleichera oleosa*) biodiesel production A, separation of glycerine layer and B, removing moisture from biodiesel heating at 80°C [Colour figure can be viewed at wileyonlinelibrary.com]

specifications of these materials are listed in (Table 1). During the experimental process, four different test fuels were prepared, denoted as KBDxAlyCNTy ("x" means volume fraction and "y" means ppm). They are KBD100 (containing 100% biodiesel in volume percentage), KBD100Al30 (containing 100% biodiesel in volume percentage and 30 ppm alumina), KBD100CNT30 (containing 100% biodiesel and 30 ppm MWCNT), and KBD100Al30CNT30 (containing 100% biodiesel, 30 ppm alumina and 30 ppm MWCNT). Amalgamation of nanoparticles in neat Kusum biodiesel (KBD) was carried using an ultrasonicator for 45 minutes at a frequency of 40 kHz. The samples had a uniform distribution of nanoparticles (Figure 3). The physicochemical (American Standard for Testing and Materials (ASTM) standard method) properties for the test fuels are represented in (Table 3).

2.3 | Hot plate ignition experimental setup

The hot stainless steel (SS) surface ignition setup encompasses of circular SS plate (152 mm diameter and 8 mm thickness), electrical-driven heater, a voltage regulator (Variac transformer), temperature controller, k-type thermocouples, glass tube, digital camcorder, and a firm stand. The hot plate was adjusted in a manner that the bottom surface of the steel plate covered the coils of the heater (Figure 4). The electric heater was insulated by mineral wool so that minimum heat is transferred to the surroundings. The sides of the ignition setup were surrounded by clay bricks to prevent any untoward incident. The SS plate that was in direct contact with the heater had a very fine polished surface with a small

TABLE 1 Specification of nanoparticles[a]

Item	Specifications	
Manufacturer	M/s. Nanobeach, India	M/s. Reinste Nano Venture, India
Chemical name	Aluminum oxide (Al_2O_3)	Multiwalled carbon nanotubes (MWCNT)
CAS No.	1344-28-1	RN-PL-MCNP-50g
Molecular weight	101.96	172.11
Purity	≥99%	≥95%
Average particle size diameter, nm	20	20
Length, μm	-	1-10
Number of walls	-	3-15
Specific surface area, m^2/g	32	330
Appearance	White	Black

[a]Hyphen indicates nil or none.

concave depression in the center of the plate to assist a definite quantity of fuel droplet. The glass tube containing fuel samples was positioned in a manner that the mouth of the burette is perpendicular to the surface of hot plate. The glass tube was held by a flexible arm at a distance of 20 mm from the SS plate and the diameter of the glass tube nozzle was 1.65 mm. Fuel through the nozzle opening was sprayed on to the hot plate by pressurizing the reservoir to 0.13 bar and setting the time duration for which the solenoid valve was kept open. The height was held fixed for all the tests. The temperature of the hot surface was rectified and maintained with the help of a voltage regulator and temperature controller. K-type thermocouples were installed at the upper surface of the plate for continuously monitoring the temperature.

As soon as the temperature of the hot plate reached a particular temperature, the droplets of fuel are allowed to drop inside a sunken shaped cavity with the help of an automated controlled solenoid valve mechanism. After every droplet test, the hot plate is glazed with a very fine grit size (90 grit) sandpaper to prevent the interfere of any impurity/trash on to the polished surface. In the beginning, the initial starting temperature of the hot plate was set at 200°C. The moment of each spray event was recorded along with the resulting ignition/no ignition outcome. Three set of readings were taken for specific surface temperature, and the values were averaged. The test fuels droplets were subjected to 10 fuel ejection event so that an impeccable probabilistic data can be obtained. After recording the data at a specified set limit, the temperature of the surface was then increased by 50°C at every stage. When the entire fuel droplet gets evaporated on the hot surface, the time was noted using the digital timer. The process of droplet-burning was recorded using a slow-motion camera (with a speed of 960 frames per second). The physical shape, finishing, and material of the hot plate along with spray characteristics (such as SMD, SSA, and spray tip penetration) are some of the

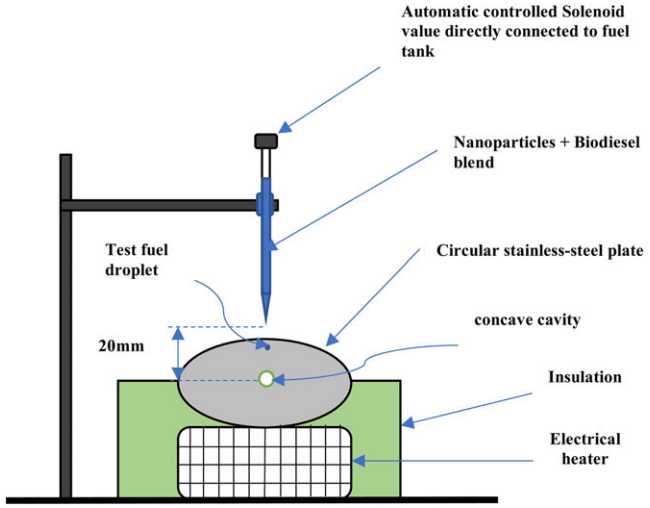

FIGURE 4 Schematic of hot plate ignition setup [Colour figure can be viewed at wileyonlinelibrary.com]

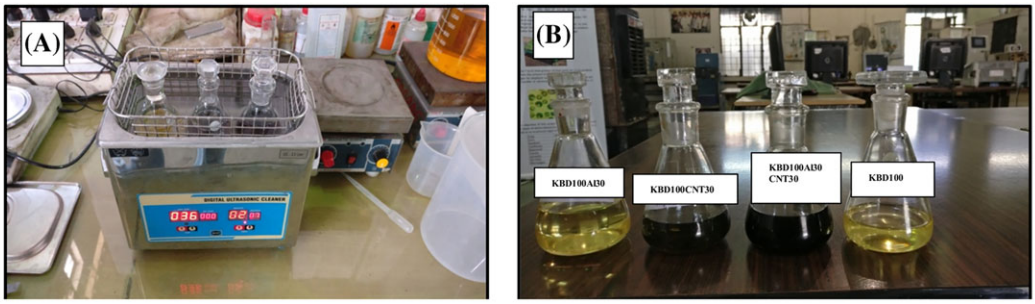

Abbreviations: KBD100, Neat Kusum Biodiesel; KBD100Al30, Kusum Biodiesel + 30 ppm Alumina; KBD100CNT30, Kusum Biodiesel + 30 ppm multiwalled carbon nanotubes; KBD100Al30CNT30, Kusum Biodiesel + 30 ppm Alumina + 30 ppm multiwalled carbon nanotubes.

FIGURE 3 Photographic view A, the ultrasonication process and B, test fuels doped with nanoparticles [Colour figure can be viewed at wileyonlinelibrary.com]

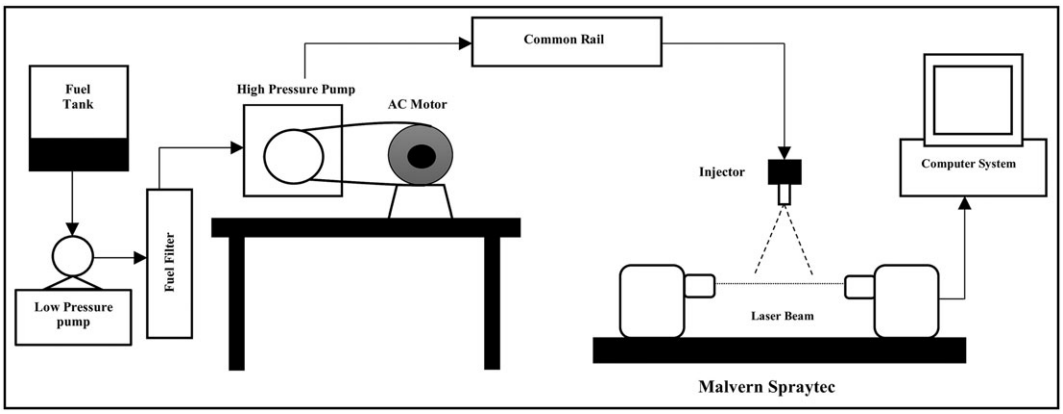

FIGURE 5 Schematic of Malvern Spraytec setup

crucial properties which govern the hot surface ignition experiment. Ignition test is also affected by the conditions of the surrounding and atmosphere such as temperatures and pressure. The investigation was performed in an air tight room at 1.013 bar pressure. During the experimental procedure, the environmental parameters such as fuel/air temperature, pressure, and droplet size were kept constant.

2.4 | Malvern Spraytec experimental setup

Atomized particle and drop size estimation are core characteristics for defining fuel performance. Malvern Spraytec is an instrument setup designed to analyze sprays of high concentrations and sprays from a robust, easy to use interface. A real-time laser diffraction measurement characterizes both intermittent and continuous events. Data regarding wide size distribution are generated rapidly and presented in a form that allows for an instant understanding of the evolution of atomization over time. The Spraytec setup comprises two different arrangements, ie, the fuel injection system (common rail) and Malvern Spraytec to record particle characteristics (Figure 5).

An automatic controlled common rail high-pressure injection setup was designed to operate and control the supply of nozzle delivering fuel. A single holed injector (which was set at a pressure of 175 bars) was used in this work. The pressure of the injector is kept constant throughout the experiment. Four different fuel samples—KBD100, KBD100Al30, KBD100CNT30, and KBD100Al30CNT30—were investigated. Malvern Spraytec setup was used to explore the droplet size and other spray properties (Figure 6). It covers the size range 0.1 to 2000 μm using a couple of lenses. The entire phenomenon of spray formation and atomization was covered within a time interval of 15 seconds. For every test fuel, five different events were conducted, and an average value is calculated to obtain statistically sound data sets.

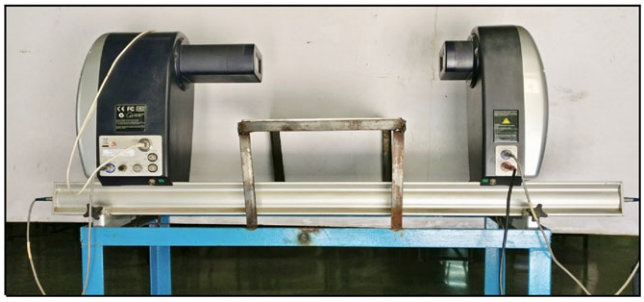

FIGURE 6 Photographic view of Malvern Spraytec setup [Colour figure can be viewed at wileyonlinelibrary.com]

2.5 | Experimental error analysis

Error in an experimental analysis is defined as the contrast between the recorded value and actual value of any measured quantity. Factors such as human interference, incorrect data entry, mistakes in experiment designing, and random errors like environmental conditions can give rise to errors in the measurement process. Hence, these parameters result in a lack of accurate measurement. There is always a need to express the inaccuracies in the experimental analysis. The variability and inherent in the measurement process is characterized by uncertainty. Uncertainty results in providing the maximum probable absolute difference between the recorded value and the true value.[34] According to the previous literature reviews, the relative uncertainty of any experimental investigation can be derived from the relation[35]:

$$\frac{U_R}{R} = \sqrt{\left(\frac{A_n}{R}\frac{\partial R}{\partial A_n}\right)^2}, \quad (1)$$

where R is the error variable and is given by the relation

$$R = R(A_1, A_2 ... A_n). \quad (2)$$

A_i is the individual measured quantity, and the partial derivative in Equation 1 $\left(\frac{\partial R}{\partial A_n}\right)$ is a measure of the sensitivity of the result.

Table 2 shows the maximum value of uncertainties of all the equipment's used in the current investigation. The overall uncertainty of all experimental instruments was calculated and found well in an acceptable range, ie, below ±4%.

3 | RESULTS AND DISCUSSION

The physicochemical properties such as density, kinematic viscosity, calorific value, flash point, cetane index, cloud point and pour point of KBD (KBD100), and other test fuels (KBD100Al30, KBD100CNT30, and KBD100Al30CNT30) were evaluated according to ASTM standards (see Table 3). The blends were kept for 80 days at the room temperature to make sure that the

TABLE 2 Maximum uncertainties of the measurements[a]

Device Used	Parameter	Measuring Range	Accuracy	Maximum Uncertainty
Fuel measuring pipette	Fuel flow, g/h	0-50 mL	±1 mL	±0.5%
Temperature indicator (k-type thermocouple)	Temperature, °C	0-1200°C	±2°C	±2%
Stop watch	Time measurement	-	±0.2 s	±0.2
GCMS-QP2010 Plus SHIMADZU	Mass analyzer and detector, m/z	1.5-1090	0.01 s	±0.1%
Malvern Spraytec	Droplet size measurement, μm	0.1-2000 μm (0.1-900 μm for 300 mm lens and 2.0-2000 μm for 750 mm lens)	≥0.01 μm	± 0.7

Abbreviations: m/z, mass to charge ratio; μm, microns.

[a]Hyphen indicates nil or none.

TABLE 3 Physicochemical properties of different test fuels[a]

Properties	Equipment	Test Method	D100	KBD100	KBD100Al30	KBD100CNT30	KBD100Al30CNT30
Density at 15°C, kg/m^3	DMA 4500, Anton Paar	ASTM D4052	834.4	860.34	861.69	861.75	861.70
Kinematic viscosity at 40°C, cSt	Visco bath, Petrotest	ASTM D445	2.51	4.269	4.458	4.420	4.494
Calorific value, MJ/kg	Parr 6100, Oxygen Bomb Calorimeter	ASTM D240	43.1	38.337	39.527	40.889	43.158
Flash point, °C	Pensky-Martens (AD0093-600)	ASTM D93	59	139	138	134	120
Cetane index	-	ASTM D4737	45	47.27	47.80	48.68	50.12
Cloud point, °C	-	-	−0.8	−2.5	−2.3	−3.8	−5.2
Pour point, °C	-	-	−8.5	−10.8	−11	−11.8	−13.7
Oxygen, wt%	CHNSO Elemental Analyzer		0	11	11.2	11.2	11.5

Abbreviations: D100, Neat diesel; KBD100, neat Kusum biodiesel; KBD100Al30, Kusum biodiesel + alumina nanoparticles; KBD100CNT30, Kusum biodiesel + multiwalled carbon nanotubes; KBD100Al30CNT30, Kusum biodiesel + alumina, multiwalled carbon nanotubes.

[a]Hyphen indicates nil or none.

nanoparticles dispersed in the neat biodiesel were free from agglomeration. After regular monitoring, it was found that KBD can be doped with these nanoparticles without any phase separation. They were examined on fifth, 10th, 20th, 30th, 40th, 50th, 70th, and 80th day. The physicochemical properties were tested on the 80th day. Comparative assessment of test fuel properties shows that the density, viscosity, and heat capacity remain relatively unchanged from that of neat biodiesel. But there is a significant improvement in the calorific value and cetane index. The maximum gain in ignition characteristics is observed with the use of both the nanoparticles blends (alumina + MWCNT) in the diesel engine.

3.1 | GC-MS analysis of KOME

The gas chromatography/mass spectroscopy (GC/MS) was carried out using GC-MS (Shimadzu, Japan, Model/Serial Number GCMS-QP2010 PLUS), to measure the percentage of fatty acids present in the biodiesel produced from the Kusum oil (Figure 7). The composition of different fatty acids obtained from GC-MS of KOME is shown in Table 3. The table patently signifies that KOME contains 40.80% saturated and 47.42% unsaturated fatty acids. The amount and type of methyl ester compounds present in the biodiesel determine the quality, compatibility, and stability of any biodiesel and if it can be used as a sustainable fuel. It was found that higher composition of unsaturated fatty acids results in low oxidative stability and poor cetane number. Figure 8 shows that KOME contains a considerable amount of tocopherols that act as an antioxidant and helps in improving the stability of KBD. KBD stability can be further enhanced by doping metal oxide nanoparticles.[36]

3.2 | Effect of hot plate temperature on evaporation time

During the experimental evaluation, it was observed that physicochemical properties such as density, viscosity remain comparatively similar to that of biodiesel. Thus, the doping of the nanoparticles does not significantly affect these properties at low concentrations. However, the calorific value shows a significant increase as that of neat KBD (KBD100). It is because the thermal conductivity of MWCNTs at room temperature is over 2000 times greater than that of biodiesel. The results for evaporation time under varying temperature with or without the addition of NP's are shown in (Figure 9). A decreasing trend in the magnitude of evaporation rate was observed at all the hot plate surface temperatures for the metal and carbon nanoparticle doped test fuels. At 425°C, minimum evaporation time was observed in the case of KBD100 and KBD100Al30. The lowest evaporation time of KBD100CNT30 was at 400°C, whereas, in the case of KBD100Al30CNT30, it was at around 360°C. The addition of MWCNT in KBD100 and KBD100Al30 mixture boosts the ignition process. The MWCNT has a unique tendency to generate the combined effect of micro explosion and secondary atomization phenomenon, which enhanced the evaporation rate of fuel blend doped with carbon-based nanoparticles.[37] However, in case of fuel blend KBD100AL30CNT30, sudden rise in evaporation time was observed after 420°C (Figure 9). The unusual phenomenon occurred because of the amount of residue remaining on the hot plate increases after subsequent burning of fuel droplets at the higher temperature. In case of fuel sample, KBD100AL30CNT30 containing multiple nanoparticles, the dosage level is more. As soon as the fuel droplet burn off from the surface, the residual of both nanoparticles combine together and forms larger size residue particles. These particles restrict the heat

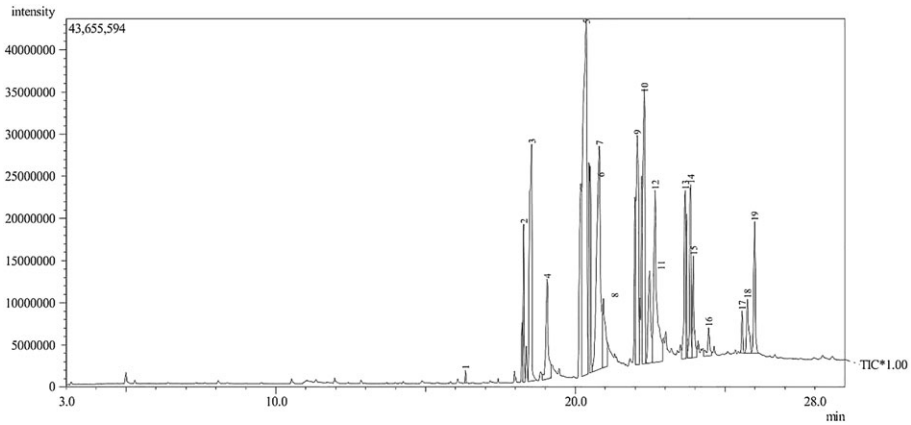

FIGURE 7 Fatty acid profile of Kusum methyl ester by gas chromatography–mass spectrometry (GC-MS)

Peak Number	Compound (Methyl Ester)	Chemical Name	Area (%)	Peak Number	Other Compound	Chemical Name	Area (%)
1	Myristic acid methyl ester(S)	$C_{15}H_{30}O_2$	0.096	4	n-Hexadecanoic acid (S)	$C_{16}H_{32}O_2$	1.44
	Tridecanoic acid methyl ester(S)	$C_{14}H_{28}O_2$	0.032		Pentadecanoic acid (S)	$C_{15}H_{30}O_2$	0.72
	Capric acid, methyl ester (S)	$C_{11}H_{22}O_2$	0.032		Octadecanoic acid (S)	$C_{18}H_{36}O_2$	0.72
2	11-Octadecenoic acid, methyl ester(UNS)	$C_{19}H_{36}O_2$	0.498		Nonadecanoic acid (S)	$C_{19}H_{38}O_2$	0.72
	Palmitoleic acid, methyl ester (UNS)	$C_{17}H_{32}O_2$	0.996	7	Oleic Acid (UNS)	$C_{18}H_{34}O_2$	5.2
	Cyclopropaneoctanoic acid 2-hexyl-,methyl ester (S)	$C_{18}H_{34}O_2$	0.498		Erucic acid (UNS)	$C_{22}H_{42}O_2$	2.6
	5-Tetracosenoic acid, methyl ester (UNS)	$C_{25}H_{48}O_2$	0.498		9-Hexadecenoic acid (UNS)	$C_{16}H_{30}O_2$	2.6
3	Palmitic acid, methyl ester (S)	$C_{17}H_{34}O_2$	8.45		E-9-Tetradecenoic acid (UNS)	$C_{14}H_{26}O_2$	2.6
5	6-Octadecenoic acid, methyl ester (UNS)	$C_{19}H_{36}O_2$	20.99	8	Octadecanoic acid (S)	$C_{18}H_{36}O_2$	1.144
6	Stearic acid, methyl ester (S)	$C_{19}H_{38}O_2$	0.45		Aqua Cera (S)	$C_{22}H_{44}O_4$	0.572
	Hexadecanoic acid, 15-methyl-,methyl ester (S)	$C_{18}H_{36}O_2$	0.45		Nonadecanoic acid (S)	$C_{19}H_{38}O_2$	0.572
	Behenic acid, methyl ester (S)	$C_{23}H_{46}O_2$	0.45		Palmitic acid (S)	$C_{16}H_{32}O_2$	0.572
	Eicosanoic acid, methyl ester (S)	$C_{21}H_{42}O_2$	0.45	9	Oleic Acid (UNS)	$C_{18}H_{34}O_2$	1.692
	Heneicosanoic acid, methyl ester (S)	$C_{22}H_{44}O_2$	0.45	11	Erucic acid (UNS)	$C_{22}H_{42}O_2$	0.732
9	Cyclopropanepentanoic acid, 2-undecyl-, methyl ester (S)	$C_{20}H_{38}O_2$	1.692		Oleic Acid (UNS)	$C_{18}H_{34}O_2$	1.464
	13-Docosenoic acid, methyl ester (UNS)	$C_{23}H_{44}O_2$	1.692		Z-8-Methyl-9-tetradecenoic acid (UNS)	$C_{15}H_{28}O_2$	0.732
	11-Octadecenoic acid, methyl ester (UNS)	$C_{19}H_{36}O_2$	1.692		Z-11-Hexadecenoic acid (UNS)	$C_{16}H_{30}O_2$	0.732
	Cyclopropanedodecanoic acid, 2-octyl-, methyl ester (S)	$C_{24}H_{46}O_2$	1.692	12	Eicosanoic acid (S)	$C_{20}H_{40}O_2$	4.866
10	Eicosanoic acid, methyl ester (S)	$C_{21}H_{42}O_2$	3.308		n-Hexadecanoic acid (S)	$C_{16}H_{32}O_2$	1.622
	Hexadecanoic acid, 15-methyl-, methyl ester (S)	$C_{18}H_{36}O_2$	3.308		Nonadecanoic acid (S)	$C_{19}H_{38}O_2$	1.622
	Pentadecanoic acid, 14-methyl-, methyl ester (S)	$C_{17}H_{34}O_2$	1.654	15	(E)-13-Docosenoic acid (UNS)	$C_{22}H_{42}O_2$	0.432
13	13-Docosenoic acid, methyl ester (UNS)	$C_{23}H_{44}O_2$	1.844		9-Octadecenal (UNS)	$C_{18}H_{34}O$	0.432
	15-Tetracosenoic acid, methyl ester (UNS)	$C_{25}H_{48}O_2$	0.922		Z-10-Pentadecen-1-ol (UNS)	$C_{15}H_{30}O$	0.432
	13-Octadecenoic acid, methyl ester (UNS)	$C_{19}H_{36}O_2$	1.844		(Z)-9-Tetradecenal (UNS)	$C_{14}H_{26}O$	0.432
14	Docosanoic acid, methyl ester (S)	$C_{23}H_{46}O_2$	4.1	16	Oleamide (UNS)	$C_{18}H_{35}NO$	0.376
15	Pentanoic acid, 10-undecenyl ester (UNS)	$C_{16}H_{30}O_2$	0.432		Tetradecanamide (S)	$C_{14}H_{29}NO$	0.188
17	Tetracosanoic acid, methyl ester (S)	$C_{25}H_{50}O_2$	0.312		Octadecanamide (S)	$C_{18}H_{37}NO$	0.188
	Heptacosanoic acid, methyl ester (S)	$C_{28}H_{56}O_2$	0.156		Dodecanamide (S)	$C_{12}H_{25}NO$	0.188
	Eicosanoic acid, methyl ester (S)	$C_{21}H_{42}O_2$	0.156	18	Z-13-Octadecenal (UNS)	$C_{18}H_{34}O$	0.72
	Heneicosanoic acid, methyl ester (S)	$C_{22}H_{44}O_2$	0.156		Cyclododecene epoxide (UNS)	$C_{12}H_{22}O$	0.36
					13-Docosenoic acid (UNS)	$C_{22}H_{42}O_2$	0.36
					Z-9-Hexadecenal (UNS)	$C_{16}H_{30}O$	0.36
				19	Behenic alcohol (S)	$C_{22}H_{46}O$	0.662
					1-Hexacosene (UNS)	$C_{26}H_{52}$	0.662
					1,1-Bis(dodecyloxy)hexadecane (S)	$C_{40}H_{82}O_2$	0.662
					Nonadecyl alcohol (S)	$C_{19}H_{40}O$	0.662
					1-Hexacosanol (S)	$C_{26}H_{54}O$	0.662

FIGURE 8 Free fatty acid profile of Kusum (*Schleichera oleosa*) biodiesel

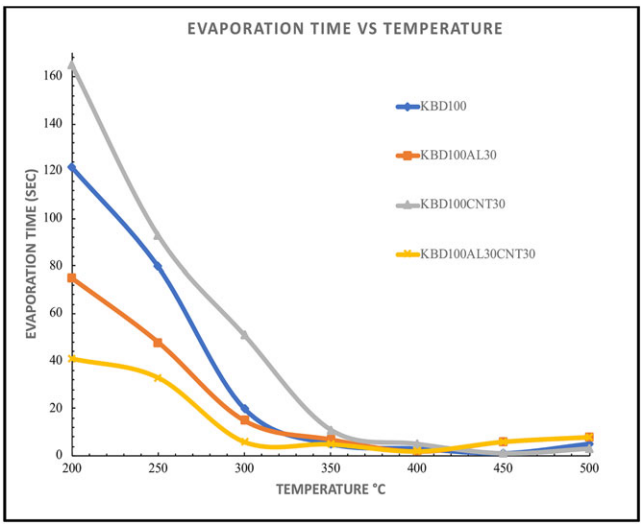

FIGURE 9 Evaporation time vs temperature for various test fuels [Colour figure can be viewed at wileyonlinelibrary.com]

transfer phenomenon and result in sudden rise of evaporation time. The cetane number also shows an increase of about 8% due to the addition of MWCNT in KBD (refer Table 2). Therefore, the evaporation rate of the fuel droplet is increased, which resulted in a shortened ignition delay.

3.3 | Effect of hot plate temperature on ignition probability

The ignition mechanism of combustible fuel droplet on a hot surface is a probabilistic phenomenon. It depends on different parameters such as temperature and material of the hot surface, particle concentration, thermal conductivity, droplet size, and distance of the hot plate from the nozzle orifice. Figure 10 showed the effect of temperature on ignition probability for neat biodiesel and its

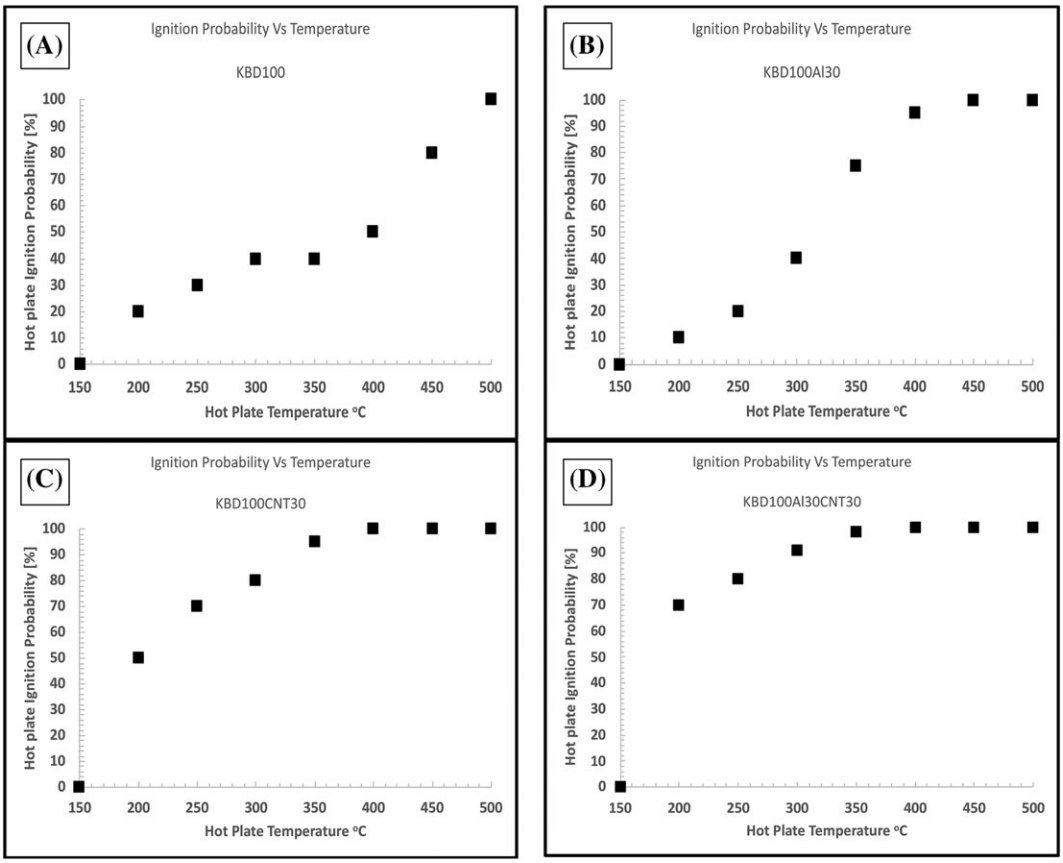

FIGURE 10 Ignition probability vs temperature A, for pure Kusum biodiesel, B, for alumina nanoparticles, C, for CNT (multiwalled carbon nanotubes [MWCNTs]), and D, for (alumina + MWCNT) nanoparticles doped Kusum biodiesel

blends. The results were obtained by ejecting the liquid fuel when the starting temperature was set at 200°C. The process continued with the increase in the hot plate temperature by 50°C till the final temperature of 450°C was achieved. Ten consecutive ignitions were conducted at each temperature. The burning of fuel droplet on a hot plate is a complex process because liquid fuel is allowed to fall on to the heated surface directly as reported in past studies.[24-26] The sufficient heat transfer can only take place when at least a portion of the liquid is evaporated and comes into contact with the hot surface. There is a transition phase in which both ignition and no ignition event occurs. The risk factor during the ignition probability experiment was calculated using logistic regression model, whereas the quality of fit was determined using the chi-squared goodness fit test.[25] The graph plotted for different fuel samples (see Figure 10A-D) suggests that experimental ignition probability obtained shows "S" curve fit of this data. Almost all the fuels exhibit a similar behavior of a longer "tail" of low ignition probability and a sharper definition of the temperature for high ignition probability. Subsequently, it can be ascertained that adding alumina and CNT nanoparticles to the biodiesel radically increases the ignition probability.

3.4 | Effect of nanoparticles on heat transfer mechanism

As per the qualitative analysis of ignition phenomenon on a hot surface, the shape of emulsion curves is divided into four different zones evaporation, nucleate boiling, transition boiling, and film boiling (Leidenfrost phenomena).[33] The Leidenfrost effect is a natural phenomenon occurs on the outer covering of the hot plate. During this period, the surface of the fluid droplet in close contact with a mass notably hotter than the fluid boiling point generates an insulating vapor layer prevents that fluid from evaporating rapidly. It is due to this resistive force, fluid droplets float over the surface of the hot plate without making physical contact with it (Figure 11). The experiments were conducted between a temperature range of 200 to 500°C. As per past literature reviews,[31] this temperature range suits best for film boiling occurrence. A uniform vapor film is formed under the droplets in the film boiling mode, and this prevents the connection of hot surface with the liquid (surface temperature [T_S] greater than Leidenfrost temperature [T_L]), the fuel droplets levitate from the surface by forming a vapor layer. As the temperature of the plate (T_S) increases, the

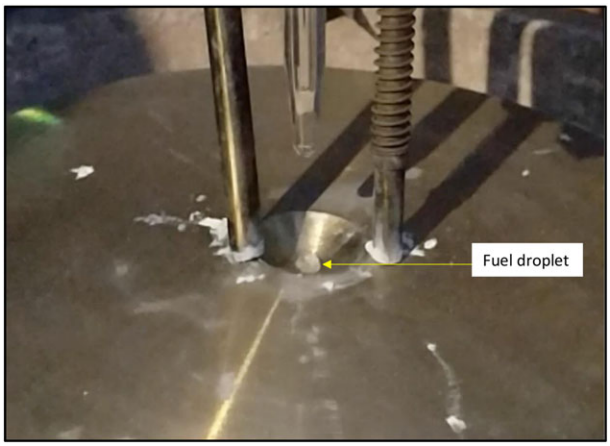

FIGURE 11 Photographic view of Leidenfrost phenomenon of test fuels over heated stainless steel plate [Colour figure can be viewed at wileyonlinelibrary.com]

rate of heat transfer increases, because of thermal radiation. This increase in T_S leads to a decrease in evaporation time of the test fuel droplets. During the hot plate evaporation mechanism of fuel droplet, the vapor acts as a medium to transmit heat from the surface of the plate to the liquid droplet. The process of conduction and radiation governs this heat transfer process. Once the surface temperature of the hot plate starts increasing, the radiation from the vapor film becomes more relevant under which heat flux also increases. This heat transfer mechanism led to an increase in ignition probability of the fuel droplet.

Thus, the experimental study confirms that with the addition of the nanoparticles, the heat conduction enhancement was not only the principal mechanism to enhance the heat transfer rate. The additional radiation absorbed by the fuel droplet also results in an increment in evaporation rate. Thus, for nanoparticles doped fuel samples, heat transfer to surrounding vapor becomes higher due to diffusion. Because of this catalytic effect caused by nanoparticles, the generation and combustion of the gas mixture were influenced, which results in better ignition characteristics. In case of neat (KBD) fuel, the rate of heat transfer becomes less compelling as compared with that of nanofuels as pure fuels are translucent to radiation. The nanofuels have higher radiation intensity as compared with that of conventional fuels because metal oxide–based nanoparticles have shorter wave length, which helps them to ingest higher heat of radiation. The moment test fuel droplet starts evaporating on a hot surface, a droplet from glass burette irrupts into the oxygen-rich open atmosphere due to the phenomenon of natural convection. The experimental investigation revealed that atmospheric air alone was not responsible for burning of fuel droplet on the hot plate, ignition will not takes place until fuel/air absorbs abundant energy. Also, the neat biodiesel (KBD100) has less heat absorption capacity compared with other test fuels; therefore, a large amount of unburnt mixture was left over the surface of the hot plate during the ignition test.

Therefore, after evaluating the physicochemical properties of the test fuels conclusion can be drafted, doping of metal oxide and carbon-based nanoparticles with the neat KBD leads to an increase in the cetane index. This result reduction in ignition delay for test fuels which contain nanoparticles. The comparative evaluation of different test fuels also displays a higher evaporation rate for nanoparticles doped test fuels. The critical surface temperatures for KBD100, KBD100Al30, KBD100CNT30, and KBD100Al30CNT30 are 340, 321, 312, and 301°C, respectively (refer Figure 9). The critical temperature (T_C) of the fuel droplet is the temperature of the surface resembling the minimum evaporation time. At this temperature (T_C), the liquid droplet disintegrates shortly as soon as significant burning starts, at the liquid-hot solid surface interface. The outcome of this event results in almost spontaneous evaporation. The value of T_C for the fuel sample KBD100Al30CNT30 is found inferior due to increment in catalytic activities (promoting a higher rate of heat transfer). Thus, the examination affirms that the issue of the ignition delay could be crouched by doping alumina/MWCNT nanoparticles to the neat biodiesel.

3.5 | Effect of nanoparticles on spray characteristics of test fuels

SMD and SSA of the test fuels were evaluated using Malvern Spraytec optical spray analyzer to investigate the effect of metal and carbon–based nanoparticles. The spray pattern plays a crucial role in estimating the quality of combustion of fuel in the combustion chamber. Figure 12 A shows the comparative result of SMD of different test fuels at a nozzle pressure of 175 bar. The mean of spray particles/fuel droplets ejected out from the nozzle for a specified set time period is known as SMD. The SMD of the of the spray particles is directly dependent upon the physical properties of the fuel such as density, viscosity, and surface tension. Biodiesel has higher SMD as compared with that of conventional fuels. The reasons behind this are due to the high friction rate between the biodiesel and nozzle surface resulting in lower injection velocity, hence, increase in SMD. During the investigation, it was observed that the mean diameter of the nanoparticles laden biodiesel is slightly different as compared with that of neat KBD. KBD100 demonstrate a significantly larger diameter than other test fuels (Figure 12A). The addition of alumina and MWCNT nanoparticles lowers the surface tension of KBD, which thereby increases the nozzle velocity, thus, reduces the mean diameter of the fuel droplet.

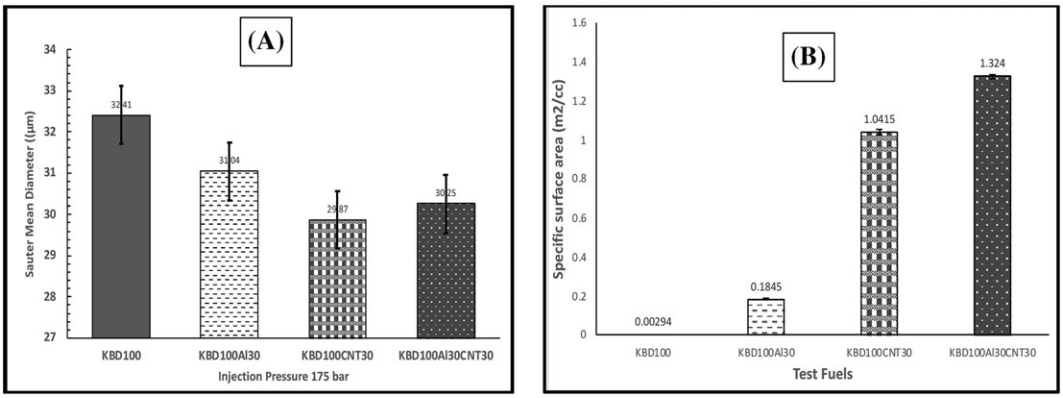

FIGURE 12 A, Sauter mean diameter (SMD) and B, specific surface area (SSA) of different test fuels

Figure 12B shows the variation of the SSA (m^2/cm^3) with or without dispersion of nanoparticles. SSA, ie, the SSA of particle which is defined as the ratio of surface area to volume of the particle is the quantity that governs the knocking characteristics in CI engine. Larger the SSA of particle lesser will be the delay period, which might ultimately result in good combustion characteristics. Interestingly, the fuel blend containing MWCNT shows maximum value for the SSA due to the secondary atomization phenomenon associated with carbon nanotubes. After investigating the spray properties of the test fuels, it can be concluded that the KBD containing (alumina and MWCNT) nanoparticles improves the atomization properties of fuel droplets by providing enhanced rapid evaporation and better fuel-air mixing qualities.

4 | CONCLUSIONS

In the present investigation, evaporation time and ignition probability for neat KBD and nanoparticle (alumina, CNT, and alumina + CNT) blended biodiesel, on stainless steel disk (as a function of surface temperatures) have been evaluated.

The following conclusions can be drawn from the experimental study.

- Nonedible vegetable oils can be utilized as a potential feedstock for biodiesel production by using the application of nanoadditives.
- The influence of adding CNT in biodiesel is more predominant than alumina nanoparticles. In the case of CNT blended biodiesel, the evaporation time is greatly reduced.
- Alumina/MWCNT nanoparticles doped test fuels show lower evaporation time as compared with that of neat KBD, till Ts is less than Tc. Beyond Tc, the evaporation time is observed to be increasing, which is the characteristic of the Leidenfrost phenomenon.
- The amplification in the evaporation rate induced due to nanoparticles incorporation at liquid-vapor interface, the possibility of ignition was observed to be much higher for nanofuels as compared with that of neat diesel.
- The value of SMD shows negligible change in physical properties such as density and kinematic viscosity with the addition of alumina and MWCNTs nanoparticles to neat KBD. However, spray property such as the SSA of KBD100Al30, KBD100CNT30, and KBD100Al30CNT30 is observed to be improved because of higher surface to volume ratio.
- The doping of metal oxide and carbon oxide nanoparticles has improved the stability, ignition, and spray characteristics of inedible biodiesel. However, some previous research showed that exposure of unburnt nanoparticles such carbon nanotubes and other metal-based nanoparticles into the atmosphere had an adverse impact on animal/plant kingdom and the human race. These nanosized particles affect the life cycle and respiratory system of aquatic and terrestrial biota and human beings.[38,39] Therefore, risk assessments associated with the unburnt nanoparticles are needed to be addressed at an early stages. Techniques such as exhaust gas treatment devices and installation of nanoparticles-membrane filtration for vehicular exhaust can trap unburnt nanoparticles from the exhaust of the engine.[40,41] Therefore, research is going on to identify appropriate and cost effective material for nano membrane fabrication. Also, technologies to control the pore size of the nano membrane are under developing stages, so that harmful particles from engine exhaust can be absorbed and treated effectively.

From the study, it is concluded that the ignition properties and spray characteristics of the fuels doped with nanoparticles are improved. Hence, the engine performance and emission characteristics are expected to be better with nanoparticles doped biodiesel in comparison with neat biodiesel.

ORCID

Mukul Tomar https://orcid.org/0000-0001-7564-8774

REFERENCES

1. Yıldız İ. 1.12 Fossil fuels. Vol 1.; 2018.
2. BP. BP Statistical Review of World Energy, June 2017. *London BP*. 2017;(June).
3. Ministry of Petroleum and Natural Gas G of I. Annual Report 2016-2017.2017:214.
4. Reşitoğlu İA, Altinişik K, Keskin A. The pollutant emissions from diesel-engine vehicles and exhaust after treatment systems. *Clean Techn Environ Policy*. 2015;17(1):15-27.
5. Sommer A. Burning fossil fuels: impact of climate change on health. *Int J Health Serv*. 2016;46(1):48-52.
6. Höök M, Tang X. Depletion of fossil fuels and anthropogenic climate change—a review. *Energy Policy*. 2013;52:797-809.
7. Stamenkovi OS, Veljkovi VB, Bankovi IB. Biodiesel production from non-edible plant oils. *Renew Sustain Energy Rev*. 2012;16:3621-3647.
8. Mofijur M, Masjuki HH, Kalam MA, Ashrafur Rahman SM, Mahmudul HM. Energy scenario and biofuel policies and targets in ASEAN countries. *Renew Sustain Energy Rev*. 2015;46: 51-61.
9. Musthafa MM, Kumar TA, Mohanraj T, Chandramouli R. A comparative study on performance, combustion and emission characteristics of diesel engine fuelled by biodiesel blends with and without an additive. *Fuel*. 2018;225(March):343-348.
10. Yadav AK, Khan ME, Dubey AM, Pal A. Performance and emission characteristics of a transportation diesel engine operated with non-edible vegetable oils biodiesel. *Case Stud Therm Eng*. 2016;8:236-244.
11. Janaun J, Ellis N. Perspectives on biodiesel as a sustainable fuel. *Renew Sustain Energy Rev*. 2010;14(4):1312-1320.
12. Mahmudul HM, Hagos FY, Mamat R, Adam AA, Ishak WFW, Alenezi R. Production, characterization and performance of biodiesel as an alternative fuel in diesel engines—a review. *Renew Sustain Energy Rev*. 2017;72(April 2016):497-509.
13. Hosseinzadeh-Bandbafha H, Tabatabaei M, Aghbashlo M, Khanali M, Demirbas A. A comprehensive review on the environmental impacts of diesel/biodiesel additives. *Energ Conver Manage*. 2018;174(June):579-614.
14. Mohd Noor CW, Noor MM, Mamat R. Biodiesel as alternative fuel for marine diesel engine applications: a review. *Renew Sustain Energy Rev*. 2018;94(February 2017):127-142.
15. Silitonga AS, Masjuki HH, Mahlia TMI, et al. Schleichera oleosa L oil as feedstock for biodiesel production. *Fuel*. 2015;156:63-70.
16. Pali HS, Mishra C, Kumar N. Production and physico-chemical characterisation of Kusum oil methyl ester as an alternative fuel in diesel engine. *J Biof*. 2013;4(1):38-46.
17. Yadav AK, Khan ME, Pal A, Dubey AM. Experimental investigations of performance and emissions characteristics of Kusum (*Schleichera oleosa*) biodiesel in a multi-cylinder transportation diesel engine. *Waste and Biomass Valorization*. 2017;8(4): 1331-1341.
18. Chandrasekaran V, Arthanarisamy M, Nachiappan P, Dhanakotti S, Moorthy B. The role of nano additives for biodiesel and diesel blended transportation fuels. *Transp Res Part D Transp Environ*. 2016;46:145-156.
19. Kumar AS. Impact on the performance of direct compression ignition engine by adding nano-particle in biodiesel. *J Material SciMech Eng*. 2015;2(7):7-9.
20. Aalam CS, Saravanan CG. Effects of nano metal oxide blended Mahua biodiesel on CRDI diesel engine. *Ain Shams Eng J*. 2017;8(4):689-696.
21. Prabu A. Nanoparticles as additive in biodiesel on the working characteristics of a DI diesel engine. *Ain Shams Eng J*. 2018;9(4): 2343–2349.
22. El-Seesy AI, Abdel-Rahman AK, Bady M, Ookawara S. Performance, combustion, and emission characteristics of a diesel engine fueled by biodiesel-diesel mixtures with multi-walled carbon nanotubes additives. *Energ Conver Manage*. 2017; 135:373-393.
23. Annamalai M, Dhinesh B, Nanthagopal K, et al. An assessment on performance, combustion and emission behavior of a diesel engine powered by ceria nanoparticle blended emulsified biofuel. *Energ Conver Manage*. 2016;123:372-380.
24. Shams Z, Moghiman M. Effect of metal oxide nanoparticles on the ignition characteristics of diesel fuel droplets: an experimental study. *J Brazilian Soc Mech Sci Eng*. 2018;40(2):1-10.
25. Somandepalli V, Kelly S, Davis S. Hot surface ignition of ethanol-blended fuels and biodiesel. SAE International 2008; 2008-01-0402.
26. Tyagi H, Phelan PE, Prasher R, et al. Increased hot-plate ignition probability for nanoparticle-laden diesel fuel. *Nano Lett*. 2008;8(5):1410-1416.
27. Sadhik Basha J, Anand RB. Performance, emission and combustion characteristics of a diesel engine using carbon nanotubes blended Jatropha methyl ester emulsions. *Alex Eng J*. 2014; 53(2):259-273.
28. Khond VW, Kriplani VM. Experimental investigation and modeling of the evaporation rate of carbon nanotube blended emulsified Neem biodiesel. *Biofuels*. 2017;0(0):1-7.
29. Ooi JB, Rajanren JR, Ismail HM, Swamy V, Wang X. Improving combustion characteristics of diesel and biodiesel droplets by graphite oxide addition for diesel engine applications. *Int J Energy Res*. 2017;41(14):2258-2267.
30. Colwell JD, Reza A. Hot surface ignition of automotive and aviation fluids. *Fire Technol*. 2005;41(2):105-123.
31. Gupta JG, Agarwal AK. Macroscopic and microscopic spray characteristics of diesel and Karanja biodiesel blends. SAE Tech Pap 2016-*01-0869*.2016;(March).
32. Chen PC, Wang WC, Roberts WL, Fang T. Spray and atomization of diesel fuel and its alternatives from a single-hole injector using a common rail fuel injection system. *Fuel*. 2013;103(10):850-861.
33. Rueda Villegas L, Tanguy S, Castanet G, Caballina O, Lemoine F. Direct numerical simulation of the impact of a droplet onto a hot surface above the Leidenfrost temperature. *Int J Heat Mass Transf*. 2017;104:1090-1109.
34. Symposia IC, Eisenhart C. The purposes of uncertainty analysis. 2013.

35. Shehata MS, Attia AMA, Razek SMA. Corn and soybean biodiesel blends as alternative fuels for diesel engine at different injection pressures. *Fuel*. 2015;161:49-58.
36. Karthikeyan S, Silaimani SM. An emission analysis on the role of TiO_2 additives in Kusum oil methyl esters on working characteristics of CI engine 2017;24(July):393–399.
37. Basha JS, Anand RB. The influence of nano additive blended biodiesel fuels on the working characteristics of a diesel engine. *J Braz Soc Mech Sci Eng*. 2013;35(3):257-264.
38. Cassee FR, van Balen EC, Singh C, et al. Exposure, health and ecological effects review of engineered nanoscale cerium and cerium oxide associated with its use as a fuel additive. *Crit Rev Toxicol*. 2011;41(3):213-229.
39. Kumar P, Robins A, Apsimon H. Nanoparticle emissions from biofuelled vehicles-their characteristics and impact on the number-based regulation of atmospheric particles. *Atmos Sci Lett*. 2010;11(4):327-331.
40. Muralikrishnan R, Swarnalakshmi M, Nakkeeran E. Nanoparticle-membrane filtration of vehicular exhaust to reduce air pollution—a review 2014;3(4):82–86.
41. Liu J, Pui DYH, Wang J. Removal of airborne nanoparticles by membrane coated filters. *Sci Total Environ*. 2011;409(22):4868-4874.

How to cite this article: Kumar N, Tomar M. Influence of nanoadditives on ignition characteristics of Kusum (*Schleichera oleosa*) biodiesel. *Int J Energy Res*. 2019;1–14. https://doi.org/10.1002/er.4446

MCML Dynamic Register Design

Neeta Pandey
Delhi Technological University
New Delhi, India
Email:n66pandey@rediffmail.com

Kirti Gupta
Bharati Vidyapeeth's College of Engineering,
New Delhi, India

Bharat Choudhary
Delhi Technological University
New Delhi, India

***Abstract*— This paper proposes MOS current mode logic (MCML) dynamic register. The register employs tristate buffers working in master-slave configuration. The paper also investigates the behavior of the registers on clock overlap and finds that it do not comply with the desired functionality. Two techniques to achieve clock skew insensitive behavior are proposed. The first technique puts constraints on timing parameter whereas the second technique modifies the enabling mechanism of the buffer. The register operation and their insensitivity towards clock skew are examined through simulations using TSMC 90 nm CMOS technology parameters. Various timing waveforms to demonstrate the effectiveness of the proposed techniques are also included.**

Keywords— MCML, tristate buffer, clock skew, register

I. INTRODUCTION

The continual shrinking of CMOS technology and increasing on-chip integration level has led to the development of mixed mode circuits where analog and digital circuits are placed on a single piece of silicon. The traditional CMOS logic is often employed in digital circuit owing to its design ease, high speed capability, high packing density and negligible static power consumption [1]. However, this logic style suffers from large current spikes during the switching event (also referred to as digital switching noise) which adversely affect resolution of on-chip analog circuits. MOS current mode logic (MCML) is a low noise logic style which is differential in nature, works on reduced voltage swing, cause cancellation of transients during switching event thereby making it a preferred choice over traditional CMOS logic [2]. Hence, MCML style has been used in the implementation of various circuits in the field of communication, digital signal processing and high speed arithmetic [3-8].

A register is extensively used in almost all the applications to store the state information as long as power is turned on and are classified as static and dynamic register. The former class holds data for a very long time and uses a positive feedback or regeneration mechanism. The other class rely on the temporary storage of charge on parasitic capacitors and are continuously clocked. The two clocks are assumed to be perfect but due to the variations in the routing path, load capacitances, overlapping in clock signals named as clock skew exist [9]. This issue is of major concern and is well addressed for CMOS registers [9]. However, it remains unattended in context of the MCML registers and is main motivation behind the present study. Two techniques to realize clock skew insensitive MCML dynamic registers are proposed. The first technique puts constraints on timing parameters while the second suggest a new buffer enabling mechanism.

The remainder of this contribution is arranged as following: the first section briefly covers MCML tristate buffer. The next section puts forward the proposed MCML dynamic register design and addresses the clock overlap problem in operation of the register. Timing waveforms are obtained through SPICE simulations using TSMC 90 nm CMOS technology parameters are included at relevant places in the paper to support the claim. The paper is finally concluded in section IV.

II. MCML TRISTATE BUFFER

A MCML gate in general consist of three main parts named as pull down network, current source and load to implement the functionality, maintain a constant bias current and to perform a current to voltage conversion as shown in Fig. 1(a). In addition to these three parts, a MCML tristate gate includes an extra circuitry for disabling it during high impedance state.

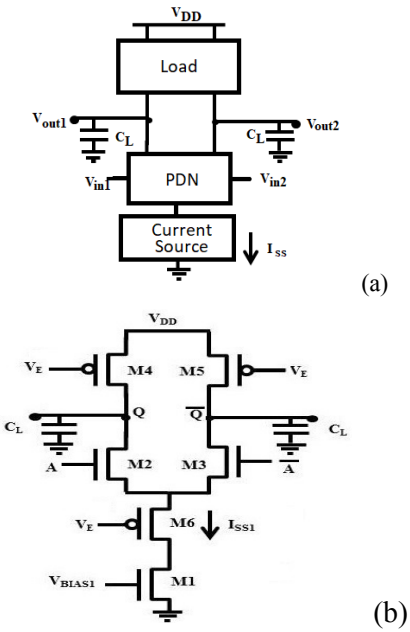

Fig. 1(a) A generic MCML gate (b) Complete schematic of MCML tristate buffer [12]

Different mechanism to achieve a high impedance are available [10-12]. Out of them, the schematic of the MCML tristate buffer [12] shown in Fig. 1(b) exhibits the best performance. The basic structure is same as a MCML buffer except that it uses a full swing control signal V_E to activate/deactivate the load (M4-M5) and the current source section (M6). A high value of the V_E signal turns OFF the transistors (M4-M6) which disconnects the power supplies from the output node and a high impedance state is attained. Conversely for a low value of the V_E signal, the transistors M4-M6 are turned ON and the circuit behaves as a regular buffer. Therefore, the procedure outlined in [12] is used to design the tristate buffer for the given specifications.

III. MCML DYNAMIC REGISTER

The most common approach for designing a register is based on master-slave configuration. An edge-triggered dynamic register can be formed by cascading two MCML tristate buffers as explained.

A. Circuit and operation

The implementation of the positive edge-triggered dynamic register consisting of tristate buffers (B1 and B2) is depicted in Fig. 2(a) The buffers B1 and B2 are enabled respectively by and signals. For low values of the CLK signal, B1 is enabled which samples the input D to the output Q_M. Analogously, when becomes CLK high, the sampled data is made available at the Q_S output of B2.

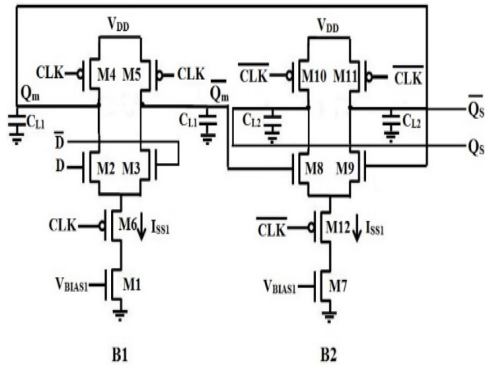

(a)

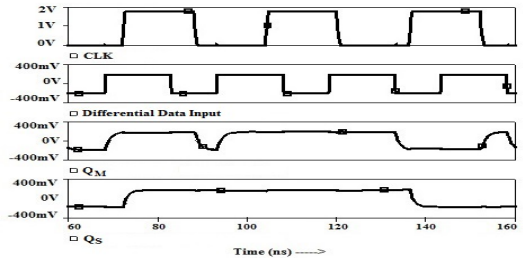

(b)

Fig. 2 (a) Complete schematic of the proposed MCML dynamic register (b) its timing waveforms

The proposed MCML dynamic register is designed for voltage swing of 400 mV and bias current of 100 µA. The timing waveforms illustrating the said functionality are displayed in Fig. 2(b).

B. Clock Oberlap issue

The above discussion on the register's operation assumes that both the buffers are being driven by perfectly inverted clocks. Practically it is not possible to achieve perfect inversion of the clocks due to unequal routing paths. Thus, there exists overlapping intervals as 0-0 and 1-1 overlap. During the 0-0 overlap condition, both the buffers (indicated by a tick mark as shown in Fig. 3(a)) are enabled due to the conducting PMOS transistors such that any changes in input D leads to changes in the state of the capacitors (C_{L1} and C_{L2}). Thus, violating the functionality of positive edge triggered register. Similarly, for 1-1 overlap, the PMOS transistors in the buffers are OFF and are removed from the Fig. 3(b). In this case, it can be observed that no state change of capacitors occurs for the changes in D input. Therefore, the circuit retains its previous output. It may be noted from timing waveforms of Fig. 3(c) that when CLK becomes 0, the QM responds to input data and this change is reflected at QS due to existence of 0-0 overlap, thus output changes at negative edge which clearly violates the functionality of positive edge triggering.

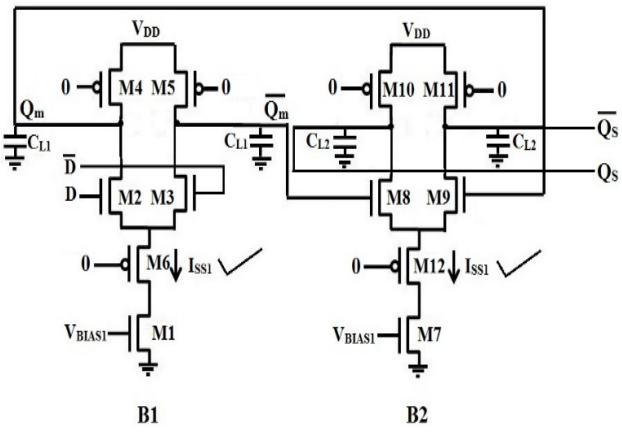

(a)

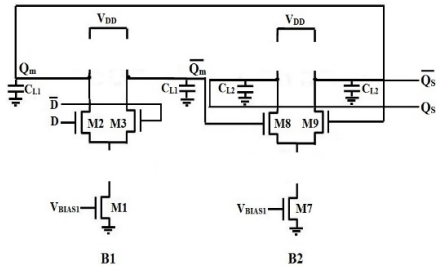

(b)

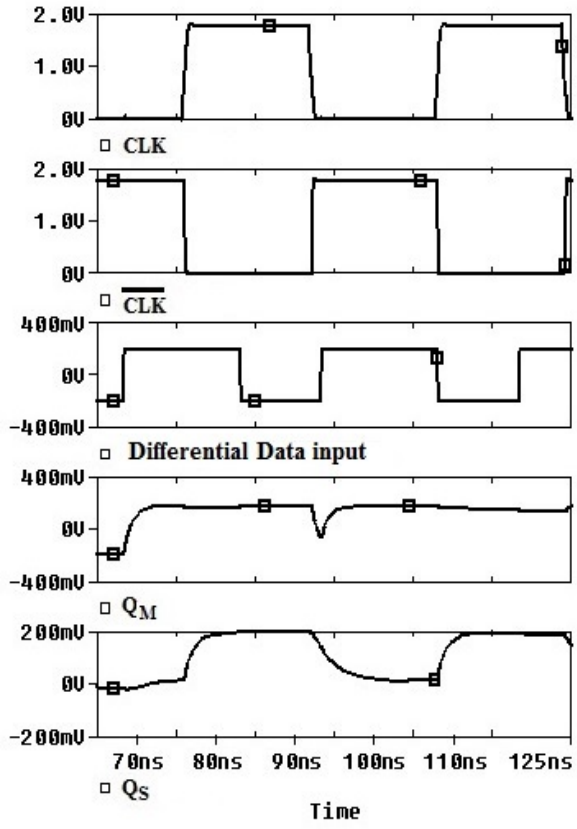

(c)

Fig. 3. Complete schematic for dynamic register during (a) 0-0 Overlap (b) 1-1 Overlap and (c) timing waveforms

It is clear that all the buffers enter in the high impedance state during 1-1 overlap therefore any change in the input does not cause any changes in the state of register whereas 0-0 overlap disturbs the register functionality. This issue can be handled either by putting constraints on the timing parameters or through circuit level the modification.

In context with the 0-0 overlap in the proposed dynamic register, if data does not change in the overlap period, there would not be any change in the state of Qm and Qs. Alternatively, if the propagation delay of master buffer B1 is larger than the overlap period, then state of the slave remains unchanged. Consequently, when $\overline{CLK}$ becomes high, the slave state will anyway enter in hold state leading to correct operation. It is thus clear that proposed dynamic registers can be made clock overlap insensitive if the timing constraints discussed above are followed.

Alternatively, an enabling circuit of the PMOS transistors in the buffers may be used. To elaborate this, the proposed positive edge-triggered dynamic register (Fig. 2(a)) is reconsidered. The PMOS transistors M10-M12 of the buffer B2 driven by the is now connected to a new signal MCLK. The circuit for its generation is shown in Fig. 4. The circuit consists of an NMOS (Tm1) driven by signal *CLK* and a weak pull-up PMOS (Tm2) transistor controlled by signal $\overline{CLK}$. The dynamic register with proposed enabling technique is shown in Fig. 5.

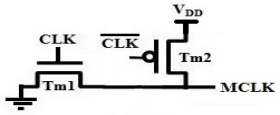

Fig. 4. Proposed circuit modification

In the 0–0 overlap condition, Tm1 is OFF and Tm2 conducts such that the signal MCLK becomes high. This causes the buffer B2 in high impedance state and prohibits the enabling of the buffer in the register. Also, it may be noted that after 0-0 overlap period, $\overline{CLK}$ attains a high logic such that Tm2 turns OFF and Tm1 remains OFF. Thus the MCLK becomes a soft node and its voltage is subject to charge leakage. The clock frequency should therefore be chosen so that soft node does not discharges to VDD - $|V_{TP}|$ (V_{TP} is threshold voltage of Tm2) enabling B2 buffer leading to malfunctioning of the circuit.

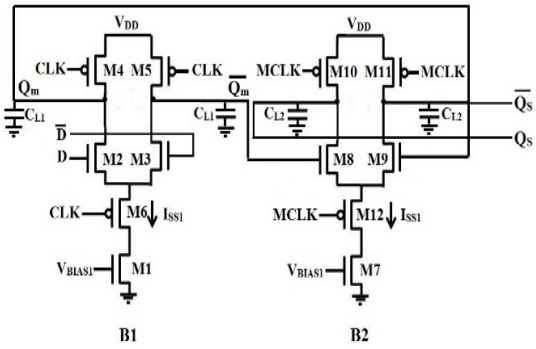

Fig. 5. Schematic of the proposed clock skew insensitive dynamic register

Analogously, during 1-1 overlap, the transistor Tm1 conducts while Tm2 remains OFF, making MCLK at low logic level. This enables the buffer B2 and maintain their previous states as before. It is also important to analyze the behavior of MCLK when 1-1 overlap is over. At this time, CLK is at logic high and attains a low logic so both Tm1 and Tm2 are ON and the circuit works as pseudo NMOS inverter. The voltage at output is computed as [7]:

$$V_{MCLK}=\left(V_{DD}-V_{TN}\right)-\sqrt{\left(V_{DD}-V_{TN}\right)^2-\frac{\mu_{p,eff}(W/L)_{Tm2}}{\mu_{n,eff}(W/L)_{Tm1}}\left(V_{DD}-|V_{TP}|\right)^2} \quad (1)$$

where $\mu_{p,eff}$ ($\mu_{n,eff}$) and $(W/L)_{Tm2}$ ($(W/L)_{Tm1}$) represent effective mobility and aspect ratio of Tm2(Tm1) respectively.

Assuming $V_{TN}=|V_{TP}|$, (1) modifies to

$$V_{MCLK} = \left(V_{DD} - V_{TN}\right)\left(1 - \sqrt{1 - x}\right) \quad (2)$$

where

$$x = \frac{\mu_{p,eff}\,(W/L)_{Tm\,2}}{\mu_{n,eff}\,(W/L)_{Tm\,1}} \quad (3)$$

It is clear from (2) that V_{MCLK} cannot attain value zero. Therefore, the subsequent buffer B2, enabled by MCLK needs to be redesigned accordingly by taking into consideration that that the load transistor is connected to a non-zero gate potential. The V_{MCLK} value can be set close to zero for very small values of x or if (W/L) Tm1>> (W/L) Tm2. But a large value of (W/L) Tm1 will affect activation of MCLK adversely due to larger capacitance. To verify this, various simulation runs were carried out by varying width of Tm1 between 0.27 µm to 1.44 µm and keeping width of Tm2 constant at 0.27 µm. The length of both the transistor is taken as 0.18 µm. The value of V_{MCLK} and delay are noted down; and are plotted in Fig. 6. It is noted that lower values of V_{MCLK} are obtained for larger Tm1 width value but at the cost of delay. Thus, to achieve a specific value of V_{MCLK}, there exists a trade-off between the size of Tm1 and delay.

The timing waveforms of the dynamic registers is depicted in Fig. 7. It may be noted that functionality of remains unaffected in presence of 0-0 and 1-1 overlaps, thereby making the register clock skew insensitive.

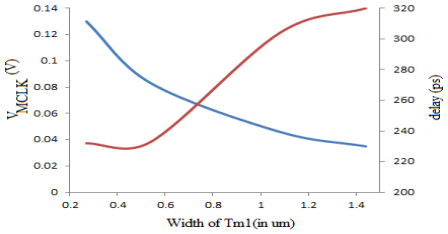

Fig. 6. Variation of V_{MCLK} and delay versus width of Tm1

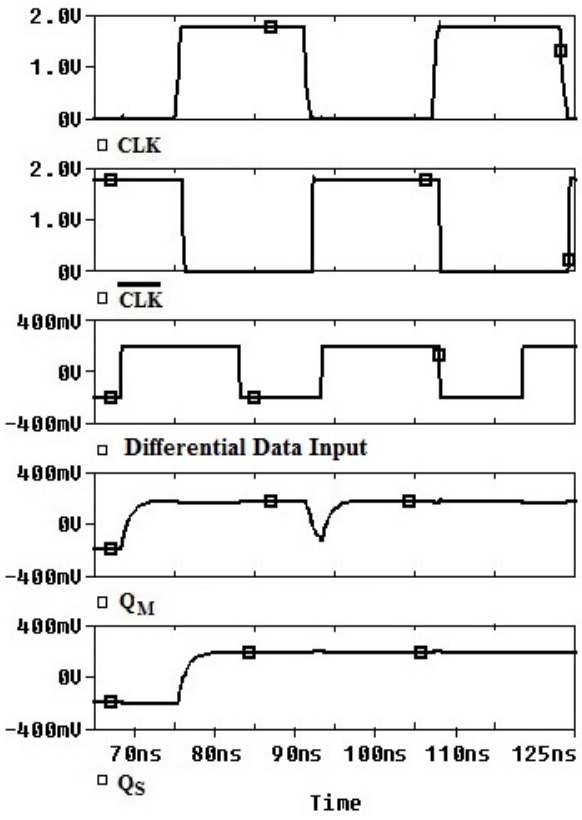

Fig. 7. Timing waveforms of the proposed clock skew insensitive MCML dynamic registers

IV. . CONCLUSIONS

In this contribution dynamic MCML tristate buffer based dynamic registers is proposed. Examination of proposed register shows that the behavior of proposed register deviates in presence of clock overlap, so two techniques are suggested for handling it. Timing constraints are used in first one while a modified buffer enabling mechanism is theme of second . The functioning of registers with modified enabling techniques is explained and it is found that registers with both techniques are insensitive to clock skew. Various timing waveforms are presented to support the investigations.

REFERENCES

[1] Weste N. H. E., & Harris, D. (2004) Principles of CMOS VLSI Design: A System Perspective. Addison-Wesley, 3rd ed..

[2] Alioto, M., & G. Palumbo, (2005) Model and design of bipolar and MOS current-mode logic (CML, ECL and SCL Digital Circuits), Netherlands: Springer.

[3] El-Hariry Y. M., & Madian, A. H. (2010) MOS Current Mode Logic Realization of Digital Arithmetic Circuits, Proc. of International Conference on Microelectronics, 128-131.

[4] Gupta, K., Pandey, N., & Gupta, M., (2013) Analysis and design of MOS current mode logic exclusive-OR gate using triple-tail cells, Microelectronics Journal, 44, 561-567.

[5] Gupta, K., Pandey, N., & Gupta, M. (2013) Low-Voltage MOS Current Mode Logic Multiplexer, Radioengineering Journal, 22, 259-268.

[6] Alioto, M., & Palumbo, G. (2008) Power Aware Design of Nanometer MCML Tapered Buffers, IEEE Transactions on Circuits and Systems-II: Express Briefs, 55, 16-20.

[7] Delcan, Y., & Morgul, A. (2009) High Performance 16-bit MCML Multiplier, Proc. of IEEE European Conference on Circuit Theory and Design, 157-160.

[8] Gupta, K., Pandey, N., & Gupta, M. (2013) MCML D-Latch Using Triple-Tail Cells: Analysis and Design," Active and Passive Electronic Component, 2013. 1-9, 2013.

[9] Rabaey, J. (2003) Digital integrated circuits (a design perspective). Prentice Hall, Englewood Cliffs, NJ, 2nd ed..

[10] Badel, S., & Leblebici, Y. (2007) Tristate buffer/bus driver circuits in MOS current- mode logic, Proc. of Research in Microelectronics and Electronics Conference 237–240.

[11] Gupta, K., Pandey, N., & Gupta, M. (2013) Low-power tristate buffer in MOS current mode logic, Analog Integrated Circuits and Signal Processing 75, 157-160.

[12] Pandey, N. & Choudhary, B. (2015). Improved tristate buffer in MOS current mode logic and its application," Analog Integrated Circuits and Signal Processing, 84, 333–340.

MĀPAN-Journal of Metrology Society of India
https://doi.org/10.1007/s12647-019-00316-w

SHORT COMMUNICATION

Measurement of Benzo(a)pyrene in PM_{10} Collected in New Delhi

J. Pokhariyal[1,2], A. Mandal[2]* and S. G. Aggarwal[1]

[1]CSIR-National Physical Laboratory, New Delhi 110012, India

[2]Delhi Technological University, Main Bawana Road, Shahbad Daulatpur, Delhi 110042, India

Received: 07 August 2018 / Accepted: 29 March 2019

© Metrology Society of India 2019

Abstract: Polyaromatic hydrocarbons (PAH) are the compound which consists of multiple benzene rings bonded in straight, groups or angular forms. They are also found in atmospheric aerosols. In the atmosphere, they can be emitted primarily as a result of incomplete combustion of natural sources (fossil fuels, forest fires, smoke etc.) or anthropogenic sources (coal burning, vehicular emissions, smoke, etc.) or secondarily by atmospheric processes. Depending on the anthropogenic sources, PAHs may occur in significant concentration in urban and industrial ambient air, i.e., bounded with particulate matter (PM). A particle whose aerodynamic diameter is $\leq$ 10 μm is called PM_{10}. Benzo(a)pyrene (BaP) is among the most toxic and carcinogenic PAHs. Both PM_{10} and BaP are among the 12 criteria pollutants listed in Indian National Ambient Air Quality Standards (NAAQS). In this paper, BaP concentration in PM_{10} collected in a representative site of New Delhi was studied during the year 2014–2015. The average concentration of BaP is varied from 0.04 to 25.7 ng m^{-3}. The uncertainty components in measurements were also estimated along with statistical analysis. The most significant uncertainty component is the purity of the BaP standard which has the highest uncertainty contribution as 77%.

Keywords: NAAQS; PM_{10}; PAHs; Benzo(a)pyrene (BaP)

1. Introduction

The primary source of polyaromatic hydrocarbons in the atmosphere is mainly due to incomplete combustion of fossil fuels emitted from suburban, natural, industrialized and vehicular sources. PAHs having small molecular weight exist in a gaseous phase in the atmosphere and also in particulate phase by the condensation after emission. PAHs having high molecular weight are mainly found as particulate in the atmosphere [1]. Thus, PAHs are ubiquitous as they are present in air, soil, and water in our environment [1, 2].

Chemically, the term "PAH" is used for compounds having carbon and hydrogen atoms. Their structure consists of multiple benzene rings bonded in straight, groups, or angular forms [3, 4].They have several sources as shown in Table 1.

There is an urgent need for monitoring the toxic compounds present in the atmosphere as they are hazardous for human health and the environment [6] International Agency for Research on Cancer (IARC) has selected few PAHs (e.g., Benzo[a]anthracene (BaA) and Benzo[a]pyrene (BaP)) as distinguished carcinogens for human [7]. Among them, BaP is referred to as a "carcinogenic substance- level 1" [8–10]. A lot of studies have been done regarding the increasing concentrations of BaP in the atmosphere all over the globe. The highest concentration of BaP (> 0.4 ng m^{-3}) was found in central and eastern part of Europe [11]. Exposure to BaP concentration beyond the permissible value was major and extensive in eastern and central part of Europe. From 2009 to 2011, 22–31% of the urban residents were exposed to BaP concentrations beyond the permissible limit of 1 ng m^{-3} [12]. In the latest report, it was observed that in summer, concentrations of BaP in the atmosphere in urban areas was averaged 3.6 ± 4.11 ng m^{-3} In winter, concentrations are higher (average 7.1 ± 5.1 ng m^{-3}) mainly because of the emission from domestic and industrial heating sources using fossil fuels.

The snow covers in the Eastern region of Moscow showed a high concentration of BaP due to its everyday fallout into the atmosphere. In 2010, the average mass of the BaP in the snow was found as 1942 ng g^{-1} while its mean values of intensity of fallout was 7.13 ng m^{-2} per

*Corresponding author, E-mail: anubha_mandal10@yahoo.co.in

Published online: 16 April 2019

Table 1 Main sources of emission in China, India and the USA for the USEPA [5]

Sources of emission	Global (%)	China (%)	India (%)	USA (%)
Biofuel	56.7	66.4	92.5	9.1
Wildfire	17.0	0	0	3.3
Consumer product wise	6.9	0.9	0.6	35.1
Traffic oil	4.8	2.0	IS	23.0
Coke production	3.7	10.7	1.3	IS
Domestic coal	3.6	14.4	IS	IS
Petroleum refining	2.4	1.0	IS	8.7
Waste incineration	1.9	IS	IS	9.5
Aluminum electrolysis	1.4	IS	IS	1.9
Open straw burning	IS	2.0	3.2	IS
Gasoline distribution	IS	IS	IS	3.0
Aerospace industry	IS	IS	IS	2.5
Other	1.5	0	2.7	3.9
Tonnes in thousand	530	114	90	32

IS Insignificant

day. Throughout the country, during winter BaP fallout varied between 0.3 and 1100 ng m^{-2} per day [13].

PM_{10}-bound BaP emitted from domestic heating sources was responsible for the lung cancer cases in various parts of cities of Poland. In rural areas, the average concentration of BaP was 1.39–4.86 ng m^{-3} [14]. PAH levels in the atmosphere are very low, i.e., $\leq$ ng m^{-3}; therefore, the measurement methods for their recording, collection and analysis study are very complex and have high uncertainties values due to low recovery in spite of large sampling volume [15]. This paper deals with the concentration of BaP in the PM_{10} samples of New Delhi collected in the year 2014–2015. The uncertainty components during sampling extraction and analysis of BaP are also taken into consideration.

2. Materials and Methods

The sampling was carried out for PM_{10} at NPL (National Physical Laboratory) in New Delhi for a year from January 2014 to January 2015 using a low-volume sampler (Envirotech APM 550) [16]. This measurement site was selected as it is a good representative site of urban aerosols of New Delhi with the mixed effect of industrial, vehicular, residential and agricultural emissions [17]. A total of 104 samples collected during year-round sampling as per NAAQS.

BaP was extracted from the exposed PM_{10} sample. The sample filter (quartz) was cut into a 14-mm-diameter disk.

Table 2 Gradient flow of mobile phase with composition and time

Time (min)	Water (%)	Acetonitrile (%)	Flow (mL/min)
0.01	50	50	0.5
20	0	100	0.5
35	0	100	0.5
40	50	50	0.5
45	50	50	0.5

The filter papers were then extracted with toluene using an ultrasonic bath. The toluene extracts was then passed through a silica gel column for the cleanup process using cyclohexane (HPLC grade) [18]. Finally, before analysis, the extract was evaporated on a rotary evaporator till dried up and was dissolved in 1 mL acetonitrile (HPLC grade). The extract obtained was then analyzed for BaP through a high-performance liquid chromatography (HPLC) system (Shimadzu Prominence Model LC-20AD) with programmed fluorescence detection (Shimadzu RX-10AXL).

Analysis of the BaP was carried out using a HPLC reversed phase C18 column (dimension 250 mm × 4.6 mm, make Shim-pack), with a elution of binary gradient from 50% acetonitrile (HPLC grade) and water mixture to 100% acetonitrile in 45 min (Table 2). BaP was detected in PM_{10} samples by means of a fluorescence detector with respect to its retention time. The fluorescence detection was done at 361 nm (excitation wavelength) and at 405 nm (emission wavelength).

The method was tested with quality assurance (verification of instrument calibration and repeatability test of the instrument). Two replicates of blank samples were used as real samples to check any contaminations of the analytes. The stock solution of standard was prepared by diluting aliquots of the BaP standard (Sigma-Aldrich, B1760). For calibration, BaP standard solution was prepared by successive dilution of stock solutions with acetonitrile (by weight). Calibration standard solutions were stored at 4 °C in the dark.

In India, the regulatory limit of BaP in National Ambient Air Quality Standards is 1 ng m^{-3} (annual). The PM_{10} sample filters were analyzed for BaP according to the ISO 16362: 2005. The data was calculated as follows.

The BaP concentration in PM_{10} samples (in ng m^{-3}) is calculated from the Eq. (1) given as:

$$\text{Concentration of BaP}\left(\text{ng m}^{-3}\right) = \frac{C(\text{ng m}^{-2}) \times A_{\text{sample}}(\text{m}^2)}{V_{\text{air}}(\text{m}^3)} \quad (1)$$

where C is the BaP concentration calculated from the analytical data and area of filter taken (ng m^{-2}), A_{sample} is

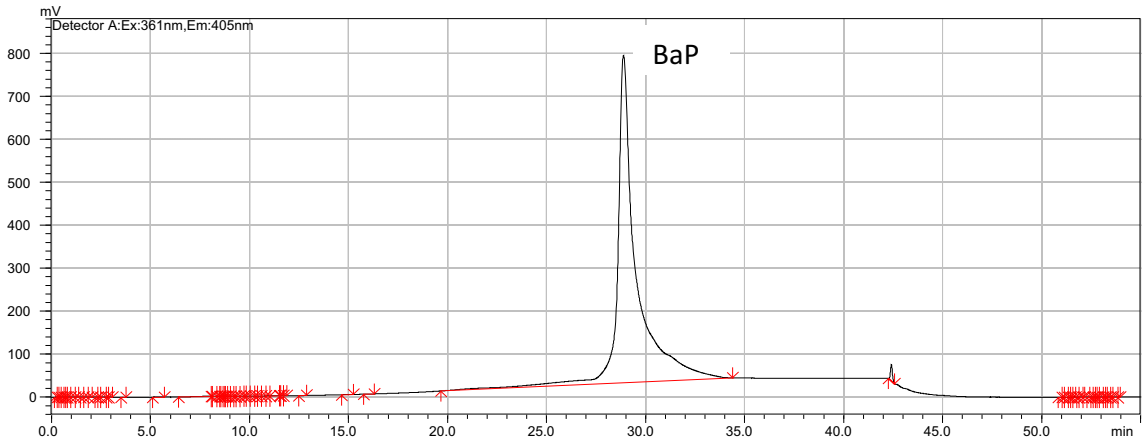

Fig. 1 HPLC chromatogram of Benzo(a)pyrene standard

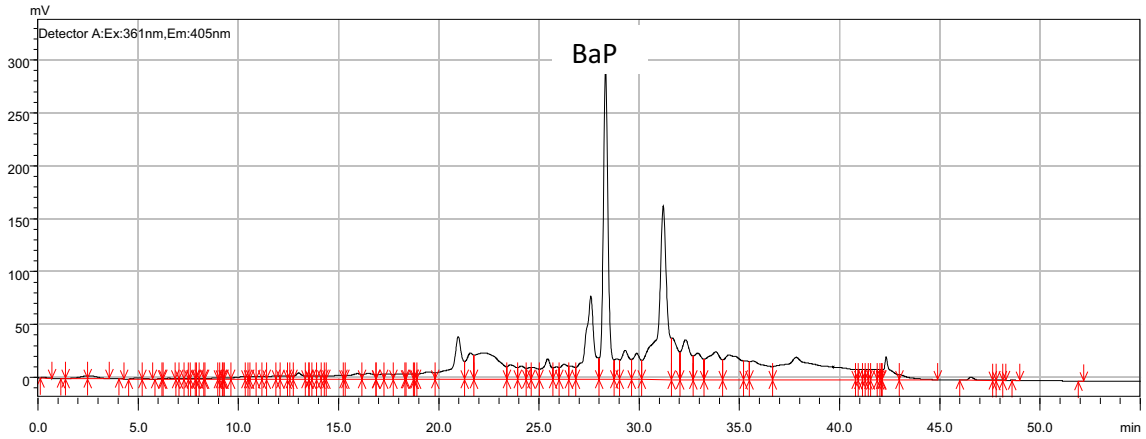

Fig. 2 HPLC chromatogram of Benzo(a)pyrene (BaP) for PM_{10} sample

the total area of the PM_{10} filter exposed (m^2), V_{air} is the volume of the sampled air (m^3).

Calibration of the instrument was done by injecting three different concentrations of BaP standards as a function of peak area using a linear curve. The peak identification of BaP in PM_{10} samples was done by comparing with the retention time of standard (Figs. 1 and 2). The instrument was calibrated after every 10 analysis of the sample. Other statistical data for instrument calibration, i.e., correlation coefficients (R^2), standard deviation (SD) etc., along with a limit of detection (LOD) and limit of quantification (LOQ) were also calculated and are listed in Table 3.

2.1. Calibration Range and Linearity

In this method, the five-point calibration curves were prepared with different concentration levels of BaP standard (Table 3). The calibration range for the method is the interval between the lower to the higher levels of BaP that have been used to determine precision, accuracy and linearity. Linearity is determined by a series of 5–6 injections of five or more BaP standards whose concentrations are 80–120% of the probable concentration range [19]. Linearity and matrix effects were calculated by a plot of the linear regression equation for BaP (Table 3).

Table 3 Statistical data for HPLC calibration

Compound name	Retention time (min)	Calibration range (ppm)	Precision (%)	Correlation coefficients (R^2)	LOD (ppm)	LOQ (ppm)
BaP	28.8	0.025–1.00	0.89	0.9928	0.011	0.021

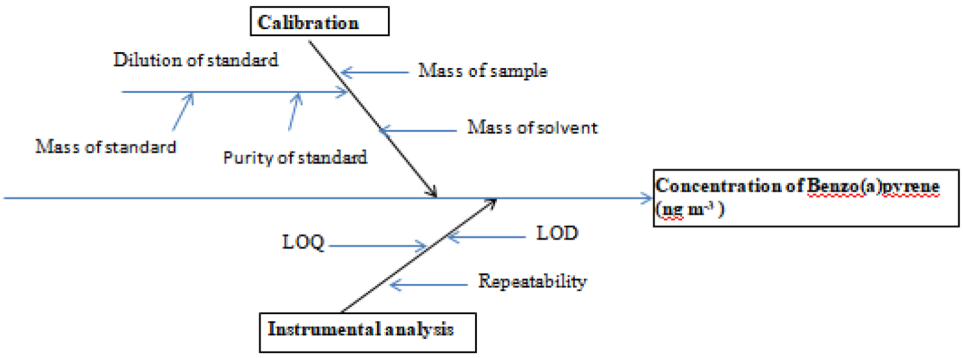

Fig. 3 Cause-and-effect diagram showing uncertainty components for the analysis of Benzo(a)pyrene

2.2. Limit of Detection (LOD) and Limit of Quantification (LOQ)

LOD was calculated to check the sensitivity of the instrument [19, 20]. LOD and LOQ were obtained by analyzing ten aliquots of PM_{10} sample with the smallest concentration of the BaP standard that will generate a valid quantifiable peak at the signal-to-noise ratio $> 3{:}1$ and 10:1, respectively, for a 20 µL of injection.

Thus, LOD was calculated according to the EURACHEM method as follows:

$$\text{LOD} = 3.3 * \text{Standard Deviation}$$

The LOQ was calculated as:

$$\text{LOQ} = 10 * \text{Standard Deviation}$$

The calculated values of LOD and LOQ were 0.01 ppm and 0.02 ppm, respectively (Table 3).

2.3. Precision

Precision is the nearness of conformity involving individual analysis results obtained under validated conditions. It is generally expressed in the form of standard deviation or relative standard deviation. The precision of method used in the analysis was obtained by the repeatability of measurements (intraday) and intermediate precision (interday) of both BaP sample and standard solutions. Precision was determined by analyzing six replicates of both BaP standard and sample solution on the intraday, i.e., same day and six times in the interday, i.e., each day for 1 week. The results obtained were expressed in terms of % RSD of the analysis. (Table 3).

2.4. Uncertainty Associated with Standard and Sample Preparation

The main sources of uncertainty in the preparations of standard stock solutions in the HPLC method as shown in Fig. 3 were as follows:

Mass of standard (Mst) and Purity of the standard (P)

Uncertainty in mass weighing was calculated for standard and sample according to Equation:

$$u(\text{Mst}) = \frac{S}{\sqrt{n}} \tag{2}$$

where s represents the standard deviation (as per the balance certificate), and n is the number of measurements of mass weighing of 20 g weight (in case of standard)and 1 g weight in case of sample), respectively.

The purity of BaP standard is given in the form $\geq y$ % and the range $(100 - y)$ % is described as the rectangular distribution. The standard uncertainty is therefore calculated as:

$$up = \frac{100 - y}{2\sqrt{3}} \tag{3}$$

3. Results and Discussion

3.1. Uncertainty Calculation Involved in the Measurement of BaP Concentrations

The uncertainty components involved in the measurement of concentration of BaP as discussed are calculated in Table 4. The major contribution of uncertainty components was of the purity of the standard (77.9%).The other parameters like mass of standard and sample contributed to 8.5% and 13.5%.

The combined uncertainty is calculated by summing up the square of all the uncertainty components calculated.

Table 4 Uncertainty components and their standard and relative uncertainties associated with the preparation of standard and sample of BaP by HPLC

Symbol	*U* component	*x*	*U*(*x*)	*U*(*x*)/*x*
Mst	Standard mass	20 g/g	$4/\sqrt{10}$ g/g = 1.265	0.06
Up	Standard purity	2 mg L^{-1}	$2/\sqrt{3}$ mg L^{-1} = 1.155	0.57
M_{sample}	Sample mass	1 g/g	$0.2/\sqrt{4}$ g/g = 0.1	0.10

The input quantities are those that are responsible for the uncertainty of the analytical method.

$$u_c = \sqrt{(\text{Mst})2 + (\text{up})2 + (\text{uM sample})2} \quad (4)$$

The combined uncertainty (u_c) is calculated as 0.35.

Calculation of the expanded uncertainty (U) is done by multiplying the combined standard uncertainty (U_c) of the input quantity with k (coverage factor). The value of k = 2.

$$u = u_c \times k \quad (5)$$

3.2. Seasonal Variation of BaP in PM_{10} Samples

The total year was classified into four seasons viz., winter, summer, monsoon and post-monsoon. The winter months are from December to February. March to May are the summer months. Monsoon starts from June to last in the month of August. Post-monsoon months are from September to November. The temperature of Delhi varies from lowest in winter to highest in summer. The average rainfall during monsoon season in Delhi is normally of the order of $\sim$ 800 mm. Delhi has a subtropical climate and, due to emission of trace gases from various sources of emission, the ambient air quality is considerably affected [21].

Figure 4 shows the monthly concentration (ng m^{-3}) of BaP calculated for the year 2014–2015 in NPL, New Delhi. The seasonal variation in concentrations of B(a)P was found to be 0.04–25.7 ng m^{-3} in PM_{10} samples collected at the sampling site from January 2014 to January 2015.

A general trend in the monthly distribution of BaP is observed. Referring to the trend graphs, we observe that

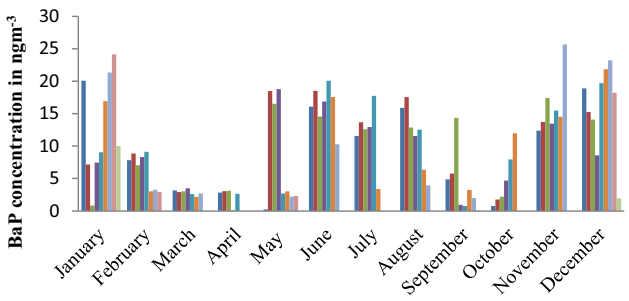

Fig. 4 Monthly BaP concentration in PM_{10} samples in the year 2014–2015

BaP concentrations decrease during the monsoon and post-monsoon season, i.e., June–September. This is possible due to the scrubbing effect of precipitation. During the rains, the suspended particulates in the air settle down, and therefore, the concentration of pollutants in the ambient air is reduced [22]. Winter months experience a great increase in BaP levels (November–January) possibly because of the additional fuel combustion, biomass burning, increase in vehicular traffic etc., [17, 23]. Major vehicular emission include both diesel and natural gas combustion, while the emissions from vehicles using coal, coke, and gasoline as fuels have a minor contribution [24]. The high BaP concentration in the winter months was due to the stable inversion layer in which the pollutants remain suspended in the air for long and have greatly increased residence times. This makes winter months particularly harmful for asthmatics and people suffering from other respiratory disorders. As the inversion layer starts to break in the summer months, the pollution level also starts decreasing.

In Delhi, there has been increase in number of vehicles over the years which affect the entire consumption of fuel. This also increases the idling time of vehicles leading to traffic congestion which finally results in increased emission of hydrocarbons, CO and NO_x [25]. As given by CPCB (Central Pollution Control Board), the average mean mass concentration of PM_1 $PM_{2.5}$ and PM_{10} was 3–4 times higher than the permitted values given in NAAQS due to emission from the crop residue burning [26].

Similar work was done on by collection of PM_{10} samples using a low-volume sampler on quartz filters for 24 h each day for a period of 15 days between October 2012 and July 2013 in Naples. The PM_{10} mass concentration was determined gravimetrically. It was observed that concentration of BaP varied from 0.065 ng m^{-3} during autumn season to 0.872 ng m^{-3} in spring season and from 0.120 ng m^{-3} during autumn season to 1.48 ng m^{-3} of winter season. The major sources observed for the increase in levels of BaP were from the traffic emission [27].

In North India, there is a high variation in all the seasons as compared to South India. In the western part of India, there are deserts and western disturbances. Apart from the natural influences, increase in the urbanization also result in the changes in the atmospheric conditions [28].

Therefore, in recent years, the concentration of BaP reported in the ambient air of India is much higher than developed countries like Germany, Italy, Greece, USA, and UK. The concentration of BaP in India was also reported higher than Asian countries like Japan, Korea, Hong Kong, and Taiwan but was comparable with China [29].

Any type of small error in the measurement of aerosols can have a strong impact on its understanding. Therefore, to understand the physical and chemical properties of aerosols, their measurements should be accurate [30]. National metrology institute (NMI) should provide the calibration requirements of industries involved in the gas and aerosol metrology. They should also work with the regulatory authorities for traceable aerosol measurement data [31]. NMI should collaborate with each other and also with other institutes for calibration and standardization of measurements which will reduce the uncertainties [32].

4. Conclusions

From the study, it can be concluded that risk associated with high PAHs concentrations still persists in New Delhi. The average annual levels are 10–20 times higher than the permitted value of 1 ng m^{-3}. The measurement of uncertainty of various parameters involved in the measurement of BaP is also calculated which is an important aspect for quality assurance and quality control studies.

BaP level is very high in winters (November–January) as compared to summers (March–May). The main reason behind the high PAHs concentration in New Delhi is the vehicular exhaust due to increase in number of vehicles over the years.

Measures should be taken to control the vehicular exhausts especially diesel exhaust by implementing strict emission norms. Also the use of solid fuels should also be reduced which will help to lower the BaP concentrations in the atmosphere.

Acknowledgements Authors are thankful to the Director, NPL for providing experimental facilities and support for the research work. JP is thankful to Prof. S.K. Singh, Head, Environmental Engineering Department, Delhi Technological University for providing the research opportunity.

References

[1] K.H. Kim, S.A. Jahan, K. Ehsanul and R.J.C. Brown, A review of airborne polycyclic aromatic hydrocarbons (PAHs) and their human health effects, Environ. Int., **60** (2013) 71–80.

[2] J. Latimer and J. Zheng, The sources, transport, and fate of PAH in the marine environment. P.E.T. Douben Eds.; PAHs: an ecotoxicological perspective, Wiley, New York (2003).

[3] J. Arey and R. Atkinson, Photochemical reactions of PAH in the atmosphere. P.E.T. Douben Eds.; PAHs: an ecotoxicological perspective, Wiley, New York (2003) pp. 47–63.

[4] D.M. Di-Toro, J.A. McGrath and D.J. Hansen, Technical basis for narcotic chemicals and polycyclic aromatic hydrocarbon criteria. I. Water and tissue, Environ. Toxicol. Chem., **9** (2000) 1951–1970.

[5] Y. Zhang and S. Tao, Global atmospheric emission inventory of polycyclic aromatic hydrocarbons (PAHs) for 2004, Atmos. Environ., **43** (2009) 812–819.

[6] A.S. Brown, R. J.C. Brown, P. J. Coleman, C. Conolly, A. J. Sweetman, K.C. Jones, D.M. Butterfield, D. Sarantaridis, B.J. Donovan, and I. Roberts, Twenty years of measurement of polycyclic aromatic hydrocarbons (PAHs) in UK ambient air by nationwide air quality networks, Environ. Sci. Process. Impacts., **15** (2013) 1199–1215.

[7] K.C. Jones, G. Grimmer, J. Jacob and A.E. Johnston, Changes in the polynuclear aromatic hydrocarbon content of wheat-grain and pasture grassland over the last century from one site in the UK, Sci. Total Environ., **78** (1989) 117–130.

[8] International Agency for Research on Cancer (IARC), Overall evaluations of carcinogenicity, IARC monogr. **42** (1987) 1–34.

[9] International Agency for Research on Cancer (IARC), Polynuclear aromatic compounds: Part 3, industrial exposures, IARC monogr. **34** (1984) 5–199.

[10] B. Maliszewska-Kordybach, Sources concentrations, fate and effects of polycyclic aromatic hydrocarbons (PAHs) in the environment. Part A: PAHs in air, Pol. J. Environ. Stud., **8** (1999) 131–136.

[11] C.B.B. Guerreiro, J. Horalek, F. de Leeuw and F.Couvidat, Benzo(a)pyrene in Europe: ambient air concentrations, population exposure and health effects, Environ. Pollut., **214** (2016) 657–667.

[12] C.B.B. Guerreiro, V. Foltescu and F. de Leeuw, Air quality status and trends in Europe, Atmos. Environ., **98** (2014) 376–384.

[13] N.S. Kasimov, N.E. Kosheleva, E.M. Nikiforova and D.V.Vlasov, Benzo[a]pyrene in urban environments of eastern Moscow: pollution levels and critical loads, Atmos. Chem. Phys., **17** (2017) 2217–2227.

[14] K.Widziewicz, W. Rogula-Kozło and G. Majewski, Lung cancer risk associated with exposure to Benzo(a)pyrene in polish agglomerations, cities and other areas, Int. J. Environ. Res., **11** (2017) 685–693.

[15] U.S. EPA, Determination of pesticides and polychlorinated biphenyls in ambient air using high volume polyurethane foam (PUF) sampling followed by gas chromatographic/multi-detector detection (GC/MD), compendium method TO-4A, second edn, Cincinnati, OH (1999).

[16] J. Pokhariyal, A. Mandal and S.G. Aggarwal, Uncertainty estimation in PM_{10} mass measurements, MAPAN-J. Metrol. Soc India (2018) 1–5.

[17] S. Kumar, S. G. Aggarwal, P.K. Gupta, and K. Kawamura, Investigation of the tracers for plastic-enriched waste burning aerosols, Atmos. Environ., **108** (2015) 49–58.

[18] ISO 16362:2005(E), Ambient air - Determination of particle-phase polycyclic aromatic hydrocarbons by high performance liquid chromatography, First edn, (2005) 2–15.

[19] ICH (International Conference for Harmonization), Validation of analytical procedures: methodology, adopted in Q2B, Geneva (1996).

[20] ISO/IEC 17025:2005(E), General requirements for the competence of testing and calibration laboratories, Second edn, (2005) 5–15.

[21] S.K. Sharma, P. Agarwal, T.K. Mandal, S.G. Karapurkar, D.M. Shenoy, S.K. Peshin, A. Gupta, M. Saxena, S. Jain, and A.

Sharma, Study on ambient air quality of megacity Delhi, India during odd–even strategy, MAPAN-J. Metrol. Soc India **32**(2) (2017) 155–165.

[22] L.C. Guo, Y. Zhang, H. Lin, W. Zeng, T. Liu, J. Xiao, S. Rutherford, J. You and W. Ma, The washout effects of rainfall on atmospheric particulate pollution in two Chinese cities. Environ. Pollut., **215** (2016) 195–202.

[23] J. Li, B.E. Carlson and A.A. Lacis, Application of spectral analysis techniques to the inter comparison of aerosol data—Part 4: Synthesized analysis of multi sensor satellite and ground-based AOD measurements using combined maximum covariance analysis, Atmos. Meas. Tech., **7** (2014) 2531–2549.

[24] A. Lakhani, Source apportionment of particle bound polycyclic aromatic hydrocarbons at an industrial location in Agra, India, Sci. World J., **2** (2012) 1–10.

[25] B.R. Gurjar, J.A. Aardenne van, J. Lelieveld and M. Mohan, Emission estimates and trends (1990–2000) for megacity Delhi and implications, Atmos. Environ., **38** (2004) 5663–5681.

[26] G.S. Saggu, S.K. Mittal, R. Agarwal and G. Beig, Epidemiological study on respiratory health of school children of rural sites of Malwa Region (India) during post-harvest stubble burning events, MAPAN-J. Metrol. Soc India, **33**(3) (2018) 281–295.

[27] P. Di Vaio, B. Cocozziello, A. Corvino, F. Fiorino, F. Frecentese, E. Magli, G. Onorati, I. Saccone, V. Santagada, G. Settimo, B. Severino and E. Perissutti, Level, potential sources of polycyclic aromatic hydrocarbons (PAHs) in particulate matter (PM10) in Naples, Atmos. Environ., **129** (2016) 186–196.

[28] M.V.S.N. Prasad, C. Sharma, B.C. Arya, T.K. Mandal, S. Singh, M.J. Kulshrestha, R. Agnihotri, S.K. Mishra and S.K. Sharma, Experimental facilities to monitor various types of atmospheric parameters in the Radio and Atmospheric Sciences Division (RASD) of CSIR-National Physical Laboratory, MAPAN-J. Metrol. Soc India, **28**(3) (2013) 193–203.

[29] L. Narayana Suvarapu and B. Sung-Ok, Review on the concentrations of Benzo[a]pyrene in the Indian environment since 1983, Polycycl. Aromat. Compd., **37** (2017) 235–256.

[30] S.G. Aggarwal, Recent developments in aerosol measurement techniques and the metrological issues, MAPAN-J. Metrol. Soc India, **25**(3) (2010) 165–189.

[31] S.G. Aggarwal, S. Kumar, P. Mandal, B. Sarangi, K. Singh, J. Pokhariyal, S.K. Mishra, S. Agarwal, D. Sinha, S. Singh, C. Sharma and P.K. Gupta, Traceability issue in $PM_{2.5}$ and PM_{10} measurements, MAPAN-J. Metrol. Soc India, **28**(3) (2013) 153–166.

[32] P. Quincey, S. Beccaceci, D. Butterfield, D. Sarantaridis and J. Tompkins, Aerosol metrology supporting air quality monitoring in the United Kingdom and Europe, MAPAN-J. Metrol. Soc India, **28**(3) (2013) 145–152.

Publisher's Note Springer Nature remains neutral with regard to jurisdictional claims in published maps and institutional affiliations.

NATIONAL SECURITY

A VIF Publication

Instructions for authors

Mitigating the threat in space: Chinese military space capability and India's response

Rahul Krishna & Aradhya Shandilya

Krishna, Rahul, Aradhya Shandilya. "Mitigating the threat in space: Chinese military space capability and India's response". National Security, Vivekananda International Foundation Vol.II (1), (2019) pp .115-136 .

https://www.vifindia.org/sites/default/files/national-security-vol-2-issue-1-article-RkAs

- This article may be used for research, teaching and private study purposes. Any substantial or systematic reproduction, re-distribution, re-selling, loan or sub-licensing, systematic supply or distribution in any form to anyone is expressly forbidden.
- Views expressed are those of the author(s) and do not necessarily reflect the views of the VIF.
- The author certifies that the article/paper is original in content, unpublished and it has not been submitted for publication/web upload elsewhere and that the facts and figures quoted are duly referenced, as needed, and are believed to be correct.

Article

Mitigating the threat in space: Chinese military space capability and India's response

Rahul Krishna
Aradhya Shandilya

Abstract

Space assets today play a pivotal node in modern warfare. In this context, the rapidly expanding Chinese space programme plays an instrumental role in supplementing the existing ground-based infrastructure and support Beijing's goals to win "Informationised local wars". The first section of the paper scrutinizes the Chinese stance regarding its space assets and how they can be employed for both offensive and deterrent purposes. Despite its claim of employing space assets for peaceful purposes, Chinese literature often advocates terms like "decisive first strike" and "information dominance". Furthermore, the speculated shift of the space programme from a support mechanism to an offensive tool has been explored. The second section brings up core structural differences between India and China in terms of their approaches to the use of space assets for military purposes. With an efficient command structure and the right ideology behind setting up the network in space, India can mitigate the Chinese threat and greatly reduce vulnerabilities in space. While the Indian space programme has made commendable advances to fulfil its military requirements, there's still a large functional void between ISRO and the military forces due to the inherent civilian nature of the former organisation. Institutional expansion for dedicated space-based military operations have been discussed through the past decade and the formation of an Integrated Space Cell offers promise. To tackle the offensive threat posed by China in space, the paper proposes a new model for deterrence through the concept of 'deterrence by denial'.

Rahul Krishna is a final year student of Electronics and Communication Engineering at Delhi Technological University (formerly DCE). His areas of research are military space policy, missile technology and new technology policy in Asia. He has previously worked with Atlantic Council and Observer Research Foundation. He has been published at Bulletin of the Atomic Scientists, The Diplomat and Columbia University among others.

Aradhya Shandilya is a final year student of Electronics and Communication Engineering at Delhi Technological University (formerly DCE). He has previously worked with the Ministry of External Affairs and the National Foundation for India. He specialises in analyzing communication technology and it's impact on security as well as economic impacts of domestic policy.

Section 1:

China's military space posture

In the era of Mao, China followed a policy of waging a "people's war", designed to fight low-sophistication, protracted warfare against more advanced invaders from the Chinese hinterland. However, over time this posture seems to have changed, particularly in the way China has approached its military space policy in modern times. Kulacki, in his paper on Chinese space policy, argues that Beijing is following the American model for development and structuring of its space capabilities rather than a lean, flexible and offensive model, which is usually the assumption.[1] However, there are exceptions which allude to a more offensive posture in space. It could be postulated that the motivation behind adopting an America like model for its space capabilities is the success the US has enjoyed with the model combined with the American approach towards China in space. Several countries, including China, took notice of the success of American space assets against Iraqi forces in the Gulf War in 1991. Additionally, instances like the non-provision of military grade GPS signal to the Indian forces during the Kargil War in 1999 by the US are also likely to have prompted the Chinese to create alternative systems in space to challenge US dominance, such as the creation of the Beidou Navigation System and the proposed Chinese space station.

China's Military Strategy of 2015 outlines Beijing's goals for winning "informationised local wars" and stresses on the importance of regional maritime operations.[2] The document emphasizes on the need for integration across command structure for "system vs system" dominance that leads to control of information in protracted military operations. There is a focus on the concept of "informationised warfare" in the document, with self-reliance advocated in this regard, which might explain the Chinese posture of creating its own capacity in key domains in space. The doctrine declares Chinese intentions to use outer space for peaceful purposes while being prepared to respond to threats against Chinese space assets. The strategy as a whole alludes to Chinese attempts to build infrastructure in space that focuses on providing a tactical advantage to military forces for terrestrial operations rather than using space as an offensive capability.

There are exceptions, however, to the theory that China is relying on space assets as a support mechanism for its military than as an offensive tool on its own. One of the most glaring displays of offensive strength has been the multiple weapons

tests conducted by China in space. While repeatedly claiming that China does not advocate for the use of weapons in space, China has conducted several Anti-Satellite (ASAT) tests. Beijing has tested a wide variety of weapons including hit-to-kill as well as directed energy blinding weapons and have launched co-orbital satellites that can allegedly be used as remote explosives and jammers. In 2018, a threat assessment report by the Director of National Intelligence of the US, estimated that not only will China reach operational capability on their counter-space weapons in the "next few years", they are also likely to use it in any military conflict to offset any adversarial advantages.[3] The report also indicates that Beijing has given importance to the integration of such counter-space capabilities with its military command structure so as to integrate counter-space assets with conventional military operations.

The Textbook for the Study of Space Operations, a publication by the PLA's Academy of Military Sciences (AMS), advocates the use of a decisive first strike in space to avoid protracted conflict and ensure dominance. The Science of Military Strategy (2013), another publication by the PLA's AMS, acknowledged the use of network warfare forces by the PLA.[4] These forces imply that the PLA has invested in network warfare capabilities and it is likely these have been used at various instances in peacetime, with some forces being part of the PLA while others are merely authorized by the PLA but do not comprise of PLA personnel. Such a statement while not directly implying the existence of offensive space capabilities, indicates Beijing's intention to adopt a strategy that binds elements of cyber, network, electronic and space-based warfare firmly with existing conventional structures. This text was one of the first admissions of the existence of such offensive forces, a departure from China's longstanding stated policy of non-aggression in cyberspace. It can be argued, based on the aforementioned developments, a declared Chinese policy of non-aggression in outer space does not imply the lack of development of capability as well as use in certain scenarios. The US, on multiple instances, has claimed that the Chinese interfered with the functioning of American space assets, using counter-space capabilities.[5]

Official documents on utilisation of space as well as their efforts at various international forums indicate that China is building its space assets as a tactical asset for its military. However, the progress made by Beijing in operationalising a counterspace capability cannot be ignored. What is certain is that China has begun the process of setting up an alternative set of infrastructures to the US in space that is likely to challenge their dominance. In doing so, China has also made its military a lot

more dependent on the availability of such capabilities, which serves as motivation for potential adversaries to target them. These vulnerabilities are augmented by China's current inability to comprehensively protect their satellites; the Chinese still do not possess capabilities such as space situational awareness, with several Chinese studies acknowledging vulnerability on this front.[6] It is also worth noting, that most Chinese texts that advocate the use of counter-space capabilities as an offensive weapon rather than a deterrent, do so against an established space network such as the US. The underlying objective is one of establishing dominance in space to assure a better-informed military rather than as a potential disruptor. The attacks on American satellites have also largely been directly over Chinese territory. It is likely that the Chinese have conducted these tests to assess whether their counter-space capabilities can enable their Anti-Area/ Access Denial (A2/AD) strategy in the maritime domain in South East and East Asia.

Organisation of China's military space capabilities

Akin to several western space programmes, the Chinese space programme was inaugurated under the auspices of the PLA, specifically the Second Artillery Corps. The Second Artillery Corps is the force in the PLA responsible for China's strategic missile arsenal, for both nuclear and conventional strike capabilities. Only in 1993, China created the China National Space Administration (CNSA), which on paper has the mandate to govern all civilian space activity. This was done in an attempt to provide a civilian governmental front to China's space activities, to make procurement and technology transfer from the West an easier task. It has often been argued that the CNSA is merely a coordinating body within the Chinese space setup, creating no real technological capability on its own.

On the military front, in 2015, China setup the Strategic Support Force (SSF), which has reportedly taken over the responsibility of several space capabilities from the Second Artillery Corps. According to a study by RAND Corporation, the setting up of such a force is another indicator of Beijing's desire to use its space capabilities as an enabler of its concept of "informationized wars" rather than a disruptive tool.[7] While the SSF appears not to have been given the status of an independent service, as is the case in US and Russia, it is considered the focal point for all outer space and cyberspace based information gathering with other wings of the military being consumers of such intelligence. The SSF brings China's cyberspace and network warfare, electronic warfare and space capabilities under a single branch of the

military. This combination of weapons with the SSF, acting as a supporting mechanism to all branches of the Chinese military, displays Beijing's desire to integrate the information component in entirety with all of its military operations. The combination of offensive capabilities such as EW and network warfare, and information gathering capabilities in space reinforce the belief that China aims to fight through short regional skirmishes in an A2/AD, enabled with complete information dominance.

Space Assets and Informationized Warfare

Inroads towards a comprehensive space-based framework are pivotal for the Chinese A2/AD strategy, especially in the West Pacific theatre. The Chinese Yaogan constellation of satellites provides Electronic Intelligence (ELINT), Synthetic Aperture Radar (SAR) and Electro-Optical (EO) capabilities for the Chinese approach to "fight and win local wars under informationized conditions".[i] Gathering electronic footprints by means of ELINT satellites surveilling in discrete formations is the primary step for the same. The coarse ELINT estimates act as cues for the SAR and EO satellites to provide imagery in order to counter infiltration or undesired presence by means of any array of surface and undersea operations. A robust surveillance system lays the groundwork for the enabling of an A2/AD bubble in tandem with conventional Air and Naval operations. Early warning satellites, combined with non-military state power are effective in the creation of bubbles where "information dominance" is possible.[8] The launches of TJS 1 and TJS 2 satellites have filled the void in the Early Warning capabilities for the Chinese Ballistic Missile Defence system. The Chinese Integrated Air Defence System (IADS) also employs the space based inputs to supplement the A2/AD strategy.

The Chinese ambitions to press for a holistic surveillance system in the Indo-Pacific have been reflected by its aggressive satellite launches in quantitative terms to secure strategic interests in its sphere of influence. Out of a total of 24 ELINT satellites operational as a part of the Yaogan constellation, the final twelve satellites have been launched in a span of months between September 2017 and April 2018.[ii] Insights into the planar orientation of the constellation further indicates a shift from the conventional formation of three satellites to a six satellite formation in the January 2018 launch of Yaogan 30. A six satellite formation aids increasing the footprint coverage between the 35 degrees North and South latitudes and thus, comprehensively monitor electronic footprint around sensitive regions of strategic

i. EO and SAR satellites are used to provide satellite imagery. EO satellites have passive payloads and thus, can't provide imagery during cloud coverage and in the absence of daylight unlike SAR sensors which provide all weather imagery even during the night.

ii. Electronic Intelligence or ELINT satellites are primarily launched in a specific formation of three satellites with respect to orbital planes in order to ensure broader coverage during a fly-by.

significance like Taiwan, the Korean peninsula, Japanese southern waters, Guam and other regions across the Indian Ocean. Additionally, the shift from conventional Low Earth Orbit to the 500 Km Sun Synchronous Orbit (SSO), used to place the Ludikancha Weixing (LKW) satellites launched this year, adds to the Chinese attempts for comprehensive surveillance.[9] A study conducted by International Strategic and Security Studies Programme at IISc. Bengaluru to monitor the amount of electronic emissions captured by five Yaogan triplets revealed a 32 per cent emission capturing capacity by the frequency of satellite revisits over Taiwan by the 15 satellites. The current framework thus, provides adequate satellite visit frequency to ensure long range coverage, however, further investments are needed to seek parity with short distance requirements.[10]

Role of Chinese ELINT Satellites

China has created a regional ELINT framework by supplementing the ground, air and sea based ELINT sensors with a roster of ELINT satellites placed in a particular formation to enhance emission coverage for a robust surveillance system. However, integrating the space-based infrastructure into broader Command, Control, Communications, Computers, Intelligence, Surveillance and Reconnaissance (C4ISR) system remains as a prime target to have an edge in "Informationised Warfare". Furthermore, technical writings from PLA affiliated sources have pressed towards a system employing ELINT sensors along with radar systems.[11] Inroads towards enhancing a terrestrial space support infrastructure have also been made to perform functions like signals transmission, reception, processing and status monitoring.

The PLA Strategic Support Force is primarily responsible for Electronic Warfare and tactical Electronic Support Measures. Its 1999 project for 10 coastal stations in Shandong province indicates an inclination towards maritime engagement in electronic warfare. China also has an array of ground stations spanning across the globe in countries like Kenya, Namibia, Pakistan and Argentina.

Chinese Space-Based ELINT capabilities receive a major boost from the alleged "piggyback" sensors mounted as secondary payloads on Chinese satellites in LEO and GEO.[iii] The scope and the intent towards the same have been stated in a paper by China Aerospace Science and Industry Corporation (CASIC) affiliated authors as:

> *"In the information age, the utilization of electronic reconnaissance satellites to obtain intelligence has become an important method [of*

iii."Piggyback" payloads serve as secondary sensors on a satellite mission. Such payloads often serve usually experimental purposes, however, as portrayed in the given scenario, they primarily execute discreet missions disguised beneath the primary payload.

> *doing so]. Geostationary electronic reconnaissance satellites provide unique advantages and are being increasingly emphasized…Using geostationary satellite platforms to engage in electronic reconnaissance is useful for the large coverage ranges available for obtaining electronic information in the air, including terrestrial and other radar signals, communications signals, satellite telemetry, etc. It also allows for the continuous, long-term surveillance of target areas; obtaining intelligence in real-time to provide rapid electronic intelligence for diplomatic and strategic military decisions."* [12]

The possibility of the same contributes to the edge in the field of intelligence due to additional footprint coverage that goes significantly unmonitored due to the discreet nature of the payloads. Furthermore, primary payloads in the GEO hold significance by providing wider coverage for holistic surveillance. Unavailability of published studies in the public domain coupled with distinct orbital configurations for an array of satellite launches in the past decade indicate towards a strong primary payload presence for ELINT purposes.[13] Chinese sources further indicate towards merging the airborne communications and ELINT payloads into combined hardware which helps monitor global communications for strategic purposes. By means of trimming the deficit faced by on-ground infrastructure by onboard processing units embedded in the payloads.

The intelligence inputs provided by the space-based ELINT sensors extend their utility towards both offensive and deterrent procedures of the PLA ranging from the conventional Air and Naval operations in the Indo-Pacific to the intricate Anti-Ship Ballistic Missile System and the Ballistic Missile Defense systems[iv] A comprehensive system of the given nature implementing the A2/AD strategy further opens ground for competent counter-space capabilities by potential adversaries are discussed separately in the paper.

Indo-Pacific is a territory of high strategic interests for China. An intricate layout of arterial trade routes coupled with disputed islands dotting the whole region attract substantial investment into deterrent assets in case of any hostile intrusion. Owing to the absence of contour matching procedures unlike in the case of land-based targets, a comprehensive ASBM attack or defence system requires space assets' inputs in fields of missile early warning, target reconnaissance, precision guidance, missile telemetry and creation of a digital battleground.

iv. Nuclear deterrent capabilities are subjected to ELINT proficiency in GEO owing to the requirement of surveillance beyond regional coverage.

Considering the expanse of conflicted territories across land and sea, especially the rugged Himalayan regions making up the majority of it, substantial investments to secure intelligence are an instrumental requisite. While the Chinese exploits in the field have been discussed in detail in the section, the Indian ELINT capabilities are more restricted to ground and air-based assets including radar stations and a fleet of Airborne Warning and Control System (AWACS) aircrafts. However, the unavailability of dedicated space-based assets may not raise significant alarm due to more regional nature of Indian intelligence gathering missions which are further backed by an 'adequate' remote sensing programme. Additionally, India is scheduled to launch EMISAT on 1st April 2019 which is listed to carry a payload which will give India electronic intelligence capabilities over the seas in the form of message interception from ships.[14] In the maritime domain, satellites like GSAT-7 launched in 2013 aid the naval operations by extending communication services. While the capabilities don't directly aid intelligence gathering, it helps provide appropriate co-ordination within the naval infrastructure for concrete surveillance procedures.

Chinese counter-space power

Beijing's roadmap for the development of a counterspace capability was highlighted in a book by Colonel Li Daguang, published by the National Defense University (NDU) of China. The book proposed a phased approach to development of a counter-space capability, with the development of a limited combat capability in space by 2010 and an advanced offensive capability beyond that which would be capable of incapacitating all "enemy space vehicles that fly in space above our sovereign territory".[15] The book makes mention of preventing US-Taiwan integration on defense systems using ASAT capabilities. This sheds light on the Chinese objective of winning localized wars using an A2/AD bubble and explains the attention given to using counterspace weapons for blacking out US satellites. It is unlikely that the US military will undergo naval operations around Taiwan without having complete remote sensing vision and command and control assets in place.

Other notable publications by the NDU highlight the need for covert development of offensive counterspace capabilities due to international sentiment on the issue. They also call for the use of a first strike during times of crisis, targeting command and control centres of the opponent to cripple their ability to carry out any military operations in the theatre of combat. These publications recommend using a shock and awe strategy as a last resort in times of emergency and coordinating a

terrestrial troop response to take advantage of the information and command and control blackout for a decisive victory.[16] Journal articles enlist GPS and centralized, space-based Command and Control structures as key targets, describing possible weapon systems that China could develop to conduct offensive strikes against these targets and indicating that these weapons are likely already under development.[17] A notable omission from these publications is countering the use of defensive strategies by an opponent in space such as redundancy and mega-constellations, however, these can be excused given that most of the publications referred to were published before 2007.

China has tested a vast variety of counterspace weapons, both hard-kill and soft-kill in nature. A 2013 paper by Chinese scientists from the Changchun Institute of Optics, Fine Mechanics and Physics, which is considered to be a part of the Chinese military space research network, claimed that China successfully tested a blinding laser on a low-orbit satellite in 2005 itself.[18] The veracity of China's claims of having a directed energy blinding weapon were verified when the US admitted that their reconnaissance satellite was blinded by lasers in orbit above China in 2006.[19] Aside from directed energy weapons such as the ones mentioned above, Beijing has also conducted several hard-kill weapons tests, most notably one in 2007 which successfully hit a Chinese weather satellite in Low Earth Orbit (LEO). The Chinese also tested their DN-2 ASAT missile in 2013 which has the capability to target satellites in "nearly geosynchronous orbit", threatening the full spectrum of satellite resources which were earlier assumed to be invulnerable as weapons capabilities were thought to be limited to the LEO.[20] Reports suggest, China has developed a potential co-orbital ASAT capability as well. In 2013, Chinese satellites displayed an ability to manoeuvre in close spaces and a robot arm was used, which Beijing claims is for servicing satellites and clearing space junk, experts are confident it could be used to tamper with enemy satellites and interrupt their functioning.[21]

The PLA's focus on asserting information dominance has led to the integration of network warfare and electronic warfare capabilities for counterspace operations as well, likely under the ambit of the SSF. The warning signs of an advanced cyber capability against space assets came through exercises conducted by China as early as 2007 and 2008. US satellites were hacked into in both these exercises and in the former, satellite communication with ground stations was interrupted for 12 minutes, displaying China's ability to suspend critical information flow of the enemy in times of conflict.[22] Beijing has continued to develop and test

these capabilities. In 2014, an American imaging satellite was hacked and was prevented from transferring remote imaging for 2 days to ground stations for processing.[23]

Such Denial of Service (DOS) attacks fit into China's plans for short, decisive victories in information dark situations for the enemy, even to transfer functions onto redundant capabilities, it would take precious time that could be used by the Chinese military to conduct offensive operations with superior information, playing into the strategy laid out in several Chinese doctrines. The only aspect that is yet to be executed is China's ability to coordinate such attacks to create an A2/AD bubble in a region, which is the PLA's eventual objective especially in maritime conflicts fought around the Chinese mainland or island groups.

To create such a bubble against a network of satellites would require not just the possession of such counterspace capabilities, but target acquisition and circumvention of defense measures. Target acquisition requires comprehensive Space Situational Awareness (SSA) capabilities,[v] which China does not possess at the moment and is unlikely to be operational in the near future. Hence, while the Chinese currently have the capability to interrupt normal functions of certain critical space-based infrastructure, it is unlikely they can create information dark zones for large satellite networks such as the ones the US possesses; they may still have the ability to acquire a tactical edge through their capabilities for short periods of time.

Section 2:

India's military space ambitions

The Doklam crisis, a India-China military standoff on Bhutanese territory, was a reminder of the importance of integrating space-based assets with military command structures. Satellite imagery was crucial in identifying Chinese infrastructure construction in areas of strategic interest to India. The situation prompted New Delhi to reassess the appropriation of its space-based capabilities, designating the Indo-Tibetan Border Police (ITBP), a paramilitary force responsible for protecting much of the border with China, as the nodal agency for the GSAT-6 satellite.[24] This move allows the paramilitary unit direct access to data rather than sending requests to ISRO, previously responsible for distributing data on the satellite largely dedicated for the armed forces.

While the move is a welcome step in making access to critical data easier for the required forces, it displays the glaring need for a doctrine as well as a capacity

v. The US military defines space situational awareness as the requisite current and predictive knowledge of the space environment and the operational environment upon which space operations depend as well as all factors, activities, and events of friendly and adversary space forces across the spectrum of conflict.

appropriation mechanism. India has a limited capacity dedicated to the military, with most of India's space-based assets being dual use in nature. With ISRO being a purely civilian-administered institution, questions and concerns over the lack of a space organization for defence in India have arisen. The first move to rectify this gap came in the form of the formulation of the Integrated Space Cell (ISC). The ISC is an agency operated by the tri-services in coordination with ISRO and the Department of Space and is responsible for operation of dual-use satellites providing critical information to the military. The solution sought to reduce the time taken for providing crucial information for the armed forces to act upon, however, the ISRO, through its various centres, still controls the satellites and gathers data with the military having little technology or know-how on how to carry out the process themselves. This structure becomes particularly troublesome when data on a particular region is required for operational planning on-ground at the unit level, with the request and subsequently the information having to travel up and down the chain of command.

There have been multiple appeals for the setting up of a defence space organisation, possibly in the form of an Aerospace Command, to rectify this situation. Four significant aspects need to be considered namely, creating capability to harness existing ISRO capabilities for military uses, forming a command structure for efficient distribution of data, coordinating with ISRO and DRDO for the creation of space and ground infrastructure tailor made for the military's needs and creating deterrence and response mechanisms to threats by adversaries.

India's doctrine on the use of space for defence

The Indian Armed Forces, while being comparatively late, have announced that they intend to form a cyber defence and a space defence agency and claim that the process to do so has begun in the 2017 Joint Doctrine.[25] The military plans to create a "triad" of capabilities in an integrated command structure comprising of cyber, space and "special operations", with these units likely to be set up under the Integrated Defence Staff and serve all three services of the Indian Armed Forces. Despite the vision being set out, the doctrine does not mention how these capabilities will be set up or used in combat. A paper presented at the Centre for Joint Warfare Studies, a Ministry of Defence think tank, suggests that the three capabilities would have independent commands with a communication grid established between them.[26] The paper recommends a study of the US Space Command structure, alluding to a top-down approach for creation of an Aerospace unit. However, this is in

contradiction to a recent statement made by the Chief of Army Staff, General Bipin Rawat, who asserted that the Armed Forces will follow a bottom-up approach to integration with regiment level exercises for cyber and space capabilities already underway.[vii]

The conversation around setting up an Aerospace Command is not a new one, the Indian military spoke of setting up an Aerospace Command as long ago as 2005, when then Air Chief Marshal, S.P. Tyagi admitted that such a command would be set up.[27] In another interview in 2005, a DRDO official close to the Chief of the DRDO at the time claimed that such a command would be set up independently to ensure effective coordination with all of the three tri-services;[28] the prevailing thought at the time was that such a command would be set up under the Indian Air Force. Since then, there has been little evidence of progress on the setting up of such a command, or on setting up of a military space organisation and it is unclear when the 2017 doctrine would come to fruition.

Assessing Indian capabilities for military use

On 27th March 2019, Prime Minister Narendra Modi announced that India had successfully tested an ASAT weapon by shooting down a live satellite in the LEO.[29] The project was codenamed Mission Shakti and has been carried out by the DRDO and appears to be entirely indigenous. In doing so, India has joined the US, China and Russia in having successfully tested an ASAT weapon. Even though the details are unclear so far, it appears to have been a kinetic kill ASAT weapon that India launched. The test comes after several appeals over the last decade for India to test its own ASAT weapon to deter China in space. In so far, New Delhi had maintained a policy of not wanting to weaponise even in the face of aggression from other countries, however, this test indicates a shift in stance.

The test seems likely to have been done by using the Agni-V missile in combination with the radar systems from the Prithvi Air Defence System. This estimate is based on claims made by former DRDO chief V.K Saraswat that India had the "building blocks", namely the above-mentioned components, necessary to develop an ASAT weapon.[30] There had been questions raised over the apparent lack of a verification mechanism- India appeared to not have an expendable satellite to test on in the LEO and there is still no word on what satellite was used for the test.

This launch puts several doubts on India's counter-space deterrent capabilities to bed. While India's intentions for the test still remain to be known, it

vi. The US military defines space situational awareness as the requisite current and predictive knowledge of the space environment and the operational environment upon which space operations depend as well as all factors, activities, and events of friendly and adversary space forces across the spectrum of conflict.

raises two possibilities for India's attempt to negotiate a treaty on the Prevention of Arms Race in Outer Space (PAROS). It indicates that either India has given up on the hope of a consensus on forming such a treaty in the future; or fears that such a treaty when negotiated might form a Nuclear Non-Proliferation Treaty (NPT) based club of powers having ASAT weapons and hence can negotiate to be a part of this group of countries.

Aside from the test, there has been little formal documentation on the space capabilities for defence use that India intends to develop. The Technology Perspective and Capability Roadmap (TPCR) 2010, a document by the Integrated Defence Staff Headquarters, was a marked departure from India's policy on space. The document stated that India would develop ASAT capabilities "for electronic or physical destruction of satellites in both LEO (up to 2,000-km altitude above earth's surface) and GEO-synchronous orbits."[31] The document was quickly taken off the website of the Ministry of Defence, with a replacement coming in 2013 which called for the deployment of "watchdog satellites" to protect space infrastructure- making no mention of ASAT capabilities.[32]

India has a host of competent dual-use capabilities in its arsenal. It has made significant headway in the remote sensing and imaging sphere, acquiring round-the-clock, and all-weather capabilities through technology transfer agreements. India has also expanded its ground station network vastly, adding a station in Vietnam recently in return for providing Vietnam images for the South East Asian region. The IRNSS constellation, which is close to being functional pending the successful launch of one more satellite, will provide the Indian military navigation and positioning capabilities across a large region where a majority of the Armed Forces' operations span. The GSAT-6 and the GSAT-7 are communication satellites dedicated to military use, for which the military is acquiring a large quantity of satellite phones for reliable communication to remote outposts.

The India military has already begun integrating such capabilities, gearing towards information warfare threats and utilising electronic and information technology assets of their own on the battlefront. An analysis of five military exercises by India, beginning from 2004, reveals the Indian Armed Forces' capability of operationalising information warfare techniques for short wars. The Indian military during the exercises showed an ability to use UAV and satellite imagery to track

adversary movements and significant advancements in the ability to integrate sensors into warfare systems.[33]

India has a host of capabilities and infrastructure in place to serve most military needs owing to the technological prowess of ISRO. However, New Delhi needs to put its weight behind the creation of a competent defence space agency, which will be able to process and disseminate data gathered from space assets and resolving a complicated flow of requests and information to allow the military to utilise such capabilities efficiently to gain a tactical advantage on the battlefield. Additionally, there needs to be a mechanism set up to create space infrastructure tailor made for the Armed Forces; to ensure there is enough coordination between commanders who are likely to benefit from such capabilities and the scientists developing them at ISRO. While there is a threat on the Chinese front that does need to be addressed, India's other major military rival, Pakistan, possesses very little by way of military space infrastructure, giving the Indian Armed Forces a considerable strategic advantage if space assets are used effectively as force multipliers.

Addressing the threat from China

It is unlikely that two nuclear weapon states will have a protracted conflict, especially given the size of militaries of both the countries in question. It is likely however, to have short, localised skirmishes for control of strategically important acreage, whether on land or at sea. This plays into Beijing's military objectives, providing them with the opportunity to press their advantage in the information warfare domain. It is imperative that New Delhi recognises the threat posed by China's capabilities and is able to mitigate the strategic advantage it gives the PLA. It is also no secret that the Indian administration does not find a solution that involves weaponizing space as a desirable alternative to mitigate the threat posed.

Keeping these factors in mind, India could follow the route of deterrence through denial as a strategy to insulate itself from Chinese aggression in space, as alluded to by former Air Force Officer M.P. Anil Kumar.[34] Glenn Snyder, in his book on the two forms of deterrence, defines deterrence through denial as, "the capability to deny the other party any gains from the move which is to be deterred".[35] The theory was originally proposed keeping conventional military conflict in mind, but can also be adapted for space based deterrence. The model being proposed focuses on reducing the strategic gains that can be made by China through aggression in space, thus 'denying' them any advantage in a conflict. This model assumes that any

offensive in space leading to the interruption of critical services would come either during or immediately before any conflict on earth between the two nations. The concept will have to be evolved by putting various practices and infrastructure in place for an effective deterrent. The military space ecosystem in India is still at a nascent stage, this needs to be leveraged to give India an upper hand. New Delhi has the opportunity to grow the ecosystem keeping the threat in mind and adapting it to mitigate such a threat proactively whereas other countries such as the US will counter it reactively. The model proposed by the authors hinges on 4 pillars to build an effective and sustainable deterrent in space:

Continuing to build dual-use infrastructure: Analysts have lamented the lack of dedicated infrastructure that the military has in space. Given Chinese capabilities, the paucity of dedicated assets may work in India's favour and the authors argue that New Delhi should continue to push this policy forth. Dual-use assets make target acquisition for deployment of counterspace weapons by the PLA more difficult. The Government Accountability Office of the US asserted that "hosted" payloads on commercial satellites may be the way to go to mitigate threat, with the Department of Defense already putting this strategy into effect with 3 hosted payloads launched.[36] With partitioning and encryption of such payloads on civilian or commercial satellites possible, data security threats are eliminated and the concept has the added advantage of managing satellites launches and capability distribution more flexibly .The strategy is likely to be effective as in most conflicts countries hesitate to attack civilian infrastructure particularly when responsibility can be easily attributed, as will be the case in space. Dual-use assets will reduce the risk of a Chinese first-strike as a precursor to a conflict and give the Indian Armed Forces uninterrupted support from space for a longer duration.

Working towards redundancy: In any system, redundancy greatly reduces the risk of a denial of service attack if switching to redundant capabilities is possible in a short period of time. Pragmatically, India will take time to build redundancy as it is still in the phase of growing its military space capabilities and is likely to prioritise growth over redundancy, however, certain practices can be put in place to facilitate such a concept when India's military space program matures. Creating a mechanism to enable the concept of an Operationally Responsive Space (ORS) is key for India. ORS involves assessing requirements of on-ground units and repurposing capabilities to augment such needs in a short span of time. It requires coordination between command units and for the capabilities to operate on the same standard so that

repurposing is possible. The ability to do so will be essential as a reaction to any counterspace measure taken; an effective mechanism is thus likely to deter the counterspace move in the first place. Mega-constellations of nano-satellites is another possible alternative to mitigate a counterspace threat. Such a form of infrastructure could be adopted from the offset for creating certain support functions in space for the military. Analysis by Secure World Foundation suggests that such a move would reduce vulnerabilities drastically but is likely to trade quality of service provided, hence this could be used for functions with comparatively low bandwidth requirements and higher margins for error.[37]

Ensuring entanglement: Entanglement involves the sharing of space-based capabilities with strategic allies to increase the cost of any offensive measure for an aggressor as it may aggrieve a non-party to the conflict. The US National Security Space Strategy alludes to such a concept, albeit advocating for multilateral governance rather than share capacity building.[38] China too has undertaken entanglement measures, using the leasing model for certain capabilities. Being a pioneer in launching capabilities and technology for several requirements, India could look to form such coalitions with a host of nations, with many of whom it already has strong relations for cooperation in outer space. Potential allies could be France- with whom India shares a deep relationship on space cooperation, Israel- which has the advantage of having the same technology on certain critical infrastructure as India and Japan- with whom India shares common interests in South and East Asia and a growing strategic partnership. Recently, Japan and India have committed to a bilateral space dialogue, the first meeting of which is scheduled to be held in March 2019. The intent to use the space-based assets of both nations is clear with the joint statement by the heads of government of the two countries calling for cooperation in areas such as Maritime Domain Awareness. Reports suggest that ISRO and the Japan Aerospace Exploration Agency (JAXA), are looking to share surveillance data on Chinese ships to ensure that both countries have access to multiple data sources in South, South-East and East Asia. Japan's endeavour to set up a Space Situational Awareness system could also be of potential benefit for India if it wants to move towards a deployable ASAT weapon. Such cooperation lays the building blocks for entanglement between two countries with similar civilian as well as military interests in space, and a strong military relationship in the region.

In March 2019, India also signed an agreement with CNES, the French Space agency, to cooperate on a joint Maritime Surveillance system beginning in May 2019. This will begin with data sharing and joint development of algorithms for data analysis between the two nations. In the future, the two countries expect to launch a constellation of LEO satellites operated jointly that give high resolution images of ship movement across the globe and particularly in the Indian Ocean Region. This along with the agreement with the Japanese is a large step towards ensuring entanglement in the surveillance and maritime domain awareness domains, capabilities that will aid the militaries of India in tracking and countering Chinese naval action in the South China Sea, East China Sea and the Indian Ocean Region.

India could look to offer certain capabilities to nations which are yet to develop the technology, to ensure entanglement, however, there would have to be a certain degree of ownership transferred to the partner nation for such a model to work. It is unlikely that capabilities such as communication would be shared to start with, but areas like remote sensing and imaging, and surveillance and early warning could be areas where India may work with strategic partners for shared ownership.

Be Ready to Punish: A noteworthy critique of Snyder's theory has been the lack of any punishment capability. Paul Davis asserts that without any means of punishment, it is unlikely that deterrence through denial is sustainable when the stakes are raised.[39] He argues that when the stakes are high, without any means to punish aggression, the adversary would undertake offensive action even if the strategic gains are minimal. Looking at it mathematically, even if the strategic gain side of the equation is reduced, not having any means to punish would amount to multiplying the cost side of the equation, thus ensuring that the gains, however little, will outweigh the cost of aggression. It is, therefore, necessary that India possess at least an ancillary capability, possibly through its ballistic missile defence system which tests in the US have shown can be adapted as an ASAT capability.[vii] With the success of the March 2019 test, India has shown that they have the capability to deploy at least a limited punishment based deterrent if the stakes are raised drastically which will certainly worry Beijing. The possession of such a capability significantly raises the cost of aggression for China considering the high level of dependence of their military on space based infrastructure and the low gains from an attack on Indian assets due to the usage of the deterrence through denial model.

Conclusion

vii. Refers to the 2008 ASAT test by the US using its Aegis Ballistic Missile Defense system to hit USA-193 in LEO.

Chinese literature and actions illustrate the objective of winning short conflicts in areas of information dominance for the PLA. China have set up an elaborate network of surveillance and early warning through space-based assets and seek to eliminate any adversary's ability to acquire information of the tense region through their own satellites. Beijing is focussed on integration of Chinese space and network capabilities to ensure effective usage in military operations.

However, the Chinese threat is largely geared towards a model of infrastructure such as the one US has in space. The PLA's strategy also centres around dominance of maritime regions with an emphasis on the Taiwanese Straits in several Chinese military texts. Indicating that these strategies are largely thought out for a forceful reunification of Taiwan and to ensure the US does not interfere in such a situation. India is still in the nascent stages of its growth of military space infrastructure. While the threat isn't as imminent for India, the Doklam standoff indicates areas where China could press its strategic advantage in space. India has the advantage of understanding the Chinese threat as it grows its military space programme and must work in a manner that mitigates the threat and reduces vulnerabilities.

Effective implementation of the model proposed combined with the creation of an Aerospace Command could help reduce vulnerabilities drastically. India needs to ensure that it mitigates threat by creating a network that is tougher to impact using China's current capabilities. Additionally, it is important to conduct a comprehensive technical threat assessment of Chinese capabilities and study forms and theatres of warfare in which space and network centric assets would provide them a significant edge. India, unlike the existing military space powers, has the benefit of developing their defence space network when threats are largely apparent and must use this to model a network that mitigates such threats while providing the military with robust and flexible services.

References

1. Kulacki, Gregory. "An Authoritative Source on China's Military Space Strategy." Union of Concerned Scientists. March 14, 2014. Accessed August 20, 2018. https://www.ucsusa.org/sites/default/files/legacy/assets/documents/nwgs/China-s-Military-Space-Strategy.pdf.
2. China's Military Strategy (2015)." Jamestown Foundation. May 2015. Accessed August 20, 2018. https://jamestown.org/wp-content/uploads/2016/07/China's-Military-Strategy-2015.pdf.
3. Coats, Daniel R. "Worldwide Threat Assessment of the United States Intelligence Community." Director of National Intelligence. February 13, 2018. Accessed August 18, 2018. https://www.dni.gov/files/documents/Newsroom/Testimonies/2018-ATA---Unclassified-SSCI.pdf.
4. McReynolds, Joe. "China's Evolving Perspectives on Network Warfare: Lessons from the Science of Military Strategy." Jamestown Foundation. April 16, 2015. Accessed August 20, 2018. https://jamestown.org/program/chinas-evolving-perspectives-on-network-warfare-lessons-from-the-science-of-military-strategy/.
5. "NRO Confirms Chinese Laser Test Illuminated U.S. Spacecraft." SpaceNews.com. December 10, 2014. Accessed August 21, 2018. https://spacenews.com/nro-confirms-chinese-laser-test-illuminated-us-spacecraft/.
6. Chase, Michael S., Jeffrey Engstrom, Tai Ming Cheung, Kristen Gunness, Scott W. Harold, Susan Puska, and Samuel K. Berkowitz, China's Incomplete Military Transformation: Assessing the Weaknesses of the People's Liberation Army (PLA). Santa Monica, CA: RAND Corporation, 2015. https://www.rand.org/pubs/research_reports/RR893.html. Also available in print form. Refer to 115-116
7. Pollpeter, Kevin L., Michael S. Chase, and Eric Heginbotham, The Creation of the PLA Strategic Support Force and Its Implications for Chinese Military Space Operations. Santa Monica, CA: RAND Corporation, 2017. https://www.rand.org/pubs/research_reports/RR2058.html. Also available in print form.
8. Military and Security Developments Involving the People's Republic of China 2018. Annual Report to the Congress. Office of the Secretary of Defense. May 16, 2018. Accessed August 23, 2018. https://media.defense.gov/2018/Aug/16/2001955282/-1/-1/1/2018-CHINA-MILITARY-POWER-REPORT.PDF.
9. Ibid 9

10. S. Chandrashekar and N.Ramani, "China's Space Power & Military Strategy – the role of the Yaogan Satellites," ISSSP Report No. 02-2018. Bangalore: International Strategic and Security Studies Programme, National Institute of Advanced Studies, July 2018.Accessed 23 August, 2018.
11. Jun Z., Jianhua Z., Jiansha Y., Tao Z., Dongpo Z., (2010). Semi-physical Simulation of Integrated Reconnaissance System of Radar and Communication Signals, Shipboard Electronic Countermeasure, pp.56-64.
12. Qiaozhong D., Weiqiang Z. (2009). Research on ELINT Satellite Techniques in GSO, Electronic Warfare, p.13.
13. Easton I., Stokes M.A. (2011). China's Electronic Intelligence Satellite Developments: Implications for U.S. Air and Naval Operations, Project 2049 Institute.p.11.
14. "India launching electronic intelligence satellite on April 1". Economic Times. March 24, 2019. https://economictimes.indiatimes.com/news/science/india-launching-electronic-intelligence-satellite-april-1/articleshow/68539756.cms
15. Pillsbury, Michael P. An Assessment of China's Anti-Satellite and Space Warfare Programs, Policies and Doctrines. Report. January 19, 2007. Accessed August 22, 2018. https://www.uscc.gov/sites/default/files/Research/An Assessment of China's Anti-Satellite and Space Warfare Programs.pdf.
16. Ibid
17. Ibid
18. Fisher Jr. R.D. (2018). China's Global Military Power Projection Challenge to the United States. Testimony Before the House Permanent Select Committee on Intelligence, United States House of Representatives. Accessed 24 Aug. 2018. https://intelligence.house.gov/uploadedfiles/hpsci_fisher_testimony_5_17_18.pdf
19. Meeks, Woodrow Anthony, Lt. Colonel. "Peace through Mutually Assured Survival - Global Transparency through Ubiquitous Satellite Imagery." Air War College. February 13, 2014. Accessed August 24, 2018. http://www.au.af.mil/au/awc/awcgate/cst/bh_2014_meeks.pdf.
20. Gertz, Bill. "China Tests Anti-Satellite Missile." Washington Free Beacon. November 09, 2015. Accessed August 24, 2018. https://freebeacon.com/national-security/china-tests-anti-satellite-missile/.
21. Cheng, Dean. "The PLA's Interest in Space Dominance Testimony before US-China Economic and Security Review Commission." The Heritage Foundation.

February 18, 2015. Accessed August 24, 2018. https://www.uscc.gov/sites/default/files/Cheng_Testimony.pdf.

22. Harrison, Todd, Kaitlyn Johnson, and Thomas G. Roberts. "Space Threat Assessment 2018." A Report Of The CSIS Aerospace Security Project. 2018. Accessed August 26, 2018. https://aerospace.csis.org/wp-content/uploads/2018/04/Harrison_SpaceThreatAssessment_FULL_WEB.pdf.
23. Ibid 25
24. Javaid, Azaan. "After Doklam Standoff, ITBP Gets Satellite Control to Keep Eye on China Border." Https://www.hindustantimes.com/. October 29, 2017. Accessed August 28, 2018. https://www.hindustantimes.com/india-news/after-doklam-standoff-itbp-gets-satellite-control-to-keep-eye-on-china-border/story-EXygJamCUO27JCQRdZJ8qJ.html.
25. "Joint Doctrine Armed Forces." Integrated Defence Staff. 2017. Accessed August 30, 2018. https://www.ids.nic.in/IDSAdmin/upload_images/doctrine/JointDoctrineIndianArmedForces2017.pdf.
26. Singh, Ranjit, Brigadier. Unified Commands in the Indian Armed Forces: Imperative for Integrated Warfighting. Centre for Joint Warfare Studies. Issue brief. New Delhi: Centre for Joint Warfare Studies. 2016. Accessed August 30, 2018. https://cenjows.gov.in/pdf/Layout_Unified Comd by Brig Ranji_03-04-17.pdf.
27. Jayaraman, K. S. "Indian Government Set To Create Aerospace Command." SpaceNews.com. December 28, 2015. Accessed August 30, 2018. https://spacenews.com/indian-government-set-create-aerospace-command.
28. Ibid
29. Miglani, Sandeep., Das, Krishna N. "India shoots down satellite in space; Modi hails major breakthrough". Reuters. March 27, 2019. https://in.reuters.com/article/india-satellite-mission-shakti/india-shoots-down-satellite-in-space-modi-hails-major-breakthrough-idINKCN1R80I6
30. Unnithan, Sandeep. ""India Has All the Building Blocks for an Anti-satellite Capability"." India Today. April 27, 2012. Accessed August 31, 2018. https://www.indiatoday.in/india/story/agni-v-drdo-chief-dr-vijay-kumar-saraswat-interview-100405-2012-04-27.
31. (2010). Technology Perspective and Capability Road Map, India.HQ Integrated Defence Staff, Ministry of Defence- Removed from public domain
32. (2013). Technology Perspective and Capability Road Map, India. HQ Integrated Defence Staff, Ministry of Defense.

33. Ladwig W.C.III. (2008). A Cold Start for Hot Wars? International Security. Vol. 32. No. 3. p. 158-190.

34. Moltz J.C. (2012). Asia's Space Race. Columbia University Press. p. 130.

35. Snyder G.H. (1959). Deterrence by Denial and Punishment. Woodrow Wilson School of Public and International Affairs, Center of International Studies, Princeton University.

36. (2018). DOD's Use of Commercial Satellites to Host Defense Payloads Would Benefit from Centralizing Data. United States Government Accountability Office.

37. Weeden, Brian. "Space Architecture Choices and Physical Dependencies." Secure World Foundation. April 14, 2009. Accessed September 1, 2018. https://swfound.org/media/205433/spacearchitec-bw-ndu-2009.pdf.

38. (2011). National Security Space Strategy- Unclassified Summary. US Department of Defense.

39. Madhumathi, D.S. "ISRO, French space agency seal agreement on maritime security". The Hindu. March 6,2019. https://www.thehindu.com/news/national/isro-french-space-agency-seal-agreement-on-maritime-security/article26449883.ece

40. Davis, Paul K. Toward Theory for Dissuasion (or Deterrence) by Denial: Using Simple Cognitive Models of the Adversary to Inform Strategy. Working paper. January 10, 2014. Accessed September 1, 2018. https://www.rand.org/content/dam/rand/pubs/working_papers/WR1000/WR1027/RAND_WR1027.pdf.

Numerical Simulation and Parametric Study of Carbon Deposition During Graphene Growth in PECVD System

Manish Kumar, Sagar Khanna, Neha Gupta, *Member, IEEE*, Ravi Gupta, *Member, IEEE*, and Suresh C. Sharma, *Member, IEEE*

***Abstract*—The aim of the present work is to understand the carbon deposition during graphene growth in plasma enhanced chemical vapor deposition system containing $Ar/C_2H_2/H_2$ gas mixture and to optimize the process parameters for the enhanced growth of graphene. In this regard, many numerical simulations have been carried out using two-dimensional axis-symmetrical inductively coupled plasma module in COMSOL multi physics 5.2a simulation software. From the simulation outcomes, it is found that the electron density, electron energy density, electric potential, and collisional power losses decrease with an increase in temperature. The number densities of various dominant ions were found to decrease and number densities of dominant neutrals were found to increase with an increase in temperature. During the carbon deposition, the formation of non-uniform horizontal graphene layer has been observed along the substrate and vertically oriented graphene sheet has been observed at the edges of the substrate. It is found that the thickness of horizontal graphene along the substrate and height of vertical graphene at the edges of the substrate increases with an increase in gas temperature. Moreover, the reduction in the carbon deposition on the substrate (growth of parallel graphene) and enhanced growth of vertical graphene sheet have been observed on applying substrate biasing. Our numerical simulation results are in good agreement with existing experimental observations and confirms the adequacy of the computational and simulation approach.**

***Index Terms*—COMSOL, graphene, ICP, PECVD, substrate biasing, temperature, vertically oriented graphene.**

I. Introduction

CARBON nanostructures such as graphene, carbon nanofilms and carbon nanotubes have recently gained scientific attention due to their miraculous applications in electron field emission devices [1], ultrafast transistors [2] and microelectrochemical systems [3]. The unique field emission characteristics of the carbon nanostructures are attributed to their size-dependent electronic properties [4]. In addition, vertically oriented carbon nanosheets and nanotubes show much enhanced field emission when exposed to low electric fields [5]. Graphene nanofilms are found to show excellent properties which make them useful in catalysis, gas separation, and energy storage etc [6]–[10]. It has also been observed that nano-films of certain materials other than carbon like cadmium telluride and zinc selenide have applications in detection of harmful gases like carbon monoxide [11], [12].

The two major techniques, namely thermal chemical vapor deposition (T-CVD) and plasma-enhanced chemical vapor deposition (PECVD) have recently gained popularity as the most preferred and widely used synthesis techniques [13]–[15] of carbon nanostructures. In PECVD, the gaseous sources exist in the ionized state in the plasma. The common source of plasma is microwave-PECVD, radio frequency-PECVD, direct current-PECVD and inductively coupled-PECVD. In reactive plasma, highly reactive positively charged ions and neutral species are generated due to collisions between electrons and other gaseous species without much rise in gas temperature. The composition of the plasma depends upon the reaction between electrons and gaseous species. Many parameters such as temperature, substrate bias, input plasma power, pressure and flow rates of the gaseous sources etc. critically influence the plasma properties such as electron density and electron temperature which ultimately affects the dissociation and ionization of neutral gaseous species. Graphene possesses a number of incredible properties, previously not witnessed at the nano scale. The observations include Quantum Hall Effect (QHE) at room-temperature, high electron mobility along with ballistic transport, large mean free paths for the electrons, high thermal conductivity, high mechanical strength, and high tremendous flexibility [16]–[19]. Moreover, many studies have been reported the multi-scale modeling of the deposition of the silicon thin films and thin films of solar cell via PECVD process to understand the deep insights of the thin film deposition [20]–[22].

The aim of the present paper is to analyze the effect of temperature and substrate biasing on the spatial distribution of the gaseous species in the localized plasma region and their surface dissociation via various surface reactions to generate carbon species which are the building blocks of graphene nanosheets. The detailed description of the model is given in Section II. Results obtained from simulation model are discussed in Section III and finally, the conclusion of the present study is summarized in Section IV.

Manuscript received October 16, 2018; revised February 14, 2019; accepted March 31, 2019. Date of publication April 11, 2019; date of current version May 1, 2019. The review of this paper was arranged by Associate Editor Mattias Borg. *(Corresponding author: Suresh C. Sharma.)*

The authors are with the Department of Applied Physics, Delhi Technological University, Delhi 231511, India (e-mail: Mannish.mannia@gmail.com; khannasagar796@gmail.com; nehagpt2105@gmail.com; ravigpt0709@gmail.com; suresh321sharma@gmail.com).

Digital Object Identifier 10.1109/TNANO.2019.2910173

1536-125X © 2019 IEEE. Personal use is permitted, but republication/redistribution requires IEEE permission.
See http://www.ieee.org/publications_standards/publications/rights/index.html for more information.

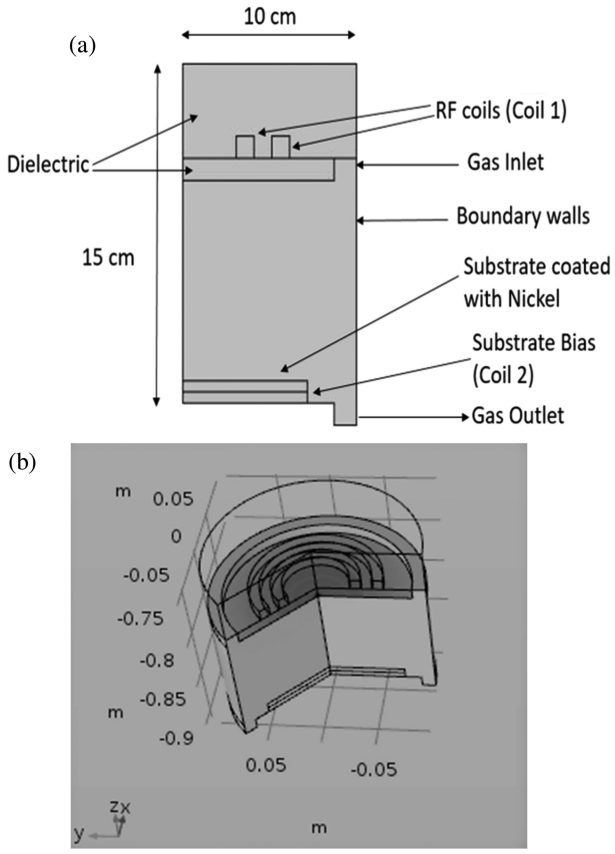

Fig. 1. Schematics of (a) 2D axis-symmetric geometry of PECVD reactor and (b) actual 3D geometry of PECVD system.

TABLE I
PROPERTIES OF THE MATERIALS USED FOR THE SIMULATION MODEL

Medium	Electrical Conductivity	Relative Permittivity	Relative Permeability
RF coils (Coil 1)	$6x10^7$ S/m	1	1
Substrate Bias (Coil 2)	$4x10^3$ S/m	1	1
Dielectrics/Insulators	0	1	4.2

II. MODEL

In the present simulation model, the growth of graphene nanosheets has been studied in $Ar/C_2H_2/H_2$ reactive plasma using COMSOL Multiphysics 5.2a modeling suite. The methodology adopted in the simulation mainly involves four physical stages.

1) Plasma interface, involves the ionization of gas mixture due to the transformer action caused by the inductively coupled RF (radio frequency) coils. This ionization leads to electron generation followed by series of electron impact reactions.
2) Heavy species transport, involves the exposure of carbon-containing gases with plasma in order to produce various ions and radicals. It also involves the interaction of plasma species with the catalyst-substrate surface.
3) Magnetic field, plays an important role in the generation of high power radio frequency wave through coils to initiate ionization of gases to form the plasma by inductive effect.
4) Substrate bias or laminar flow, supports the directed flow of various hydrocarbon species towards the catalyst coated substrate Catalyst coated substrate plays an important role in the control of nanostructure morphology. It provides the route for the nucleation process.

These physical interfaces are coupled in the 2D axis symmetric geometry constructed in the inductively coupled plasma (ICP) module in COMSOL Multiphysics 5.2. as shown in Fig. 1. The two-dimensional PECVD model of $Ar/C_2H_2/H_2$ gas mixture at low-pressure (20mTorr) and low temperature (below 723 K) has been developed to study the growth of graphene nanosheets. To make the analysis simpler, the actual 3D model is taken as a 2D axis-symmetric geometry. The actual 3D geometry structure of PECVD system considered is also shown in Fig. 1 that consist the metallic cylinder having radius and height of 10 cm and 15 cm, respectively. A substrate platform of radius 7 cm is kept at the bottom of the chamber. A four-turn spiral antenna (inductive coils) [23] named as coil 1is placed at the top of the plasma chamber and is connected to 13.56 MHz generator. These RF coils are the main ICP source. The antenna configuration is considered to generate low-temperature plasmas having non-uniform density profiles along the radial direction [24]. A negative substrate bias named coil 2 is also placed beneath the substrate consisting of DC voltage source with biasing ranged from -10 V to -400 V DC. Insulators around high-power magnetic coils are used to electrically isolate them from the surrounding and plasma chamber. The properties of the materials used in the present model are listed in Table I. Inlet and outlet are provided to supply gases into/off the plasma chamber.

The other assumptions of the model are: (i) coating of nickel as catalyst material on silicon (100) substrate in pre-plasma conditions, (ii) operating conditions in the chamber are uniform, (iii) frequency transient study of the system is analyzed using COMSOL Multiphysics 5.2a, (iv) convection of heavy species present in a plasma can often be neglected due to the low operating pressure, (v) the surface loss (boundary walls) of hydrogen atoms is assumed to be zero, (vi) ion impact electron emission is set to zero. Moreover, complete absorption or neutralization of ions are considered on arriving at the chamber boundary with the only transitional change in the state of Ar, and (vii) the excited hydrogen and argon atoms are set to revert to their ground states when they contact with the walls.

Meshing is a critical step in plasma model which is needed to capture the separation of space charge between the electrons and ions close to the wall. Inductively coupled plasma and heavy species transport is computationally meshed using COMSOL Multiphysics 5.2a. The material and spatial domains are meshed using finer settings having minimum quality of 0.001 m. The plasma chamber domains are meshed using extra fine element size with the free triangular entity. The boundary layer property involves a total of 5 boundary layers with the stretching factor of 1.4.

In this simulation model, the numerical modeling of reactive PECVD process is carried out using COMSOL. The model

involves the solution of multiple volumetric reactions in the bulk plasma and various surface reactions over the catalyst surface for a number of reactants and intermediate species. These reactions are provided with tens of finite rate reaction steps and varying rate coefficients. The solutions of such rigid sets of equations are difficult and the inbuilt solver of COMSOL does the job accurately and very fast. COMSOL has an easy to use graphical user interface (GUI) and also provide the several inbuilt equations solver (using Finite element method) with various Multiphysics options.

A. Physics and Equations Involved

The model incorporates various physics interfaces. When a time-varying electric current is supplied to the RF coils at 13.56 MHz, it produces a time-varying magnetic field in the plasma chamber filled with gases. As per Lenz's law, a time-varying electric current flows inside the chamber gases in opposite direction to oppose the magnetic field. This electric current in the gas chamber ionizes the gases to form the plasma by transformer action. The plasma interface is used to study the general plasma parameters such as electron density, electric potential, and electron temperature. The heavy species transport interface is a mass balance interface for all non-electron species formed in the plasma chamber. This physics interface also makes it possible to add electron impact reactions, chemical reactions, surface reactions, and species, including charged, neutral, and electronically excited species into the model to simulate the actual reactions that take place experimentally.

The electron transport properties are computed from the reduced transport properties using the equation $\mu_e = \frac{\mu_{red}}{N_n}$, where N_n is the number density and μ_{red} is the reduced mobility of electrons. The cross-section data is used to define source coefficients in the model, here the Maxwellian electron energy distribution function (EEDF) is used to define source coefficients $f(\varepsilon) = \varphi^{-3/2}\beta_1 \exp(-(\frac{\varepsilon\beta_2}{\varphi}))$, where $\beta_1 = \Gamma(\frac{5}{2})^{3/2}\Gamma(\frac{3}{2})^{-5/2}, \beta_2 = \Gamma(\frac{5}{2})\Gamma(\frac{3}{2})^{-1}, \varphi$ is the mean electron energy in eV, ε is the electron energy in eV, and Γ is the incomplete gamma function.

$$\frac{\partial(n_e)}{\partial t} + \nabla.\Gamma_e = \mathrm{R}_e, \tag{1}$$

$$\frac{\partial(n_\varepsilon)}{\partial t} + \nabla.\Gamma_\varepsilon + E.\Gamma_e = \mathrm{R}_\varepsilon, \tag{2}$$

$$\Gamma_e = -n_e(\mu_e E) - D_e\nabla n_e, \tag{3}$$

$$\Gamma_\varepsilon = -n_\varepsilon(\mu_\varepsilon E) - D_\varepsilon\nabla n_\varepsilon, \tag{4}$$

$$\mathrm{R}_e = \sum_{j=1}^{M} x_j k_j N_n n_e, \tag{5}$$

$$\mathrm{R}_\varepsilon = \sum_{j=1}^{P} x_j k_j N_n n_e \Delta\varepsilon_j, \tag{6}$$

$$k_j = \gamma\int_0^\infty \varepsilon\sigma_j(\varepsilon)f(\varepsilon)d\varepsilon, \tag{7}$$

$$\gamma = (2q/m)^{1/2}, \tag{8}$$

TABLE II
PARAMETERS USED IN SIMULATION

Parameters	Value
Input Plasma Power	1200 W
Gas Pressure	20 mTorr
Reduced Electron Mobility	$4x10^{24}V^{-1}\ m^{-1}s^{-1}$
Area of the substrate	154 cm^2
Thickness of Nickel Coating	200 nm
Initial Electron Density	10^{13} /m^3
Plasma Power frequency	13.56 MHz (Radiofrequency)
Initial Density of Gases	10^{13} /m^3

TABLE III
DIFFERENT SPECIES CONSIDERED IN THE Ar/C_2H_2/H_2 PLASMA, WHERE ADS STANDS FOR ADSORPTION AND b STANDS FOR BULK

Molecules	Ions	Radicals	Surface Species
Ar	Ar^+, ArH^+	Ars	
C_2H_2	C_2H^+, C_2H^+, $C_2H_3^+$	C_2H, C_2H_3	C_2H_2(ads),C_2H(ads), C(b)
H_2	H^+, H_2^+, H_3^+	H	H(ads), H_2(ads), H(b)

COMSOL Multiphysics solves a pair of drift-diffusion for the electron density viz. Eqns. 1, 3, and 5 and for the electron energy density viz Eqns. 2, 4, and 6. Where Γe is the flux of diffusing electron termed as Fick's law of diffusion, where D_e is the diffusion constant. Re is the source term, where *kj* is the rate coefficient for reaction *j*, $\Delta\varepsilon_j$ is the energy loss from reaction j, N_n is the number density of reactants, E is the electric field in the chamber, n_e is the electron density, m is the electron mass, ε is energy, σ_j is the collision cross section, x_j is the mole fraction for the target species of reaction j, and *f* is the electron energy distribution function. The plasma potential is computed from Poisson's equation $-\nabla.\varepsilon_o\varepsilon_r\nabla V = \rho$. The space charge density ρ is computed from the number densities of electrons and other charged species by Eq. 9.

$$\rho = q\left(\sum_{k=1}^{M} Z_k n_k - n_e\right), \tag{9}$$

Surface reactions can be specified in terms of rate or sticking coefficients. The surface rate constant is determined using Eq. 10.

$$K_{f,i} = \left(\frac{\gamma_i}{1-\gamma_i/2}\right)\left(\frac{1}{(\Gamma_{tot})^m}\right)\left(\frac{1}{4}\right)\sqrt{\frac{8RT_e}{\pi M_n}}, \tag{10}$$

γ_i is the sticking coefficient given by $\gamma_i = a_1 {T_e}^{b_1}\exp(-\frac{e_i}{RT_e})$, where M_n is the mean molecular weight of the gas mixture, R is the gas constant, T_e is the electron temperature, and a_1 and b_1 are constants.

The carbon species generated over the catalyst substrate surface via various reactions diffuse along the substrate interface. Hence, the velocity of the interface can be mathematically expressed by an equation $v_y = \frac{\vec{j}_m.\hat{n}_y}{\rho_{carbon}}$, where vy is the interface velocity and $\vec{j}\,m.\hat{n}y$ is the mass flux in the y-direction and

TABLE IV
REACTIONS INVOLVED

Electron Impact reactions, where Ars represents the meta-stable state of the Argon atom i.e., when it strikes the walls, gets converted into the ground state Ar atom.

No	Reaction	Type	Threshold(eV)	Ref.
1	e^- +Ar → e^- +Ar	Elastic	0	[25],[26]
2	e^- +Ar → e^- +Ars	Excitation	11.5	[25],[26]
3	e^- +Ars → e^- +Ar	Super elastic	-11.5	[25],[26]
4	e^- +Ar → 2 e^- + e^-	Ionization	15.8	[25],[26]
5	e^- +Ars → 2 e^- +Ar^+	Ionization	4.24	[25],[26]
6	Ars+Ars → e^- +Ar	Penning Ionization		[25],[26]
7	Ars+Ar → Ar +Ar	Metastable quenching		[25],[26]

Plasma chamber Wall Surface reaction

No	Reaction	Sticking Coefficient	Ref.
8	Ars → Ar	1	[26]
9	Ars^+ → Ar	1	[26]

Reactions

No	Reaction	Rate Coefficients $m^3/(s.mol)$)	Ref.
10	Ar^++C_2H_2 → $C_2H_2^+$+Ar	25.29 x10^8	[27]
11	Ar^++H_2 → Ar+H_2^+	0.448 x10^8	[27]
12	$C_2H_2^+$+H_2 → $C_2H_3^+$+H	0.1656 x10^6	[27]
13	H_2^++H → H^++H_2	1.062 x10^7	[27]
14	C_2H_2+H^+ → C_2H^++H_2	0.713 x10^8	[27]
15	$C_2H_3^+$+H → $C_2H_2^+$+H_2	1.126 x10^6	[27]
16	C_2H^++H_2 → $C_2H_2^+$+H	0.182 x10^8	[27]
17	$C_2H_2^+$+H^+ → $C_2H_2^+$+H_2	0.713x10^8	[27]

Surface Reactions on the substrate

No	Reaction	Type	Sticking Coeffici-ent	Ref.
18	C_2H^+ → 2C(b)+H_2	Dissociation of hydrocarbon	1	[28]-[32]
19	C_2H^+ → C_2H	Stabilization of ions	0.8	[28]-[32]
20	C_2H_2 → C_2H_2(ads)	Adsorption of Hydrocarbons on the nickel coated (catalyst) silicon substrate surface	0.5	[28]-[32]
21	C_2H → C2H(ads)		0.8	[28]-[32]
22	H → H(ads)	Adsorption of hydrogen species on the nickelcoated (catalyst) silicon substrate surface	0.0 1	[28]-[32]
23	H_2 → H_2(ads)		0.0 2	[28]-[32]
24	C_2H^++C_2H(ads) → 2C(b)+H(b)+C_2H^+	Ion-induced dissociation of hydrocarbons and hydrogen generation	0.9	[28]-[32]
25	C_2H2^++C_2H(ads) → 2C(b)+H(b)+$C_2H_2^+$		0.9	[28]-[32]
26	$C_2H_2^+$+C_2H_2(ads) → 2C(b)+H_2+$C_2H_2^+$		0.9	[28]-[32]
27	C_2H_2(ads) → 2C(b)+2H	Thermal dissociation of hydrocarbons	1	[28]-[32]
28	C_2H(ads) → 2C(b)+H		1	[28]-[32]
29	C_2H2^++C_2H_2(ads) → 2C(b)+H+$C_2H_2^+$	Ion-induced dissociation of Hydrocarbons	0.9	[28]-[32]
30	C_2H^++C_2H_2(ads) → 2C(b)+H+C_2H^+		0.9	[28]-[32]
31	C_2H_2(ads)+H → C_2H_3	Interaction of hydrocarbons with atomic hydrogen	0.3	[28]-[32]
32	C_2H(ads)+H → C_2H_2		0.5	[28]-[32]
33	C_2H_2(ads) → C_2H_2	Desorption of hydrocarbons	0.5	[28]-[32]
34	C_2H(ads) → C_2H		0.8	[28]-[32]

$\rho_{carbon} (= 2.267\ \mathrm{g/cm^3})$ is density of carbon. Hence, the thickness (d) of the segregated carbon material (planar graphene nanofilms) can be calculated by equation $d = vy * t$, where't' is time.

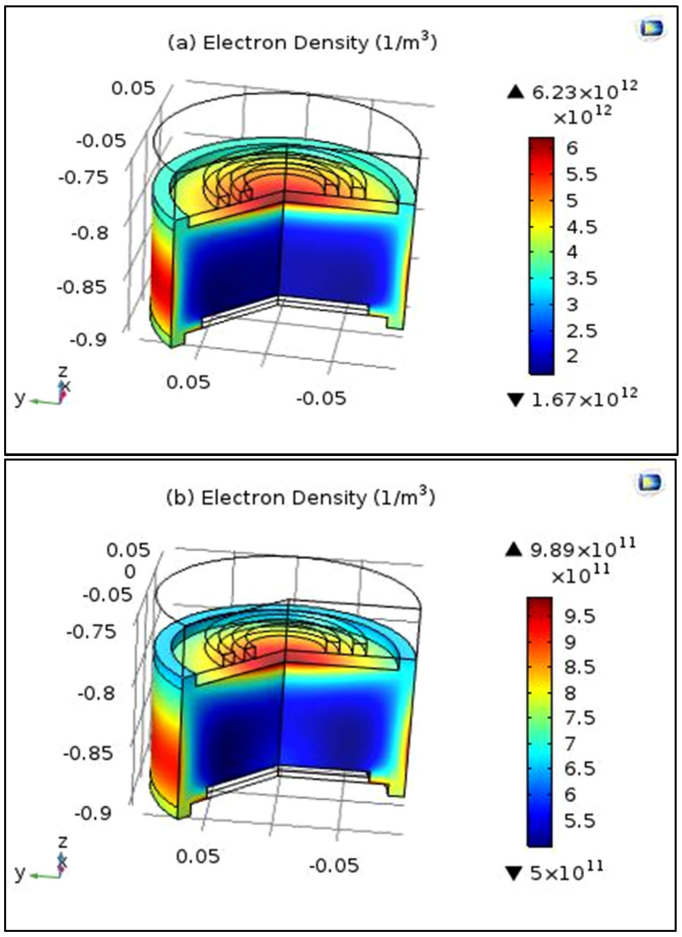

Fig. 2. 3D distribution of Electron Density inside the PECVD chamber (a) at room temperature of 300 K and (b) at threshold temperature for sensitive substrates at 723 K.

Using the above plasma module, simulations are performed for $Ar/C_2H_2/H_2$ for plasma operated at the parameters given in Table II. The numerous plasma species accounted in the present simulation are given in Table III and the various reactions between plasma species in bulk plasma and over the catalyst surface are given in Table IV. The plasma species and chemical reactions considered in the present simulation are justified in order to generate 2D analysis of the number densities and fluxes of various species involved which are vital for nano assembly of selected carbon-based nanostructures. The limited species have been accounted to reduce the computational coast and duration.

III. RESULTS AND DISCUSSIONS

In the present study, the simulations were performed for two different cases, i.e., the effect of temperature at fixed substrate bias and effect of substrate bias at fixed temperature.

Figs. 2(a) and 2(b) represent the 3D electron densities profiles calculated at temperatures 300 K (room temperature) and 723 K (threshold temperature for temperature sensitive substrate), respectively. The peak value of electron density is observed to be

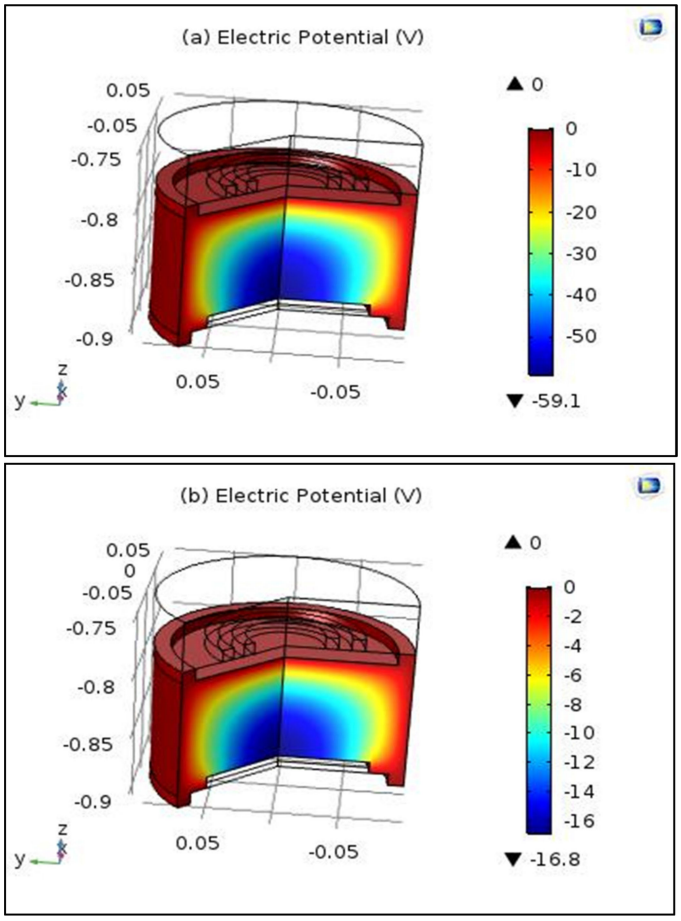

Fig. 3. 3D distribution of Electric Potential inside the PECVD chamber (a) at 300 K and (b) at 723 K.

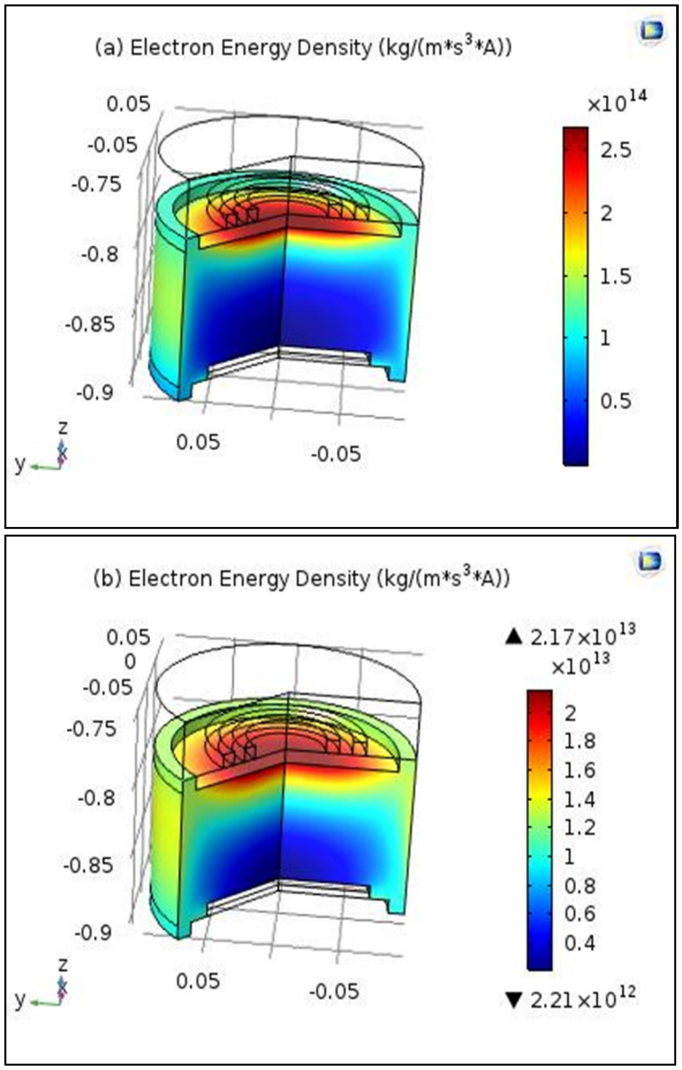

Fig. 4. 3D distribution of Electron Energy Density inside the PECVD chamber Electron energy density at (a) 300 K and (b) at 723K.

6.33×10^{12} m^{-3} and 9.89×10^{11} m^{-3} for 300 K and 723 K, respectively, in the inductive region (below the power coil).

Fig. 3(a) and Fig. 3(b) display the electric potential distribution at 300 K and 723 K, respectively. The peak value of electric potential is found to be negative with numerical values 59.1V and 16.9V for 300 K and 723 K, respectively, in the localized plasma region. The distribution of electron energy density at 300 K and 723 K are shown in Fig. 4(a) and Fig. 4(b) respectively. The Peaks are observed near the coils having numerical values 2.69×10^{14} kg/(m.s^{3}·A) and 2.17×10^{13} kg/(m.s^{3}·A) for 300 K and 723 K, respectively. The electron energy density is found to be greater at 300 K.

The reason for the decrease in electron density, electron energy density and electric potential with an increase in temperature can be inferred from the collision theory [33]. One can expect the increase in the rate of reaction with the increase in temperature. However, in reality, an opposite scenario takes place. With an increase in the temperature, random motion of the molecules increases due to which greater proportion of molecules in the chamber will have the minimum energy for effective collision. Thus, the fraction of molecules available for electron impact reaction decreases and leads to decrease in the rate of reaction and suppresses the overall electron generation.

Fig. 5(a) and Fig. 5(b) show the collision power loss distribution in the plasma chamber at 300 K and 723 K, respectively. When the electrons and fluxes of different constituents of gases collide with each other, the electrons transfer their momentum and tend to lose their energy [34]. This phenomenon of loss of energy is signified as collisional power loss. The collision power losses are found to be 800 W/m^3 and 25 W/m^3 at 300 K and 723 K, respectively. Thus, one can see that at high temperature, the number of electrons in the plasma are less and consequently, show low collisional power loss.

A. Plasma Chemistry and the Surface Phenomenon

The average volume number densities of various plasma components including radicals, ions, and neutrals define the surface interaction with the catalyst coated substrate. The density profiles of the plasma species, i.e., Ar+, C_2H^+, $C_2H_2{}^+$, $C_2H_3{}^+$, and H_2 at 300 K and 723 K can be seen from Fig. 6 to 10. These carbon-containing species mostly being singly positively charged are electrically attracted towards the negatively biased

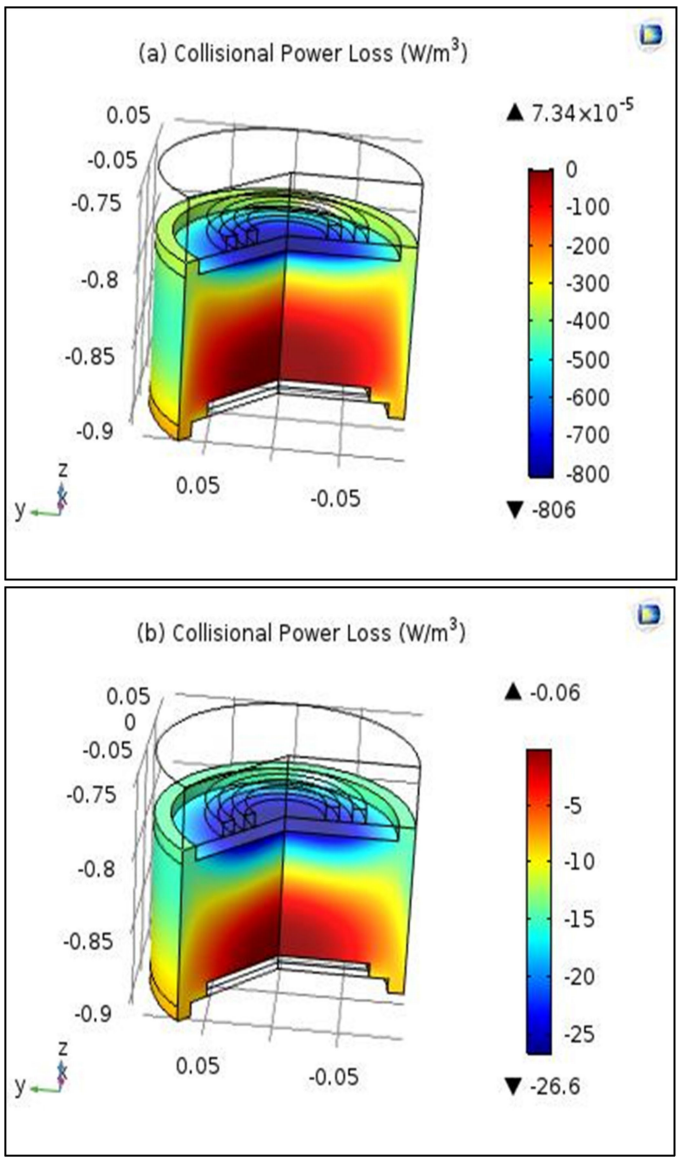

Fig. 5. Collision Power Loss distribution inside PECVD chamber (a) at 300 K and (b) at 723 K.

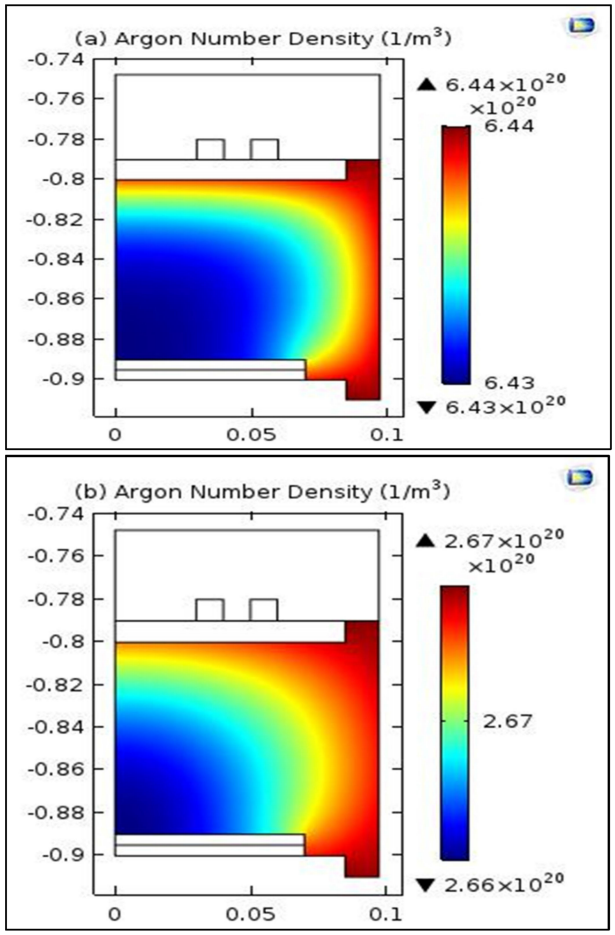

Fig. 6. Two-dimensional plot of number density of argon gas (a) at 300 K and (b) at 723 K.

substrate leading to interaction with surface catalyst surface via various surface processes listed in Table III.

Fig. 6(a) & 6(b) show the Argon ion density in the chamber after plasma formation for 300 K and 723 K, respectively. It can be observed that the density of argon ions decreased when the temperature is increased. This is because the overall electron density is reduced at high temperature which in turn leads to the lesser collision with neutral argon species (argon gas) to produce argon ions.

After activation of gaseous sources of plasma, the carbon-containing gas dissociates into constituent radicals and neutrals which later interacts with catalyst surface. Fig. 7(a) and 7(b) shows the number density distribution of C_2H^+ ion over the catalyst substrate surface. The density of C_2H^+ is found to be low at substrate contact point with increasing concentration outwards due to the generation of hydrogen and C_2H^+ by ion-induced decomposition of the various other hydrocarbon species [cf. Table III].

Figs. 8(a) and 8(b) shows the number density distribution of $C_2H_2{}^+$ ion over the catalyst substrate surface at 300 K and 723 K, respectively. The number density of $C_2H_2{}^+$ is observed to be low compared to C_2H^+ in the plasma due to the low intensity of dissociation of the much heavier $C_2H_2{}^+$. It is found that density $C_2H_2{}^+$ is higher at substrate contact point with decreasing concentration outwards because the rate of absorption of $C_2H_2{}^+$ is higher than the rate of desorption. Moreover, the concentration also decreases outwards due to the continuous ion induced decomposition of the hydrocarbons which leads to the continuous generation of carbon species. Fig. 9(a) and 9(b) shows the $C_2H_3{}^+$ number density distribution in the plasma at 300 K and 723 K, respectively. It follows the same pattern as followed by C_2H^+, i.e., the lowest density at substrate plasma interface and increasing density outwards. This is because of the loss of hydrocarbons due to the interaction with atomic hydrogen at the catalyst-substrate surface.

The overall effect of temperature on number densities of ions and neutral species can be seen from Fig. 10(a) and 10(b), respectively. From the bar graph it can be seen that the ion densities of various ionic component decrease when operative temperature is raised. This is because of the decrease in the fraction

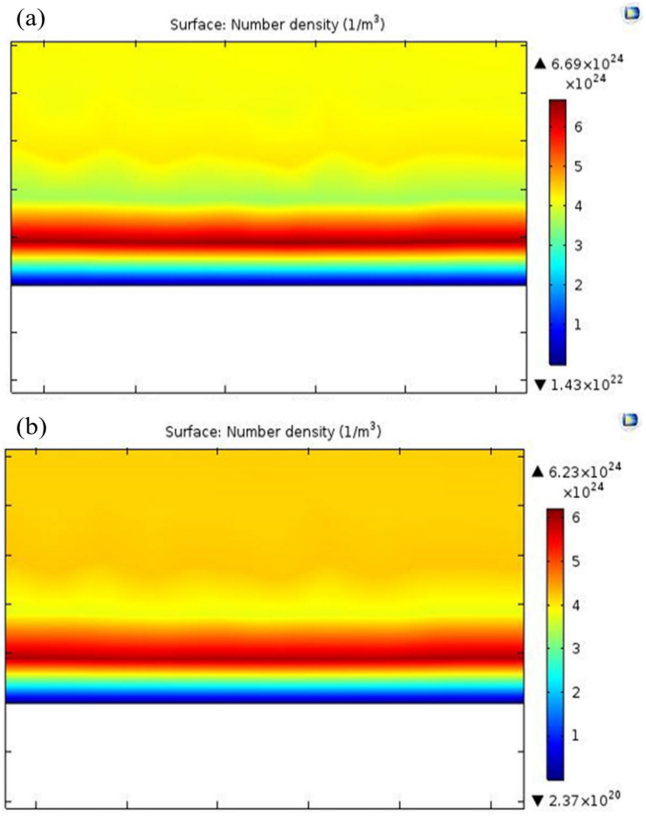

Fig. 7. Two-dimensional profile of C_2H^+ ion number density (a) at 300 K and (b) at 723 K.

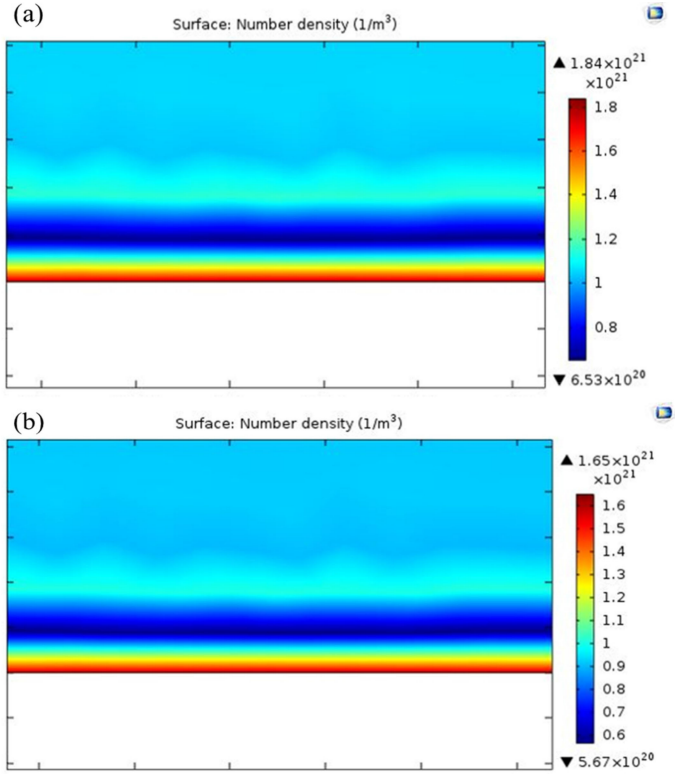

Fig. 8. Two-dimensional profile of $C_2H_2^+$ ion density at 300 K and (b) at 723 K.

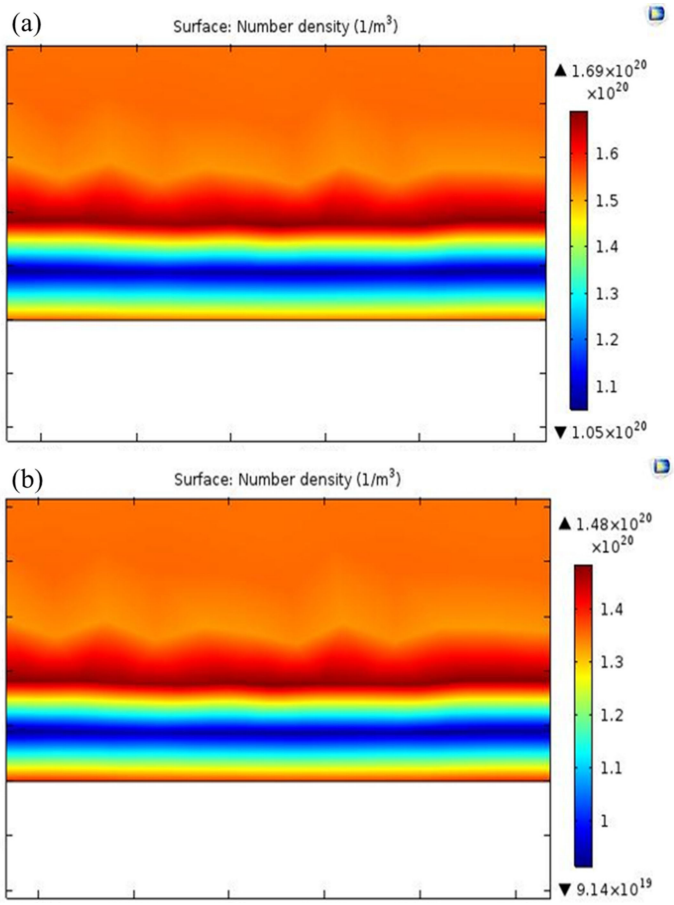

Fig. 9. Two-dimensional profile of $C_2H_3^+$ ion density at 300 K and (b) at 723 K.

of gaseous molecules available for collision [34]. However, the densities of C_2H_2 and C_2H_3 increases with an increase in temperature because of the loss of hydrocarbons neutrals (C_2H_2 and C_2H_3) from adsorbed state to gaseous state on interaction with atomic hydrogen.

Accumulated carbon growth on substrate

The carbon deposition (graphene sheet growth) over the substrate surface in $Ar/C_2H_2/H_2$ gas mixture at a fixed temperature is highly dependent on the substrate biasing. Fig. 11(a) and Fig. 11(b) shows the accumulated carbon height with biasing (-50 V) and without biasing, respectively, at 723 K. It can be seen that the deposition of planar graphene sheet along the substrate surface is found to be non-uniform with thickness varying from 48–60 nm, however, vertical growth of graphene sheet is observed at the edges of the catalyst substrate surface. The height of this vertical carbon nanostructure is found to be 223 nm. When the bias voltage at the substrate surface is removed, the carbon deposition over the catalyst substrate surface and vertical carbon growth at the edges increases and found to be in the range 340–400 nm and 660 nm respectively. Fig. 12(a) and Fig. 12(b) show the 3D accumulated carbon growth on the substrate at -50 V DC bias and no bias, respectively.

There is a significant 8-fold decrease in carbon growth height on the substrate which makes it suitable for thin film deposition

Fig. 10. (a) Number density of various ions at 300 K & 723 K and (b) Number density of various neutrals at 300 K & 723 K.

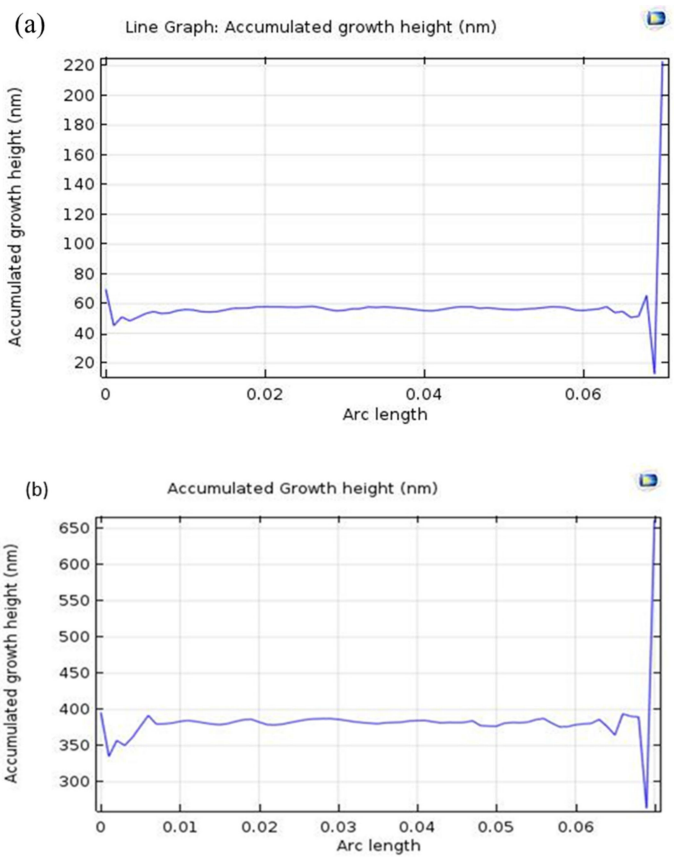

Fig. 11. Accumulated carbon growth height along the substrate arc (a) with −50 V DC bias; (b) without bias.

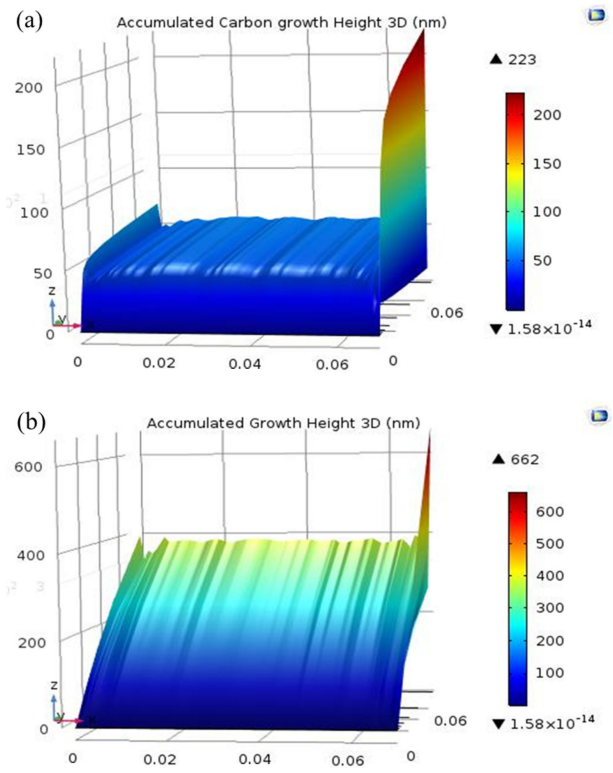

Fig. 12. 3D plot of accumulated carbon growth height along the substrate arc (a) at −50 V DC bias; (b) without bias.

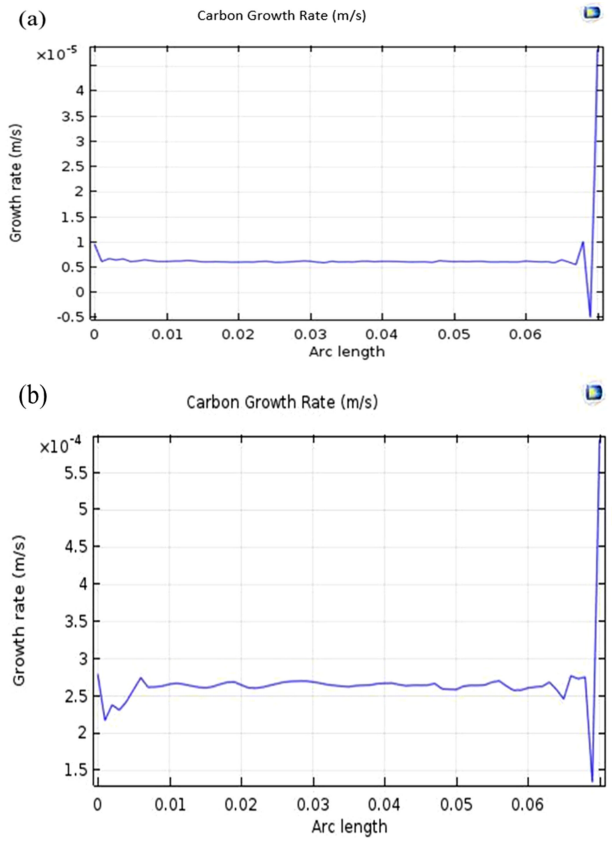

Fig. 13. Accumulated carbon growth rate along substrate arc length (a) at −50 V DC bias; (b) without bias.

on desired materials. The thickness of the horizontal graphene sheet decreases on applying biasing, because of the effective etching of the energetic ion at the sheet [35]–[37]. In the absence of biasing the flux of the energetic ions towards the substrate decreases due to which the effective etching is reduced [37]. Also, the thickness of the sheet is non-uniform due to the non-uniform flux of species as can be seen from Figs. 6 to Fig. 10.

The growth of 2D graphene takes along the plane due to coalescence and coalition of accumulated graphene islands formed on the catalyst-substrate surface because of diffusion and attachment of clusters (bunch of carbon species). However, due to temperature gradient, ion bombardment, and lattice mismatch between the graphitic layer and catalyst-substrate edges. an internal stress is developed at the edges of the substrate.

This internal stress tends the free edges of the planar graphene sheets to bend vertically upward. Further, under the resultant action of tensile stress, alignment force (exerted by the electric field induce in the plasma sheath) and continuous carbon species, the graphene sheet attains vertical orientation and continues to grow in the direction normal to the substrate surface [37]. After some time, the growth termination stage is achieved when rate of carbon deposition is balanced by the rate of etching of graphene sheet. Relative growth of vertical graphene is higher when biased is applied as compared to without biased growth. On applying substrate bias, ion flux towards the substrate surface increases which leads to the larger ion-induced dissociation of hydrocarbons which results in the sufficient supply of building units and thus, enhance the vertical growth.

The carbon growth rate along the different part of the substrate is not same in both the cases, i.e., with bias and without bias as shown in Fig. 13(a) and Fig. 13(b), respectively. With the substrate biasing, the deposition rate of the carbon in the form of the sheet is observed to be uniform except at the edge. However, in the absence of biasing non-uniform deposition rate of carbon is observed. From Fig. 12(a) and 12(b) the growth rate is found to be maximum in case of no bias, i.e., 2.2×10^{-4} m/s to 2.6×10^{-4} m/s along substrate and 6×10^{-4} m/s at the edge whereas, a constant growth rate of 5×10^{-6} m/s along substrate and 55×10^{-6} m/s at the edge is observed when bias is applied.

The simulation for $Ar/C_2H_2/H_2$ gas mixture with nickel as a catalyst is performed at two different temperatures 300 K and 723 K and a fixed bias of -50 V, resulted into formation of irregular 2D nanosheet-like structures on the substrate. The graphene sheets having thickness of 50–60 nm are seen growing parallel to the substrate surface at 300 K. Moreover, the vertical carbon growth having height of 220 nm has been also observed at the edges of the substrate when biasing is applied as shown in Fig. 14(a). The vertical carbon growth along edge resembles vertical graphene-like structure. At 723 K accumulation and growth of carbon is also observed to be same with a thickness of 200 nm parallel to the substrate as shown in Fig. 14(b). At the edges of the substrate, the growth of the graphene sheet is observed to be 1 micrometer.

This is due to the vertical bending of the graphene sheet (vertical alignment of the graphene sheet) at the edges of the substrate.

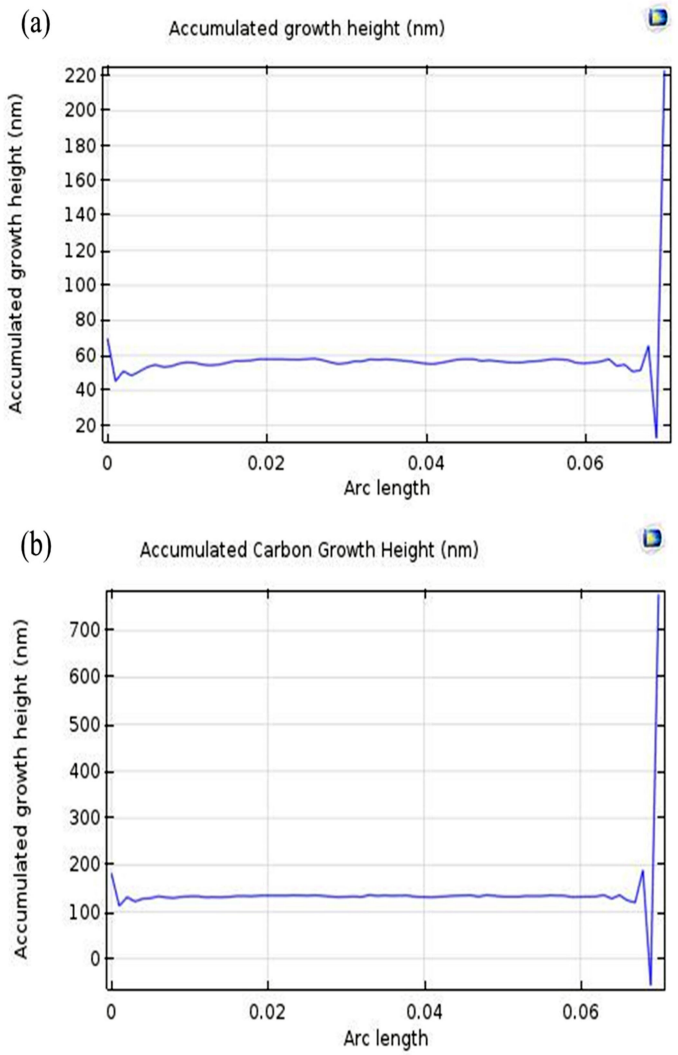

Fig. 14. Accumulated carbon growth along the substrate arc (a) at 300 K (b) at 723 K for a fixed dc bias of -50 V.

Due to the combined effect of internal stress and alignment force exerted by plasma sheath electric field, vertical growth began [37]. The thickness of the horizontal graphene sheet increases on increasing temperature because of the effective increase in breaking of constituent gases at the sheet surface. This is because of the increase in surface reaction due to the collision enhancement between the constituent gases. This increases the carbon availability for deposition. Also, the thickness of the sheet is non-uniform due to the non-uniform flux of various species. Fig. 15(a) and Fig. 15(b) shows the 3D accumulated carbon growth on the substrate at -50 V dc bias and no bias, respectively. There is a significant 4-fold decrease in carbon growth height on the substrate which makes it suitable for thin film deposition on desired materials. All these simulation results have been compared with the experimental observations of Rao *et al.* [38], where the same type of growth i.e, horizontal graphene along the substrate and vertical graphene at the edges is observed for low temperature Rf-PECVD for $Ar/CH_4/H_2$.

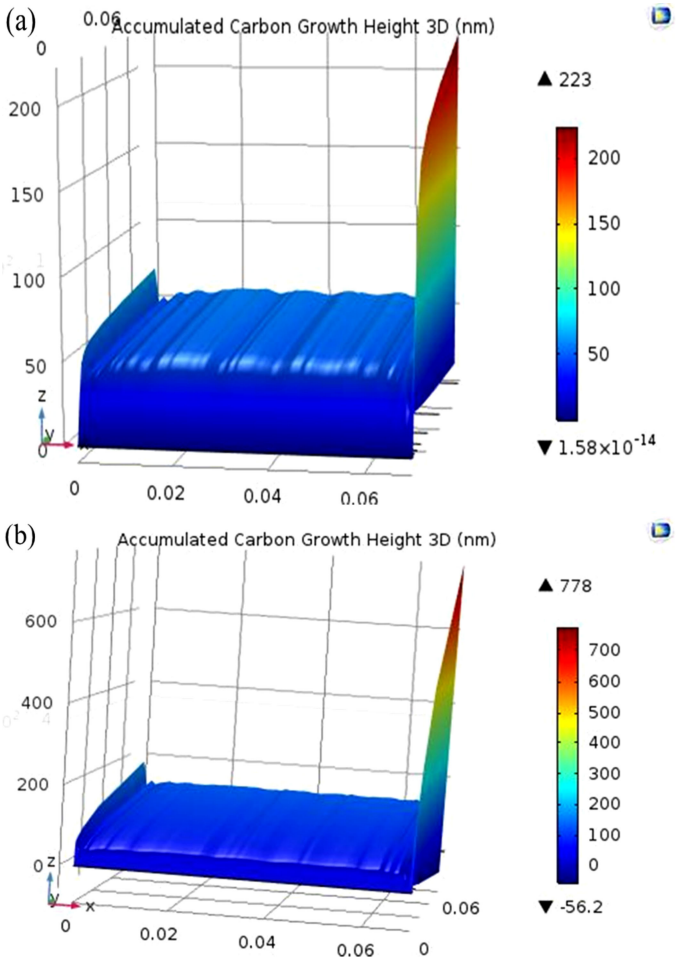

Fig. 15. Accumulated carbon growth along the substrate arc (a) at 300 K (b) at 723 K for a fixed dc bias of −50 V.

IV. Conclusion

Plasma enhanced CVD techniques are the most suitable synthesis technique for the growth of graphene carbon nanostructures compared to other techniques as the temperature attained for the production of plasma is comparatively low. This advantage plays an important role in the commercial and industrial production of graphene and other carbon based nanostructuresin semiconductor industries where the fabricating materials cannot withstand high temperature.

In the present paper, COMSOL Multiphysics 5.2a based numerical simulations have been carried for the parametric study of $Ar/C_2H_2/H_2$ reactive plasma and their effect on growth dynamics of graphene. From the simulation model, a non-uniform distribution of various parameters i.e., electron density, electron energy density, electric potential and collisional power loss have been observed and found to decrease with an increase in temperature. Moreover, we have also found that the number densities of dominant ions decreases and number density of neutrals increases with an increase in temperature.

At the nickel catalyst coated substrate surface, horizontal graphene growth is observed to be non-uniform having thickness varying from 40–60 nm. Also, vertically oriented graphene growth is observed at the edges of substrate with height ranging from 223–660 nm. It was also observed that the substrate biasing and gas temperature have prominent effect on the carbon growth on substrate in PECVD system. On applying substrate biasing, the growth of carbon deposition (growth of parallel graphene) reduced significantly as effective etching by energetic ions increases. On increasing the gas temperature carbon deposition increases. However, the growth of vertically oriented graphene increases when substrate biasing is applied.

References

[1] W. B. Choi *et al.*, "Fully sealed, high-brightness carbon-nanotube field-emission display," *Appl. Phys. Lett.*, vol. 75, 1999, Art. no. 3129.
[2] S. J. Tans, A. R. M. Verschueren, and C. Dekker, "Room-temperature transistor based on a single carbon nanotube," *Nature*, vol. 393, pp. 49–52, 1998.
[3] M. B. Nardelli and J. Bernholc, "Electronic transport in extended systems: Application to carbon nanotubes," *Phys. Rev. B*, vol. 60, 1999, Art. no. 7828.
[4] L. Nilsson, O. Groening, O. Kuettel, P. Groening, L. Schlapbach, and J. Vac, "Microscopic characterization of electron field emission," *J. Vacuum Sci. Technol. B, Microelectron. Nanometer Structures Process., Meas. Phenomena*, vol. 20, p. 326, 2002.
[5] L. Delzeit *et al.*, "Growth of multiwall carbon nanotubes in an inductively coupled plasma reactor," *J. Appl. Phys.*, vol. 91, 2002, Art. no. 6027.
[6] Y. Z. Bin, Q. Y. Chen, Y. Nakamura, and K. Tsuda Matsuo, "Preparation, and characterization of carbon films prepared from poly(vinyl alcohol) containing metal oxide and nanofibers with iodine pretreatment," *Carbon*, vol. 45, pp. 1330–1339, 2007.
[7] D. Yang *et al.*, "Preparation and characterization of an ultrathin carbon shell coating a silver core for shell-isolated nanoparticle-enhanced Raman spectroscopy," *Chem. Commun.*, vol. 47, pp. 5873–5875, 2011.
[8] H. C. Foley, "Carbogenic molecular sieves: Synthesis, properties and applications," *Microporous Mater.*, vol. 4, pp. 407–433, 2005.
[9] K. Y. Sheem, E. H. Song, and Y. H. Lee, "High-rate charging performance using high-capacity carbon nanofilms coated on alumina nanoparticles for lithium-ion battery anode," *Electrochimica Acta*, vol. 78, pp. 223–228, 2012.
[10] S. C. Tsang, V. Caps, I. Paraskevas, D. Chadwick, and D. Thompsett, "Magnetically separable, carbon-supported nanocatalysts for the manufacture of fine chemicals," *Angewandte Chem. Int. English*, vol. 43, pp. 5645–5649, 2005.
[11] S. O. Podgorny, I. P. Demeshko, and O. T. Podgornaya, "Cadmium telluride nanofilms application in carbon monoxide detection," in *Proc. IEEE Dyn. Syst. Mechanism Mach.*, 2016, pp. 1–4.
[12] S. O. Podgornyi *et al.*, "Zinc selenide nanofilms application in carbon monoxide detection," *Procedia Eng.*, vol. 152, pp. 474–477, 2016.
[13] M. Meyyappan, L. Delzeit, A. Cassell, and D. Hash, "Carbon nanotube growth by PECVD: A review," *Plasma Sources Sci. Technol.*, vol. 12, p. 205, 2003.
[14] Z. L. Tsakadze, K. Ostrikovab, J. D. Longa, and S. Xua, "Self-assembly of uniform carbon nanotip structures in chemically active inductively coupled plasmas," *Bull. Amer. Phys. Soc.*, vol. 13, no. 10, pp. 1923–1929, Oct. 2004.
[15] C. Bower, W. Zhu, S. Jin, and O. Zhou, "Plasma-induced alignment of carbon nanotubes," *Appl. Phys. Lett.*, vol. 77, 2000, Art. no. 830.
[16] C. Lee, X. Wei1, W. Jeffrey, and J. H. Kysar, "Measurement of the elastic properties and intrinsic strength of monolayer graphene," *Science*, vol. 321, 2008, Art. no. 385.
[17] A. B. TaisukeOhta, T. Seyller, K. Horn, and E. Rotenberg, "Controlling the electronic structure of bilayer graphene," *Science*, vol. 313, pp. 951–954, 2006.
[18] Y.-W. Son, M. L. Cohen, and S. G. Louie, "Half-metallic graphene nanoribbons," *Nature*, vol. 444, pp. 347–349, 2006.
[19] S. H. Tsai, F. K. Chiang, T. G. Tsai, F. S. Shieu, and H. C. Shih, "Synthesis and characterization of the aligned hydrogenated amorphous carbon nanotubes by electron cyclotron resonance excitation," *Thin Solid Films*, vol. 366, no. 1, pp. 11–15, 2000.
[20] M. Crose, W. Zhang, A. Tran, and P. D. Christofides, "Multiscale three-dimensional CFD modeling of PECVD of amorphous silicon thin films," *Comput. Chem. Eng.*, vol. 113, pp. 184–195, 2018.

[21] M. Crose, A. Tran, and P. D. Christofides, "Multiscale computational fluid dynamics: Methodology and application to PECVD of thin film solar cells," *Coatings*, vol. 7 no. 2, p. 22, 2017.
[22] M. Crose, J. S. I. Kwon, A. Tran, and P. D. Christofides, "Multiscale modeling and run-to-run control of PECVD of thin film solar cells," *Renewable Energy*, vol. 100, pp. 129–140, 2017.
[23] T. Okumura, "Inductively coupled plasma sources and applications," *Phys. Res. Int.*, vol. 2010, 2010, Art. no. 164249.
[24] T. Okumura and I. Nakayama, "New inductively coupled plasma source using a multi-spiral coil," *Rev. Sci. Instrum.*, vol. 66, no. 11, pp. 5262–5265, 1995.
[25] T. G. Beuthe and J. S. Chang, "Chemical kinetic modelling of non-equilibrium Ar-H2," *Japanese J. Appl. Phys.*, vol. 38, p. 4576, 1991.
[26] A. Bogaerts, K. de Bleecker, V. Georgieva, I. Kolev, M. Madani, and E. Neyts, "Computer simulations for processing plasmas," *Plasma Processes and Polymers*, vol. 3, pp. 110–119, Feb. 2016.
[27] UMIST, Manchester, U.K., 2012. [Online]. Available: http://udfa.ajmarkwick.net/index.php?mode=species
[28] I. Denysenko and N. A. Azarenkov, "Formation of vertically aligned carbon nanostructures in plasmas: Numerical modelling of growth and energy exchange," *J. Phys. D, Appl. Phys.*, vol. 44, no. 17, p. 31, 2011.
[29] I. Denysenko and K. Ostrikov, *J. Phys. D, Appl. Phys.*, vol. 42, 2009, Art. no. 015208.
[30] Z. Marvi, S. Xu, G. Foroutan, and K. Ostrikov, "Contribution of radicals and ions in catalyzed growth of single-walled carbon nanotubes from low-temperature plasmas," *Phys. Plasmas*, vol. 22, 2015, Art. no. 013504.
[31] I. Denysenko and K. Ostrikov, "Ion-assisted precursor dissociation and surface diffusion: Enabling rapid, low-temperature growth of carbon nanofibers," *Appl. Phys. Lett.*, vol. 90, 2007, Art. no. 251501.
[32] H. Mehdipour, K. Ostrikov, and A. E. Rider, "Low- and high-temperature controls in carbon nanofiber growth in reactive plasmas," *Nanotechnology*, vol. 21, no. 45, 2010, Art. no. 455605.
[33] R. S. Myers, "Collision theory," *J. Chem. Edu.*, vol. 55, no. 4, p. 243, 1978.
[34] M. Gryziński, "Theoretical description of collisions in plasma: Classical methods," *J. Physique Colloques*, vol. 40, pp. 171–177, 1979.
[35] C. S. Cojocaru, A. Senger, and F. L. Normand, "A nucleation and growth model of vertically-oriented carbon nanofibers or nanotubes by plasma-enhanced catalytic chemical vapor deposition," *J. Nanosci, Nanotechnol.*, vol. 6, pp. 3761–4099, 2006.
[36] M. Rodriguez, "A review of catalytically grown carbon nanofibers," *J. Mater. Res.*, vol. 8, 1993, Art. no. 3233.
[37] J. W. G. Wildoer, L. C. Venema, A. G. Rinzler, R. E. Smalley, and C. Dekker, "Electronic structure of atomically resolved carbon nanotubes," *Nature*, vol. 391, pp. 59–62, 1998.
[38] B. Purna Chandra Rao, R. Maheswaran, S. Ramaswamy, O. Mahapatra, C. Gopalakrishanan, and D. John Thiruvadigal, "Low temperature growth of carbonnanostructures by radio frequency-plasmaenhanced chemical vapor deposition (Low) temperature growth of carbon nanostructures by RF-PECVD), fullerenes," *Nanotubes Carbon Nanostructures*, vol. 17, pp. 625–635, 2009, https://doi.org/10.1080/1536383090329140
[39] I. Denysenko, K. Ostrikov, M. Y. Yu, and N. A. Azarenkov, "Effects of ions and atomic hydrogen in plasma-assisted growth of single-walled carbon nanotubes," *J. Appl. Phys.*, vol. 102, 2007, Art. no. 074308.

Manish Kumar was born in Patna, Bihar, India. He received the Bachelor's in Engineering degree in electrical and engineering from the Bhilai Institute of Technology, Raipur, Raipur, India, and received the Master of Technology degree in nanoscience and technology from the Delhi Technological University, Delhi, India. His current area of expertise is COMSOL Multiphysics based simulation of synthesis of PECVD based carbon-nanostructures.

Sagar Khanna was raised and brought up in Delhi. He received the Bachelor of Technology degree in electronics and communication engineering from Delhi. He is currently working toward the Master of Technology degree in nanoscience and technology from Delhi Technological University, Delhi, India. He has presented his major in plasma physics in which he studied effect on various parameters of plasma using COMSOL multiphysics simulation software.

Neha Gupta was born in Delhi, India. She received the master's degree in physics from the University of Delhi, Delhi, India, in 2013 and the Ph.D. degree in physics from the Delhi Technological University, Delhi, India, in 2018. She has authored 14 research papers in the journals of international repute and proceedings of international conferences. Her current area of expertise is analytical and numerical simulation of plasma processing of nanomaterials and their applications in field emission devices. She has also been a part of DST-SERB, Government of India funded research project.

Ravi Gupta was born in Delhi, India and received the master's degree in physics from the University of Delhi, Delhi, India, in 2013 and the Ph.D. degree in physics from the Delhi Technological University, Delhi, India, in 2018, He is currently working as an Assistant Professor with the Department of Physics, Bhaskaracharya College of Applied Sciences, Delhi University, Delhi, India. He authored 13 research papers in the journals of international repute and proceedings of international conferences. His current area of expertise is nucleation and growth plasma grown nanostrcuture. He has also attended 9 international conferences/symposium/workshops across the globe.

Suresh C. Sharma is working as a Professor with the Department of Applied Physics, Delhi Technological University, Delhi, India. He was a Monbusho Postdoctoral Fellow under Japanese Government Fellowship, Department of Physics, Faculty of Science, Ehime University, Matsuyama, Japan from October 1997 to March 1999. In addition, he was a JSPS (Invitation) Postdoctoral Fellow and a Visiting Researcher from May 2004 to October 2005 with the Center for Atomic and Molecular Technologies, Osaka University, Japan. He worked on several research projects in India and abroad. He has guided numerous Ph.D., M. Tech and B. Tech students. He has authored 157 research papers in journals of international and national repute and proceedings of international and national conferences. His current research interest includes plasma physics/plasma applications, nanotechnology, high power microwave devices, dusty plasma/strongly coupled dusty plasma, THz radiation emission/short pulse lasers, and plasma medicines.

Prof. Sharma was awarded the Young Scientist project as a principal Investigator by the Department of Science and Technology, Government of India for a two year duration (1997–1999) and worked with the Department of Physics and Astrophysics, University of Delhi from January 6, 1997 to October 14, 1997. Besides, he was awarded Senior Research Associate under the Scientist's Pool Scheme by CSIR, Government of India for three years duration (1999–2002) and worked with the Department of Physics and Astrophysics, University of Delhi from April 1999 to January 2002. He is a member of the American Physical Society, USA; a member of the International Association of Engineers, Hong Kong; a member of the National Academy of Sciences, India; a life member-Plasma Science Society of India; a life member–Indian Science Congress Association, and a life member-Indian Society for Technical Education, New Delhi, India.

DOI 10.12694/scpe.v20i2.1513
Scalable Computing: Practice and Experience ISSN 1895-1767
Volume 20, Number 2, pp. 223–235. http://www.scpe.org © 2019 SCPE

ONTOLOGY DRIVEN SOCIAL BIG DATA ANALYTICS FOR FOG ENABLED SENTIC-SOCIAL GOVERNANCE

AKSHI KUMAR* AND ABHILASHA SHARMA†

Abstract. Conventional e-government has many practical infrastructure development and implementation challenges. The recent surge of SMAC (Social media, Mobile, Analytics, Cloud) technologies re-defines the e-governance ecosystem. Cloud-based e-governance has numerous operational challenges which range from development to implementation. Moreover, the contemplation and vocalization of public opinion about any government initiative is quintessential to be cognizant of how citizens perceives and get benefitted from cloud/fog enabled governance. This research puts forward a semantic knowledge model for investigating public opinion towards adaption of fog enabled services for governance and comprehending the significance of two s-components (sentic and social) in aforesaid structure that specifically visualize fog enabled Sentic-Social Governance. The results using conventional TF-IDF (Term Frequency-Inverse Document Frequency) feature extraction are empirically compared with ontology driven TF-IDF feature extraction to find the best opinion mining model with optimal accuracy. The results depict that the implementation of ontology driven opinion mining for feature extraction in polarity classification outperforms the traditional TF-IDF method validated over baseline supervised learning algorithms. An average of 7.3% improvement in accuracy and approximately 38% reduction in features has been reported.

Key words: Fog Computing, Government Intelligence Cloud , Opinion Mining, Feature Selection, Ontology

AMS subject classifications. 68M14, 97R50, 91D30

1. Introduction.

Government-to-Citizen (G2C) is a concept [1] that speaks about the connectivity between public administration organizations and citizens of a country. The relationship specifies ICT (Information and communication technologies) based solution that streamlines the interaction and association between governing bodies and citizens. The ultimate goal of G2C [2] governance is to serve the society by offering various ICT services with the use of cutting edge technologies in a more productive and profitable way. It also plays up to increase people participation in governance both in terms of quantity and quality. G2C interactions empower citizens by apprising them with the government policies, practices, rules, regulations, strategies and services. Several countries have developed their respective framework of G2C technology for enhancing public participation in governmental proceedings.

Digital India [3] is a flagship programme launched by Government of India to transform the nation into a digitally empowered society and knowledge economy. The objective is to explore innovative ideas and practical solutions by exploiting digital technologies such as cloud computing, mobile applications, Internet of Things (IoT) etc. It is a "citizen-centric" campaign that concentrates on three prime parameters [4]: digital infrastructure as a utility to every citizen, governance and services on demand, and digital empowerment of citizens. The initiative includes coupling of multiple government ministries and departments with several thoughts and ideas transforming into a single comprehensive vision but its practical implementation is very demanding and challenging. Large development and implementation cost, lack of internet accessibility, lack of computing skills among citizens, insufficient technology requirements, requisite of email addresses, lack of privacy are certain issues [5] that makes it difficult for governing bodies to reach out citizens. The nine growth pillars of Digital India [6] that contribute towards the economic and electronic dissemination of government information in public are represented in figure 1.1. Several policies, schemes, campaigns, and initiatives are undertaken by different government officials with the purpose to reinforce these growth pillars. Thus, the holistic development of these growth pillars is the need of the hour.

Electronic governance or e-governance [7], an application of ICT and framework for G2C communication, plays a significant role in information exchange of government services to citizens. It is an electronic execution of governance [8] that facilitates a simple, rapid, efficient and highly transparent process of information broadcasting, delivery of government services in order to promote good governance. It signifies the reformation of government with the implementation of technology in government processes and functions. This technological revolution in governance can modernize the modus operandi of any society.

*Department of Computer Science & Engineering, Delhi Technological University, Delhi-42, India (akshi.kumar@gmail.com).
†Department of Computer Science & Engineering, Delhi Technological University, Delhi-42, India (abhi16.sharma@gmail.com)

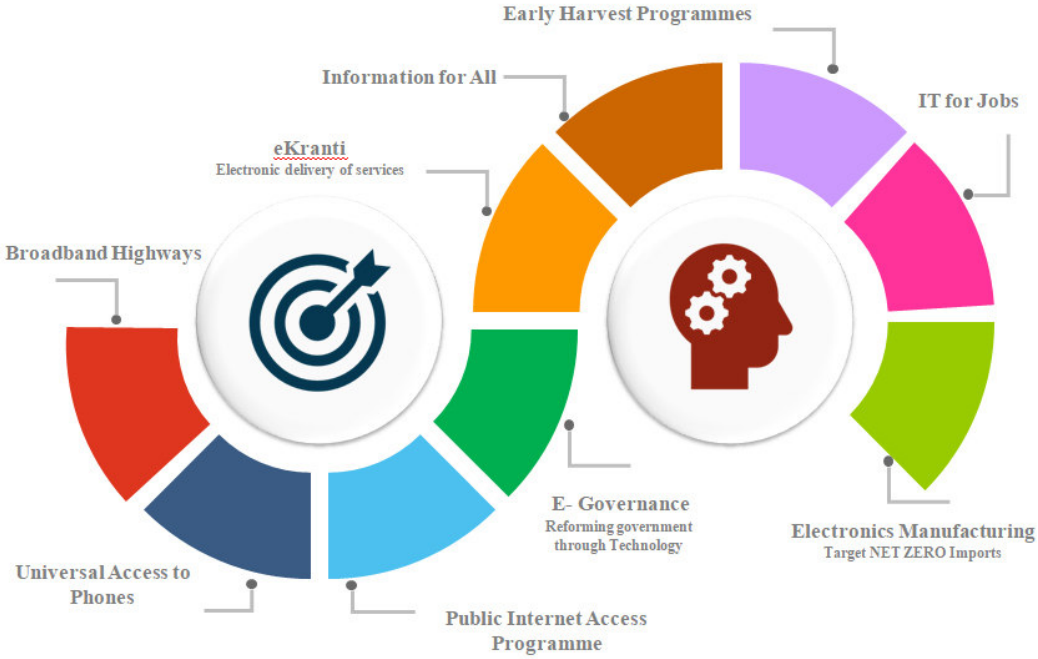

FIG. 1.1. *Nine Growth Pillars of Digital India [6]*

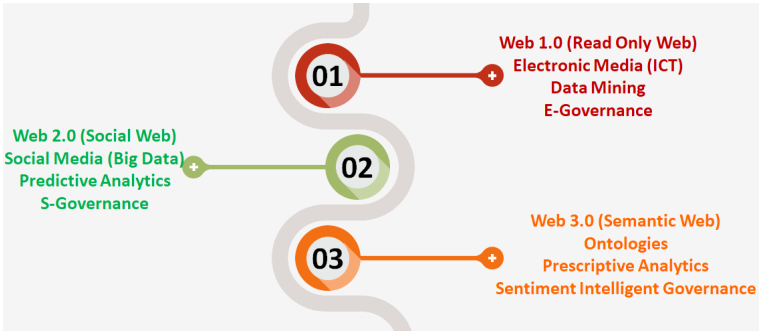

FIG. 1.2. *Evolution of Media, Analytics and Governance with Web*

Digital information and communication technologies have come forth as wave maker that can transform an entire economy, build up smart citizens and realize a well established form of socio-political organizations across globe. In view of this, convergence of four technologies namely Social media, Mobile, Analytics, Cloud (SMAC paradigm) [9] is the driving force of governance ecosystem. A voluminous amount of data (big data) has been generated through various sources of *social media* and *mobile* applications that require optimized techniques for data *analytics*. Cloud computing characterizes the on-demand delivery of computing services over the internet. This virtualization technology offers self-service capability, scalability, flexibility, and affordability. The evolving web has changed the traditional model of governance into digital governance model turning the [10] paradigm shift from e-governance to s-governance (social governance). It also turns the corners of social media as well as data analytics. The evolution timeline of all four factors has been depicted in figure 1.2.

Cloud computing [11] makes a big shift from the conventional methods of governance due to various reasons such as infrastructure cost reduction, quick provision of computing resources, scalability in terms of delivering right amount of IT services, improves productivity and performance, procuring more secure environment and much more. It proffers a simple way to access servers, storage, databases and a broad set of application services

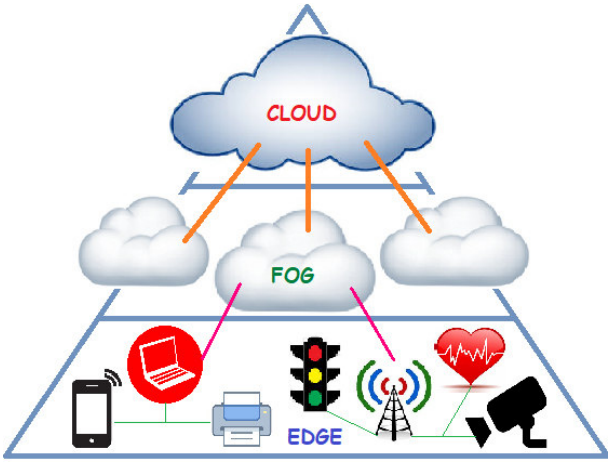

FIG. 1.3. *Big Data Processing Layer Stack [13]*

over the Internet. Cloud computing, the name is so because information accessed is found in "the cloud" and provides user a anywhere, anytime access. Fog computing, dew computing, cloudlet and edge computing are extended variants that lies at different levels in hierarchy of cloud computing architecture. Figure 1.3 represents how the [12] storage, accessibility and maintenance of huge amount of data i.e. big data available over web is being maintained and processed by cloud, fog and edge computing.

Fog computing brings the benefits, services and power of cloud to the edge of the network. It has closer proximity to end users i.e. performing short term data analytics at the edge and larger geographical distribution. It acts as an interface between cloud and edge device layers [14] deciding what data needs to be pushed to cloud and what needs to be analyzed locally at the edge. The goal of fogging is to improve efficiency, reducing data transportation to cloud, security and compliance. All these factors put accent on the adoption of fog layered architecture for adapting governance infrastructure. The role and need of cloud/fog based governance has been studied across literature. Various literary resources are available online which discuss the practical and potential application of cloud in the governance ecosystem. Certainly, fog enabled governance is the non-trivial buzzword within the contemporary paradigm for government intelligence. *MeghRaj: the national cloud* is one such the government intelligence cloud initiative [15] launched by Government of India.

The contemplation and vocalization of public opinion about any governmental processes or practices is quintessential as they are entitled to enjoy all the legal rights and privileges granted by the government. It is equally important to be cognizant of how citizens perceives and get benefitted from cloud/fog enabled governance. Consequently, addition of one more s-factor (sentiment based) in s-governance reforms the existing model into a *sentic-social* governance (S-governance) with a view to make it more sustainable. Opinion mining facilitates this implementation and formalization of the S-governance model. It is referred to as the computational study [16,17] to extract and analyze public opinion/sentiment about any topic, subject, event or entity for better decision making process by applying various intelligent techniques over a large volume of user generated data (social big data) over web. The use of different intelligent learning techniques such as machine learning, lexicon-based, hybrid and concept based has been reported across pertinent literature studies [18] within the domain. As an attempt to comprehend public opinion on the induction and adoption of cloud-based governance model, this research put forwards an optimized predictive learning model based on real-time data.

The vital sub-task of the polarity classification (opinion polarity: positive, negative, neutral) process is feature extraction, which converts the input data (unstructured textual data indicative of opinion), into an array of representative features. Commonly, the feature extraction task is done using intrinsic filtering methods which are fast, classifier-independent methods that rank features according to predetermined numerical functions based on the measure of the importance of the terms. A variety of scoring functions such as, tf-idf, chi-square, mutual information, information gain, cross-entropy etc., have been used as statistical measures to pick features with the highest scores [19].The accuracy of the classifier strongly depends on the selection of high quality

data features that is the training dataset. Moreover, the training sets are typically prepared manually. Past literature conforms that an optimal feature selection [20] improves the classifier performance (in terms of speed, predictive power and simplicity of the model), reduces dimensionality, removes noise and helps visualizing the data for model selection. In feature selection the features are kept intact and n best features are chosen among them, removing the redundant and co-linear features. This sub-task of selecting the relevant subset of features and discarding the non-essential ones is computationally challenging and expensive task. Motivated by these issues, in this research we propose a semantic knowledge based polarity classification process.

An ontology [21,22] which is specification of conceptualization is utilized as a filtering method for finding important as well as hidden features. Ontologies are primarily tools which can drive the feature engineering process by:

- Structuring semantic information as concepts, properties, instances and hierarchies for feature identification.
- Extracting explicit features to build the feature space using relationship between concepts.
- Uncover important features using concept hierarchy defined by the ontology.

Hence, to optimize the feature space without sacrificing remarkable classification accuracy in this work, we put forward an intelligent ontology based data analytics solution for opinion prediction in social big data concerning fog enabled governance. The proffered solution is put to test for the sentiment classification tasks on tweets pertaining to *"Meghraj: The National Cloud"*, a government intelligence cloud initiative launched by Government of India. The conventional classification process is done using TF-IDF (Term Frequency-Inverse Document Frequency) feature extraction method on the cleaned dataset. Five supervised machine learning classifiers namely Nave Bayesian (NB), Support Vector Machines (SVM), Multilayer Perceptron (MLP), k-Nearest Neighbour (k-NN), and Decision Tree (DT) are empirically compared. Ontology based feature optimization is then performed to semantically analyze the concept and make rise in reusability, interoperability, knowledge acquisition and its verification. Thus, the contribution of this research is to build an optimal opinion mining model as follows:

- To implement five supervised learning algorithms to classify opinion polarity using tf-idf feature extraction: NB, DT, SVM, kNN & MLP
- To build a domain ontology for optimal feature extraction: Domain Ontology for Meghraj (DOM)
- To implement five supervised learning algorithms using ontology guided feature extraction method: TF-IDF on ontological features
- Performance analysis on the basis of efficacy measures

The objective of this paper is to implement and evaluate an opinion mining model for analysing public opinion on government cloud initiative. It is characterized as a semantic knowledge (ontology) based model of fog enabled services offered by government and consequently comprehends the significance of two s-components (sentic and social) within the Fog enabled Sentic-Social Governance.

The subsequent sections are lined up as follows: Section 2 discusses the background work related to fog enabled services in governance and ontology driven opinion mining. Section 3 abstracts the information about Meghraj as a techno typhoon for government prosperity and its scope in the landscape of Indian governance. Section 4 explicates the proffered model for ontology driven opinion prediction of fog enabled governance It also illustrates the dataset details and implementation process. Section 5 determines the opinion classification of the chosen concept as per tweets polarity. It substantiates the ontological model by comparing classifier performance for optimal feature extraction with baseline supervised learning techniques to analyse public opinion about the program. At last, section 6 sums up the inferences drawn from the results and discusses the future work as an open scope of this research work.

2. Related Literature Review of Cloud/Fog enabled Services for Digital Governance. Conventional e-governance faces many challenges in terms of cost, software and hardware requirements, network, security, business & policy adoption and implementation etc. Recent years have shown cloud computing as a technology to solve these problems. Pokharel et al. [23] proposed cloud computing as the future solution for e-governance. Mukherjee et al. [24] put forward a future framework for e-governance based on cloud computing consisting of three layers. Sharma et al. [25] enlisted the applications of cloud computing in e-governance. Work done by authors Cellary et al. [26] discussed about cloud computing and service-oriented architecture for

e-governance. In the research done by Yeh et al. [27], cloud computing has been used in e-governance to change its function towards service, push forward the green technology and promote industrial upgrading. Author Rastogi [28] proposed a model-based framework to implement cloud computing in e-governance. Tripathi & Parihar in 2011, Alshomrani & Qamar in 2013 [29,30] analysed cloud computing and its applications in e-governance and explained how cloud may lead to cost savings.

The term, *Opinion Mining*, also known as sentiment analysis or sentiment mining, was initially witnessed in the published work by Dave et al. [31] in 2003 and since then both primary and secondary studies have been reported across pertinent literature [18,32,33]. As discussed, various techniques have been used to perform the task of opinion mining namely: machine learning, concept based, lexicon based, and hybrid. Pertinent literature reveals [18] various application areas of opinion mining namely, business intelligence, information and security analysis, market intelligence, sub component technology, government intelligence, smart society services etc. Government intelligence (GI) has been the least explored application area with only few relevant studies done within the domain, which include GI using concept based opinion mining, lexicon-based opinion mining , hybrid approach , and opinion mining using machine learning. Recently, Kumar & Sharma [34, 35] proposed few models/frameworks for opinion mining in the different application area of digital governance. To the best of our knowledge, no related work on mining public opinion to understand adoption and acceptance process of a cloud based e-governance initiative has been done.

Feature extraction primarily transforms raw data into features suitable for modelling. For example textual features include n-grams, word2vec and TF-IDF etc [36]. The training set is high-dimensional and the classifiers accuracy strongly depends on the quality of hand-crafted features. To deal with the dimensionality of training feature sets for improved classifier performance, various techniques have been successfully applied. Feature selection [37] and dimensionality reduction [38] approaches have been used to select features with the highest "importance"/influence on the target variable, from a set of existing features. The higher the number of features, more challenging and computationally expensive it gets to visualize the training set. Ontology guided feature extraction can thus be used as a feasible and to optimize the feature space representative of the training dataset. Domain ontologies can be used in selection of features for improved feature-based opinion mining. Pealver-Martnez et al. [39] have discussed the concept of ontological feature based opinion mining based on recent studies. The two major dimensions were given attention namely, opinion classification and feature based opinion mining. They reviewed the improvement process of feature level opinion mining by incorporating the concept of ontology. Also, a proposed approach for ontology-supported polarity mining (OSPM) has been examined for the sake of enhancing the process of opinion classification.

3. *Meghraj: The National Cloud* - An Initiative by Indian Government for Proliferation of Fog/Cloud in Governance. In May 2016, National e-Governance Plan (NeGP) [40] was initiated by Government of India for better accessibility of all government services to citizens. The vision is to access these services in the citizens own locality in a cost-effective manner via common service delivery outlets. As a step towards this different states have placed and setup their respective ICT infrastructure. The deployment and installation of application software has been done through assistance and funding provided by central government. Although, the whole process has been outsourced but still the entire endeavour was strapped for time due to inadequate application development initiatives, detailed and exhaustive procurement process, shortage of in-house experts for managing large procurements etc. The government was looking forward for a common shared platform to gain momentum in the implementation process. This infused the need for the adoption of a government private cloud environment that would expedite the ICT enabled service enrichment process with an affordable cost in and among various government departments at state or central level. Figure 3.1 represents the hierarchy of adoption of cloud [41] in Indian governmental structure.

Meghraj, the GI cloud initiative [15,42] was launched by Government of India under the Department of Electronics and Information Technology (DeitY), Ministry of Communications and Information Technology. The major objective(s) is to (a) accelerate the development and deployment of eGov applications (b) ensure optimal use of resources and infrastructure (c) make standardized and certified applications available (d) replicate successful applications in order to reduce effort, time and cost across states and much more. The functional flow of GI cloud system [42] is illustrated in figure 5. The architecture of GI cloud follows specific standards, guidelines and a set of protocols issued by Government of India. The task of GI cloud services directory is

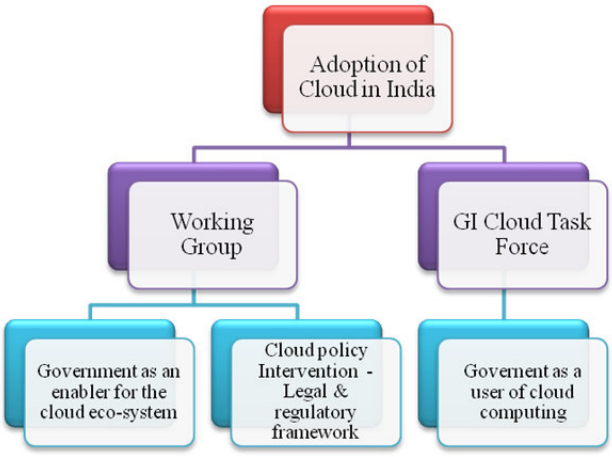

FIG. 3.1. *The National Cloud Initiative [41]*

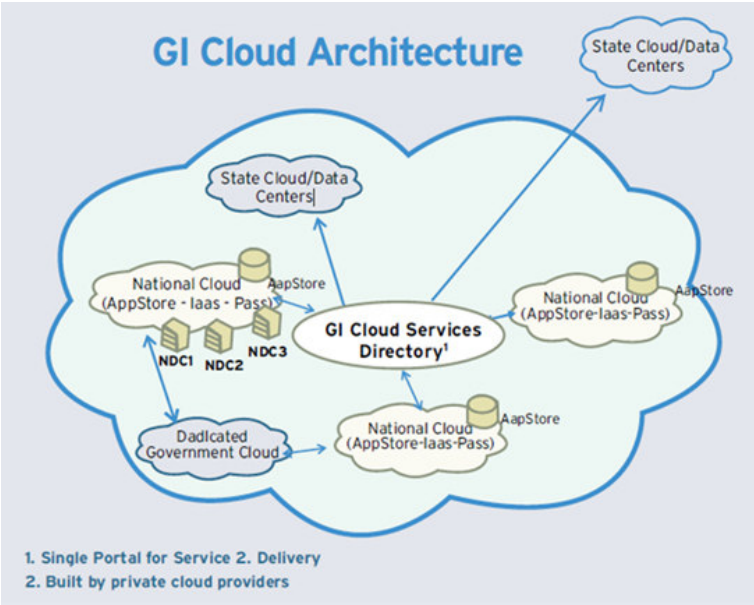

FIG. 3.2. *GI Cloud System Flow [42]*

to publish the services proffered by GI cloud. It comprises of discrete and multiple private cloud computing environments at national and state levels with a view to provide high level blueprint of ICT enabled government functions. The architecture allows the state data centres (SDCs) or state clouds of different states to associate with GI cloud either by acting as independent cloud environments or by lending their IT Infrastructure as part of GI Cloud but these states can have their own data centres as well that exists outside the GI cloud environment. All such states are motivated to jump on GI cloud resources as and when they exhausted their own. SDCs of 21 states have been made operational and running numerous applications such as e-Procurement, Bhoomi, commercial tax, mandi board etc. SDCs of 4 states are in advanced stage of implementation and cloud adoption.

National Cloud was launched in February 2014 under Meghraj initiative and implemented by National Informatics Centre (NIC) [43] offers various services: Infrastructure as a Service (IaaS), Platform as a Service (PaaS), Software as a Service (SaaS) and Storage as a Service (STaaS). Table 3.1 enlists various potential

TABLE 3.1
Key drivers and issues of GI cloud

Benefit(s)	Hazard(s)
Optimal usage of available resources and infrastructure	Application design approaches and cloud standards
Rapid deployment and Reusability	Intensive change management and lack of skilled resources
Security, Scalability, Manageability and Maintainability	Vendor lock-in and data location
Reduced time, effort and cost in managing technology	Loss of portability and control
Increased standardisation and user mobility	Licensing and funding model

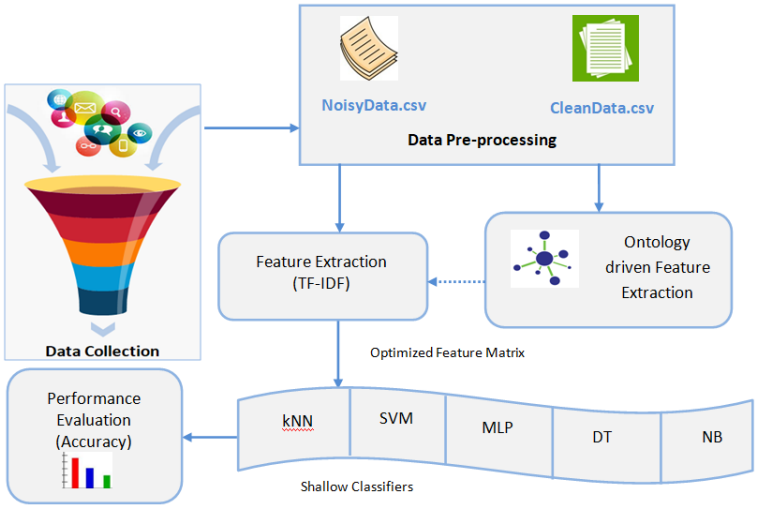

FIG. 4.1. *System Architecture of Ontology based Opinion Prediction Model*

benefits and risks of GI cloud.

There are three adoption phases for the establishment of GI cloud [44] namely, (i) Strategy, policy and guidelines establishment (ii) Implementation and (iii) Monitoring, management and ongoing improvement. The first phase focuses over the formation of practices, strategies, rules and guidelines in order to prepare a development plan. Implementation phase executes the prepared program in a well planned manner and the last phase monitors the present workings, evaluates the shortfalls and works towards continuous improvements. In this paper, the evaluation of GI cloud initiative has been done by capturing opinionated response of citizens for predictive analytics. Domain Ontology has been built to model the feature space and it is optimized using the conventional statistical feature extraction TF-IDF filter. The proposed framework is proposes in the following section.

4. Ontology based Opinion Predictive Analytics. The proposed framework comprises of four phases namely, data collection, data pre-processing, ontology driven optimal feature extraction and classification. Figure 4.1 depicts the system architecture of ontology based opinion prediction model.

4.1. Data Acquisition. Collection of data is the foremost step in the process of opinion mining. Various social media portals are available for capturing real-time data of public perception about any topic, subject, event or area of concern. Analysis of real-time data sets relevant to any phenomena provides more accurate results or evaluation of the system and hence improves the overall performance. Twitter, being the most popular micro blogging site [45] has been used in this research work to capture the public sentiments about Meghraj. It is one of the most prominent social media platforms exercised by government for facilitating

TABLE 4.1
Weekly record of tweets collected

Duration	Tweet Count	Duration	Tweet Count
Week 1	192	Week 4	328
Week 2	194	Week 5	160
Week 3	402	Week 6	140

TABLE 4.2
Tweets Distribution based on Polarity

Week	N	Nu	P	Total
Week 1	29	14	149	192
Week 2	23	16	155	194
Week 3	19	76	307	402
Week 4	11	65	252	328
Week 5	4	79	77	160
Week 6	1	85	54	140
Total	87	335	994	1416

direct government citizen interaction. A huge volume of users share their views, ideas, suggestions and update themselves with the information posted on twitter. The diversity of opinion in various public communities attributed to their regional, cultural, social, economical and educational backgrounds is considered in order to obtain a realistic view of the system. Provision of various APIs (Application Program Interfaces) accelerate the process of tweets extraction over a specific topic using #(hash tag) leading with the topic name(#topicname). The process of tweet extraction has been done by running scripts using an application developed in python. The search query comprises and executes with various hash tag words such as #meghraj, #gicloud, #meghrajcloud, #nationalcloud. A .csv file has been created with the tweets relevant to #topicname as a result of search query. Tweets associated with hashtags for national cloud have been collected near the launch date of program for a duration 6 weeks. A count of 1416 tweets have been gathered in this duration in order to figure out the public inclination about the program. Table 4.1 enlists the weekly status of tweets collected.

The tweets are classified into three polarity categories namely, positive, negative and neutral. Table 4.2 reflects the tweets distribution based on their opinion polarity.

For the selected duration, MeghRaj able to capture a count of 1416 tweets that consists of 950 positive tweets, 335 neutral tweets and 126 negative tweets. A graphical depiction of the aforesaid stats of weekly polarity distribution of tweets is represented in figure 4.2. Approximately 70% of tweets were positive, whereas the percentage of neutral and negative tweets was 23.6% and 6.1% respectively. Deprecation in the count of positive tweets has been reported after week 3 whereas an average rise of tweet count can be observed in neutral tweets after week 2. However, there is a continuous deterioration in the frequency of negative tweets. Week 3 was reported as a critical week being the maximum number of positive tweets whereas week 6 reflects the maximum number of neutral tweets. The percentage of negative tweets was high in the initial phases due to certain technical limitations in implementing procedure of this scheme. Also, the gradual increase in the neutral tweets by the time is due to the rapid occurrence of informational tweets posted by government, allied agencies, and media or civic. This information was all about the campaign features, functionality, latest updates and future processing's and hence making the polarity of tweet neutral. Python packages like Scipy, nltk, Numpy, Scikit-learn etc., machine learning and python scripts (version 3.6) have been used for implementation.

4.2. Pre-processing of data. The outcome of data collection is a .csv file that contains data with a lot of noise. The second phase, data pre-processing, is another essential step performed in order to transform the existing file into a new one for feature selection by cleansing the collected data. This conversion of NoisyData.csv file to CleanData.csv file and the pre-processing procedure includes following steps:

- Removing tweets replication, stop words, number in tweets with placeholders, mentions etc.
- Replacement of URLs.
- Eliminating figures, special characters such as , #.
- Natural Language tool-Kit (NLTK) [46,47] for tokenization.

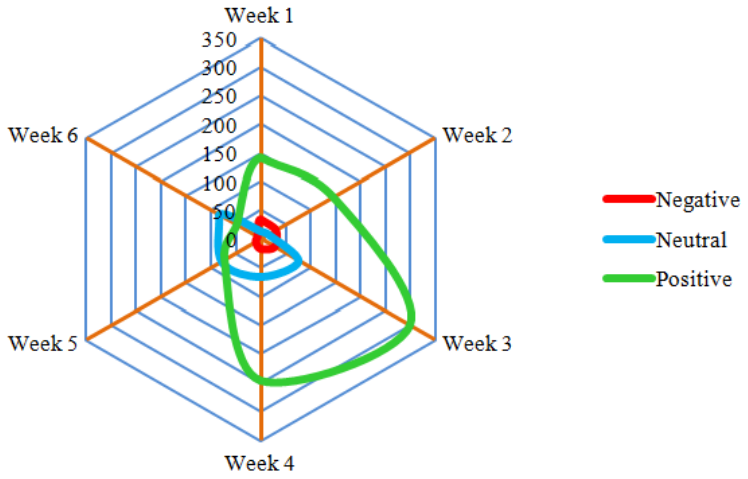

FIG. 4.2. *Polarity distribution of tweets on weekly basis for Meghraj*

- Porter's stemmer [48,49] for stemming to the root word.
- Removal of non-ASCII English character.

This cleansed data is then utilised for feature extraction. Some keywords for the selected attributes are: projects, e-services, IT giants, operational, future computing, cloud solution, departments, deployment, infrastructure, server, administration etc.

4.3. Feature Extraction. Feature extraction is one of the critical and complex tasks in opinion mining. The objective is to recognize the entity (person, service or an object) that is being referred in opinion. The automation of the process of feature identification in opinion analysis with the use of NLP (Natural language processing) techniques makes it harder to comprehend. In this paper, the two methods used for feature extraction are as follows:

- **Conventional Feature Extraction (TF-IDF based)**
  TF-IDF stands [50,51] for Term Frequency - Inverse Document Frequency. It is a weight statistically measured to evaluate the importance of a word to a document in a corpus. The importance of a word increases as its frequency increases in a document but is offset by the frequency of word in corpus. The Term Frequency, TF(t, d) simply counts the frequency of a term in a document as follows:

$$TF(t,d) = \left(\frac{No.\ of\ times\ term\ t\ appears\ in\ a\ document\ d}{Total\ no.\ of\ terms\ in\ the\ document} \right)$$

  The Inverse Document Frequency, IDF (t, D) checks whether the word is rare or common in the corpus so as to measure how much information is provided by a specific word. It is calculated as follows:

$$IDF(t,D) = log_e \left(\frac{Total\ no.\ of\ documents}{No.\ of\ documents\ with\ term\ t\ in\ it} \right).$$

  Thus, TF-IDF is calculated as:

$$TF - IDF(t,d,D) = TF(t,d) * IDF(w,D)$$

  where t denotes the terms; d denotes each document and D denotes the collection of documents.

- **Optimal Feature Extraction (Ontology driven TF-IDF)**
  Ontology is specifically defined as [22,52] a conceptual reference model that describes the semantics of a system or domain. It represents the relationship between concepts; both in human comprehensible

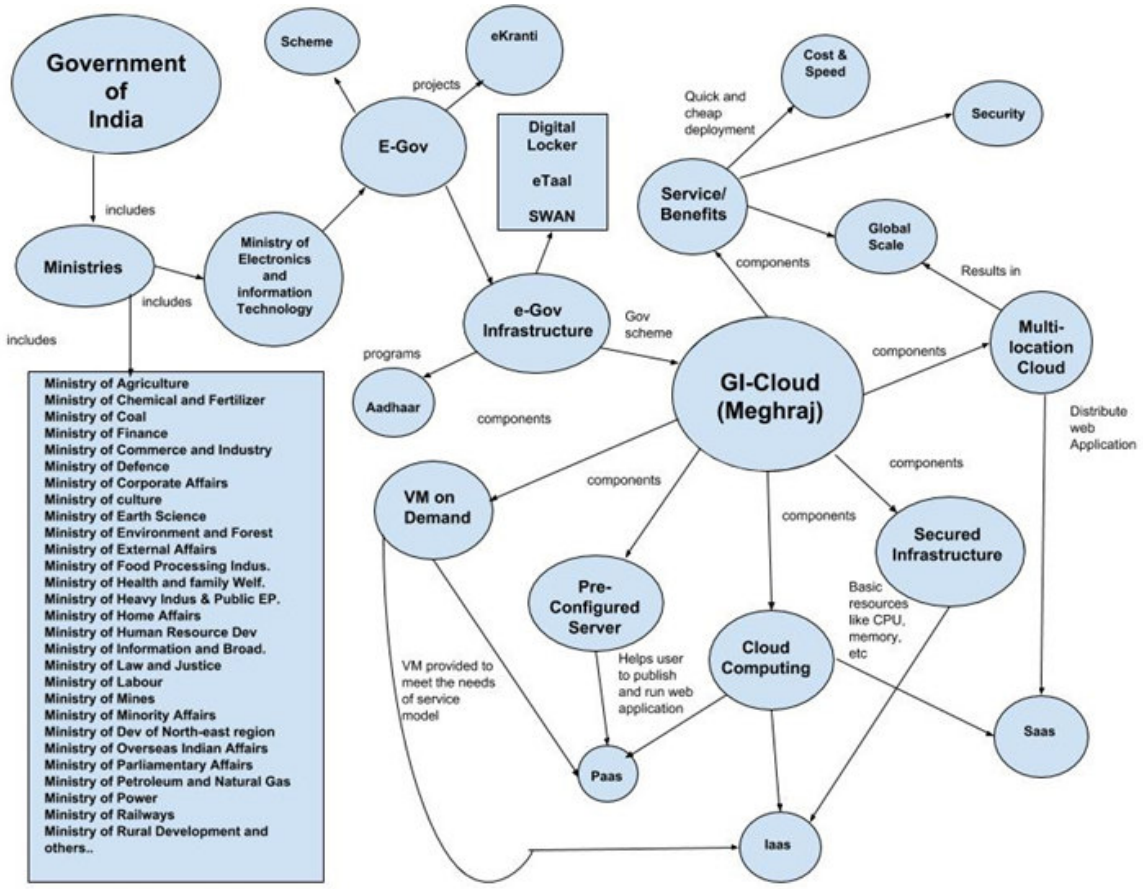

FIG. 4.3. *Domain Ontology of Meghraj (DOM): An initiative towards fog enabled governance*

and machine processable manner. It represents a concept or categories of a particular subject area that exhibits the characteristics and relationship between them. The ontological representation of the concept of Meghraj (DOM - an initiative taken by government of India to provide fog enabled services for a sentic-social facet of governance) is illustrated in figure 4.3 that represents the existing entities, how they are grouped and related in a hierarchy and sub classified based on their similitude & dissimilarity. The ontology represents various ministries that come under the umbrella of government of India. Among those, Ministry of Electronics and Information Technology provides the facility of electronic delivery of services i.e. e-Governance to facilitate citizens. Various components that comprise e-Governance are policies; projects (such as e-Kranti) and infrastructure (include programs such as aadhar, services such as digital locker, eTaal, SWAN etc., schemes). Meghraj, the first Indian GI cloud is one of the prime governmental schemes enhancing the e-Governance infrastructure. Different sub components that combines to form Meghraj are cloud computing, secured infrastructure, multi-location cloud, pre-configured server and VM (virtual machine) on demand. The figure depicts the sub components of cloud computing, elements of services offered by MeghRaj and the inter-relationship between these components along with remaining elements of ontology.

4.4. Opinion Polarity Classification. In this phase, polarity of opinion is classified into three pre-defined categories namely, positive, negative and neutral. The optimal feature set generated in the earlier step are used to build the training and testing sets of the classifier. In this paper, five supervised learning based classifiers namely, Support Vector Machine (SVM), Decision Trees (DT), Nave Bayesian (NB), k-Nearest Neighbour (k-NN) and Multi-Layer Perceptron (MLP) have been implemented. All the machine learning techniques are

TABLE 4.3
Accuracy obtained using conventional and optimal feature extraction

Technique Used	Conventional Approach (TF-IDF) Accuracy (%)	Optimal Approach (Ontology + TF-IDF) Accuracy (%)	Increase In Accuracy (%)
NB	82.2	91.9	9.7
DT	89.8	96.6	6.8
SVM	92.6	98.5	5.9
k-NN	91.3	97.7	6.4
MLP	90.2	98.3	8.1

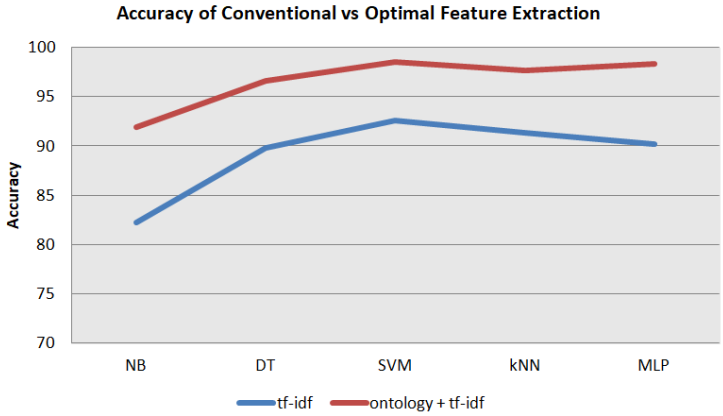

FIG. 4.4. *Accuracy obtained using conventional and optimal approach*

described in detail [34,53] across relevant literature.

4.5. Results and Discussions. This section discusses about the performance of classifiers for selected machine learning techniques (NB, DT, SVM, kNN & MLP) based on accuracy. It also compares and contrasts the difference between conventional feature extraction (using TF-IDF) and optimal feature extraction (ontological TF-IDF) techniques. The results along with percentage increase in accuracy have been listed in Table 4.3.

Result states that the best accuracy with conventional feature extraction over collected data set has been obtained by Support Vector Machine (SVM) algorithm with 92.6%. Next is k-Nearest Neighbour (kNN) with a classification accuracy of 91.3% followed by Multi-Layer Perceptron (MLP) with 90.2% and Decision Trees (DT) with 89.8. Amongst all, Naive Bayesian (NB) attained the lowest accuracy of 82.2%. The best accuracy using ontology driven feature extraction is achieved by SVM, i.e. 98.5% followed by MLP with 98.3%. k-NN and DT have occupied the next level with 97.7% and 96.6% respectively. Amongst all, NB showed the lowest accuracy of around 91.9%. The graphical comparison is represented in figure 4.4.

The maximum accuracy gain was obtained by NB (9.7%) followed by MLP (8.1%) while SVM, k-NN showed an appreciable gain in accuracy (approximately 6%). The average accuracy gain is of 7.38%.

The count of features selected in both the approaches is listed in Table 4.4. In conventional approach all the classification algorithms used the same number of features (866). After applying ontology for feature extraction the minimum number of features selected was 507 (SVM) which is 58.5% selection and maximum was 574 (NB) which is 66.2% selection. The Table 4.4 reflects an average of 62.02% features was selected.

5. Conclusion. User-generated big data from online social portals is a goldmine for extracting and analyzing stance and opinion. This knowledge discovery framework within the unstructured web data setting defines a novel socially aware and sentiment driven governance. Based on this, the work proffered in this research made two primary contributions to evaluate the response of citizens towards government initiatives, schemes or policies. Firstly, the role of social media analytics in government intelligence was investigated. Public opinion in tweets for the national cloud initiative of Government of India was examined. This opinionated information

TABLE 4.4
Number of features obtained using conventional and optimal approach

Technique	Conventional Approach (TF-IDF) #Features (%)	Optimal Approach (Ontology + TF-IDF) #Features (%)	Features Selected (%)
NB	866	574	66.2
DT	866	526	60.7
SVM	866	507	58.5
k-NN	866	547	63.1
MLP	866	534	61.6

can be an imperative phase in a government stratagem for public policy evaluation. Secondly, the learning for the predictive model of opinion mining was driven using optimal semantics-driven feature space generation. Domain ontology for Meghraj (DOM) was built and used for feature extraction with the intrinsic TF-IDF filtering method. The results demonstrated an average accuracy gain of 7.3%. SVM outperformed all the other classifiers (NB, DT, k-NN, MLP) for both conventional and ontology-drive model training. The use of ontology also built an optimal feature space automatically with only 62% of the features selected.

REFERENCES

[1] E-GOVERNANCE, https://en.wikipedia.org/wiki/E-governance
[2] WHAT IS GOVERNMENT-TO-CITIZEN (G2C), https://www.igi-global.com/dictionary/government-to-citizen-g2c/12392
[3] INTRODUCTION OF DIGITAL INDIA, https://digitalindia.gov.in/content/introduction
[4] VISION OF DIGITAL INDIA, https://digitalindia.gov.in/content/vision-and-vision-areas
[5] DIGITAL INDIA, https://www.mygov.in/group/digital-india/
[6] HOW DIGITAL INDIA WILL BE REALIZED: PILLARS OF DIGITAL INDIA., https://digitalindia.gov.in/content/programme-pillars
[7] DAWES, S. S, *The evolution and continuing challenges of egovernance*, Public Administration Review., 68 (2008), S86-S102.
[8] LEE-GEILLER, S. AND LEE, T. D., *Using government websites to enhance democratic E-governance: A conceptual model for evaluation.*, Government Information Quarterly., (2019)
[9] SMAC - THE PARADIGM SHIFT - CREATING FUTURE OF THE ENTERPRISE., https://home.kpmg/in/en/home/insights/2014/09/smac-theparadigmshift.html
[10] KUMAR, A. AND SHARMA, A., *Paradigm shifts from e-governance to s-governance*, The Human Element of Big Data: Issues, Analytics, and Performance., 213(2016)
[11] ARMBRUST, M., FOX, A., GRIFFITH, R., JOSEPH, A. D., KATZ, R., KONWINSKI, A., ET AL., *A view of cloud computing.*, Communications of the ACM., 53(4) (2010), 50-58
[12] VAQUERO, L. M. AND RODERO-MERINO, L., *Finding your way in the fog: Towards a comprehensive definition of fog computing.*, ACM SIGCOMM Computer Communication Review, 44(5)(2014), 27-32.
[13] FOG COMPUTING VS EDGE COMPUTING., https://erpinnews.com/fog-computing-vs-edge-computing
[14] GUPTA, H., VAHID DASTJERDI, A., GHOSH, S. K. AND BUYYA, R, *iFogSim: A toolkit for modeling and simulation of resource management techniques in the Internet of Things, Edge and Fog computing environments.*, Software: Practice and Experience, 47(9) (2017), 1275-1296.
[15] ABOUT MEGHRAJ., https://cloud.gov.in/about.php
[16] LIU, B., *Sentiment analysis and opinion mining.*, Synthesis lectures on human language technologies, 5(1) (2012), 1-167.
[17] PANG, B. AND LEE, L., *Opinion mining and sentiment analysis.*, Foundations and Trends in Information Retrieval, 2(12) (2008), 1-135.
[18] KUMAR, A. AND SHARMA, A., *Systematic Literature Review on Opinion Mining of Big Data for Government Intelligence.*, Webology, 14(2) (2017).
[19] CHANDRASHEKAR, G. AND SAHIN, F., *A survey on feature selection methods.*, Computers & Electrical Engineering, 40(1) (2014), 16-28.
[20] KUMAR, A., KHORWAL, R. AND CHAUDHARY, S, *A survey on sentiment analysis using swarm intelligence.*, Indian Journal of Science and Technology, 9(39) (2016).
[21] GRUBER, T., *Ontology.*, Encyclopedia of database systems.1963-1965.
[22] MAEDCHE, A. AND STAAB, S., *Ontology learning for the semantic web.*, IEEE Intelligent systems, 16(2) (2001), 72-79.
[23] POKHAREL, M. AND PARK, J.S., *Cloud computing: future solution for e-governance.*, In Proceedings of the 3rd international conference on Theory and practice of electronic governance (pp. 409-410) (2009). ACM.
[24] MUKHERJEE, K. AND SAHOO, G., *Cloud computing: future solution for e-governance.*, nternational Journal of Computer Applications, 7(7) (2010), pp.31-34.
[25] SHARMA, M.K. AND THAPLIYAL, M.P., *G-Cloud(e-Governance in Cloud).*, International Journal Engg. TechSci, 2(2) (2011), pp.134-137.

[26] Cellary, W. and Strykowski, S., *E-government based on cloud computing and service-oriented architecture.*, In Proceedings of the 3rd international conference on Theory and practice of electronic governance (2009)(pp. 5-10). ACM.
[27] Yeh, C., Zhou, Y., Yu, H. and Wang, H., *Analysis of E-government service platform based on cloud computing.*, In Information Science and Engineering (ICISE), 2010 2nd International Conference (2010) (pp. 997-1000). IEEE.
[28] Rastogi, A., *A model based approach to implement cloud computing in e-Governance.*, International Journal of Computer Applications, 9(7) (2010), pp.15-18.
[29] Tripathi, A. and Parihar, B., *E-governance challenges and cloud benefits.*, In Computer Science and Automation Engineering (CSAE), 2011 IEEE International Conference on (Vol. 1, pp. 351-354). IEEE. 2011, June
[30] Alshomrani, S. and Qamar, S., *Cloud based e-government: benefits and challenges.*, International Journal of Multidisciplinary Sciences and Engineering, 4(6) (2013), pp.1-7.
[31] Dave K, Lawrence S, Pennock DM, *Mining the peanut gallery: Opinion extraction and semantic classification of product reviews.*, Proceedings of the 12th international conference on World Wide Web. ACM. 2003; 519-528.
[32] Kumar, A. and Jaiswal, A, *Systematic literature review of sentiment analysis on Twitter using soft computing techniques.*, Concurrency and Computation: Practice and Experience, e5107.
[33] Gamal, D., Alfonse, M., M El-Horbaty, E. S. and M Salem, A. B., *Analysis of Machine Learning Algorithms for Opinion Mining in Different Domains.*, Machine Learning and Knowledge Extraction, 1(1) (2019), 224-234.
[34] Kumar, A. and Sharma, A., *Socio-Sentic framework for sustainable agricultural governance.*, ustainable Computing: Informatics and Systems.(2018)
[35] Kumar, A. and Sharma, A., *Opinion Mining of Saubhagya Yojna for Digital India.*, In International Conference on Innovative Computing and Communications (2019) (pp. 375-386). Springer, Singapore.
[36] Asghar, M. Z., Khan, A., Ahmad, S. and Kundi, F. M., *A review of feature extraction in sentiment analysis..*, Journal of Basic and Applied Scientific Research, 4(3) (2014), 181-186.
[37] Chandrashekar, G. and Sahin, F., *A survey on feature selection methods.*, Computers & Electrical Engineering, 40(1) (2014), 16-28.
[38] Sorzano, C. O. S., Vargas, J. and Montano, A. P., *A survey of dimensionality reduction techniques.*, arXiv preprint arXiv:1403.2877. (2014)
[39] Pealver-Martnez, I., Valencia-Garca, R. and Garca-Snchez, F., *Ontology-guided approach to feature-based opinion mining.*, In International Conference on Application of Natural Language to Information Systems (2011, June) (pp. 193-200). Springer, Berlin, Heidelberg.
[40] National e-Governance Plan, `https://meity.gov.in/divisions/national-e-governance-plan`
[41] Indian Government Cloud Initiative (GI Cloud - MeghRaj), `https://www.slideshare.net/nasscom/meghraj-nasscom`
[42] GI Cloud (MeghRaj), `https://meity.gov.in/content/gi-cloud-meghraj`
[43] GI Cloud Initiative - Meghraj, `http://vikaspedia.in/e-governance/national-e-governance-plan/gi-cloud-initiative-meghraj`
[44] Government of India's GI Cloud (Meghraj) strategic Direction Paper, `https://meity.gov.in/writereaddata/files/GI-Cloud\%20Strategic\%20Direction\%20Report\%281\%29_0.pdf`
[45] A. Kumar and T.M. Sebastian, *Sentiment analysis on twitter.*, IJCSI International Journal of Computer Science, vol. 9, no. 4, pp. 372-378, Jul. 2012.
[46] Natural Language Toolkit, `https://www.nltk.org/`
[47] Natural Language Toolkit, `https://en.wikipedia.org/wiki/Natural_Language_Toolkit`
[48] Porter Stemmer, `http://people.scs.carleton.ca/~armyunis/projects/KAPI/porter.pdf`
[49] Porter's Algorithm., `http://people.ischool.berkeley.edu/~hearst/irbook/porter.html`
[50] Aizawa, A., *An information-theoretic perspective of tfidf measures.*, Information Processing & Management, 39(1) (2003), 45-65.
[51] Jing, L. P., Huang, H. K. and Shi, H. B., *A Improved feature selection approach TFIDF in text mining.*, In Machine Learning and Cybernetics, 2002. Proceedings. 2002 International Conference on (Vol. 2, pp. 944-946). IEEE.
[52] Cristani, M. and Cuel, R., *A survey on ontology creation methodologies.*, International Journal on Semantic Web and Information Systems (IJSWIS), 1(2) (2005), 49-69.
[53] Kumar, A. and Jaiswal, A., *Empirical Study of twitter and tumblr for sentiment analysis using soft computing techniques.*, In Proceedings of the World Congress on Engineering and Computer Science (2017) (Vol. 1).

Edited by: Anand Nayyar
Received: Feb 18, 2019
Accepted: Mar 20, 2019

Wireless Personal Communications
https://doi.org/10.1007/s11277-019-06382-2

Operational Transresistance Amplifier Based Wienbridge Oscillator and Its Harmonic Analysis

Gurumurthy Komanapalli[1] · **Rajeshwari Pandey**[1] · **Neeta Pandey**[1]

© Springer Science+Business Media, LLC, part of Springer Nature 2019

Abstract
In this paper, operational transresistance amplifier (OTRA) based Wien bridge oscillator is presented which uses an OTRA, two RC sections, and a buffer. The frequency of oscillation and the condition of oscillation have been derived, and the effect of device non-ideality on these parameters has also been analyzed. Further, harmonic analysis is carried out to characterize the linear performance of the proposed oscillator. Workability of the proposed Wien bridge oscillator is verified through SPICE simulations followed by experimental results. The total harmonic distortion (THD) is calculated and found to be less than 1%. Low THD value is a significant performance criterion for many high frequency applications.

Keywords OTRA · Wien bridge oscillator · THD · Current mode · RF

1 Introduction

Sinusoidal oscillators are essential building blocks for communication, instrumentation, measurement and control systems [1]. A wide variety sinusoidal oscillator designs are available in the literature, and Wien bridge oscillator is one among those and provides sinusoids with high linearity [2]. Sinusoidal waveforms with high linearity performance are significant for the circuits which are operating at RF frequencies.

Traditionally operational amplifiers are used to realize Wien bridge oscillator [3, 4] however their high-frequency operations are limited due to constant gain-bandwidth product and low slew rate [5–8]. To overcome this shortcoming numerous new analog building blocks (ABBs) [5–8] based on current mode (CM) approach [8] having wider bandwidth independent of closed loop gain, greater linearity, and large dynamic range as compared to operational amplifiers came into being. These ABBs are being used for wide variety of analog applications as presented in [5, 6] and references cited therein. The OTRA [9–11] is one of these active building blocks. The input terminals of OTRA being internally grounded eliminate response limitations due to parasitic capacitances, thus making OTRA a suitable choice for high-frequency applications. In literature Wien bridge topologies using Operational Transconductance

✉ Gurumurthy Komanapalli
murthykgm@gmail.com

[1] Department of Electronics and Communication Engineering, Delhi Technological University, Delhi, Delhi, India

Published online: 20 April 2019

Amplifiers (OTA) [13], second-generation current conveyors (CCIIs) [13–19] Current Feedback Operational Amplifiers (CFOA) [16], and modified current controlled current differencing transconductance amplifier (MCCCDTA) [20] have been presented.

Harmonic distortion (HD) analysis is usually carried out to characterize the linearity performance of a circuit [22]. There are different methods and models discussed in the literature [2, 22–25]. By applying these methods which we can study the nonlinear behavior of the topologies producing sinusoids. The method outlined in [2] evaluates the HD of an opamp based Wien bridge oscillator topology, and the same method has been used to calculate the HD for tunnel diode oscillator [23]. The method presented in [24] is used to enumerate the HD of OTA based oscillator.

The distinctive features of available Wienbridge oscillators [4, 13–20] are summarized in Table 1 and it may be observed that

- Wien bridge configurations [15, 18, 20, 21] give current whereas [3, 4, 12–14, 16, 17, 19] provide voltage output
- only [3, 4, 12, 13, 16] provide voltage output at low impedance node
- detailed harmonic analysis has been presented in [2], and [24] only.

Thus it may be concluded that only four Wien bridge configurations [3, 4, 13, 16] providing voltage output at appropriate impedance level are available. Further, the opamp based structure [3, 4] is not suitable for high-frequency applications. Therefore, in this communication, an OTRA based Wien bridge topology is proposed which provides voltage output at low impedance node and may be used for high-frequency applications as well due to its internally grounded input terminals. Additionally, this work also focuses on presenting the detailed harmonic analysis of the proposed structure to characterize its linearity adapting the method outlined in [2, 25] and verify the same through simulations and experimental results.

The paper has been arranged in the following manner: Sect. 2 gives the description of OTRA; Sect. 3 describes proposed OTRA based Wienbridge oscillator circuit. The nonideality and Harmonic analysis are shown in Sects. 3 and 4 respectively. The experimental and simulation results for functional verification are placed in Sect. 5. In this section, Harmonic distortion factors by considering two and three harmonics (HD2 and HD3) for proposed oscillator have also been evaluated through SPICE simulations and are compared with theoretical values. Finally, the conclusion is presented in Sect. 6.

2 OTRA

OTRA is a high gain current input voltage output analog building block [9–11]. The input terminals of OTRA are internally grounded, thereby eliminating response limitations due to parasitic capacitances and resistances and hence is a suitable choice for high-frequency applications. The circuit symbol of OTRA is shown in Fig. 1 and the port characteristics are given by Eq. (1) which signifies the output voltage (V_o) is equal to the product of the difference between two input currents (I_p, I_n) and transresistance gain R_m. For ideal operations, the R_m of OTRA approaches infinity and forces the input currents to be equal

$$\begin{bmatrix} V_p \\ V_n \\ V_o \end{bmatrix} = \begin{bmatrix} 0 & 0 & 0 \\ 0 & 0 & 0 \\ R_m & -R_m & 0 \end{bmatrix} \begin{bmatrix} I_p \\ I_n \\ I_o \end{bmatrix} \tag{1}$$

Table 1 Comparison of available Wien bridge oscillators designed using different ABB

References/Figures	Active element	No. of active elements	No. of passive elements (Floating (F)/grounded (G)	Simulation frequency (kHz)	Electronic tuning	Harmonic analysis/measured THD	Output type (I/V)	Output impedance
[3] /Fig. 3a/Fig. 3b	OPAMP	1	4R(2F, 2G) + 2C(1F, 1G)	5.5–50	N	None/–	V	Low
	OPAMP	2	6R(4F, 2G) + 2C(1F, 1G)	do	N	None/–	V	Low
[4] /Fig. 4	OPAMP	2	6R(3F, 3G) + 2C(1F, 1G)	10.6–52.2	N	Yes/–	V	Low
[12] /Fig. 3c	OTA	3	1R(G) + 2C(1F, 1G)	3–200	Y	None/–	V	High
[13] /Fig. 2a/Fig. 2b	CCII+	1	2R(G) + 2C(1F, 1G)	1–30	N	None/–	V	Low
	CCII+	1	2R(1F, 1G) + 2C(G)	do	N	None/–	V	Low
[14] /Fig. 3	CCII	1	4R(3F, 1G) + 2C(G)	0.0398	Y	None/0.54%	V	High
[15] /Fig. 5b–d	CCII	2	4R(1F, 3G) + 2C(1F, 1G)	15.887	N	None/–	I	High
[16] /Fig. 3a/Fig. 3b/Fig. 8	CCII+	1	3R(G) + 2C(1F, 1G)	8.36, 98.67, 1019	Y	None/< 1%	V	High
	CCII+	1	3R(G) + 2C(1F, 1G)	8.30, 97.25, 1145	Y	None/< 1%	V	High
	CFA	1	4R(2F, 2G) + 2C(1F, 1G)	8.25, 95.8, 843	Y	None/< 0.3%	V	Low
[17] /Fig. 1 (Ckt. 1, 2, 3, 4)/ Fig. 1 (Ckt. 7, 8, 11, 12)	CCII-	2	3R(G) + 3C(G)	6150	Y	None/–	V	High
	CCII-	2	4R(G) + 3C(G)	6150	Y	None/–	V	High
[18] /Fig. 4	CCII-	2	4R(3 F, 1G) + 3C(3 F, 1G)	215.1	Y	None/–	I	High
[19] /Fig. 4a, 5a, 6b/Fig. 4b, 5b	CCII	2	4R(1 F, 3G) + 2C(2G)	–	Y	None/–	V	High
	ICCII	2					V	High
[20] /Fig. 3	MCCCDTA	1	2R(2 F) + 2C(1 F, 1G)	76.556	Y	None/0.13%	I	High
[21] /Fig. 3a/Fig. 3b/Fig. 8	MCCCDTA	1	2C(1F, 1G)	–	N	None/–	I	High
	MCCCDTA	1	1R(G) + 2C(1F, 1G)	–	N	None/–	I	High
	MCCCDTA	1	1R(G) + 2C(1F, 1G)	765.556	Y	None/–	I	High
Proposed	OTRA	2	4R(3F, 1G) + 2C(1F, 1G)	300	Y	Yes/< 1%	V	low

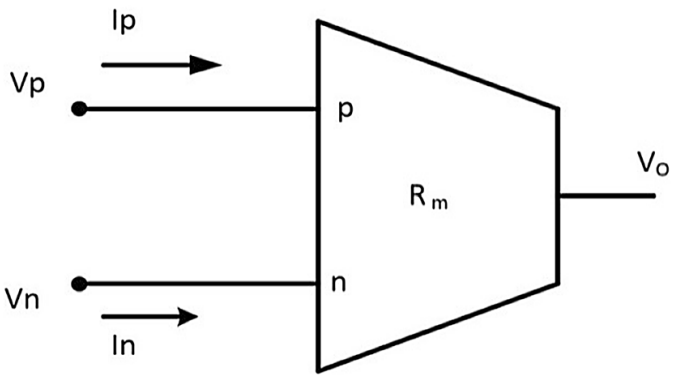

Fig. 1 OTRA symbol

3 Circuit Description of the Proposed Oscillator

The OTRA based Wien bridge oscillator is shown in Fig. 2 which uses two RC sections a buffer and an OTRA. As the OTRA is a current controlled voltage source, the combination of buffer and OTRA is used as a voltage controlled voltage source which forms a forward path of gain K given by Eq. (2).

$$K = \frac{R_4}{R_3} \tag{2}$$

The feedback factor H(s) involving two RC sections is expressed by Eq. (3)

$$H(s) = \frac{Z_2(s)}{Z_1(s) + Z_2(s)} \tag{3}$$

where $Z_1(s) = R_1 || \frac{1}{sC_1}$ and $Z_2(s) = R_2 || \frac{1}{sC_2}$.

Substituting the values of Z_1 and Z_2 in Eq. (3) the H(s) can be expressed as

$$\mathrm{H}(s) = \frac{sC_1R_2}{s^2C_1C_2R_1R_2 + s\left[C_1R_1 + C_2R_2 + C_1R_2\right] + 1} \tag{4}$$

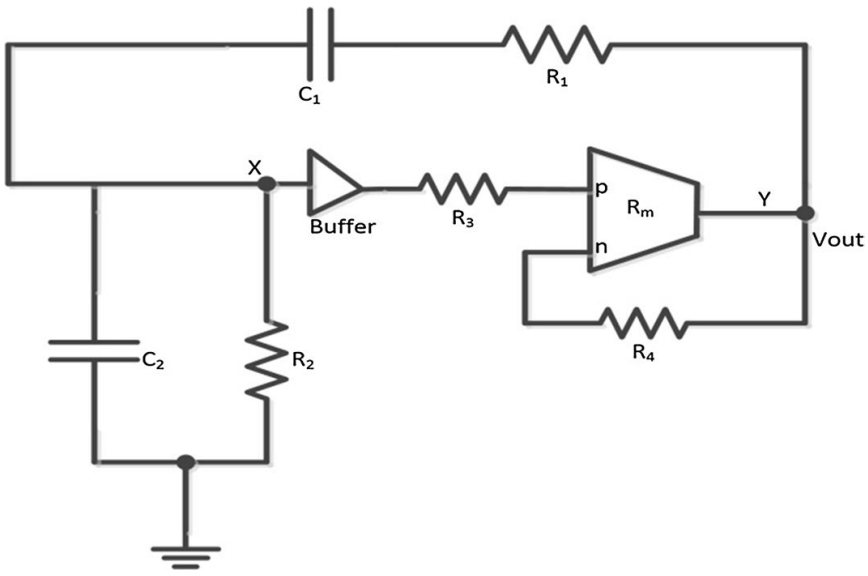

Fig. 2 OTRA based Wien Oscillator

Fig. 3 Symbol of IC AD 844

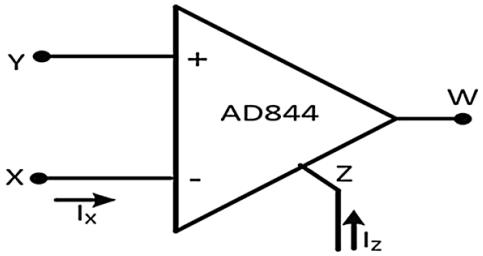

The well-known Barkhausen criterion [1] for sustained oscillations can also be expressed in terms of the characteristic equation of the system as given

$$1 - KH(s) = 0 \tag{5}$$

Substituting Eq. (2) and Eq. (4) in Eq. (5) the characteristic equation of the circuit of Fig. 2 may be obtained as

$$s^2 C_1 C_2 R_1 R_2 + s\left[C_1 R_1 + C_2 R_2 + C_1 R_2 - \frac{C_1 R_2 R_4}{R_3}\right] + 1 = 0 \tag{6}$$

Considering $C_1 = C_2 = C$ and equating real and imaginary parts of Eq. (6) the condition of oscillation (CO) and frequency of oscillation (FO) can be determined as

$$\text{CO} : K = 2 + \frac{R_1}{R_2}; \quad \text{FO} = \frac{1}{2\pi C\sqrt{R_1 R_2}} \tag{7}$$

From Eq. (7) it may be observed that both CO and FO can be adjusted independently, i.e. the FO can be tuned using C whereas the CO can be adjusted through R_3 and R_4.

3.1 Realization of OTRA and Buffer Using IC AD844 and Associated Non-idealities

To compare the simulation and experimental results, the OTRA and buffer are implemented using available ICAD844 (CFOA) since the OTRA is not available as off shelf IC. Therefore this section presents the realization of OTRA and buffer using ICAD844 [26]. The symbol of CFOA is shown in Fig. 3, and terminal characteristics are given in Eq. (8). The influence of CFOA parasites on the proposed structure has also been discussed in this section.

$$V_X = V_Y; I_Y = 0; I_Z = I_X; V_W = V_Z \tag{8}$$

3.2 The OTRA and Buffer Realization

An OTRA can be realized using two AD844 ICs [27] connected as shown in Fig. 4a. Using terminal equations of CFOA, Fig. 4 may be analyzed to verify the terminal characteristics of OTRA as given below.

$$V_p = V_{x1} = V_{y1} = 0 \tag{9}$$

$$V_n = V_{x2} = V_{y2} = 0 \tag{10}$$

$$V_{01} = V_{Z1} = V_{2n} = V_{2p} = 0 \tag{11}$$

$$I_{Z1} = I_{X1} = I_p \tag{12}$$

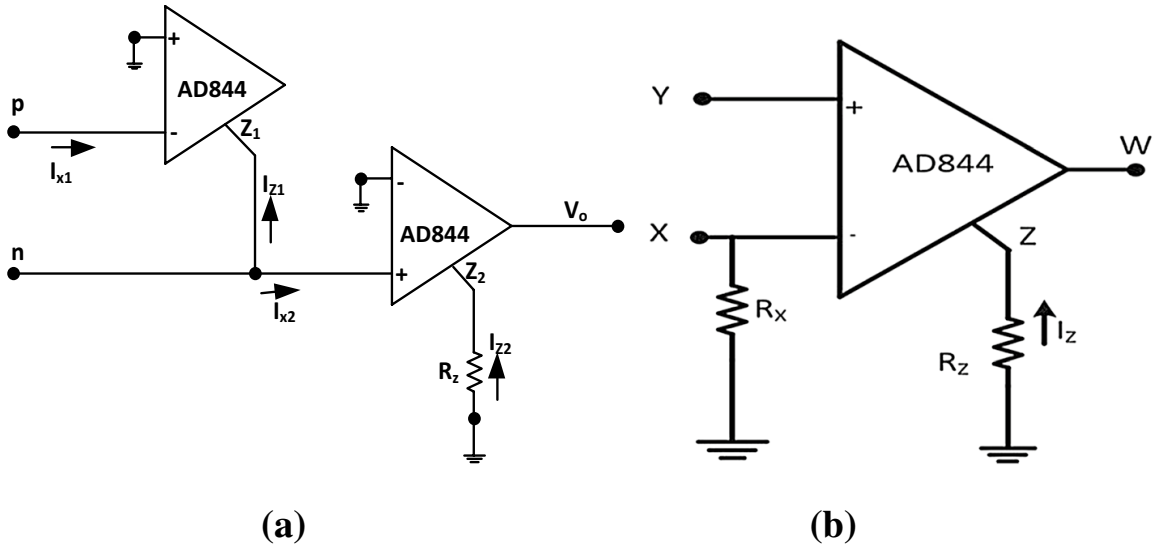

Fig. 4 IC AD 844 based **a** OTRA [26], **b** buffer implementations

$$I_{Z2} = I_{X2} = I_n - I_{Z1} = I_n - I_p \tag{13}$$

$$V_0 = V_{Z2} = -I_{Z2}.R_Z = -R_Z\left(I_n - I_p\right) \tag{14}$$

$$V_0 = R_Z\left(I_n - I_p\right) \tag{15}$$

It may be observed that Eq. (15) is similar to Eq. (1) provided the value of R_Z be very high. To have high resistance gain the resistance R_Z at Z terminal of the second AD844 is kept high. By applying the CFOA properties Eq. (8), we can realize buffer as shown in Fig. 4b, i.e.

$$V_X = V_Y = I_X R_X; I_X = -\frac{V_X}{R_X} = -\frac{V_Y}{R_X};$$

$$I_Z = -\frac{V_Z}{R_X} = I_X; \tag{16}$$

$$V_Z = V_Y; V_W = V_Y \tag{17}$$

Thus implementing a buffer as a voltage of V_Y is now available at a low impedance terminal W.

3.3 Impact of AD844 Non-idealities on the Proposed Oscillator

The above analysis is done by considering the ideal characteristics of the CFOA. However, in practice, the output of the oscillator may deviate due to a non-ideal behavior of CFOA. Therefore, the effect of the CFOA parasites needs to be taken into consideration. For this, the nonideal model of AD844 [28] which includes a finite input resistance at X terminal, parasitic impedances $\left(R_y||C_y\right)$ and $\left(R_z||C_z\right)$ at Y and Z terminals respectively.

Considering the CFOA parasitic impedances, the proposed structure of Fig. 2 can be redrawn as shown in Fig. 5. Further, the parasitic impedance at Y terminal of CFOA can be neglected in OTRA implementation since this port is grounded as shown in Fig. 4.

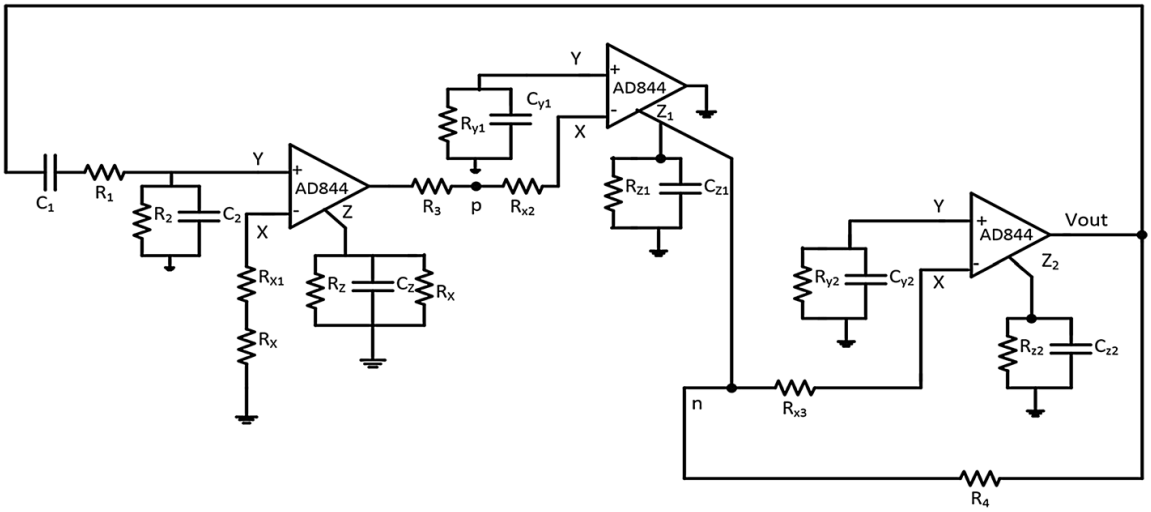

Fig. 5 Proposed oscillator including Nonidealities

Considering the non-idealities outlined, above Eq. (6) modifies to Eq. (18).

$$\frac{sC_1R_2}{s^2C_1C_2R_1R_2+s\left[C_1R_1+C_2R_2+C_1R_2\right]+1}\frac{\left(R_X+R_{X1}\right)\left(1+sC_ZR_{eq}\right)}{R_{eq}}$$
$$\frac{R_{Z1}R_{Z2}R_4}{\left(R_3+R_{X2}\right)\left[R_{Z1}R_{Z2}-R_{X3}R_4\left(1+sC_{Z1}R_{Z1}\right)\left(1+sC_{Z2}R_{Z2}\right)+R_{Z1}R_{X3}\left(1+sC_{Z2}R_{Z2}\right)\right]}=1 \tag{18}$$

$$\text{where}\quad R_{eq}=\frac{R_ZR_X}{R_Z+R_X}\approx R_X;\ \text{As}\ R_Z>>R_X \tag{19}$$

$$\text{As}\ R_3>>R_{X2};\left(R_3+R_{X2}\right)\approx R_3\ \text{and}\ R_X>>R_{X1};R_X+R_{X1}\approx R_{X1}; \tag{20}$$

$$\frac{sC_1R_2}{s^2C_1C_2R_1R_2+s\left[C_1R_1+C_2R_2+C_1R_2\right]+1}\frac{R_X\left(1+sC_ZR_{eq}\right)}{R_X}$$
$$\frac{R_{Z1}R_{Z2}R_4}{R_3\left[R_{Z1}R_{Z2}-R_{X3}R_4\left(1+sC_{Z1}R_{Z1}\right)\left(1+sC_{Z2}R_{Z2}\right)+R_{Z1}R_{X3}\left(1+sC_{Z2}R_{Z2}\right)\right]}=1 \tag{21}$$

By substituting Eqs. (19) and (20) in Eq. (18) results in Eq. (21) Selecting the FO to be much smaller than $\frac{1}{C_{Z1}R_{Z1}}$ and $\frac{1}{C_{Z2}R_{Z2}}$, Eq. (21) reduces to Eq. (6) and therefore expressions for FO and CO remain unchanged.

4 Harmonic Distortion Analysis

The HD analysis is a method to characterize the linear performance of any oscillator, and is evaluated in terms of total harmonic distortion (THD). The low value of THD is always necessary to avoid the harmful effects such as the heating effect of electronic equipment etc.

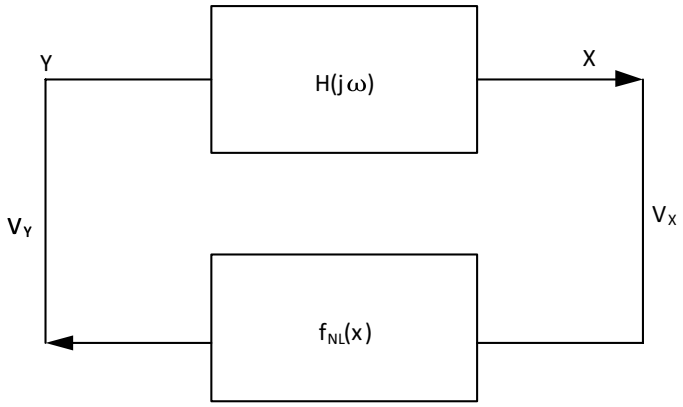

Fig. 6 Generic block diagram of sinusoidal oscillator [24]

Literature survey on oscillators shows that only a few structures [2, 23, 25] have been analyzed from HD point of view Therefore this section is devoted to HD analysis of the proposed structure.

The HD analysis method is given in [2] which is based on separating the nonlinear function from the frequency dependent linear transfer function has been adapted for calculation of THD. The second and third harmonic distortion (HD_2, HD_3) factors are computed by comparing the proposed oscillator topology of Fig. 2 with generic oscillator block diagram of Fig. 6.

Considering only first three harmonics the voltage at node X may be represented in phasor notation as

$$V_X(t) = \mathrm{Re}\left[V_{X1}e^{j\omega_o t} + V_{X2}e^{j2\omega_o t} + V_{X3}e^{j3\omega_o t}\right] \tag{22}$$

where ω_o, oscillation frequency, and V_{Xi}, complex quantity with magnitude and phase as $|V_{Xi}|$ and $\angle V_{Xi}$ respectively ($i = 1, 2, 3$).

Assuming the fundamental as the real number, the phase of second and third harmonics is computed with respect to fundamental. Taking nonlinearity of OTRA into account, the output at node Y is modeled as

$$V_Y = a_1(\omega_o)V_X + a_2(\omega_o)V_X^2 + a_3(\omega_o)V_X^3 \tag{23}$$

The coefficients a_1, a_2, a_3 can be frequency independent, and their values are obtained by analyzing Fourier components of voltage V_Y. The calculations are presented in "Appendix". The voltage $V_Y(t)$ and $V_X(t)$ are related by

$$V_Y = V_X * H(j\omega) \tag{24}$$

where the * operator is used to computing the output of nonlinear block and indicates that function is to be computed at incoming signal frequency [2, 22]. Combining Eqs. (22) and (23) for evaluation of product terms between real part of the sum of phasors yields

$$V_Y(t) = \mathrm{Re}\left[V_{Y1}e^{j\omega_o t} + V_{Y2}e^{j2\omega_o t} + V_{Y3}e^{j3\omega_o t}\right] \tag{25}$$

where the terms up to third harmonics are retained, and dc component and higher terms are neglected [2]. The terms V_{Y1}, V_{Y2}, V_{Y3} are computed as

$$V_{Y1} = a_1(\omega_o)V_{X1} + \frac{3}{4}a_3(\omega_o)V_{X1}^3 \tag{26}$$

$$V_{Y2} = a_1(2\omega_o)V_{X2} + \frac{1}{2}a_2(\omega_o)V_{X1}^2 + \frac{3}{2}a_3(\omega_o)V_{X1}^2 V_{X2} \tag{27}$$

$$V_{Y3} = a_1(3\omega_o)V_{X3} + a_2(\omega_o)V_{X1}V_{X3} + \frac{1}{4}a_3(\omega_o)V_{X1}^3 \tag{28}$$

The voltage V_X of linear section may be obtained by retracing feedback path, and its value is given by

$$V_X(t) = \mathrm{Re}\left[V_{Y1}e^{j\omega_o t}H(j\omega_o) + V_{Y2}e^{j2\omega_o t}H(2j\omega_o) + V_{Y3}e^{j3\omega_o t}H(3j\omega_o)\right] \tag{29}$$

The V_{X1},V_{X2} and V_{X3} may be evaluated by substituting Eqs. (26–28) in Eq. (29) and comparing the resulting expression with Eq. (22).

$$\text{Calculation of } V_{X1}: \quad V_{X1} = \left[a_1(\omega_o)V_{X1} + \frac{3}{4}a_3(\omega_o)V_{X1}^3\right]H(j\omega_o) \tag{30}$$

$$V_{X1} = \left[V_{X1} + \frac{3}{4}\frac{a_3}{a_1}V_{X1}^3\right]a_1H(j\omega_o)$$

where $a_1H(j\omega_o)$ is the loop gain of the linearized system. Simplification of Eq. (30) gives

$$V_{X1} = 2\sqrt{\frac{\frac{1}{H(j\omega_o)} - a_1}{3a_3}} \tag{31}$$

Substituting $s = j\omega$ in Eq. (4), the value of $H(j\omega)$ at $\omega = \omega_o$ maybe expressed as

$$H(j\omega)\Big|_{\omega=\omega_o} = \frac{1}{1+u+v} \quad \text{where} \quad u = \frac{R_1}{R_2}; v = \frac{C_1}{C_2}$$

$$\text{Calculation of } V_{X2}: \quad V_{X2} = \left[a_1(2\omega_o)V_{X2} + \frac{1}{2}a_2(\omega_o)V_{X1}^2 + \frac{3}{2}a_3(\omega_o)V_{X1}^2V_{X2}\right]H(j2\omega_o) \tag{32}$$

Solving Eq. (32) yield

$$V_{X2} = \frac{1}{2}\frac{a_2}{a_1}\frac{a_1H(j2\omega_o)}{1 - \left(1 + \frac{3}{2}\frac{a_3}{a_1}V_{X1}^2\right)a_1H(j2\omega_o)}V_{X1}^2 \tag{33}$$

$$\text{where} \quad H(2j\omega_o) = \frac{1}{-3 + j\sqrt{\frac{v}{u}}(1+u+1/v)}$$

$$\text{Calculation of } V_{X3}: \quad V_{X3} = \left[\begin{array}{r} a_1(3\omega_o)V_{X3} + a_2(\omega_o)V_{X1}V_{X3} + \\ \frac{1}{4}a_3(\omega_o)V_{X1}^3 \end{array}\right]H(j3\omega_o) \tag{34}$$

$$\text{Or} \quad V_{X3} = \frac{1}{4}\frac{a_3}{a_1}\frac{a_1H(j3\omega_o)}{1 - a_1H(j3\omega_o)}\left[1 + \frac{2a_2^2}{a_1a_3}\frac{a_1H(j2\omega_o)}{1 - \left(1 + \frac{3}{2}\frac{a_3}{a_1}V_{X1}^2\right)a_1H(j2\omega_o)}\right]V_{X1}^3 \tag{35}$$

$$\text{where} \quad H(2j\omega_o) = \frac{1}{-3 + j\sqrt{\frac{v}{u}}(1 + u + 1/v)} \tag{36}$$

The term $\frac{a_1 H(j3\omega_o)}{1-a_1 H(j3\omega_o)}$ can be evaluated and is given by

$$\frac{a_1 H(j3\omega_o)}{1 - a_1 H(j3\omega_o)} = \frac{j3a_1\sqrt{\frac{v}{u}}}{-8 + j3\sqrt{\frac{v}{u}}\left(1 + u + \frac{1}{v}a_1\right)} \tag{37}$$

By considering (31), (33) and (35), HD_2 and HD_3 are evaluated as

$$HD_2 = 20\log\left|\frac{V_{X2}}{V_{X1}}\right| = 20\log\frac{|a_2|V_{X1}}{\sqrt{9u\left(\frac{3}{4}a_3V_{X1}^2 + a_1 - 1 - u\right) + \left(\frac{-9}{4}a_3V_{X1}^2 - 9a_1\right)^2}} \tag{38}$$

$$\begin{aligned} HD_3 &= 20\log\left|\frac{V_{X3}}{V_{X1}}\right| \\ &= 20\log\frac{\frac{3}{4}|a_3|V_{X1}^2}{\sqrt{64u\left(\frac{3}{4}a_3V_{X1}^2 + a_1 - 1 - u\right) + \frac{81}{16}a_3^2V_{X1}^4}} \\ &\quad \cdot \sqrt{\frac{9u\left(\frac{3}{4}a_3V_{X1}^2 + a_1 - 1 - u\right) + \left(\frac{-9}{4}a_3V_{X1}^2 - 9a_1 + \frac{a_2^2}{a_3}\right)^2}{9u\left(\frac{3}{4}a_3V_{X1}^2 + a_1 - 1 - u\right) + \left(\frac{-9}{4}a_3V_{X1}^2 - a_1\right)^2}} \end{aligned} \tag{39}$$

The minimum values of HD_2 and HD_3 can be obtained by choosing optimum u value which may be determined by differentiating Eqs. (38) and (39) with respect to u. The optimal value of u is computed as

$$u_{opt} = \frac{3}{8}a_3V_{X1}^2 + \frac{1}{2}(a_1 - 1) \tag{40}$$

The values of HD_2 and HD_3 depend on V_{X1}(amplitude); coefficients a_1, a_2, a_3 and also on the parameter u. From App. A. it is clear that the coefficients a_1, a_2, a_3 will depend on $\frac{R_4}{R_3}$,V_{X1} and saturation voltage of OTRA (V_{sat}). In order to allow amplitude stabilization mechanism, the values of $\frac{R_4}{R_3}$ and V_{X1} must be chosen to satisfy the condition of Eq. (41).

$$\frac{R_4}{R_3} >> \frac{V_{sat}}{V_{X1}} \tag{41}$$

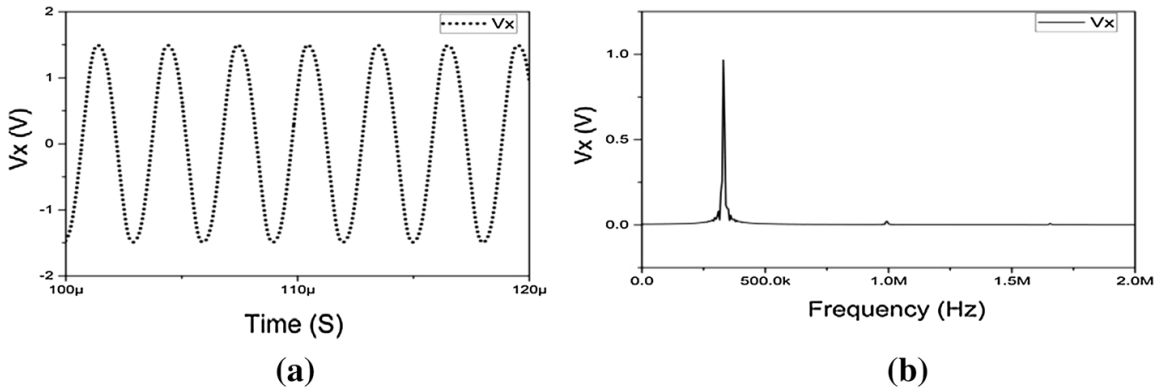

Fig. 7 **a** Transient output, **b** frequency spectrum

Table 2 Example design parameters

S. No.	V_{X1}	R (kΩ)	C (pF)	u_{opt}
1	0.5 V	$R_1=16$, $R_2=2$, $R_3=1$, $R_4=10.1$	94	4.5
2	1 V	$R_1=9$, $R_2=3$, $R_3=1$, $R_4=5.1$	102	2.5
3	1.65 V	$R_1=R_2=5.2$, $R_3=1$, $R_4=3.1$	102	1.5

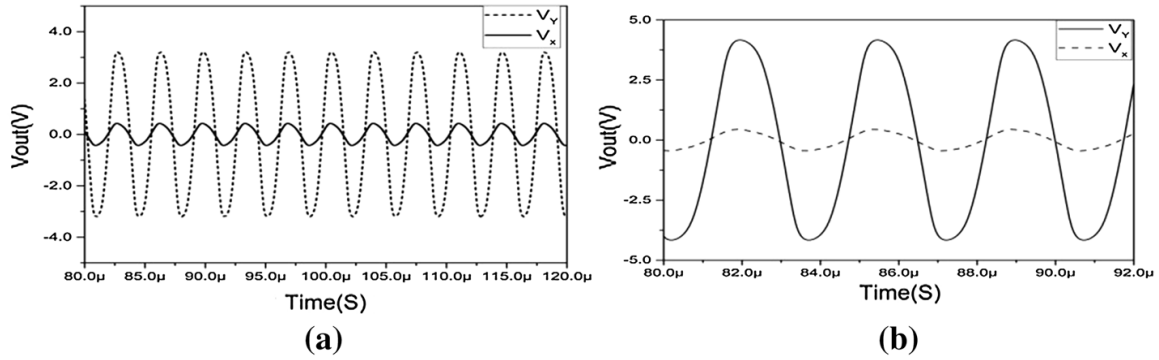

Fig. 8 Simulated waveforms for V_X and V_Y (Settings of S. No. 1 of Table 2) with **a** $R_4/R_3=10.1$, **b** $R_4/R_3=11$

5 Simulation Results

The functionality of the proposed Wien bridge oscillator has been verified through SPICE simulations where the OTRA and the buffer are realized using commercially available IC AD844 N as shown in Figs. 4 and 5 respectively. The supply voltages are chosen as ± 8.5 V. The proposed oscillator is designed for an FO of 300 kHz for which the components are computed as $R_1=9$ kΩ, $R_2=3$ kΩ, $R_3=1$ kΩ, $R_4=5.1$ kΩ and C = 104 pF. Transient output and corresponding frequency spectrum obtained through simulation are depicted in Fig. 7. Simulated value of THD is observed as 0.8%. Next, the simulations are carried out to examine the harmonic distortion of the oscillator.

For the chosen supply voltages V_{SAT} of 5 V is obtained for OTRA from SPICE simulation. To examine the impact of R_4/R_3 on HD_2 and HD_3, different peak amplitudes of 0.5 V, 1 V, and 1.65 V are considered.

The corresponding R, C values and u_{opt} for these peak voltages are shown in Table 2. The simulated waveforms of V_X and V_Y for settings at serial number 1, 2 and 3 of Table 2

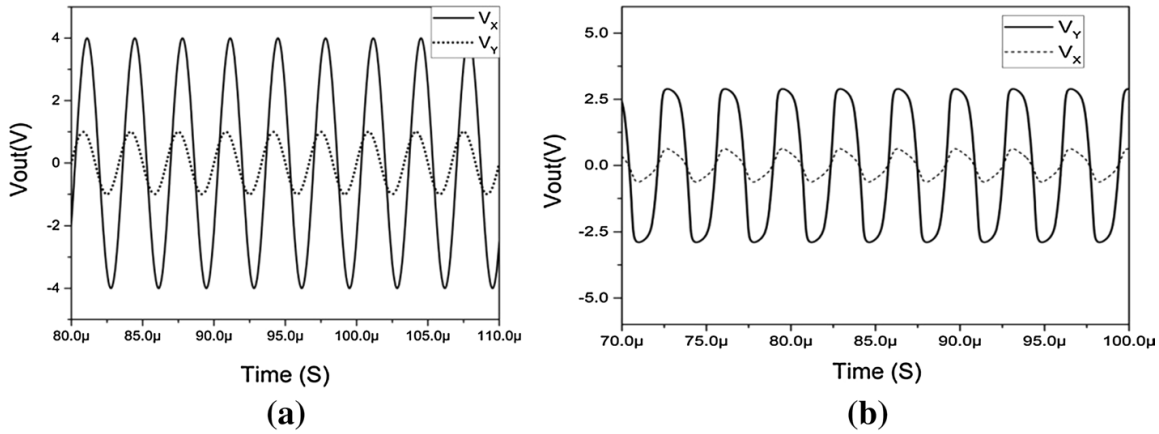

Fig. 9 Simulated waveforms for V_X and V_Y (Settings of S. No. 2 of Table 2) with **a** $R_4/R_3 = 5.1$, **b** $R_4/R_3 = 6$

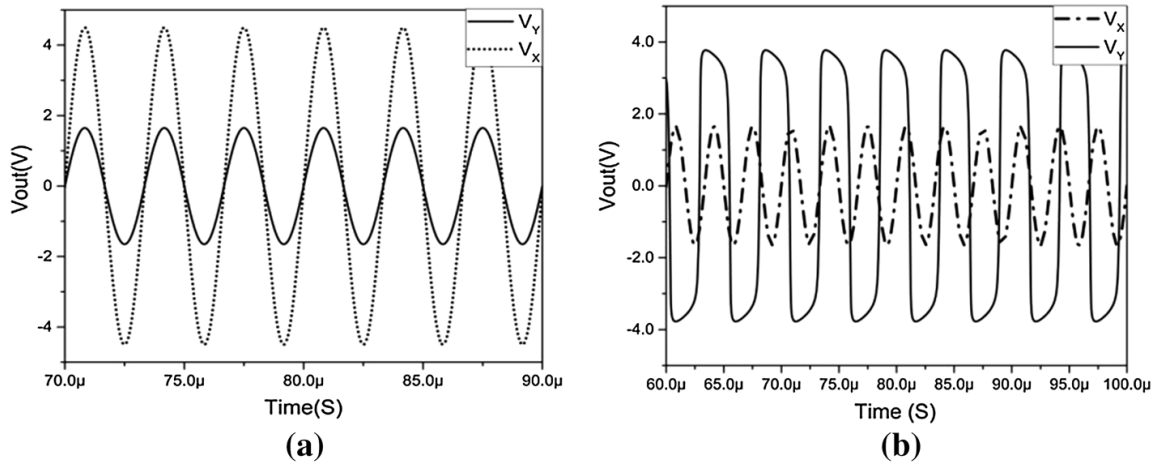

Fig. 10 Simulated waveforms for V_X and V_Y (Settings of S. No. 3 of Table 2) with **a** $R_4/R_3 = 3.1$, **b** $R_4/R_3 = 4$

Table 3 Theoretical and simulated values of HD_2 and HD_3

V_{X1}	Theoretical		Simulated	
	HD_2 (dB)	HD_3 (dB)	HD_2 (dB)	HD_3 (dB)
0.5 V $(R_4/R_3) = 10$	−46.71	−54.65	−48.80	−52.34
1 V $(R_4/R_3) = 5$	−45.52	−48.40	−46.65	−48.89
1.65 mV $(R_4/R_3) = 3$	−45.51	−46.64	−42.27	−41.68

are depicted in Figs. 8a, 9a and 10a respectively. It has been discussed in section V that signal distortion occurs mainly due to active element saturation mechanism [2]. To validate this point, R_4/R_3 is changed from settings given in Table 2, and corresponding waveforms are placed as Figs. 8b, 9b and 10b which are slightly distorted waveform thus confirming the mentioned fact.

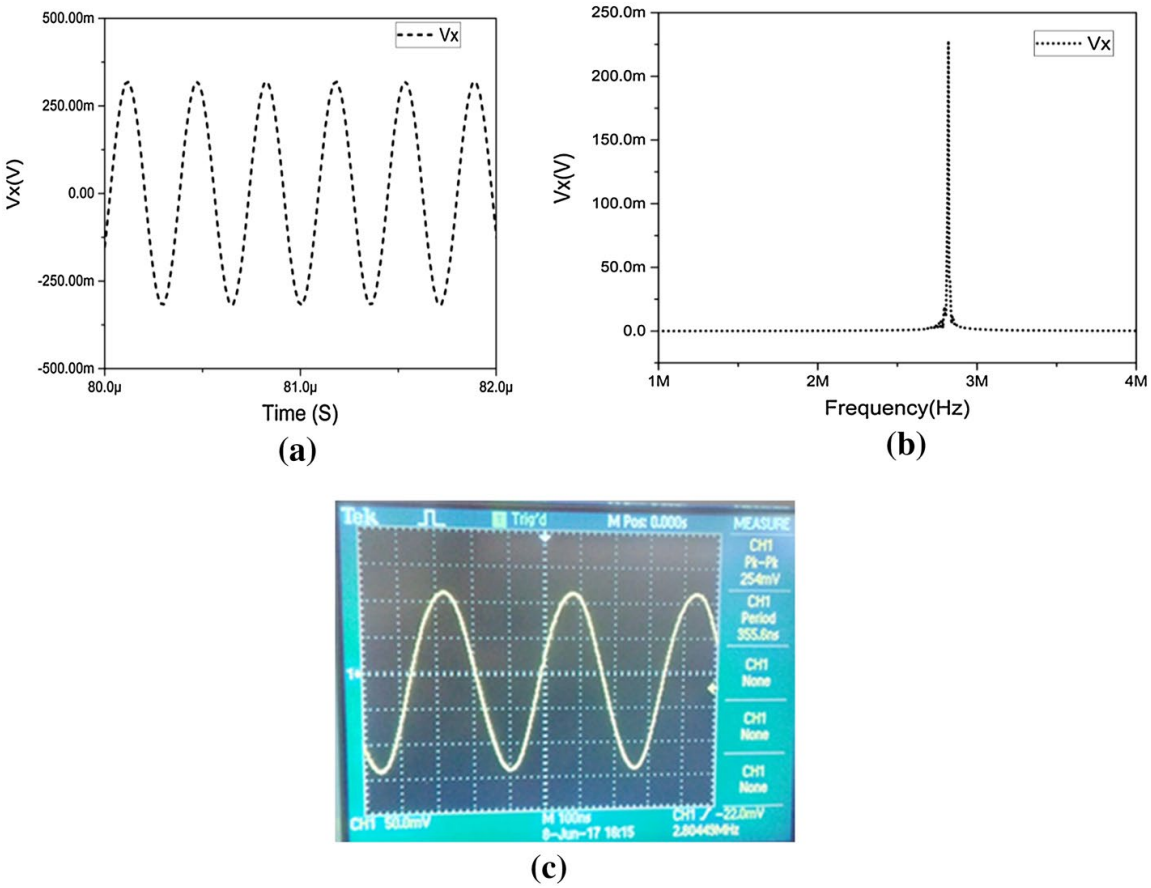

Fig. 11 **a** Simulated transient output waveform and **b** its frequency spectrum, **c** experimental output waveform

Table 3 enlists simulated and theoretical values of HD_2 and HD_3 for the three cases discussed above. There is close agreement between the two. The THD for the three cases is within 1%.

5.1 Experimental Results

The functionality of proposed Wien bridge oscillator is also verified through experimentation for which the circuit is breadboarded using AD844 ICs [26]. The passive components are chosen as $R_1 = 16$ kΩ, $R_2 = 2$ kΩ, $R_3 = 1$ kΩ, $R_4 = 10.1$ kΩ and $C = 10$ pF corresponding to FO of 2.82 MHz.

The simulated transient output waveform and its frequency spectrum are shown in Fig. 11a, b respectively. The experimental output is depicted in Fig. 11c. The observed values of FO closely match with the theoretical values. Simulated THD value at FO of 2.82 MHz is found to be 0.7%.

6 Conclusion

OTRA based voltage output Wien bridge oscillator has been presented in this paper which is a suitable choice for high-frequency applications. The FO and the CO for the proposed structure have been enumerated and have also been analyzed in the light of device

non-idealities. The detailed harmonic analysis is carried out to characterize the linear performance of the proposed oscillator. Verification of workability of the proposed oscillator is presented through SPICE simulations and experimental prototyping. The total harmonic distortion (THD) for the proposed design is found to be less than 1%.

Appendix

Consider the circuit of buffer and OTRA separating Z_1 and Z_2 from Fig. 2, and assume the input V_X as pure sinusoidal voltage as given by (42) with amplitude V_{X1} and frequency ω_0. Assume the output voltage V_Y of the circuit given by (23) can be rewritten as given in (43)

$$V_X = V_{X1}\cos(\omega_o t) \tag{42}$$

$$V_Y = a_1(\omega)V_X + a_2(\omega)V_X^2 + a_3(\omega)V_X^3 \tag{43}$$

Substituting the expression of V_X into (43), we get

$$V_Y = a_1(\omega_o)V_{X1}\cos(\omega_o t) + a_2(\omega_o)V_{X1}^2\left(\frac{1+\cos(2\omega_o t)}{2}\right) + a_3(\omega_o)V_{X1}^3\left(\frac{\cos(3\omega_o t)+3\cos(\omega_o t)}{4}\right) \tag{44}$$

By neglecting the DC term [25] in (44) and considering frequency dependent terms V_{Y1}, V_{Y2} and V_{Y3} we get

$$V_{Y1} = a_1(\omega_o)V_{X1} + \frac{3}{4}a_3(\omega_o)V_{X1}^3; V_{Y2} = a_2(\omega_o)\frac{V_{X1}^2}{2}$$

$$V_{Y3} = \frac{1}{4}a_3(\omega_o)V_{X1}^3 \tag{45}$$

Equation (45) relates coefficients a_1, a_2 and a_3 to the magnitude of the harmonics of V_{Y1},V_{Y2} and V_{Y3} resp.

$$a_1 = \frac{V_{Y1}-3V_{Y3}}{V_{X1}}; a_2 = -\frac{V_{Y2}}{V_{X1}^2}; a_3 = 4\frac{V_{Y3}}{V_{X1}^3} \tag{46}$$

To compute the coefficients a_1, a_2, a_3 first, we derive the components V_{Y1}, V_{Y2} and V_{Y3} by using the Fourier integral as given in (47). By tedious mathematical calculations, we get the coefficients a_1, a_2, a_3 which are frequency independent as shown in (48–50). The Fourier integral is evaluated in three different regions namely when $V_Y(t) < -V_{sat}$, $V_Y(t) \leq -V_{sat}$ and $V_Y(t) > -V_{sat}$ by assuming signal distortion is due to the output voltage saturation mechanism. The value of V_Y for these three different regions are $-V_{sat}, \left(\frac{R_4}{R_3}V_{X1}\cos(\omega_o t)\right)$ and V_{sat} resp.

$$V_{Y,k} = \frac{1}{\pi}\int_0^{2\pi} V_Y(t)e^{jk\omega_o t}d(\omega_o t) \tag{47}$$

where $k = 1, 2, 3$

$$a_1 = \frac{R_4}{R_3}\left[1 - \frac{2}{\pi}\arccos\frac{V_{sat}R_3}{V_{X1}R_4} + \frac{2}{\pi}\frac{V_{sat}R_3}{V_{X1}R_4}\left(3 - 2\left(\frac{V_{sat}R_3}{V_{X1}R_4}\right)^2\right)\sqrt{1 - \left(\frac{V_{sat}R_3}{V_{X1}R_4}\right)^2}\right] \tag{48}$$

$$a_2 = -\frac{4}{3\pi}\frac{R_4}{R_3}.\frac{2\frac{V_{sat}R_3}{V_{X1}R_4}.\left[1 - \left(\frac{V_{sat}R_3}{V_{X1}R_4}\right)^2\right]\sqrt{1 - \left(\frac{V_{sat}R_3}{V_{X1}R_4}\right)^2}}{V_{X1}} \tag{49}$$

$$a_3 = -\frac{16}{3\pi}\frac{R_4}{R_3}.\frac{\frac{V_{sat}R_3}{V_{X1}R_4}.\left[1 - \left(\frac{V_{sat}R_3}{V_{X1}R_4}\right)^2\right]\sqrt{1 - \left(\frac{V_{sat}R_3}{V_{X1}R_4}\right)^2}}{V_{X1}^2} \tag{50}$$

References

1. Adel, S., & Kenneth, C. S. (2015). *Microelectronic circuits*, 7th edn. New York: Oxford University Press. ISBN 978-0-19-933913-6.
2. Gaetano, P., Melita, P., & Salvatore, P. (2008). Wien-type oscillators: Evaluation and optimization of harmonic distortion. *Circuits and Systems II: Express Briefs, IEEE Transactions, 55*(7), 628–632.
3. Aram, B., & Kevin, N. (1981). Operational amplifier circuits for the Wien Bridge oscillator. *IEEE Transactions on Circuits and Systems, 28*(9), 930–934.
4. Carlosena, A., Martinez, P., & Porta, S. (1990). An improved Wien bridge oscillator. *IEEE Transactions on Circuits and Systems, 37*(4), 543–546.
5. Biolek, D., Senani, R., Biolkova, R., & Kolka, Z. (2008). Active elements for analog signal processing: Classification, review, and newproposals. *Radioengineering, 17*(4), 15–32.
6. Muhammad Taher, A. (2017). Recent developments in current-mode sinusoidal oscillators, circuits and active elements. *Arabian Journal for Science and Engineering, 42*(7), 2583–2614.
7. Sheikhajaz, B., & Shah, N. A. (2012). Active device usage in filter design—An overview. *International Journal of Scientific and Research Publications, 2*(6), 1–8.
8. Toumazou, C., Lidgey, F. J., & Haigh, D. G. (1990). *Analog IC design: The current-mode approach*. London: IET. ISBN 0863412971, 9780863412974.
9. Mostafa, H., & Soliman, A. M. (2006). A modified CMOS realization of the operational transresistance amplifier. *Frequency, 60*(3–4), 70–76.
10. Khaled, N. S., & Ahmed, M. S. (1999). CMOS operational transresistance amplifier for analog signal processing applications. *Microelectronics Journal, 30*(3), 235–245.
11. Jiann-jong, C., Hen-wai, T., & Chen, C. C. (1992). Operational transresistance amplifier using CMOS technology. *IET Electronics Letters, 28*(22), 2087–2088.
12. Senani, R., & Kumar, B. A. (1989). Linearly tunable Wien bridge oscillator realized with operational transconductance amplifiers. *IET Electronics Letters, 25*(1), 19–21.
13. Muhammad Taher, A., & Humood, N. (1987). Two new minimum component Wienbridge oscillators using current-conveyors. *International Journal of Electronics, 63*(5), 669–672.
14. Ahmed, M. S., & Elwakil, A. (1999). Wien oscillators using current conveyor. *Computers Electrical Engineering, 25*(1), 45–55.
15. Ahmed, M. S. (1998). Current-mode oscillators using single output current conveyors. *Microelectronics Journal, 29*(11), 907–912.
16. Pedro, A. M., Santiago, C., & Inmaculada, G. (1995). Wien-type oscillators using CCII+. *Analog Integrated Circuits and Signal Processing, 7*(2), 139–147.

17. Muhammad Taher, A., Alghumaiz, A. A., & Khan, M. H. (1995). Novel CCII-based single-element controlled oscillators employing grounded resistors and capacitors. *International Journal of Electronics, 78*(6), 1107–1112.
18. Ahmed, M. S. (1998). Novel generation method of current mode Wien-type oscillators using current conveyors. *International Journal of Electronics, 85*(6), 737–747.
19. Ahmed, M. S. (2010). Generation of CCII and ICCII based Wien oscillators using nodal admittance matrix expansion. *AEU-International Journal of Electronics and Communications, 64*(10), 971–977.
20. Yongan, L. (2012). A new single MCCCDTA based Wien-bridge oscillator with AGC. *AEU-International Journal of Electronics and Communications, 66*(2), 153–156.
21. Yongan, L. (2014). Three current-mode Wien-bridge oscillators using single modified current controlled current differencing transconductance amplifier. In W. Wang (Ed.), *Mechatronics and automatic control systems. Lecture notes in electrical engineering* (pp. 693–700). Cham: Springer.
22. Cannizzaro, S. O., Gaetano, P., & Salvatore, P. (2006). Effects of nonlinear feedback in the frequency domain. *IEEE Transactions on Circuits and Systems I: Regular Papers, 53*(2), 225–234.
23. Gaetano, P., Melita, P., & Salvatore, P. (2006). Analysis and evaluation of harmonic distortion in the tunnel diode oscillator. In *Proceedings of IEEE international symposium on circuits and systems*, Greece (pp. 5135–5138). IEEE.
24. Cannizzaro, S. O., Gaetano, P., & Salvatore, P. (2005). Accurate estimation of high-frequency harmonic distortion in two-stage miller OTAs. *IET Circuits, Devices and Systems, 152*(5), 417–424.
25. Gaetano, P., Melita, P., & Salvatore, P. (2009). Approach to analyze and design nearly sinusoidal oscillators. *IET Circuits, Devices and Systems, 3*(4), 204–221.
26. AD844. (1990). *Current feedback op-amp data sheet*. Norwood, NJ: Analog Devices Inc.
27. Chen, J., Tsao, H., Liu, S., & Chui, W. (1995). Parasitic capacitance insensitive current-mode filters using operational transresistance amplifier. *IET Circuits, Devices and Systems, 142,* 186–192.
28. Pandey, R., Pandey, N., Negi, T., & Vivek, G. (2013). CDBA based universal inverse filter. *ISRN Electronics, 2013,* 1–6, Article ID 181869.

Publisher's Note Springer Nature remains neutral with regard to jurisdictional claims in published maps and institutional affiliations.

Gurumurthy Komanapalli received his B.Tech. (Electronics and Communication) from JNTU Kakinada, Andhra Pradesh and his MTECH in VLSI design from Delhi Technological University (DTU) (formerly Delhi College of Engineering), New Delhi in 2014 and Currently he is working towards Ph.D. degree from DTU. He published more than ten research papers in reputed international journals, conferences. His research interests are in Analog circuit design and Microelectronics.

Rajeshwari Pandey is currently working as Professor in Department of Electronics and Communication Engineering, Delhi Technological University, Delhi, India. She did her M.E. (Electronics and Control) from BITS, Pilani, Rajasthan, India and Ph.D. from Faculty of Technology, Delhi University, India. Her research interests include Analog Integrated Circuits, and Microelectronics. She has published several papers in International, Journals of repute and conferences. She is life member of IETE, ISTE and member of IEEE, IEEE WIE for 15 years.

Neeta Pandey received her M.E. in Microelectronics from Birla Institute of Technology and Sciences, Pilani and Ph.D. from Guru Gobind Singh Indraprastha University, Delhi. She has served in Central Electronics Engineering Research Institute, Pilani, Indian Institute of Technology, Delhi, Priyadarshini College of Computer Science, Noida and Bharati Vidyapeeth's College of Engineering, Delhi in various capacities. At present, she is professor in ECE department, Delhi Technological University. A life member of ISTE, and member of IEEE, USA, she has published papers in international, national journals of repute and conferences. Her research interests are in analog and digital VLSI design.

ResearchGate

See discussions, stats, and author profiles for this publication at: https://www.researchgate.net/publication/332137631

Optimization of protein extraction from detoxified Jatropha seed cake using response surface methodology and amino acid analysis

Article *in* International journal of Environmental Science and Technology · April 2019

DOI: 10.1007/s13762-019-02340-4

CITATIONS
0

READS
24

6 authors, including:

Avanish Kumar Shrivastav
Delhi Technological University
2 PUBLICATIONS **1** CITATION
SEE PROFILE

Ravi kumar Goswami
University of Delhi
2 PUBLICATIONS **1** CITATION
SEE PROFILE

Some of the authors of this publication are also working on these related projects:

Development of alternative sustainable fish feeds to promote human health using novel non- conventional indigenous ingredients View project

All content following this page was uploaded by Avanish Kumar Shrivastav on 02 April 2019.

The user has requested enhancement of the downloaded file.

International Journal of Environmental Science and Technology
https://doi.org/10.1007/s13762-019-02340-4

ORIGINAL PAPER

Optimization of protein extraction from detoxified Jatropha seed cake using response surface methodology and amino acid analysis

S. Ahluwalia[1] · R. Bidlan[1] · A. K. Shrivastav[1] · R. K. Goswami[2] · P. Singh[3] · J. G. Sharma[1]

Received: 23 July 2018 / Revised: 6 March 2019 / Accepted: 18 March 2019
© Islamic Azad University (IAU) 2019

Abstract

Jatropha seed cake is a by-product of biodiesel industry which is rich in proteins and carbohydrates and contains many bioactive compounds. Besides having a good protein quality, the essential amino acid content (except lysine) is also high in *Jatropha* seed cake, and therefore, *Jatropha* proteins can be exploited for many technical applications. The major hindrance for its use as a protein supplement is the presence of anti-nutritional factors and toxins, especially the phorbol esters. The detoxification of *Jatropha* seed cake for the removal of phorbol esters has been shown in our earlier studies. Proteins were extracted from the detoxified *Jatropha* seed cake and analyzed for amino acid content. Various parameters such as temperature, solubilization pH, precipitation pH and extraction time were studied for their effect on protein content, and the process was optimized using response surface methodology among 5 best samples selected based on protein content and protein yield from dry concentrates. The amount of dry matter, protein content and protein yield of 17.1%, 41.98% and 38.66%, respectively, was obtained under the optimized conditions of 60 °C temperature, solubilization pH 11.0, precipitation pH 4.41 and extraction time of 0.78 h. Amino acid contents revealed that the extracted samples contained a higher concentration of essential amino acids, especially leucine (4.40 ± 0.98 g/100 g). The results indicated that the protein extraction procedure from *Jatropha* seed cake affected the amino acid content, yet the values were close to FAO/WHO reference protein, and thus, the *Jatropha* proteins can be explored further for their use as feed supplement.

Keywords *Jatropha* proteins · Isoelectric precipitation · Amino acids · Response surface methodology · Optimization process

Introduction

Jatropha seed cake which is the by-product of biodiesel industry is rich in proteins and carbohydrates and contains many bioactive compounds and has found many economical and technical applications (Ahluwalia et al. 2018). The seed cake can be used as a substitute for other organic fertilizers because of good content of nitrogen, phosphorus and potassium [NPK (%) 4.44: 2.09: 1.68] (Manyuchi et al. 2018) which is much higher than the NPK values of organic fertilizers such as cow manure [NPK (%) 0.97: 0.69: 1.66], compost of municipal wastes [NPK (%) 1.25: 0.25: 0.65] and Karanj oil cake [NPK (%) 4.0: 1.0: 1.0] (Achten et al. 2010). Also, the biological decomposition of *Jatropha* seed cake helps in improving soil fertility which enhances crop production (Jakub et al. 2016). Many researchers have reported the increase in yields when *Jatropha* press cake was used as an organic fertilizer (Ghosh et al. 2012). Being nutritionally rich, the seed cake can be used as animal feed, but the presence of toxins like phorbol esters makes it unsuitable for animal consumption, and therefore, the seed cake needs to be detoxified (Ahluwalia et al. 2017). Despite of this, the use of *Jatropha* protein is advantageous as the protein quality and the essential amino acid content (except lysine) are high in *Jatropha* seed cake as compared to Food and Agricultural Organization (FAO) reference protein (Yinuo et al. 2018; Makkar and Becker 2009). Amino acids are very important chemical compounds and play a major role as structural

Editorial responsibility: Parveen Fatemeh Rupani.

✉ S. Ahluwalia
shilpi.ahluwalia@gmail.com

[1] Department of Biotechnology, Delhi Technological University, Delhi, India

[2] Department of Zoology, University of Delhi, Delhi, India

[3] Department of Mechanical Engineering, Delhi Technological University, Delhi, India

Published online: 01 April 2019

and functional components of the body. Many studies have been conducted on the functions of amino acids (essential or nonessential), their composition in proteins, their effect on promoting muscle strength and function, etc. Various analytical methods for the determination of amino acids have been explored like high-performance liquid chromatography (HPLC) using diode array detector (Calull et al. 1991) which has many photodiode arrays for obtaining information over different wavelengths at one time and which makes it different from other methods. Fluorescence detector has a high sensitivity and has been used for the analysis of amino acids after reaction with fluorescence reagent (Tateda et al. 1998). Combined HPLC system with mass spectrometry is another method which is accurate and has high precision and has been used by many authors in their study (Krumpochova et al. 2015; Vilches et al. 2017). It involves the separation of analytes by ion pair chromatography, and the detection is done by multiple reaction monitoring positive ion mode. Nuclear magnetic resonance (NMR) technique has been used by many research groups for the determination of amino acids (Sugiki et al. 2017; Mati et al. 2015). This method involves simple procedures for sample preparation, and the spectra are obtained is few minutes unlike other methods (Lars et al. 2004). Jimenez et al. (2012) and Monia et al. (2017) have used gas chromatography (GC) method coupled with mass spectroscopy for amino acid analysis which requires derivatization of polar amino acids before GC analysis which makes them less reactive and more volatile. The method is preferred over HPLC if the availability of instrumentation and operational costs is considered; however, the major disadvantage of this method is its sensitivity to moisture which results in unstable derivatized analytes. The proteins extracted from raw *Jatropha* seed cake were successfully used as reactive component in polyketone-based wood adhesive formulations which not only improved the performance but also contributed in making the process economical (Hamarneh et al. 2010). Also, *Jatropha* proteins have good functional properties such as emulsifying properties, foaming properties, solubility, film-forming properties which widen up the possibilities of using this protein for various technical applications like emulsifier or paper adhesive (Lestari et al. 2011), coating material for food packaging applications (Gabriele et al. 2015), etc. Several studies have been conducted on *Jatropha* protein extraction which includes steam injection (Devappa and Swamylingappa 2008) by which a yield of 70–77% was obtained, counter current multistage extraction (Lestari et al. 2010) resulted in 82% protein recovery, by isoelectric precipitation method (Hamarneh et al. 2010; Makkar et al. 2008) 40–53% proteins were recovered, and enzyme-assisted extraction process (Gofferje et al. 2014) yielded 76% proteins.

Every geographic region carries significance as far as the toxins like phorbol esters and other anti-nutritional factors are concerned. This study focuses on the J*atropha* seed cake obtained from the Delhi region of North India after the extraction of oil for biodiesel production. In our earlier studies, we have already shown the presence of various phorbol esters in these samples and the bio-detoxification, removing significant amounts of phorbol esters using the strain *Pseudomonas aeruginosa* DS1. In the present study, this detoxified *Jatropha* seed cake was analyzed for the presence of essential and nonessential amino acids. This study is important as India is an agriculture-based country with huge number of cattle and other animals being reared that demand for healthy feed. The population of India is increasing at an alarming rate, thereby making it imperative to focus on the food and feed requirements. The emergence of biofuel sector has given a sigh of relief for the scientists in protecting the environment, especially the air quality. The by-products of biodiesel industry using *Jatropha* seeds would produce tons of oil press seed cake carrying various anti-nutritional factors and other toxins like phorbol esters. These seed cakes can get in to the environment and lead to various other unstudied complications. Unintentional intake of these materials by animals might have a severe blow on the backbone of Indian agriculture, economy and heritage. The aim of this study was to extract proteins from detoxified *Jatropha* seed cake by applying the principle of isoelectric precipitation. Optimization of the process was done using one-factor-at-a-time approach and RSM. The effect of various factors such as extraction temperature, time, solubilization pH, precipitation pH variations was also studied for obtaining a high protein yield with high protein and amino acid content. Therefore, the present study carries a lot of significance in terms of safeguarding India from future set back and is a small step toward this.

Materials and methods

Materials

Jatropha seed cake, after the extraction of the oil from whole seeds by screw press, was obtained from Biodiesel Centre, Delhi Technological University (DTU), Delhi, India. All the chemicals used in the work were purchased from Fischer Scientific and were of analytical grade. For the detoxification of *Jatropha* seed cake, submerged fermentation was carried out using *Pseudomonas aeruginosa* DS1 isolated in our laboratory. Complete degradation of phorbol esters resulted when the seed cake was fermented for 15 h at 37 °C, pH 7, 100 rpm (Ahluwalia et al. 2017).

Methods

Protein extraction

The extraction of protein from detoxified *Jatropha* seed cake at different conditions was done according to the method described by Makkar et al. (2008) which followed the principle of isoelectric precipitation. 10-g seed cake was suspended in 100 ml water, and the pH was adjusted using 1 mol L^{-1} NaOH. The mixture was stirred for 1 h at different temperatures (Table 1). The pH was checked after every 20 min and adjusted to desired pH (shown in Table 1) using 1 M NaOH. The contents were then centrifuged at 6700*g* for 15 min to collect the supernatant. The acidic pH of the supernatant was adjusted using 4 M HCl. The mixture was stirred for 10 min and centrifuged at 6700*g* for 15 min for the separation of protein precipitates. The pellet was air dried, and the weight (dry wt.) was noted. Each experiment was done in duplicates.

Protein analysis

Protein content of the detoxified *Jatropha* seed cake and protein precipitates was determined by Kjeldahl method (AACC 2000), which consists of three steps: digestion, distillation and titration. The sample is digested in boiling concentrated sulfuric acid in the presence of a catalyst (potassium sulfate and cupric sulfate in 5:1 ratio) for complete dissolution and oxidation. The nitrogen in the sample is converted to ammonium sulfate. In the distillation step, sodium hydroxide is added into the solution, which converts the ammonium ion to ammonia, which is distilled and received in a boric acid solution. The amount of ammonia released and thus the amount of nitrogen present in the sample are then determined by titration. The results are expressed in % N, % NH_3 or protein (%N × factor). Dry matter recovery and protein yield were calculated according to the formula:

$$\text{Dry matter (\%)} = \frac{\text{Dry matter weight of protein precipitate}}{\text{Initial dry weight of seed cake}} \times 100$$

$$\text{Protein yield (\%)} = \frac{\text{dry mass extract (g)} \times \text{Protein content extract (\%)}}{\text{initial weight of seed cake (g)} \times \text{protein content in seed cake (\%)}} \times 100$$

Pilot-scale experiments

One-factor-at-a-time approach was applied to study the effect of temperature, solubilization pH and precipitation pH on protein content and protein yield. For this study, the following extraction conditions were performed: (1) temperature 25, 40, 55, 70, 85 °C; (2) solubilization pH 7.5, 8.5, 9.5, 10.5, 11.5; (3) precipitation pH 2, 3, 4, 5, 6. After analyzing the data of the former parameter, its optimum value was fixed in the subsequent experiments of pilot-scale studies. The quadratic model and R^2 value for each factor were found out. Similar methodology was followed by Chen et al. (2012) in their studies for cultural optimization of biosurfactant produced by *Acinetobacter* genus.

Optimization of protein extraction using RSM

Four different parameters, i.e., temperature, solubilization pH, precipitation pH and time, were varied at five levels for studying the combined effect of these independent variables on three response variables, i.e., dry matter, protein content and protein yield. Response surface methodology (RSM) was used to study the process and optimization of different parameters for the extraction of proteins from *Jatropha* seed cake. The experimental plan consisted of four factors at five levels. The optimal concentrations of each factor from the quadratic models (from pilot-scale experiments) were adjusted slightly and were applied as central value. Different levels of variation and codes of the independent variables of temperature (*A*), solubilization pH (*B*), precipitation pH (*C*) and time (*D*) are presented in Table 1. As per Central Composite Rotatable Design (CCRD), thirty sets of experiments were performed with varying levels of parameters. The analysis of variance was performed to evaluate the effect of the independent variables on the response variables. Design Expert (DX-11) was used for the selecting

Table 1 Levels and codes of the independent variables

Variables	Codes	Levels (coded and real values)				
		−2	−1	0	1	2
Temperature (°C)	*A*	30	40	50	60	70
Solubilization pH	*B*	8	9	10	11	12
Precipitation pH	*C*	3.5	4	4.5	5	5.5
Time (h)	*D*	0.5	0.75	1	1.25	1.75

appropriate model, and multiple regression analysis was performed considering a full second-order polynomial model.

Elemental analysis

Five best samples of dried protein concentrates on the basis of protein yield and protein content were selected and analyzed for carbon, hydrogen, oxygen, nitrogen and sulfur contents in CHNSO analyzer (Vario micro tube, Germany).

Amino acid analysis

The amino acid content of the five protein concentrates was estimated by amino acid analyzer (Hitachi, Model L-8900) using the method described by You Shin et al. (2013). In brief, the protein sample is made to pass through a cation exchange column where it is separated into amino acid components which are detected at a wavelength of 570 nm. Quantification was done by comparing sample chromatogram peaks with the standards. Proline and hydroxyproline (imino acids) have no absorbance maxima within the visible light spectrum and are therefore detected at 440 nm. In the deamination column, 20 µL of sample was injected with a flow rate of 0.35 mL min^{-1} and the column temperature was 30–70 °C. In reaction column, reaction temperature was 135 °C with a Ninhydrin flow rate of 0.30 mL min^{-1}.

Results and discussion

Pilot-scale experiments

The quadratic model and R^2 value for each factor (temperature, solubilization pH, precipitation pH) are shown in Fig. 1. On the basis of these models, the optimal concentration for each factor was used as a central value for optimization by RSM.

No significant change in the protein yield was seen at temperatures 25, 40 and 55 °C (Fig. 1a); however, a slight increase in protein yield was observed. As the temperature was increased from 55 to 85 °C, a significant decrease in protein yield was observed from 45.5 to 17.6%. An increase

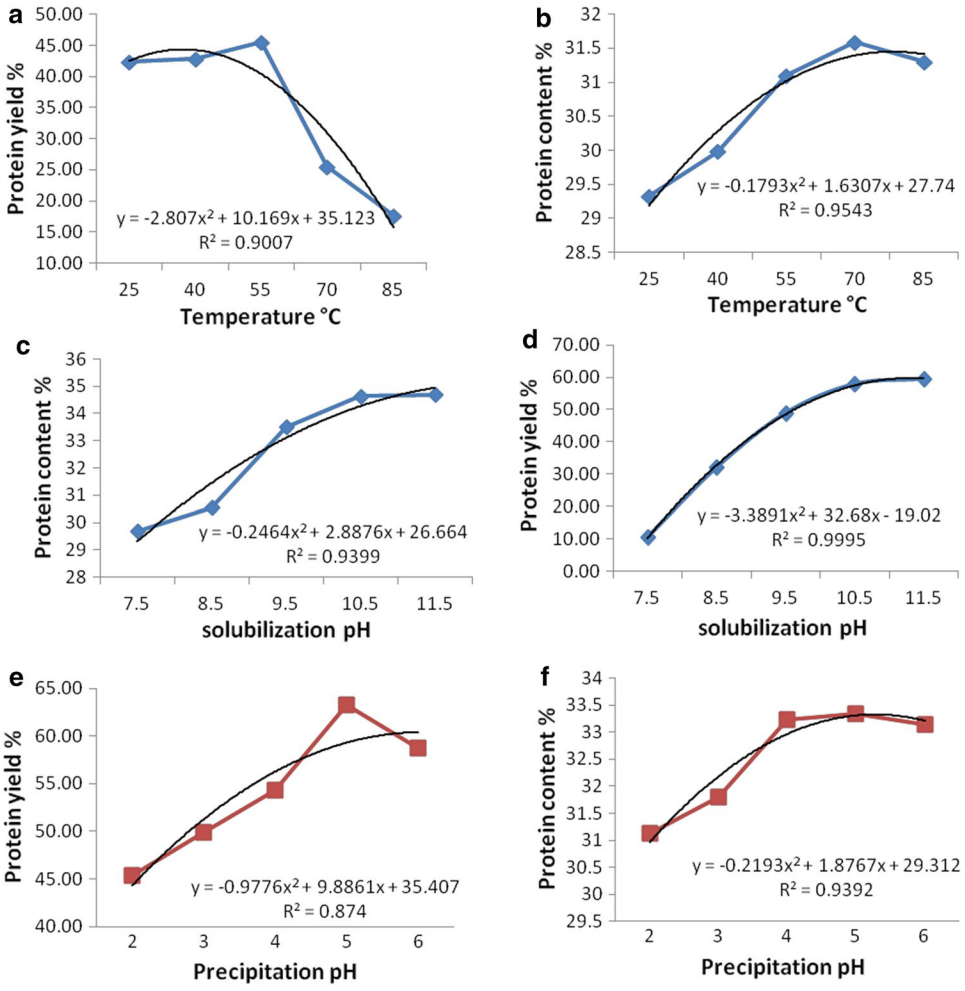

Fig. 1 Quadratic model and related equation for each factor after one-factor-at-a-time analysis

in protein content was observed with the increase in extraction temperature (Fig. 1b).

Figure 1c shows the increasing pH had a positive effect on the protein content of the concentrates. There was a gradual increase in the protein content when the pH was raised from 7.5 to 10.5; however, no significant change in protein content was observed when the pH reached 11.5. The highest protein content of 34.69% was observed in samples when they were solubilized at 11.5. The graphs in Fig. 1d clearly show that the alkaline conditions significantly affect the protein extraction yield and higher yields were obtained at pH 11.5 compared with pH 10.5.

There was a steady increase in protein yield when the precipitation pH was increased from 2 to 5. However, further increase in pH resulted in sharp decline in protein yield (Fig. 1e). This suggests that the isolectric point of *Jatropha* protein is between pH 4.5 and 5 which results in the maximum recovery of the solubilized proteins at this pH. The increase in protein content was observed when precipitation pH was raised from pH 2 to 4, and it was comparable at pH 4 and 5 while a decline in protein content was observed when the extraction was performed at pH6 (Fig. 1f).

Recoveries of protein concentrates

The data in Table 2 show the recoveries of dry matter, protein yield and protein content of protein concentrate (from detoxified *Jatropha* raw seed cake). The protein concentrate had protein content in the range from 29.47 to 45.62%, and the protein yield varied from 11.7 to 50.9%.

Optimization of protein extraction from detoxified *Jatropha* seed cake using RSM

Thirty experiments were performed according to CCRD to determine the effect of four parameters, i.e., temperature,

Table 2 Average values of the response parameters

S. no.	Temperature (°C)	Solubilization pH	Precipitation pH	Time (h)	Dry matter (%)	Protein content (%)	Protein yield (%)
1	40	9	4	0.75	6.1	31.72	11.7
2	60	9	4	0.75	10.8	30.07	18.4
3	40	11	4	0.75	15	31.11	26
4	60	11	4	0.75	17.5	37.02	36
5	40	9	5	0.75	8.2	30.12	13.7
6	60	9	5	0.75	8	33.58	15
7	40	11	5	0.75	15.6	31.72	27.5
8	60	11	5	0.75	15.2	40.87	34.5
9	40	9	4	1.25	12.5	32.98	23
10	60	9	4	1.25	18.3	33.72	34.2
11	40	11	4	1.25	11.7	33.17	21.6
12	60	11	4	1.25	20.1	42.18	47.1
13	40	9	5	1.25	15.3	31.72	31
14	60	9	5	1.25	17.5	35.18	34.2
15	40	11	5	1.25	16.7	31.94	29.6
16	60	11	5	1.25	23.1	42.75	50.9
17	30	10	4.5	1.00	11.2	34.54	21.5
18	70	10	4.5	1.00	16.7	45.62	42.3
19	50	8	4.5	1.00	9.1	29.47	14.9
20	50	12	4.5	1.00	19	39.56	41.8
21	50	10	3.5	1.00	16	30.61	27.2
22	50	10	5.5	1.00	17.1	33.35	31.7
23	50	10	4.5	0.50	11.8	33.12	21.7
24	50	10	4.5	1.50	18.4	36.31	37.1
25	50	10	4.5	1.00	16.8	34.88	32.6
26	50	10	4.5	1.00	17.5	35.33	34.3
27	50	10	4.5	1.00	16.1	34.01	30.4
28	50	10	4.5	1.00	17.3	35.01	32.6
29	50	10	4.5	1.00	16.4	34.98	32.9
30	50	10	4.5	1.00	15.9	35.97	31.4

solubilization pH and precipitation pH and time on dry matter, protein content and protein yield. All the experiments were performed in triplicates, and the average values of the responses were calculated and are given in Table 2.

Effect of parameters on dry matter

Experimental runs were performed, and the results were modeled according to a polynomial quadratic equation to identify the variables that affected significantly or non-significantly. The analysis of variance (ANOVA) was performed and is given in Table 3. Determination coefficient ($R^2 = 0.95$) illustrates that only 5% of the total variations are not described by the model. Adjusted determination coefficient (adjusted $R^2 = 0.92$) is also high, which indicates the model is highly significant. As shown in Table 3, the value of lack of fit (0.095) was nonsignificant which implies accuracy of the model. The response surface equation for dry matter obtained after eliminating the nonsignificant terms is:

$$\begin{aligned}\text{Dry Matter} = {} & 16.55 + 1.68A + 2.42B + 0.40C + 2.17D \\ & - 0.83AC + 1.01AD - 1.39BD + 0.77CD \\ & - 0.73A^2 - 0.71B^2 - 0.45D^2\end{aligned}$$

The probability value p is < 0.05 which indicates that the model is significant. The coefficients in the equation indicated that all the parameters significantly affect the dry matter content. The dry matter content was found to increase with the increase in temperature, pH and time. In a work done by Makkar et al. (2008), the increase in temperature increased the dry matter and protein recovery in seed cake when the extraction was carried out at pH 10. In our study as well, there was significant rise in dry matter content when the extractions were carried out at high temperatures. The response surface plots of dry matter content affected by temperature, solubilization pH, time and precipitation pH are shown in Fig. 2.

Effect of parameters on protein content

The protein content of the detoxified seed cake ranged from 30.07 to 45.62%. The second-order polynomial model had a high correlation coefficient ($R^2 = 0.95$), and it indicated that the model fitted suitably with the observed data. The analysis of variance (ANOVA) after omitting the nonsignificant terms is given in Table 4. The 3-D plots of protein content as a function of temperature, solubilization pH, precipitation pH and time are shown in Fig. 3. The response surface equation after removing the nonsignificant terms for protein content is:

$$\begin{aligned}\text{Protein Content} = {} & 34.50 + 2.63A + 2.16B + 0.47C \\ & + 0.99D + 1.80AB + 0.80AC \\ & - 1.17A^2 - 0.85C^2\end{aligned}$$

The coefficients of the first-order term in the equation showed that the protein content of the concentrate increased with the increase in temperature, solubilization pH, precipitation pH and time. An increase in protein content was observed with the increase in temperature which could possibly be due to the reason that high temperatures break the

Table 3 Pooled ANOVA showing the variables as a linear, quadratic and interaction terms on dry matter of *Jatropha* seed cake

Source	Sum of squares	*df*	Mean square	*F* value	*p* value
Model	421.46	11	38.31	34.06	< 0.0001
A—temp	68.01	1	68.01	60.46	< 0.0001
B—solubilization pH	140.17	1	140.17	124.62	< 0.0001
C—precipitation pH	4.00	1	4.00	3.56	0.0755
D—time	112.67	1	112.67	100.17	< 0.0001
AC	11.22	1	11.22	9.98	0.0054
AD	16.40	1	16.40	14.58	0.0013
BD	30.80	1	30.80	27.39	< 0.0001
CD	9.61	1	9.61	8.54	0.0091
A^2	15.23	1	15.23	13.54	0.0017
B^2	14.21	1	14.21	12.64	0.0023
D^2	5.67	1	5.67	5.04	0.0376
Residual	20.25	18	1.12		
Lack of fit	18.15	13	1.40	3.34	0.0957^{ns}
Pure error	2.09	5	0.4187		
Cor total	441.70	29			
				R^2	0.95
				Adj R^2	0.92

ns not significant terms and others are significant at 95% confidence

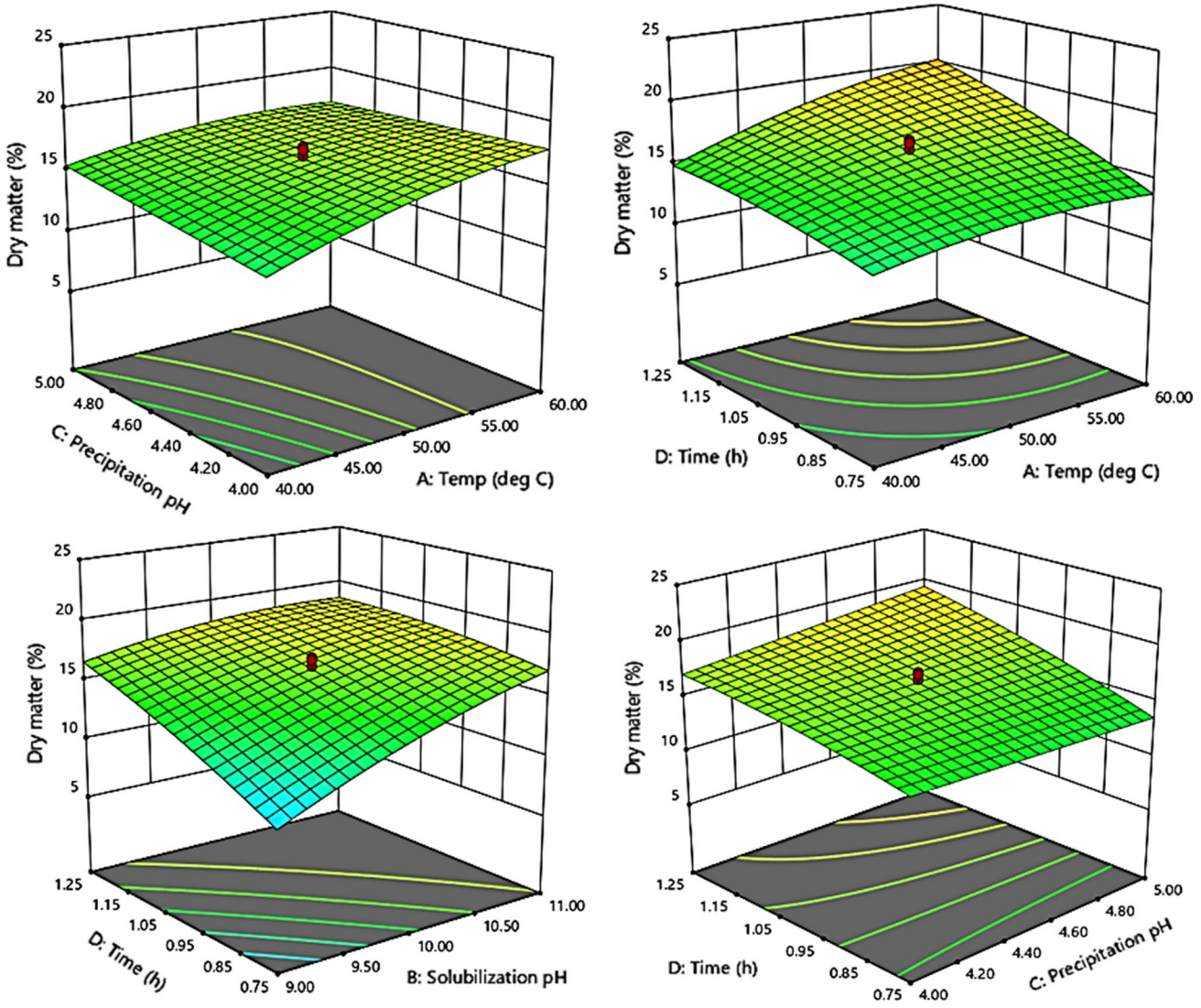

Fig. 2 Response surface plots of dry matter content affected by temperature, solubilization pH, time and precipitation pH

bonds in protein structure which increases the dissolution rate resulting in high protein content (Oliyaei et al. 2017; Liliana et al. 2013). However, temperature beyond a certain range may cause overheating and result in protein denaturation and the addition of impurities which may affect the protein content in the protein concentrate. In our study, temperature up to 70 °C was also found to be suitable for the extraction of proteins from detoxified *Jatropha* seed cake with good protein content.

Many researchers have observed increased protein content at higher pH because of the better solubility of proteins at alkaline pH which may attribute to good protein content in the protein concentrate (Rhee et al. 1972; Gisele et al. 2014). An increase in protein content was also observed with time as longer extraction time results in more solubility of proteins with a good amount of protein. According to Kain et al. (2009), the solubility of proteins is minimum at isoelectric pH because of balance between positive and negative charges which minimizes the repulsion forces among amino acids and thus reduces the solubility of proteins. Rhee et al. (1972) observed a decrease in protein content when the pH was increased beyond the isoelectric point. The positive coefficient of the interaction terms (AB and AC) indicated an increase in protein content with the addition of these variables.

Effect of parameters on protein yield

The analysis of variance (ANOVA) was performed to evaluate the effect of four factors on the protein yield. As shown in Table 5, the value of lack of fit (0.091) was non-significant which implies accuracy of the model. The R^2 and the adjusted R^2 value of the model was 0.96 and 0.94,

Table 4 ANOVA showing the variables as a linear, quadratic and interaction terms on protein content of *Jatropha* seed cake

Source	Sum of squares	*df*	Mean square	*F* value	*p* value
Model	435.99	8	54.50	52.00	< 0.0001
A—temp	165.64	1	165.64	158.03	< 0.0001
B—solubilization pH	112.02	1	112.02	106.87	< 0.0001
C—precipitation pH	5.41	1	5.41	5.16	0.0338
D—time	23.62	1	23.62	22.54	0.0001
AB	52.09	1	52.09	49.70	< 0.0001
AC	10.35	1	10.35	9.88	0.0049
A^2	38.86	1	38.86	37.08	< 0.0001
C^2	20.85	1	20.85	19.89	0.0002
Residual	22.01	21	1.05		
Lack of fit	19.97	16	1.25	3.06	0.1105^{ns}
Pure error	2.04	5	0.4079		
Cor total	458.00	29			
				R^2	0.95
				Adj R^2	0.93

ns not significant terms and others are significant at 95% confidence

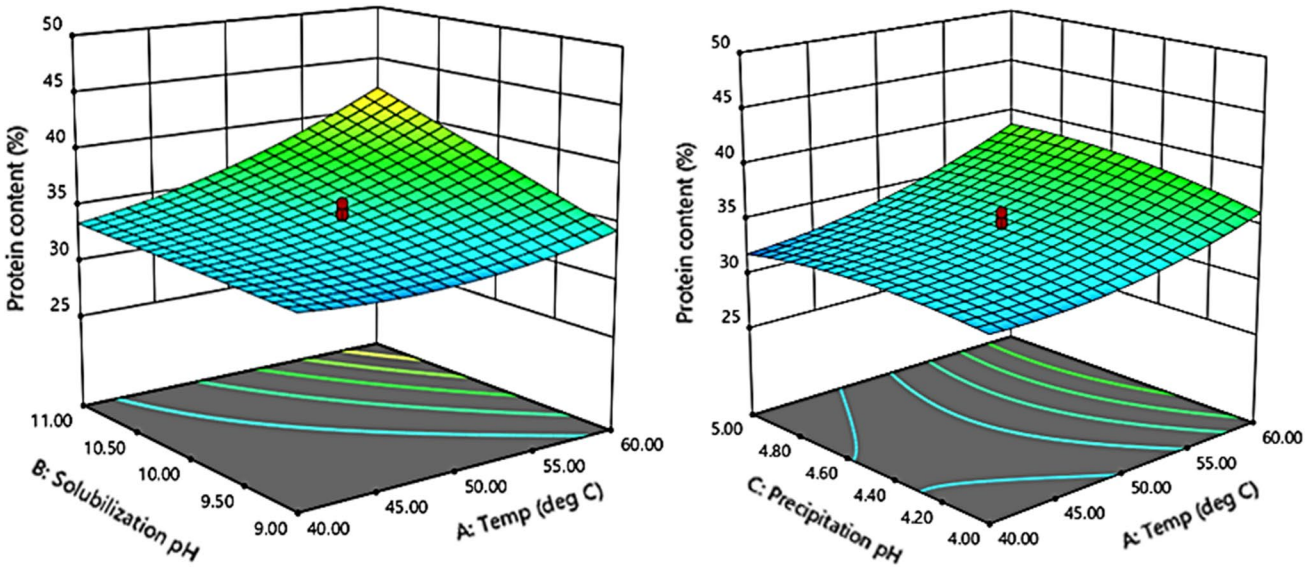

Fig. 3 Response surface plots of protein content affected by temperature, solubilization pH, time and precipitation pH and residual distribution plot

respectively, so it can be conferred that the obtained model is accurate and can be predicted for mentioned response. The independent variables having $p < 0.05$ indicate the significant model terms.

The response surface equation for protein yield after removing the nonsignificant terms in coded values is:

$$\begin{aligned}\text{Protein Yield} = {} & 31.97 + 5.32A + 6.08B + 1.14C + 4.98D \\ & + 2.59AB - 1.29AC + 2.26AD - 2.40BD \\ & + 1.33CD - 1.18B^2 - 0.90C^2 - 0.92D^2\end{aligned}$$

It can be observed from the response equation that all the four independent variables, i.e., temperature (*A*), solubilization pH (*B*), precipitation pH (*C*) and time (*D*), were showing significant effect on the protein yield. The interaction of temperature and solubilization pH had a positive effect on protein yield while all other interaction terms were negative.

As shown in Fig. 4, the increase in protein yield was observed with the increase in process temperature. In a work done by Selling et al. (2013), the highest protein yield (35%) was obtained when pennycress seeds were extracted with

Table 5 ANOVA showing the variables as a linear, quadratic and interaction terms on protein yield of *Jatropha* seed cake

Source	Sum of squares	*df*	Mean square	*F* value	*p* value
Model	2598.74	12	216.56	44.53	< 0.0001
A—temp	680.53	1	680.53	139.94	< 0.0001
B—solubilization pH	885.73	1	885.73	182.14	< 0.0001
C—precipitation pH	31.28	1	31.28	6.43	0.0213
D—time	596.01	1	596.01	122.56	< 0.0001
AB	107.12	1	107.12	22.03	0.0002
AC	26.52	1	26.52	5.45	0.0320
AD	81.90	1	81.90	16.84	0.0007
BD	92.16	1	92.16	18.95	0.0004
CD	28.09	1	28.09	5.78	0.0279
B^2	39.25	1	39.25	8.07	0.0113
C^2	23.13	1	23.13	4.76	0.0435
D^2	23.77	1	23.77	4.89	0.0410
Residual	82.67	17	4.86		
Lack of fit	73.74	12	6.14	3.44	0.0910^{ns}
Pure error	8.93	5	1.79		
Cor total	2681.41	29			
				R^2	0.96
				Adj R^2	0.94

ns not significant terms and others are significant at 95% confidence

water at 77 °C. In another work by Aleksandra et al. (2018), proteins were extracted from rape seed cake and primrose cake using a eutectic solvent and water at different processing temperatures and high yields of protein precipitates were obtained with increasing temperature. The rate of extraction varies linearly with temperature, and the increase in temperature causes molecules to move fast, thereby increasing the mass transfer rate between solid and liquid resulting in good solubility and increased extraction rate. But further increase in temperature resulted in decrease in protein yield. In a work done by Kain et al. (2009), the extraction of proteins from peanut at high temperatures (60 °C) resulted in decrease in protein yield. According to Chenyan et al., (2011), extractions at higher temperatures result in a decline in protein yield which could be due to thermal degradation or denaturation of proteins. In our study, temperature up to 60 °C resulted in a good protein content and protein yield, but as the temperature was further raised to 70 °C, protein yield declined, but the protein content was still higher. pH also plays a significant role on the extraction of proteins and protein yield. As the solubilization pH was increased an increase in protein yield was observed which could be due to increased extractability of proteins. In a study, the extraction of proteins from fish was done by the isoelectric precipitation method and high protein recovery was observed at pH 12 than pH 10 (Oliyaei et al. 2017). Similar results were obtained in various studies where a high protein yield was obtained at high alkaline pH (Martin et al. 2010; Saha et al. 2016; Shaviklo et al. 2017). Different studies have also shown an increase in solubility at precipitation pH. The graphs of precipitation pH indicated a good protein yield at pH 5. This suggests that the isolectric point of *Jatropha* protein is between pH 4.5 and 5 which results in the maximum recovery of the solubilized proteins at this pH. According to Kain et al. (2009), the solubility of proteins is minimum at isolectric pH because of balance between positive and negative charges which minimizes the repulsion forces among amino acids and thus reduces the solubility of proteins. Each protein has its own isoelectric pH depending upon its amino acid composition. Likewise, the method of extraction also affects the isoelectric pH of a particular protein. According to Yu et al. (2007), the maximum amount of peanut protein was extracted from supernatant when the extraction was carried out at pH 4. While in another work reported by Wu et al. (2009), pH 4.5 was found to be the isoelectric pH for the precipitation of peanut protein. The protein yield also increased with the increase in extraction time which is similar to the findings of Qiaoyun et al. 2017 who also observed a sharp increase in protein yield when the extractions were carried out for longer periods.

The interaction terms of solubilization pH and precipitation pH (*BC*) and precipitation pH and time (*CD*) were also found to be positive and significantly affecting the protein yield. It has been cited in many reports that both solubilization pH and precipitation pH influence the solubility properties of proteins in a solution and hence the protein yield. Since the interaction terms of solubilization pH and time

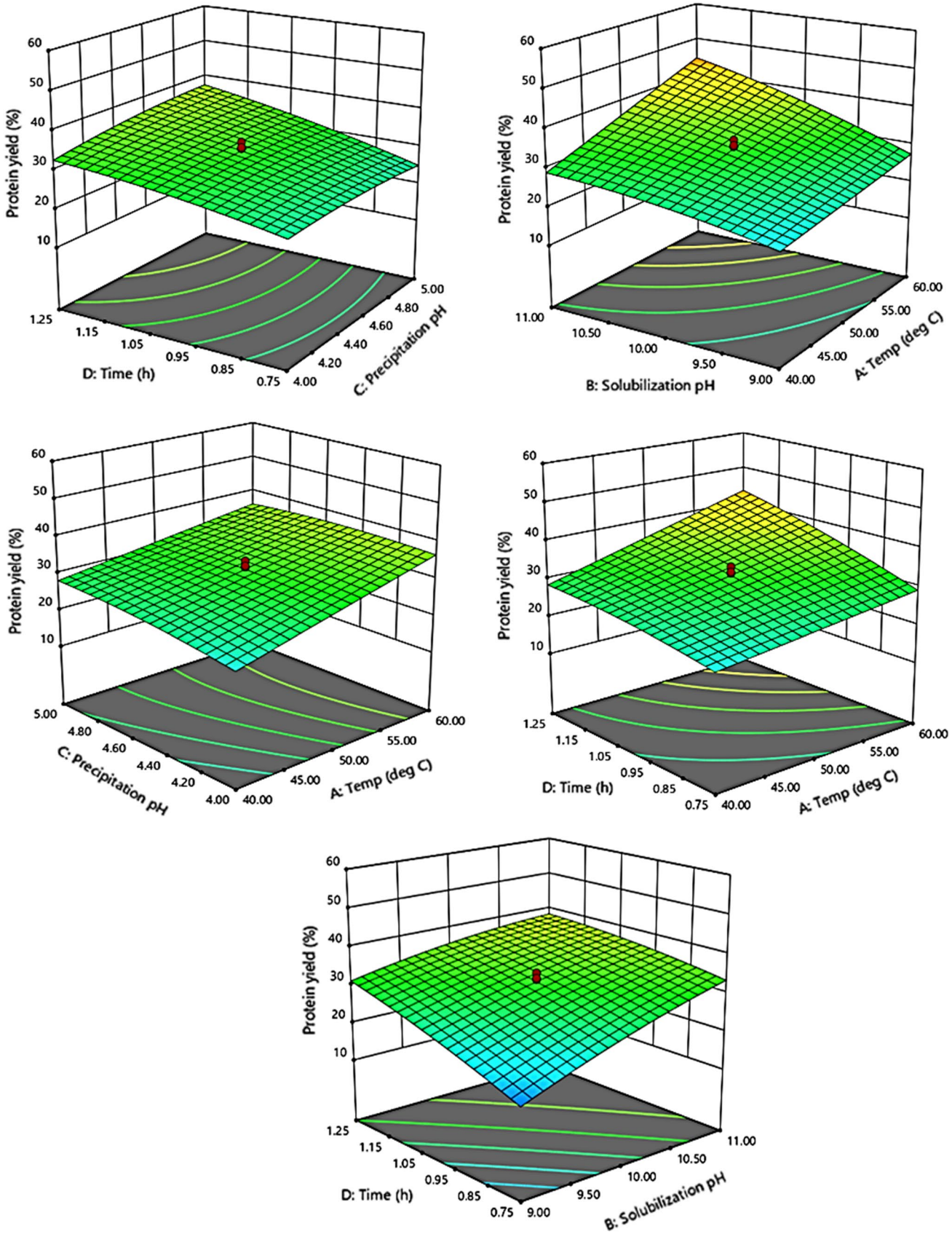

Fig. 4 Response surface plots of protein yield affected by temperature, solubilization pH, time and precipitation pH

were not significant, these factors are not dependant on each other in the chosen range.

Optimization

The optimum values as obtained by differentiation of the quadratic model, for achieving dry matter, protein content and protein yield, were temperature = 60 °C, solubilization pH = 11, time = 0.78 h and precipitation pH = 4.41. The predicted optimal dry matter, protein content and protein yield corresponding to these values were 17.4%, 41.12% and 39.86%, respectively. Additional experiments were performed in triplicates using these optimized levels to verify the accuracy of the model for predicting the three responses, i.e., dry matter, protein content and protein yield. The average of triplicate experiments yielded a dry matter, protein content and protein yield of 17.1%, 41.98% and 38.66%, respectively. In comparison, a good compliance between the experimental and predicted values was observed which confirms the reliability of model as well as the existence of optimal point.

Elemental analysis

Five best samples of dried protein concentrates were selected with the highest protein content and protein yield. These were analyzed for carbon, hydrogen, nitrogen and sulfur contents in CHNSO analyzer (Vario micro tube, Germany). The results are given in Table 6. The highest elemental percentage distribution recorded was 55.94% of carbon, and the lowest was of sulfur 0.19% in sample 2. The nitrogen content of protein concentrates varied from 5.81 to 7.30% while the C/N ratio ranged from 7.36 to 9.62. The lowest C/N ratio was obtained for sample 5 which is in suitable range for the application in soil amendments. Low C/N ratio allows fast mineralization which allows plants to take up nutrients easily but as the ratio increases, the decomposition and mineralization slow down.

Table 6 CHNS analysis of protein concentrates

	Samples				
	1	2	3	4	5
N (%)	6.33	5.81	5.90	6.75	7.30
C (%)	53.79	55.94	54.94	55.43	53.75
H (%)	7.21	8.41	8.32	8.43	8.05
S (%)	0.29	0.19	0.39	0.50	0.67
Protein (%)	39.56	36.31	36.87	42.18	45.62
N area	13,664	16,999	15,528	20,345	16,993
C area	71,450	102,715	90,143	106,530	78,773
H area	31,311	51,201	45,077	53,763	38,781
S area	23,970	23,639	29,308	35,801	36,130
C/*N* ratio	8.49	9.62	9.31	8.21	7.36
C/*H* ratio	7.46	6.64	6.59	6.57	6.68

Amino acid analysis

Amino acid composition of protein concentrates is an indicative of their nutritional value. The concentrations of amino acids (essential and nonessential) in all the samples (five best and optimized) varied considerably indicating the effect of extraction conditions on the structure and solubility of amino acids (Table 7). However, it was observed that *Jatropha* seed cake contained higher amounts of nonessential amino acids than essential amino acids. Leucine, valine, phenylalanine, isoleucine were the major essential amino acids found in all the samples of protein concentrates while the concentration of glutamic acid (10.92 g/100 g) and arginine (7.18 g/100 g) was higher in nonessential amino acids in *Jatropha* protein concentrates. Similar results were also observed by Makkar et al. (2008) and Ugbogu et al. (2014), who have reported higher percentages of these amino acids (leucine, valine, phenylalanine, isoleucine) in *Jatropha* seed cake which suggests that *Jatropha* seed cake can serve as a good source of these essential amino acids. Based on the results obtained for samples 1 and 2, it was observed that during the extraction of proteins, solubilization pH more toward alkaline side resulted in better recovery of amino acids from the protein concentrates. However, in case of tryptophan, acidic pH during extraction affected its content as lower pH leads to its degradation (Csapo et al. 2008). Sample 5 was found to have higher content of essential amino acids than sample 1 indicating the extraction of proteins at 60 °C didn't affect the amino acid concentration. According to Line et al. (2018), in the production of specialized protein products, heating at high temperatures resulted in oxidation, loss of cysteine, tryptophan and methionine which indicated that high temperatures lead to many undesirable physical and chemical changes. In a study by Beuk et al. (1948), there was complete retention of all amino acids (except cysteine) when the samples were autoclaved suggesting the thermo stability of amino acids except cysteine. Comparing the results obtained for sample 4 and sample 5, the amount of amino acids in sample 5 was higher than in sample 4 which suggested that the extraction of proteins at pH 5 (precipitation pH) is more efficient than at pH 4.

When the extraction pH was decreased slightly from 5 to 4.41, it was observed that the yield was comparable in 0.78 h (optimized sample, Table 7) to that of pH 5 in 1.25 h (sample 5, Table 7). This indicates that higher yield of amino acids can be obtained in less treatment time with slight variation in pH under same set of conditions. Further, these optimized conditions were validated with triplicate samples and found to be the best, yielding the maximum essential as well as nonessential amino acids, and the values were close to FAO/

Table 7 Amino acid content of five protein concentrate samples and optimized sample

S. no.	Amino acids	Concentration (g/100 g)					
		Sample 1 (50 °C, 12, 4.5, 1 h)	Sample 2 (50 °C, 10, 4.5, 1.5 h)	Sample 3 (60 °C, 11, 5, 0.75 h)	Sample 4 (60 °C, 11, 4, 1.25 h)	Sample 5 (60 °C, 11, 5, 1.25 h)	Optimized sample (60 °C, 11, 4.41, 0.78 h)
Essential							
1	Histidine (His)	1.21 ± 0.19	1.09 ± 0.46	1.19 ± 0.09	1.38 ± 0.69	1.45 ± 0.70	1.49 ± 0.51
2	Isoleucine (Ile)	2.32 ± 0.42	1.70 ± 0.71	2.28 ± 1.19	2.57 ± 2.19	2.63 ± 2.21	2.57 ± 0.30
3	Leucine (Leu)	3.91 ± 0.07	3.59 ± 2.17	3.94 ± 0.17	4.44 ± 2.28	4.63 ± 2.19	4.40 ± 0.98
4	Lysine (Lys)	1.40 ± 0.17	1.37 ± 0.72	1.43 ± 0.04	1.73 ± 0.75	1.82 ± 0.81	1.70 ± 0.06
5	Methionine (Met)	0.81 ± 0.01	0.64 ± 0.80	0.69 ± 0.57	0.73 ± 1.24	0.84 ± 0.12	0.75 ± 1.08
6	Phenylalanine (Phe)	2.51 ± 0.65	2.21 ± 1.35	1.44 ± 0.10	2.82 ± 1.26	2.91 ± 0.88	2.88 ± 0.75
7	Threonine (Thr)	1.77 ± 0.89	1.20 ± 0.00	–	2.17 ± 0.00	2.10 ± 2.60	2.15 ± 1.10
8	Tryptophan (Trp)	0.31 ± 0.00	0.29 ± 0.00	0.46 ± 0.00	0.51 ± 0.00	0.57 ± 0.00	0.51 ± 0.00
9	Valine (Val)	2.78 ± 0.41	2.23 ± 2.83	2.44 ± 1.43	2.87 ± 2.45	2.96 ± 2.75	2.84 ± 1.23
	Total EAA	17.58	14.36	13.89	19.26	19.94	19.32
Nonessential							
1	Alanine (Ala)	2.48 ± 0.27	2.20 ± 0.98	2.38 ± 0.04	2.72 ± 1.35	2.89 ± 1.33	2.78 ± 0.88
2	Arginine (Arg)	5.74 ± 0.87	5.38 ± 0.69	6.29 ± 0.67	6.66 ± 1.71	7.18 ± 2.07	6.70 ± 0.82
3	Aspartate (Asp)	4.61 ± 0.42	–	–	–	5.71 ± 0.00	5.53 ± 0.01
4	Cysteine (Cys)	0.59 ± 0.24	0.84 ± 0.10	0.94 ± 0.22	0.79 ± 0.59	0.67 ± 1.32	0.72 ± 0.72
5	Glutamic acid (Glu)	8.86 ± 0.32	8.37 ± 0.00	4.94 ± 0.00	9.95 ± 0.00	10.92 ± 3.95	10.04 ± 0.12
6	Glutamine (Gln)	–	–	3.99 ± 0.00	–	–	–
6	Glycine (Gly)	2.56 ± 0.45	2.32 ± 0.41	2.46 ± 0.33	2.84 ± 1.31	2.99 ± 1.21	2.82 ± 1.01
7	Proline (Pro)	1.33 ± 0.18	1.06 ± 0.46	1.11 ± 1.61	1.46 ± 0.40	1.46 ± 0.10	1.46 ± 0.75
8	Serine (Ser)	2.16 ± 1.00	1.55 ± 0.00	2.76 ± 0.00	3.02 ± 2.88	3.00 ± 0.66	3.03 ± 0.98
9	Tyrosine (Tyr)	1.48 ± 0.13	1.37 ± 0.37	1.62 ± 1.82	1.91 ± 0.60	1.99 ± 0.88	1.94 ± 0.65
10	Phosphoserine (p-Ser)	0.17 ± 0.08	0.12 ± 0.15	0.08 ± 0.00	–	0.24 ± 0.00	0.19 ± 0.02
11	Phospho ethanol amine (PEA)	0.01 ± 0.02	0.03 ± 0.00	0.04 ± 0.00	–	0.009 ± 0.00	–
12	α-Amino-n-adipic acid (a-AAA)	0.024 ± 0.00	–	–	–	–	–
13	α-Amino-*n*-butaric acid (a-ABA)	0.05 ± 0.02	0.04 ± 0.01	0.07 ± 0.16	0.07 ± 0.12	0.07 ± 0.12	0.07 ± 0.17
14	Cystathionine (Cysthi)	0.09 ± 0.00	8.04 ± 0.10	0.13 ± 0.53	0.12 ± 0.20	0.67 ± 1.32	0.44 ± 0.20
15	β-Alanine (b-Ala)	0.04 ± 0.03	0.05 ± 0.01	0.06 ± 0.05	0.03 ± 0.11	0.12 ± 0.00	0.04 ± 0.02
16	β-Amino isobutyric acid (b-AiBA)	0.03 ± 0.00	1.00 ± 0.00	0.11 ± 0.00	0.03 ± 0.00	0.05 ± 0.09	0.03 ± 0.05
17	ϒ-Amino butyric acid (g-AiBA)	0.01 ± 0.00	0.01 ± 0.01	0.009 ± 0..04	0.02 ± 0.00	0.01 ± 0.00	0.02 ± 0.01
18	Ethanol amine ($EOHNH_2$)	0.01 ± 0.00	0.01 ± 0.00	0.04 ± 0.00	0.05 ± 0.00	0.05 ± 0.00	0.05 ± 0.00
19	Ornithine (Orn)	0.04 ± 0.00	0.03 ± 0.04	0.03 ± 0.03	0.03 ± 0.02	0.03 ± 0.04	0.03 ± 0.06
20	1 Methyl histidine (1 Mehis)	0.08 ± 0.00	0.08 ± 0.00	0.06 ± 0.00	0.04 ± 0.00	0.05 ± 0.00	0.05 ± 0.00
21	Hydroxyproline (Hypro)	–	0.036 ± 0.00	–	0.04 ± 0.00	–	–
	Total	30.44	24.50	27.18	29.78	38.20	35.98

The range of detection of amino acids by the analyzer was 0.5–2 nM. The values presented here are within this range

WHO reference (1985; report 935), and thus, *Jatropha* proteins can therefore be used as feed supplement.

Conclusion

Various parameters such as temperature, solubilization pH, precipitation pH, and extraction time were tested for the extraction of proteins from the bio-detoxified *Jatropha* seed cake. The extraction was optimized using CCRD model of RSM. Four factors at five levels were allowed to interact in a set of 30 experiments. Multivariate ANOVA indicated that temperature and pH were the significant parameters affecting the protein content and protein yield. The optimum values of temperature, solubilization pH, precipitation pH and time for the extraction of protein from detoxified *Jatropha* seed cake were 60 °C, 11.0, 4.41 and 0.78 h, respectively, which yielded the maximum dry matter, protein content and protein yield of 17.1%, 41.98% and 38.66%, respectively. Elemental analysis showed the highest nitrogen and sulfur content of 7.3% and 0.67%, respectively, in sample 5. Amino acid contents were determined, and the results elaborate that though the extraction procedure affected the amino acid content, yet the values were close to FAO/WHO reference. The overall essential amino acid content was 19.32 g/100 g while the nonessential amino acids constituted 35.98 g/100 g under the optimized conditions of extraction. These *Jatropha* proteins can be used as food and feed supplement. Though this is a small step toward the essence of creating healthy environment and healthy livestock for future, further studies need to be carried out to ascertain the effect of these supplements on the overall health of animals. However, the present study indicates the high possibilities of supplementing the feed with essential amino acids, and the avenues for nutraceutical research are widely open for the development of suitable food and feed formulations.

Acknowledgements The first two authors acknowledge DTU and UGC for providing research fellowships.

References

AACC (2000) Approved methods of American Association of Cereal Chemists. American Association of Cereal Chemists Inc., St. Paul

Achten WMJ, Almeida J, Fobelets V, Bolle E, Mathijs E, Singh VP, Tewari DN, Verchot LV, Muys B (2010) Life cycle assessment of Jatropha biodiesel as transportation fuel in rural India. Appl Energy 87(12):3652–3660

Ahluwalia S, Sharma JG, Singh P (2017) Degradation of phorbol esters In *Jatropha* seed cake by *Pseudomonas aeruginosa* DS1. Int J Pharm Bio Sci 8(2):542–546

Ahluwalia S, Sharma JG, Singh P (2018) Modeling and Analysis of critical factors for phorbol ester degradation in *Jatropha* seed cake using ISM and MICMAC. Int J Environ Waste Manag 21(4):287–305

Aleksandra G, Eduardo M, Angel C, Radosław G, Filip B, Avtar SM (2018) Enhanced protein extraction from oilseed cakes using glycerol-choline chloride deep eutectic solvents: a biorefinery approach. ACS Sustain Chem Eng 6(11):15791–15800. https://doi.org/10.1021/acssuschemeng.8b04359

Beuk JF, Chornock FW, Rice EE (1948) The effect of severe heat treatment upon the amino acids of fresh and cured pork. J Biol Chem 175:291–298

Calull M, Fabregas J, Marce RM, Borrull F (1991) Determination of free amino acids by precolumn derivatization with phenylisothiocyanate. Application to wine samples. Chromatographia 31:272–276

Chen J, Huang PT, Zhang KY, Ding FR (2012) Isolation of biosurfactant producers, optimization and properties of biosurfactant produced by Acinetobacter sp. from petroleum-contaminated soil. J Appl Microbiol 112:660–671

Chenyan LV, Xiaoling J, Meiliang L, Jingyun Y, Guanghua Z (2011) Optimization of extraction process of crude protein from grape seeds by RSM. Food Sci Technol Res 17(5):437–445

Csapo J, Csapo ZK, Albert C, Loki K (2008) Hydrolysis of proteins performed at high temperatures and for short times with reduced racemization, in order to determine the enantiomers of D- and L-amino acids. Acta Univ Sapientiae Aliment 1:31–48

Devappa RK, Swamylingappa B (2008) Biochemical and nutritional evaluation of *Jatropha* protein isolate prepared by steam injection heating for reduction of toxic and antinutritional factors. J Sci Food Agric 88:911–919

Gabriele G, Markus S, Andreas S (2015) Characterization of *Jatropha curcas* L. Protein cast films with respect to packaging relevant properties. Int J Political Sci 2015:1–9. https://doi.org/10.1155/2015/630585

Ghosh A, Chikara J, Chaudhary DR (2012) Value addition of Jatropha cake and its utilisation as manure in Jatropha and other crops. In: Carels N, Sujatha M, Bahadar B (eds) Jatropha, challenges for a new energy crop. Farming, economics and biofuel, vol 1. Springer, New York

Gisele LAM, Roseli SL, Hulda NCM, Patricia AC, Ana MQBB, Catarina AG, Paulo JAS (2014) Effect of alkaline agent and pH on the composition of freeze-dried proteins extracted from castor bean (*Ricinus communis L.*) cake. Chem Eng Trans 37:697–702

Gofferje G, Klingele S, Stabler A, Schweiggert-Weisz U, Floter E (2014) Comparison of two protein extraction techniques utilizing aqueous de-oiled residue from *Jatropha* curcas L. Waste Biomass Valor 5:33–41

Hamarneh AI, Heeres HJ, Broekhuis AA, Picchioni F (2010) Extraction of *Jatropha* curcas proteins and application in polyketone-based wood adhesives. Int J Adhes Adhes 30:615–625

Jakub E, Petr S, Magdalena DV, Lukas PA, Petr S, Jindrich K, Zdenek HD, Martin B, Eliska K (2016) Jatropha seed cake and organic waste compost: the potential for improvement of soil fertility. Ecol Chem Eng S 23(1):131–141

Jimenez ME, Ruiz J, Perez Palacios T, Silva A, Antequera T (2012) Gas chromatography-mass spectrometry method for the determination of free amino acids as their dimethyl-tert-butylsilyl (TBDMS) derivatives in animal source food. J Agric Food Chem 60:2456–2463

Joint FAO/WHO/UNU expert consultation: Protein and amino acid requirements in human nutrition: report, World Health Organization, 1985 (WHO technical report series, no. 935)

Kain RJ, Chen Z, Sonda TS, Abu-Kpawoh JC (2009) Study on the effects of enzymatic hydrolysis on the physical, functional and chemical properties of peanut protein isolates extracted from defatted heat pressed peanut meal flour (*Arachis hypogaea L.*). Pak J Nutr 8(6):818–825

Krumpochova P, Bruyneel B, Molenaar D, Koukou A, Wuhrer M, Niessen WM, Giera M (2015) Amino acid analysis using chromatography-mass spectrometry: an inter platform comparison study. J Pharm Biomed Anal 114:398–407. https://doi.org/10.1016/j.jpba.2015.06.001

Lars IN, Pia V, Jens OD (2004) Quantification of organic and amino acids in beer by 1H NMR spectroscopy. Anal Chem 76(16):4790–4798

Lestari D, Mulder W, Sanders J (2010) Improving *Jatropha curcas* seed protein recovery by using counter current multistage extraction. Biochem Eng J 50(1–2):16–23

Lestari D, Mulder WJ, Sanders JPM (2011) *Jatropha* seed protein functional properties for technical applications. Biochem Eng J 53(3):297–304

Liliana LL, Gloria DO, Cristian JM, Humberto HS (2013) Sequentially integrated optimization of the conditions to obtain a high-protein and low-antinutritional factors protein isolate from edible *Jatropha curcas* seed cake. ISRN Biotechnol 2013:1–7

Line RN, Marianne NL, Michael JD, Jacob HN, Soren BN (2018) Effect of free cysteine on the denaturation and aggregation of holo α-lactalbumin. Int Dairy J 79:52–61

Makkar HPS, Becker K (2009) *Jatropha curcas*, a promising crop for the generation of biodiesel and value-added coproducts. Eur J Lipid Sci Technol 111(8):773–787

Makkar HPS, Francis G, Becker K (2008) Protein concentrate from *Jatropha curcas* screw-pressed seed cake and toxic and anti-nutritional factors in protein concentrate. J Sci Food Agric 88:1542–1548

Manyuchi MM, Mbohwa C, Muzenda E (2018) Bio stabilization of Jatropha Curcas Cake to bio fertilizers through vermicomposting. In: Proceedings of the international conference on industrial engineering and operations management, Paris, France, 26–27 July 2018, pp 9–13

Martin AMM, Israel LM, Samuel RM (2010) Optimization of protein concentrate preparation from Bambara bean using Response Surface Methodology. J Food Process Eng 33:398–412

Mati M, Staruch L, Soral M (2015) Use of NMR spectroscopy in the analysis of carnosine and free amino acids in fermented sausages during ripening. Chem Pap 69(10):1319–1324. https://doi.org/10.1515/chempap-2015-0148

Monia SA, Siluana KTS, Gabriela R, Claudia BB, Marcel P, Luciano VG, de Daniel BF et al (2017) Free amino acid determination by GC-MS combined with a chemometric approach for geographical classification of bracatinga honeydew honey (*Mimosa scabrella Bentham*). Food Control 78:383–392

Oliyaei N, Ghorbani M, Moosavi-Nasab M, Sadeghimahoonak AR, Maghsoudloo Y (2017) Effect of temperature and alkaline pH on the physicochemical properties of the protein isolates extracted from the whole ungutted Lanternfish (*Benthosema pterotum*). J Aquat Food Prod Technol 26(10):1134–1143. https://doi.org/10.1080/10498850.2014.940564

Qiaoyun CUI, Xinghong NI, Liang Z, Zheng TU, Jin L, Kang S, Xuan C, Xinghui LI (2017) Optimization of protein extraction and decoloration conditions for Tea residues. Horticul Plant J 3(4):172–176

Rhee KC, Cater CM, Mattil KF (1972) Simultaneous recovery of protein and oil from raw peanuts in an aqueous system. J Food Sci 37:90–93

Saha J, Chakraborty S, Deka SC (2016) A comparative study between Response Surface Methodology and genetic algorithm in optimization and extraction of leaf protein concentrate from *Diplazium esculentum* of Assam. Int J Biotechnol Wellness Ind 5:111–120

Selling GW, Hojilla-Evangelista MP, Evangelista R, Isbell T, Price N, Doll KM (2013) Extraction of proteins from pennycress seeds and press cake. Ind Crop Prod 41:113–119

Shaviklo AR, Rezapanah S, Motamedzadegan A, DamavandiKamali N, Mozafari H (2017) Optimum conditions for protein extraction from tuna processing by-products using isoelectric solubilization and precipitation processes. Iran J Fish Sci 16(2):774–792

Sugiki T, Kobayashi N, Fujiwara T (2017) Modern technologies of solution nuclear magnetic resonance spectroscopy for three-dimensional structure determination of proteins open avenues for life scientists. Comput Struct Biotechnol J 15:328–339. https://doi.org/10.1016/j.csbj.2017.04.001

Tateda N, Matsuhisa K, Hasebe K, Kitajima N, Miura T (1998) High performance liquid chromatographic method for rapid and highly sensitive determination of histidine using postcolumn fluorescence detection with o-phthaldialdehyde. J Chromatogr B 718:235–241

Ugbogu AE, Akubugwo EI, Uhegbu FO, Chinyere CG, Ugbogu OC, Oduse KA (2014) Quality assessment profile of *Jatropha curcas* (L) seed oil from Nigeria. Int Food Res J 21(2):735–741

Vilches AP, Norstrom SH, Bylund D (2017) Direct analysis of free amino acids by mixed-mode chromatography with tandem mass spectrometry. J Sep Sci 40(7):1482–1492. https://doi.org/10.1002/jssc.201601097

Wu H, Wang Q, Ma T, Ren J (2009) Comparative studies on the functional properties of various proteins concentrate preparations of peanut protein. J Food Res Int 42:343–348

Yinuo Z, Yubao W, Haifeng W, Yueming W, Harinder PM, Jianxin L (2018) Nutritional value of detoxified *Jatropha curcas* seed cake protein isolates using rats as an animal model. Anim Nutr 4:429–434

You Shin S, Won-Jin Y, Jaeho H, Dongwon S, Kwang-Won L, Woo-Young L, Kwang-Il K et al (2013) Method validation of 16 types of structural amino acids using an automated amino acid analyzer. Food Sci Biotechnol 22(6):1567–1571

Yu J, Aahmedna M, Goktepe I (2007) Peanut proteins concentrate: production and functional properties as affected by processing. Food Chem 103:121–129

View publication stats

JOC The Journal of Organic Chemistry

Subscriber access provided by DELHI TECH UNIV

Article

Phosphazene Superbase-mediated Regio- and Stereoselective Iodoaminocyclization of 2-(1-Alkynyl)benzamides for the Synthesis of Isoindolin-1-ones

Saurabh Mehta, and Dhirendra Brahmchari

J. Org. Chem., **Just Accepted Manuscript** • DOI: 10.1021/acs.joc.9b00452 • Publication Date (Web): 15 Apr 2019

Downloaded from http://pubs.acs.org on April 20, 2019

Just Accepted

"Just Accepted" manuscripts have been peer-reviewed and accepted for publication. They are posted online prior to technical editing, formatting for publication and author proofing. The American Chemical Society provides "Just Accepted" as a service to the research community to expedite the dissemination of scientific material as soon as possible after acceptance. "Just Accepted" manuscripts appear in full in PDF format accompanied by an HTML abstract. "Just Accepted" manuscripts have been fully peer reviewed, but should not be considered the official version of record. They are citable by the Digital Object Identifier (DOI®). "Just Accepted" is an optional service offered to authors. Therefore, the "Just Accepted" Web site may not include all articles that will be published in the journal. After a manuscript is technically edited and formatted, it will be removed from the "Just Accepted" Web site and published as an ASAP article. Note that technical editing may introduce minor changes to the manuscript text and/or graphics which could affect content, and all legal disclaimers and ethical guidelines that apply to the journal pertain. ACS cannot be held responsible for errors or consequences arising from the use of information contained in these "Just Accepted" manuscripts.

ACS Publications

is published by the American Chemical Society. 1155 Sixteenth Street N.W., Washington, DC 20036

Published by American Chemical Society. Copyright © American Chemical Society. However, no copyright claim is made to original U.S. Government works, or works produced by employees of any Commonwealth realm Crown government in the course of their duties.

Phosphazene Superbase-mediated Regio- and Stereoselective Iodoaminocyclization of 2-(1-Alkynyl)benzamides for the Synthesis of Isoindolin-1-ones

Saurabh Mehta,* and Dhirendra Brahmchari

Department of Applied Chemistry, Delhi Technological University, Delhi, 110042 India

Abstract

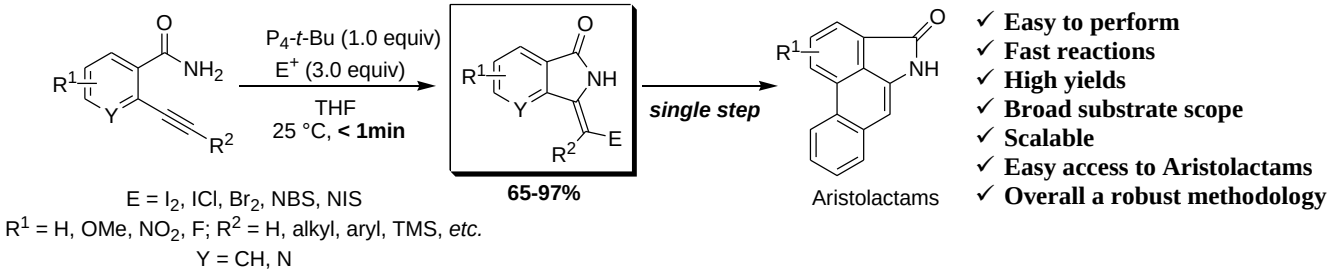

Phosphazene superbase P_4-*t*-Bu mediated iodoaminocyclization of 2-(1-alkynyl)benzamides is reported. The reaction works under ambient conditions, and instantaneously results in the synthesis of isoindolin-1-ones in 65-97% yields, in a regio- and stereoselective manner. The exclusive formation of products with *Z*-geometry (across the exo C=C bond) has been confirmed through X-ray crystallography. The methodology also provides an easy access to Aristolactams, an important class of natural products. This has been successfully demonstrated by synthesizing two Aristolactam derivatives (including Cepharanone B).

Introduction

Isoindolinones, also known as phathalimidines, are important nitrogenous compounds. This important heterocyclic scaffold is present in many pharmacologically important natural products such as Isoindolinomycin (Idm) **(I)**,[1] Lennoxamine **(II)**,[2]

Aristolactams **(III)**,[3] *etc*.[4] (Figure 1). Additionally, several medicinally important synthetic compounds containing isoindolin-1-ones scaffold are also known, such as Chlortalidone **(IV)**,[5] Dopamine receptor ligand (*S*)-PD 172938 **(V)**,[6] Pagoclone (Cl-1043) **(VI)**,[7] Pazinaclone **(VII)**,[8] *etc*.[9] (Figure 1).

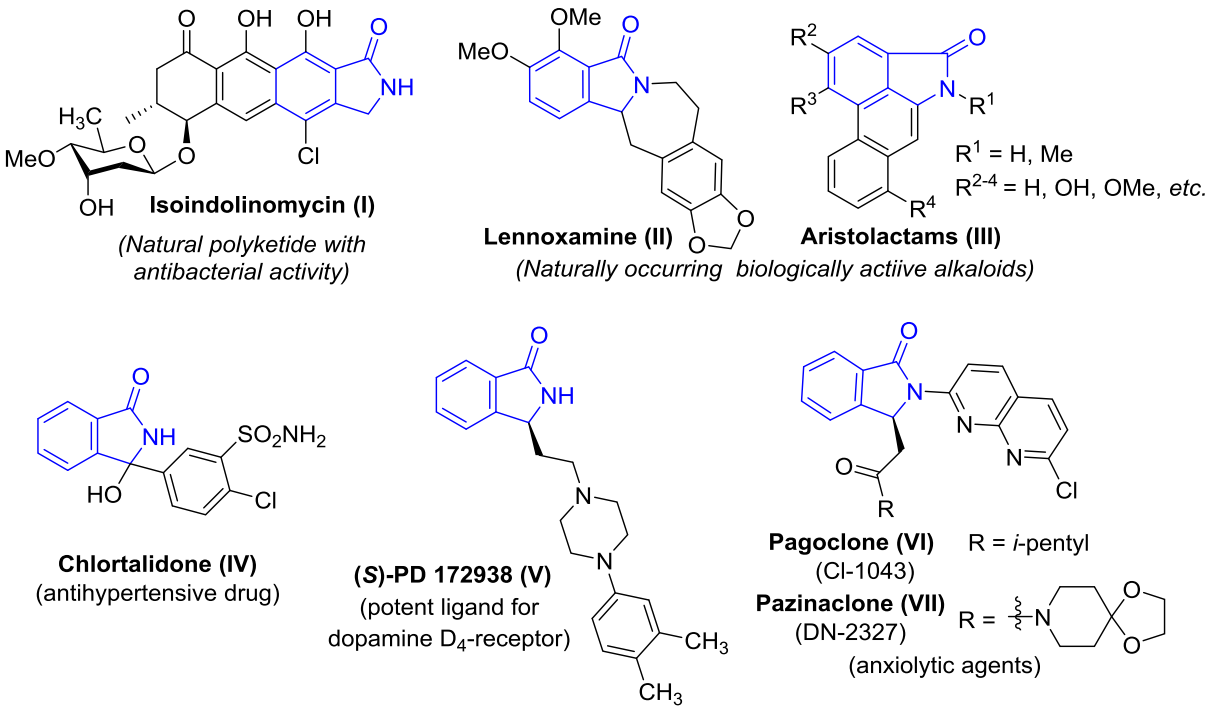

Figure 1. Selected examples of natural (I-III) and synthetic (IV-VII) biologically active compounds with the isoindolin-1-one skeleton.

Due to the medicinally privileged nature of isoindolinone scaffold, several synthetic organic as well as medicinal researchers have reported various interesting approaches for the synthesis of the isoindolin-1-ones.[10-16] Also, various alkyne annulation reactions, such as metal-catalyzed annulations,[17-20] base-mediated annulations,[21-23] aza-conjugate additions,[24,25] *etc*. have been extensively used for synthesizing a variety of isoindolinone derivatives.

Electrophilic cyclization reactions of functionalized alkynes have emerged as very useful synthetic tools in organic chemistry.[26-28] Over the years, we have been interested in developing novel strategies for the synthesis of heterocyclic and polyheterocyclic compounds through iodocyclization methodology.[29,30] More particularly, we and others have studied the

synthesis of isoindolinones and their regio-isomeric cyclic imidates, through the electrophilic cyclization reactions of *o*-alkynyl benzamides.[31-35] In this context, it may be noted that Amide group ($-CONH_2$) is known to be an ambident nucleophile.[36-42] Further, it may be summarized that the cyclization of *o*-alkynyl benzamides in the absence of a base (using NIS in DCM),[31] or in presence of weak base (using I_2/ICl with $NaHCO_3$ in MeCN),[32-34] leads to the *O*-cyclization yielding the corresponding cyclic imidates (Scheme 1a). It may also be noted that some of these cyclic imidates were mis-characterized as isoindolinones and isoquinolones before[32] and this was later corrected by us and also by Opatz *et al*.[33,34] Furthermore, we later accomplished the *N*-cyclization for *o*-alkynyl benzamide substrates by using a stronger base *n*-BuLi with I_2/ICl (Scheme 1b).[35] Although the use of BuLi worked reasonably well, the scope of the methodology was found to be limited with respect to the substrate functionality, for example the substrates with trimethylsilyl (TMS) or bromo (-Br) groups did not yield the desired products. Also, the reaction yields were moderate in most cases. Moreover, *n*-BuLi being a highly reactive reagent, is difficult to handle, and is not a preferred choice of synthetic/industrial chemists.

We believe that due to the ambident nature of the amide group, it is still a synthetic challenge to accomplish an efficient and regioselective *N*-cyclization for the alkynyl amides and related substrates.[39-42] Moreover, we think that there is still scope for the development of a robust methodology for the synthesis of isoindolin-1-ones, especially one that allows further diversification, and possible extension to natural product synthesis. Therefore, we decided to develop a simple, straight-forward and efficient methodology for the iodoaminocyclization of *o*-alkynyl benzamides. We wondered if the use of an organic, non-nucleophilic superbase would be suitable for such iodocyclizations. One important class of such superbases is phosphazenes, which are very strong, metal free, non-nucleophilic bases.[43-45] In this context, one member of the phosphazene superbase family, namely P_4-*t*-Bu

(Figure 2) is particularly established as an extremely strong (pK_a = 42.7 in MeCN) and useful superbase in organic synthesis.[46,47]

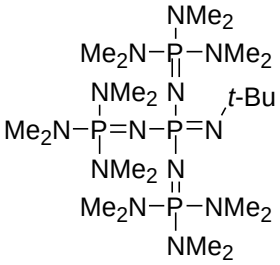

Figure 2. Phosphazene Superbase P_4-*t*-Bu.

Upon a thorough search of the literature, we didn't find any report of the use of a superbase in iodocyclization of functionally-substituted alkynes. Although we came across a few papers where Terada *et al.* reported superbase-catalyzed intramolecular cyclization of *o*-alkynylphenyl ethers[48] and *o*-alkynylbenzamides,[49] however, no electrophiles (other than H^+) were explored for that methodology. Also, in many cases mixtures of *E*/*Z* stereoisomers were obtained as a result of cyclization reaction of *o*-alkynylbenzamides (Scheme 1c).[49] Therefore, we decided to explore the use of P_4-*t*-Bu in halocyclization reactions, and here we report the results of our studies on superbase P_4-*t*-Bu mediated stereo- and regioselective halocyclization reactions of 2-(1-alkynyl) benzamides (Scheme 1d).

Scheme 1. Base-mediated Cyclizations of 2-(1-Alkynyl)benzamides

(a) Electrophilic Cyclization of 2-(1-Alkynyl)benzamides yielding Cyclic Imidates[33]

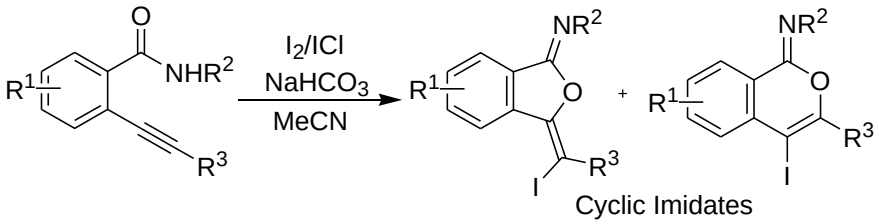

(b) *n*-Butyl Lithium-mediated Iodocyclization of 2-(1-Alkynyl)benzamides Generating isoindolin-1-ones[35]

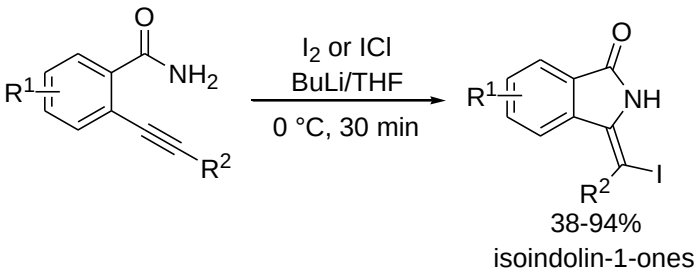

38-94%
isoindolin-1-ones

(c) P_4-*t*-Bu Catalyzed Cyclization of *o*-Alkynylbenzamide forming isoindolinones[49]

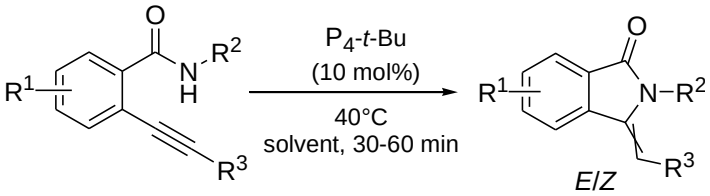

E/*Z*

(d) Present work: P_4-*t*-Bu mediated Stereoselective Electrophilic Cyclization of *o*-Alkynylbenzamides

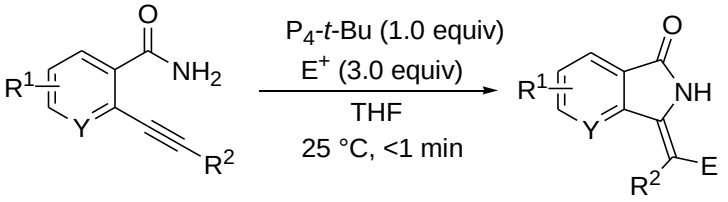

Stereoselective

Results and Discussion

The starting materials, 2-(1-alkynyl)benzamides, were prepared through a two-step strategy (Scheme 2). It involved the reaction of commercially available *o*-halobenzoic acids **(1a-1e)** with thionyl chloride, followed by the reaction with ammonia/primary amine, resulting in the formation of *o*-halobenzamides **(2a-2g),** which were then subjected to Sonogashira coupling[50] with appropriate terminal alkyne **(3)** affording *o*-alkynylbenzamides **(4a-4aa)** in good to excellent yields (Table 1).

Scheme 2. Strategy for the Synthesis of 2-(1-alkynyl)benzamides[a]

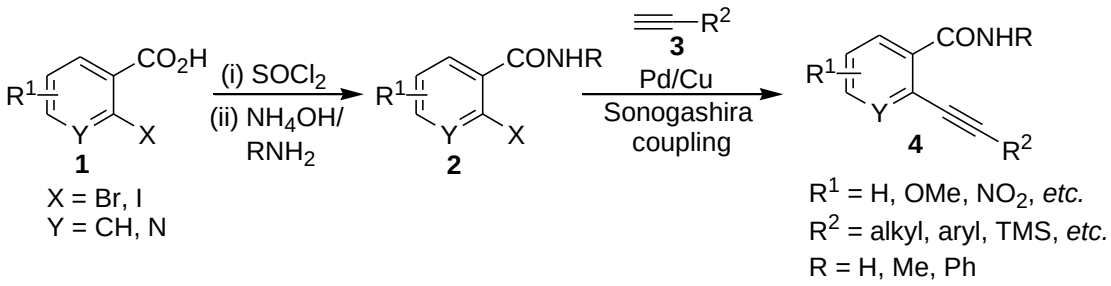

Table 1. Sonogashira Coupling: Preparation of 2-(1-Alkynyl)benzamides[a]

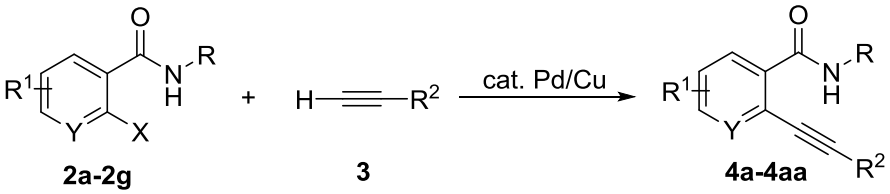

entry	product	Y	R^1	R	R^2	isolated yield
1	**4a**	CH	H	H	Ph	96
2	**4b**	CH	H	H	2-Me-C_6H_4	96
3	**4c**	CH	H	H	3-Me-C_6H_4	72
4	**4d**	CH	H	H	4-Me-C_6H_4	69
5	**4e**	CH	H	H	4-OMe-C_6H_4	66
6	**4f**	CH	H	H	4-NMe_2-C_6H_4	77
7	**4g**	CH	H	H	4-F-C_6H_4	67
8	**4h**	CH	H	H	4-Br-C_6H_4	74[b]
9	**4i**	CH	H	H	2-Br-C_6H_4	76[b]
10	**4j**	CH	4,5-$(OMe)_2$	H	2-Br-C_6H_4	95[b]
11	**4k**	CH	H	H	3-Cl-C_6H_4	50
12	**4l**	CH	H	H	*n*-hexyl	75
13	**4m**	CH	H	H	cyclohexyl	83
14	**4n**	CH	H	H	cyclohexenyl	86
15	**4o**[c]	CH	H	H	TMS	94[d]
16	**4q**	CH	H	H	3-thienyl	92
17	**4r**	CH	4,5-$(OMe)_2$	H	Ph	91[e]

18	**4s**	CH	5-F	H	Ph	94
19	**4t**	CH	5-F	H	4-Me-C_6H_4	95
20	**4u**	CH	5-F	H	3-thienyl	93
21	**4v**	CH	5-NO_2	H	Ph	96
22	**4w**	CH	5-NO_2	H	4-Me-C_6H_4	94
23	**4x**	N	H	H	Ph	84[f]
24	**4y**	N	H	H	*n*-hexyl	90[f]
25	**4z**	CH	H	Me	Ph	85
26	**4aa**	CH	H	Ph	4-Me-C_6H_4	96

[a]All reactions were carried using the 0.50 mmol *o*-iodo/bromo amide substrate in DMF (see experimental section for details). [b]The reaction was carried out in THF:DIPA (50:1) as solvent. [c]This compound **4o** (2 mmol) was used for preparing **4p** through TMS group deprotection. [d]This reaction was performed on a 3 mmol scale. [e]15 mol% of catalyst was used and the reaction was carried out at 80 °C. [f]THF was used as a solvent and the reaction was carried out at 50 °C.

Our efforts for the superbase P_4-*t*-Bu mediated synthesis of isoindolin-1-ones began by taking 2-(phenylethynyl)benzamide (**4a**) as the substrate for the cyclization reaction. The summary of the results of the optimization studies are compiled in Table 2.

Table 2. Optimization Studies for Halocyclization Reaction[a,b]

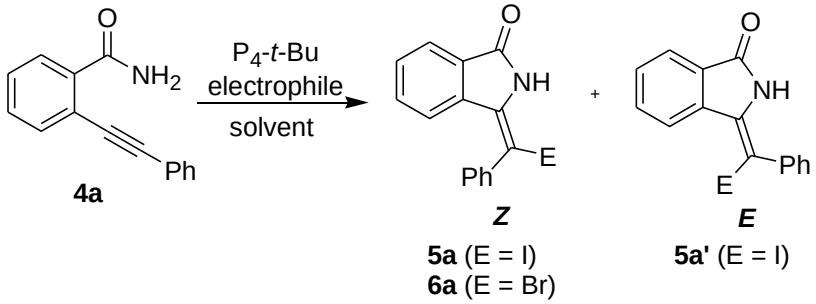

S. No.	base equiv.	solvent	temp (°C)	time (min)	electrophile	total isolated yield (5a + 5a') or (6a) (%)	*Z*/*E* ratio (5a:5a')
1	0.10	THF	25	30	I_2	63[c]	82/18
2	0.10	THF	25	1	I_2	63[c]	82/18
3	0.20	THF	25	1	I_2	72[c]	82/18
4	0.20	THF	25	30	I_2	72[c]	82/18
5	0.30	THF	25	1	I_2	78[c]	84/16

6	0.30	THF	25	30	I_2	78[c]	84/16
7	0.50	THF	25	1	I_2	85	88/12
8	0.50	THF	25	30	I_2	85	88/12
9	**1.0**	**THF**	**25**	**1**	**I_2**	**87**	**100/0**
10	1.0	THF	25	30	I_2	87	100/0
11	1.0	THF	0	1	I_2	87	90/10
12	1.0	THF	50	1	I_2	83	100/0
13	1.0	THF	25	1	1 I_2	72[c]	71/29
14	1.0	THF	25	1	2 I_2	84	73/27
15	1.0	THF	25	1	ICl	82	100/0
16	1.0	THF	25	1	NIS	81	100/0
17	1.0	THF	25	1	Br_2	71[d]	-
18	1.0	THF	25	1	NBS	68[d]	-
19	1.0	DCM	25	1	I_2	78	100/0
20	1.0	MeCN	25	1	I_2	73	100/0

[a]Unless otherwise indicated, all reactions were performed on 0.25 mmol scale using 3.0 equiv of the electrophile. [b]Unless otherwise indicated, the reactions were complete in less than 1 min, however, for the uniform comparison of yields, the reactions were stopped after 1 min/30 min**.** [c]Starting material was not consumed completely. [d]Only *Z*-isomer (**6a**) was obtained.

Firstly, the superbase P_4-*t*-Bu was used as a catalyst (10%) (entry 1). We were pleased to observe the formation of the desired *N*-cyclized product **(5)**, the structure of which was confirmed by comparing its spectroscopic data with the previously published results.[35] Notably the major product (**5a**) was found to have *Z*-configuration across the exocyclic C=C bond. The same result was obtained when the reaction was stopped after 1 minute (entry 2). Increasing the amount of the base led to the improvement in the product yield and stereoselectivity (entries 3-8). Nevertheless, it was observed that for all the experiments where P_4-*t*-Bu was used as catalyst (10-50%), the starting material was not completely consumed and/or the *E*-isomer of the product (**5a'**) was also formed in small quantities (entries 1-8). The best isolated yield of the exclusively formed *Z*-isomer (87%) was obtained with 1 equiv of the superbase (entry 9). The same result was obtained when the reaction was

run for 30 minutes (entry 10). The lowering of the reaction temperature led to the formation of the *E*-isomer (entry 11) as minor co-product, whereas the increase in temperature resulted in the slight reduction of the product yield (entry 12). On reducing the amount of the electrophile (I_2), the reaction either didn't complete (starting material was remaining with 1 equiv), and/or a significant amount of *E*-isomer was also formed (entries 13 and 14). The methodology also worked well with ICl, NIS (entry 15-16) as well as with bromine electrophiles such as Br_2 and NBS (entry 17-18), although the product yield was lower as compared to reactions with I_2. The use of other solvents such as DCM or MeCN (entries 19-20) also resulted in formation of the desired product but the yield could not be further improved. In all the cases, the product yield remained unchanged when the reaction was run for longer durations (30 minutes). Therefore the optimized conditions involve stirring of *o*-alkynylbenzamide (1.0 equiv), P_4-*t*-Bu superbase (1.0 equiv.), I_2 (3.0 equiv) in THF at ambient temperature.

Having optimized the reaction conditions, we then focused on studying the scope of the iodocyclization reaction. The reactions were performed with the *o*-alkynyl benzamide substrates (**4a-4y**) using iodine electrophile and the results are presented below (Table 3), where the structures of the products along with the isolated yields are indicated. Additionally, a few reactions were also performed using ICl as electrophile and where applicable, the corresponding yields are reported in the parentheses.

Table 3. Scope for P_4-*t*-Bu Mediated Iodocyclization Reaction[a]

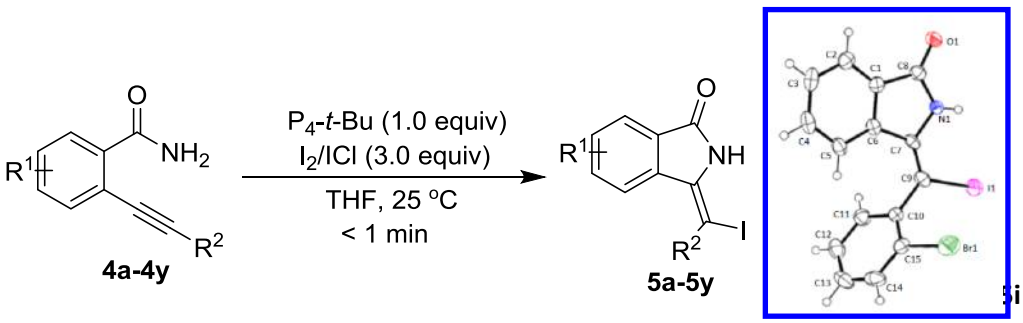

5i

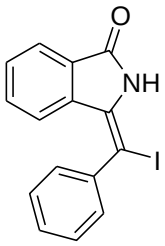

5a, 87%
(82%)

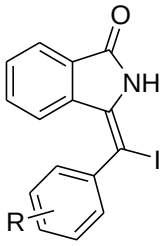

5b (R = *o*-methyl), 94%
5c (R = *m*-methyl), 93% (83%)
5d (R = *p*-methyl), 86% (84%)

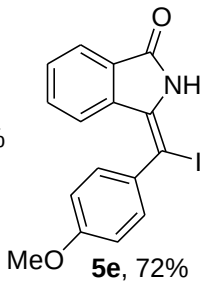

5e, 72%
(65%)

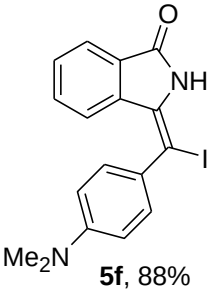

5f, 88%
(82%)

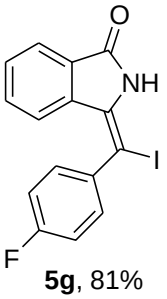

5g, 81%
(75%)

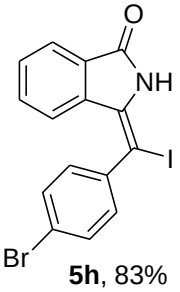

5h, 83%
(79%)

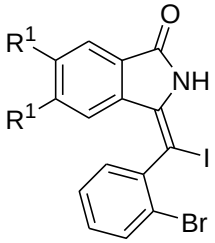

5i (R^1 = H), 86%
5j (R^1 = OMe), 96%

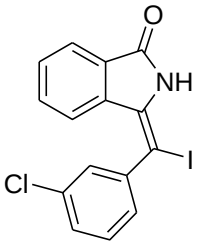

5k, 89%
(84%)

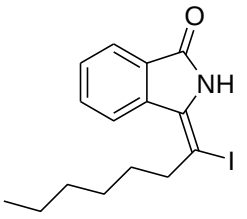

5l, 91%
(84%)

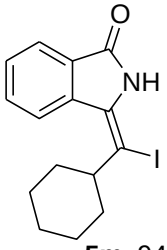

5m, 94%
(80%)

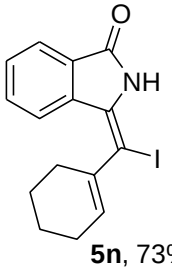

5n, 73%
(69%)

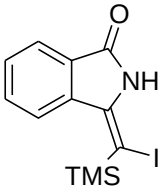

5o, 91%
(88%)

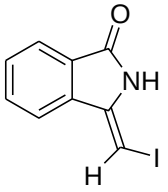

5p,[c] 94%
(85%)

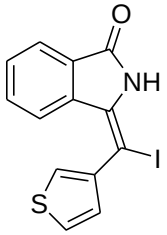

5q, 90%

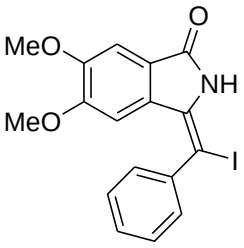

5r, 91%
(91%)

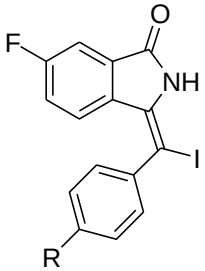

5s, R = H, 90%
5t, R = Me, 96%

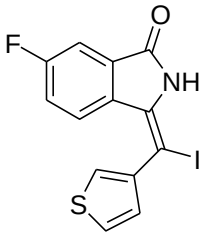

5u, 96%

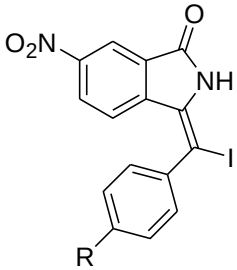

5v, R = H, 97%
5w, R = Me, 93%

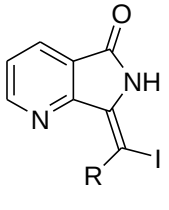

5x, R = Ph, 94%
5y, R = *n*-hexyl, 91%

[a]All reactions were run using 0.25 mmol of *o*-(alkynyl)benzamide and 1.0 equiv of P_4-*t*-Bu (0.8 M in Hexane), 3.0 equiv I_2 in dry THF at 25 °C. [b]The yields in the parentheses correspond to the reactions that were performed using 3.0 equiv ICl as the electrophile. [c]This reaction was also performed at 1 mmol scale (isolated yield: 96%).

When substrates containing the electron donating/withdrawing groups on the phenyl ring at the distal end of the alkyne were subjected to the cyclization conditions, the desired isoindolin-1-ones were formed (**5b**-**5k**) in good yields (Table 3). The cyclization of halogen (-F, -Cl, -Br) containing substrates was particularly interesting, and in all these cases the desired products (**5g-5k**) were isolated in good yields. It is noteworthy that the substrate containing the bromo and chloro groups were efficiently transformed into corresponding cyclized products in good yields and no dehalogenated product was observed in either case. The reaction was also successful with the substrate having aliphatic chain (*n*-hexyl) to give the corresponding product **5l** in 91% yield. The alkyne substrate containing cyclohexyl group was cyclized to give the desired product **5m** in excellent yield (94%). Even the cyclohexenyl group was well tolerated to give product **5n** in good yield (73%). Next, the cyclization of alkynyl substrate containing a highly labile trimethylsilyl (TMS) functional group resulted in the formation of cyclized product **5o** in 91% yield, with TMS group intact. When the terminal alkyne (**4p**) was subjected to the cyclization conditions, the cyclized product **5p** was formed in excellent yield (94%). Notably the reaction with the same substrate (**4p**) at higher scale (1 mmol) afforded the desired product at even higher isolated yield of 96%. The substrate containing the heterocyclic moiety (3-thienyl) also worked well under the reaction conditions and resulted in the thienyl containing isoindolin-1-one **5q** in 90% yield. The reaction also worked for the alkynyl substrates containing various electron-donating (**5r**) and withdrawing groups (**5s**-**5w**) on the benzamide ring. With fluoro (-F) substitution on the benzamide ring, the substrates containing the phenyl, *p*-tolyl and even 3-thienyl groups at the alkyne-terminal afforded the corresponding products **5s**-**5u** in excellent yields. Substrates with electron withdrawing nitro group on benzamide ring afforded products **5v** and **5w** in excellent yields, 97% and 93%, respectively. The introduction of heteroatom (nitrogen) in the benzamide ring was also well accommodated and the reaction resulted in the isolation of the desired

heteroatom containing isoindolinone derivatives **5x** and **5y** in 94% and 91% yield, respectively.

As indicated above, a few reactions that were performed with ICl as the source of electrophile also afforded the desired products; however, the yields were generally slightly lower as compared to the reactions when iodine was used. The results indicate that iodine is the electrophile of choice for this methodology.

The iodocyclization of secondary amide substrates (*N*-methyl and *N*-phenyl substituted) was also attempted (Scheme 3). Although these substrates underwent cyclization *via* the nitrogen atom of the amide group to form the corresponding isoindolinones, however, the iodine atom (C-I bond) was found to be absent in the isolated products. Also, the geometry of the resulting products **7a** and **7b** was found to be different (the nitrogen atom is *trans* with respect to the incoming H) as compared to the products (**5a-5y**) obtained from primary amide substrates (where the nitrogen atom is *cis* with respect to the incoming I). This observation is discussed in the mechanism section (Scheme 4).

Scheme 3. Cyclization of *N*-substituted *o*-alkynylbenzamides

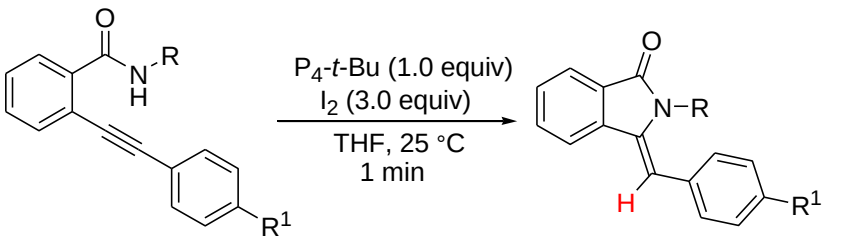

4z (R = Me, R^1 = H)
4aa (R = Ph; R^1 = Me)

7a (R = Me; R^1 = H) 81 %
7b (R = Ph; R^1 = Me) 77 %

Thus, the above results indicate that it is an efficient methodology for the synthesis of isoindolin-1-ones, and it is superior to our previously reported BuLi-mediated iodocyclization on several important criteria. These include the ease of setting up the reactions, as well as having metal-free and ambient reaction conditions. Also, the reactions are cleaner, faster,

generally afford better yields, and are scalable. The present methodology also has a broader scope, as trimethylsilyl group as well as the halogens are well tolerated. The tolerance of halogens, particularly bromo group, offers the possibility of further expansion of the present methodology for the synthesis of more complex derivatives as well as natural products. This type of expansion was not possible for the BuLi-mediated iodocyclization methodology, due to the debromination of the bromo-containing substrates during the reaction. Moreover, the present methodology also works with a secondary amide group, leading to the formation of the desired isoindolinone (although without the incorporation of iodo group). Thus, the new and successful substrates in this work either expand the scope of this methodology, and/or provide insights for the possible mechanism of the reaction. Overall, we think that these results reported here constitute a significant advancement in the area of electrophilic cyclization of alkynes, and will further advance this interesting area of organic synthesis.

In order to explain the interesting results obtained through the superbase-mediated electrophilic cyclization reaction, we considered various factors affecting the reaction, as well as the various types of intermediates that may be involved. [35,51] Moreover, we came across the literature evidence for an intimate ion pair intermediate that was reported to be isolated and characterized through X-ray crystallography,[52] for a base-mediated iodocyclization reaction of a metallabenzene. In view of the literature evidence available in this regard, along with our combined observations with bases BuLi as well as P_4-*t*-Bu, we propose a similar kind of intermediate *i.e.* an intimate ion pair intermediate, for the mechanism of this reaction (Scheme 4). It appears that, the first step of the base-mediated cyclization of 2-(1-alkynyl)benzamides involves the generation of the amide anion (I).[36-38] Thereafter, in presence of iodine, the aminocyclization of primary amide containing substrates proceeds through the intimate ion pair (II) intermediate (path a). As far as the quantity of the base is concerned, it seems that a stoichiometric amount of superbase is required for quick and

complete generation of the intermediate, as well as for the cyclization reaction. It must also be mentioned here that while we believe that involvement of an intimate ion pair is likely, alternatively the involvement of a cationic intermediate cannot be completely ruled out.

Scheme 4. Plausible Mechanism for iodoaminocyclization reaction

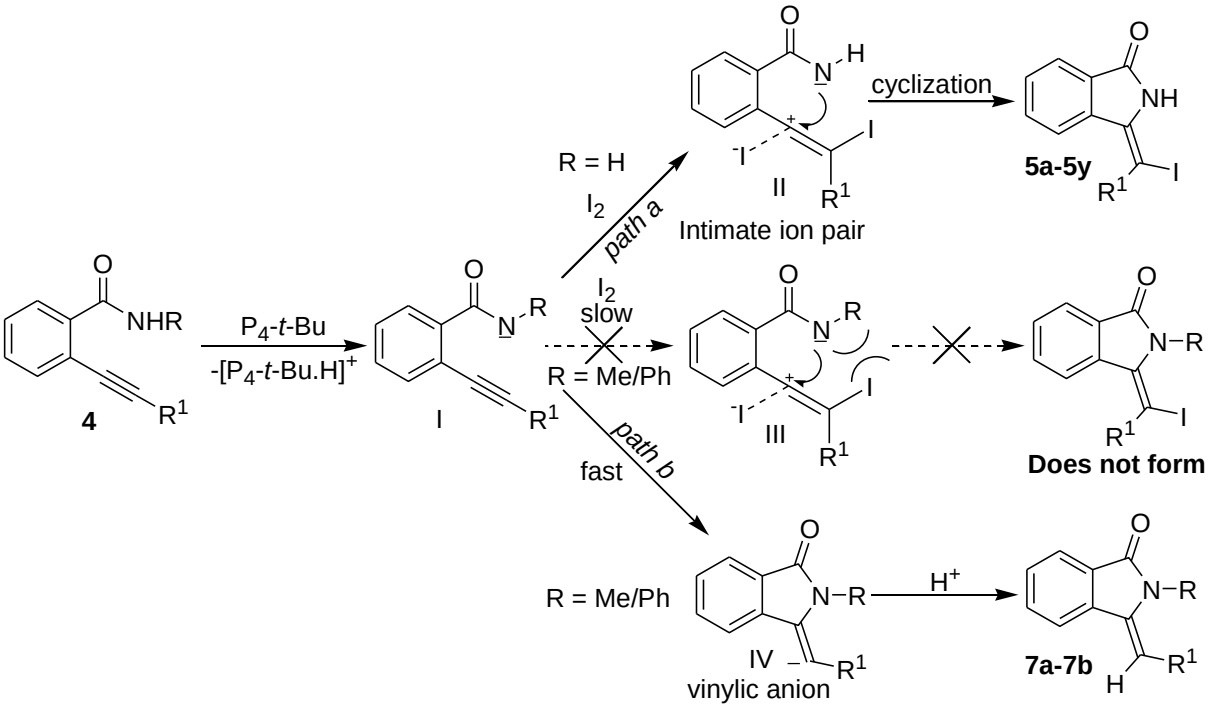

Furthermore, in case of the secondary amide substrates (**4z** and **4aa)**, the formation of the corresponding intimate ion pair (III) is presumably slow due to the steric hindrance. It appears that the cyclization proceeds through an alternate mechanism (path b), *i.e.* a relatively fast anionic mechanism in this case, where the vinylic anion intermediate (IV) seems to be quenched with H^+ (presumably during the reaction work-up), leading to the isolation of the corresponding isoindolinones (**7a** and **7b)** without iodine incorporation. It may be noted that when the substrate was subjected to the BuLi-mediated iodocyclization conditions, the *N*-cyclization was disfavored and the reaction resulted in the isolation of the *O*-cyclized product.[35] The combined observations suggest that being a kinetically-controlled reaction, the presence of a free amide group is necessary for the successful iodoaminocyclization. Any

steric hindrance at the nitrogen atom of the amide functionality either leads to the *N*-cyclized product without iodine incorporation (for P_4-*t*-Bu mediated cyclization), or *O*-cyclization (for BuLi-mediated cyclization). Finally, the nature of the base also appears to be an important factor for the cyclization, and interestingly the use of P_4-*t*-Bu seems to favor *N*-cyclization.[49]

The presence of C-I bond, as well as the free *–NH* group in the iodocyclized products provide easy handles for further functionalization. It has been previously demonstrated through various metal-catalyzed transformations such as Sonogashira alkynylation, Heck reaction, Suzuki-Miyaura coupling, *etc*. on iodo-containing heterocycles;[53,54] as well as through alkylation/arylation of the lactam *(–NH)*.[35] Further, we considered testing the utility of our superbase-mediated iodocyclization methodology for the synthesis of important natural products. As mentioned above, the isoindolinone core is prevalent in a variety of biologically active natural products, and we believe that there is still scope for the development of new and efficient methodologies for the synthesis of important natural products and their analogues. One such example is Aristolactams that is an important class of naturally occurring phenanthrene lactam alkaloids, found in the leaves and roots of several plants families such as Aristolochiaceae, Piperaceae, *etc*.[55,56] In East Asia, traditionally the aristolactams have been used as folk medicines and have also displayed important biological properties including anticancer, anti-inflammatory, antiplatelet and neuro-protective activities.[57-59] We thought of devising a new synthetic route for Aristolactams using our iodocyclization methodology. For demonstrating this utility, we were particularly interested in synthesizing a particular Aristolactam derivative, namely Aristolactam BII (also known as Cepharanone B), due to its known antitumor[60] and antitubercular activities.[61]

As indicated above, the substrates containing halogens are easily tolerated under our iodocyclization conditions (see products **5i** and **5j** in Table 3). This feature of our methodology may be used for further extension. We considered using this feature to

synthesize Aristolactam derivatives. Using a brief retrosynthetic analysis (Scheme 5), we envisioned that the Aristolactam derivatives could indeed be conveniently synthesized by constructing the **'C'** ring through an annulation reaction (such as free redical-mediated annulation) of a suitably substituted isoindolinone derivative obtained from our iodocyclization methodology.

Scheme 5. Retrosynthetic Analysis for the Synthesis of Aristolactams

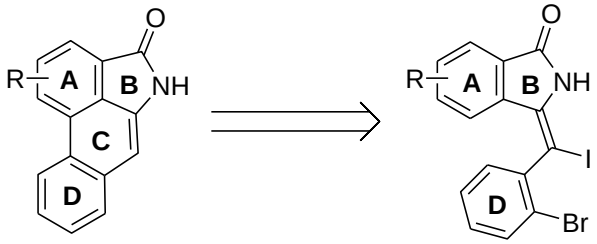

In this context, the *Z* geometry at the exo C=C double bond of the cyclized products (confirmed through the X-ray crystallographic studies of the cyclized product **5i** (Table 3) seems to be favorable for a subsequent annulation reaction.

Scheme 6. Synthesis of Aristolactam Derivatives

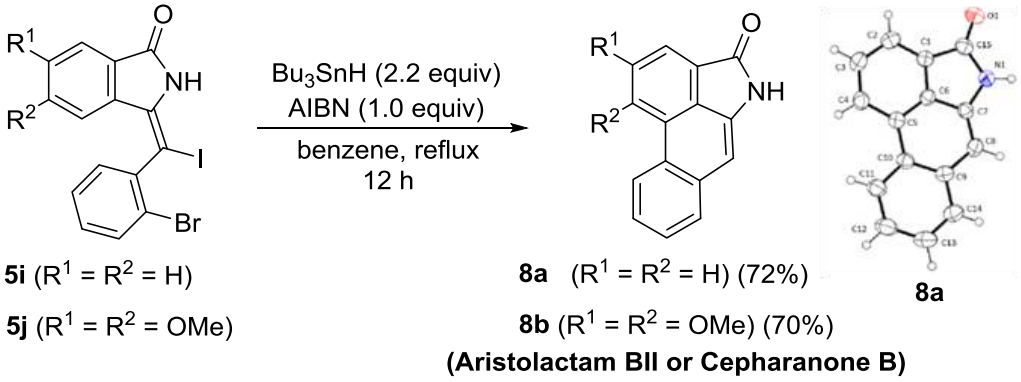

5i ($R^1 = R^2 = H$)

5j ($R^1 = R^2 = OMe$)

8a ($R^1 = R^2 = H$) (72%)

8b ($R^1 = R^2 = OMe$) (70%)

(Aristolactam BII or Cepharanone B)

The isoindolinones containing bromo group when subjected to free radical cyclization using tributyltin hydride and AIBN,[62,63] resulted in the formation of the Aristolactam derivative **8a** and Cepharanone B/Aristolactam BII **(8b)** in good yields of 72% and 70% respectively (Scheme 6). The structure of **8a** was also confirmed through single crystal X-ray crystallography (see ORTEP diagram in Scheme 6). Thus, it has been demonstrated that the

methodology offers scope for the synthesis of novel isoindolinones as well as related natural products and their derivatives.

Conclusions

In summary, we have developed a simple and robust methodology for the regio- and stereoselective synthesis of isoindolinones. This is the first report of a superbase-mediated electrophilic cyclization/iodocyclization reaction. The reaction is easy to perform, accommodates a variety of sensitive functional groups (including TMS, halogens, *etc*.), works with other halogen electrophiles (such as ICl, Br_2, NBS, *etc*.), and is also scalable. It is notable that in addition to the broader scope; the yields are generally higher (on average 15-20%) as compared to the yields obtained through *n*-BuLi-mediated iodoaminocyclization. Moreover, the suitably substituted iodocyclized products may be conveniently converted into the corresponding Aristolactam derivatives. We believe that this methodology will be of interest to the synthetic/medicinal chemists, and may find applications in the pharmaceutical industry.

EXPERIMENTAL SECTION

General information

The ^{1}H NMR and ^{13}C NMR spectra were obtained at 400 and 100 MHz, respectively, with Tetramethylsilane (TMS) as the internal standard, using deuterated chloroform ($CDCl_3$) or deuterated Dimethyl sulfoxide (DMSO-d_6) as the solvent. Crystal structure analysis was performed on single needles X-ray diffractometer. Reaction progress was monitored by thin-layer chromatography (TLC) analysis, that was performed on commercially available silica gel 60 F_{254} 0.25 mm precoated aluminium foil plates and visualization was done with short wavelength UV light (254 nm). HRMS data was recorded on an Agilent G6530A (LC-HRMS-Q-TOF) mass spectrometer equipped with an electrospray source with a mass accuracy > 2 ppm having HPLC pressure 600 Bar and MS pressure 10^{-4} to 10^{-5} Torr.

Compounds purification was performed by column chromatography using commercially available silica having mesh size 100-200, and using ethylacetate-hexane as solvent. All melting points are uncorrected.

Reagents and Solvents. Unless otherwise indicated, all reagents and solvents were used as obtained commercially.

2-Halobenzoic Acids (1a-1e). Commercially available, and were used as received.

Terminal Alkynes (3). Commercially available terminal alkynes were used as received.

Superbase P_4-*t*-Bu (0.8 M in hexane) was used as received (Sigma Aldrich, SKU 79421).

Procedure for the synthesis of 2-Halobenzamides:

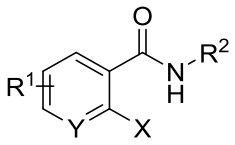

2a-2g

R^1 = H, R^2 = H, X = I, Y = CH (**2a**)
R^1 = 5-F, R^2 = H, X = I, Y = CH (**2b**)
R^1 = 5-NO_2, R^2 = H, X = Br, Y = CH (**2c**)
R^1 = H, R^2 = H, X = Br, Y = N (**2d**)
R^1 = 4,5-$(OMe)_2$, R^2 = H, X = I, Y = CH (**2e**)
R^1 = H, R^2 = Me, X = I, Y = CH (**2f**)
R^1 = H, R^2 = Ph, X = I, Y = CH (**2g**)

To an oven-dried round bottom flask, added corresponding 2-Halobenzoic acid **1a-1e** (1 gm) followed by the addition of 5 mL of thionyl chloride ($SOCl_2$). The solution was allowed to reflux for 7 hours. After the completion of the reaction, the excess of thionyl chloride was removed under reduced pressure and the residue was cooled to 0 °C using ice-bath. The primary amine was added dropwise while vigorously stirring the reaction mixture. The amide (**2a-2g)** was formed as white solid, which were filtered in scintered flask and washed with water several times to remove any traces of starting acid. The moist amide was dried in a hot air oven at 50 °C for 12 hours, weighed and used as such.

2-Iodobenzamide (2a).[64] This compound was prepared by performing the reaction on a 10 mmol scale. Yield: 2.42 g (98%).

5-Fluoro-2-iodobenzamide (2b).[65] Yield: (976.3 mg, 98%).

2-Bromo-5-nitrobenzamide (2c). Yield: (956.0 mg, 96%); White solid: TLC R_f = 0.18 (30% EtOAc:Hexanes, UV); mp 130-132 °C; **IR** (KBr, cm^{-1}) 3361, 3186, 1627, 639; **^{1}H NMR** (400 MHz, DMSO-d_6) δ 8.18-8.16 (m, 2H), 8.12 (s, 1H), 7.97 (d, J = 8.40 Hz, 1H), 7.85 (s, 1H); **^{13}C{^{1}H} NMR** (100 MHz, DMSO-d_6) δ 167.6, 147.0, 140.8, 135.0, 126.9, 125.5, 123.5; **HRMS** (ESI-TOF) *m/z*: $[M + H]^+$ Calcd for $C_7H_6BrN_2O_3$ 244.9556; Found 244.9554.

2-Bromonicotinamide (2d). Yield: (776.1 mg, 78%); White solid: TLC R_f = 0.26 (50% EtOAc:Hexanes, UV); mp 185-187 °C; **IR** (KBr, cm^{-1}) 3329, 3153, 1669, 629; **^{1}H NMR** (400 MHz, DMSO-d_6) δ 8.45-8.44 (m, 1H), 8.05 (s, 1H), 7.90-7.88 (m, 1H), 7.78 (s, 1H), 7.49-7.46 (m, 1H); **^{13}C{^{1}H} NMR** (100 MHz, DMSO-d_6) δ 167.4, 150.5, 146.7, 138.3, 133.9, 123.5; **HRMS** (ESI-TOF) *m/z*: $[M + H]^+$ Calcd for $C_6H_6BrN_2O$ 200.9658; Found 200.9651.

2-Iodo-4,5-dimethoxybenzamide (2e). Yield: (966.8 mg, 97%); White solid: TLC R_f = 0.15 (40% EtOAc:Hexanes, UV); mp 186-188 °C; **IR** (KBr, cm^{-1}) 3364, 319, 2964, 1638, 1256 ; **^{1}H NMR** (400 MHz, DMSO-d_6) δ 7.67 (s, 1H), 7.39 (s, 1H), 7.28 (s, 1H), 6.96 (s, 1H), 3.76 (s, 3H), 3.75 (s, 3H); **^{13}C{^{1}H} NMR** (100 MHz, DMSO-d_6) δ 170.1, 149.7, 148.3, 134.6, 121.9, 111.8, 81.8, 55.9, 55.6; **HRMS** (ESI-TOF) *m/z*: $[M + H]^+$ Calcd for $C_9H_{11}INO_3$ 307.9778; Found 307.9780.

2-Iodo-N-methylbenzamide (2f).[64] Yield: (979 mg, 93%).

2-iodo-N-phenylbenzamide (2g).[35] Yield: (1.27 g, 98%).

Procedure for Sonogashira coupling for the preparation of 2-(1-Alkynyl)benzamides:

The starting bromo/iodo amide (0.50 mmol) was placed in DMF (6 mL) in an oven-dried round bottom flask. $Pd(PPh_3)_2Cl_2$ (4 mol %) and Copper iodide (2 mol %) were added to the flask and the reaction mixture was placed under Argon atmosphere. The reaction mixture was stirred (5 min) at room temperature, and triethylamine (4.0 equiv) was added by a syringe. The temperature was then increased to 70 °C. The terminal alkyne (1.2 equiv)

dissolved in DMF (2 mL) was added drop wise over 5 minutes. The reaction mixture was allowed to stir at 70 °C for 2 hours, and the reaction was monitored by TLC to establish completion. After the reaction was over, it was allowed to cool, and was quenched with aqueous NH_4Cl (10 mL) and water (10 mL). The aqueous layer was extracted with EtOAc (3 × 20 mL). The combined organic layer was washed with brine, dried using anhydrous Na_2SO_4, and was evaporated under reduced pressure. The crude product thus obtained was purified through the column chromatography.

Substrates **4h, 4i** and **4j** were synthesized using the slightly modified procedure, as the reaction was carried at 50 °C in THF:DIPA (50:1) as the solvent, and that the terminal alkyne in THF (2 mL) was added very slowly over a period of 30 min. Substrate **4r** was prepared as before.[35] For preparing substrate **4x** and **4y**, the reaction was carried out at 50 °C using THF as the solvent. The terminal alkyne **4p** was prepared from **4o** as before on a 2 mmol scale, as per a modified literature procedure.[29,66]

2-(Phenylethynyl)benzamide (4a).[67] Yield: (106.1 mg, 96%).

2-(o-Tolylethynyl)benzamide (4b). Yield: (112.9 mg, 96%); White solid; TLC R_f = 0.28 (30% EtOAc:Hexanes, UV); mp 131-133 °C; **IR** (KBr, cm^{-1}) 3380, 3179, 3019, 2214, 1650, 1397; **^{1}H NMR** (400 MHz, DMSO-d_6) δ 7.82 (s, 1H), 7.58-7.56 (m, 2H), 7.52-7.49 (m, 1H), 7.46-7.38 (m, 3H), 7.28-7.27 (m, 2H), 7.22-7.16 (m, 1H), 2.43 (s, 3H); **^{13}C{^{1}H} NMR** (100 MHz, DMSO-d_6) δ 169.2, 139.9, 139.4, 132.5, 131.6, 129.6, 129.5, 128.8, 128.4, 127.5, 125.8, 122.2, 120.0, 91.7, 91.6, 20.3; **HRMS** (ESI-TOF) *m/z*: $[M + H]^+$ Calcd for $C_{16}H_{14}NO$ 236.1070; Found 236.1081.

2-(m-Tolylethynyl)benzamide (4c).[35] Yield: (84.7 mg, 72%).

2-(p-Tolylethynyl)benzamide (4d).[68] Yield: (81.2 mg, 69%).

2-((4-Methoxyphenyl)ethynyl)benzamide (4e).[67] Yield: (82.9 mg, 66%).

2-((4-(Dimethylamino)phenyl)ethynyl)benzamide (4f).[35] Yield: (101.8 mg, 77%).

2-((4-Fluorophenyl)ethynyl)benzamide (4g).[68] Yield: (80.2 mg, 67%).

2-((4-Bromophenyl)ethynyl)benzamide (4h).[35] Yield: (111.0 mg, 74%).

2-((2-Bromophenyl)ethynyl)benzamide (4i).[35] Yield: (114.0 mg, 76%).

2-((2-Bromophenyl)ethynyl)-4,5-dimethoxybenzamide (4j). Yield: (171.0 mg, 95%); Yellow solid; TLC R_f = 0.45 (30% EtOAc:Hexanes, UV); mp 138-140 °C; **IR** (KBr, cm^{-1}) 3436, 3150, 2961, 2202, 1671, 1263, 1067; **^{1}H NMR** (400 MHz, $CDCl_3$) δ 7.86 (s, 1H), 7.70 (s, 1H), 7.60-7.54 (m, 2H), 7.32-7.28 (m, 1H), 7.22-7.18 (m, 1H), 7.04 (s, 1H), 6.56 (s, 1H), 3.94 (s, 3H), 3.93 (s, 3H); **^{13}C{^{1}H} NMR** (100 MHz, $CDCl_3$) δ 167.5, 150.9, 149.5, 133.4, 132.4, 130.0, 127.2, 124.9, 124.3, 115.3, 115.3, 112.8, 112.5, 93.3, 91.9, 56.0. **HRMS** (ESI-TOF) *m/z*: $[M + H]^+$ Calcd for $C_{17}H_{14}BrNO_3$ 360.0230; Found 360.0223.

2-((3-Chlorophenyl)ethynyl)benzamide (4k).[19] Yield: (63.9 mg, 50%).

2-(Oct-1-yn-1-yl)benzamide (4l).[69] Yield: (86.0 mg, 75%).

2-(Cyclohexylethynyl)benzamide (4m).[68] Yield: (94.3 mg, 83%).

2-(Cyclohex-1-en-1-ylethynyl)benzamide (4n).[67] Yield: (96.9 mg, 86%).

2-((Trimethylsilyl)ethynyl)benzamide (4o).[67] This reaction was performed on a 3 mmol scale. Yield: (612.7 mg, 94%).

2-Ethynylbenzamide (4p).[67] This reaction was performed on a 2 mmol scale. Yield: (278.6 mg, 96%).

2-(Thiophen-3-ylethynyl)benzamide (4q).[67] Yield: (104.6 mg, 92%).

4,5-Dimethoxy-2-(phenylethynyl)benzamide (4r).[35] Yield: (127.9 mg, 91%).

5-Fluoro-2-(phenylethynyl)benzamide (4s).[67] Yield: (112.4 mg, 94%); White solid; TLC R_f = 0.54 (30% EtOAc:Hexanes, UV); mp 160-162 °C; **^{1}H NMR** (400 MHz, $CDCl_3$) δ 7.87-7.84 (m, 1H), 7.63-7.60 (m, 1H), 7.53-7.51 (m, 2H), 7.41-7.37 (m, 4H), 7.21-7.17 (m, 1H), 6.35 (s, 1H); **^{13}C{^{1}H} NMR** (100 MHz, $CDCl_3$) δ 166.8, 163.7, 137.0, 135.5, 131.5, 129.3, 128.6, 121.7, 117.7, 117.3, 116.2, 95.6, 86.6. **HRMS** (ESI-TOF) *m/z*: $[M + H]^+$ Calcd for $C_{15}H_{11}FNO$ 240.0819; Found 240.0827.

5-Fluoro-2-(p-tolylethynyl)benzamide (4t). Yield: (120.2 mg, 95%); Light yellow solid; TLC R_f = 0.47 (30% EtOAc:Hexanes, UV); mp 191-193 °C; **IR** (KBr, cm^{-1}) 3367, 3167, 2957, 2213, 1644, 1376; **^{1}H NMR** (400 MHz, $CDCl_3$) δ 7.87-7.84 (m, 1H), 7.62-7.58 (m, 2H), 7.42-7.40 (m, 2H), 7.20-7.15 (m, 3H), 6.31 (s, 1H), 2.38 (s, 3H); **^{13}C{^{1}H} NMR** (100 MHz, $CDCl_3$) δ 166.7, 163.6, 139.7, 135.5, 135.4, 131.3, 129.3, 118.6, 117.6, 117.3, 116.5, 95.9, 86.0, 21.5; **HRMS** (ESI-TOF) *m/z*: $[M + H]^+$ Calcd for $C_{16}H_{13}FNO$ 254.0976; Found 254.0994.

5-Fluoro-2-(thiophen-3-ylethynyl)benzamide (4u). Yield: (114.0 mg, 93%); Yellow solid; TLC R_f = 0.41 (30% EtOAc:Hexanes, UV); mp 105-107 °C; **IR** (KBr, cm^{-1}) 3353, 3175, 2204, 1651, 1384;**^{1}H NMR** (400 MHz, DMSO-d_6) δ 7.88 (s, 1H), 7.80-7.79 (m, 1H), 7.64 (s, 1H), 7.63-7.58 (m, 2H), 7.36-7.28 (m, 2H), 7.18-7.17 (m, 1H); **^{13}C{^{1}H} NMR** (100 MHz, DMSO-d_6) δ 167.7, 162.5, 141.6, 134.9, 134.8, 129.9, 129.5, 127.0, 121.2, 117.0, 115.0, 88.0, 86.2; **HRMS** (ESI-TOF) *m/z*: $[M + H]^+$ Calcd for $C_{13}H_9FNOS$ 246.0383; Found 246.0352.

5-Nitro-2-(phenylethynyl)benzamide (4v). Yield: (127.8 mg, 96%); Yellow solid; TLC R_f = 0.59 (30% EtOAc:Hexanes, UV); mp 176-177 °C; **IR** (KBr, cm^{-1}) 3368, 3186, 2209, 1650, 1342; **^{1}H NMR** (400 MHz, DMSO-d_6) δ 8.32-8.29 (m, 2H), 8.13 (s, 1H), 7.92-7.86 (m, 2H), 7.62-7.56 (m, 2H), 7.48-7.45 (m, 3H); **^{13}C{^{1}H} NMR** (100 MHz, DMSO-d_6) δ 167.5, 146.8, 141.1, 134.4, 132.1, 130.3, 129.4, 127.0, 124.8, 123.1, 122.0, 98.0, 87.2; **HRMS** (ESI-TOF) *m/z*: $[M + H]^+$ Calcd for $C_{15}H_{11}N_2O_3$ 267.0764; Found 267.0779.

5-Nitro-2-(p-tolylethynyl)benzamide (4w). Yield: (131.7 mg, 94%); Yellow solid; TLC R_f = 0.55 (30% EtOAc:Hexanes, UV); mp 217-219 °C; **IR** (KBr, cm^{-1}) 3373, 3203, 2925, 2209, 1641, 1350; **^{1}H NMR** (400 MHz, DMSO-d_6) δ 8.34-8.28 (m, 2H), 8.12 (s, 1H), 7.86-7.84 (m, 2H), 7.51-7.42 (m, 2H), 7.30-7.28 (m, 2H), 2.35 (s, 3H); **^{13}C{^{1}H} NMR** (100 MHz, DMSO-d_6) δ 167.6, 146.7, 140.8, 140.3, 134.0, 131.9, 130.0, 127.3, 124.5, 122.5, 118.5, 98.4, 86.4, 21.4; **HRMS** (ESI-TOF) *m/z*: $[M + H]^+$ Calcd for $C_{16}H_{13}N_2O_3$ 281.0921; Found 281.0928.

2-(Phenylethynyl)nicotinamide (4x). Yield: (93.4 mg, 84%); White solid; TLC R_f = 0.27 (50% EtOAc:Hexanes, UV); mp 201-202 °C; **IR** (KBr, cm^{-1}) 3370, 3173, 2223, 1648; **^{1}H NMR** (400 MHz, DMSO-d_6) δ 8.63-8.61 (m, 1H), 8.03 (s, 1H), 7.91-7.88 (m, 1H), 7.74 (s, 1H), 7.57-7.51 (m, 2H), 7.47-7.43 (m, 4H); **^{13}C{^{1}H} NMR** (100 MHz, DMSO-d_6) δ 168.0, 150.5, 139.0, 136.0, 135.4, 131.6, 129.5, 128.8, 123.1, 121.6, 91.5, 87.8; **HRMS** (ESI-TOF) *m/z*: $[M + H]^+$ Calcd for $C_{14}H_{11}N_2O$ 223.0866; Found 223.0872.

2-(Oct-1-yn-1-yl)nicotinamide (4y). Yield: (103.6 mg, 90.0%); Yellow viscous liquid; TLC R_f = 0.20 (30% EtOAc:Hexanes, UV); **IR** (KBr, cm^{-1}) 3370, 3174, 2957, 2924, 2232, 1650; **^{1}H NMR** (400 MHz, $CDCl_3$) δ = 8.65-8.63 (m, 1H), 8.42-8.40 (m, 1H), 7.74 (s, 1H), 7.35-7.32 (m, 1H), 6.51 (s, 1H), 2.54-2.50 (m, 2H), 1.69-1.62 (m, 2H), 1.48-1.40 (m, 2H), 1.31-1.27 (m, 4H), 0.89-0.86 (m, 3H); **^{13}C{^{1}H} NMR** (100 MHz, $CDCl_3$) δ = 166.6, 151.8, 139.9, 138.3, 130.3, 122.7, 98.1, 79.6, 31.2, 28.7, 27.9, 22.4, 19.5, 13.9; **HRMS** (ESI-TOF) *m/z*: [M + H]$^+$ Calcd for $C_{14}H_{19}N_2O$ 231.1492; Found 231.1495.

N-Methyl-2-(phenylethynyl)benzamide (4z).[33] Yield: (100.0 mg, 85%).

N-Phenyl-2-(p-tolylethynyl)benzamide (4aa).[70] Yield: (149.4 mg, 96%).

Procedure for Iodocyclization Reaction:

To an oven dried round bottom flask, the appropriate alkyne substrate **4** (0.25 mmol) was taken in 2 mL of THF at 25 °C, and flushed with Argon. 1.0 equiv of P_4-*t*-Bu (0.8 M in

Hexane) superbase was added by a syringe. Iodine (3 equiv)/[ICl (3 equiv; 1.0 molar in THF)] dissolved in 1 ml THF, was added by a syringe and the reaction was stirred for 1 minute (since the addition of superbase). The reaction was quenched by the addition of saturated aq. NH_4Cl (3 ml), followed by the addition of satd. aq. $Na_2S_2O_3$ (3 ml). Water (10 ml) was added and the product was extracted with ethyl acetate (3 × 10 ml). The combined organic layer was dried using anhydrous Na_2SO_4, evaporated under reduced pressure, and the residue was purified by column chromatography (using hexane-EtOAc as eluent) to afford the pure isoindolin-1-one product **5**.

(Z)-3-(Iodo(phenyl)methylene)isoindolin-1-one (5a).[35] Yield: (75.5 mg, 87%).

(E)-3-(Iodo(phenyl)methylene)isoindolin-1-one (5a').[35] Yield: (10 mg, 12%).

(Z)-3-(Iodo(o-tolyl)methylene)isoindolin-1-one (5b). Yield: (84.6 mg, 94%); Light yellow solid; TLC R_f = 0.36 (30% EtOAc:Hexanes, UV); mp 144-145 °C; **IR** (KBr, cm^{-1}) 3170, 2959, 1708, 1467; **^{1}H NMR** (400 MHz, DMSO-d_6) δ 10.27 (s, 1H), 7.67 (d, J = 7.6 Hz, 1H), 7.45-7.41 (m, 1H), 7.37-7.28 (m, 4H), 7.26-7.21 (m, 1H), 6.02 (d, J = 8.0 Hz, 1H), 2.10 (s, 3H); **^{13}C{^{1}H} NMR** (100 MHz, DMSO-d_6) δ 167.4, 140.8, 138.5, 135.6, 134.6, 132.4, 131.2, 130.8, 129.4, 129.3, 129.1, 127.0, 123.1, 122.0, 77.4, 18.9; **HRMS** (ESI-TOF) *m/z*: $[M + H]^+$ Calcd for $C_{16}H_{13}INO$ 362.0036; Found 362.0047.

(Z)-3-(Iodo(m-tolyl)methylene)isoindolin-1-one (5c).[35] Yield: (83.9 mg, 93%).

(Z)-3-(Iodo(p-tolyl)methylene)isoindolin-1-one (5d).[35] Yield: (77.6 mg, 86%).

(Z)-3-(Iodo(4-methoxyphenyl)methylene)isoindolin-1-one (***5e***).[35] Yield: (67.9 mg, 72%).

(Z)-3-((4-(Dimethylamino)phenyl)iodomethylene)isoindolin-1-one (5f).[35] Yield: (85.8 mg, 88%).

(Z)-3-((4-Fluorophenyl)iodomethylene)isoindolin-1-one (5g).[35] Yield: (73.9 mg, 81%).

(Z)-3-((4-Bromophenyl)iodomethylene)isoindolin-1-one (5h).[35] Yield: (88.4 mg, 83%).

(Z)-3-((2-Bromophenyl)iodomethylene)isoindolin-1-one (5i). Yield: (91.6 mg, 86%); Yellow solid; TLC R_f = 0.54 (30% EtOAc:Hexanes, UV); mp 172-174 °C; **IR** (KBr, cm^{-1}) 3219, 3058, 1707, 1471; **^{1}H NMR** (400 MHz, $CDCl_3$) δ 7.80-7.78 (m, 2H), 7.73-7.71 (m, 1H), 7.44-7.40 (m, 4H), 7.35-7.28 (m, 1H), 6.27 (d, J = 8.4 Hz, 1H). **^{13}C{^{1}H} NMR** (100 MHz, $CDCl_3$) δ 167.2, 140.4, 138.8, 134.2, 133.8, 132.6, 131.6, 131.3, 130.8, 129.5, 128.4, 124.1, 123.9, 122.7, 76.3; **HRMS** (ESI-TOF) *m/z*: $[M + H]^+$ Calcd for $C_{15}H_{10}BrINO$ 425.8985; Found 425.8978.

(Z)-3-((2-Bromophenyl)iodomethylene)-5,6-dimethoxyisoindolin-1-one (5j). Yield: (116.6 mg, 96%); Yellow solid; TLC R_f = 0.43 (50% EtOAc:Hexanes, UV); mp 174-175 °C; **IR** (KBr, cm^{-1}) 3198, 2913, 1710, 1463, 1356; **^{1}H NMR** (400 MHz, DMSO-d_6) δ 10.32 (s, 1H), 7.67-7.65 (m, 1H), 7.61-7.59 (m, 2H), 7.41-7.39 (m, 1H), 7.19 (s, 1H), 6.60 (s, 1H), 3.91 (s, 3H), 3.85 (s, 3H); **^{13}C{^{1}H} NMR** (100 MHz, DMSO-d_6) δ 169.0, 153.0, 150.8, 135.1, 134.8, 132.5, 131.6, 131.3, 128.8, 127.9, 123.3, 121.4, 104.2, 103.1, 72.0, 56.2, 55.8; **HRMS** (ESI-TOF) *m/z*: $[M + H]^+$ Calcd for $C_{17}H_{14}BrINO_3$ 485.9196; Found 485.9212.

(Z)-3-((3-Chlorophenyl)iodomethylene)isoindolin-1-one (5k).[35] Yield: (84.9 mg, 89%).

(Z)-3-(1-Iodoheptylidene)isoindolin-1-one (5l).[35] Yield: (80.8 mg, 91%).

(Z)-3-(Cyclohexyliodomethylene)isoindolin-1-one (5m).[35] Yield: (83.0 mg, 94%).

***(Z)-3-(Cyclohex-1-en-1-yliodomethylene)isoindolin-1-one* (5n)**.[35] Yield: (64.0 mg, 73%).

(Z)-3-(Iodo(trimethylsilyl)methylene)isoindolin-1-one (5o). Yield: (78.0 mg, 91%); Yellow solid; TLC R_f = 0.37 (20% EtOAc:Hexanes, UV); mp 157-159 °C; **IR** (KBr, cm^{-1}) 3180, 2917, 1708, 1467; **^{1}H NMR** (400 MHz, $CDCl_3$) δ 8.22 (s, 1H), 7.51-7.48 (m, 2H), 7.45-7.43 (m, 2H), 0.23 (s, 9H); **^{13}C{^{1}H} NMR** (100 MHz, $CDCl_3$) δ 167.3, 140.0, 135.4, 135.1, 132.2,

131.0, 123.9, 123.9, 71.8, 0.2; **HRMS** (ESI-TOF) *m/z*: $[M + H]^+$ Calcd for $C_{12}H_{15}INOSi$ 343.9962; Found 343.9978.

(Z)-3-(Iodomethylene)isoindolin-1-one (5p).[35] Yield: (63.7 mg, 94%), Yield at 1 mmol scale: 260.0 mg, 96%.

(Z)-3-(Iodo(thiophen-3-yl)methylene)isoindolin-1-one (5q).[35] Yield: (79.4 mg, 90%).

(Z)-3-(Iodo(phenyl)methylene)-5,6-dimethoxyisoindolin-1-one (5r).[35] Yield: (92.6 mg, 91%).

(Z)-6-Fluoro-3-(iodo(phenyl)methylene)isoindolin-1-one (5s). Yield: (82.1 mg, 90%); White solid; TLC R_f = 0.42 (30% EtOAc:Hexanes, UV); mp 176-178 °C; **IR** (KBr, cm^{-1}) 3342, 1706, 1478, 1362; **^{1}H NMR** (400 MHz, $CDCl_3$) δ 7.85 (s, 1H), 7.49-7.41 (m, 6H), 6.95-6.90 (m, 1H), 6.47-6.43 (m, 1H); **^{13}C{^{1}H} NMR** (100 MHz, $CDCl_3$) δ 166.0, 164.2, 140.7, 136.8, 134.0, 133.9, 130.4, 129.4, 129.2, 125.2, 119.9, 119.7, 78.5; **HRMS** (ESI-TOF) *m/z*: $[M + H]^+$ Calcd for $C_{15}H_{10}FINO$ 365.9786; Found 365.9781.

(Z)-6-Fluoro-3-(iodo(p-tolyl)methylene)isoindolin-1-one (5t). Yield: (91.0 mg, 96%); White solid; TLC R_f = 0.38 (30% EtOAc:Hexanes, UV); mp 202-204 °C; **IR** (KBr, cm^{-1}) 3174, 2957, 2957, 1707, 1478, 1367; **^{1}H NMR** (400 MHz, $CDCl_3$) δ 7.72 (s, 1H), 7.43-7.41 (m, 1H), 7.33-7.31 (m, 2H), 7.27-7.21 (m, 3H, including solvent proton), 6.97-6.92 (m, 1H), 6.56-6.52 (m, 1H), 2.45 (s, 3H); **^{13}C{^{1}H} NMR** (100 MHz, $CDCl_3$) δ 166.1, 164.2, 139.6, 137.8, 136.6, 133.9, 130.4, 129.9, 129.3, 125.2, 119.9, 119.6, 79.2, 24.6; **HRMS** (ESI-TOF) *m/z*: $[M + H]^+$ Calcd for $C_{16}H_{12}FINO$ 379.9942; Found 379.9936.

((Z)-6-Fluoro-3-(iodo(thiophen-3-yl)methylene)isoindolin-1-one (5u). Yield: (89.0 mg, 96%); White solid; TLC R_f = 0.33 (30% EtOAc:Hexanes, UV); mp 182-183 °C; **IR** (KBr, cm^{-1}) 3205, 1709, 1466, 1364; **^{1}H NMR** (400 MHz, DMSO-d_6) δ 10.45 (s, 1H), 7.76-7.74 (m, 1H), 7.69-7.68 (m, 1H), 7.48-7.46 (m, 1H), 7.32-7.27 (m, 1H), 7.15-7.14 (m, 1H), 6.50-

6.47 (m, 1H); **^{13}C{^{1}H} NMR** (100 MHz, DMSO-d_6) δ 166.2, 163.6, 141.7, 138.3, 133.6, 130.9, 128.2, 127.8, 125.9, 124.8, 120.0, 109.7, 72.0; **HRMS** (ESI-TOF) *m/z*: $[M + H]^+$ Calcd for $C_{13}H_8FINOS$ 371.9350; Found 371.9367.

(Z)-3-(Iodo(phenyl)methylene)-6-nitroisoindolin-1-one (5v). Yield: (95.0 mg, 97%); Light yellow solid; TLC R_f = 0.45 (30% EtOAc:Hexanes, UV); mp 190-192 °C; **IR** (KBr, cm^{-1}) 3172, 1705, 1463, 1342; **^{1}H NMR** (400 MHz, $CDCl_3$) δ 8.61-8.60 (m, 1H), 8.25 (s, 1H), 8.11-8.08 (m, 1H), 7.51-7.42 (m, 5H), 6.62 (d, *J* = 8.8 Hz, 1H); **^{13}C{^{1}H} NMR** (100 MHz, $CDCl_3$) δ 165.0, 147.9, 140.3, 138.3, 136.6, 133.0, 130.0, 129.4, 129.1, 127.0, 124.2, 119.4, 84.2; **HRMS** (ESI-TOF) *m/z*: $[M + H]^+$ Calcd for $C_{15}H_{10}IN_2O_3$ 392.9731; Found 392.9722.

(Z)-3-(Iodo(p-tolyl)methylene)-6-nitroisoindolin-1-one (5w). Yield: (94.4 mg, 93%); Yellow solid; TLC R_f = 0.41 (30% EtOAc:Hexanes, UV); mp 235-237 °C; **IR** (KBr, cm^{-1}) 3167, 2924, 1704, 1342; **^{1}H NMR** (400 MHz, $CDCl_3$) δ 8.60-8.60 (m, 1H), 8.13-8.10 (m, 2H), 7.33-7.28 (m, 4H), 6.71 (d, *J* = 8.8 Hz, 1H), 2.46 (s, 3H); **^{13}C{^{1}H} NMR** (100 MHz, DMSO-d_6) δ 166.1, 148.0, 139.6, 139.4, 137.9, 132.9, 130.4, 129.7, 129.4, 127.6, 124.5, 118.6, 79.7, 21.5; **HRMS** (ESI-TOF) *m/z*: $[M + H]^+$ Calcd for $C_{16}H_{12}IN_2O_3$ 406.9887; Found 406.9858.

(Z)-7-(Iodo(phenyl)methylene)-6,7-dihydro-5H-pyrrolo[3,4-b]pyridin-5-one (5x). Yield: (81.8 mg, 94%); Light yellow solid; TLC R_f = 0.38 (50% EtOAc:Hexanes, UV); mp 221-223 °C; **IR** (KBr, cm^{-1}) 3427, 1702, 1466; **^{1}H NMR** (400 MHz, $CDCl_3$) δ 9.95 (s, 1H), 9.05-9.04 (m, 1H), 8.58-8.55 (m, 1H), 7.58-7.52 (m, 5H), 7.47-7.44 (m, 1H); **^{13}C{^{1}H} NMR** (100 MHz, DMSO-d_6) δ 161.8, 155.2, 152.4, 147.7, 137.5, 135.5, 129.5, 128.1, 122.5, 120.4, 79.2 (1 peak missing due to overlap); **HRMS** (ESI-TOF) *m/z*: $[M + H]^+$ Calcd for $C_{14}H_{10}IN_2O$ 348.9832; Found 348.9820.

(Z)-7-(1-Iodoheptylidene)-6,7-dihydro-5H-pyrrolo[3,4-b]pyridin-5-one (5y). Yield: (162.0 mg, 91.0%); Light yellow solid; TLC R_f = 0.20 (30% EtOAc:Hexanes, UV); mp 142-144 °C;

IR (KBr, cm^{-1}) 3310, 2958, 2924, 1707, 1459; **^{1}H NMR** (400 MHz, $CDCl_3$) δ 11.71 (s, 1H), 9.01-9.00 (m, 1H), 8.61-8.59 (m, 1H), 7.43-7.40 (m, 1H), 1.81-1.74 (m, 2H), 1.54-1.47 (m, 2H), 1.37-1.33 (m, 2H), 1.27-1.23 (m, 4H), 0.91-0.88 (m, 3H); **^{13}C{^{1}H} NMR** (100 MHz, $CDCl_3$) δ 164.0, 155.3, 153.2, 148.2, 136.1, 121.5, 119.8, 79.5, 38.7, 31.4, 28.9, 28.3, 22.5, 14.0; **HRMS** (ESI-TOF) *m/z*: $[M + H]^+$ Calcd for $C_{14}H_{18}IN_2O$ 357.0458; Found 357.0464.

(Z)-3-(Bromo(phenyl)methylene)isoindolin-1-one (6a).[71] Yield: (53.2 mg, 71%); Light yellow solid; TLC R_f = 0.37 (30% EtOAc:Hexanes, UV); mp 214-216 °C; **IR** (KBr, cm^{-1}) 3171, 1704, 1469; **^{1}H NMR** (400 MHz, $CDCl_3$) δ 7.90 (s, 1H), 7.83-7.81 (d, *J* = 7.6 Hz, 1H), 7.51-7.47 (m, 5H), 7.44-7.40 (m,1H), 7.29-7.25 (m, 1H), 6.65-6.63 (d, J = 8.0 Hz, 1H); **^{13}C{^{1}H} NMR** (100 MHz, $CDCl_3$) δ 167.2, 137.4, 135.0, 135.4, 132.2, 130.9, 130.1, 129.8, 129.2, 129.1, 123.8, 122.7, 103.7; **HRMS** (ESI-TOF) *m/z*: $[M + H]^+$ Calcd for $C_{15}H_{11}BrNO$ 300.0019; Found 300.0016.

(Z)-3-Benzylidene-2-methylisoindolin-1-one (7a).[72] This reaction was performed twice. Yield: (47.6 mg, 81%); Light yellow solid; TLC R_f = 0.48 (30% EtOAc:Hexanes, UV); mp 182-183 °C; **^{1}H NMR** (400 MHz, $CDCl_3$) δ 7.86-7.84 (m, 1H), 7.75-7.73 (m, 1H), 7.59-7.57 (m, 1H), 7.50-7.47 (m, 1H), 7.40-7.31 (m, 5H), 6.78 (s, 1H), 3.03 (s, 3H); **^{13}C{^{1}H} NMR** (100 MHz, $CDCl_3$) δ 168.8, 137.9, 136.1, 134.6, 131.7, 129.5, 128.9, 128.4, 128.0, 127.4, 123.1, 119.2, 106.4, 30.4.

(Z)-3-(4-methylbenzylidene)-2-phenylisoindolin-1-one (7b).[73] Yield: (60.0 mg, 77%). Light yellow Solid; TLC R_f = 0.28 (10% EtOAc:Hexanes, UV); **^{1}H NMR** (400 MHz, $CDCl_3$) δ 7.96 (d, *J* = 8.0 Hz, 1H), 7.86 (d, *J* = 7.6 Hz, 1H), 7.68-7.64 (m, 1H), 7.55-7.51 (m, 1H), 7.11-7.08 (m, 5H), 6.80 (s, 1H), 6.76-6.71 (m, 4H), 2.19 (s, 3H); **^{13}C{^{1}H} NMR** (100 MHz, $CDCl_3$) δ 167.9, 136.4, 135.9, 133.6, 132.3, 130.5, 129.0, 128.9, 127.8, 127.6, 127.2, 127.0, 126.7, 123.8, 119.2, 107.9, 21.1.

Procedure for the Synthesis of Aristolactam Derivatives:[63]

The isoindolin-1-one derivative (**5i** or **5j**) was dissolved (0.25 mmol) in dry, degassed benzene (20 mL), and the solution was heated at reflux under Argon atmosphere. A solution of *n*Bu_3SnH (2.2 equiv, 0.55 mmol) and AIBN (1.0 equiv, 0.25 mmol) in dry, degassed benzene (4 mL) was added by syringe over 30 minutes. Once the addition was complete, the reaction mixture was refluxed for 12 hours. Benzene was evaporated under reduced pressure, and the residue was dissolved in CH_3CN (10 mL). The solution was washed with hexane (3×50 mL) and concentrated in vacuum to give the crude product, which was purified by column chromatography using Hexanes-EtOAc as the eluent.

Dibenzo[cd,f]indol-4(5H)-one (8a). Yield: (39.5 mg, 72%); Light yellow solid; TLC R_f = 0.61 (30% EtOAc:Hexanes, UV); mp 154-156 °C; **IR** (KBr, cm^{-1}) 3414, 1707; **^{1}H NMR** (400 MHz, DMSO-d_6) δ 10.96 (s, 1H), 8.86 (d, J = 8.0 Hz, 1H), 8.69 (d, J = 7.2 Hz, 1H), 8.04-8.02 (m, 1H), 7.97 (d, J = 8.4 Hz, 1H), 7.92-7.88 (m, 1H), 7.61-7.54 (m, 2H), 7.24 (s, 1H); **^{13}C{^{1}H} NMR** (100 MHz, DMSO-d_6) δ 168.9, 135.6, 134.9, 134.2, 131.7, 129.4, 129.2, 129.0, 128.6, 127.7, 126.9, 125.3, 123.5, 123.4, 105.5. **HRMS** (ESI-TOF) *m/z*: $[M + H]^+$ Calcd for $C_{15}H_{10}NO$ 220.0757; Found 220.0774.

1,2-Dimethoxydibenzo[cd,f]indol-4(5H)-one (8b).[74] Yield: (48.9 mg, 70%); Light yellow solid; TLC R_f = 0.14 (30% EtOAc:Hexanes, UV); mp 250-251°C; **^{1}H NMR** (400 MHz, DMSO-d_6) δ 10.84 (s, 1H), 9.12-9.09 (m, 1H), 7.95-7.93 (m, 1H), 7.85 (s, 1H), 7.60-7.54 (m, 2H), 7.13 (s 1H), 4.04 (s, 3H), 4.02 (s, 3H); **^{13}C{^{1}H} NMR** (100 MHz, DMSO-d_6) δ 168.4, 154.2, 150.4, 135.1, 134.8, 129.1, 127.5, 126.9, 125.9, 125.4, 123.3, 121.6, 119.9, 109.9, 104.6, 59.9, 56.9.

ASSOCIATED CONTENT

Supporting Information

The Supporting Information is available free of charge on the ACS Publications website.

X-ray crystallographic information for compounds **5i** (CCDC 1864768) and **8a** (CCDC 1865767) (CIF), and copies of the NMR spectra for all products **(2a-2g, 4a-4aa, 5a-5y, 6a, 7a-7b, 8a-8b)** (PDF).

AUTHOR INFORMATION

Corresponding Author
**E-mail: saurabh.mehta@dtu.ac.in*

ORCID ID

Saurabh Mehta: 0000-0002-9174-128X

Dhirendra Brahmchari: 0000-0003-1787-5762

Notes

The authors declare no competing financial interest.

ACKNOWLEDGMENTS

We gratefully acknowledge the Delhi Technological University, and the Technical Education Quality Improvement Programme, Phase III (TEQIP-III) of Government of India for financially supporting this work. We also acknowledge USIC-CIF, University of Delhi, for acquiring the NMR, Mass and SC-XRD data, and the instrumentation facility at DTU for IR analysis. We are thankful to Dr. P. K. Sudhadevi (crystallographer) at SAIF, IIT Madras for solving the SC-XRD data for **5i** and **8a**. We are also thankful to Mr. Mange Ram Mangyan (DTU) for his support in experimental work, and Dr. Om Prakash Yadav (ARSD College) for his help in collecting NMR data. Finally we thank Professor N. G. Ramesh (IIT Delhi) for useful discussions.

REFERENCES

(1) Thong, W. L.; Shin-ya, K.; Nishiyama, M.; Kuzuyama, T. Discovery of an antibacterial isoindolinone-containing tetracyclic polyketide by cryptic gene activation and characterization of its biosynthetic gene cluster. *ACS Chem. Biol.*, **2018**, *13*, 2615–2622.

(2) Yao, T.; Guo, Z.; Liang, X.; Qi, L. Regio- and stereoselective electrophilic cyclization approach for the protecting-group-free synthesis of alkaloids Lennoxamine, Chilenine, Fumaridine, 8-Oxypseudoplamatine, and 2-*O*-(Methyloxy)fagaronine. *J. Org. Chem.* **2018**, *83*, 13370-13380.

(3) Reddy, M. C.; Jeganmohan, M. Total synthesis of aristolactam alkaloids *via* synergistic C–H bond activation and dehydro-Diels-Alder reactions. *Chem. Sci.* **2017**, *17*, 4130-4135 and references cited therein.

(4) Kim, Y. H.; Kim, M.; Yoo, M.; Kim, J. E.; Lee, H. K.; Heo, J.-N.; Lee, C. O.; Yoo, M.; Jung, K.-Y.; Yun, C.-S.; Moon, S. W.; Chang, H. K.; Chung, C.-W.; Pyo, S.; Choi, S. U.; Park, C. H. A natural compound, aristoyagonine, is identified as a potent bromodomain inhibitor by mid-throughput screening. *Biochem. Biophys. Res. Commun.* **2018**, *503*, 882-887.

(5) The ALLHAT Officers and Coordinators for the ALLHAT Collaborative Research Group. Major outcomes in high-risk hypertensive patients randomized to angiotensin-converting enzyme inhibitor or calcium channel blocker vs diuretic the antihypertensive and lipid-lowering treatment to prevent heart attack trial (ALLHAT). *JAMA J. Am. Med. Assoc.* **2002**, *288*, 2981–2997.

(6) Belliotti, T. R.; Brink, W. A.; Kesten, S. R.; Rubin, J. R.; Wustrow, D. J.; Zoski, K. T.; Whetzel, S. Z.; Corbin, A. E.; Pugsley, T. A.; Heffner, T. G.; Wise, L. D. Isoindolinone enantiomers having affinity for the Dopamine D_4 receptor. *Bioorg. Med. Chem. Lett.* **1998**, *8*, 1499–1502.

(7) Stuk, T. L.; Assink, B. K.; Bates, R. C., Jr.; Erdman, D. T.; Fedij, V.; Jennings, S. M.; Lassig, J. A.; Smith, R. J.; Smith, T. L. An efficient and cost-effective synthesis of Pagoclone. *Org. Process Res. Dev.* **2003**, *7*, 851–855.

(8) Linden, M.; Hadler, D.; Hofmann, S. Randomized, double-blind, placebo-controlled trial of the efficacy and tolerability of a new isoindoline derivative (DN-2327) in generalized anxiety. *Hum. Psychopharmacol.* **1997**, *12*, 445-452.

(9) Atack, J. R. The benzodiazepine binding site of $GABA_A$ receptors as a target for the development of novel anxiolytics. *Expert Opin. Investig. Drugs* **2005**, *14*, 601-618.

(10) Lorion, M.; Couture, A.; Deniau, E.; Grandclaudon, P. Complementary Synthetic Approaches to constitutionally diverse *N*-Aminoalkylated isoindolinones: Application to the synthesis of Falipamil and 5-HT_{1A} receptor ligand analogues. *Synthesis* **2009**, 1897–1903.

(11) Chen, Z.-Y.; Wu, L.-Y.; Fang, H.-S.; Zhang, T.; Mao, Z.-F.; Zou, Y.; Zhang, X.-J.; Yan, M. Intramolecular hydroamidation of *ortho*-vinyl benzamides promoted by Potassium *tert*-Butoxide/*N*,*N*-Dimethylformamide. *Adv. Synth.Catal.* **2017**, *359*, 3894-3899.

(12) Bisai, V.; Suneja, A.; Singh, V. K. Asymmetric alkynylation/lactamization cascade: An expeditious entry to enantiomerically enriched isoindolinones. *Angew. Chem. Int. Ed.* **2014**, *53*, 10737–10741.

(13) Adachi, S.; Onozuka, M.; Yoshida, Y.; Ide, M.; Saikawa, Y.; Nakata, M. Smooth isoindolinone formation from isopropyl carbamates via Bischler–Napieralski-type cyclization. *Org. Lett.* **2014**, *16*, 358–361.

(14) Tiso, S.; Palombi, L.; Vignes, C.; Di Mola, A.; Massa, A. Organocatalysts and sequential asymmetric cascade reactions in the synthesis of functionalized isoindolinones and benzoindolizidinones. *RSC Adv.* **2013**, *3*, 19380-19387.

(15) Chen, X.; Ge, F.-F.; Lu, T.; Zhou, Q.-F. Stereoselective synthesis of 3-methyleneisoindolin-1-ones via base-catalyzed intermolecular reactions of electron-deficient alkynes with *N*–Hydroxyphthalimides. *J. Org. Chem.* **2015**, *80*, 3295−3301.

(16) Cao, H.; McNamee, L.; Alper, H. Syntheses of substituted 3-methyleneisoindolin-1-ones by a palladium-catalyzed sonogashira coupling−carbonylation−hydroamination sequence in phosphonium salt-based ionic liquids. *Org. Lett.* **2008**, *10*, 5281− 5284.

(17) Hazarika, D.; Phukan, P. Copper-catalyzed stereoselective domino synthesis of (*Z*)-3-methyleneisoindolin-1-one. *ChemistrySelect* **2018**, *3*, 2474-2478 and references cited therein.

(18) Mancuso, R.; Pomelli, C. S.; Raut, D. S.; Marino, N.; Giofrè,S. V.; Romeo, R.; Sartini, S.; Chiappe, C.; Gabriele, B. Copper-catalyzed recyclable synthesis of (*Z*)-3-alkylideneisoindolinones by cycloisomerization of 2-alkynylbenzamides in ionic liquids. ChemistrySelect 2017, 2, 894−899 and references cited therein.

(19) Kundu, N. G.; Khan, M. W. Palladium-catalysed heteroannulation with terminal alkynes: a highly regio- and stereoselective synthesis of (*Z*)-3-Aryl(alkyl)idene isoindolin-1-ones. *Tetrahedron* **2000**, *56*, 4777–4792.

(20) Kondo, Y.; Shiga, F.; Murata, N.; Sakamoto, T.; Yamanaka, H. Condensed heteroaromatic ring systems. XXIV. Palladium-catalyzed cyclization of 2-substituted phenylacetylenes in the presence of carbon monoxide. *Tetrahedron* **1994**, *50*, 11803−11812.

(21) Koradin, C.; Dohle, W.; Rodriguez, A. L.; Schmid, B.; Knochel, P. Synthesis of polyfunctional indoles and related heterocycles mediated by cesium and potassium bases. *Tetrahedron* **2003**, *59*, 1571−1587.

(22) Tan, J.; Tong, Y.; Chen, Z. Alkali-metal promoted chemo- and regioselective cycloisomerization reactions to (*Z*)-3-alkylideneisoindolin-1-ones: Unusual positive role of H_2O. *ChemistrySelect* **2018**, *3*, 3886–3890.

(23) Wu, M.-J.; Chang, L.-J.; Wei, L.-M.; Lin, C.-F. A direct anionic cyclization of 2-alkynylbenzonitrile to 3-substituted-1(2*H*)-isoquinolones and 3-benzylideneisoindol-2-ones initiated by methoxide addition. *Tetrahedron* **1999**, *55*, 13193−13200.

(24) Royo, S.; Chapman, R. S. L.; Sim, A. M.; Peacock, L. R.; Bull, S. D. *Aza*-conjugate addition methodology for the synthesis of *N*-Hydroxy-isoindolin-1-ones. *Org. Lett.* **2016**, *18*, 1146–1149.

(25) Cao, Z.; Zhu, H.; Meng, X.; Guan, J.; Zhang, Q.; Tian, L.; Sun, X.; Chen, G.; You, J. Metal-free reaction of *ortho*-carbonylated alkynyl-substituted arylaldehydes with common amines: Selective access to functionalized Isoindolinone and Indenamine derivatives. *Chem. Eur. J.* **2016**, *22*, 16979−16985.

(26) Aggarwal, T.; Kumar, S.; Verma, A. K. Iodine-Mediated Synthesis of Heterocycles *via* Electrophilic Cyclization of Alkynes. *Org. Biomol. Chem.* **2016**, *14*, 7639–7653.

(27) Godoi, B.; Schumacher, R. F.; Zeni, G. Synthesis of Heterocycles via Electrophilic Cyclization of Alkynes Containing Heteroatom. *Chem. Rev.* **2011**, *111*, 2937–2980.

(28) Issaian, A.; Tu, K. N.; Blum, S. A. Boron–Heteroatom Addition Reactions via Borylative Heterocyclization: Oxyboration, Aminoboration, and Thioboration. *Acc. Chem. Res.*, **2017**, *50*, 2598–2609.

(29) Mehta, S.; Waldo, J. P.; Larock, R. C. Competition Studies in Alkyne Electrophilic Cyclization Reactions. *J. Org. Chem.* **2009**, *74*, 1141–1147.

(30) Mehta, S.; Larock, R. C. Iodine/Palladium Approaches to the Synthesis of Polyheterocyclic Compounds. *J. Org. Chem.* **2010**, *75*, 1652–1658.

(31) Chinta, B. S.; Sanapa, H.; Vasikarla, K. P.; Baire, B. Highly regioselective, electrophile induced cyclizations of 2-(prop-1-ynyl)benzamides. *Org. Biomol. Chem.* **2018**, *16*, 3947-3951.

(32) Yao, T.; Larock, R. C. Regio- and Stereoselective Synthesis of Isoindolin-1-ones via Electrophilic Cyclization. *J. Org. Chem.* **2005**, *70*, 1432−1437.

(33) Mehta, S.; Yao, T.; Larock, R. C. Regio- and Stereoselective Synthesis of Cyclic Imidates via Electrophilic Cyclization of 2-(1-Alkynyl)benzamides. A Correction. *J. Org. Chem.* **2012**, *77*, 10938−10944.

(34) Schlemmer, C.; Andernach, L.; Schollmeyer, D.; Straub, B. F.; Opatz, T. Iodocyclization of *o*-Alkynylbenzamides Revisited: Formation of Isobenzofuran-1(3*H*)-imines and 1*H*-Isochromen-1-imines Instead of Lactams. *J. Org. Chem.* **2012**, *77*, 10118−10124.

(35) Brahmchari, D.; Verma, A. K.; Mehta, S. Regio- and Stereoselective Synthesis of Isoindolin-1-ones through BuLi-Mediated Iodoaminocyclization of 2-(1-Alkynyl)benzamides. *J. Org. Chem.* **2018**, *83*, 3339−3347 and references cited therein.

(36) Mayr, H.; Breugst, M.; Ofial, A. R. Farewell to the HSAB Treatment of Ambident Reactivity. *Angew. Chem., Int. Ed.* **2011**, *50*, 6470−6505.

(37) Breugst, M.; Zipse, H.; Guthrie, J. P.; Mayr, H. Marcus Analysis of Ambident Reactivity. *Angew. Chem., Int. Ed.* **2010**, *49*, 5165−5169.

(38) Breugst, M.; Tokuyasu, T.; Mayr, H. Nucleophilic Reactivities of Imide and Amide Anions. *J. Org. Chem.* **2010**, *75*, 5250−5258.

(39) Robin, S.; Rousseau, G. Electrophilic cyclization of unsaturated amides. *Tetrahedron* **1998**, *54*, 13681−13736.

(40) Bian, M.; Yao, W.; Ding, H.; Ma, C. Highly Efficient Access to Iminoisocoumarins and α-Iminopyrones *via* AgOTf-Catalyzed Intramolecular Enyne−Amide Cyclization. *J. Org. Chem.* **2010**, *75*, 269−272.

(41) Bianchi, G.; Chiarini, M.; Marinelli, F.; Rossi, L.; Arcadi, A. Product Selectivity Control in the Heteroannulation of *o*-(1-Alkynyl)benzamides. *Adv. Synth. Catal.* **2010**, *352*, 136−142.

(42) Okitsu, T.; Nakahigashi, H.; Sugihara, R.; Fukuda, I.; Tsuji, S.; In, Y.; Wada, A. Silyl Group-Directed 6-*exo-dig* Iodocyclization of Homopropargylic Carbamates and Amides. *Chem. Eur. J.* **2018**, *24*, 18638-18642.

(43) Saame, J.; Rodima, T.; Tshepelevitsh, S.; Kütt, A.; Kaljurand, I.; Haljasorg, T.; Koppel, I. A.; Leito, I. Experimental Basicities of Superbasic Phosphonium Ylides and Phosphazenes. *J. Org. Chem* **2016**, *81*, 7349–7361.

(44) Ishikawa, T. *Superbases for Organic Synthesis: Guanidines, Amidines, Phosphazenes and Related Organocatalysts*; Ishikawa, T., Ed.; John Wiley & Sons, Ltd: Chichester, UK, 2009.

(45) Schwesinger, R.; Hasenfratz, C.; Schlemper, H.; Walz, L.; Peters, E.-M.; Peters, K.; von Schnering, H. G. How Strong and How Hindered Can Uncharged Phosphazene Bases Be?. *Angew. Chem. Int. Ed.* **1993**, *32*, 1361–1363.

(46) Kolonko, K. J.; Reich, H. J. Stabilization of Ketone and Aldehyde Enols by Formation of Hydrogen Bonds to Phosphazene Enolates and Their Aldol Products. *J. Am. Chem. Soc.* **2008**, *130*, 9668–9669.

(47) Imahori, T.; Hori, C. Kondo, Y. Functionalization of Alkynes Catalyzed by *t*-Bu-P4 Base. *Adv. Synth. Catal.* **2004**, *346*, 1090-1092 and references cited therein.

(48) Kanazawa, C.; Goto, K.; Terada, M. Phosphazene base-catalyzed intramolecular cyclization for efficient synthesis of benzofurans *via* carbon–carbon bond formation. *Chem. Commun.* **2009**, 5248–5250.

(49) Kanazawa, C.; Terada, M. Dichotomous Control of *E*/*Z*-Geometry in Intramolecular Cyclization of *o*-Alkynylbenzamide Derivatives Catalyzed by Organic Superbase P4- *t*Bu in the Presence/Absence of Water. *Chem. Asian J.* **2009**, *4*, 1668–1672.

(50) Sonogashira, K.; Tohda, Y.; Hagihara, N. A convenient synthesis of acetylenes: catalytic substitutions of acetylenic hydrogen with bromoalkenes, iodoarenes and bromopyridines. *Tetrahedron Lett.* **1975**, *16*, 4467–4470.

(51) Volpe, R.; Aurelio, L.; Gillin, M. G.; Krenske, E. H.; Flynn, B. L. Mapping the Interactions of I_2, $I^{\cdot}$, I^{-}, and I^{+} with Alkynes and Their Roles in Iodocyclizations. *Chem. - Eur. J.* **2015**, *21*, 10191−10199.

(52) Wang, T.; Zhang, H.; Han, F.; Long, L.; Lin, Z.; Xia, H. Key Intermediates of Iodine-Mediated Electrophilic Cyclization: Isolation and Characterization in an Osmabenzene System. *Angew. Chem., Int. Ed.* **2013**, *52*, 9251–9255.

(53) Mehta, S.; Waldo, J. P.; Neuenswander, B.; Lushington, G. H.; Larock, R. C. Solution-Phase Parallel Synthesis of a Multisubstituted Cyclic Imidate Library. *ACS Comb. Sci.* **2013**, 15, 247−254.

(54) Dubrovskiy, A. V.; Markina, N. A.; Larock, R. C. Iodocyclization, Followed by Palladium-Catalyzed Coupling: A Versatile Strategy for Heterocyclic Library Construction. *Comb. Chem. High Throughput Screen.* **2012**, *15*, 451-472.

(55) Houghton, P. J.; Ogutveren, M. Aristolochic acids and Aristolactams from *Arilstolochia auricularia*. *Phytochemistry* **1991**, *30*, 253–254.

(56) Zhang, Y.-N.; Zhong, X.-G.; Zheng, Z.-P.; Hu, X.-D.; Zuo, J.-P.; Hu, L.-H. Discovery and synthesis of new immunosuppressive alkaloids from the stem of *Fissistigma oldhamii* (Hemsl.) Merr. *Bioorg. Med. Chem.* **2007**, *15*, 988–996.

(57) Chen, Y.-C.; Chen, J.-J.; Chang, Y.-L.; Teng, C.-M.; Lin, W.-Y.; Wu, C.-C.; Chen, I.-S. A new Aristolactam alkaloid and anti-platelet aggregation constituents from *Piper taiwanense*. *Planta Med.* **2004**, *70*, 174–177.

(58) Kim, S. R.; Sung, S. H.; Kang, S. Y.; Koo, K. A.; Kim, S. H.; Ma, C. J.; Lee, H.-S.; Park, M. J.; Kim, Y. C. Aristolactam BII of *Saururus chinensis* attenuates glutamate-induced neurotoxicity in rat cortical cultures probably by inhibiting nitric oxide production. *Planta Med.* **2004**, *70*, 391–396.

(59) Marti, G.; Eparvier, V.; Morleo, B.; Le Ven, J.; Apel, C.; Bodo, B.; Amand, S. Dumontet, V.; Lozach, O.; Meijer, L.; Guéritte, F.; Litaudon, M. Natural Aristolactams and Aporphine alkaloids as inhibitors of CDK1/Cyclin B and DYRK1A. *Molecules* **2013**, *18*, 3018-3027 and references cited therein.

(60) Choi, Y. L.; Kim, J. K.; Choi, S.-U.; Min, Y.-K.; Bae, M.-A.; Kim, B.-T.; Heo, J.-N. Synthesis of aristolactam analogues and evaluation of their antitumor activity. *Bioorg. Med. Chem. Lett.* **2009**, *19*, 3036-3040.

(61) Mata, R.; Morales, I.; Pérez, O.; Rivero-Cruz, I.; Acevedo, L.; Enriquez-Mendoza, I.; Bye, R.; Franzblau, S.; Timmermann, B. Antimycobacterial compounds from *Piper sanctum*. *J. Nat. Prod.* **2004**; *67*, 1961–1968.

(62) Couture, A.; Deniau, E.; Grandclaudon, P.; Rybalko-Rosen, H.; Léonce, S.; Pfeiffer, B.; Renard, P. Synthesis and Biological Evaluation of Aristolactams. *Bioorg. Med. Chem. Lett.* **2002**, *12*, 3557-3559 and references cited therein.

(63) Rys, V.; Couture, A.; Deniau, E.; Grandclaudon, P. A Short Total Synthesis of the Alkaloids Piperolactam C, Goniopedaline, and Stigmalactam. *Eur. J. Org. Chem.* **2003**, *2003*, 1231–1237.

(64) Songsichan, T.; Promsuk, J.; Rukachaisirikul, V.; Kaeobamrung, J. Synthesis of Quinazolinones from 2-Iodobenzamides and Enaminones *via* Copper-Catalyzed Domino Reactions. *Org. Biomol. Chem.* **2014**, *12*, 4571–4575.

(65) Kong, L.-L.; Fan, L.-Y. Magnetically recyclable copper modified GO/Fe_3O_4 catalyst for efficient synthesis of quinazolinones. *Chinese Chem. Lett.* **2016**, *27*, 827–831.

(66) Spivey, A. C.; McKendrick, J.; Srikaran, R.; Helm, B. A. Solid-Phase Synthesis of an A-B Loop Mimetic of the Cε3 Domain of Human IgE: Macrocyclization by Sonogashira Coupling. *J. Org. Chem.* **2003**, *68*, 1843–1851.

(67) Long, Y.; She, Z.; Liu, X.; Chen, Y. Synthesis of 1-Aminoisoquinolines by Gold(III)-Mediated Domino Reactions from 2-Alkynylbenzamides and Ammonium Acetate. *J. Org. Chem.* **2013**, *78*, 2579–2588.

(68) Minami, H.; Sueda, T.; Okamoto, N.; Miwa, Y.; Ishikura, M.; Yanada, R. Copper-Catalyzed Tandem Amide *N*-Arylation and Regioselective Cyclization of 2-Alkynylbenzamides. *Eur. J. Org. Chem.* **2016**, *2016*, 541–548.

(69) Praveen, C.; Dheenkumar, P.; Perumal, P. T. Super acid catalysed sequential hydrolysis/cycloisomerization of *o*-(acetylenic)benzamides under microwave condition: Synthesis, antinociceptive and antiinflammatory activity of substituted isocoumarins. *J. Chem. Sci.* **2013**, *125*, 71–83.

(70) Dev, K.; Maurya, R. Facile synthesis of 11-aryl-6*H*-isoindolo[2,1-*a*]indol-6-ones *via* hypervalent iodine(III)-promoted cascade cyclization. *RSC Adv.* **2015**, *5*, 13102–13106.

(71) Hong, S. Y.; Son, J.; Kim, D.; Chang, S. Ir(III)-Catalyzed Stereoselective Haloamidation of Alkynes Enabled by Ligand Participation. *J. Am. Chem. Soc.* **2018**, *140*, 12359–12363.

(72) Munoz, S. B.; Aloia, A. N.; Moore, A. K.; Papp, A.; Mathew, T.; Fustero, S.; Olah, G. A.; Prakash, G. K. S. Synthesis of 3-substituted isoindolin-1-ones *via* a tandem desilylation, cross-coupling, hydroamidation sequence under aqueous phase-transfer conditions. *Org. Biomol. Chem.* **2016**, *14*, 85–92.

(73) Gogoi, A.; Guin, S.; Rout, S. K.; Majji, G.; Patel, B. K. A Cu-catalysed synthesis of substituted 3-methyleneisoindolin-1-one. *RSC Adv.* **2014**, *4*, 59902–59907.

(74) Kim, J. K.; Kim, Y. H.; Nam, H. T.; Kim, B. T.; Heo, J.-N. Total Synthesis of Aristolactams via a One-Pot Suzuki-Miyaura Coupling/Aldol Condensation Cascade Reaction. *Org. Lett.* **2008**, *10*, 3543–3546.

This article has been accepted for publication in a future issue of this journal, but has not been fully edited. Content may change prior to final publication. Citation information: DOI 10.1109/TIE.2019.2905835, IEEE Transactions on Industrial Electronics

Power Quality Enhancement Using Euclidean Direction Search Based Control Technique

Manoj Badoni, *Member, IEEE,* Alka Singh*, Senior Member, IEEE*, Bhim Singh, *Fellow, IEEE*

***Abstract*—This paper proposes the design and control of a three phase four wire DSTATCOM (Distribution Static Compensator) for elimination of several PQ (Power Quality) issues namely harmonics, reactive power, load unbalancing and neutral current. A three phase VSC (Voltage Source Converter) and a zig-zag transformer based configuration, is utilized as a DSTATCOM. The zig-zag transformer is operated to provide a suitable path for load neutral current and other power quality problems are mitigated by designing a suitable control for VSC. The control of VSC is developed using EDS (Euclidean Direction Search) technique based adaptive control theory. This control algorithm is designed to extricate fundamental constituents from the load current and used to generate switching pulses for VSC. The improved behavior of proposed EDS based control is observed by comparing it with other existing controllers. Real time performance of the EDS control is verified on a developed prototype in the laboratory using VSC and DSP- dSPACE1104 R&D controller.**

***Index Terms*—Harmonics, reactive power, power quality, DSTATCOM, adaptive control**

NOMENCLATURE

DSTATCOM	Distribution static compensator.
PQ	Power quality.
VSC	Voltage source converter.
EDS	Euclidean direction search.
TPFW	Three-phase four-wire.
u_{pa}, u_{pb}, u_{pc}	Unit in-phase components.
V_t	PCC voltage magnitude.
i_{ln} ,i_{zn}, i_{sn}	Load, zig-zag transformer and grid neutral currents
i_{za}, i_{zb}, i_{zc}	Zig-zag transformer currents
i_{pdc}	DC link PI controller output.
$X(n)$	Input data vector.
i_{lest}	Estimated load current.
e_n	Error between actual and estimated load current.
J_n	Least square objective function.
β	Exponential weighting factor.
g	Search direction.
λ	Forgetting factor.
α	Step size.
Q, r	Coefficient and vector matrices.
i_{lpa}, i_{lpb}, i_{lpc}	Fundamental active weight components of load current.
i_{pm}, i_p	Average and reference active weight components.
i_{pa}^*, i_{pb}^*, i_{pc}^*	Reference active components of grid currents.
u_{qa}, u_{qb}, u_{qc}	Unit quadrature components.
i_{lqa}, i_{lqb}, i_{lqc}	Fundamental reactive weight components of load current.
i_t	AC bus PI controller output.
i_{qm}, i_q	Average reactive and reference reactive components.
i_{qa}^*, i_{qb}^*, i_{qc}^*	Reference reactive components of grid currents.
i_{sa}^* , i_{sb}^* , i_{sc}^*	Reference grid currents.
PWMCC	Pulse width modulation current controller.
LMS	Lease mean square.
RLS	Recursive least square.
DPF	Displacement power factor.

Manuscript received April 05, 2018; revised July 01, 2018, September 18, 2018, November 08, 2018 and January 28, 2019; accepted February 25, 2019.

Manoj Badoni is with the Electrical and Instrumentation Engineering Department, Thapar Institute of Engineering and Technology, Patiala, Punjab, India (e-mail: manojbadoni23@gmail.com).

Alka Singh is with the Electrical Engineering Department, Delhi Technological University, Delhi, India (e-mail: alkasingh.dr@gmail.com).

Bhim Singh is with the Electrical Engineering Department, Indian Institute of Technology, Delhi, India (e-mail: bhimsinghiitd61@gmail.com).

I. INTRODUCTION

The increasing dependency on power electronics based devices at the utilization level, has injected high level of harmonics in electrical supply system. A large number of consumer equipment draw non-sinusoidal currents and act as nonlinear loads, which pollute the electrical supply system. Power quality issues manifest at PCC (Point of Common Coupling), which is connected to other loads. Issues such as voltage harmonics, surge, sag/dip, swell and so on, affect the performance of connected loads and their lifespan. Moreover, problems concerning the input currents drawn from mains include harmonics, reactive power, and unbalanced currents and neutral current [1]. A number of standards have been developed by different organizations (IEEE and IEC), in order to limit numerous power quality problems. Various solutions to power quality (PQ) issues are suggested in the literature. These include passive, active and hybrid filters. A group of devices used at the distribution system named custom power devices (CPDs) is operated to solve PQ issues. These devices comprise of a shunt compensator as DSTATCOM (Distribution Static Compensator), series compensator as DVR (Dynamic Voltage Restorer) and series-shunt compensator as UPQC (Unified Power Quality Conditioner). Among these, DSTATCOM is used to minimize current based PQ issues [2]. Configurations of DSTATCOM namely three-phase three-wire (TPTW) and three-phase four-wire (TPFW) are mainly reported in the literature [3]. Three-phase three-wire

0278-0046 (c) 2018 IEEE. Personal use is permitted, but republication/redistribution requires IEEE permission. See http://www.ieee.org/publications_standards/publications/rights/index.html for more information.

This article has been accepted for publication in a future issue of this journal, but has not been fully edited. Content may change prior to final publication. Citation information: DOI 10.1109/TIE.2019.2905835, IEEE Transactions on Industrial Electronics

DSTATCOM is applicable for regulating load reactive power, eliminating harmonics current at distribution system. TPFW shunt active compensator is utilized for reduction of neutral current and unbalanced load currents together with reactive power compensation and reduction of supply current harmonics. Different topologies of shunt compensator for neutral current reduction with other compensation features, are reported in the literature. Few of them are based on four-leg voltage source converter (VSC), three-leg VSC (split capacitors), three leg VSC with star/delta transformers, three leg VSC with zigzag transformers and three leg VSC with T-connected transformer [4]. Three-leg VSC with zigzag transformer type topology is preferred because it requires a three leg VSC, which is a standard configuration, popular and easily controlled using a low cost controller [5]. Various control approaches are reported for estimation of the fundamental currents (from distorted load currents) and control pulses for IGBTs (Insulated Gate Bipolar Transistors) of VSC used as a DSTATCOM. These control algorithms include synchronous reference frame (SRF) [6], Icosϕ [7], Lyapunov stability theory [8], moving average filter [9], model predictive control [10], modulated carrier control using on-time doubler [11], Chebyshev function operated ANN controller [12] and adaptive Volterra second-order filter (AVSF) [13].

Adaptive theory based control utilizes feedback mechanism and performs self-adjustment of internal parameters of the controller [14]. Some of them are reported in the literature to develop control algorithm for the shunt compensator [15]. Few of them, include adaptive model-based technique for harmonic diagnosis [16] based on the data-driven conception, adaptive neural filtering [17], which is recursive notch filter for fundamental frequency of the grid, model reference adaptive control [18], adaptive recursive inverse [19], LMS (Least Mean Square) based NN (Neural Network) structure [20], and variable forgetting factor RLS (VFFRLS) [21].

The LMS adaptive controllers have been widely used for the shunt compensator as it is computationally simple to implement [22]. However, the use of this technique results in slow convergence of weight and higher steady state error. Therefore, performance of LMS technique is just satisfactory and better algorithms may be required. Recursive least square (RLS) algorithm gives fast convergence of weights and lower steady state error. However, the complex mathematical equations of RLS may prohibit its use in real time applications. An adaptive control theory based on Euclidean Direction Search (EDS) has been first introduced by Fang and Bose [23] and it combines the benefits of both computational efficiency of LMS and fast convergence of RLS technique [24]-[26]. Its application in electrical power distribution systems, has not been reported in the literature.

In this paper, an EDS based control approach is designed, developed and tested for improving power quality in TPFW distribution system under a wide variation of loading conditions. Multiple objectives are achieved from the proposed EDS control viz. alleviating harmonics, providing load reactive power, correcting power factor and supply currents balancing. A standard three-phase, three-leg topology of DSTATCOM is used with an additional zigzag transformer associated for recompense of neutral current. Appropriate comparison with RLS and LMS algorithms, shows fast tracking can be achieved even with low computational burden. This makes real time implementation of adaptive controllers attractive under constantly varying and unpredictable loads.

II. Developed Three Phase Four Wire Shunt Compensator

The equivalent diagram of a four wire compensator with zig-zag transformer is presented in Fig. 1. This system generates compensating currents, which are required to compensate PQ issues viz. harmonics, immoderate reactive power, unbalancing and load neutral current.

A. System Configuration

Three phase four wire load is connected to the AC mains having an impedance (inductor and resistor) corresponding to the line inductance (L_s) and resistance (R_s). The shunt compensator is coupled to the AC mains at the PCC via interfacing inductors (L_f). This consists of a voltage source converter (VSC) made up of IGBTs with antiparallel diode and self-sustained DC link. A passive ripple filter consists of series resistive and capacitive (R_f-C_f) connected at the PCC for suppressing switching noise generated by VSC. Series impedance (L_{sn} and R_{sn}) is connected across supply side neutral wire. The designed values of capacitance and voltage at DC link, interfacing inductors, ripple filters and VSC rating, are given in Appendix.

B. Zig-Zag Transformer Design

A zig-zag transformer attenuates the neutral current on the grid side and offers a passage for load neutral current through it [7], [27]. It is designed with three single-phase transformers (T_1, T_2 andT_3) of rating 2.5 kVA, 110/110V (turn ratio 1:1) each comprising the neutral conductor, which offers path for zero sequence current. The zig-zag transformer is designed by using two similar windings per phase coupled in series phase opposition as depicted in Fig. 2. Terminal a_1 of transformer T_1 is attached to c_2 terminal (in phase opposition) of transformer T_3. Terminal b_1 of transformer T_2 is connected to terminal a_2 (in phase opposition) of transformer T_1 and terminal c_1 of transformer T_3 is attached to terminal b_2 (in phase opposition) of transformer T_2. During unbalanced load condition, the neutral current in the load (i_{ln}), passes through the zig-zag transformer neutral (i_{zn}) and is distributed equally (equal in phase and magnitude) across three output terminals.

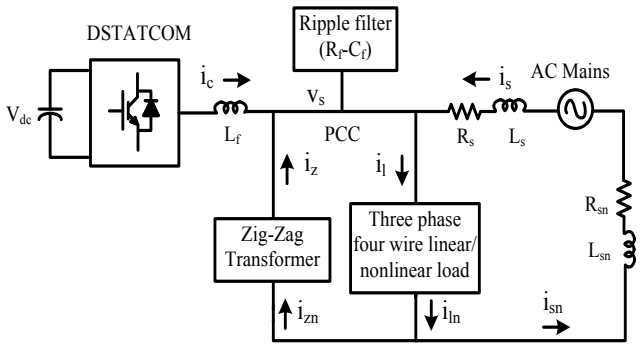

Fig. 1 Equivalent diagram of four wire shunt compensator

0278-0046 (c) 2018 IEEE. Personal use is permitted, but republication/redistribution requires IEEE permission. See http://www.ieee.org/publications_standards/publications/rights/index.html for more information.

This article has been accepted for publication in a future issue of this journal, but has not been fully edited. Content may change prior to final publication. Citation information: DOI 10.1109/TIE.2019.2905835, IEEE Transactions on Industrial Electronics

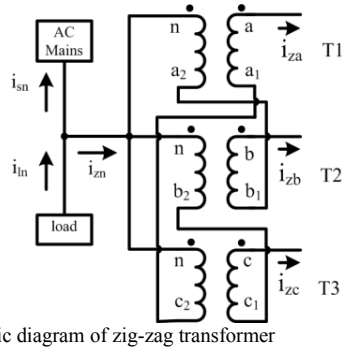

Fig. 2 Schematic diagram of zig-zag transformer

III. Control Algorithm

The block diagram of EDS (Euclidean Direction Search) based control for a shunt compensator, is shown in Fig. 3. This control is utilized to obtain fundamental components of load currents with unit templates in phase of PCC voltages. This control is implemented in a DSP-dSPACE 1104 as shown in Fig. 1.The mathematical formulation of EDS based control, is given here.

A. Reference Active Grid Current Computation

The in-phase (unit magnitude) components (u_{pa}, u_{pb} and u_{pc}), of PCC voltages (v_{sa}, v_{sb} and v_{sc}) are calculated as,

$$u_{pa} = v_{sa}/V_t;\ u_{pb} = v_{sb}/V_t;\ \text{and}\ u_{pc}\, v_{sc}/V_t \quad (1)$$

where, V_t is the magnitude of PCC voltage, which is determined as,

$$V_t = \sqrt{2(v_{sa}^2 + v_{sb}^2 + v_{sc}^2)/3} \quad (2)$$

In Fig. 1, DC link voltage (V_{dc}) is the voltage at the DC link capacitor (C_{dc}) connected at DC side of VSC. This voltage is sensed using voltage sensor (LEM LV-25p), which is connected across DC link. This voltage (V_{dc}) is detected and subtracted from the set voltage (V_{dc}^*), to compute an error signal (v_{de}). This error signal (v_{de}) is fed to proportional integral (PI) controller. The PI controller output (i_{pdc}), is utilized to set DC link voltage at specified reference value and also to realize the switching losses in VSC [21].

The fundamental active constituents of load currents, are extracted using EDS based control. This control is designed to minimize the cost function and update the weights.

For the input load current (i_l), let *X(n)* be the input data vector, which is represented by unit in-phase and the unit quadrature vector for this case as, [$u_{pa}u_{qa}u_{5pa}u_{5qa}$…]. Theses vectors are computed in following section. Let $i_{lp}(n)$ be the fundamental weight vector of the control, the estimated quantity (or load current, i_{lest}) is given as,

$$i_{lest} = X^T(n) i_{lp}(n) \quad (3)$$

Therefore, the error is given as,

$$e_n = i_l^*(n) - X^T(n) i_{lp}(n) \quad (4)$$

The least square objective function, J_n is defined as,

$$J_n(w) = \min_{i_{lpa} \in R^N} \left\{ \sum_{i=1}^{n} \beta(n,p) \left(i_l(p) - i_{lp}(n)^T X(p) \right)^2 \right\} \quad (5)$$

where exponential weighting factor, $\beta(n, p)=\lambda^{n-i}$, i=1,2,…, n and forgetting factor (λ) lie within the range $0 \leq \lambda \leq 1$. Here in (5), n be the number of coefficients of the controller and $i_{lp}(n)$ be the weight vector.

The weight updation equation of EDS control for load current, is performed using [23],

$$i_{lp}(n) = i_{lp}(n-1) + \alpha \quad (6)$$

where α is step size to minimize least square objective function and symbol g denotes the search direction. This is an *N×1* column matrix with *N-1* "0" elements and only one "1" element, the step size α is given as,

$$\alpha = -\left. g^T \left(Q(n) i_{lp}(n) - r(n) \right) \right/ g^T Q(n) g \quad (7)$$

The coefficient matrix Q(n) and vector r(n), are updated as given as,

$$Q(n) = \sum_{i=1}^{n} \lambda^{n-i} X(i) X(i)^T = \lambda Q(n-1) + X(n) X(n)^T \quad (8)$$

$$r(n) = \sum_{i=1}^{n} \lambda^{n-i} i_l^*(i) X(i) = \lambda r(n-1) + i_l^*(n) X(n) \quad (9)$$

The weight updation equation for three phases of load currents are defined as,

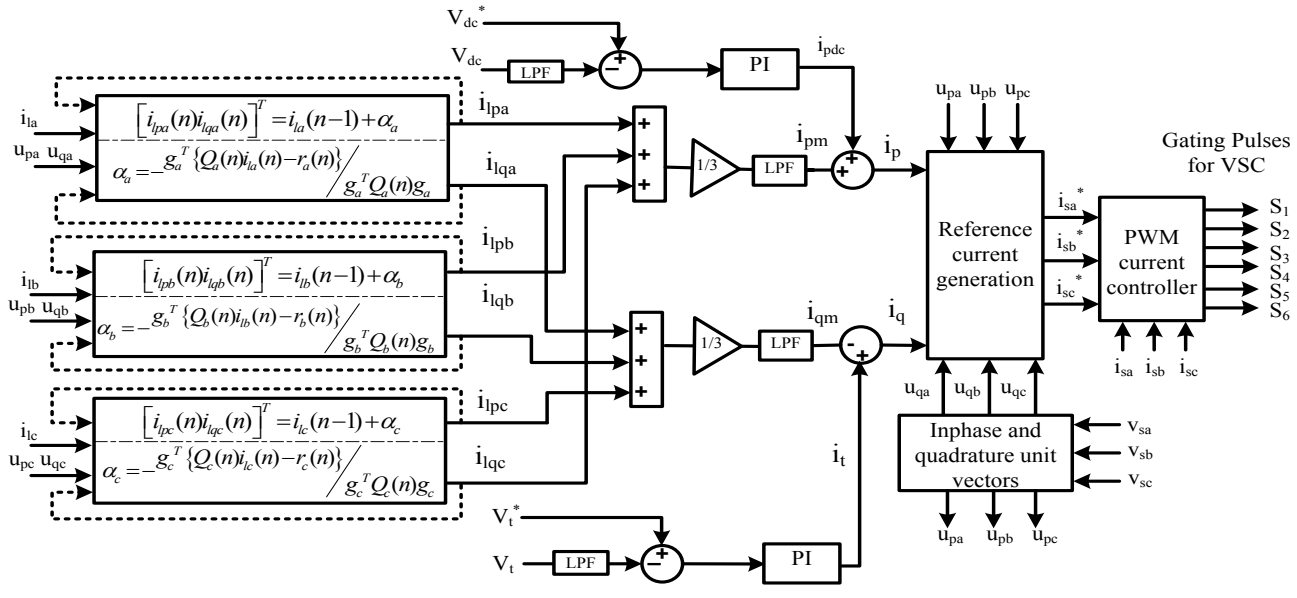

Fig. 3 Block diagram of Euclidean direction search based control technique

0278-0046 (c) 2018 IEEE. Personal use is permitted, but republication/redistribution requires IEEE permission. See http://www.ieee.org/publications_standards/publications/rights/index.html for more information.

This article has been accepted for publication in a future issue of this journal, but has not been fully edited. Content may change prior to final publication. Citation information: DOI 10.1109/TIE.2019.2905835, IEEE Transactions on Industrial Electronics

$$i_{lpa}(n) = i_{lpa}(n-1) + \alpha_a \quad (10)$$
$$i_{lpb}(n) = i_{lpb}(n-1) + \alpha_b \quad (11)$$
$$i_{lpc}(n) = i_{lpc}(n-1) + \alpha_c \quad (12)$$

The weights estimated from load currents (i_{la}, i_{lb} and i_{lc}) given in (10) to (12) are used to compute average weight value (i_{pm}), which is given as,

$$i_{pm} = (i_{lpa} + i_{lpb} + i_{lpc})/3 \quad (13)$$

This average weight (i_{pm}) (computed in (13)) and PI controller output (i_{pdc}) are added to determine reference active weight (i_p) given as,

$$i_p = i_{pm} + i_{pdc} \quad (14)$$

The reference active currents (i_{pa}^*, i_{pb}^* and i_{pc}^*) are determined by reference active weight component (i_p) and in-phase components (u_{pa}, u_{pb} and u_{pc}) as,

$$i_{pa}^* = i_p u_{pa},\ i_{pb}^* = i_p u_{pb} \text{ and } i_{pc}^* = i_p u_{pc} \quad (15)$$

These estimated active currents are utilized along with reference reactive currents (estimated in the following sub section) to evaluate the reference currents.

B. Estimation of Reference Reactive Currents

The components u_{pa}, u_{pb} and u_{pc} computed in (1) are used to determine u_{qa}, u_{qb} and u_{qc} (quadrature components with unit amplitude) of PCC voltages as,

$$u_{qa} = -u_{pb}/\sqrt{3} + u_{pc}/\sqrt{3} \quad (16)$$
$$u_{qb} = \sqrt{3}\,u_{pa}/2 + (u_{pb} - u_{pc})/2\sqrt{3} \quad (17)$$
$$u_{qc} = -\sqrt{3}\,u_{pa}/2 + (u_{pb} - u_{pc})/2\sqrt{3} \quad (18)$$

There is some voltage drop at PCC due to internal impedance of the utility and the distribution network. Hence an additional PI controller is required to adjust amplitude of PCC voltage (V_t) at set value. The error (v_{te}) between PCC voltage magnitude (V_t) and set voltage (V_t^*) is computed and processed using PI controller. The output of AC bus PI controller (i_t) is defined as given in [21].

The reactive weights (i_{lqa}, i_{lqb} and i_{lqc}) are estimated using EDS control given in (6) as,

$$i_{lqa}(n) = i_{lqa}(n-1) + \alpha_a \quad (19)$$
$$i_{lqb}(n) = i_{lqb}(n-1) + \alpha_b \quad (20)$$
$$i_{lqc}(n) = i_{lqc}(n-1) + \alpha_c \quad (21)$$

The above given reactive weights (i_{lqa}, i_{lqb} and i_{lqc}) estimated from EDS controller are averaged and the averaged reactive component (i_{qm}) is given as,

$$i_{qm} = (i_{lqa} + i_{lqb} + i_{lqc})/3 \quad (22)$$

The average reactive weight (i_{qm}) is now subtracted from the AC bus PI controller output (i_t) to determine reference reactive constituent (i_q) as,

$$i_q = i_t - i_{qm} \quad (23)$$

The reactive component (i_q) is used along with unit quadrature components (u_{qa}, u_{qb} and u_{qc}) given in (16), (17) and (18) to estimate fundamental reference reactive currents as,

$$i_{qa}^* = i_q u_{qa},\ i_{qb}^* = i_q u_{qb} \text{ and } i_{qc}^* = i_q u_{qc} \quad (24)$$

These estimated reference reactive currents (24) are used to determine total reference grid currents (only fundamental component), which is formulated in following sub section.

C. Gating Pulse Generation for VSC

The summation of i_{pa}^*, i_{pb}^*, i_{pc}^* and i_{qa}^*, i_{qb}^*, i_{qc}^* fundamental reference currents estimated in (15) and (24), are used to determine reference grid currents (i_{sa}^*, i_{sb}^* and i_{sc}^*) as,

$$i_{sa}^* = i_{pa}^* + i_{qa}^*,\ i_{sb}^* = i_{pb}^* + i_{qb}^* \text{ and } i_{sc}^* = i_{pc}^* + i_{qc}^* \quad (25)$$

The above determined reference grid currents are compared with sensed grid currents (i_{sa}, i_{sb} and i_{sc}) and error signals are produced. Moreover these errors are passed through PWM current controller (PWMCC). The PWMCC generates gating pulses of VSC used in DSTATCOM.

IV. Results and Discussion

A prototype of a three phase four wire compensator, is implemented in the laboratory using three phase IGBTs based voltage source converter (VSC) as shown in Fig. 4. The voltage and current sensors (Hall Effect) with appropriate buffer circuitry, are utilized to sense PCC voltages, load and grid currents. The EDS controller is realized in DSP (dSPACE 1104 R&D controller) and gating pulses to IGBTs of VSC, are provided with the help of appropriate gating circuitry. Experimental results are demonstrated for control behavior at steady state load conditions and dynamic load conditions using EDS based control under linear/nonlinear loads.

A. Behavior of EDS Based Control Under Nonlinear Load

Fig. 5 illustrates numerous intermediate signals of EDS based control when tested experimentally on a developed DSTATCOM. Fig. 5(a) depicts wave-shapes of PCC voltage (v_{sa}), filtered PCC voltage (v_{saf}), unit in-phase component obtained from PCC voltage (u_{pa}) and load current (i_{lc}). There is switching noise (high frequency) in the PCC voltage (v_{sa}), which is filtered out by passing it through band pass filter. This filtered voltage signal is provided to the control. Fig. 5(b) shows wave-shapes of various parameters of controller such as forgetting factor (λ), component of vector matrices (Q and r) and step size parameter (α). Fig. 5(c) presents fundamental weight component of load current (i_{lpa}), average weight component of all three phases of load (i_{pm}), PI controller output (i_{pdc}) and active weight (i_p). In this figure, the load is disconnected at some instant and it is observed that fundamental active weight component (i_{lpa}), average weight component (i_{pm}) are reduced. There are also some changes in PI controller output, which is settled after few cycles due to PI

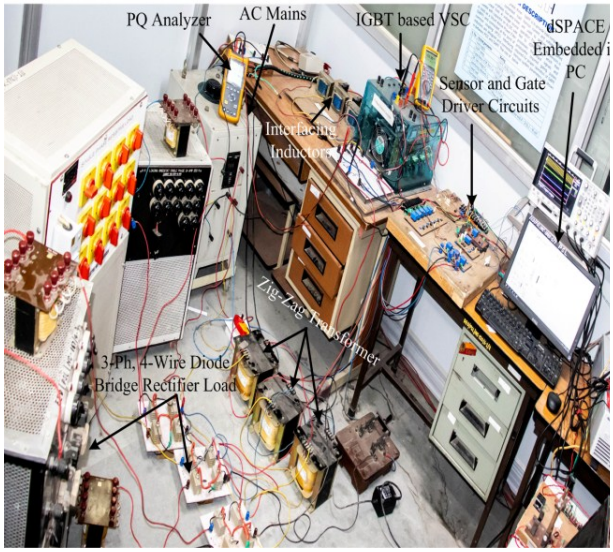

Fig. 4 Experimental prototype of three phase 4-wire shunt compensator

0278-0046 (c) 2018 IEEE. Personal use is permitted, but republication/redistribution requires IEEE permission. See http://www.ieee.org/publications_standards/publications/rights/index.html for more information.

This article has been accepted for publication in a future issue of this journal, but has not been fully edited. Content may change prior to final publication. Citation information: DOI 10.1109/TIE.2019.2905835, IEEE Transactions on Industrial Electronics

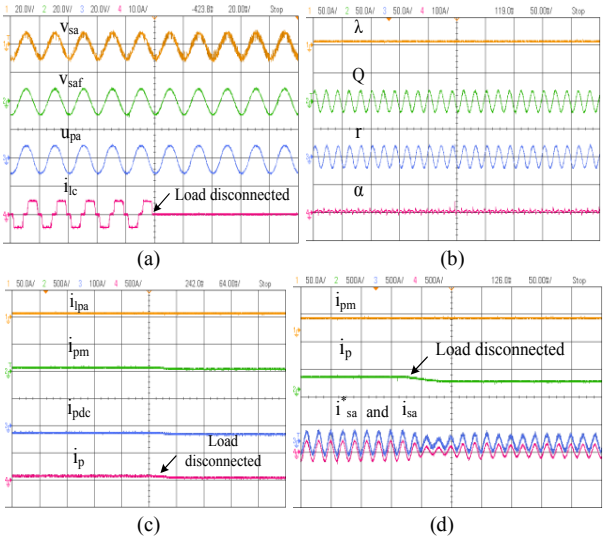

Fig. 5 Behavior of EDS based control on four wire shunt compensator (a) PCC voltage (v_{sa}), filtered PCC voltage (v_{saf}), u_{pa} and i_{lc} (b) forgetting factor (λ), component of vector matrices (Q and r) , step size (α) (c) i_{lpa}, i_{pm}, $i_{pdc,}$ and i_p (d) i_{pm}, i_p, i_{sa} and i^*_{sa}

controller action. Fig. 5(d) presents reference grid current (i_{sa}^*) and sensed grid current (i_{sa}) along with average weight (i_{pm}) and reference active weight (i_p). These results show good response of the EDS control implemented for a shunt compensator. The grid current perfectly follows the reference current generated from the control at various load conditions.

B. *Recompense of Reactive Power Under Linear Load*

Fig. 6 presents the shunt compensator behavior for compensating reactive power demand of a linear load. Figs. 6(a)-(c) depict power (real and reactive) delivered by AC mains (P_s and Q_s), power (real and reactive) demanded by linear load (P_l and Q_l) and reactive power supplied from compensator (Q_c). It is noticed from the plot of Fig. 6(b) that active power demand of load is 490W and reactive power demands is 364VAR. Total demand (active power) of load including losses (560W), is supplied by source. It is observed

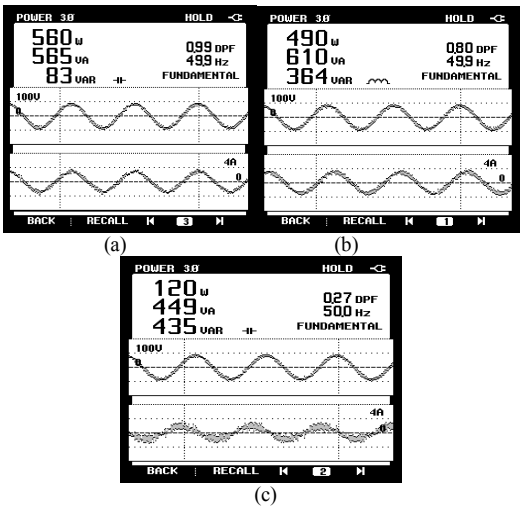

Fig. 6 Power flow in steady state condition under linear load (a) supply P_s and Q_s along with v_{sa}, i_{sa} (b) load P_l and Q_l along with v_{sa}, i_{la} (c) compensator P_c and Q_c along with v_{sa}, i_{ca}

that the entire reactive power demand of the system (435VAR) (includes load plus line inductors) is provided by the shunt compensator. Hence the compensator supplies reactive power demand and grid displacement power factor (DPF) is improved to 0.99, as shown in Fig. 6(a).

C. *Operation of DSTATCOM at Balanced Nonlinear Load*

Fig. 7 exhibits behavior of DSTATCOM considering the case of nonlinear load (balanced). Figs. 7(a)-(c) present wave-shapes of only one phase grid current (i_{sa}), load current (i_{la}) and DSTATCOM current (i_{ca}) plotted with PCC voltage (v_{sa}). Fig. 7(b) shows distorted load current, which becomes sinusoidal after compensator action (Fig. 7(a)). Highly distorted compensator current is observed in Fig. 7(c). Figs.7(d)-(f) illustrate harmonic spectra of grid current (i_{sa}), load current (i_{la}) and PCC voltage (v_{sa}).These results present significant improvement in the harmonic distortion of grid current (3.4% THD) after compensation, though there is 32.2% THD in load current and THD of PCC voltage is 3.5%. Therefore, the shunt compensator is able to reduce harmonics distortion in grid current according to international standards. Figs. 7(g)-(i) illustrate wave shapes of grid neutral, load neutral and zig-zag transformer neutral wire currents ($i_{sn,}$ i_{ln} and i_{zn}) for a case when neutral current exists in the load. It is observed from these results that neutral current present in the load (i_{ln}) is compensated by the zig-zag transformer and nearly zero neutral current flows in the supply neutral, as desired.

D. *Operation of DSTATCOM at Unbalanced Nonlinear Load*

Fig. 8 presents behavior of the shunt compensator when one phase of load is detached and the system becomes unbalanced. Sudden disconnection of one phase of load can be treated as

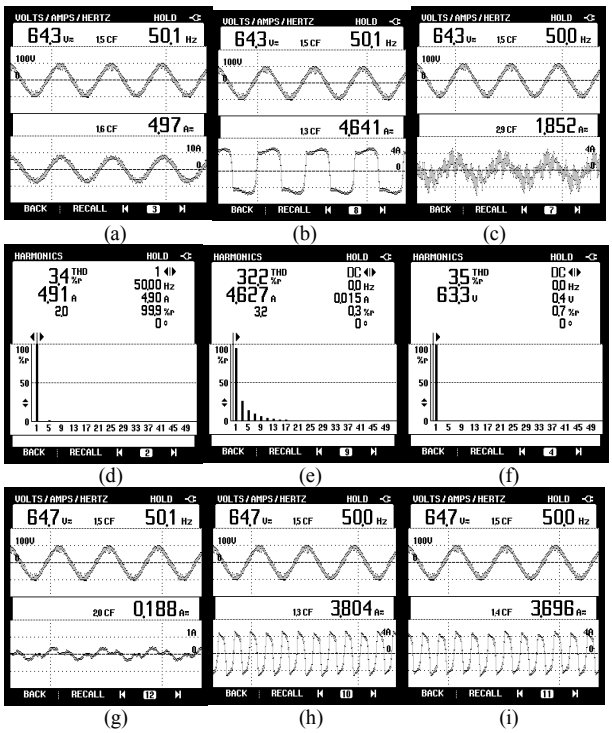

Fig. 7 Steady state behavior of shunt compensator (a-c) i_{sa}, i_{la} and i_{ca} along with v_{sa} (d-f) harmonic spectra of i_{sa}, i_{la} and v_{sa} (g-i) neutral current i_{sn}, i_{ln} and i_{zn}

0278-0046 (c) 2018 IEEE. Personal use is permitted, but republication/redistribution requires IEEE permission. See http://www.ieee.org/publications_standards/publications/rights/index.html for more information.

This article has been accepted for publication in a future issue of this journal, but has not been fully edited. Content may change prior to final publication. Citation information: DOI 10.1109/TIE.2019.2905835, IEEE Transactions on Industrial Electronics

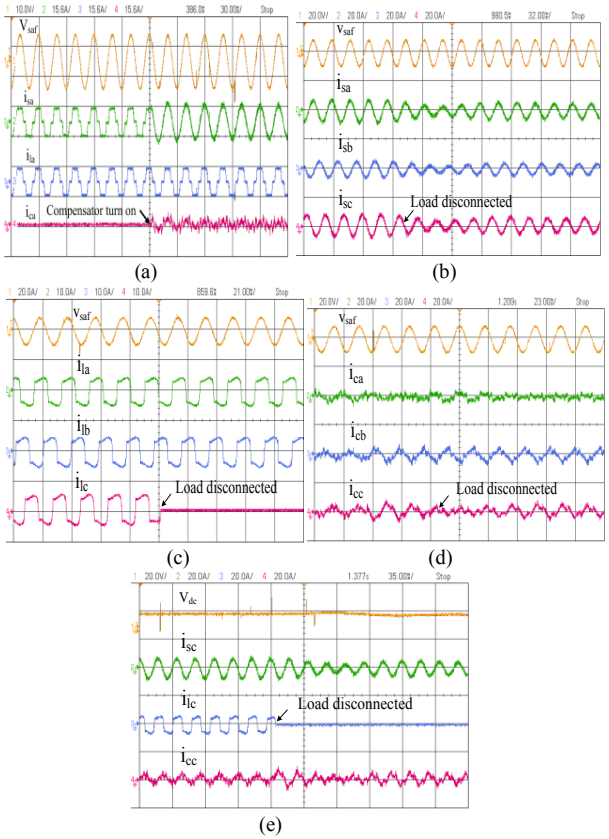

Fig. 8 Behavior of shunt active compensator at unbalanced load condition (a) PCC voltage, supply current, load current and compensator current without and with compensator switched on (b-d) supply, load and compensator currents along with v_{saf} (e) V_{dc}, i_{sc}, i_{lc} and i_{cc}

severe case of load unbalancing. Fig. 8 (a) presents phase 'a' of PCC voltage (v_{sa}), grid current (i_{sa}), load current (i_{la}) and compensator current (i_{ca}) without and with compensator switched on. Figs. 8(b)-(d) illustrate wave shapes of the grid (i_{sa}, i_{sb} and i_{sc}), load (i_{la}, i_{lb} and i_{lc}) and DSTATCOM currents (i_{ca}, i_{cb} and i_{cc}) along with PCC voltage phase 'a' (v_{sa}) under dynamic load condition. Performance results in Fig. 8, indicate that the grid currents are sinusoidal and appear balanced even if one of the phase of load is detached. Fig. 8(e) exhibits wave-shapes of one phase of grid, load and compensator current (i_{sc}, i_{lc} and i_{cc}) with DC link voltage during load removal. The EDS control action is fast and quick to adapt to changing load conditions. Moreover, voltage at DC link of VSC is adjusted at its set value.

Figs. 9(a)-(c) present dynamic behavior of the grid, load and zig-zag transformer neutral currents with PCC voltage, load current and DC link voltage of VSC. Fig. 9(a) illustrates behavior of load and zig-zag neutral currents (i_{ln} and i_{zn}) with load current (i_{lc}) and PCC voltage (v_{sa}). The load is suddenly disconnected and it is perceived that neutral current starts flowing in the load neutral wire. Fig. 9(b) shows behavior of grid neutral current (i_{sn}) and i_{zn} with grid current (i_{sa}). Fig. 9(c) presents performance of i_{sn}, i_{ln} and i_{zn} along with DC link voltage (V_{dc}). One can observe from these results that there is almost negligible neutral current burden on grid side even if neutral current in the load (i_{ln}) is passing through neutral

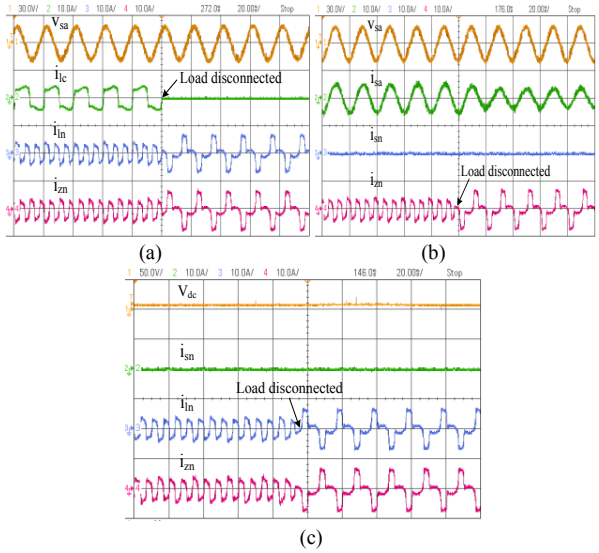

Fig. 9 Behavior of shunt active compensator during unbalanced load condition (a) v_{sa}, i_{lc}, i_{ln} and i_{zn} (b) v_{sa}, i_{sa}, i_{sn} and i_{zn} (c) V_{dc}, i_{sn}, i_{ln} and i_{zn}

conductor, which compensates neutral current with the zig-zag transformer in the proposed system configuration.

E. Comparative Performance of EDS Control with Conventional Controls

Performance of EDS control is compared with LMS and RLS controls on various criteria such as weight convergence for different loading conditions, type of control, harmonics compensation capability, error between actual and estimated load current and sampling time taken [20]-[21]. Figs. 10(a) and (b) show convergence of weights with RLS, EDS and LMS controls under numerous load conditions (steady state and unbalanced). It is noticed from the wave-shapes that there are large magnitude and persistent oscillations with LMS controller, oscillations with reduced amplitude are observed with RLS controller and significantly reduced amplitude oscillations than LMS and RLS controllers, are observed with EDS controller in several load conditions throughout t=0.3s to 0.4s, when a phase of load is detached. These results are affected under unbalanced conditions.

Fig. 11 shows the error between actual and estimated load currents using EDS, RLS and LMS controls. It can be concluded from these results that there is significantly reduced error using EDS controller than RLS and LMS controllers. Figs. 12(a)-(d) show harmonic spectra of grid current using EDS, LMS, RLS and load current, respectively. These results show 1.76%, 4.28% and 3.35% THD in phase 'a' of grid current (i_{sa}) with EDS, LMS and RLS based controllers when THD of 26.55% is observed in similar phase of load current (i_{la}). It is noticed from these harmonics spectra that EDS controller is much more effective in mitigating harmonics in the grid current than LMS and RLS controllers. Therefore, from the above explanation, it is determined that EDS controller gives improved performance in weight convergence, error minimization and harmonics mitigation. Performance of all three controls based on various parameters is summarized in Table-I. It clearly shows superior performance of EDS control compared to LMS and RLS based controls.

0278-0046 (c) 2018 IEEE. Personal use is permitted, but republication/redistribution requires IEEE permission. See http://www.ieee.org/publications_standards/publications/rights/index.html for more information.

This article has been accepted for publication in a future issue of this journal, but has not been fully edited. Content may change prior to final publication. Citation information: DOI 10.1109/TIE.2019.2905835, IEEE Transactions on Industrial Electronics

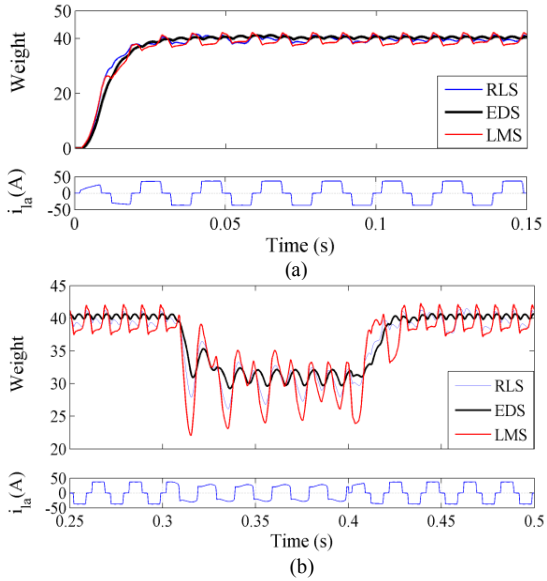

Fig. 10 Convergence of weights using LMS, EDS and RLS controllers in (a) steady state and (b) dynamic load condition

V. CONCLUSIONS

A TPFW shunt compensator has been developed using the three leg VSC and a zig-zag transformer. PQ issues in distribution systems viz. harmonics, immoderate reactive power, load unbalancing and neutral current, have been compensated with the proposed system. The neutral current compensation has been performed with a zig-zag transformer. An adaptive control based on EDS algorithm has been suitably developed to compute reference grid currents. The EDS control algorithm has been verified on an implemented DSTATCOM in the laboratory using VSC and DSP at linear and nonlinear loads. The THDs of 1.76% and 3.4% have been obtained in the grid current with proposed control with simulation and experimental results, respectively. The grid side DPF has improved to 0.99, which shows that the load reactive power demand has been met by the shunt compensator. Performances of EDS control, have been compared with LMS and RLS based controls in terms of weight convergence, complexity, harmonic compensation and steady state error. It has been found that proposed controller presents improved performance over LMS and RLS controls.

APPENDIX

AC grid, 110V (L-L), 50Hz; DC link voltage, V_{dc}=200V; DC link capacitor, C_{dc}=1650µF, interfacing inductor, L_f=3mH; ripple filter, R_f=5Ω, C_f=5Ω; VSC rating, 25kVA; linear load, 0.61kVA, 0.8 DPF; nonlinear load, uncontrolled diode rectifier (3-Ø), R=15Ω, L=100mH.

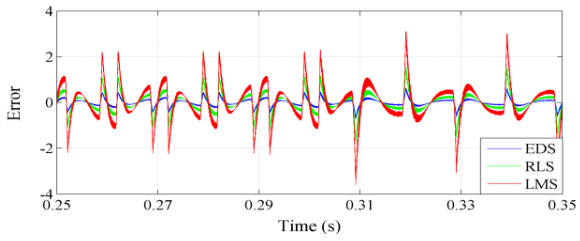

Fig. 11 Error between actual and estimated load current for EDS, RLS and LMS

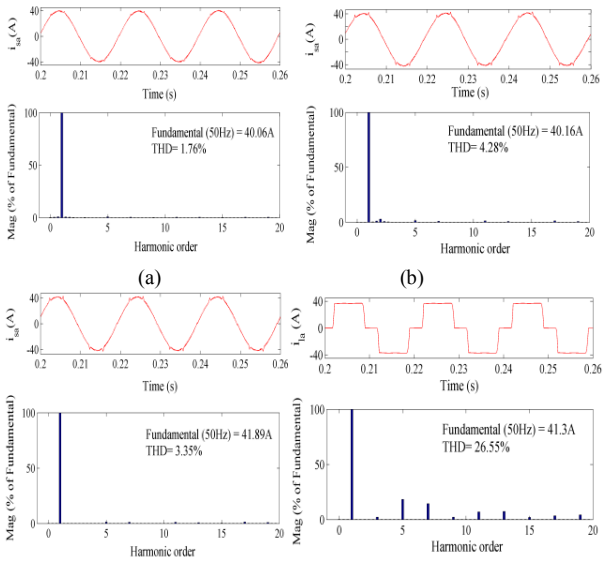

Fig. 12 Harmonic spectra of phase 'a' of supply current, i_{sa} (a) EDS controller (b) LMS controller (c) RLS controller and (d) load current, i_{la}

TABLE-I
COMPARATIVE PERFORMANCE OF EDS CONTROLLER WITH RLS AND LMS

Operations		**EDS**	**RLS**	**LMS**
Type		Adaptive filter	Adaptive filter	Adaptive filter
Convergence		Faster	Slower than EDS	Slower than RLS
Complexity		Less	More	Less
Convergence of weights	Steady State condition	Fast with very less oscillations	Sustained oscillation with lower amplitude	Sustained oscillation with higher amplitude
	Dynamic condition	Converges within a cycle	Convergence takes more than one cycle	Sustained oscillations
Steady state error		Significantly Less	More than EDS	Higher than RLS
Harmonic compensatio	Grid current, i_{ga}	40.06A, THD 1.76%	41.89A, THD 3.35%	40.16A, THD 4.28%
	Load current, i_{la}	41.3A THD 26.55%	41.3A THD 26.55%	41.3A THD 26.55%
Sample time, T_s		60µs	75µs	65µs

ACKNOWLEDGMENT

The authors are thankful to the Department of Science and Technology (DST), Government of India for the Sponsored Project (EMR/2016/001874).

REFERENCES

[1] G. Benysek and M. Pasko, *Power Theories for Improved Power Quality*, Springer-Verlag, London, 2012.

0278-0046 (c) 2018 IEEE. Personal use is permitted, but republication/redistribution requires IEEE permission. See http://www.ieee.org/publications_standards/publications/rights/index.html for more information.

This article has been accepted for publication in a future issue of this journal, but has not been fully edited. Content may change prior to final publication. Citation information: DOI 10.1109/TIE.2019.2905835, IEEE Transactions on Industrial Electronics

[2] A. F. Zobaa and Shady H.E. Abdel Aleem, *Power Quality in Future Electrical Power Systems*, Institution of Engineering and Technology, U.K., March 2017.
[3] E. L. L. Fabricio, S. C. S. Júnior, C. B. Jacobina and M. B. de Rossiter Corrêa, "Analysis of main topologies of shunt active power filters applied to four-wire systems," *IEEE Trans. Power Elect.*, vol. 33, no. 3, pp. 2100-2112, March 2018.
[4] F. Li, F. He, Z. Ye, T. Fernando, X. Wang and X. Zhang, "A simplified PWM strategy for three-level converters on three-phase four-wire active power filter," *IEEE Trans. Power Elect.*, vol. 33, no. 5, pp. 4396-4406, May 2018.
[5] B. Singh, P. Jayaprakash, T. R. Somayajulu and D. P. Kothari, "Reduced rating VSC with a zig-zag transformer for current compensation in a three-phase four-wire distribution system," *IEEE Trans. Power Del.*, vol. 24, no. 1, pp. 249-259, Jan. 2009.
[6] R. Pandey, R. N. Tripathi and T. Hanamoto, "Multiband HCC for cascaded H-bridge multilevel inverter based DSTATCOM," in *Proc. IEEE 11th Conf. on Industrial Electronics and Applications (ICIEA)*, Hefei, 2016, pp. 607-612.
[7] P. Jayaprakash, B. Singh and D. P. Kothari, "IcosΦ algorithm based control of zig-zag transformer connected three phase four wire DSTATCOM," in *Proc. IEEE International Conference on Power Electronics, Drives and Energy Systems (PEDES)*, Bengaluru, 2012.
[8] H. Komurcugil and O. Kukrer, "A new control strategy for single-phase shunt active power filters using a Lyapunov function," *IEEE Trans. Ind. Elect.*, vol. 53, no. 1, pp. 305-312, Feb. 2006.
[9] S. Devassy and B. Singh, "Design and performance analysis of three-phase solar PV integrated UPQC," *IEEE Trans. Ind. Applications*, vol. 54, no. 1, pp. 73-81, 2018.
[10] K. Antoniewicz, M. Jasinski, M. P. Kazmierkowski and M. Malinowski, "Model predictive control for three-level four-leg flying capacitor converter operating as shunt active power filter," *IEEE Trans. Ind. Elect.*, vol. 63, no. 8, pp. 5255-5262, 2016.
[11] G. Son, H. J. Kim and B. H. Cho, "Improved modulated carrier control with on-time doubler for a single-phase shunt active power filter," *IEEE Trans. Power Elect.*, vol.33, no.2, pp.1715-1723, Feb. 2018.
[12] P. Chittora, A. Singh and M. Singh, "Chebyshev functional expansion based artificial neural network controller for shunt compensation," *IEEE Trans. Ind. Informatics*, vol. 14, iss. 9, Sept. 2018.
[13] M. T. Ahmad, N. Kumar and B. Singh, "AVSF-based control algorithm of DSTATCOM for distribution system," *IET Gen. Trans. Distri.*, vol. 11, no. 13, pp. 3389-3396, 2017.
[14] S. Kumar, I. Hussain, B. Singh, A. Chandra and K. Al-Haddad, "An adaptive control scheme of SPV system integrated to AC distribution system," *IEEE Trans. Ind. Applications.*, vol. 53, no. 6, pp. 5173-5181, 2017.
[15] D. J. Hogan, F. J. Gonzalez-Espin, J. G. Hayes, G. Lightbody and R. Foley, "An adaptive digital-control scheme for improved active power filtering under distorted grid conditions," *IEEE Trans. Ind. Elect.*, vol. 65, no. 2, pp. 988-999, Feb. 2018.
[16] C. I. Chen and Y. C. Chen, "Application of adaptive model-based scheme for harmonic diagnosis and compensation of grid-connected converters," *IEEE Trans. Ind. Elect.*, vol.65, no.1, pp.770-777, Jan. 2018.
[17] M. Cirrincione, M. Pucci, G. Vitale and A. Miraoui, "Current harmonic compensation by a single-phase shunt active power filter controlled by adaptive neural filtering," *IEEE Trans. Ind. Elect.,* vol. 56, no. 8, pp. 3128-3143, 2009.
[18] K. K. Shyu, M. J. Yang, Y. M. Chen and Y. F. Lin, "Model reference adaptive control design for a shunt active-power-filter system," *IEEE Trans. Ind. Elect.*, vol. 55, no. 1, pp. 97-106, 2008.
[19] M. Badoni, A. Singh and B. Singh, "Adaptive recursive inverse-based control algorithm for shunt active power filter," *IET Power Electron.*, vol. 9, no. 5, pp. 1053-1064, 2016.
[20] R. K. Agarwal, I. Hussain and B. Singh, "Application of LMS-based NN structure for power quality enhancement in a distribution network under abnormal conditions," *IEEE Trans. Neural Net. Learn. Sys.*, vol. 29, no. 5, pp. 1598-1607, May 2018.
[21] M. Badoni, A. Singh and B. Singh, "Variable forgetting factor recursive least square control algorithm for DSTATCOM," *IEEE Trans. Power Del.*, vol. 30, no. 5, pp. 2353-2361, 2015.
[22] N. Beniwal, I. Hussain and B. Singh, "Hybrid VSS–LMS–LMF based adaptive control of SPV-DSTATCOM system under distorted grid conditions," *IET Renew. Power Gen.*, vol. 12, no. 3, pp. 311-322, 2018.
[23] G. F. Xu, T. Bose and J. Schroeder, "The Euclidean direction search algorithm for adaptive filtering," in *Proc. IEEE Inter. Symposium on Circuits and Systems*, Orlando, FL, 1999, pp. 146-149.
[24] G. F. Xu and T. Bose, "Analysis of the Euclidean direction set adaptive algorithm," in *Proc. of Inter. Conference on Acoustics, Speech and Signal Processing*, Seattle, April 1998, pp. 1689-1692.
[25] R. A. Fayadh, H. A. Fadhil, F. S. Abdullah, F. Malek and S. A. Dawood, "Selective update euclidean direction search algorithm for adaptive filtering in indoor wireless rake-receiver," in *Proc. Inter. Conf. on Computer, Communications, and Control Technology*, Langkawi, 2014, pp. 329-332.
[26] B. Xie and T. Bose, *Partial Update Least-Square Adaptive Filtering*, Morgan & Claypool Publishers, Williston, USA, 2014.
[27] H. L. Jou, J. C. Wu, K. D. Wu, W. J. Chiang and Y. H. Chen, "Analysis of zig-zag transformer applying in the three-phase four-wire distribution power system," *IEEE Trans. Power Del.*, vol. 20, no. 2, pp. 1168-1173, 2005.

Manoj Badoni (M'17) received the B. Tech. in Instrumentation Engineering form University Science and Instrumentation Centre, Srinagar Garhwal, Uttrakhand in 2006, M.E. degree in Electronics Engineering from Punjab Engineering College, Chandigarh, India in 2008 and Ph.D degree in Electrical Engineering from Delhi Technological University, Delhi, India in 2016.
In 2017, he has joined Department of Electrical and Instrumentation Engineering, Thapar Institute of Engineering and Technology, Patiala as Assistant Professor. His areas of research interest include power electronics, power quality, and distributed generation.

Alka Singh (SM'15) received the B.E. degree in Electrical Engineering from Delhi College of Engineering, Delhi, India, in 1996, the M.Tech. Degree in Power Systems from the Indian Institute of Technology, New Delhi, India, in 2001, and the Ph.D. degree from Netaji Subash Institute of Technology (Delhi University), Delhi, India, in 2006. Currently, she is working as an Professor in the Department of Electrical Engineering, Delhi Technological University, Delhi. Her research interests include power systems, and power quality. She has more than 15 years of teaching and industrial experience. She is a Life Member of the Indian Society for Technical Education.

Bhim Singh (SM'99–F'10) received the B.E. (Electrical) degree from the University of Roorkee, Roorkee, India, in 1977 and the M.Tech. (Power Apparatus & Systems) and Ph.D. degrees from the Indian Institute of Technology (IIT) Delhi, New Delhi, India, in 1979 and 1983, respectively. In 1983, he joined the Department of Electrical Engineering, University of Roorkee, as a Lecturer. He became a Reader there in 1988. In December 1990, he joined the Department of Electrical Engineering, IIT Delhi, as an Assistant Professor, where he became an Associate Professor in 1994 and a Professor in 1997. He has guided 74 Ph.D. dissertations and 166 M.E./M.Tech. theses. Prof. Singh has more than 37 patents. He has executed more than seventy five sponsored and consultancy projects. Prof. Singh is a Fellow of the Indian National Academy of Engineering (FNAE), The Indian National Science Academy (FNA), The National Academy of Science, India (FNASc), The Indian Academy of Sciences, India (FASc), The World Academy of Sciences (FTWAS), Institute of Electrical and Electronics Engineers (FIEEE), the Institute of Engineering and Technology (FIET), Institution of Engineers (India) (FIE), and Institution of Electronics and Telecommunication Engineers (FIETE) and a Life Member of the Indian Society for Technical Education (ISTE), System Society of India (SSI), and National Institution of Quality and Reliability (NIQR).

0278-0046 (c) 2018 IEEE. Personal use is permitted, but republication/redistribution requires IEEE permission. See http://www.ieee.org/publications_standards/publications/rights/index.html for more information.

Talanta 201 (2019) 465–473

Contents lists available at ScienceDirect

Talanta

journal homepage: www.elsevier.com/locate/talanta

Protein functionalised self assembled monolayer based biosensor for colon cancer detection

Tarun Narayan[a,1], Saurabh Kumar[a,b,1], Suveen Kumar[a,c], Shine Augustine[a], B.K. Yadav[d,e], Bansi D. Malhotra[a,*]

[a] Nanobioelectronics Laboratory, Department of Biotechnology, Delhi Technological University, Delhi, 110042, India
[b] Centre for Nano Science and Engineering (CeNSE), Indian Institute of Science, Bengaluru, 560012, India
[c] Department of Chemistry, University of Delhi, Delhi, 110007, India
[d] Rajiv Gandhi Cancer Institute and Research Centre, Delhi, 110085, India
[e] National Liver Disease Biobank, Institute of Liver and Biliary Sciences, Delhi, 110070 India

ARTICLE INFO

Keywords:
Cancer biomarker
Endothelin-1
Biosensor
Surface plasmon resonance
Electrochemical impedance spectroscopy

ABSTRACT

We report results of the studies relating to the fabrication of a surface plasmon resonance (SPR) based label-free immunosensor for real-time monitoring of endothelin-1 (ET-1), a colon cancer biomarker. A gold disk modified with a self-assembled monolayer (SAM) of 11-mercaptoundecanoic acid (11-MUA) was functionalised via covalent immobilization of monoclonal anti-ET-1 antibodies using EDC-NHS (1-(3-(dimethylamine)-propyl)-3-ethylcarbodiimide hydrochloride, *N*-hydroxy succinimide) chemistry. This immunosensing platform (ethanolamine/anti-ET-1/11-MUA/Au) was characterized via atomic force microscopy (AFM), contact angle (CA) and Fourier transform infrared (FT-IR) spectroscopic techniques. The fabricated SPR electrode was further used to detect ET-1 in the broad concentration range 2–100 pg mL^{-1}, with a detection limit of 0.30 pg mL^{-1} and remarkable sensitivity of 2.18 m^{o} pg^{-1}mL. The adsorption mechanism was studied using monophasic model and the values of association (k_a) and dissociation (k_d) constants for anti-ET-1 and ET-1 binding were calculated to be $4.4 \pm 0.4 \times 10^{5}\,M^{-1}s^{-1}$ and $2.04 \pm 0.0003 \times 10^{-3}\,s^{-1}$, respectively. The results obtained via analysis of serum samples of colorectal cancer patients were found to be in good agreement with those obtained from enzyme-linked immunosorbent assay (ELISA) technique. Further, electrochemical studies were performed to prove the efficacy of the fabricated platform as a point of care device for the detection of ET-1.

1. Introduction

Colon cancer, also known as colorectal cancer (CRC), is presently the third most death causing cancer [1]. According to WHO (2012), it is the third most death causing cancer globally [2]. The CRC rates are found to be usually higher in men as compared to women with increased mortality rates in countries having limited resources and inadequate health infrastructure. In India, the five-year survival rates of CRC is less than 40% [3]. CRC usually begins as a non-cancerous polyp that develops on the inner side of the colon and rectum, eventually leading to cancer. The various genetic, environmental and lifestyle-related factors have been reported to contribute to the development of CRC. The environmental and physiological factors that have been observed to affect CRC are age and gender [4], ulcerative colitis [5], long-term immunosuppression [6], diabetes mellitus [7,8], alcohol consumption [9], consumption of red meat [10], obesity [11] and cigarette smoking [12].

The diagnosis of CRC is particularly challenging since the conventional techniques such as physical examination, blood tests [13], colonoscopy [14], histopathology, radiology, and PET-CT scan [15,16] are solely based on evaluation of the symptoms resulting in limited accuracy. Moreover, other techniques, such as biopsy [14], double-contrast barium enema and flexible sigmoidoscopy, depend on the phenotypic properties of the tumor and possess numerous challenges. Despite being sophisticated and selective, these diagnostic techniques are complex, less sensitive, labor-intensive, time-consuming, and have a

Abbreviations: SPRi, Surface plasmon Resonance imaging; LSPR, localized Surface Plasmon Resonance; CA 15-3, Cancer antigen 15-3; GTF2B, General Transcription Factor 2B; ALCAM, Activated leukocyte cell adhesion molecule

* Corresponding author.
E-mail address: bansi.malhotra@gmail.com (B.D. Malhotra).
[1] These authors contributed equally.

https://doi.org/10.1016/j.talanta.2019.04.039
Received 26 February 2019; Received in revised form 12 April 2019; Accepted 15 April 2019
Available online 18 April 2019
0039-9140/ © 2019 Elsevier B.V. All rights reserved.

risk of complications like bleeding and bowel tears. Moreover, these methods require advanced instrumentation and well-trained experts for diagnosis. Thus, there is an urgent need to develop an alternative method that is user-friendly, has high throughput screening and is relatively inexpensive for CRC diagnosis.

With the advancement in the stages of CRC, the levels of biomarkers fluctuate indicating state of the disease. Inspection and quantification of these CRC biomarkers can be useful for its timely detection. The biomarkers that are secreted during CRC are carcinoembryonic antigen (CEA) [17], cancer antigen 19-9 (CA 19-9) [18–20], cancer antigen 125 (CA 125), miRNA [21] (miRNA-29a and miRNA-92a), ssDNA [22] (colorectal cancer gene), etc. Among these, CA 19-9 has been found to be less sensitive and is a poor diagnostic marker [23–25]. Moreover, the role of miRNA as a biomarker for CRC detection is not yet well established. The major disadvantage of using ssDNA as a biomarker for cancer detection is that it can be released by the dying tumor cell that remains in circulation as it is highly stable [26]. The challenges posed by these biomarkers open a window for exploring the potential of new markers.

Endothelin-1 (ET-1) is a vasoconstrictor peptide chain of 21 amino acids and can be isolated from endothelial cells [27]. In CRC patients the level of ET-1 in the blood plasma has been found to be elevated in comparison to the normal value [28]. Immunohistochemical analysis of CRC specimens has shown the heterogeneous distribution of ET-1 around tumor cells [29]. Moreover, it is known that ET-1 increases the tumor size when it is added to the growth medium [30–32]. Studies have shown the reported level of ET-1 in serum samples for control subjects to be around $\sim 2.78\ pg\ mL^{-1}$ and in the primary tumor case, it may increase up to $3.9\ pg\ mL^{-1}$. In a patient with metastasis, the ET-1 value rises to $\geq 4.5\ pg\ mL^{-1}$ [33,34]. Many studies have reported that plasma/serum ET-1 concentration rises significantly in the case of CRC [35–37]. Thus, the elevated levels of ET-1 may exhibit a strong correlation with CRC prognosis [28,33,34,38].

The surface plasmon resonance (SPR) is a highly sensitive method that can be used to monitor biomolecular interactions in real-time and can be utilized as a label-free detection for a wide array of molecular interactions, ranging from small ions and viruses to multimolecular complexes [39,40]. The SPR technique allows real-time monitoring of binding kinetics, affinity, specificity, and concentration [41]. Moreover, it also offers fast, label-free detection and is reliable.

We report, for the first time, results of the systematic studies relating to the development of ET-1 immunosensor for detection and real-time monitoring of CRC. Under optimal conditions, the fabricated immunoelectrode exhibited high sensitivity ($2.18\ m^{o}\ pg^{-1}$ mL) and covered the physiological range of ET-1 biomarker secreted in serum samples of CRC patients. Besides this, we investigated the kinetics of interaction of ET-1 with anti-ET-1 using monophasic model. The immobilization process and binding response were also studied by electrochemical impedance spectroscopy (EIS). The SPR immunosensor exhibited a highly specific interaction between anti-ET-1 and ET-1 biomolecules as compared to other methods. This immunoelectrode was used for the analysis of serum samples from CRC patients and the results showed good correlation with those obtained via the ELISA technique.

2. Materials and reagents

11-mercaptoundecanoic acid, ethanolamine, and 1-(3-(dimethylamine)-propyl)-3-ethylcarbodiimide hydrochloride (EDC), *N*-hydroxysuccinimide (NHS) of AR grade were purchased from Sigma Aldrich, India. Disodium hydrogen phosphate, sodium hydroxide, sodium acetate, potassium chloride (KCl), and polysorbate 20 (tween 20) were procured from Fisher Scientific. Ethanol and acetic acid were purchased from Merck. Sodium dodecyl sulphonate (SDS) was procured from SRL Pvt. Ltd. India. Endothelin-1 (ET-1), and anti-endothelin-1 (monoclonal) were purchased from Biorbyt, USA. 50 nm thick gold-coated BK-7 glass disks (24-mm diameter) were procured from Metrohm Autolab, Netherlands. ET-1 ELISA kit was purchased from Ray Biotech, Inc., India. Patient serum samples were obtained from Rajiv Gandhi Cancer Institute and Research Centre, New Delhi. All experiments were conducted in triplicates (n = 3).

2.1. Preparation of running buffer, regeneration buffer and deactivation solution

Fresh phosphate buffer saline tween (PBST) solution of pH 7.4 was prepared by dissolving salts such as Na_2HPO_4 (0.01 M), NaCl (0.138 M), KCl (0.027 M), and Tween-20 in 200 mL Milli-Q-water. The deactivation solution was prepared using 1 M ethanolamine (pH was adjusted to 8.5 using 1 M HCl) and was used for neutralizing the reactive sites present on the SAM surface. The regeneration buffer was prepared by mixing 10 mM of sodium acetate with 0.1% of SDS (pH was adjusted to 4.5 using acetic acid) and was utilized to remove the analyte present on the surface for re-using the sensor disk. For electrochemical analysis, PBS solution (50 mM, pH 7.4) containing 5 mM $[Fe(CN)_6]^{3-/4-}$ was used. All solutions were prepared in Milli-Q-water (resistivity: 18.2 MΩ cm) and stored at 4 °C.

2.2. Immobilization of anti-ET-1 over the SPR gold disk

Prior to the formation of the desired SAM, the gold (Au) disk was sequentially cleaned with ethanol, acetone and deionized water. Subsequently, the cleaned Au disk was immersed in a solution of 11-MUA (20 mM) in ethanol for 12 h for uniform SAM formation. The strong interaction between the gold and sulfur led to more orderly monolayer formation. The SAM-modified Au Disk (11-MUA/Au) was rinsed with ethanol to remove the unbound 11-MUA molecules. Further, the monoclonal ET-1 antibodies were immobilized onto the 11-MUA/Au disk using EDC–NHS covalent chemistry. Briefly, the 11-MUA/Au disk was flushed with PBST (pH 7.4) for 120 s to obtain a steady baseline, followed by introducing a mixture (30 µL) of 0.4 M EDC and 0.1 M NHS in the ratio of 1:1 for 900 s at 25 °C for activation of 11-MUA SAM surface. Subsequently, 50 µL of monoclonal anti-ET-1($100\ \mu g\ mL^{-1}$) was added onto the EDC-NHS treated 11-MUA/Au disk for covalent immobilization. The activated 11-MUA SAM was bound to the $–NH_2$ group of the anti-ET-1 via EDC-NHS coupling resulting in the formation of an amide bond (Scheme 1). After this, the deactivated buffer of ethanolamine (EA, pH-8.5) solution was introduced for 300s to the anti-ET-1/11-MUA Au disk to deactivate the unbound active sites on the disk. Finally, 30 µL of regeneration buffer (acetic acid + 0.1% SDS; pH 4.5) was added onto the electrode to regenerate and reuse the surface.

2.3. Characterization

The SPR measurements were carried out on SPR TWINGLE (Autolab, Netherlands) instrument having Kretschman configuration. The contact angle measurements were done using SEO Pheonix 300T goniometer (Korea). The Fourier transform infrared (FT-IR) spectroscopic studies of Au disk, 11-MUA/Au disk, and EA/anti-ET-1/11-MUA/Au disk were carried out using a Shimadzu IR Affinity 1S FTIR spectrophotometer. The surface morphology studies on 11-MUA/Au, and anti-ET-1/11-MUA/Au disk was carried out using atomic force microscope (NT-MDT Spectrum Instruments Ltd). Electrochemical impedance spectroscopy (EIS) studies were conducted on an Autolab Potentiostat/Galvanostat (Metrohm, Netherlands) using a three-electrode cell with the modified gold electrode as a working electrode, Ag/AgCl as the reference electrode and platinum as the counter electrode in phosphate buffer saline (PBS, 50 mM, pH 7.4) containing $Fe(CN)_6^{3-/4-}$. The enzyme-linked immunosorbent assay (ELISA) for quantification of ET-1 concentration in the serum samples was conducted using a Bio-Rad microplate absorbance reader.

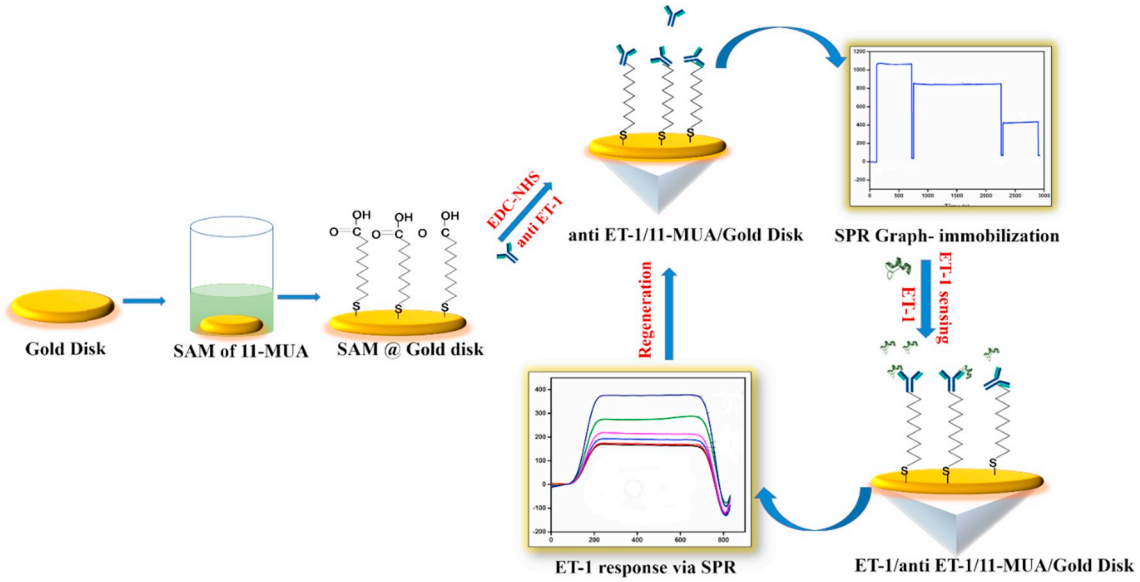

Scheme 1. Schematic illustration of gold disk modification for SPR biosensing.

3. Results and discussion

3.1. Optimization of anti-ET-1 concentration

The optimization of antibody concentration is a crucial step in the fabrication of a biosensor. In this study, the observed change in the response angle was obtained as a function of different concentration (50, 70, 100 and 150 μg mL^{-1}) of anti-ET-1 antibodies. The maximum change in angle was observed for 100 μg mL^{-1} of anti-ET-1 (Fig. 1A). However, at higher concentration (150 μg mL^{-1}) of anti-ET-1, the saturation of SPR angle occurred possibly because of steric hindrance. The observed saturation at 100 μg mL^{-1} was attributed to the complete immobilization of anti-ET-1 onto the activated sites of the SAM surface. Thus, 100 μg mL^{-1} of monoclonal anti-ET-1 was chosen for the fabrication of immunosensor. Fig. 1B shows the plot obtained between the SPR response angle (m°) and time(s), which clearly reveals the binding of anti-ET-1 at each step. The immobilization curve shows a baseline for 11-MUA/Au with continuous buffer flow at 10 μL/min. Thereafter 35 μL of EDC-NHS was added to activate the carboxyl groups of 11-MUA/Au (curve b). Further injection of anti-ET-1 leading to electrostatic interaction and coupling of the ligand on 11-MUA/Au matrix is shown by curve c. Next, 1 M ethanolamine was used to deactivate unreacted NHS-esters and remove electrostatically bound ligands (curve d) followed by baseline curve e. The change in the baseline toward the higher value indicated the modification of 11-MUA/Au disk with the linker (EDC-NHS) and anti-ET-1 antibodies. This could be assigned to the change in the refractive indices at each step of modification.

3.2. Fourier transform infrared spectroscopy studies

FT-IR spectroscopic studies were conducted in the 4000-500 cm^{-1} range to investigate the presence of functional groups or intermolecular binding occurring onto the (A) Au disk (B) 11-MUA/Au disk, and (C) anti-ET-1/11-MUA/Au disk (Fig. 2). The sharp peak at 1697 cm^{-1}

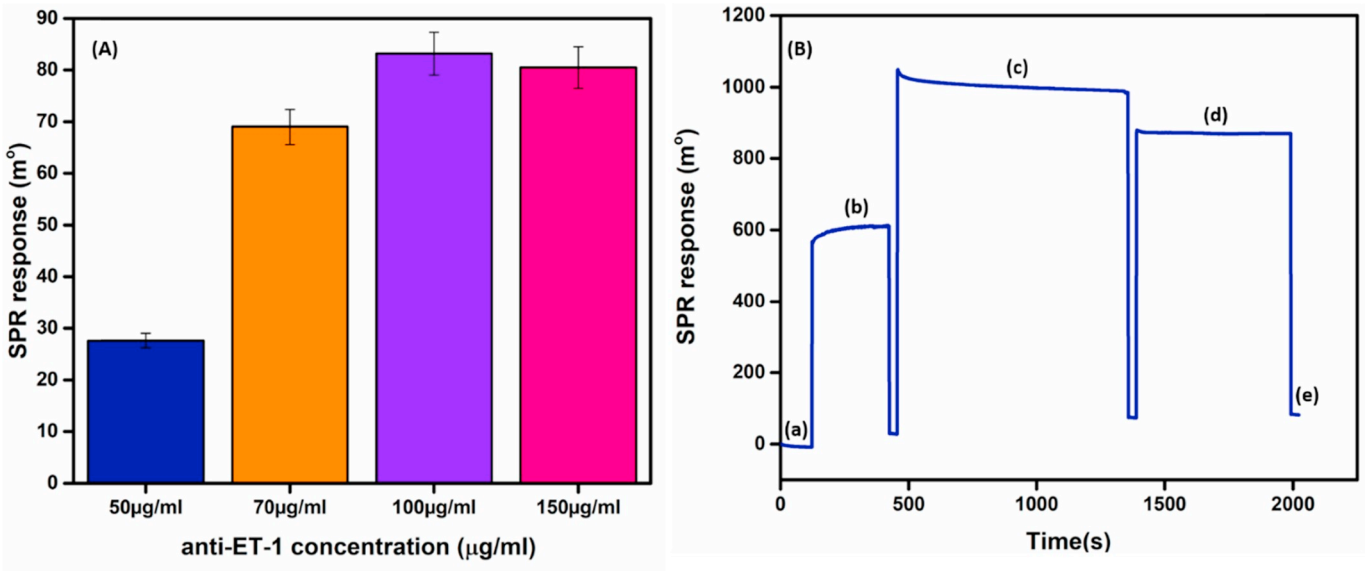

Fig. 1. (A) Optimization of anti-ET-1 immobilization using different concentration of 50 μg mL^{-1}, 70 μg mL^{-1},100 μg $mL^{-1}$and 150 μg mL^{-1}(difference in baseline obtained before immobilization and baseline after ethanolamine deactivation) (B) Immobilization of anti-ET-1 (a) Baseline of 11-MUA/Au, (b) EDC-NHS activation on 11-MUA/Au and (c) anti-ET-1/11-MUA/Au (d) ethanolamine deactivation (e) baseline.

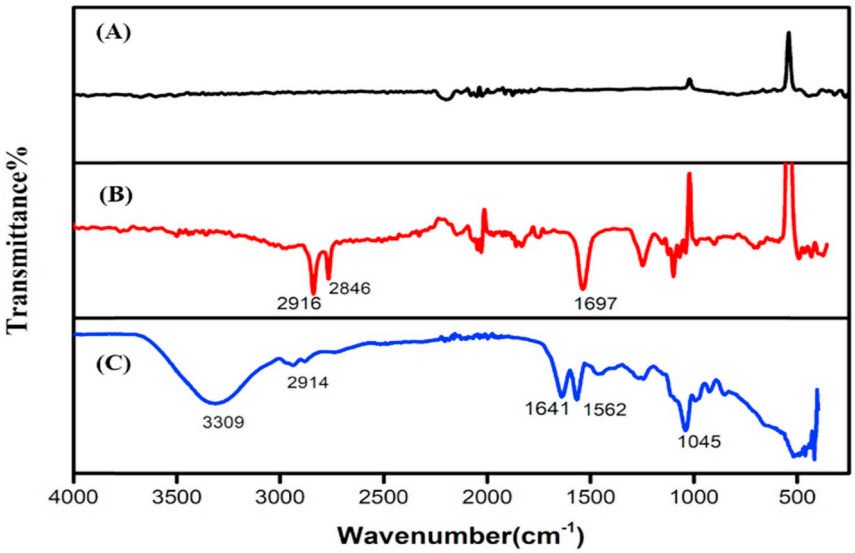

Fig. 2. FTIR spectra of (A) Au Disk, (B) 11-MUA/Au disk, (C) anti-ET-1/11-MUA/Au disk.

observed in the IR spectra (Fig. 2B) indicated the presence of –COOH groups of 11-MUA molecules confirming the formation of the 11-MUA SAM on the Au Disk (Fig. 2B). The other peaks are seen at 2916, and 2846 cm^{-1} corresponding to the stretching vibration of saturated $–CH_3$ groups further revealed the formation of 11-MUA layer onto the gold surface [42]. After anti-ET-1 immobilization the characteristic peaks obtained at 1641 and 1562 cm^{-1} were assigned to the presence of amide-I and amide-II bonds formed between the –COOH group of SAM and $–NH_2$ group of ET-1 antibody (Fig. 2C). The other peaks found at 3309 cm^{-1} and 1045 cm^{-1} were attributed to the presence of —OH and C—OH stretching vibrations of antibodies [43], respectively. These results confirmed the successful immobilization of anti-ET-1 with 11-MUA of the SAM layer on the gold disk.

3.3. Contact angle studies

To investigate the hydrophilic/hydrophobic properties of the modified Au disks, contact angle (CA) studies were conducted (Fig. 3A & B). After the 11-MUA SAM formation (Fig. 3A), the CA value was found to be 53.6° indicating increased hydrophilicity due to free –COOH groups introduced on to the Au disk. Interestingly, the CA angle decreased to 31.3° after anti-ET-1 immobilization (Fig. 3B). This increase in hydrophilicity was due to the hydrophilic nature of antibodies indicating the immobilization of anti-ET-1 onto the 11-MUA/Au electrode [44].

3.4. Atomic force microscopic studies

The atomic force microscopic (AFM) studies were conducted to investigate the changes in the surface morphology of the fabricated electrode. The average surface roughness of the gold disk modified with 11-MUA was found to be ~4.1 nm (Fig. 3C), confirming the smooth, dense and uniform SAM formation onto the Au disk. After the anti-ET-1 immobilization onto the 11-MUA/Au disk, the average roughness increased to ~9.8 nm (Fig. 3D) due to the globular structure of the antibodies that further covered the smooth surface of the SAM/Au disk [45]. The results of the AFM studies indicated the successful formation of the SAM onto the Au disk and the immobilization of anti-ET-1 biomolecules and were in agreement with the FT-IR studies.

3.5. Binding, response and kinetic analysis of ET-1

The SPR measurements were conducted to gain insight of the binding kinetics and biomolecular interactions of this novel biomarker (ET-1). This technique was used to investigate the binding response of the fabricated immunoelectrode as a function of ET-1 concentration. In SPR, the surface plasmon wave is generated and propagated along the boundary of metal and the dielectric. The propagation constant of the surface plasmon wave can be expressed as (Eq. (1))

$$\beta = \frac{\omega}{c}\sqrt{\frac{\varepsilon_M \varepsilon_D}{\varepsilon_M + \varepsilon_D}} \quad (1)$$

where ω is the angular frequency, εM and εD are the dielectric functions of metal and dielectric, respectively, and c is the speed of light. The change in the refractive index of the dielectric medium as a function of concentration resulted in a change in the intensity of surface plasmon wave that in turn led to the change in the SPR angle.

Fig. 4A shows the change in the SPR reflectance curve obtained at different concentrations of ET-1 as a function of time at room temperature (298 K). It was found that the shift in the curve was directly proportional to the increase in ET-1 concentration. Further, a calibration curve was plotted (Fig. S-1 A) between the change in SPR response in equilibrium versus ET-1 concentration (2–100 pg mL^{-1}). The change in R_{eq} with increasing concentration was found to be linear in the range, 2–100 pg mL^{-1} with an R^2 value of 0.99 and follows Eq. (2).

$$y = 2.18\,x + 165.05 \quad (2)$$

where *y* represents the change in SPR angle (Δm^o), and x represents the ET-1 concentration. Further, the sensitivity of the immunosensor was evaluated by using the slope of the curve and was found to be 2.18 m^o pg^{-1} mL, and the limit of detection (LOD) was calculated to be 0.30 pg mL^{-1} using Eq. (3).

$$\text{Limit of detection} = 3\sigma/\text{sensitivity} \quad (3)$$

where σ is the standard deviation of intercept. The shift observed in the SPR dip angle with increasing concentration of ET-1 (Fig. 4A) revealed that the refractive index changed along with the change in the surface density. Further, electrochemical impedance spectroscopy (EIS) studies were performed to investigate the dynamics of the antibody and antigen interaction occurring at the EA/anti-ET-1/11-MUA/Au electrode interface. In EIS, the Randles circuit is used for modelling the EIS data which consists of the capacitance of dielectric layer (C_{dl}), Warburg impedance (Z_w), and charge transfer resistance (R_{ct}) in series with electrolyte resistance (R_s). The typical Nyquist plot has a semicircle region which indicates the charge transfer limited process followed by a linear region revealing the mass transfer process. Fig. S-3 shows the Nyquist plot of (a) bare Au electrode, (b) 11-MUA/Au and (c) EA/anti-

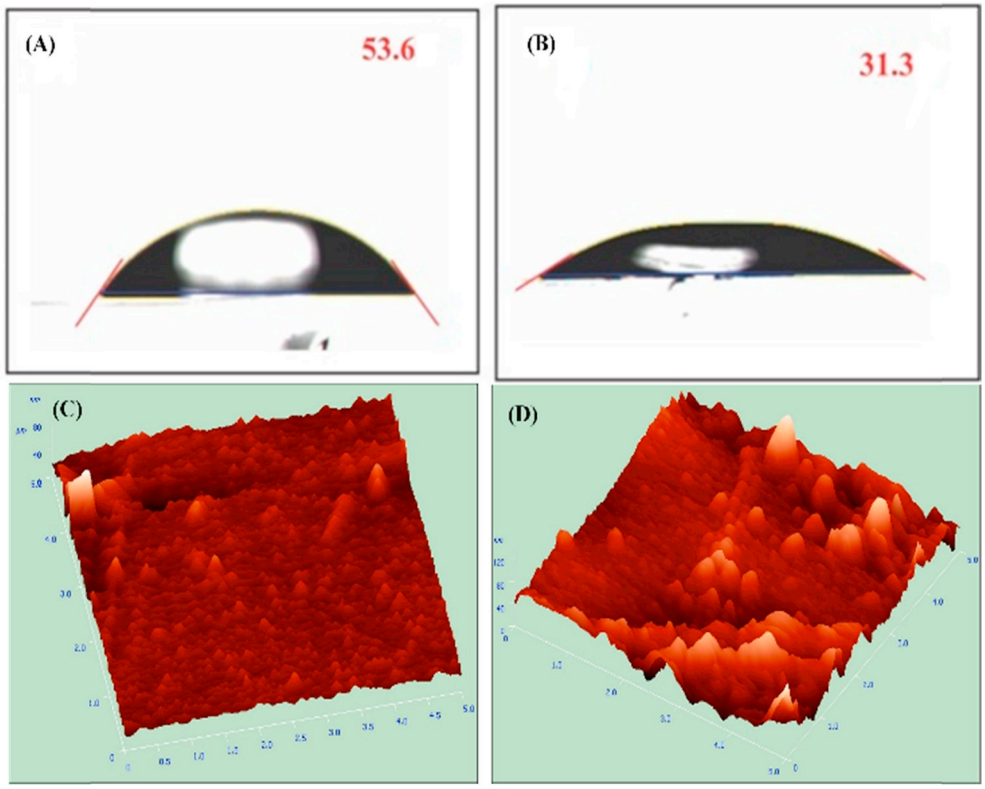

Fig. 3. Contact angle studies of (A) 11-MUA/Au electrode and (B) anti-ET-1/11-MUA/Au electrode. AFM micrographs of (C) 11-MUA/Au electrode and (D) anti-ET-1/11-MUA/Au electrode.

ET-1/11-MUA/Au electrode in PBS (pH-7.4) containing 5 mM $[Fe(CN)_6]^{4-/3-}$ in the frequency range, 10^5-0.1 Hz at a potential of 10 mV. The electron transfer resistance (R_{ct}) values for the bare gold, SAM-modified and antibody immobilized electrode were found to be 17.1 Ω, 1.33 kΩ, and 8.78 kΩ, respectively. The change in R_{ct} values with modification of the film indicated increased insulating characteristics of the SAM. The increased R_{ct} value after antibody immobilization was attributed to the insulating nature of the biomolecules that hindered the electron transport from bulk to the electrode surface. The heterogeneous electron transfer rate (k°) for bare Au, 11-MUA/Au, and EA/anti-ET-1/11-MUA/Au electrodes were calculated using Eq. (4).

$$k^{\circ} = RT/n^2F^2AR_{ct}C \quad (4)$$

where T is the temperature (~298 K), R is the molar gas constant, n is the number of electrons, C is the concentration of electroactive species (5×10^{-3} M), and A is the active surface area of the electrode (0.25 cm^2). The k° values of the bare Au, 11-MUA/Au, and EA/anti-ET-1/11-MUA/Au were determined to be 0.17 cm s^{-1}, 2.2×10^{-3} cm s^{-1} and 3.4×10^{-4} cm s^{-1}, respectively. Further, the impedimetric response of EA/anti-ET-1/11-MUA/Au as a function of the different

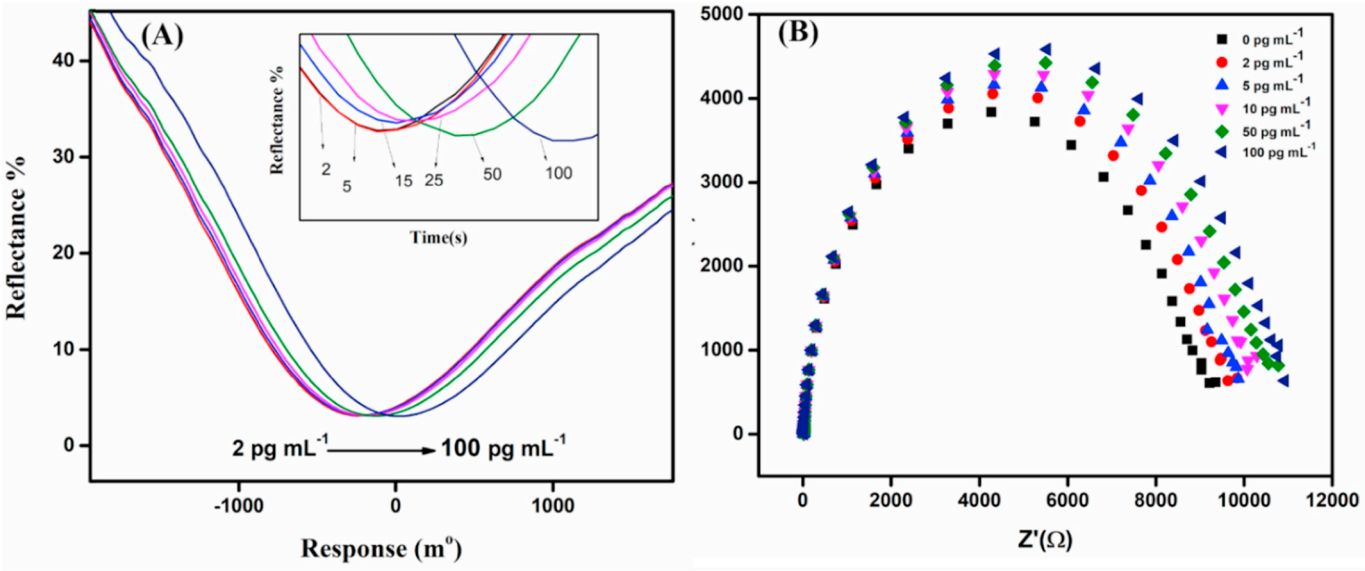

Fig. 4. Sensing response obtained for anti-ET-1 immobilized electrode exposed to different concentration of ET-1 (2–100 pg mL^{-1}) (A) SPR reflectance curve, (B) Impedance spectra.

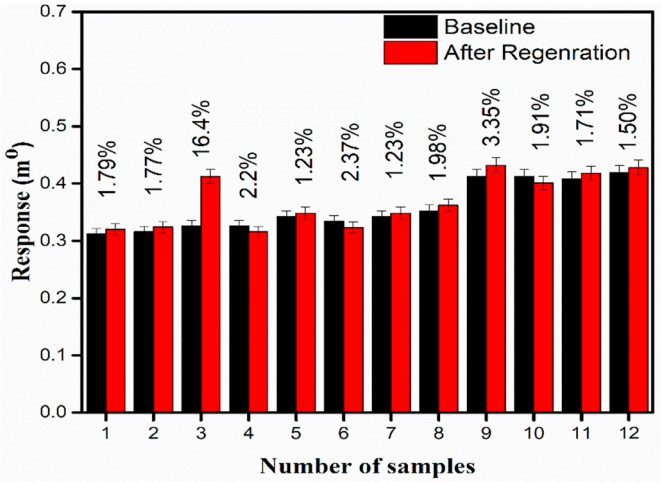

Fig. 5. Bar graph depicting the change in response angle of baseline after regeneration of immunosensor with the concentration of 5 pg mL^{-1}.

concentration of ET-1 (2–100 pg mL^{-1}) was obtained from the Nyquist plot (Fig. 4B). As the concentration of ET-1 was increased, the attachment of antigens on the modified electrode increased resulting in increased R_{ct} arising due to the formation of insulating antigen-antibody complexes. The calibration plot between the R_{ct} and ET-1 concentration exhibited a linear behaviour in the range (2–100 pg mL^{-1}) (Fig. S-1 B). The detection limit was calculated to be 0.36 pg mL^{-1} using Eq. (3).

Further, the binding kinetics of ET-1 onto the immunosensor surface undergoes two phases i.e., association and dissociation phase with ka and kd as an association constant and dissociation constant, respectively. The interaction between the ligand (anti-ET-1) and the analyte (ET-1) resulted in the formation of immunocomplex at the SPR sensor disk (EA/anti-ET-1/11-MUA/Au). The kinetics involved in the immunocomplex formation was evaluated using the observed experimental data. The dissociation phase was followed by the regeneration phase to reuse the electrode. The association constant of the analyte binding with the ligand was determined by a non-linear curve fitting using the SPR kinetic evaluation software. (Fig. S-2). Further, a monophasic model was assumed where the binding of the analyte at the sensor surface was considered to be in the ratio of 1:1 and was a single step process represented using the integrated rate equation (Rt) [46] involved during the association phase (Eq. (5)).

$$R_t = \frac{k_a C R_{max}}{k_a C + k_d}\left(1 - e^{-(k_a C + k_d)t}\right) + R_o \quad (5)$$

where C is the amount of ET-1 bound on the surface R_o is the response of signal at zero seconds, $k_aC\ R_{max}/k_aC + k_d$ is the maximal change in the binding response. The values of k_a and k_d were determined to be $4.4 \pm 0.4 \times 10^5\ M^{-1}\ s^{-1}$, and $2.04 \pm 0.0003 \times 10^{-3}\ s^{-1}$, respectively. Thus, the equilibrium constant K_A ($=k_a/k_d$) for association was obtained as $K_A = 2.15 \times 10^8\ M^{-1}$. The advantage of SPR immunosensor over the conventional techniques such as ELISA is reusability of the sensor surface. During the regeneration phase, the antigen is removed from the antibody while maintaining the functionality and reusability of the antibody at the sensor surface. Here, we observed the negligible difference in the SPR signal obtained before antigen sensing and after regeneration stage revealing successful recovery of the active surface of the immunoelectrode. This could perhaps be attributed to the fact that at low pH the protein binding sites tended to fold and repel each other making the molecules move apart. The % change in response to baseline after regeneration of the sensor surface is shown in Fig. 5. It was observed that the sensor could be regenerated more than ten times (~% RSD = 2.5).

Table 1
Characteristics of the 11-MUA based SPR biosensor along with those reported in the literature for colorectal cancer detection.

Method	Detection technique	Biosensing platform	Sample	Target Analyte	Label used	Degree of invasiveness	Range	Limit of detection (LOD)	Sensitivity	Reference
Colonoscopy	Visual Imaging	–	Tissue	–	–	High	–	–	–	[1]
Sigmoidoscopy	Visual Imaging	–	Tissue	–	–	High	–	–	–	[1]
Double Contrast barium enema	X-Ray Imaging	–	Tissue	–	–	High	–	–	–	[1]
Biosensor	SPR	Gold/ZnO nanocomposite	Serum	CA 15–3	No	Low	1–40 U mL^{-1}	0.0125 U ml^{-1}	–	[47]
	LSPR	Gold/MHDA/TAA	Serum	GTF2b and EDIL3	No	Low	50 ng mL^{-1} to 1 μg mL^{-1}	10 ngmL^{-1}and 5 ng mL^{-1}	–	[48]
	SPRi	OEG and COOH–OEG SAM Layer	Serum	CEA	No	Low	–	–	–	[49]
	SPRi	Gold/DNA probe H1	Serum	miRNA-15a	Yes	Low	0.5-5 fM	0.56 fM	–	[50]
	LSPR	Mixed PEG/GNR	Serum	ALCAM	No	Low	0.05 nM–25 nM	15 pM		[51]
	SPR	Gold/MUA	Serum	ET-1	No	Low	2 pg mL^{-1}-100 pg mL^{-1}	0.30 pgmL^{-1}	2.38 m° pg^{-1} mL	This work

3.5.1. Non-specific interaction and interferent studies

Reducing non-specific interaction is crucial as it helps to obtain good binding curves. To reduce nonspecific interaction on the SPR sensor surface, we introduced salts such as NaCl (0.138 M), KCl (0.027 M) and tween 20 into the running buffer as it reduces the charge interactions by shielding effect. Moreover, we also used ethanolamine (EA) to reduce the interaction of other proteins on the sensor surface and on the attached ligand. To evaluate the specificity of this SPR immunosensor towards ET-1, interferent studies were conducted. In serum samples of cancer patients, several biological molecules such as glucose (100 mg dL^{-1}), cardiac troponin I (cTnI 0.40 ng mL^{-1}), cytokeratin 19 fragments (CYFRA-21-1 3.5 ng mL^{-1}), and carcinoembryonic antigen (CEA 3 ng mL^{-1}) are known to be present and are potential interferents. The fabricated SPR sensor disk was subjected to these different interferents starting with ET-1 followed by incorporation of cTnI, CYFRA-21-1, CEA and glucose. The obtained SPR response angle did not exhibit any significant change when subjected to various interferents (Fig. S-4), revealing high specificity of the immunosensor to ET-1. Table 1 shows the characteristics of this ET-1 SPR immunosensor along with those reported in the literature for colorectal cancer detection.

3.6. Serum sample analysis

A study was conducted to assess the applicability of the fabricated SPR immunosensor towards the serum samples taken from CRC patients. These results were validated against those obtained by ELISA (Table 2). The detailed procedures of sample collection and analysis by SPR and ELISA have been provided in the supplementary data Section 1.1 and 1.2.

Fig. S-5 shows the bar graph representation comparing the change in response angle with respect to the patient samples and standard samples with an acceptable %RSD (0.63–1.64). The LOD for the serum sample was calculated to be 4.6 pg mL^{-1}. The small deviation in sensitivity of serum samples with respect to the standard samples may perhaps be due to other interfering compounds present in natural serum samples of the patients. This SPR based detection was found to be more sensitive, less time consuming and exhibited a better LOD than ELISA kit. The results obtained using this SPR immunosensor, ELISA and EIS towards the determination of ET-1 levels have been tabulated in Table 3.

4. Conclusions

In this study, a simple, label-free SPR immunosensor has been fabricated for real-time detection of ET-1, a colorectal cancer biomarker for the first time. The SPR Au sensor disk has been initially modified with SAM (11-MUA) followed by immobilization of anti-ET-1 and EA. This ET-1 based SPR sensor disk has been characterized via contact angle, FT-IR, and AFM techniques. The interaction mechanism of antigen (ET-1) and antibody (anti-ET1) was evaluated by different model amongst which the monophasic model revealed better results. The

Table 2
Determination of ET-1 concentration in the serum sample of colorectal patients by ELISA technique and EA/anti-ET-1/11-MUA/Au SPR immunosensor.

Patient sample	Concentration of ET-1 in serum sample determined from ELISA (pg mL^{-1})	Concentration of ET-1 in serum sample determined by developed SPR disk (pg mL^{-1})	%RSD (n = 3)
1	9.4	9.7	2.22
2	10.3	10.04	1.81
3	10.5	10.21	1.98
4	10.9	10.3	4.0
5	11.5	11.2	1.87
6	15	15.4	1.86

Table 3
Comparison between different techniques used in this study to determine the presence of ET-1.

Techniques	Linear range (pg mL^{-1})	LOD (pg mL^{-1})	Advantages	Limitations	Ref.
RayBio Human Endothelin-1 ELISA Kit	10–1000	10	Gold standard technique Specific and sensitive	Time-consuming, Labor intensive	[52]
SPR	2–100	0.30	Real-time monitoring, Kinetic studies, label-free, sensitive	Plasmon effect limited to gold or silver surface.	Present study
EIS	2–100	0.36	Highly Sensitive, Miniaturization possible	Kinetic interaction cannot be studied, no real-time interaction monitoring,	

linear range of this sensor has been found to be 2–100 pg mL^{-1} with a LOD of 0.36 pg mL^{-1} and a remarkable sensitivity of 2.18 m^{o} pg^{-1} mL. Real-time analysis of the serum sample obtained using this SPR sensor has been compared with ELISA and electrochemical impedance spectroscopy results. The fabricated biosensor shows remarkable sensitivity, selectivity, and reproducibility in real time sensing of ET-1. The excellent performance of SPR biosensor for ET-1 detection as a potential biomarker for CRC detection paves the way for effective diagnosing method towards cancer detection as compared to conventional methods. Further efforts should also be made to fabricate a portable SPR biosensor for point-of-care diagnostics.

Acknowledgements

We thank Prof. Yogesh Singh, Vice Chancellor, Delhi Technological University (DTU), Delhi, India for providing the facilities. TN is thankful to DBT, India (BT/PR12530/MED/32/385/2015) for providing financial assistance. BDM thanks Science & Engineering Research Board (Govt. of India) for the award of a Distinguished Fellowship (SB/S9/YSCP/SERB-DF/2018(1)). Saurabh Kumar and Suveen Kumar acknowledge Department of Science and Technology, New Delhi, India for DST INSPIRE Faculty Award (DST/INSPIRE/04/2017/002750 and DST/INSPIRE/04/2017/001336, respectively).

Appendix A. Supplementary data

Supplementary data to this article can be found online at https://doi.org/10.1016/j.talanta.2019.04.039.

References

[1] R.L. Siegel, K.D. Miller, S.A. Fedewa, D.J. Ahnen, R.G. Meester, A. Barzi, A. Jemal, Colorectal cancer statistics, 2017, Ca - Cancer J. Clin. 67 (3) (2017) 177–193.
[2] L.A. Torre, F. Bray, R.L. Siegel, J. Ferlay, J. Lortet-Tieulent, A. Jemal, Global cancer statistics, Ca - Cancer J. Clin. 65 (2) (2012) 87–108 2015.
[3] C. Allemani, H.K. Weir, H. Carreira, R. Harewood, D. Spika, X.-S. Wang, F. Bannon, J.V. Ahn, C.J. Johnson, A. Bonaventure, Global surveillance of cancer survival 1995–2009: analysis of individual data for 25 676 887 patients from 279 population-based registries in 67 countries (CONCORD-2), Lancet 385 (9972) (2015) 977–1010.
[4] A. Jemal, R. Siegel, J. Xu, E. Ward, Cancer statistics, Ca - Cancer J. Clin. 60 (5) (2010) 277–300 2010.
[5] A. Ekbom, C. Helmick, M. Zack, H.-O. Adami, Ulcerative colitis and colorectal cancer: a population-based study, N. Engl. J. Med. 323 (18) (1990) 1228–1233.
[6] M.G. Collins, E. Teo, S.R. Cole, C.-Y. Chan, S.P. McDonald, G.R. Russ, G.P. Young, P.A. Bampton, P.T. Coates, Screening for colorectal cancer and advanced colorectal neoplasia in kidney transplant recipients: cross sectional prevalence and diagnostic accuracy study of faecal immunochemical testing for haemoglobin and colonoscopy, BMJ 345 (2012) e4657.
[7] E. Giovannucci, Insulin and colon cancer, Cancer Causes Control 6 (2) (1995) 164–179.
[8] H. Yuhara, C. Steinmaus, S.E. Cohen, D.A. Corley, Y. Tei, P.A. Buffler, Is diabetes mellitus an independent risk factor for colon cancer and rectal cancer? Am. J. Gastroenterol. 106 (11) (2011) 1911–1921.
[9] E. Cho, J.E. Lee, E.B. Rimm, C.S. Fuchs, E.L. Giovannucci, Alcohol consumption and the risk of colon cancer by family history of colorectal cancer, Am. J. Clin. Nutr. 95 (2) (2012) 413–419.
[10] Y. Kimura, S. Kono, K. Toyomura, J. Nagano, T. Mizoue, M.A. Moore, R. Mibu, M. Tanaka, Y. Kakeji, Y. Maehara, Meat, fish and fat intake in relation to subsite-specific risk of colorectal cancer: the Fukuoka colorectal cancer study, Cancer Sci. 98 (4) (2007) 590–597.
[11] D. Harriss, G. Atkinson, A. Batterham, K. George, N. Tim Cable, T. Reilly, N. Haboubi, A.G. Renehan, Lifestyle factors and colorectal cancer risk (2): a systematic review and meta-analysis of associations with leisure-time physical activity, Colorectal Dis. 11 (7) (2009) 689–701.
[12] B. Ji, Q. Dai, Y. Gao, A. Hsing, J. McLaughlin, J. Fraumeni Jr., W. Chow, Cigarette and alcohol consumption and the risk of colorectal cancer in Shanghai, China, Eur. J. Cancer Prev. 11 (3) (2002) 237–244.
[13] P. Thirunavukarasu, S. Sukumar, M. Sathaiah, M. Mahan, K.D. Pragatheeshwar, J.F. Pingpank, H. Zeh, C.J. Bartels, K.K. Lee, D.L. Bartlett, C-stage in colon cancer: implications of carcinoembryonic antigen biomarker in staging, prognosis, and management, JNCI: J. Natl. Cancer Inst. 103 (8) (2011) 689–697.
[14] P.J. Pickhardt, C. Hassan, S. Halligan, R. Marmo, Colorectal cancer: CT colonography and colonoscopy for detection—systematic review and meta-analysis, Radiology 259 (2) (2011) 393–405.
[15] N. Wasserberg, O. Purim, V. Bard, Y. Kundel, N. Gordon, D. Groshar, N. Goldberg, H. Kashtan, A. Sulkes, B. Brenner, Early postoperative 18F-FDG PET/CT in high-risk stage III colorectal cancer, Clin. Nucl. Med. 40 (4) (2015) e222–e227.
[16] F. Tixier, A.M. Groves, V. Goh, M. Hatt, P. Ingrand, C.C. Le Rest, D. Visvikis, Correlation of intra-tumor 18F-FDG uptake heterogeneity indices with perfusion CT derived parameters in colorectal cancer, PLoS One 9 (6) (2014) e99567.
[17] H.J. Wanebo, B. Rao, C.M. Pinsky, R.G. Hoffman, M. Stearns, M.K. Schwartz, H.F. Oettgen, Preoperative carcinoembryonic antigen level as a prognostic indicator in colorectal cancer, N. Engl. J. Med. 299 (9) (1978) 448–451.
[18] P. Byström, Colorectal Cancer Treatment and Early Response Evaluation, How do We Best Evaluate Treatment Response?, Institutionen för Onkologi-Patologi/Department of Oncology-Pathology, (2010).
[19] W. Zhong, Z. Yu, J. Zhan, T. Yu, Y. Lin, Z.-S. Xia, Y.-H. Yuan, Q.-K. Chen, Association of serum levels of CEA, CA199, CA125, CYFRA21-1 and CA72-4 and disease characteristics in colorectal cancer, Pathol. Oncol. Res. 21 (1) (2015) 83–95.
[20] A. Nicolini, P. Ferrari, M.J. Duffy, A. Antonelli, G. Rossi, M.R. Metelli, F. Fulceri, L. Anselmi, M. Conte, P. Berti, Intensive risk-adjusted follow-up with the CEA, TPA, CA19. 9, and CA72. 4 tumor marker panel and abdominal ultrasonography to diagnose operable colorectal cancer recurrences: effect on survival, Arch. Surg. 145 (12) (2010) 1177–1183.
[21] Z. Huang, D. Huang, S. Ni, Z. Peng, W. Sheng, X. Du, Plasma microRNAs are promising novel biomarkers for early detection of colorectal cancer, Int. J. Cancer 127 (1) (2010) 118–126.
[22] K.-J. Feng, Y.-H. Yang, Z.-J. Wang, J.-H. Jiang, G.-L. Shen, R.-Q. Yu, A nano-porous CeO 2/Chitosan composite film as the immobilization matrix for colorectal cancer DNA sequence-selective electrochemical biosensor, Talanta 70 (3) (2006) 561–565.
[23] G.Y. Locker, S. Hamilton, J. Harris, J.M. Jessup, N. Kemeny, J.S. Macdonald, M.R. Somerfield, D.F. Hayes, R.C. Bast Jr., ASCO 2006 update of recommendations for the use of tumor markers in gastrointestinal cancer, J. Clin. Oncol. 24 (33) (2006) 5313–5327.
[24] M. Duffy, R. Lamerz, C. Haglund, A. Nicolini, M. Kalousová, L. Holubec, C. Sturgeon, Tumor markers in colorectal cancer, gastric cancer and gastrointestinal stromal cancers: european group on tumor markers 2014 guidelines update, Int. J. Cancer 134 (11) (2014) 2513–2522.
[25] F. Lumachi, F. Marino, R. Orlando, G.B. Chiara, S.M. Basso, Simultaneous multianalyte immunoassay measurement of five serum tumor markers in the detection of colorectal cancer, Anticancer Res. 32 (3) (2012) 985–988.
[26] L. Tao, K. Zhang, Y. Sun, B. Jin, Z. Zhang, K. Yang, Anti-epithelial cell adhesion molecule monoclonal antibody conjugated fluorescent nanoparticle biosensor for sensitive detection of colon cancer cells, Biosens. Bioelectron. 35 (1) (2012) 186–192.
[27] M. Yanagisawa, H. Kurihara, S. Kimura, Y. Tomobe, M. Kobayashi, Y. Mitsui, Y. Yazaki, K. Goto, T. Masaki, A novel potent vasoconstrictor peptide produced by vascular endothelial cells, Nature 332 (6163) (1988) 411–415.
[28] I.A. Abdel-Gawad, H. Hassanein, N.A. Bahgat, M. Abdel Sattar, A.H. El-Sissy, M.A. Altaweel, A.M. Helal, Study of endothelin-1 and vascular endothelial growth factor in patients with cancer colon, J. Egypt. Natl. Cancer Inst. 20 (3) (2008) 216–223.
[29] H. Inagaki, A.E. Bishop, T. Eimoto, J.M. Polak, Autoradiographic localization of endothelin-1 binding sites in human colonic cancer tissue, J. Pathol. 168 (3) (1992) 263–267.
[30] M. Shichiri, Y. Hirata, T. Nakajima, K. Ando, T. Imai, M. Yanagisawa, T. Masaki, F. Marumo, Endothelin-1 is an autocrine/paracrine growth factor for human cancer cell lines, J. Clin. Investig. 87 (5) (1991) 1867.
[31] A. Bagnato, R. Tecce, V. Di Castro, K.J. Catt, Activation of mitogenic signaling by endothelin 1 in ovarian carcinoma cells, Cancer Res. 57 (7) (1997) 1306–1311.
[32] S. Moraitis, S. Langdon, W. Miller, Endothelin expression and responsiveness in human ovarian carcinoma cell lines, Eur. J. Cancer 33 (4) (1997) 661–668.
[33] E. Asham, A. Shankar, M. Loizidou, S. Fredericks, K. Miller, P. Boulos, G. Burnstock, I. Taylor, Increased endothelin-1 in colorectal cancer and reduction of tumour growth by ET, Br. J. Canc. 85 (11) (2001) 1759–1763.
[34] A. Shankar, M. Loizidou, G. Aliev, S. Fredericks, D. Holt, P. Boulos, G. Burnstock, I. Taylor, Raised endothelin 1 levels in patients with colorectal liver metastases, Br. J. Surg. 85 (4) (1998) 502–506.
[35] J. Knowles, M. Loizidou, Irving Taylor, Endothelin-1 and angiogenesis in cancer, Curr. Vasc. Pharmacol. 3 (4) (2005) 309–314.
[36] J. León, J. Casado, S.M. Jiménez Ruiz, M.S. Zurita, C. González-Puga, J.D. Rejón, A. Gila, P. Muñoz de Rueda, E.J. Pavón, Russel J. Reiter, Angela Ruiz-Extremera, Javier Salmerón, Melatonin reduces endothelin-1 expression and secretion in colon cancer cells through the inactivation of FoxO-1 and NF-κβ, J. Pineal Res. 56 (4) (2014) 415–426.
[37] R. Cianfrocca, L. Rosanò, P. Tocci, R. Sestito, V. Caprara, V. Di Castro, R. De Maria, A. Bagnato, Blocking endothelin-1-receptor/β-catenin circuit sensitizes to chemotherapy in colorectal cancer, Cell Death Differ. 24 (2017) 1811.
[38] H. Ali, M. Loizidou, M. Dashwood, F. Savage, C. Sheard, I. Taylor, Stimulation of colorectal cancer cell line growth by ET-1 and its inhibition by ET A antagonists, Gut 47 (5) (2000) 685–688.
[39] Z. Matharu, A.J. Bandodkar, G. Sumana, P.R. Solanki, E.M. Ekanayake, K. Kaneto, V. Gupta, B. Malhotra, Low density lipoprotein detection based on antibody immobilized self-assembled monolayer: investigations of kinetic and thermodynamic properties, J. Phys. Chem. B 113 (43) (2009) 14405–14412.
[40] B.D. Malhotra, M.A. Ali, Nanomaterials for Biosensors: Fundamentals and Applications, William Andrew, 2017.
[41] M. Corr, A.E. Slanetz, L.F. Boyd, M.T. Jelonek, S. Khilko, B.K. Al-Ramadi, Y.S. Kim, S.E. Maher, A.L. Bothwell, D.H. Margulies, T Cell Receptor-MHC Class I Peptide Interactions: Affinity, Kinetics, and Specificity, Science-New York then Washington, 1994 946-946.

[42] R. Zhu, J. Song, Q. Ma, Y. Zhou, J. Yang, S. Shuang, C. Dong, A colorimetric probe for the detection of aluminum ions based on 11-mercaptoundecanoic acid functionalized gold nanoparticles, Anal. Methods 8 (39) (2016) 7232–7236.
[43] I. Tubía, J. Paredes, E. Pérez-Lorenzo, S. Arana, Antibody biosensors for spoilage yeast detection based on impedance spectroscopy, Biosens. Bioelectron. 102 (2018) 432–438.
[44] S. Kumar, J. Singh, V. Agrawal, M. Ahamad, B.J.A.M. Malhotra, Biocompatible self-assembled monolayer platform based on (3-glycidoxypropyl) trimethoxysilane for total cholesterol estimation, 3 (10) (2011) 2237–2245.
[45] S. Kumar, S. Kumar, S. Tiwari, S. Augustine, S. Srivastava, B.K. Yadav, B.D. Malhotra, Highly sensitive protein functionalized nanostructured hafnium oxide based biosensing platform for non-invasive oral cancer detection, Sensor. Actuator. B Chem. 235 (2016) 1–10.
[46] R.B. Schasfoort, Handbook of Surface Plasmon Resonance, Royal Society of Chemistry, 2017.
[47] C.-C. Chang, N.-F. Chiu, D.S. Lin, Y. Chu-Su, Y.-H. Liang, C.-W. Lin, High-sensitivity detection of carbohydrate antigen 15-3 using a gold/zinc oxide thin film surface plasmon resonance-based biosensor, Anal. Chem. 82 (4) (2010) 1207–1212.
[48] M. Soler, M.-C. Estevez, R. Villar-Vazquez, J.I. Casal, L.M. Lechuga, Label-free nanoplasmonic sensing of tumor-associate autoantibodies for early diagnosis of colorectal cancer, Anal. Chim. Acta 930 (2016) 31–38.
[49] J. Ladd, H. Lu, A.D. Taylor, V. Goodell, M.L. Disis, S. Jiang, Direct detection of carcinoembryonic antigen autoantibodies in clinical human serum samples using a surface plasmon resonance sensor, Colloids Surfaces B Biointerfaces 70 (1) (2009) 1–6.
[50] F. Hu, J. Xu, Y. Chen, Surface plasmon resonance imaging detection of sub-femtomolar MicroRNA, Anal. Chem. 89 (18) (2017) 10071–10077.
[51] J.-H. Pai, C.-T. Yang, H.-Y. Hsu, A.B. Wedding, B. Thierry, Development of a simplified approach for the fabrication of localised surface plasmon resonance sensors based on gold nanorods functionalized using mixed polyethylene glycol layers, Anal. Chim. Acta 974 (2017) 87–92.
[52] Raybiotech, Human Endothelin-1 ELISA, (2019) https://www.raybiotech.com/human-endothelin-1-elisa/.

International Journal of Computer Networks and Applications (IJCNA)
DOI: 10.22247/ijcna/2019/49618 Volume 6, Issue 2, March – April (2019)

RESEARCH ARTICLE

QoS and Fuzzy Logic Based Routing Protocol for CRN

Gagan Deep Dhand
Department of Computer Science and Engineering, Bharati Vidyapeeth's College of Engineering, New Delhi, India.
gdgagan696@gmail.com

Rohit Kumar
Department of Computer Science and Engineering, Bharati Vidyapeeth's College of Engineering, New Delhi, India.
rohitkumar.050505@gmail.com

Rishabh
Department of Computer Science and Engineering, Bharati Vidyapeeth's College of Engineering, New Delhi, India.
rishabh421996@gmail.com

Devashish Ghildiyal
Department of Computer Science and Engineering, Bharati Vidyapeeth's College of Engineering, New Delhi, India.
devashishghildiyal@gmail.com

Rachna Jain
Department of Computer Science and Engineering, Bharati Vidyapeeth's College of Engineering, New Delhi, India.
rachna.jain@bharatividyapeeth.edu

Published online: 17 April 2019

Abstract – The tremendous development in wireless technologies and multimedia applications persuaded upsurge in spectrum utilization in the past. One of the adequate clarifications to overwhelm this limitation is by using Cognitive Radios (CR). These networks are likely to boost spectrum consumption professionally by permitting Secondary Users (SUs) to take advantage of the use of the approved spectrum of primary users (PUs). CR is a kind of a sensible radio that can sense the extraneous surroundings, analyze the past and build perspicacious conclusions to switch its transmission factors in step with the current state of the atmosphere. An Ad-hoc Network engaging Cognitive Radios (CR) can often be termed as Cognitive Radio Adhoc Network (CRAHN). Routing in CRAHN is not an easy mission due to spectrum availability, power, link stability, etc. Among all the parameters, the one among the best parameter for route selection is throughput. Since several applications need a high value of throughput like Audio & Video Broadcasting, Interactive audio & Video Streaming, etc. and some require the low value of throughput like E-mail, Telnet, etc. This paper design a routing strategy based on finding an optimal throughput path using fuzzy logic. To show the efficiency of a designed scheme it is compared with the shortest path routing mechanism. Our result shows that the proposed method is efficient than Shortest Spectrum.

Index Terms – Cognitive radios, Fuzzy Logic, Mamdami-Fuzzy Logic Controller, Quality of Service (QoS), Shortest Spectrum.

1. INTRODUCTION

Nowadays wireless technologies are shattering due to which spectrum's rectification is in demand. The radio frequency spectrum faces the deficiency issue in many nations subsequently the effective and convenient utilization of spectrum is needed. Solution to this problem can be Cognitive Radio (CR) [1, 2]. This technology looks forwards to intensify the spectral utilization in the licensed frequencies [3, 4, 5]. Cognitive radio [6, 7] can be presumed as a sensible radio that can sense extraneous surroundings, analyze the past and build perspicacious conclusions to switch its transmission factors in step with the current state of the atmosphere.

Cognitive Radio Ad-Hoc Network is a term for Ad hoc Network employing Cognitive Radios (CR). The two forms of users, one is Cognitive User (CU) and the other is Primary User (PU) play a significant role in CR [8, 9, 10]. PU's have their endemic frequency band due to which they are also admitted as licensed users while secondary users use the primary user's spectrum for communication due to which they are also admitted as unlicensed users.

The main notion of CR is to consume the unoccupied bands for communications resolutions [11]. As a CU, CR should not any harm to the PUs. Also, once a PU returns to its own channel, CU should abandon the channel rapidly and find

RESEARCH ARTICLE

another free channel [12]. CR permits the SUs to alter their transmission parameters (in reference to time and frequency domain) in accordance with the spectrum atmosphere while not inflicting any dangerous interference to PUs. There are certain limitations a protocol has to follow in order to provide efficient and reliable communication between a pair of distant nodes which are given below [13]:

- Limited Bandwidth
- Transmission Range
- Limitation in Power of Battery
- Mobility of Nodes

Certain applications require variable throughput [14] which is given in Table 1.

Type of Application	Traffic Class	Throughput (bps)
Non Real Time and Asymmetric	Web Browsing	<30.5K
Non Real Time and Asymmetric	Enhanced Web Browsing	<24K
Non Real Time and Asymmetric	Email	<10K
Non Real Time and Asymmetric	FTP	High
Non Real Time and Asymmetric	Telnet	<1K
Non Real Time and Symmetric	Internet, Relay Chat	<1K
Real Time and Highly Asymmetric	Audio Broadcasting	56-64K
Real Time and Highly Asymmetric	Video Broadcasting	1.2 to 60 M
Real Time and Highly Asymmetric	Interactive Audio on Demand	32-448K
Real Time and Highly Asymmetric	Interactive Video on Demand	1.2 to 60 M
Real Time and Highly Asymmetric	Telemetry	2K-52M
Real Time and Symmetric	Audio Conferencing	5.3 to 64K
Real Time and Symmetric	Audio graphics Conferencing	9.6-19.6K
Real Time and Symmetric	Video Conferencing	64 to 1920K
Real Time and Symmetric	Videophony	64 to 1920k
Real Time and Symmetric	Voice over IP	5.3 to 64K

Table 1: Throughput Requirement for various applications

Keeping aforementioned aspects in view we proposed a routing protocol based on QoS, which takes into consideration throughput along with the availability of a channel for path formation. Our paper is further designed as follows: the succeeding segment gives the literature survey. The proposal is given in section 3 followed by simulation set-up, results, conclusion, and references.

2. RELATED WORK

This section gives a broad analysis of routing protocols stated in the past research for CRN are enlisted.

Bahareh Najafi et al. [15] in their routing protocol used transmission count and channel selection to improve the performance of the protocol. They consider the spectrum and topology of the network to efficiently utilize the available channels. Cuimei Cui et al. [16] in their protocol used channel availability for path selection. To improve the performance of available spectrum Dual-Stage Collaborative Spectrum Sensing (DCSS) is used. Per-hop node performance was tried to maximize along their path by their protocol.

Bădoi, C. et al. [17] in their routing protocol considered hop-by-hop routing, geographical location, and spectrum availability. They also used basic information like the position of nodes and channel information and then take a hop-by-hop decision. Zhou, X. et al. [18] in their routing protocol consider destinations' node location. The direction of routing is found on the basis of the location of the source and destination nodes.

Bowen LI et al. [19] proposed a routing protocol based on Ant Colony. They used two types of ants on their proposed work. Forward ants (F-ants) are used to utilize spectrum achievable routes to destination and backward ants (B-ants) to accumulate data about the network and to keep routing table up-to-date.

Behrouz Jashni et al. [20] in their routing protocol make use of delay for path selection. They used queuing delay and transmission delay. They collected the information from the neighboring nodes and then evaluated the delays of all possible links and then select the optimal out of all for communication.

Anirudha R. Kulkarni and Anjali Agarwal [21] proposed protocol which considers end-to-end transmission power, channel availability, Presence of PU and link strength for route formation. Zhaoxia Song et al. [22] proposed a routing protocol which applied swarm intelligence into CRN routing protocol. They consider channel availability as a metric. Their proposed protocol minimizes delay.

Yongkang Liu et al. [23] designed a routing protocol based on geographical location details and channel availability. Next hop relay is selected by SU on the basis of locality and channel. They utilized Cognitive Transport Throughput (CTT) to evaluate the relay gain. K.R. Chowdhury and M.D. Felice [24] in their protocol undertake path and channel availability into consideration. They also consider node mobility during path formation. Their routing protocol minimized the hop count.

Nitul Dutta and Hiren Kumar Deva Sarma [25] in their protocol consider the probability of stability of channel for building the path from source to destination.

All listed available routing methods in literature are not beneficial for a specific type of application. Our proposal tries to solve this issue addressed by other routing protocols. The next section discusses the proposed protocol in detail.

International Journal of Computer Networks and Applications (IJCNA)
DOI: 10.22247/ijcna/2019/49618 Volume 6, Issue 2, March – April (2019)

RESEARCH ARTICLE

3. PROPOSED MODELLING

This section discusses the proposed work in detail along with the algorithm used.

3.1. Flow Diagram of Proposed Work:

The flow diagram of the proposed routing arrangement based on throughput is shown in Figure 1.

The procedure to select the best possible route can be explained as:-

1. First, the all possible route from source to destination is calculated along with the throughput of all those routes.
2. Of the entire possible path generated in step 1, Mamdami-Fuzzy Logic Controller (FLC) [26, 27] is applied to calculate the output weights.
3. For data transfer, the path having the maximum output weight is selected.

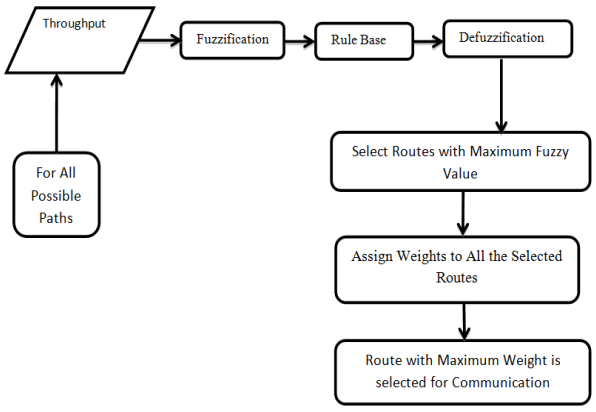

Figure 1 Flow Diagram of Proposed Scheme

3.2. Proposed Algorithm

```
1.  PU=16                    //Number of Primary Users
2.  SU=20                    //Number of Secondary User
3.  P=0                      //PDR
4.  H=0                      //Hop Count
5.  Delay=0                  //Delay
6.  Throughput=0
7.  Counter=0
8.  Temp=0
9.  allPath=[]               //Stores all Possible Path
10. a=[]
11. min=99999;
12. fuzzy=0;
13. S=floor(random(SU))      //Source Node
14. D=floor(random(SU))      //Destination
15. If(path_existes(S-D)
        a. {Counter++
        b. Temp++
        c. H=length(path)-2
        d. D=H*random(2)
        e. for( i=1 to path.length-1){
                i. if(PU[path[i]].rate<min){
                        1. min=PUarr[path[i]].rate;}
                        }
        f. Throughput=min
        g. a.push(H)
        h. a.push(D)
        i. a.push(Throughput)
        j. fuzzy=Fuzzification(path)
                        //Calculates Fuzzy Value
        k. a.push(fuzzy)
        l. a.push(temp)
        m. allPath.push(a)
        n. }
        o. else
        p. {
        q. Counter++;
        r. }
16. Function getPath()
        a. {
        b. Pos=-1;
        c. maxFuzzy=maxFuzz()
                        //Calculates Maximum Fuzzy Value
        d. for(i=0;i<allPath.length;i++)
                i. {If(allPath[i][3]==maxFuzzy){
                        a. Pos=i}}}
                        b. P=allPath[pos][4]/Counter
        }
```

Algorithm 1 Proposed Algorithm.

The proposed algorithm is represented in Algorithm 1. Where "PU" represents the Primary User nodes and "SU" represents the Secondary User nodes. To calculate the PDR "Counter" and "Temp" is used. "Temp" is used to stores count of a number of times the path from source to destination is formed. "S" represents the randomly generated source node whereas "D" denotes the randomly generated destination node. "a" stores all relevant information about the specific path and "allPath" stores the all possible path from particular source to destination. Fuzzification function is used to calculate the fuzzy value of the path which is stored in the

International Journal of Computer Networks and Applications (IJCNA)
DOI: 10.22247/ijcna/2019/49618 Volume 6, Issue 2, March – April (2019)

RESEARCH ARTICLE

fuzzy variable. "P", "H", "D" represents PDR, Hop Count, and Delay respectively.

The fundamental blocks of Fuzzy Logic Controller (FLC) are enlightened as underneath [28, 29, 30]:-

- **Input-** To calculate the optimal path the input i.e. throughput is feed to the fuzzy logic Controller (FLC).
- **Fuzzification-** It is the process of changing crisp value into fuzzy values with the help of membership function (Crisp values) as shown in Figure 2.

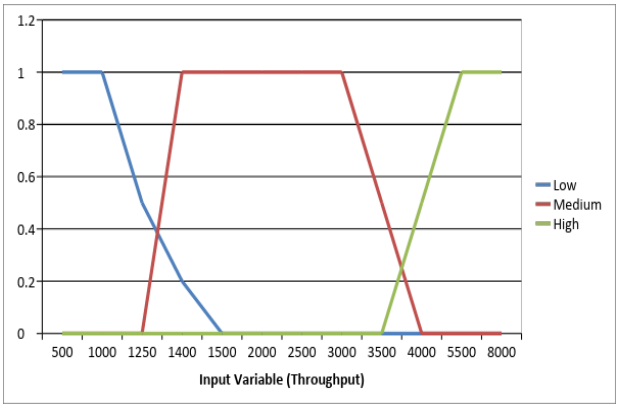

Figure 2 Crisp Values for Throughput

- **Membership Function of FLC Input-** Crisp Value for inputs can be same but membership function will be different. The semantic variable used as input is classified as below:-

$$T\ (input) = \{(low, medium, high)\}$$

- **Fuzzification Equation-** For fuzzification of input Table 2 is used in which Throughput (TH) is mapped according to Table 2 and output obtained is Optimality of Path (OP).

Membership Function	Optimality of path (OP)	Throughput (Input)
Low	1	$0 < TH \leq 1000$
	$3 - 0.002 * TH$	$1000 < TH \leq 1500$
Medium	$0.00095 * TH - 1904$	$1250 < TH \leq 1400$
	1	$1400 < TH \leq 3000$
	$4 - 0.001 * TH$	$3000 < TH \leq 4000$
High	$0.0005 * TH - 1.75$	$3500 < TH \leq 5500$
	1	$5500 < TH \leq 8000$

Table 2 Equations for Fuzzification

- **Rule Base-** Information related to the procedure of the process of the domain is stored in this. It is generally of the form IF-THEN. Rule base used in our proposal is given below:

1. If (Throughput is high) then (output is best)
2. If(Throughput is med) then (output is moderate)
3. If(Throughput is low) then (output is poor)

- **Defuzzification-** The reduction of a fuzzy set into a crisp set member is known as defuzzification. Proposed work used the Centre of Gravity (CoG)[31, 32] method employed for defuzzification is given in the below equation:-

$$Output = (m1 * A1 + m2 * A2)/(A1 + A2)$$

Where, m1 and m2 signify the membership functions calculated with the help of process of Fuzzification as {Poor, Moderate, and Best} and A1, A2 are the areas in the particular region.

- **FLC Output's Membership Function -** Output variable used in FLC basically defined optimality of route. The semantic variable used for output is categorized as below:

$$T\ (output) = \{(Poor, Moderate, Best)\}$$

It can be observed from Figure 3 that the path's optimality is less than or equal to 1.

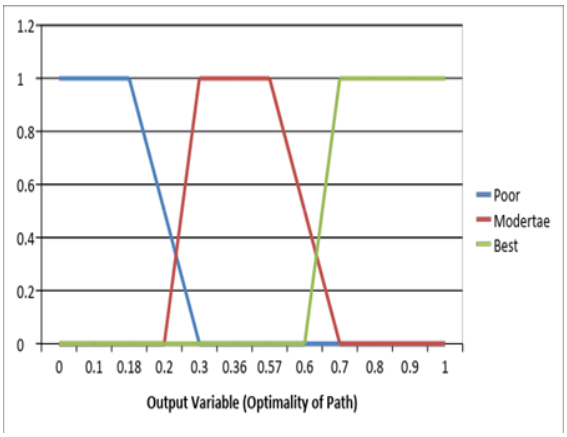

Figure 3 Crisp Values for Output

- **Defuzzification Equation-** For the defuzzification process Table 3 is used. It also characterizes the membership functions. It produces output weight taking Optimality of Path (OP) as input.
- **Weight-**Outputs are assigned some weights and the preference to maximum weight is selected as the optimal route.

RESEARCH ARTICLE

Membership Function	Output Weight	Optimality of path (input)
Poor	1	$0 < OP \leq 0.18$
	$2 - 5.56 * OP$	$0.18 < OP \leq 0.36$
Moderate	$10 * OP - 2$	$0.20 < OP \leq 0.30$
	1	$0.30 < OP \leq 0.57$
	$5.38 - 7.69 * OP$	$0.57 < OP \leq 0.70$
Best	$11.11 * OP - 6.67$	$0.60 < OP \leq 0.69$
	1	$0.69 < OP \leq 1$

Table 3 Equation for Defuzzification

4. SIMULATION SET-UP

The proposed routing protocol based on QoS is executed on JavaScript and comparison is done with the shortest spectrum is known routing protocol. This given segment provides information about the following:

- Setup Parameters,
- Portraits of the proposed scheme and
- Performance metrics used for comparison.

4.1. Simulation set-up parameters

Set-Up parameters employed to assess the efficiency of the proposed mechanism are given in Table 4.

Position of SU	Random
Position of PU	Fixed
Area	1500X1500
Number of PU nodes	16
Number of SU Nodes	20
Transmission Range of SU	300,400,450,500 Units
Mobility model	Random waypoint Model
Pause time	5 seconds
Simulation Time	50 sec
Throughput	8 Mbps Maximum
Number of Channels	2
Number of Iterations	15
Software Used	Javascript and its library p5.js

Table 4 Set-Up parameters

4.2. Portraits:

The path formed from source to destination using the proposed method is shown in Figure 4. PU nodes which are immovable are denoted by white color while SU nodes which are arbitrarily positioned and also movable are denoted by orange color. The Green line in Figure 4 demonstrates the path achieved from our proposed Quality of Service (QoS) based protocol.

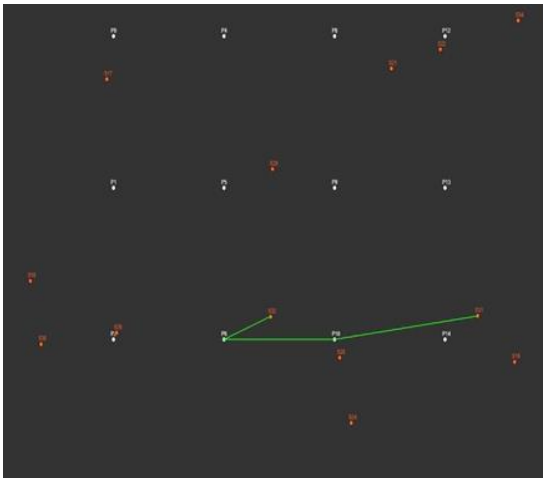

Figure 4 Visualization of Path Formation by our Proposed Method

4.3. Performance metrics used:

- **Packet Delivery Ratio (PDR):** The proportion of a number of packets delivered to the total number of packets sent from source [33] [34] is known as PDR.
- **Delay:** The time required to exchange a packet from beginning to end is known as Delay [35] [36].
- **Hop Count:** Number of intermediate nodes from a source to destination is known as hop count [37].
- **Throughput:** The speed in bits per seconds of the received data is known as throughput [38].

5. RESULTS AND DISCUSSIONS

To estimate the efficiency of the proposed protocol, the transmission range was varied as 350,400,450 and 500 units. The number of nodes is given above in the set-Up parameters.

The average throughput of our proposed protocol is higher than the shortest spectrum aware which can be seen from Figure 5 because our proposed protocol utilizes throughput during path selection while the latter consider hop count.

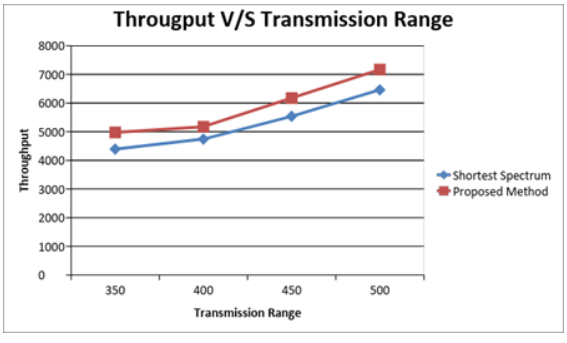

Figure 5 Throughput V/S Transmission Range

RESEARCH ARTICLE

Average Packet Delivery Ratio (PDR) in our proposed protocol is lower than the shortest spectrum aware as can be seen from Figure 6 as the latter has less hop count which boosts the PDR. Additionally, with an increase in transmission range PDR increases. This happened as with rising in transmission range the destination will most likely lie in the range of the nodes.

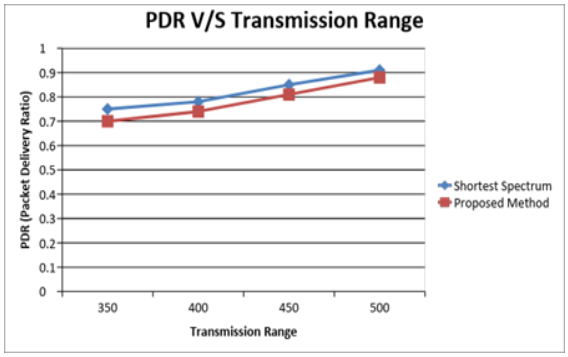

Figure 6 PDR V/S Transmission Range

Hop count in our proposed protocol is higher than the shortest spectrum aware as can be seen from Figure 7 because the shortest spectrum aware takes into account hop count and our proposed protocol takes into account throughput.

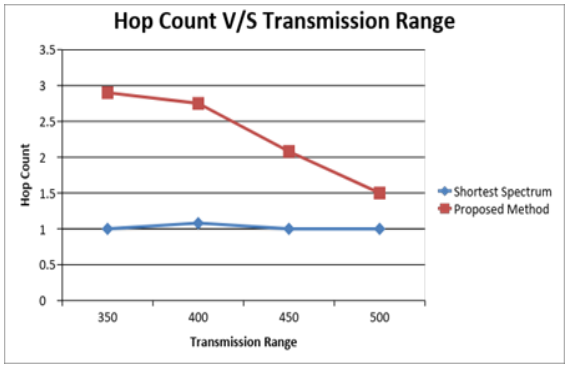

Figure 7 Hop Count V/S Transmission Range

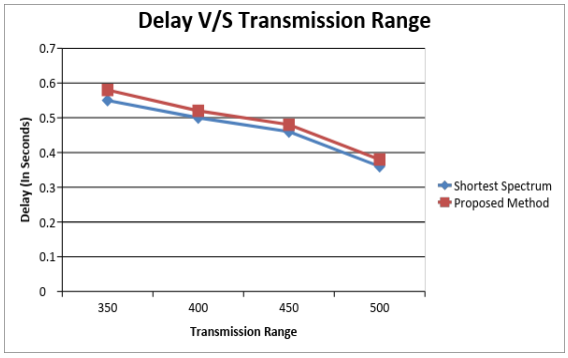

Figure 8 Delay V/S Transmission Range

Delay in our proposed protocol is higher than the shortest spectrum aware as can be seen from Figure 8 because the shortest spectrum aware selects the shortest path. Also, a number of hop counts are minimum in the shortest spectrum aware than our proposed routing protocol which also affects the delay.

6. CONCLUSION

This paper proposes a routing protocol which depends on one Quality of Service (QoS) Parameter i.e. throughput. It is an imperative parameter since different applications require variable values of throughput such as Live streaming requires a higher value of throughput in contrast to email transfer. Important corollaries which can be drawn from the results are as follows:

- Our protocol has high throughput since it selects the path which has maximum throughput.
- PDR is almost the same for both the routing scheme i.e. shortest path routing and the proposed scheme.
- Hop count and Delay values are high in case of the proposed scheme since it undertakes throughput for path selection instead of hop count.

REFERENCES

[1] Akyildiz, I. F., Lee, W. Y., Vuran, M. C., & Mohanty, S. "A survey on spectrum management in cognitive radio networks", IEEE Communications Magazine. Copyright 2008 IEEE, 2008, pp.40-48.

[2] Chen, D., Zhang, Q., & Jia, W. "Aggregation aware spectrum assignment in cognitive ad-hoc networks.", In 2008 3rd International Conference on Cognitive Radio Oriented Wireless Networks and Communications (CrownCom 2008), 2008, pp. 1-6.

[3] G. Cheng, W. Liu, Y. Li and W. Cheng, "Spectrum Aware On-Demand Routing in Cognitive Radio Networks," 2007 2nd IEEE International Symposium on New Frontiers in Dynamic Spectrum Access Networks, Dublin, 2007, pp. 571-574.

[4] Liang, Y. C., Zeng, Y., Peh, E., & Hoang, A. T. "Sensing-throughput tradeoff for cognitive radio networks", In 2007 IEEE International Conference on Communications, 2007, pp. 5330-5335.

[5] Akyildiz, I. F., Lee, W. Y., Vuran, M. C., & Mohanty, S. "Next generation dynamic spectrum access cognitive radio wireless networks: A survey", Computer networks, Vol.50, Issue 13, 2006, pp. 2127-2159.

[6] Akyildiz, I. F., Lee, W. Y., & Chowdhury, K. R. "CRAHNs: Cognitive radio ad hoc networks. AD hoc networks", Vol.7, Issue 5, 2009 pp.810-836.

[7] Letaief, K. B., & Zhang, W. "Cooperative communications for cognitive radio networks", Proceedings of the IEEE, Vol. 97, Issue 5, 2009, pp. 878-893.

[8] S. M. Kamruzzaman, E. Kim and D. G. Jeong, "An Energy Efficient QoS Routing Protocol for Cognitive Radio and Ad Hoc Networks" International Conference on Advance Communication Technology (ICACT), 2011, pp.344-349.

[9] Dutta, N., Sarma, H. K. D., Srivastava, A., & Verma, S. "A SINR Based Clustering Protocol for Cognitive Radio Ad Hoc Network

RESEARCH ARTICLE

(CRAHN)" , International Conference on Information Technology,2009, pp. 69-75.

[10] Letaief, K. B., & Zhang, W. "Cooperative communications for cognitive radio networks" Proceedings of the IEEE, Vol.97, Issue 5, 2009, pp. 878-893.

[11] S. Kulkarni and S. Markande, "Comparative study of routing protocols in Cognitive Radio Networks," International Conference on Pervasive Computing (ICPC), Pune, 2015, pp. 1-5.

[12] Ren Han and Xiaoxia Huang, "Reliable link routing in Cognitive Radio networks," 2010 2nd International Asia Conference on Informatics in Control, Automation and Robotics (CAR 2010), Wuhan, 2010, pp. 55-58.

[13] Pradeep Kyasanur and Nitin H. Vaidya, "Protocol Design Challenges for Multi-hop Dynamic Spectrum Access Networks," International Symposium on New Frontiers in Dynamic Spectrum Access Networks, 2005, pp.645-648.

[14] Chen, Y., Farley, T., & Ye, N., "QoS Requirements of Network Applications on the Internet" ,Information Knowledge Systems Management,Vol.4, 2004, pp.55-76.

[15] Najafi, B., Keshavarz-Haddad, A., & Jamshidi, A., "A new spectrum path diversity routing protocol based on AODV for cognitive radio ad hoc networks," In 7th International Symposium on Telecommunications (IST'2014), 2014, pp. 585-589, IEEE.

[16] Cui, C., Man, H., Wang, Y., & Liu, S., "Cooperative spectrum-aware opportunistic routing in cognitive radio ad hoc networks," In 2014 IEEE Global Conference on Signal and Information Processing (GlobalSIP), 2014, pp. 1238-1241, IEEE.

[17] Bădoi, C. I., Croitoru, V., & Prasad, R., "IPSAG: an IP spectrum aware geographic routing algorithm proposal for multi-hop cognitive radio networks," In 2010 8th International Conference on Communications, 2010, pp. 491-496, IEEE.

[18] Zhou, X., Zhou, D., Kong, X., & Sheng, Q., "ACK signal based on-demand routing ,algorithm in Cognitive Radio Networks," In 2009 IEEE Pacific Rim Conference on Communications, Computers and Signal Processing, 2009,pp. 774-779,IEEE.

[19] Li, B., Li, D., Wu, Q. H., & Li, H., "ASAR: Ant-based spectrum aware routing for cognitive radio networks," In 2009 International Conference on Wireless Communications & Signal Processing,2009, pp. 1-5, IEEE.

[20] Jashni, B., Tadaion, A. A., & Ashtiani, F., "Dynamic link/frequency selection in multi-hop cognitive radio networks for delay sensitive applications," In 2010 17th International Conference on Telecommunications, 2010, pp. 128-132, IEEE.

[21] Kulkarni, A. R., & Agarwal, A., "Energy-efficient QoS based route management in cognitive radio networks," In 2015 IEEE International Conference on Data Science and Data Intensive Systems, 2015, pp. 304-310, IEEE.

[22] Song, Z., Shen, B., Zhou, Z., & Kwak, K. S., "Improved ant routing algorithm in cognitive radio networks," In 2009 9th International Symposium on Communications and Information Technology, 2009, pp. 110-114,IEEE.

[23] Liu, Y., Cai, L. X., & Shen, X. S., "Spectrum-aware opportunistic routing in multi-hop cognitive radio networks," IEEE Journal on Selected Areas in Communications, Vol. 30, Issue 10, 2012, pp. 1958-1968.

[24] Chowdhury, K. R., & Felice, M. D., "Search: A routing protocol for mobile cognitive radio ad-hoc networks," Computer Communications, Vol. 32, Issue 18, 2009, pp.1983-1997.

[25] Dutta, N., & Sarma, H. K. D., "A probability based stable routing for cognitive radio adhoc networks," Wireless Networks, Vol. 23, Issue 1, 2017, pp.65-78.

[26] H. Zhou, H. Ying, "A method for deriving the analytical structure of a broad class of typical interval type-2 mamdani fuzzy controllers," IEEE Trans. 420 Fuzzy Syst. Vol. 21, Issue 3, 2013, pp.447–458.

[27] El Masri, "A fuzzy-based routing strategy for multihop cognitive radio networks", International Journal of Communication Networks and Information Security, IJCNIS-2011, Vol. 3, Issue 1, 2011. pp. 74–82.

[28] Kukreja, V., Gupta, S., & Bhushan, B. "A fuzzy-based routing protocol for cognitive radio networks" International Journal of Fuzzy Computation and Modelling, Vol. 1, Issue 1, 2014, pp. 97-122.

[29] Castillo, O., Amador-Angulo, L., Castro, J. R., & Garcia-Valdez, M. "A comparative study of type-1 fuzzy logic systems, interval type-2 fuzzy logic systems and generalized type-2 fuzzy logic systems in control problems." Information Sciences, Vol. 354, 2016, pp.257-274.

[30] Nagpal, C.K., & Gupta, S. "A Delay and Spectrum Aware Fuzzy Logic Based Routing Protocol for CRN" International Journal of Computer Networks and Applications, Volume 3, Issue 1, 2016, pp.16-24.

[31] Amini, A., & Nikraz, N. "Proposing two defuzzification methods based on output fuzzy set weights" International Journal of Intelligent Systems and Applications, Vol. 8, Issue 2, 2016,pp.1-12.

[32] Namazov, M., & Basturk, O. "DC motor position control using fuzzy proportional-derivative controllers with different defuzzification methods," TJFS: Turkish Journal of Fuzzy Systems, Vol.1, No.1, 2010, pp.36-54.

[33] Rohal, P., Dahiya, R., & Dahiya, P. "Study and analysis of throughput, delay and packet delivery ratio in MANET for topology based routing protocols (AODV, DSR and DSDV)" International Journal for advance research in engineering and technology, Vol.1,Issue 2, 2013,pp.54-58.

[34] M. F. Khan, E. A. Felemban, S. Qaisar and S. Ali, "Performance Analysis on Packet Delivery Ratio and End-to-End Delay of Different Network Topologies in Wireless Sensor Networks (WSNs)," 2013 IEEE 9th International Conference on Mobile Ad-hoc and Sensor Networks, Dalian, 2013, pp. 324-329.

[35] B.Ruxanayasmin, B.Ananda Krishna, T.Subhashini, "Minimization of Power Consumption in Mobile Adhoc Network" International Journal of Communication Networks and Information Security (IJCNIS), 2014, pp. 38-44.

[36] Shah, S., Khandre, A., Shirole, M., & Bhole, G. "Performance evaluation of ad hoc routing protocols using NS2 simulation," Conference of Mobile and Pervasive Computing (CoMPC), 2008, pp.167-171.

[37] M. Youssef, M. Ibrahim, M. Abdelatif, L. Chen and A. V. Vasilakos, "Routing Metrics of Cognitive Radio Networks: A Survey," in IEEE Communications Surveys & Tutorials, Vol. 16, No. 1, 2014, pp. 92-109.

[38] Kadhim, A. S., & Alsabbagh, H. M. "Throughput Analysis for Cognitive Radio (CR) Systems", International Journal of Computer Networks & Communications, Vol.4, No.4, 2012, pp.211-222.

Authors

Gagan Deep Dhand, a student of B.Tech. in Computer Science Engineering Department at Bharati Vidyapeeth's College of Engineering, Affiliated to Guru Gobind Singh Indraprastha University, Paschim Vihar, New Delhi, India. His interest is in networking.

RESEARCH ARTICLE

Rohit Kumar, a student of B.Tech. in Computer Science Engineering Department at Bharati Vidyapeeth's College of Engineering, Affiliated to Guru Gobind Singh Indraprastha University, Paschim Vihar, New Delhi, India. His interest is in networking.

Rishabh, a student of B.Tech. in Computer Science Engineering Department at Bharati Vidyapeeth's College of Engineering, Affiliated to Guru Gobind Singh Indraprastha University, Paschim Vihar, New Delhi, India. His interest is in networking.

Devashish Ghildiyal, a student of B.Tech. in Computer Science Engineering Department at Bharati Vidyapeeth's College of Engineering, Affiliated to Guru Gobind Singh Indraprastha University, Paschim Vihar, New Delhi, India. His interest is in networking.

Dr. Rachna Jain, currently working as Assistant Professor (Computer Science Department) in Bharati Vidyapeeth's College of Engineering (GGSIPU) since 2007. She did her Ph.D. from Banasthali Vidyapith in Computer Science in 2017. She received ME degree in the year 2011 from Delhi college of engineering (Delhi University) with specialization in Computer Technology and Applications. She did her B.tech (Computer Science) in 2006 from N.C College of Engineering, Kurukshetra University. Her current research interests are Cloud Computing, Image Processing, Network, and information security, Swarm Intelligence, Big Data, and IoT. A total of 12+ Years of Academic / Research Experience with more than 20+ Publications in various National, International Conferences cum International Journals(Scopus/ISI/SCI) of High Repute.

Defence Science Journal, Vol. 69, No. 3, May 2019, pp. 298-302, DOI : 10.14429/dsj.69.12976
© 2019, DESIDOC

Resonator to Laser Cavity Decoupling Interface for Chemical Oxygen Iodine Laser

A.K. Varshney[#,*], Rajeev Kr. Dohare[#], Gaurav Singhal[#], and Mainuddin[@]

[#]*DRDO-Laser Science and Technology Centre, Delhi - 110 054, India*
[@]*Department of Electronics and Communication Engineering, Jamia Millia Islamia, New Delhi - 110 025, India*
[*]*E-mail: anujkumarvarshneya@lastec.drdo.in*

ABSTRACT

In the present work, the conventional chemical oxygen iodine laser (COIL) source has been technologically upgraded and successfully tested after implementation of decoupling interface between laser cavity and resonator. In the technique, anti-reflection coated fused silica windows mounted in suitable mechanical assemblies are placed between resonator mirrors and laser cavity in such a way that the generated laser beam is out coupled through the resonator during the laser operation. The implemented decoupling assemblies isolate the caustic environment produced in low pressure laser cavity from that of resonator mirrors. Thus requirement of using isolation valves and cavity limbs between laser cavity and resonator as in conventional COIL source is eliminated. Such decoupling mechanism therefore effectively reduces the number of associated components as well as overall length of the laser source which in turn further reduces the overall weight of the laser making it suitable for use onto a mobile platform. Moreover the technique provides accrued benefits in terms of reduction in readiness time and checking of optical alignment of the laser source at will in practical operation scenarios.

Keywords: COIL; Laser cavity; Resonator; Decoupling; Isolation

1. INTRODUCTION

Chemical oxygen iodine laser (COIL)[1] is a high power chemical laser in which the required pumping energy for population inversion is released via a chemical reaction. This eliminates the need of electrical power supply for laser operation at remote locations. Among other chemical lasers, COIL has the advantages of power scalability, fairly short laser wavelength (1.315 μm) compatible with fiber[2] and also better laser material interaction. These attributes make COIL the choice for both military[3,4] as well as industrial applications[5]. The current literature[6-9] indicates that there are number of research activities related to advanced subsystems development and diagnostics for COIL in the US, Russia, Japan, Germany, Israel, Czech Republic, India, China, and South Korea.

COIL operates on the $I^*(^2P_{1/2})$ – $I(^2P_{3/2})$ transition of atomic iodine at a wavelength of 1.315 μm as

$$I^*\left(^2P_{1/2}\right)+h\nu \rightarrow I\left(^2P_{3/2}\right)+2h\nu(1.315\mu m) \quad (1)$$

The atomic iodine (I^*) is populated by near resonant energy transfer from singlet oxygen molecules.

$$O_2(^1\Delta_g)+I(^2P_{3/2}) \Leftrightarrow I^*(^2P_{1/2})+O_2(^3\Sigma_g) \quad (2)$$

Singlet oxygen is generated by the reaction between chlorine gas (Cl_2) and basic hydrogen peroxide (BHP) as given by the equation

$$Cl_2+2KOH+H_2O_2 \rightarrow 2KCl+2H_2O+O_2\left(^1\Delta_g\right) \quad (3)$$

The interaction of singlet oxygen with atomic iodine at appropriate flow conditions results in the generation of laser gain medium inside the laser cavity from where the laser output power is extracted using optical resonator. In conventional COIL source, the laser effluents produced in the laser cavity during laser operation are kept separate from the laser mirrors using isolation valves and cavity limbs between laser cavity and resonator. These isolation valves are operated using actuators and associated circuitry. All these components increase the overall length and weight of the laser source. In addition, the increased length of resonator support structure corresponding to that of isolation valves, cavity limbs and rubber bellows also enhances the overall weight of the laser source. However military applications necessitate the deployment of mobile or transportable high power laser system of limited size and weight.

At Laser Science and Technology Centre (LASTEC), Delhi, the conventional COIL source has been technologically upgraded by implementation of decoupling interface between laser cavity and resonator which provides comparatively reduced-weight laser source suitable for mobile applications by reducing the number and length of components associated with the conventional COIL source. The reduced length of the laser cavity not only helps in reducing overall weight of the laser source but also makes resonator less sensitive to angular misalignment generated due to thermal gradient and gravitational displacement.

2. CONVENTIONAL COIL CAVITY CONFIGURATION

The conventional COIL source as shown schematically in Fig. 1 consists of various subsystems. BHP preparation tank is used to prepare BHP solution by mixing hydrogen peroxide and

Received : 29 June 2018, Revised : 03 January 2019
Accepted : 05 February 2019, Online published : 30 April 2019

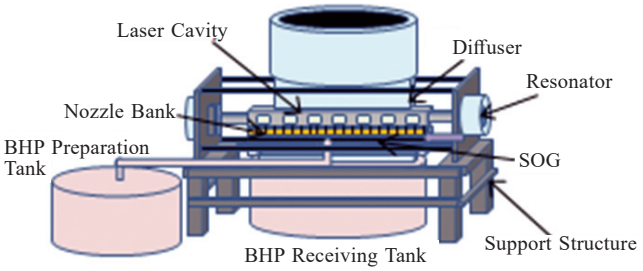

Figure 1. Schematic of COIL.

potassium hydroxide solutions in certain proportion. Singlet Oxygen Generator (SOG) where reaction between BHP and chlorine gas takes place is used to generate singlet oxygen molecules. BHP receiving tank collects back the BHP solution for further recirculation. Supersonic mixing nozzle bank is used for mixing the primary flow consisting of singlet oxygen molecules with nitrogen gas and secondary flow consisting of iodine molecules with nitrogen gas. The nozzle bank is followed by laser cavity wherein population inversion takes place and lasing phenomenon occurs. Optical resonator consisting of a set of mirrors is used for extraction of power from laser cavity. Diffuser is a low pressure system to exhaust the COIL effluents from sub atmospheric pressure to above atmospheric pressure.

The material used for laser cavity as shown in Fig. 2 is SS-316 due to its compatibility with chlorine. It has an active medium length of 350 mm with cavity cross-section of 60 mm x 60 mm. At one end, it is connected to the nozzle bank which ensures the entry of the laser gases into the laser cavity. At the other end, it is connected to the supersonic diffuser for exhaust of the effluent gases. An expansion of 4^0 is typically used to compensate the active medium boundary layer effect. The viewing window arrays with 7 view-ports on each side of the laser cavity are used to observe the chemical reaction occurring in the laser cavity. This helps in drawing the conclusion regarding the gain medium formation in the laser cavity.

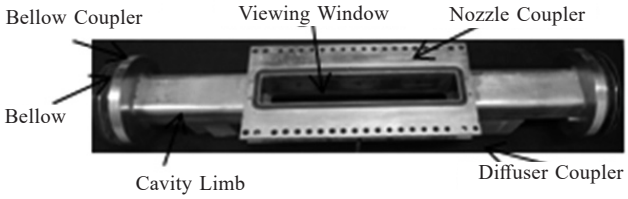

Figure 2. Laser cavity of COIL.

The laser cavity has cavity limb on both sides of it. The laser cavity through bellow coupler is connected with resonator flanges on the resonator assembly structure as shown in Fig. 3 using rubber bellows. These rubber bellows help in the alignment of the optic axis of resonator mirrors with the center of the laser gain medium and also keep the resonator insensitive to mechanical vibrations. The resonator support rods enhance the rigidity of the resonator flanges against vacuum created in the laser cavity. Resonator boxes are used to prevent the resonator optics from the sudden shock that occurs during evacuation of the laser cavity.

In high power COIL system, the laser cavity or gain region is typically separated from the resonator boxes using

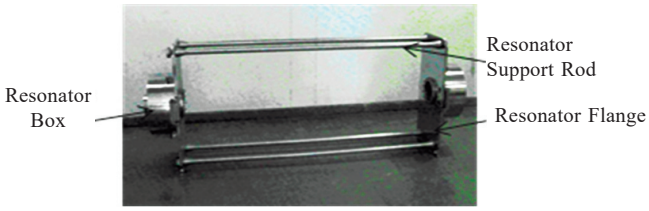

Figure 3. Resonator assembly structure of conventional COIL.

an isolation valve on each side of the cavity region. The two isolation valves and two cavity limbs along with rubber bellows increase the length of the COIL laser source. The conventional COIL source has typically 1000 mm separation between two resonator mirrors in comparison to 350 mm active medium length. It should also be noted that these systems are mounted onto support structure. The length of the support structure must be sum of the length of the laser cavity plus the lengths of the cavity limbs, the isolation valves and the bellow couplers. Such systems also include a vacuum pump and purge gases that are used to create the positive pressure in the resonator boxes so that the flow of the gases is out of the box and the gases do not flow back into the resonator boxes. It should be noted that back flow of the laser cavity exhaust may cause caustic damage to the precision optics inside the resonator boxes. It should also be noted that the optical isolation valves completely block the line of sight of the laser when not open. The closed valve prevents the monitoring of the optics within the boxes thereby limiting the ability to make adjustments to the optics for the alignment of the laser resonator. Each valve has an associated actuator system that also increases the mass of the laser source. Such laser source may be required to be mounted on transportable system. Reducing the overall size and mass of the laser source is appreciable to make it efficient for transportable system.

3. IMPLEMENTATION OF DECOUPLING INTERFACE

Figure 4 shows the schematic of the decoupling interface to be used to isolate the laser cavity from the resonator. In this technique, suitable mechanical assemblies of thickness 25mm made of aluminum as shown in Fig. 5 having heat and chemical resistant fused silica windows of 100 mm diameter and 10 mm thickness are placed on each end of the laser cavity to isolate the resonator mirrors in such a way that the generated laser beam is out coupled through the resonator during the laser operation.

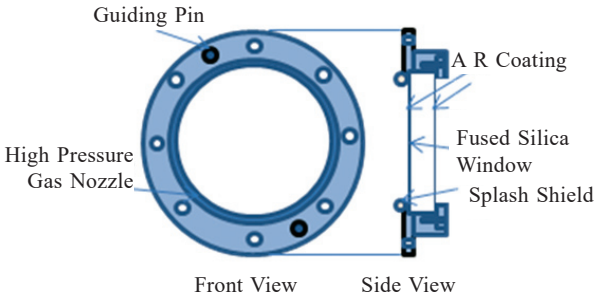

Figure 4. Schematic of decoupling interface.

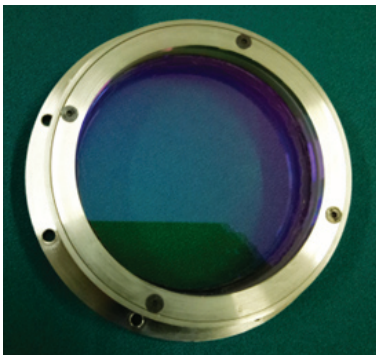

Figure 5. Developed decoupling interface hardware.

Fused silica windows have anti-reflective coating (R<0.5%) on both the surfaces at lasing wavelength of 1.315µm. The laser cavity is directly sealed against mechanical assemblies from both the ends. This allows resonator boxes to be non-pressurised which may further be removed. Mechanical assemblies include a high pressure gas source which may direct high pressure gas through the nozzles to wash the surfaces of optical windows to prevent the impingement of contaminants coming from laser cavity. Typically nitrogen gas at 2-3 bar pressure has been used in the laser experiments which does not react with the chemicals used in the COIL operation. In addition, a splash shield has also been disposed adjacent to fused silica window. The splash shield coupled to an actuator and a controller helps in preventing the caustic material within the cavity from contacting the optical windows during the period just prior to lasing.

The implemented decoupling assembly isolates resonator mirrors from the reactive laser gases produced in laser cavity. Thus requirement of using isolation valves and cavity limbs between laser cavity and resonator as in conventional COIL source is eliminated. The effective length of the laser cavity is therefore reduced from 1000mm to nearly 400mm, which also includes both decoupler interfaces. The resonator assembly structure remains of no use due to isolation between laser cavity and resonator. As a result of which total length of the support structure becomes shorter than the length of the structure earlier required. This effectively reduces the overall weight of the laser source. Therefore the present approach reduces 20 per cent to 30 per cent overall weight of the COIL source making it effective for mobile platform.

Since the decoupling interface isolates the low pressure laser cavity from the resonator mirrors, it greatly simplifies alignment of resonator optics. Once the resonator optics are aligned, the assembly is unaffected by the occurrence of shocks and vibrations occurred during COIL operation thereby eliminating the need for repeated alignment. Further, the alignment may be checked at will as there are no interfering isolation valves or shutter between the mirrors. The accrued benefit is also in terms of reduction in readiness time of the laser system in practical operation scenarios.

4. RESULTS AND DISCUSSION

At LASTEC, the conventional COIL source as described above has been technologically upgraded by implementing decoupling interface between laser cavity and resonator. The cavity limbs as well as the resonator assembly structure have been dispensed with and resonator mirrors are mounted separately. The laser cavity and resonator have been tested in conjunction with the rest of the subsystems of the COIL during the laser runs. The COIL source has been operated with the help of dedicated data acquisition and control system.

Laser test runs for typical COIL input parameters were carried out to make a comparative study and to prove the efficacy of decoupling interface. The liquid reagent (BHP) of a molar ratio (KOH : H_2O_2) of 6.5 : 7.0 was used at optimal temperature range of -20 °C to -18 °C to minimise generated water vapor at generator exit. Chlorine flow rate employed was nearly 450 mmol s^{-1} with a primary nitrogen dilution of N_2: Cl_2:: 2.5:1. The flow rates are precisely controlled using choked flow orifices. The generator efficiency is essentially a function of chlorine utilisation and singlet oxygen yield. The former is measured using in-house developed measurement setup based on absorption spectroscopy at 330 nm in which a portion of the singlet oxygen generator flow exit medium is passed through an optical cell of 25 cm length and 2.5 cm diameter. UV mercury lamp is used as a light source along with 330±5 nm interference filter. Collimated light is passed through the cell and detected using silicon photodiode (RS component stock no. 303-674). The molar flow rate of exit (residual) chlorine is estimated by calculating the partial pressure of chlorine (using Beer Lambert's law and perfect gas law) and substituting the expression for the partial pressure in Dalton's law. The detailed experimentations show a typical chlorine utilisation of greater than 90 per cent. Singlet oxygen yield is measured using optical emission spectroscopy based singlet oxygen diagnostic system. The details of the singlet oxygen measurement technique have been given in reference (10). The emitted photons which are collected using a one-inch lens fixed in the diagnostic cell are focused on to a liquid nitrogen cooled germanium photodiode of 5 mm diameter (EG & G Judson, Model No. JD16-M204). An interference filter with 1270±5 nm wavelength is introduced between the lens and the photodiode. The estimated singlet oxygen yield at the exit of the generator inside the plenum is 60 per cent - 70 per cent. The observed flow rate of molecular iodine is nearly 10 mmol s^{-1}.

Figure 6 shows typically variation of pressures at various critical locations inside the gas dynamic tunnel of COIL laser source. The measured pressure at SOG, Plenum, Cavity and Pitot for both cases of conventional operation and operation with decoupling interface are shown. In both cases, Plenum ~ 20 torr, Cavity of 3- 4 torr and Pitot ~ 9 torr are found to be nearly identical, which clearly shows that the introduction of decoupling assembly does not in any way perturb the laser medium flow. There is marginal variation in SOG pressure from ~ 25 torr to ~ 20 torr owing to local effects of variation of condition of BHP injector plates and is apparently not due to introduction of decoupling interface. This is imperative for optimal functioning of the laser source. The small signal gain for the laser source is also measured using distributed feedback laser diode as a probe laser in conjunction with a germanium photo-detector. The observed small signal gain lies in the range of 0.0025 cm^{-1} - 0.003 cm^{-1} and remains unchanged for both cases.

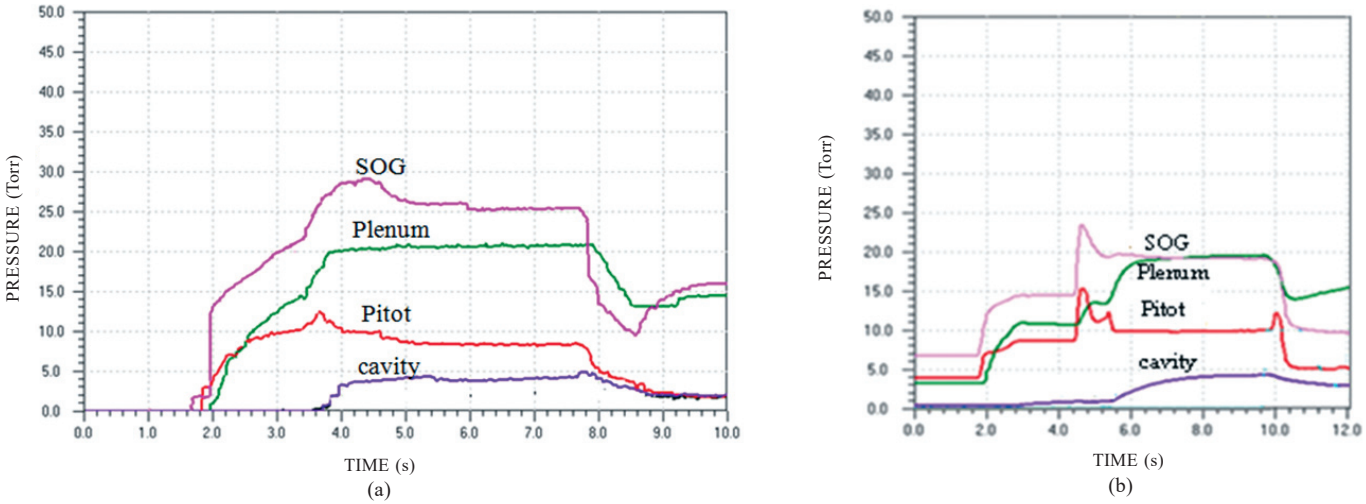

Figure 6. Temporal variation of pressures at different locations inside COIL: (a) Conventional and (b) With decoupling interface.

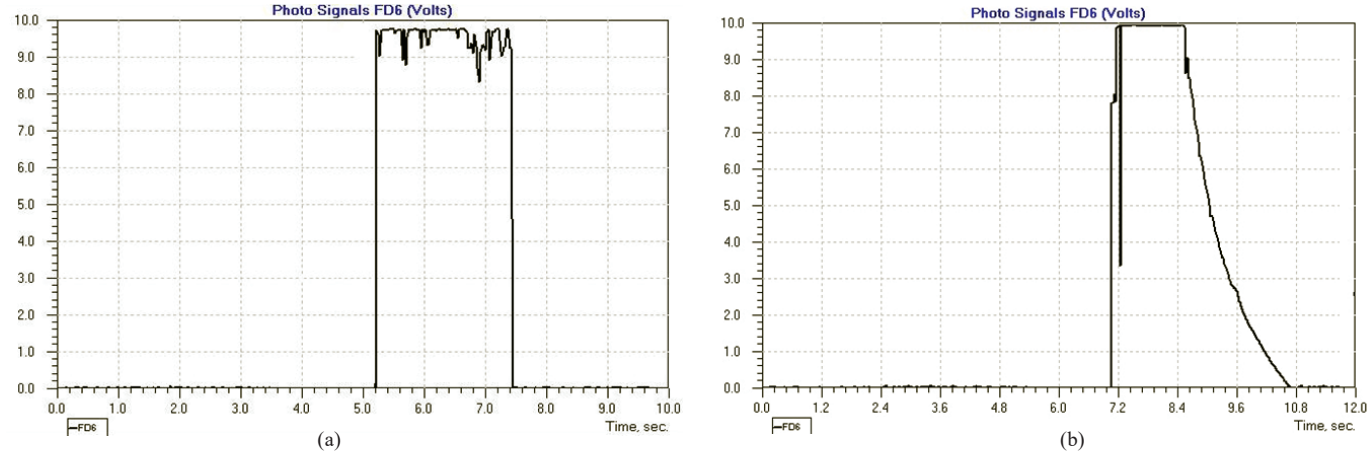

Figure 7. Temporal variation of laser power: (a) Conventional and (b) With decoupling interface.

The temporal variation of the laser power is measured using a germanium photo-detector by collecting the back scattered radiation from the rear mirror, refer Fig. 7, showing a pulse duration of ~ 2 s. A slight variation after 1.5 s showing signal trail off with decoupling interface is primarily due to the flutter of the guiding mechanism directing the back scatter into the detector.

The laser was operated repeatedly for its specified input parameters under both scenarios of conventional operation and with implementation of decoupling interface. The laser output power is measured using cone type laser calorimeter and has been shown in Fig. 8 for typical laser run case, which clearly indicates that the upgraded COIL source with decoupling interface provides nearly 10 kW stable laser output power which is identical to that obtained with conventional COIL source i.e. without decoupling interface.

In the present work, gain medium length as well as inter-mirror spacing of the COIL source has been kept same in both conventional and decoupling interface cases during experimentation. Therefore, longitudinal as well as transverse properties of the laser beam remain unaltered. Typical line width in case of multimode COIL systems with T~ 200 K and P~ 4 torr are reported to be 25 MHz[11]. The multi-mode laser

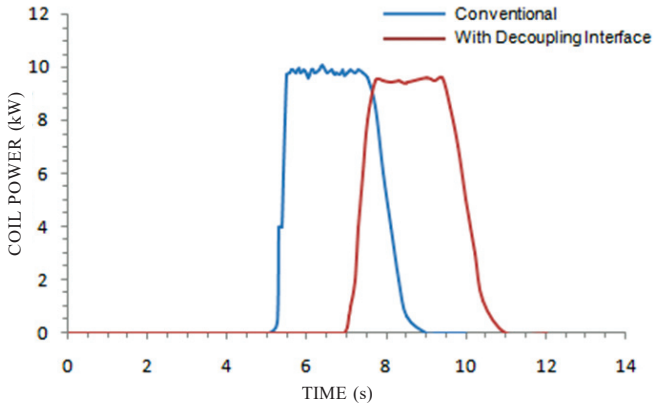

Figure 8. Temporal variation of laser power in both conventional and with decoupling interface.

output has been successfully achieved in both the cases in all the power runs. Exhaustive power runs for both operation cases have shown a typical maximum variation of 5 per cent. This is may possibly be due to insertion of two extra intra-cavity optical windows. Hence, it is inferred that the overall efficiency of the COIL source essentially remains unaffected by implementing the decoupling mechanism. Further, for large scale systems the benefits accruing from reduction in weight

and volume of the laser cavity and resonator assembly far offset the marginal penalty on power output.

5. CONCLUSIONS

Practical operation scenarios require that overall footprint of the laser source as lucrative as COIL, which is capable of being scaled to large power levels in single aperture output, be reduced as far as possible. One of the contributing sub-system towards larger size and weight of COIL laser source is the resonator assembly. The present paper examines an alternative approach to implementation of resonator using a decoupling optical interface. This enables decoupling of the low pressure cavity flow field from the resonator optics and its effects thereof during system operation. The developed decoupling interface has been implemented in the COIL source and tested successfully showing a maximum typical variation of 5 per cent in power output as compared to conventional operation. Hence, it is inferred that overall performance of the COIL source essentially remains unaffected by implementing the decoupling mechanism. Further, for high power COIL systems the miniscule reduction in power, if any, is far compensated by largely diminished footprint of the laser source.

REFERENCES

1. McDermott, W.E.; Pchelkin, N.R.; Benards, D.J. & Bousek, R.R. An electronic transition chemical laser. *Appl. Phy. Lett.*, 1978, **32**, 469. doi: 10.1063/1.90088.
2. Grunewald, K.; Bdin, W.L.; Duschek, F.; Hankle, J. & Schall, W.O. High-power COIL fiber transmission for D&D application. *In* Proceeding of SPIE, 2004, **5479**, 35. doi: 10.1117/12.558188.
3. Duff, E.A. & Truesdell, K.A. Chemical oxygen iodine laser (COIL) technology and development. *In* Proceedings of SPIE, 2004, **5414**, 52. doi: 10.1117/12.554472.
4. Boreisho, A.S.; Barkan, A.B.; Vasil'ev, D.N.; Evdokimov, I.M. & Savin, A.V. High efficient CW chemical oxygen iodine laser with transonic iodine injection and a nitrogen buffer gas. *Quantum Electronics*, 2005, **35(6)**, 495. doi: 10.1070/QE2005v035n06ABEH002866.
5. Carroll, D.L.; King, D.M.; Focker, L.; Stromberg, D.; Madden, T. J.; Solomon, W.C. & Sentman, L.N. COIL for industrial applications. *AIAA Paper,* 1998, **98,** 2992. doi: 10.2514/6.1998-2992.
6. Jia, S.; Li, Q.; Jin, Y.; Zhang, Y.; Geng, Z.; Li, Y.; Zhang, P.; Shi, W.; Fang, B. & Sang, F. A chemosorption vacuum pump for a chemical oxygen iodine laser with CO_2 buffer gases. *J. Russian Laser Res.*, 2017, **38**(1), 96. doi: 10.1007/s10946-017-9624-x.
7. Zagidullin, M.V.; Malyshev, M.S. & Azyazov, V.N. Kinetics of an oxygen iodine active medium with iodine atoms optically pumped on the $^2P_{1/2}$-$^2P_{3/2}$ transition. *Quantum Electronics*, 2015, **45**, 720. doi: 10.1070/QE2015v045n08ABEH015619.
8. Singhal, G.; Subbarao, P.M.V.; Mainuddin; Tyagi, R.K. & Dawar, A.L. Performance comparison of supersonic ejectors with different motive gas injection schemes applicable for flowing medium gas laser. *Thermophy. Aeromechanics*, 2017, **24**(3), 449. doi: 10.1134/S086986431703012X.
9. Mainuddin; Singhal, Gaurav; Tyagi, R.K. & Maini, A.K. Development of safe infrared gas lasers. *J. Optics Laser Technol.,* 2013, **47**, 56. doi: 10.1016/j.optlastec.2012.07.026.
10. Mainuddin; Singhal, Gaurav; Varshney, A.K.; Dohare, R. & Tyagi, R.K. Optical diagnostics of singlet oxygen for chemical oxygen iodine laser. *In* Advances in Laser Physics and Technology, Cambridge University Press, India, ISBN 978-93-84463-41-0, pp 120, 2015.
11. Copeland, D.A. & Bauer, A.H. Optical saturation and extraction from the chemical oxygen iodine laser medium. *IEEE J. Quantum Electron.*, 1993, **29**(9), 2525. doi: 10.1109/3.247711.

ACKNOWLEDGEMENT

This work is supported by the Ministry of Electronics and Information Technology, Government of India under the Visvesvaraya PhD scheme.

CONTRIBUTORS

Mr A.K. Varshney received his MTech (Laser Technology) from Devi Ahilya University, Indore, in 1999. Currently, he is working as a Scientist at DRDO-Laser Science and Technology Centre, Delhi, India. His area of research includes : Integrated optics, microchip lasers and high power lasers specifically chemical oxygen iodine laser.
In the current study, he contributed towards the design, implementation and testing of the decoupling interface to isolate the resonator from the laser cavity of the chemical oxygen iodine laser.

Mr Rajeev Kr Dohare obtained his MTech (Electronics & Communication Engineering) from Amity University, Noida, in 2013. Presently, he is working as a Scientist in DRDO-Laser Science and Technology Centre, Delhi, India. His field of interest includes data acquisition and control/ electronics/ high power lasers.
In the current study, he has carried out data acquisition and control during operation and testing of the chemical oxygen iodine laser.

Dr Gaurav Singhal received BE (Mechanical Engineering) from JMI, New Delhi, in 1998 and PhD from IIT, Delhi, in 2008. Presently, he is working as a Scientist in DRDO-Laser Science and Technology Centre, Delhi. His research interests include : High power lasers, high speed unsteady flows, turbulent mixing, laser diagnostics, CFD techniques etc.
In the current study, he has contributed towards the design, implementation and testing of COIL source both with and without decoupling interface.

Dr Mainuddin received his ME from Delhi College of Engineering, Delhi, in 2003 and PhD in 2008 from JMI, New Delhi. He is presently working as a Professor in Department of Electronics & Communication Engineering, JMI, New Delhi. His research interests include : Optical diagnostics, high power lasers, data communication, optical communication and computer networks.
In the current study, he has been instrumental in design and realisation of data acquisition employed for the operation of COIL source with and without decoupling interface.

This article has been accepted for inclusion in a future issue of this journal. Content is final as presented, with the exception of pagination.

Securing Data in Internet of Things (IoT) Using Cryptography and Steganography Techniques

Manju Khari, Aditya Kumar Garg, Amir H. Gandomi, *Senior Member, IEEE*, Rashmi Gupta, *Member, IEEE*, Rizwan Patan, and Balamurugan Balusamy

***Abstract*—Internet of Things (IoT) is a domain wherein which the transfer of data is taking place every single second. The security of these data is a challenging task; however, security challenges can be mitigated with cryptography and steganography techniques. These techniques are crucial when dealing with user authentication and data privacy. In the proposed work, the elliptic Galois cryptography protocol is introduced and discussed. In this protocol, a cryptography technique is used to encrypt confidential data that came from different medical sources. Next, a Matrix XOR encoding steganography technique is used to embed the encrypted data into a low complexity image. The proposed work also uses an optimization algorithm called Adaptive Firefly to optimize the selection of cover blocks within the image. Based on the results, various parameters are evaluated and compared with the existing techniques. Finally, the data that is hidden in the image is recovered and is then decrypted.**

***Index Terms*—Confidential data, cryptography, data security, Internet of Things (IoT), steganography, user authentication.**

I. Introduction

THE INTERNET of Things (IoT) is a network of connected vehicles, physical devices, software, and electronic items that facilitate data exchange. The purpose of IoT is to provide the IT-infrastructure for the secure and reliable exchange of "Things" [1]. The foundation of IoT mainly consists of the integration of sensors/actuators, radio frequency identification (RFID) tags, and communication technologies. The IoT explains how a variety of physical items and devices can be integrated with the Internet to permit those objects to cooperate and communicate with each other to reach common goals. The IoT consists mostly of little materials that are associated together to facilitate collaborative calculating situations. Constraints of the IoT include energy budget, connectivity, and computational power [2].

Although IoT devices have made life easier, little attention has been given to the security of these devices. Currently, the focus of developers is to increase the capabilities of these devices, with little emphasis on the security of the devices. The data that is transferred over the IoT network is vulnerable to attack. This data is needed to be secured to protect the privacy of the user. If there is no data security, then there is a possibility of data breach and thus, personal information can be easily hacked from the system. Some of the important concepts of IoT involve identification and authentication. These concepts are inter-related to each other as cryptographic functions that are necessary to ensure that the information is communicated to the correct device and if the source is trusted or not. With the lack of authentication, a hacker can easily communicate to any device.

Whenever two devices communicate with each other, there is a transfer of data between them. The data can also be very sensitive and personal. Therefore, when this sensitive data is moving from device to device over the IoT network, then there is a need for encryption of the data. Encryption also helps to protect data from intruders. The data can be easily encrypted with the help of cryptography, which is the process of converting simple text into unintelligible text. The primary objectives of cryptography are confidentiality, integrity, nonrepudiation, and authentication. Elliptic curve cryptography (ECC) is one of the cryptographic algorithms that is used in the proposed work. ECC is a public key cryptographic technique based on the algebraic structure of elliptic curves over finite fields.

In addition, to the cryptographic techniques, another method, named steganography is used in the proposed work which helps to provide additional security to the data. Steganography hides encrypted messages in such a way that no one would even suspect that an encrypted message even exists in the first place. In modern digital steganography, encryption of data occurs using typical cryptographic techniques. Next, a special algorithm helps to insert the data into redundant data that is part of a file format, such as a JPEG image. The proposed work uses Matrix XOR steganography to provide additional security. The image block is optimized with the help of Adaptive Firefly algorithm in which the encrypted data is hidden in a selected block from a huge image block.

The remaining part of this paper is organized as follows. Section II discussed work that relates to the security of IoT communication. Section III proposes methodology for

Manuscript received July 22, 2018; revised October 16, 2018; accepted February 20, 2019. This paper was recommended by Associate Editor Y. Yuan. *(Corresponding author: Amir H. Gandomi.)*

M. Khari, A. K. Garg, and R. Gupta are with the Department of CSE, Ambedkar Institute of Advanced Communication Technology and Research, New Delhi 110031, India (e-mail: manjukhari@yahoo.co.in; adityagarg2607@gmail.com; rashmig71@yahoo.com).

A. H. Gandomi is with the Analytics and Information Systems, School of Business, Stevens Institute of Technology, Hoboken, NJ 07030 USA (e-mail: a.h.gandomi@stevens.edu).

R. Patan and B. Balusamy are with the School of Computing Science and Engineering, Galgotias University, Greater Noida 201310, India (e-mail: prizwan5@gmail.com; kadavulai@gmail.com).

Color versions of one or more of the figures in this paper are available online at http://ieeexplore.ieee.org.

Digital Object Identifier 10.1109/TSMC.2019.2903785

2168-2216 © 2019 IEEE. Personal use is permitted, but republication/redistribution requires IEEE permission.
See http://www.ieee.org/publications_standards/publications/rights/index.html for more information.

This article has been accepted for inclusion in a future issue of this journal. Content is final as presented, with the exception of pagination.

improvements in medical data security. Section IV describes the experimental setup and results. Section V concludes this paper.

II. Related Work

This section presents an overview of existing studies of healthcare data security within the IoT network.

Daniels *et al.* [3] introduced security microvisor (SμV) middleware, which uses software virtualization and assembly level code verification to provide memory isolation and custom security. Banerjee *et al.* [4] presented energy-efficient datagram transport layer security (eeDTLS), which is a low-energy variant of datagram transport layer security (DTLS) that had the same security strength but a lower energy requirement.

Manogaran *et al.* [5] proposed a system in which medical sensor devices are embedded in the human body to collect clinical measurements of patients. Significant changes in respiratory rate, blood pressure, heart rate, blood sugar, and body temperature that exceed standard levels are detected by the sensors, which generate an alert message containing relevant health information that is sent to the doctor, with the help of a wireless network. This system uses a vital management security mechanism to protect large amounts of data in the industry.

There is an urgent need for the securing the data that is transmitted every second over the IoT network. Some of the existing studies for data security are shown below.

Sun *et al.* [6] proposed CloudEyes, a cloud-based anti-malware system. The proposed system provided efficient and trusted security services to the devices in the IoT network. Ukil *et al.* [2] studied the requirements of embedded security, provided methods and solutions for resisting cyber-attacks, and provided technology for tamper proofing the embedded devices based on the concept of trusted computing.

Chervyakov *et al.* [7] provided a data storage scheme for the least probability of data redundancy, data loss, and the speed of encoding and decoding, that can cope with different objective preferences, workloads, and storage properties. This analysis showed that if the selection of redundant residue number system (RRNS) parameters is accurate, then it not only allows increased safety and reliability but it also helps to increase the speed of processing the encrypted data. The applications used on IoT platforms generally require more data than traditional applications. Raza *et al.* [8] presented lightweight secure CoAP for the IoT (Lithe), which helped in the development of a novel DTLS header compression scheme designed to reduce energy consumption with the help of 6LoWPAN. Moreover, security is not compromised with the DTLS header compression scheme. Vučinić *et al.* [9] proposed object security architecture (OSCAR), which is the architecture for end-to-end security in the IoT. OSCAR is based on the concept that the security of an object is related to the security of the application payload.

Yang *et al.* [10] proposed the lightweight break-glass access control (LiBAC) system in which medical files can be encrypted in two ways: 1) attribute-based access and 2) break-glass access. In standard situations, a medical worker can decrypt and access data if the attribute set satisfies the access policy of a medical file. In an emergency, a break-glass access mechanism is used that can bypass the access policy of the medical file so that emergency medical care workers or rescue workers can access the data in a timely fashion.

Safety and confidentiality of information sent over the IoT network is a priority for the healthcare and medical industries. Bairagi *et al.* [11] developed three methods for hiding information so that communication over the IoT network can be preserved with the help of steganography. Information is hidden in the deepest layer of the image with the help of minimal distortion in the least significant bit (LSB) and the sign of the information can also be utilized. This technique improved imperceptibility and ability when compared to the actual method.

Huang *et al.* [12] presented a steganography scheme that employs vector quantization (VQ) transformation in which LSB embeds secret data into a cover image. In the first level, the pixels of a 4×4 VQ-transformed image block are separated into two different groups: 1) the LSB group and 2) the secret data group. In the second level, VQ indexes are embedded in the LSB group and secret data are embedded in the secret group. Shanableh *et al.* [13] proposed the flexible macro-block ordering (FMO) feature of H.264/AVC to hide message bits. The macroblocks are assigned to arbitrary slice groups with reference to the content of the message bits to be hidden. In the proposed method, a maximum payload of three message bits per macroblock is achieved.

Liao *et al.* [14] proposed a new medical JPEG image steganographic scheme that is based on the dependencies of interblock coefficients. The basic strategy that is used in this paper consists of preserving the differences among discrete cosine transform (DCT) coefficients at the same position in adjacent DCT blocks as much as possible.

The development of IoT was related to the security of end-user's privacy and communication. However, the technical heterogeneity, materials, and asymmetric nature of communication between the Internet and sensor nodes created challenging security issues.

III. Proposed Approach

A. Elliptic Galois Cryptography and Steganography Protocol

This paper proposes the elliptic Galois cryptography (EGC) protocol for protection against data infiltration during transmission over the IoT network. In the proposed work, different devices in the IoT network transmit data through the proposed protocol as a part of the controller. The encrypted algorithm within the controller encrypts the data using the EGC protocol and then the encrypted and secured message is hidden in layers of the image, with help from the steganography technique. The image can then be easily transferred throughout the Internet such that an intruder cannot extract the message hidden inside the image. Initially, the EGC technique encrypts confidential data. Subsequently, the encoded secret message is inserted within the image by the XOR steganography

This article has been accepted for inclusion in a future issue of this journal. Content is final as presented, with the exception of pagination.

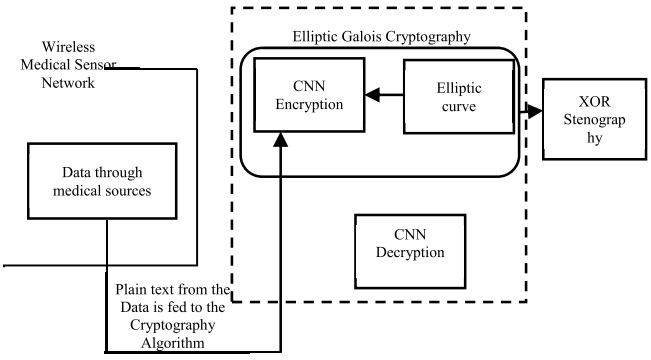

Fig. 1. EGC.

technique. Next, an optimization algorithm called the Adaptive Firefly algorithm is used to select a block in the image.

1) Elliptic Galois Cryptography: ECC, commonly known as the public key encryption technique, is based on elliptic curve theory. The keys are generated by using the properties of elliptic curve equations instead of traditional methods.

The proposed work uses EGC (Fig. 1). For improving the efficiency of calculations and to reduce the complexities of rounding errors, the elliptic curve over the Galois field (F_a) is used. The value of the Galois field must be greater than one. The elements of a Galois field GF(P) are as follows:

$$\begin{aligned}\mathrm{GF}(P) = {} & (0, 1, 2, \ldots, P-1)U \\ & (P, P+1, P+2, \ldots, P+P-1)U \\ & \left(P^2, P^2+1.P^2+2, \ldots, P^2+P-1\right)U \cdots U \\ & \left(P^{n-1}, P^{n-1}{+}1, P^{n-1}{+}2, \ldots, P^{n-1}{+}P-1\right) \text{ [15]}\end{aligned}$$

where $P \in \mathbb{P}$ and $n \in Z_+$. The order of the Galois field is given by P^n and P is called the characteristic of the field. GF stands of Galois Field. The degree is at most $n-1$ for each polynomial [15].

The secret key/public key is generated by the owner of the medical data and is used to access the authorized data. The generation of the key is crucial as both the public key and the private key need to be generated. The message will be encrypted by the user's public key and the message can only be decrypted with the help of a private key. Every user on the network develops key pairs that are used for encryption and decryption.

An elliptic curve over a Galois field GF (P) greater than three ($P > 3$) that was formed with the help of variables g and h within the field GF (P) and elements such as (x, y) gives the following equation [15]:

$$y^2 = x^3 + h \bmod P + gx. \tag{1}$$

For different inputs and values of h and g, different elliptic curve points with values x and y exist that are within the range of the Galois field [x, y belongs to GF (P)]. The public key thus generated is a random point that lies on the elliptic curve and the random number generated is the private key. Multiplication of the private key by the generator point G in the curve provides the public key.

Let P and Q be two points on an elliptic curve such that [15]

$$U = GR \tag{2}$$

where U is the public key, R is the private key, and G is the generator point. An elliptic curve group is formed with the help of this point only if no repeated factors are contained in $27h^2 + 4g^3 = 0(\mathrm{mod}P)$ and $x^3 + gx + h$.

The mathematical structure for addition over GF (P), emulating the conditions are given by the following equation.

Let $P(x_1,\ y_1)$ and $Q(x_2, y_2)$ be components of the elliptic curve graph. Then, $P + Q = (x_3,\ y_3)$ where

$$x_3 = \lambda^2 - x_1 - x_2 \text{ and } y_3 = \lambda(x_1 - x_3) - y_1. \tag{3}$$

Then, λ resolves as

$$\lambda = \begin{cases} \frac{3x_1^2+a}{2y_1} \text{ if } P = Q \\ \frac{y_2-y_1}{x_2-x_1} \text{ if } P \neq Q. \end{cases} \tag{4}$$

After the completion of the key generation step, encryption can be performed with the chaotic neural network, as described below.

a) Encryption based on the chaotic neural network: Suppose there is a chaotic neural network with n inputs and outputs. The input to this network is the plain text that is converted into cipher text with the help of ECC-based Galois field. The input text is denoted as $(P_1, P_2, \ldots, P_n)$ and the cipher text is denoted as $(C_1, C_2, \ldots, C_n)$.

Step 1: Generate a chaotic sequence

$$(g(n),\ g(n+1), \ldots, g(n+n+1)).$$

This chaotic sequence is known as the cipher text.

Step 2: The plain text is input into the network $(P_1, P_2, \ldots, P_n)$ and is then converted into the chain of binary data. The binary sequence thus generated is denoted by $(b_1, b_2, \ldots, b_n)$ and the formula used to generate this binary data is as follows:

$$b(8n-8)b(8n-7)\cdots b(8n-2)b(8n-1)$$

where

$$n = 1, 2, \ldots, n.$$

Step 3: The binary sequence that was generated in the previous step helps to perform weight factor generation, which varies based on input functions. The equation for weight factor generation is as follows:

$$W_j = \left\{ \begin{array}{ll} 1 & \text{if } b(j+8\times n) = 0 \\ -1 & \text{if } b(j+8\times n) = 1 \end{array} \right\}. \tag{5}$$

According to the above equation, there are different weight factors for different inputs and the value of j varies from zero to seven.

Step 4: After the creation of weight factors, a bias function is introduced for every chaos, which is generated by using weight factors. The problem of singularity is avoided with the help of this bias function.

The equation for the bias function is as follows:

$$d_j' = f\left(W_j \times d_j\right) \tag{6}$$

This article has been accepted for inclusion in a future issue of this journal. Content is final as presented, with the exception of pagination.

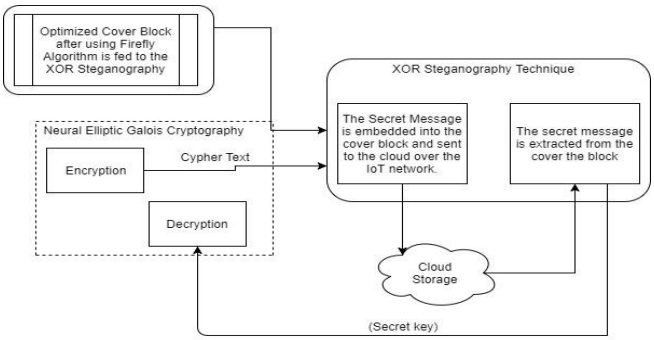

Fig. 2. Proposed Matrix-XOR steganography technique.

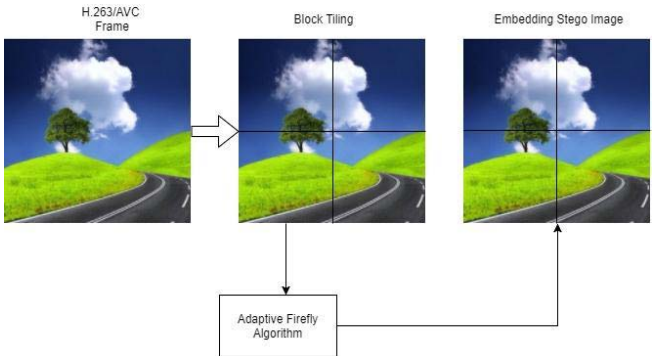

Fig. 3. Adaptive Firefly optimization.

d'_j is the bias function, W_j is the weight factor, and d_j is the input function.

Step 5: The cipher text is generated, based on the weight factor and the input function

$$g(i) = x_n(n) \times (1 - y_n) + d'_j. \tag{7}$$

In the above equation, (x_n, y_n) are the points on the elliptic curve (secret key). After creation of the cipher text, this text is stored on a cloud platform with the help of the Matrix XOR Encoding steganography technique.

b) Matrix XOR*:* Matrix XOR is a technique for hiding encrypted data in which the encrypted data is hidden inside the H.264 video file [16]. For this technique, the Firefly optimization technique is used to optimize the blocks of the image. With the help of this optimization technique, block selection among the whole image is possible.

The proposed OM-XOR steganography technique is shown in Fig. 2. The initial image is tiled and the secret data is hidden on the cover block with the help of Adaptive Firefly optimization. The tiled image is recombined and decoded. Finally, the encrypted message is decoded by using the secret key.

Step 1 (Permutative Straddling): When there is no need to use the full size to hide the encrypted message, the fragment of the image remains unused. Permutative straddling is used to eliminate this problem. This technique scatters the secret message over the complete carrier medium; i.e., over the complete image. Permutation depends on a key-based password. If the user has the correct key, the same permutation can be repeated.

Step 2 (Encoding): There are many algorithms for embedding secret information into an image block. By introducing the Matrix XOR encoding technique, the proposed work enhances the embedding efficiency. The conversion of triple(f, k, $g(i)$) to quad(e, k, $g(i)$) and the compression of the encrypted message enhances the efficiency of this technique.

The Matrix XOR technique embeds the $g(i)$ chaotic sequence (secret data) in the optimized image block (cover block). In this process, the one-bit block from the cover block is replaced with the encrypted information block. The one-bit embedding process is carried out using the following equation:

$$M_e = D \oplus C \tag{8}$$

where the binary data bit is D and C is the binary image bit block. Two conditions must be satisfied to carry out this embedding process.

Condition 1: For the two blocks, if the XOR operation results in a zero, then there is no requirement to change the last bit position.

Condition 2: For the two blocks, if the XOR operation does not result in zero, then there is a change of the cover block (i.e., zero to one or one to zero).

After deciding the bit position for the cover block, the embedding process is executed based on the following equation:

$$M_e = \left\{\left((d(i) \oplus c(i))c'(i)\right) + (d(i) \oplus c(i))' c'(i)\right)\right\}. \tag{9}$$

Optimization of the cover block is handled with the help of the Firefly algorithm, as discussed below.

Step 3 (Adaptive Firefly Optimization): The Adaptive Firefly algorithm (Fig. 3) is described by these three standard rules.

1) All the fireflies are unisex so that all fireflies are attracted to each other.
2) Attractiveness between the fireflies is proportional to their brightness; thus, a less bright firefly will move toward a brighter one. With increased distance between fireflies, both the attractiveness and brightness decrease.
3) The brightness of a firefly is determined by the landscape of the objective function. Two important issues persist in the Firefly algorithm: a) formulation of the attractiveness and b) the variation of light intensity [17].

The main motive is to reduce the count of the pixel blocks. For this, some control parameters are initialized, such as:

1) initial brightness $b = 0.4$;
2) randomization parameter $\eta = 0.5$;
3) coefficient of light absorption $\gamma = 0.5$.

The following equation is used to calculate multiobjective functions [17]:

$$f(x) = [\min\{(c)\}]. \tag{10}$$

For a given medium with a fixed light absorption coefficient, the light intensity I varies with the distance c, according to the following equation [17]:

$$I = I_0 e^{-\gamma c} \tag{11}$$

This article has been accepted for inclusion in a future issue of this journal. Content is final as presented, with the exception of pagination.

where I_0 is the original light intensity, In (10), the cost function "c" should be minimal in order to optimize the number of blocks of an image. As attractiveness of fireflies is directly related to LI with a neighboring firefly, β is defined as follows [17]:

$$\beta(r) = \beta_0 e^{-\gamma c^k}; \quad k \geq 1 \tag{12}$$

where β_0 is defined as attraction per $c = 0$ and γ is defined as the illuminated saturation immersion coefficient. $\gamma = [0, \infty]$ and $\gamma = 1$. In certain circumstances, β_0 is expressed as $\beta_0 = 1$ and $k = 2$ since most fireflies are visible due to a constrained separation.

Suppose that, for two fireflies i and j, room arrangement is n-dimensional. The distance between the x_i and y_i, the individual count can be create using Cartesian (c) count calculation, as follows:

$$c = \sqrt{\left(\sum_{k=1}^{d} \left(x_j - x_i\right)^2\right) + \left(y_i - y_j\right)}. \tag{13}$$

Next, a time-varying AW is developed to update the position of the fireflies. Over the period, the AW diminishes. The AW value is updated with the following equation:

$$S_{\text{new}}(t+1) = f(x) + \beta_0 e^{-\gamma c^m}\left(x_j - x_i\right) + \alpha \varepsilon_i. \tag{14}$$

Equation (14) shows that the ith firefly moves toward the jth firefly, which is more attractive in the optimization.

Where location of the ith firefly is $S_{\text{new}}(t+1)$, after $t+1$th interchange; randomization parameter is α; $\alpha \in [0, 1]$ in place of major difficulties $\alpha = 0.1$. The random numbers vector is ε_i. Thus, the ith element is updated as follows:

$$S_{\text{new}} = S_{\text{old}} + S_{\text{new}}(t+1). \tag{15}$$

Thus, complexity is reduced with the help of the Firefly optimization algorithm and helps to achieve better performance and results in the case of block selection.

c) Data retrieval: On the receiver side, data is retrieved with the help of the OM-XOR retrieval process. Encrypted data that was stored in the cloud is retrieved with the OM-XOR decoding process. Finally, the decoded information that was encrypted using the steganography technique is then decrypted with the help of CNN decryption using the private key of the user.

IV. Experimental Results and Discussion

The MATLAB simulation tool is used for implementation of the proposed work. The proposed work uses H.264/AVC video standards.

A. Database Description

Some official videos, such as MPEG 2 and MPEG 4 help to achieve a high compression ratio. Although high-performance efficiency is achieved, there is a loss in the compression ratio [18]. This problem is solved with supreme progressive film coding model up-to-date. H.264 MPEG-4 is similarly used for this process and the video quality of this H.264/AVC is

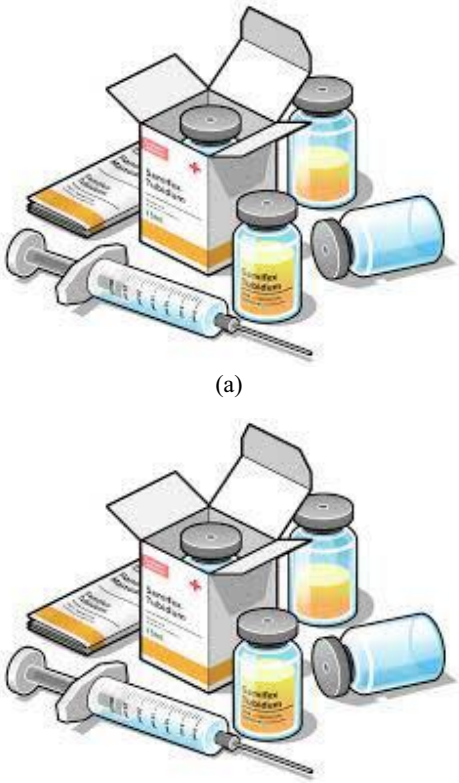

(a)

(b)

Fig. 4. Matrix XOR stegno image and cover image. (a) Cover image. (b) Stegno image.

H.264, and each video has 30 frames/s. Video resolution is 304 × 204 pixels.

The cover block image, which is the converted frame for the H.264/AVC video, is depicted in Fig. 4(a). Fig. 4(b) corresponds to the stegno image in which medical data is hidden in the profound layer of the cover block. Thus, with the help of the proposed method, the medical data of the patient is securely hidden within the image.

The data that is hidden with the proposed method cannot be extracted by any unauthorized person since only the ECC secret key can retrieve the original data.

B. Parameter Evaluation

For showing the efficiency of the proposed EGC system, embedding efficiency, carrier capacity, peak signal to noise ratio (PSNR), mean square error (MSE), and time complexity were evaluated. The results of all these parameters were compared to some of the existing methods, such as LSB steganography, FMO steganography, and optimized modified matrix encoding (OMME) steganography. Various graphs have been put-up to efficiently show the comparison between the proposed work and the existing methods. The parameters are evaluated as follows.

1) Embedding Efficiency (E_η): Embedding efficiency is defined as the rate of the amount of secrets bits stored and embedded in an image block, which helps to show the

This article has been accepted for inclusion in a future issue of this journal. Content is final as presented, with the exception of pagination.

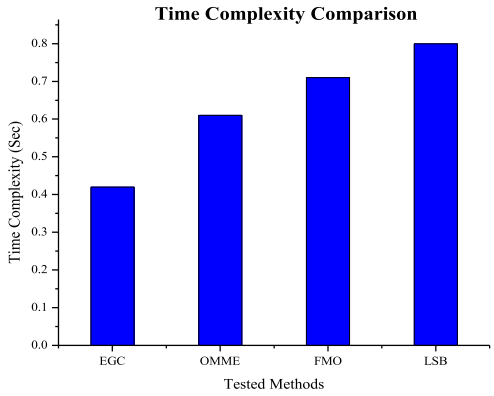

Fig. 5. Time complexity comparison analysis.

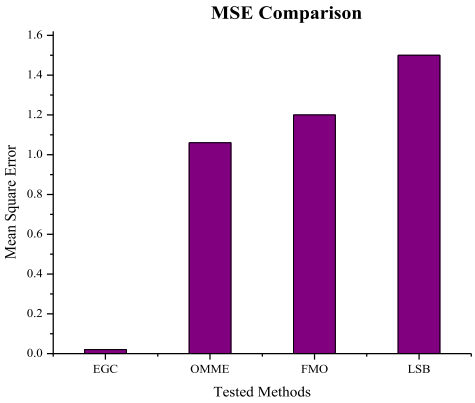

Fig. 6. MSE comparison analysis.

effectiveness of the system

$$E_\eta = \frac{k+1}{k} n \tag{16}$$

where k is the bit in the cover block and n is the total quantity of secret bits within the embedding technique.

2) Carrier Capacity (C): Carrier capacity is the ability of the system to hide encrypted data inside the cover block. The value of carrier capacity is directly proportional to the performance

$$C = \frac{\text{Total number of secret bits}}{\text{Number of bits in the cover block}}. \tag{17}$$

Carrier capacity is the other name for hiding capacity and is measured in terms of bits per pixel (BPP).

3) Mean Square Error: MSE is the amount of similarity and the range of distortion in an image and it also helps in the measurement of the amount of reliability

$$\text{MSE} = \frac{1}{N} \sum_{i=X,Y}^{n} (X - Y)^2. \tag{18}$$

N is the total pixel within the image, X is the initial image, and Y is the final Stegno image.

4) Peak Signal to Noise Ratio: PSNR calculates the invisibility of the image. PSNR can also be used for dynamic range images

$$\text{PSNR} = 10 \log_{10} \frac{255^2}{\text{MSE}}. \tag{19}$$

Time Complexity: Time complexity is the amount of time taken between the encryption and decryption process. To increase the efficiency of the system, time complexity must be lowered.

Comparative analyses are shown in Figs. 4–6.

The EGC protocol gave better performance regarding embedding efficiency, carrier capacity, PSNR, MSE, and time complexity as compared to other techniques, such as LSB steganography, FMO steganography, and OMME steganography. As depicted in Figs. 5 and 6, the MSE and time complexity of the proposed EGC protocol is very low, as compared to existing methods. The proposed protocol yielded better PSNR performance as compared to LSB, FMO, and OMME (32.42%, 45.62%, and 52.24% better performance,

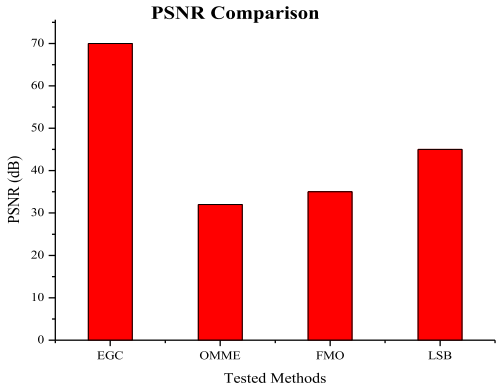

Fig. 7. PSNR comparison analysis.

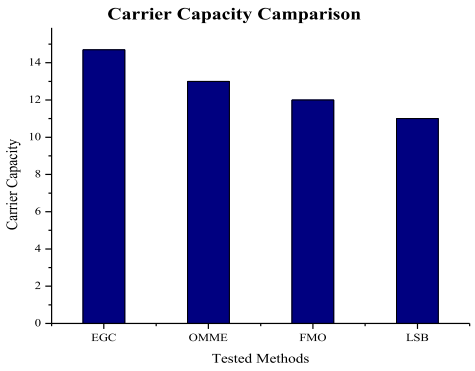

Fig. 8. Carrier capacity analysis.

respectively), as depicted in Fig. 7. Fig. 8 shows that the proposed protocol yielded better carrier capacity performance as compared to LSB, FMO, and OMME (0.33%, 16.35%, and 9.36% better performance, respectively). As shown in Fig. 9, the proposed protocol yielded better embedding efficiency performance as compared to LSB, FMO, and OMME (31%, 21%, and 1.16% better performance, respectively). Therefore, overall the proposed method is well optimized and yielded better results when compared to the existing protocols.

This article has been accepted for inclusion in a future issue of this journal. Content is final as presented, with the exception of pagination.

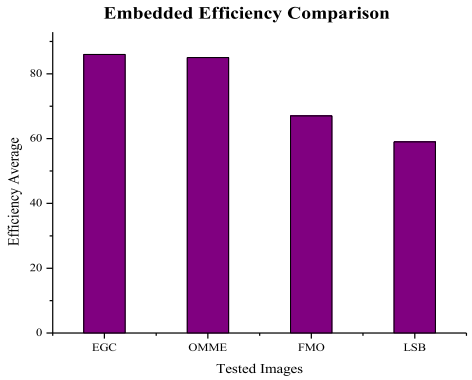

Fig. 9. Embedding efficiency analysis.

V. Conclusion

The EGC protocol generated high levels of data security to serve the purpose of protecting data during transmission in the IoT. With the novel ECC over Galois field, the proposed EGC protocol provided better security. Due to the enhanced embedding efficiency, advanced data hiding capacity can be achieved. With the help of the proposed protocol and Adaptive Firefly optimization, any amount of data can be easily transmitted over the IoT network securely hidden within the profound layers of images. Performance is evaluated with parameters, such as embedding efficiency, PSNR, carrier capacity, time complexity, and MSE. Finally, the proposed work is implemented in a MATLAB simulator, and approximately 86% steganography embedding efficiency was achieved. Results from this proposed protocol were compared to existing methods, such as OMME, FMO, and LSB.

References

[1] R. H. Weber, "Internet of Things—New security and privacy challenges," *Comput. Law Security Rev.*, vol. 26, no. 1, pp. 23–30, 2010.

[2] A. Ukil, J. Sen, and S. Koilakonda, "Embedded security for Internet of Things," in *Proc. 2nd Nat. Conf. Emerg. Trends Appl. Comput. Sci. (NCETACS)*, Mar. 2011, pp. 1–6.

[3] W. Daniels *et al.*, "SμV-the security microvisor: A virtualisation-based security middleware for the Internet of Things," in *Proc. ACM 18th ACM/IFIP/USENIX Middleware Conf. Ind. Track*, Dec. 2017, pp. 36–42.

[4] U. Banerjee, C. Juvekar, S. H. Fuller, and A. P. Chandrakasan, "eeDTLS: Energy-efficient datagram transport layer security for the Internet of Things," in *Proc. GLOBECOM IEEE Glob. Commun. Conf.*, Dec. 2017, pp. 1–6.

[5] G. Manogaran, C. Thota, D. Lopez, and R. Sundarasekar, "Big data security intelligence for healthcare industry 4.0," in *Cybersecurity for Industry 4.0*. Cham, Switzerland: Springer, 2017, pp. 103–126.

[6] H. Sun, X. Wang, R. Buyya, and J. Su, "CloudEyes: Cloud-based malware detection with reversible sketch for resource-constrained Internet of Things (IoT) devices," *Softw. Pract. Exp.*, vol. 47, no. 3, pp. 421–441, 2017.

[7] N. Chervyakov *et al.*, "AR-RRNS: Configurable reliable distributed data storage systems for Internet of Things to ensure security," *Future Gener. Comput. Syst.*, vol. 92, pp. 1080–1092, Mar. 2019.

[8] S. Raza, H. Shafagh, K. Hewage, R. Hummen, and T. Voigt, "Lithe: Lightweight secure CoAP for the Internet of Things," *IEEE Sensors J.*, vol. 1, no. 10, pp. 3711–3720, Oct. 2013.

[9] M. Vučinić *et al.*, "OSCAR: Object security architecture for the Internet of Things," *Ad Hoc Netw.*, vol. 32, pp. 3–16, Sep. 2015.

[10] Y. Yang, X. Liu, and R. H. Deng, "Lightweight break-glass access control system for healthcare Internet-of-Things," *IEEE Trans. Ind. Informat.*, vol. 14, no. 8, pp. 3610–3617, Aug. 2017.

[11] A. K. Bairagi, R. Khondoker, and R. Islam, "An efficient steganographic approach for protecting communication in the Internet of Things (IoT) critical infrastructures," *Inf. Security J. Glob. Perspective*, vol. 25, nos. 4–6, pp. 197–212, 2016.

[12] C.-T. Huang, M.-Y. Tsai, L.-C. Lin, W.-J. Wang, and S.-J. Wang, "VQ-based data hiding in IoT networks using two-level encoding with adaptive pixel replacements," *J. Supercomput.*, vol. 74, no. 9, pp. 4295–4314, 2018.

[13] T. Shanableh, "Data hiding in MPEG video files using multivariate regression and flexible macroblock ordering," *IEEE Trans. Inf. Forensics Security*, vol. 7, no. 2, pp. 455–464, Apr. 2012.

[14] X. Liao, J. Yin, S. Guo, X. Li, and A. K. Sangaiah, "Medical JPEG image steganography based on preserving inter-block dependencies," *Comput. Elect. Eng.*, vol. 67, pp. 320–329, Apr. 2018.

[15] C. J. Benvenuto, *Galois Field in Cryptography*, Univ. Washington, Seattle, WA, USA, 2012.

[16] T. Wiegand, G. J. Sullivan, G. Bjontegaard, and A. Luthra, "Overview of the H.264/AVC video coding standard," *IEEE Trans. Circuits Syst. Video Technol.*, vol. 13, no. 7, pp. 560–576, Jul. 2003.

[17] A. H. Gandomi, X. S. Yang, and A. H. Alavi, "Mixed variable structural optimization using firefly algorithm," *Comput. Struct.*, vol. 89, nos. 23–24, pp. 2325–2336, 2011.

[18] R. Hegde and S. Jagadeesha, "An optimal modified matrix encoding technique for secret writing in MPEG video using ECC," *Comput. Stand. Interfaces*, vol. 48, pp. 173–182, Nov. 2016.

Manju Khari received the B.Tech. degree from the Indira Gandhi Institute of Technology under Guru Gobind Singh Indraprastha (GGSIP) University, New Delhi, India, in 2004, the M.Tech. degree in information security from the Ambedkar Institute of Technology under GGSIP University in 2010, and the Ph.D. degree in computer science and engineering from the National Institute of Technology Patna, Patna, India, in 2016.

She is an Assistant Professor with the Ambedkar Institute of Advanced Communication Technology and Research, Under Govt. of NCT Delhi affiliated with Guru Gobind Singh Indraprastha University. She is also the Professor-in-Charge of the IT Services of the Institute and has experience of over 12 years in Network Planning and Management. She has 70 published papers in refereed National/International Journals and Conferences, such as IEEE, ACM, Springer, Inderscience, and Elsevier, 6 book chapters in a Springer. She has also coauthored two books published by NCERT of XI and XII. Her current research interests include software testing, software quality, software metrics, information security, optimization, and nature-inspired algorithm.

Aditya Kumar Garg is currently pursuing the B.Tech. degree in computer science with the Ambedkar Institute of Communication Technologies and Research, New Delhi, India.

His current research interests include developing Web Applications, image processing, machine learning algorithms, and their applications.

This article has been accepted for inclusion in a future issue of this journal. Content is final as presented, with the exception of pagination.

Amir H. Gandomi (SM'19) received the Ph.D. degree in engineering from the University of Akron, Akron, OH, USA, in 2015.

He used to be a Lecturer in several universities. He was a Distinguished Research Fellow in headquarter of BEACON NSF Center located at Michigan State University, East Lansing, MI, USA. He is an Assistant Professor of Analytics and Information Systems with the School of Business, Stevens Institute of Technology, Hoboken, NJ, USA. He has published over 130 journal papers and four books. Some of those publications are now among the hottest papers in the field and collectively have been cited over 11 000 times with an *H*-index of 53. He has been named as Highly Cited Researcher (top 1%) for two consecutive years, 2017 and 2018, and One of the World's Most Influential Scientific Minds. He is currently ranked 19th in GP bibliography among over 11 000 researchers. He is part of a NASA Technology cluster on big data, artificial intelligence, and machine learning. His current research interests include global optimization and (big) data mining using machine learning and evolutionary computations in particular.

Dr. Gandomi has also served as an Associate Editor, an Editor, and a Guest Editor in several prestigious journals and has delivered several keynote/invited talks.

Rashmi Gupta (M'13) received the B.Tech. degree from the Institute of Electronics and Telecommunication Engineers under Delhi University, New Delhi, India, in 1997, and the M.E. and Ph.D. degrees in electronics and communication engineering from the Delhi College of Engineering under Delhi University, New Delhi, in 2005 and 2014, respectively.

He was a Senior Engineer with Calcom Group of companies from 1991 to 1999, a Lecturer with the Electronics and Communication Engineering Department, Hindu Institute of Technology, Sonipat, India, and a Senior Lecturer with the Maharaja Agrasen Institute of Technology, New Delhi, from 1999 to 2003. She is currently a Professor with the Electronics and Communication Engineering Department, Ambedkar Institute of Communication Technologies and Research (Govt. of NCT of Delhi). She has authored over 70 research papers in various renowned international journal and conferences. Her current research interests include machine learning, computer vision, and signal and image processing.

Dr. Gupta is a Fellow Member of IETE.

Rizwan Patan received the B.Tech. and M.Tech. degrees in computer science and engineering from Jawaharlal Nehru Technological University Anantapur, Anantapur, India, in 2012 and 2014, respectively, and the Ph.D. degree in computer science and engineering from the School of Computer Science and Engineering, Vellore Institute of Technology, Vellore, India, in 2017.

He is an Assistant Professor with the School of Computing Science and Engineering, Galgotias University, Greater Noida, India. He has published reputed 8 SCI journals and 20 free Scopus indexed journals, and also presented paper in National/International Conferences, published book chapters in CRC Press, IGI Global, Elsevier, and edited as books. He has two Indian patents.

Dr. Patan is a Guest Editor of the *International Journal of Grid and Utility Computing* (Inderscience), Recent Patents on Computer Science, and Information Medical Unlock (Elsevier).

Balamurugan Balusamy received the B.E. degree in computer science and engineering from Bharathidasan University, Tiruchirappalli, India, in 2001, the M.E. degree in computer science and engineering from Anna University, Chennai, India, in 2005, and the Ph.D. degree in computer science and engineering from VIT University, Vellore, India, in 2015.

He is a Professor with the School of Computing Science and Engineering, Galgotias University, Greater Noida, India. His current research interests include big data, network security, and cloud computing. He is pioneer researcher in the areas of big data and IoT and has published over 70 papers in various top international journals.

Short-Term PV Power Forecasting Using Adaptive Neuro-Fuzzy Inference System

Harendra Kumar Yadav
Ph.D Research Scholar
School of Renewable Energy and Efficiency
NIT Kurukshetra Haryana, India
nitkkrharendra@gmail.com

Yash Pal
Department Electrical Engineering
NIT Kurukshetra Haryana, India
yashpal@nitkkr.ac.in

M.M. Tripathi
Department of Electrical Engineering
Delhi Technological University
New Delhi, India
mmtripathi@dce.ac.in

***Abstract*—Due to the rapid increase in electricity demand and dwindling energy resources, people have begun to think about renewable energy resources. Solar photovoltaic energy is the dominating source of renewable energy. In this paper, the ANFIS model (adaptive neuro-fuzzy inference systems) is used to predict photovoltaic power. One-year historical data for PV, direct solar radiation, diffuse solar radiation and temperature are used for training and testing purposes. The forecasted result of the model is appreciable and evidence shows that the prediction error of the proposed model has significantly good accuracy with the other existing models.**

Keywords—solar irradiation, temperature, ANFIS, PV power Forecasting and restructuring.

I. INTRODUCTION

Form few last decades, restructuring of the electrical market occurring throughout the worldwide. The countries are minimizing their generation cost as well as maximizing their profit. In the process of maximizing their profit, producer, retailer, brokers, power pool operator, consumers and prosumers are trying to interact with each other through electricity market. Two electricity market structures are generally considered worldwide:

- Bilateral electricity market
- A pool electricity market

Most countries are developing a competitive environment at different levels to meet their demand for electricity in the restructured electricity market. But the satisfaction of the demand is only possible if the generation is appropriate [1]. Therefore, electricity markets, encouraging competition from the level of production both from the point of view of bulk production at the generation level as well as the generation of distributed power (DG) at the distribution level.

Recent studies have suggested a good level of integration of renewable energies in smart grid systems [2]. The photovoltaic system (PV) is the largest renewable energy source and universally adopted as a key solution to meet the demand for electricity in the present and in the future in the world. The level of penetration of the photovoltaic system is increasing rapidly worldwide due to the development of technology, the exponential increase in demand and the lower cost of the panels. The following integration technique encourages production departments to participate in the restructured electricity market at all levels to increase the penetration of photovoltaic energy in the smart grid.

- Large-scale integration to transmission power system
- Small-scale (DG) integration to the distribution system (Medium Voltage)
- Rooftop generation integration to the distribution system (Low Voltage)

In the recent years a numerous research has been done in the field of forecasting. Recently a number of hard, soft and hybrid forecasting models have been proposed to forecast accurately the load, demand, electricity price, wind power and solar irradiance etc.

Many researchers have proposed different models for the PV power forecasting in two decades. Most of the researchers used indirect [3]-[5] and direct [6]-[10] approaches for the PV power forecasting. PV power output is forecasted directly in the direct approach and solar irradiation is forecasted in the indirect approach.

The techniques of statistical intelligence and artificial intelligence are frequently used for prediction. All recently developed models use the persistence model as a reference model for both types of forecasts. ARIMA [4], support vector regression (SVR), artificial neural network (ANN) and ANN-based hybrid methods [5], adaptive wavelet neural network (AWNN) [11], hybrid intelligent system (HIS), neural network with Wavelet Transform (NNWT) has also recently been proposed and the cascade neuro evolutionary Algorithm (CNEA) [10] is the development of prediction models with some specific advantages and disadvantages for the prediction of wind energy, the speed of the wind and the load, etc.

A combination of two or more techniques offers a good compromise between the accuracy of the forecast and the calculation time used for the indirect forecast, as well as for the direct prediction of the PV output power. In recent years, many researchers have also used support vector regression (SVR) [6] - [8], ANN [9], fuzzy logic [10], ANFIS [18] and other hybrid methods [11]. These methods have an advantage and a disadvantage for each other. All the models mentioned above are developed for the forecast of the specific time horizon, mainly for the day.

Rest of the paper is arranged in the following manner. Sections II discuss the correlation of the input variables with PV power. Section III explains adaptive network-based inference system. Section IV highlights the proposed approach and section V presents various performance

978-1-5386-7339-3/18/$31.00 ©2018 IEEE

measurement parameters. Results and discussions are presented in section VI. Section VII presents the conclusion.

II. CORRELATION OF INPUT VARIABLES

Selection of input variables for the forecasting model is a big task. Forecasting models accuracy is highly dependent upon the model input variables. In this paper pearson correlation coefficient r is also used to study the correlation between the input variables and PV power output. Pearson coefficient r is calculated by the following Eq. (1) [13].

$$r = \frac{\sum AB - \frac{\sum A \sum B}{N}}{\sqrt{\left(\sum A^2 - \frac{\sum A^2}{N}\right) - \left(\sum B^2 - \frac{\sum B^2}{N}\right)}} \quad (1)$$

Where A is PV power output, B is the input variables and N is the number of samples.

One week of data from four seasons was used to analyze the correlation between the input variables and the photovoltaic power. Table 1 shows the correlation between the photovoltaic power and the input variables, such as direct solar radiation, diffuse solar radiation and atmospheric temperature. It is clear that direct solar radiation shows a linear autocorrelation with photovoltaic power with an autocorrelation coefficient of 0.99, 0.99, 0.99 and 0.99 for the winter, summer, rain and autumn seasons, respectively. The diffuse solar radiation shows a slightly lower autocorrelation with photovoltaic power with autocorrelation coefficients of 0.87, 0.90, 0.90 and 0.86 respectively in winter, summer, rainy season and autumn. The coefficient of autocorrelation of the atmospheric temperature is moderate with photovoltaic energy with coefficients of autocorrelation of 0.61, 0.68, 0.68 and 0.71 in winter, summer, rainy season and autumn respectively [20-21].

Table 1. Correlation of input Vs PV power

S. N.	Season	Influence Factor	Correlation Coefficient (r)
1.	Winter	Direct solar radiation Diffuse solar radiation Atmospheric temperature	0.99 0.87 0.61
2.	Summer	Direct solar radiation Diffuse solar radiation Atmospheric temperature	0.99 0.90 0.68
3.	Rainy	Direct solar radiation Diffuse solar radiation Atmospheric temperature	0.99 0.90 0.68
4.	Autumn	Direct solar radiation Diffuse solar radiation Atmospheric temperature	0.99 0.86 0.71

III. ADAPTIVE NEURO-FUZZY INFERENCE SYSTEMS

The adaptive network-based inference system (ANFIS) [16-17] is a data-driven procedure that represents a neural network approach to solving function approximation problems. ANFIS can be applied to non-linear forecasts where past data is used to predict future data. ANFIS includes NN's self-learning ability with the linguistic expression function of fuzzy inference [18-19]. Here, the type 3 fuzzy inference system proposed by Takagi and Sugeno is used. In this inference system, the result of each rule is a linear combination of input variables added by a constant term. The end result is the weighted average of the production of each rule. The corresponding equivalent ANFIS structure is shown in Fig 1. The ANFIS network is composed of five layers. Each layer contains several nodes described by the node function.

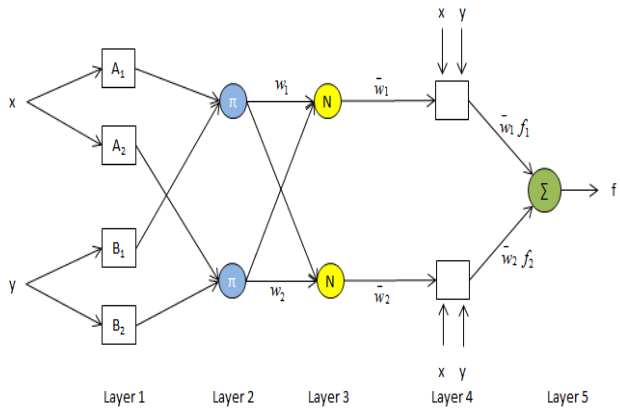

Fig. 1. Structure of ANFIS

The individual layers of this ANFIS structure are explained below. In layer 1 every node *i* is adaptive with a node function:

$$O_i^1 = \mu A_i(x) \quad (2)$$

Where x is input and A_i is a linguistic label for the corresponding node.

The generalized bell functions are used as a membership functions for input variables:

$$\mu A_i(x) = \frac{1}{1+\left|\frac{x-r_i}{a_i}\right|^{2b_i}} \quad (3)$$

where x denotes input and (a_i, b_i, r_i) shows premise parameter set

In layer 2 every node is fixed and used to calculate the firing strength w_i of rule. The product of all incoming signals at the node is the output of that node as described in Eq. (4). In this layer all parameters are referred as premise parameters.

$$O_i^2 = w_i = \mu A_i(x) \times \mu B_i(y), \quad i = 1,2 \quad (4)$$

In the layer 3 every node is also fixed and each node calculates the ratio of the respected node rule firing strength to the summation of strength of all firing rules. The results of the layer are called normalized firing strengths as explained in Eq. (5).

$$O_i^3 = \overline{w_i} = \frac{w_i}{w_{1+}w_2}, \quad i = 1,2 \quad (5)$$

In layer 4, all node computes contribution of respected ith rule to complete output as shown in Eq.(6).

$$O_i^4 = \overline{w_i} \times f_i = \overline{w_i} \times (a_i x + b_i y + c_i)$$

$$i = 1,2 \tag{6}$$

where $\overline{w_i}$ is result of layer 3 and $\{a_i, b_i, c_i\}$ is resultant parameter set.

Layer 5 has a single node and it computes final outputs by summing the all incoming signals given in Eq.(7).

$$O_i^5 = \sum_i \overline{w_i} \times f_i = \frac{\sum_i w_i \times f_i}{\sum_i w_i} \tag{7}$$

So we can say that, an adaptive network is functionally same as to the Sugeno-type fuzzy inference system. This paper implements the ANFIS to forecast the solar PV power. Parameters of the membership functions are adjusted by hit and trial methods. This method has the advantage of being less computational cost for a given size of network topology. The triangular shape membership functions are considered in this study.

IV. Proposed Approach

This paper uses ANFIS to forecast the PV power output. In pre-processing stage data is normalized, missing values are replaced by zero and clustered into four groups according to seasons. Then, the future values of these constitutive series are forecasted using ANFIS. The membership functions of ANFIS structure are tuned with the help of hit and trial method to attain a lower error. Finally, the forecasted PV power is renormalized into the actual values for performance evaluation.

V. Performance Measure Parameters

Root mean squared error (RSME), mean absolute percentage error (MAPE) and mean absolute error (MAE) are used to evaluate the accuracy and ability of proposed PV power forecasting model as given by Eq. 8 to Eq. 11 respectively [3]-[4].

Root mean square error

$$RMSE = \sqrt{\frac{1}{N}\sum_{j=1}^{N}(X_{mj} - X_{cj})^2} \tag{8}$$

Mean absolute percentage error

$$MAPE = \frac{100}{N}\sum_{j=1}^{N}\frac{\left(X_{mj} - X_{cj}\right)}{\bar{X}_m} \tag{9}$$

$$\bar{X}_m = \frac{1}{N}\sum_{j=1}^{N} X_m \tag{10}$$

Mean absolute error

$$MAE = \frac{1}{N}\sum_{j=1}^{N}\left|(X_{mj} - X_{cj})\right| \tag{11}$$

Where X_{mj} is j^{th} measured value, X_{cj} is j^{th} calculated value and N is the number of measurement taken. $\bar{X}m$ is the average PV power of the forecast period. The average PV power is used in the equation. 9 to stay away from the negative results of photovoltaic power close to zero.

VI. Results and Discussion

The ANFIS model is applied to forecast the one-week ahead PV power output in Indian electricity market. Fig. 2 to fig. 5 show the forecasted result vs actual solar PV power as well as mean absolute error (MAE) in forecasting for one week using the proposed hybrid approach for winter, summer, rainy and autumn respectively. The results are computed using MATLAB on a machine with 3GB of RAM and a 2.40 GHz I-3 based processor.

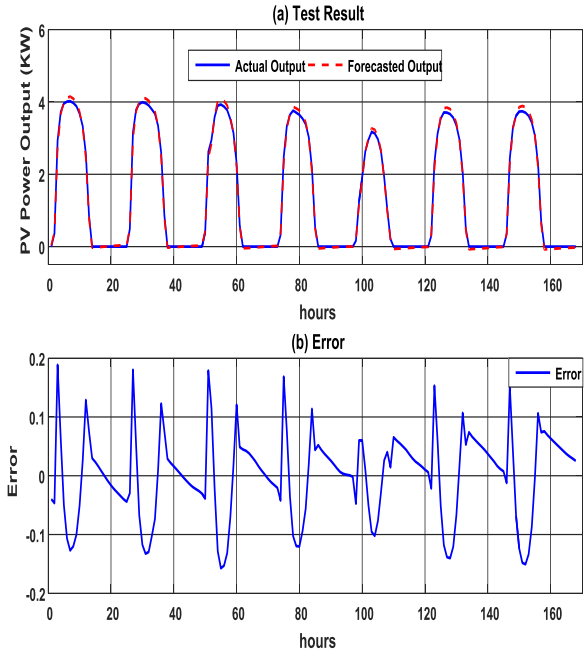

Fig. 2. Forecasted result of the winter season

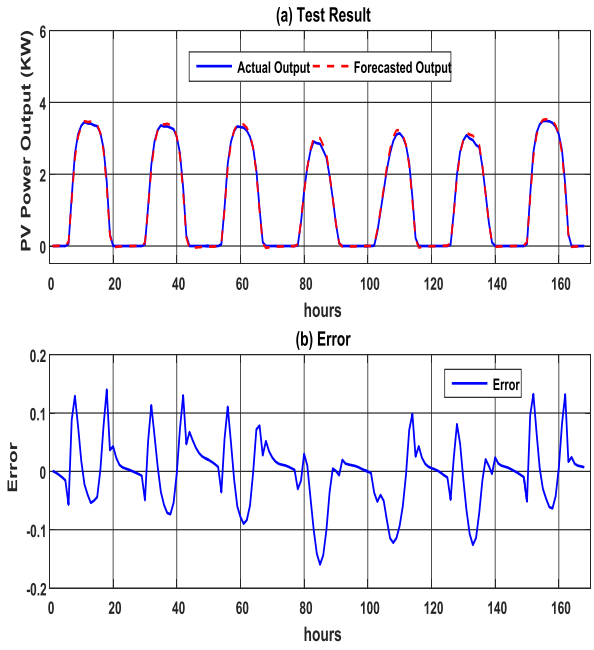

Fig. 3. Forecasted result of the summer season

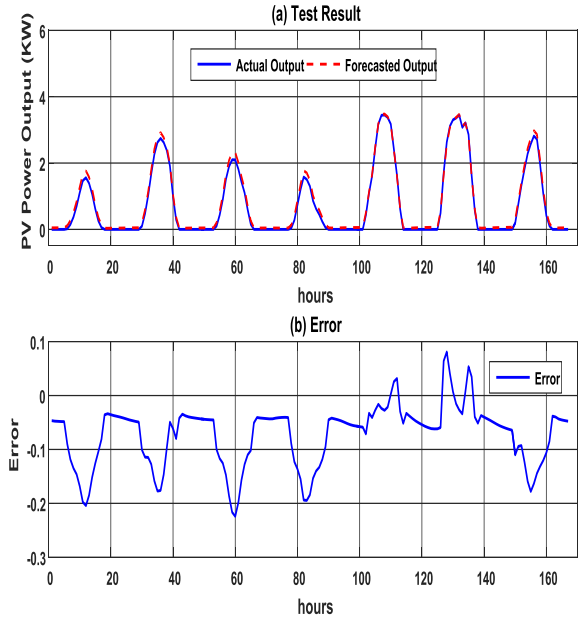

Fig. 4. Forecasted result of the rainy season

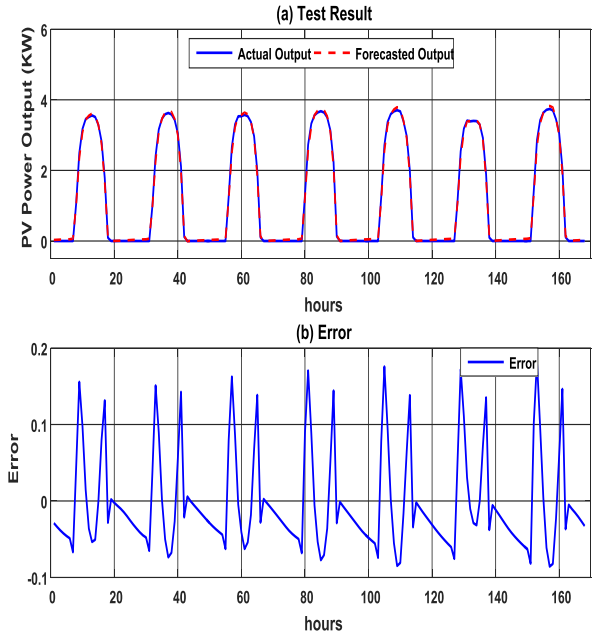

Fig. 5. Forecasted result of the auntumn season

Table 2 presents the summarized result of the proposed approach with some pre-existing approaches. The proposed approach presents better result with 4.092%, 3.161%, 9.337% and 3.932% MAPE for winter, summer, rainy and autumn season respectively. From the above discussion it is clear that the proposed ANFIS approach performs better accuracy and gives better result as compared to ARIMA and ANN approach in summer and autumn seasons and result of winter season is also comparable with ANN method, and better with ARIMA. Proposed method outperform in the rainy season as compared to the ANN method because of random behavior of nature in rainy time. So the forecast results indicate that all season results are quite good and able to perform PV forecasting with an acceptable error. All the three error parameters MAPE, RMSE, and MAE are best for the summer season and poor for the rainy season due to the reasons stated above. The proposed approach has less complexity of design, less computation time and better accuracy, so it is very useful for the real life application.

Table 2. Summarized result of all four seasons

Forecasting Season	Evaluation Metrics	Forecasting Methods		
		ARIMA	ANN	ANFIS
Winter	MAPE	24.699	**3.019**	4.092
	MAE	0.344	**0.042**	0.057
	RMSE	0.434	**0.066**	0.073
Summer	MAPE	24.585	3.960	**3.161**
	MAE	0.315	0.051	**0.041**
	RMSE	0.404	0.076	**0.056**
Rainy	MAPE	24.429	**7.488**	9.337
	MAE	0.315	**0.056**	0.077
	RMSE	0.407	**0.097**	0.092
Autumn	MAPE	26.326	7.847	**3.932**
	MAE	0.328	0.098	**0.049**
	RMSE	0.468	0.166	**0.064**

Fig. 6 to Fig. 8 shows the comparative analysis of the mean absolute percentage error (MAPE), mean absolute error (MAE) and root mean squared error (RSME) of the forecasted result of all four winter, summer, rainy and autumn seasons respectively. It is evident from these plots that the proposed model is able to forecast the week ahead solar PV power output with least error. The MAPE, MAE and RSME errors are compared with the existing ARIMA and ANN methods. All calculated performance measure as explained above show that the proposed model errors are least in the summer and autumn seasons as compared to the existing methods ARIMA and ANN. Error for winter season is comparable with the ANN method. In rainy season performance of the proposed method is poor as compared with the old ANN method.

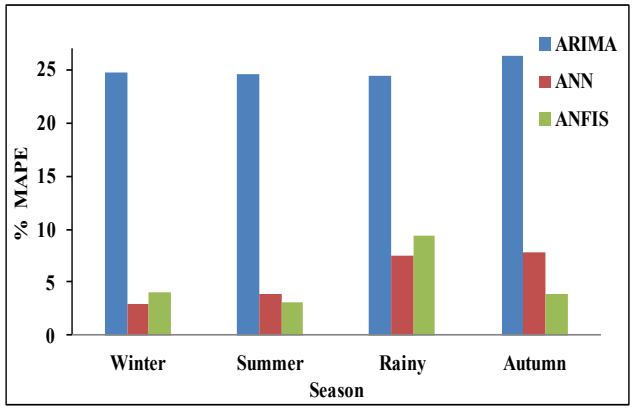

Fig. 6. Comparative MAPE of the forecasted result

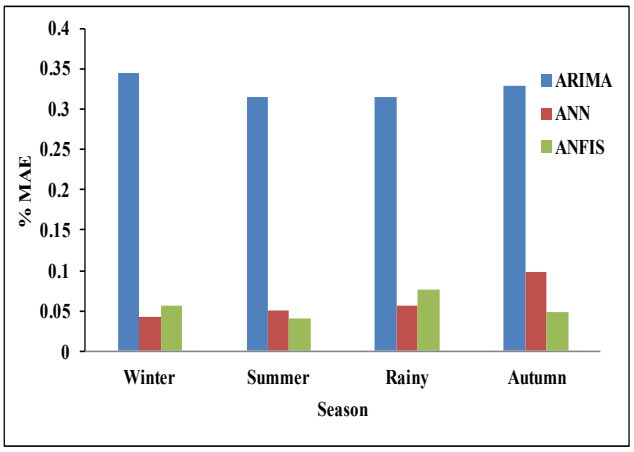

Fig. 7. Comparative MAE of the forecasted result

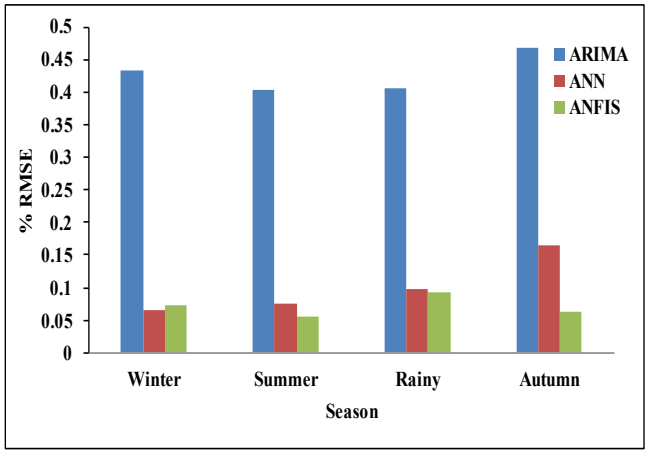

Fig. 8. Comparative RMSE of the forecasted result

VII. CONCLUSION

The solar photovoltaic energy forecast is very crucial for the reliable, safe and efficient operation of the grid and the economic functioning of the electricity market. This paper proposes an ANFIS model for the short-term prediction of photovoltaic energy, which is the combination of the neural network and the fuzzy inference system. The proposed model is trained and tested using actual measured data from India and weekly solar PV forecasts were made using a new dataset from the same region. The error results show that the average MAPE for the winter, summer, rainy and fall seasons is 4.092%, 3.161%, 9.337% and 3.932%, respectively, while the MAPE average for all stations becomes 5.13%. The performance of the proposed model is also compared to existing models and has outperformed existing models in terms of forecast accuracy.

ACKNOWLEDGMENT

The author Harendra Kumar Yadav would like to thank renewable ninja community for providing hourly PV power and wind speed simulated data for the site located in the India.

REFERENCES

[1] O. Ellabban, H. Abu Rub and F. Blaabjerg, "Renewable energy resources: current status future prospects and their enabling technology," Renew. Sust. Energy, Rev 39, pp.748–764, 2014.

[2] D. Connolly, H. Lund, B. V. Mathiesen and M. Leahy, "The first step towards a 100% renewable energy-system for Ireland," Application Energy 88(2), pp.502–507, February 2011.

[3] P. Lauret, C. Voyant, T. Soubdhan, M. David and P. Poggi, "A benchmarking of machine learning techniques for solar radiation forecasting in an insular context," Solar Energy (112), pp.446-457, 2015.

[4] H. K. Yadav, Y. Pal and M. M. Tripathi, "Photovoltaic power forecasting methods in smart power grid," Annual IEEE India Conference (INDICON), pp. 1–6, December 2015.

[5] A. Mellit and A. M. Pavan, "A 24-h forecast of solar irradiance using artificial neural network: Application for performance prediction of a grid-connected PV plant at Trieste, Italy," Solar Energy 84, pp. 807-821, 2010.

[6] H. T. Yang, C. M. Huang, Y. C. Huang and Yi-Shiang Pai, "A weather based hybrid method for 1- day ahead hourly forecasting of PV power output," IEEE transactions on susta. energy, VOL.5, NO.3, pp.917-926, 2014.

[7] J. Shi, W. J. Lee, Y. Liu, Y. Yang and P. Wang, "Forecasting power output of photovoltaic system based on weather classification and support vector machine," IEEE transaction on industry applications, vol.48, no.3, pp.1064-1069, June 2012.

[8] K. A. Baharin, H. A. Rahman, M.Y. Hassan and C. K. Gan(2016), "Short-term forecasting of solar photovoltaic output power for tropical climate using ground-based measurement data," Journal of renewable and sustainable energy 8, pp. 053701-1-053701-19, 2016.

[9] J. P. S. Catalao, S. J. P. S. Mariano, V. M. F. Mendes, and L. A. F. M. Ferreira, "Short-term electricity prices forecasting in a competitive market: A neural network approach," Electric Power System Res., vol. 77, no. 10, pp. 1297–1304, Aug 2007.

[10] J. P. S. Catalao, H. M. I. Pousinho, and V. M. F. Mendes, "Hybrid wavelet-PSO-ANFIS approach for short-term electricity prices forecasting," IEEE Transaction Power System, vol. 26, no. 1, pp. 137–144, Feb. 2010.

[11] N. M. Pindoriya, S. N. Singh, and S. K. Singh, "An adaptive wavelet neural network-based energy price forecasting in electricity markets," IEEE Trans. Power Syst., vol. 23, no. 3, pp. 1423–1432, Aug. 2008.

[12] N. Amjady and F. Keynia, "Day-ahead price forecasting of electricity markets by mutual information technique and cascaded neuro-evolutionary algorithm," IEEE Trans. Power Syst., vol. 24, no. 1, pp. 306–318, Feb. 2009.

[13] L.M. Saini, S.K. Aggarwal and A. Kumar, "Parameter optimisation using genetic algorithm for support vector machine-based price-forecasting model in National electricity market," IET Gener. Transm. Distrib., Vol. 4, Iss. 1, pp. 36–49, 2010.

[14] L. L. Li, P. Cheng, H. C. Lin and H. Dong, "Short-term output power forecasting of photovoltaic systems based on the deep belief net," Advances in mechanical engineering, Vol. 9, pp.1-13, 2017.

[15] J. S. R. Jang, "ANFIS: Adaptive-network-based fuzzy inference systems," IEEE Trans. on Syst., Man and Cybern., vol. 23, no. 3, pp. 665–684, May/June 1993.

[16] Z. Yun, Z. Quan, S. Caixin, L. Shaolan, L. Yuming, and S. Yang, "RBF neural network and ANFIS-based short-term load forecasting approach in real-time price environment," IEEE Trans. Power Syst., vol. 23, no. 3, pp. 853–858, Aug. 2008.

[17] J. -S. R. Jang, "ANFIS: Adaptive-network-based fuzzy inference system," IEEE Trans. Syst., Man., Cybern., vol. 23, no. 3, pp. 665–685, May–Jun. 1993.

[18] M. A. Shoorehdeli, M. Teshnehlab, A. K. Sedigh, and M. A. Khanesar, "Identification using ANFIS with intelligent hybrid stable learning algorithm approaches and stability analysis of training methods," Appl. Soft. Comput., vol. 9, pp. 833–850, 2009.

[19] M. A. Shoorehdeli, M. Teshnehlab and A. Sedigh, “Novel hybrid learning algorithms for tuning ANFIS parameters using adaptive weighted PSO,” In Fuzzy Systems Conference, fuzzy IEEE 2007, IEEE International , pp. 1-6, 2007.

[20] Pfenninger, Stefan, Staffell and Iain, “ Long-term patterns of European PV output using 30 years of validated hourly reanalysis and satellite data,” Energy-114, pp. 1251-1265, 2016. Doi:10.1016/j.energy.2016.08.060.

[21] Staffell, Iain, Pfenninger and Stefan, “Using Bias-Corrected Reanalysis to Simulate Current and Future Wind Power Output,” Energy -114, pp. 1224-1239, 2016. Doi:10.1016/j.energy.2016.08.068

Wireless Personal Communications
https://doi.org/10.1007/s11277-019-06476-x

Single-Feed Dual-Polarized High Gain Microstrip Antenna

Chandan Roy[1] · **Taimoor Khan**[2]

© Springer Science+Business Media, LLC, part of Springer Nature 2019

Abstract
In this work, a novel single-feed stacked microstrip antenna is proposed for high gain and dual polarization application. The designed antenna is useful at two purposes. In one hand, its lower operating frequency demonstrates high gain and on the other hand, the upper operating frequency shows circular polarization. The proposed design consists of two pairs of small parallel slots on the radiating surface as well as in the ground plane with a view to achieving significant amount of gain (approximately 8.3 dB) at its lower operating frequency (~6 GHz). An interesting aspect of this work is its polarization diversity. The designed antenna is capable of showing circular polarization at its upper operating frequency (~6.8 GHz). At this frequency, the axial ratio of the antenna has been kept below 3 dB for circular polarization applications. This circular polarization has been introduced by truncating the corners of radiating patch at different shapes. High gain and dual polarization play a major role on different antenna performance parameters. This antenna meets these two applications simultaneously. A prototype has been fabricated and characterized in order to validate the results. An outstanding agreement between experimental results and simulated results is achieved.

Keywords Microstrip antenna · Rectangular stacked patch · Slotted patch · Truncated corner · Defected ground surface · Dual-polarization

1 Introduction

Wireless communication systems like Wi-Fi and Wi-MAX utilize the dual-polarized antenna to overcome multipath fading problem and reuse the frequency for increasing channel capacity or to optimize the complete system performance by enhancing the channel throughput [1, 2]. Dual-band circularly polarized [3] and multi-band circularly polarized [4] characteristics of microstrip antennas (MSAs) have been investigated. Various

✉ Chandan Roy
roy.chandan.eee@gmail.com

Taimoor Khan
ktaimoor@gmail.com

[1] Department of Electrical Engineering, Ecole Polytechnique de Montréal, University of Montreal, Montreal, Canada

[2] Department of Electronics and Communication Engineering, NIT Silchar, Silchar, India

Published online: 04 May 2019

dual-polarization techniques for different geometries have been highlighted on existing works [5–18]. Single-feed dual-polarized antennas having advantages over dual-feed antennas such as cost effective, less in weight, simple in structure and fabrication procedure and having less RF loss. A hexagonal shaped slot loaded single-feed dual-frequency square shape MSA is presented having polarization planes of two frequencies perpendicular to each other and providing better bandwidth [12]. Two U-slot loaded patches are introduced for obtaining better bandwidth, high gain and dual-polarized performance in different bands [13]. A multilayered, dual-frequency and dual-polarized antenna is designed consisting of two DGSs of spiral and dumbbell shape [14]. In [15], a drum shape compact dual-band dual-polarized MSA is designed by utilizing a single co-axial feed line having resonant frequencies of 1.593 GHz and 1.797 GHz. An arrow shaped patch antenna is described in for application of dual-band and dual-polarization using single microstrip feed line [16]. By introducing a Boolean particle swarm optimization technique, a dual-band dual-polarized single-feed MSA is designed [17]. In the application of compass navigation satellite system, a dual-band dual-polarized antenna operating on L- and S-band, is presented [18].

The slot behavior of microstrip antennas follows the Babinet's principle which states that two complementary screens produce the similar diffraction patterns. This develops a relation between the radiated fields and the impedance along with the facility of low cost, low profile, compact size, easier fabrication process and conformability. In general, slot antennas having approximately $\lambda/2$ length elongated slot that cut in a conductive plate as well as excited in the center. In case of microstrip slot antenna, microstrip feed that couples electromagnetic waves which travels through the slot above and slot radiates them. A microstrip-fed slot antenna provides an excellent isolation between the material and the feed with respect to microstrip-fed microstrip antenna. Microstrip slot antennas are compact and easy to integrate with different active and passive devices. This compactness can be found by altering the current path. Here, current covers more distance which results in the antenna size reduction as well as lowering the resonant frequency.

Single feed circularly polarized antennas are more efficient, as the external polarizer is not required which makes the antenna more compact in size and simple in design. In case of dual feed, Circular polarization is used to obtain by exciting two orthogonal patch modes in phase quadrature along with the relative phase determining polarization hand sign which can be done in various ways. On the other hand, the circular polarization can be achieved by perturbing the patch at the optimized location as compared to the feed location to excite two orthogonal modes with a quadrature phase shift. It can be done by truncating the patch corners of a single-feed square microstrip antenna. In case of Defected Ground Surface (DGS), a designed defect on the ground surface that causes the effective capacitance and inductance. The equivalent value of R, L and C of the DGS can be calculated by the structure of DGS. In general, any defected place under the patch effects within the cavity. As a result, the modulation takes place in the input along with the radiation characteristics of the microstrip antenna which is subjected to the geometrical shape of the defect [19–21].

Performance by slot antennas are described here from some of the existing works [22–32]. In [22], a dual-band dual-polarized omni-directional antenna has been designed. The operating frequencies are approximately 1.57 GHz and 2.45 GHz, respectively. Corresponding bandwidths are 18 MHz and 32 MHz, which is not up to the mark as compared to other antennas. Furthermore, the antenna demonstrates 0.7 dBi and 1.0 dBi at the respective frequencies which is insignificant. A dual band circularly polarized antenna has been designed for the application of BeiDou navigation satellite system [23]. A high gain slotted has been designed in with support vector machine optimization techniques [24]. In

[25], a T-shaped triple-band dipole antenna has been designed which has trident shaped ground-plane. The antenna covers a major portion of L, S and C bands. The average gain of 1.6 dBi, 3.4 dBi and 3 dBi has been observed for 1.5, 4 and 5.4 GHz, respectively. A metamaterial based leaky wave antenna has been designed for passive radar applications [26]. A wideband printed monopole antenna has been designed with back-to-back triangular shaped patches which are excited by a single feed-line [27]. A GPS, Bluetooth and Wi-Fi bands covering wideband planar antenna has been proposed in [28]. Based on CRLH MTMs unit-cells, a multiband planar patch antenna has been presented [29]. Here, a L-shaped slit is etched on the radiating patch by the help of an inductive spiral that is grounded by employing a via-hole. In [30], two planar slotted-antennas are proposed with good radiation characteristics at different bands of UHF and SHF bands. Metamaterial unit-cells are utilized in these antennas and those are constituted from etched capacitive slots on the radiating patch as well as the grounded spiral shaped inductive stubs. A wideband planar antenna has been designed by capacitive slits on radiating patch and truncated ground plane [31]. A coplanar waveguide fed Hexa-band antenna has been proposed with fork-shaped radiating elements [32]. This proposed antenna resonant frequencies are 1.3, 1.75, 3.35, 4.85, 6.5 and 7.6 GHz which covers 7 major bands of wireless applications.

In the proposed communication, a single-feed dual-frequency dual-polarized MSA loaded with assemblies of parallel slots on the radiating surface as well as in the ground plane is proposed. This paper is summarized into following sections: Sect. 2 describes the antenna geometry with design procedure, Sect. 3 describes the results and validation. Comparison of the proposed antenna has been shown in Sect. 4. Conclusion followed by references is then discussed in Sect. 5.

2 Antenna Geometry

The top-view and bottom-view of the proposed antenna is shown in Fig. 1a, b, respectively. Different abbreviations used in antenna geometry are also mentioned here. A rectangular patch of dimensions 41.3×48.5 mm^2 is designed using stacking of two Rogers Duroid 5880 ($\varepsilon_{r1} = \varepsilon_{r2} = 2.2$ and $h_1 = h_2 = 0.762$ mm) substrates sheets of equal size 70.0×70.0 mm^2. For exciting the patch, a 50 Ω-microstrip feed line of dimensions 14.35×1.20 mm^2, is used. The antenna is designed using FEM (finite element method) based HFSS (high frequency structure simulator) software [29].

In Sect. 1, benefit of introducing slots on radiating patch for improving the radiation characteristics has been explained with proper references. In this design, two assemblies of slots have been imposed. These assemblies of slots are done horizontally and vertically

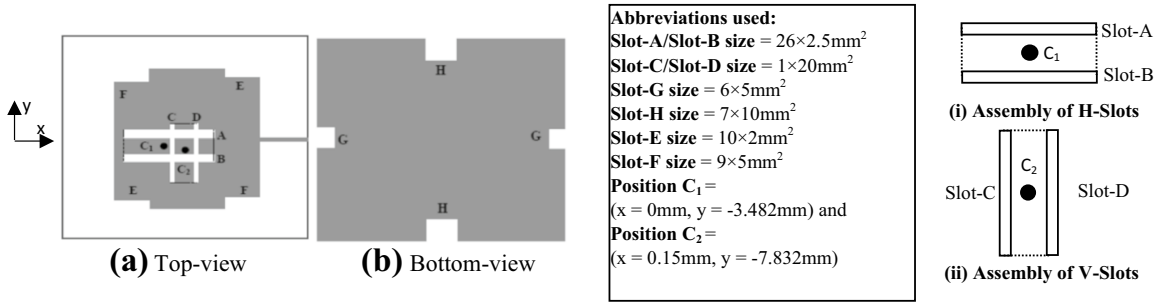

Fig. 1 Geometry of proposed antenna

at the same time. Assembly of horizontal slot consists of two slots (slot-A and slot-B) of equal size 26×2.5 mm^2 whereas assembly of vertical slots consists of two slots (slot-C and slot-D) of equal size: 1×20 mm^2. The position of assembly of horizontal slots is optimized at C_1(x = 0 mm, y = − 3.482 mm) whereas for assembly of vertical slots, it is optimized at C_2(x = 0.15 mm, y = − 7.832 mm).

The four corners of the patch have been truncated for achieving circular polarization as well as the impedance matching and the bandwidth improvement. In order to achieve circular polarization at the upper frequency, the opposite corners of the rectangular patch are truncated by introducing small sized slots (slot-E and slot-F). Finally, the sizes of these slots are optimized as 10×2 mm^2 and 9×5 mm^2, respectively. In addition, truncation of the corners causes to resonate the antenna at higher frequencies [34, 35]. Consequently, the combined effect of both the corner truncation and slot insertion on the patch arise the bandwidth of the proposed antenna. The truncated corner and the slotted patch also make the single-feed microstrip antenna more compact. Moreover, the ground plane for the proposed designs is also modified by inserting another two pairs of slots (slot-G and slot-H). The sizes of these slots are optimized as 6×5 mm^2 and 7×10 mm^2. As soon as the rectangular shaped defect is inserted near the non-radiating edges of the patch, cross polarization, gain along with the input impedance bandwidth of microstrip antenna are outstandingly changed. Because of the rectangular geometry of the defects, the fields become highly concentrated at radiating edge whereas it becomes weak near the non-radiating edges. This defected ground surface excites a resonant band, but it arises a problem of circular polarization raised. The circular polarization at upper band is acquired by cutting out the two opposite edges of the ground plane which are symmetrical to each other. Here, the axial ratio is improved by optimizing the dimensions of the four slots along the corners of the rectangular patch. The mismatch of axial ratio and resonant frequency was removed by introducing the slots in the ground of the patch.

The proposed antenna has basically two-fold; a dual-frequency antenna with high gain is designed firstly and then in the second step, a circular polarization at the second frequency is achieved. High gain is achieved by stacking of two substrates and inserting two pairs of parallel slots on radiation surface as well as in the ground plane. The circular polarization is obtained at one frequency by truncating four corners of the radiating patch perfectly. These slot introduction and corner truncation makes the designed antenna more compact, efficient radiator and diversely polarized.

3 Results and Validation

The proposed antenna geometry discussed in the previous section is analyzed in the reference of the center position and off-center position of the substrate. The overall assembly of slot-A, slot-B, slot-C and slot-D, is firstly placed in the reference of the center position of the substrate. This position is then slightly varied and finally the two optimized positions (viz. position C_1 and position C_2). Position C_1 corresponds to the center position of assembly of horizontal slots (slot-A and slot-B) whereas C_2 corresponds to the center position of assembly of vertical slots (slot-C and slot-D). For circular polarization, the four opposite corners of the patch are truncated by inserting slot-E and slot-F, simultaneously. The S_{11} values variation with and without truncation is depicted in Fig. 2 to both center and off center positions.

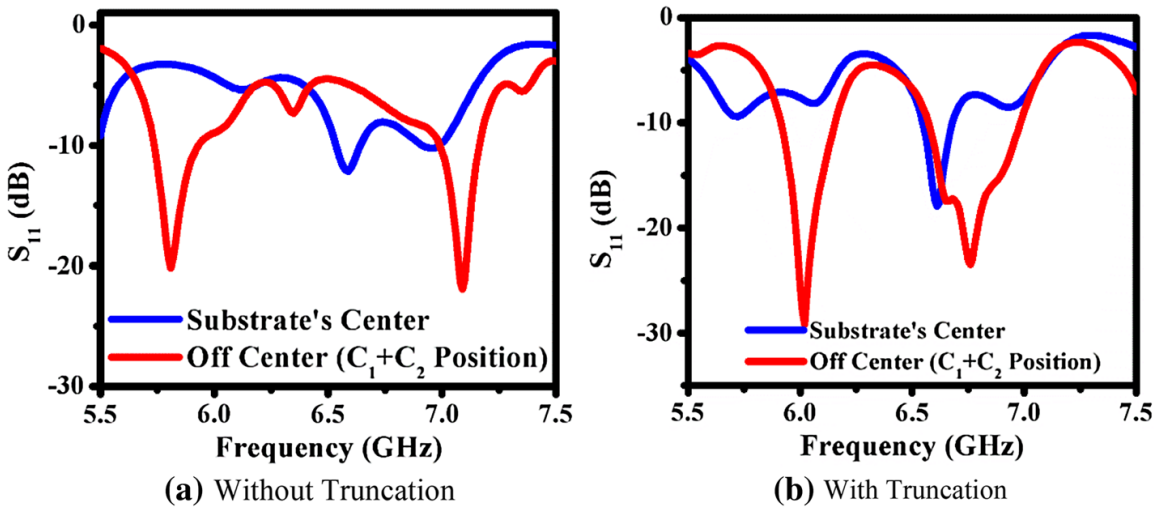

Fig. 2 Effect of truncation on S_{11} values (Simulated)

Figure 2a depicts the variations in S_{11} values for both substrate's center position and substrate's off-center position without truncation of the corners. In this case both TM_{10} and TM_{10} modes are excited. There is only one effective resonating dip ($S_{11} = 12.3$ dB at frequency = 6.6 GHz) is observed while both the horizontal assembly and vertical assembly are positioned in the center of the substrate. Now if the positions of these assemblies are made off-centered, then a fair improvement is observed. By placing the horizontal assembly at position C_1 and vertical assembly at position C_2, a drastic improvement is observed. In this case two resonating dips; first dip ($S_{11} = 20$ dB at frequency = 5.8 GHz) and second dip ($S_{11} = 22$ dB at frequency = 7.1 GHz), are observed. Eventually, these two positions are providing perfect matching, hence the improvement is observed.

The effect of variation of center and off-center position on the performance of horizontal slots assembly and vertical slots assembly is also plotted in Fig. 3. Figure 3a illustrates the improvement in S_{11} values when the horizontal slots assembly is shifted from the center position of the substrate to the off center position C_1. The improvement is observed in the excitement of TM_{10} mode. The similar behavior is observed after shifting the position of vertical slots assembly from the center position of the substrate to the off center position

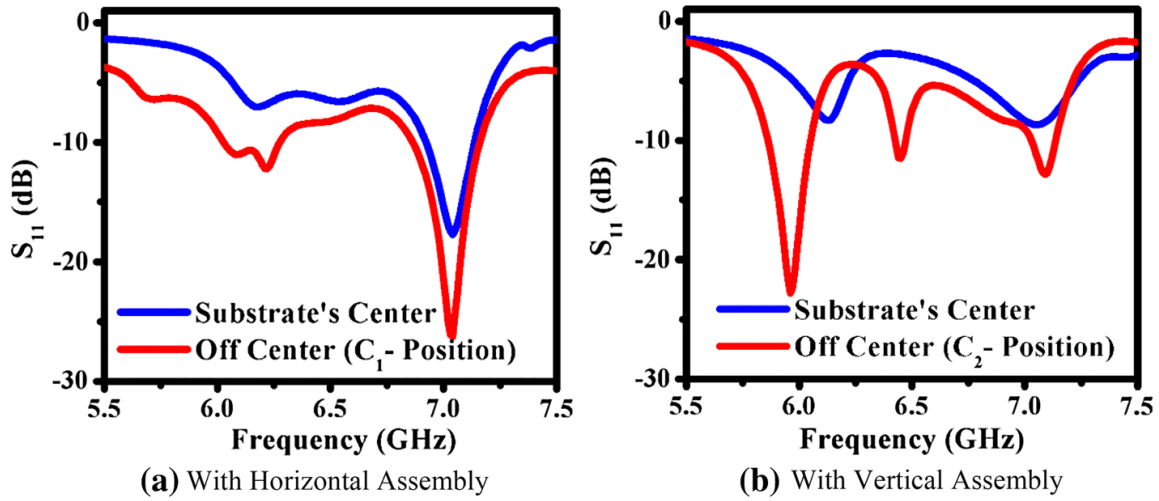

Fig. 3 Effect of variation of slots assembly positions(Simulated)

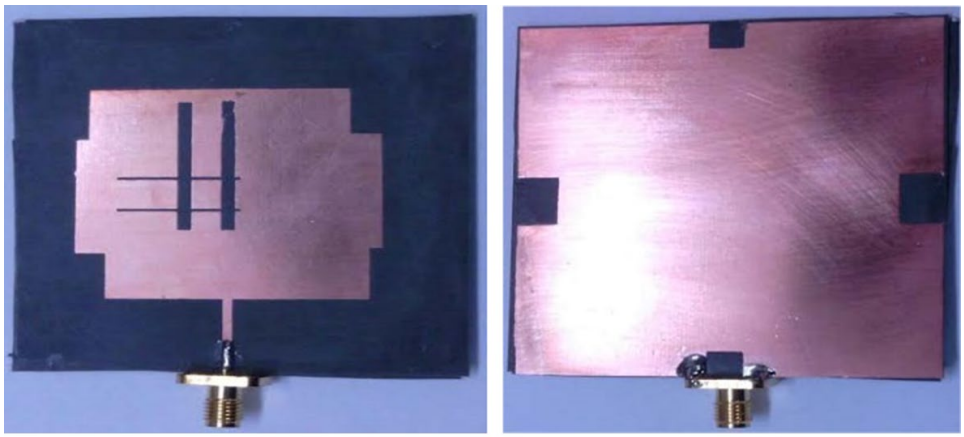

(a) Top-view **(b)** Bottom-view

Fig. 4 Snapshots of fabricated prototype

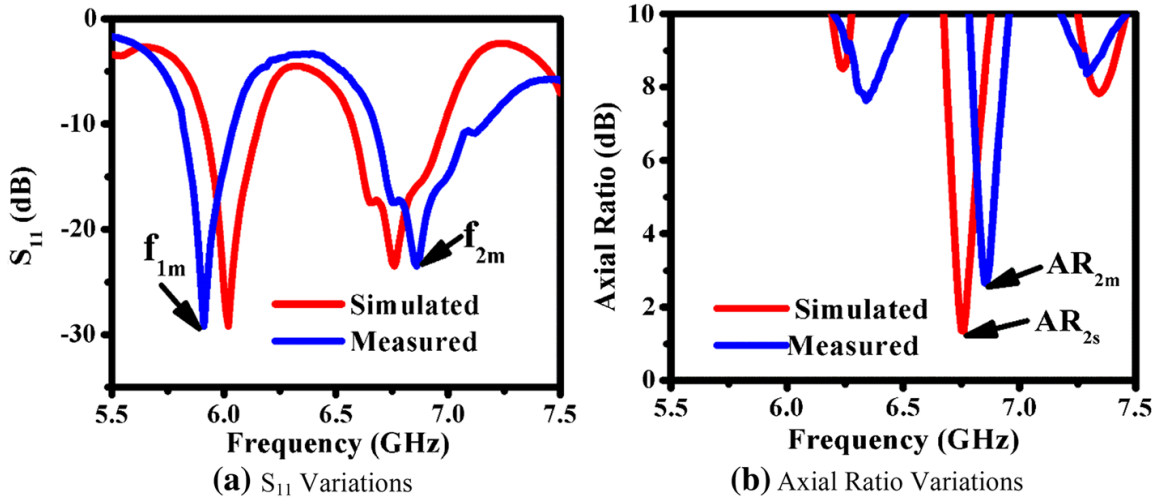

(a) S_{11} Variations **(b)** Axial Ratio Variations

Fig. 5 Comparison of measured and simulated results

C_2. For validating the designed antenna, its prototype is fabricated and characterized. The top-view and bottom-view are shown in Fig. 4. The S_{11} values of the fabricated prototype are measured using Agilent N5230A network analyzer. A comparison between measured and simulated -parameters is depicted in Fig. 5.

The simulated resonant frequencies are observed as 6.020 GHz and 6.755 GHz, respectively whereas their corresponding measured values are observed as 5.900 GHz and 6.860 GHz. Thus, a very good conformity is achieved if these simulated values (i.e., 6.020 GHz and 6.755 GHz) are compared to their corresponding measured values (5.900 GHz and 6.860 GHz). Moreover, the difference between them might be due to the error in fabricating the prototype especially staking of two substrates. Furthermore, the simulation does not include the effect of the connector as well as the amount of solder wire used to connect the PCB board to the connector.

The bandwidth of the designed antenna is also calculated both for simulated and measured results. During simulation, the bandwidth of 3.99% or 240 MHz (5.915 GHz to 6.155 GHz) is achieved for $S_{11} \leq -10$ dB corresponds to first resonant frequency and 5.98% or 405 MHz (6.575–6.98 GHz) corresponds to second resonant frequency. During measurement, it is

Table 1 Effect of DGS on performance comparison

Antenna	Frequency (GHz)	Gain (dB)	Axial Ratio (dB)
Without DGS	6.0010 & 6.7910	6.4019 & 2.4914	16.7169 & 4.8349
With DGS	6.0200 & 6.7550	8.3279 & 2.0822	15.2427 & 1.0913

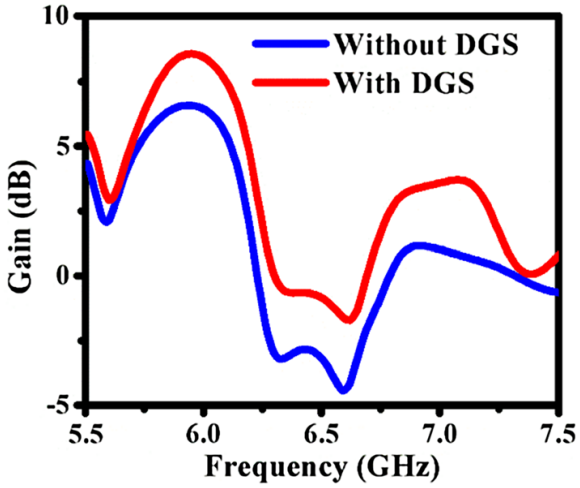

Fig. 6 Effect of DGS on antenna gain (Simulated)

achieved as 3.98% or 235 MHz (5.815–6.05 GHz) and 6.99% or 480 MHz (6.675–7.155 GHz) is achieved corresponding to first and second resonant frequency, respectively. Overall, a good agreement is achieved between simulated bandwidth and measured bandwidth.

Figure 5b depicts the comparison of measured and simulated axial ratio. The axial ratio corresponds to simulated 6.755 GHz is observed as 1.0913 dB whereas 2.6 dB axial ratio corresponds measured frequency of 6.86 GHz. Consequently, both the values are under 3 dB i.e., capable of circular polarization. Further, the 3 dB axial ratio bandwidth is observed as 60 MHz (6.72–6.78 GHz) corresponding to 6.775 GHz frequency and 30 MHz (6.84–6.87 GHz) corresponding 6.86 GHz frequency. To recapitulate, first frequency provides linear polarization for both simulation and measured results.

The performance of designed antenna is also analyzed by considering a ground plane (GP) of size 188×188 mm^2 which is about three times of the size of the substrate [36, 37]. The performance of the designed antenna has been observed up to satisfaction level but only at the cost of increased size of designed antenna. Hence, the overall size of the antenna geometry is reduced from 188×188 mm^2 to only 70.0×70.0 mm^2 by using DGS. The DGS is created by inserting four small-size slots in the grounding surface. The dimensions of the inserted slots have already been described in section II. Hence, by this modification in the ground plane, the size of designed antenna remains as the size of the substrate and the performance also increases. This performance improvement is observed in terms of dual-resonance, gain, axial ratio, radiation patterns, etc. The effect of inserting DGS on the performance of dual-resonance, gains and axial ratio is mentioned in Table 1 whereas the gain improvement without and with DGS is illustrated in Fig. 6. The comparison of measured and simulated values of performance parameters are also illustrated in Table 2.

The gain values corresponding to dual-resonance are also calculated using Friis Transmission equation as mentioned below:

$$P_R = \frac{P_T G_T G_r \lambda^2}{(4\pi R)^2} \tag{1}$$

Table 2 Simulated and measured performance comparison

Parameters	Optimized antenna	
	Simulated values	Measured value
Frequencies	$f_{1s} = 6.020$ GHz & $f_{2s} = 6.775$ GHz	$f_{1m} = 5.900$ GHz & $f_{2m} = 6.860$ GHz
Gains	$G_{1s} = 8.3279$ dB & $G_{2s} = 2.0822$ dB	$G_{1m} = 8.18$ dB & $G_{2m} = 2.19$ dB
Axial Ratio	$AR_1s = 15.2427$ dB & $AR_2s = 1.0913$ dB	$AR_{1m} = 18.33$ dB & $AR_{2m} = 2.6$ dB

For the used experimental setup, the different variables have the values as follows:

P_T = Cable Loss = − 8.5 dB,
P_{1R} = Received Power (Max. at 0^0) at $f_1 = -44.7$ dB,
P_{2R} = Received Power (Max. at 0^0) at $f_2 = -52$ dB and
R = distance between testing antenna and horn antenna = 200 cm.

Now the wavelength, λ for both frequencies is computed as:

$$\lambda_1 = \frac{c}{f_1} = 5.08 \text{ cm} \tag{2}$$

$$\lambda_2 = \frac{c}{f_2} = 4.37 \text{ cm} \tag{3}$$

The intermediate factor used in (1) is computed as follows:

$$K_1 = \left(\frac{\lambda_1}{4\pi R}\right)^2 = \left(\frac{5.08}{4 \times 3.14 \times 200}\right)^2 = -53.88 \text{ dB}\left[10\log_{10} \text{K}\right] \tag{4}$$

$$K_2 = \left(\frac{\lambda_2}{4\pi R}\right)^2 = \left(\frac{4.37}{4 \times 3.14 \times 200}\right)^2 = -55.19 \text{ dB } \left[10\log_{10} \text{K}\right] \tag{5}$$

Now, finally the gain (dB) is computed as follows:

$$G_{1r} = P_{1r} - P_T - G_T - K_1 = 8.18 \text{ dB} \tag{6}$$

$$G_{2r} = P_{2r} - P_T - G_T - K_2 = 2.19 \text{ dB} \tag{7}$$

These calculated gain values are also compared in Table 2.

Achieved radiation efficiency from simulated results has been found as around 95% which is illustrated in Fig. 7. The achieved radiation patterns of the designed antenna are shown in Fig. 7. Figure 8a, b illustrate E- and H-patterns at 6.02 GHz, Fig. 8c, d illustrate E- and H-patterns at 6.65 GHz, Fig. 8e, f illustrate E- and H-patterns at 6.755 GHz while Fig. 8g, h illustrate E- and H-pattern sat 6.90 GHz. Radiation patterns of 6.65 GHz, 6.755 GHz and 6.90 GHz are shown as they are all corresponding to the operating band of circularly polarized frequency. Nearly 20 dB of difference between co- and cross-polarization is observed in all patterns. Simulated and measured patterns

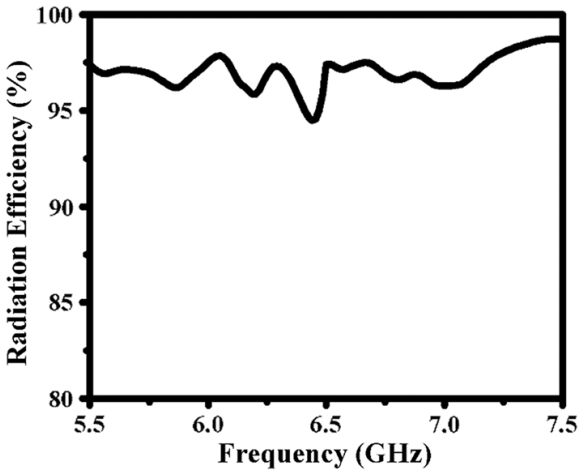

Fig. 7 Radiation efficiency versus frequency (Simulated)

support each other which is displayed in same graph. Thus, the designed microstrip antenna is qualified enough in terms of polarization purity.

4 Comparison of Proposed Antenna

A comparison of investigated salient characteristics, i.e., antenna size, frequency range, maximum gain and maximum radiation efficiency of the designed antenna with published works is enlisted in Table 3. Kenari et al. [25–32] has done a substantial work on slot antennas for wideband applications [25–32]. Few of these works are studied in Sect. 1 and compared with this work in Table 3. The proposed antenna structure in this paper has simpler structure, dual polarization application, reasonable bandwidth (around 4% and 7%), better gain (maximum 8.3 dB), excellent radiation efficiency (minimum radiation efficiency ~95%) and more than 20 dB separation between co and cross polarization. Thus, this antenna demonstrates better performance in terms of design, bandwidth, gain and polarization purity.

5 Conclusion

In this communication, a rectangular patch has been proposed to improve gain for the dual-frequency and dual-polarization application. Eight numbers of small slots on the radiating patch as well as four numbers of small slots in the ground plane have been used to achieve improved gain with dual-polarization. For validation purpose, a prototype has also been fabricated and characterized. A very good convergence between measured and simulated results has been achieved over the entire operating band which supports the effectiveness of the proposed work. A significant amount of improvement in antenna gain has also been observed by inserting the slots on the radiating surface as well as in the ground plane.

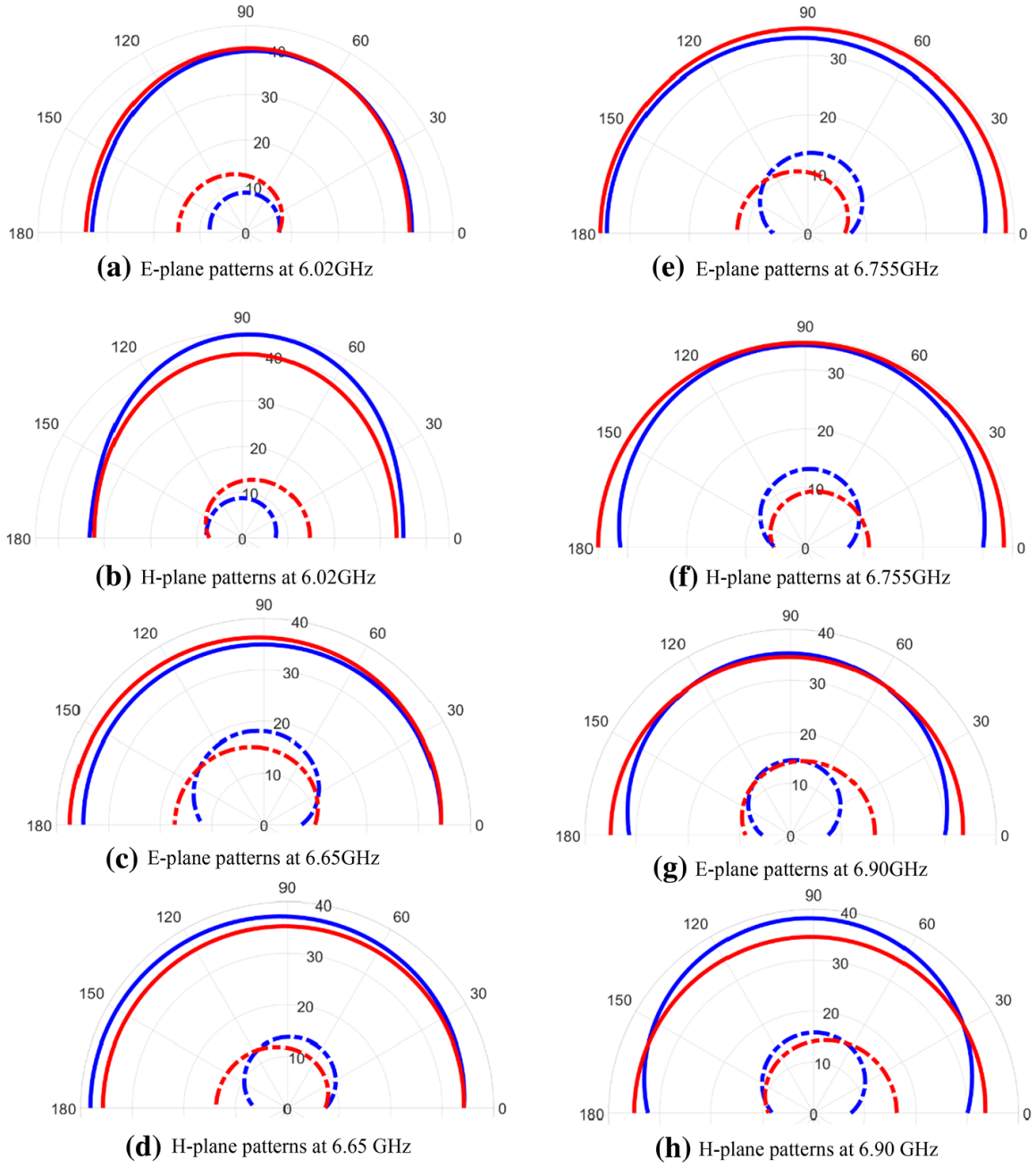

Fig. 8 Achieved radiation patterns for antenna-4 (blue lines indicate simulated and red lines indicate measured results). (Color figure online)

Circular polarization is obtained for second resonant frequency by corner truncation of the patch. The Encouraging amount of gain at first resonant frequency and circular polarization at second resonant frequency help to act it as a better candidate for high gain, dual-frequency as well dual-polarization applications in wireless communications.

Table 3 Comparison of the proposed antenna with existing reference

Reference	Antenna size (mm^3)	Frequency range (GHz)	Maximum gain (dB)	Maximum efficiency (%)
[23]	24.12×24.12×15.48	1.40–2.70	6.38	90
[24]	41.3×48.5×1.52	1.75–2.50	7.02	95.00
[25]	19×16×0.8	0.50–6.60	4.00	83.00
[26]	54.91×68.18×14.55	0.10–0.90	1.20	57.10
[27]	48.32×43.72×0.80	0.115–2.90	2.35	78.85
[28]	15×15×0.80	0.50–3.05	3.05	48.00
[29]	23×17×1.60	0.48–6.5	3.70	73.00
[30]	25.9×10.90×1.60	1.00–4.20	1.50	35.00
	25.9×10.90×1.60	0.75–4.50	3.50	60.00
[31]	13.50×12.70×0.80	1.00–5.00	5.35	84.12
[32]	35×26×1.60	0.50–12.50	5.27	81.30
This paper	41.3×48.5×1.52	5.5–7.5	8.33	98.00

References

1. Kumar, S., Kanaujia, B. K., Sharma, A., Khandelwal, M. K., & Gautam, A. K. (2014). Single-feed cross-slot loaded compact circularly polarized microstrip antenna for indoor WLAN applications. *Microwave and Optical Technology Letters, 56*(6), 1313–1317.
2. Kumar, C., & Guha, D. (2012). linearly polarized elliptical microstrip antenna with improved polarization purity and bandwidth characteristics. *Microwave and Optical Technology Letters, 54*(10), 2309–2314.
3. Kumar, S., Kanaujia, B. K., Khandelwal, M. K., & Gautam, A. K. (2015). Single-feed circularly polarized stacked patch antenna with small-frequency ratio for dual-band wireless applications. *International Journal of Microwave and Wireless Technologies, 8*(8), 1207–1213.
4. Khandelwal, M. K., Kanaujia, B. K., Dwari, S., Kumar, S., & Gautam, A. K. (2015). Triple band circularly polarized compact microstrip antenna with defected ground structure for wireless applications. *International Journal of Microwave and Wireless Technologies, 8*(6), 943–953.
5. Gao, S., & Sambell, A. (2005). Simple broadband dual-polarized printed antenna. *Microwave and Optical Technology Letters, 46*(2), 144–148.
6. Liang, X.-L., Zhong, S.-S., & Wang, W. (2005). Design of a dual-polarized microstrip patch antenna with excellent polarization purity. *Microwave and Optical Technology Letters, 44*(4), 329–331.
7. Row, J.-S., Yeh, S.-H., & Wong, K.-L. (2000). Compact dual-polarized microstrip antennas. *Microwave and Optical Technology Letters, 27*(4), 284–287.
8. Yang, T. Y., Hong, W., & Zhang, Y. (2015). Wideband high-gain low-profile dual-polarized stacked patch antenna array with parasitic elements. *Microwave and Optical Technology Letters, 57*(9), 2012–2016.
9. Gao, S., & Sambell, A. (2005). Dual-polarized broad-band microstrip antennas fed by proximity coupling. *IEEE Transactions on Antennas and Propagation, 53*(1), 526–530.
10. Sim, C.-Y.-D., Chang, C.-C., & Row, J.-S. (2009). Dual-feed dual-polarized patch antenna with low cross polarization and high isolation. *IEEE Transactions on Antennas and Propagation, 57*(10), 3321–3324.
11. Shad, Saeideh, Rahimian, Zahra, & Bemani, Mohammad. (2016). Design of a wideband dual-polarized microstrip patch antenna with novel structure for WLAN application. *Microwave and Optical Technology Letters, 58*(7), 1599–1602.
12. Shynu, S. V., Raj, R. K., Chandran, A. R., & Anandan, C. K. (2004). Single-feed dual-frequency dual polarized microstrip antenna with hexagonal slot. *IEEE Antennas and Propagation Society Symposium, 4,* 4380–4383.

13. Lin, S., Qi, S.-S., Wu, W., Fang, D.-G. (2013). Single-fed dual-band dual-polarized U-slot patch antenna. In *Microwave workshop series on RF and wireless technology biomedical and healthcare application (IMWS-BIO), 2013 IEEE MTT-S International* (pp. 1–3).
14. Prajapati, P. R., Patnaik, A., & Kartikeyan, M. V. (2014) Design of single feed dual band dual polarized microstrip antenna with defected ground structure for aeronautical and radio navigation applications. In *General assembly and scientific symposium (URSI GASS), 2014 XXXIth URSI* (pp. 1–4).
15. Kundukulam, S. O., Paulson, M., Aanandan, C. K., Mohanan, P., & Vasudevan, K. (2000). Dual-band dual-polarized compact microstrip antenna. *Microwave and Optical Technology Letters, 25*(5), 328–331.
16. Paulson, M., Kundukulam, S. O., Aanandan, C. K., & Mohanan, P. (2001). A new compact dual-band dual-polarized microstrip antenna. *Microwave and Optical Technology Letters, 29*(5), 328–331.
17. Afshinmanesh, F., Marandi, A., & Shahabadi, M. (2008). Design of a single-feed dual-band dual-polarized printed microstrip antenna using a boolean particle swarm optimization. *IEEE Transactions on Antennas and Propagation, 56*(7), 1845–1852.
18. Yuan, H. Y., Zhang, J. Q., Qu, S. B., Zhou, H., Wang, J. F., Ma, H., et al. (2012). Dual-band dual-polarized microstrip antenna for compass navigation satellite system. *Progress in Electromagnetics Research C, 30,* 213–223.
19. Uddin, N., Chen, Z. N., & Qing, X. (2012). Compact circularly polarized asymmetric-slotted microstrip patch antennas. *Microwave and Optical Technology Letters, 54*(8), 1920–1927.
20. Kumar, S., Kanaujia, B. K., Khandelwal, M. K., & Gautam, A. K. (2014). Stacked dual-band circularly polarized microstrip antenna with small frequency ratio. *Microwave and Optical Technology Letters, 56*(8), 1933–1937.
21. Chakraborty, S., & Chattopadhyay, S. (2016). Substrate fields modulation with defected ground structure: a key to realize high gain, wideband microstrip antenna with improved polarization purity in principal and diagonal planes. *Int J RF and Microwave CAE, 26,* 174–181.
22. Liu, Y., Li, X., Yang, L., & Liu, Y. (2017). A dual-polarized dual-band antenna with omni-directional radiation patterns. *IEEE Transactions on Antennas and Propagation, 65*(8), 4259–4262.
23. Chen, K., Yuan, J., & Luo, X. (2017). Compact dual-band dual circularly polarized annular-ring patch antenna for BeiDou navigation satellite system application. *IET Microwaves, Antennas and Propagation, 11*(8), 1079–1085.
24. Roy, C., Khan, T., & Kanaujia, B. K. (2017). Performance parameters prediction of slotted microstrip antennas with modified ground plane using support vector machine. *International Journal of Microwave and Wireless Technologies, 9*(5), 1169–1177.
25. Alibakhshikenari, M., Virdee, B. S., & Limiti, E. (2018). Triple-band planar dipole antenna for omni-directional radiation. *Microwave and Optical Technology Letters, 60,* 1048–1051.
26. Alibakhshikenari, M., Virdee, B. S., Ali, A., & Limiti, E. (2018). A novel monofilar-Archimedean metamaterial inspired leaky-wave antenna for scanning application for passive radar systems. *Microwave and Optical Technology Letters, 60,* 2055–2060.
27. Alibakhshikenari, M., Virdee, B. S., See, C. H., Abd-Alhameed, R., Ali, A., Falcone, F., et al. (2018). Wideband printed monopole antenna for application in wireless communication systems. *IET Microwaves, Antennas and Propagation, 12*(7), 1222–1230.
28. Alibakhshikenari, M., Limiti, E., Naser-Moghadasi, M., Virdee, B. S., & Sadeghzadeh, R. A. (2017). A new wideband planar antenna with band-notch functionality at GPS, Bluetooth and WiFi bands for integration in portable wireless systems. *International Journal of Electronics and Communications, 72,* 79–85.
29. Alibakhshikenari, M., Virdee, B. S., Ali, A., & Limiti, E. (2018). "Miniaturized planar-patch antenna based on metamaterial L-shaped unit-cells for broadband portable microwave devices and multiband wireless communication systems. *IET Microwaves, Antennas and Propagation, 12*(7), 1080–1086.
30. Alibakhshi-Kenari, M., Naser-Moghadasi, M., Sadeghzadeh, R. A., Virdee, B. S., & Limiti, E. (2017). New CRLH-based planar slotted antennas with helical inductors for wireless communication systems, RF-circuits and microwave devices at UHF-SHF bands. *Wireless Personal Communications, 92*(3), 1029–1038.
31. Alibakhshi-Kenari, M., Naser-Moghadasi, M., Sadeghzadeh, R. A., Virdee, B. S., & Limiti, E. (2016). Bandwidth extension of planar antennas using embedded slits for reliable multiband RF communications. *International Journal of Electronics and Communications, 70*(7), 910–919.
32. Alibakhshi-Kenari, M., Naser-Moghadasi, M., Sadeghzadeh, R. A., & Virdee, B. S. (2016). Hexa-band planar antenna with asymmetric fork-shaped radiators for multiband and broadband communication applications. *IET Microwaves, Antennas and Propagation, 10*(5), 471–478.
33. Ansoft HFSS 14.0, Ansoft Corporation, Pittsburgh, PA.

34. Baudha, S., & Kumar, V. D. (2015). Corner truncated broadband patch antenna with circular slots. *Microwave and Optical Technology Letters, 57*(4), 845–849.
35. Gautam, A. K., & Kanaujia, B. K. (2013). A novel dual-band asymmetric slit with defected ground structure microstrip antenna for circular polarization operation. *Microwave and Optical Technology Letters, 55*(6), 1198–1201.
36. Huang, J. (1983). The finite ground plane effect on the microstrip antenna radiation patterns. *IEEE Transactions on Antennas and Propagation, 31*(4), 649–653.
37. Lier, E., & Jakobsen, K. R. (1983). Rectangular microstrip patch antennas with infinite and finite ground plane dimensions. *IEEE Transactions on Antennas and Propagation, 31*(6), 978–984.

Publisher's Note Springer Nature remains neutral with regard to jurisdictional claims in published maps and institutional affiliations.

Chandan Roy has obtained his M.Tech. degree in Communication and Signal Processing Engineering specialization in 2016 from National Institute of Technology (An Institute of National Importance, Ministry of HRD, Government of India), Silchar, India under Bangladesh Scholarship Scheme, 2014–2016. Prior to that, he has obtained his B.Sc. degree in Electrical and Electronic Engineering from Khulna University of Engineering and Technology, Bangladesh in 2013. Currently he is working toward the Ph.D. degree in Electrical Engineering from Poly-Grames Research Center, Ecole Polytechnique de Montreal, Montreal, Quebec, Canada. His research interests include Artificial Neural Networks (ANN), microwave device and circuit modeling, and computer-aided design of tunable devices.

Dr. Taimoor Khan is an Assistant Professor in the Department of Electronics and Communication Engineering at National Institute of Technology (An Institute of National Importance, under Ministry of Human Resource Development, Government of India) Silchar, India, where he serves as a full-time faculty member from 2014. He worked as a Visiting Assistant Professor in Telecommunication Field of Study at Asian Institute of Technology, Bangkok, Thailand under Secondment Program of Ministry of HRD, Government of India for the duration of September–December, 2016. Prior to joining National Institute of Technology Silchar, he served several organizations such as Delhi Technological University (Formerly Delhi College of Engineering), Government of NCT of Delhi, Delhi, India for more than 2 years; Netaji Subhas Institute of Technology Patna, India for more than 1 year and Shobhit Institute of Engineering and Technology (a Deemed University), Meerut, India for more than 9 years. Dr. Khan had awarded his Ph.D. degree in Electronics and Communication Engineering from National Institute of Technology (An Institute of National Importance, under Ministry of Human Resource Development, Government of India) Patna, India in the year 2014. He obtained his Master's degree in Communication Engineering from Shobhit Institute of Engineering and Technology (a Deemed University), Meerut, India (2009); Bachelor degree in Electronics and Communication Engineering from The Institution of Engineers (India), Kolkata, India (2005), and Polytechnic diploma in Electronics Engineering from Government Polytechnic Saharanpur, India (2001). His active research interest includes Communication Engineering, Printed Microwave and Millimeter Wave Circuits, Electromagnetic Band gap Structures, Computational Electromagnetics, and Artificial Intelligence Paradigms in Communication Engineering. He has published over 28 research papers in international journals, including IEEE, Wiley, PIER, etc. as well as in international/national conference proceedings, including AEMC, APACE, ISMOT, etc. In addition, he has successfully organized several academic events such as Workshop, Faculty Development Program, Expert Lecture Series, etc. as well as attended several

international/national conferences of repute. He is an active member of IEEE (USA), life member of IEI (India), and life member of IAE (Hong Kong).

SVM Tuned NARX Method for Wind speed & power Prediction in Electricity Generation

Vijay kumar
School of Renewable Energy and Efficiency
NIT Kurukshetra Haryana, India
Vijay5686@gmail.com

Yash Pal
Department of Electrical Engineering
NIT Kurukshetra Haryana, India
yashpal@nitkkr.ac.in

M.M. Tripathi
Department of Electrical Engineering
Delhi Technological University
New Delhi, India
mmtripathi@dce.ac.in

***Abstract*—Due to continuous depleting of conventional energy reserves as well as global warming issues has diverted world attention towards non conventional energy sources. Out of different non conventional energy sources wind can be consider the cleanest source with minimum possible pollution or harmful emissions and has the potential to decrease the relying on conventional energy sources .Wind energy can play a major role to meet our energy demands, however, it faces various problems such as intermittent nature, instability in frequency. To reduce such issues the idea of futuristic wind speed trends and weather conditions are required. This paper suggests a method for wind speed, power forecasting using NARX and Support Vector Machine (SVM). This hybrid technique can select most suitable data segment from available data. These data segments are used for the training and validation of SVM model. The historical data used is from Kolkata region wind energy farm.**

Keywords—Wind power forecasting, Artificial Neural Network, NARX, SVM, Size optimization, Mean Absolute Percentage Error.

I. INTRODUCTION

The people of world today faces two, significant problem, first to enhance energy generation to meet the required demand and secondly to minimize the global warming effect due to energy generation and utilization by conventional sources. To reduce these significant problems we have to increase the contribution of non conventional energy sources in electricity generation such as wind power. As wind is highly unpredictable and its reliability for energy generation is not up to mark [1], [2]. So, forecasting of wind speed with minimum possible error will help in the improvement of reliable power generation, risk minimization and highly economical operation. Wind power generation is proportional to the cube of wind speed so any error in speed prediction will lead error in power generation. For reliable power generation accurate wind speed prediction is essential. For accuracy point of view the estimation of future value of wind speed with certainty is very difficult [3]. Currently various techniques are used for the prediction of wind speed and power such as Physical method, Numerical weather Prediction, artificial intelligence method, ARMA model, Persistence method, Statistical method, hybrid approach etc. Physical method is generally good for long term forecasting which involved physical based equations for the conversion of data from certain period of time to forecasted value [4]. Statistical method is pattern based technique and more effective for short term forecasting as it involve curve fitting for prediction [5]. Artificial intelligence (AI) method is also used for wind speed forecasting, the beauty of AI technique is that future time series data can be predicted without knowledge of any prior defined mathematical model. With the occurrence similar patterns probability of error can be minimized and simultaneously and accuracy significantly decreases with increase in time horizon [6]. In Numerical weather prediction (NWP) model, parameters selections are very crucial steps, and involve geographical area, special resolution, temporal resolution, time horizon and accuracy of computational time [7]. This work mainly suggests the implementation of SVM and NARX for prediction of speed & power of wind available from historical wind data of Indian wind energy farms.

II. ARTIFICIAL NEURAL NETWORK APPROACH

In early days artificial neural network (ANN) was mainly used for the conventional load and price forecasting in power market. Now days it is widely used in wind power forecasting. Due to non linear nature of wind speed many researchers used ANN for wind speed and power forecasting as ANN is a great tool and easily understands the complication and non-linear bonding between the data without any prior assumption [8]. Its structure is composed basic element in parallel and work on the basis of biological nervous systems. To perform a particular function ANN can be trained by changing weights of its different connections. After receiving the input neuron it gives the output through the activation function compared from its output and depending on conditions weights are modified to meet the best output. Artificial neural networks can extract the dependency of the variable in training process by showing a non linear complex relationship [9]. For non linear function approximation, time series based estimation of climate variables in separate time horizon ANN gives better result as compare to traditional methods [10]-[11].

For wind speed and power prediction Artificial Neural Network is a considerably accurate technique. Feed forward and error back-propagation algorithm based model used by Lapedes for the wind speed prediction gives the satisfactory result. [12]. On the other hand Song also proposed an ANN based model to estimate one-step ahead wind speed and power prediction and it provide good result as compare to Lapedes when wind data variation rate is very low [13]. Figure 1 and figure 2 shows the Feed forward- back propagation (FFBP) and Radial basis neural network structure.

Basic elements for the activation pattern or input vector can be supply by input layer source nodes that involve the input signal for the hidden layer neurons and output of hidden layer will work as input to output layer of the network.

978-1-5386-7339-3/18/$31.00 ©2018 IEEE

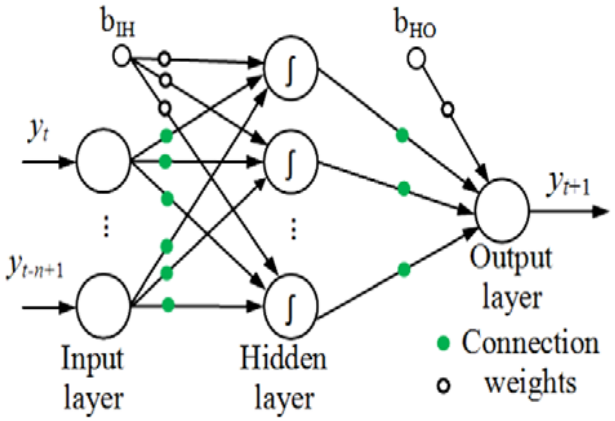

Fig. 1. Feed forward- back propagation network

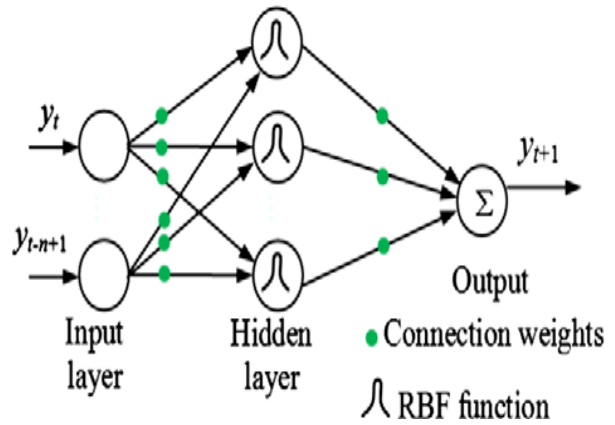

Fig. 2. Radial basis function neural network

The Radial basis function neural network takes multi-input and gives the single-output it have three basic layer such as input, hidden and output layer. The Radial basis function network output nodes shows linear relationship of a function called as basis function. The basis function gives nonzero response in hidden layer only when input ranges in small localized value of the input [14].

III. NARX Neural Network

For time series modeling a nonlinear autoregressive exogenous model (NARX) is used, which associate exogenous input of the current value to the past value of same time series or current and past value of driving (exogenous) series. This model can be represented algebraically as equation 1.

$$Y_t = F\left(y_{t-1}, y_{t-2}, y_{t-3}, \ldots, u_t, u_{t-1}, u_{t-2}, u_{t-3}, \ldots \right) + \varepsilon_t \ldots (1)$$

Here y is the variable of interest, u is the externally determined variable and εt error .This structures has capacity to perform nonlinear modeling without any previous knowledge of relationships between input variables and output variables.

Figure 3 indicate a multilayer ANN. The bias unit is denoted by labeled "+1" and corresponds to the intercept term. The Layer1, Layer2 and Layer3 are called as input layer, hidden layer and output layer respectively. This network has 3 input 3 hidden and 1 output units. Its parameters are indicated as below.

(W, b) = (W(1), b(1), W(2), b(2)) where Wij(l) indicate weight associated with unit j in layer l , and i unit in layer l + 1, bi(l) is the associated bias with unit i in layer l+1and ai(l) indicate the activation of unit i in layer l.

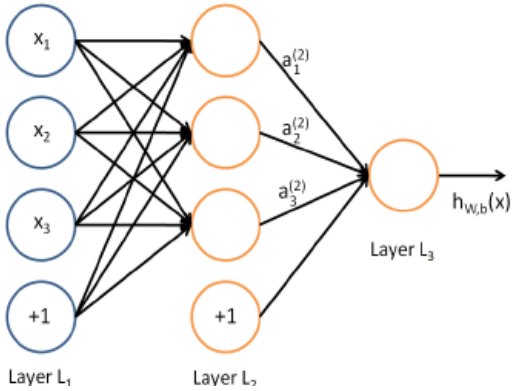

Fig. 3. Multilayer Artificial Neural Network

Neurons and network output are given by equations. 2, 3, 4 and 5.

$$a_1^{(2)} = f\left(W_{11}^{(1)} x_1 + W_{12}^{(1)} x_2 + W_{13}^{(1)} x_3 + b_1^{(1)} \right) \ldots \quad (2)$$

$$a_2^{(2)} = f\left(W_{21}^{(1)} x_1 + W_{22}^{(1)} x_2 + W_{23}^{(1)} x_3 + b_2^{(1)} \right) \ldots \quad (3)$$

$$a_3^{(2)} = f\left(W_{11}^{(1)} x_1 + W_{32}^{(1)} x_2 + W_{33}^{(1)} x_3 + b_3^{(1)} \right) \ldots \quad (4)$$

$$h_{W,b}(x) = f\left(W_{11}^{(2)} a_1^{(2)} + W_{12}^{(2)} a_2^{(2)} + W_{13}^{(1)} a_3^{(3)} + b_1^{(2)}\right). \quad (5)$$

NARX neural network with exogenous inputs uses the previous data as input for the prediction the future time series [15].

Historical wind speed and power Data has collected from Kolkata region wind energy farms during 2015 and utilizes the wind parameters such as speed, density, direction, temperature, power respectively to predict the future value of wind speed and power. All the data are normalized in the range of -1 to +1. For the complete neural network, design of three basic fields such as input, output neurons and hidden elements are essential. Feed forward activity connections are used which connects al the neuron of field 1 to the every neurons of field 2.Two weights, one denoting for the activation of neurons of hidden layer, second for determination the activation of output neuron. By implementing the BP algorithm, in every training historical data set, the weights of different connections can be change to minimize the error between the predicted and actual data. These changes can be start from the output, through each hidden layer, up to last condition is reached. Forecasted wind data such as speed and power is used for comparison with the actual data. Error between actual and forecasted can be minimize by compromising the total weights, hidden layers, delay, learning parameter [16] & [17].

Figure 4 indicate the Procedure for forecasting wind speed and power by NARX.

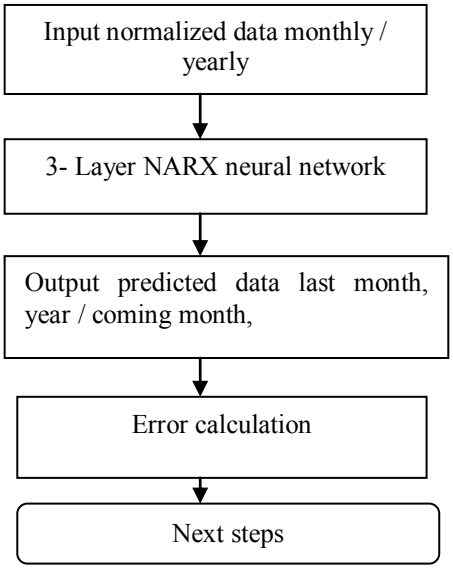

Fig. 4. Procedure for forecasting

IV. Error Parameters

Performance of any forecasting model is examined by various parameters such as root mean square error (RMSE), mean bias error (MBE) and mean absolute error (MAE). Equation 6, 7 and 8 shows the expression for these indicators [22]-[23].

(i) Root mean square error (RMSE)

$$RMSE = \sqrt{\frac{1}{N}\sum_{j=1}^{N}(P_{mj} - P_{cj})^2} \qquad (6)$$

(ii) Mean bias error (MBE)

$$MBE = \frac{1}{N}\sum_{j=1}^{N}\left(P_{mj} - P_{cj}\right) \qquad (7)$$

(iii) Mean absolute error (MAE)

$$MAE = \frac{1}{N}\sum_{j=1}^{N}\left|(P_{mj} - P_{cj})\right| \qquad (8)$$

Where Pmj is jth measured value, Pcj is jth calculated value and N is the number of times that observation taken. In this work, mean absolute percentage error (MAPE) is calculated for the predicted error. Where Pmj is jth measured value, Pcj is jth calculated value and N is the number of measurement taken. In this work, mean absolute error (MAE) is calculated for the predicted error.

V. Support Vector Machine (SVM)

Support vector machine comes n the category of learning method and advantages is that it involve less computational steps and suitable to provide globally optimal result. Instead of many advantages it has some disadvantages also such as data segment searching for same pattern from large data. So before training of SVM data processing is very important for proper forecast result [18]-[19]. SVM is very good for dealing the nonlinear classification / regression with implementing kernel function that changes the nonlinear low dimension problem into high dimension linear space. It consist mainly two parts SVC and SVR [20]-[21]. Figure 5 shows the proposed SVM model for the prediction of wind parameters such as speed and power. In this model first we normalized the value of available historical wind speed and power data for Kolkata region during the year of 2015. Processed data set which are highly correlated are used for training and validation of Support Vector Machine model and forecasted parameters such as wind speed and power is used for the calculation of maximum absolute percentage error (MAPE) and square mean error (SME).

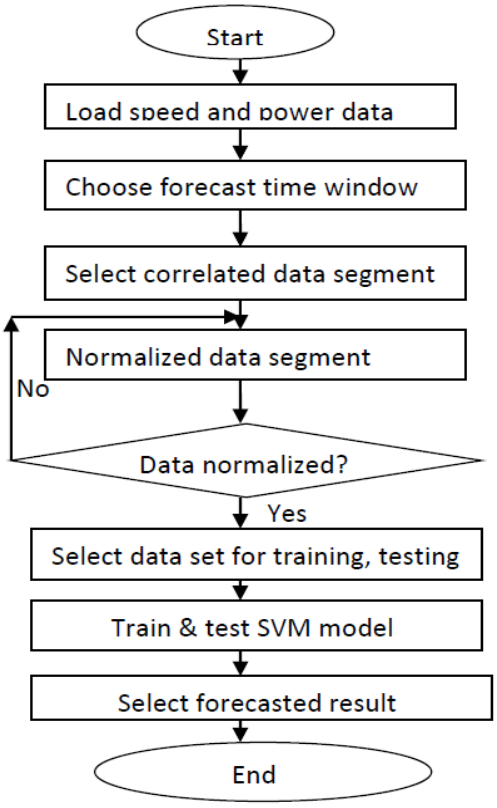

Fig. 5. Proposed SVM model

VI. Results and Discussion

In this paper, forecasted parameters of wind such as speed and power is carried out with NARX and SVM model. Multi layer ANN is used in the condition for the optimum number of hidden neurons can be achieved by repeated simulations for the minimization of predicted error (MAPE) and to improvement in regression. When same data is forecasted with SVM it gives the better result as compare to NARX by improving the MAPE.

A. Wind speed & power forecasting by NARX

The historical data of wind such as direction, speed, air density, power & temperature for the prediction of wind speed, after getting the forecasted wind speed it is further utilize to predict the power [23]. Forecasted parameters accuracy estimated with the calculation of MAPE. Wind speed and power forecasting has been carried out by using historical data for the time span hour, day, week and month

from Kolkata region wind energy farm. Figure 6, 7and 8 represent the hourly , day ahead and weekly forecasting of wind speed with ANN and SVM, and corresponding MAPE of wind speed and power as the function of each month, as well as wind speed training and validation time response by NARX and SVM are shown in figure 9, 10, 11, and 12 respectively.

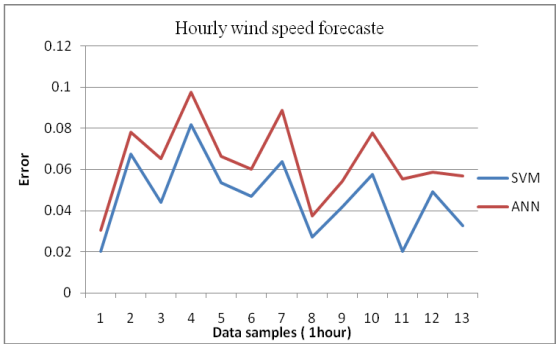

Fig. 6. Hourly wind speed forecast by ANN & SVM

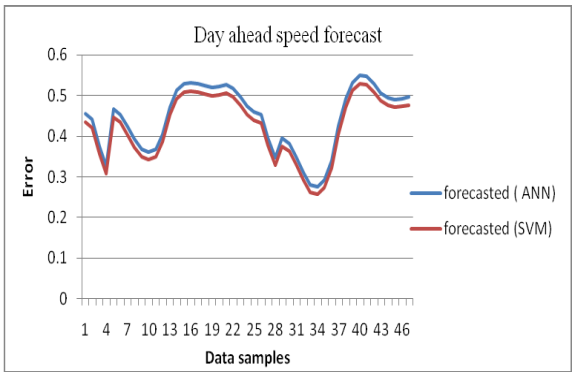

Fig. 7. Day Ahead wind speed forecast by ANN & SVM

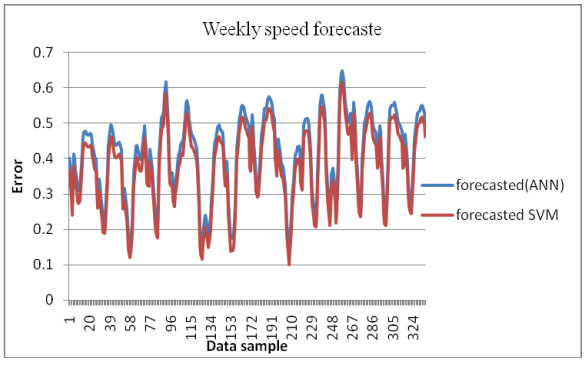

Fig. 8. Weekly wind speed forecast by ANN & SVM

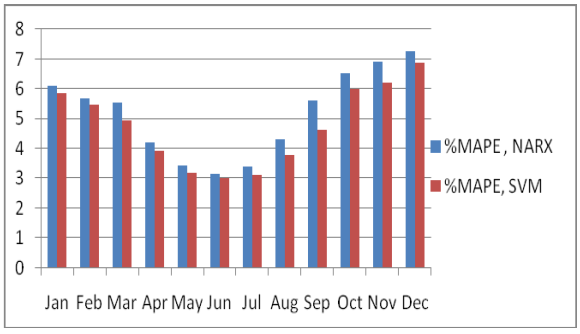

Fig. 9. MAPE for wind speed by NARX and SVM-2015

B. *Power forecasting with NARX & SVM*

By using the historical data sets of wind such as speed, power, direction, temperature and considering speed, power as input and forecasted value of speed and power is obtained. The historical wind data set 2015 of Kolkata region wind energy farm is used in this paper. Wind power is predicted by NARX and SVM model. The accuracy of error forecasting parameters such as speed and power is evaluated in terms of MAPE [22].

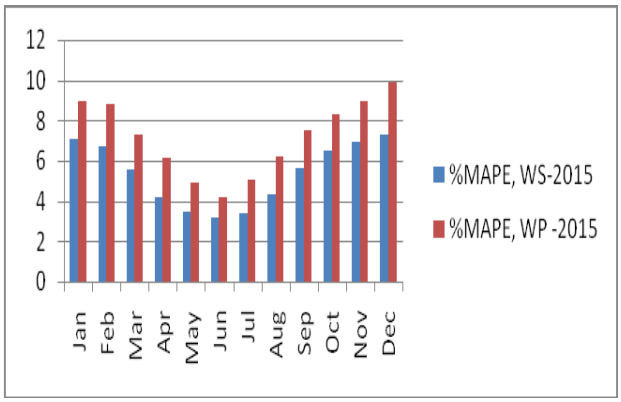

Fig. 10. MAPE for wind speed, power by NARX -2015

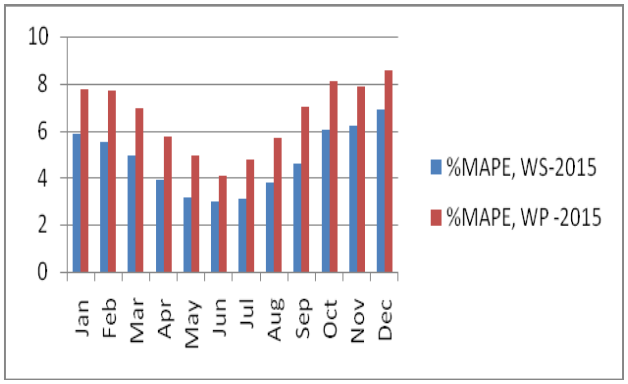

Fig. 11. MAPE for wind speed, power by SVM -2015

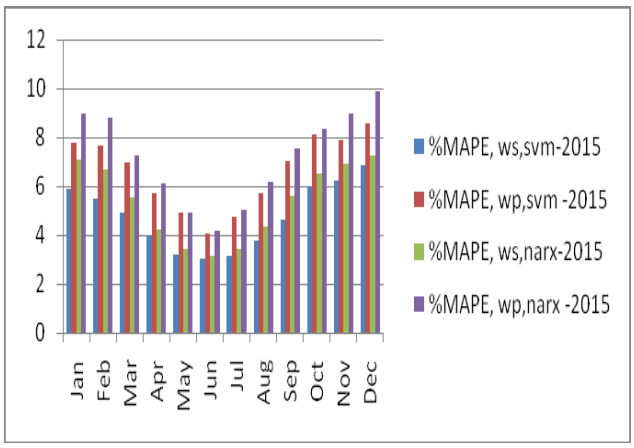

Fig. 12. MAPE for wind speed, power by SVM and NARX

All the forecasted value of wind speed and power are shown in Table-I and Table-II, as well as MAPE values are depicted in Table III.

TABLE I. FORECASTING WIND SPEED RESULT

Time	Actual speed (m/s)	Forecasted speed NARX	Forecasted speed SVM
5:30 AM	2.453	2.052	2.141765
6:30 AM	3.571	3.241	3.330765
7:30 AM	6.075	5.986	6.075765
8:30 AM	7.133	6.982	7.071765
9:30 AM	7.439	6.234	6.323765
10:30AM	7.693	6.345	6.434765
11:30AM	7.544	7.234	7.323765
12:30 PM	6.626	6.345	6.434765
1:30 PM	5.788	5.897	5.986765
2:30 PM	5.508	5.673	5.762765
3:30 PM	4.762	4.345	4.434765
4:30PM	3.865	3.452	3.541765
5:30 PM	4.28	3.986	4.075765
6:30 PM	4.366	4.123	4.212765
7:30PM	4.738	4.342	4.431765
8:30 PM	5.069	5.324	5.413765
9:30PM	5	4.896	4.985765
10:30PM	4.732	4.324	4.413765
11:30 PM	4.36	3.245	3.334765
MSE		56.43	52.32
MAPE		8.64	7.34

TABLE II. FORECASTING WIND POWER RESULT

Time	Actual power (kW)	Forecasted power NARX	Forecasted power SVM
5:30 AM	0.054	0.076	0.049
6:30 AM	0.301	0.21	0.298
7:30 AM	1.778	1.52	1.653
8:30 AM	2.85	2.45	2.56
9:30 AM	3.217	3.17	3.11
10:30 AM	3.518	3.21	3.56
11:30AM	3.335	2.98	3.56
12:30 PM	2.303	1.97	2.13
1:30 PM	1.54	1.41	2.13
2:30 PM	1.316	1.13	1.21
3:30 PM	0.831	0.76	0.987
4:30PM	0.408	0.29	0.567
5:30 PM	0.587	0.46	0.453
6:30 PM	0.626	0.52	0.564
7:30PM	0.818	0.96	0.986
8:30 PM	1.021	1.12	1.34
9:30PM	0.972	1.01	1.23
10:30PM	0.814	0.98	0.932
11:30 PM	0.621	0.897	0.612
MSE		52.23	49.12
MAPE		9.25	7.67

TABLE III. % MAPE FOR NARX AND SVM

Input parameters	Forecasted parameters	MAPE (NARX)	MAPE (SVM)
Wind speed 2014	Wind speed 2015	15.25	14.87
Wind power 2014	Wind power 2015	17.56	15.34
Wind speed January 2014	Wind power January 2015	9.91	11.43
Wind speed 2014	Wind power of 2015	14.36	12.67
Wind speed of 1h	Wind speed of next hour	8.78	7.89
Wind speed of 1h	Wind power of 1h	9.56	8.25
Wind speed of 1 day	Wind speed of next day	7.58	7.37
Wind speed of 1 day	Wind power of 1 day	10.34	10.12
Wind speed of 1 week	Wind speed of next week	11.34	9.89

VII. CONCLUSIONS

For the correct forecasting of wind power the accuracy of wind speed is very important. In this work long-term and short term prediction of wind speed and power is carried out for historical data available Kolkata region wind energy farm during 2015 using NARX neural network and SVM. The main purpose of this work is to predict the normal trend of the wind speed and corresponding power with minimum possible MAPE for coming year by analyzing the previous trends of the wind speed and power for the previous years that may improve the forecasted results of long and short term. With the development of hybrid model with NARX and SVM the accuracy of wind speed and power can also improve. In this work NARX and SVM both are used for forecasting and result shows that SVM provide the better result than NARX in term of forecasted error, MAPE and MSE.

REFERENCES

[1] E. W. E. Association, "Large scale integration of wind energy in the European power supply: Analysis, issues,and recommendations,"publications/grid/051215_Grid_report.pdf, 2005.

[2] 2006 Minnesota P. S. Georgilakis, "Technical challenges associated with the integration of wind power into power systems," Renew. Sustain. Energy Rev., vol. 12, no. 3, pp. 852–863,2008.

[3] Integration S.-D. Kwon, "Uncertainty analysis of wind energy potential assessment," Appl. Energy, vol. 87, no. 3, pp. 856–865, 2010.

[4] Z. Zheng, Y. Chen and M. M. Huo., "An overview: The development of prediction technology of wind and photovoltaic power generation," Energy Procedia, vol.12,pp.601–608, 2011.

[5] S. S. Soman, H. Zareipour, O. Malik et al., "A review of wind power and wind speed forecasting methods with different time horizons," in Proc. North Amer. Power Symp.(NAPS),Arlington,TX, USA,pp.1–8. 2010.

[6] W. Yuan-Kang and H. Jing-Shan, "A literature review of wind forecasting technology in the world," in Proc. IEEE Lausanne Power

[7] Niya chen, Zheng Qian, Ian T. Nabney and Xiaofeng Meng, "Wind Forecasts Using Gaussian Processes and Numerical Weather Prediction," IEEE Trans.Power Syst. Vol.29, No.2, pp. 656-665, March 2014.

[8] Aoife M. Foley, Paul G. Leahy, Antonino Marvuglia, and Eamon J. McKeogh, "Current methods and advances in forecasting of wind power generation, Renewable Energy 37 (2012) pp. 1-8.

[9] J. P. S. Catalão, H. M. I. Pousinho, and V. M. F. Mendes, "An Artificial Neural Network Approach for Short-Term Wind Power Forecasting in Portugal"Intelligent System Applications to Power Systems, ISAP '09. 15th International Conference. 2009.

[10] K. Philippopoulos and D. Deligiorgi, "Application of artificial neural networks for the spatial estimation of wind speed in a coastal region with complex topo-graphy," Renew. Energy, vol. 38, no. 1, pp. 75–82, 2012.

[11] D.A.Fadare,"The application of artificial neural networks to mapping of wind speed profile for energy application in Nigeria," Appl. Energy, vol. 87, no. 3, pp. 934–942, 2010.

[12] Lapedes A, Farber R. Nonlinear signal processing using neural networks: forecast and system modeling. Los Alamos National Lab. Los Alamos, NM. Technical report LAUR872662; 1987.

[13] Song YD. A new approach for wind speed prediction.Wind Eng 2000;24(1): pp.35–47.

[14] Kisi O. Comparison of different ANN techniques in river flow prediction. Civ Eng Environ Syst 2007(24), pp.211–31.

[15] I.M. Yassin ,M. N. Taib , A.Zabidi ;,H. A. Hassan,"Comparison between NARX parameter estimation methods with Binary Particle Swarm Optimization-based structure selection method" ,Evolutionary Computation (CEC), 2010 IEEE Congress , 18-23 July 2010, Barcelona.

[16] K. G. Upadhyay, A. K. Choudhary and M. M.Tripathi, "Shortterm Wind Speed Forecasting using Feed-forward Backpropagation Neural Network",International Journal of Engineering, Science and Technology (IJEST) ISSN: 2141-2839, Vol. 3, No. 5, 2011, pp. 107-112.

[17] A. K. Choudhary, K. G. Upadhyay and M. M.Tripathi, "Soft computing applications in wind speed and power prediction for wind energy", 5th IEEE Power India Conference, Dec. 2012, Murthal, India.

[18] Qianyao Xu, Dawei He, Ning Zhang, and Chongqing Kang. "A short-term wind power forecasting approach with adjustment of numerical weather prediction input by data mining". IEEE Transactions on Sustainable Energy, pp.1283–1291, 2015.

[19] Hanieh Borhan Azad, Saad Mekhilef, and Vellapa Gounder Ganapathy. "Long-term wind speed forecasting and general pattern recognition using neural networks". IEEE Transactions on Sustainable Energy, pp.546–553, 2014.

[20] L. Zhu, Q. H. Wu, M. S. Li, and L. Jiang. "Support vector machine-based short-term wind power prediction with false neighbors filtered". In International Conference on Renewable Energy Research and Applications, pp.740–744, 2013.

[21] Yi Ren, P. Suganthan, and N. Srikanth. "A novel empirical mode decomposition with support vector regression for wind speed forecasting". IEEE Transactions on Neural Networks & Learning Systems, pp. 1-7, 2014.

[22] Harendra Kumar Yadav, Yah Pal, M.M Tripathi. ― Photovoltaic power forecasting methods in smart power grid‖, IEEE India conference (INDICON), 2015.

[23] Jyothi Varanasi, M.M.Tripathi. " Artificial Neural Network based wind speed and power forecasting in US wind energy farms." IEEE 1st International Conference on power Electronics, Intelligent Control and Energy Systems (ICPEICES), 2016.

Pattern Analysis and Applications
https://doi.org/10.1007/s10044-019-00811-5

SHORT PAPER

Text area segmentation from document images by novel adaptive thresholding and template matching using texture cues

Seba Susan[1] · **K. M. Rachna Devi**[1]

Received: 27 September 2018 / Accepted: 22 March 2019
© Springer-Verlag London Ltd., part of Springer Nature 2019

Abstract
This paper presents a new perspective of text area segmentation from document images using a novel adaptive thresholding for image enhancement. Using sliding windows, the texture of the enhanced image is matched with that of a fixed training template image containing the typed letters 'dB.' The affine-invariant, low-dimensional difference theoretic texture feature set is used for the texture measurement. The distance matrix is binarized using Otsu threshold, and the '0' pixels indicate the text area. One primary contribution of this paper is the novel adaptive thresholding for document image enhancement prior to the extraction of texture cues. The proposed adaptive thresholding mimics the ability of the human eye to iteratively adjust to varying light intensities through iterative gamma correction followed by contrast stretching so that the text becomes well defined against the background clutter. The text blobs so segmented are binarized using Yanowitz and Bruckstein method of text binarization, and the results are applied for evaluation with respect to the ground-truth annotations. We tested our algorithm on the benchmark DIBCO 2009, 2010, 2011, 2012, 2013 document image datasets in comparison with the state of the art. The high precision–recall and *F*-score values establish the efficiency of our approach.

Keywords Adaptive thresholding for document images · Thresholding · Gamma correction · Text binarization · Text area localization · Difference theoretic texture features

1 Introduction

The problem of text binarization and segmentation from document images has been consistently the focus of the research community [1] due to its potential in the field of education, digitization of libraries and preservation of old manuscripts and historical documents [2]. The Web-based deployment of text locating systems [3] and ever-growing online repositories of digitized historical documents [4, 5] are examples of the relevance of this topic in today's context. The problems usually encountered in text binarization are torn, smeared or dirty documents, poor resolution and illumination, background noise and aging artifacts [6, 7]. Several works have been proposed to address these problems [6], some examples being background light intensity normalization [8] and background noise reduction by optimal binarization [9].

The discrimination of the text area from the non-text area is the primary concern in the text binarization problem. Some methods use edge points for segmenting out the text [10], while some others rely on shape information [1], contour tracing [9], contrast enhancement techniques [11, 12] and texture analysis techniques like the Gabor filter [13]. Statistical methods like the conditional random field [14] and Hidden Markov Models [15] have also been used. Machine learning techniques like the support vector machine (SVM) that is used for distinguishing the text from the non-text area in [16] have the disadvantage that the training for the non-text area is just not enough with a wide range of possibilities. The separation of text strings irrespective of font style, size and orientation is achieved in [17] by generating connected components and grouping them using Hough transform into text and graphics categories. In [18], texture discrimination mask was used to segment images of printed documents into text and graphics. This is because a document consists of different physical entities other than text such as figures, tables and background [19] without considering the imaging and aging artifacts.

✉ Seba Susan
seba_406@yahoo.in

[1] Department of Information Technology, Delhi Technological University, New Delhi, India

Published online: 03 April 2019

In our work, we seek to discriminate text from non-text through a new adaptive thresholding followed by affine-invariant texture analysis in order to locate text in any illumination, orientation, font and size in any background. Some other works that consider text as a form of texture are [16, 20] in which support vector machines are used for high efficiency. Texture feature extraction was not investigated though, with mere intensities being used as the features. Language-free segmentation of text using texture features was also explored in [21]. The texture features extracted from the text area were found distinctly different from that of the background in [22]. Gabor filter-based texture features were used for text extraction in [22]. However, its use was limited to printed pages, with handwritten pages not contributing to a uniform texture. In [23], no single texture feature was found sufficient for text extraction. In this paper, we propose a novel document image enhancement based on iterative gamma correction followed by the extraction of affine-invariant texture cues and distance-based matching with a template image. The organization of this paper is as follows: The new adaptive thresholding for document images and the overall methodology of text area segmentation are described in Sect. 2, the results are analyzed in Sect. 3 and the overall conclusions are drawn in Sect. 4.

2 Text area segmentation from document images

The primary contribution of this paper is the combination of a novel adaptive thresholding with affine texture analysis performed on sliding image windows. The texture cues computed from the enhanced image are matched with that of a fixed template image containing a short typewritten word and the areas that match form text blobs that are ultimately binarized displaying the text. The other existing methods on text area segmentation, some of which find mention in the previous section, use parts of this procedure to obtain quick results. While some methods execute text binarization directly [24], others focus on extracting features based on texture, shape, contour or edge points [22], and some others just investigate image enhancement [11]. Our method is a more comprehensive collection of image enhancement, texture analysis, text blob segmentation and binarization, targeting higher segmentation accuracy at the cost of a slight increase in the computational complexity. One significant advantage is the absence of any training module as with SVM classifiers to distinguish text area from non-text area as in [20]. The single template image used is the common reference image for all the document image datasets in our experiments.

2.1 Novel adaptive thresholding of document images incorporating iterative gamma correction

Gamma correction [25] mimics the way our eyes perceive shades or light intensities. We perceive very bright light to be only a fraction brighter than normal light. A work which studies the human response to light is [26], which suggests displaying high-contrast images on limited dynamic range display systems by a logarithmic compression of intensities. We propose an adaptive thresholding scheme involving iterative gamma correction for segregating out the text area from the document image. When the eye adjusts to a scene, it does so in an iterative manner, by adjusting the contrast continually till the intensities stabilize and our eye can distinguish the brighter pages of the document against the darker blur of the background noise. The method by which the eye picks up the salient object in varying light intensities is summarized in a few steps below in the context of our work.

For a grayscale document image with intensities in the range [0, 255], do:

- Perform gamma correction with the gamma value γ less than one, so that the brighter shades (text area) appear less bright and overall contrast is reduced.
- Threshold the document image to separate out the bright (white background in page) cluster from the dark (both text/graphics and noise/artifacts) cluster.
- Iterate the above two steps till the intensities (and therefore the threshold) stabilize and the salient object becomes meaningfully defined; in our case, very dark document details (since threshold has been much lowered) including text are highlighted clearly against the background.
- Finally, increase the overall contrast of the image by stretching the intensities lying above the computed threshold to 1 and stretch the intensities below threshold to 0.

The gamma correction of an image $\boldsymbol{I}$ (with gray-level intensities ranging between 0 and 255) by a factor of γ is defined by

$$I' = (I)^{\gamma} \tag{1}$$

where I' is the gamma-corrected image of the same size as I. To reduce the contrast of the image with intensities in the range [0, 255], we set $\gamma < 1$. However, in order for the iterative process to converge quickly by fine-tuning, γ is set just below 1, about 0.97 for all images, as is the procedure for adjusting of system gammas [27]. A recent work on text binarization [28] is based on a similar principle of the removal of degradation by L0 minimization algorithm and use of contrast feature for enhancing the foreground.

Some of the existing approaches to determine thresholds are Otsu thresholding computed from histograms [29], bi-level thresholding [28] and the Bayesian approach [30].

2.2 Experimental steps

The steps of our proposed method are described below. There are three stages of experimentation as elucidated in the process flowchart in Fig. 1. The initial step is document image enhancement by adaptive thresholding, followed by matching of texture cues from sliding image windows and formation of the distance image (with respect to the fixed template). The last step is the binarization of text blobs derived from the distance image. The three stages are explained below in more detail.

2.2.1 Step 1: image enhancement

This stage comprises of thresholding the image by the new adaptive thresholding algorithm incorporating gamma correction followed by contrast stretching, the steps of which are detailed as follows.

1. Initially binarize the input image $\boldsymbol{I}$ using Otsu thresholding [29]. Let the Otsu threshold computed be T.
2. Let G_1 (brighter cluster with pixel values greater than T) and G_2 (darker cluster with pixel values less than or equal to T) be the two images derived from $\boldsymbol{I}$ after thresholding which are of the same size as $\boldsymbol{I}$. The image intensities are substituted for all the '1' pixels in the binarized image and the '0' intensities are left as it is.
3. Perform gamma correction on G_1 as shown in (1) to obtain the gamma-corrected image G_1'

$$G_1' = (G_1)^{\gamma} \tag{2}$$

4. Store the existing threshold T as T_{old} and compute the new value of T from the average intensity of the bright cluster G_1'. Use the new value of T to threshold $\boldsymbol{I}$ into two clusters G_1 and G_2.
5. Repeat steps 2–4, till the threshold value T stabilizes and converges to T_{old}, up to two decimal places. At this juncture, the dark blur in the second (dark) cluster approximately equals the black intensities in the first (bright) cluster and that is why the threshold converges to a stable value.
6. In order to compensate for the loss of contrast while performing the iterative gamma correction, the contrast stretching [25] of G_1' is achieved as shown below.

$$G_1'' = \left(\frac{1}{1 + \left(\frac{T}{G_1'} \right)^{E}} \right) \tag{3}$$

Contrast stretching involves increasing the brightness of the pixels above the final threshold T and decreasing the intensity of the pixels below T in a nonlinear manner. This highlights only the relevant part of the document containing the text, while the portion containing the noisy artifacts is totally eliminated. In the above equation, E is considered to be 4, determined after lots of empirical trials and sensitivity analysis for obtaining best results. G_1'' is the resulting contrast enhanced image that is next subjected to feature extraction as described below in step 2. Figure 2 demonstrates the image enhancement for a sample document image used in our experiments (sample no. 14 document image from DIBCO 2012).

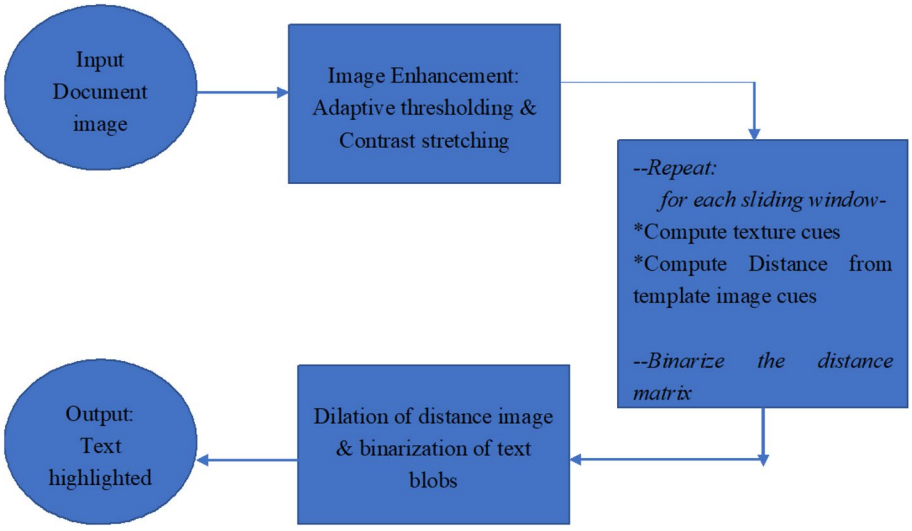

Fig. 1 Process flowchart for our method

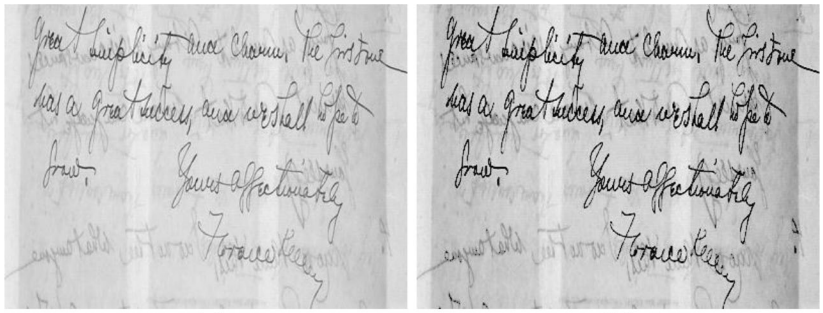

(a) **(b)**

Fig. 2 **a** Original image. **b** Image formed after proposed adaptive thresholding and contrast stretching

2.2.2 Step 2: affine-invariant texture analysis and text blob segmentation

This stage involves segmenting text blobs from the enhanced image G_1'' using the eleven-dimensional affine-invariant difference theoretic texture features (DTTF) [31] based on gray-level difference statistics. The texture recognition problem is addressed in the literature using various means such as co-occurrence matrices [32], Gabor filters [13], Markov random fields [33] and wavelet decompositions [34]. Affine-invariant feature sets are, however, the requirement when it comes to recognizing text of any size or orientation in poor lighting conditions. The feature set in [31] is proved to outperform the rotation-invariant LBP [35], LBPV [36] and the scale-invariant MRS4 filter bank features [37] for texture identification and classification [31]. Due to averaging, these features are invariant to scale, and the use of local and global differences instead of actual intensities brings about illumination invariance. A cyclic reordering of the features starting with the orientation having maximum differences renders it rotation invariant. The high texture recognition rates achieved using the 1-nearest-neighbor classifier in [31] (98.845% for 64,800 scaled, rotated and differently lighted monochrome Brodatz texture samples) are the reason for our choice of the DTTF (source code online [38]) in our current experiment on text segmentation from document snapshots, which require adequate feature representation of slanted, scaled text under uneven lighting conditions.

We create a random image containing the typed word 'dB' (a small letter and a full letter combination) of size 15×20, shown in Fig. 3a, and use it as the training template for identifying the text in all test documents from various sources.

1. From the enhanced image G_1'' resized to 300×400, for a sliding window of size 15×20 (1:20 ratio, same size as template image used for matching) centered at pixel (i, j), find the worst-case (maximum) city-block distance between the 11 template features $\text{DTTF}_{\text{template}}$ and the 11

(a)

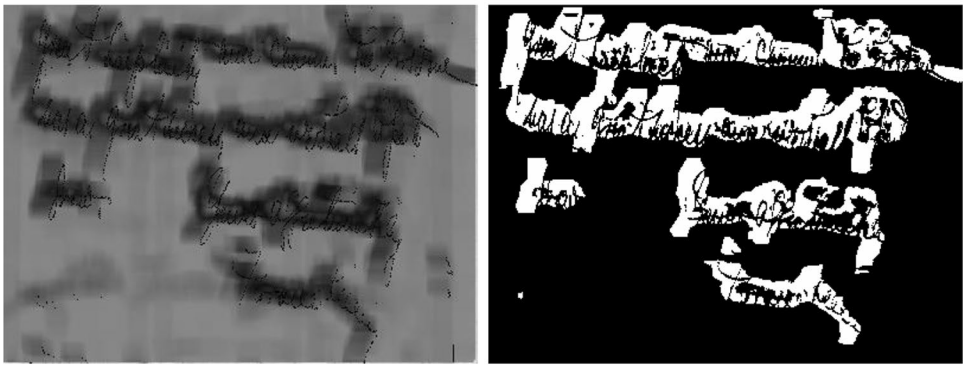

(b) **(c)**

Fig. 3 **a** 15×20 template. **b** Distance matrix based on template matching using DTTF. **c** Thresholded distance matrix

difference theoretic texture features computed from the sliding image window $\mathrm{DTTF}_{\mathrm{window}}(i,j)$ as shown below.

$$\mathrm{dist}(i,j) = \max_{\forall 1,2,\ldots,11 \text{ features}} \left| \mathrm{DTTF}_{\mathrm{template}} - \mathrm{DTTF}_{\mathrm{window}}(i,j) \right| \quad (4)$$

2. The distance matrix being equal to the size of the image is binarized using Otsu threshold to separate the text (dark pixels indicating a match with the template) from the non-text (brighter pixels indicating a mismatch). The outputs for steps 1 and 2 are shown in Fig. 3b, c, respectively, for the sample document image in Fig. 2.
3. The binarized image indicates text area which when multiplied with the original image gives the text blobs in gray scale against a black background.

2.2.3 Step 3: formation of text blobs and binarization

This stage involves the formation and binarization of text blobs derived from the thresholded distance matrix obtained in the previous stage. The detailed steps are as follows:

1. Dilate the binarized distance image using a rectangular (7×10) structuring element. The size of the structuring element is taken to be half of the size of the sliding window (15×20) in step 2 to compensate for the missing parts of words detected in some cases along the boundaries of the detected text.
2. Obtain the original image pixel values for the white ('1') pixels in the dilated image to obtain text blobs.
3. Binarize the segmented text blobs using the Yanowitz and Bruckstein method in [24]. Their method involves interpolating the gray-level values at high-gradient-magnitude regions for constructing a threshold surface. This method is a standard for text binarization though it cannot distinguish text from the foreign objects in the scene like pen, fingers, etc.

The results of applying the above steps on the partial outputs in Fig. 3 are shown in Fig. 4. The binarized text in Fig. 4b is the final output of the proposed method for the document image in Fig. 2.

3 Experimental results and discussions

The coding is implemented in MATLAB 7.9 version software on a 2.3 GHz Pentium processor. Our code for adaptive thresholding of document images is made available online at [39]. We have tested our text segmentation method on five benchmark document image datasets of DIBCO 2009, DIBCO 2010, DIBCO 2011, DIBCO 2012 and DIBCO 2013 [40–43] containing 66 document images in all and provided with ground-truth annotations. All our images are resized to 300×400, and the standard reference template is of size 15×20 as discussed in the previous section. The software implementation of DTTF texture features is available online at [38]. We compare our results with some of the state-of-the-art text binarization methods such as Yanowitz and Bruckstein [24] which was proved in [6, 44] to be the best text binarization tool among several existing methods. Other methods that we have compared with are Niblack's local image thresholding [45] available online at [46] and Sauvola and Pietikäinen's method [47] available online at [48]. The precision, recall and F-score of the text segmentation achieved by all methods for the five datasets are computed and listed in Tables 1, 2, 3, 4 and 5 with the text samples numbered. As observed from the mean precision, recall and F-score values in Tables 1–5, the proposed text segmentation and binarization consistently gives the best results as compared to all other methods. The average or 'Avg' rows in Tables 1–5 indicate a high precision and F-score for the proposed method for all datasets (best values for each database shown highlighted in bold in the last row of each table). The high precision is due to the low number of false positives due to a good discrimination between the text and background. However, in our quest for excluding the

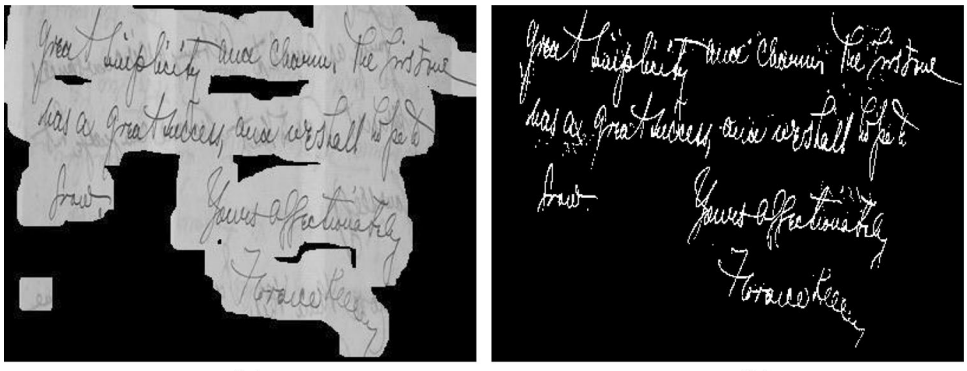

(a) (b)

Fig. 4 **a** Dilation of thresholded distance matrix with values from original image embedded. **b** Binarization of the segmented text blobs using Yanowitz and Bruckstein technique (final output of the proposed method)

Table 1 Results on DIBCO 2009 dataset

Image no.	Proposed method			Yanowitz and Bruckstein [24]			Niblack [45]			Sauvola and Pietikäinen [47]		
	Precision	Recall	*F*-score	Precision	Recall	*F*-score	Precision	Recall	*F*-score	Precision	Recall	*F*-score
1	84.46	90.02	87.15	86.95	88.85	87.89	84.38	91.73	87.90	74.76	95.02	83.68
2	42.94	99.45	59.98	26.26	99.56	41.56	17.49	99.04	29.73	25.39	99.89	40.49
3	79.90	91.08	85.13	72.29	95.55	82.31	68.87	93.33	79.26	51.93	99.81	68.32
4	66.89	83.16	74.14	48.02	98.28	64.51	50.07	96.70	65.98	27.09	99.63	42.60
5	54.92	61.14	57.86	53.07	95.90	68.33	60.86	93.90	73.86	18.82	94.94	31.41
6	82.52	93.34	87.60	76.37	95.24	84.77	71.28	90.27	79.66	58.58	99.69	73.80
7	93.42	92.92	93.17	90.27	95.14	92.64	86.12	91.99	88.96	83.97	99.62	91.13
8	96.61	94.51	95.55	95.62	93.46	94.53	86.13	89.86	87.96	92.20	98.94	95.45
9	79.68	94.66	86.52	69.67	98.19	81.50	73.41	95.24	82.91	59.44	99.83	74.52
10	78.10	93.56	85.13	75.26	94.03	83.60	70.94	88.97	78.94	61.38	99.60	75.96
Avg.	**75.9440**	89.38	**81.22**	69.3780	95.42	78.16	66.9550	93.10	75.51	55.3560	**98.69**	67.73

Table 2 Results on DIBCO 2010 dataset

Image no.	Proposed method			Yanowitz and Bruckstein [24]			Niblack [45]			Sauvola and Pietikäinen [47]		
	Precision	Recall	*F*-score	Precision	Recall	*F*-score	Precision	Recall	*F*-score	Precision	Recall	*F*-score
1	96.01	76.82	85.35	98.26	70.15	81.86	94.13	83.30	88.39	90.38	87.03	88.67
2	88.33	90.54	89.42	89.10	88.11	88.60	78.99	93.42	85.60	77.56	89.09	82.90
3	92.63	84.63	88.45	91.39	82.81	86.89	70.94	87.68	78.43	81.57	90.94	86.00
4	82.01	94.37	87.76	84.98	92.00	88.35	82.53	94.63	88.17	82.52	87.46	84.92
5	54.82	98.75	70.50	41.67	99.17	58.68	36.97	98.92	53.83	30.53	99.96	46.77
6	87.23	84.45	85.82	87.73	80.85	84.15	80.78	87.10	83.82	76.41	90.12	82.70
7	81.62	93.07	86.97	78.12	94.51	85.54	61.69	96.74	75.34	71.11	97.89	82.38
8	85.94	55.87	67.72	83.35	74.83	78.86	76.96	86.17	81.30	73.95	84.36	78.82
9	83.39	88.95	86.08	87.13	84.79	85.94	82.73	92.71	87.44	79.32	85.21	82.16
10	80.76	80.29	80.52	85.40	76.07	80.47	83.94	79.11	81.45	64.94	81.79	72.40
Avg	**83.2740**	84.77	**82.85**	82.7130	84.32	81.93	74.9660	**89.97**	80.37	72.8290	89.38	78.77

background efficiently, some text pixels are missing leading to a marginally higher number of false negatives and thus a lower recall value in Tables 1–5. Niblack's as well as Sauvola and Pietikäinen's methods give the best recall values in Tables 1–5 though they select a substantial amount of the background as well, as evident from their low precisions. Simple morphological operations like opening, closing, erosion and dilation could be used for further enhancing the text segmented by the proposed method. The sizes of the structural elements would be based on average text size that can be deduced from the height of the text blobs segmented in our method. Automation of the post-processing procedure irrespective of the text size, and improvising recall, forms the future scope of our work.

Figures 5, 6, 7, 8 and 9 summarize the text binarization results for some samples of the five DIBCO datasets used for the experimentation, and their corresponding precision–recall and *F*-score values are given in Tables 1–5 by matching sample numbers given in the figure subscripts. Our results are overall visually impressive since they exclude the smears, smudges, shadow writing with only the main text highlighted (Figs. 4–9 all being examples). Especially in Fig. 9, the text in the left side of the page is highlighted only, while the shadow writing on the right side of the page is not detected. The number of missing characters in the binarized text is very less as compared to the other methods. An exception is shown in Fig. 10 where some text lies in a discolored part of the page and is missed out in our results. Even in this case, the precision (and *F*-score) is found best for our method though recall values are less due to the missing words as shown in Table 1 (sample no. 4 from DIBCO 2009 dataset). The text portion is highlighted darkly against the background by our adaptive thresholding technique as shown in Fig. 2b and in all other cases as well. The synthetically created template image for the printed word 'dB' shown in Fig. 3a, sized at 15×20, is found to detect text in all cases with accuracy irrespective of font size, orientation and style

Table 3 Results on DIBCO 2011 dataset

Image no.	Proposed method			Yanowitz and Bruckstein [24]			Niblack [45]			Sauvola and Pietikäinen [47]		
	Precision	Recall	*F*-score	Precision	Recall	*F*-score	Precision	Recall	*F*-score	Precision	Recall	*F*-score
1	80.04	85.40	82.63	71.24	95.85	81.73	64.01	96.07	76.83	59.52	98.04	74.32
2	87.99	89.45	88.71	84.29	94.90	89.28	74.35	96.38	83.94	71.34	96.83	82.15
3	82.25	82.12	82.18	86.81	79.02	82.73	80.26	86.19	83.12	58.10	91.80	71.17
4	74.39	86.83	80.13	62.09	89.89	73.45	62.08	89.35	73.26	41.03	92.93	56.93
5	83.46	93.04	87.99	80.44	94.87	87.06	72.61	93.62	81.79	64.05	99.30	77.87
6	79.17	75.46	77.27	66.30	86.45	75.05	62.09	88.87	73.10	48.18	82.52	60.84
7	62.21	93.93	74.85	37.56	96.16	54.02	29.47	96.06	45.10	31.83	97.77	48.03
8	85.66	91.42	88.45	87.43	91.80	89.56	88.32	88.14	88.23	79.20	96.42	86.92
9	94.58	88.37	91.37	78.98	89.49	83.91	67.50	86.14	75.69	78.14	99.42	87.50
10	68.64	94.41	79.49	65.56	95.03	77.59	60.80	89.80	72.51	49.30	99.50	65.93
11	94.42	90.03	92.17	89.74	91.08	90.41	79.95	87.91	83.74	81.18	98.35	88.95
12	90.59	95.63	93.04	75.74	96.90	85.03	68.26	95.15	79.49	60.97	99.90	75.73
13	75.54	92.00	82.96	67.40	93.51	78.34	70.60	93.68	80.52	56.46	99.54	72.05
14	77.06	96.18	85.56	32.14	98.63	48.48	32.49	95.49	48.48	25.23	99.79	40.27
15	89.21	88.35	88.78	68.61	95.55	79.87	44.41	91.37	59.76	49.90	98.77	66.30
16	91.57	81.14	86.04	93.15	79.04	85.52	88.70	82.00	85.22	84.57	86.29	85.42
Avg	**82.2988**	88.98	**85.10**	71.7175	91.76	78.87	65.3688	91.01	74.42	58.6875	**96.07**	71.27

Table 4 Results on DIBCO 2012 dataset

Image no.	Proposed method			Yanowitz and Bruckstein [24]			Niblack [45]			Sauvola and Pietikäinen [47]		
	Precision	Recall	*F*-score	Precision	Recall	*F*-score	Precision	Recall	*F*-score	Precision	Recall	*F*-score
1	71.43	93.47	81.08	71.37	93.74	81.04	60.18	93.71	73.29	51.44	98.94	67.69
2	79.47	92.05	85.30	82.35	90.43	86.20	77.83	93.95	85.13	71.17	88.16	78.76
3	81.12	94.40	87.26	81.87	92.01	86.64	80.95	96.86	88.19	59.54	98.64	74.26
4	86.03	91.77	88.81	81.18	93.95	87.10	79.89	92.91	85.91	74.70	97.93	84.75
5	63.06	96.73	76.35	51.67	98.96	67.89	43.70	99.41	60.72	40.00	99.81	57.11
6	48.71	98.42	65.17	43.86	99.06	60.80	40.51	99.40	57.56	35.18	99.57	51.99
7	81.28	87.77	84.40	82.04	86.47	84.20	79.70	87.00	83.19	73.63	94.56	82.79
8	68.61	98.81	80.99	59.78	99.89	74.80	65.47	99.68	79.03	40.89	100.0	58.05
9	95.98	90.36	93.09	96.78	88.52	92.47	95.16	89.55	92.27	91.68	95.47	93.69
10	89.42	93.94	91.63	95.33	87.49	91.24	92.17	90.28	91.22	89.40	94.47	91.86
11	90.95	87.91	89.40	95.78	82.91	88.88	91.87	88.12	89.95	84.91	89.52	87.15
12	84.98	83.08	84.02	87.17	82.28	84.66	81.04	93.10	86.65	78.74	83.53	81.07
13	86.77	68.88	76.80	90.91	71.00	79.73	86.43	86.93	86.68	75.43	69.14	72.15
14	73.97	95.45	83.35	64.35	98.66	77.89	52.53	99.21	68.69	49.33	99.04	65.85
Avg	**78.6986**	90.9314	**83.4036**	77.4600	90.3836	81.6814	73.3879	**93.5793**	80.6057	65.4314	93.4843	74.7979

and in any lighting condition. This is attributed to the affine-invariant nature of the texture features used in our work. Some examples of images with the computed distance matrix (with very dark pixels in the distance matrix indicating a match with template) are shown in Fig. 11. These examples verify the utility of a single random training template for detecting handwritten or typed text in any lighting condition or the presence of foreign objects like fingers, pen, etc. Figure 11f shows how the main text is represented by very dark pixels and the shadow writing by lighter pixels in the distance matrix, leading to easy and simple text discrimination by Otsu thresholding. We also conducted a robustness analysis for our adaptive thresholding technique, and the result in the form of the stability of the computed threshold is plotted in Fig. 12 for different quanta of additive Gaussian noise [standard deviation: 0 to 50 considered for six document images]. As shown in Fig. 12, the standard deviation of the computed threshold

Table 5 Results on DIBCO 2013 dataset

Image no.	Proposed method			Yanowitz and Bruckstein [24]			Niblack [45]			Sauvola and Pietikäinen [47]		
	Precision	Recall	*F*-score	Precision	Recall	*F*-score	Precision	Recall	*F*-score	Precision	Recall	*F*-score
1	66.47	67.76	67.11	58.10	83.49	68.52	50.41	91.45	64.99	44.81	94.23	60.73
2	90.25	89.14	89.70	81.63	94.11	87.42	76.34	95.01	84.66	68.07	98.93	80.65
3	78.47	77.04	77.75	81.32	76.64	78.91	72.33	84.03	77.75	69.85	80.75	74.90
4	73.87	99.78	84.89	54.77	99.85	70.74	46.04	99.97	63.05	59.97	100	74.97
5	19.93	99.82	33.23	18.45	99.90	31.15	13.97	100	24.52	19.50	100	32.63
6	58.52	98.35	73.38	58.47	98.36	73.34	50.32	99.41	66.82	47.06	99.76	63.95
7	83.05	23.72	36.90	82.40	44.04	57.40	80.06	71.82	75.71	71.15	56.99	63.29
8	49.89	99.01	66.35	44.49	99.61	61.50	40.35	99.62	57.44	31.44	99.88	47.83
9	80.78	91.80	85.94	73.70	98.52	84.32	60.31	98.70	74.87	65.31	98.97	78.69
10	83.15	98.92	90.35	75.20	99.63	85.71	62.88	99.05	76.93	63.37	99.99	77.57
11	92.36	94.89	93.61	92.62	91.36	91.99	84.58	94.76	89.38	86.54	95.26	90.69
12	86.16	88.46	87.29	83.69	96.52	89.65	81.75	96.43	88.48	44.46	99.50	61.46
13	89.54	92.76	91.12	82.22	97.63	89.27	87.04	93.83	90.31	68.56	99.90	81.31
14	61.84	95.01	74.92	60.84	96.18	74.53	58.27	96.87	72.77	46.09	99.94	63.09
15	93.74	92.46	93.10	93.19	91.58	92.38	91.33	88.46	89.87	86.13	97.44	91.44
16	56.26	96.47	71.08	49.65	98.59	66.04	47.93	96.58	64.06	40.70	99.52	57.77
Avg	**72.7675**	87.8369	**76.0450**	68.1713	91.6256	75.1794	62.7444	94.1244	72.6006	57.0631	**95.0663**	68.8106

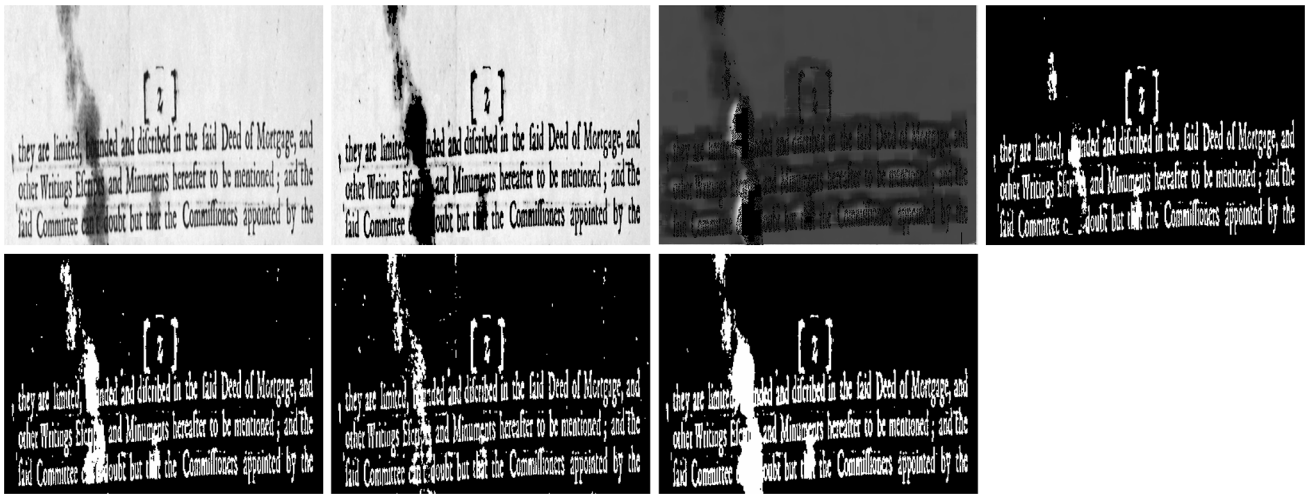

Fig. 5 Text binarization results of a DIBCO 2009 sample (no. 9): proposed method (first row—in the order from left to right): original image, enhanced image, affine-invariant texture analysis, template matching results (distance matrix) and text binarization; comparison methods (second row—in the order from left to right): Yanowitz and Bruckstein [24], Niblack [45] and Sauvola [47]

is minimal for the images corrupted by Gaussian noise with standard deviation up to 5–7, after which the threshold values slightly decline.

4 Conclusions

A novel text segmentation and binarization algorithm is proposed in this paper that is based on a new adaptive thresholding incorporating iterative gamma correction followed by affine-invariant texture cue extraction and template matching. The result is efficient text binarization from benchmark datasets with state-of-the-art comparisons proving the efficiency of our approach. Our results display legible text with a good exclusion of externally induced artifacts and discrimination from non-text matter as reflected from the high *F*-score values.

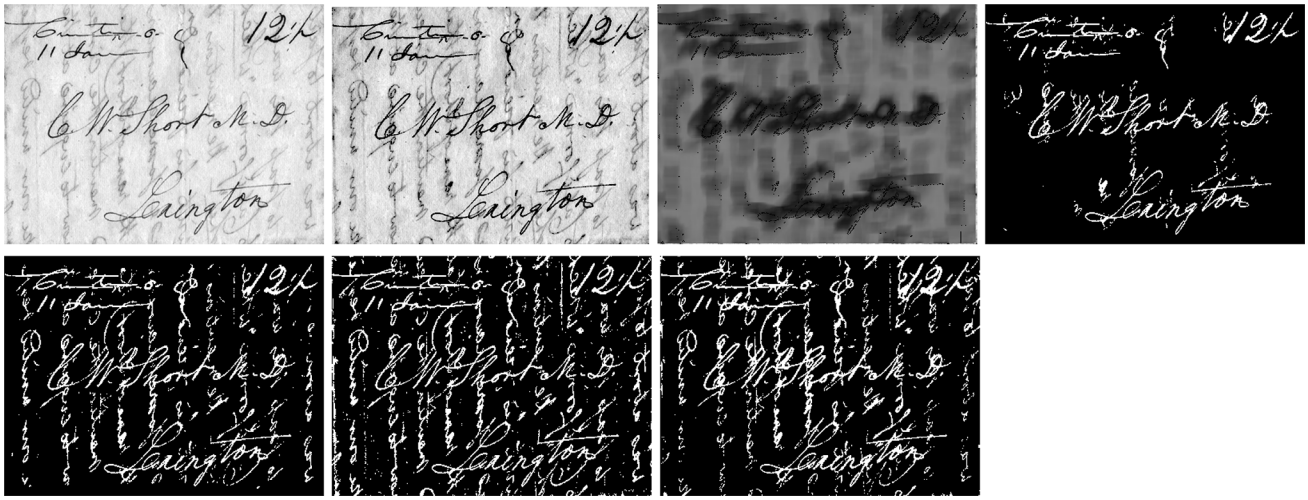

Fig. 6 Text binarization results of a DIBCO 2010 sample (no. 7): proposed method (first row—in the order from left to right): original image, enhanced image, affine-invariant texture analysis, template matching results (distance matrix) and text binarization; comparison methods (second row—in the order from left to right): Yanowitz and Bruckstein [24], Niblack [45] and Sauvola [47]

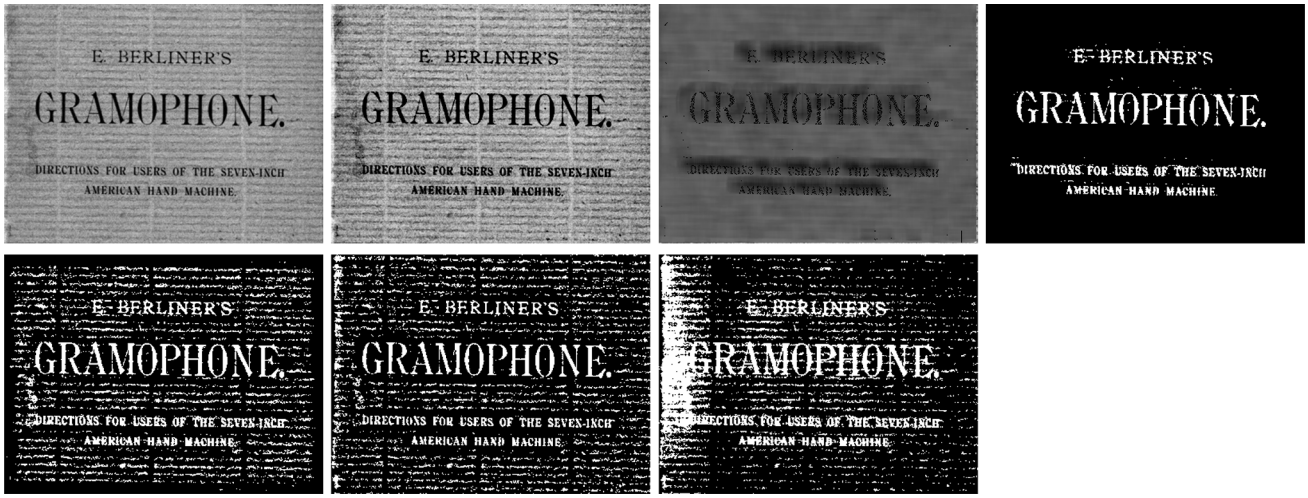

Fig. 7 Text binarization results of a DIBCO 2011 sample (no. 15): proposed method (first row—in the order from left to right): original image, enhanced image, affine-invariant texture analysis; template matching results (distance matrix) and text binarization; comparison methods (second row—in the order from left to right): Yanowitz and Bruckstein [24], Niblack [45] and Sauvola [47]

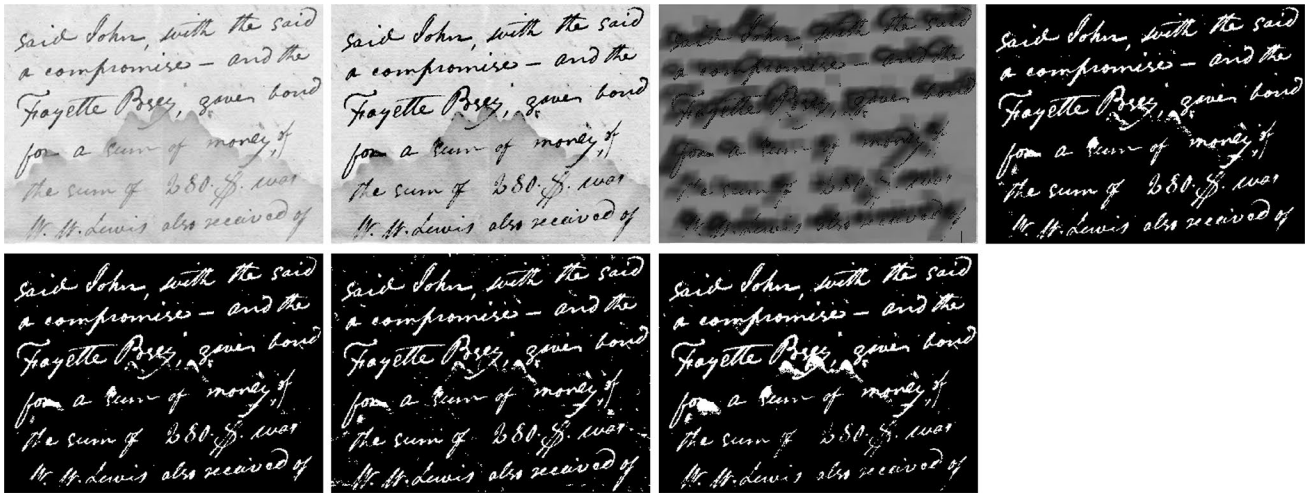

Fig. 8 Text binarization results of a DIBCO 2012 sample (no. 2): proposed method (first row—in the order from left to right): original image, enhanced image, affine-invariant texture analysis, template matching results (distance matrix) and text binarization; comparison methods (second row—in the order from left to right): Yanowitz and Bruckstein [24], Niblack [45] and Sauvola [47]

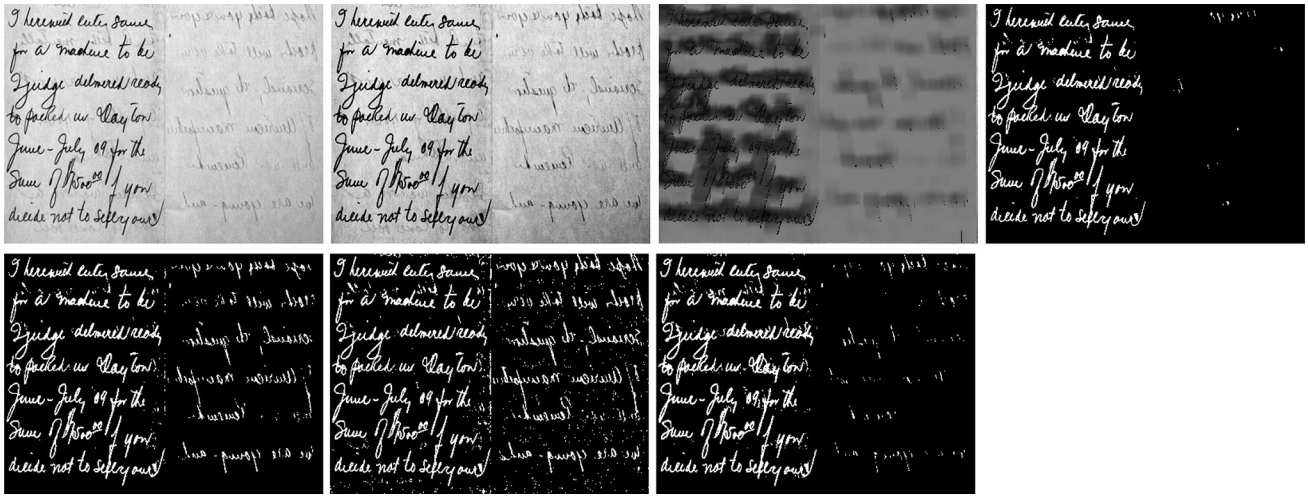

Fig. 9 Text binarization results of a DIBCO 2013 sample (no. 4): proposed method (first row—in the order from left to right): original image, enhanced image, affine-invariant texture analysis, template matching results (distance matrix) and text binarization; comparison methods (second row—in the order from left to right): Yanowitz and Bruckstein [24], Niblack [45] and Sauvola [47]

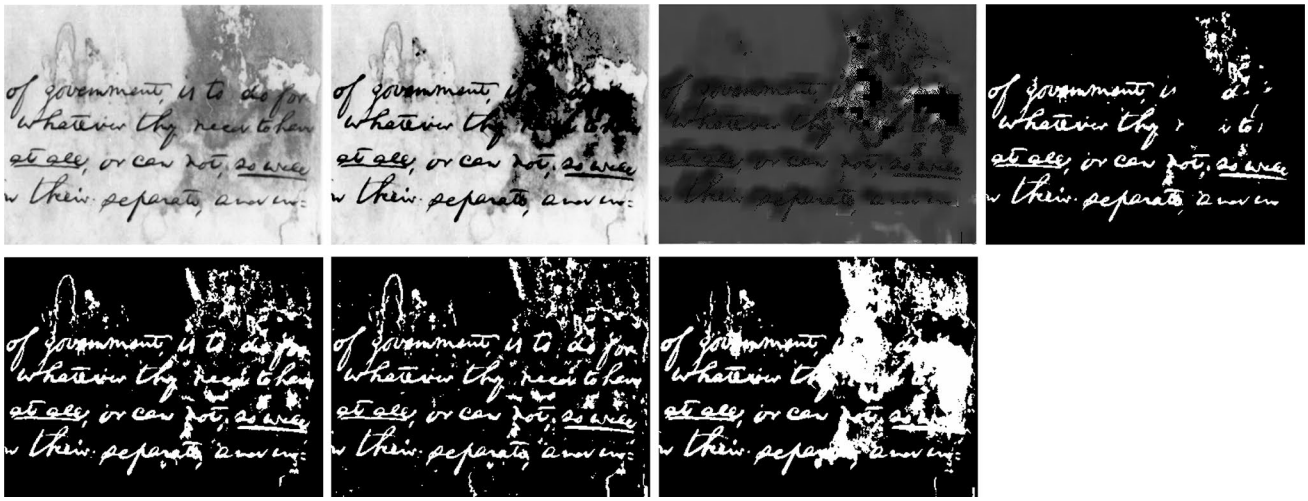

Fig. 10 Text binarization results of a DIBCO 2009 sample (no. 4): proposed method (first row—in the order from left to right): original image, enhanced image, affine-invariant texture analysis, template matching results (distance matrix) and text binarization; comparison methods (second row—in the order from left to right): Yanowitz and Bruckstein [24], Niblack [45] and Sauvola [47]

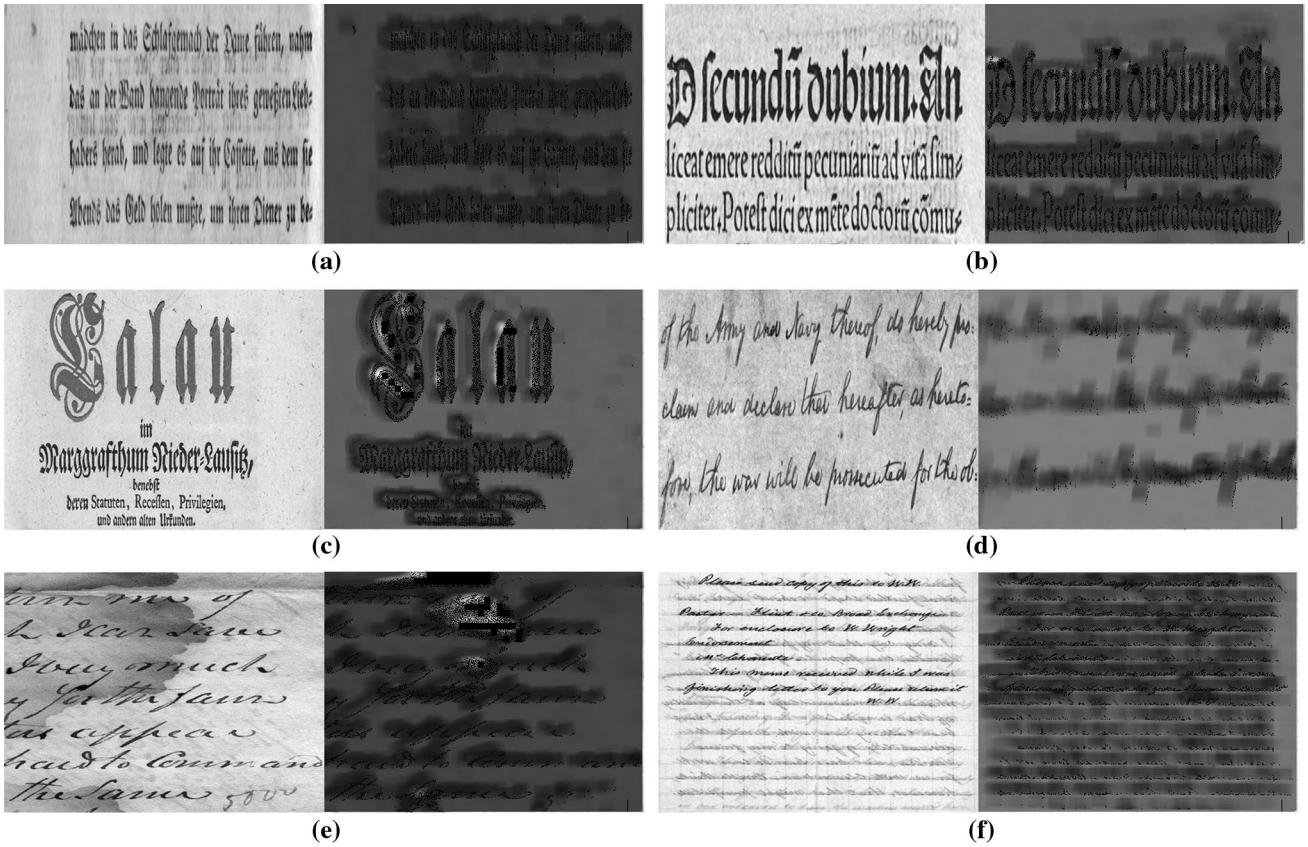

Fig. 11 **a–f** Pair-wise images of text in different fonts, size and styles in the five datasets and the results of texture-based template matching (in the order: original image, distance matrix after matching with template with very dark pixels indicating a match)

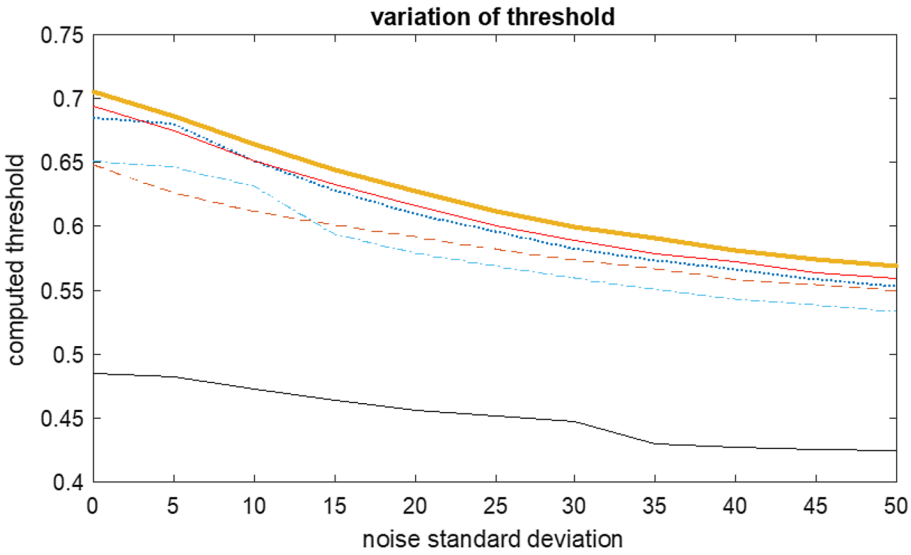

Fig. 12 Robustness analysis of the proposed adaptive thresholding for six instances of document images corrupted by Gaussian noise

Compliance with ethical standards

Conflict of interest The authors declare that they have no conflict of interest.

References

1. Jamal AT, Suen CY (2013) Shape-based analysis for automatic segmentation of Arabic handwritten text. In: Advances in artificial intelligence, Springer, Berlin, Heidelberg, pp 334–339
2. Eskenazi S, Gomez-Krämer P, Ogier J-M (2017) A comprehensive survey of mostly textual document segmentation algorithms since 2008. Pattern Recognit 64:1–14
3. Lucas SM (2005) ICDAR 2005 text locating competition results. In: Eighth international conference on document analysis and recognition, 2005. Proceedings, IEEE, pp 80–84
4. Bukhari SS, Kadi A, Jouneh MA, Mir FM, Dengel A (2017) anyOCR: an open-source OCR system for historical archives. In: 2017 14th IAPR international conference on document analysis and recognition (ICDAR), IEEE, vol 1, pp 305–310
5. Sulaiman A, Omar K, Nasrudin MF (2017) A database for degraded Arabic historical manuscripts. In: 2017 6th international conference on electrical engineering and informatics (ICEEI), IEEE, pp 1–6
6. Leedham G, Chen Y et al (2003) Comparison of some thresholding algorithms for text/background segmentation in difficult document images. In: Proceedings of the seventh international conference on document analysis and recognition, vol 2
7. Likforman-Sulem L, Zahour A, Taconet B (2007) Text line segmentation of historical documents: a survey. Int J Doc Anal Recognit 9(2-4):123–138
8. Shi Z, Govindaraju V (2004) Historical document image enhancement using background light intensity normalization. In: ICPR 2004, Proceedings of the 17th international conference on pattern recognition, 2004, IEEE, vol 1
9. Chamchong R, Fung CC (2011) Character segmentation from ancient palm leaf manuscripts in Thailand. In: Proceedings of the 2011 workshop on historical document imaging and processing, ACM
10. Yuan Q, Tan CW (2001) Text extraction from gray scale document images using edge information. In: Proceedings, sixth international conference on document analysis and recognition, 2001, IEEE
11. Rumley SD (1990) Document scanner. U.S. Patent 4,961,117. Issued 2 October 1990
12. Maurer RP, Barash D (2004) Method for enhancing compressibility and visual quality of scanned document images. U.S. Patent 6,731,821. Issued 4 May 2004
13. Bovik AC, Clark M, Geisler WS (1990) Multichannel texture analysis using localized spatial filters. IEEE Trans Pattern Anal Mach Intell 12(1):55–73
14. Li M et al (2010) Conditional random field for text segmentation from images with complex background. Pattern Recognit Lett 31(14):2295–2308
15. Yamron JP, et al (1998) A hidden Markov model approach to text segmentation and event tracking. In: Proceedings of the 1998 IEEE international conference on acoustics, speech and signal processing, IEEE, vol 1
16. Chen D, Odobez J-M (2002) Comparison of support vector machine and neural network for text texture verification. IDIAP, Martigny
17. Fletcher LA, Kasturi R (1988) A robust algorithm for text string separation from mixed text/graphics images. IEEE Trans Pattern Anal Mach Intell 10(6):910–918
18. Jain AK, Karu K (1996) Learning texture discrimination masks. IEEE Trans Pattern Anal Mach Intell 18(2):195–205
19. Namboodiri AM, Jain AK (2007) Document structure and layout analysis. In: Chaudhuri BB (ed) Digital document processing. Springer, London, pp 29–48
20. Kim KI, Jung K, Kim JH (2003) Texture-based approach for text detection in images using support vector machines and continuously adaptive mean shift algorithm. IEEE Trans Pattern Anal Mach Intell 25(12):1631–1639
21. Jain AK, Zhong Yu (1996) Page segmentation using texture analysis. Pattern Recognit 29(5):743–770
22. Jain AK, Bhattacharjee S (1992) Text segmentation using Gabor filters for automatic document processing. Mach Vis Appl 5(3):169–184
23. Ye Q, Huang Q, Gao W, Zhao D (2005) Fast and robust text detection in images and video frames. Image Vis Comput 23(6):565–576
24. Yanowitz SD, Bruckstein AM (1989) A new method for image segmentation. Comput Vis Graph Image Process 46(1):82–95

25. Gonzalez RC, Woods RE (2002) Digital image processing, 2nd edn. Publishing House of Electronics Industry, Beijing, p 455
26. Drago F, Myszkowski K, Annen T, Chiba N (2003) Adaptive logarithmic mapping for displaying high contrast scenes. Comput Graph Forum 22(3):419–426
27. Iida H, King P-S (1983) Video system having an adjustable digital Gamma correction for contrast enhancement. U.S. Patent 4,394,688. Issued 19 July 1983
28. Jennifer Ranjani J (2014) Bi-level thresholding for binarisation of handwritten and printed documents. IET Comput Vis 9(1):41–50
29. Otsu N (1979) A threshold selection method from gray-level histograms. IEEE Trans Syst Man Cybernet 9(1):62–66
30. Zhang H, Liu G, Chow TWS, Liu W (2011) Textual and visual content-based anti-phishing: a Bayesian approach. IEEE Trans Neural Netw 22(10):1532–1546
31. Susan S, Hanmandlu M (2013) Difference theoretic feature set for scale-, illumination-and rotation-invariant texture classification. IET Image Process 7(8):725–732
32. Susan S, Hanmandlu M (2013) A non-extensive entropy feature and its application to texture classification. Neurocomputing 120:214–225
33. Cross GR, Jain AK (1983) Markov random field texture models. IEEE Trans Pattern Anal Mach Intell 1:25–39
34. Unser M (1995) Texture classification and segmentation using wavelet frames. IEEE Trans Image Process 4(11):1549–1560
35. Ojala T, Pietikaenen M, Maenepae T (2002) Multi-resolution gray scale and rotation invariant texture classification with LBP. IEEE Trans Pattern Anal Mach Intell 24(7):971–987
36. Guo Z, Zhang L, Zhang D (2010) Rotation invariant texture classification using LBP variance with global matching. Pattern Recognit 43:706–719
37. Leung T, Malik J (2001) Representing and recognizing the visual appearance of materials using three-dimensional textons. Int J Comput Vis 43(1):29–44
38. https://in.mathworks.com/matlabcentral/fileexchange/70290-dttf-difference-theoretic-texture-features. Accessed 14 Feb 2019
39. https://in.mathworks.com/matlabcentral/fileexchange/70291-adaptive-thresholding-for-document-images. Accessed 15 Feb 2019
40. Gatos B, Ntirogiannis K, Pratikakis I (2009) ICDAR 2009 document image binarization contest (DIBCO 2009). In: ICDAR, vol 9, pp 1375–1382
41. Pratikakis I, Gatos B, Ntirogiannis K (2010) H-DIBCO 2010-handwritten document image binarization competition. In: 2010 international conference on frontiers in handwriting recognition (ICFHR), IEEE, pp 727–732
42. Pratikakis I, Gatos B, Ntirogiannis K (2012) ICFHR 2012 competition on handwritten document image binarization (H-DIBCO 2012). In: 2012 international conference on frontiers in handwriting recognition (ICFHR), IEEE, pp 817–822
43. Pratikakis I, Gatos B, Ntirogiannis K (2013) ICDAR 2013 document image binarization contest (DIBCO 2013). In: 2013 12th international conference on document analysis and recognition (ICDAR), IEEE, pp 1471–1476
44. Trier OD, Taxt T (1995) Evaluation of binarization methods for document images. IEEE Trans Pattern Anal Mach Intell 17(3):312–315
45. Niblack W (1985) An introduction to digital image processing. Strandberg Publishing Company, Birkeroed
46. http://www.mathworks.in/matlabcentral/fileexchange/40849-niblack-local-image-thresholding. Accessed 14 Feb 2019
47. Sauvola J, Pietikäinen M (2000) Adaptive document image binarization. Pattern Recognit 33(2):225–236
48. http://www.mathworks.in/matlabcentral/fileexchange/40266-sauvola-local-image-thresholding. Accessed 14 Feb 2019

Publisher's Note Springer Nature remains neutral with regard to jurisdictional claims in published maps and institutional affiliations.

ResearchGate

See discussions, stats, and author profiles for this publication at: https://www.researchgate.net/publication/332268701

THE IMPACT OF TECHNOLOGY ADOPTION ON AGRICULTURAL PRODUCTIVITY IN ETHIOPIA: ARDL APPROACH

Article *in* Indian Journal of Economics and Business · January 2019

CITATIONS
0

READS
6

3 authors:

Aynalem Shita
Debre Markos University
4 PUBLICATIONS **0** CITATIONS
SEE PROFILE

Nand Kumar
Delhi Technological University
36 PUBLICATIONS **51** CITATIONS
SEE PROFILE

Seema Singh
Delhi Technological University
34 PUBLICATIONS **22** CITATIONS
SEE PROFILE

Some of the authors of this publication are also working on these related projects:

Dates Extended for Full manuscript Submission at ICAPIE 2016, Delhi, India View project

Efficiency analysis banks in India. View project

All content following this page was uploaded by Nand Kumar on 08 April 2019.

The user has requested enhancement of the downloaded file.

Indian Journal of Economics & Business, Vol. 19, No.1 (2019) : 255-262

THE IMPACT OF TECHNOLOGY ADOPTION ON AGRICULTURAL PRODUCTIVITY IN ETHIOPIA: ARDL APPROACH

AYNALEM SHITA[*], NAND KUMAR[**] AND SEEMA SINGH[***]

Abstract

This paper investigates the impact of technology adoption on agricultural productivity by using Autoregressive Distributed Lag (ARDL) approach for the period of 1990-2016. The result of bounds testing procedure and the coefficient of error correction term indicates the existence of long-run relationship among variables. The study finds that technology adoption (as captured by fertilizer consumption) and real GDP affect agricultural productivity positively and significantly both in the long-run and short-run. Area of arable land affects agricultural productivity positively in the long-run but negatively in the short-run. The speed of adjustment in the error correction term is found to be 0.54.

Keywords: *Agricultural Productivity, ARDL, Ethiopia, Fertilizer, Technology adoption. JEL: O13, O33*

INTRODUCTION

Agriculture remains an important sector in the Ethiopian economy. The sector accounts for 36.7% of the GDP and generates 88.8% of export earnings. Crops take up 71.9% share of the agriculture sector (NBE, 2016).

Since more than 80% of the population lives in the rural area where agriculture is the source of their livelihood, its growth is a major driver of poverty reduction in rural Ethiopia. Towards the goal of reducing poverty and food insecurity in the country, the government of Ethiopia has planned to increase agricultural productivity through the adoption of agricultural technologies among other strategies (FDRE-GTP II, 2016).

Adoption of agricultural technologies can help to increase productivity, ensuring food security and reducing poverty. It is believed that that improved agricultural technologies such as improved seeds, fertilizers, pesticides, modern farming

[*] PhD Scholar in Economics, Delhi Technological University, Delhi-110042
[**] Associate Professor of Economics, , Delhi Technological University, Delhi-110042
[***] Professor of Economics, Delhi Technological University, Delhi-110042

machines and irrigation techniques are crucial for rural development through increment in agricultural productivity.

The bulk of the literature on the green revolution technologies argues that the higher yielding plant varieties, the greater use of fertilizers and the increased irrigation have been essential for the decline of poverty in Asia (Mendola, 2007). While Green revolution has significantly increased productivity in many Asian and Latin America countries, in Africa, the level of adoption and its impact were not promising due to little interest shown by farmers for these technologies (Toborn, 2011; Grfftin, 1979). In this regard, Andersen and Hazell (1985) argued that in order to reap the benefits of Green Revolution, its implementation should be properly integrated into the overall development strategy and accompanied by appropriate public policy and institutional changes.

Researches in the area assure the advantage of agricultural technologies through increment of food availability and lowering its prices. De Janvry and Sadoulet (2002) argue that the effect of modern agricultural technologies on poverty in Africa is directly while the effect in Asia and Latin America is indirectly through employment and linkage effect respectively.

Hossain (1989) explained that for agricultural growth to be increased, the adoption of improved technology is a key since expansion of arable land become a minimal source for output increment. In this regard, Ahmed and Heng (2012) found that fertilizer is the major determinant for the growth of agriculture productivity in Pakistan both in the short-run and in the long-run.

Studies done in Ethiopia related to the impact of technology adoption on agricultural productivity are very scanty. Among them Kefyalew (2010) based on household survey in Ethiopia argue that the effect of fertilizer use on the value of agricultural production and yield is positive but the magnitude with which the value of production responds to a change in fertilizer use is low. Likewise, a study by Tigist (2017) by using micro-level evidence from Rural Ethiopia found the a 1 percent increase in high variety yield inputs and inorganic fertilizer use will lead to 7.37 percent and 6.32 percent increase in farm value of production respectively.

However, the existing researches in Ethiopia which relate technology adoption to agricultural productivity have been done based on only micro –level factors which ignored the possible influence of macro variables (Kefyalew, 2010; Tigist, 2017). Hence, this study focuses on the impact of technology adoption on agricultural productivity based on macroeconomic variables.

Material and Methodology

Material

This study is employed based on four Ethiopian macroeconomic variables which include agricultural productivity, technology adoption (fertilizer consumption), real

gross domestic product (GDP) and area of arable land. For this study, secondary data were taken from World Development Indicators of the World Bank database. The period cover was fixed over 1990 to 2016 based on data availability. Moreover, the values for fertilizer consumption from the period 1990 to 2001 were filled using backward extrapolation technique due to unavailability of data.

Methodology

In order to investigate the impact of technology adoption on agricultural productivity, three explanatory variables were included; fertilizer consumption as a proxy for technology adoption, Real GDP and arable land. These three variables were selected due to their strong relationship with technology adoption.

Hence, the model is identified as;

$$lnP = f(lnF, lnRGDP, lnL) \quad (1)$$

While *ln* refers to natural logarithm of variables, the description of variables is presented below.

Agricultural productivity (lnP) is the dependent variable which is measured by the average amount of cereal yield in kg per hectare.

Fertilizer consumption (lnF): It is measured as the use of fertilizer in kg per hectare of arable land. Fertilizer significantly enhances natural soil nutrients and as a result per acre production is increased (Ahmad and Heng, 2012). Hence it is expected that fertilizer affects agricultural productivity positively.

***Real Gross Domestic Product (lnRGDP)*:** This variable reflects the impact income on agricultural productivity. It is measured in USD at 2010 constant price. It is expected that as income increases farmers will adopt agricultural technologies such as improved seed, fertilizer and pesticides etc which will increase productivity. Hence real GDP was expected to have a positive impact on agricultural productivity.

Arable Land (lnL): In this research land is defined as the average amount of arable land in hectare per household. However, the impact of land size on agricultural productivity is inconclusive. Barker and Herdt (1978) argued that large farmers had higher rate for hybrid usage and were therefore more productive than the smaller one. In contrary, Ekborm (1998) conclude that smaller farms are often forced to intensify production to sustain household welfare and hence a negative relationship is found between farm size and agricultural productivity. On the other side, Karanja *et al* (1999) show scale has no effect on productivity. Smallholders lag behind in adoption but later catch up and will increase productivity (Hassan and Karanja, 1997).

Most researchers used Engle and Granger (1987) two-step co-integration test to examine short run and long run relationships between variables. However, this method can only be applied when all the variables in the model are integrated of order one, I(1). Moreover, this method requires large sample size. However,

autoregressive distributed lag (ARDL) technique avoids the above problems and allows when the variables included in the model can be either integrated of order 0 or 1 but not I(2). In addition, its estimation technique provides efficient results for small samples (Pesaran et al. (1999). As a result, in this study, Autoregressive Distributed Lag (ARDL) model has been selected since some of the variables included in the model are integrated of order zero, I(0) and others are I(1). Stationary test were conducted by using both Augmented Dickey Fuller (ADF) and Phillips-Peron (PP) tests.

Hence, following Pesaran *et al.* (1999), the ARDL model is written as;

$$\Delta\, lnP = \alpha_0 + \sum_{i=1}^{n_1} \alpha_{1i} \Delta lnP_{t-1} + \sum_{i=1}^{n_2} \alpha_{2i} \Delta lnF_{t-1} + \sum_{i=1}^{n_3} \alpha_{3i} \Delta lnRGDP_{t-1} + \sum_{i=1}^{n_4} \alpha_{4i} \Delta lnL_{t-1} + \beta_1 lnP_{t-1} + \beta_2\, lnF_{t-1} + \beta_3\, lnRGDP_{t-1} + \beta_4\, lnL_{t-1} + \mu_t \quad \ldots\ldots\ldots\

either zero or one, I(0) or I(1). Hence, in this study the stationary test were done by using both Augmented Dicky-Fuller (ADF) test and Phillips-Perron (PP) test as shown by table 1 below.

Table 1: Unit Root Test

Variables	ADF Test Level	First Difference	PP -Test Level	First Difference	Decision
lnP	-2.388710	-6.462341 ***	-1.762008	-12.72201***	I(1)
lnF	-4.394415***	-8.279203***	-4.753968***	-15.76028***	I(0)
ln RGDP	-2.498128	-5.625599***	-2.465112	-4.754740***	I(1)
lnL	-2.609176	-2.806256***	1.253334	-2.687295***	I(1)

Note: *** indicates 1% significance level.

The unit root test results reported in Table 1 indicates that *lnF* is stationary at level (integrated of order zero, I(0)) while the other three variables, *ln*P, *ln*RGDP and *lnL* are stationary at their first difference(integrated of order one, I(1)) by both the ADF and PP tests. Hence, it implies that the ARDL approach may be better to be used since the variables are either I (0) or I (1).

Before applying the ARDL model, determination of the appropriate lag length is required since the results are sensitive to it. Therefore, in this study, we used Akaike Information Criterion (AIC) to select the optimum lag length and it is found that one lag was determined for and whereas for and RGDP zero lag was selected.

Table 2: Bound Test for Co-integration

Test Statistic	Value	K	Critical Value Bonds		
F-statistic	6.286516	3	Significance	Lower Bound	Upper Bound
			5%	2.79	3.67
			1%	3.65	4.66

As shown by table 2 above, the results clearly indicates the existence of co-integration between variables included in the model since the computed F-statistic is greater than the critical values.

Therefore, now we are in a position to develop and analyze the long-run coefficients of the ARDL model. Hence, the long-run coefficients are presented table 3.

Table 3: Estimated Long Run Coefficients Using the ARDL Approach (Dependent Variable: *lnP*)

Variable	Coefficient	Std. Error	t-Statistic	Prob.
lnF	0.145339	0.044389	3.274242	0.0038***
lnRGDP	0.417392	0.047071	8.867330	0.0000***
lnL	0.371031	0.195077	1.901970	0.0717*
C	-2.275472	0.963643	-2.361323	0.0285**

Note: "***", "**","*", indicates significant level at 1%, 5% and 10% respectively.

The results of above table shows that all estimated coefficients are significant and their signs are consistent with the theoretical principles. In line with the priori expectation, it is found that fertilizer consumption has a positive and significant (at 1%) impact on agricultural productivity. A 1 percent increase in the amount of fertilizer consumption will lead to 0.14 percent increase in agricultural productivity. The coefficient, 0.42 implies that a one percent increase in real gross domestic product will result in 0.42 percent increment in agricultural productivity at 1 % significance level. Finally, the increase in the amount of arable land in hectares, will impacted on a 0.37% increase in agricultural productivity, but at 10% level of significance.

Table 4 presents the error correction representation of the selected ARDL model. The estimated lagged error correction term (ECM-1) is negative and statistically significant at 1%. This result indicates the co-integration among the variables included in the model. The coefficient of error correction term (i.e. -0.54) implies that 54 percent of the disequilibrium is adjusted toward equilibrium annually.

Table 4: Error Correction Representation of ARDL Model, ARDL (1, 0, 0, 1) (Dependent Variable:)

Variable	**Coefficient**	**Std. Error**	**t-Statistic**	**Prob.**
D(lnF)	0.102677	0.013832	7.423189	0.0000***
D(ln*FGDP*)	0.298853	0.123270	2.424378	0.0249**
D(lnL)	-0.427720	0.244082	-1.752362	0.0950*
CointEq(-1)	-0.537032	0.132723	-4.046267	0.0006***

Note: "***", "**","*", indicates significant level at 1%, 5% and 10% respectively.

As it was expected, fertilizer consumption and real GDP affects agricultural productivity not only in the long-run but also in the short-run positively and significantly. A 1 percent increase in the amount of fertilizer consumption will result in 0.10 percent increase agricultural productivity where as a 1 percent increase in real GDP will lead to 0.30 percent increase in productivity. However, the short-run effect of arable land on agricultural productivity was found negative and significant at 10% level of significance.

Table 5 presents the diagnostic tests applied to the error correction model on serial correlation. The result indicated the absence of serial correlation since the probability value is greater than 5% which is actually 7.75%.

Table 5: Breusch-Godfrey Serial Correlation LM Test:

F-statistic	2.203878	Prob. F(2,18)	0.1393
Obs*R-squared	5.114375	Prob. Chi-Square(2)	0.0775

Moreover, in order to check the stability of the long-run coefficients together with the short run dynamics, the figure of Cumulative Sum (CUSUM) was constructed. As shown in the figure 1, the cumulative sum of recursive residuals remains within the 5 percent critical bounds which indicate that the model is stable.

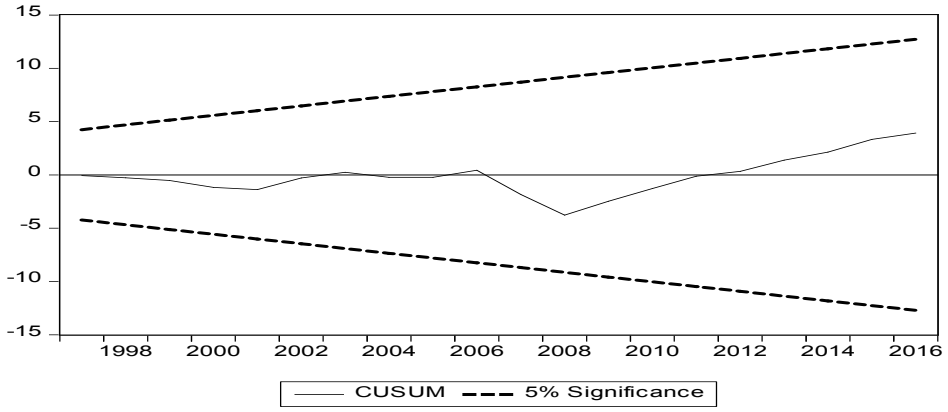

Figure 1: Plot of Cumulative Sum of Recursive Residuals.

Conclusion

This study emphasizes on the impact of technology adoption on agricultural productivity. It identified three explanatory variables, namely fertilizer consumption as the main proxy for technology adoption, real GDP and area of arable land by expecting their influence on agricultural technology adoption of farmers and affects productivity indirectly. The study Employed autoregressive distributed lag (ARDL) model using data for the period 1990-2009 retrieved from World Development Indicators of the World Bank data base. The bounds test and the estimated coefficient of error correction term indicate that there exists a long-run equilibrium relationship between agricultural productivity, fertilizer consumption, real GDP and arable land. The study found that fertilizer consumption and real GDP affect agricultural productivity positively and significantly both in the long-run and in the short-run. However, the impact of arable land was found positive in the long-run where as its effect in the short-run was negative both at 10 % significance level. The coefficient of error correction term implies that 54 percent of the disequilibrium error is corrected toward equilibrium annually. The performance of the co-integration model as it was checked by the Breusch-Godfrey Serial Correlation LM Test confirms the absence of serial correlation where as the CUSUM test reveals the stability of the model.

References

Ahmed, K. and Heng, A.C.T (2012), Determinants of Agriculture Productivity Growth in Pakistan, International Research Journal of Finance and Economics 95: 163-172

Barker, R. and R.W. Herdt (1978). "Equity implication of technology changes". In Interpretative analysis of selected papers from changes in rice farming in selected areas of Asia. Los Banos: International Development Rice Research Institute.

De Janvry, A. and E. Sadoulet (2002a). World poverty and the role of agricultural technology: direct and indirect effects. Journal of Development Studies 38 (4), 1–26.

Ekborm (1998). Some determinants to agricultural productivity-an application to Kenyan highlands. Paper presented at the World Conference of Environmental Economics, Venice Italy, 25-27 June 1998.

Engle, R. and C. Granger (1987). Cointegration and error correction representation: Estimation and testing. *Econometrica* 55: 251-276.

Federal Democratic Republic of Ethiopia (FDRE), (2016), Growth and Transformation Plan II (GTP II), (2015/16-2019/20), National Planning Commission, Addis Ababa, Ethiopia .

Grfftin K. (1979) The Political Economy of Agrarian Change: An Essay on the Green Revolution, Second Edition, The Macmillan Press Ltd., London.

Hassan, R.M. and D.D. Karanja (1997)**.** Increasing maize production in Kenya: technology, institutions and policy. In Byelee, D. and C.K. Eicher (eds). Africa emerging maize revolution. Boulders, Lynne Rienner Publishers**.**

Hossain, M. (1989). Green revolution in Bangladesh: Impact on growth and distribution of income. University Press.

Karanja, D., T.S. Jayne and P. Strasberg (1999). Determinant of input use and maize productivity in Kenya: implication of cereals marker reforms Kenya. Agricultural marketing and policy analysis project, Tegemeo Institute/Michigan State

Kefyalew E. (2010), Fertilizer Consumption and Agricultural Productivity in Ethiopia, the Ethiopian Development Research Institute Working Paper (003), Addis Ababa, Ethiopia

National Bank of Ethiopia (2016), Annual Report , Addis Ababa, Ethiopia.

Owens, T., J. Hoddinott, and B. Kinsey (2003). The impact of agricultural extension on farm production in resettlement areas of zimbabwe. Economic Development and Cultural Change 51 (2), 337–357

Pesaran, M. H. and Y. Shin (1999). An autoregressive distributed lag modelling approach to cointegration analysis. In Storm, S. (eds), *Econometrics and Economic Theory in 20th Century*: *The Ragnar Frisch Centennial Symposium*. Cambridge: Cambridge University Press.

Pesaran, M. H., Y. Shin and R. J. Smith (2001). Bounds testing approaches to the analysis of level relationships. *Journal of Applied Econometrics* 16: 289-326

Pinstrup-Andersen, P. and P. B. Hazell (1985). The impact of the green revolution and prospects for the future. Food Reviews International 1 (1), 1–25.

Tigist M. (2017), Productivity and household welfare impact of technology adoption: Micro level evidence from rural Ethiopia, United Nations University working paper: 20017-007.

Toborn, J. (2011). Adoption of agricultural innovations, converging narratives, and the role of swedish agricultural research for development. Discussion Paper

Trigo, E. J. and E. J. Cap (2004). The impact of the introduction of transgenic crops in argentinean agriculture.

View publication stats

IEEE Access
Multidisciplinary | Rapid Review | Open Access Journal

SPECIAL SECTION ON DATA MINING FOR INTERNET OF THINGS

Received March 12, 2019, accepted March 25, 2019, date of publication April 4, 2019, date of current version April 23, 2019.

Digital Object Identifier 10.1109/ACCESS.2019.2909400

The Role of Wearable Technologies in Supply Chain Collaboration: A Case of Pharmaceutical Industry

MUHAMMAD NOMAN SHAFIQUE[1], MUHAMMAD MAHBOOB KHURSHID[2], HAJI RAHMAN[3], ASHISH KHANNA[4], DEEPAK GUPTA[4], AND JOEL J. P. C. RODRIGUES[5,6,7], (Senior Member, IEEE)

[1]Dongbei University of Finance and Economics, Dalian 116023, China
[2]Department of Examinations, Virtual University of Pakistan, Lahore 54000, Pakistan
[3]University of Buner, Buner 17290, Pakistan
[4]Maharaja Agrasen Institute of Technology, GGSIP University, Delhi 110078, India
[5]National Institute of Telecommunications (Inatel), Santa Rita do Sapucaì 37540-000, Brazil
[6]Instituto de Telecomunicações, 1049-001 Lisbon, Portugal
[7]Federal University of Piauí, Teresina 64049-550, Brazil

Corresponding authors: Muhammad Mahboob Khurshid (mehboob.khursheed@vu.edu.pk) and Joel J. P. C. Rodrigues (joeljr@ieee.org)

This work was supported in part by the National Funding from the FCT -Fundação para a Ciência e a Tecnologia through the Project UID/EEA/50008/2019, in part by the RNP, with resources from MCTIC, through the Centro de Referência em Radiocomunições (CRR) project of the Instituto Nacional de Telecomunicações (Inatel), Brazil, under Grant 01250.075413/2018-04, and in part by the Brazilian National Council for Research and Development (CNPq) under Grant 309335/2017-5.

ABSTRACT The technological transformation has led to the introduction of mini computers as wearable computers which facilitate users to use the Internet, different applications, messaging, and for calls all on one platform. The focus of these wearable computers in earlier studies has been on consumers and technical aspects, and their application has not been explored from an organizational perspective. This means that the recent introduction of wearable technology has great potential, which is untapped in the organizational context, especially for supply chain collaboration (SC). In this study, wearable technology is thought to offer huge potential for organizations in SC. Therefore, the purpose of this study is to empirically examine the role of wearable technology i.e. Smartwatch in enhancing collaboration among supply chain members with mediating roles of green training (GT) and emotional intelligence (EI). The population of this study is the pharmaceutical industry in Pakistan. Simple random sampling method has been used to collect data from 150 sample size. Data have been collected through offline and online survey method. Data have been analyzed through partial least square–structure equation modeling (PLS–SEM) technique. The results of this study have empirically tested the established conceptual framework. Continuance intention to use smartwatch has a positive effect on SC. Furthermore, GT and EI have mediating roles between continuance intention to use smartwatch and SC. It is concluded that the continuance intention to use smartwatch will increase SC. GT and EI will strengthen the relationship between continuance intention to use smartwatch and SC. The use of wearable technology will motivate employees to communicate rapidly and to monitor their supply chain activities using web-based and other applications. This study has practical implications in organizations and theoretical contribution to literature.

INDEX TERMS Internet of things, emotional intelligence, green training, smart watch, supply chain collaboration, theory of planned behavior, wearable technologies.

I. INTRODUCTION

The advancement in information technology has increased the demand for wearable technologies very rapidly. In 2014, 22 million units of wearable technologies were sold, which increased to over 250 million in 2018 [1], [3]. In addition, it has been estimated to reach wearable devices market to be of worth $25 billion by 2019 [2]. The most common wearable devices are wrist bands, smartwatches, wearable cameras and smart eye-wears. In China, Xiaomi has sold

The associate editor coordinating the review of this manuscript and approving it for publication was Sherali Zeadally.

2169-3536 © 2019 IEEE. Translations and content mining are permitted for academic research only.
Personal use is also permitted, but republication/redistribution requires IEEE permission.
See http://www.ieee.org/publications_standards/publications/rights/index.html for more information.

wearable wrist bands more than of any country in the world. This sales trend predicts the increase of sale of wristwatches included Samsung, Apple, and Pebble in the future more than previous years. The wrist-worn wearable devices will be more dominant in the coming years and most of the market share will be captured by smartwatches [3], [4].

Currently, smartwatches can perform multiple operations at one time. Smartwatches have different display and include different resolution schemes. They can be connected to mobile phones as well as Bluetooth devices to enable wearers to respond to calls and messages. Furthermore, different social and communication applications can be used in smartwatches [5], [6]. Smartwatches can also track health related activities to monitor work, count steps, sleep time, swimming and other activities. They can track and store health record of users. These smartwatch features have attracted the attention of users to make their life more convenient [4], [7].

In previous literature, wearable technologies have been focused on the perspective of sales, market growth [8], battery life, power absorption capability, wireless communication [9], [10], smartwatch interfaces and resolution [11], diffusion of innovation (DOI) [12], and use of wearable technologies [3]. However, literature has ignored the importance of wearable devices, especially smartwatches, to increase organizational performance and especially supply chain collaboration. Therefore, this study has changed the trend of usage of wearable devices from the user and technological perspective to organizational perspective. This study has focused on wearable technology to use smartwatch and increase the supply chain collaboration, which is a more practical issue, and to fill the literature gap.

II. LITERATURE REVIEW

A. THEORY OF PLANNED BEHAVIOR (TPB)

Theory of planned behavior is the extension of theory of reasoned action (TRA). In information technology literature, theory of planned behavior was considered to evaluate the user's behavior on adoption of technologies [13]. Theory of planned behavior was proposed by Ajzen in 1991 [14]. In this study, theory of planned behavior has been employed as a lens to establish the conceptual framework for study. Three antecedents which are attitude, subjective norms and perceived behavior are used to measure the user's continuance intention to use smartwatch. In previous literature, theory of planned behavior has grounded the explanation about individual adoption behavior in wearable technologies [15], healthcare, technology, politics and different fields [15]–[17].

Wearable technology i.e. smartwatch is a new innovation that can play a significant role in enhancing supply chain collaboration and TPB model with three constructs of attitude, subjective norms, and perceived behavior is expected to give a more satisfactory explanation of adoption intention. TPB model asserts that human behavior to use a technology is a direct function of human behavioral intention. However, behavioral intention is the function of attitude, subjective norms as well as perceived behavior instead of attitude and subjective norms only [14] used in theory of reason action (TRA).

In previous literature, attitude has been defined as ''the effect of positive or negative feelings of individuals in performing a particular behavior'' [18]. Thus, attitude is the one of major psychological antecedents of intention. In previous literature of theory of planned behavior in different fields, attitude has been found to have a positive effect on intention. In this study, consistent pattern has been followed, as attitude has positive effect on continuance intention to use smartwatch [18].

Subjective norms construct is the second major factor considered in theory of planned behavior to measure intention. Subjective norms construct has been defined as ''the individual's perception of the likelihood that the potential referent group or individuals approve or disapprove of performing the given behavior'' [18]. In previous literature, subjective norms have positive effect to evaluate the user intention. In this study, same pattern has been followed and positive relationship between subjective norms and continuance intention to use smartwatch has been considered [5].

Perceived behavior is described as ''the perceived ease or difficulty of performing the behavior, and it is assumed to reflect experience as well as anticipated impediments and obstacles'' [14]. Perceived behavior is the third factor which influences on user's intention. In previous literature, perceived behavior has positive effect on the intention. In this study, the direct effect of perceived behavior on continuance intention to use smartwatch has been focused [18].

B. SMARTWATCHES

Smartwatches are mini computers because they do more than only show the time as do traditional watches. Smartwatches are wrist wearing technology, which is the advancement in wrist wearing technology from smart wristbands to smart watches. Smartwatches have reduced the usage of smartphones because user can use their smartphones on their wrist. So, it will increase the attention of consumers towards smartwatches. In previous literature, smartwatches have been considered a luxury product which can show email, calls, messages, and other apps on the wrist, which is more convenient [5], [19].

Smartwatches have numerous functions which will facilitate users to do their work. For example, smartwatches or wrist-worn devices like wristbands, smart bracelets or smart watches can trace human pulse to measure blood pressure and other health related information. Smartwatches can also be used to collect, store and retrieve all recorded health-related information on laptops and smartphones which can be utilized anytime and whenever it is needed [5]. Furthermore, those applications can also be installed in smartwatches which cannot be installed on wristbands e.g. Fitbit Surge and Nike Fuelband. So, smartwatches are better than other wrist-worn devices and have greater functionality [15], [20].

Smartwatches can be connected to the Internet through Bluetooth and Wi-Fi devices. More than 10,000 apps can be installed on iOS smartwatch, and 4000 apps can be installed on Android smartwatch. Battery life and smartwatch design is improving day by day to attract the attention of users. Furthermore, smartwatches also offer large size and touch-screen display. These functions are not available on smart wristbands [5]. In this study, smartwatches have been used for the benefit of organizations, to communicate in real time, and present a more cost effective and convenient method of operation, which will enhance supply chain collaboration.

C. GREEN TRAINING

Green human-resource practices are the emerging trends in human resource management. Green human resource management practices have a positive effect on operational performance and Green Supply Chain Performance (GSCP). In this study, green training has focused as one of the prominent practices of green human resource management. Green training or environmental training can be defined as ''on-job education and training of organizational employees to achieve organizational environment management goals'' [21]. So, the green training will create green awareness and environmentally friendly thinking among the employees through green education, which will be implemented in the organizations [22], [23].

In green human resource management literature, green training can develop the environmental understanding in all level of employees (from the top, senior, middle to lower level) within the organization. Furthermore, employees can implement their green knowledge into their operational activities. Green training will enable organizations to integrate their routine activities to green practices and play their role to protect the environment. So, the ultimate goal of green training is to achieve environmental performance [23]–[25].

In green training literature, it is highlighted that green training has a positive impact on greening the organization because GT enables all the employees to think and go green, which will lead to improving the green practices in the organization at all levels. Furthermore, green training also develops green teams in the organizations to achieve an environmentally friendly environment in the organizations [26]. In Spain, for example, green training motivated organizations to adopt advanced green practices, protect the environment, and contribute to environmental performance [25], [27].

D. EMOTIONAL INTELLIGENCE

Emotional intelligence is not a very old concept, having emerged for the first time in 1920's. Emotional intelligence was divided into three concepts of abstract, mechanical and social intelligence. These three concepts were studied for the first time in emotional intelligence. In 1980's, the concept of emotional intelligence was first conceptualized by Steiner [28]. Emotional intelligence was studied in different disciplines such as human resource, organizational behaviors, and other disciplines [29]. Furthermore, emotional intelligence has been categorized as inter-emotional and intra-emotional intelligence in previous literature [30], [31].

Emotional intelligence is the part of social intelligence. Emotional intelligence is the ability of individuals to understand one's emotions and feelings [29]. Emotional intelligence enables individuals to differentiate and manage their actions and reasoning in all fields of endeavor. In addition, emotional intelligence is the individual's capability to identify, access and produce emotions which will facilitate the individual to make judgements, make decisions for different actions [32]. So, the emotional intelligence plays the most important role in understanding and regulating the individual's feelings and emotions [30].

Emotional intelligence is the complete mental process which starts from articulating and appraising of self-emotions. In the next phase, it will enable individuals to understand the verbal and nonverbal emotions and words of others. The next step is to adopt the self and others' emotions. Individuals can then use the emotions of self and others for specific actions and reasons. So, individuals can regulate the emotions of others. This complete process will become the overall process of emotional intelligence [30].

E. SUPPLY CHAIN COLLABORATION

Supply chain collaboration is the process of planning and execution of activities which will enable supply chain partners to respond according to dynamic changes in the market [33], [34]. Supply chain collaboration is the complete mechanism to integrate organizational internal and external resources, activities, and team members to achieve specific organizational goals which were not possible to achieve alone [35], [36]. Supply chain collaboration is very beneficial for organizations to develop the relationship with other supply chain members [37], [38].

The primary purpose of supply chain collaboration is to satisfy customer needs through the integration of operations and team members with each other [39]. In addition, supply chain collaboration develops close and strong relationship between supply chain partners, enabling them to share information with each other [40]. Therefore, supply chain collaboration is not an option for the organization, rather it is the basic necessity to achieve organizational goals [41].

Supply chain collaboration is the important factor to develop and sustain competitive advantage. This is because supply chain collaboration will enhance the communication among team members, which will reduce the errors in the supply chain operations. So, the supply chain collaboration will enhance productivity and increase the trust level between supply chain partners to achieve competitive advantage and organizational goals [36], [42]–[44].

In this study, the relationship between attitude, subjective norms, perceived behavior, continuance intention to use smartwatch (as theory of planned behavior) has been considered to have a positive effect on supply chain collaboration. In addition, green training and emotional intelligence have been hypothesized to have mediating effects

FIGURE 1. Conceptual framework.

TABLE 1. Profile of respondents (N=150).

Demographic Factor	Frequency	Percentage
Gender		
Female	35	23.3
Male	115	76.7
Education		
Intermediate	10	6.7
Bachelor	120	80
Master	20	13.3
Age in Years		
18 – 25	18	12
26 – 35	56	37.3
36 – 40	40	26.7
Above 40	36	24
Experience in Years		
1 – 3	20	13.3
4 – 6	56	37.3
7 – 9	55	36.7
Above 9	19	12.7
Position		
Lower level management	35	23.3
Middle level management	86	57.3
Upper management	29	19.4

FIGURE 2. Research design.

between the continuance intention to use smartwatch and collaborative behavior. The overall conceptual model has been drawn graphically in Figure 1 as schematic diagram.

III. METHODOLOGY

A. RESEARCH DESIGN

Research design is the pictorial representation of stages through which a study is conducted. Figure 2 demonstrate the design of this research. Stage 1, stage 2, and stage 3 in the research design have been discussed in Section I and Section II. In Section III, stage 4 is being elaborated in detail. In Section IV, stage 5 has been elaborated.

B. SAMPLE AND DATA COLLECTION PROCEDURE

Pharmaceutical industry in Pakistan is the targeted population of this study. The sample has been derived from population through simple random sampling technique. The sampling size is 150 employees from pharmaceutical companies taken from Lahore (the capital of Punjab province) and Islamabad (the capital of Pakistan), because more competitive environment has been observed in these big cities. Organizations in these cities face greater competition to gain market share, thus they invest in the training and development of their employees and in the advancement of information communication technologies. Furthermore, the employees are more competent and innovative. In these big cities, people are more aware and use of wearable technologies are higher than other cities in Pakistan. In addition, the success of pharmaceutical industry is based on smooth flow of information and medicines throughout the market. This is only possible if pharmaceutical companies have strong supply chain collaborative system. In previous literature of wearable technologies, health care industry has been focused [45]. Thus, support for the pharmaceutical industry as population of this study is consistent with previous research [45].

In this study, survey method has been used to collect the data from respondents. Both offline and online questionnaires have been designed to conduct the survey. Questionnaire has been divided into two parts; first part is related to demographic questions related to information about respondents and the second part of questionnaire has inquired about research phenomena. These research questions have been adapted and measured on five-point Likert scale. Online survey method is a more convenient and rapid data collection method. It will collect and store the survey responses automatically. On the other hand, in offline questionnaire, physical survey has been conducted during the period of September to October 2018 from Lahore and Islamabad. The results of demographics of respondents have been mentioned in Table 1, which provide the information about respondents.

C. WHY USE PLS-SEM

The advancement in information communication technology has facilitated the researchers to conduct their studies such that these technologies facilitate research process and enhance research quality. In this study, the online questionnaire has been developed through the use of Lime survey, which is a web-based application. The use of this application will enable researchers to develop online survey. It will create the hyperlink of survey to send through email or through any other social media. Respondents can open the survey, complete the questionnaire and submit it on line. Lime survey will collect and store the responses automatically. These responses can be downloaded in comma separated values (CSV) format. This format can be imported directly into Smart PLS for further data analysis [46].

Partial least square structure equation modeling (PLS – SEM) is the advanced statistical methodology to analyze the data [46]. There are two main reasons to use PLS – SEM. In this study, analysis has been done on 5000 bootstrap subsamples method to avoid sample size issue [47]–[49]. The first reason is that it can work more effectively on small sample data size. This is because this method did not consider the normality assumptions for analysis, which was considered in traditional software like AMOS [50]. It gives more accurate results in small sample data size [51]. Second, this method is more accurate in the exploratory stage of any phenomena because PLS – SEM can elaborate the phenomena more precisely at exploratory stage [52]–[54]. In this study, the relationship between intention to use smartwatch, emotional intelligence, green training and supply chain collaboration is at exploratory stage which was not developed in previous literature. So, PLS – SEM will statistically test this conceptually developed relationship at exploratory stage.

The research report has been written and formatted through the use of Microsoft Word 2016, and Microsoft Excel 2016 has facilitated to present the analysis tables in order to reduce the unnecessary information from output tables. Endnote X9 has been used for citation and references to avoid any human error from citation and references portion. This is because it is very difficult to mention all citations and references without the use of citation software. After the completion of paper, English grammar has been checked through the use of Grammarly premium account to remove major mistakes from the report. Furthermore, English will be double checked by human if necessary.

D. RESEARCH INSTRUMENT

In this study, all the questions have been adapted and measured on five-point Likert scale. The validity of items was measured through construct validity, content validity, and convergent validity which were tested through factor loading. Items having factor loading less than 0.6 have been deleted and not considered for further analysis.

Attitude (AT): Attitude was measured through six questions and adapted from literature [55], [56].

Subjective Norms (SN): Subjective Norms was measured through four questions and adapted from literature [55], [56].

Perceived Behavior (PB): Perceived behavior was measured through three questions and adapted from literature [55], [56].

Continuance Intention to use smartwatch (INT): Intention to use smartwatch was measured through four questions and adapted from literature [57].

Emotional Intelligence (EI): Emotional intelligence was measured through sixteen questions and adapted from literature [58].

Green Training (GT): Green training was measured through ten questions and adapted from literature [22], [26].

Supply Chain Collaboration (SC): Supply chain collaboration was measured through four questions and adapted from literature [36].

IV. FINDINGS

A. COMMON METHOD VARIANCE

Common method variance is also called common method bias. The common method bias is different from instrument variance method. This is because it is related to methodology instead of instrument and refers to the chance that this issue will arise when data of independent and dependent variables has been collected at the same time from same respondents through the use of single questionnaire [59]. The chances of common method bias can be reduced if the questionnaire has been divided into different pages, which will separate the independent variable from dependent variable [59]. In this study, cross sectional data collection method has been used. So, the data regarding independent and dependent variables has been collected from the same respondents at one time, which is why the chances of common method variance are high in this study.

Common method variance can be analyzed statistically. There are three common techniques to analyze common method variance, which are Harman Method, Lindell & Whitney Method and Bagozzi approach. In this study, Bagozzi approach has been used to analyze the common method bias because it is a very common and easy method to use. Bagozzi method suggests that if the correlation among variables is less than 0.9, there is no common method bias issue [60]. So, data can be used for further analysis. In this study, researcher has used Bagozzi method to measure the common method bias. The correlation between variables can be checked through correlational matrix, which was mentioned in Table 2. The correlation value of each variable is less than 0.9, which showed there is no common method bias issue in the data.

B. MEASUREMENT MODEL

Structural equation modeling method consists of two models. The first is measurement model, which measures the reliability and validity of data [61]. Reliability is also measured through Cronbach's Alpha and composite reliability. Validity can be measured through content, convergent and discriminant validity [52], [62].

TABLE 2. Fornell-Larcker Criterion Method for Discriminant Validity.

	1	2	3	4	5	6	7
AT	**0.876**						
INT	0.813	**0.890**					
EI	0.882	0.827	**0.803**				
GT	0.829	0.827	0.865	**0.830**			
PB	0.739	0.762	0.740	0.737	**0.768**		
SN	0.780	0.828	0.799	0.772	0.686	**0.790**	
SC	0.835	0.881	0.886	0.869	0.718	0.821	**0.887**

FIGURE 3. Cronbach's Alpha values.

1) CRONBACH'S ALPHA

Reliability is the internal consistency of items. In this study, reliability was measured through Cronbach's Alpha test. The minimum acceptable value for Cronbach's Alpha value is 0.6 [52], [63], [64]. In this study, the Cronbach's Alpha values of reliability of attitude, subjective norms, perceived behavior, intention to use smartwatch, green training, emotional intelligence, and supply chain collaboration is more than 0.6, which is greater than minimum acceptable values. So, the data is reliable for further analysis. Reliability values have been mentioned in Table 3, while Figure 3 shows the reliability of each variable, which shows the minimum acceptable value and the graphical Cronbach's Alpha values of each item.

2) COMPOSITE RELIABILITY

Composite reliability (CR) is the overall reliability of all items of specific variable [54]. Composite reliability can be measured through PLS – SEM. In PLS – SEM, composite reliability was measured when the items are reflective. On the other hand, if items are measured through formative items, the variance inflation factor (VIF) test was used [65], [66]. In this study, attitude, subjective norms, perceived behavior, intention to use smartwatch, green training, emotional intelligence, and supply chain collaboration have been measured through reflective items. So, composite reliability test has been used. The minimum acceptable value for composite reliability is 0.6 [51], [66]. In this study, composite reliability of all variables is shown in Table 3, and graphical illustration shown in Figure 4, which show the minimum acceptable value of composite reliability and individual composite reliability of each variable.

TABLE 3. Factor Loadings, t – statistics, Reliability, and Average Variance Extract.

Construct	Item Loading	t-statistics	Cronbach's Alpha	CR & AVE
Attitude (at)				
at1	0.909	69.935	0.939	CR =
at2	0.894	54.605		0.952
at3	0.885	52.676		AVE =
at4	0.916	51.512		0.767
at5	0.822	32.776		
at6	0.823	35.488		
Subjective Norms (sn)				
Sn1	0.765	17.745	0.799	CR =
Sn2	0.793	19.726		0.869
Sn3	0.813	23.624		AVE =
Sn4				0.624
	0.787	20.884		
Perceived Behavior (pb)				
pb1	0.875	41.694	0.701	CR =
pb2	0.694	8.710		0.810
pb3				AVE =
				0.589
	0.721	8.511		
Intention to use smartwatch (int)				
in1	0.900	43.599	0.912	CR =
in2	0.871	37.254		0.938
in3	0.897	59.721		AVE =
in4				0.792
	0.892	44.526		
Emotional Intelligence (ie)				
ei1	0.784	23.439	0.921	CR =
ei2	0.822	24.594		0.936
ei3***	0.865	41.069		AVE =
ei4	0.751	17.930		0.645
ei5	0.779	20.246		
ei6	0.836	29.465		
ei7	0.766	18.099		
ei8	0.817	29.395		
Green Training (gt)				
gt1	0.800	18.905	0.909	CR =
gt2	0.827	26.500		0.930
gt3	0.869	38.206		AVE =
gt4	0.859	36.599		0.689
gt5	0.842	30.865		
gt6	0.780	19.156		
Supply chain collaboration (sc)				
sc1	0.876	39.644	0.909	CR =
sc2	0.892	41.935		0.936
sc3	0.895	44.239		AVE =
sc4				0.786
	0.883	45.064		

3) CONTENT VALIDITY

Content validity is related to the construction of items. The content validity shows the logical flow and grammatical correctness of each item. If all items have logical flow and they are grammatically correct, the reader and respondents can understand the items completely. Content validity enables respondents to respond to the items well. Content validity can be measured through factor loading of each item. The minimum acceptable item loading is 0.6 of all items to have content validity [51], [52], [66]. In this study, factor loading was measured through smart PLS and the results are shown

FIGURE 4. Composite reliability values.

in Table 3. The results showed that all items have factor loadings greater than 0.6 which showed all items have content validity.

4) CONVERGENT VALIDITY

Convergent validity shows the theoretical relationship between variables. The convergent validity showed how much variables are interlinked with each other, how much they are correlated with each other. Because if variables have no correlation with each other then they cannot integrate in to single framework of the study. In this study, attitude, subjective norms, perceived behavior, intention to use smartwatch, green training, emotional intelligence, and supply chain collaboration has considered and their convergent validity has tested through factor loading. The minimum acceptable item loading is 0.6 of all items to have convergent validity [51], [52], [66]. In this study, factor loading has measured through smart PLS and the results have mentioned in Table 3. The results showed that all items have factor loadings more than 0.6 which showed all items have convergent validity.

5) DISCRIMINANT VALIDITY

Discriminant validity is the opposite of convergent validity. It shows the degree to which variables are different from each other. If the variables are the same as other variables, there is no need to consider them as a separate variable. So, discriminant validity showed whether the variables are completely the same or if they have some difference from each other. Discriminant validity can be measured through two ways. First, it can be measured through the square root of average variance extracted (AVE) and this value is then compared with correlation among the variables [47], [51], [62]. If the values are higher than the correlation, there is no discriminant validity issue. Moreover, PLS – SEM can test the discriminant validity through Fornell-Larker criterion method. The Fornell-Larker criterion method also measures the correlation and square root of AVE values [51]. In this study, the discriminant validity was measured through Fornell-Larker criterion method as shown in Table 2. In addition, if the items have AVE values greater than 0.5, they are discriminant valid. Second, factor loading can also be used to measure the discriminant validity. If the items have factor loadings greater than 0.6, they have discriminant validity [67].

The overall results of factor loadings, t-statistics, Cronbach's Alpha, composite reliability and average variance extracted values can be used for the validation of measurement model in PLS – SEM. In this study, the results of all values are in favor to accept the measurement model as shown in Table 3.

TABLE 4. Collinearity statistics.

Indicators	VIF	Indicators	VIF	Indicators	VIF
at1	4.919	ei1	2.271	gt1	2.431
at2	3.825	ei2	2.601	gt2	2.481
at3	4.524	ei3	3.247	gt3	3.026
at4	4.819	ei4	2.054	gt4	2.923
at5	2.518	ei5	2.081	gt5	2.775
at6	2.271	ei6	2.554	gt6	1.901
sn1	1.520	ei7	2.128	pb1	1.184
sn2	1.627	ei8	2.467	pb2	1.635
sn3	1.782	sc1	2.576	pb3	1.664
sn4	1.545	sc2	3.011		
in1	3.036	sc3	3.050		
in2	2.565	sc4	2.645		
in3	2.895				
in4	2.857				

6) COLLINEARITY

Collinearity issue occurs when two constructs of formative nature are correlated with each other. However, the issue becomes more critical if more than two formative indicators are correlating with each other named as multicollinearity [52], [62]. It is indicated as Variance Inflation Factor (VIF) in SmartPLS 3.0 software. The maximum threshold value of VIF is 5. Therefore, VIF value of each indicator should be below 5. Since VIF value of each indicator is below 5, there is no collinearity issue found. Although collinearity statistics need not to be evaluated in reflective measurement models [52], [62], yet VIF values of all indicators for assurance of results are shown in Table 4.

C. STRUCTURAL MODEL

Structural model is the second model in structural equation modeling technique. In structural model, explanatory factors (R^2) and significant values (p values) are the most crucial values to assess the structural model [47], [48], [62]. In advanced PLS – SEM software, the values of all possible direct and indirect paths of the conceptual model can be statistically analyzed, which was not possible in traditional techniques. In smart PLS, small sample size data can be assessed. This is because this software does not require the normality assumptions [50]. Instead, it works on bootstrapping subsample technique which is more advanced and accurate. The minimum recommended bootstrapping subsample size is 500 [49]. But in this study, bootstrapping subsample size is taken as 5000 to get more accurate results. All the possible direct and indirect paths of conceptual model have been statistically tested and

TABLE 5. Path Coefficients, t – statistics, and significant values.

All Possible Direct and Specific Indirect Paths	R^2	T Statistics	P Values	Result
Attitude -> Continuance Intention to use smartwatch	0.298	4.487	0.000	Supported
Continuance Intention to use smartwatch -> Emotional Intelligence	0.827	31.145	0.000	Supported
Continuance Intention to use smartwatch -> Green Training	0.827	30.159	0.000	Supported
Continuance Intention to use smartwatch -> Supply Chain Collaboration	0.387	5.203	0.000	Supported
Emotional Intelligence -> Supply Chain Collaboration	0.361	3.945	0.000	Supported
Green Training -> Supply Chain Collaboration	0.237	2.957	0.003	Supported
Perceived Behavior -> Continuance Intention to use smartwatch	0.252	4.582	0.000	Supported
Subjective Norms -> Continuance Intention to use smartwatch	0.423	6.448	0.000	Supported
Attitude -> Continuance Intention to use smartwatch -> Emotional Intelligence	0.246	4.219	0.000	Supported
Perceived Behavior -> Continuance Intention to use smartwatch -> Emotional Intelligence	0.208	4.740	0.000	Supported
Subjective Norms -> Continuance Intention to use smartwatch -> Emotional Intelligence	0.350	6.321	0.000	Supported
Attitude -> Continuance Intention to use smartwatch -> Green Training	0.246	4.376	0.000	Supported
Perceived Behavior -> Continuance Intention to use smartwatch -> Green Training	0.208	4.580	0.000	Supported
Subjective Norms -> Continuance Intention to use smartwatch -> Green Training	0.350	6.228	0.000	Supported
Attitude -> Continuance Intention to use smartwatch -> Supply Chain Collaboration	0.115	3.125	0.002	Supported
Perceived Behavior -> Continuance Intention to use smartwatch -> Supply Chain Collaboration	0.097	3.570	0.000	Supported
Subjective Norms -> Continuance Intention to use smartwatch -> Supply Chain Collaboration	0.164	4.374	0.000	Supported
Attitude -> Continuance Intention to use smartwatch -> Emotional Intelligence -> Supply Chain Collaboration	0.089	3.111	0.002	Supported
Perceived Behavior -> Continuance Intention to use smartwatch -> Emotional Intelligence -> Supply Chain Collaboration	0.075	2.852	0.004	Supported
Continuance Intention to use smartwatch -> Emotional Intelligence -> Supply Chain Collaboration	0.299	3.911	0.000	Supported
Subjective Norms -> Continuance Intention to use smartwatch -> Emotional Intelligence -> Supply Chain Collaboration	0.126	3.131	0.002	Supported
Attitude -> Continuance Intention to use smartwatch -> Green Training -> Supply Chain Collaboration	0.058	2.305	0.021	Supported
Perceived Behavior -> Continuance Intention to use smartwatch -> Green Training -> Supply Chain Collaboration	0.049	2.435	0.015	Supported
Continuance Intention to use smartwatch -> Green Training -> Supply Chain Collaboration	0.196	2.891	0.004	Supported
Subjective Norms -> Continuance Intention to use smartwatch -> Green Training -> Supply Chain Collaboration	0.083	2.619	0.009	Supported

the results of their explanatory factors (R^2), t – statistics and their significant values are shown in Table 5.

There is no hard and fast rule for explanatory factors (R^2) values which show the minimum acceptable value [72], [68]. However, in previous literature, the values of R^2 0.02, 0.13 and 0.26 are categorized as low, medium and high explanatory variance [69]. The objective of structural model is only to explain the variance between independent and dependent variables. The path coefficient values of attitude to continuance intention to use smartwatch, continuance intention to use smartwatch to emotional intelligence, continuance intention to use smartwatch to green training, continuance intention to use smartwatch to supply chain collaboration, emotional intelligence to supply chain collaboration, green training to supply chain collaboration, perceived behavior to continuance intention to use

FIGURE 5. Path coefficients.

FIGURE 6. Path coefficients for supply chain collaboration.

TABLE 6. Model fit indexes.

	Saturated Model	Estimated Model
SRMR	0.072	0.097
d_ULS	3.305	5.959
d_G	1.546	1.788
Chi-Square	1,170.365	1,262.779
NFI	0.779	0.761

smartwatch, and subjective norms to continuance intention to use smartwatch are shown in graphical form in Figure 5. These are all possible direct paths and show the path coefficients (R^2) values of independent to dependent variables. All values are positive which showed that if the values of independent variable were to increase or decrease, the value of dependent variable will also increase or decrease in the same manner. However, the magnitude of change in value will be different in each relationship.

The overall structural model of PLS – SEM model has been imported from software and shown in Figure 6. The outer model is consisting of factor loadings of each item and the inner model shows the value of R^2 as mentioned on paths and inside the circles of each dependent variable. As shown, the statistical values have empirically supported the conceptual model.

The overall model fitness can be analyzed through model fit index in smart PLS. The overall model fit index shows the model fitness of whole model. In PLS – SEM, the overall model fitness can be analyzed through two values. First, Standardized Root Mean Square Residual (SRMR), in which the minimum recommended acceptable value is less than 0.08 [70]–[72]. The second model fit index is Normed Fit Index (NFI). The NFI is related to chi square index, where higher values are more preferred. The minimum recommended value for NFI is 0.9 [73], [74]. In this study, the values of overall model fit have been analyzed through saturated and estimated models. The values of both saturated and estimated model values are closer to the recommended values. So, both SRMR and NFI values are in favor of statistically tested model, which is why the whole conceptual model has been accepted through empirical results. The values of both saturated and estimated models are shown in Table 6.

V. CONCLUSION AND DISCUSSION

The usage of smartwatches is becoming very common. This usage is opening new opportunities for IT professionals, consumers, and organizations. Smartwatches are handheld wearable technology. Smartwatches are different from mobile and tablet devices because they have scanning and sensory features that differ from other devices [10]. Furthermore, smartwatches can be connected to mobile phones to attend calls and to use different applications on them. These wearable devices can also be used to count steps, track sleep, make enjoyment, provide ease in communication and many other features that encourage consumers to continue using them.

In this study, theory of planned behavior has been used to understand the continuance intention to use smartwatch. This study has developed the relationship between intention, green training and emotional intelligence to achieve supply chain collaboration. This relationship has been empirically tested through advanced statistical technique PLS – SEM. The path coefficient results are significant, which are in favor to accept the conceptual framework. So, this study showed that the continuance intention to use smartwatch, green training and emotional intelligence will enhance supply chain collaboration.

Theory of planned behavior has been used to measure the continuance intention to use smartwatch through three constructs; attitude, subjective norms, and perceived behavior. These three constructs have positive effect on continuance intention to use smartwatch. Results of this study are consistent with previous studies on theory of planned behavior [15], [18]. The results have proven that the attitude of consumer, subjective norms of society and perceived behavior of consumer will encourage the consumers to use wearable technology and motivate them to use these wearable technologies continuously.

In this study, emotional intelligence and green training has mediating the relationship between continuance intention to use smartwatch and supply chain collaboration. This mediating effect has measured through PLS – SEM using measurement and structural models. The results showed that high intention to use smartwatch will increase the supply chain collaboration. Furthermore, the indirect mediating paths of intention to use smartwatch through emotional intelligence and green training has the significant effect on supply chain collaboration. The results showed the partial mediation of both mediators of emotional intelligence and green training between continuance intention to use smartwatch and supply chain collaboration.

In this study, a multidisciplinary framework has been introduced and empirically tested which was not found in literature. The wearable technologies have focused in computer science and information communication technologies studies and many consumer behavior related studies [4], [45]. However, the organizational perspective and utilization of wearable technology, especially smartwatch, has been ignored in supply chain studies. In this study, the relationship between wearable technology (IT perspective), green training (human resource management), emotional intelligence (psychology) and supply chain collaboration (supply chain management) has been developed and empirically tested, which give a big picture of the utilization of wearable technologies in supply chain. So, this study will open new horizons in literature and open new practical implications of wearable technologies in organizations.

The advancement in wearable technologies, especially smartwatch, has introduced new features to attract consumer attention. So, consumers get emotionally involved in it, which is why organizations must understand this reality and move towards the wearable technologies to communicate with their team members. In addition, organizations must hold training sessions about the use of new wearable technologies especially smartwatches. Organizations must integrate their communication activities through smartwatches, which is more convenient and can track and record the health and usage information of their team members.

In organizations, people are moving rapidly towards the use of smartwatches. In addition, supply chain team members are very engaged, and they are reducing the usage of their mobile phones and increasing the usage of wearable technologies. The frequency of using smartwatch is beginning to increase. Users are also recommending that others should use smartwatches. Furthermore, the employees would be tracked in the advancement of technology, and when the new series or model of smartwatch are introduced, they will prefer to buy them. This is because they think new version has more advanced features which will make it easier for them to use.

In summary, this study has established a multidisciplinary relationship to use of wearable technologies and their practical implication for organizational benefits. Theory of planned behavior has helped to establish this relationship. The PLS – SEM results showed that continuance intention to use smartwatch has positive effect on supply chain collaboration. Furthermore, green training and emotional intelligence played the mediating effect between continuance intention to use smartwatch and supply chain collaboration. The overall model fit index showed that the conceptual model is fit. In addition, the advanced PLS – SEM technique based on both measurement model and structural model empirically supported the conceptual model.

VI. LIMITATIONS AND FUTURE DIRECTIONS

In this study only, smartwatch has been considered as wearable technology, while the other wearable technologies like Bluetooth hand free, smart eye wear, wearable camera, wearable wrist bands and many other wearable technologies has been ignored. In future studies, other wearable technologies can be considered. In this study, the survey method has been used to collect the data. It is recommended for future studies to consider interview method for data collection because people have innovative ideas to improve wearable technologies. Their feedback is very important and can be recommended to organization which will facilitate to design and develop customized features for the new models in wearable technologies. This study has been limited to intention to use smartwatch, emotional intelligence, green training, and supply chain collaboration while many other factors like regulations, peer pressure, market demands, and many other important factors have been ignored in this study. So, it is highly recommended to consider these factors in future studies. This study has focused on Pakistani population but in future other developing counties like India, Sri Lanka, Bangladesh and Nepal can be focused. The implication of this study in other countries will generalize this study.

REFERENCES

[1] C-Insight. (2014). *Smartwatches and Smart Bands Dominate Fast-Growing Wearables Market*. Accessed: Dec. 30, 2018. [Online]. Available: https://www.ccsinsight.com/press/company-news/1944-smartwatches-and-smart-bands-dominate-fast-growing-wearables-market

[2] C-Insight. (2015). *Wearables Market to Be Worth $25 Billion by 2019*. [Online]. Available: https://www.ccsinsight.com/press/company-news/2332-wearables-market-to-be-worth-25-billion-by-2019-reveals-ccs-insight

[3] H. Leggatt. (2014). *Forecast: 250 Million Smart Wearables in Use by 2018*. Accessed: Dec. 30, 2018. [Online]. Available: http://www.bizreport.com/2014/08/forecast-250-million-smart-wearables-in-use-by-2018.html

[4] J.-C. Hong, P.-H. Lin, and P.-C. Hsieh, "The effect of consumer innovativeness on perceived value and continuance intention to use smartwatch," *Comput. Hum. Behav.*, vol. 67, pp. 264–272, Feb. 2017.

[5] S. H.-W. Chuah, P. A. Rauschnabel, N. Krey, B. Nguyen, T. Ramayah, and S. Lade, "Wearable technologies: The role of usefulness and visibility in smartwatch adoption," *Comput. Hum. Behav.*, vol. 65, pp. 276–284, Dec. 2016.

[6] J. Choi and S. Kim, "Is the smartwatch an IT product or a fashion product? A study on factors affecting the intention to use smartwatches," *Comput. Hum. Behav.*, vol. 63, pp. 777–786, Oct. 2016.

[7] H. Kalantarian and M. Sarrafzadeh, "Audio-based detection and evaluation of eating behavior using the smartwatch platform," *Comput. Biol. Med.*, vol. 65, no. 1, pp. 1–9, 2015.

[8] IDC. (2018). *Global Wearables Market Grows 7.7% in 4Q17 and 10.3% in 2017 as Apple Seizes the Leader Position*. Accessed: Dec. 30, 2018. [Online]. Available: https://www.idc.com/getdoc.jsp?containerId=prUS43598218

[9] C. Min *et al.*, "Exploring current practices for battery use and management of smartwatches," in *Proc. ACM Int. Symp. Wearable Comput.*, 2015, pp. 11–18.

[10] B. Reeder and A. David, "Health at hand: A systematic review of smart watch uses for health and wellness," *J. Biomed. Informat.*, vol. 63, pp. 269–276, Oct. 2016.

[11] T. Starner, "The challenges of wearable computing: Part 2," *IEEE Micro*, vol. 21, no. 4, pp. 54–67, Jul. 2001.

[12] E. M. Rogers, *Diffusion of Innovations*. New York, NY, USA: Free Press, 1983.

[13] R. J. Holden and B. T. Karsh, "The technology acceptance model: Its past and its future in health care," *J. Biomed. Inform.*, vol. 43, no. 1, pp. 159–172, 2010.

[14] I. Ajzen, "The theory of planned behavior," *Org. Behav. Hum. Decis. Process.*, vol. 50, no. 2, pp. 179–211, 1991.

[15] H.-M. Chuang, "Factors influencing behavioral intention of wearable symbiotic devices–case study of the Mi band," *Soochow J. Econ. Bus.*, vol. 93, pp. 1–24, Dec. 2016.
[16] J. Cheon, S. Lee, S. M. Crooks, and J. Song, "An investigation of mobile learning readiness in higher education based on the theory of planned behavior," *Comput. Edu.*, vol. 59, no. 3, pp. 1054–1064, 2012.
[17] F. D. Davis, "Perceived usefulness, perceived ease of use, and user acceptance of information technology," *MIS Quart.*, vol. 13, no. 3, pp. 319–340, 1989.
[18] M. Fishbein and I. Ajzen, *Belief, Attitude, Intention, and Behavior: An Introduction to the Theory and Research*. Reading, MA, USA: Addison-Wesley, 1975.
[19] J. Carlson. (2015). *Apple Watch Becomes a Study on Attention*. [Online]. Available: https://www.seattletimes.com/business/apple-watch-becomes-a-study-on-attention/
[20] K. J. Kim and D.-H. Shin, "An acceptance model for smart watches: Implications for the adoption of future wearable technology," *Internet Research*, vol. 25, no. 4, pp. 527–541, 2015.
[21] B. F. Daily and S.-C. Huang, "Achieving sustainability through attention to human resource factors in environmental management," *Int. J. Oper. Prod. Manage.*, vol. 21, no. 12, pp. 1539–1552, 2001.
[22] A. A. Teixeira, C. J. C. Jabbour, A. B. L. de Sousa Jabbour, H. Latan, and J. H. C. de Oliveira, "Green training and Green supply chain management: Evidence from Brazilian firms," *J. Cleaner Prod.*, vol. 116, pp. 170–176, Mar. 2016.
[23] M. Shafique, A. Rashid, I. Bajwa, R. Kazmi, M. Khurshid, and W. Tahir, "Effect of IoT capabilities and energy consumption behavior on Green supply chain integration," *Appl. Sci.*, vol. 8, no. 12, p. 2481, 2018.
[24] P. Paillé, Y. Chen, O. Boiral, and J. Jin, "The impact of human resource management on environmental performance: An employee-level study," *J. Bus. Ethics*, vol. 121, no. 3, pp. 451–466, 2014.
[25] K. Muduli, K. Govindan, A. Barve, and Y. Geng, "Barriers to Green supply chain management in Indian mining industries: A graph theoretic approach," *J. Cleaner Prod.*, vol. 47, pp. 335–344, May 2013.
[26] B. F. Daily, J. W. Bishop, and J. A. Massoud, "The role of training and empowerment in environmental performance: A study of the Mexican *maquiladora* industry," *Int. J. Oper. Prod. Manage.*, vol. 32, no. 5, pp. 631–647, 2012.
[27] J. Sarkis, P. Gonzalez-Torre, and B. Adenso-Diaz, "Stakeholder pressure and the adoption of environmental practices: The mediating effect of training," *J. Oper. Manage.*, vol. 28, no. 2, pp. 163-176, 2010.
[28] C. Steiner, "Emotional literacy," *Trans. Anal. J.*, vol. 14, no. 3, pp. 162–173, 1984.
[29] P. Salovey and J. Mayer, "Emotional intelligence," *Imag., Cogn. Pers.*, vol. 9, no. 3, pp. 185–211, 1990.
[30] M. Asrar-ul-Haq, S. Anwar, and M. J. F. B. J. Hassan, "Impact of emotional intelligence on teacher's performance in higher education institutions of Pakistan," *Future Bus. J.*, vol. 3, no. 2, pp. 87–97, 2017.
[31] H. Gardner, *Multiple Intelligences: The Theory in Practice*. New York, NY, USA: Basic Books, 1993.
[32] J. D. Mayer, D. R. Caruso, and P. Salovey, "Emotional intelligence meets traditional standards for an intelligence," *Intelligence*, vol. 27, no. 4, pp. 267–298, 1999.
[33] Y. S. Wei and Q. Wang, "Making sense of a market information system for superior performance: The roles of organizational responsiveness and innovation strategy," *Ind. Marketing Manage.*, vol. 40, no. 2, pp. 267–277, 2011.
[34] C. Blome, A. Paulraj, and K. Schuetz, "Supply chain collaboration and sustainability: A profile deviation analysis," *Int. J. Oper. Prod. Manage.*, vol. 34, no. 5, pp. 639–663, 2014.
[35] J. Hoyt, F. Huq, and P. Kreiser, "Measuring organizational responsiveness: The development of a validated survey instrument," *Manage. Decis.*, vol. 45, no. 10, pp. 1573–1594, 2007.
[36] Z. G. Zacharia, N. W. Nix, and R. F. Lusch, "Capabilities that enhance outcomes of an episodic supply chain collaboration," *J. Oper. Manage.*, vol. 29, no. 6, pp. 591–603, 2011.
[37] S. de Leeuw and J. Fransoo, "Drivers of close supply chain collaboration: One size fits all?" *Int. J. Oper. Prod. Manage.*, vol. 29, no. 7, pp. 720–739, 2009.
[38] F. Wiengarten, P. Humphreys, A. McKittrick, and B. Fynes, "Investigating the impact of e-business applications on supply chain collaboration in the German automotive industry," *Int. J. Oper. Prod. Manage.*, vol. 33, no. 1, pp. 25–48, 2013.
[39] M. Cao, M. A. Vonderembse, Q. Zhang, and T. Ragu-Nathan, "Supply chain collaboration: Conceptualisation and instrument development," *Int. J. Prod. Res.*, vol. 48, no. 22, pp. 6613–6635, 2010.
[40] M. Cao and Q. Zhang, "Supply chain collaboration: Impact on collaborative advantage and firm performance," *J. Oper. Manage.*, vol. 29, no. 3, pp. 163–180, 2011.
[41] A. Matopoulos, M. Vlachopoulou, V. Manthou, and B. Manos, "A conceptual framework for supply chain collaboration: Empirical evidence from the agri-food industry," *Supply Chain Manage., Int. J.*, vol. 12, no. 3, pp. 177–186, 2007.
[42] Z. Cai, Q. Huang, H. Liu, and L. Liang, "The moderating role of information technology capability in the relationship between supply chain collaboration and organizational responsiveness: Evidence from China," *Int. J. Oper.*, vol. 36, no. 10, pp. 1247–1271, 2016.
[43] A. Vereecke and S. Muylle, "Performance improvement through supply chain collaboration in Europe," *Int. J. Oper. Prod. Manage.*, vol. 26, no. 11, pp. 1176–1198, 2006.
[44] U. Ramanathan, "Supply chain collaboration for improved forecast accuracy of promotional sales," *Int. J. Oper. Prod. Manage.*, vol. 32, no. 6, pp. 676–695, 2012.
[45] Y. Gao, H. Li, and Y. Luo, "An empirical study of wearable technology acceptance in healthcare," *Ind. Manage. Data Syst.*, vol. 115, no. 9, pp. 1704–1723, 2015.
[46] C. M. Ringle, S. Wende, and J.-M. Becker. (2015). *SmartPLS 3. Bönningstedt1: SmartPLS*. [Online]. Available: http://www.smartpls.com
[47] W. W. Chin, "How to write up and report PLS analyses," in *Handbook of Partial Least Squares*. Berlin, Germany: Springer, 2010, pp. 655–690.
[48] G. Sanchez, *PLS Path Modeling With R*. Berkeley, CA, USA: Trowchez Editions, 2013.
[49] M. Wetzels, G. Odekerken-Schröder, and C. van Oppen, "Using PLS path modeling for assessing hierarchical construct models: Guidelines and empirical illustration," *MIS Quart.*, vol. 33, no. 1, pp. 177–195, 2009.
[50] C. B. Astrachan, V. K. Patel, and G. Wanzenried, "A comparative study of CB-SEM and PLS-SEM for theory development in family firm research," *J. Family Bus. Strategy*, vol. 5, no. 1, pp. 116–128, 2014.
[51] C. Fornell and D. F. Larcker, "Evaluating structural equation models with unobservable variables and measurement error," *J. Marketing Res.*, vol. 18, no. 1, pp. 39–50, 1981.
[52] J. F. Hair, C. M. Ringle, and M. Sarstedt, "PLS-SEM: Indeed a silver bullet," *J. Marketing Theory Pract.*, vol. 19, no. 2, pp. 139–152, 2011.
[53] S. Petter, D. Straub, and A. Rai, "Specifying formative constructs in information systems research," *MIS Quart.*, vol. 31, no. 4, pp. 623–656, 2007.
[54] J. Henseler, C. M. Ringle, and R. R. Sinkovics, "The use of partial least squares path modeling in international marketing," in *New Challenges to International Marketing*. Bingley, U.K.: Emerald Group Publishing, 2009, pp. 277–319.
[55] I. Ajzen. (2012). *Constructing a Theory of Planned Behavior Questionnaire*. Accessed: Jan. 12, 2019. [Online]. Available: http://people.umass.edu/~aizen/pdf/tpb.measurement.pdf
[56] S. Taylor and P. A. Todd, "Understanding information technology usage: A test of competing models," *Inf. Syst. Res.*, vol. 6, no. 2, pp. 144–176, 1995.
[57] A. Bhattacherjee, "Understanding information systems continuance: An expectation-confirmation model," *MIS Quart.*, vol. 25, no. 3, pp. 351–370, 2001.
[58] C.-S. Wong and K. S. Law, "The effects of leader and follower emotional intelligence on performance and attitude: An exploratory study," *Leadership Quart.*, vol. 13, no. 3, pp. 243–274, 2002.
[59] P. M. Podsakoff, S. B. MacKenzie, J.-Y. Lee, and N. P. Podsakoff, "Common method biases in behavioral research: A critical review of the literature and recommended remedies," *J. Appl. Psychol.*, vol. 88, no. 5, p. 879, 2003.
[60] R. P. Bagozzi, Y. Yi, and L. W. Phillips, "Assessing construct validity in organizational research," *Administ. Sci. Quart.*, vol. 36, no. 3, pp. 421–458, 1991.
[61] C. Barclay, C. Higgins, and R. Thompson, "The partial least squares (PLS) approach to causal modeling: Personal computer adoption and use as an illustration," *Technol. Stud.*, vol. 2, no. 2, pp. 285–309, 1995.
[62] W. W. Chin, "The partial least squares approach to structural equation modeling," *Mod. Methods Bus. Res.*, vol. 295, no. 2, pp. 295–336, 1998.
[63] J. C., Nunnally, I. H. Bernstein, and J. M. T. Berge, *Psychometric Theory*, vol. 226. New York, NY, USA: McGraw-Hill, 1967.
[64] J. C. Nunnally and I. H. Bernstein, *Psychological Theory*. New York, NY, USA: MacGraw-Hill, 1994.
[65] M. H. Kutner, C. Nachtsheim, J. Neter, and W. Li, *Applied Linear Statistical Models*. New York, NY, USA: McGraw-Hill, 2005.

[66] J. F. Hair, W. C. Black, B. J. Babin, R. E. Anderson, and R. L. Tatham, *Multivariate Data Analysis*, no. 3. Upper Saddle River, NJ, USA: Prentice-Hall, 1998.
[67] W. W. Chin, B. L. Marcolin, and P. R. Newsted, "A partial least squares latent variable modeling approach for measuring interaction effects: Results from a Monte Carlo simulation study and an electronic-mail emotion/adoption study," *Inf. Syst. Res.*, vol. 14, no. 2, pp. 189–217, 2003.
[68] J. Hulland, "Use of partial least squares (PLS) in strategic management research: A review of four recent studies," *Strategic Manage. J.*, vol. 20, no. 2, pp. 195–204, 1999.
[69] J. Cohen, *Statistical Power Analysis for the Behavioral Sciences*, 2nd ed. Hillsdale, MI, USA: Erlbaum Associates, 1988.
[70] L. T. Hu and P. M. Bentler, "Cutoff criteria for fit indexes in covariance structure analysis: Conventional criteria versus new alternatives," *Struct. Equ. Model.*, vol. 6, no. 1, pp. 1–55, 1999.
[71] L.-T. Hu and P. M. Bentler, "Fit indices in covariance structure modeling: Sensitivity to underparameterized model misspecification," *Psychol. Methods*, vol. 3, no. 4, p. 424, 1998.
[72] J. Henseler *et al.*, "Common beliefs and reality about PLS: Comments on Rönkkö and Evermann (2013)," *Org. Res. Methods*, vol. 17, no. 2, pp. 182–209, 2014.
[73] J.-B. Lohmöller, "Predictive vs. structural modeling: PLS vs. ML," in *Latent Variable Path Modeling and Partial Least Squares*. Physician-Verlag, 1989, pp. 199–226.
[74] J.-B. Lohmöller, *Latent Variable Path Modeling With Partial Least Squares*. Springer, 2013.

MUHAMMAD NOMAN SHAFIQUE received the M.Phil. degree in business administration from Pakistan. He is currently pursuing the Ph.D. degree in business administration with the Dongbei University of Finance and Economics, China. He is learning new research techniques and implementing his studies. He has completed many research certifications and has published few research papers in different journals.

MUHAMMAD MAHBOOB KHURSHID received the M.Sc. degree in project management from the COMSATS Institute of Information Technology, Islamabad. He is currently pursuing the Ph.D. degree in information systems with the Universiti Teknologi Malaysia. He is currently serving as an Assistant Controller of Examinations with the Department of Examinations, Virtual University of Pakistan (VUP). He has ten years of professional experience carrying out operations regarding examinations in VUP.

HAJI RAHMAN a man of ambitions to take the challenges in his field. He remained a hardworking human with an excellent academic career. He received the M.S. degree in engineering management from UET, Taxila, Pakistan, and the Ph.D. degree in management sciences (HRM) from Preston University, Islamabad, on HEC scholarships. He was a faculty member for more than nine years at the Ghulam Ishaq Khan Institute with best result producing teacher awards. He has remained as an Assistant Professor with Preston University, Islamabad campus for two years. He is also a Visiting Faculty Member at the IIUI, Islamabad, and Federal Urdu University of Arts Sciences and Technology, Islamabad. He also delivered training modules at CDA Training Academy and Pakistan Manpower Institute, Islamabad. He is currently an Assistant Professor with the Department of Management Science, University of Buner. He also holds the additional charge as a Director Quality Enhancement Cell (QEC) at University of Buner. He is the author of a number of international and national research papers. He has also presented his research articles in a number of international research conferences. He received the Punctuality and Efficiency Awards for Fall Semester 2015, Spring Semester 2016, Fall 2016, and Spring 2017 from Preston University.

ASHISH KHANNA is a highly qualified individual with around 15 years of rich expertise in Teaching, Entrepreneurship, and Research & Development with specialization in Computer Science Engineering Subjects. He received the B.Tech. and M.Tech. degrees from GGSIP University, Delhi, in 2004 and 2009, respectively, and the Ph.D. degree from the National Institute of Technology, Kurukshetra. He has been a part of various seminars, paper presentations, research paper reviews, and conferences, as a convener and a session chair, and a guest editor in journals, and has coauthored several books in publication house and papers in national journals, international journals, and conferences. He has published many research papers in reputed journals and conferences. He also has papers in SCI-indexed and Springer journals. He has coauthored 10 Text books and edited books i.e. *Distributed Systems*, *Java Programming and Website Development*, *Java Programming*, *Computer Graphics*, *Computer Graphics and Multimedia*, *Computer Networks*, *Computer Networks and Data Communication Networks*, *Success Mantra for IT interviews*, and *Fundamental of Computing*. He has also an edited book in Lambert publication. He recently successfully managed Smart India Hackathon in 2017 at MAIT, GGSIP University with teams under him winning prices at their distributed systems, cloud computing, vehicular ad hoc networks, and opportunistic networks. He displayed vast success in continuously acquiring new knowledge and applying innovative pedagogies and has always aimed to be an effective educator and have a global outlook which is the need of today. He is currently associated with some Springer and IEEE conferences and managing special sessions for them and looking forward for some more challenging tasks. He was a reviewer in some SCI indexed Journals, like *Cluster Computing* (Springer) and IEEE conferences. He is also a Reviewer and a Session Chair of IEEE international conference ICCCA 2016 and 2017. He has designed the syllabus for cloud computing, Java Programming, and distributed systems for GGSIP University. He was a Guest Editor in IEEE conference-IC3TSN-2017 and managing a special session on Parallel and Distributed Network-based Computing Systems. He was a Guest Editor in Springer Conference at ICDMAI-2018 and managing a special session on Computational Intelligence for Data Science.

DEEPAK GUPTA received the M.E. degree from the Delhi College of Engineering, in 2010and the Ph.D. degree from Dr APJ Abdul Kalam Technical University (AKTU), in 2017. He is currently an Assistant Professor with the Department of Computer Science and Engineering, Maharaja Agrasen Institute of Technology, GGSIP University, Delhi, India. He has published many scientific papers in SCI journals, like JoCS, IAJIT, and FGCS. In addition, he has authored/edited over 25 books (Elsevier, Springer, IOS Press, and Katson) and six journal special issues. His research area includes software usability, human-computer interaction, nature-inspired computing, machine learning, and soft computing. He is a Convener and an Organizer of ICICC-2018 springer conference. He has also started a research unit under the banner of Universal Innovator. He is also associated with various professional bodies, like ISTE, IAENG, IACSIT, SCIEI, ICSES, UACEE, the Internet Society, SMEI, IAOP, and IAOIP.

JOEL J. P. C. RODRIGUES (S'01–M'06–SM'06) received the five-year B.Sc. degree (licentiate) in informatics engineering from the University of Coimbra, Portugal, the M.Sc. degree and the Ph.D. degree in informatics engineering from UBI, the Habilitation degree in computer science and engineering from the University of Haute Alsace, France, and the Academic Title of Aggregated Professor in informatics engineering from UBI. He is currently a Professor with the National Institute of Telecommunications (Inatel), Brazil, a Senior Researcher with the Instituto de Telecomunicações, Portugal, and a Visiting Professor with the federal University of Piauí, Brazil. He is also the Leader of the Internet of Things Research Group (CNPq), the Director for Conference Development-IEEE ComSoc Board of Governors, the IEEE Distinguished Lecturer, a Technical Activities Committee Chair of the IEEE ComSoc Latin America Region Board, and the President of the scientific council at ParkUrbis-Covilhã Science and Technology Park. He has authored or coauthored over 700 papers in refereed international journals and conferences and three books. He holds two patents. He is a member of many international TPCs and participated in several international conferences organization. He was a recipient of several Outstanding Leadership and Outstanding Service Awards from the IEEE Communications Society and several best papers awards. He was the Chair of the IEEE ComSoc Technical Committee on eHealth and the IEEE ComSoc Technical Committee on Communications Software, a Steering Committee Member of the IEEE Life Sciences Technical Community and a Publications Co-Chair, and a Member Representative of the IEEE Communications Society on the IEEE Biometrics Council. He is the Editor-In-Chief of the *International Journal on E-Health and Medical Communications* and an Editorial Board Member of several high-reputed journals. He has been a General Chair and a TPC Chair of many international conferences, including IEEE ICC, IEEE GLOBECOM, IEEE HEALTHCOM, and IEEE LatinCom. He is a licensed Professional Engineer (as a Senior Member), a member of the Internet Society, and a Senior Member of ACM.

International Journal of Research in Engineering and Innovation (IJREI)
journal home page: http://www.ijrei.com
ISSN (Online): 2456-6934

Thermodynamic performance evaluation of single effect Li/Br H_2O vapour absorption refrigeration system cascaded with vapour compression system using ecofriendly HFC-134a and HFO-1234yf refrigerants

R.S. Mishra

Department of Mechanical and Production Industrial and Automobiles Engineering, Delhi Technological University, Delhi, India

Abstract

Vapour Absorption system is an attractive method for using the low grade energy directly for cooling. In this paper the effect of performance parameters on the thermodynamic performances of two single effect Li/Br H_2O systems cascaded by vapour compression refrigeration cycle at -53ºC of evaporator temperature have been studied in detailed. The comparisons were made for two systems in terms of thermal performances. System-1: consisting of single effect vapour absorption refrigeration system cascaded with vapour compression system using ecofriendly refrigerant (i.e.HFC-134a) and system-2 consisting of single effect vapour absorption refrigeration system cascaded with vapour compression system using ecofriendly refrigerant (HFO-1234yf) (system-2). Numerical computation was carried out using thermal model developed for -53ºC of low temperature evaporator circuit by varying various thermodynamic parameters (i.e. such as effect of temperature overlapping (i.e. approach) , generator temperature, absorber temperature, evaporator temperature of single effect Li/Br VARS cycle and evaporator temperature of VCRS cycle, etc.) and it is found that single effect cascade vapour absorption system using HFO-1234yf (System-2) has slightly lower thermodynamic performances in terms of overall coefficient of performances, and exergetic efficiency around 3% lower than single effect Li/Br H_2O vapour absorption refrigeration system cascaded with vapour compression system using ecofriendly HFC-134a refrigerant (system-1). On first law efficiency ($COP_{Cascade}$) and exergetic efficiency of overall system have been presented and found that there is significant effect of performance parameters on overall coefficient of performance and exergetic efficiency of cascade system, i.e. COP is 1.434%, exergetic efficiency is 3.2156% and both types-EDRs is 5.922 lower than using HFC-134a (in system-1)

© 2019 ijrei.com. All rights reserved

Keywords: Thermo-dynamic performance Comparison, Ecofriendly refrigerants, Cascade single effect VAR System

1. Introduction

Vapour Absorption system is an attractive method for using the low grade energy directly for cooling. Simple vapour absorption system consists of an absorber, a pump, a generator and a pressure reducing valve to replace the compressor of vapour compression system. This is an important advantage as compared to the conventional vapour compression system which operates on high grade energy. Another important feature of these systems is that they do not use any moving component except for a very small liquid pump. Vapour absorption system consists of four basic components viz. an evaporator, an absorber (located on low pressure side), a generator and a compressor (located on high pressure side). Refrigerant flows from the condenser to the evaporator, then through absorber to the generator and back to condenser, while the absorbent passes from absorber to the generator and back to absorber. For maximum efficiency, the pressure difference between the low pressure side and high pressure side is maintained as small as possible. In some places there is a fluctuation in the amount of heat availability which generates cyclic temperature changes in the cooling volume. This change alters the quality of the stored materials like fruits, meat, bakery products etc. The simple vapour absorption system consists of an absorber, a pump, a generator and a pressure reducing valve to replace the compressor of vapour

Corresponding author: Prof. R.S. Mishra
Email Address: hod.mechanical.rsm@dtu.ac.in

compression system. The other components of the system are condenser, receiver, expansion valve and evaporator as in the vapour compression system. In Lithium bromide absorption system, a solution of lithium bromide and water is used. Water is being used as the refrigerant and Lithium bromide acts as an absorbent. Lithium bromide is a hydroscopic salt with high affinity for water vapour due to its very low vapour pressure. This system is generally used in air conditioning systems due to not very low temperature (above 0˚C) requirements.

In a Li/Br-H_2O bromide vapour absorption system. The absorber and the evaporator are placed in one compartment which operates at the same low pressure of the system. The generator and condenser are placed together in another chamber that operates at the same high pressure of the system. In the absorber, the lithium bromide solution absorbs the water refrigerant, which creates a weak solution of water and lithium bromide. This weak solution is pumped by the pump to the generator where the solution is heated by the available waste heat. The water refrigerant gets vapourized and flows to the condenser where it is cooled while the strong solution of lithium bromide flows back to the absorber where it further absorbs water coming from the Evaporator. In condenser, water refrigerant loses heat and changes its phase into liquid. Then it passes to the evaporator through an expansion valve where pressure is reduced drastically. In evaporator water is sprayed at low pressure which absorbs the heat from the area to be cooled and gets converted into vapour state. The effect of various thermodynamic parameters (such as effect of temperature overlapping i.e. approach , generator temperature, absorber temperature, evaporator temperature of VCRS cycle, Evaporator temperature of single effect Li/Br VARS cycle, heat exchanger effectiveness, etc.) have been presented.

2. Literature Review

Getu and Bansal [1] carried out thermodynamic analysis of cascade refrigeration system using carbon dioxide–ammonia (R744–R717) to optimize operating parameters of the system

Kilicarslan [2] carried out theoretical and experimental investigation of a two-stage vapor compression cascade refrigeration system using R-134a as the refrigerant.

Lee et al. [3] studied carbon dioxide and ammonia as refrigerants in the cascade refrigeration system and carried out thermodynamic analysis to determine the optimal condensing temperature of the cascade condenser to maximize the COP and minimize the exergy destruction of the system

Arora et.al. [4-5] developed energy and exergy analysis of single effect and series flow double effect water– lithium bromide absorption system and found that the irreversibility is highest in the absorber in both systems as compared to other systems.

Gomri [6] developed the thermal models of single effect and double effect absorption refrigeration systems and found the best possible generator temperature and also observed that the first law efficiency (COP) of double effect system is around twice the first law efficiency (COP) of single effect system.

Kilic and Kaynakli [7] carried out energy analysis for finding the performance of a single stage water lithium bromide absorption refrigeration system by varying inputs parameters and found that that the maximum energy loss occurs in generator of the system. S.B. Riffat N. Shankland [8] designed the different types of absorption systems integration with vapour-compression systems. The double-effect parallel continuous absorption systems and their integration with vapour compression systems have been carried out.

Garimella and Brown [9] studied a NH3/H2O cascaded absorption–compression system coupled with subcritical CO2 vapor–compression cycle to breed low-temperature refrigerant. Cimsit and Ozturk [8] carried out thermodynamic analysis of vapour compression absorption cascaded refrigeration system (VCACRS) with H_2O-LiBr and NH_3-H_2O and improved the system performances with lesser amount of energy input. Chinnappa et al. [9] developed a compression-absorption cascaded refrigeration system which consist a conventional refrigerants with a solar operated, NH_3-H_2O, VARS for air conditioning application. Rogdakis and Antonopoulos [10] carried out absorption refrigeration system NH_3/H_2O running by waste heat and found COP lower as compared LiBr absorption refrigeration system. Fernández–Seara et al. [11] proposed a cascaded vapor NH_3/H_2O absorption refrigeration system with a CO2 compression vapour refrigeration system at an evaporation temperature of -45°C and found its COP using energy and exergy analysis.

Mishra [12-15] modelled the cascaded half effect vapour absorption refrigeration cycle coupled with vapour compression cycle. He has improved COP by 40% using the half effect LiBr/H_2O vapour absorption refrigeration cascaded with vapour compression cycle using HFC-134a. It was evidenced that the performances of single effect cascaded vapour absorption refrigeration system coupled with vapour compression cycle significantly higher than that of existing cycle. Thermodynamic analysis of cascade single effect ammonia-water (NH_3-H_20) vapour absorption refrigeration system coupled with vapour compression refrigeration using ecofriendly refrigerants in the low temperature cycle of VCRS system have been carried out and it is found that the dichloro-1-fluoroethane and Penta-fluoro-propane gives improved thermodynamic performances. The method for enhancement in the thermal performances of vapour absorption refrigeration system by using heat pipes developed by Mishra and Dewedi [16] by utilizing the waste heat in the condenser and found increase in COP of vapour absorption refrigeration system.

The above investigators have not gone through detailed analysis for finding performance improvement and the effect of performance parameters using HFC/ 134A and HFO/1234yf refrigerants in vapour compression refrigeration cycle cascaded with single effect LiBr/ H_2O vapour absorption system.

3. Results and Discussions

Following input data have been taken for numerical computation of single effect Li/Br vapour absorption refrigeration system cascaded with vapour compression refrigeration systems using HFC-134a (system-1) and HFO-

1234yf (system-2) refrigerants**.**

(i) Effect of temperature overlapping (Approach= Temperature of cascade condenser vapour compression refrigeration cycle- cascade evaporator temperature of vapour absorption refrigeration cycle) variation from 0 to 18 using HFC-134a and HFO-1234yf refrigerants
(ii) Compressor efficiency= 0.80
(iii) Generator temperature variation single effect Li//Br vapour absorption refrigeration from 70 ^{o}C to 115 ^{o}C,
(iv) Evaporator temperature vapour compression refrigeration system from $T_{_EVA_VCRS}$ = - 53^{o}C.
(v) Evaporator temperature vapour absorption refrigeration system $T_{_EVA_VARS}$= 05^{o}C,
(vi) Refrigeration effect of vapour absorption refrigeration system =29.167 "kW'

3.1 Effect of temperature overlapping(approach =$T_{_Cond_VCRS}$ -$T_{_Eva_VARS}$)

Table-1 (a-b) shows the variation of approach with variation of thermal performances such as first law efficiency in terms of coefficient of performance (COP) of cascaded vapour absorption system & second law efficiency in terms of exergetic efficiency and exergy destruction ratio based on exergy of fuel of single effect Li/Br-H_2O vapour absorption refrigeration system cascaded with vapour compression refrigeration using HFC-134a refrigerant and it is found that when temperature overlapping in terms of approach (means condenser temperature of vapour compression refrigeration minus evaporator temperature of vapour absorption refrigeration system) is increasing , the thermodynamic performances in terms of ($COP_{_Cascade}$, exergetic efficiency $_{Cascade\ System}$) is decreasing and $EDR_{_}$ is increasing. Similarly exergy destruction ratio based on the exergy of product (EDR_Cascade) is also decreasing as shown in table-1(b) respectively.

Table-1 (c) shows the variation of approach with variation of thermal performances such as first law efficiency in terms of coefficient of performance (COP) of cascaded single effect vapour absorption system & second law efficiency in terms of exergetic efficiency and exergy destruction ratio based on exergy of fuel of single effect Li/Br-H_2O vapour absorption refrigeration system cascaded with vapour compression refrigeration using HFO-1234yf refrigerant and it is found that when temperature overlapping in terms of approach (means condenser temperature of vapour compression refrigeration minus evaporator temperature of vapour absorption refrigeration system) is increasing, the thermodynamic performances in terms of ($COP_{_Cascade}$, Exergetic $efficiency_{_Cascade\ System}$) is decreasing and $EDR_{_Rational}$ is increasing. Similarly exergy destruction ratio based on the exergy of product ($EDR_{_Cascade}$) is also decreasing as shown in table-1(d) respectively.

The performance of single effect Li/Br-H_2O vapour absorption system cascaded with vapour compression system using HFC-134a and HFO-1234yf for low temperature circuit evaporator at -53^{o}C and generator temperature at 110^{o}C have been compared and also shown in Tables-1 to Tables-2 respectively and it is found that thermodynamic performances using HFO-1234yf in cascaded vapour absorption system (system-2) in terms of COP is 1.434% lower and exergetic efficiency is 3.2156% lower than using HFC-134a For both type of EDRs 5.922% decreasing as temperature overlapping approach is increasing.

(A) Input Parameters for vapour single effect Li/Br-H_2O refrigeration system

- Generator temperature= 110 ^{o}C,
- $T_{_EVA_VARS}$= 5^{o}C,
- Refrigerating Effect=35.167 "kW'
- Condenser temperature ($T_{_Cond}$)=35^{o}C
- Absorber temperature ($T_{_Cond}$)=35^{o}C

(B) Performance of single effect Vapour Absorption System using energy-exergy method

- First law Efficiency (COP_VARS) =0.741,
- Exergy Destruction Ratio (EDR)=3.412, ,
- Exergetic Efficiency_VARS=0.2241,

(C) PerforCmance of single effect Vapour Absorption System using entropy generation method

- First law Efficiency (COP_VARS) =0.741,
- Exergy Destruction Ratio (EDR)=3.759, ,
- Exergetic Efficiency_VARS=0.2101,

(D) *Input Parameters for vapour compression refrigeration system using HFC-134a*

- Compressor efficiency= 0.80
- $T_{_EVA_VCRS}$ = - 53^{o}C.
- Effect of Approach; 0 to 20

Table-1(a) Effect of approach on exergy destruction ratio ($EDR_{_Rational}$) of single *effect vapour absorption refrigeration cascaded with vapour compression refrigeration system*

Temperature overlapping / Approach(^{o}C)	$COP_{_Cascade}$	$EDR_{_Cascade}$	Cascaded System Second Law Efficiency
0	1.036	0.8522	0.5399
2	1.024	0.9024	0.5256
4	1.012	0.9530	0.5118
6	1.0	1.006	0.4984
8	0.9888	1.06	0.4854
10	0.9774	1.116	0.4727
12	0.9660	1.172	0.4603
14	0.9548	1.231	0.4483
16	0.9436	1.291	0.4365
18	0.9325	1.353	0.4251

(A) Input Parameters for vapour Double effect Li/Br-H_2O refrigeration system

- Generator temperature= 110 ^oC,
- $T_{_EVA_VARS}$= 5^oC,
- RE=35.167 "kW'
- Condenser temperature (T_ Cond)=35^oC
- Absorber temperature ($T_{_\ Absorber}$)=35^oC

(B) Performance of single effect Vapour Absorption System

- First law Efficiency (COP_VARS) =0.741,
- Exergy Destruction Ratio (EDR)=3.412, ,
- Exergetic Efficiency_VARS=0.2241,

(C) Performance of single effect Vapour Absorption System using entropy generation method

- First law Efficiency (COP_VARS) =0.741,
- Exergy Destruction Ratio (EDR)=3.759, ,
- Exergetic Efficiency_VARS=0.2101,

(D) Input Parameters for vapour compression refrigeration system

- Effect of Approach; 0 to 20 using HFO-1234yf,
- Compressor efficiency= 0.80
- $T_{_EVA_VCRS}$ = - 53^oC.

Table-1(b) Effect of approach on exergy destruction ratio ($EDR_{_Rational}$) of single *effect vapour absorption refrigeration cascaded with vapour compression refrigeration system*

Temperature overlapping / Approach(^oC)	$COP_{_VCRS}$	$EDR_{_VCRS}$	VCRS Second Law Efficiency
0	2.378	0.1862	0.8431
2	2.271	0.2418	0.8053
4	2.171	0.2991	0.7698
6	2.077	0.3581	0.7363
8	1.988	0.419	0.747
10	1.903	0.4819	0.6748
12	1.823	0.5470	0.6464
14	1.747	0.6143	0.6195
16	1.675	0.6841	0.5938
18	1.606	0.7566	0.5693

- Effect of Approach; 0 to 20 using HFO-1234yf, Compressor efficiency= 0.80
- Generator temperature= 110 ^oC, $T_{_EVA_VCRS}$ = - 53^oC. $T_{_EVA_VARS}$= 5^oC, RE=35.167 "kW'
- Performance of Vapour Absorption System: COP_VARS=1.121, EDR=3.241,
- Exergetic Efficiency_VARS=0.2358,

Table-1(c) Effect of Approach on exergy Destruction Ratio (EDR) of single effect vapour absorption refrigeration cascaded with vapour compression refrigeration system

Temperature overlapping / Approach(^oC)	$COP_{_Cascade}$	$EDR_{_Cascade}$	Cascaded System Second Law Efficiency
0	1.027	0.8893	0.5293
2	1.014	0.9448	0.5142
4	1.001	1.002	0.4995
6	0.9886	1.061	0.4852
8	0.9760	1.122	0.4712
10	0.9634	1.186	0.4575
12	0.9509	1.252	0.44441
14	0.9383	1.320	0.4311
16	0.9258	1.391	0.4182
18	0.9133	1.465	0.4057

- Effect of Approach; 0 to 20 using HFO-1234yf, Compressor efficiency= 0.80
- Generator temperature= 110 ^oC, $T_{_EVA_VCRS}$ = - 53^oC. $T_{_EVA_VARS}$= 5^oC, RE=35.167 "kW'
- Performance of Vapour Absorption System:
- $COP_{_VARS}$=1.121, $EDR_{_VARS}$=3.241,
- $ExergeticEfficiency_{_VARS}$=0.2358

Table-1(d) Effect of Approach on exergy Destruction Ratio (EDR) of single *effect vapour absorption refrigeration cascaded with vapour compression refrigeration system*

Temperature overlapping / Approach(^oC)	$COP_{_VCRS}$	$EDR_{_VCRS}$	VCRS Second Law Efficiency
0	2.298	0.2273	0.8148
2	2.188	0.2891	0.7758
4	2.084	0.3533	0.7390
6	1.986	0.420	0.7042
8	1.893	0.4897	0.6713
10	1.805	0.5624	0.6401
12	1.722	0.6384	0.6101
14	1.641	0.7181	0.5821
16	1.565	0.8017	0.5550
18	1.493	0.8898	0.5292

3.2 Effect of of low temperature evaporator temperature of vapour compression refrigeration cycle on thermal performances of single effect vapour absorption refrigeration cascaded with vapour compression refrigeration system

Table-2 (a) shows the variation of low temperature evaporator circuit temperature with variation of thermal performances such as first law efficiency in terms of coefficient of performance (COP) of cascaded vapour absorption system & second law efficiency in terms of exergetic efficiency and exergy destruction ratio based on exergy of fuel of single effect Li/Br-H_2O vapour absorption refrigeration system cascaded with vapour compression refrigeration using HFC-134a refrigerant and it is found that when low temperature evaporator circuit temperature of vapour absorption

refrigeration system is increasing, the thermodynamic performances in terms of (COP_{Cascad},) is decreasing and exergetic efficiency$_{Cascade\ System}$ is also decreasing and $EDR_{Rational}$ is increasing . Similarly exergy destruction ratio based on the exergy of product ($EDR_{Cascade}$) is also decreasing and exergetic efficiency is increasing.as shown in table-2(b) respectively. The optimum values of single effect vapour absorption refrigeration cycle cascaded with vapour compression cycle for generator temperature of 110ºC and condenser temperature and absorber temperature of 35ºC by using HFO-1234yf refrigerant(system-2) has 1.353% lower COP and 3.036% lower exergetic efficiency and 5.703% higher EDR than System-1 using HFC-134a

(A) Input Parameters for vapour single effect Li/Br-H_2O refrigeration system

- Generator temperature= 110 ºC,
- T_{EVA_VARS}= 5ºC,
- RE=29.167 "kW'
- Condenser temperature (T_ Cond)=35ºC
- Absorber temperature ($T_{Absorber}$)=35ºC

(B) Performance of single effect Vapour Absorption System

- COP_VARS=0.7410, (vii) EDR=3.462,
- ExergeticEfficiency_VARS=0.2241

(C) Performance of single effect Vapour Absorption System using entropy generation method

- COP_VARS=0.7410, (vii) Irreversibility Ratio=3.759.
- Exergetic Efficiency_VARS=0.2101

(D) Performance of single effect Vapour Absorption System

- COP_VARS=0.7410,
- Maximum COP_VARS=1.815
- Exergetic Efficiency_VARS=0.4083

(E) Input Parameters for vapour compression refrigeration system

- Effect of Approach; 10 using HFC-134a,
- Compressor efficiency= 0.80
- T_{EVA_VCRS} = - 53ºC.

Table-2(a) Effect of evaporator Temperature VCRS Evaporator on thermal performances of single effect vapour absorption refrigeration cascaded with vapour compression refrigeration system

Temperature VCRS Evaporator $T_{Evaporator}$(ºC)	$COP_{Cascade}$	$EDR_{Cascade}$	Cascaded System Second Law Efficiency
- 40	0.9774	1.116	0.4727
- 45	0.9839	1.112	0.4735
-50	0.9904	1.108	0.4743
-51	0.9970	1.105	0.4751
-52	1.030	1.092	0.4781
-53	1.099	1.083	0.4802

*(A) Input Parameters for vapour **single** effect Li/Br-H_2O refrigeration system*

- Generator temperature= 110 ºC,
- T_{EVA_VARS}= 5ºC,
- RE=35.167 "kW'
- Condenser temperature (T_ Cond)=35ºC
- Absorber temperature ($T_{Absorber}$)=35ºC

(B) Performance of single effect Vapour Absorption System

- COP_VARS=07410, (vii) EDR=3.759,
- ExergeticEfficiency_VARS=0.2101,

(C) Performance of single effect Vapour Absorption System

- COP_VARS=07410, (vii) EDR=3.462
- ExergeticEfficiency_VARS=0.2241

(D) Performance of single effect Vapour Absorption System

- COP_VARS=07410, (vii) EDR=3.759,
- ExergeticEfficiency_VARS=0.2101,

(E) Input Parameters for vapour compression refrigeration system

- Effect of Approach; 10 using HFC-134a,
- Compressor efficiency= 0.80
- T_{EVA_VCRS} = - 53ºC.

Table-2(b) Effect of evaporator Temperature VCRS Evaporator on thermal performances of single effect vapour absorption refrigeration cascaded with vapour compression refrigeration system

Temperature VCRS Evaporator $T_{Evaporator}$(ºC)	COP_{VCRS}	EDR_{VCRS}	VCRS Second Law Efficiency
- 40	1.903	0.4819	0.6748
- 45	1.951	0.4713	0.6797
-50	2.0	0.4607	0.6846
-51	2.05	0.4501	0.6896
-52	2.33	0.3981	0.7153
-53	3.063	0.2952	0.7721

(A) Input Parameters for vapour single effect Li/Br-H_2O refrigeration system:

- Generator temperature= 110 ºC,
- T_{EVA_VARS}= 5ºC,
- RE=29.167 "kW'
- Condenser temperature (T_ Cond)=35ºC
- Absorber temperature ($T_{Absorber}$)=35ºC

(B) Performance of single effect Vapour Absorption System using entropy generation method

- COP_VARS=07410, (vii) EDR=3.759,
- ExergeticEfficiency_VARS=0.2101,

(C) Performance of single effect Vapour Absorption System

- COP_VARS=07410, (vii) EDR=3.462,
- ExergeticEfficiency_VARS=0.2241,

(D) Performance of single effect Vapour Absorption System

- COP_VARS=07410, (vii) EDR=3.759,
- ExergeticEfficiency_VARS=0.2101,

(E) Input Parameters for vapour compression refrigeration system

- Effect of Approach; 10 using HFO-1234yf,
- Compressor efficiency= 0.80
- $T_{_EVA_VCRS}$ = - 53ºC.

Table-2(b) Effect of evaporator Temperature VCRS Evaporator on thermal performances of single effect vapour absorption refrigeration cascaded with vapour compression refrigeration system

Temperature VCRS Evaporator $T_{_Evaporator}$ (ºC)	$COP_{_Cascade}$	$EDR_{_Cascade}$	Cascaded System Second Law Efficiency
- 40	0.9634	1.186	0.4575
- 45	0.9702	1.180	0.4587
-50	0.9770	1.175	0.4599
-51	0.9839	1.169	0.4610
-52	1.019	1.147	0.4658
-53	1.054	1.131	0.4692

(A) Input Parameters for vapour single effect Li/Br-H_2O refrigeration system

- Generator temperature= 110 ºC,
- $T_{_EVA_VARS}$= 5ºC,
- RE= 35.167"kW'
- Condenser temperature (T_ Cond)=35ºC
- Absorber temperature ($T_{_Absorber}$)=35ºC

(B) Performance of single effect Vapour Absorption System using entropy generation method

- COP_VARS=0.7410, (vii) EDR=3.759,
- ExergeticEfficiency_VARS=0.2101,

(C) Performance of single effect Vapour Absorption System

- COP_VARS=07410, (vii) EDR=3.462,
- ExergeticEfficiency_VARS=0.2241.

(D) Performance of single effect Vapour Absorption System

- COP_VARS=07410, (vii) EDR=3.759,
- Exergetic Efficiency_VARS=0.2101,

(E) Input Parameters for vapour compression refrigeration system

- Effect of Approach; 10 using HF-134a,
- Compressor efficiency= 0.80
- $T_{_EVA_VCRS}$ = - 53ºC.

Table-2(b) Effect of evaporator Temperature VCRS Evaporator on thermal performances of single effect vapour absorption refrigeration cascaded with vapour compression refrigeration system

Temperature VCRS Evaporator $T_{_Evaporator}$(ºC)	$COP_{_VCRS}$	$EDR_{_VCRS}$	VCRS Second Law Efficiency
- 40	1.805	0.5624	0.6401
- 45	1.852	0.5496	0.6453
-50	1.901	0.5369	0.6507
-51	1.951	0.5243	0.6560
-52	2.227	0.4626	0.6837
-53	2.553	0.4023	0.7131

The optimum value of second law efficiency of single effect Li/Br H_2O vapour absorption refrigeration system at 5ºC of VARS evaporator temperature using HFO-1234yf occurred between VCRS evaporator temperature -30ºC to -34ºC (i.e. -31ºC, -32ºC and -33ºC. The optimum exergetic efficiency is 46.67% with exergy destruction ratio is 1.143 and rational exergy destruction ratio is 0.5333) and similar second law performance (exergetic efficiency= 46.66%) which is less than optimum exergetic efficiency occurred at -30ºC and -34ºC. Table-2 (b) shows the variation of low temperature evaporator circuit temperature with variation of thermal performances such as first law efficiency in terms of coefficient of performance (COP) of cascaded vapour absorption system & second law efficiency in terms of exergetic efficiency and exergy destruction ratio based on exergy of fuel of single effect Li/Br-H_2O vapour absorption refrigeration system cascaded with vapour compression refrigeration using HFO-1234yf refrigerant and it is found that when low temperature evaporator circuit temperature of single effect Li/Br H_2O vapour absorption is increasing, the thermodynamic performances in terms of ($COP_{_Cascade}$) &Exergetic $efficiency_{_Cascade\ System}$ is decreasing and $EDR_{_Rational}$ is increasing. Similarly exergy destruction ratio based on the exergy of product ($EDR_{_Cascade}$) is also decreasing and low temperature evaporator circuit temperature increasing along with exergetic efficiency of cascaded system is increasing as shown in table-2(d) respectively. The performance of single effect Li/Br-H_2O vapour absorption system cascaded with vapour compression system using HFC-134a and HFO-1234yf for low temperature circuit evaporator at -53ºC have been compared and also shown in Table-2(a) & Table-2(d)

respectively and it is found that thermodynamic performances using HFO-1234yf in cascaded vapour absorption system in terms of COP is 1.643 % and exergetic efficiency is 3.201% lower than using HFC-134a.

3.3 Comparison between VCRS performance using HFC-134a and HFO-1234yf refrigerants at T $_{Evaporator}$ = -30 (^oC)

(A) Input Parameters for vapour single effect Li/Br-H_2O refrigeration system

- Generator temperature= 110 ^oC,
- $T_{_EVA_VARS}$= 5^oC,
- RE=35.167 "kW'
- Condenser temperature (T_ Cond)=35^oC
- Absorber temperature ($T_{_\ Absorber}$)=35^oC

(B) Performance of single effect Vapour Absorption System

- COP_VARS=0.7410, (vii) EDR=3.462,
- Exergetic Efficiency_VARS=0.2241,

(C) Performance of single effect Vapour Absorption System using entropy generation method

- COP_VARS=0.7410, (vii) EDR=3.759,
- Exergetic Efficiency_VARS=0.2101,

(D) Performance of single effect Vapour Absorption System

- COP_VARS=0.7410, (vii) Maximum $COP_{_VARS}$=1.815
- Second law (Exergetic) $Efficiency_{_VARS}$=0.4083,

(E) Input Parameters for vapour compression refrigeration system

- Using HFC-134a, R1234ze and R-1234yf
- Effect of Approach; 10
- Compressor efficiency= 0.80
- $T_{_EVA_VCRS}$ = - 30^oC.

Table-3(a) Effect of ecofriendly refrigerants in the VCRS on thermal performances of single *effect vapour absorption refrigeration cascaded with vapour compression refrigeration system*

Ecofriendly Refrigerants	$COP_{Cascade}$	Rational $EDR_{_Cascade}$	Cascaded System Second Law Efficiency
R134a	1.135	1.088	0.4790
R1234ze	1.133	1.094	0.4776
R1234yf	1.127	1.121	0.4716

(A) Input Parameters for vapour single effect Li/Br-H_2O refrigeration system

- Generator temperature= 110 ^oC,
- $T_{_EVA_VARS}$= 5^oC,
- RE=29.167 "kW'
- Condenser temperature (T_ Cond)=35^oC
- Absorber temperature ($T_{_\ Absorber}$)=35^oC

(B) Performance of single effect Vapour Absorption System

- COP_VARS=1.121, (vii) EDR=3.24,
- Exergetic Efficiency_VARS=0.2358,

(C) Input Parameters for vapour compression refrigeration system

- Using HFC-134a, R1234ze and R-1234yf
- Effect of Approach; 10
- Compressor efficiency= 0.80
- $T_{_EVA_VCRS}$ = - 30^oC.

Table-3(b) Effect of ecofriendly refrigerants in the VCRS on VCRS thermal performances of vapour compression refrigeration system cascaded with single *effect vapour absorption refrigeration system.*

Ecofriendly Refrigerants	COP_{VCRS}	Rational $EDR_{_Cascade}$	Cascaded System Second Law Efficiency
R134a	3.555	0.2428	0.8046
R1234ze	3.535	0.2499	0.8001
R1234yf	3.444	0.2829	0.7795

Table-3(a) and Table-3(b) show, the effect of ecofriendly HFC-134a and HFO refrigerants in low temperature circuit with variation of thermal performances such as first law efficiency in terms of coefficient of performance (COP) of cascaded vapour absorption system & second law efficiency in terms of exergetic efficiency and exergy destruction ratio based on exergy of fuel of single effect Li/Br-H_2O vapour absorption refrigeration system cascaded with vapour compression refrigeration at -30^oC and it is found that the performance of HFC-134a refrigerant and HFO-1234ze are nearly similar with the variation of 0.5626% in first law efficiency and 0.559% in second law efficiency while the performance of HFC-134a is superior than HFO- 1234yf refrigerant. Therefore both HFO refrigerants can replace HFC-134a refrigerant in near future due to its very low global warming potential (i.e. GWP of R1234ze is 6 and GWP of R1234yf is 4 respectively as compared to GWP of HFC-134a is 1360).

3.4 Variation of vapour absorption refrigeration system evaporator temperature of vapour absorption system, when absorber temperature is same as condenser temperature

- Evaporator temperature ($T_{_EVA_VARS}$) varying from 5ºC to 10ºC
- Generator temperature =110 ºC
- VCRS using HFC-134a , Compressor efficiency= 0.80
- Approach=10, $T_{_EVA_VCRS}$ = - 53ºC. $T_{_EVA_VARS}$= 5ºC, RE=35.167 "kW'
- Performance of Vapour compression System COP_VCRS=1.71, EDR=,0.6492
- Exergetic Efficiency_VCRS=0.6064, $EDR_{_Rational}$ =0.3936

Table-5(a) Effect of vapour absorption refrigeration system evaporator temperature on thermal performances of single effect vapour absorption refrigeration cascaded with vapour compression refrigeration system

Vapour absorption system evaporator temperature (ºC)	$COP_{_Cascade}$	$EDR_{_Cascade}$	Cascaded System Second Law Efficiency
05	0.9773	1.116	0.4726
06	0.9745	1.168	0.4613
07	0.9717	1.222	0.4501
08	0.9891	1.277	0.4391
09	0.9665	1.335	0.4283
10	0.9641	1.394	0.4177

- Evaporator temperature ($T_{_EVA_VARS}$) varying from 5ºC to 10ºC
- Generator temperature =110 ºC
- VCRS using HFC-134a , Compressor efficiency= 0.80
- Approach=10, $T_{_EVA_VCRS}$ = - 53ºC. $T_{_EVA_VARS}$= 5ºC, RE=35.167 "kW'
- Performance of Vapour compression System: COP_VCRS=1.71, EDR=,0.6492
- Exergetic efficiency_VCRS=0.6064, $EDR_{_Rational}$ =0.3936

Table-5(b) Effect of Vapour absorption system evaporator temperature ($T_{_evaporator}$)*on thermal performances of single e effect vapour absorption refrigeration cascaded with vapour compression refrigeration system*

Vapour absorption system evaporator temperature ($T_{_evaporator}$)	$COP_{_VARS}$	$EDR_{_VARS}$	VARS Second Law Efficiency
05	0.7410	3.462	0.2241
06	0.7438	3.68	0.2137
07	0.7466	3.921	0.2032
08	0.7496	4.19	1.927
09	0.7527	4.491	1.821
10	0.7560	4.832	0.1715

- Evaporator temperature ($T_{_EVA_VARS}$) varying from 5ºCto 10ºC
- Generator temperature =110 ºC
- VCRS using HFC-134a , Compressor efficiency= 0.80
- Approach=10, $T_{_EVA_VCRS}$ = - 53ºC. $T_{_EVA_VARS}$= 5ºC, RE=35.167 "kW'
- Performance of Vapour compression System: COP_VCRS= 1.71, EDR=,0.6492
- Exergetic Efficiency_VCRS=0.6064, $EDR_{_Rational}$ =0.3936.

Table-5(d) Effect of generator temperature on thermal performances of single effect vapour absorption refrigeration cascaded with vapourcompression refrigeration system

Vapour absorption system evaporator temperature ($T_{_evaporator}$)	$COP_{_VARS}$	$EDR_{_VARS}$	VARS Second Law Efficiency
05	0.7410	3.759	0.2101
06	0.7438	3.939	0.2025
07	0.7466	4.36	0.1946
08	0.7496	4.19	1.866
09	0.7527	4.609	1.783
10	0.7560	4.89	0.1698

- Evaporator temperature ($T_{_EVA_VARS}$) varying from 5ºCto 10ºC
- Generator temperature =110 ºC
- VCRS using HFC-134a , Compressor efficiency= 0.80
- Approach=10, $T_{_EVA_VCRS}$ = - 53ºC. $T_{_EVA_VARS}$= 5ºC, RE=35.167 "kW'
- Performance of Vapour compression System: COP_VCRS=1.71, EDR=,0.6492
- Exergetic Efficiency_VCRS=0.6064, $EDR_{_Rational}$ =0.3936.

Table-5(d) Effect of generator temperature on thermal performances of single effect vapour absorption refrigeration cascaded with vapou rcompression refrigeration system

Vapour absorption system evaporator temperature ($T_{_evaporator}$)	$COP_{_VARS}$	Maximum COP_VARS	VARS Second Law Efficiency
05	0.7410	1.815	0.4083
06	0.7438	1.884	0.3947
07	0.7466	1.959	0.3812
08	0.7496	2.038	0.3678
09	0.7527	2.124	0.3543
10	0.7560	2.217	0.3410

- Evaporator temperature ($T_{_EVA_VARS}$) varying from 5ºC to 10ºC
- Generator temperature =110 ºC
- VCRS using HFC-1234yf , Compressor efficiency= 0.80
- Approach=10, $T_{_EVA_VCRS}$ = - 53ºC. $T_{_EVA_VARS}$= 5ºC, RE=35.167 "kW'
- Performance of Vapour compression System: COP_VCRS=1.588, EDR=,0.7759
- Exergetic Efficiency_VCRS=0.5631, $EDR_{_Rational}$ =0.4369.

Table-5(c) Effect of Vapour absorption system evaporator temperature ($T_{_evaporator}$) *on thermal performances of single effect vapour absorption refrigeration cascaded with vapour compression refrigeration system*

Vapour absorption system evaporator temperature ($T_{_evaporator}$) (°C)	$COP_{_Cascade}$	$EDR_{_Cascade}$	Cascaded System Second Law Efficiency
05	0.9613	1.197	0.4552
06	0.9577	1.255	0.4434
07	0.9542	1.316	0.4317
08	0.9508	1.379	0.4203
09	0.9474	1.445	0.4090
10	0.9441	1.513	0.3979

- Evaporator temperature ($T_{_EVA_VARS}$) varying from 5°Cto 10°C
- Generator temperature =110 °C
- VCRS using HFC-1234yf , Compressor efficiency= 0.80
- Approach=10, $T_{_EVA_VCRS}$ = - 53°C. $T_{_EVA_VARS}$= 5°C, RE=35.167 "kW'
- Performance of Vapour compression System:COP_VCRS=1.588, EDR=,0.7759
- ExergeticEfficiency_VCRS=0.5631, $EDR_{_Rational}$ =0.4369.

Table-5(d) Effect of generator temperature on thermal performances of single effect vapour absorption refrigeration cascaded with vapour compression refrigeration system

Vapour absorption system evaporator temperature ($T_{_evaporator}$)	$COP_{_VARS}$	$EDR_{_VARS}$	VARS Second Law Efficiency
05	0.7410	3.462	0.2241
06	0.7438	3.68	0.2137
07	0.7466	3.921	0.2032
08	0.7496	4.19	1.927
09	0.7527	4.491	1.821
10	0.7560	4.832	0.1715

- Evaporator temperature ($T_{_EVA_VARS}$) varying from 5°Cto 10°C
- Generator temperature =110 °C
- VCRS using HFC-1234yf , Compressor efficiency= 0.80
- Approach=10, $T_{_EVA_VCRS}$ = - 53°C. $T_{_EVA_VARS}$= 5°C, RE=35.167 "kW'
- Performance of Vapour compression System:COP_VCRS=1.588, EDR=,0.7759
- ExergeticEfficiency_VCRS=0.5631, $EDR_{_Rational}$ =0.4369 .

Table-5(d) Effect of generator temperature on thermal performances of single effect vapour absorption refrigeration cascaded with vapourcompression refrigeration system using entropy generation method

Vapour absorption system evaporator temperature ($T_{_evaporator}$)	$COP_{_VARS}$	$EDR_{_VARS}$	VARS Second Law Efficiency
05	0.7410	3.759	0.2101
06	0.7438	3.939	0.2025
07	0.7466	4.36	0.1946
08	0.7496	4.19	1.866
09	0.7527	4.609	1.783
10	0.7560	4.89	0.1698

- Evaporator temperature ($T_{_EVA_VARS}$) varying from 5°Cto 10°C
- Generator temperature =110 °C
- VCRS using HFC-1234yf , Compressor efficiency= 0.80
- Approach=10, $T_{_EVA_VCRS}$ = - 53°C. $T_{_EVA_VARS}$= 5°C, RE=35.167 "kW'
- Performance of Vapour compression System:COP_VCRS=1.588, EDR=,0.7759
- Exergetic Efficiency_VCRS=0.5631, $EDR_{Rational}$ = 0.4369.

Table-5(d) Effect of generator temperature on thermal performances of single effect vapour absorption refrigeration cascaded with vapour compression refrigeration system

Vapour absorption system evaporator temperature	$COP_{_VARS}$	Maximum COP_VARS	VARS Second Law Efficiency
05	0.7410	1.815	0.4083
06	0.7438	1.884	0.3947
07	0.7466	1.959	0.3812
08	0.7496	2.038	0.3678
09	0.7527	2.124	0.3543
10	0.7560	2.217	0.3410

Table-5 (a) shows the variation of Vapour absorption system evaporator temperature ($T_{_evaporator}$)with variation of thermal performances such as first law efficiency in terms of coefficient of performance (COP) of cascaded vapour absorption system & second law efficiency in terms of exergetic efficiency and exergy destruction ratio based on exergy of fuel of single effect Li/Br-H_2Ovapour absorption refrigeration system cascaded with vapour compression refrigeration using HFC-134a refrigerant and it is found that when Vapour absorption system evaporator temperature ($T_{_evaporator}$)of vapour absorption refrigeration system is increasing, the thermodynamic performances in terms of ($COP_{_Cascad}$,) is decreasing and Exergetic efficiency $_{_CascadeSystem}$ is increasing and $EDR_{_Rational}$ is decreasing . Similarly exergy destruction ratio based on the exergy of product ($EDR_{_Cascade}$) is also decreasing and exergetic efficiency is increasing.as shown in table-5(b) respectively. Table-5 (c) shows the variation of generator temperature with variation of thermal performances such as first law efficiency in terms of coefficient of performance (COP) of cascaded vapour absorption system & second law efficiency in terms of exergetic efficiency and exergy destruction ratio based on exergy of fuel of single effect Li/Br-H_2O vapour absorption refrigeration system cascaded with vapour compression refrigeration using HFO-1234yf refrigerant and it is found that when generator temperature of tripple effect Li/Br H_2O vapour absorption is increasing , the thermodynamic performances in terms of ($COP_{_Cascade}$) &$EDR_{_Rational}$ is decreasing and Exergetic efficiency$_{_Cascade\ System}$) is increasing. Similarly exergy destruction ratio based on the exergy of product ($EDR_{_Cascade}$) is also decreasing and generator temperature increasing along with exergetic efficiency of cascaded system is increasing as shown in table-5(d) respectively.

The performance of single effect Li/Br-H_2O vapour absorption system cascaded with vapour compression system using HFC-134a and HFO-1234yf for low temperature circuit evaporator

at -53ºC and Vapour absorption system evaporator temperature at 5ºC have been compared and also shown in Table-5(a) to Tables-5(d) respectively and it is found that thermodynamic performances using HFO-1234yf (system-2)in cascaded vapour absorption system in terms of COP is 3.87223% and exergetic efficiency is 4.2815 % lower than using HFC-134a (system-1)with increasing 7.9875% at 8ºC of evaporator of single effect vapour absorption systems. .

3.5 Variation of generator temperature of vapour absorption system, when absorber temperature is same as condenser temperature

Table-6 (a) shows the variation of generator temperature with variation of thermal performances such as first law efficiency in terms of coefficient of performance (COP) of cascaded vapour absorption system & second law efficiency in terms of exergetic efficiency and exergy destruction ratio based on exergy of fuel of single effect Li/Br-H_2Ovapour absorption refrigeration system cascaded with vapour compression refrigeration using HFC-134a refrigerant and it is found that when generator temperature of vapour absorption refrigeration system is increasing , the thermodynamic performances in terms of ($COP_{_Cascad}$) is decreasing and Exergetic $efficiency_{_Cascade\ System}$ is increasing and $EDR_{_Rational}$ is decreasing . Similarly exergy destruction ratio based on the exergy of product ($EDR_{_Cascade}$) is also decreasing and exergetic efficiency is increasing.as shown in table-6(b) respectively. Table-6 (c) shows the variation of generator temperature with variation of thermal performances such as first law efficiency in terms of coefficient of performance (COP) of cascaded vapour absorption system & second law efficiency in terms of exergetic efficiency and exergy destruction ratio based on exergy of fuel of single effect Li/Br-H_2O vapour absorption refrigeration system cascaded with vapour compression refrigeration using HFO-1234yf refrigerant and it is found that when generator temperature of single effect Li/Br H_2O vapour absorption is increasing , the thermodynamic performances in terms of ($COP_{_Cascade}$) &$EDR_{_Rational}$ is decreasing and Exergetic $efficiency_{_Cascade\ System}$) is increasing. Similarly exergy destruction ratio based on the exergy of product ($EDR_{_Cascade)}$ is also decreasing and generator temperature increasing along with exergetic efficiency of cascaded system is increasing as shown in table-6(b) respectively. The performance of single effect Li/Br-H_2O vapour absorption system cascaded with vapour compression system using HFC-134a and HFO-1234yf for low temperature circuit evaporator at -53ºC and generator temperature at 110ºC have been compared and also shown in Table-6(a) to Tables-6(d) respectively and it is found that thermodynamic performances using HFO-1234yf (system-2) in cascaded vapour absorption system in terms of COP is 1.4322% lower and exergetic efficiency is 3.3044 % lower than using HFC-134a(System-1).

- Generator temperature varing from 80 to 115 ºC
- VCRS using HFC-134a , Compressor efficiency= 0.80
- Approach=10, $T_{_EVA_VCRS}$ = - 53ºC. $T_{_EVA_VARS}$= 5ºC, RE=29.167 "kW'
- Performance of Vapour compression System: COP_VCRS=1.903,
- Exergetic $Efficiency_{_VCRS}$=0.6748 , $EDR_{_VCRS}$=0.4819.

Table-6(a) Effect of generator temperature on thermal performances of single effect vapour absorption refrigeration cascaded with vapour compression refrigeration system

$T_{_generator}$ (ºC)	$COP_{_Cascade}$	Rational $EDR_{_Cascade}$	Cascaded System Second Law Efficiency
80	1.013	0.792	0.5580
85	1.004	0.8497	0.5406
90	0.9968	0.9062	0.5246
95	0.9901	0.9614	0.5099
100	0.9845	1.015	0.4963
105	0.9802	1.067	0.4839
110	0.9774	1.116	0.4727
115	0.975	1.163	0.4623

- Generator temperature varing from 80 to 115 ºC
- VCRS using HFC-134a , Compressor efficiency= 0.80
- Approach=10, $T_{_EVA_VCRS}$ = - 53ºC. $T_{_EVA_VARS}$= 5ºC, RE = 35.167 "kW'
- Performance of Vapour compression System: COP_VCRS =1.903,
- Exergetic $Efficiency_{_VCRS}$=0.6748 , $EDR_{_VCRS}$=0.4819.

Table-6(b) Effect of generator temperature on thermal performances of single effect vapour absorption refrigeration cascaded with vapour compression refrigeration system

$T_{_generator}$ (ºC)	$COP_{_VARS}$	$EDR_{_VARS}$	VARS Second Law Efficiency
80	0.7752	1.995	0.3339
85	0.7669	2.256	0.3071
90	0.7596	2.513	0.2847
95	0.7532	2.763	0.2658
100	0.7479	3.006	0.2496
105	0.7438	3.24	0.2359
110	0.7410	3.462	0.2241
115	0.7388	3.678	0.2138

- Generator temperature varing from 80 to 115 ºC
- VCRS using HFC-134a , Compressor efficiency= 0.80
- Approach=10, $T_{_EVA_VCRS}$ = - 53ºC. $T_{_EVA_VARS}$= 5ºC, RE= 35.167 "kW'
- Performance of Vapour compression System: COP_VCRS= 1.903,
- $ExergeticEfficiency_{_VCRS}$=0.6748 ,
- $EDR_{_VCRS}$=0.4819.

Table-6(b) Effect of generator temperature on thermal performances of single effect vapour absorption refrigeration cascaded with vapour compression refrigeration system using entropy generation method

$T_{_generator}$ (°C)	$COP_{_VARS}$	Irreversibility Coefficient	VARS Second Law Efficiency
80	0.7752	3.555	0.2195
85	0.7669	3.603	0.2172
90	0.7596	3.646	0.2152
95	0.7532	3.684	0.2135
100	0.7479	3.717	0.2120
105	0.7438	3.742	0.2109
110	0.7410	3.759	0.2101
115	0.7388	3.773	0.2095

- Generator temperature varing from 80 to 115 °C
- VCRS using HFC-134a , Compressor efficiency= 0.80
- Approach=10, $T_{_EVA_VCRS}$ = - 53°C. $T_{_EVA_VARS}$= 5°C, RE=35.167 "kW'
- Performance of Vapour compression System: COP_VCRS=1.903,
- Exergetic $Efficiency_{_VCRS}$=0.6748 , $EDR_{_VCRS}$=0.4819.

Table-6(b) Effect of generator temperature on thermal performances of single effect vapour absorption refrigeration cascaded with vapour compression refrigeration system

$T_{_generator}$ (°C)	$COP_{_VARS}$	Maximum COP_VARS	VARS Second Law Efficiency
80	0.7752	1.181	0.6562
85	0.7669	1.294	0.5925
90	0.7596	1.404	0.5409
95	0.7532	1.511	0.4985
100	0.7479	1.615	0.463
105	0.7438	1.716	0.4334
110	0.7410	1.815	0.4083
115	0.7388	1.911	0.3866

- Generator temperature varing from 80 to 115 °C
- VCRS using HFO-1234yf , Compressor efficiency= 0.80
- Approach=10, $T_{_EVA_VCRS}$ = - 53°C. $T_{_EVA_VARS}$= 5°C, RE=35.167 "kW'
- Performance of Vapour compression System:COP_VCRS=1.805, EDR=,1.117
- ExergeticEfficiency_VCRS=0.5624, $EDR_{_VCRS}$=0.6401 .

Table-6(c) Effect of generator temperature on thermal performances of single *effect vapour absorption refrigeration cascaded with vapour compression refrigeration system*

$T_{_generator}$ (°C)	$COP_{_Cascade}$	$EDR_{_Cascade}$	Cascaded System Second Law Efficiency
80	0.9983	0.8575	0.5383
85	0.9898	0.9160	0.5219
90	0.9824	0.9733	0.5088
95	0.9759	1.029	0.4928
100	0.9704	1.084	0.4799
105	0.9662	1.136	0.4682
110	0.9634	1.186	0.4575
115	0.9601	1.234	0.4476

- Generator temperature varing from 80 to 115 °C
- VCRS using HFC-1234yf , Compressor efficiency= 0.80
- Approach=10, $T_{_EVA_VCRS}$ = - 53°C. $T_{_EVA_VARS}$= 5°C, RE=35.167 "kW'
- Performance of Vapour compression System: COP_VCRS=1.805,
- Exergetic $Efficiency_{_VCRS}$=0.6748 , $EDR_{_VCRS}$=0.6401.

Table-6(b) Effect of generator temperature on thermal performances of triple effect vapour absorption refrigeration cascaded with vapour compression refrigeration system

$T_{_generator}$ (°C)	$COP_{_VARS}$	$EDR_{_VARS}$	VARS Second Law Efficiency
80	0.7752	1.995	0.3339
85	0.7669	2.256	0.3071
90	0.7596	2.513	0.2847
95	0.7532	2.763	0.2658
100	0.7479	3.006	0.2496
105	0.7438	3.24	0.2359
110	0.7410	3.462	0.2241
115	0.7388	3.678	0.2138

- Generator temperature varying from 80 to 115 °C
- VCRS using HFC-134a , Compressor efficiency= 0.80
- Approach=10, $T_{_EVA_VCRS}$ = - 53°C. $T_{_EVA_VARS}$= 5°C, RE=35.167 "kW'
- Performance of Vapour compression System: COP_VCRS=1.805,
- Exergetic $Efficiency_{_VCRS}$=0.6748, $EDR_{_VCRS}$=0.6401.

Table-6(b) Effect of generator temperature on thermal performances of single *effect vapour absorption refrigeration cascaded with vapour compression refrigeration system*

$T_{_generator}$ (°C)	$COP_{_VARS}$	Irreversibility Coefficient	VARS Second Law Efficiency
80	0.7752	3.555	0.2195
85	0.7669	3.603	0.2172
90	0.7596	3.646	0.2152
95	0.7532	3.684	0.2135
100	0.7479	3.717	0.2120
105	0.7438	3.742	0.2109
110	0.7410	3.759	0.2101
115	0.7388	3.773	0.2095

- Generator temperature varing from 80 to 115 °C
- VCRS using HFC-1234yf , Compressor efficiency= 0.80
- Approach=10, $T_{_EVA_VCRS}$ = - 53°C. $T_{_EVA_VARS}$= 5°C, RE=29.167 "kW'
- Performance of Vapour compression System: COP_VCRS=1.805,
- ExergeticEfficiency_$_{VCRS}$=0.6748 , $EDR_{_VCRS}$=0.6401.

Table-6(b) Effect of generator temperature on thermal performances of single *effect vapour absorption refrigeration cascaded with vapour compression refrigeration system*

$T_{_generator}$ (°C)	$COP_{_VARS}$	Maximum COP_VARS	VARS Second Law Efficiency
80	0.7752	1.181	0.6562

85	0.7669	1.294	0.5925
90	0.7596	1.404	0.5409
95	0.7532	1.511	0.4985
100	0.7479	1.615	0.463
105	0.7438	1.716	0.4334
110	0.7410	1.815	0.4083
115	0.7388	1.911	0.3866

3.6 Variation of condenser temperature of vapour absorption system, when absorber temperature is same as condenser temperature

- Evaporator temperature of VARS using HFC-134a = - 53ºC, Compressor efficiency= 0.80
- Single effect Li/Br-H_2O VARS
- Approach=10, $T_{generator}$= 110ºC. T_{EVA_VARS}= 05ºC, RE =29.167 "kW', T_Absorber=T_Cond
- Performance of Vapour compression System: COP_VCRS=1.903,
- Exergetic Efficiency$_{VCRS}$=,0.2630, EDR$_{VCRSl}$=0.4822.

Table-7(a) Effect of condenser temperature of VARS on thermal performances of single effect vapour absorption refrigeration cascaded with vapour compression refrigeration system when $T_{Cond}=T_{Absorber}$

T_Cond	COP$_{Cascade}$	EDR$_{Cascade}$	Cascaded System Second Law Efficiency
31	0.9827	1.109	0.4741
32	0.9414	1.111	0.4738
33	0.9801	1.112	0.4734
34	0.9787	1.114	0.4730
35	0.9773	1.116	0.4726
36	0.9760	1.118	0.4722
37	0.9747	1.119	0.4719
38	0.9735	1.121	0.4715
39	0.9724	1.222	0.4712
40	0.9713	1.123	0.4709

- Evaporator temperature of VARS using HFC-134a = - 53ºC, Compressor efficiency= 0.80
- Double effect Li/Br-H_2O VARS
- Approach=10, $T_{generator}$= 110ºC. T_{EVA_VARS}= 05ºC, RE=35.167 "kW', T_Absorber=T_Cond
- Performance of Vapour compression System:COP_VCRS=1.903,
- ExergeticEfficiency$_{VCRS}$=,0.2630, EDR$_{VCRSl}$=0.4822.

Table-7(b) Effect of condenser temperature of VARS on thermal performances of single *effect vapour absorption refrigeration cascaded with vapour compression refrigeration system when $T_{Cond}=T_{Absorber}$*

T_Cond	COP$_{VARS}$	EDR$_{VARS}$	VARS Second Law Efficiency
31	0.7461	3.432	0.2256
32	0.7449	3.439	0.2253
33	0.7437	3.447	0.2249
34	0.7423	3.455	0.2245
35	0.7410	3.759	0.2241
36	0.7398	3.47	0.2237
37	0.7385	3.478	0.2233
38	0.7374	3.484	0.2230
39	0.7363	3.491	0.2227
40	0.7353	3.497	0.2224-

- Evaporator temperature of VARS using HFC-134a = - 53 ºC, Compressor efficiency= 0.80
- Double effect Li/Br-H_2O VARS
- Approach=10, $T_{generator}$= 110ºC. T_{EVA_VARS}= 05ºC, RE= 35.167 "kW', T_Absorber=T_Cond
- Performance of Vapour compression System: COP_VCRS=1.903,
- Exergetic Efficiency$_{VCRS}$= 0.2630, EDR$_{VCRSl}$= 0.4822.

Table-7(b) Effect of condenser temperature of VARS on thermal performances of single *effect vapour absorption refrigeration cascaded with vapour compression refrigeration system when $T_{Cond}=T_{Absorber}$ using entropy generation method*

T_Cond	COP$_{VARS}$	EDR$_{VARS}$	VARS Second Law Efficiency
31	0.7461	3.327	0.2126
32	0.7449	3.734	0.2112
33	0.7437	3.742	0.2109
34	0.7423	3.750	0.2105
35	0.7410	3.759	0.2101
36	0.7398	3.767	0.2098
37	0.7385	3.774	0.2095
38	0.7374	3.782	0.2091
39	0.7363	3.788	0.2088
40	0.7353	3.94	0.2086

- Evaporator temperature of VARS using HFC-134a = - 53 ºC, Compressor efficiency= 0.80
- Double effect Li/Br-H_2O VARS
- Approach=10, $T_{generator}$= 110ºC. T_{EVA_VARS}= 05ºC, RE=35.167 "kW', T_Absorber=T_Cond
- Performance of Vapour compression System: COP_VCRS=1.903,
- Exergetic Efficiency$_{VCRS}$=,0.2630, EDR$_{VCRSl}$=0.4822.

Table-7(b) Effect of condenser temperature of VARS on thermal performances of single *effect vapour absorption refrigeration cascaded with vapour compression refrigeration system when $T_{Cond}=T_{Absorber}$*

T_Cond	COP$_{VARS}$	Maximum COP$_{VARS}$	VARS Second Law Efficiency
31	0.7461	2.206	0.3383
32	0.7449	2.097	0.3552
33	0.7437	1.996	0.3725
34	0.7423	1.903	0.3902
35	0.7410	1.815	0.4083
36	0.7398	1.733	0.4269
37	0.7385	1.656	0.4460
38	0.7374	1.584	0.4656
39	0.7363	1.516	0.4857
40	0.7353	1.791	0.5065

- Evaporator temperature of VARS using HFO-1234yf = -53ºC, Compressor efficiency= 0.80
- Single effect Li/Br-H_2O VARS
- Approach=10, $T_{_generator}$= 110ºC. $T_{_EVA_VARS}$= 05ºC, RE=35.167 "kW', T_Absorber=T_Cond
- Performance of Vapour compression System: COP_VCRS=1.791,
- Exergetic efficiency$_{_VCRS}$=0.6349,EDR$_{_VCRSl}$=0.5751.

Table-7(c) Effect of condenser temperature of VARS on thermal performances of single *effect vapour absorption refrigeration cascaded with vapour compression refrigeration system when* $T_{_Cond}=T_{_Absorber}$

T_Cond	COP$_{_Cascade}$	EDR$_{_Cascade}$	Cascaded System Second Law Efficiency
31	0.9665	1.190	0.4566
32	0.9653	1.192	0.4563
33	0.9640	1.193	0.4559
34	0.9626	1.195	0.4556
35	0.9613	1.197	0.4552
36	0.960	1.199	0.4548
37	0.9587	1.20	0.4545
38	0.9575	1.202	0.4542
39	0.9564	1.203	0.4539
40	0.9554	1.205	0.4536

- Evaporator temperature of VARS using HFO-1234yf = -53 ºC, Compressor efficiency= 0.80
- Double effect Li/Br-H_2O VARS
- Approach=10, $T_{_generator}$= 110ºC. $T_{_EVA_VARS}$= 05ºC, RE=35.167 "kW', T_Absorber=T_Cond
- Performance of Vapour compression System:COP_VCRS=1.791,
- Exergetic Efficiency$_{_VCRS}$=0.6349, EDR$_{_VCRSl}$=0.3630,

Table-7(d) Effect of condenser temperature of VARS on thermal performances of single *effect vapour absorption refrigeration cascaded with vapour compression refrigeration system when* $T_{_Cond}=T_{_Absorber}$

T_Cond	COP$_{_VARS}$	EDR$_{_VARS}$	VARS Second Law Efficiency
31	0.7461	3.432	0.2256
32	0.7449	3.439	0.2253
33	0.7437	3.447	0.2249
34	0.7423	3.455	0.2245
35	0.7410	3.759	0.2241
36	0.7398	3.47	0.2237
37	0.7385	3.478	0.2233
38	0.7374	3.484	0.2230
39	0.7363	3.491	0.2227
40	0.7353	3.497	0.2224-

- Evaporator temperature of VARS using HFO-1234yf = -53 ºC, Compressor efficiency= 0.80
- Double effect Li/Br-H_2O VARS
- Approach=10, $T_{_generator}$= 110ºC. $T_{_EVA_VARS}$= 05ºC, RE=35.167 "kW', T_Absorber=T_Cond
- Performance of Vapour compression System: COP_VCRS=1.791,
- Exergetic Efficiency$_{_VCRS}$=0.6349, EDR$_{_VCRSl}$=0.3630,

Table-7(d) Effect of condenser temperature of VARS on thermal performances of single *effect vapour absorption refrigeration cascaded with vapour compression refrigeration system when* $T_{_Cond}=T_{_Absorber}$

T_Cond	COP$_{_VARS}$	EDR$_{_VARS}$	VARS Second Law Efficiency
31	0.7461	3.327	0.2126
32	0.7449	3.734	0.2112
33	0.7437	3.742	0.2109
34	0.7423	3.750	0.2105
35	0.7410	3.759	0.2101
36	0.7398	3.767	0.2098
37	0.7385	3.774	0.2095
38	0.7374	3.782	0.2091
39	0.7363	3.788	0.2088
40	0.7353	3.94	0.2086

- Evaporator temperature of VARS using HFC-134a = - 53 ºC, Compressor efficiency= 0.80
- Double effect Li/Br-H_2O VARS
- Approach=10, $T_{_generator}$= 110ºC. $T_{_EVA_VARS}$= 05ºC, RE=35.167 "kW', T_Absorber=T_Cond
- Performance of Vapour compression System: COP_VCRS=
- Exergetic Efficiency$_{_VCRS}$=,EDR$_{_VCRSl}$=0.

Table-7(b) Effect of condenser temperature of VARS on thermal performances of single *effect vapour absorption refrigeration cascaded with vapour compression refrigeration system when* $T_{_Cond}=T_{_Absorber}$

T_Cond	COP$_{_VARS}$	Maximum COP$_{_VARS}$	VARS Second Law Efficiency
31	0.7461	2.206	0.3383
32	0.7449	2.097	0.3552
33	0.7437	1.996	0.3725
34	0.7423	1.903	0.3902
35	0.7410	1.815	0.4083
36	0.7398	1.733	0.4269
37	0.7385	1.656	0.4460
38	0.7374	1.584	0.4656
39	0.7363	1.516	0.4857
40	0.7353	1.791	0.5065

Table-7 (a) shows the variation of condenser temperature with variation of thermal performances such as first law efficiency in terms of coefficient of performance (COP) of cascaded vapour absorption system & second law efficiency in terms of exergetic efficiency and exergy destruction ratio based on exergy of fuel of single effect Li/Br-H_2Ovapour absorption refrigeration system cascaded with vapour compression refrigeration using HFC-134a refrigerant and it is found that when condenser temperature of vapour absorption refrigeration system is increasing, the thermodynamic performances in terms of (COP$_{_Cascad}$,) and Exergetic

efficiency_Cascade System both are decreasing and EDR_Rational is increasing . Similarly exergy destruction ratio based on the exergy of product (EDR_Cascade) is also increasing as exergetic efficiency is decreasing. Table-7 (b) shows the variation of low temperature evaporator circuit temperature with variation of thermal performances such as first law efficiency in terms of coefficient of performance (COP) of cascaded vapour absorption system & second law efficiency in terms of exergetic efficiency and exergy destruction ratio based on exergy of fuel of single effect Li/Br-H_2O vapour absorption refrigeration system cascaded with vapour compression refrigeration using HFO-1234yf refrigerant and it is found that when absorber temperature of double effect Li/Br H_2O vapour absorption is increasing , the thermodynamic performances in terms of (COP_Cascade) &Exergetic efficiency_Cascade System is decreasing and EDR_Rational is increasing. Similarly exergy destruction ratio based on the exergy of product (EDR_Cascade) is also increasing .Table-7 (c) shows the variation of condenser temperature with variation of thermal performances such as first law efficiency in terms of coefficient of performance (COP) of cascaded vapour absorption system & second law efficiency in terms of exergetic efficiency and exergy destruction ratio based on exergy of fuel of single effect Li/Br-H_2Ovapour absorption refrigeration system cascaded with vapour compression refrigeration using HFC-134a refrigerant and it is found that when condenser temperature of vapour absorption refrigeration system is increasing , the thermodynamic performances in terms of (COP_Cascad,) and Exergetic efficiency_Cascade System both are decreasing and EDR_Rational is increasing . Similarly exergy destruction ratio based on the exergy of product (EDR_Cascade) is also increasing and exergetic efficiency is decreasing. The performance of single effect Li/Br-H_2O vapour absorption system cascaded with vapour compression system using HFC-134a and HFO-1234yf for low temperature circuit evaporator at -53ºC and generator temperature at 110ºC have been compared and also shown in Table-7(a) to Table7(d) respectively and it is found that thermodynamic performances using HFO-1234yf (ystem-2) in cascaded vapour absorption system in terms of COP, is 1.6372 % lower than using HFC-134a (system-1)at 35ºC of condenser temperature and 1.643% lower than using HFC-134a at 35ºC of condenser temperature respectively. Similarly. The exergetic efficiency using HFO-1234yf is 3.682% lower than R134a at 35ºC and exergy destruction ratio is 7.256% higher than system-1 at 35ºC respectively.

3.7 Effect of absorber temperature of single effect vapour absorption cascaded vapour absorption refrigeration system on thermal performances

- Evaporator temperature of VCRS using HFC-134a = -53ºC, Compressor efficiency= 0.80
- Single effect Li/Br-H_2O VARS
- Approach=10, T_generator= 110ºC. T_EVA_VARS= 05ºC, RE=29.167 "kW', T_Cond=35ºC
- Performance of Vapour compression System performance of Vapour compression System: COP_VCRS=1.903, EDR= 0.4822 Exergetic Efficiency_VCRS=,0.6747, EDR_Rational =0.3253.

Table-8(a) Effect of absorber temperature of VARS on thermal performances of single -effect vapour absorption refrigeration cascaded with vapour compression refrigeration system

T_Absorber (ºC)	COP_Cascade	EDR_Cascade	Cascaded System Second Law Efficiency
30	0.9853	1.106	0.4749
35	0.9773	1.116	0.4726
40	0.9713	1.124	0.4709
45	0.9669	1.129	0.4697

- Evaporator temperature of VCRS using HFC-134a = -53ºC, Compressor efficiency= 0.80
- Single effect Li/Br-H_2O VARS
- Approach=10, T_generator= 110ºC. T_EVA_VARS= 05ºC, RE=29.167 "kW', T_Cond=35ºC
- Performance of Vapour compression System:Performance of Vapour compression System: COP_VCRS=1.903, EDR= 0.48242 ExergeticEfficiency_VCRS=,0.6747, EDR_Rational =0.3253.

Table-8(b) Effect of absorber temperature of VARS on thermal performances of single effect vapour absorption refrigeration cascaded with vapour compression refrigeration system

T_Absorber (ºC)	COP_VARS	EDR_ VARS	VARS Second Law Efficiency
30	0.7486	3.417	0.2264
35	0.7410	3.482	0.2241
40	0.7353	3.497	0.2224
45	0.7312	3.522	0.2211

- Evaporator temperature of VCRS using HFC-134a = -53ºC, Compressor efficiency= 0.80
- Single effect Li/Br-H_2O VARS
- Approach=10, T_generator= 110ºC. T_EVA_VARS= 05ºC, RE=29.167 "kW', T_Cond=35ºC
- Performance of Vapour compression System:Performance of Vapour compression System: COP_VCRS=1.903, EDR= 0.48242ExergeticEfficiency_VCRS=,0.6747, EDR_Rational =0.3253.

Table-8(b) Effect of absorber temperature of VARS on thermal performances of single effect vapour absorption refrigeration cascaded with vapour compression refrigeration system using entropy generation method

T_Absorber (ºC)	COP_VARS	Rational EDR_ VARS	VARS Second Law Efficiency
30	0.7486	3.712	0.2122
35	0.7410	3.759	0.2101
40	0.7353	3.795	0.2086
45	0.7312	3.821	0.2074

- Evaporator temperature of VCRS using HFC-134a = -53ºC, Compressor efficiency= 0.80

- Single effect Li/Br-H_2O VARS
- Approach=10, $T_{_generator}$= 110ºC. $T_{_EVA_VARS}$= 05ºC, RE=29.167 "kW', T_Cond=35ºC
- Performance of Vapour compression System: COP_VCRS=1.903, EDR= 0.48242Exergetic Efficiency_VCRS=, 0.6747, $EDR_{_Rational}$ =0.3253.

Table-8(b) Effect of absorber temperature of VARS on thermal performances of single effect vapour absorption refrigeration cascaded with vapour compression refrigeration system

T_Absorber (ºC)	$COP_{_VARS}$	Maximum COP_VARS	VARS Second Law Efficiency
30	0.7486	1.815	0.4125
35	0.7410	1.815	0.4083
40	0.7353	1.815	0.4051
45	0.7312	1.815	0.4029

Table-8 (a) shows the variation of absorber temperature with variation of thermal performances such as first law efficiency in terms of coefficient of performance (COP) of cascaded vapour absorption system & second law efficiency in terms of exergetic efficiency and exergy destruction ratio based on exergy of fuel of single effect Li/Br-H_2Ovapour absorption refrigeration system cascaded with vapour compression refrigeration using HFC-134a refrigerant and it is found that when absorber temperature of vapour absorption refrigeration system is increasing , the thermodynamic performances in terms of ($COP_{_Cascad}$,) is decreasing and Exergetic $efficiency_{_Cascade\ System}$ is increasing and $EDR_{_Rational}$ is decreasing . Similarly exergy destruction ratio based on the exergy of product (EDR_Cascade) is also decreasing and exergetic efficiency is increasing.as shown in table-8(b) respectively.Table-8 (c) shows the variation of low temperature evaporator circuit temperature with variation of thermal performances such as first law efficiency in terms of coefficient of performance (COP) of cascaded vapour absorption system & second law efficiency in terms of exergetic efficiency and exergy destruction ratio based on exergy of fuel of single effect Li/Br-H_2O vapour absorption refrigeration system cascaded with vapour compression refrigeration using HFO-1234yf refrigerant and it is found that when absorber temperature of single effect Li/Br H_2O vapour absorption is increasing , the thermodynamic performances in terms of ($COP_{_Cascade}$) & Exergetic $efficiency_{_Cascade\ System}$ is decreasing and $EDR_{_Rational}$ is increasing. Similarly exergy destruction ratio based on the exergy of product (EDR_Cascade) is also decreasing and absorber temperature increasing along with exergetic efficiency of cascaded system is increasing as shown in table-8(d) respectively.

The performance of single effect Li/Br-H_2O vapour absorption system cascaded with vapour compression system using HFC-134a and HFO-1234yf for absorber temperature at 35ºC have been compared and also shown in Tables-7 to Tables-8 respectively and it is found that thermodynamic performances using HFO-1234yf in cascaded vapour absorption system in terms of COP is1.637 % lower and , exergetic efficiency is 3.682 % lower than using HFC-134a at 35ºC of vapour compression absorber temperature.

- Evaporator temperature of VCRS using HFO-1234yf = -53 ºC, Compressor efficiency= 0.80
- singleeffect Li/Br-H_2O VARS
- Approach=10, $T_{_generator}$= 110ºC. $T_{_EVA_VARS}$= 05ºC, RE=29.167 "kW', T_Cond=35ºC
- Performance of Vapour compression System:Performance of Vapour compression System:
- Performance of Vapour compression System:
- COP_VCRS=1.791, EDR= 0.5751,
- ExergeticEfficiency_VCRS=, 0.6349, $EDR_{_Rational}$ =0.3451.

Table-8(c) Effect of absorber temperature of VARS on thermal performances of single effect vapour absorption refrigeration cascaded with vapour compression refrigeration system

T_Absorber (ºC)	$COP_{_Cascade}$	$EDR_{_Cascade}$	Cascaded System Second Law Efficiency
30	0.9690	1.187	0.4573
35	0.9613	1.197	0.4552
40	0.9554	1.205	0.4536
45	0.9512	1.210	0.4524

- Evaporator temperature of VCRS using HFO-1234yf = -53 ºC, Compressor efficiency= 0.80
- Single effect Li/Br-H_2O VARS
- Approach=10, $T_{_generator}$= 110ºC. $T_{_EVA_VARS}$= 05ºC, RE=29.167 "kW', T_Cond=35ºC
- Performance of Vapour compression System:
- COP_VCRS=1.791, EDR= 0.5751,
- Exergetic Efficiency_VCRS=,0.6349, $EDR_{_Rational}$ =0.3451.

Table-8(d) Effect of absorber temperature of VARS on thermal performances of single effect vapour absorption refrigeration cascaded with vapour compression refrigeration system

T_Absorber (ºC)	$COP_{_VARS}$	$EDR_{_VARS}$	VARS Second Law Efficiency
30	0.7486	3.417	0.2264
35	0.7410	3.462	0.2241
40	0.7353	3.497	0.2224
45	0.7312	3.522	0.2211

- Evaporator temperature of VCRS using HFO-1234yf = -53 ºC, Compressor efficiency= 0.80
- Single effect Li/Br-H_2O VARS
- Approach=10, $T_{_generator}$= 110ºC. $T_{_EVA_VARS}$= 05ºC, RE=29.167 "kW', T_Cond=35ºC
- Performance of Vapour compression System:
- COP_VCRS=1.791, EDR= 0.5751,
- Exergetic Efficiency_VCRS=,0.6349, $EDR_{_Rational}$ =0.3451.

Table-8(d) Effect of absorber temperature of VARS on thermal performances of single effect vapour absorption refrigeration cascaded with vapour compression refrigeration system using entropy generation method

T_Absorber (°C)	COP_VARS	EDR_ VARS	VARS Second Law Efficiency
30	0.7486	3.712	0.2122
35	0.7410	3.759	0.2101
40	0.7353	3.795	0.2086
45	0.7312	3.821	0.2074

- Evaporator temperature of VCRS using HFO-1234yf = -53 °C, Compressor efficiency= 0.80
- Single effect Li/Br-H_2O VARS
- Approach=10, $T_{_generator}$= 110°C. $T_{_EVA_VARS}$= 05°C, RE=29.167 "kW', T_Cond=35°C
- Performance of Vapour compression System:
- COP_VCRS=1.791, EDR= 0.5751,
- Exergetic Efficiency_VCRS=,0.6349, $EDR_{Rational}$ =0.3451.

Table-8(d) Effect of absorber temperature of VARS on thermal performances of single effect vapour absorption refrigeration cascaded with vapour compression refrigeration system

T_Absorber (°C)	COP_VARS	Maximum COP_VARS	VARS Second Law Efficiency
30	0.7486	1.815	0.4125
35	0.7410	1.815	0.4083
40	0.7353	1.815	0.4051
45	0.7312	1.815	0.4029

4. Conclusions and Recommendations

The following conclusions were drawn from present investigations.

(i) The thermodynamic performances of single effect Li/Br H_2O vapour absorption refrigeration system cascaded with vapour compression system HFO-1234yf refrigerants(system-2) in terms of COP is 1.435% lower and exergetic efficiency is 3.216%lower than The thermodynamic performances of single effect Li/Br H_2O vapour absorption refrigeration system cascaded with vapour compression system using HFC-134a (system-1) For both type of EDRs 5.922% at 10°C approach and also decreases as temperature overlapping (approach) is increasing.

(ii) The thermal performance of single effect Li/Br H_2O vapour absorption refrigeration system cascaded with vapour compression system using HFO -1234yf refrigerant is always than the single effect Li/Br H_2O vapour absorption refrigeration system cascaded with vapour compression system (system-1)using HFC -134a refrigerants. The thermodynamic performances using HFO-1234yf (system-2) in cascaded vapour absorption system in terms of COP is 1.353 % lower and exergetic efficiency is 3.036% lower than using HFC-134a in the vapour compression refrigeration system.

(iii) The variation of low temperature evaporator circuit temperature in single effect Li/Br vapour absorption refrigeration system on thermal performance of single effect Li/Br H_2O vapour absorption refrigeration system cascaded with vapour compression system using HFO -1234yf refrigerant when low temperature evaporator circuit temperature of vapour absorption refrigeration system is increasing , the thermodynamic performances in terms of ($COP_{_Cascad}$,) is decreasing and $Exergeticefficiency_{_Cascade\ System}$ is also decreasing and $EDR_{_Rational}$ is increasing . Similarly exergy destruction ratio based on the exergy of product ($EDR_{_Cascade}$) is also decreasing and exergetic efficiency is increasing; The optimum values of single effect vapour absorption refrigeration cycle cascaded with vapour compression cycle for generator temperature of 110°C and condenser temperature and 35°C of absorber temperature using HFC-134a refrigerant (system-1) comes to be 1.353% COP and 3.036% higher exergetic efficiency) with reduction in 5.702% in exergy destruction ratio of cascade system than cascade vapour absorption Li/Br H2O system using R1234yf refrigerant in compression refrigerating cycle (system-2).

(iv) The variation of temperature of generator in single effect Li/Br vapour absorption refrigeration system on thermal performance of single effect Li/Br H_2O vapour absorption refrigeration system cascaded with vapour compression system using HFO -1234yf refrigerant is 6.0 % to 7% lower than the single effect Li/Br H_2O vapour absorption refrigeration system cascaded with vapour compression system using HFC -134a refrigerants.

(v) For single effect Li/Br-H_2O vapour absorption refrigeration system cascaded with vapour compression refrigeration at -30°C , the performance of HFC-134a refrigerant and HFO-1234ze are nearly similar with the variation of 0.5626% in first law efficiency and 0.559% in second law efficiency while the performance of HFC-134a is 3.1196% superior than HFO- 1234yf refrigerant (system-2) . Therefore both HFO refrigerants can replace HFC-134a refrigerant in near future due to its very low global warming potential (i.e. GWP of R1234ze is 6 and GWP of R1234yf is 4 respectively as compared to GWP of HFC-134a is 1360) (iv) Thermodynamic performances of single effect Li/Br-H_2O vapour absorption refrigeration system cascaded with vapour compression refrigeration using HFO-1234yf in cascaded vapour absorption system in terms of COP is 1.643 % lower and exergetic efficiency is 3.201% lower than using HFC-134a. For both type of EDRs 6.261% decreasing as heat exchanger effectiveness is increasing.

(vi) The performance of single effect Li/Br-H_2O vapour absorption system cascaded with vapour compression system using HFC-134a and HFO-1234yf for low temperature circuit evaporator at -53°C and generator

temperature at 180°C thermodynamic performances using HFO-1234yf in cascaded vapour absorption system in terms of COP is1.643% lower and exergetic efficiency is 3.201 % lower than using HFC-134a in the vapour compression refrigeration cycle.

(vii) The performance of single effect Li/Br-H_2O vapour absorption system cascaded with vapour compression system using HFC-134a and HFO-1234yf for low temperature circuit evaporator at -53°C and Vapour absorption system evaporator temperature at 5°C have been compared and it is found that thermodynamic performances using HFO-1234yf in cascaded vapour absorption system in terms of COP is 1.643% and exergetic efficiency is 3.201 % lower than using HFC-134a.

(viii) The performance of single effect Li/Br-H_2O vapour absorption system cascaded with vapour compression system using HFC-134a and HFO-1234yf for low temperature circuit evaporator at -53°C and generator temperature at 130°C have been compared and it is found that thermodynamic performances using HFO-1234yf in cascaded vapour absorption system in terms of COP, is 1.9563 % lower than using HFC-134a at 30°C of condenser temperature and 1.643% lower than using HFC-134a at 35°C of condenser temperature respectively. Similarly The exergetic efficiency using HFO-1234yf is 3.5033% lower than R134a at 30°C and 3.20% lower than HFC-134a at 35°C respectively.

(ix) The performance of single effect Li/Br-H_2O vapour absorption system cascaded with vapour compression system using HFC-134a and HFO-1234yf for absorber temperature at 40°C have been compared and it is found that thermodynamic performances using HFO-1234yf in cascaded vapour absorption system in terms of COP is1.637 % lower and , exergetic efficiency is 3.682 % lower than using HFC-134a at 35°C of vapour compression absorber temperature.

(x) In the single effect Li/Br-H_2Ovapour absorption refrigeration system cascaded with vapour compression refrigeration using HFC-134a refrigerant and it is found that absorber temperature of Tripple effect Li/Br vapour absorption refrigeration system is increasing , the thermodynamic performances in terms of ($COP_{_Cascad}$,) is decreasing and Exergetic $efficiency_{_Cascade\ System}$ is increasing and $EDR_{_}$ is decreasing.

(xi) In the single effect Li/Br-H_2Ovapour absorption refrigeration system cascaded with vapour compression refrigeration using HFC-134a refrigerant and it is found that when condenser temperature of vapour absorption refrigeration system is increasing , the thermodynamic performances in terms of ($COP_{_Cascad}$,) and Exergetic $efficiency_{_Cascade\ System}$ both are decreasing and $EDR_{_Rational}$ is increasing.

(xii) In the single effect Li/Br-H_2Ovapour absorption refrigeration system cascaded with vapour compression refrigeration using HFC-134a refrigerant and it is found that when generator temperature of vapour absorption refrigeration system is increasing , the thermodynamic performances in terms of ($COP_{_Cascad}$,) is decreasing and Exergetic $efficiency_{_Cascade\ System}$ is increasing and $EDR_{_Rational}$ is decreasing.

(xiii) In the single effect Li/Br-H_2Ovapour absorption refrigeration system cascaded with vapour compression refrigeration using HFC-134a refrigerant and it is found that when Vapour absorption system evaporator temperature ($T_{_evaporator}$)of vapour absorption refrigeration system is increasing , the thermodynamic performances in terms of ($COP_{_Cascad}$,) is decreasing and Exergetic $efficiency_{_Cascade\ System}$ is increasing and $EDR_{_Rational}$ is decreasing . Similarly exergy destruction ratio based on the exergy of product ($EDR_{_Cascade}$) is also decreasing and exergetic efficiency is increasing.

(xiv) In the single effect Li/Br-H_2Ovapour absorption refrigeration system cascaded with vapour compression refrigeration using HFC-134a refrigerant and it is found that when heat exchanger effectiveness of vapour absorption refrigeration system) is increasing , the thermodynamic performances in terms of ($COP_{_Cascade}$) &exergetic $efficiency_{_Cascade\ System}$) is increasing and $EDR_{_cascade}$ is decreasing when heat exchanger effectiveness is increasing.

(xv) In the single effect Li/Br-H_2Ovapour absorption refrigeration system cascaded with vapour compression refrigeration using HFC-134a refrigerant and it is found that when temperature overlapping in terms of approach (means condenser temperature of vapour compression refrigeration minus evaporator temperature of vapour absorption refrigeration system) is increasing , the thermodynamic performances in terms of ($COP_{_Cascade}$, Exergetic $efficiency_{_Cascade\ System}$) is decreasing and $EDR_{_Rational}$ is increasing.

References

[1] H.M. Getu, P.K. Bansal,[2008] "Thermodynamic Analysis of an R744–R717 Cascade Refrigeration System", International Journal of Refrigeration, vol. 31, pp. 45-54,

[2] A. Kilicarslan [2004] "An Experimental Investigation of a Different Type Vapor Compression Cascade Refrigeration System", Applied Thermal Engineering, vol. 24, pp. 2611–2626.

[3] Lee T-S, Liu C-H, Chen T-W.[2006] Thermodynamic analysis of optimal condensing temperature of cascade-condenser in CO_2/NH_3 cascade refrigeration systems. International Journal of Refrigeration.;Vol-29:No.1,page-100-118.

[4] A Arora and S.C. Kaushik [2009]Theoretical analysis of LiBr/H_2O absorption refrigeration system, International Journal of Energy Research, 33(15), page-1321 - 1340

[5] Kaushik, S.C., Arora, A. [2009], Energy and Exergy analysis of single effect and series flow double effect water lithium bromide absorption refrigeration systems, International Journal of Refrigeration, Vol. 32, pp.1247-1258.

[6] Gomri, R.[2009], Second law comparison of single effect and double effect vapour absorption refrigeration systems, Energy Conversion and Management,Vol. 50, pp.1279-1287).

[7] Kilic, M. and Kaynakli, O. [2007], Theoretical study on the effect of operating conditions on performance of absorption refrigeration system, Energy Conversion and Management, Vol. 48, pp. 599-607 .

[8] S.B. Riffat N. Shankland [1993] Integration of absorption and vapourcompression systems, Applied Energy, Vol-46, Issue-4,1993,

Pages 303-316.
[9] Garimella S, Brown AM, Nagavarapu AK. Waste heat driven absorption/vapor-compression cascade refrigeration system for megawatt scale, high-flux, low-temperature cooling. International Journal of Refrigeration. 2011;34:1776-85
[10] *C Cimsit, I Ozturk.[2012] Analysis of compression-absorption cascade refrigeration cycles, Applied Thermal Engineering, 40, 311-317.*
[11] J Chinnappa, M Crees, SS Murthy, K Srinivasan.[1993] Solar-assisted vapor compression/absorption cascaded air-conditioning systems, Solar Energy, 50(5), 453-458
[12] Fernández-Seara J, Sieres J, Vázquez M. [2006], Compression–absorption cascade refrigeration system. Applied Thermal Engineering.Vol-26:page-502-12.
[13] Rogdakis ED, Antonopoulos KA. Performance of a low- temperature NH3H2O absorption-refrigeration system. Energy. 1992;17:477-84
[14] R.S. Mishra (2019) Comparison of half effect absorption-compression cascaded refrigeration system using thermodynamic (energy-exergy) analysis. International Journal of Research in Engineering and Innovation Vol-3, Issue-1 (2019), 6-11
[15] R.S. Mishra (2019) Thermal performances (first law efficiency, exergy destruction ratio &exergetic efficiency) of cascade single effect ammonia-water (NH_3-H_20) vapour absorption refrigeration system coupled with vapour compression refrigeration using ecofriendly refrigerants in the low temperature cycle of VCRS system, International Journal of Research in Engineering and Innovation Vol-3, Issue-1, (2019), 1-5
[16] R.S. Mishra (2018) Comparison of thermal performances of single effect, double effect and triple effect LiBr-H2O absorption system cascaded with vapour compression refrigeration systems using ecofriendly refrigerants, International Journal of Research in Engineering and Innovation Vol-2, Issue-6 , 610-621.
[17] R.S. Mishra Ankit Dewedi [2017] Methods for improving thermal performances of vapour absorption system using heat pipes International Journal of Research in Engineering and Innovation (IJREI) journal home page: http://www.ijrei.com ISSN (Online): 2456-6934, Vol-1, Issue-3), 118-125
[18] Ankit Dewedi & R.S. Mishra [(2017)] A thermodynamic analysis of ejector type vapour refrigeration system using eco-friendly refrigerants International journal of research in engineering and innovation (IJREI), vol 1, issue 2, page-40-48.

Cite this article as: R.S. Mishra, Thermodynamic performance evaluation of single effect Li/Br H_2O vapour absorption refrigeration system cascaded with vapour compression system using ecofriendly HFC-134a and HFO-1234yf refrigerants, International Journal of Research in Engineering and Innovation Vol-3, Issue-3 (2019), 165-182.

Check for updates

Article

Threshold Effect of Bank-specific Determinants of Non-performing Assets: An Application in Indian Banking

Journal of Emerging Market Finance
18(1S) 1S–34S, 2019
© 2019 Institute for Financial Management and Research
Reprints and permissions:
in.sagepub.com/journals-permissions-india
DOI: 10.1177/0972652719831546
journals.sagepub.com/home/emf
SAGE

Samaresh Bardhan[1]
Rajesh Sharma[2]
Vivekananda Mukherjee[3]

Abstract

The article investigates role of bank-specific factors on non-performing assets (NPAs) in Indian banking system in a panel threshold framework (Hansen, 1999, *Journal of Econometrics*, *93*(2), 345–368), using an unbalanced panel of 82 scheduled commercial banks over the period of 1995–1996 to 2010–2011. We consider capital to risk-weighted assets ratio (CRAR) and credit growth as alternative threshold variables (and regime dependent) along with relevant bank-specific variables treated as regime independent. Findings reveal that CRAR exerts negative and significant impact on NPAs once it reaches a critical threshold. Possible implication is that banks extend less risky loans in a high CRAR regime

[1] Department of Humanities and Social Sciences, Indian institute of Technology Ropar, Rupnagar, Punjab, India.
[2] University School of Management and Entrepreneurship, Delhi Technological University, Delhi, India.
[3] Department of Economics, Jadavpur University, Kolkata, West Bengal, India.

Corresponding author:
Samaresh Bardhan, Department of Humanities and Social Sciences, Indian Institute of Technology Ropar, Nangal Road, Rupnagar, Punjab 140001, India.
E-mail: samaresh@iitrpr.ac.in

than in low CRAR regime that helps reduce NPAs. With credit growth as threshold as well as regime dependent, we observe statistically significant non-linear effect of credit growth on NPAs. Beyond threshold, credit growth exerts significant negative effect on NPAs that may imply that banks extend good quality loans. However, we cannot rule out the possibility of evidence of 'ever-greening hypothesis' of bad debts in Indian banking, that is, banks just roll over previous bad debts into fresh performing loans.

JEL Classification: G21, G28, C13, C33

Keywords

Banks, non-performing assets, threshold regression, panel data models

1. Introduction

Much of the recent debates on loan default arise in the context of banking troubles around the globe during the 1990s and the beginning of the 2000s.[1] Growing incidence of non-performing assets (NPAs) observed in loan portfolio of failing banks is identified as one of the most significant factors behind systemic bank failures. However, causes and intensities of such failures, associated problems of loan default and resulting burden of NPAs have been different in different countries. While close bank–firm relationship is identified as the most important source behind accumulation of bad loans and consequent banking troubles in few countries in Asia (Krugman, 1998), credit crunch arising out of reluctance of banks to commit new loans and thereby take new risks is partially attributable to bad loans in countries like Mexico during post 1995 crisis (Krueger & Tornell, 1999). In Indonesia, banks become vulnerable immediately after contagion effects of exchange rate turmoil in Thailand (Agung et al., 2001). In Indian subcontinent, however, incidence of loan default is attributed mainly to lack of effective monitoring and supervision on the part of banks, lack of effective lenders' recourse, weaknesses of legal infrastructure and lack of effective debt recovery strategies.

It has been widely observed that banks having large incidence of NPAs try to overcome the problem through two related ex post strategies. First, loss making banks ask for insertion of more capital as it typically happens in developing country banking systems such as India and second, banks very often grow aggressively in order to *gamble for resurrection* (Kane, 1989) by extending more risky loans. As a reaction, regulators require

banks to maintain its capital above a certain level, ex ante, so that it can absorb a reasonable amount of loss and at the same time, keep its risky asset portfolio under control and comply with statutory capital requirements. Regulators usually follow the Basel Committee on Banking Supervision (BCBS) recommendations to set capital to risk-weighted asset ratio (CRAR) requirement of banks.[5] Theory does not provide a clear-cut answer as to whether high CRAR succeeds to create a dampening effect on NPAs of banks and avoid banking failure. Intuitively, on the one hand, if banks avoid forwarding risky loans to increase their CRAR, it should have a dampening effect on NPAs over time. On the other hand, if they pursue moral hazard strategy to forward more risky-high return loans, maintaining stipulated CRAR might be difficult unless these banks manage to maintain their own capital. This tendency might increase NPAs in bank's balance sheet in the future. It is also argued that weak accounting practices and poor disclosure measures in developing country banking systems, in particular, very often, allow banks to extend additional loans to already troubled borrowers: bad debts roll through process of lending and re-lending in order to cover extent of damages from NPAs (Sarkar, 1999). This might lead to *ever-greening* of loans where fresh loans are given to repay old loans and apparently bank's balance sheets show a rosy picture which may not be the case, in reality. Niinimaki (2007) theorises *gambling for resurrection* that advocates in favour of growth of credit through rolling over previous bad debts[6] where worst loans are often considered those that are reported as current as banks roll over their old bad loans. Amidst these possibilities, we also conjecture that growth of credit might also in‡uence NPAs of banks, whether good or bad.

Against this background, the article hypothesises that there are threshold effects of both CRAR and credit growth on NPAs of banks and argue that response of NPAs of banks below respective thresholds are likely different from those above critical thresholds. We test these hypotheses in case of Indian banks for CRAR and credit growth separately. To the best of our knowledge, this is the first attempt to investigate threshold effects of regulatory instrument of bank as well as credit growth on NPAs of Indian banks. While previous existing studies on Indian banking mostly look into linear effects of bank-specific determinants of NPAs (Bardhan & Marjit, 2005; Bardhan & Mukherjee, 2016; Das & Ghosh, 2007), current article models NPAs in a non-monotonic framework and identify threshold effects of CRAR and credit growth on NPAs. In this study, first, we examine, whether there are non-linear effects of CRAR on NPAs in case of Indian banks, that is, does the effect of CRAR on NPA differs on either side of threshold. Second, given the fact that risk characteristics

of loans form an integral part of loan decision-making process, we separately examine, whether depending upon risk weights attached to various types of loan assets, credit growth leads to a dampening effect on NPAs of banks once a critical threshold is attained where banks extend better quality, less risky loans. In order to answer above empirical questions, we use an unbalanced panel dataset of 82 scheduled commercial banks covering public sector banks (PSBs), Indian private banks and foreign banks (FBs) operating in India and apply the panel threshold regression model (Hansen, 1999).

Empirical flndings show that up to a critical threshold (threshold value is estimated to be in the range of 10%–12%), CRAR does not exert any discernible impact on NPA of banks. Beyond the threshold, higher CRAR leads to a signiflcant decline in NPA. Fortunately, in Indian banking sector, number of banks above the threshold has substantially increased over the study period. With credit growth as threshold variable, the panel threshold model also exhibits presence of non-linear effects of credit growth: when credit growth exceeds the threshold, NPA decreases. However, on an average, over the study period, only 47 per cent of Indian banks had their credit growth above the threshold. Among PSBs, which have higher share of loans in Indian credit market relative to other banks, during the study period, on an average, only 46 per cent had their credit growth above the threshold. Therefore, the hypothesis of '*gambling for resurrection*' does not seem to have much support in India. On average, it appears that over time, asset portfolio of Indian banks of all types became less risky and banks with high credit growth forwarded less risky loans which contributed to signiflcant reduction of their NPAs. Results provide strong empirical reason behind resilience of Indian banks to flnancial crisis.

The rest of the article is structured as follows: Section 2 presents a brief overview of Indian scenario. Section 3 presents survey of relevant extant literature. Section 4 provides data sources. Section 5 presents details of methodology used. Section 6 provides results and discussions. Finally, Section 7 concludes the article.

2. Indian Scenario

Indian banking system is claimed to be resilient to global financial crisis because of stringent capital adequacy requirements imposed by Reserve Bank of India (RBI) following Basel Principles.[7] With respect to Basel I, India's banking industry performed reasonably well, with an average CRAR of about 12 per cent, which is not only higher than the

internationally acceptable level of 8 per cent, but also higher than India's own regulatory requirement of 9 per cent (Sarma & Nikaido, 2007). The data shows that over the period of 1995–1996 to 2010–2011, Indian banks across all bank groups, that is, PSBs, old private sector banks (OPBs), new private banks (NPBs) and FBs, on average, maintained their CRAR much above the stipulated level (see Table 1) and the minimum requirement was not binding for them.

As far as risk taking behaviour of Indian banks is concerned, ownership also matters. For example, FBs, in general, are more concerned with financing export-oriented industries than agriculture and small-scale industries in the priority sector. In contrast, PSBs along with private domestic banks are committed to extend more loans under directed credit programme.[8] Accordingly, risk characteristics of loans are likely to be different for different ownership group of banks depending on type of loans. The cost of raising capital is also different for different ownership group of banks. Banks which are 'too big to fail' expect higher probability of capital infusion from the government.

Table 1. Movement of CRAR by Bank Groups

Year (end March)	Public Sector Banks	Old Pvt. Banks	New Pvt. Banks	Foreign Banks	All Banks
1995–1996	8.76	17.65	20.56	14.56	14.26
1996–1997	9.21	11.84	17.22	13.61	11.83
1997–1998	11.13	11.74	14.96	15.09	12.68
1998–1999	10.6	12.1	11.8	10.8	11.3
1999–2000	10.1	12.4	13.4	11.9	11.1
2000–2001	10.2	11.9	11.5	12.6	11.4
2001–2002	10.9	12.5	12.3	12.9	12
2002–2003	12.2	12.8	11.3	15.2	12.7
2003–2004	13.1	13.7	10.2	15	12.9
2004–2005	13.2	12.5	12.1	14	12.8
2005–2006	12.2	11.7	12.6	13	12.3
2006–2007	12.4	12.08	12.0	12.4	12.3
2007–2008	12.02	14.08	14.4	13.1	13.1
2008–2009	12.04	14.3	15.1	15.0	13.2
2009–2010	12.11	13.8	18.1	18.1	13.6
2010–2011	12.03	13.3	17.7	17.71	13.0
2011–2012	11.88	12.47	14.90	17.30	12.9
2012–2013	11.31	12.33	15.71	18.76	12.8

Source: Authors' calculations.
Notes: Data on CRAR is based on BASEL I.

3. Review of Literature

Existing body of literature on NPAs of banks investigates relative importance of various bank-specific and macroeconomic determinants of NPAs of banks and examines the nature of causal relationship between NPAs and efficiency of banks. Role of capital, credit and deposit growth arise in both contexts. Berger and DeYoung (1997), in a seminal paper, investigate inter-temporal causality among NPAs, cost efficiency and bank capital in a sample of US banks and find that for a consistently efficient set of banks, increase in measured cost efficiency leads to an increase in NPAs thereby supporting *skimping hypothesis* (that efficient banks willingly skimp on monitoring costs today in exchange for higher loan loss provision in the future). They also find evidence of the *moral hazard hypothesis* (that poorly capitalised banks suffering reductions in capital will take greater risks and hence, on average, end up with higher loan loss provision) where thinly capitalised banks face higher incidence of NPAs in their balance sheet. Salas and Saurina (2002) find evidence of negative and statistically significant effect of solvency ratio on NPAs in Spanish banks and lend support to the *moral hazard hypothesis*. Williams (2004) examines intertemporal relationship between loan loss provision, efficiency and capitalisation in a Granger causality framework for European banks during 1990 and 1998. This study presents a robustness test of the findings of Berger and DeYoung (1997) for US banks and find strong evidences of *bad management hypothesis* (that low measured cost efficiency is a signal for poor bank management: as poor managers, they may also choose investment projects with very little credit-worthiness or they may not properly judge the true value of collateral pledged against the loans. Consequently, a significant number of loan accounts may turn out to be non-performing as time goes on). However, unlike US banks, the study hardly finds any evidence of *skimping hypothesis* (that efficient banks willingly skimp on monitoring costs today in exchange for higher loan loss provision in the future), *moral hazard hypothesis* and *bad luck hypothesis* (that banks with high loan loss provision suffer a reduction in operating efficiency). Hu, Li, and Chiu (2004) assess effect of ownership structure across Taiwanese banks and find that non-performing loans (NPLs) decrease up to certain critical threshold level of government ownership, thereafter it starts increasing. Podpiera and Weill (2008) assess causal link between cost efficiency and NPLs across banks in Czech Republic over the period of 1994–2005 and find that cost inefficiency precedes increase in NPLs. Louzis, Vouldis, and Metaxas (2011) find negative and statistically significant effect of

cost efficiency on NPA in case of Greek banks. However, they do not find support of the moral hazard hypothesis because relatively smaller size of Greek banking creates disincentives towards risk taking behaviour of banks. Klein (2013) investigates NPLs in Central, Eastern and Southeastern Europe (CESEE) in the period of 1998–2011 and finds that the level of NPLs can be attributed to both macroeconomic conditions and banks' specific factors. However, bank-specific factors are found to have a relatively low explanatory power. Leung, Taylor, and Evans (2015) find a positive relationship between bank risk taking and NPLs in the context of United States. However, maintaining of large tier 1 capital buffer mitigates the risk and leads to lower exposure to shocks in market-wide default risks.[9] Ghosh (2015) examines determinants of NPLs of commercial banks and savings institutions across 50 US states and the District of Columbia for 1984–2013 and finds that bank-specific factors such as capitalisation, liquidity risks, poor credit quality, greater cost inefficiency, etc., raise NPLs, while greater bank profitability lowers it. Vithessonthi (2016) finds evidence for the time-varying relationship between bank credit growth and NPLs in a sample of 82 publicly listed commercial banks in Japan during the period 1993–2013. The author finds that while an increase in bank credit may lead to an increase in the level of non-performing loans, it it does not necessarily lead to higher profitability. Zhang, Cai, Dickinson, and Kutan (2016) evaluate effect of increasing NPAs on loan qualities in Chinese context and find evidence in support of the *moral hazard hypothesis* in which increased NPA leads to risky behaviour of banks further leading to deterioration in the asset quality.

In Indian context, we flnd few studies which identify reasons behind the growing incidence of NPAs. Rajaraman and Vasishtha (2002) provide evidence of signiflcant bivariate relationship between operating ineffIciency indicator and problem loans of PSBs. Muniappan (2002) identifles several internal as well as external factors behind growing incidence of NPAs in Indian banks. Ranjan and Dhal (2003) provide evidences of crucial link between terms of credit given to borrowers and NPAs in Indian context. Mukherjee (2003) identifles that relative contribution of non-priority sector in NPAs of banks has increased compared to priority sector. Das and Ghosh (2007) empirically examine various indicators such as asset size, credit growth and macroeconomic conditions and flnd that at the macro level, GDP growth and at the bank level, real loan growth and bank size play an important role in in‡uencing problem loans. Reddy (2004) argues that banks' lending policy could have crucial in‡uence on NPAs of banks. Mallick and Marjit (2004) advocate in favour of monitoring of collateral asked by banks as private monitoring by banks fall short of

optimal monitoring desired by the regulator. As regulators in developing country banking systems, in general, bail out the troubled banks, there is a tendency of a section of these banks, particularly PSBs, not to properly monitor their collateral. Authors design an incentive mechanism that calls for auditing in good state and show that regulator does not need to regulate when success probability is very high. Bardhan and Marjit (2005) raise doubts over the efficacy of official definition of NPA in Indian banking system which is entirely based on loan repayment status and propose a concept of *tolerable limit* of NPAs based on actual conditions of a bank's health and measure severity of problem loans as difference between actual level of NPAs and tolerable level of NPA. Pandey, Tilak, and Deokar (2013) look into the phases and dimension of the problem of NPAs in Indian banking during post-liberalisation period and observe the tendency of Indian banks towards more retail and priority sector lending which adversely affects the borrowings of the corporate sector. The article also suggests for a separate audit in order to control mounting burden of NPAs and advocates in favour of early warning signal, setting up of nodal offices for recovery of loans in PSBs. Samantaraya (2016) explores reasons behind surge in NPAs of Indian banks and observes that excessive credit growth in the past has led to significant increase in current NPAs. It also identifies that contemporary economic conditions, capital adequacy and overall levels of efficiency of banks contributed to the incidence of NPAs in Indian banking. As a policy recommendation, the study suggests that macro-prudential aspects such as counter-cyclical capital buffer, dynamic provisioning and issues related to corporate governance need to be strengthened. Misra, Rajmal, and Verma (2016) scrutinise the determinants of recovery of defaulted loan in Indian banking and advocate in favour of a stronger and effective insolvency regime in order to improve debtor–creditor relationship and credit environment. The study also emphasises on the type of collateral used, stronger credit appraisal system, favourable macroeconomic environment and tapping alternative sources of funds by debtors such as capital market towards recovery of bad loans. Bardhan and Mukherjee (2016) examine the role of bank-specific factors while explaining the dynamics of NPAs of Indian banks in a linear panel GMM framework over the post liberalisation period and shows that, among other observations, bank-specific indicators such as lagged capital adequacy ratio significantly reduces current NPAs of banks. It also shows that larger banks are more prone to default than smaller banks. Sengupta and Vardhan (2017) make a comparative assessment of causes and magnitudes of incidence of NPAs and associated banking troubles in Indian banking during 1997–2002 immediately after introduction of

flnancial liberalisation in the early 1990s and also in the aftermath of 2008 global flnancial crisis. Authors identify few favourable factors that emerged during 2003–2008 in Indian economy such as cyclical nature of macroeconomic factors as the source of impairment of bank balance sheet, sharp macroeconomic recovery in the aftermath of crisis. These, in turn, helped resolution of banking crisis that emerged in the late 1990s. In contrast, post 2008 banking crisis is identifled to be more critical and growth recovery in post 2011 period was much slow compared to that in early 2000. Monetary contraction consequent upon demonetisation in November 2016 also acted as a further drag in Indian economy and may contribute to worsening of NPAs of Indian banks. Goyal (2017) examines issues of NPAs of Indian banks and slowdown in credit growth along with few other related issues and argues that although Indian banking system, as a whole, is stable, lower quality of assets and higher concentration of loans to large corporates in non-priority sector given by PSBs led to greater incidence of NPAs. Moreover, higher interest rate adversely affected corporate debt and hence led to slowdown in credit growth and accumulation of NPAs. This observation is speciflc to post global flnancial crisis period. The article also argues that contrary to traditional perception that PSBs are always underperformers, they performed well in post reform period.

4. Data and Preliminary Statistical Diagnostics

We use four alternative proxies of NPAs following official definitions of NPAs of Indian banks.[10] These are *net NPA to net advances ratio (NNPNA)*, *gross NPA to gross advance ratio (GNPGA)*, *net NPA to total asset* ratio (NNPTA) and *gross NPA to total asset ratio (GNPTA)*.[11] *Capital adequacy ratio* (CRAR) and *credit growth* (*credit*) are treated as alternative threshold variables. In addition to these, few other relevant bank-specific variables such as ratio of operating expenses to total assets (*opeta*), market share (*mshare*), ratio of net profit to total assets (*profit*) and rate of growth of deposit (*deposit*) have also been taken. We also included two ownership dummies, *private* and *foreign* (representing private and foreign sector banks) in the threshold regression model with the group of PSBs taken as the base category. The two dummies: *private* and *foreign* are defined ownership dummies that take the value 1 if a bank belongs to the private sector and foreign sector, respectively, and 0 otherwise. These variables including ownership dummies are treated as regime independent variables. Nominal values of credit and deposit are

deflated at 2004–2005 prices before computing growth rates (Table A1 in appendix A1 for description of variables).

We construct an unbalanced panel of 82 scheduled commercial banks in India over the period 1995–1996 to 2010–2011.[12] Our sample consists of 28 PSBs, 31 private sector banks and 23 FBs that yield 1,051 observations. All relevant balance sheet data is retrieved from *Statistical Tables Relating to Banks in India* published by RBI (1995-2005). For few years, data on NPAs for the banks in our sample are collected from *Database on Indian Banking* published by the Indian Bank's Association (IBA, 2006) and *Money and Banking* published by the Centre for Monitoring Indian Economy (CMIE, 2006). Data on CRAR of all banks in our sample is based on BASEL I.[13] Average statistics of our sample over the study period is presented in Table 2.

Table 2 shows that average NPAs of PSBs, private banks and FBs were at comparable level in the study period irrespective of the measure of NPA used. Average CRAR was higher in FBs compared to public and private sector banks. As we compare average deposit and credit growth rates, both were the highest for FBs and the lowest for PSBs. For all the bank classes, credit growth rate was higher than deposit growth rate. While market share was the highest for PSBs, it is the lowest for FBs. Although FBs, on average, have highest operating expenses to total assets, they enjoy the highest net proflt to total assets. On both these accounts, PSBs occupied the lowest position. However, in most of variables, variation within the class of FBs was higher than that within either PSBs or private sector banks.

Figures 1 and 2 show various plots for NPA indicators against capital adequacy ratio and credit growth, respectively. Figure 3 displays movement of average CRAR across different bank groups.

In Figure 1, a point represents a combination of average value of a given NPA indicator and average value of CRAR of a particular bank. Figure 1 suggests that cutting across banks, a positive association exists between average CRAR and average NPA irrespective of measures of NPA used. Figure 2 suggests a negative association between average credit growth rate and average NPA across banks. However, these plots do not capture probable non-linearity in the relationship between the variables. It is also evident from scatter plots that certain banks record extremely large values of NPA, CRAR and credit growth. In order to control such extreme observations and negative value of variables in the sample, we use a semi-log transformation of all variables following Ghosh and Phillips (1998)[14] where we take natural logarithm of observations with values greater than 1, and observations for which value is less than 1 are also

Table 2. Summary Statistics by Bank Groups: 1995–2011

	Public Sector Banks					Private Banks					Foreign Banks				
Variables	Obs.	Mean	SD	Min.	Max.	Obs.	Mean	SD	Min.	Max.	Obs.	Mean	SD	Min.	Max.
NNPANA	461	4.43	4.46	0	26.01	447	4.11	4.85	0	50.96	373	4.88	16.11	–0.11	261.54
GNPAGA	459	8.69	7.65	0.63	39.12	438	7.69	8.86	0	126.93	364	9.81	18.76	0	179.85
NNPATA	461	1.81	1.6	0	10.56	447	1.88	2.21	0	23.66	372	1.83	5.05	–0.06	58.24
GNPATA	461	3.85	3.08	0	19.39	447	3.69	5.43	0	78.28	372	5.15	14.36	0	208.16
CAR	460	11.72	2.38	1	20.12	447	13.59	6.14	0	60	373	26.34	23.71	0	175.47
DEPOSIT GROWTH	433	12.09	9.15	–21.02	71.9	416	22.1	59.2	–88.69	975.14	350	19.57	65.5	–92.03	548.96
CREDIT GROWTH	433	14.85	10.47	–16.07	48.42	416	23.05	57.27	–36.6	894.21	350	41.93	312.73	–94.93	4099
MSHARE	461	2.81	3.72	0.49	24.12	447	0.61	1.22	0.01	9.95	372	0.29	0.47	0.001	2.01
OPETA	457	2.15	0.66	0.56	4.55	407	2.28	1.2	0.58	18.67	356	5.39	27.88	0.44	332.01
PROFIT	461	0.69	0.74	–7.51	1.76	447	0.83	1.21	–11.28	13.73	372	2.72	17.56	–25.41	291.68

Source: Authors' calculations.

Notes: NNPANA, GNPAGA, NNPATA and GNPATA denote net non-performing assets and *gross non-performing assets* expressed as percentage of net advances, gross advances and total *assets*, respectively. MSHARE, OPETA and CAR denote market share, *operating expenses* and capital to risk-weighted assets ratio of banks, respectively. Figures reported in this table are in percentage terms.

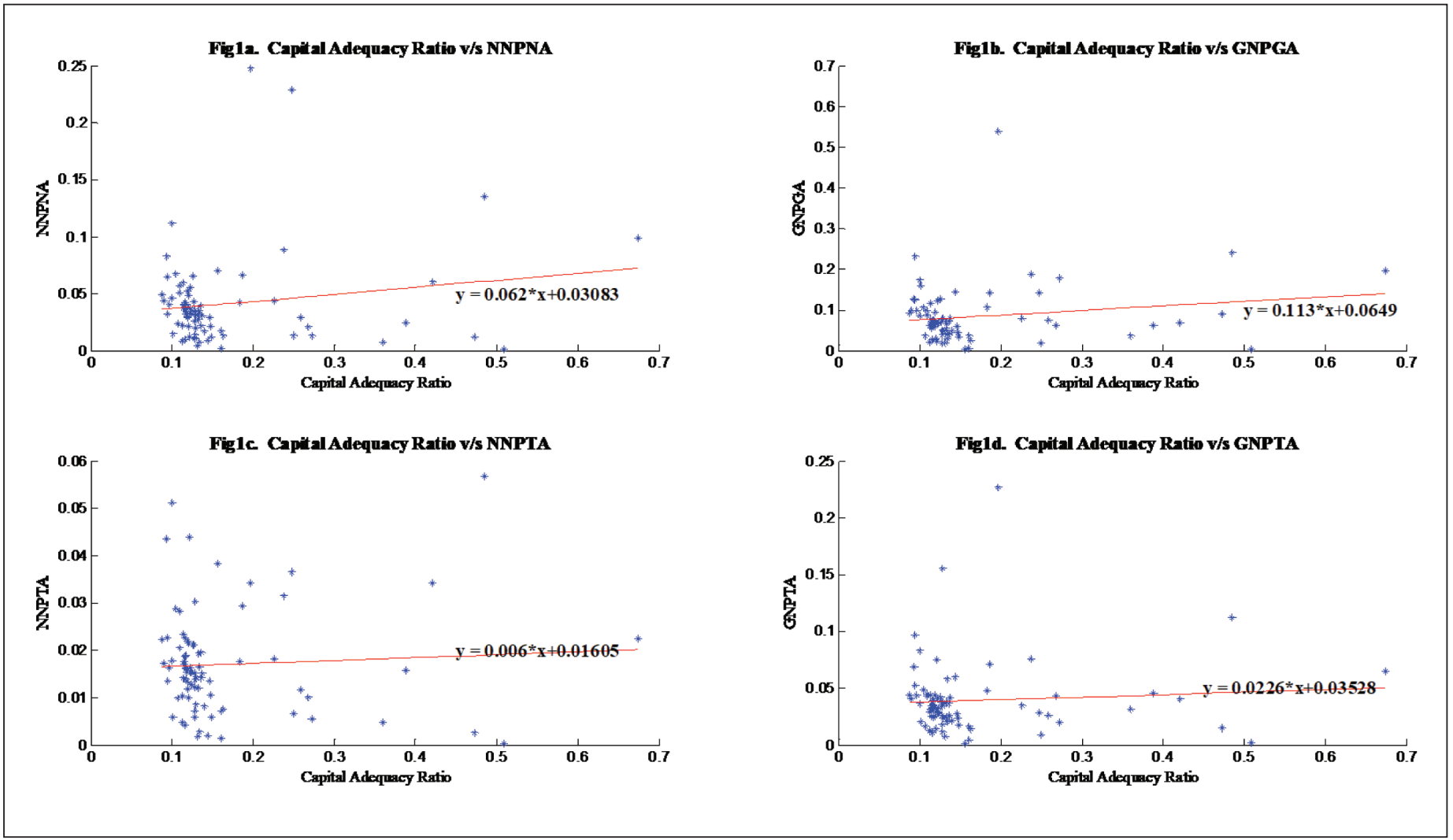

Figure 1. Average NPA and Average Capital Adequacy Ratio

Source: Authors' calculations.

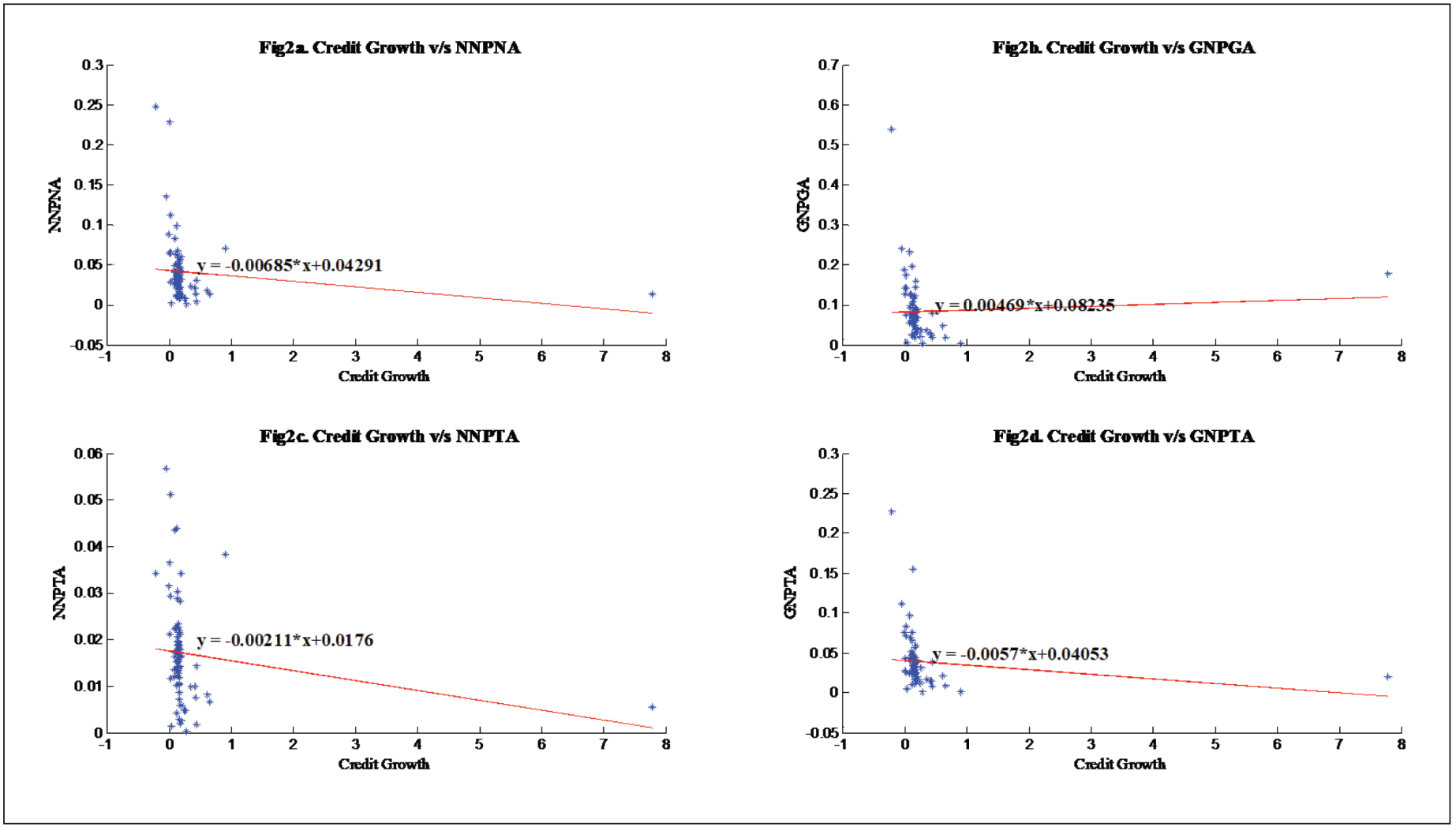

Figure 2. Average NPA and Average Credit Growth

Source: Authors' calculations.

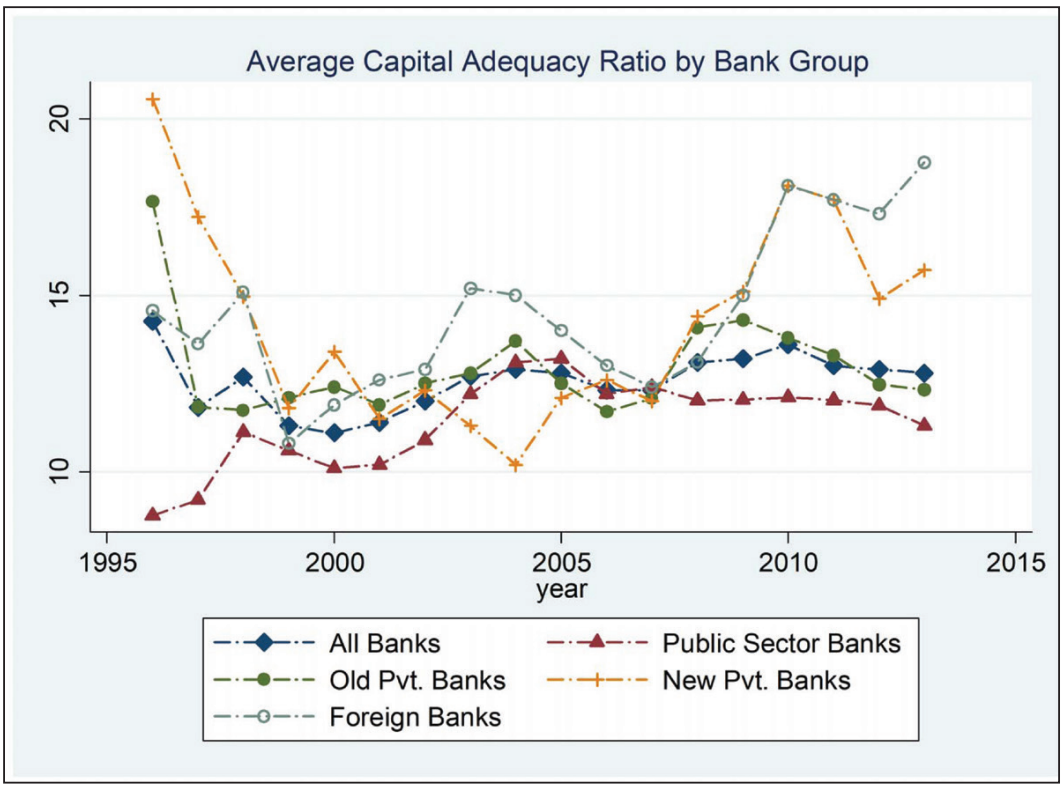

Figure 3. Movement of Average Capital Adequacy Ratio by Bank Groups

Source: Authors' calculations.

re-scaled for the sake of continuity. One beneflt of this transformation is that distribution of most of the variables becomes symmetrical rather than skewed and effects of outliers are negated to a large extent.

5. Econometric Methodology

5.1 Econometric Model

We apply panel threshold regression technique developed by Hansen (1999). A two-regime threshold regression model is specified as:

$$y_{it} = \begin{cases} \mu_i + \beta'_1 x_{it-1} + e_{it}, & q_{it-1} \leq \gamma, \\ \mu_i + \beta'_2 x_{it-1} + e_{it}, & q_{it-1} > \gamma \end{cases} \quad (1)$$

where, i denotes cross-sectional unit and t denotes time, y_{it} is the dependent variable, x_{it-1} is the vector of explanatory variables and e_{it} denotes error term which is assumed to be independently and identically

distributed (i.i.d.) with zero mean and finite variance σ^2. q_{it-1} is the threshold variable that splits the sample into different regimes depending on whether threshold variable q_{it-1} is smaller or larger than the threshold γ, where γ is the threshold parameter endogenously determined by the model. Two regimes are distinguished by differing regression coefficients β'_1 and β'_2 For identification of β'_1 and β'_2, it is required that elements of x_{it-1} are not time invariant. The i.i.d. assumption precludes lagged dependent variable to be included in the vector of explanatory variables. Alternative NPA indicators are considered as dependent variable in our empirical model; x_{it-1} is the vector of explanatory variables. In our empirical models, credit growth, deposit growth, capital adequacy ratio (CRAR), market share, ratio of operating expenses and profit to total assets, ownership of banks are considered as explanatory variables.[15] We consider lagged explanatory variables as well as threshold variable in our empirical models as bank-specific variables such as credit growth and CAR are likely to exert effect on NPAs with a significant time lag. For example, tight monitoring and supervision of loan quality have reflections in declining trend of NPAs across different bank groups over the post-liberalisation periods where incremental NPAs have been low. Similarly, stipulation of maintaining higher CAR is also likely to have lagged effects on NPAs rather than contemporaneous effect as there is a time gap between adjusting riskiness of assets and maintaining capital and effective impact on volume of NPAs of banks.

While estimating threshold and slope parameters, we flrst remove flxed effects μ_i by suitable transformation such that individual bank-speciflc effects are eliminated without violating distributional assumptions underlying Hansen (1999). However, we apply the following forward orthogonal deviation transformation suggested by Arellano and Bover (1995):

$$\varepsilon^*_{it} = \sqrt{\frac{T-t}{T-t+1}}[\varepsilon_{it} - \frac{1}{T-t}(\varepsilon_{i(t+1)} + \ldots + \varepsilon_{iT})].$$

T is the maximum possible time period in the data-set and e is the variable for which forward deviation transformation is conducted.

In forward orthogonal deviation transformation, average of all future available observation of the variable are subtracted from each observation instead of subtracting previous observation from current observation (as in flrst differencing usually applicable in dynamic panels) or subtracting mean from each observation (as is done in within transformation). Beneflt of forward orthogonal transformation is that the serial correlation in error terms is avoided and the distribution theory developed by Hansen (1999) is applicable to panel data. Moreover, by the virtue of forward orthogonal

deviation transformation, gaps in data series are not amplified as it occurs in first difference transformation. Moreover, if a variable is i.i.d. before transformation, it still remains i.i.d. even after fixed effect transformation (Roodman, 2009). After removing fixed effects, coefficient vector $(\beta'_1 \quad \beta'_1)$ in Equation (1) is estimated via least squares for a fixed threshold γ and resulting sum of squared residuals is denoted by $S_1(\gamma)$. This step is repeated for every value of threshold variable q and estimate of threshold variable is the one which corresponds to minimum sum of squared residuals, that is, the least squares estimator of γ as follows:

$$\hat{\gamma} = \underset{\hat{\gamma}}{argmin} S_1(\gamma)$$

In order to ascertain minimum number of observations in either regime, Hansen (1999) suggests trimming of certain percentage of observations (10% or 15%) in either regime[16] that ensures that threshold parameter does not sort too few observations in either regime which may be potential outliers. Once $\hat{\gamma}$ is determined, slope coefficients are estimated using the following ordinary least square (OLS) estimation:

$$\hat{\beta}(\hat{\gamma}) = (X(\hat{\gamma})' X(\hat{\gamma}))^{-1} X(\hat{\gamma})' Y$$

As our focus is on threshold variable, we consider only the threshold variable to be regime dependent and other variables are considered as regime independent which implies that effect of other variables except the threshold variable is assumed to be linear.

5.2 Test of Threshold

Following Hansen (1999), we test whether threshold effect is significant or not. With reference to Equation (1), null hypothesis of no threshold effect can be represented as follows:

$$H_0: \beta_1 = \beta_2.$$

Under H_0, the model is reduced to be linear as follows:

$$y_{it} = \mu_i + \beta'_i x_{it} + e_{it}.$$

After forward orthogonal transformation, the model becomes:

$$y^*_{it} = \beta'_i x^*_{it} + e^*_{it} . \qquad (2)$$

Hansen (1996) suggests the following likelihood ratio test (LRT):

$$F = (S_0 - S_1(\hat{\gamma}))/\hat{\sigma}^2, \tag{3}$$

where $S_0 = \tilde{e}^{*'}\tilde{e}^*$ and $\sigma^2 = \frac{1}{n(T-1)} S_1(\hat{\gamma}_2)$.

Test of this hypothesis involves estimation of nuisance parameter (threshold parameter), that is why classical tests have non-standard distributions in this case. As asymptotic distribution of this likelihood ratio statistic is non-standard, Hansen (1996) suggests use of bootstrapping method for obtaining critical values of *F*-statistic and flnds bootstrapped *p*-values to be asymptotically valid. In this article, we apply wild bootstrap (WB) for generating pseudo data for the dependent variable which is panel extension of bootstrap procedure proposed by Goncalves and Killian (2004) used in time series[17] (see Appendix B for details of bootstrapping procedure).

6. Results and Discussions

6.1 Threshold Effects of Capital Adequacy Ratio on Non-performing Assets

Table 3 presents estimates of threshold regression for full sample of banks with CRAR as threshold variable. Threshold estimates of CRAR ranges between 10 and 12 per cent for alternate measures of NPAs. Beyond the critical threshold, CRAR exerts negative and significant impact on NPAs of Indian banks. Below the threshold, impact is insignificant. Results show on the one hand that banks which had their CRAR high enough above the critical threshold in previous period could manage to reduce their NPAs in next period. These finding are consistent with the hypothesis that banks with lower levels of capital have moral hazard incentives to assume more risks and relatively well capitalised banks are less prone to risk. Therefore, moral hazard incentive for banks with high CRAR did not work; on the other hand, banks with CRAR lower than threshold might have taken recourse to *gamble for resurrection*.[18] Our findings are also consistent with previous evidence that banks with poor 'Equity to Assets ratio' go for higher risks in their loan portfolios reflected in higher NPAs (Berger & Deyoung, 1997; Klein, 2013; Salas & Saurina, 2002). These findings support *moral hazard hypothesis* that banks with lower levels of capitalisation have the motivation to increase riskiness of their loan portfolio.

Table 3. Panel Threshold Regression Results CRAR as Threshold

Dependent Variable	NNPNA	GNPGA	NNPTA	GNPTA
Threshold estimate (%)	10.54	10.99	11.05	11.66
Confidence interval	[10.41–11.66]	[10.31–11.68]	[10.93–11.74]	[10.31–11.78]
Regime Dependent Variable				
Beta 1	–0.0831	–0.1051	–0.0389	–0.2023**
	(0.1182)	(0.1635)	(0.0831)	(0.1133)
Beta 2	–0.2720***	–0.2438*	–0.1586**	–0.2784***
	(0.1034)	(0.1484)	(0.0744)	(0.1058)
Regime Independent Variables				
Deposit growth	–0.0008	–0.0061	–0.0006	–0.0069**
	(0.0035)	(0.0038)	(0.0025)	(0.0030)
Credit growth	–0.0093*	–0.0186***	–0.0011	–0.0057
	(0.0048)	(0.0061)	(0.0032)	(0.0041)
Operating expenses	0.6852***	0.6208***	0.5458***	0.5826***
	(0.1186)	(0.1235)	(0.0847)	(0.0994)
Market share	0.7816***	0.6707***	0.5901***	0.5903***
	(0.1040)	(0.0968)	(0.0761)	(0.0765)
Profit	–0.1276***	–0.1440***	–0.0857***	–0.1452***
	(0.0405)	(0.0491)	(0.0238)	(0.0471)
Private	0.6359***	0.5051***	0.4622***	0.3865***
	(0.0453)	(0.0385)	(0.0357)	(0.0353)
Foreign	0.2105***	0.3131***	0.1837***	0.2845***
	(0.0581)	(0.0667)	(0.0474)	(0.0573)
F-test (*p*-value)	45.8523***	39.1753***	44.3064***	27.7648***
	(0.0000)	(0.0000)	(0.0000)	(0.0000)
Wald test (*p*-value)	4.7505***	3.9391***	4.0039***	2.9418***
	(0.0000)	(0.0000)	(0.0000)	(0.0016)

Source: Authors' calculations.

Notes: Robust standard errors are presented in parenthesis. *, ** and *** denote statistical significance at 10%, 5% and 1%, respectively. *F*-test bootstrap *p*-value is obtained through 500 bootstrap replications.

Model diagnostics also predict that *F*-test is signiflcant which shows evidence of signiflcant threshold effect of CRAR on NPA. In addition to *F*-test, we also carry out test of whether coefflcient estimates of regime dependent variable are statistically same (i.e., $\beta_1 = \beta_2$) across the regimes using Wald test.[19] Wald test for equality of coefflcients of CRAR in two regimes also implies that sample splitting by threshold parameter produces different parameter estimates in two regimes.

In case of regime independent variable, results indicate that lagged operating expenses positively and signifl cantly affect NPAs in next period. Higher operating expenses acts as a signal of low-cost effl ciency. 'Bad Management hypothesis' also postulates that low-cost effl ciency acts as a symptom of poor managerial effl ciency and lead to higher NPAs in next periods. Market share as a proxy of bank's size in relation to banking industry as a whole exerts positive and signifl cant effect on NPAs for the grand sample. In contrast to fl ndings of previous literature which fl nd that the effect of size on NPAs is negative, our analysis of NPAs of Indian banks shows positive effect of NPAs. In fact, bank size is very often treated as a proxy of diversifl cation. The common argument is that bigger size helps banks to diversify their portfolio and also help in improving quality of their loans and thus effectively reduce the rate of NPAs as they have more resources to evaluate lending activities (Hu et al., 2004; Lis, Pages, & Saurina, 2000; Ranjan & Dhal, 2003; Salas & Saurina, 2002). However, *too-big-to fail hypothesis* based on moral hazard also predicts that banks may resort to excessive risk taking extending more risky loans since market discipline is not imposed on those banks who expect government protection in case of a bank's failure (Louzis et al., 2011; Stern & Feldman, 2004). Therefore, it may end up with higher incidence of bad loans in bank's balance sheet subsequently. This typically happens in case of PSBs because market discipline is poorly exercised in these banks and there is an expectation that government will bail out in case of bank run. Coeffl cients of deposit growth appear to be insignifl cant in most cases while explaining NPAs of banks. However, credit growth exerts negative and signifl cant coeffl cient in most cases. This observation reinforces that Indian bank, in general, extended good quality loans during the period under investigation. Lagged Profl t of banks measured by net profl t as a proportion of total asset gives negative and signifl cant coeffl cient in all the models. Lower profl t re‡ects that overdue of repayment of outstanding loans result in accumulation of NPAs over time. Negative coeffl cients of profl t in all estimated models imply that repayment of loans gets adversely affected following decrease in profl t. This, in turn, leads to an increase in NPAs in next period.[20] This particular observation supports 'Bad Management Hypothesis' which postulates that performance is negatively associated with increases in future NPLs. In fact, there are two possible interpretations of 'Bad Management Hypothesis'. First, interpretation of this negative causation from lagged profl t and NPAs in future is that worse performance may act as a proxy for bad skills in terms of lending activities of banks. Second, interpretation is that past performance is considered as a proxy for the quality of management of a bank and performance in previous

period is negatively associated with increases in future NPAs. This finding is also consistent with the hypothesis that worse performance may proxy for bad quality loans (Louzis et al., 2011). According to this hypothesis, past performance is regarded as a proxy of the quality of management. However, in our threshold regression models, we rule out the possibility of reverse causation from NPAs to profit as we measure our dependent variable, NPA at time t and all other explanatory variables including profit have been measured at time $t - 1$ (see Hasan & Wu, 2016, p. 9)

As far as ownership dummies are concerned, we find positive and significant coefficients of both private as well as foreign dummies in all alternative threshold regression models (Table 3). Results indicate that both private banks as well as FBs operating in India record higher levels of NPAs compared to PSBs. In fact, performance of different ownership group of banks in India is not uniform during the period under investigation. Despite the fact that PSBs in India contribute to the bulk of NPAs, compared to private banks and FBs, shares of NPAs have been different for different ownership group of banks during pre-crisis and post-crisis periods.[21] In fact, share of private banks particularly NPBs and FBs in total NPAs have gone up during the post-crisis period. On the other hand, share of PSBs in total NPAs has declined during the post-crisis period, as compared to the pre-crisis period. Similarly, the old private banks account for lesser NPAs during the post-crisis period compared to that in pre-crisis period (Lokare, 2014). It is argued that FBs witnessed a greater impairment in their asset quality as their NPAs during the post-crisis period. There are certain re‡ections to these facts in Table 2. These factors have been instrumental for positive and significant coefficient of private and foreign dummies.

6.2 Threshold Effects of Credit Growth on Non-performing Assets

Table 4 presents threshold effect of credit on NPAs of Indian banks while we consider credit growth as threshold variable. For aggregate sample, threshold estimate of credit growth appears to be approximately 15 per cent across all the models estimated. Ownership group-wise threshold estimations reveal that threshold estimates of credit growth for PSBs are consistently significant compared to those of private and FBs.[22] Findings also reveal that above the threshold, credit growth in case of aggregate sample, exerts negative and significant effect on NPAs However, in most cases, below the threshold, credit growth exerts insignificant effect on NPAs. Threshold estimates of credit growth are found to be not significant

Table 4. Panel Threshold Regression Results (credit growth as threshold): All Bank Groups

Dependent variable	NNPNA	GNPGA	NNPTA	GNPTA
Threshold estimate (%)	14.71	14.68	14.68	14.68
Confidence interval	[10.38–15.70]	[10.53–16.02]	[10.53–17.19]	[11.48–16.11]
Regime dependent variable				
Beta 1	0.0015	–0.0081	0.0067**	0.0033
	(0.0050)	(0.0064)	(0.0033)	(0.0041)
Beta 2	–0.1273***	–0.1331***	–0.0876***	–0.1058***
	(0.0166)	(0.0173)	(0.0131)	(0.0147)
Regime independent variables				
Deposit growth	0.0008	–0.0044	0.0008	–0.0055*
	(0.0035)	(0.0038)	(0.0024)	(0.0030)
CAR	–0.2544**	–0.2158	–0.1460*	–0.2474**
	(0.1116)	(0.1510)	(0.0790)	(0.1078)
Operating expenses	0.6769***	0.6081***	0.5454***	0.5575***
	(0.1137)	(0.1209)	(0.0805)	(0.0974)
Market share	0.7810***	0.6739***	0.5957***	0.5856***
	(0.1034)	(0.0966)	(0.0745)	(0.0754)
Profit	–0.1408***	–0.1543***	–0.0941***	–0.1502***
	(0.0396)	(0.0488)	(0.0230)	(0.0462)
Private	0.6569***	0.5227***	0.4794***	0.4009***
	(0.0460)	(0.0374)	(0.0357)	(0.0340)
Foreign	0.2746***	0.3718***	0.2308***	0.3250***
	(0.0579)	(0.0680)	(0.0490)	(0.0585)
F-test *F*-Test	43.6333***	42.8690***	38.9030***	44.0634***
(*p*-value)	(0.0000)	(0.0000)	(0.0000)	(0.0000)
Wald test	7.0224***	6.6451***	6.6185***	6.8815***
Wald test (*p*-value)	(0.0000)	(0.0000)	(0.0000)	(0.0000)

Source: Authors' calculations.

Notes: Robust standard errors are presented in parenthesis. *, ** and *** denote statistical significance at 10%, 5% and 1%, respectively. *F*-test bootstrap *p*-value is obtained through 500 bootstrap replications.

in case of private and FBs as in PSBs (ownership group-wise results are not reported). In fact, ownership of banks plays a significant role in this respect. Although we have more or less even representation of different ownership group of banks in our aggregate sample, over the years, it is observed, in general, that credit growth is relatively more stable in case

of PSBs compared to those in private and FBs.[23] Although, above findings of threshold effects of credit growth look to be promising, however, we do not rule out the possibility that high growth of credit may be a signal of rolling over previous bad loans into fresh performing loans that immediately lowers current NPAs, as it typically happens in developing country banking systems. Wald test of equality of coefficients across regimes is significant in almost all the models with alternate indicator of NPAs as the dependent variable. As far as regime independent variables including ownership dummies are concerned, we obtain similar evidences in case of most of the variables as in Table 3.

In Figure 4, we plot percentage of banks in second regime separated by CRAR and credit growth as threshold variables (based on threshold estimation results with only net NPA as proportion of net advances [NNPNA] as dependent variable, corresponding to column 1 of Tables 3 and 4, respectively). Observe around 35 per cent of sample banks have CRAR higher than threshold level of 10.54 per cent in 1996. However, percentage of banks maintaining CRAR well above threshold increased to 100 per cent by 2012. It indicates that Indian banks maintain CRAR well above RBI stipulated requirement which partially explains that Indian banking system remains immune to global financial crisis. However, more stringent CRAR requirements as well as risk-weightage norms as per BASEL III posits a challenge of huge capital insertion in case of bigger PSBs, in particular (Reserve Bank of India [RBI], 2014). In terms of credit growth as threshold variable, we observe that percentage of banks posting credit growth exceeding 14.71 per cent increases from 20 per cent in 2002 to almost 70 per cent by 2006 before experiencing significant decline during the global recession of 2007–2009 and remained low thereafter (Figure 4).

6.3 Robustness Check

In order to avoid large effects of outlier observations (as observed in Figures 1 and 2) that might affect parameter estimates or significance, we exclude extreme 1 per cent observations corresponding to capital adequacy ratio as well as credit growth and re-run panel threshold regression models. We only report results corresponding to NNPNA as dependent variable with capital adequacy ratio and credit growth as threshold variable and (Table 5).[24] Observe there is no qualitative change in parameter estimates of threshold variable in both regimes. For instance, statistical significance of CRAR remained the same as in Table 3 (see column 2), while parameter estimate of CRAR in second regime changed

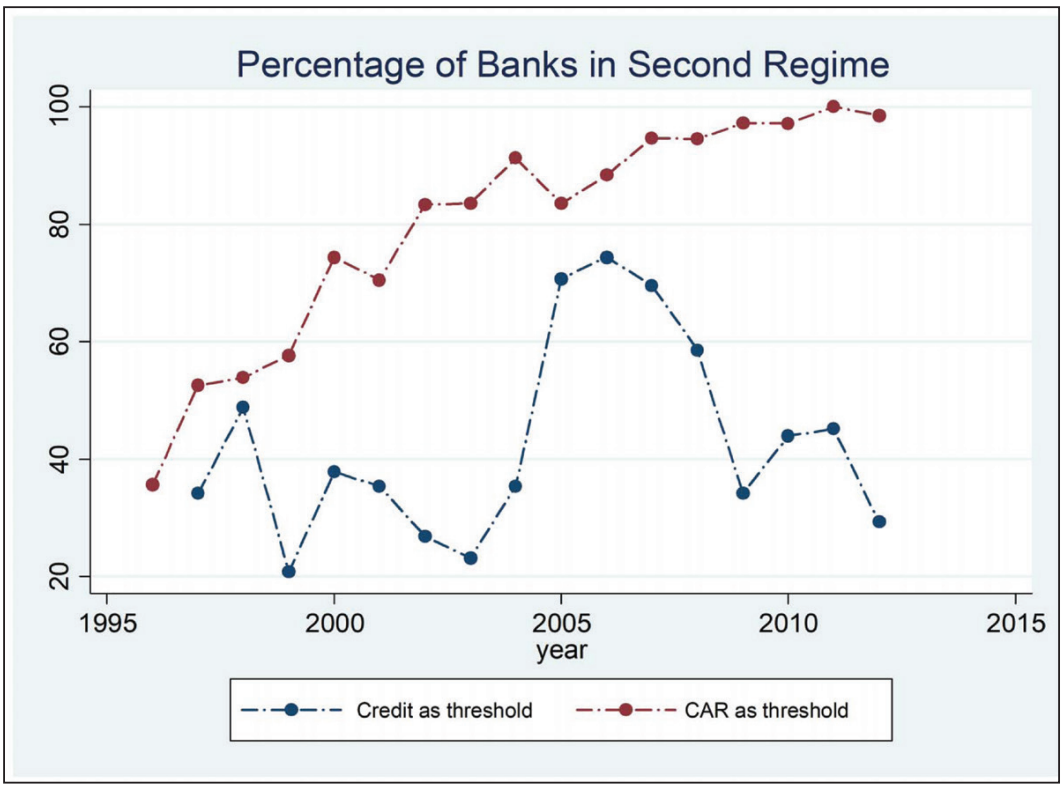

Figure 4. Percentage of Banks in Second Regime with CAR and Credit as Threshold Variable

Source: Authors' calculations.

Table 5. Panel Threshold Results Excluding Outliers

Dependent Variable	NNPNA	NNPNA
Threshold Variable	Capital Adequacy Ratio	Credit Growth
Threshold estimate (%)	10.54	14.71
Confidence interval	[10.41–11.66]	[10.47–15.55]
	Regime Dependent	
Beta1	–0.0443	0.0014
	(0.1269)	(0.0050)
Beta 2	–0.2352**	–0.1370***
	(0.1118)	(0.0167)
	Regime Independent	
Deposit growth	–0.0009	–0.0004
	(0.0042)	(0.0036)
Credit growth	–0.0102**	
	(0.0052)	
Car		–0.2420**
		(0.1141)

(Table 5 continued)

(Table 5 continued)

Dependent Variable	NNPNA	NNPNA
Operating expenses	0.6864***	0.6730***
	(0.1203)	(0.1159)
Market share	0.7940***	0.7849***
	(0.1060)	(0.1083)
Profit	–0.1279***	–0.1391***
	(0.0411)	(0.0394)
Private	0.6389***	0.6478***
	(0.0452)	(0.0459)
Foreign	0.2331***	0.2775***
	(0.0610)	(0.0590)
F-test	46.2543**	50.8446***
	(0.0000)	(0.0000)
Wald test	4.7733***	7.5935***
	(0.0000)	(0.0000)

Source: Authors' calculations.

Notes: Robust standard errors are presented in parenthesis. *, ** and *** denote statistical significance at 10%, 5% and 1%, respectively. *F*-test bootstrap *p*-value is obtained through 500 bootstrap replications.

marginally from –0.2720 to –0.2352 which leads us to conclude that evidences in support of threshold effects are not driven by outlier observations.

7. Conclusions

We investigate the role of bank-specific factors on NPAs in Indian banking sector in a panel threshold framework. We find significant evidence of threshold effect of CRAR on NPAs in the range of 10–12 per cent, and beyond which CRAR leads to a reduction in NPAs. This finding resembles evidence observed by Berger and DeYoung (1997) in a linear framework where increase in capital in thinly capitalised banks results in decrease of NPAs in case of US banks. Although, CRAR of Indian banking industry is maintained well above BASEL I and II requirements, on an average, Indian banks including many PSBs still require capital infusion in order to comply with high capital requirements stipulated in BASEL III norms. With credit growth as threshold variable, we also find significant threshold effects close to 15 per cent above which it exerts negative and significant effect on NPAs. Observe, a significant number of banks posit credit

growth in excess of 15 per cent till the beginning of worldwide recession, which resulted in substantial fall in NPAs in Indian banking system during this period. High credit growth rate is not only crucial in terms of reduction of NPAs and increased profitability but also bears positive implications for the economy as commercial banks constitute the major source of external financing in developing countries such as India. However, too high growth of credit may also signal towards ever-greening of bad assets in a given bank as it typically happens in a developing country banking system such as India (Sarkar, 1999). We also observe that bigger banks especially in public sector are plagued with high NPAs. It is counter-intuitive in the sense that bigger banks are expected to have better credit monitoring mechanism, higher financial strength for credit monitoring and are, therefore, likely to experience smaller incidence of NPAs in their balance-sheet. We also observe that higher operating expenses increase NPLs that supports bad *management hypothesis* (Berger & DeYoung, 1997). In public sector, in particular, personnel expenses constitute the major component of operating expenses, reduction of which may lead to better monitoring of advances, which, in turn, is expected to have dampening effect on NPLs.

The article has important policy implications for stability of Indian banking system. Results suggest that in order to reduce the burden of NPAs regulatory and monitoring mechanisms needs to be strengthened by enforcing strict and transparent auditing schemes to increase transparency in commercial banks' operations which have their CRAR below the threshold and thereby reduce incidence of NPAs. For the banks having their credit growth above the threshold, RBI should be vigilant to prevent roll-over of bad loans to mitigate the possibility of ever-greening in Indian banking system.

Declaration of Conflicting Interests

The authors declared no potential conflicts of interest with respect to the research, authorship and/or publication of this article.

Funding

The authors received no financial support for the research, authorship and/or publication of this article.

Appendix A

Table A1. Description of Variables

Variables	Description	Source
	Indicators of loan default	
NNPANA	Net non-performing assets (NNPA) as a proportion of net advances,	*Statistical Tables Relating to Banks in India*, Reserve Bank of India; *Database of Indian Banking*, Indian Bank's Association; *Money and Banking, Centre for Monitoring Indian Economy*, relevant years
GNPANA	Gross non-performing assets (GNPA) as a proportion of gross advances (GA)	
NNPATA	Net non-performing assets (NNPA) as a proportion of total assets	
GNPATA	Gross non-performing assets (GNPA) as a proportion of total assets	
	Other bank-specific variables	
CAR	Capital adequacy ratio	*Statistical Tables Relating to Banks in India*, Reserve Bank of India, relevant years
DEPOSIT	Rate of growth bank deposits (annual %)	
CREDIT	Rate of growth of bank credit (annual %)	
OPETA	Ratio of operating expenses to total assets	
MSHARE	Current banks total assets/ assets of entire banking industry	
PROFIT	Net profit as a proportion of total assets	

Bootstrapping Procedure

We apply residual-based wild bootstrap (WB) which is of fixed-design nature. We use wild bootstrapping in following manner to generate pseudo data of dependent variable. First, we transform all variables through forward orthogonal transformation (FOT), regress them as per Equation (1) and obtain OLS estimates and estimated residuals as follows:

$$\hat{e} = Y_T - \hat{Y}$$

where Y_T is the transformed dependent variable. We also calculated

$$\text{LRT} = \frac{\text{SSE}_{H_0} - \text{SSE}_{H_1}}{\text{SSE}_{H_1}} * n.$$

Before re-sampling, we rescale the residuals as suggested by McKinnon (2002) as follows:

$$\ddot{e} = \left(\frac{n}{n-1}\right)^{1/2}\left(\frac{\hat{e}_t}{(1-h_t)} - \frac{1}{n}\sum_{s=1}^{n}\frac{\hat{e}_s}{(1-h_s)^{1/2}}\right).$$

As per McKinnon (2002), by doing so, transformed residuals have the same variance if the error terms are homoscedastic and by subtracting the mean of residuals from each transformed residual, the mean of transformed residuals is zero. By multiplying the transformed residual by square root of $\left(\frac{n}{n-1}\right)$, we undo the shrinkage caused by subtracting the mean. Second, we generate bootstrap residuals e_b through the WB method as follows:

$$e_b = \ddot{e} * \mu_{it}$$

where μ_{it}~*iid*(0,1). We generate pseudo-dependent (bootstrap) dependent variables as follows:

$$Y_b = \hat{Y} + e_b$$

Finally, we re-run regression under null hypothesis (linear) against alternative (threshold model) using bootstrap dependent variable based on Equations (2) and (1) respectively (Y_b) and estimate likelihood ratio test (LRT) for threshold effect as follows:

$$\text{LRT}_b = \frac{\text{SSE}_{H_0} - \text{SSE}_{H_1}}{\text{SSE}_{H_1}} * n$$

where n is the number of observations and SSE_{H_0}, SSE_{H_1} are sum of squared errors from null and alternate hypothesis, respectively. Above steps are repeated numbers of times to generate empirical distribution of likelihood ratio statistic and obtain the 90 per cent, 95 per cent, and 99 per cent critical values for the LR.

Notes

1. NPAs are recognised as an important indicator of bank asset quality (Meeker & Gray, 1987).
2. 'CRAR' and 'CAR' are interchangeably used in this article. CRAR is defined as total capital expressed as a percentage of a bank's risk-weighted credit

exposures: CRAR = ([tier 1 capital + tier 2 capital]/risk weighted assets), where tier I capital consists of equity capital and disclosed reserves and tier II capital comprises of general provisions, undisclosed reserves, revaluation reserves, etc. Following the definition, measure of risk-weighted assets is generally obtained by considering loan types and their risk-proneness. In fact, bank's assets are weighted by five categories of credit risk—0, 10, 20, 50 and 100 per cent. Since banks may vary loan types from time to time, ratio also keeps changing.

3. Fleming, Chu, and Bakker (1996) exemplify loan rollovers and gambling for resurrection in case of Lithuanian bank, where an insolvent bank refinances its defaulted borrowers by rolling over their loans which leads to an expansion of its asset base from US$16 million in 1993 to the US$77 million in 1994 and up to US$169 million in 1995.
4. In pursuance of the Narasimhan Committee recommendations, India adopted Basel I norms for commercial banks in 1992, the market risk amendment of Basel I in 1996 and implement Basel II with effect from March 2008 (RBI, 2015). Recent financial crisis that hit the global economy in 2008 points towards weaknesses of Basel II CRAR norm in order to withstand widespread risks and it paved the way for Basel III which led to more stringent capital requirements in the form additional buffer of capital to the tune of 2.5 per cent for taking care of excessive credit growth along with the introduction of liquidity standards in order to ensure stable source of short-term and medium-term funding of bank's assets. In India, implementation of Basel III norms commenced from 1 April 2013 in a phased manner, with full compliance initially targeted to be fulfilled by 31 March 2018 but extended to 31 March 2019 following guidelines from Bank of International Settlements (BIS, 2011).
5. In fact, FBs operating in India with less than 20 branches have no mandatory requirement to contribute towards agriculture. Most of these banks cover their priority sector requirement by contributing towards the export sector. Since most of the PSBs as well as domestic private banks have more than 20 branches, these banks must comply with mandatory requirements of credit to the priority sectors. The CRAR of FBs tends to be quite high and in some cases with the average of more than 25 per cent. This may be because these banks are operating in a foreign country and pursue aggressive marketing policies.
6. Research may have found that capital requirements mitigates the risk arising out of contagion, but it is also observed that excess capital management by banks is positively associated with excess risk taking by banks and vice versa (Shrieves & Dahl, 1992).
7. An NPA has been defined as a loan advance in respect of which payment of interest or repayment of instalment of principal or both remains unpaid for a certain period of time. At present, in Indian banking system an NPA is defined as an advance where payment of interest or repayment of instalment of principal (in case of term loans) remains unpaid for a period of one-quarter

or more. In fact, Narasimham Committee (Muniappan, 1998), as a part of the second phase of reforms of the banking sector, recommended tightening of asset classification and provisioning norms with an objective of moving towards international standard. Accordingly, RBI has moved over to the one-quarter norm (90 days) since 2004. Net NPAs are obtained from gross NPAs after adjusting (a) balance in interest suspense account, (b) claims received from credit guarantors and kept in suspense account and (c) part payment received and kept in suspense account and total provisions (RBI, 1997). The term NPA in our article is treated as synonymous to NPLs as in official definition of NPA in Indian banking system, only loan assets are considered.

8. While gross NPA reflects quality of loans, net NPA reflects actual burden of a bank. In Indian banking system, there is a time lag involved in the process of recovery and detailed safeguards are placed before the write-off of NPAs. Consequently, banks even after making provisions for the advances considered irrecoverable continue to hold such advances, which are termed as gross NPA (RBI, 1999).
9. We consider this period in our analysis as in this period, a proper objective and transparent yardstick for measurement of problem loans were introduced by RBI in Indian banking replacing earlier 'Health Code System' (RBI, 1999). Moreover, we have consistent data of relevant variables of a larger set of banks in our sample during this period.
10. We use statistical data of CRAR of Indian banks based on Basel I framework only in this article because data on CRAR based on Basel I across different ownership groups as well as individual banks are consistently available during the period under investigation. Statistical data of CRAR based on Basel II are only available from 2008 to 2009 onwards.
11. Drukker, Gomis-Porqueras, and Hernandez-Verme (2005) and Khan and Senhadji (2001) apply semi-log transformation of inflation for analysing the effect of inflation on growth of GDP per capita. Semi-log transformation given by:

$$x_{it} = \begin{cases} x_{it} - 1 & if\ x_{it} \leq 1 \\ \ln(x_{it}), & if\ x_{it} > 1 \end{cases}$$

deposit growth, credit growth, capital adequacy ratio and NPA indicators are transformed using semi-log transformation. Market share, operating expenses are transformed using logarithmic transformation.
12. In our estimated threshold regression models, we did not include time dummies. Following specific arguments of Schularick and Taylor (2012, p. 1044) regarding the inclusion of time dummies, perhaps, we also cannot predict truly what is going to happen in NPAs in period t as effect of time is not known ex ante, if we would know that, ex post, it essentiality means that RBI could undertake regulations accordingly, in order to reduce the incidence of NPAs. Therefore, perhaps, it would be difficult to draw certain policy implications based on time as RBI is not supposed to look at time as determinant of NPA. Rather, RBI looks at policy variable such as CAR of bank or other

bank-specific determinants such as market share or profit as possible determinant of NPA.

13. In this article, we consider 15 per cent trimming as we have many extreme observations, the reason for this being that many new private sector banks came into existence in this period and this is the period in which many foreign sector banks entered into Indian banking system. These banks usually had very high values of capital adequacy ratio or very low NPA values in their initial years of operation.
14. The WB was originally proposed by Wu (1986) and Liu (1988) in the context of cross section regressions with unconditional heteroscedasticity. Its application to the time series autoregressive context was considered by Goncalves and Killian (2004). The recursive design version of this bootstrapping has been applied in panel context by Everaert and Pozzi (2007) for bias correction in LSDV estimator and theory for WB in panel context is developed by Goncalves and Kaffo (2015).
15. We conduct separate threshold regressions for different ownership groups of banks operating in India. However, results are not reported in the article. Ownership group wise findings reveal that for public sector as well as private banks, results are mostly in conformity with observations in aggregate sample. In case of FBs, threshold estimates appear to be higher than those observed in case of PSBs as well as private banks. It is observed that FBs in India mostly concentrate their activities in investment banking and operations in foreign exchange market with less emphasis on expansion of credit (Mohan, 2006). Comparatively higher threshold of CRAR of FBs operating in India mainly arises due to less risky assets and more equity capital assumed by these banks.
16. The null hypothesis of Wald test is that the parameter estimates of regime dependent variable is statistically the same in both regimes, that is, H_0: $\beta_1 = \beta_2$ against H_0: $\beta_1 \neq \beta_2$. The Wald test is calculated as $W = \frac{|\beta_1 - \beta_2|}{se(\beta_1 - \beta_2)}$ and $W \sim N(0,1)$.
17. As there may be issues relating to reverse causality between profits and NPAs we cannot rule out such a possibility. However, we cannot control for reverse causation, as Hansen (1999) method does not allow us to control for potential endogeneity of the explanatory variables.
18. Literature identifies three distinct phases in terms of growth of NPAs and growth of total advances of banks. During 2001–2006, there has been a sharp decline in NPAs and gradual acceleration in growth of credit. Improvement in asset quality, increased banking competition and financial deepening are few important factors which contributed to growth of credit during this period. However, during 2006–2009, there has been a trend reversal when NPAs grew and credit growth registered a slowdown.
19. These findings are not reported in the article, available from authors on demand.

20. Foreign and private sector banks operating in Indian financial system are relatively newer as compared to PSBs. In particular, many FBs started their operation in Indian banking system since the mid-1990s with comparatively lower capital base than established PSBs.
21. Results corresponding to other indicators as dependent variable are qualitatively the same and are available from authors.

References

Agung, J., Kusmiarso, B., Pramono, B., Hutapea, E. G., Prasmuko, A., & Prastowo, N. J. (2001). *Credit crunch in Indonesia in the aftermath of the crisis: Facts, causes and policy implications* (Bank Indonesia Occasional Paper). Jakarta: Bank Indonesia.

Arellano, M., & Bover, M. O. (1995). Another look at the instrumental variable estimation of error-components models. *Journal of Econometrics*, *68*(1), 29–51.

Bank of International Settlements (BIS). (2011). *Basel III: A global regulatory framework for more resilient banks and banking systems*. Basel: Bank of International Settlements Publications.

Bardhan, S., & Marjit, S. (2005). Non-performing assets of Indian commercial banks: An analytical Exercise. In T. T. Rammohan, R. R. Nitsure, & M. Joseph (Eds.), *Regulation of financial intermediaries in emerging markets* (pp. 210–249). New Delhi: Response Books, SAGE Publications.

Bardhan, S., & Mukherjee, V. (2016). Bank-specific determinants of non-performing assets of Indian banks. *International Economics and Economic Policy*, *13*(3), 483–498.

Berger, A. N., & DeYoung, R. (1997). Problem loans and cost efficiency in commercial banks. *Journal of Banking & Finance*, *21*(6), 849–870.

Centre for Monitoring Indian Economy (CMIE). (2006). *Money and banking* (pp. 279–280). Bombay: Centre for Monitoring Indian Economy.

Das, A., & Ghosh, S. (2007). Determinants of credit risk in Indian state-owned banks: An empirical investigation. *Economic Issues*, *12*(2), 27–46.

Drukker, D., Gomis-Porqueras, P., & Hernandez-Verme, P. (2005). *Threshold effects in the relationship between inflation and growth: A new panel-data approach* (Working Paper, pp. 1–18). University of Texas. Retrieved from http://www.uh.edu/~cmurray/TCE/papers/Drukker.pdf

Everaert, G., & Pozzi, L. (2007). Bootstrap-based bias correction for dynamic panels. *Journal of Economic Dynamics and Control*, *31*(4), 1160–1184.

Fleming, A., Chu, L., & Bakker, M. H. (1996). *The Baltics-banking crises observed* (World Bank Policy Research Working Paper No.1647). Washington, DC: The World Bank.

Ghosh, A. (2015). Banking-industry specific and regional economic determinants of non-performing loans: Evidence from US states. *Journal of Financial Stability*, *20*(C), 93–104.

Ghosh, A., & Phillips, S. (1998). Warning: Inflation may be harmful to your growth. *IMF Staff Papers*, *45*(4), 672–710.

Goncalves, S., & Kaffo, M. (2015). Bootstrap inference for linear dynamic panel data models with individual fixed effects. *Journal of Econometrics*, *186*(2), 407–426.

Goncalves, S., & Kilian, V. (2004). Bootstrapping autoregressions with conditional heteroskedasticity of unknown form. *Journal of Econometrics*, *123*(1), 89–120.

Goyal, A. (2017). Indian banking: Perception and reality. *Economic & Political Weekly*, *52*(12), 77–84.

Hansen, B. E. (1996). Inference when a nuisance parameter is not identified under the null hypothesis. *Econometrica*, *64*(2), 413–430.

———. (1999). Threshold effects in non-dynamic panels: Estimation, testing, and inference. *Journal of Econometrics*, *93*(2), 345–368.

Hasan, I., &, Wu, D. (2016). *How large banks use CDS to manage risks: Bank-firm-level evidence* (Bank of Finland Discussion Paper No. 10/2016). Retrieved from https://helda.helsinki.fi/bof

Hu, J. L., Li, Y., & Chiu, Y. H. (2004). Ownership and non-performing loans: Evidence from Taiwan's banks. *Developing Economies*, *42*(3), 405–420.

Indian Banks' Association (IBA). (2006). *Database of Indian banking: 2001–02 to 2004–05* (Special Issue). Mumbai: Indian Banker.

Kane, E. (1989). *The S&L insurance mess: How did it happen?* Washington, DC: The Urban Institute Press.

Khan, M. S., & Senhadji, A. S. (2001). Threshold effects in the relationship between inflation and growth. *IMF Staff Papers*, *48*(1), 1–21.

Klein, N. (2013). *Non-performing loans in CESEE : Determinants and impact on macroeconomic performance* (IMF Working Paper No. 13/72). Washington, DC: IMF.

Krueger, A., & Tornell, A. (1999). *The role of bank restructuring in recovering from crises: Mexico 1995–98* (NBER Working Paper No. 7042). Retrieved from http://www.nber.org/papers/w7042.pdf

Krugman, P. (1998). *What happened to Asia?* (Working Paper). Cambridge, MA: Massachusetts of Technology. Retrieved from http://web.mit.edu/krugman/www/DISINTER.html

Leung, W. S., Taylor, N., & Evans, K. P. (2015). The determinants of bank risks: Evidence from the recent financial crisis. *Journal of International Financial Markets, Institutions and Money*, *34*(C), 277–293.

Lis, S. F. de, Pages, J. M., & Saurina, J. (2000). Credit growth, problem loans and credit risk provisioning. provisioning in Spain (Working Paper 0018). The Bank of Spain.

Liu, R. Y. (1988). Bootstrap procedures under some non-I.I.D. models. *Annals of Statistics*, *16*(4), 1696–1708.

Lokare, M. S. (2014). *Re-emerging stress in the asset quality of Indian banks: Macro-financial linkages* (RBI Working Paper Series (DEPR): 03/2014, pp. 1–43). Mumbai: RBI.

Louzis, D. P., Vouldis, A. T., & Metaxas, V. L. (2011). Macroeconomic and bank-specific determinants of non-performing loans in Greece: A comparative

study of mortgage, business and consumer loan portfolios. *Journal of Banking & Finance*, *36*(4), 1012–1027.

Mallick, I., & Marjit, S. (2004). Collateral monitoring and banking regulation. *Economic & Political Weekly*, 39(12), 1259–1262.

McKinnon, J. G. (2002). Bootstrap inference in econometrics. *Canadian Journal of Economics*, *35*(4), 615–645.

Meeker, L. G., & Gray, L. (1987). A note on non-performing loans as an indicator of asset quality. *Journal of Banking & Finance*, *11*(1), 161–168.

Misra, R., Rajmal, & Verma, R. (2016). Determinants of recovery of stressed assets in India. *Economic & Political Weekly*, *51*(43), 62–71.

Mohan, R. (2006, June). *Financial sector reforms and monetary policy: The Indian experience*. Paper presented at Conference of Economic Policy of Asia, organised by Stanford Centre for International development and Stanford Institute for Economic Policy and Research, Stanford.

Mukherjee, P. (2003). Dealing with NPAs: Lessons from international experiences. *Money & Finance*, *12*(12), 64–90.

Muniappan, G. (2002, April 2). *The NPA overhang, magnitude, solution and legal reforms*. Paper prepared for the CII Banking Summit 2002, 1–11, Mumbai.

——— (1998). *Report of the Narasimham Committee on the banking sector reforms*. New Delhi: (Narasimham Committee II), Ministry of Finance.

Niinimaki, J. P. (2007). Evergreening in banking. *Journal of Financial Stability*, *3*(4), 368–393.

Pandey, S. J., Tilak, V. G., & Deokar, B. (2013). Non-performing assets of Indian banks. *Economic & Political Weekly*, *48*(24), 91–93.

Podpiera, J., & Weill, L. (2008). Bad luck or bad management? Emerging banking market experience. *Journal of Financial Stability*, *4*(2), 135–148.

Rajaraman, I., & Vasishtha, V. (2002). Non-performing loans of PSU banks: Some panel results. *Economic & Political Weekly*, *37*(5), 429–435.

Ranjan, R., & Dhal, S. (2003). Non-performing loans and terms of credit of public sector banks in India: An empirical assessment. *Reserve Bank of India Occasional Paper*, *24*(3), 81–121.

Reddy, G. S. (2004). Management of non-performing assets (NPA's) in public sector banks. *Journal of Banking and Finance*, *17*(3), 17–21.

Reserve Bank of India (RBI). (1995–2005). *Statistical tables relating to banks in India, various issues*. Mumbai: RBI.

———. (1997). *Report on trend and progress in banking.* Mumbai: RBI.

———. (1999). Some aspects and issues relating to the NPAs in commercial banks. *RBI Bulletin*, *53*(7), 913–916.

———. (2014). *Master circular on Basel III capital regulations*. Retrieved from http://www.rbi.org.in

———. (2015). *Master circular—Prudential norms on capital adequacy—Basel I framework*. Retrieved from http://www.rbi.org.in

Roodman, D. (2009). How to do xtabond2: An introduction to difference and system GMM in Stata. *Stata Journal*, *9*(1), 86–136.

Salas, V., & Saurina, J. (2002). Credit risk in two institutional regimes: Spanish commercial and savings banks. *Journal of Financial Services Research*, *22*(3), 203–224.

Samantaraya, A. (2016). Pro-cyclical credit growth and bank NPAs in India. *Economic & Political Weekly*, *51*(12), 112–119.

Sarkar, J. (1999). India's banking sector: Current status, emerging challenges, and policy imperatives in a globalised environment. In J. A. Hanson & S. Kathuria (Eds.), *India: A financial sector for the twenty-first century* (pp. 71–131). New Delhi: Oxford University Press.

Sarma, M., & Nikaido, Y. (2007). India's capital adequacy regime. *Economic & Political Weekly*, *42*(43), 66–71.

Schularick, M., & Taylor A. M. (2012). Credit booms gone bust: Monetary policy, leverage cycles, and financial crises, 1870–2008. *American Economic Review*, *102*(2), 1029–1061.

Sengupta, R., & Vardhan, H. (2017). Non-performing assets in Indian banks: This time it is different. *Economic & Political Weekly*, *52*(12), 85–95.

Shrieves, R. E., & Dahl, D. (1992). The relationship between risk and capital in commercial banks. *Journal of Banking & Finance*, *16*(2), 439–457.

Stern, G., & Feldman, R. (2004). *Too big to fail: The hazards of bank bailouts*. Washington, DC: The Brookings Institution.

Vithessonthi, C. (2016). Deflation, bank credit growth, and non-performing loans: Evidence from Japan. *International Review of Financial Analysis*, *45*(C), 295–305.

Williams, J. (2004). Determining management behaviour in European banking. *Journal of Banking & Finance*, *28*(10), 2427–2460.

Wu, C. F. J. (1986). Jackknife, bootstrap and other re-sampling methods in regression analysis. *Annals of Statistics*, *14*(4), 1261–1295.

Zhang, D., Cai, J., Dickinson, D. G., & Kutan, A. M. (2016). Non-performing loans, moral hazard and regulation of the Chinese commercial banking system. *Journal of Banking & Finance*, *63*, 48–60.

SCIENTIFIC REPORTS

OPEN

Two-dimensional transition metal dichalcogenides assisted biofunctionalized optical fiber SPR biosensor for efficient and rapid detection of bovine serum albumin

Received: 18 January 2019
Accepted: 15 April 2019
Published online: 06 May 2019

Siddharth Kaushik[1,2], Umesh K. Tiwari[1,2], Akash Deep[1,2] & Ravindra K. Sinha[1,3]

The present study reports an alternative method of functionalizing the optical fiber Surface Plasmon Resonance (SPR) sensing probe with antibodies for label-free detection of bovine serum albumin (BSA) protein. In this novel approach, the gold coated fiber was first modified with Molybdenum disulfide (MoS_2) nanosheets followed by its bio-functionalization with Anti-BSA antibodies. The developed technique not only allowed the amplification of the SPR signals by synergic effects of MoS_2 and gold metallic thin film but also enabled a direct and chemical-free attachment of representative antibodies through hydrophobic interactions. The sensitivity of the MoS_2 modified sensing probe with detection limit of 0.29 μg/mL was improved as compared to the fiber optic SPR biosensor without MoS_2 overlayer (Detection limit for BSA was 0.45 μg/mL). The developed biosensor has good specificity, and environmental stability. Accordingly, the proposed design of the MoS_2 based SPR optical biosensor can offer the development of a simplified optical device for the monitoring of various biomedical and environmental parameters.

Biosensors have been the focus of cutting-edge research in recent years as they possess desirable properties of high sensitivity, excellent specificity, good stability, easy operation, fast response and cost-effective analysis[1]. Considering these imperative features, a plethora of biosensing platforms including photoelectrochemical[2–5], impedance-based[6–8] and optical[9,10], were reported for sensitive and specific detection of chemical compounds and biomolecules. As diseases caused by pathogens including diarrhea[11], typhoid[12] and pneumonia[13,14] etc., are major public health concern in developing nations, a sensitive and portable biosensor is needed to rapidly detect the target analyte in a different matrices without delayed intermediate sample processing. SPR sensors offer a specific, rapid, sensitive and label-free detection method preferable for the medical diagnostics and chemical analyses[15]. For the last three decades, since its inception in 1982 as a gas sensor[16], the Surface Plasmon Resonance (SPR) sensors have evolved as the propitious sensing platform for wide range of applications[17–22]. For medical and environmental applications different SPR based configurations had been explored which includes prism-based SPR sensor[23,24], optical fiber SPR sensors[25–28].

The prism configuration has certain limitations including large size with many optical and mechanical components which limit their use for on-site sensing application[29]. The optical fiber-based sensors have the potential to be used for the on-site sensing of analytes as they allow the designing of devices with advantageous features of compactness, cost-effectiveness, robustness, and rapid response[30–34]. An easier tuning of the resonance wavelength in optical fiber SPR sensors compared to the prism-based SPR sensors is also of great benefit[35,36]. As such, the resonance characteristics depend upon the core refractive index (RI) and RI of the surrounding layer, metal layer thickness, and the length of the sensing probe[37–40]. Additionally, the optical fiber sensors are immune to

[1]CSIR-Central Scientific Instruments Organization, Chandigarh, 160030, India. [2]Academy of Scientific and Innovative Research, CSIR-CSIO Campus, Chandigarh, 160030, India. [3]TIFAC-Centre of Relevance and Excellence in Fiber Optics and Optical Communication, Department of Applied Physics, Delhi Technological University, Delhi, 110042, India. Correspondence and requests for materials should be addressed to U.K.T. (email: uktiwari_2003@yahoo.co.in)

electromagnetic interference and undesired influences of ionization radiation[41–43]. Hence the fiber optic SPR sensors are practically advantageous as compared to the other optical sensors in different fields of sensing.

The electromagnetic waves excited by the charge density oscillations that exist along the metal–dielectric interface is known as surface plasmon polaritons (SPPs)[44]. SPR is the quantum of these oscillations and the wave associated with it is called surface plasmon wave (SPW). The SPWs which propagates along the interface are transverse in nature and exponentially decay in both the dielectric and metal medium. TM polarized light excite the surface plasmon at the phase matching condition. As the propagation constant of the TM polarized light matches with the SP wave propagation constant, it results in the generation of surface plasmon resonance (SPR). The normalized transmission power of the fiber optic SPR sensor is presented in eq. (1)[45]

$$T.\ P. = \frac{\int_{\varnothing_{cr}}^{\frac{\pi}{2}} R^{N(\varnothing)} \frac{{n_1}^2\, Sin2\varnothing}{2\,(1-{n_1}^2 Cos^2\varnothing)^2} d\varnothing}{\int_{\varnothing_{cr}}^{\frac{\pi}{2}} \frac{{n_1}^2 Sin2\varnothing}{2\,(1-{n_1}^2\, Cos^2\varnothing)^2} d\varnothing} \tag{1}$$

Where n_1 is the RI of the core and $\varnothing$ is the angle of the incidence of the light with the normal at the core-cladding interface in the sensing region. The total reflection by the incident light is denoted by $N(\varnothing)$. The field intensity decays exponentially with the formation of SPR exhibiting a sharp dip of SP wave in the spectral response of the transmitted light. Hence, the variations in the RI at the surface of the sensing platform within the evanescent wave region due to the interaction between immobilized bioreceptor (e.g., aptamers, antibodies, lectins, etc.) and target molecules in samples may shift the resonant wavelength significantly[46].

The optical fiber SPR sensing technology is also beneficial for the detection of biomolecules. To frame the optical fiber biosensor specific towards desired analytes, they must be functionalized by bio-recognition molecules, such as proteins, RNA, DNA, cells, etc. This adherence of the biomolecules over the optical fiber surface is generally achieved via some chemical linkers ((3-Aminopropyl) triethoxysilane, N-Succinimidyl 4-Maleimidobutyrate, etc[47–49]. Most of the above-mentioned surface modifications approaches are tedious and do not necessarily provide a homogenous bio coating.

Recently, the 2D transition metal dichalcogenides (TMDs), particularly MoS_2, have attracted significant attention of researchers in different scientific fields, due to their high electron conductivity, tuneable band gap, and high optical absorption efficiency[50–53]. The hydrophobic nature, large surface area and presence of free sulphur atoms are distinctive features of MoS_2 which makes it a potential material to develop biosensing interfaces[54,55]. Moreover, the MoS_2 layers have been employed to inhibit the oxidation of metallic layers such as aluminium in SPR sensors[56].

The present research outlines a novel method for biofunctionalization and sensitivity enhancement of the optical fiber SPR sensor for biosensing applications. The interfacing of MoS_2 sheets facilitates simple and rapid antibodies immobilization on transducer's surface via a convenient method of hydrophobic interaction[57]. In this way, the developed sensor avoids the requirement of any harsh chemical or muti-step treatments to the fiber which affects the sensitivity of the sensor by forming additional layer between antibodies and sensing probe.

Materials and Methods

Reagents. Sodium sulfide (Na_2S), Poly (ethylene glycol) (PEG), Fluorescein isothiocyanate (FITC), 3-mercaptopropionic acid, n-methyl pyrrolidone (NMP) was purchased from Sigma-Aldrich, India. Umicore, India supplied molybdenum sheets (99.5% purity), Hydrofluoric acid (48% w/w), Anti-Bovine serum albumin (monoclonal), Bovine serum albumin and 10 mM Phosphate buffer saline (pH 7.4 at 25 °C) were obtained from Merck, India. All the other chemicals used were of the analytical grade. All the solutions were prepared in double deionized water >18 mΩ.cm (specific resistivity) at 25 °C, Millipore.

Analytical instruments. The optical absorbance spectrum of the MoS_2 functionalized optical fiber sensor was recorded at a scan rate of 600 nm min^{-1} over a wavelength range of 200–800 nm by a UV-Vis spectrophotometer (Varian Cary 5000, Agilent Technologies, U.S.A). The X-Ray diffraction analysis was achieved with a Bruker D8 diffractometer using Cu Kα radiation (wavelength = 1.546 Å) at the scan rate of 4° min^{-1}. The morphological characterization of the fabricated biosensor was performed by field-emission scanning electron microscope (Hitachi S4800; accelerating voltage 2–4 KV). The Raman analysis was performed using a Raman spectrophotometer (excitation wavelength: 514 nm) (Renishaw, UK). The confocal laser scanning microscopic (LSM 510) (Zeiss, Germany) was used for morphological analysis of the bio functionalized sensing probe. The exfoliated MoS_2 nanosheets were analysed using a transmission electron microscope (TEM) (Applied voltage: 200 kV) (JEOL 2010, Japan).

Experimental setup. The experimental setup employed to study the SPR biosensor performance is presented in Fig. 1. The developed sensor (Anti-BSA/MoS_2/Au optical fiber) was positioned in a glass flow cell having definite inlet and outlet passages. Non-polarized polychromatic light from broadband source (wavelength range: 360–2400 nm; output power: 6.7 mW; Ocean Optics, HL-2000,) was launched at one end of the fiber optic sensor. The transmission spectra were recorded through charge-coupled device (CCD) spectrometer (λ: 200–1160 nm; resolution: 0.09–20 nm; Avantes, ULS2048XL-EVO) connected to another end of the sensor. The computer was interfaced with the spectrometer to record the spectral response at different concentrations of the BSA.

Synthesis of MoS_2 nanosheets. MoS_2 nanosheets were synthesized by the electro-dissolution method. Briefly, the cathode having molybdenum sheet was intercalated with Na^+ ions. The Ag/AgCl, molybdenum sheets and Pt wire were forgathered in an electrochemical cell as the reference, cathode (working) and anode (counter) electrodes respectively. 1 M sodium sulfide (Na_2S) solution was taken as the electrolyte. The chrono-amperometry

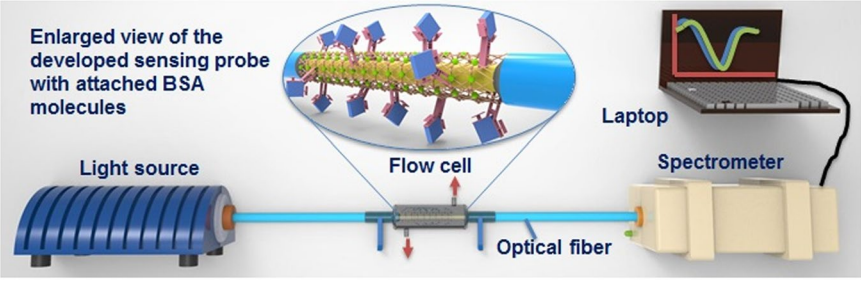

Figure 1. Diagrammatic representation of the SPR biosensor experimental system for the detection of BSA. The time of interaction between Anti-BSA antibodies and BSA sample was 15 minutes.

mode was applied, keeping the potential constant at 1 V. The electrolysis process was repeated for multiple cycles to obtain better product yield. The hydroxyl and oxygen radicals generated by the oxidation of water react with the grain boundaries and edge sites of the molybdenum sheets creating defective sites. The Na^+ ions intercalate in these defective sites causing interlayer separation. The Na^+ intercalated MoS_2 sheets dissolution was clear, as the colorless electrolyte organic solution transformed primarily to pale yellow and ultimately to dark yellow colour with the trickling of MoS_2 sheets into the solution. The extracted material was separated by centrifugation at 20000 rpm for 30 min. After washing three times with DI water followed by centrifugation, the supernatant was suspended in DI water and ultrasonicated for 2 hours resulting in the exfoliation of Mo into few-layered MoS_2 nanosheets. This method is rapid and highly efficient for producing MoS_2 nanosheets.

Fabrication of the sensing probe. *Chemical etching of multimode optical fiber.* The optical fiber SPR sensor was fabricated in a plastic cladded multimode step-index fiber (core diameter: 400 μm). For developing the sensing region, cladding layer was initially removed by thermal process to expose a 1 cm uncladded fiber length. After depletion of the cladding layer, the core region of the optical fiber was subjected to the chemical etching process. It was performed by exposing the fiber to Hydrofluoric acid (HF) for 38 minutes at room temperature (25 °C ± 2 °C). The acid solution was intermittently agitated to allow a uniform etching. The etching reaction proceeded at an etch rate of 3 microns/minute. Subsequently, the etched fiber was washed with methanol and DI water. The tapered optical fibers were stored in glass desiccator under dry conditions.

DC Magnetron sputtering unit assisted gold thin film deposition on the optical fiber (PVD method). The gold thin film coating on the tapered optical fiber was achieved through a DC Magnetron Sputtering deposition instrument which consisted of a DC sputter source (Excel Instruments, India). The optical fiber was placed at a distance of 10 cm in front of the target. A glow discharge was created by applying high voltage. The acceleration of argon ions to a pre-mounted gold target surface led to the ejection of gold particles, which subsequently got adhered as a sputtered coating layer onto the optical fiber. During the above experiment, the sputtering gas (Argon) was introduced in the chamber with a flow rate of 30 standard cubic centimetre per minute (SCCM) at a pressure of 2.1 Pa. To achieve good sensitivity, the gold layer thickness is considered as an important parameter. The fiber was rotated for different cycles (4, 5, 6, 7, 8, 9) to optimize the gold layer deposition to achieve best results and it was observed that after 7 cycles, the sensitivity of the fabricated sensor towards 6% w/v sucrose solution (RI: 1.3420 at 25 °C) was highest as compared to the other rotations of certain time interval as presented in Fig. S1(a) (Supplementary Information). To introduce a uniform coating, 7 cycles of rotation was done under the inert conditions. The chromium (~5 nm) was initially coated on the optical fiber for good adhesion of gold on optical fiber. The DC power of 40 W was used during the total deposition time. The thickness of the coated gold was 50 nm ± 4 nm which is comparable to the thickness reported in preceding studies[58].

Functionalizing the MoS_2 nanosheets on the gold coated optical fiber. The MoS_2 overlayer were deposited on the gold coated fiber optic SPR sensor via dip coating technique. The gold coated fiber was incubated with 1 mL solution of the MoS_2 nanosheets. To optimize the nanosheets functionalization process the dip coating was done for 2, 3, 4, 5, 6, 7 cycles. Each cycle was accomplished by dipping the optical fiber in the MoS_2 nanosheets solution for 30 seconds and subsequently drying for 120 seconds. After different cycles, the MoS_2 functionalized sensing probe was annealed for 1 hour at 60 °C to confirm the proper robustness of the MoS_2 interfacing with the gold layer. The MoS_2 functionalized sensing probes were further treated with Anti-BSA antibodies and the biofunctionalized sensing probes were tested for detection of BSA (10 μg/mL). The dip coating process of 05 cycles was selected for the development of proposed sensor as best resonance wavelength shift was obtained at this optimal thickness of MoS_2 layers as depicted in Fig. S1(b) (Supplementary Information). The Raman spectroscopy and scanning electron microscopy characterization confirmed the uniform interfacing of the MoS_2 on the gold coated fiber.

In SPR based sensing, temperature is an important parameter which affects metal properties through phonon-electron scattering and electron-electron scattering, signal-to-noise ratio (SNR) and sensitivity of the sensor[59]. The metal dielectric function is also related with temperature variation. It has been reported that plasma frequency and collision frequency of metal layer is related to temperature, the RI of core and RI of the sensing layer are also affected by temperature through thermo-optic coefficient. The blue shift in resonance wavelength and broadening of SPR curve was noted with increase in temperature in previous studies[60]. We have performed

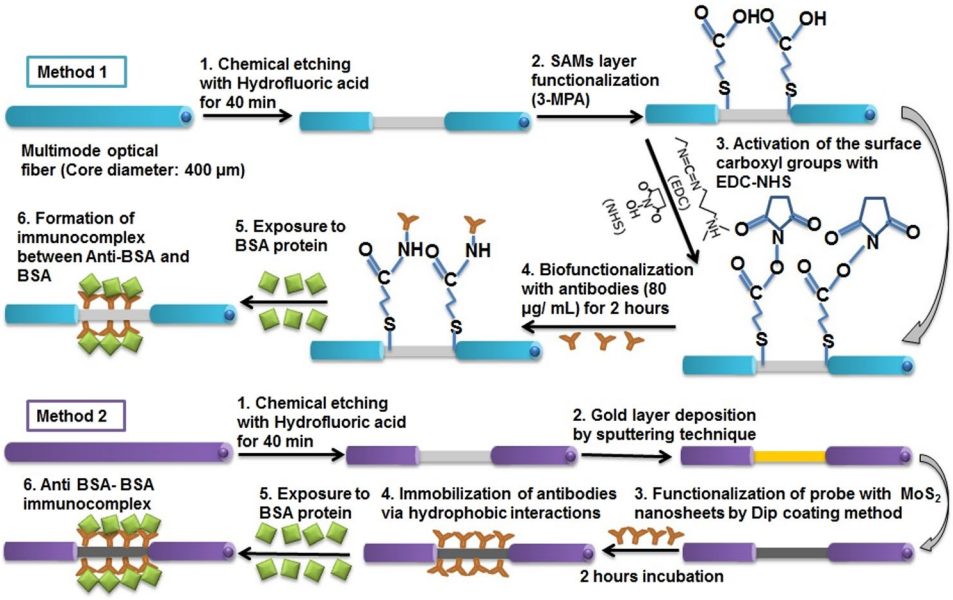

Figure 2. Schematic delineation of the development process of optical fiber SPR biosensor without MoS_2 overlayer and the MoS_2 modified optical fiber SPR biosensor.

our experiments at room temperature (25 °C ± 2 °C) to eliminate the temperature effect on spectral response of the proposed sensing platform.

Biofunctionalization of Anti-BSA on MoS_2/gold/optical fiber. The MoS_2 functionalized surface of the optical fiber was incubated with the 80 µg/mL solution of anti-BSA (monoclonal antibodies) in PBS solution (pH 7.4) for two hours at room temperature. After immobilization of anti-BSA antibodies, the sensing platform was incubated for 20 minutes with 35 µL of 1-mM polyethylene glycol solution as a blocking agent to occlude the non-specific sites of the sensing probe. After an incubation, the fiber was washed three times with DI water for removal of unbound molecules.

Sample preparation for characterization of the bio functionalized sensing probe. We have immobilized the FITC conjugated anti-bovine serum albumin antibodies on MoS_2/Au/optical fiber through simple physical adsorption route. Briefly, 500 µL of FITC (0.2 mg/mL prepared in DMF) and 80 µg/mL of anti-*BSA* antibodies were mixed together. The mixed solution was incubated for 1 hour in dark at 25 °C. Desalting spin column was used to remove excess FITC molecules. The 1 mg/mL solution of FITC/anti-BSA in PBS solution (pH 7.4) was prepared and then left to incubate with the MoS_2 functionalized surface of the optical fiber for 40 min at room temperature. For the Raman spectroscopic analysis, the MoS_2/Au/optical fiber was first carefully diced using a surgical blade, then mounted on the glass slide. A 50X objective was employed to focus the laser beam (514 nm) and collect Raman signal at room temperature.

Quantitative analysis of Bovine serum albumin (BSA). The performance of the antibody immobilized optical fiber sensor with MoS_2 overlayer was collated with antibody immobilized gold coated optical fiber sensor without MoS_2 overlayer. In this conventional design, the gold coated optical fiber was modified with 3-mercaptopropionic acid (3-MPA) by immersing the gold coated fiber in 10 mM ethanolic solution of 3-MPA for 6 hours. It was then incubated with 1 mL of PBS solution having 1 mM EDC and 2 mM NHS to activate –COOH groups of the sensing probe. Incubation of the anti-BSA antibodies was finally performed at 37 °C for an hour. The remaining binding sites on the sensing probe were blocked by treating the developed sensor with with 1 M ethanolamine hydrochloride (pH 8.6) for 45 min. The developed biosensor was then thoroughly washed with distilled water three times, dried by nitrogen gas, and stored at 4 °C before using for the BSA detection. The complete process for fabrication of SPR biosensor without MoS_2 overlayer and MoS_2 assisted biofunctionalized SPR sensing probe is presented in Fig. 2. Different concentration of BSA, ranging from 10 µg/mL to 50 µg/mL in PBS solution was prepared. These samples were then inserted through flow cell to interact with the antibody immobilized MoS_2/gold/optical fiber sensor for 15 minutes and then the resulting transmission spectra were recorded. The spectral response in terms of shift in resonance wavelength of the sensor was then correlated with the defined concentrations of BSA.

Results and Discussion

Structural analysis of exfoliated MoS_2 nanosheets and developed optical fiber SPR sensor. The exfoliated MoS_2 nanosheets have been characterized by well-established microscopic and spectroscopic techniques. In UV-Vis absorption spectrum [Fig. 3(a)], the exfoliated MoS_2 nanosheets have shown the absorption peaks at 617 nm and 672 nm, due to direct transitions at the K point of the Brillion zone[61]. The broad peak at 395

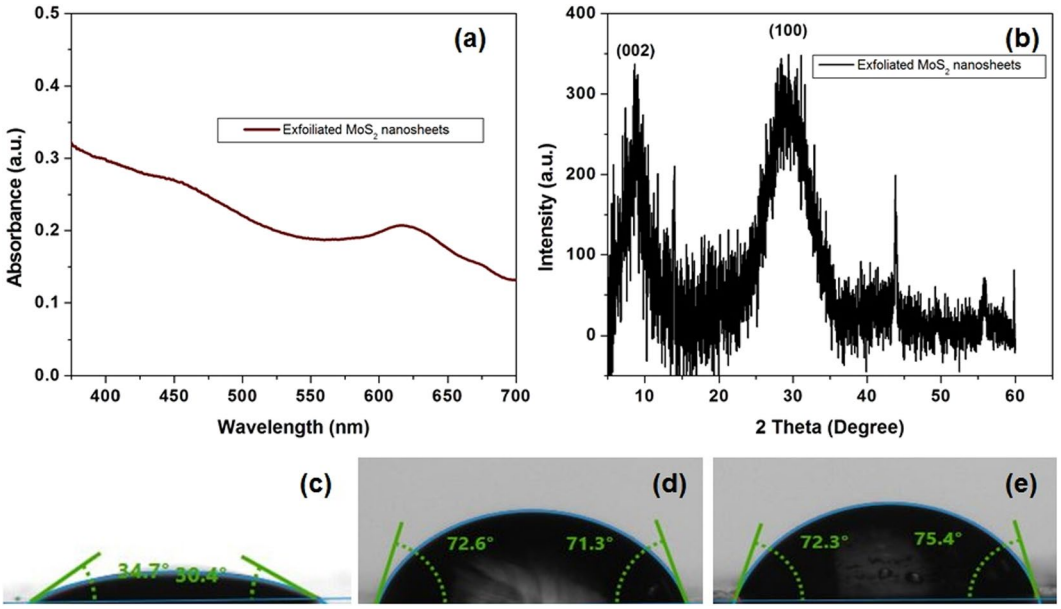

Figure 3. **(a)** UV-Vis spectra of exfoliated MoS_2; **(b)** XRD analysis of exfoliated MoS_2 nanosheets; The water contact angle of **(c)** silicon substrate (SiO_2) **(d)** gold (Au) and **(e)** MoS_2 layer to determine the hydrophobic characteristics of different substrates. The mean water contact angle of MoS_2, Au, and SiO_2 substrate are 32.55°, 71.95°, and 73.85° respectively.

around 453 nm originating after the linear transition of electrons from deep valence band to the conduction band are noted as mentioned in the reported studies[62].

In XRD analysis of the bulk MoS_2 powder many peaks are evident owing to the lattice plane reflections from the multiple layers of MoS_2 [Fig. 3(b)]. However, the XRD spectra of exfoliated MoS_2 nanosheets shows the strong distinctive (002) peak of bulk MoS_2 (at around 14° was shifted to 9°) signifying lattice expansion. The shift is due to an increased lattice strain and reduction in crystallite size. The exfoliation causes increase in the interlayer distance of the (002) lattice plane thereby changing the diffraction at a lower angle. The manifestation of XRD peaks at 33° corresponds with planes of (100) as per the typical hexagonal MoS_2 structure. The broadening of these peaks are correlated with the reduction of particle size in the corresponding planes[63].

To determine the hydrophobicity of the exfoliated MoS_2 nanosheets, drop shape analysis (DSA) was performed. The contact angle was measured by the image of sessile water drop at the points of contact with the target surface as shown in Fig. 3(c–e). The glass substrate is hydrophilic in nature with mean contact angle of 32.55°. The mean contact angle of gold coated surface (71.95°) is relatively less hydrophobic as compared to MoS_2 nanosheets functionalized surface (73.85°). The higher hydrophobicity of MoS_2 nanosheets helps in proper adsorption of proteins and antibodies without any cross likers. Hence, MoS_2 nanosheets are potential 2 D nanomaterials for rapid and simple immobilization of antibodies.

Raman spectroscopy is an important technique used to determine the layers of the 2D materials. The peak position and intensity of in-plane (E^1_{2g}) and out-of-plane (A_{1g}) modes offers specific identification of discrete and few layers of MoS_2[64,65]. The E^1_{2g} (384 cm^{-1}) peaks and A_{1g} (404 cm^{-1}) peaks were observed in Fig. 4, in accordance with the previous studies[66]. The red shift in the E^1_{2g} peaks and the blue shift in the A_{1g} peaks were observed indicating decrease in layer thickness from bulk MoS_2 to exfoliated MoS_2.

The microscopic analysis as shown in Fig. 5(a,b) signifies morphological changes on the surface of sensing probe after MoS_2 functionalization. It can be observed that the dip coating method explored for the nanosheets functionalization aid in uniform deposition of MoS_2 on the optical fiber. The FESEM images confirm the homogenous interfacing of MoS_2 nanosheets, thereby providing higher antibodies binding sites as compared to the fiber optic SPR sensor without MoS_2 nanosheets.

The formation of the nanostructures with uniform dimensions is evident from the TEM images is presented in Fig. 5(c). The sheets like morphology of the exfoliated MoS_2 are well demonstrated by the TEM image. The uniform fluorescence signals originating from the FITC/anti-BSA antibodies/MoS_2/Au/optical fiber as depicted in Fig. 5(d) of confocal laser scanning microscope (CLSM) study affirm the successful immobilization of anti-BSA antibodies over MoS_2/Au/optical fiber. As a control experiment, sensing platform without bioreceptors (antibodies) under the similar conditions was also observed by CLSM and no fluorescent signals were detected. Thus, the fluorescence perceived in the sensing probe can be attributed to the immobilization of Anti-BSA monoclonal antibodies.

Comparative study of spectral response characteristics. To investigate the output characteristics of the developed SPR biosensor, spectral response was measured for known concentrations of BSA in buffer solution with an Ab/Au/optical fiber (SPR biosensor without MoS_2 overlayer) and Ab/MoS_2/Au/optical fiber (developed

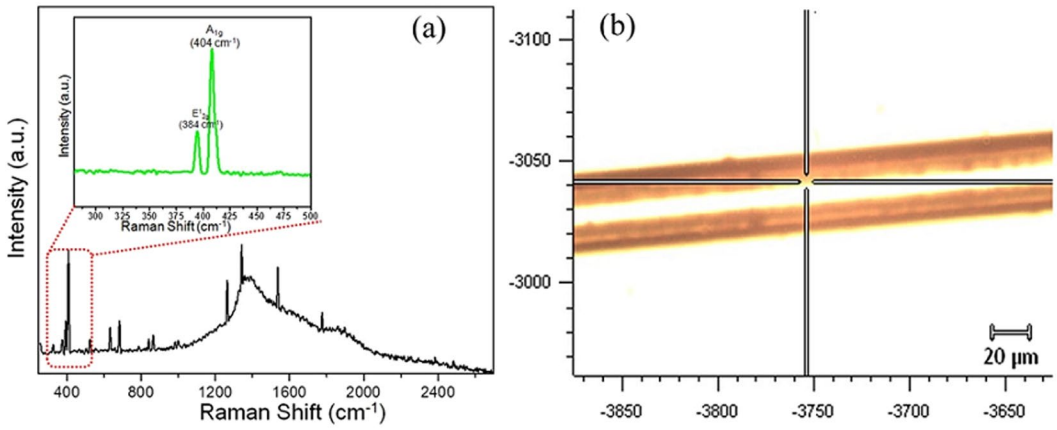

Figure 4. Raman analysis of the MoS_2 nanosheets functionalized sensing probe **(a)** Characteristic in-plane E^1_{2g} (~384 cm^{-1}) and out-of-plane A_{1g} (~404 cm^{-1}) Raman vibrational modes of exfoliated MoS_2; **(b)** Point of analysis on sensing probe.

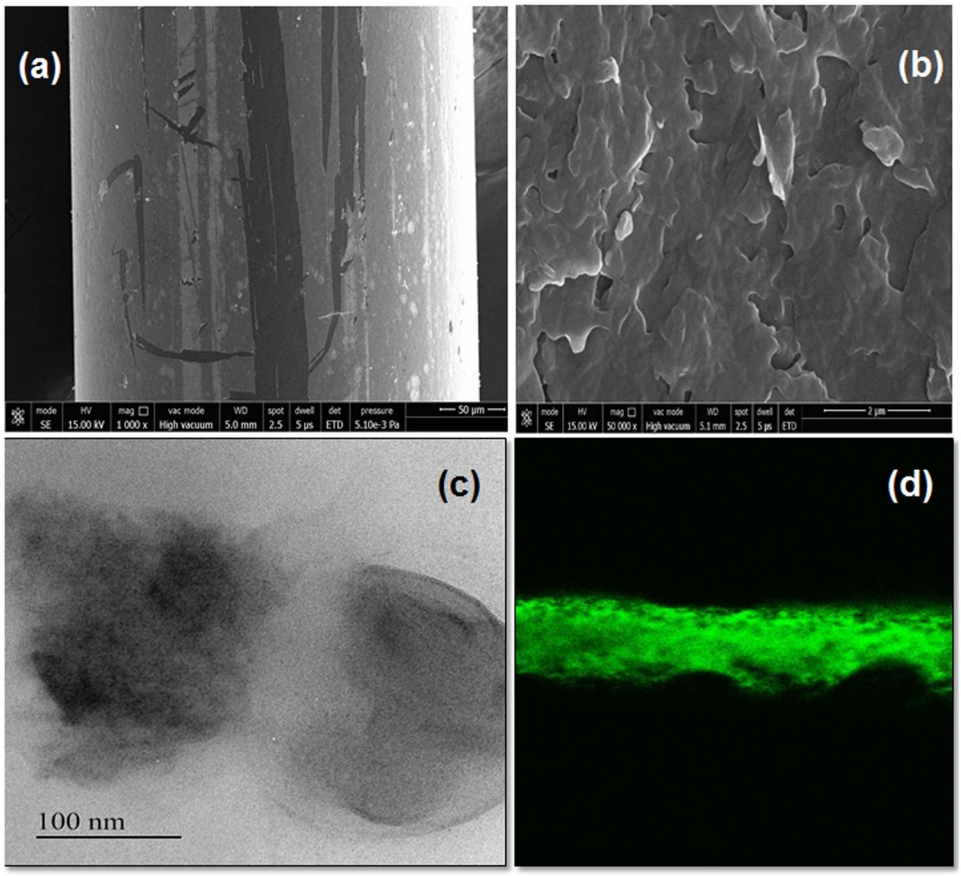

Figure 5. FESEM analysis of **(a)** developed SPR sensor scratched at different points to show the functionalized layers of MoS_2 nanosheets on the gold coated optical fiber; **(b)** Enlarged view of functionalized MoS_2 nanosheets; **(c)** TEM analysis of the exfoliated MoS_2 nanosheets; **(d)** Confocal image of the Anti-BSA monoclonal antibodies immobilized MoS_2/Au/optical fiber.

SPR biosensor). The resonance wavelength observed after the immobilization of the antibodies was regarded as reference peak. The SPR spectra attained with SPR biosensor without MoS_2 overlayer for different concentration of BSA ranging from 10 µg/mL to 50 µg/mL in PBS solution is depicted in Fig. 6(a). The transmission spectra were measured after 15 minutes of analyte addition in the glass flow cell. For each sample with certain concentration, resonance wavelength was measured. As the concentration of the BSA increases, red shift in the resonance wavelength can be observed. Figure 6(c) shows the respective shift in the resonance wavelength with each sample (BSA) by developed biosensor. The error bar graph shown in Fig. 6(b,d) clearly shows the increase in the

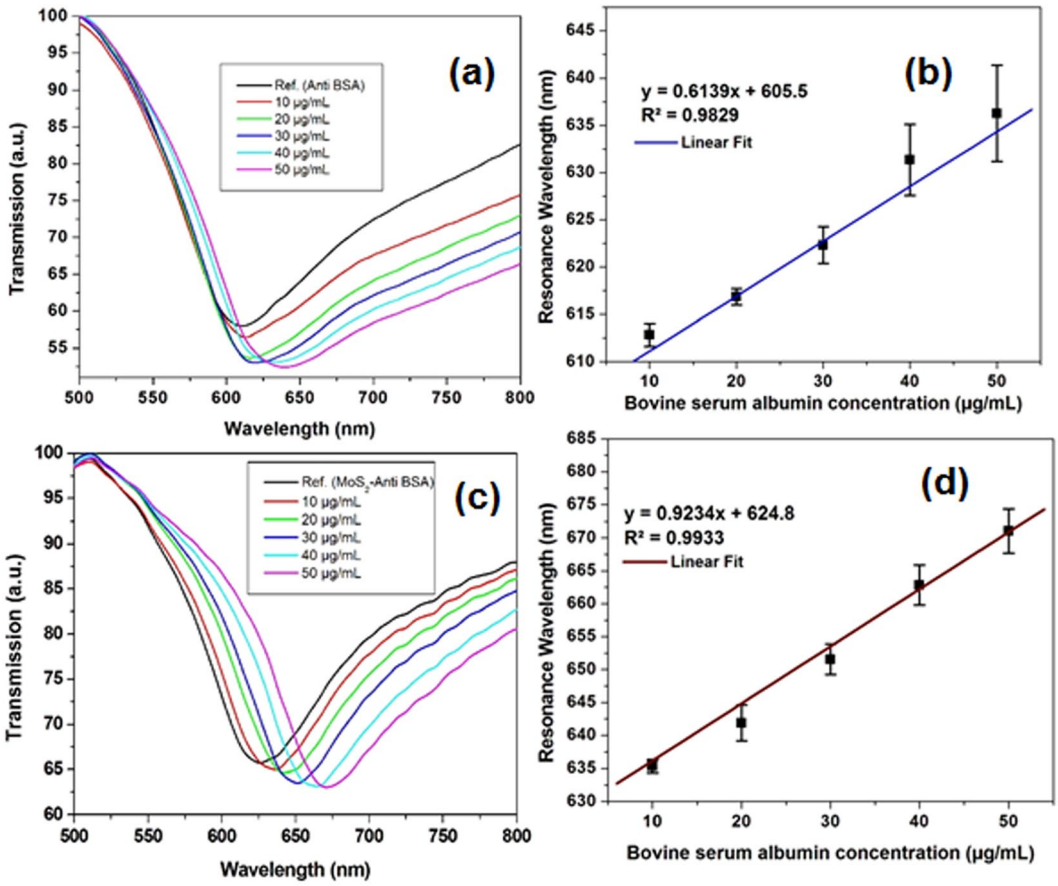

Figure 6. Spectral characteristics towards BSA in PBS solution of the **(a)** optical fiber SPR biosensor without MoS_2 overlayer and **(c)** developed SPR biosensor; Standard calibration plot of **(b)** Ab/gold/fiber; **(d)** Ab/MoS_2/gold/fiber against varying concentration of BSA in PBS solution (pH 7.4); The error bars represent the standard deviation, Experiment for each sample was repeated three times (n = 3).

resonance wavelength increases linearly with the BSA concentration in PBS solution by Ab/Au/fiber, in PBS solution by Ab/MoS_2/Au/ fiber. Experiment for the analysis of individual sample was done in triplicates. The probe was treated with DI water for removal of bonded molecules after each experiment. The shift in the resonance wavelength was because BSA and Anti-BSA antibodies interaction results in the formation of immune-complex which changes the surrounding refractive index and modifies the properties of the interacting evanescent wave. The concentration of the BSA protein is directly proportional to the change in the refractive index and the difference in refractive index is marked by the shift in resonance wavelength of the transmission spectra. The level of wavelength shift is higher in the proposed Ab/MoS_2/Au/optical fiber demonstrating better sensor sensitivity as shown in Fig. S2 (Supplementary Information). Due to high surface to volume ratio of functionalized MoS_2 nanosheets, the density of functionalized antibodies increases leading to binding of large number of target analytes (*BSA*). It is also important to note that the MoS_2 single layer has higher refractive index (4.49 @ $\lambda = 651$ nm) as compared to gold layer[67]. Due to large RI, the MoS_2 nanosheets can sustain evanescent waves even at smaller thicknesses. Accordingly, high proportion of evanescent field can be propagated in the sensing region by thin layers (8 ± 2 µm) of these nanosheets. Similarly, as the sensitivity is related to the electrical intensity's overlap integral in the surrounding medium which depends on the interaction between analytes and guided wave, the greater interaction of analytes and guided waves increases the sensitivity of the immunosensor. It was noted that the proposed SPR biosensor provide better sensitivity with LOD of 0.29 µg/mL [(calculated by the slope of the regression line equation) with $R^2 = 0.9933$] than conventional fiber optic SPR biosensor without MoS_2 overlayer (0.45 µg/mL with $R^2 = 0.9829$).

Researchers have reported graphene oxide (GO) functionalized biosensor for the selective detection of BSA (detection limit: 265 µg/mL). This aggregation-induced emission (AIE) based sensing platform utilizes disulfonated tetraphenylethene (TPE-SO3Na) and GO for the detection of BSA molecules[68]. Similarly, quantum dots based fluorescent probes were studied for BSA detection. The binding of BSA to the sensing probe resulted in photoluminescence quenching. The limit of detection of this sensing method was 100 µg/mL[69]. In recent years, the fiber optic sensing platforms have been studied for the detection of BSA. A fiber optic Mach-Zehnder interferometer based BSA detection has been reported with the detection limit of 0.257 µg/mL. The sensing platform was highly sensitive nevertheless, the specificity of the developed sensor was not reported[70]. Nayak *et al.*, 2017 have studied the fiber optic biosensor coated with gold nanoparticles and graphene oxide (GO) for BSA detection.

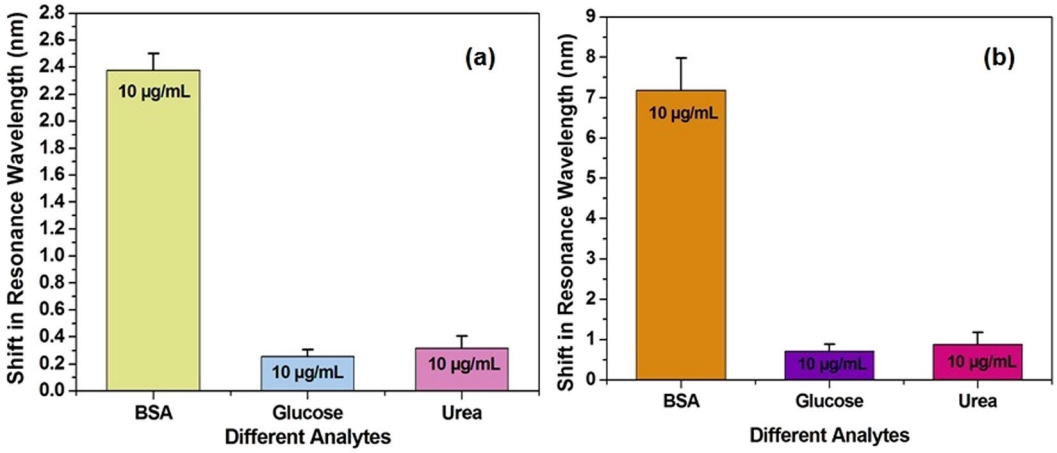

Figure 7. Comparison of specificity **(a)** optical fiber SPR biosensor without MoS_2 overlayer and **(b)** developed optical fiber SPR biosensor with MoS_2 overlayer for different compounds in PBS solution.

This sensing probe functionalized with nanoparticles was studied for detection of 10 µg/mL of BSA[71]. In comparison to the previous studies for the BSA detection, the present work encompassing MoS_2 nanosheets provide label-free, specific and rapid detection of BSA with comparable sensitivity (detection limit: 0.29 µg/mL). The addition of MoS_2 nanosheets in the transducer layer increases the light absorption in the sensing medium leading to enhancement of the evanescent field, thereby improving the performance of fiber optic SPR sensor. Though the sensor has better sensitivity towards target analyte (BSA) as compared to the reported fiber optics biosensors, the sensitivity of electrochemical biosensor[72], differential pulse voltammogram[73], cyclic voltammetry based sensor[74], Fluorescence based assay and resonance light scattering spectra (RLS) based assay[75] is higher as compared to the developed sensor reported in the present study.

Specificity studies. The specificity towards target analyte is an essential feature of good biosensor. To study the specificity of both the SPR biosensor without MoS_2 overlayer and the developed MoS_2 modified SPR biosensor, the spectral analysis was done for cross-reactants like glucose (10 µg/mL) and urea (10 µg/mL). The measured response of both the sensing probes expressed as shift in resonance wavelength towards each compound is shown in Fig. 7(a,b). Comparison of the performance of the developed biosensor with the SPR biosensor without MoS_2 overlayer indicates that the MoS_2 based developed biosensor is more sensitive and specific towards the detection of BSA.

Statistical analysis. To study the significant difference in the mean wavelengths statistically, One-way analysis of variance (ANOVA) was used. The ANOVA test indicate a statistically substantial difference in the resonant wavelength across at least one of the analyte sample ($F\ 3, 8 = 1662.612$, $p < 0.001$), obtained using the MoS_2 modified sensor. To perform pair-wise comparisons while controlling the family-wise alpha to 0.05 the Tukey's Honest Significant Difference (HSD) post hoc test was used. Mean wavelength in the detection of BSA observed to be significantly different from that of other analyte including glucose ($p < 0.001$), urea ($p < 0.001$), and blank sample ($p < 0.001$). When compared to the blank sample, no significant difference in mean wavelength in the detection of glucose ($p = 0.095$) and urea ($p = 0.547$) was observed. Table S1 (Supplementary Information) presents the pair wise comparison of mean resonance wavelength across different samples. The statistical test was performed by SPSS software version 15.0 (SPSS South Asia, Bangalore). The results confirm the high specificity of the developed biosensor for BSA detection.

Conclusion

In summary, MoS_2 nanosheets assisted biofunctionalized optical fiber SPR sensor has been successfully demonstrated for specific detection of BSA protein. The sensing probe functionalization with nanosheets and antibodies was characterized by different analytical techniques including Raman spectroscopy, TEM, UV-Vis spectroscopy, FESEM, confocal imaging and XRD analysis. The optimization of the parameters in the development of sensing probe was performed to attain the good analytical performance. The probe was introduced for the concentration range of 10 µg/mL to 50 µg/mL. The sensing capabilities of the developed biosensor was compared with the fiber optic SPR biosensor without MoS_2 overlayer. The senstivity of the designed probe (LOD: 0.29 µg/mL) was better as compared to the optical fiber SPR biosensor without MoS_2 overlayer (LOD: 0.45 µg/mL). The developed sensing probe was highly specific towards target analyte (BSA) even in the presence of cross-reactive compounds. Though the present study has presented some promising results, few limitations require attention including fragile nature of optical fiber and time consuming gold coating process. The alternative method of simple biofunctionalization may open new horizons towards the development of new generation optical fiber sensor with advantage of fabrication simplicity while offering real time monitoring and ultra-low quantitative analysis.

Data Availability

All data analyzed during this study are included in form of graphs in this article (and its Supplementary Information).

References

1. Yu, Z., Tang, Y., Cai, G., Ren, R. & Tang, D. Paper Electrode-Based Flexible Pressure Sensor for Point-of-Care Immunoassay with Digital Multimeter. *Analytical Chemistry* **91**, 1222–1226, https://doi.org/10.1021/acs.analchem.8b04635 (2019).
2. Qiu, Z., Shu, J., Liu, J. & Tang, D. Dual-Channel Photoelectrochemical Ratiometric Aptasensor with up-Converting Nanocrystals Using Spatial-Resolved Technique on Homemade 3D Printed Device. *Analytical Chemistry* **91**, 1260–1268, https://doi.org/10.1021/acs.analchem.8b05455 (2019).
3. Zeng, R. *et al*. Photoelectrochemical bioanalysis of antibiotics on rGO-Bi2WO6-Au based on branched hybridization chain reaction. *Biosensors and Bioelectronics* **133**, 100–106, https://doi.org/10.1016/j.bios.2019.02.067 (2019).
4. Qiu, Z., Shu, J. & Tang, D. Plasmonic resonance enhanced photoelectrochemical aptasensors based on gC 3 N 4/Bi 2 MoO 6. *Chemical Communications* **54**, 7199–7202 (2018).
5. Da, H., Liu, H., Zheng, Y., Yuan, R. & Chai, Y. A highly sensitive VEGF165 photoelectrochemical biosensor fabricated by assembly of aptamer bridged DNA networks. *Biosensors and Bioelectronics* **101**, 213–218 (2018).
6. Lin, J. *et al*. An impedance immunosensor based on low-cost microelectrodes and specific monoclonal antibodies for rapid detection of avian influenza virus H5N1 in chicken swabs. *Biosensors and Bioelectronics* **67**, 546–552 (2015).
7. Tang, J., Lu, M. & Tang, D. Target-initiated impedimetric proximity ligation assay with DNAzyme design for *in situ* amplified biocatalytic precipitation. *Analyst* **139**, 2998–3001, https://doi.org/10.1039/C4AN00523F (2014).
8. Tang, J., Tang, D., Zhou, J., Yang, H. & Chen, G. Nuclease cleavage-assisted target recycling for signal amplification of free-label impedimetric aptasensors. *Chemical Communications* **48**, 2627–2629, https://doi.org/10.1039/C2CC17536C (2012).
9. Dash, J. N. & Jha, R. Highly sensitive side-polished birefringent PCF-based SPR sensor in near IR. *Plasmonics* **11**, 1505–1509 (2016).
10. Srinivasan, R., Umesh, S., Murali, S., Asokan, S. & Siva Gorthi, S. Bare fiber Bragg grating immunosensor for real-time detection of *Escherichia coli* bacteria. *Journal of biophotonics* **10**, 224–230 (2017).
11. Nilima *et al*. Prevalence, patterns, and predictors of diarrhea: a spatial-temporal comprehensive evaluation in India. *BMC public health* **18**, 1288–1288, https://doi.org/10.1186/s12889-018-6213-z (2018).
12. Crump, J. A. Progress in typhoid fever epidemiology. *Clinical Infectious Diseases* **68**, S4–S9 (2019).
13. Shi, T. *et al*. Global and Regional Burden of Hospital Admissions for Pneumonia in Older Adults: A Systematic Review and Meta-Analysis. *The Journal of infectious diseases* (2019).
14. Pradhan, S. M., Rao, A. P., Pattanshetty, S. M. & Nilima, A. R. Knowledge and perception regarding childhood pneumonia among mothers of under-five children in rural areas of Udupi Taluk, Karnataka: A cross-sectional study. *Indian Journal of Health Sciences* **9**(1), 35 (2016).
15. Shrivastav, A. M., Mishra, S. K. & Gupta, B. D. Fiber optic SPR sensor for the detection of melamine using molecular imprinting. *Sensors and Actuators B: Chemical* **212**, 404–410 (2015).
16. Liedberg, B., Nylander, C. & Lunström, I. Surface plasmon resonance for gas detection and biosensing. *Sensors and Actuators* **4**, 299–304, https://doi.org/10.1016/0250-6874(83)85036-7 (1983).
17. Abdulhalim, I., Zourob, M. & Lakhtakia, A. Surface plasmon resonance for biosensing: a mini-review. *Electromagnetics* **28**, 214–242 (2008).
18. Singh, P. SPR Biosensors: Historical Perspectives and Current Challenges. *Sensors and Actuators B: Chemical* **229**, 110–130, https://doi.org/10.1016/j.snb.2016.01.118 (2016).
19. Mishra, A. K., Mishra, S. K. & Singh, A. P. Giant Infrared Sensitivity of Surface Plasmon Resonance-Based Refractive Index Sensor. *Plasmonics*, 1–8 (2017).
20. Gupta, B. D., Srivastava, S. K. & Verma, R. *Fiber optic sensors based on plasmonics*. (World Scientific, 2015).
21. Rehman, S.-u., Rahmouni, A., Mahfoud, T., Nesterenko, D. V. & Sekkat, Z. Determination of the optical thickness of sub 10-nm thin metal films by SPR experiments. *Plasmonics* **9**, 381–387 (2014).
22. Penezic, A. *et al*. Carbohydrate–lectin interaction on graphene-coated surface plasmon resonance (SPR) interfaces. *Plasmonics* **9**, 677–683 (2014).
23. Jha, R. & Sharma, A. K. Chalcogenide glass prism based SPR sensor with Ag–Au bimetallic nanoparticle alloy in infrared wavelength region. *Journal of Optics A: Pure and Applied Optics* **11**, 045502 (2009).
24. Homola, J., Koudela, I. & Yee, S. S. Surface plasmon resonance sensors based on diffraction gratings and prism couplers: sensitivity comparison. *Sensors and Actuators B: Chemical* **54**, 16–24 (1999).
25. Slavík, R., Homola, J., Čtyroký, J. & Brynda, E. Novel spectral fiber optic sensor based on surface plasmon resonance. *Sensors and Actuators B: Chemical* **74**, 106–111 (2001).
26. Kim, Y.-C., Peng, W., Banerji, S. & Booksh, K. S. Tapered fiber optic surface plasmon resonance sensor for analyses of vapor and liquid phases. *Optics letters* **30**, 2218–2220 (2005).
27. Srivastava, S. K., Verma, R. & Gupta, B. D. Surface plasmon resonance based fiber optic sensor for the detection of low water content in ethanol. *Sensors and Actuators B: Chemical* **153**, 194–198 (2011).
28. Baliyan, A. *et al*. Surface plasmon resonance based fiber optic sensor for the detection of triacylglycerides using gel entrapment technique. *Sensors and Actuators B: Chemical* **188**, 917–922 (2013).
29. Sharma, A. K., Jha, R. & Gupta, B. Fiber-optic sensors based on surface plasmon resonance: a comprehensive review. *IEEE Sensors Journal* **7**, 1118–1129 (2007).
30. Mishra, S. K., Tripathi, S. N., Choudhary, V. & Gupta, B. D. SPR based fibre optic ammonia gas sensor utilizing nanocomposite film of PMMA/reduced graphene oxide prepared by *in situ* polymerization. *Sensors and Actuators B: Chemical* **199**, 190–200 (2014).
31. Cennamo, N. *et al*. Sensors based on surface plasmon resonance in a plastic optical fiber for the detection of trinitrotoluene. *Sensors and Actuators B: Chemical* **188**, 221–226 (2013).
32. Kaushik, S., Pandey, A., Tiwari, U. K. & Sinha, R. K. A label-free fiber optic biosensor for Salmonella Typhimurium detection. *Optical Fiber Technology* **46**, 95–103 (2018).
33. Dwivedi, Y. S., Sharma, A. K. & Gupta, B. Influence of design parameters on the performance of a surface plasmon sensor based fiber optic sensor. *Plasmonics* **3**, 79–86 (2008).
34. Christopher, C., Subrahmanyam, A. & Sai, V. Gold sputtered U-bent plastic optical fiber probes as SPR-and LSPR-based compact plasmonic sensors. *Plasmonics* **13**, 493–502 (2018).
35. Klantsataya, E., Jia, P., Ebendorff-Heidepriem, H., Monro, T. M. & François, A. Plasmonic fiber optic refractometric sensors: From conventional architectures to recent design trends. *Sensors* **17**, 12 (2016).
36. Nayak, J. K., Maharana, P. K. & Jha, R. Dielectric over-layer assisted graphene, its oxide and MoS_2-based fibre optic sensor with high field enhancement. *Journal of Physics D: Applied Physics* **50**, 405112 (2017).
37. Ong, B. H., Yuan, X., Tjin, S. C., Zhang, J. & Ng, H. M. Optimised film thickness for maximum evanescent field enhancement of a bimetallic film surface plasmon resonance biosensor. *Sensors and Actuators B: Chemical* **114**, 1028–1034 (2006).
38. Kanso, M., Cuenot, S. & Louarn, G. Sensitivity of optical fiber sensor based on surface plasmon resonance: modeling and experiments. *Plasmonics* **3**, 49–57 (2008).

39. Maharana, P. K., Srivastava, T. & Jha, R. On the performance of highly sensitive and accurate graphene-on-aluminum and silicon-based SPR biosensor for visible and near infrared. *Plasmonics* **9**, 1113–1120 (2014).
40. Du, B., Yang, Y., Zhang, Y. & Yang, D. SPR Label-Free Biosensor with Oxide-Metal-Oxide-Coated D-Typed Optical Fiber: a Theoretical Study. *Plasmonics*, 1–7 (2018).
41. Kaushik, S. *et al*. In *AIP Conference Proceedings*. 020110 (AIP Publishing).
42. Ju, S. *et al*. Fabrication and Optical Characteristics of a Novel Optical Fiber Doped with the Au Nanoparticles. *Journal of Nanoscience and Nanotechnology* **6**, 3555–3558, https://doi.org/10.1166/jnn.2006.055 (2006).
43. Hao, T. & Chiang, K. S. Graphene-Based Ammonia-Gas Sensor Using In-Fiber Mach-Zehnder Interferometer. *IEEE Photonics Technology Letters* **29**, 2035–2038, https://doi.org/10.1109/LPT.2017.2761981 (2017).
44. Mishra, S. K., Zou, B. & Chiang, K. S. Surface-Plasmon-Resonance Refractive-Index Sensor With Cu-Coated Polymer Waveguide. *IEEE Photonics Technology Letters* **28**, 1835–1838, https://doi.org/10.1109/LPT.2016.2573322 (2016).
45. Shukla, S., Sharma, N. K. & Sajal, V. Sensitivity enhancement of a surface plasmon resonance based fiber optic sensor using ZnO thin film: a theoretical study. *Sensors and Actuators B: Chemical* **206**, 463–470 (2015).
46. Mariani, S. & Minunni, M. Surface plasmon resonance applications in clinical analysis. *Analytical and bioanalytical chemistry* **406**, 2303–2323 (2014).
47. Liu, C. *et al*. Graphene oxide functionalized long period grating for ultrasensitive label-free immunosensing. *Biosensors and Bioelectronics* **94**, 200–206 (2017).
48. Kaushik, S. *et al*. In *International Conference on Fibre Optics and Photonics*. Th3A. 59 (Optical Society of America) (2016).
49. Kaushik, S. *et al*. Label-free detection of E scherichia coli bacteria by cascaded chirped long period gratings immunosensor. *Review of Scientific Instruments* **90**, 025003 (2019).
50. Singh, E., Kim, K. S., Yeom, G. Y. & Nalwa, H. S. Two-dimensional transition metal dichalcogenide-based counter electrodes for dye-sensitized solar cells. *RSC Advances* **7**, 28234–28290 (2017).
51. Mishra, A. K., Mishra, S. K. & Verma, R. K. Graphene and beyond graphene MoS_2: a new window in surface-plasmon-resonance-based fiber optic sensing. *The Journal of Physical Chemistry C* **120**, 2893–2900 (2016).
52. Sharma, A. K. & Kaur, B. Chalcogenide fiber-optic SPR chemical sensor with MoS_2 monolayer, polymer clad, and polythiophene layer in NIR using selective ray launching. *Optical Fiber Technology* **43**, 163–168, https://doi.org/10.1016/j.yofte.2018.05.003 (2018).
53. Sridhar, S., Sebastian, S. & Asokan, S. Temperature sensor based on multi-layer MoS_2 coated etched fiber Bragg grating. *Applied optics* **58**, 535–539 (2019).
54. Tuteja, S. K., Duffield, T. & Neethirajan, S. Liquid exfoliation of 2D MoS_2 nanosheets and their utilization as a label-free electrochemical immunoassay for subclinical ketosis. *Nanoscale* **9**, 10886–10896 (2017).
55. Lee, J. *et al*. Two-dimensional layered MoS_2 biosensors enable highly sensitive detection of biomolecules. *Scientific reports* **4**, 7352 (2014).
56. Xu, Y., Wu, L. & Ang, L. K. Based Highly Sensitive Near-Infrared Surface Plasmon Resonance Refractive Index Sensor. *IEEE Journal of Selected Topics in Quantum Electronics* **25**, 1–7, https://doi.org/10.1109/JSTQE.2018.2868795 (2019).
57. Kaushik, S., Tiwari, U. K., Pal, S. S. & Sinha, R. K. Rapid detection of *Escherichia coli* using fiber optic surface plasmon resonance immunosensor based on biofunctionalized Molybdenum disulfide (MoS_2) nanosheets. *Biosensors and Bioelectronics* **126**, 501–509 (2019).
58. Iga, M., Seki, A. & Watanabe, K. Gold thickness dependence of SPR-based hetero-core structured optical fiber sensor. *Sensors and Actuators B: Chemical* **106**, 363–368 (2005).
59. Chiang, H. P., Wang, Y. C., Leung, P. T. & Tse, W. S. A theoretical model for the temperature-dependent sensitivity of the optical sensor based on surface plasmon resonance. *Optics Communications* **188**, 283–289, https://doi.org/10.1016/S0030-4018(00)01175-5 (2001).
60. Sharma, A. K. & Gupta, B. D. Influence of temperature on the sensitivity and signal-to-noise ratio of a fiber-optic surface-plasmon resonance sensor. *Applied Optics* **45**, 151–161, https://doi.org/10.1364/AO.45.000151 (2006).
61. Xu, S., Li, D. & Wu, P. One-pot, facile, and versatile synthesis of monolayer MoS_2/WS2 quantum dots as bioimaging probes and efficient electrocatalysts for hydrogen evolution reaction. *Advanced Functional Materials* **25**, 1127–1136 (2015).
62. Kukkar, M. *et al*. Molybdenum disulfide quantum dot based highly sensitive impedimetric immunoassay for prostate specific antigen. *Microchimica Acta* **184**, 4647–4654 (2017).
63. Joensen, P., Crozier, E., Alberding, N. & Frindt, R. A study of single-layer and restacked MoS_2 by X-ray diffraction and X-ray absorption spectroscopy. *Journal of Physics C: Solid State Physics* **20**, 4043 (1987).
64. Zhao, Y. *et al*. Interlayer breathing and shear modes in few-trilayer MoS_2 and WSe2. *Nano letters* **13**, 1007–1015 (2013).
65. Gopalakrishnan, D., Damien, D. & Shaijumon, M. M. MoS_2 quantum dot-interspersed exfoliated MoS_2 nanosheets. *ACS nano* **8**, 5297–5303 (2014).
66. Lee, C. *et al*. Anomalous lattice vibrations of single-and few-layer MoS_2. *ACS nano* **4**, 2695–2700 (2010).
67. Zhang, H. *et al*. Measuring the refractive index of highly crystalline monolayer MoS_2 with high confidence. *Scientific reports* **5**, 8440 (2015).
68. Xu, X., Huang, J., Li, J., Yan, J. Qin, J. & Li, Z. A graphene oxide-based AIE biosensor with high selectivity toward bovine serum albumin. *Chem. Commun*. **47**, 12385e12387 (2011).
69. Kumar, P., Deep, A., Sharma, S. C. & Bharadwaj, L. M. Bioconjugation of InGaP quantum dots for molecular sensing. *Analytical Biochemistry* **421**, 285–290, https://doi.org/10.1016/j.ab.2011.10.037 (2012).
70. Li, Z. *et al*. Label-free detection of bovine serum albumin based on an in-fiber Mach-Zehnder interferometric biosensor. *Optics Express* **25**, 17105–17113, https://doi.org/10.1364/OE.25.017105 (2017).
71. Nayak, J. K. & Jha, R. In *Frontiers in Optics 2017*. FTh3A.6 (Optical Society of America) (2017).
72. Pinwattana, K. *et al*. CdSe/ZnS quantum dots based electrochemical immunoassay for the detection of phosphorylated bovine serum albumin. *Biosensors and Bioelectronics* **26**, 1109–1113, https://doi.org/10.1016/j.bios.2010.08.021 (2010).
73. Chen, H.-J., Zhang, Z.-H., Luo, L.-J. & Yao, S.-Z. Surface-imprinted chitosan-coated magnetic nanoparticles modified multi-walled carbon nanotubes biosensor for detection of bovine serum albumin. *Sensors and Actuators B: Chemical* **163**, 76–83, https://doi.org/10.1016/j.snb.2012.01.010 (2012).
74. Kukkar, M., Sharma, A., Kumar, P., Kim, K.-H. & Deep, A. Application of MoS_2 modified screen-printed electrodes for highly sensitive detection of bovine serum albumin. *Analytica Chimica Acta* **939**, 101–107, https://doi.org/10.1016/j.aca.2016.08.010 (2016).
75. Pan, H., Tao, X., Mao, C., Zhu, J.-J. & Liang, F. Aminopolycarboxyl-modified Ag2S nanoparticles: Synthesis, characterization and resonance light scattering sensing for bovine serum albumin. *Talanta* **71**, 276–281, https://doi.org/10.1016/j.talanta.2006.03.057 (2007).

Acknowledgements

This research was supported by Council of Scientific and Industrial Research, India (EMR 0001), (MLP 0059) and University Grant Commission, New Delhi (P-90807). The authors sincerely express gratitude to Ms. Nilima at the Indian Institute of Public Health-Delhi for helping in statistical analysis. The authors are gratified to Dr. A.K. Paul, Dr. Praveen Kaushik and Kamalpreet Singh of CSIO for prolific discussions. The authors are thankful to Dr. Amit L. Sharma, CSIO for XRD analysis.

Author Contributions

S.K., U.K.T. and A.D. designed the study, S.K. and U.K.T. performed the experiments, S.K., U.K.T. and R.K.S. interpreted data, S.K. wrote the manuscript, all authors reviewed the manuscript.

Additional Information

Supplementary information accompanies this paper at https://doi.org/10.1038/s41598-019-43531-w.

Competing Interests: The authors declare no competing interests.

Publisher's note: Springer Nature remains neutral with regard to jurisdictional claims in published maps and institutional affiliations.

Open Access This article is licensed under a Creative Commons Attribution 4.0 International License, which permits use, sharing, adaptation, distribution and reproduction in any medium or format, as long as you give appropriate credit to the original author(s) and the source, provide a link to the Creative Commons license, and indicate if changes were made. The images or other third party material in this article are included in the article's Creative Commons license, unless indicated otherwise in a credit line to the material. If material is not included in the article's Creative Commons license and your intended use is not permitted by statutory regulation or exceeds the permitted use, you will need to obtain permission directly from the copyright holder. To view a copy of this license, visit http://creativecommons.org/licenses/by/4.0/.

© The Author(s) 2019

Proc. Natl. Acad. Sci., India, Sect. A Phys. Sci.
https://doi.org/10.1007/s40010-019-00595-7

RESEARCH ARTICLE

Two-Stage Spectrum Sensing Using Fuzzy Logic for Cognitive Radio Networks

Bhawna Ahuja[1] · **Gurjit Kaur**[2]

Received: 5 April 2015 / Revised: 10 September 2018 / Accepted: 1 February 2019
© The National Academy of Sciences, India 2019

Abstract In this paper, we present a two-stage detection scheme using fuzzy logic for spectrum sensing. The first stage consists of the dynamic double-threshold energy detector, whereas the second stage uses of a fuzzy logic system. Fuzzy logic detector utilizes estimated energy and estimated eigenvalue of the signal and gives a decision in confused state. The novelty of the proposed spectrum sensing technique lies in its decision-making capability at individual nodes without adding any overhead to the system in terms of control channel which ultimately reduces the bandwidth consumption. It has been observed from the results that the proposed system yields improved performance in comparison with the conventional two-stage detection schemes. The proposed scheme was also analyzed in cooperative sensing scenario where it outperforms the conventional cooperative spectrum sensing schemes to a considerable extent.

Keywords Cooperative spectrum sensing · Spectrum sensing technique · Fuzzy logic · Two-stage detector · Eigenvalue detector

✉ Gurjit Kaur
gurjeet_kaur@rediffmail.com; gurjitkaur@dtu.ac.in

Bhawna Ahuja
bhawnaajuneja@gmail.com

[1] Galgotias College of Engineering, Greater Noida, India

[2] Department of Electronics and Communication Engineering, Delhi Technological University, Delhi, India

1 Introduction

Cognitive radio (CR) has always been considered as the enabler technology for effective utilization of frequency spectrum, and it accurately and reliably senses the spectral conditions of the frequency spectrum. It aims to recognize the presence and absence of the licensed user usually referred to as primary user (PU) in the licensed frequency spectrum. If PU is absent, it allocates the spectrum of PU to the secondary user (SU). SUs are low-preference users who avail the spectrum without causing interference to PUs under certain conditions [1].

Till now, a number of researchers reported various spectrum sensing techniques. They mainly include cyclostationary-based detection, covariance-based detection, energy detection (ED), matched filter and multi-taper spectrum estimation. All these techniques have already shown to provide different trade-offs between complexity and detection capability [2, 3]. Among them, ED is used for its simple architecture, fast sensing and lesser implementation cost, and moreover, it doesn't require any prior data about the PU, so its complexity is very low. Classical energy detector (CED) uses only one threshold, but the performance of CED seems to degrade at low SNR values [4]. The only potential solution to overcome this limitation is to design multi-stage methods.

A two-stage spectrum sensing technique was proposed that consists of coarse and fine detection process [5]. The two-stage spectrum sensing techniques are able to do faster detection in comparison with single-stage spectrum sensing techniques [6]. Another two-stage detection scheme was reported where CED is followed by cyclostationary detection, and it significantly improves the detection performance [7]. However, it has been observed from all of the above that increment in gain is always achieved at the

Published online: 15 April 2019

cost of more complexity and more sensing time. Cyclostationary detection and ED detection are chosen depending on the estimation of SNR value, but SNR estimation usually results in increased complexity [8, 9].

Sensing performance depends on the optimality of the detection threshold. Due to uncertainty in the noise level, it usually seems a bit intricate to set the optimal value of threshold which ultimately leads to reduced detection performance [10]. Multiple energy methods have been employed for the first stage followed by adaptive threshold technique at the second stage to reduce the noise problem [11]. Preferably, the first stage of any sensing method should be simpler because when spectrum is vacant the decision should be taken through a simple method so that the system overheads are reduced. Usually, the second stage considers the difference of threshold value and the energy level value which is inadequate to take the decision in the confused region. The hidden nodes, multi-path fading and shadowing are also responsible for the deterioration in the performance of the spectrum sensing techniques. A good solution for this problem is to use cooperative spectrum sensing (CSS) technique which involves collaborative use of available sensing information at various positions to take decision about the availability of the spectrum with improved accuracy [12–14].

Recently, the use of the fuzzy logic has drawn a lot of attention in spectrum sensing techniques due to its ability to provide the decision even in difficult conditions. Till now, fuzzy logic has already been implemented in different areas of CR network including handoff, cross-layer optimization and spectrum access techniques [15]. But still there is a large scope to exploit its advantages in spectrum sensing techniques. A fuzzy logic-based scheme was proposed which gives greater flexibility and good performance by using fuzzy logic controller [16].

A number of spectrum sensing techniques have been reported in the literature where fuzzy logic-based approach has been used for two-stage spectrum sensing [17]. But in their research work fuzzy logic controller is used at the centralized level. Because of the centralized level fuzzy controller the system consumes a large bandwidth for communicating with all other nodes on control channel and increases the overhead in terms of bandwidth which is already a scarce resource in CR. The other issue with the previous centralized techniques is that if the central node fails the other nodes become paralyzed.

In this research work, a novel two-stage spectrum sensing technique is proposed which is less complex and provides the output with better accuracy. A simple classical dynamic double-threshold ED is used in the first stage followed by fuzzy logic-based detection. We propose fuzzy logic-based detection utilizing both energy- and eigenvalue-based parameters as the input to the fuzzy logic system for taking detection decision at second stage.

2 System Model Description

Let $x(t)$ represent the signal transmitted by the PU with $h(t)$ as the impulse response of the channel. $a(t)$ denotes the additive white Gaussian noise (AWGN) with mean equal to 0 and variance being equal to σ_n^2, and $y(t)$ represents the signal received by the user. SU discrimination is needed in the following hypothesis in order to detect the PU's nth time instant.

$$y(n) = \begin{cases} a(n); & H_0 \\ x(n) * h(n) + a(n); & H_1 \end{cases} \quad (1)$$

Here, H_0 denotes the null hypothesis which represents that PU is not communicating, while, on the other hand, the PU's existence is indicated by the alternative hypothesis H_1. In the already existing double-threshold methods, the values between two thresholds are generally ignored due to which these techniques are not reliable. In our proposed scheme, if the test statistic lies in between these two thresholds, fuzzy logic detector takes the decision using two new decision metrics. The whole process of the fuzzy logic detector is described in the next section. This two-stage detection scheme not only improves the performance but reliability as well, even at low SNR. In addition, to overcome the noise uncertainty problem, the above-mentioned thresholds can be configured according to maximum and minimum noise variance, thereby making these thresholds adaptive.

2.1 Dynamic Double-Threshold-Based Energy Detection Scheme

This is a blind spectrum sensing scheme where the received signal energy is measured over a certain observation period [18].

$$E = \sum_{n=1}^{N} |y(n)|^2 \quad (2)$$

The PU's absence or presence can be decided by the comparison of energy with a threshold λ_{ED} as illustrated in Fig. 1. For this purpose, let W be the bandwidth of the signal. As per sampling theorem, we approximately need $2u$ samples for representing the energy of infinite number of terms over a duration T, where $u = TW$ represents the time–bandwidth product. In hypothesis H_0, only noise is present and PU is absent. For this case, the sum of the squares of variance σ_n^2 and $2u$ Gaussian variables that has zero mean represents test statistic Y.

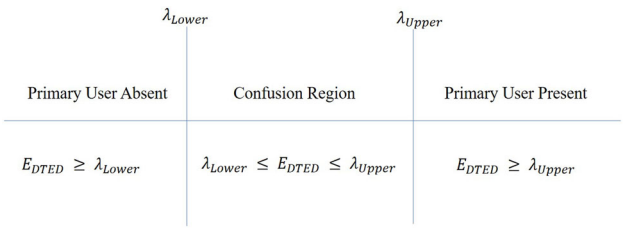

Fig. 1 Proposed technique with dynamic double thresholds at the first stage

$$E_{\mathrm{DTED}} \sim \begin{cases} X_{2u}^2, & H_0 \\ X_{2u}^2, (2\zeta), & H_1 \end{cases} \tag{3}$$

For given λ, the P_d is defined as

$$P_d = P\left(E_{\mathrm{DTED}} > \lambda | H_1\right) = \int_{\lambda}^{\infty} Q_u\left(\sqrt{\frac{2\gamma}{\sigma_n^2}}, \sqrt{\frac{\lambda}{\sigma_n^2}}\right) f(\zeta)\mathrm{d}x \tag{4}$$

where Q_u represents the generalized Marcum Q-function, ζ the SNR, and $\bar{\zeta}$ the PDF of the channel effect with average SNR.

$$f(\gamma) = \frac{1}{\bar{\zeta}} \exp\left(-\frac{\zeta}{\bar{\zeta}}\right), \quad \zeta \geq 0 \tag{5}$$

$$P_f = P(E_{\mathrm{DTED}} > \lambda | H_0) = \int_{\zeta}^{\infty} f_{\chi^2}(\zeta)\mathrm{d}\zeta = \frac{\Gamma\left(u, \zeta/2\sigma_n^2\right)}{\Gamma(u)} \tag{6}$$

where ζ represents the signal-to-noise ratio with $\Gamma(,)$ and $\Gamma(\cdot)$ as the incomplete and complete gamma functions [18]. Thus, the computation of threshold λ for a given P_f is described as:

$$\lambda_{\mathrm{DTED}} = 2\sigma_n^2 \Gamma^{-1}\left(u, P_f \Gamma(u)\right) \tag{7}$$

where incomplete gamma function inverse is represented $\Gamma^{-1}(\cdot,\cdot)$. This technique holds the ability to ease the implementation process with faster decision-making capability that too with low complexity. But under low SNR, its performance usually degrades. However, since noise variance has direct effect on the threshold, the precise knowledge of noise power is what we need for accurate results. Even though the estimation of the noise variance is theoretically possible, in practice, noise power always seems to change with location and time. Thus, in practice, we conclusively state that noise uncertainty exists. To calculate noise uncertainty, let us assume $[(1-\rho)\sigma_n^2, (1+\rho)\sigma_n^2]$ as the interval of estimated noise variance. Here q quantifies noise power uncertainty and is always in between 0 and 1. In order to increase the accuracy and reliability of the proposed technique, the upper threshold (λ_{upper}) for ED has been chosen in correspondence with noise variance's upper limit. Hence,

$$\lambda_{\mathrm{upper}} = (\rho + 1)\lambda_{\mathrm{DTED}} \tag{8}$$

2.2 Fuzzy Logic Detector for Spectrum Sensing

Unlike classical set theory, fuzzy sets allow objects to have partial membership with unique capability for making logical decisions in a case of imprecision, incompleteness and uncertainty of information [19–21]. We, therefore, propose a fuzzy logic detector (FLD) method at stage two for increasing the performance of local sensing. Moreover, it can be modified easily as it is governed by user-defined rules. Fuzzy inference engine determines the value of output variables by using If–Then rule base. Inference engine evaluates these rules and decides how to process these rules, and the results of various rules are summed up to produce a fuzzy output set. This process produces membership function for each output variable to represent their appropriateness. The structure of fuzzy logic detector is represented in Fig. 2. Defuzzifier computes an appropriate crisp value as the actual output. Max-product and triangular membership function are used as inference method for fuzzification, and the centroid of area has been used as a defuzzification method.

3 Proposed Fuzzy Logic-Based Two-Stage Detection Method

In the proposed scheme, two stages are used for detection. At first stage, dynamic double-threshold-based ED is used and if value of the energy level lies in between the two thresholds, then FLD is used for second-stage detection. The originality of our work is reflected by the fact that the final decision is made by FLD by making use of two different parameters which increases the reliability of sensing, i.e., Credibility_energy and Credibility_eigen. In this scheme, the final decision is given by the fuzzy logic detector at individual user. Moreover, for the first- and second-stage detection, preliminary knowledge about the PU signal is not needed which is perhaps a constraint for most of the fine sensing schemes. Figure 3 represents the proposed two-stage spectrum sensing technique using Rayleigh channel. The signal is detected by using the square law device which gives energy E. H_1 is declared in case energy E is greater than λ_{upper}. However, if E is less than λ_{lower} then H_0 is declared, whereas when E lies in between both these thresholds then fuzzy logic detection is employed to take the final decision. Two input parameters are provided to FLD for decision making as it is a multi-valued logic, first one of which is based on signal energy and upper threshold.

For the given purpose, new decision metric called Credibility_energy is introduced and defined as:

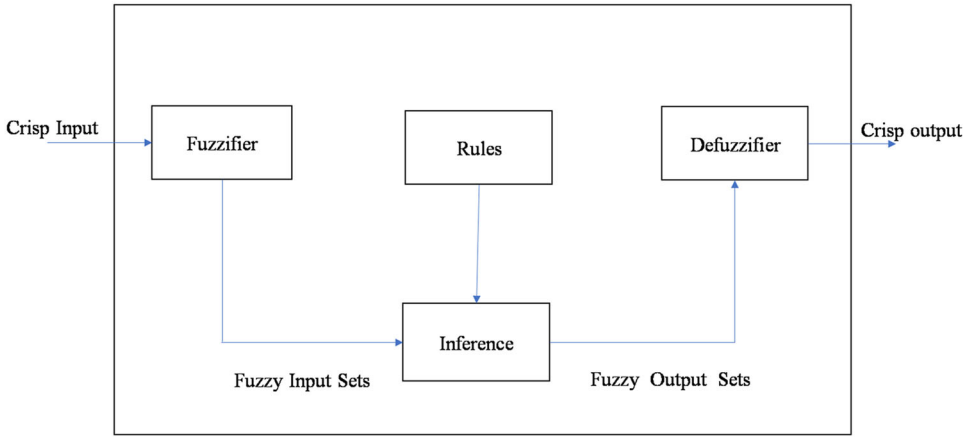

Fig. 2 Structure of fuzzy logic detector

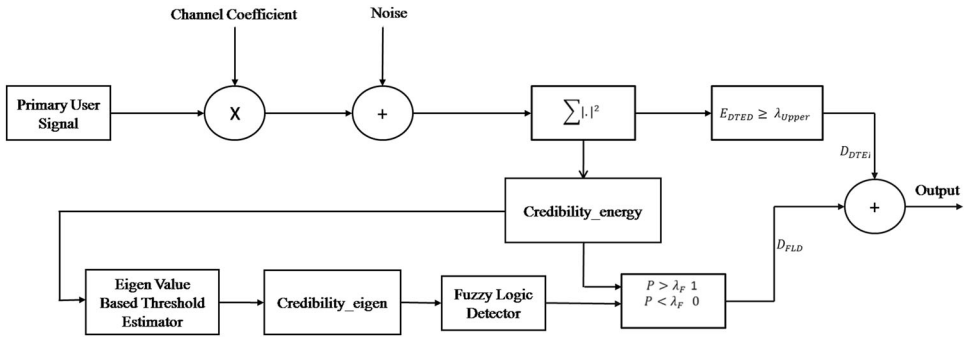

Fig. 3 Proposed scheme block diagram

$$\text{Credibility_energy} = 1 - \frac{(\lambda_{\text{upper}} - E)}{\lambda_{\text{upper}}} \tag{9}$$

Here, E seems closer to the threshold if the Credibility_energy is high. Hence, this decision metric represents the closeness of decision to either H_1 or H_0. The decision is closer to H_1 if Credibility_energy comes out to be high; otherwise, the decision is closer to H_0. If this difference is small, there is probability of the signal to be present, but it may not be detected because of low SNR arising out of fading or channel conditions.

In order to enhance the sensing capability further, an additional parameter based on the eigenvalue of the received signal is introduced. This metric is defined as the credibility eigenvalue, which is represented as

$$\text{Credibility_eigen} = \frac{\gamma - T}{\gamma} \tag{10}$$

The proposed metric involves computation of test statistics (T) and threshold (γ) through MME algorithm, which is expressed as

$$R_{\text{received}}(N) = R_{\text{transmitted}}(N) + R_{\text{noise}}(N) \tag{11}$$

where $R_{\text{received}}(N), R_{\text{transmitted}}(N)$ and $R_{\text{noise}}(N)$ denote the autocorrelation matrices of signal received at SU, transmitted by PU and noise, respectively. Here, AWGN noise has been taken into consideration with zero mean and σ_n^2 variance. Therefore, the equation defined above can be rewritten as

$$R_{\text{received}}(N) = R_{\text{transmitted}}(N) + \sigma_n^2 I_L \tag{12}$$

Let $\rho_{\max}$ and $\rho_{\min}$ denote the maximum and minimum eigenvalues of $R_{\text{transmitted}}(N)$. So,

$$\alpha_{\max} = \rho_{\max} + \sigma_n^2 \tag{13}$$

$$\alpha_{\min} = \rho_{\min} + \sigma_n^2 \tag{14}$$

Therefore, when the PU signal is absent, we have

$$\alpha_{\max} = \alpha_{\min}, \tag{15}$$

whereas in the presence of PU signal $\alpha_{\max} > \alpha_{\min}$.

Hence, for the detection of PU the following ratio is chosen as the test statistics.

$$T(N) = \frac{\alpha_{\max}}{\alpha_{\min}} \tag{16}$$

All this provides us the mathematical ground for MME (maximum to minimum eigenvalue) algorithm. The algorithm is further expressed as

Step 1 Sample covariance matrix of the received signal is computed. Here, the following expression represents the received signal covariance matrix.

$$R_{\text{received}}(N) = \begin{bmatrix} K(0) & K(1) & \dots & K^*(L-1) \\ K^*(0) & K(1) & \dots & K(L-1) \\ \vdots & \vdots & \vdots & \vdots \\ \vdots & \vdots & \vdots & \vdots \end{bmatrix} \tag{17}$$

where

$$K(l) = \frac{1}{N}\sum_{m=0}^{N-1} r(m)r(m-l)^* \tag{18}$$

with $l = 0, 1, \ldots, L-1$.

Here, N is the number of collected samples.

Step 2 Calculate the max and min eigenvalues of the covariance matrix $R_{\text{received}}(N)$, i.e., $\alpha_{\max}$ and $\alpha_{\min}$.

Step 3 Derive test statistics

$$T(N) = \frac{\alpha_{\max}}{\alpha_{\min}} \tag{19}$$

Step 4. Sensing decision

$$D = \begin{cases} 0; & \text{if } T(N) < \gamma \\ 1; & \text{if } T(N) > \gamma \end{cases} \tag{20}$$

where D is the threshold of the MME pre-computed based on N, S, P_f irrespective of signal noise and power.

It has been observed from various experiments that at a considerable amount of received signal finite samples, the sample covariance matrix $R_{\text{received}}(N)$ seems to diverge from the statistical covariance matrix R_{received}. Therefore, due to the following reason the eigenvalue distribution of $R_{\text{received}}(N)$ becomes too complicated which ultimately makes the choice of threshold quite difficult. Apart from this, since we have no information about signal, obtaining the threshold on the basis of P_d seems quite difficult. So, we tried to choose threshold based on P_f. To obtain the threshold for the given algorithm, theorem based on certain latest random matrix theories has been taken into consideration. Without any signal $R_{\text{received}}(N)$ turns out to be $R_{\text{noise}}(N)$, and then

$$R_{\text{noise}}(N) \underline{\text{def}} \frac{1}{N}\sum_{m=0}^{N-1} n_0(m)n_0(m-l)^* \tag{21}$$

Here, $R_{\text{noise}}(N)$ represents a special matrix which has been known for many years for its joint PDF. Even though the joint PDF of ordered eigenvalues is known to us for quite a long time, the closed form expression is still not available due to the complexity of the PDF expression. However, recent work helps us to find the distribution of largest and smallest eigenvalues that are within our area of concern by theorems which are expressed as follows [22–25]:

Theorem 1 *Assume noise to be real. Let*

$$A(N) = \frac{N}{\sigma_N^2} R_{\text{noise}}(N) \tag{22}$$

$$u = \left(\sqrt{N-1} - \sqrt{FS}\right)^2 \tag{23}$$

$$v = \left(\sqrt{N-1} + \sqrt{FS}\right).\left(\frac{1}{\sqrt{N-1}} + \frac{1}{\sqrt{FS}}\right)^{1/3} \tag{24}$$

where N, F and S denote the number of samples, oversampling factor and smoothing factor of the received signal, respectively.

Now, assuming $\lim_{N\to\infty} \frac{FS}{N} = y(0<y<1)$, $\frac{\alpha_{\max}(A(N))-u}{v}$ seems to converge (with probability 1) to the TW distribution of order 1.

Theorem 2 *Again taking the same assumption* $\lim_{N\to\infty} \frac{FS}{N} = y(0<y<1)$, *here in this theorem* $\lim_{N\to\infty} \alpha_{\min} = y(0<y<1)$ *(with probability equal to one).*

Based on both the above-mentioned theorems, when N is quite large enough, the smallest and largest eigenvalues of $R_{\text{noise}}(N)$ turn out to be $\frac{\sigma_n^2}{N}\left(\sqrt{N} - \sqrt{FS}\right)^2$ and $\frac{\sigma_n^2}{N}\left(\sqrt{N} + \sqrt{FS}\right)^2$, respectively.

Furthermore, Theorem 1 provides the largest eigenvalue distribution of N, which ultimately helps to find the min and max eigenvalues of $R_{\text{noise}}(N)$.

Let f_1 and f_1^{-1} be the CDF and its inverse for TW distribution of order 1, respectively. The probability of false alarm for MME algorithm is represented as

$$P_f = P(\alpha_{\max} > \gamma\alpha_{\min}) \tag{25}$$

$$= P\left(\frac{\sigma_n^2}{N}\alpha_{\max}(A(N)) > \gamma\alpha_{\min}\right) \tag{26}$$

$$\approx P\left(\alpha_{\max}(A(N)) > \gamma\left(\sqrt{N} - \sqrt{FS}\right)^2\right) \tag{27}$$

$$= P\left(\frac{\alpha_{\max}(A(N)) - u}{v} > \frac{\gamma\left(\sqrt{N} - \sqrt{FS}\right)^2 - u}{v}\right) \tag{28}$$

$$= 1 - f_1\left(\frac{\gamma\left(\sqrt{N} - \sqrt{FS}\right)^2 - u}{v}\right) \tag{29}$$

$$f_1\left(\frac{\gamma\left(\sqrt{N} - \sqrt{FS}\right)^2 - u}{v}\right) = 1 - P_f \tag{30}$$

leading to

$$\left(\frac{\gamma\left(\sqrt{N} - \sqrt{FS}\right)^2 - u}{v}\right) = f_1^{-1}\left(1 - P_f\right) \tag{31}$$

$$\gamma = \frac{\left(\sqrt{N}+\sqrt{FS}\right)^2}{\left(\sqrt{N}-\sqrt{FS}\right)^2}\cdot\left(1+\frac{\left(\sqrt{N}+\sqrt{FS}\right)^{-2/3}}{(NFS)^{1/6}}f_1^{-1}(1-P_f)\right) \tag{32}$$

Here, in order to calculate the output P, the two parameters, namely Credibility_eigen and Credibility_energy, are provided as the inputs to the fuzzy logic detection system. The decision regarding final sensing consists of two stages:

1. Dynamic double-threshold-based ED
2. Fuzzy logic detector.

ED follows the following rule:

$$D_{\text{DTED}} = \begin{cases} 1\ E > \lambda_{\text{upper}} & H_1 \text{ declared: Channel Occupied} \\ 1\ E > \lambda_{\text{upper}} & H_1 \text{ declared: Channel Occupied} \\ D_{\text{FLD}}\lambda_{\text{lower}} < E < \lambda_{\text{upper}} & \text{Decision taken by Fuzzy Logic Detector} \end{cases} \tag{33}$$

where the fuzzy logic system decision, D_{FLD}, is as follows

$$D_{\text{FLD}} = \begin{cases} 1 \quad \text{if } P > \lambda_{FL} & H_1 \text{ declared: Channel Occupied} \\ 0 \quad \text{if } P > \lambda_{FL} & H_0 \text{ declared: Channel Unoccupied} \end{cases} \tag{34}$$

where P represents the output of the fuzzy logic detection system with λ_{FL} being the threshold value, set for taking rational decisions. For the sake of convenience, here the value of λ_{FL} has been taken to be 0.5.

Final decision is concluded by the following expression:

$$0 = D_{\text{DTED}} + D_{\text{FLD}} \tag{35}$$

$$0 = \begin{cases} D_{\text{DTED}} + D_{\text{FLD}} > 0 H_1 \text{ declared : Channel is Occupied} \\ \text{else} H_0 \text{ declared: Unoccupied Channel} \end{cases} \tag{36}$$

where D_{DTED} and D_{FLD} represent two events that are mutually exclusive.

In the proposed fuzzy logic detection stage, linguistic variables are mainly divided into three levels described as low, medium and high for the representation of Credibility_eigen and Credibility_energy. By definition, Credibility_energy is reflecting the possibility of PU presence by energy detection method. If Credibility_energy is high, it means energy is near upper threshold and hence high possibility of user presence and vice versa. Similarly, Credibility_eigen is reflecting the possibility of PU detection by eigenvalue method. If both credibilities are low then the presence of user is low and so on. In our proposed work, we have taken three membership functions for each input and there are 2 inputs, so total rule base is 3^2 = 9 rules which are given in Table 1. Further, there are five levels of divisions for consequence P (primary user presence possibility), namely very high, high, medium, low and very low. Figure 4 depicts the membership functions (MFs) which represent antecedent and consequent variables used for the proposed case. In the proposed system there are 3 fuzzy subsets and 2 antecedents and 9 rules formulation. Tables 1, 2 and 3 show the rule and range values for the proposed fuzzy-based system.

Table 1 Fuzzy logic detection system rule base

Antecedent 1 (Credibility_energy)	Antecedent 2 (Credibility_eigen)	Consequent P (possibility of PU)
Low	Low	Low
Low	Medium	Very low
Low	High	Medium
Medium	Low	Very low
Medium	Medium	Medium
Medium	High	Very high
High	Low	Medium
High	Medium	Very high
High	High	High

On the basis of our input parameters and applications in spectrum sensing techniques triangular and Gaussian membership functions are best suited. However, due to simplicity and less computational complexity, we have chosen triangular membership function. Moreover, we cannot easily calculate the arithmetic operations in case of bell, sigmoid, asymmetric and LR, etc.

3.1 The Proposed Algorithm

1. Take into consideration a continuous-time received signal $y(n)$.
2. Obtain n samples of the concerned signal $\{y_1, y_2, y_3, \ldots, y_n\}$.
3. Calculate λ_{ED} according to P_f and estimated noise variance.
4. Calculate λ_{upper} and λ_{lower} according to P_f and max–min value of noise variance for the double-threshold-based energy detection scheme.
5. Calculate the required test statistic that is $E(y) \leftarrow$ Enery of the signal, at the first stage.
6. If test statistic $E(y) \geq \lambda_{\text{upper}}$

$D_{\text{DTED}} \leftarrow H_1$;

else if $E(y) \leq \lambda_{\text{lower}}$

$D_{\text{DTED}} \leftarrow H_0$;

else $\lambda_{\text{lower}} < E(y) < \lambda_{\text{upper}}$

(a) Evaluate credibility of the user in terms of energy as

$$\text{Credibility_energy} = 1 - \left[\frac{(\lambda_{\text{upper}} - E}{\lambda_{\text{upper}}}\right]$$

(b) Calculate max and min eigenvalues of the received signal denoted by $\alpha_{\max}$ and $\alpha_{\min}$

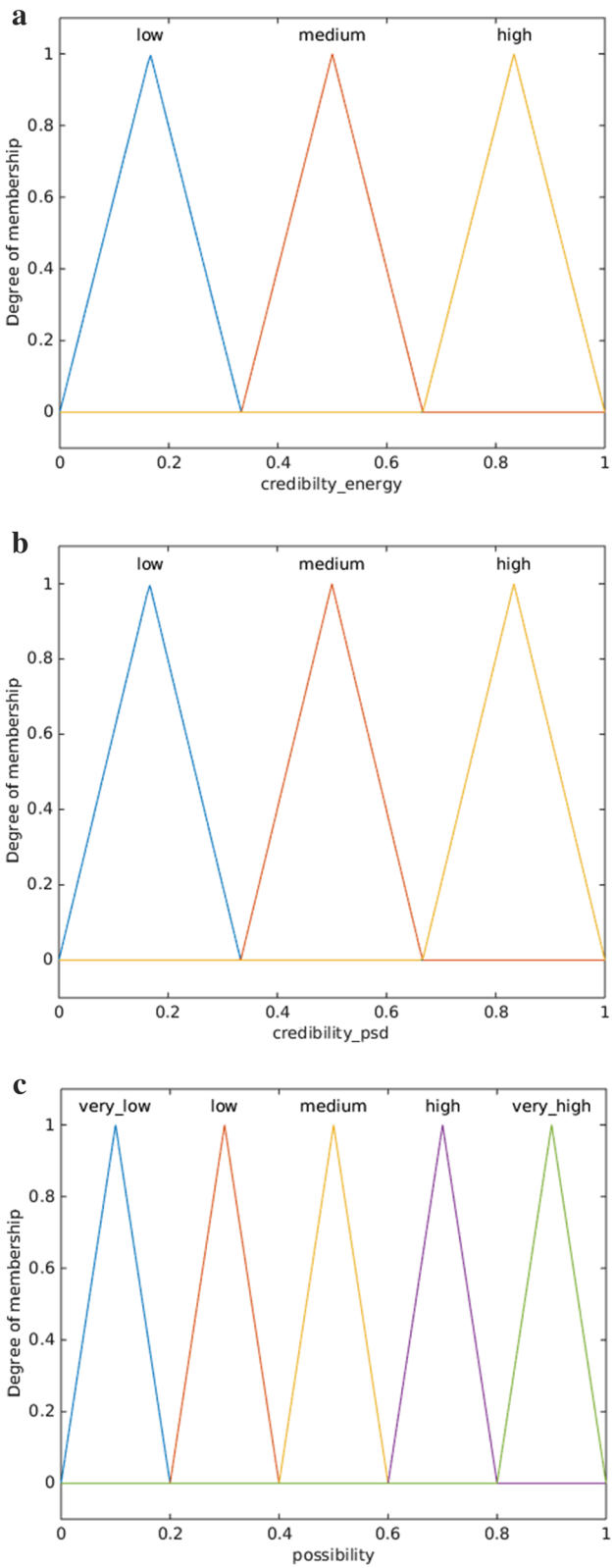

Fig. 4 Membership function of **a** antecedent 1 (Credibility_energy), **b** antecedent 2 (Credibility_eigen) and **c** consequent about possibility of the presence of PU

(c) Calculate eigenvalue-based test statistics as

$T \leftarrow$ Ratio of max to min eigen value of the received signal

$$T = \frac{\alpha_{\max}}{\alpha_{\min}}$$

7. Calculate γ, threshold of the max–min eigenvalue detection algorithm (MME).
8. Calculate credibility of eigenvalue of the concerned signal by Credibility_eigen $= (\gamma - T/\gamma)$
9. *Provide inputs* [Credibility_eigen, Credibility_energy] to the fuzzy logic-based detection system in the second stage, and evaluate decision taken by another test statistic P given as follows:

$P \leftarrow$ Primary User Presence Possibility

10. If $P > \lambda_{\text{FLD}} = 0.5$

$D_{\text{FLD}} \leftarrow H_1$;

else

$D_{\text{FLD}} \leftarrow H_0$

where λ_{FLD} denotes the threshold value of fuzzy logic detection system.

11. Final decision is thus given by $0 = D_{\text{DTED}} + D_{\text{FLD}}$.

The proposed scheme has two stages where the first stage is simple double-threshold-based ED and the second stage is based on the eigenvalue estimator. If the signal lies in the first and second stages then these stages give the decision quickly. If the signal could not identify its state in these two stages only then it goes to the fuzzy detector. Means computation by fuzzy logic comes into the picture only when signal lies in confused region. So, the proposed system offers low computational complexity. Implementation complexity of cooperative spectrum sensing is high as it needs a separate fusion controller. Moreover, control/reporting channels need to be assigned separately. Communication cost in terms of reporting channel and reporting time also increases with the number of cooperative users. Computation complexity also depends on the number of users. Hence, the optimized scheduling is needed to allocate sensing task in CSS. In the proposed scheme at local sensing, no separate fusion center is needed. However, good processing capability is needed at local nodes; however, that is used only opportunistically. Computational complexity of the proposed scheme is:

$$(1 - P)\ \text{Complexity (ED)} + P(\text{Complexity ED} + \text{Eigen} + \text{FLD}) \quad (37)$$

Table 2 Range values of the two parameters for three linguistic variables

Linguistic variable	Credibility_energy	Credibility_eigen
Low	0–0.33	0–0.33
Medium	0.33–0.66	0.33–0.66
High	0.66–1	0.66–1

Table 3 Range values of inference of the fuzzy logic system output

Lower output value	Higher output value	Inference
0.8	1	Very high
0.6	0.8	High
0.4	0.6	Medium
0.2	0.4	Low
0	0.2	Very low

4 Cooperative Spectrum Sensing Using the Proposed Scheme

The center of fusion in this section is responsible for the combination of all local decisions with the fuzzy logic scheme. The fusion process in this scheme is categorized mainly into two types: First is the hard combination for decision fusion, while the second is the soft combination for data fusion. The data fusion type technique is responsible for aggregating all the users data from all the respective cooperative user at the fusion center, where all the information is being combined according to some particular set of rules, e.g., SNR-based weight in MRC scheme. Since all the data are being sent to the fusion center, this scheme is therefore expected to occupy sufficiently large part of the bandwidth. On the other hand, in decision fusion or data hard combination type, cooperative secondary user decides at the local level with one-bit decision transmitted to the center of fusion. However, all the decisions at the fusion center are taken by combing all the individual decisions based on the AND, OR and the MAJORITY rules. When all the other users give the decision about the spectrum occupancy only then the AND rule declares the presence of the primary user. The mathematical expressions for the cooperative probability of false alarm P_{FD} and cooperative probability of detection P_{CD} for the AND rule are given as follows:

$$P_{CD}(U) = \prod_{i=1}^{U} (P_{d,i}) \tag{38}$$

$$P_{FD}(U) = \prod_{i=1}^{U} (P_{f,i}) \tag{39}$$

OR rule, on the other hand, signifies the presence of primary signal when at least one among all users indicates the presence of PU. The respective P_{CD} probability of detection and P_{FD} probability of false alarm for the given OR rule are expressed as follows:

$$P_{CD}(U) = 1 - \prod_{i=1}^{U} (1 - P_{\text{detection},i}) \tag{40}$$

$$P_{FD}(U) = 1 - \prod_{i=1}^{U} (1 - P_{\text{falsealarm},i}) \tag{41}$$

where U represents the number of secondary users subscribing cooperation. The $P_{\text{falsealarm},i}$ and $P_{\text{detection},i}$ here represent the probability of false alarm and detection for each secondary user. In the paper, one of the prime objectives is to enhance the cooperative sensing performance through fusion of decision where the proposed fuzzy logic-based two-stage spectrum sensing method is applied to every secondary user at the node level. In this regard, the block diagram of the proposed cooperative spectrum sensing (CSS) scheme with the proposed method is depicted in Fig. 5.

For the uncorrelated decision case, the detection probability for decision fusion is provided very well by $P_{D,CD} = \sum_{i=k}^{n} \binom{n}{i} P_D^i (1 - P_D)^{n-i}$, where P_D is the probability of detection of a single user with n being the total number of cooperative nodes in the proposed method. Setting $n = 1$ in the OR rule helps us to evaluate further the performance of cooperation for the given system

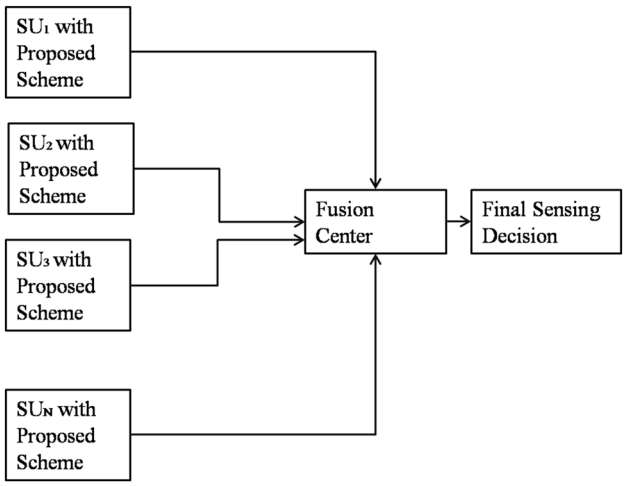

Fig. 5 CSS scheme with the proposed method

5 Results and Discussion

We provide the performance analysis of the proposed scheme with the existing ones through computer simulation results in MATLAB, version 12.0. The system parameters that are assumed for system modeling are as follows: PU signal: QPSK with 1 MHz carrier frequency, delay vector of Rayleigh fading channel accompany = [0 4 8 12] μs, sampling frequency = 50 MHz, Doppler shift = 4 Hz, gain vector = [0 − 3 − 6 − 9]. For the purpose, twenty thousand iterations were performed so that results converged properly. The probability of miss detection (P_{md}) versus SNR depicted in Fig. 6 provides the performance analysis of the proposed scheme with that of the conventional ED with a single user.

From the results it has been observed that at $P_f = 0.1$ the proposed scheme provides better results in comparison with the conventional ED schemes. For the typical value of SNR = − 9 dB, the proposed method yields $P_{md} = 0.1$, while it is 0.78 for the CED. The other interesting fact about the proposed scheme is that it gives better results even at low value of SNR, i.e., − 9 dB, which is the main requirement of the IEEE 802.22 standard, resulting in significant improvement in the detection performances. Figure 7 shows the performance at different settings of P_f in terms of P_d. Though smaller P_f is desirable it seems to reduce P_d. For typical setting of $P_f = 0.01$, the proposed scheme gives detection provability $P_d = 0.9$ at SNR = − 7 dB. In Fig. 8, it is observed that our scheme offers better results as compared to the already existing ED and cyclostationary methods [7]. Also it brings 13.3% improvement in the performance at SNR value of − 10 dB. This performance is also better as compared to the already existing two-stage schemes utilizing ADT and MED [11]. We have used dynamic double-threshold-based ED method at the very first stage, whereas in [11] multiple energy detectors were employed at the local node level, resulting in unnecessary increases in cost and complexity.

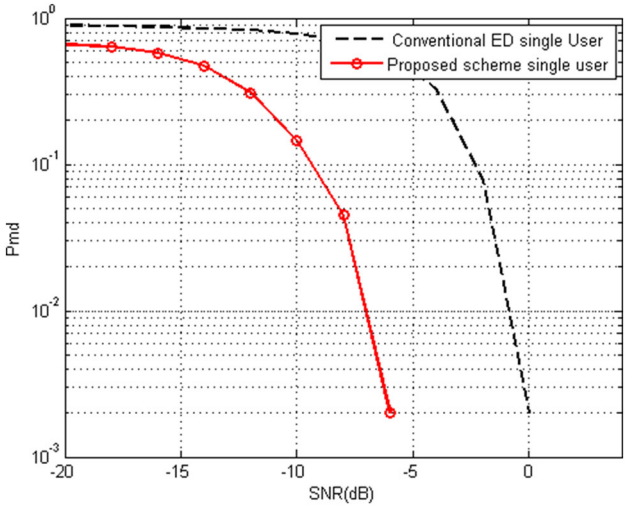

Fig. 6 P_{md} versus SNR at $P_f = 0.1$

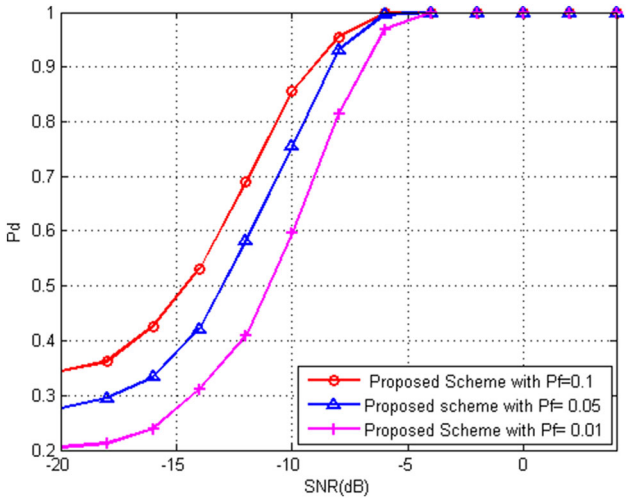

Fig. 7 P_d versus SNR with $P_f = 0.1$, 0.05, 0.01 and 0.001 for the proposed scheme

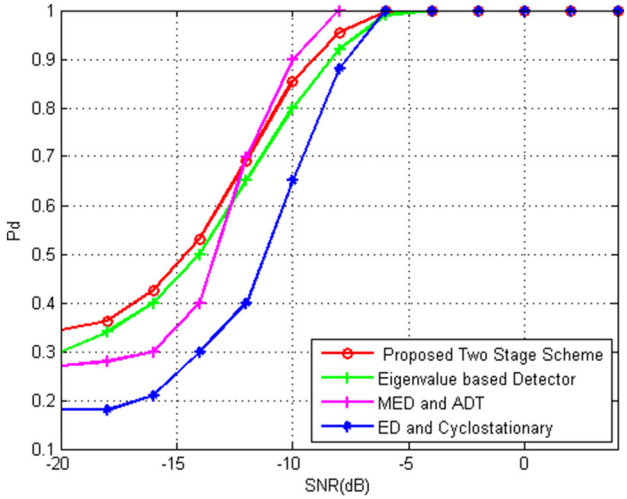

Fig. 8 P_d versus SNR at $P_f = 0.1$ for the proposed scheme

In Figs. 9 and 10, results for CSS detection with three CR users in consideration are depicted. From Fig. 9, it is observed that the proposed scheme with a single user provides better results in comparison with the conventional CED with and without the OR hard combination.

In Fig. 10, it is observed that the desired P_d of 0.9 dB is achieved at − 14 dB, − 4 dB and − 6 dB for the proposed OR rule CSS, OR hard combination and cooperative CED with MRC soft combination schemes, respectively. From this it has been observed that the proposed scheme seems to provide better results in comparison with the conventional CSS detection with OR and MRC by 10 dB and 8 dB, respectively, for $P_d = 0.9$. Moreover, communication

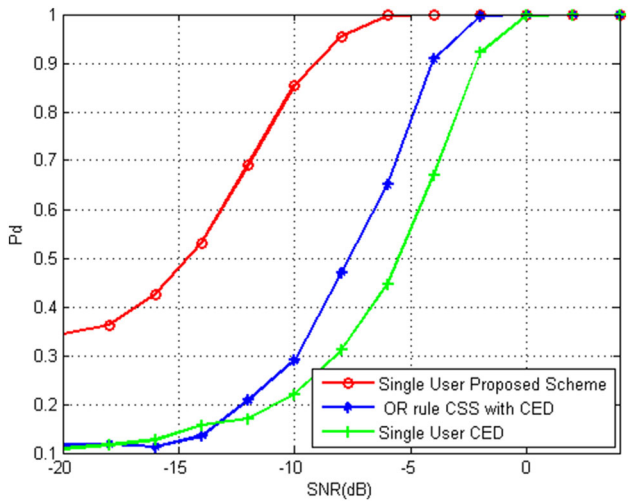

Fig. 9 P_d versus SNR at $P_f = 0.1$ and $k = 3$

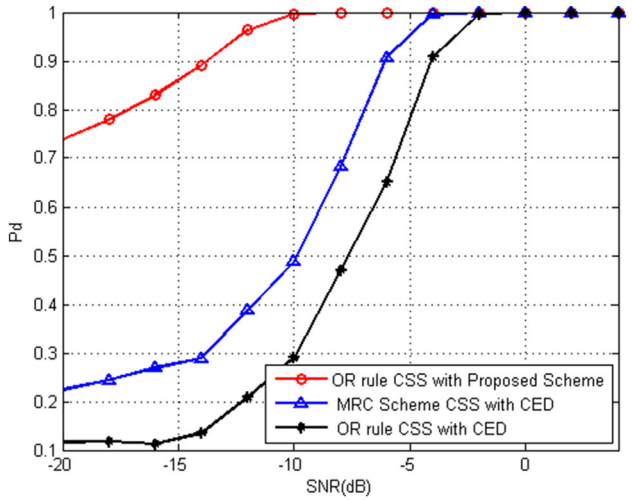

Fig. 10 Comparison of the detection performance at $P_f = 0.1$ and $k = 3$

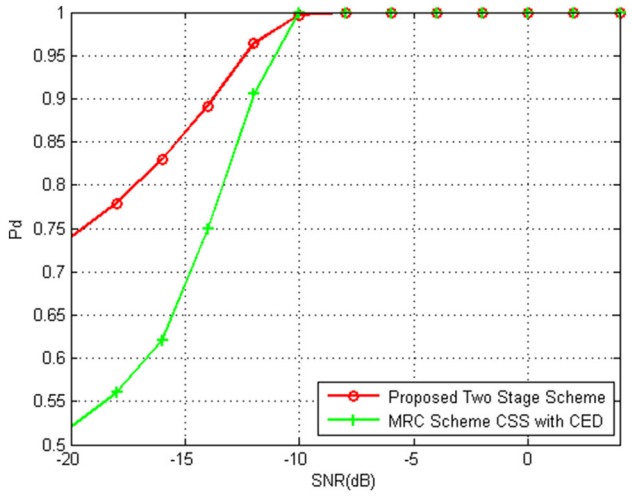

Fig. 11 P_d versus SNR at $P_f = 0.1$ and $k = 3$ for cooperative scheme

overheads are also observed to be low in comparison with the MRC. Figure 11 illustrates the comparison of MRC scheme with the proposed scheme [11]. Results show that the desirable value of $P_d = 0.9$ is achieved at SNR value of -10.2 dB in the MED and ADT, while the method proposed in this paper yields $P_d = 0.9$ at SNR $= -12$ dB, which comes under significant lower SNR region.

6 Conclusion

The paper brings a novel fuzzy logic-based two-stage spectrum sensing scheme for CR networks. The proposed scheme in this paper outperforms the conventional spectrum sensing schemes that had existed for a long time over the years. It does not show any prior urge of information about the PU, which ultimately results in reduction in the overall complexity of the system along with the sensing time. Also, the proposed scheme seems to show nearly comparable results with MED and ADT with energy detection scheme being used at the very first stage. Another advantage that comes into the picture of the proposed scheme is that its first stage is way less complex. Therefore, due to all these things, the cooperative sensing scheme was also implemented using the proposed method. For the given $P_d = 0.9$, results show 10 dB and 8 dB respective improvement as compared to the already existing techniques, i.e., OR schemes and cooperative CED with MRC scheme. Moreover, it has been observed that the proposed solution reduces the overheads in the entire process. Therefore, it is concluded that the proposed method brings significant improvement in terms of bandwidth requirements and system complexity.

References

1. Haykin S (2005) Cognitive radio: brain-empowered wireless communications. IEEE J Sel Areas Commun 23(2):201–220
2. Axell E, Leus G, Larsson EG, Vincent H (2012) Spectrum sensing for cognitive radio: state-of-the-art and recent advances. IEEE Signal Process Mag 29(3):101–116
3. Lu L, Zhou X, Onunkwo U, Li G (2012) Ten years of research in spectrum sensing and sharing in cognitive radio. EURASIP J Wirel Commun Netw 28:1–16
4. Yucek T, Arslan H (2009) A survey of spectrum sensing algorithms for cognitive radio applications. IEEE Commun Surv Tutor 11(1):116–130
5. Benko J, Cheong YC, Cordeiro C (2006) A PHY/MAC proposal for IEEE 802.22 WRAN systems—part 1: the PHY, IEEE 802.22-06/0004r1
6. Luo L, Neihart NM, Roy S, Allstot DJ (2009) A two-stage sensing technique for dynamic spectrum access. IEEE Trans Wirel Commun 6:3028–3037
7. Maleki S, Pandharipande A, Leus G (2010) Two-stage spectrum sensing for cognitive radios. In: Proceedings of the IEEE

international conference on acoustics, speech, and signal processing, pp 2946–2949
8. Ejaz W, Hasan N, Kim HS (2012) SNR-based adaptive spectrum sensing for cognitive radio networks. Int J Innov Comput Inf Control 8:6095–6105
9. Nair PR, Vinod AP, Smitha KG, Krishna AK (2012) Fast two stage spectrum detector for cognitive radios in uncertain noise channels. IET Commun 11:1341–1348
10. Tandra R, Sahai A (2008) SNR walls for signal detection. IEEE J Sel Top Signal Process 2:4–17
11. Bagwari A, Tomar GS (2013) Two-stage detectors with multiple energy detectors and adaptive double threshold in cognitive radio networks. Int J Distrib Sens Netw 2013:1–8
12. Akyildiz IF, Lo BF, Balakrishnan R (2011) Cooperative spectrum sensing in cognitive radio networks: a survey. Phys Commun 4:40–62
13. Do T, Mark LB (2012) Improving spectrum sensing performance by exploiting multiuser diversity. In: Cheng S (ed) Foundation of cognitive radio systems. InTech Open, London, pp 119–140
14. Ma J, Zhao G, Li Y (2008) Soft combination and detection for cooperative spectrum sensing in cognitive radio networks. IEEE Trans Wirel Commun 7:4502–4507
15. Baldo N, Zorzi M (2009) Cognitive network access using fuzzy decision making. IEEE Trans Wirel Commun 8:3523–3535
16. Matinmikko M, Rauma T, Mustonen M, Harjula I, Sarvanko H, Mammela A (2009) Application of fuzzy logic to cognitive radio systems. IEICE Trans Commun 12:3572–3580
17. Hasan MH, Nasar OA (2011) Adaptive spectrum sensing of wireless microphones with noise uncertainty. In: IEEE 22nd international symposium on personal, indoor and mobile radio communication, pp 445–450
18. Digham FF, Alouini MS, Simon MK (2007) On the energy detection of unknown signals over fading channels. IEEE Trans Wirel Commun 55:21–24
19. Zadeh LA (2008) Is there a need for fuzzy logic? Inf Sci 178:2751–2779
20. Stocia P, Moses R (2005) Spectral analysis of signals. Prentice Hall, Upper Saddle River
21. Kyperountas S, Correal N, Shi Q, Ye Z (2008) Performance analysis of cooperative spectrum sensing in Suzuki fading channels. In: IEEE international conference on cognitive radio oriented wireless networks and communications, pp 428–432
22. Johnstone IM (2001) On the distribution of largest eigenvalue in principle component analysis. Ann Stat 29(2):295–327
23. Johannson K (2001) Shape fluctuations and random matrices. Commun Math Phys 209:437–476
24. Bai ZD (1999) Methodologies in spectral analysis of large dimensional random matrices: a review. Stat Sin 9:611–677
25. Ahuja B, Kaur G (2017) Design of an improved spectrum sensing technique using dynamic double thresholds for cognitive radio networks wireless personal communication. Springer, New York. https://doi.org/10.1007/s11277-017-4539-y

Publisher's Note Springer Nature remains neutral with regard to jurisdictional claims in published maps and institutional affiliations.

Wireless Personal Communications
https://doi.org/10.1007/s11277-019-06389-9

Ultra Wide Band CPW-Fed Circularly Polarized Microstrip Antenna for Wearable Applications

Saumya Das[1] · Hashinur Islam[1] · Tanushree Bose[1] · Nisha Gupta[2]

© Springer Science+Business Media, LLC, part of Springer Nature 2019

Abstract

A conformal rigid microstrip ultra-wideband (UWB) circularly polarized wearable antenna is proposed to overcome the behavioural irregularities of flexible body-worn antennas. The design demonstrates the inclusion of two L shaped radiators along with an L shape feed and also a vertically protruded stub embedded with the ground plane for achieving the required ultra-wide bandwidth and circular polarization. Coplanar waveguide (CPW) feed is used to overcome the bandwidth limitation of circular polarization. The proposed low profile antenna with dimensions $75 \times 63 \times 1.52$ mm^3 yields a 10 dB impedance bandwidth of 111.4% (1.28–4.5 GHz) and a 3 dB axial ratio bandwidth of 45.61% (2.2–3.5 GHz). On body performance measurement of this planar antenna validates its applicability under body worn condition. Specific absorption rate (SAR) assessment has also been evaluated for this antenna on a hypothetical body model to justify its acceptance for the wearable application. It is observed that the maximum radiation amount absorbed by the body model is restricted to a maximum SAR value of 1.19 W/kg and 1.43 W/kg over 1 g and 10 g average body mass respectively. The time-domain characteristics such as group delay and waveform response, also exhibit satisfactory UWB performance of the proposed antenna. A lumped wideband equivalent circuit model of the antenna is also developed for estimating the broadband matching ability.

Keywords Ultra-wideband (UWB) · Axial ratio (AR) · Coplanar waveguide (CPW) · Circular polarization (CP) · On body performance · Specific absorption rate (SAR)

✉ Saumya Das
saumya.das@smit.smu.edu.in

Nisha Gupta
ngupta@bitmesra.ac.in

[1] ECE Department, Sikkim Manipal Institute of Technology, Sikkim Manipal University, Sikkim, India

[2] ECE Department, Birla Institute of Technology, Mesra, Ranchi, Jharkhand, India

Published online: 22 April 2019

1 Introduction

In recent times, fixed and movable target localization and tracking have received significant concern in the research community for several upcoming wearable wireless applications. In particular, wireless wearable devices are becoming popular day by day for the purpose of monitoring human activities in workshops, sports, battlefields, and health care. Ultra-wideband (UWB) RF technology is widely accepted because of its inherent features such as high localization accuracy, low cost, low power, portability, high data rate and better integration ability with microelectromechanical systems (MEMS) [1]. In addition, very low power spectral density exists over the UWB band making it less prone to interferences [2]. Moreover, the impact of UWB radiation is almost negligible on the human body and it is considered to be one of the most promising technologies for the wearable application worldwide. Wearable systems require supporting UWB wearable antennas for efficient wireless transmission and reception. Many researchers considered flexible textile material such as jeans, cotton, fabric, perforated plastic, etc. as a substrate for designing UWB wearable antennas as textile material could be worn easily on different body parts [3–7]. Pasting of the copper tape on the textile material is the most common method for designing the wearable antennas [8–10]. However, the characteristics of flexible wearable textile antennas deteriorate heavily because of several unavoidable issues. One of the major issues is the crumpling of textile material due to different body gesture which affects the antenna performance significantly by changing the effective current path length [11]. Secondly, the copper tape pasting causes uneven air gap formation between the textile and the copper tape which leads to unreliable and unrepeatable antenna characteristics [12]. In addition, the washing of the clothes embedded with a textile antenna may cause deterioration of antenna performance over time [13]. Therefore, it is worthwhile to develop a rigid pocket size compact UWB wearable antenna made of a copper laminated material to overcome the behaviour irregularities of the flexible antenna due to body bending, copper tape pasting, cloth crumpling, and cloth washing. This compact planar antenna can be installed over a pocket-size UWB wearable system. The UWB wearable systems are widely used for tracking the flow of workers inside a warehouse. As shown in Fig. 1, every worker carries a UWB system inside the pocket while performing their regular duties. The movement of workers could be monitored through a control computer and a data management server. Use of a UWB system for long working hours is also very safe in terms of radiation exposure. Therefore, a more efficient work environment could be achieved with UWB wearable systems.

In this proposed work, an ultra-wideband circularly polarized coplanar waveguide fed planar patch wearable antenna is presented. The antenna is developed on a rigid substrate to overcome the problems related to flexible wearable antennas. The circular polarization property is another important performance parameter of the wearable antenna to be considered, since the movement and position of the human body may disturb the polarization matching of the body-worn antenna. This is incorporated in the proposed antenna, by introducing the generation of two orthogonal current paths. The coplanar waveguide (CPW) feeding is used to compensate for the bandwidth limitation due to circular polarization. Initially, HFSS simulation software is used for simulation and analysis purpose. Then the importing tool of CST-MWS software is explored to bring the original HFSS model on CST-MWS platform. Thus, two different simulation tools are utilized for verification of simulation results of the proposed antenna. The proposed antenna characteristics are also compared with the characteristics of some recently published antennas in terms of antenna

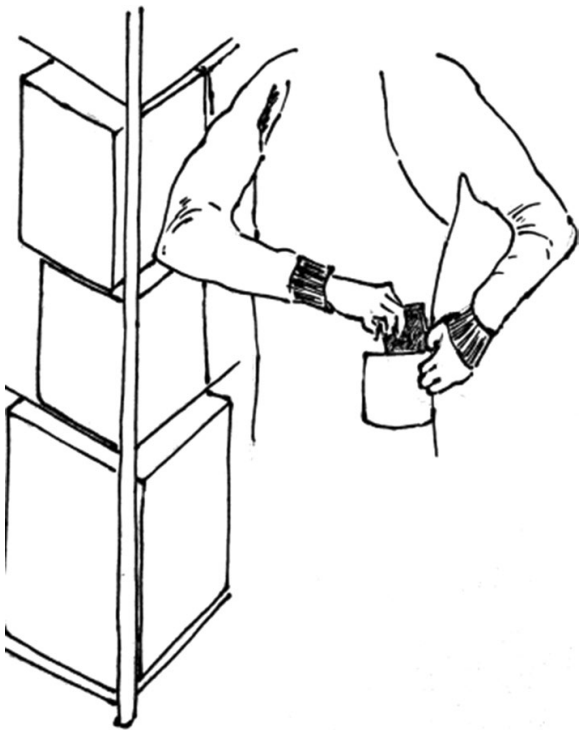

Fig. 1 Use of UWB wearable system for tracking the movement of workers in a warehouse

dimension, 10 dB impedance bandwidth and 3 dB axial ratio and peak gain. Further, CST-MWS is used to evaluate the Specific Absorption Rate (SAR) on a hypothetical body model due to the electromagnetic radiation of the proposed antenna under body worn condition. The SAR value of the proposed design is compared with other previously reported 2.45 GHz wearable antennas. A prototype model of this wearable antenna is fabricated and some important antenna performance parameters are measured for the purpose of validation. Additionally, the antenna is kept inside the shirt pocket of a volunteer to measure the on body performances of the radiator experimentally. Experimental and simulation results are found to be in good agreement for this wearable antenna. The CST-MWS is also used to explore the time domain characteristics for ensuring satisfactory UWB performance of the proposed antenna. Lumped wideband equivalent circuit models of the proposed antenna is also developed in CST design studio for estimating the broadband matching ability.

2 Wearable Antenna Geometry and Body Model Designing

In this antenna design, two L shape patch sections (A, B) are fed by another L shaped feed section (C) and all sections are merged to form the complete radiator as shown in Fig. 2. The proposed patch design is printed over the Rogers RO4232 substrate ($\varepsilon_r = 3.2$, loss tangent $\tan\delta = 0.0018$) with thickness 1.52 mm. The overall dimension of the proposed antenna is $63 \times 75 \times 1.52$ mm^3. The C section of width 3.2 mm is considered as the CPW feed for the wearable antenna. The D and E sections are assigned as a co-planner ground for this antenna. A vertical protrude part of dimension 10×1.5 mm^2 is included in the E section to improve the axial ratio for circular polarization. Figure 3 shows the fabricated prototype following the antenna geometry.

For evaluating the SAR value of the human body cell, a hypothetical layered body model of dimension $200 \times 200 \times 40$ mm^3 has been developed using CST-MWS. As shown in Fig. 4, layers of skin, fat, muscle and bone are considered for modelling the body model.

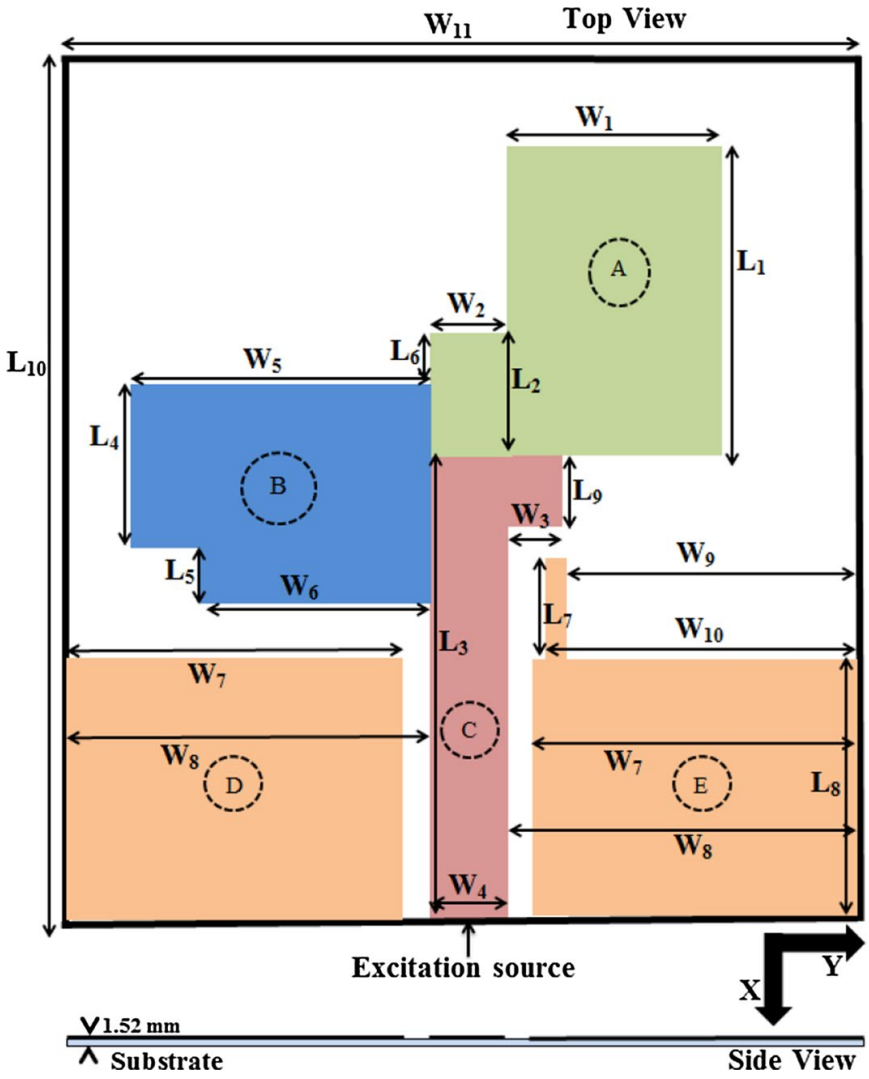

Fig. 2 Geometry of the proposed antenna where $W_1 = 18$, $W_2 = 3.2$, $W_3 = 2.5$, $W_4 = 3.2$, $W_5 = 23$, $W_6 = 15.2$, $W_7 = 29.4$, $W_8 = 29.9$, $W_9 = 27$, $W_{10} = 28.5$, $W_{11} = 63$, $L_1 = 30$, $L_2 = 16.5$, $L_3 = 35.5$, $L_4 = 15.5$, $L_5 = 3.2$, $L_6 = 7$, $L_7 = 10$, $L_8 = 20$, $L_9 = 3.2$, $L_{10} = 75$, (unit: mm)

Table 1 shows the thickness of each layer for building the layered structure. The position of the proposed antenna in the hypothetical model is also illustrated in Fig. 4.

3 Gradual Progress of Antenna Designing for Bandwidth and Axial Ratio Improvement

3.1 Steps of Antenna Designing

The progressive steps of final antenna designing are explained using two different approaches to examine the influence of each section on 10 dB impedance bandwidth and 3 dB axial ratio bandwidth precisely in Fig. 5. The 1st approach narrates the design procedure with a sequence as follows:-

Step 1 Design of a symmetrical ground plane with the L shaped CPW feed
Step 2 Protruded part inclusion with a ground plane

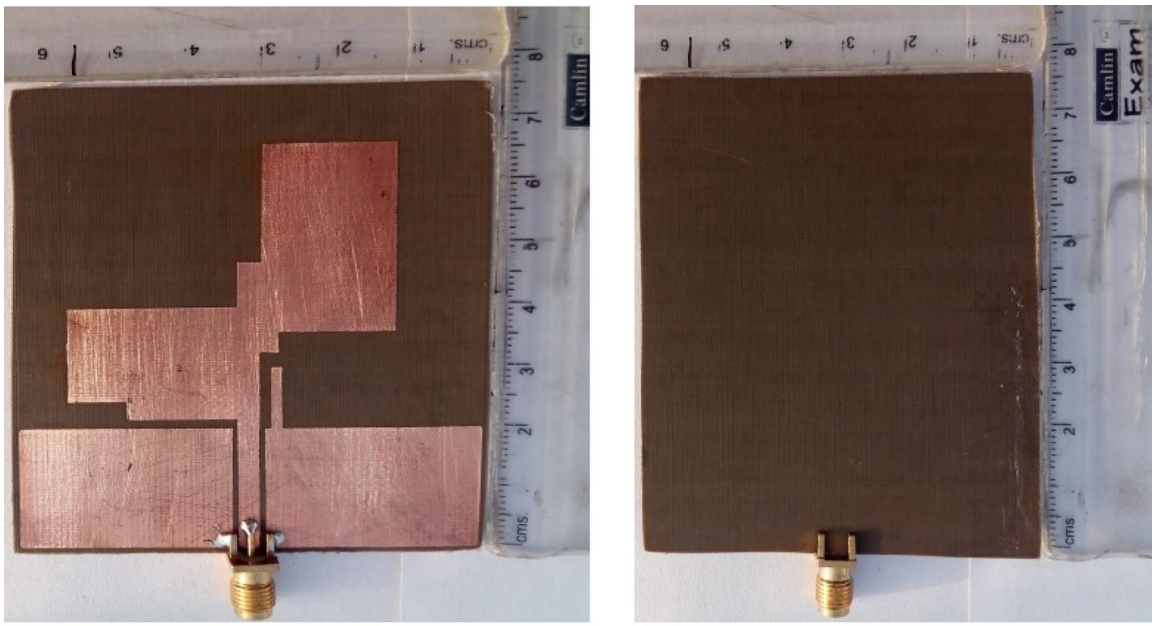

Fig. 3 Prototype Model (**a**) Front view (**b**) Back view

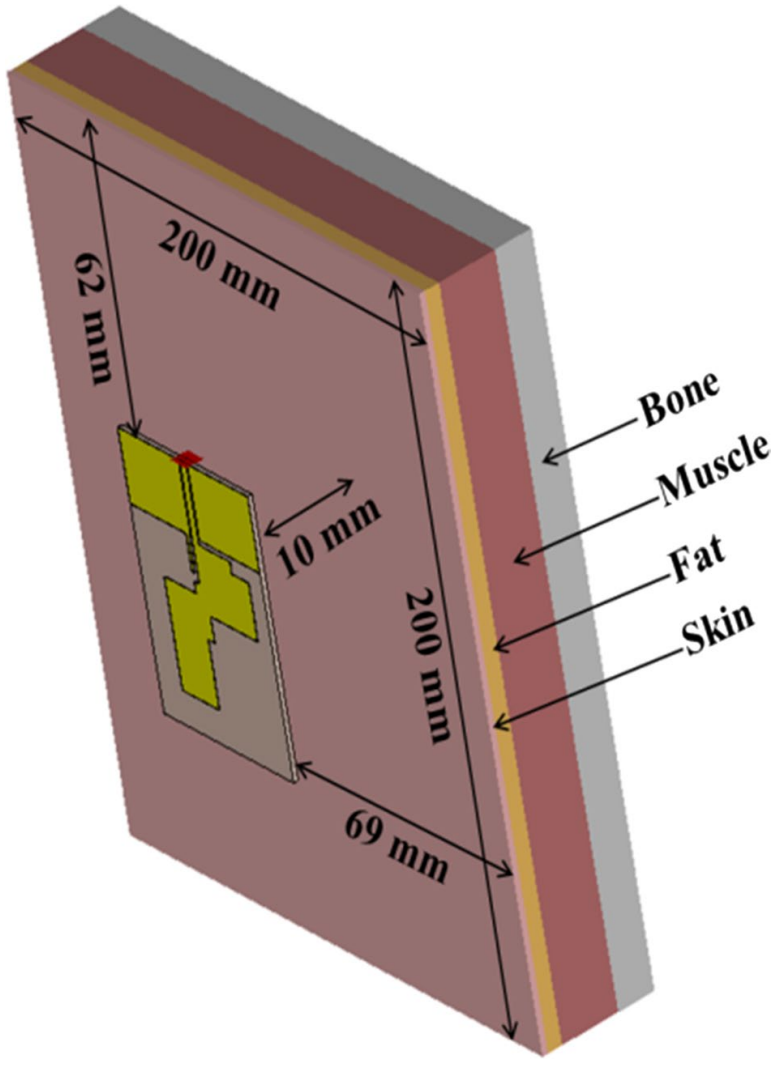

Fig. 4 Body model including proposed antenna

Table 1 Multilayer thickness specification

Layer	Thickness (mm)
Skin	2
Fat	5
Muscle	20
Bone	13

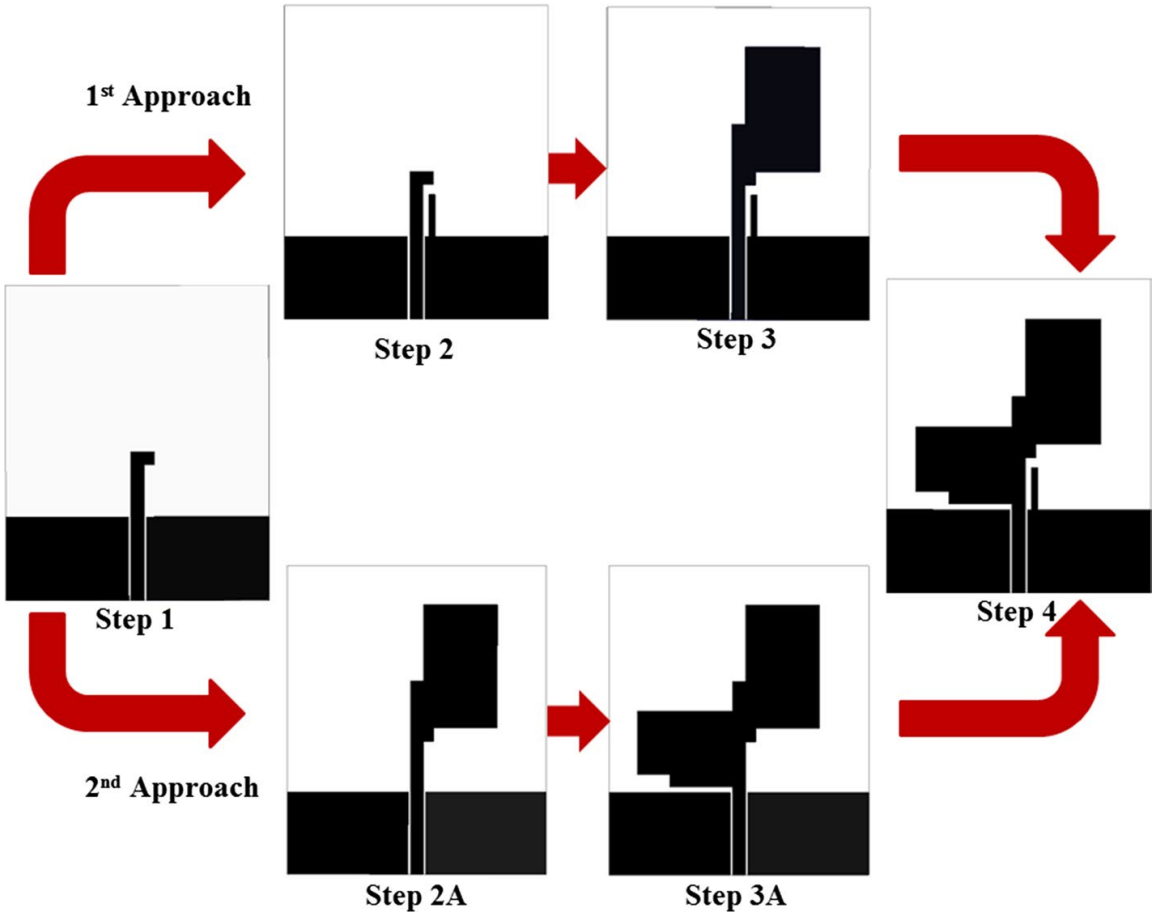

Fig. 5 Steps of progression of the proposed antenna

Step 3 Vertical L shaped part attached to the feed structure
Step 4 Horizontal L shaped part inclusion with the Step 3 model

The 2nd approach sequence is as follows:-

Step 1 Design of a symmetrical ground plane with the L shaped CPW feed
Step 2A Vertical L shaped part attached to the feed structure
Step 3A Horizontal L shaped part inclusion with the Step 2A model
Step 4 Protruded part inclusion with a ground plane

Step 1 includes an L shaped feed (Section 'C', Fig. 2) with two symmetrical ground planes (Section 'D' and 'E', Fig. 2). The advantage of considering L shaped feed over

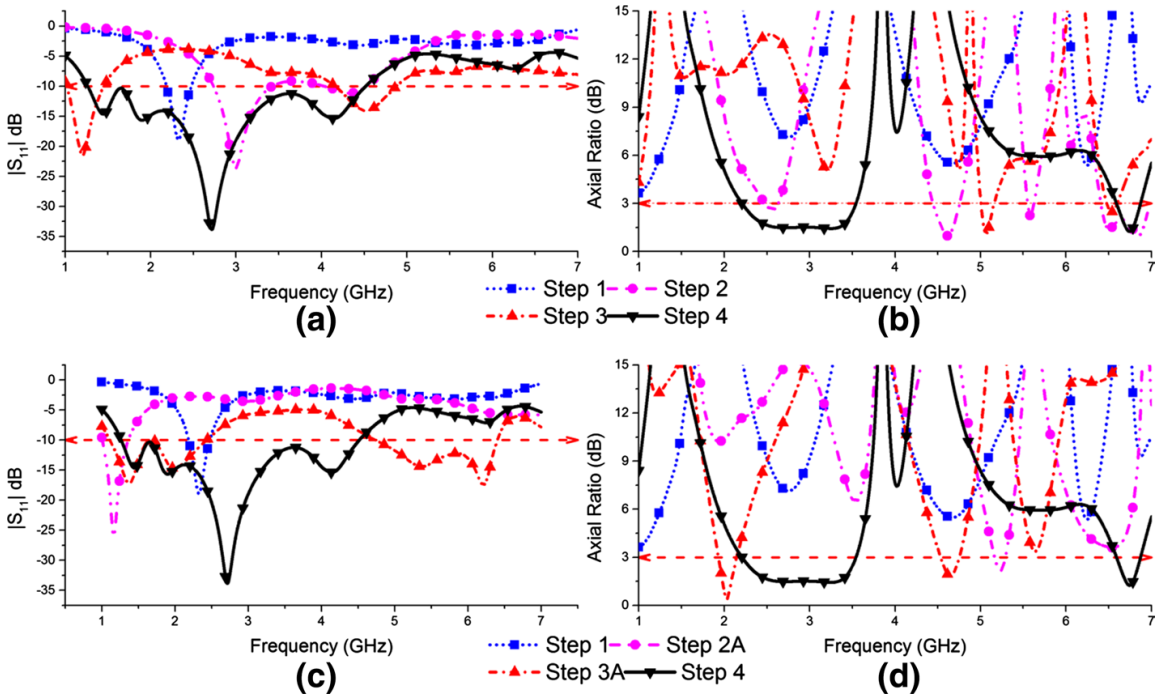

Fig. 6 Stepwise improvement of S_{11} and AR

straight line feed is to increase the effective current path length, to make the structure resonate at lower frequencies [14]. It is observed in the Step 1 analysis that a straight line feed with a length 38 mm the configuration resonates at 2.8 GHz, whereas with the L shaped feed of the same length, it resonates at 2.3 GHz as shown in Fig. 6a. The ground plane on both sides of the feed line is considered to be symmetrical and current distributions over the left half and right half rotate with directions opposite to each other thus, forcing the fields due to these currents to cancel out. Hence, in spite of the current rotation, the circular polarization cannot be achieved with the symmetrical ground plane structure.

The Step 2 transforms the ground plane (Section 'D' and 'E', Fig. 2) configuration from symmetric to asymmetric by introducing a protruded stub part with 'E' part that almost holds the rotation of the current on 'E' section. Thereby rotation of the current in the part 'D' dominates to support circular polarization with the asymmetric ground plane and axial ratio is brought below 3 dB value as shown in Fig. 6b. However, the inclusion of the protruded part causes the resonant frequency to shift right by about 700 MHz as shown in Fig. 6a. Additionally, another resonant frequency at 4.5 GHz is obtained due to the protruded stub length of 30 mm (including the ground width) which is equal to half wavelength, making it a dual band design.

A vertical L shaped part (Section 'A', Fig. 2) is introduced in Step 3 in the feed part. As a result, the total length of the current path is almost doubled and the resonant frequency shifts from 3 GHz to 1.2 GHz while the protruded stub maintains the resonance at 4.5 GHz. But the circular polarization suffers because of the inclusion of section 'A' that makes the axial ratio value above 3 dB.

Finally, in Step 4, another horizontal L shaped part (Section 'B', Fig. 2) is embedded to achieve two almost equal current paths with 90° phase difference along Section 'A' and Section 'B' and thus circular polarization is again achieved with significant 3 dB axial ratio bandwidth in the desired frequency band. The horizontal L shaped part also

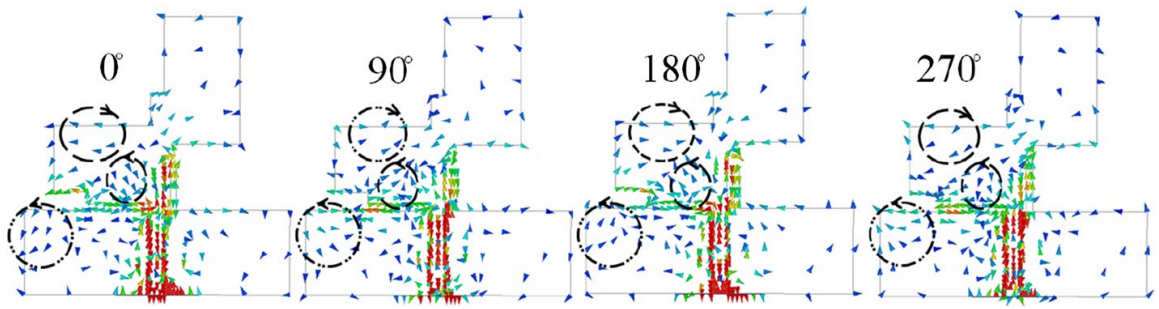

Fig. 7 Surface current distributions on the proposed antenna at 2.85 GHz for four different phases of excitations

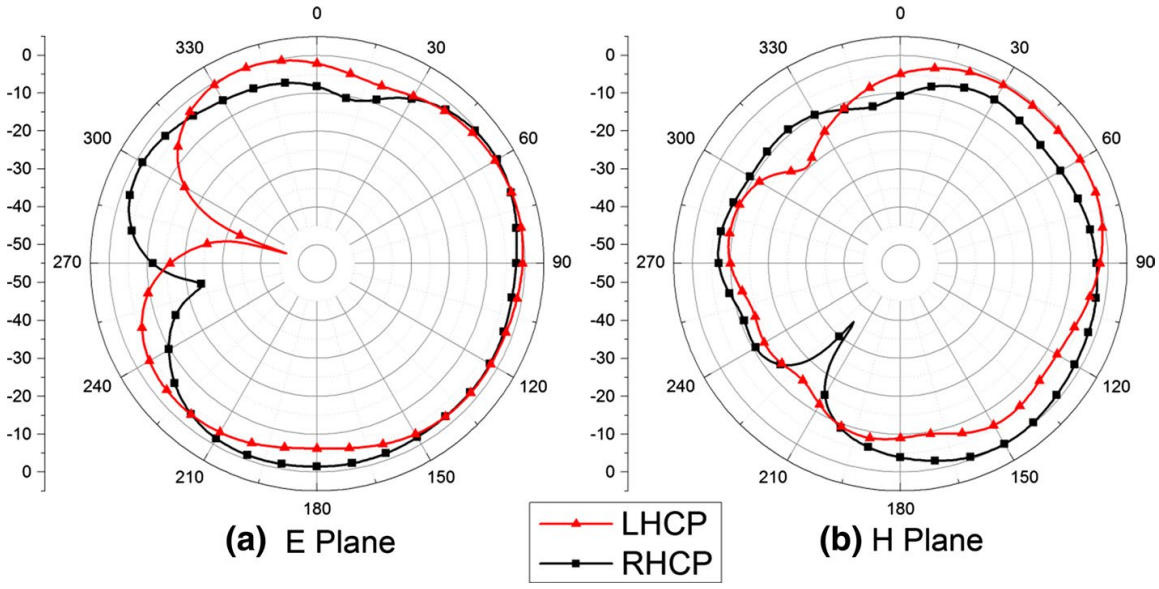

Fig. 8 Normalized LHCP and RHCP pattern at 2.85 GHz (**a**) E Plane (**b**) H Plane

includes another resonant frequency in between 2 GHz to 3 GHz with a current path length of about 33 mm as shown in Fig. 6a.

Step 2A confirms the outcome of inclusion of vertical L shaped part with the feed structure as explained in Step 3. Also, the absence of resonant frequency at 4.5 GHz as shown in Fig. 6c ensures the absence of protruding stub in Step 2A.

As shown in Fig. 6c, the reflection coefficient graph of Step 3A ensures the resonant frequency at 2.1 GHz as expected in the first approach due to the inclusion of the horizontal L shaped part along with Step 2A model and the absence of 4.5 GHz resonant band confirms that the protruded stub is still not incorporated.

Proper parametric optimization is carried out to merge all the resonant frequencies well below the -10 dB value of reflection coefficient so that the proposed structure can be suitably used in ultra-wideband wireless systems.

The surface current distribution of the final antenna is observed at four different phases (0°, 90°, 180°, 270°) for 2.85 GHz as shown in Fig. 7. Rotational current elements are encircled over four phases to ensure the circular polarization for the proposed structure. Simulated E plane and H plane radiation pattern in Fig. 8 affirm the dominance of Left Hand Circular Polarization (LHCP) over Right Hand Circular Polarization (RHCP) at 2.85 GHz.

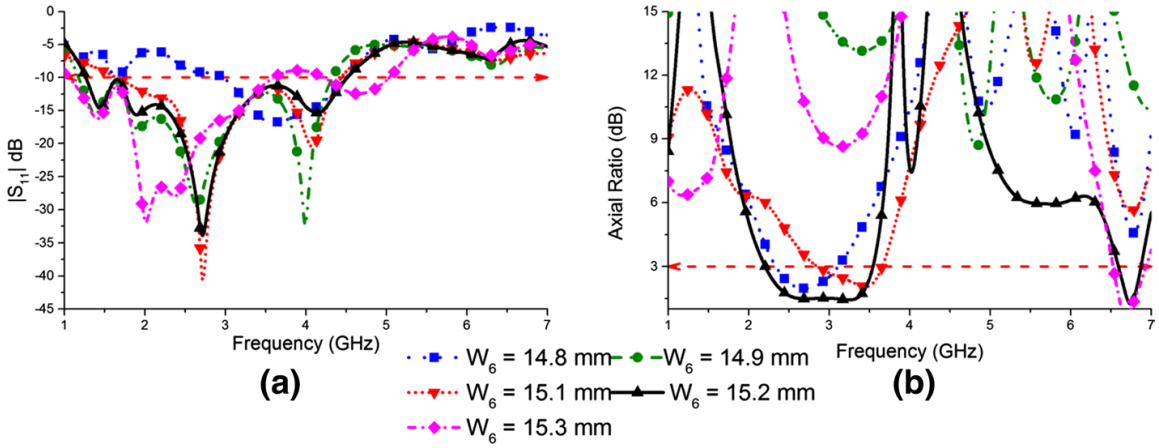

Fig. 9 Effect of length W_6 on (**a**) S_{11} (**b**) AR

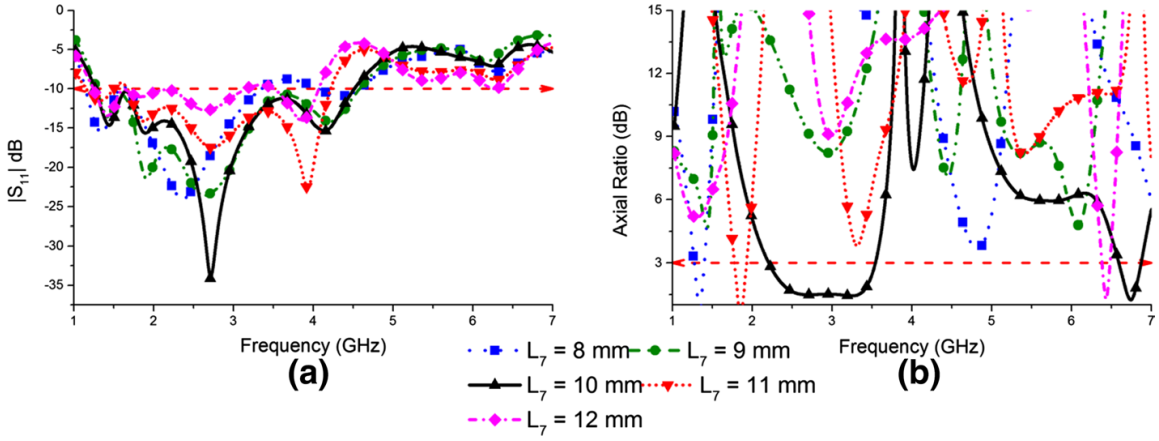

Fig. 10 Effect of length L_7 on (**a**) S_{11} (**b**) AR

3.2 Parametric Analysis

For this particular antenna configuration, even a small variation in four parameters, namely W_6, L_7, L_6, and W_3 causes significant changes in the antenna characteristics.

3.2.1 Effect of Parameter W_6 on Bandwidth and Axial Ratio

Figure 9 illustrates the influence of W_6 parameter on the return loss and axial ratio of the proposed antenna precisely. The length of W_6 is varied from 14.8 mm to 15.3 mm with an increment of 0.1 mm. Both 10 dB impedance bandwidth and 3 dB AR bandwidth are at their maximum level for $W_6 = 15.2$ mm.

3.2.2 Effect of Parameter L_7 on Bandwidth and Axial Ratio

Effect of length L_7 on reflection coefficient and axial ratio is considered in Fig. 10. Although the variation of L_7 between the range 8 mm to 12 mm does not show any

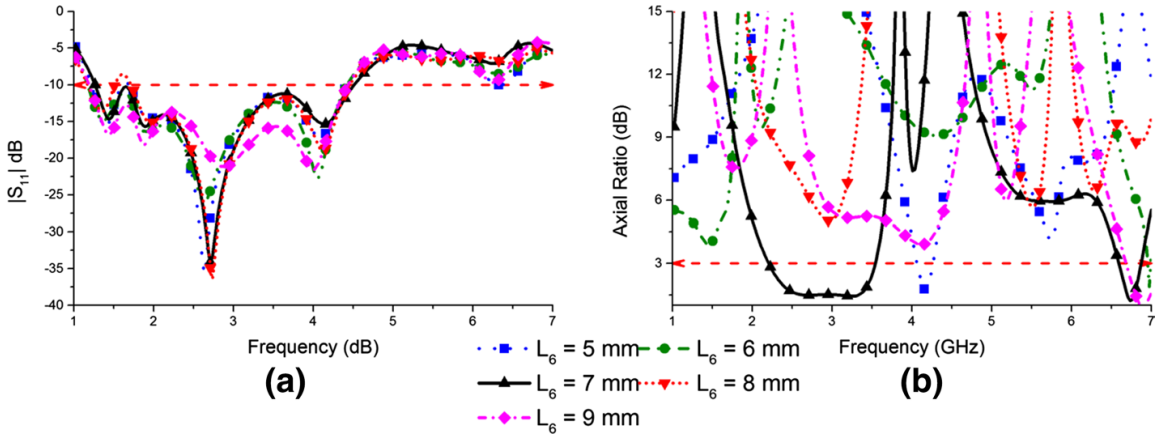

Fig. 11 Effect of length L_6 on (**a**) S_{11} (**b**) AR

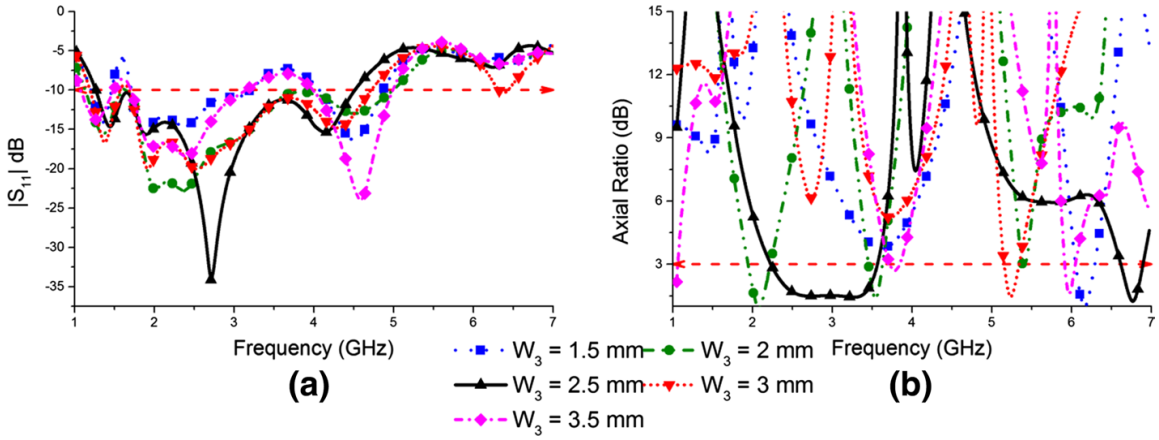

Fig. 12 Effect of length W_3 on (**a**) S_{11} (**b**) AR

significant change in 10 dB bandwidth but affects the AR bandwidth greatly. At $L_7 = 10$ mm 3 dB AR bandwidth attains its highest value of 1300 MHz.

3.2.3 Effect of Parameter L_6 on Bandwidth and Axial Ratio

The length of L_6 is another important parameter for influencing the axial ratio bandwidth as shown in Fig. 11. However, its effect on S_{11} is almost negligible. The maximum 3 dB AR bandwidth is obtained at $L_6 = 7$ mm.

3.2.4 Effect of Parameter W_3 on Bandwidth and Axial Ratio

The parameter W_3 is also one of the prime factors for deciding S_{11} and AR bandwidth for the proposed antenna. The length of W_3 is varied from 1.5 mm to 3.5 mm with an increment of 0.5 mm. Maximum 10 dB impedance bandwidth and 3 dB AR bandwidth are obtained with $W_3 = 2.5$ mm as shown in Fig. 12.

Thus, it can be concluded that the optimal design for 10 dB impedance bandwidth and 3 dB AR bandwidth, is obtained with $W_6 = 15.2$ mm, $L_7 = 10$ mm, $L_6 = 7$ mm and $W_3 = 2.5$ mm.

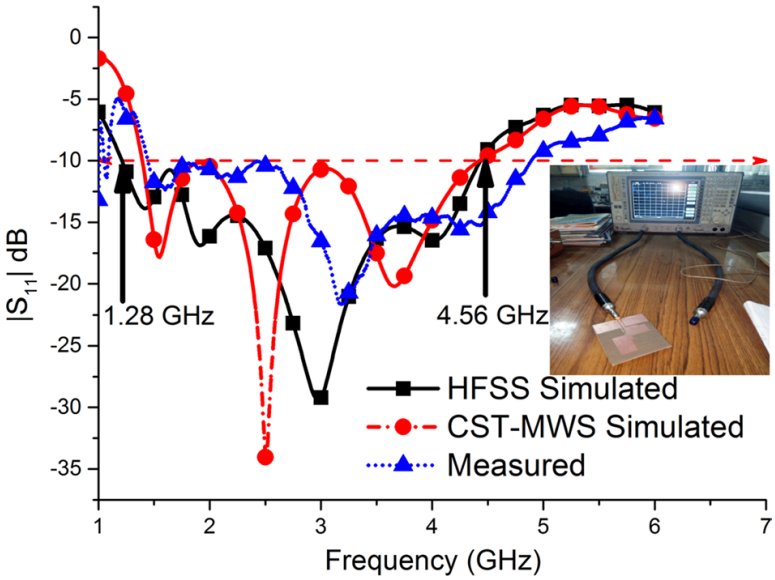

Fig. 13 Simulated and measured S_{11}

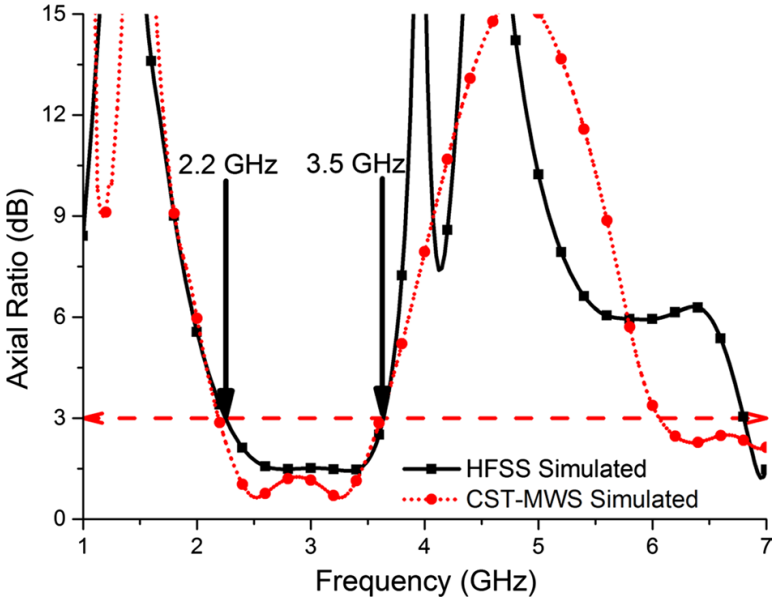

Fig. 14 Simulated axial ratio

4 Result Analysis and Discussion

4.1 Antenna Performance

Two simulation results along with the experimental result for S_{11} are presented in Fig. 13. Both of the simulation results, almost confirm the 10 dB impedance bandwidth of 111.4% (1.28 to 4.56 GHz). The simulated 3 dB AR bandwidth obtained from HFSS and CST is 45.61% (2.2 to 3.5 GHz) as shown in Fig. 14. From Fig. 13, it is evident that there is some deviation in S_{11} of the simulated antenna model and the prototype model and this deviation is maximum at the frequency around 4.56 GHz. The difference in the two results may be attributed to the fabrication errors along with variation in the substrate parameter used in fabrication. The proposed antenna design becomes worthy because of its ability to combine several bands for achieving wide bandwidth. As per FCC standard, the UWB antennas must possess a fractional bandwidth of the order of greater than 20%. The proposed antenna exhibits a fractional bandwidth of 1.11, therefore it can be considered for UWB

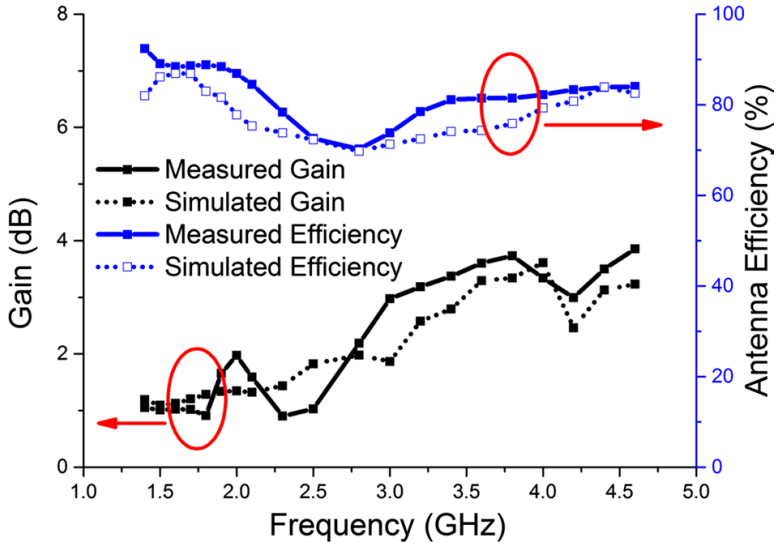

Fig. 15 Gain and Antenna Efficiency for the proposed antenna

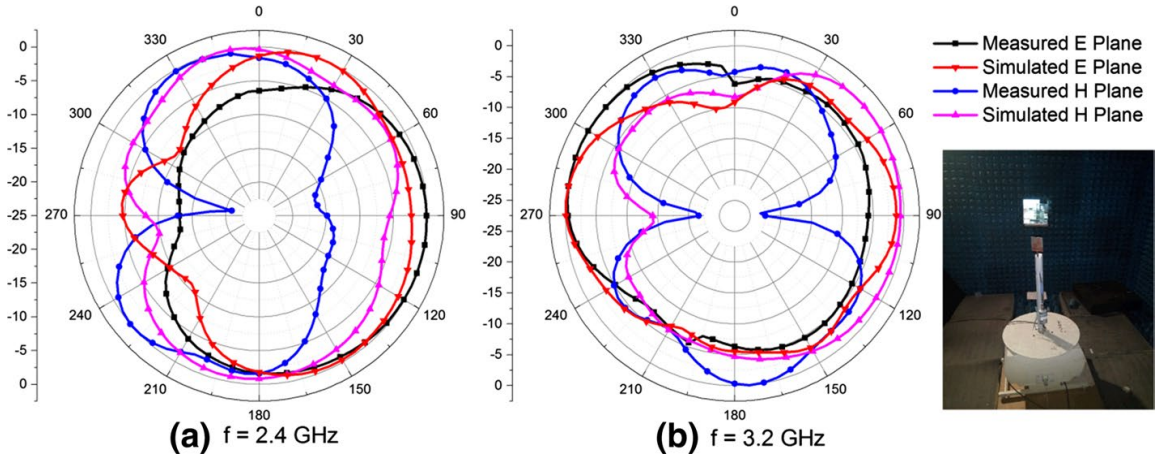

Fig. 16 E plane and H plane radiation pattern at (**a**) 2.4 GHz (**b**) 3.2 GHz

Table 2 Performance Comparison table

Reference	Dimension (mm^3)	Impedance bandwidth (%)	Axial ratio bandwidth (%)	Peak gain
[15]	73×65×1.6	71.63	27.45 and 7.1	2.5 dB
[16]	65.5×42.4×1.6	20.9	4.7	7 dBic
[17]	50×50×1.524	19.5	12.9	9.8 dBi
[18]	25×25×0.80	52	16.6	3.6 dBic
Proposed Work	73×65×1.52	111.4	45.61	3.5 dB

application. The gain and efficiency of this antenna over the achieved bandwidth lies in between 1.5 and 3.5 dB as shown in Fig. 15. The normalized E plane and H plane radiation patterns at 2.4 GHz and 3.2 GHz for the proposed antenna confirm almost omnidirectional characteristics as sketched in Fig. 16. A comparative study is carried out to compare the characteristics of the proposed antenna with some other references, and is listed in Table 2.

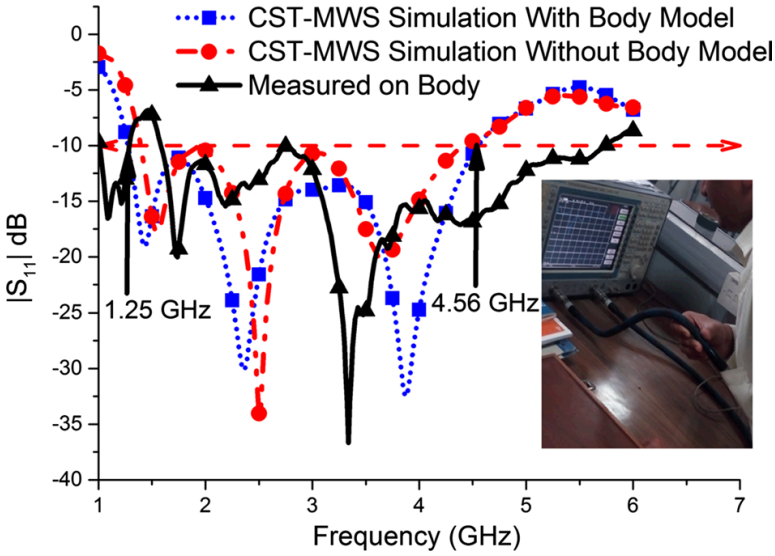

Fig. 17 On body measurement of S_{11}

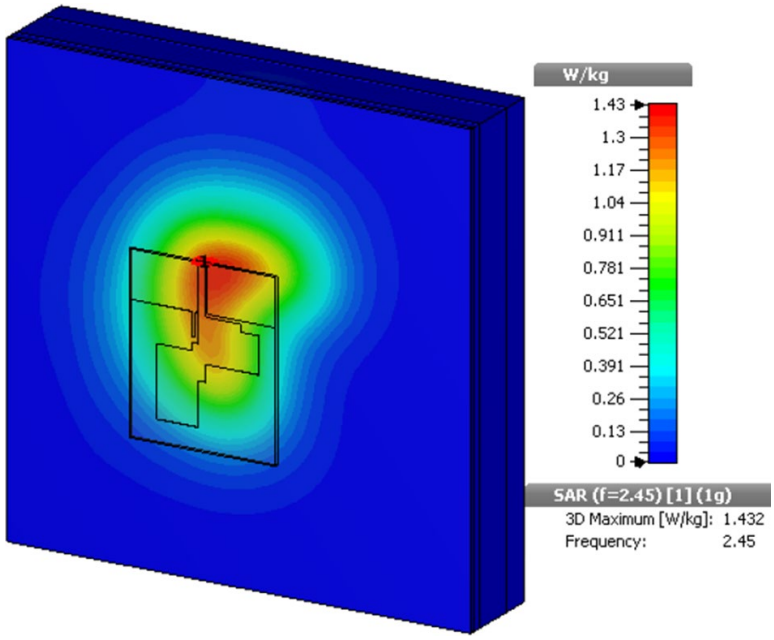

Fig. 18 Evaluated SAR with CST-MWS at 2.45 GHz

4.2 On Body Measurement

The simulated and experimental measurement of the reflection coefficient under on body condition is shown in Fig. 17. It confirms the acceptance of the presented wearable antenna for UWB application. To accept the proposed antenna for wearable application, the SAR value should be limited to 1.6 W/kg over 1 g of tissue mass as per the Federal Communication Commission (FCC) and to 2 W/kg over 10 g tissue mass as per the International Electrotechnical Commission (IEC). The SAR calculation of the proposed antenna is carried out with CST-MWS software assuming an input power of 0.5 W. The SAR value for the exposed body model is obtained as a maximum value of 1.43 W/kg and 1.19 W/kg over 1 g and 10 g average models at 2.45 GHz respectively as shown in Fig. 18 which satisfy its acceptability as wearable antenna. Table 3 includes a comparison of SAR values among a few wearable antennas operating at 2.45 GHz to examine the suitability of the proposed antenna for body worn application. The radiation gain pattern with body model in Fig. 19

Table 3 SAR Comparison table

References	Frequency considered (GHz)	Max SAR (W/kg)	Averaged mass
[10]	F = 2.45	6.62 (Without EBG)	10 g Tissue
[19]	F = 2.45	1.88 (Without EBG)	1 g Tissue
[20]	F = 2.45	0.14	10 g Tissue
[21]	F = 2.45	13.12 (Without Ferrite Sheet) 7.23 (Without Ferrite Sheet)	1 g Tissue 10 g Tissue
[22]	F = 2.45	0.316	10 g Tissue
[23]	F = 2.45 F = 2.45	2 (Diode is off) 0.29 (Diode is on)	1 g Tissue 1 g Tissue
Proposed Work	F = 2.45	1.43 1.19	1 g Tissue 10 g Tissue

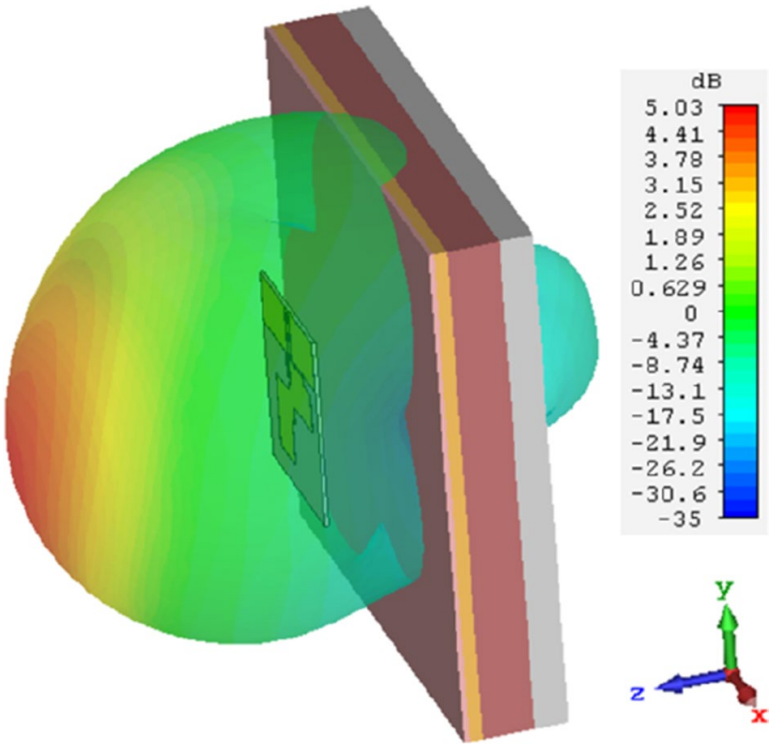

Fig. 19 Radiation gain pattern with body model

shows that the gain has its maximum value in the outward direction, thus protecting the body from the antenna radiation exposure.

4.3 Time Domain Performance

The time domain analysis of the UWB antennas has significant importance as those antennas impose a severe impact on the waveforms [24]. Thus a satisfactory time domain performance needs to be considered in the designing of UWB antennas. For this proposed antenna, two time-domain characteristics, group delay and waveform response, are analysed using post-processing tools of CST-MWS. A linear phase response (constant group delay) is required to overcome waveform distortion over the desired frequency range [25]. The group delay curve of the proposed antenna

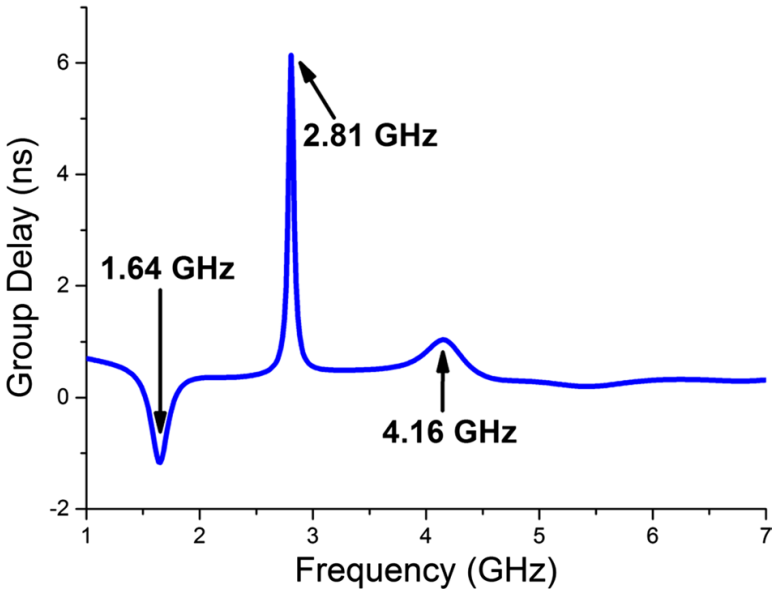

Fig. 20 Group delay of the proposed antenna

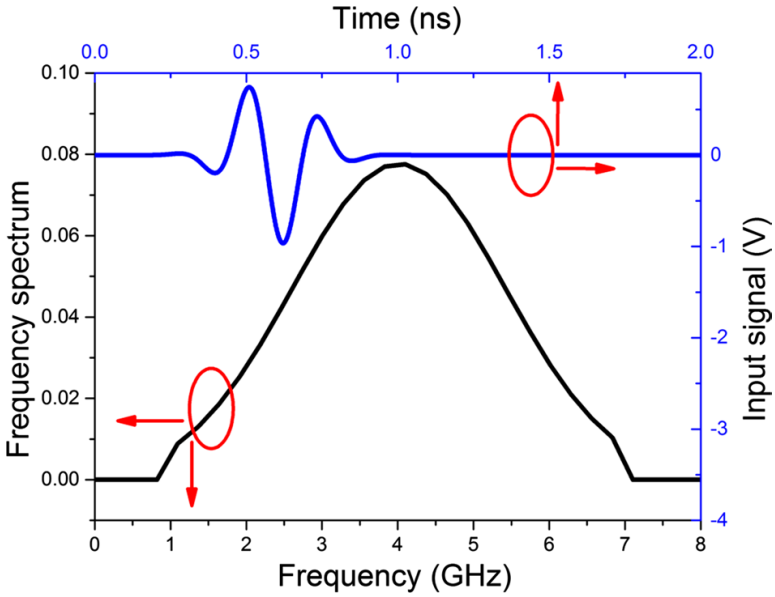

Fig. 21 Input signal at the antenna terminal

is exhibited in Fig. 20. It shows an almost ignorable variation on broader bandwidth except for distortions at three center frequencies of 1.64 GHz, 2.81 GHz, and 4.16 GHz.

The waveform response allows intuitionistic understanding of antenna performance [25]. As illustrated in Fig. 21, a transient Gaussian pulse is taken as the input signal for the proposed antenna. This Gaussian pulse has a frequency range from 1 to 7 GHz. The

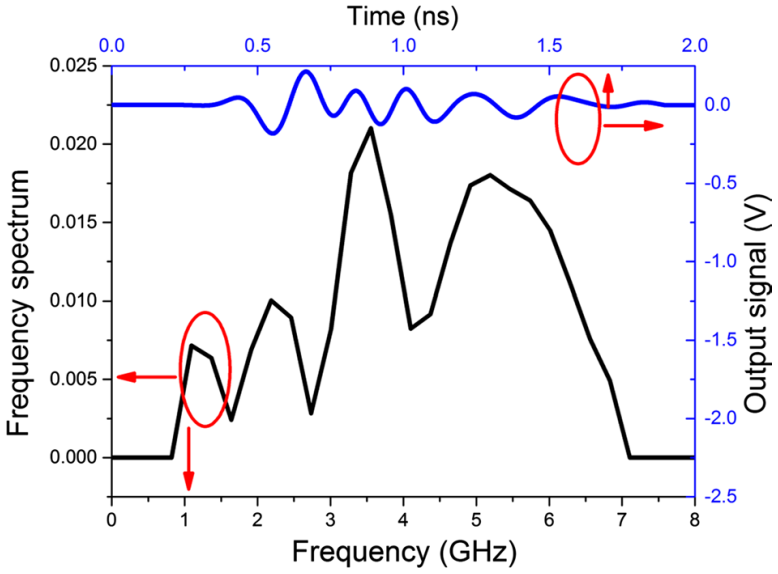

Fig. 22 Output signal at the antenna terminal

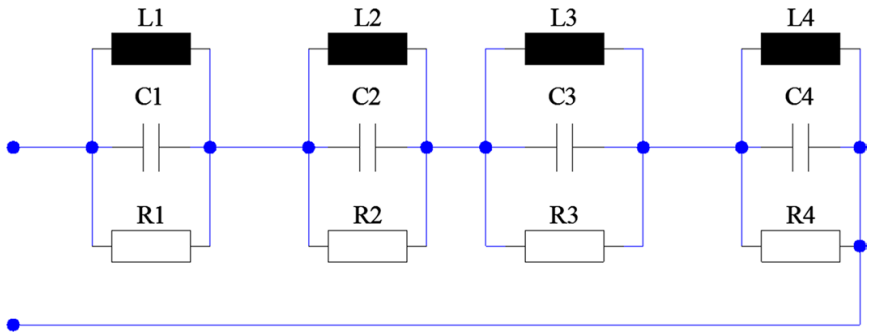

Fig. 23 Equivalent circuit model of the proposed antenna

signal at the output terminal is presented in Fig. 22 for comparison. It is found from the Fig. 22 that, the output waveform is attenuated by four-fold and ringing distortions are present at the frequencies of 1.64 GHz, 2.81 GHz, and 4.16 GHz. However, the output frequency spectrum almost holds the same pattern as the input frequency spectrum.

5 Equivalent Circuit Model

In this section, an equivalent lumped circuit model of the proposed antenna is developed. As shown in Fig. 23, the concept of cascaded resonant parallel RLC circuits is considered for constructing this equivalent circuit model [26, 27]. The S_{11} output from the equivalent model is compared with that of the CST-MWS model in the Fig. 24 in order to comprehend and predict the wideband response.

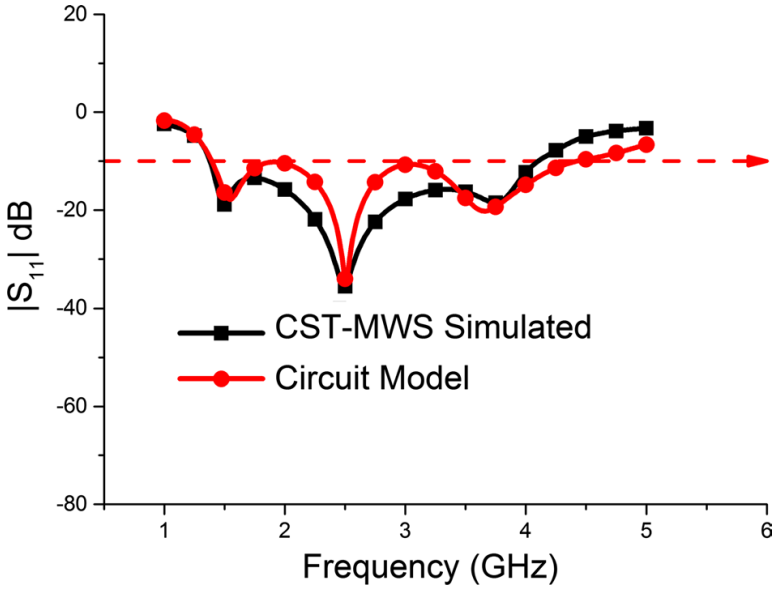

Fig. 24 S_{11} results from CST-MWS and Circuit model

6 Conclusion

In this proposed work, the advantage of a rigid, compact, monopole like structure is considered for wearable antenna application to overcome the effect of body bending, cloth crumpling and cloth washing on antenna characteristics. A detailed description of antenna geometry has been presented for achieving an ultra-wide 10 dB impedance bandwidth (111.4%) and a significant AR bandwidth (45.61%). Satisfactory time domain characteristics are also displayed over the desired frequency band. The proposed antenna is expected to be useful in wide applications in GPS-L1 (1575.42 MHz), DCS-1800 (1710–1880 MHz), PCS-1900 (1850–1990 MHz), Bluetooth (2400–2480 MHz), WLAN (2400–2484 MHz, 3657–3692 MHz), ISM band (2400–2500 MHz), WiMAX (2500–2690 MHz, 3200–3800 MHz). The SAR analysis using a four-layered body model is also carried out in order to examine its acceptance in the wearable application. It is observed that the amount of maximum radiation absorbed by the body model is limited to a maximum SAR value of 1.19 W/kg and 1.43 W/kg over 1 g and 10 g tissue mass respectively. More patterns of L shapes could be appended to obtain more resonating frequencies in the proposed design. However, merging all the resonating frequencies to achieve larger bandwidth and axial ratio require very efficient matching techniques.

Compliance with Ethical Standards

Conflict of interest The authors report no conflicts of interest. The authors alone are responsible for the content and writing of the paper.

References

1. Bharadwaj, R., Swaisaenyakorn, S., Parini, C. G., Batchelor, J. C., Alomainy, A., et al. (2017). Impulse radio ultra-wideband communications for localization and tracking of human body and limbs

movement for healthcare applications. *IEEE Transactions on Antennas and Propagation, 65*(12), 7298–7309.
2. Gao, Y., Zheng, Y., Diao, S., Toh, W. D., Ang, C. W., Je, M., et al. (2011). Low-power ultrawideband wireless telemetry transceiver for medical sensor applications. *IEEE Transactions on Biomedical Engineering, 58*(3), 768–772.
3. Singh, V. K., Dhupkariya, S., Bangari, N., et al. (2017). Wearable ultra wide dual band flexible textile antenna for WiMax/WLAN application. *Wireless Personal Communications, 95*(2), 1075–1086.
4. Bolaños-Torres, M. Á., Torrealba-Meléndez, R., Muñoz-Pacheco, J. M., del Carmen Goméz-Pavón, L., Tamariz-Flores, E. I., et al. (2018). Multiband flexible antenna for wearable personal communications. *Wireless Personal Communications, 100,* 1–12.
5. Alqadami, A. S. M., & Jamlos, M. F. (2014). Design and development of a flexible and elastic UWB wearable antenna on PDMS substrate. In 2014 *IEEE Asia-Pacific conference on applied electromagnetics (APACE)* (pp. 27–30). IEEE.
6. Ahmed, M. I., Ahmed, M. F., Shaalan, A. E. H., et al. (2018). SAR calculations of novel textile dual-layer UWB lotus antenna for astronauts spacesuit. *Progress In Electromagnetics Research, 82,* 135–144.
7. Kumar, R., Kumar, P., Gupta, N., Dubey, R., et al. (2017). Experimental investigations of wearable antenna on flexible perforated plastic substrate. *Microwave and Optical Technology Letters, 59*(2), 265–270.
8. Lee, H., Tak, J., Choi, J., et al. (2017). Wearable antenna integrated into military berets for indoor/outdoor positioning system. *IEEE Antennas and Wireless Propagation Letters, 16,* 1919–1922.
9. Ashyap, A. Y., Abidin, Z. Z., Dahlan, S. H., Majid, H. A., Shah, S. M., Kamarudin, M. R., et al. (2017). Compact and low-profile textile EBG-based antenna for wearable medical applications. *IEEE Antennas and Wireless Propagation Letters, 16,* 2550–2553.
10. Velan, S., Sundarsingh, E. F., Kanagasabai, M., Sarma, A. K., Raviteja, C., Sivasamy, R., et al. (2015). Dual-band EBG integrated monopole antenna deploying fractal geometry for wearable applications. *IEEE Antennas and Wireless Propagation Letters, 14,* 249–252.
11. Bai, Q., Rigelsford, J., Langley, R., et al. (2013). Crumpling of microstrip antenna array. *IEEE Transactions on Antennas and Propagation, 61*(9), 4567–4576.
12. Jalil, M. E. B., Abd Rahim, M. K., Samsuri, N. A., Murad, N. A., Majid, H. A., Kamardin, K., et al. (2013). Fractal koch multiband textile antenna performance with bending, wet conditions and on the human body. *Progress In Electromagnetics Research, 140,* 633–652.
13. Scarpello, M. L., Kazani, I., Hertleer, C., Rogier, H., Ginste, D. V., et al. (2012). Stability and efficiency of screen-printed wearable and washable antennas. *IEEE Antennas and Wireless Propagation Letters, 11,* 838–841.
14. Dong, J., Yu, X., & Hu, G. (2016). Design of a compact quad-band slot antenna for integrated mobile devices. *International Journal of Antennas and Propagation*, *2016*, 3717681.
15. Saini, R. K., Dwari, S., Mandal, M. K., et al. (2017). CPW-fed dual-band dual-sense circularly polarized monopole antenna. *IEEE Antennas and Wireless Propagation Letters, 16,* 2497–2500.
16. Santosa, C. E., Sri Sumantyo, J. T., Urata, K., Chua, M. Y., Ito, K., Gao, S., et al. (2018). Development of a low profile wide-bandwidth circularly polarized microstrip antenna for C-band airborne CP-SAR sensor. *Progress In Electromagnetics Research, 81,* 77–88.
17. Ding, K., Gao, C., Qu, D., Yin, Q., et al. (2017). Compact broadband circularly polarized antenna with parasitic patches. *IEEE Transactions on Antennas and Propagation, 65*(9), 4854–4857.
18. Rafii, V., Nourinia, J., Ghobadi, C., Pourahmadazar, J., Virdee, B. S., et al. (2013). Broadband circularly polarized slot antenna array using sequentially rotated technique for *C*-band applications. *IEEE Antennas and Wireless Propagation Letters, 12,* 128–131.
19. Raad, H. R., Abbosh, A. I., Al-Rizzo, H. M., Rucker, D. G., et al. (2013). Flexible and compact AMC based antenna for telemedicine applications. *IEEE Transactions on Antennas and Propagation, 61*(2), 524–531.
20. Rais, N. H. M., Soh, P. J., Malek, M. F. A., Vandenbosch, G. A., et al. (2013). Dual-band suspended-plate wearable textile antenna. *IEEE Antennas and Wireless Propagation Letters, 12,* 583–586.
21. Augustine, R., Alves, T., Sarrebourse, T., Poussot, B., Mathew, K. T., Laheurte, J. M., et al. (2010). Polymeric ferrite sheets for SAR reduction of wearable antennas. *Electronics Letters, 46*(3), 197–198.
22. Fernandez, M., Espinosa, H. G., Thiel, D. V., & Arrinda, A. (2018). Wearable slot antenna at 2.45 GHz for off-body radiation: Analysis of efficiency, frequency shift, and body absorption. *Bioelectromagnetics, 39*(1), 25–34.

23. Saeed, S. M., Balanis, C. A., Birtcher, C. R., Durgun, A. C., & Shaman, H. N. (2017). Wearable flexible reconfigurable antenna integrated with artificial magnetic conductor. *IEEE Antennas and Wireless Propagation Letters, 16,* 2396–2399.
24. Akhoondzadeh-Asl, L., Fardis, M., Abolghasemi, A., & Dadashzadeh, G. R. (2008). Frequency and time domain characteristic of a novel notch frequency UWB antenna. *Progress In Electromagnetics Research, 80,* 337–348.
25. Peng, L., & Ruan, C. L. (2013). Design and time-domain analysis of compact multi-band-notched UWB antennas with EBG structures. *Progress In Electromagnetics Research, 47,* 339–357.
26. Chu, Q. X., & Yang, Y. Y. (2008). A compact ultrawideband antenna with 3.4/5.5 GHz dual band-notched characteristics. *IEEE Transactions on Antennas and Propagation, 56*(12), 3637.
27. Jam, S., & Malekpoor, H. (2016). Analysis on wideband patch arrays using unequal arms with equivalent circuit model in X-band. *IEEE Antennas and Wireless Propagation Letters, 15,* 1861–1864.

Publisher's Note Springer Nature remains neutral with regard to jurisdictional claims in published maps and institutional affiliations.

Saumya Das received B.Tech degree in Electronics and Telecommunication from Institute of Electronics and Telecommunication Engineers (IETE, India) and M.E in Electronics and Communication from Delhi College of Engineering, Delhi University in 2002 and 2010 respectively. Presently he is a research scholar at Sikkim Manipal Institute of Technology, India in Electronics and Communication department. His research interest includes different feeding techniques for microstrip and dielectric resonator antennas, Flexible and wearable antenna for tracking and medical application, Computational Mathematics for antenna designing, RF exposure testing on human bodies, Electromagnetic Compatibility etc.

Hashinur Islam completed his B.Tech in Electronics and Telecommunication from Institute of Electronics and Telecommunication Engineers (IETE, India) in the year 2014. Presently he is a final year M.Tech student of Sikkim Manipal Institute of Technology, India and doing his project on conformal microstrip antennas and dielectric resonator antennas. His area of interest includes multiband antennas, fractal antenna, circular polarization on antennas, feeding mechanism for antenna, PIFA antenna, and antenna for embedded systems etc. He has published two research papers in International Journals and three international conference papers.

Tanushree Bose was born in Ranchi, Jharkhand on 4th September 1979. She completed her PhD in Design of Printed Antennas using Neural Network in the Department of Electronics and Communication Engineering, B.I.T., Mesra, India in the year 2011. Presently, she is working as an associate professor in Sikkim Manipal Institute of Technology, India. She worked extensively in the field of RF and Microwave antennas with soft computation. Her current research interests are multiband antennas for handsets and networks, miniature antennas, reconfigurable antennas, EBG application on conformal antennas, flexible and wearable antennas, smart antennas etc. She has published over 50 refereed papers in journals and conference proceedings and has served on many national and international technical committees. She successfully completed one AICTE sponsored research project on Patch antenna designing using artificial neural network and successfully guided her research scholars.

Nisha Gupta received Bachelor's and Master's degrees in Electronics Telecommunication and Electrical & Electronics engineering both from Birla Institute of Technology, Mesra, Ranchi, India and also Ph.D. degree from the Indian Institute of Technology, Kharagpur, India. She was a Maintenance Engineer at Shreeram Bearings Ltd., Ranchi during 1982-83 and a Programmer at Ranchi University, Ranchi from 1983 to 1986. She was a Junior Scientific Officer in a DRDO sponsored project, at Department of Electronics and Electrical Communication Engineering, Indian Institute of Technology, Kharagpur, from 1986 to 1989 and a Institute Research Scholar and Research Associate (CSIR) in the same department from 1990 to 1996. She was a post doctoral fellow at University of Manitoba, Canada from 1997 to 1998 before joining the Department of Electronics and Communication Engineering, Birla Institute of Technology in 1999 as a Reader. Currently, she is a Professor and Head in the same department. She has authored and coauthored more than 40 technical journal articles. Her research interests are Computational Electromagnetics, RF circuits and Antennas for Wireless Communication and AI techniques in Wireless and Mobile Communication.

Check for updates

Article

Understanding the Nuances of Employees' Safety to Improve Job Satisfaction of Employees in Manufacturing Sector

Journal of Health Management
1–11
© 2019 Indian Institute of
Health Management Research
Reprints and permissions:
in.sagepub.com/journals-permissions-india
DOI: 10.1177/0972063419835125
journals.sagepub.com/home/jhm

Meha Joshi[1]

Abstract

Safety of employees is one of the important concerns of the manufacturing organizations and needs to be addressed carefully. It was once, not in ambit of focus but the realization of making safety management as an integral part of the organization is gaining pace. The research article attempts to study the influence of safety perception of the employees on their job satisfaction level in selected small and medium manufacturing enterprises of Uttarakhand in India. A self-developed 29 items scale was used to determine the safety level of employees and job satisfaction inventory by Paul and Spector was used for assessing the job satisfaction level of employees. Linear regression analysis was used to find the degree of influence of safety on job satisfaction level of employees. Stepwise multiple regressions were used to identify the safety factor which contributes the most for employee's job satisfaction. The research highlights positive influence of safety perception of employees on their job satisfaction level and draws attention towards safety as predictor of job satisfaction. Training and supervision and work procedures were identified as the most contributing factors to enhance job satisfaction of the employees. This study could be helpful for organizations to identify most contributing safety factor which lead to improving the level of job satisfaction among employees.

Keywords

Small and medium enterprises, training, safety, job satisfaction

Introduction

Micro, Small and medium enterprises (MSME) are emerging as an important sector of the economy over the last five decades. It can be considered as one of the most vibrant sectors of the economy. Small and medium enterprises have a vital role to play in the economic development of the country.

[1] Delhi School of Management, Delhi Technological University, New Delhi, India.

Corresponding author:
Meha Joshi, Delhi School of Management, Delhi Technological University, Shahbad Daulatpur, Main Bawana Road, Delhi, 110042, India.
E-mail: mehajoshi83@gmail.com

According to the estimates of Ministry of MSME, Government of India, the sector generates around 100 million jobs through over 46 million units situated throughout the geographical expanse of the country. The role of this sector can be well understood by its 38 per cent contribution to the nation's GDP and 45 per cent contribution to manufacturing sector.

MSME not only help in industrialization of the rural and urban areas but also help in creating employment opportunities to the people of the country, thereby combating regional imbalances. In twenty-first century with the growth of technology, the associated hazards also grew with it. The employees are exposed to various kinds of risks. Safety of employees is one of the important concerns of the manufacturing organizations and needs to be addressed carefully. It was once, not in ambit of focus but the realization of making safety management as an integral part of the organization is gaining pace. Assuming it as one of the prime responsibilities of the employer and issues of great concern, the government is paying more attention to the safety and health by formulating National Policy of Safety and Health at workplace. It is believed that if the employees feel safe at workplace, it increases their level of job satisfaction.

Literature Review

Small and medium enterprises hold a special place across the globe. They are the most vibrant and a constant source of growth for the national and international arena.

The economic integration of globe is changing the competitive spirit in which the businesses operate, requiring an expansion strategy to impact long-term growth and survival in a positive manner (Karagozoglu & Lindell, 1998).

According to Shridhar (2006), the small sector is emerging as one of the most important sectors for positively impacting the growth of national economies. Inherently, there are many disadvantages being faced by small and medium enterprises as they are transiting into the international environment (Chen & Huang, 2004).

In the manufacturing organization, employees are often faced with a lot of risk related to safety and health. These risks directly and indirectly affect business operations. Consequently, for a company to grow and prosper, it is pertinent that risks are effectively managed, because the organizational health, assets and opportunities can be better taken advantage of, if they are taken care of (Fuller, 1997). According to Husain (2010), Occupational safety is an important element of social responsibility. He defines safety as freedom from danger and injury, insuring against hurt and other dangers of risk.

According to Terry E. McSween (2003) unsafe work behaviour takes place as a result of the physical factors which have a bearing in pursuit of existing business.

It has been reported that in 2011–2012, the number of fatal accidents reported per 100,000 man days worked in India were 1,083 (Report of Labour Bureau, 2012). This rate is alarming and calls for existence of safety culture in the organization.

Safety culture can be defined as 'Assembly of characteristics and attitudes in an organization and individuals, which establishes that, as an overriding plant safety issues receive attention warranted by their significance' (International Atomic Energy Authority [IAEA], 1986).

Safety culture is an enduring feature of the organization and forms an integral part of organization culture (Kennedy & Kirwan, 1998).

Zohar emphasized the importance of safety culture by stating that it encourages employees to follow safety behaviour and it leads to the development of safety attitude.

To understand the state of organization with respect to safety, often safety surveys are employed as they can be best viewed as ideally predicting the state of safety performance of an organization. It has been suggested that safety climate surveys are good predictors of state of organizational safety performance as it does not suffer from traditional biases of reporting and post hoc analysis. Safety culture in particular is a relatively enduring characteristic of organization.

Ojanen, Seppala, and Aaltonen (1998) recommended that safety attitude determination should form an important aspect to understand the real safety level of the organization clubbed with other safety surveys. They claimed that changes in the safety behaviour of the employees in the organization can be indicated well through measuring safety climate, which can further be useful in evaluating the programmes and drive related to safety in the organization. Davies, Spencer, and Dooley (2001) described safety climate as current variation or nuances of long-term culture as the tangible outputs of an organization's health and safety culture, as perceived by individuals or work groups, at some point in time.

Safety climate in the organization can be evaluated typically using employee questionnaires to assess the attitude. Various researchers have emphasized on different aspects of safety to assess the safety level in the organizations.

According to Prakash (2010), safety training is a safety measure to enable workers to handle unforeseen hazards.

Richter and Koch (2004) indicated that employee involvement is also important by defining it as the shared and learned meaning, experiences and interpretation of work and safety, expressed symbolically and which guides people. Husain (2010) reinstated in his study that employee involvement is a behaviour-oriented technique involved in the employees in the upward communication flow and decision-making process of the organization. In a study by Fleming (2001), four factors were found to be having a positive impact on how people perceive safety and they are valuing their subordinates, frequently visiting worksites, safety communication and participation of workers in management

Guest, Peccei, and Thomas (1994) in his study found that communication is an important issue to reinforce safety culture. Mearns, Flin, and Whitaker (2001) pinpointed that likelihood of accident is more in absence of job communication and thus it supported the view that safety communication is important for reducing risk of safety and for ensuring safety culture. Reason (1997) studied the importance of safety reporting in the organization. The study by Guest et al. (1994) indicated the existence of 'macho' attitude among the workers towards safety and studied the importance of involvement and participation of staff. Thus for the assessing the safety level of employees in the organization, the various parameters can be used.

Job Satisfaction

The concept of employee satisfaction has been a focus for research and practice for the last two decades in particular (Greasley et al., 2005) and considered to be a critical issue for organizational performance. A number of scholars and management 'gurus' stressed the importance of employee satisfaction and its influences on organizational performance as much as customer satisfaction (Chen et al., 2006). The concept of employee satisfaction is a multi-dimensional and interdisciplinary term that has attracted the attention of researchers and practitioners from different disciplines such as psychology, human resource management, organizational behaviour, TQM and so forth. However there is no universal definition of employee satisfaction that exposes all these dimensions at the same time (Bernal, Castel, Navarro, & Torres, 2005).

Most of the definitions emphasize the importance of employees' job-related perceptions that link the expectations of them and what they receive in return. Some researchers focus on the overall job satisfaction or even life satisfaction of employees (Judge et al., 2005).

There are several studies showing the relationship between safety and job satisfaction. In one of the studies by Havold (2007), it was established that there is positive correlation between safety and job satisfaction. Job satisfaction is associated with the indicators of safety and safety perception (Gyekye & Salminen, 2006). Nielsen, Mearns, Mattheisen, and Eid (2011) stated the existence of positive correlation between job satisfaction and safety climate. Ongoing through the literature review, it was established that there is a dearth of research evidence available in India in the area of safety, health and welfare of employees with respect to the manufacturing concerns of small and medium type of organizations.

Objectives of the Study

1. To determine that whether there is any significant difference in the safety perception level with respect to nature of industry.
2. To determine that whether there is any significant difference in the safety perception level with respect to type of organization.
3. To study the impact of safety perception level on job satisfaction level of employees.
4. To determine the safety factor which contributes the most towards the job satisfaction level of employees.

Hypotheses of the Study

H_1: There is no significant difference in the perception of employees regarding safety levels among groups based on nature of industry (chemical, packaging, automobile, food, safety equipment, heavy equipment).

H_2: There is no significant difference in the perception of employees regarding Safety levels between among groups based on type of organization (small or medium).

H_3: There is no significant impact of perception of employees about safety levels of organization on job satisfaction levels of employees.

Research Design

The framework within which the research was conducted was basically descriptive in nature and the target population in this regard is defined as consisting of 215 shop floor employees of small and medium type in manufacturing organizations in Sitarganj area of SIDCUL (State Infrastructure Development Corporation of Uttarakhand Ltd) in India. The research was conducted on shop floor employees of 15 organizations belonging to six types of manufacturing industries that is, chemical, automobile, packaging, food, safety equipment, heavy equipment. Stratified random sampling method was adopted for selecting the samples. The respondents' age varied from 20 years to 50 years. Survey methods were used to collect data from respondents with the help of self-administered questionnaires.

A self-developed scale comprising 29 items clubbed into eight factors was used to determine the safety perception level of employees on a 5-point Likert scale. This questionnaire was the result of extensive literature review conducted. In the process of literature review, eight factors were identified for determining the safety perception of employees. Job satisfaction inventory by Paul and Spector was used for assessing the job satisfaction level of employees. For both the scales 1 meant Strongly disagree, 2 meant Disagree, 3 meant Neutral, 4 meant Agree, 5 meant Strongly agree. The process of data collection took a period of over 3 months. Participation of workers in the survey was voluntary. Safety perception of employees was measured using a self-developed 29 item scale with eight factors of safety, that is, safety training and supervision, involvement of staff, work procedures, safety reporting culture, management commitment towards safety, injury management, communication and safety leadership. For assessing the job satisfaction level of employees, the scale developed by Spector was used. This was chosen as it is considered as a reliable and most common inventory for assessing the level of job satisfaction. On both the inventories, reliability analysis was done by using Cronbach's alpha test and the score came out to be more than 0.7 which indicated that the statements are internally consistent. One way analysis of variance (ANOVA) was used to measure the industry variations (nature of industry) and type of organization (small or medium) variations on safety perception of employees. Linear regression analysis was used to find the degree of influence of various factors of safety on job satisfaction level of employees. Stepwise multiple regressions were used to determine the factor which contributes the most towards safety of the organization.

Data Analysis

Table 1 shows the mean and standard deviation of responses obtained from the respondents on 29 items scale put into eight factors of safety. The self-developed scale aimed at finding the level of safety perception of employees with respect to various factors responsible for ensuring safety in the organization. The factors with their mean scores and standard deviations are as follows:

From Table 1, it can be established that employees showed strong agreement to the factors such as safety training and supervision, involvement of staff, safety leadership, communication, work procedures and safety reporting culture whereas they showed slight disagreement towards factors pertaining to injury management and commitment of management towards safety.

Table 1. Mean and Standard Deviation of Responses for Various Factors of Safety

Factors	Mean	Standard Deviation
Safety training and supervision	4.31	0.56
Involvement of staff	4.25	0.73
Work procedures	4.18	0.61
Safety reporting culture	4.23	0.64
Management commitment towards safety	2.10	0.58
Injury management	2.15	0.89
Communication	4.23	0.71
Safety leadership	4.34	0.70

Source: The authors.

H_1: There is no significant difference in the perception of employees regarding safety levels among groups based on nature of industry (chemical, packaging, automobile, food, safety equipment, heavy equipment).

The effects of nature of industry on employees' perception were studied using one-way ANOVA test. The test was performed to find out whether there is any significant difference among the group using ANOVA with all groups taken together. The results of ANOVA are presented in Table 2. It is evident from *F*-value (2.3) and *p*-value (0.045) which is less than 0.05) that there is a significant difference in employees' perception about safety with respect to six different types of industries, that is, chemical, automobile, packaging, food, safety equipment and heavy equipment.

Thus the null hypothesis (H_1) stating that there is no significant difference in the perception of employees regarding safety levels among different types of industries is not accepted and alternate hypothesis stating that there is a significant difference in the perception of employees with respect to different types of industries is accepted.

H_2: There is no significant difference in the perception of employees regarding safety levels among different groups based on the type of organization (small or medium).

The effects of type of organization on employees' perception were studied using one-way ANOVA test. The test was performed to find out whether there is any significant difference among the group using ANOVA with all groups taken together. The results of ANOVA are presented in Table 3. It is evident from *F*-value (0.298) and *p*-value (0.58 which is more than 0.05) that there is no significant difference in employees' perception about safety with respect to two different types of organizations, that is, small and medium.

Thus the null hypothesis (H_2) stating that there is no significant difference in the perception of employees regarding safety levels among different types of organizations is rejected.

H_3: There is no significant impact of perception of employees about safety levels of organization on job satisfaction levels of employees.

The bivariate relationship between job satisfaction and safety perception was tested using the responses gathered from employees. SPSS 21software was used for this purpose. The results of the same

Table 2. Analysis of Variance of Various Factors of Safety with Respect to Nature of Industry

Nature of Industry	*N*	Mean	Standard Deviation	*F*-value	*P*-value
Chemical	45	3.7322	0.520		
Automobile	31	3.8708	0.594		
Packaging	72	3.9271	0.441		
Food	21	3.6955	0.128	2.315	0.045
Safety	9	3.9438	0.081		
Heavy equipment	37	3.9872	0.352		
Total	215	3.8666	0.451		

Source: The authors.

Table 3. Analysis of Variance for Safety Perception with Respect to Type of Organization

Type of organization	*N*	Mean	Standard Deviation	*F*-value	*P*-value
Small	84	3.84	0.41		
Medium	131	3.88	0.47	0.298	0.586
Total	215	3.86	0.45		

Source: The authors.

Table 4. Bivariate Correlationship Between Safety and Job Satisfaction

		Job Satisfaction	Safety
Job satisfaction	Pearson correlation	1	0.798*
	Sig. (2-tailed)		0.000
	N	215	215
Safety	Pearson correlation	0.798*	1
	Sig. (2-tailed)	0.000	
	N	215	215

Source: The authors.
Note: *Correlation is significant at the 0.01 level (2-tailed).

are shown below in Table 4. The overall perception of employee towards safety was found to be positively correlated, that is, 0.798 at significance level of 0.01 indicating that there exists a positive relationship between safety perception of workers and job satisfaction level of employees, thereby indicating that safety perception can be used for predicting the job satisfaction level of employees.

Linear regression analysis was performed to investigate the relationship between the impacts of employees' perception about safety on job satisfaction of employees. The perception of employees towards safety (independent factor) was treated as a predictor variable for job satisfaction level (dependent factor). The results are presented in Table 5.

The results of *F*-statistics with respect to safety perception indicate that the equation is significant as $p < 0.01$ and hence it can be used for explanation purpose. The R^2 value (0.597) indicates that safety perception explains 63.9 per cent of variance in the dependent variable and from the table, it can be inferred that statistics for both independent and dependent variables have come out to be significant as $p < 0.01$ in explaining the variation. Hence null hypothesis (H_3) stating that there is no significant impact of perception of employees about safety level of employees on job satisfaction is not accepted and alternate hypothesis stating that there is significant impact of perception of employees about safety level of employees on job satisfaction is accepted.

Stepwise multiple regressions for predicting the most contributing factor towards safety in the organization.

The model summary shows that value of R^2 is 0.394 (model 1) shows that 39.4 per cent changes in response variable (job satisfaction). It is because of changes in controlled variable (work procedures). This explains that safe work procedure is the major contributing factor to job satisfaction. In model 2, the value of R^2 is 0.489 ($R = 0.674$) which shows that 48.9 per cent changes in response variable occurred is due to two controlled variable (Training and Supervision and work safety). By comparing both the variables, model 2 is a better fit to the data than model 1. This is because the higher the value of R^2, the better the model fits into the data.

Table 5. Result of Linear Regression Analysis

R = 0.798 R^2 = 0.639	Adjusted R^2 = 0.597 Standard Error of the Estimate = 0.174	F = 40.188	Significance 0.000*
Factor	Beta	T	Significance
Safety perception	0.456	6.339	0.000**

Source: The authors.
Note: *Indicates $p < 0.01$.

Table 6. Model Summary

Model	R	R^2	Adjusted R^2	Std Error of the Estimate
1	0.640[a]	0.394	0.380	0.90799
2	0.674[b]	0.489	0.463	0.89226

Source: The authors.

Table 7. ANOVA

ANOVA[a]						
Model		Sum of Squares	*df*	Mean Square	*F*	Sig.
1	Regression	42.206	1	42.206	51.192	0.000[b]
	Residual	175.608	213	0.824		
	Total	217.814	214			
2	Regression	49.034	2	24.517	80.795	0.000[c]
	Residual	168.780	212	0.796		
	Total	217.814	214			

Source: The authors.
Notes: a. Dependent variable: job satisfaction.
b. Predictors: (constant), training and supervision.
c. Predictors: (constant), training and supervision, work procedures.

This part of analysis helps in testing that whether the model best predicts the outcome. Here in the table, for the first model the value of F ratio is 51.19 which is likely to be not happened by chance ($p < 0.001$) whereas for the second model the value of F ratio is 80.79, which is highly significant. Thus we can conclude that the model 2 can better help in predicting the outcome variable.

Table 8 can be divided into two parts. The first part contains training and supervision and the second part contains two variables, that is, training supervision and work procedures. In this table, we need concentrate on model 2 as it contains all the predictor variables that make significant contribution to predict the job satisfaction (outcome variable). The B-value here tells about the relationship between predictor variables and job satisfaction. The positive B-value of the predictor variables indicates that there is a positive relationship between the variables in both the models. Since the t-statistics associated with B-value is coming to be significant in both cases, they can be taken as predictors of job satisfaction. However the training and supervision seem to be having a slightly large impact on

Table 8. Model Parameters

Model		Unstandardized Coefficients		Standardized Coefficients		
		B	Std Error	Beta	*T*	Sig.
1	(Constant)	0.490	0.475		1.031	0.304
	Training and supervision	0.780	0.109	0.440	7.155	0.000
2	(Constant)	0.605	0.504		−0.130	0.897
	Training and supervision	0.568	0.129	0.320	4.386	0.000
	work procedures	0.352	0.120	0.214	2.929	0.004

Source: The authors.

outcome as compared to work safety because the lower the significance value, the more contribution it is making on the outcome. From the magnitude of *t*-statistics, training and supervision has slightly more impact than work procedures.

Discussion

The results highlight that there is a significant difference in the perception of safety level of employees based on the nature of industry but there is no significant difference in safety perception level of employees based on small and medium enterprises.

The results from the sample of small and medium enterprises' employees of manufacturing concerns also show that there exists a strong correlation between safety level of employees and job satisfaction level of employees. The existence of relationship between job satisfaction and safety is further supported by the previous studies by Huang (2004). which says that there is a relationship between safety and job satisfaction. Additionally, occupational safety and health (OSH) can also increase employees' job satisfaction. This is similar to the statement that the company's OSH policy is an investment in human resources, not only with regard to the workplace physical safety but also because it could also improve employee satisfaction (Huang, 2004). As a result of the present study conducted, the following equation can be used to predict the level of job satisfaction on the basis of safety level of employees.

$$\text{Job satisfaction} = 1.93 + 0.456 \times \text{safety perception}$$

This equation can help one to predict the level of job satisfaction of employees on the basis of safety perception of employees.

Moreover, from the study it was established that the safety factors which contribute the most towards job satisfaction level of employees are

1. training and supervision and
2. work procedures.

This clearly shows that if organizations wish to increase the job satisfaction level of employees, they need to provide better safety training and supervision to the employees and keeping the work procedures safe would help in increasing the job satisfaction level of the employees.

Future studies may be conducted to examine and investigate the relationship between variables using longitudinal designs of study. The study can also be further extended to finding out the relationship between safety, job satisfaction and organizational productivity.

Conclusion

It can be concluded that in order to increase job satisfaction level of employees, the safety perception level of employees needs to be worked upon. Moreover imparting effective training and improving the work procedures can be very instrumental in enhancing the job satisfaction level of employees, which can further lead to improved safety culture.

Declaration of Conflicting Interests

The author declared no potential conflicts of interest with respect to the research, authorship and/or publication of this article.

Funding

The author received no financial support for the research, authorship and/or publication of this article.

References

Bernal, J. G., Castel, A. G., Navarro, M. M., & Torres, P. R. (2005). Job satisfaction: Empirical gender differences. *Women in Management Review*, *20*(4), 279–288.

Chen, H. L., & Huang, Y. (2004). The establishment of global marketing strategic alliances by small and medium enterprises. *Small Business Economics*, *22*(5), 365–377.

Chen, S. H., Yang, C. C., Shiau, J. Y., & Wang, H. H. (2006). The development of an employee satisfaction model for higher education. *The TQM Magazine*, *18*(5), 484–500.

Davies, F., Spencer, R., & Dooley, K. (2001). *Summary guide to safety climate tools*. Sudbury: HSE Books.

Fleming, M. (2001). *Safety culture maturity model*. Sudbury: HSE Books.

Fuller, C. W. (1997). Key performance indicators for benchmarking health and safety management in intra- and inter-company comparisons. *Benchmarking for Quality Management & Technology*, *4*(3), 165–174.

Greasley, K., Bryman, A., Dainty, A., Price, A., Soetanto, R., & King, N. (2005). Employee perceptions of empowerment. *Employee Relations*, *27*(4), 354–368.

Guest, D. E., Peccei, R., & Thomas, A. (1994, January). Safety culture and safety performance: British Rail in the aftermath of the Clapham Junction disaster. In *Bolton Business School Conference on Changing Perceptions of Risk.*

Gyekye, S. A., & Salminen, S. (2006). The self defensive attribution hypothesis in work environment: Co-worker's perspective. *Safety Science*, *44*, 157–168.

Havold, J. I. (2007). *From safety culture to safety orientation; developing a tool to measure safety in shipping*. Trondhum: Faculty of Social Sciences and Technology, Department of Industrial Economics and Technology Management, Norwegian University.

Huang, Y. (2004). The establishment of global marketing strategic alliances by small and medium enterprises. *Small Business Economics*, *22*(5), 365–377.

Husain, N. H. (2010). *The critical success factor in implement occupational safety and health* (Master of Science (Management) Thesis). College of Business, University Utara Malaysia, Malaysia.

International Atomic Energy Authority (IAEA). (1986). *Summary report on the post accident review meeting on the Chernobyl accident 75-INSAG-1*. Vienna: IAEA.

Judge, T. A., Bono, J. E., Erez, A., & Locke, E. A. (2005). Core self-evaluations and job and life satisfaction: The role of self-concordance and goal attainment. *Journal of Applied Psychology*, *90*(2), 257.

Karagozoglu, N., & Lindell, M. (1998). Internationalization of small and medium-sized technology-based firms: An exploratory study. *Journal of Small Business Management*, *36*(1), 44–59.

Kennedy, R., & Kirwan, B. (1998). Development of a hazard and operability-based method for identifying safety vulnerabilities in high risk systems. *Safety Science*, *30*, 249–274.

Labour Bureau. (2012). Report on employment and unemployment 2011–12. Ministry of Labour and Employment, Government of India.

McSween, T. E. (2003). *Behaviour based safety* (2nd ed.). Canada: John Wiley.

Mearns, K., Flin, R., & Whitaker, S. (2001). Benchmarking safety climate in hazardous environment: A longitudinal and inter organizational approach. *Risk Analysis*, *21*(4), 771–786.

Nielsen, M. B., Mearns, K., Mattheisen, S. B., & Eid, J. (2011). Using job demand resource model to investigate risk perception, safety climate and job satisfaction in safety critical organizations. *Scandinavian Journal of Psychology*, *52*(5), 465–475.

Ojanen, K., Seppala, A., & Aaltonen, M. (1998). Measurement methodology for the effects of accident prevention program. *Scandinavian Journal of Work, Environment and Health*, *14*(Suppl 1), 95–96.

Prakash, R. (2010). *Framework for understanding the relationship between lean and safety in construction: A thesis*. Graduate Studies of Texas A&M University in partial fulfilment of the requirements for the degree of Master of Science. Major Subject: Construction Management.

Reason, J. (1997). *Managing the risks of organisational accidents*. London: Ashgate.

Richter, A., & Koch, C. (2004). Integration, differentiation and ambiguity in safety cultures. *Safety Science*, *48*(8), 703–722.

Shridhar, M. (2006). Incubators and science parks: Strategies for developing countries. Retrieved from www.anprotec.org.br/idisc/pdfs/ publishers/155.doc

International Journal of Engineering

Journal Homepage: www.ije.ir

Voltage Differencing Buffered Amplifier based Voltage Mode Four Quadrant Analog Multiplier and its Applications

P. Gupta*, R. Pandey

Department of Electronics and Communication Engineering, Delhi Technological University, Delhi, India

P A P E R I N F O

Paper history:
Received *25 July 2018*
Received in revised form *20 January 2019*
Accepted 07 March 2019

Keywords:
Analog Building Blocks
Voltage Differencing Buffered Amplifier
Four Quadrant Analog Multiplier
Quarter Square Algebraic Identity

A B S T R A C T

In this paper a voltage mode four quadrant analog multiplier (FQAM) using voltage differencing buffered amplifier (VDBA) based on quarter square algebraic identity is presented. In the proposed FQAM the passive resistor can be implemented using MOSFETs operating in saturation region thereby making it suitable for integration. The effect of non idealities of VDBA has also been analyzed in this paper. Theoretical propositions are verified through SPICE simulations at 0.18µm CMOS technology node and the simulation results are found in close agreement with theoretical values. The supply voltage is taken as ± 1V and the value of the bias current is set to 40µA. The simulated total harmonic distortion (THD) is observed to be under 3% and the total power dissipation is found as 627µW. The workability of the proposed FQAM is also tested through two applications, namely, an amplitude modulator and a rectifier. The simulated results corroborate the theoretical propositions.

doi: *10.5829/ije.2019.32.04a.10*

NOMENCLATURE

V	Volt	**Greek Symbols**	
R	Resistance	ε	Tracking error
n	nano	$\alpha_{p,n}$	$1-\varepsilon_{gmp,n}$
A	Ampere	$\beta_{p,n}$	$1-\varepsilon_{p,n}$
µ	Micro	Ω	Ohms

1. INTRODUCTION

The FQAM performs multiplication of two bipolar signals and preserves the polarity relationship. Analog multiplier is used extensively for nonlinear applications such as a modulator, equalizer, frequency doublers, and neural computing [1]. A large number of analog multipliers are available in literature [2-14] using different analog building blocks (ABBs) having there own pros and cons.

On the other hand, researchers are continuously striving to explore different ABBs with attributes like higher bandwidth, higher slew rate, lower power consumption, and better linearity [15]. This journey initiated way back in 1966 with current conveyor [16] and still continues. As a result numerous applications using different ABBs have already being developed [17-23]. The voltage differencing buffered amplifier (VDBA) has emerged as an outcome of this consistent effort relatively recently [17]. Apart from possessing the above mentioned attributes the VDBA also provides electronic tunability through its transconductance. Various applications based on VDBA and their variants are available in the literature [15,18-21]. However, limited literature is available on VDBA based non linear applications. So the aim of this study is to present VDBA-based FQAM using the quarter square technique. All available analog multipliers [2-14] are summarized in Table 1 to identify the gap in the previous research and to justify the proposition of voltage mode VDBA based FQAM. Some of the inferences from Table 1 are:

*Corresponding Author Email: *priyankagupta09@gmail.com* (P. Gupta)

Please cite this article as: P. Gupta, R. Pandey, Voltage Differencing Buffered Amplifier based Voltage Mode Four Quadrant Analog Multiplier and its Applications, International Journal of Engineering (IJE), IJE TRANSACTIONS A: Basics Vol. 32, No. 4, (April 2019) 528-535

TABLE 1. Comparison of previously reported analog multipliers

Reference No.	ABB	Number of ABBs	Numberof extra transistors	Passive resistors	Four quagrant	Input range	output range	Supply voltage	Type of Input signal	Type of ouput signal	Power dissipation (mW)	3 dB Frequency
[2]	CCCII+	2	0	0	No	-	-	±5V	Current	Current	-	20 MHz
[3]	OTA	3	0	0	Yes	±.8mA	±.8mA	±10V	Current	Current	-	155 MHz
[4]	Op-Amp	5	0	8	Yes	2.62V	±200mV	±2.4V	Voltage	Voltage	-	840 KHz
[5]	CCCII	1	0	1	No	-	-	±2.5V	Current	Current	3.82	-
		1	0	1	Yes			±2.5V	Current	Current	3.82	
[6]	OTRA	1	6	0	Yes	±200mV	±350mV	±1.5V	Voltage	Voltage	-	25 MHz
[7]	CDBA	1	6	0	Yes	±250mV	±180mV	±5V	Voltage	Voltage	-	82.3 MHz
[8]	CDBA	1	4	0	Yes	±1V	±0.6V	±5V	Voltage	Voltage	-	10 MHz
[9]	CDTA	2	0	0	Yes	-	-	±5V	Current	Current	-	30 MHz
[10]	OTA	4	16	0	Yes	±0.1V	±0.015V	±1V	Voltage	Voltage	0.588	3.96 GHz
[11]	CTTA	1	0	0	Yes	±150uA	±40uA	±1.5V	Current	Current	1.83	53.1MHz
[12]	OTA	3	0	0	Yes	±1mA	±1mA	±10V	Current	Current	-	162 MHz
[13]	VSDVG	3	6	0	Yes	±150mV	±600mv	±1.5V	Voltage	Voltage	0.550	10 MHz
[14]	OTRA	1	4	0	Yes	±300mV	±100mV	±1.5V	Voltage	Voltage	0.830	8 MHz
Proposed	VDBA	2	10	0	Yes	±50mV	±15mV	±1V	Voltage	Voltage	0.627	220 MHz

- The structures discussed in literature [2-9, 12] are not suitable from portability view point due to higher power supply requirements. Structures discussed in literature [2-4, 10, 12 and 13] use a large number of ABBs.
- The bandwidth of all the listed configurations other than reported value [10] is smaller as compared to the proposed configurations.
- Multipliers reported literature [4, 5] use passive components which is not suitable for integrated circuit.
- Voltage output is available at a high impedance in literature [10] making a buffer necessary to drive the voltage input circuits.
- The work presented in literature [2] is a two quadrant, while the multiplier designed in another paper [5] can work as a two or four quadrant multiplier.

Thus the intention of this paper is to propose a VDBA based FQAM which operates at the low power supply consumes less power and provides higher bandwidth.

2. CIRCUIT DESCRIPTION

In this section, the generalized quarter square algebraic identity based FQAM [1] is described first which has been adapted for implementation with VDBA.

2. 1. Generic FQAM based on Quarter Square Algebraic Identity An FQAM can be implemented using well known quarter square algebraic identity given below:

$$(V_{in1}+V_{in2})^2-(V_{in1}-V_{in2})^2=4V_{in1}V_{in2} \quad (1)$$

It may be observed from Equation (1) that FQAM based on quarter square algebraic identity can be designed with the help of adder, subtractor and squarer circuits arranged as depicted in Figure 1

2. 2. Proposed VDBA based FQAM The circuit symbol of VDBA is shown in Figure 2, the terminals *p* and *n* are high impedance input voltage differencing terminals. The *z* represents a high impedance output current terminal and the *w*-(*w*+) is the low impedance buffered inverted (non inverted) output terminal. Due to the high input and low output impedances, this block is well suited for voltage mode operation. The port relationship of the VDBA is described in Eq. (2).

$$\begin{bmatrix} I_z \\ V_{w+} \\ V_{w-} \\ I_p \\ I_n \end{bmatrix} = \begin{bmatrix} 0 & 0 & 0 & g_m & -g_m \\ 1 & 0 & 0 & 0 & 0 \\ -1 & 0 & 0 & 0 & 0 \\ 0 & 0 & 0 & 0 & 0 \\ 0 & 0 & 0 & 0 & 0 \end{bmatrix} \begin{bmatrix} V_z \\ I_{w+} \\ I_{w-} \\ V_p \\ V_n \end{bmatrix} \quad (2)$$

where g_m represents the transconductance of VDBA and is g_m is expressed as follows:

$$g_m = \sqrt{\frac{\mu n \, Cox \, W}{L} I_b} \quad (3)$$

It may be observed that the value of g_m can be controlled through bias current I_b.

The proposed VDBA based FQAM is shown in Figure 3. The circuit comprising of VDBA I and resistance R_1 represents an adder whereas VDBA II along with resistance R_1 performs the subtraction operation.

The current and voltage outputs of VDBA I are expressed in Equations (4) and (5), respectively: Similarly, for VDBA II Equations (6) and (7) represent the current and voltage outputs.

$$I_{z1} = g_{mv}(V_{in1} + V_{in2}) \quad (4)$$

$$V_{w1+} = -V_{w1-} = g_{mv} R_1 (V_{in1} + V_{in2}) \quad (5)$$

$$I_{z2} = g_{mv}(V_{in1} - V_{in2}) \quad (6)$$

$$V_{w2+} = -V_{w2-} = g_{mv} R_1 (V_{in1} - V_{in2}) \quad (7)$$

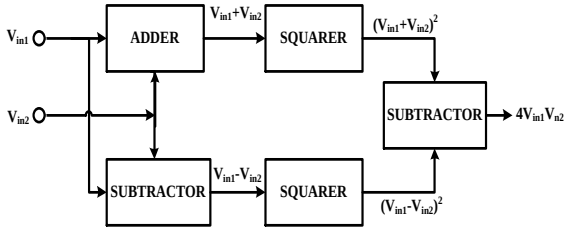

Figure 1. Block diagram of Quarter square algebraic identity [1]

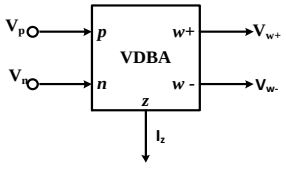

Figure 2. The VDBA Circuit Symbol

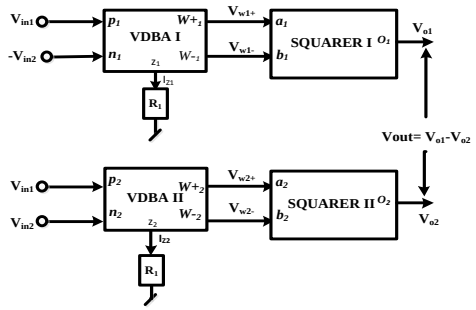

Figure 3. Proposed VDBA based FQAM

where g_{mv} represents the transconductance of VDBA

It may be seen from Equation (5) that V_{w1+} is proportional to the sum of the input voltages whereas V_{w1-} is an inversion of V_{w1+} Equation (7) shows that buffered outputs of VDBA II are proportional to the difference of input voltages with opposite polarities. The squarer block [13] having *a* and *b* as two inputs and *O* as the output terminalis shown in Figure 4. Using routine analysis the output voltage of the squarer circuit (V_{SQ}) may be derived and expressed as Equation (16) provided transistors M_{s1} and M_{s2} are perfectly matched and all the transistors are biased in the saturation region. Further aspect ratio of M_{s3} is considered to be twice as that of M_{s1} and M_{s2}.

For the nmos transistor in saturation region, the drain current is given as follows:

$$I_d = \frac{K}{2}\left[(V_{gs} - V_{TH})^2\right] \quad (8)$$

where K is transconductance parameter.

From Figure 4 Current through MS3 can be written as follows:

$$I_{MS3} = I_{MS1} + I_{MS2} \quad (9)$$

$$\text{As } K_{MS1} = K_{MS2} = K = 0.5K_{MS3} \quad (10)$$

$$\frac{2K}{2}(V_{SQ} - V_{SS} - V_{TH})^2 = \frac{K}{2}[(+V_x - V_{SQ} - V_{TH})^2 + (-V_x - V_{SQ} - V_{TH})^2] \quad (11)$$

$$V_{SQ} = -\frac{V_x^2}{2(V_{SS} + 2V_{TH})} + \frac{V_{SS}}{2} \quad (12)$$

where V_x is the applied input voltage. V_{SQ} is the output of the squarer circuit. Using Equations (8) and (10) current through respectively can be written as follows:

$$I_{MS3} = K(V_{SQ} - V_{SS} - V_{TH})^2 \quad (13)$$

Now putting the value of $V_{SQ}$from Equation (12) into Equation (13),

$$I_{MS3} = \frac{K(V_x^4 + 2V_x^2(V_{ss} + 2V_{TH})^2 + (V_{ss} + 2V_{Th}))}{4(V_{ss} + 2V_{TH})^2} \quad (14)$$

For small signals, $V_x^4 \approx 0$

$$I_{MS3} = \frac{K}{2}V_x^2 + \frac{K}{4}(V_{SS} + 2V_{TH})^2 \quad (15)$$

$$V_{SQ} = \frac{I_{MS3}}{g_{ms}} = \frac{K}{2g_{ms}}V_x^2 + \frac{K}{4g_{ms}}(V_{ss} + 2V_{TH})^2 \quad (16)$$

Equation (16) suggests that the output voltage of the squarer circuit (V_{SQ}) is proportional to the square of the input voltage (V_x). The outputs of VDBA I and VDBA II as expressed by Equations (5) and (7) serve as inputs to the squarer blocks of Figure 3. Using Equation (16)

the output voltages of the squarer I and squarer II, may be written as Equations (17) and (18), respectively.

$$V_{o1} = \frac{K_s}{2g_{ms}} V_{w1}^2 + \frac{K_s}{4g_{ms}} (V_{ss} + 2V_{TH})^2 \quad (17)$$

$$V_{o2} = \frac{K_s}{2g_{ms}} V_{w2}^2 + \frac{K_s}{4g_{ms}} (V_{ss} + 2V_{TH})^2 \quad (18)$$

Where g_{ms} represents the transconductance of squarer. The output voltage (V_{out}) can be determined as follows:

$$V_{out} = V_{o1} - V_{o2} = \frac{K_s}{2g_{ms}} (V_{w1}^2 - V_{w2}^2) \quad (19)$$

From Equations (5), (7) and (19)

$$V_{out} = \frac{K_s}{2g_{ms}} g_{mv}^2 R_1^2 ((V_{in1} + V_{in2})^2 - (V_{in1} - V_{in2})^2) = CV_{in1}V_{in2} \quad (20)$$

Where , $C = \frac{2K_s}{g_{ms}} g_{mv}^2 R_1^2$ (21)

Thus, it may be concluded from Equation (21), the output voltage is proportional to the multiplication of the two input signals. The passive resistors consume a large chip area as compared to active resistors. Thus from integration view point, it is always preferred to implement a passive resistor using MOSFETs operating in the linear region.

The resistance R_1 in Figure 3 can be realized using MOSFETs as shown in Figure 5 where both the transistors ($M_{R1}$and M_{R2} with aspect ratio as W_{MR}/L_{MR}) are operating in saturation. The equivalent resistor R may be expressed as follows:

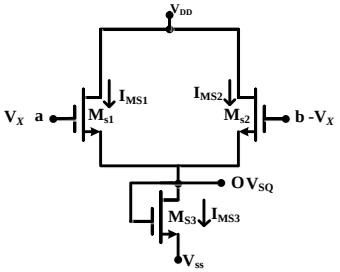

Figure 4. Squarer Circuit [13]

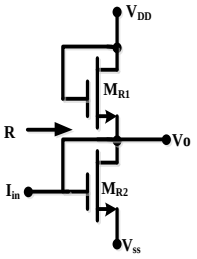

Figure 5. The NMOS based resistor (R) realization

$$R = \frac{V_o}{I_{in}} = \frac{L_{MR}}{2\mu C_{ox} W_{MR} (V_{DD} - V_{TH})} = \frac{1}{2K_R (V_{DD} - V_{TH})} \quad (22)$$

Substituting the value of R_1 from Equation (22) into Equation (20) the V_{out} may be expressed as follows:

$$V_{out} = \frac{2K_s}{g_{ms}} \left(\frac{g_{mv}}{2K_R (V_{DD} - V_{TH})} \right)^2 \left((V_{in1} + V_{in2})^2 - (V_{in1} - V_{in2})^2 \right) = CV_{in1}V_{in2} \quad (23)$$

and the C of Equation (21) modifies to following expression:

$$C = \frac{2K_s}{g_{ms}} \left(\frac{g_{mv}}{2K_R (V_{DD} - V_{TH})} \right)^2 \quad (24)$$

3. NON-IDEAL ANALYSIS

In the analysis so far, the VDBA characteristics are considered to be ideal. However, in CMOS implementation of VDBA transconductance and voltage tracking errors may exist due to device mismatch which may lead to deviation from the ideal behavior. Therefore, the effect of non-idealities of VDBA needs to be considered on the performance of the proposed FQAM configuration. Taking the tracking errors into consideration Equation (2) modifies to following expression:

$$\begin{bmatrix} I_z \\ V_{w+} \\ V_{w-} \\ I_p \\ I_n \end{bmatrix} = \begin{bmatrix} 0 & 0 & 0 & \alpha_p g_m & -\alpha_n g_m \\ \beta_p & 0 & 0 & 0 & 0 \\ -\beta_n & 0 & 0 & 0 & 0 \\ 0 & 0 & 0 & 0 & 0 \\ 0 & 0 & 0 & 0 & 0 \end{bmatrix} \begin{bmatrix} V_z \\ I_{w+} \\ I_{w-} \\ V_p \\ V_n \end{bmatrix} \quad (25)$$

where $\alpha_p(\alpha_n)$ represents transconductance transfer ratio from p(n) to z terminal and similarly $\beta_p(\beta_n)$ represent voltage transfer ratio from z to w+(w-) terminal. The non-idealities of VDBA have been summarized in Table 2.

Including the non-idealities of VDBA the outputs of VDBA I and VDBA II of Figure 3 represented by Equations (5) - (7) get modified as Equations (26)-(29):

$$V_{w1+_n} = \frac{\beta_p g_{mv} (\alpha_p V_{in1} + \alpha_n V_{in2})}{2K_R (V_{DD} - V_{TH})} \quad (26)$$

TABLE 2. VDBA Non-Idealities

Parameter	Value from *p* to *z*	Value from *n* to *z*	Value from *z* to *w+*	Value from *z* to *w-*
Voltage transfer ratio	-	-	$\beta_p=(1-\varepsilon_p)$	$\beta_n=(1-\varepsilon_n)$.
Transconductance transfer ratio	$\alpha_p=(1\varepsilon_{gmp})$	$\alpha_n=(1-\varepsilon_{gm})$	-	-
Tracking error	ε_{gmp} ($\|\varepsilon_{gmp}\|<<1$)	ε_{gmn} ($\|\varepsilon_{gmn}\|<<1$)	ε_p ($\|\varepsilon_p\|<<1$)	ε_n ($\|\varepsilon_n\|<<1$)

$$V_{w1-_n} = -\frac{\beta_n g_{mv}(\alpha_p V_{in1} + \alpha_n V_{in2})}{2K_R(V_{DD} - V_{TH})} \quad (27)$$

$$V_{w2+_n} = \frac{\beta_p g_{mv}(\alpha_p V_{in1} - \alpha_n V_{in2})}{2K_R(V_{DD} - V_{TH})} \quad (28)$$

$$V_{w2-_n} = -\frac{\beta_n g_{mv}(\alpha_p V_{in1} - \alpha_n V_{in2})}{2K_R(V_{DD} - V_{TH})} \quad (29)$$

Considering $\beta_n = \beta_p = \beta$,

$$V_{w1+_n} = \frac{\beta g_{mv}(\alpha_p V_{in1} + \alpha_n V_{in2})}{2K_R(V_{DD} - V_{TH})} = -V_{w1-_n} \quad (30)$$

$$V_{w2+_n} = \frac{\beta g_{mv}(\alpha_p V_{in1} - \alpha_n V_{in2})}{2K_R(V_{DD} - V_{TH})} = -V_{w2-_n} \quad (31)$$

Using Equations (16), (30) and (31), the output voltage of the FQAM can be written as follows:

$$V_{out_n} = \left(\frac{K_s}{2g_{ms}}\left(\frac{\beta g_{mv}}{2K_R(V_{DD} - V_{TH})}\right)^2\right)\left((\alpha_p V_{in1} + \alpha_n V_{in2})^2 - (\alpha_p V_{in1} - \alpha_n V_{in2})^2\right) \quad (32)$$

$$V_{out_n} = \frac{K_s}{2g_{ms}}\left(\frac{\beta g_{mv}}{2K_R(V_{DD} - V_{TH})}\right)^2 \left(4\alpha_p \alpha_n V_{in1} V_{in2}\right) \quad (33)$$

For $\alpha_p = \alpha_n = \alpha$, the resultant output voltage may be expressed as follows:

$$V_{out_n} = (\alpha\beta)^2 C V_{in1} V_{in2} \quad (34)$$

However, the deviation caused in the output due to tracking errors may be ignored as the values of ε_{gmp}, ε_{gmn}, ε_n and ε_p are much smaller than unity.

4. SIMULATION RESULTS

The working of the proposed FQAM circuit is confirmed through SPICE simulations. The CMOS implementation of the VDBA [21] shown in Figure 6 is used and 0.18µm technology node is used for simulations.

The supply voltage used is ±1V. The value of the bias current is set to 40µA. The aspect ratios for the transistors used in VDBA, squarer circuit, and R_1 implementation are given in Table 3.

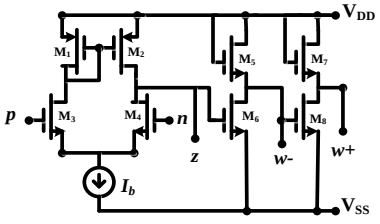

Figure 6. CMOS Implementation of VDBA [21]

TABLE 3. Aspect Ratio of the transistors

Transistor	M_1-M_4	M_5 - M_8	M_{S1}-M_{S2}	M_{S3}	M_{R1}-M_{R3}
(W/L) µm	0.36/0.18	21.6/0.72	5.4/0.27	10.8/0.27	0.27/0.27

The values of α_p and α_n are found 0.934 and 0.933, respectively. Similarly, β_p and β_n were obtained as 0.95 and 0.97, respectively.

4. 1. The DC Characteristics The DC transfer characteristics for the proposed FQAM is depicted in Figure 7(a) with the variation of V_{in2} from -40 mV to 40 mV. It is observed from Figure 7(a) that the proposed circuit is an FQAM. The output voltage varies linearly with V_{in1} as observed from Figure 7(a). The nonlinearity curve for the proposed FQAM is shown in Figure 7(b) which depicts that over the entire input range maximum nonlinearity is less than 0.03%. The simulated power consumption is found to be 627µW when V_{in1} and V_{in2} are kept grounded.

4. 2. AC Characteristics The simulated frequency response for output voltage is presented in Figure 8. A DC voltage source is applied to V_{in2} while V_{in1} is taken as AC source of 100 mV. The 3dB bandwidth of the proposed FQAM circuit is found to be 220 MHz.

4. 3. Total Harmonic Distortion The Total Harmonic Distortion (THD) is a measure to estimate the degree to which a system is nonlinear. Therefore the variation in THD as a function of input signal amplitude is observed. For this, a constant DC voltage of 50 mV is applied to V_{in2} while a sinusoidal signal of 100 kHz is applied to V_{in1} with amplitude varying. The measured THD is plotted in Figure 9.

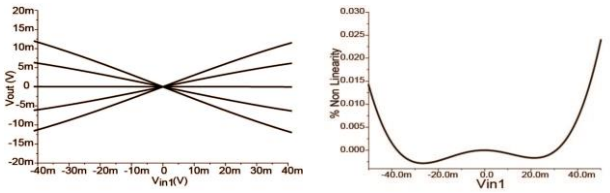

(a) (b)

Figure 7. (a) DC characteristics of proposed multiplier (b) % Nonlinearity curve

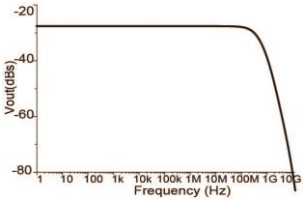

Figure 8. AC characteristics

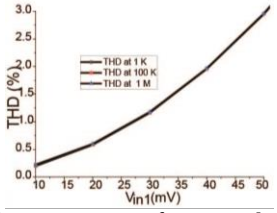

Figure 9. THD vs V_{in1} of proposed multiplier

The similar measurements are obtained for two other input signals having frequencies 1 kHz and 1 MHz, respectively and found that for input signals < 50 mV the maximum THD remains under 3% for the proposed FQAM for all three cases.

4. 4 Noise Analysis The noise limits the minimum signal level that a circuit can process with acceptable quality. Therefore, the effect of noise on the proposed circuit is examined through SPICE simulations. The equivalent input noise and the equivalent output noise are plotted in Figures 10(a) and 10(b), respectively with varying input frequency. For simulations, V_{in1} is taken as a 100 mV AC signal whereas V_{in2} is chosen as 80 mV DC value. The obseved Vinoise and Vonise are 21.75 nV/√Hz and 10.38 nV/√Hz, respectively.

5. APPLICATIONS

5. 1. Amplitude Modulator An amplitude modulator can be designed provided the carrier and modulating signals are applied to the two inputs of an FQAM, respectively. To validate the functionality of proposed FQAM as an amplitude modulator, two sinusoids of 100 mV/100 kHz and 100 mV/10 kHz frequencies were applied at $V_{in1}$and V_{in2}, respectively. The input transient and corresponding spctrum are shown in Figures 11(a) and 11(b), respectively. Similarly, Figure 12(a) depicts the amplitude modulated output with its spectrum in Figure 12(b). The output frequency spectrum has two frequency components of 90 kHz and 110 kHz thereby confirming the modulation operation.

5. 2. Rectifier The rectifier can be implemented using multiplier by taking one of the inputs as pulse type having frequency same as that of the signal which is to be rectified. To verify the workability of rectifier two inputs namely a sinusoidal signal and a square wave of 100 kHz/100 mV each were applied to the respective inputs of FQAM.

The input transient is shown in Figure 13(a) and the rectified output is presented in Figure 13(b). The simulated ripple factor curve is plotted in Figure 13 (c).

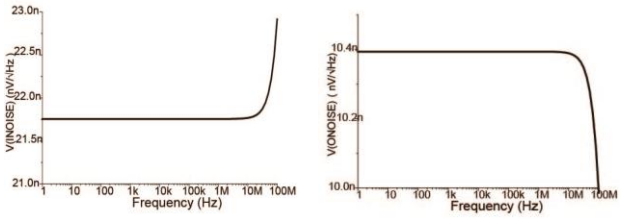

(a) (b)

Figure 10. (a) Input Noise (b) Output Noise

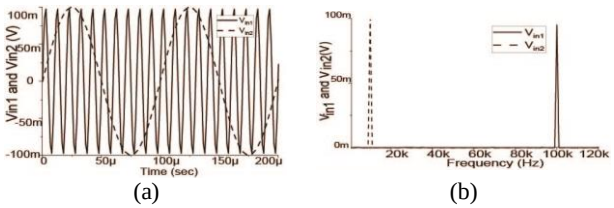

(a) (b)

Figure 11. (a) Input transient (b) Frequency spectrum

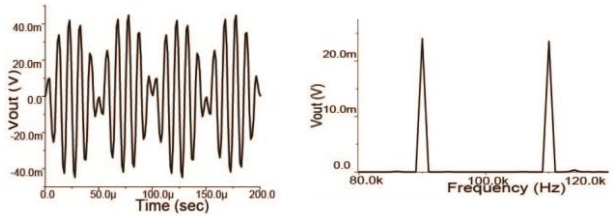

(a) (b)

Figure 12. (a) output transient (b) Frequency spectrum

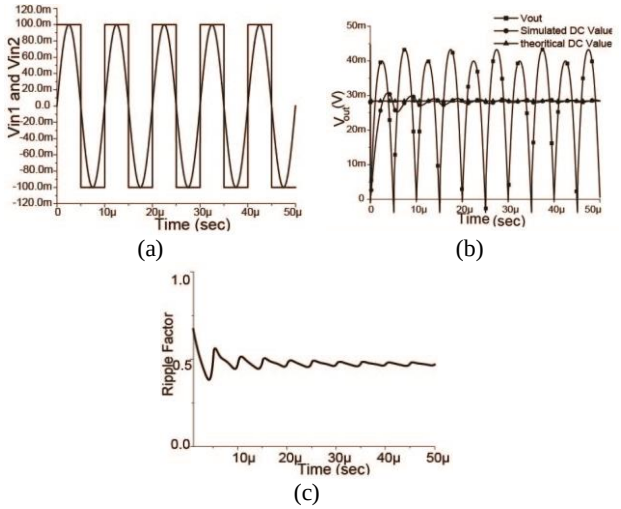

(a) (b)

(c)

Figure 13. Time domain representation of (a) input signals (b) output signal (c) ripple factor

The maximum value of the ripple factor is observed to be less than 0.5.The DC value is found to be 28.54 mV which is in close agreement of the calculated value of 28.42 mV.

6. CONCLUSION

A voltage mode FQAM based on quarter square - algebric identity employing VDBA is proposed in this paper. The circuit is suitable for integration as passive resistor may suitably be implemented using MOSFETs. The theoretical propositions have been verified through SPICE simulations using 0.18µm CMOS process parameters. The power dissipation is found low as compared to other available structures and the simulated THD is well below 3%. Applications like amplitude modulator and rectifier are predesigned using proposed structure to show its applicability and results are in total agreement with the theory.

7. REFERENCES

1. Hsiao, S.Y., and Wu, C.Y., "A 1.2 V CMOS four-quadrant analog multiplier",Proceedings of 1997 IEEE International Symposium on Circuits and Systems, (1997), 241–244.
2. Abuelma'atti Muhammad, M.T., "A current-mode current-controlled current-conveyor-based analogue multiplier/divider",***International Journal of Electronics***, Vol. 85, No. 1, (1998), 71–77.
3. Kaewdang, K., Fongsamut, C. and Surakampontorn, W., "A wide-band current-mode OTA-based analog multiplier-divider",Proceedings of the 2003 IEEE International Symposium on Circuits and Systems, (2003).
4. Riewruja, V. and Rerkratn, A., "Four-quadrant analogue multiplier using operational amplifier", ***International Journal of Electronics***, Vol. 98, No. 4, (2011), 459–474.
5. Yuce, E., "Design of a Simple Current-Mode Multiplier Topology Using a Single CCCII+", ***IEEE Transactions on Instrumentation and Measurement***, Vol. 57, No. 3, (2008),631–637.
6. Chadha, U. and Arora, T., "Four quadrant analog multiplier/divider employing single OTRA", Proceedings of the International Conference on Communication and Computing Systems,(2016),635–639.
7. Pathak, J.K., Singh, A.K. and Senani, R. "New Multiplier/Divider Using a Single CDBA",***American Journal of Electrical and Electronic Engineering***, Vol. 2, No. 3,(2014), 98–102.
8. Keskin, A. Ü.,"A Four Quadrant Analog Multiplier Employing Single CDBA",***Analog Integrated Circuits and Signal Processing***,Vol.40, No. 1,(2004), 99–101.
9. Tangsrirat, W., Pukkalanun, T., Mongkolwai, P., and Surakampontorn, W.,"Simple current-mode analog multiplier, divider, square-rooter and squarer based on CDTAs",***AEU - International Journal of Electronics and Communications***, Vol. 65, No. 3,(2011), 198–203.
10. Hidayat, R., Dejhan, K., Moungnoul, P. and Miyanaga, Y.,"OTA-based high frequency CMOS multiplier and squaring circuit:, IEEE2008 International Symposium on Intelligent Signal Processing and Communications Systems,(2009),1-4.
11. Surakampontorn, W.,Kaewdang, K. and Fongsamut, C..,"A Simple Current-Mode Analog Multiplier- Divider Circuit Using OTAs", 2002 International Technical Conference on Circuits, Computers and Communications, Thailand,(2002), pp. 658–61.
12. Pisutthipong, N. and Siripruchyanun, M.,"A novel simple current-mode multiplier/divider employing only single multiple-output current controlled CTTA". TENCON 2009 IEEE Region 10 Conference, (2009), 1–4.
13. Boonchu, B. and Surakampontorn, W.,"Power Detector Voltage-Mode CMOS Squarer/Multiplier Circuit,"International Technical Conference on Circuits,(2002),8–11.
14. Pandey, R., Pandey, N., Sriram, B. and Paul, S. K., "Single OTRA Based Analog Multiplier and Its Applications",***ISRN Electronics***, Vol. 2012,(2012),1–7.
15. Kaçar, F., Yeşil, A. and Noori, A., "New CMOS realization of voltage differencing buffered amplifier and its biquad filter applications",***Radioengineering***, Vol.21, No. 1,(2012), 333–339.
16. Toumazou, C., Lidgey, F. J. and Haigh, D.,"Analogue IC design: the current-mode approach", IET, (1993), 1st Ed. London.
17. Biolek, D., Senani, R. and Biolková, V., "Active Elements for Analog Signal Processing: Classification , Review , and New Proposals", ***Radioengineering***, Vol. 17, No. 4, (2008), 15-32
18. Herencsar, N., Cicekoglu, O., Sotner, R., Koton, J. and Vrba, K., "New resistorless tunable voltage-mode universal filter using single VDIBA", ***Analog Integrated Circuits and Signal Processing***, Vol.76, No. 2,(2013), 251–260.
19. Guney, A., Alaybeyoglu, E. and Kuntman, H.,"New CMOS realization of Z Copy Voltage Differencing Buffered Amplifier and its current-mode filter application", IEEE 8th International Conference on Design & Technology of Integrated Systems in Nanoscale Era, (2013), 68–71.
20. Khatib, N. and Biolek, D.,"New voltage mode universal filter based on promising structure of Voltage Differencing Buffered Amplifier", IEEE 23rd International Conference Radioelektronika, (2013),177–181. 25.
21. Sotner, R., Jerabek, J. and Herencsar, N.,"Voltage Differencing Buffered/Inverted Amplifiers and Their Applications for Signal Generation", ***Radioengineering***,Vol. 22, No. 2, (2013), 490–504.
22. Farshidi, E. and Keramatzadeh, A., "A New Approach for low voltage CMOS based on current-controlled conveyors", ***International Journal of Engineering, Transactions B: Applications***, Vol. 27, No. 5, (2014),723-730.
23. Singh, S. V., Tomar, R. S. and Chauhan D. S., "A New Trans-Admittance-Mode Biquad Filter Suitable for Low Voltage Operation", ***International Journal of Engineering, Transactions B: Applications***, Vol. 28, No. 12, (2015), 1738-1745.

Voltage Differencing Buffered Amplifier based Voltage Mode Four Quadrant Analog Multiplier and its Applications

P. Gupta, R. Pandey

Department of Electronics and Communication Engineering, Delhi Technological University, Delhi, India

P A P E R I N F O

Paper history:
Received *25 July 2018*
Received in revised form *20 January 2019*
Accepted 07 March 2019

Keywords:
Analog Building Blocks
Voltage Differencing Buffered Amplifier
Four Quadrant Analog Multiplier
Quarter Square Algebraic Identity

چکیده

در این مقاله یک حالت ولتاژ چهار ضریب آنالوگ چهارگانه (FQAM) با استفاده از تقویت کننده بافر ولتاژ (VDBA) بر اساس هویت جبری مربع ارائه شده است. در FQAM پیشنهادی، مقاومت منفعل را می توان با استفاده از MOSFET های عامل در منطقه اشباع اجرا کرد و بنابراین آن را برای ادغام مناسب می کند. در این مقاله اثر غیر آرایشی VDBA نیز مورد تحلیل قرار گرفته است. گزاره های نظری از طریق شبیه سازی SPICE در گره فن آوری CMOS 0.18μm تایید شده و نتایج شبیه سازی در توافق نزدیک با مقادیر نظری یافت می شود. ولتاژ منبع تغذیه به عنوان ± ۱V محاسبه می شود و مقدار جریان تعادلی به ۴۰μA تنظیم می شود. اعوجاج هارمونیک کل تداخل (THD) کمتر از ۳٪ مشاهده می شود و کل قدرت تخلیه به ۶۲۷μW می رسد. کارایی پیشنهاد FQAM نیز از طریق دو برنامه کاربردی، یعنی یک مدولاتور دامنه و یک یکسو کننده، مورد آزمایش قرار می گیرد. نتایج شبیه سازی گزاره های نظری را تأیید می کند.

***doi**: 10.5829/ije.2019.32.04a.10*